Journal of
Marine Science and Engineering

CFD Simulations of Marine Hydrodynamics

Edited by
Yigit Kemal Demirel

Printed Edition of the Special Issue Published in
Journal of Marine Science and Engineering

www.mdpi.com/journal/jmse

MDPI

CFD Simulations of Marine Hydrodynamics

CFD Simulations of Marine Hydrodynamics

Editor

Yigit Kemal Demirel

MDPI • Basel • Beijing • Wuhan • Barcelona • Belgrade • Manchester • Tokyo • Cluj • Tianjin

Editor
Yigit Kemal Demirel
University of Strathclyde
UK

Editorial Office
MDPI
St. Alban-Anlage 66
4052 Basel, Switzerland

This is a reprint of articles from the Special Issue published online in the open access journal *Journal of Marine Science and Engineering* (ISSN 2077-1312) (available at: http://www.mdpi.com).

For citation purposes, cite each article independently as indicated on the article page online and as indicated below:

LastName, A.A.; LastName, B.B.; LastName, C.C. Article Title. *Journal Name* **Year**, *Volume Number*, Page Range.

ISBN 978-3-0365-2335-4 (Hbk)
ISBN 978-3-0365-2336-1 (PDF)

Cover image courtesy of Yigit Kemal Demirel

Contents

About the Editor

Dr Yigit Kemal Demirel is currently a Senior Lecturer (Associate Professor) in the Department of Naval Architecture, Ocean and Marine Engineering (NAOME) at the University of Strathclyde, Glasgow. He is also a member of the University Senate. His research interests lie in computational (CFD) and experimental hydrodynamics. He is actively engaged in fundamental and industry-focussed research on the effect of roughness (hull fouling and fouling-control coatings) on ship performance, energy efficiency of ships, hull-propeller optimisation and energy saving devices (ESDs). Dr Demirel worked on a number of internationally collaborated projects, published numerous papers in highly ranked journals and presented his research at several international conferences and workshops. In 2017, Dr Demirel was appointed to the Resistance and Propulsion Committee of the International Towing Tank Conference (ITTC), which sets best-practice standards for large-scale hydrodynamics facilities worldwide. He was appointed as an Advisory Board Member of the European University of the Seas (SEA-EU) Alliance in December 2019 for a duration of 3 years.

Preface to "CFD Simulations of Marine Hydrodynamics"

Marine Hydrodynamics covers plenty of subjects relevant to naval architecture, ocean and marine engineering, and it has been one of the essential interests of researchers for a long time. There is a plethora of ways to deal with Marine Hydrodynamics problems. Computational Fluid Dynamics (CFD) approach has been routinely employed in naval architecture and ocean engineering due to the availability of ever-increasing computational power and the potential advantages of CFD over other methods. For example, CFD can overcome the difficulties of nonlinear problems faced in theoretical studies, and it is normally more cost-efficient than physical experiments. For these reasons, the CFD method has been prevalently used to investigate different types of marine hydrodynamics problems such as the ship resistance, propeller performance, ship self-propulsion performance, seakeeping and maneuverability as well as the tidal turbine performance.

This Special Issue, therefore, comprises 24 original articles from both academia and industry that advance state-of-the-art CFD applications in marine hydrodynamics or review the progress and future directions of research in this field. The published articles cover a wide range of subjects relevant to naval architecture and ocean engineering, including but not limited to; ship resistance and propulsion, seakeeping and maneuverability, hydrodynamics of marine renewable energy devices, validation and verification of computational fluid dynamics, EFD/CFD combined methods, fouling/coating hydrodynamics.

Yigit Kemal Demirel
Editor

Journal of *Marine Science and Engineering*

MDPI

Editorial

Structure–Seabed Interactions in Marine Environments

Zhen Guo [1,†], Yi Hong [1,†] and Dong-Sheng Jeng [2,*,†]

[1] College of Civil Engineering and Architecture, Zhejiang University, Hangzhou 310058, China; nehzoug@163.com (Z.G.); yi_hong@zju.edu.cn (Y.H.)
[2] School of Engineering & Built Environment, Griffith University Gold Coast Campus, Gold Coast, QLD 4222, Australia
* Correspondence: d.jeng@griffith.edu.au
† These authors contributed equally to this work.

The phenomenon of soil–structure interactions in marine environments has attracted much attention from coastal and geotechnical engineers and researchers in recent years. One of the reasons for the growing interest is the rapid development of marine resources (such as the oil and gas industry, marine renewable energy, and fish farming industry), as well as the damage to marine infrastructure that has occurred in the last two decades. To assist practical engineers in the design and planning of coastal geotechnical projects, a better understanding of the mechanisms of structure–soil interactions in marine environments is desired. The purpose of this Special Issue is to report the recent advances in the problems of structure–seabed interactions. This Special Issue will provide practical engineers and researchers with information on recent developments in this field.

Nine (9) papers are included in this Special Issue: one review article [1] and eight research articles covering two main themes—(1) the mechanisms of marine sediments in the Yellow River Delta [2] and a field study [3] and (2) structure–seabed interactions in the vicinity of tunnels [4,5], spudcans [6], pile foundations [7], breakwaters [8], and pipelines [9]. More details on each contribution are summarized here.

In the early stages of research on this topic, most theoretical studies were based on linear wave theory and analytical approximations for wave-induced seabed responses without a structure or in front of a structure. This is not particularly relevant to the interactions between seabeds and structures due the difficulty of handling the complicated boundaries near the structure. Therefore, numerical simulation, as well as physical modeling, are effective techniques.

Diaz-Carrasco et al. [1] summarize the recent advances in numerical simulations for wave–structure–seabed interactions with a focus on breakwaters. In this review article, the authors discuss the concept of scour and how the wave–structure–seabed interaction process contributes to the scour for the design of marine protection structures. They outline the most recent studies in the field, many of which are based on one-way coupling. In addition to the conventional approach to wave–structure–seabed interactions, the authors outlined the full multi-phase approach, which includes air, water, and sediment phases in both mass and momentum conservation equations. However, this review article focuses on the oscillatory mechanism only and limits its scope to poro-elastic seabed models. Other mechanisms, such as residual liquefaction and associated poro-elastoplastic models (which are equally important in the field of wave–seabed–structure interactions), are not included.

Marine sediments have quite different soil properties and mechanical behaviors compared with the onshore soils due to various physical processes and loading mechanisms in marine environments. It is particularly important to gain a better understanding of the physical properties of marine sediments and the associated changes under dynamic loading for the design of foundations of marine infrastructures.

The highly concentrated sediments from the middle and lower reaches of the Yellow River are normally deposited at the estuary. The nearshore seabed of the Yellow River Delta (YRD) is repeatedly re-deposited and excess pore-water pressure and upward seepage

Citation: Guo, Z.; Hong, Y.; Jeng, D.-S. Structure–Seabed Interactions in Marine Environments. *J. Mar. Sci. Eng.* **2021**, *9*, 972. https://doi.org/10.3390/jmse9090972

Received: 30 August 2021
Accepted: 1 September 2021
Published: 7 September 2021

appear in the newly deposited seabed. Tang et al. [2] reported a series of laboratory experiments carried out on the newly deposited sediments in the Yellow River Delta in their O-tube flume. They focused on the critical hydraulic gradient for seepage failure, which has a significant effect on the erosion and re-suspension of sediments.

Most studies available in the literature focus on the prediction or evaluation of seabed liquefaction under various dynamic loading processes, such as ocean waves, currents, and earthquakes. Measurements of the rheological characteristics of liquefied sediments are limited. Zhang et al. [3] introduced an on-site test device based on the shear column theory. The device was tested in the Yellow River Delta. To verify the field measurements, the authors also conducted a series of laboratory rheological tests. The authors further outlined the applicability of the in situ device in offshore areas.

The construction of a tunnel in the marine environment has attracted much attention from coastal and geotechnical engineers due to the ongoing demands of tunnel construction in coastal cities. To appropriately model the physical properties of coastal sand during the construction of tunnels, Zhu et al. [4] presented a series of experimental results of triaxial compression tests for dry and saturated sand with different initial void ratios. The experimental results were used to modify the disturbance function in terms of the parametric constant (K) and friction angle of the soil (ϕ), utilizing disturbed state concept (DSC) theory. Based on the proposed disturbance function, a modified Duncan–Chang model taking into account construction disturbance was proposed. The developed constitutive framework was further incorporated into the well-known commercial software, ABAQUS, to simulate the ground movement during tunnel construction.

An immersed tunnel may be constructed in a submerged trench. Although the artificial slope is temporary during construction, its stability under wave loading needs to be guaranteed until the end of the construction period. Chen et al. [5] investigated the slope stability of the submerged trench of the immersed tunnel under combined solitary wave and current loading. In their study, the commercial software FLOW-3D was adopted to simulate the solitary wave propagation, and the FEM seabed model was governed by Darcy's flow with the continuity of pressure at the water–seabed interface. The seabed behavior was described by the Mohr–Coulomb constitutive model. The stability of the slope could be calculated by 2D plane strain approximation with the Mohr–Coulomb yield criterion. In their study, they drew the following conclusions. First, as the slope ratio increases, the factor of safety (FOS) decreases. The maximum deformation is likely to concentrate at the bottom of the slope with an increasing slope ratio. Second, when the foundation trench takes the form of a two-stage slope, the slope ratio of the lower slope has a more significant influence on the stability of the whole slope compared with that of the upper slope.

Spudcan foundations have been used to support offshore jack-up platforms, which are extensively used in the offshore industry for drilling and exploration activities. In many previous studies, the "installation effects" are largely disregarded; however, these effects are widely known to affect various aspects of spudcan behavior. Lin et al. [6] re-evaluated the elastic stiffness coefficients of spudcan foundations after the proper consideration of spudcan installation effects using the commercial FEM software, ABAQUS. From this paper, expressions for the dimensionless elastic stiffness coefficient of spudcan are provided. The product of the reduction factor and the elastic stiffness coefficient thus gives the elastic stiffness of spudcan foundations with the consideration of the spudcan installation effects. In practical applications, these coefficients can be directly employed as the boundary conditions in structural analysis for the design of the spudcan.

Pile-type foundations have been used to support various offshore infrastructures, such as platforms, cross-sea bridges, etc. In this paper, Dou et al. [7] attempts to simulate the entire process of steel-pipe pile jacking in saturated fine-grained soil. Based on numerical simulation, it was concluded that during pile installation, the negative excess pore-water pressure near the ground surface around the pile and at a certain depth below the pile tip would increase the effective stress and hence the penetration resistance.

Breakwaters are one of the key nearshore coastal structures used for protection of coastlines. Jeng et al. [8] proposed the use of a mesh-free method for examining the wave-induced soil response around a submerged breakwater. Both regular and irregular wave loadings are considered. This study could be the first attempt at the application of a mesh-free method for the problem of wave-induced seabed response around a breakwater. However, this study is limited in that only the oscillatory soil response and 2D conditions are considered. The further development of the mesh-free model could include extension to 3D and the consideration of the residual soil response in the future.

Offshore pipelines are key marine infrastructures for various purposes, such as the transportation of oil and gas from offshore to onshore regions. Therefore, the damage caused to a pipeline due to seabed instability has been a main concern of offshore pipeline projects. Wu et al. [9] proposes a new fractional cyclic model for capturing the state dependency, non-associativity, and cyclic mobility behavior of sand. The proposed model is validated using two-way stress- and strain-controlled undrained cyclic tests of Karlsuhe find sand. Then, the model is further adapted for the practical engineering problem of an offshore pipeline fully buried in a trenched layer with different backfilled materials. In their study, second-order Stokes wave theory is used to describe the dynamic wave loading. As reported in this study, the non-associativity of sand has an important effect on the accumulation of wave-induced excess pore pressure and plastic strain. Furthermore, soils at the top of the pipeline are more prone to wave-induced liquefaction than they are at other locations within the seabed. Moreover, a trench layer of non-liquefiable materials with a high permeability is found to be useful for preventing seabed liquefaction in submarine pipelines.

In summary, this Special Issue not only provides information on recent advances in the field of structure–seabed interaction in the marine environment but also highlights scopes for future research in this field. This will light several possible research directions in the field for the readers.

Author Contributions: D.-S.J.: writing—original draft preparation; Z.G.: writing—review and editing; Y.H.: writing—review and editing. All authors have read and agreed to the published version of the manuscript.

Funding: This research received no external funding.

Acknowledgments: The authors are grateful for the support from all authors and reviewers.

Conflicts of Interest: The authors declare no conflicts of interest.

References

1. Diaz-Carrasco, P.; Croquer, S.; Tamini, V.; Lacey, J.; Poncel, S. Advances in numerical Reynolds-Averaged Navier–Stokes modelling of wave-structure-seabed interactions and scour. *J. Mar. Sci. Eng.* **2021**, *9*, 611, doi: 10.3390/jmse9060611. [CrossRef]
2. Tang, M.; Jia, Y.; Zhang, S.; Wang, C.; Liu, H. Impacts of consolidation time on the critical hydraulic gradient of newly deposited silty seabed in the Yellow River Delta. *J. Mar. Sci. Eng.* **2021**, *9*, 270, doi: 10.3390/jmse9030270. [CrossRef]
3. Zhang, H.; Li, X.; Chen, A.; Li, W.; Lu, Y.; Guo, X. Design and application of an in situ test device for Rheological characteristic measurements of liquefied submarine sediments. *J. Mar. Sci. Eng.* **2021**, *9*, 639, doi: 10.3390/jmse9060639. [CrossRef]
4. Zhu, J.F.; Zhao, H.Y.; Xu, R.Q.; Luo, Z.Y.; Jeng, D.S. Constitutive modeling of physical properties of coastal sand during tunneling construction disturbance. *J. Mar. Sci. Eng.* **2021**, *9*, 167, doi: 10.3390/jmse9020167. [CrossRef]
5. Chen, W.; Wang, D.; Xu, L.; Lv, Z.; Wang, Z.; Gao, H. On the slope stability of the submerged trench of the immersed tunnel subjected to solitary wave. *J. Mar. Sci. Eng.* **2021**, *9*, 526, doi: 10.3390/jmse9050526. [CrossRef]
6. Lin, W.L.; Wang, Z.; Liu, F.; Yi, J.T. The effects of installation on the elastic stiffness coefficients of spudcan foundations. *J. Mar. Sci. Eng.* **2021**, *9*, 429, doi: 10.3390/jmse9040429. [CrossRef]
7. Dou, J.; Chen, J.; Liao, C.; Sun, M.; Han, L. Study on the Correlation between Soil Consolidation and Pile Set-Up Considering Pile Installation Effect. *J. Mar. Sci. Eng.* **2021**, *9*, 705, doi: 10.3390/jmse9070705. [CrossRef]
8. Jeng, D.S.; Wang, X.X.; Tsai, C.C. Meshless Model for Wave-Induced Oscillatory Seabed Response around a Submerged Breakwater Due to Regular and Irregular Wave Loading. *J. Mar. Sci. Eng.* **2021**, *9*, 15, doi: 10.3390/jmse9010015. [CrossRef]
9. Wu, L.; Cheng, W.; Zhu, Z. Fractional-Order elastoplastic modeling of sands considering cyclic mobility. *J. Mar. Sci. Eng.* **2021**, *9*, 354, doi: 10.3390/jmse9040354. [CrossRef]

Journal of
Marine Science and Engineering

MDPI

Article

Virtual Replica of a Towing Tank Experiment to Determine the Kelvin Half-Angle of a Ship in Restricted Water

Momchil Terziev [1], Guangwei Zhao [1], Tahsin Tezdogan [1,*], Zhiming Yuan [1] and Atilla Incecik [2]

[1] Department of Naval Architecture, Ocean and Marine Engineering, University of Strathclyde, Glasgow G4 0LZ, UK; momchil.terziev@strath.ac.uk (M.T.); guangwei.zhao@strath.ac.uk (G.Z.); zhiming.yuan@strath.ac.uk (Z.Y.)

[2] Faculty of Engineering, University of Strathclyde, Glasgow G1 1XJ, UK; atilla.incecik@strath.ac.uk

* Correspondence: tahsin.tezdogan@strath.ac.uk

Received: 9 March 2020; Accepted: 1 April 2020; Published: 6 April 2020

Abstract: The numerical simulation of ship flows has evolved into a highly practical approach in naval architecture. In typical virtual towing tanks, the principle of Galilean relativity is invoked to maintain the ship as fixed, while the surrounding water is prescribed to flow past it. This assumption may be identified, at least partly, as being responsible for the wide-scale adoption of computational solutions within practitioners' toolkits. However, it carries several assumptions, such as the levels of inlet turbulence and their effect on flow properties. This study presents an alternative virtual towing tank, where the ship is simulated to advance over a stationary fluid. To supplement the present work, the free surface disturbance is processed into Fourier space to determine the Kelvin half-angle for an example case. The results suggest that it is possible to construct a fully unsteady virtual towing tank using the overset method, without relying on Galilean relativity. Differences between theoretical and numerical predictions for the Kelvin half-angle are predominantly attributed to the assumptions used by the theoretical method. The methods presented in this work can potentially be used to validate free-surface flows, even when one does not have access to experimental wave elevation data.

Keywords: CFD; shallow water; restricted water; KCS; spectral analysis of free surfaces

1. Introduction

Computational fluid dynamics (CFD) has become widely accepted as a useful tool to predict the flow around a ship. This is facilitated by the increase in available computational power, which has allowed practitioners to re-create the flow around a vessel even on a standard computer. Thus, the number of cells or, more generally, the computational effort required to perform a numerical simulation in model-scale is not thought to be prohibitive for practical applications.

Regardless of the advances in every field of numerical modelling, CFD is not yet considered a replacement of model-scale experimentation. This is because it is not possible to guarantee that a particular numerical model will perform with the same level of accuracy across all possible case studies. For example, new energy-saving devices, or novel underwater shapes may require research into the best applicable modelling approaches. Additionally, the consequences of implementing modelling assumptions may not be fully understood. Specifically, although in model-scale computations, a significant portion of the ship hull is covered by a laminar layer, most turbulence models assume the flow is fully turbulent. Yet, results with accuracy of a few percentage error can be found in the open literature [1–7].

There are also different aspects of the problem of modelling ship flows that can be validated with different levels of confidence. For instance, the resistance of a ship can be measured accurately.

However, velocities in the wake of the ship or free surface elevations require complex and expensive equipment. Thus, in the course of validating a numerical result, researchers typically analyse the error in observed integral quantities (resistance, motions, etc.) but tend to assume that other flow features are also accurately modelled as a consequence. Although this may be the true in many cases, an approach to validate aspects of the flow around a ship, such as the generated wave field, is necessary. Ideally, such a method would not rely on expensive equipment nor complex mathematics; in other words, it should be accessible. It is important to mention that some experimental campaigns report on a wide range of features of the flow around the ship, for instance, the flow properties in the wake [8,9].

The research presented herein is motivated primarily by the manner in which the problem of ship resistance is typically solved. That is, the principle of Galilean relativity is invoked (also called frame invariance; further information can be found in [10]). Namely, the water is flowing over a stationary ship (in the direction of the incoming flow). This assumption has several consequences. Those particularly important to the naval architect are:

(1) Levels of inlet turbulence.

This can have an impact on the overall properties of the flow [11] and may require calibration in some cases. For example, according to Lopes et al. [12], the onset of transition from laminar to turbulent boundary layer is strongly dependent on the level of free-stream turbulence. Some two-equation models, such as the SST k–ω model (which is widely used in marine hydrodynamics), are known to predict excessive decay of free-stream turbulence, which may affect the results. More recently, Lopes et al. [13] examined the same topic. According to them, even if one were to employ a more advanced eddy-viscosity model, capable of accounting for transition, the location of where laminar–turbulent transition occurs is highly dependent on the level of inlet turbulence.

(2) Wave reflections and their damping.

In cases where the volume of fluid (VOF) method is used [14], a damping length is often prescribed. That is, a length over which all waves are damped, extending from the boundary it is applied to in the normal direction. Setting an inappropriate damping length can have severe consequences to the predicted parameters [15].

(3) The temporal dependency of free surface flows.

The simulation of free surface flows via CFD cannot be solved using steady-state solvers (except in rare academic cases), because they require that properties are convected through the domain [14]. Theoretically, in the frame of reference of the ship, the flow—once converged—is steady. Therefore, ship resistance is frequently classed as a pseudo-steady problem. In reality, towing takes place over time and is a fundamentally unsteady process. Here, the presence of turbulence, which is by definition time-dependent [16], should also be kept in mind.

A second aspect inspiring this work partly stems from point (2) above. Although these may be of less interest to the naval architect, they carry their own importance nonetheless. Specifically, this concerns the destruction of ship waves, regardless of whether or not damping is prescribed. Once a ship-generated wave reaches the outlet, it is irreversibly destroyed, and the information it carries is lost. In shallow and restricted waters, ship waves are of great importance because they cause bank erosion and may even lead to destruction of coastal features/infrastructure [17,18]. In extreme cases, they may even be the cause of loss of life, as stated by Soomere [19]. Therefore, the accurate modelling of ship waves and their interactions with riverbeds or canal sides is important. Soomere [19] also advances a criticism of ship-induced flow predictions, pointing out that the flow is only described at a distance of few ship lengths.

Clearly, ship waves are both of practical and research interest. Therefore, the validation of numerical ship-generated waves is of high importance. In this respect, the work Caplier et al. [20], Fourdrinoy et al. [21], and Gomit et al. [22] is important to mention. The authors of the

aforementioned references systematically developed and implemented a technique to capture and analyse ship-generated waves from a model experiment. Of interest to the present researchh is the fact that in their studies, the authors proved the dispersion relation in deep and shallow water and demonstrated its validity for ships experimentally. Since the developed technique relies primarily on spectral representation of the wave field, it is thought prudent to attempt its application to a numerically generated free surface disturbance caused by a ship. It is expected that, if applied correctly, it is possible to validate a numerical wave field simply by means of processing a virtual free surface, which would be undoubtedly of practical use. Such a method has the potential to change how numerical solutions of surface piercing bodies are treated.

The present paper will attempt to apply the aforementioned spectral technique on a different type of numerical towing tank. Instead of relying on Galilean relativity, the present paper will present a numerical replica of a towing tank, where the ship advances over a stationary fluid. This is achieved via the overset domain method, where the ship is encased in what is essentially a moving box. To perform the numerical simulations, the commercial Reynolds-averaged Navier–Stokes (RANS) solver, Star-CCM+ version 13.06, is used. The specific case studies adopted in this paper are selected to maximise the practical relevance of the study. Specifically, the New Suez Canal is replicated, alongside a standard rectangular canal, which were investigated experimentally by Elsherbiny et al. [23]. The KRISO container ship (KCS) with a scale factor of 1:75, following the available experimental data, is used for all simulations.

The aim of this paper is primarily to demonstrate that it is possible to create a virtual towing tank where the ship is towed using the overset method, i.e., a virtual towing tank that does not rely on Galilean relativity. The generated wave field will then be used to estimate the Kelvin half-angle for an example case. The adopted approach also allows one to split the near- and far-field wave systems, which is used on the fully nonlinear disturbance, generated by the KCS at a variety of speeds in two different canals.

This work is organised as follows. Section 2 contains a description of the adopted case studies, while Section 3 explains the adopted methodology, which is split into the two techniques used in this paper, namely the computational set-up and the spectral representation techniques. Section 4 is dedicated to results and their discussion, whereas Section 5 contains conclusions and summary.

2. Case Studies

As mentioned in the previous section, the case studies adopted for this work are taken from the experimental work of by Elsherbiny et al. [23]. The rationale behind this choice relates to the particular objective of this study. To elaborate, shallow-water studies are a natural choice for the examination of ship-generated waves. This is because they present several features that are absent in deep-water ship-generated waves. Shallow-water waves are nonlinear, and their Kelvin half-angle is speed-dependent [24,25]. This is illustrated in Figure 1, which is constructed via Havelock's [17] linear method. Here, the Kelvin wake angle increases from its deep-water value of ≈19.47° to 90°. The theory predicts that at a depth Froude number ($F_h = U/\sqrt{gh}$, where U is the ship speed in m/s, g is the gravitational acceleration and h is the water depth) of one, $F_h = 1$, the ship-generated waves will travel at the same speed as the disturbance, indicating the Kelvin wedge fills the entire half-plane aft of the disturbance, i.e., at a half-angle of $\theta = 90°$. The relationships derived by Havelock [17] are omitted in the present work, as they are available in the open literature.

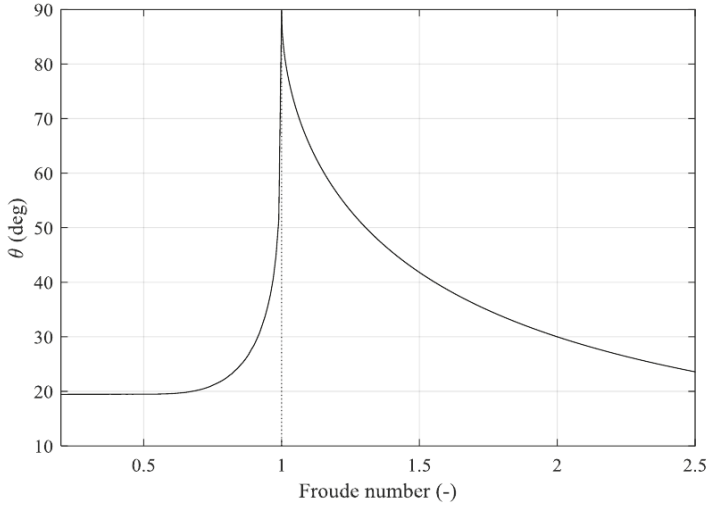

Figure 1. Kelvin half-angle of ship-generated waves in shallow waters as a function of the depth Froude number.

Ship-generated waves are also of greater concern in restricted areas than in deep waters, because they may affect the surrounding environment detrimentally. In navigational fairways, bank erosion is of particular concern, which has led to authorities restricting the speed with which vessels are legally allowed to operate [26]. Such a restriction simultaneously guards against groundings.

The case studies adopted herein are chosen to reflect the aforementioned points. In this respect, the recent work of Elsherbiny et al. [24] is used as a benchmark. From their experimentally investigated cases, two different canal cross-sections are selected: the New Suez Canal and a standard rectangular canal. These are graphically depicted in Figure 2.

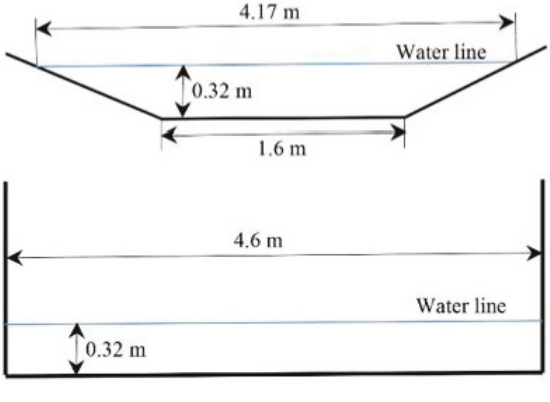

Figure 2. Graphical depiction of the cross-section of the selected case studies. Top: New Suez Canal; bottom: rectangular canal.

The ship used in this study also follows from the experimental campaign of Elsherbiny et al. [23]. Namely, the KCS hull form is used, scaled by a factor of 1:75. This translated into a depth-to-draught ratio of 2.2, based on the ship's design draught. In order to ensure that a well-defined Kelvin wake is simulated, the chosen depth Froude numbers are towards the high end of the experimentally available

conditions. The ship's particulars are given in Table 1, whereas test matrix alongside the predicted Kelvin half-angles (via Havelock's [17] method) are described in Table 2. It should be noted that Havelock's [17] method was originally devised for point sources and is therefore not expected to be perfectly accurate for nonlinear three-dimensional surface piercing bodies. Nonetheless, it is a useful starting point. Additionally, turbulence, viscosity and vorticity may influence ship-generated waves, particularly in the near-field [27].

Table 1. Ship characteristics.

Quantity	Symbol	Value	Unit
Scale Factor	λ	75	-
Length	L	3.067	m
Beam	B	0.429	m
Draught	T	0.144	m
Depth	D	0.253	m
Water depth	h	0.32	m
Block coefficient	C_B	0.651	-
Longitudinal Centre of Gravity	LCG	1.488	m
Wetted area	S	1.694	m^2

Table 2. Test matrix and resultant Kelvin half-angles according to Havelock's [17] method.

Canal	Case Number	Depth-to-Draught (h/T)	Depth Froude Number (F_h)	Ship Speed (m/s)	Kelvin Half-Angle (°) [17]
Rectangular canal	1	2.2	0.57	1.01	19.52
	2		0.77	1.364	21.58
New Suez Canal	3		0.47	0.815	19.47
	4		0.57	1.01	19.52

The relatively high depth Froude numbers ensure the numerically generated wave field will be discernible. The spectral method used also performs best at high speeds, where the near- and far-field disturbances generated by the ship are well visible. This can be seen by consulting the results of Caplier et al. [20].

3. Methodology

This section is presented in two major parts. These reflect the methodologies used in this work. The first section presents the numerical set-up, which is followed by an explanation of the spectral method in the second subsection.

3.1. Numerical Aspects

The solver, Star-CCM+ version 13.06, employs the finite volume method to model the flow, which uses the integral form of the incompressible RANS equations and divides the computational domain into a finite number of adjoining cells. Continuity and momentum are linked via a predictor–corrector approach. Further details pertaining to the implementation and algorithms used can be accessed in Siemens [28] and Ferziger and Peric [29].

To account for turbulence within the fluid, the k–ω model of Wilcox [30] is used. This choice is made following previous work, which showed the particular model to be stable and provide the fastest solution time of all two-equation variants [31]. Benefits of using the k–ω model include its seamless application to low y^+ type meshes ($y^+ < 1$). This is a desirable feature, because it avoids the use of wall

functions, or any other bifurcations of the solution, as is the case with the k–ε model [28]. Although wall functions can predict the forces acting on a body with good accuracy, they may introduce errors in the modelling of hydrodynamic properties in the wake of a ship. For instance, they are unable to account for flow separation [32]. To facilitate a good representation of turbulent properties, a second-order convection scheme is applied throughout all simulations.

To characterise the fluid interphase, the volume of fluid (VoF) method is used [33]. Moreover, Star-CCM+ offers a high-resolution interphase-capturing (HRIC) scheme to enhance the definition of the free surface, which is employed in this study [34]. Vertical ship movements, i.e., sinkage and trim, are not accounted for to reduce the complexity of the simulations. Instead, the ship's position in the x–z plane is adjusted prior to initiating the simulation according to the published results of Elsherbiny et al. [23,35]. This is done in an attempt to reduce the discrepancy between the experimental results and those derived herein. However, some difference is expected to persist since the experimental data, reported by Elsherbiny et al. [23], were determined for a free to sink and trim KCS model.

3.1.1. Computational Domain

As stated previously, frame invariance is not used in this work. Instead, the ship is given the corresponding velocity, which can be consulted in Table 2 for each canal. To model the motion of the ship along the canal, the overset domain approach is used. Thus, the ship is towed in the virtual environment over a static fluid. This has two main consequences. Firstly, the computational domain can no longer conform to the recommendations of the ITTC [36] relating to the positioning and dimensions of the computational boundaries. Instead, an attempt is made to replicate the towing tank used for the experimental work, which is used as a benchmark. Specifically, the towing tank at the Kelvin Hydrodynamics Laboratory at the University of Strathclyde. Naturally, the width and depth of the computational domain must satisfy the test cases (given in Table 2). On the other hand, the length of the computational domain is set as 60 m long. The dimensions are kept the same across case studies (pertaining to the overset domain and the length of the tank). These are shown in Figure 3. The height of the static domain is set as 1.23 ship lengths from the undisturbed water surface in all cases to eliminate any possible effects stemming from the height of the domain.

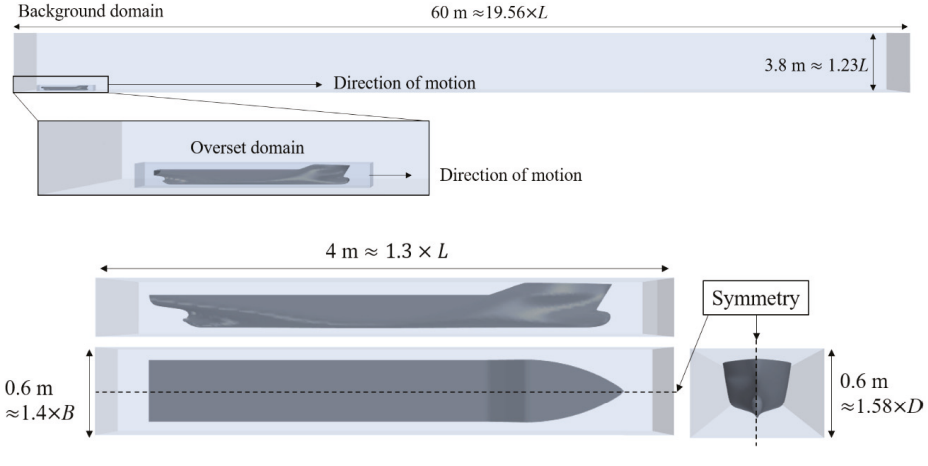

Figure 3. Length of the computational domain and dimensions of the overset domain.

The dimensions of the overset domain, which are maintained identical across case studies, are also shown in Figure 3. It should be noted that for visualisation purposes the figures have been mirrored about the central plane. Other than the boundary, coincidental with the canal and ship centrelines

where a symmetry condition is imposed, all other boundaries within the background domain are no-slip walls. This is in line with our goal of designing a more realistic representation of a towing tank. Specifically, so-called 'open boundaries' do not exist in reality [37]. Examples of such boundaries include velocity inlets and pressure outlets. Although it is easier to define the conditions at such boundaries mathematically, they are a definite source of modelling error as discussed earlier.

The manner in which the computational domain is constructed allows the removal of wave damping. Moreover, the definition of turbulent properties on boundaries (such as levels of inlet turbulence) of the fluid is not necessary since there are no inlets nor outlets present. However, it should be noted that the initial conditions in terms of turbulence in the fluid must be specified. In this study, a turbulent viscosity ratio of 0.1% is used, which decays rapidly and is effectively zero in the nondisturbed region of the domain at the end of the acceleration phase, limiting its influence to the early stages of the simulation.

3.1.2. Computational Mesh

The computational mesh is generated entirely within the automatic facilities of Star-CCM+. As stated earlier, the near-wall mesh is generated so that $y^+ < 1$ over the wetted area of the ship. This is achieved via the prism layer mesher, offered by Star-CCM+. It should be noted that no prism layer refinement has been applied to the side walls and canal bottom. Therefore, wall functions are employed on these boundaries. The choice of background and overset mesh is of critical importance. This must be done in a way that enables the solver to adequately capture flow properties as they transition from the background into the overset mesh. The cell distribution of each domain is depicted graphically in Figure 4, whereas Figure 5 depicts the y^+ distribution on the hull at a physical time of 40 s for the $F_h = 0.77$ case.

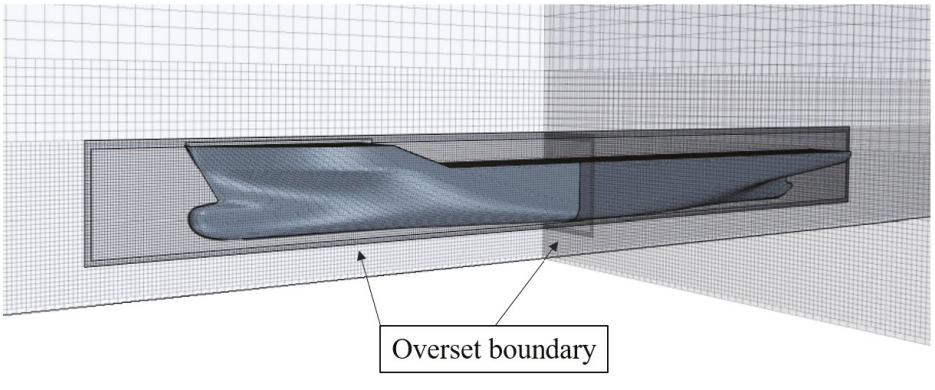

Figure 4. Three-dimensional depiction of the computational mesh.

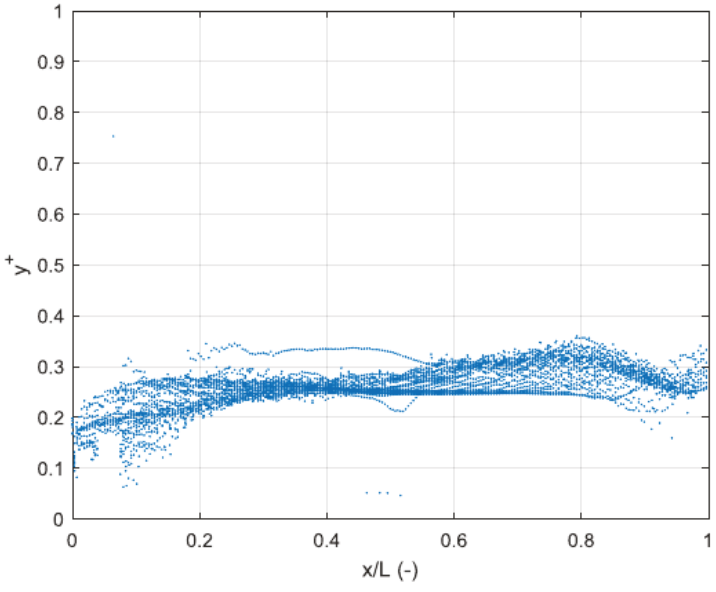

Figure 5. The y^+ distribution on the ship hull at $F_h = 0.77$, sampled at 40 s physical time.

The arrangement of the mesh does not vary across case studies; the total cell numbers for each canal are shown in Table 3. The circa 8 million cell difference between the two adopted canals is a direct result of the smaller wetted volume occupied by the Suez Canal.

Table 3. Cell numbers for both canals.

Canal	Background Cells	Overset Cells	Total
Rectangular canal	29,312,452	766,402	30,078,854
Suez Canal	21,496,179	766,402	22,262,581

Figure 4 also depicts the manner in which the mesh coarsens as the distance from the waterline is increased. This gradual coarsening is implemented to reduce the overall number of computational cells.

3.1.3. Time-Step Selection

Time-step selection is of high importance in CFD. In this respect, the Courant–Friedrichs–Lewy (CFL) number may be used as an assessment criterion. The CFL number is defined as the product of the flow speed and time-step, divided by the mesh size [29]. As a fluid parcel propagates through the mesh, one would ideally aim to capture its properties at each cell. This is satisfied when CFL < 1. Since the mesh is kept identical for all cases, the highest speed can be used to assess the CFL condition. Moreover, a CFL condition onto the background domain is not a meaningful metric, since the majority of the fluid is static. Instead, the CFL number within the overset box is monitored throughout the duration of the simulation.

Typically, when solid body motion is present, the time-step requirements are relatively low. In this work, a trial with a time-step of $0.0035L/U$, where L is the ship length and U is the ship speed in m/s was used. The results indicated satisfactory agreement with experimental data, as will be demonstrated in the following section. For this reason, the time-step is set at $0.0035L/U$ for all simulations. For the highest speed, the average CFL within the overset domain did not exceed 0.7, which is considered

adequate for a first-order temporal discretisation scheme. It should also be borne in mind that if the time-step is too low, severe numerical noise may be noticed in the solution time-history [38].

3.1.4. Time-History of the Solution

An example time-history of the resistance of the ship is given in Figure 6. The figure is characterised by two distinct regions. Firstly, the ship velocity is linearly increased up to the target velocity. This is done by linking the time-step and velocity. The specific approach adopted requires the ship speed to reach its steady value at the end of the first 1000 time-steps. In other words, the ship's velocity is increased by $U_{target}/1000$ each time-step. Thus, after an initial oscillatory behaviour, the resistance time-history exhibits oscillatory convergence towards its steady-state value. The oscillations are liked with the reflections of waves from the side walls, which also impact the observed resistance [39]. All final values reported in this work are obtained by averaging over one period of oscillation of the resistance curve. The specific point where averaging is performed is chosen to be sufficiently far from the acceleration phase to eliminate its effect.

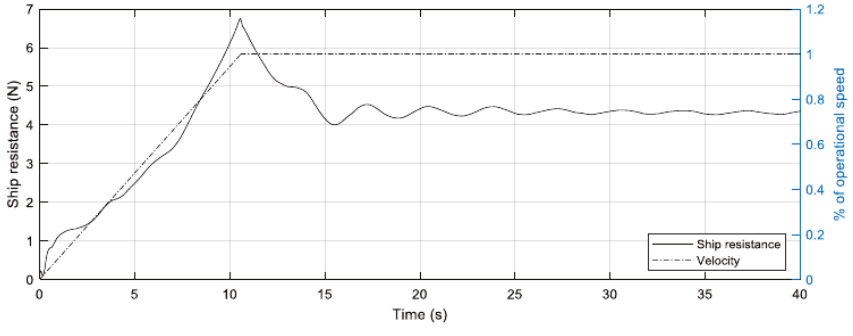

Figure 6. Example time-history of the solution (depicted: $F_h = 0.57$).

3.1.5. Verification

This section contains the numerical verification of the case study in the rectangular canal, $F_h = 0.57$. The numerical uncertainties are estimated via the grid convergence index (GCI) method. This is the standard way to report numerical uncertainties in ship CFD [40]. It is assumed that the remaining cases are characterised by similar levels of numerical uncertainty.

The GCI method requires three systematically coarsened solutions for the same case. In this study, the recommendations of the ITTC [40] are followed. Specifically, the refinement ratio, $r = \sqrt{2}$ is adopted. The refinement ratio is used to coarsen and lessen the grid size and time-step, respectively. The GCI method assumes that all three solutions are close to the asymptotic range and are sufficiently different, which may be difficult to achieve in practice. The proximity to the asymptotic range is typically characterised by the convergence ratio, p, which is shown in Equation (1).

$$p = \ln(\varepsilon_{32}/\varepsilon_{21})/\ln r \tag{1}$$

where $\varepsilon_{32} = f_3 - f_2$ and $\varepsilon_{21} = f_2 - f_1$. Here, f_n represents the n-th solution, generated by a systematic coarsening/lessening of the input parameter (grid or time-step). If $p = 2$, then the grid or time-step can be deemed asymptotic [41]. The convergence properties, however, can be determined in a different manner, which also carries information on what type of convergence/divergence is achieved with refinement. This is known as the convergence ratio, $R = \varepsilon_{21}/\varepsilon_{32}$ [42]. Based on the value of R, the following may be interpreted:

1. Monotonic convergence is observed if $0 < R < 1$;

2. Oscillatory convergence is observed if $R < 0$;
3. Divergence is observed if $R > 1$.

The GCI method is only applicable in case (1). Next, an error estimate (e_{21}) is defined as [43]:

$$e_{21} = (f_1 - f_2)/f_1 \quad (2)$$

Once the error is known, the numerical uncertainty can be calculated as shown in Equation (3) [44]:

$$GCI = 1.25 e_{21} / \left(r_k^p - 1\right) \quad (3)$$

where k represents the k-th input variable (grid or time-step). The factor 1.25 in the numerator of the expression, defining the numerical uncertainty represents a factor of safety. This has been devised to ensure that the true solution lies within the bracket provided by the GCI with 95% confidence. The results from the convergence study can be seen in Table 4.

Table 4. Grid and time independence (rectangular canal, $F_h = 0.57$). Experimental result: 4.5047 N.

Parameter	Mesh	Time-Step	Units
r	$\sqrt{2}$	$\sqrt{2}$	-
f_1	4.325 (29,312,452 cells)	4.325	N
f_2	4.356 (10,955,825 cells)	4.381	N
f_3	5.045 (4,155,326 cells)	4.446	N
R	0.044	0.852	-
p	9.005	0.463	-
GCI (%)	0.6704	19.609	-

The successive grid coarsening resulted in 10,955,825 and 4,155,326 cells for the medium and coarse solutions, respectively. In terms of spatial dependence, the solution exhibited rapid ranges with reduction in cell numbers. This 'superconvergence' can be deduced by examining the order of accuracy, p. While in the case of grid coarsening it is approximately 9, when the time-step is lessened, the solution changes according to $p_{time} = 0.463$. According to Eca and Hoekstra [45], orders of accuracy between in the range 0.5 and 2 can still be treated as asymptotic. Eca and Hoekstra [45] devised a procedure based on a least-squares fit to estimate the numerical uncertainty. Their method is not employed in this study, because it requires a minimum of four solutions. Further coarsening of the computational mesh resulted in divergent behaviour in the simulation. The consequence of the time-step exhibiting the above order of accuracy means that the GCI method predicts large numerical uncertainties, even though the overall change between the coarse and fine solution is less than 3% of the fine solution's value.

It should be noted that the time-step is kept at the smallest value while coarsening the grid. Conversely, the finest grid was maintained throughout the temporal convergence analysis. To ensure that the ratio of overset cell to background cell dimension is kept constant, both domains were coarsened simultaneously. In this study, it is assumed that all examined cases will exhibit similar levels of spatial and temporal dependence. For this reason, the above procedure is not repeated.

3.2. Spectral Representation of the Wave Field

In this section, the method devised by Caplier et al. [20] and Gomit et al. [22] is briefly examined. This method has previously been used to determine a ship's speed via satellite imagery [46,47]. The essence of the approach is to process an available water surface in Fourier space. To achieve this, a 2D Fourier transform is used to represent the disturbance in the spectral space (k_x, k_y). These arise by defining the angular wavenumber, k, as a vector containing x and y components, $k = \sqrt{k_x^2 + k_y^2}$. The spatial equivalent of these components are used to calculate the extents of the spectrum.

The x-direction length of the entire water surface (L_x) becomes $k_{x,max}$; similarly, using the extent in the y-direction (L_y) one obtains $k_{y,max}$, as shown in Equation (4). Likewise, the resolution of the water surface in real space dictates the steps in Fourier space Δk_x and Δk_y in the x and y directions, respectively (Equation (5)).

$$k_{x,max} = 2\pi/L_x,\ k_{y,max} = 2\pi/L_y \tag{4}$$

$$\Delta k_x = \frac{1}{2} \times \frac{2\pi}{\Delta X}, \Delta k_y = \frac{1}{2} \times \frac{2\pi}{\Delta Y} \tag{5}$$

where ΔX and ΔY are the resolutions in the x and y directions, respectively.

If surface tension is ignored, the dispersion relation in shallow water may be expressed via the angular frequency (ω) of the waves as shown in Equation (6). This is justified, because surface tension becomes important only in waves characterised by wavelengths smaller than 7 cm. Alternatively, the travelling disturbance should propagate with a speed higher than 0.23 m/s [48] for surface tension to be negligible.

$$\omega(k) = \pm\sqrt{gk\tanh kh} \tag{6}$$

A moving ship will cause the waves to be Doppler-shifted, and setting $\omega' = \omega - Uk_x$ and $k' = k$, the resulting dispersion relation becomes [20]:

$$\omega'(k) = \pm\sqrt{gk\tanh kh} - Uk_x \tag{7}$$

To obtain the locus of the dispersion relation, Equation (7) is solved for $\omega'(k) = 0$ [49], which yields:

$$U^2k_x^2 - g\sqrt{k_x^2 + k_y^2}\tanh\left(h\sqrt{k_x^2 + k_y^2}\right) = 0 \tag{8}$$

Equation (8) is symmetrical with respect to both axes [50]. This is demonstrated in Figure 7, which includes computed loci (this is used to represent the solutions of Equation (8)) for $F_h = 0.57, 0.77$, according to the adopted cases. Alongside these, the critical depth Froude number is depicted to demonstrate the effect of ship speed on the dispersion relation in shallow water. It should be noted that the dispersion relation is speed-independent in deep water [20]. The arms of the loci always begin at $k_{y,x}/\left(g/U^2\right) = 1$ in deep water. This is also the cut-off wavenumber. In shallow waters on the other hand, the cut-off wavenumber varies with speed. This can be seen by consulting Figure 7, specifically, where the curves cross the abscissa. Here, the case for $F_h = 0.47$ is not shown, as it is practically impossible to distinguish it from the $F_h = 0.57$ case. Deep and shallow water cases are essentially identical when $kh \gg 1$.

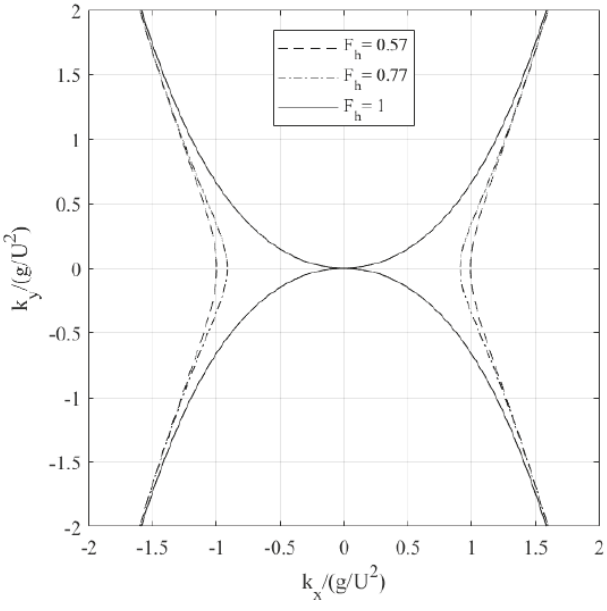

Figure 7. Solutions to Equation (8). Figure depicts the examined loci alongside the critical depth Froude number (F_h = 1) to demonstrate the effect of speed.

The cut-off wavenumber separates the near-field disturbance from the far-field waves generated by the ship. Thus, useful analysis with applications to loads on coastal structures may be performed by removing the near-field disturbance, which does not propagate away from the ship. To determine the cut-off wavenumber (k_x^c) in shallow water, Caplier et al. [20] solved Equation (9).

$$U^2 k_x^c - g k_x^c \tanh(h k_x^c) = 0 \tag{9}$$

Finally, the Kelvin half-angle may be determined by computing $\tan\theta = \left(dk_y/dk_x\right)^{-1}$ at the inflection point. According to Nakos and Sclavounos [51], numerical errors will manifest near cut-off wavenumbers. This can be deduced by examining Figure 7. Even a small deviation in the intersection between the locus and the abscissa will lead to large errors. The specific example given demonstrates the relatively short distance between the intersection points of F_h =0.57 and 0.77. On the other hand, as the speed is increased further, the locus approaches the origin. At the critical depth Froude number, the locus will transition into crossing the origin and progressing into a quadrant characterised by opposite signs of the abscissa and ordinate.

The manner in which a numerical free surface generates this pattern is in terms of maxima of the spectrum in Fourier space. This can be extracted and compared to the theoretical prediction provided by Equation (8). Caplier et al. [20] demonstrated that the relationship holds well despite its neglect of nonlinear and three-dimensional terms. Thus, if one can prove that a numerically generated free surface (once processed to the spectral domain) provides maxima near the locus, then the free surface can be considered validated. This is explored in the following section.

4. Results and Discussion

The presentation and analysis of the results generated in this study are split into two major parts. The first relates to the computed ship resistance coefficients, while the second subsection relates to the spectral analysis of ship waves.

4.1. Ship Resistance

In this subsection, the numerically obtained resistance is briefly discussed and compared to the experimental data. To begin with, the total resistance coefficients are presented in Figure 8 for all cases. The experimental data of Elsherbiny et al. [23] is included alongside each numerical result to enable comparison. Figure 8 clearly indicates the numerical prediction has a well-defined tendency to underpredict the experimental data. Here, the subscripts refer to depth Froude number. As one might expect, the ship's resistance at higher speeds becomes more challenging to predict by CFD. This is evident, especially in the resistance characteristics at the highest depth Froude number for each case.

The overall agreement between the experimental and numerical data is encouraging. This is the first sign that the constructed towing tank is capable of providing good predictions for the resistance of a ship. Possible sources of discrepancy are suspected to stem from the fact that the numerical approach did not model sinkage and trim. In shallow waters, their combined effect, termed ship squat, is attributed greater relative importance than in deep waters. Thus, the imperfect modelling adopted may have been partly the cause of the observed levels of discrepancy between the experimental and numerical results. Moreover, as the ship speed is increased, the difference also grows. This matches the pattern observed in the sinkage and trim curves for a ship, both theoretically [52,53] as well as numerically [54]. Turbulence modelling is also a source of error in the results presented herein. Based on previous research, it is expected and indeed observed that the k–ω model has a tendency to underpredict resistance [31]. More sophisticated modelling approaches, such as those accounting for transition or those resolving large parts of the turbulent kinetic energy spectrum, should be used to assess the sensitivity of the adopted approach to turbulence modelling. Recent studies have demonstrated that the latter approach can be highly beneficial in terms of accuracy [55].

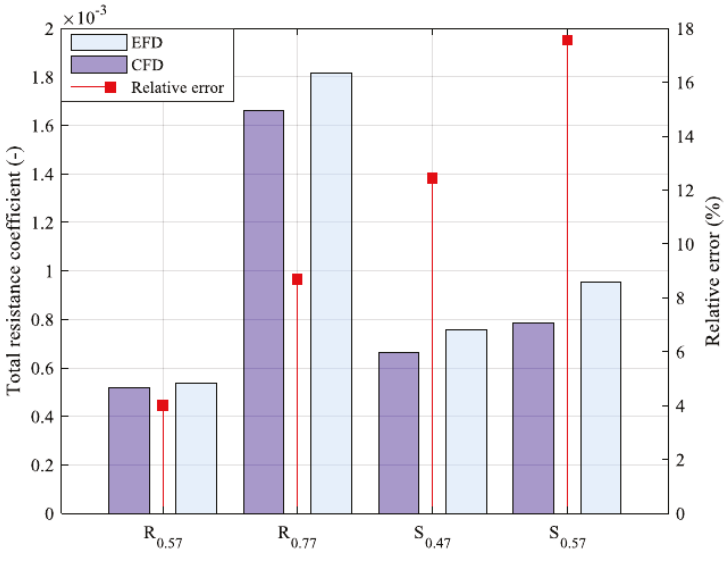

Figure 8. Comparison of total resistance coefficients for all cases (R indicates the rectangular canal case, whereas S indicates the Suez Canal). Subscripts refer to depth Froude number. Relative error computed as (EFD − CFD)/EFD × 100.

In practice, the cell numbers used in this study tend towards being prohibitively high. As stated earlier, a virtual towing tank where the principle of Galilean invariance has been utilised will consist of no more than 2–3 million cells. Such simulations can be performed within a few days on a standard computer. Thus, the adopted approach of virtually towing the ship may not become widespread soon.

Nevertheless, the additional information that may be extracted from a case such as this can be useful. An example of this is given in the following subsection.

4.2. Spectral Analysis of the Numerical Free Surface

We begin by examining the highest speed, simulated in the virtual towing tank, $F_h = 0.77$ in the rectangular canal. The numerical free surface is depicted in Figure 9. Here, the far-field waves generated by the ship are clearly visible. Due to the lateral restriction, waves have reflected approximately 2.5 ship lengths aft of the ship. It should be noted that Figure 9 and other figures are reflected around the central symmetry plane to enable a better visualisation.

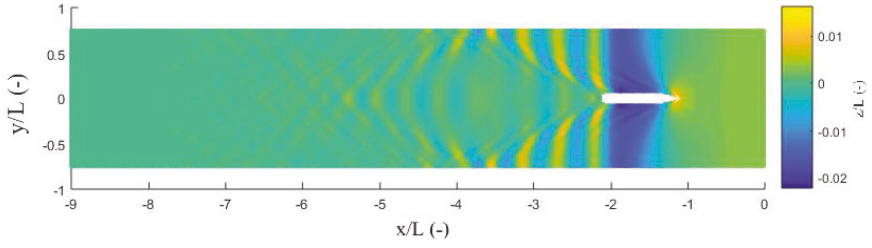

Figure 9. Generated wave field in the rectangular canal at $F_h = 0.77$.

At this point, it is useful to attempt to determine the wave angle. According to Havelock's [17] method, the Kelvin half-angle is $\theta = 21.58°$. Figure 10 depicts an attempt at solving this problem by projecting a (dashed) straight line from the forward perpendicular (FP) to the sides (and its reflection) at an angle of 21.58°. The line 'lands' at a wave trough on the canal wall—clearly, this is not the correct approach. The solid line in Figure 10 represents the same process but in this case beginning from the nearest peak downstream at the wall and projecting in both directions. The line intersects the ship approximately $^1/_4\,L$ from the forward perpendicular. Then, the broken line is initiated at the highest peak at the wall, where wave reflection occurs. This intersects the ship approximately $^3/_4\,L$ from the FP. Finally, the dotted line shows the same process. It originates at the point of the ship defined by [min(x), max(y)], representing the point where the aft wave system is generated.

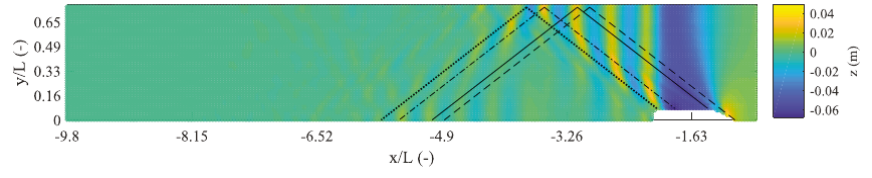

Figure 10. Generated wave field in the rectangular canal at $F_h = 0.77$ and corresponding half-angle according to Havelock [17]. Dashed line originates at FP; solid line originates at the nearest downstream peak, where the dashed line is reflected. Broken line originates at the highest wave elevation on the wall; dotted line originates at the ship coordinates representing the point where the aft wave system is generated.

Clearly, neither line in Figure 10 accounts for the wave angle well. This is not surprising since the method used to estimate the half-angle is linear and devised for a point source. In this case, the spectral representation may be used to approach the problem. As explained earlier, the first step is to calculate the Fourier transform of the wave field. This is performed in MATLAB, which uses grayscale images. For this reason, the images used henceforth to represent the free surface will be shown in the grayscale format used to perform the analysis. By doing so, other researchers may cross-reference results obtained herein by analysing the provided images.

Figure 11 depicts the process used in this study. Specifically, the image is first represented in Fourier space. Then, for each column of the matrix defining the Fourier transform, a maximum is identified. The k_x, k_y components of these maxima are then compared to the theoretical relationship provided by Equation (8). A polynomial fit is constructed from these points to demonstrate the accuracy of large and small k_x on the fit. In the present case, it is apparent that as one progresses in the k_x range to higher values, agreement deteriorates quickly. According to Nakos and Sclavounos [51], insufficient grid resolution will be manifest as numerical dispersion in the k_x, k_y plane being curved towards high values of k_x, eventually forming closed curves. Since this is not what is observed in the present study, it may be concluded that the numerical wave field is represented with sufficient grid resolution. Nonlinear phenomena will be revealed in the appearance of additional branches in the spectrum. In each quadrant, a branch, emanating from the origin and propagating linearly to the edge of the plot, where it reflects, is observed. Moreover, smaller branches of the dispersion relation are observed, with origins at higher k_x values, indicating nonlinearity [21]. These lead to deformation of the wake in the real space.

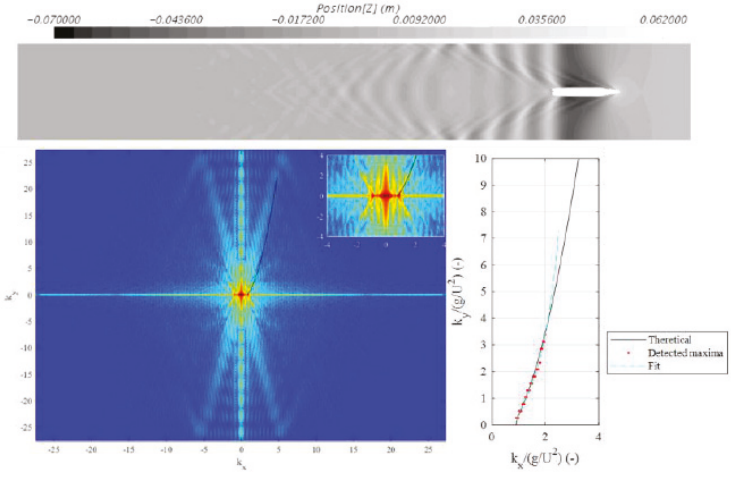

Figure 11. Processing of the wave field. Depicted: $F_h = 0.77$ in the rectangular canal. Top: the raw image, where real space extents are 32 m in the stream-wise and 4.6 m in the span-wise directions. Bottom left: the Fourier representation of the wave field. Bottom right: detected maxima and fit, superimposed onto the theoretical relationship, Equation (8).

Now, it is important to deduce the origin of the apparent disagreement in the high k_x region, as well as its effect on the predicted Kelvin half-angle. One source of disagreement inevitably stems from the fact that the dispersion relation used for comparison is linear [56]. Ship waves, particularly in shallow water, are nonlinear. Even in deep waters, Ma et al. [57] found significant nonlinear influence on the dynamic pressure of the KCS. On the other hand, the experimental data presented in Caplier et al. [20] suggest that the theory approximates real ship waves very well for the Wigley hull. This may not be a fair comparison, because nonlinear effects for the Wigley hull are known to be small [57–59]. In other words, using the parabolic hull plays to the method's strengths.

The neglect of nonlinear terms is chiefly manifest in the near-field disturbance, close to the ship. Although a modification to the Kelvin half-angle may be produced as a consequence of modified pressure in the near-field, the magnitude of such an effect is not known. Interference between transverse and divergent waves, generated at the ship's bow, may be one cause of the observed disagreement [60]. This interference effect, along with the nonlinearity exhibited by the KCS, and the influence of viscosity are all thought to be the contributing to the observed discrepancy.

There is one more aspect of the solution that one should consider carefully. This relates to the curve fit used to approximate the numerical dispersion for higher k_x values than maxima were detected for. In shallow waters, the arms of the locus are typically not well developed [20]. Thus, it is difficult to extract a sufficient number of points to perform the analysis. For this reason, the only fair assessment recommended is within the range where maxima have been detected from the Fourier transform. The range $k_x/(g/U^2) \in [1, 2.5]$ is used to perform all subsequent analysis. This includes part of the fit over which no maxima have been detected to illustrate the effect of limited data samples.

Figure 12 contains the derivatives dk_y/dk_x for deep and shallow water, alongside the numerically generated fit from CFD. This is shown because upon evaluating dk_y/dk_x at the inflection point, the Kelvin half-angle can be obtained. Moreover, Nakos and Sclavounos [51] recommend the examination of these derivatives to highlight differences between numerical and theoretical dispersion relations. Figure 12 also includes the area under each curve for reference. Clearly, assessing solely the area under each curve is not a good approach to determine an apparent disagreement, or error, which is −3.901% in this case. This is the case because different parts of the k_x range over which the derivative is shown may attenuate or reinforce the total favourably. On the other hand, the RMS (root mean square) of the difference between the theoretical and numerical curve is predicted as 0.456. The effect of this on the predicted half-angle is illustrated in Figure 13, where the consequences of the previously examined differences are highlighted.

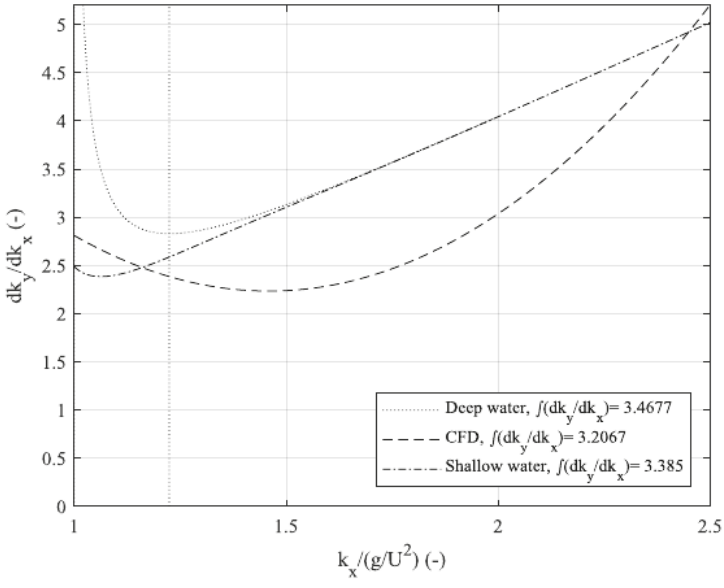

Figure 12. Derivatives dk_y/dk_x for deep water, shallow water and numerical shallow water cases.

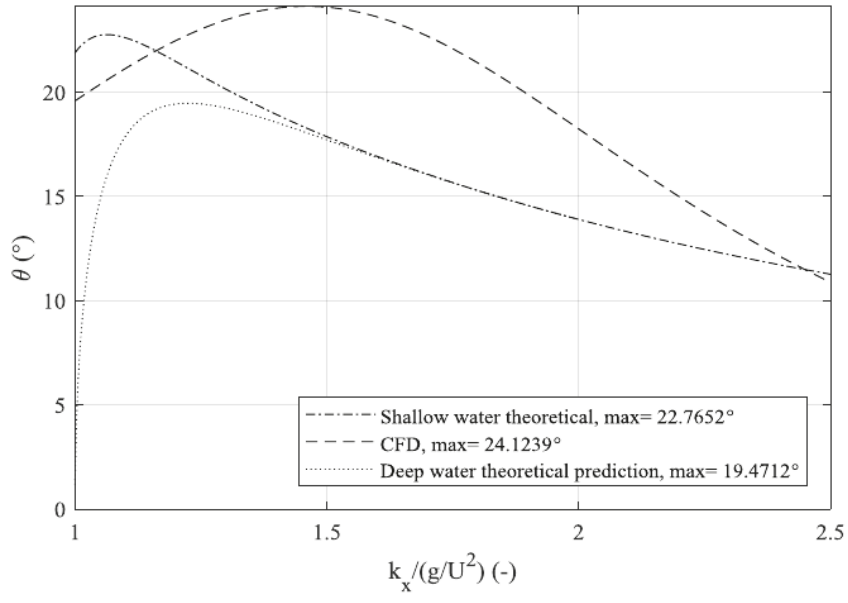

Figure 13. Predicted and theoretical half-angles.

The net effect of the difference between the fit and theoretical curves is translated into a difference of approximately 2.6° in the predicted half-angle. This is not considered as a substantial discrepancy. However, the locations where inflection occurs are significantly different between the two sets of data. This occurs at $k_{x,theory}/(g/U^2) = 1.06$ according to the theoretical relationship, whereas CFD predicts this at $k_{x,CFD}/(g/U^2) \approx 1.46$. The identification of this half-angle does not help in visualising the wake better. Plotting a line with origins at the bow with an angle of 24.1° causes an intersection with the wall earlier than what is shown in Figure 10. The relative error between the two predictions is 5.93% (arrived at by computing $|(\theta_{theory} - \theta_{CFD})/\theta_{theory} \times 100)|$).

There are several aspects of this technique that should be improved. Firstly, the range over which it is acceptable to find maxima of the Fourier transform should be defined. The only way to accomplish this is via an extensive experimental campaign. If such an interval is known, then it may be possible to define a metric expressing the degree to which waves are correctly modelled. It may also be possible to link specific parts of the computational free surface with increased error in the representation of ship waves. The only manner in which this can be achieved is via experimental work, which should demonstrate the validity of the assumptions as they apply to waves generated by a ship, rather than point sources. Specifically, this concerns ships causing highly nonlinear flows, thereby generating waves that may not resemble the method's predictions well.

This work proceeds with the next aspect of the solution, which one may obtain via the spectral representation. Specifically, this concerns splitting the near-field from the far-field components. This is illustrated for the rectangular case study at $F_h = 0.77$ in Figure 14, where the cut-off wave number is $k_x^c = 4.7885$. Here, the shape of the ship leaves a small effect onto the corresponding near- and far-field systems because the outline of the vessel forms part of the free surface itself. The intensity of the spectrum depends on the input and can be changed based on the brightness of the supplied input. The range of the spectrum is therefore not shown.

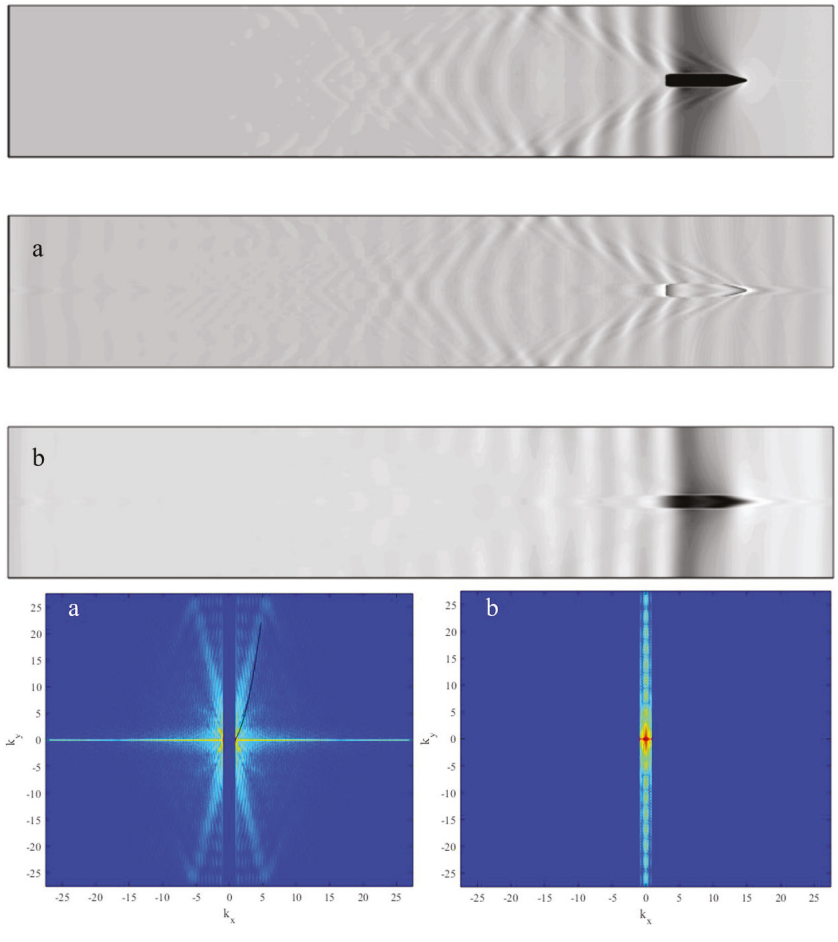

Figure 14. Splitting of near- and far-field components via manipulations of the spectrum (cut-off wave number $k_x^c = 4.7885$). Top: original free surface; (**a**) indicates the far-field component, whereas (**b**) indicates the near-field disturbance and their corresponding Fourier representations. Longitudinal extent: 32 m.

The near-field disturbance is not confined in the immediate vicinity of the ship in Figure 14, contrary to expectations. Instead, it is shed from the ship downstream, with its influence being clearly visible near the domain walls. This representation also allows the detection of the far-field waves, as well as their reflection from the side walls, with ease. It is apparent that the wave system is convex with respect to the ship centreline. Once reflected, this is not as clearly visible. The full spectrum for this case can be consulted in Figure 11.

Figure 15 shows the spectral decomposition process as applied to the rectangular canal for $F_h = 0.57$. Here, the arms of the spectrum, previously used to extract maxima and compare with the theoretical relationship, are not formed. This is consistent with findings of other researchers [20]. Specifically, the higher the depth Froude number is, the more clearly the arms of the spectrum are formed. The physical origins of this relate to the relatively small far-field disturbance generated by the ship in the examined speed range. Simultaneously, speeds corresponding to $F_h \geq 1$ are impractical, which is why they have not been investigated. Experimental data in terms of resistance are also not

available for the adopted case studies at the aforementioned speeds. In any case, several features of the spectrum can be observed. Firstly, the low-intensity arms, observed in Figures 11 and 14, extending into the far field are reproduced. However, in Figure 15, the arms are not reflected from the boundaries of the plot; instead, they exhibit periodic structures, which vanish near the limits.

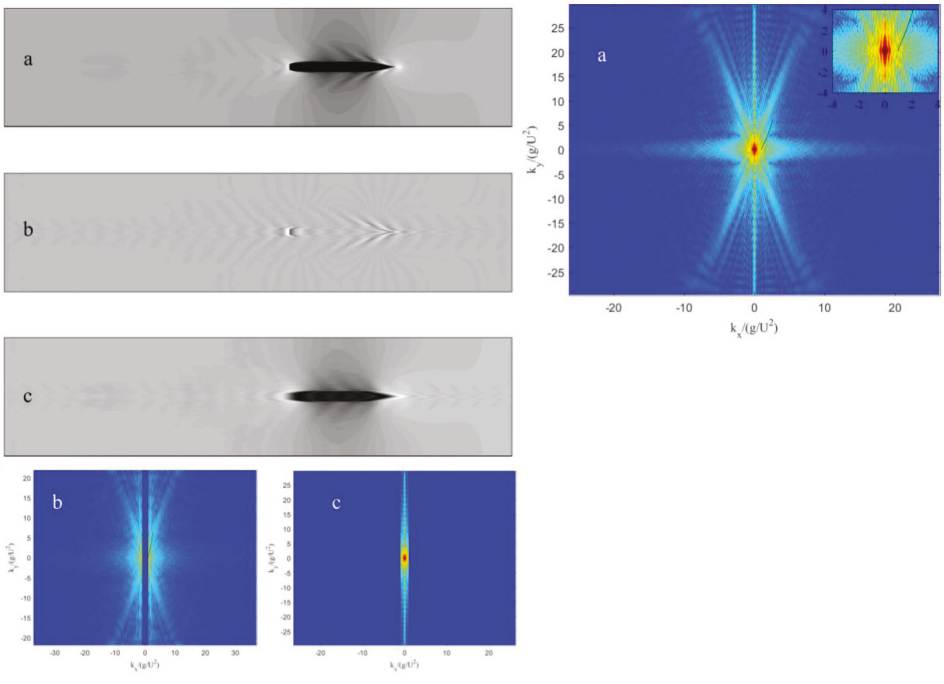

Figure 15. Free surface disturbance in the rectangular canal, $F_h = 0.57$; (**a**) Computed free surface. (**b**) Far-field and (**c**) near-field representations in the real and spectral space ($k_x^c = 9.5796$). Longitudinal extent: 16.5 m.

It is now appropriate to shift the focus onto the Suez Canal and the spectral representation of the wave field obtained. As before, the higher speed ($F_h = 0.57$) is examined first, as shown in Figure 16. An immediately apparent difference relates to the structure of the wave field. Specifically, the slopped canal banks have caused a rundown of the water surface. Since the theoretical relationship used to plot the solid line in the plot can only account for a single depth, it is not seen to represent the Fourier representation of the numerical wave field well. Interestingly, the spectrum contains maxima arranged in semi-circular arcs. An interpretation of this is not attempted at present; instead, this is left for a more theoretical piece of work. Such research would need to determine the form of the dispersion relation in nonconstant water depths. The cut-off wave number used to produce Figures 15 and 16 is the same ($k_x^c = 9.5796$ m^{-1}) for this reason. As was the case for $F_h = 0.77$, the near-field disturbance is trapped near the canal walls and shed over a great distance downstream.

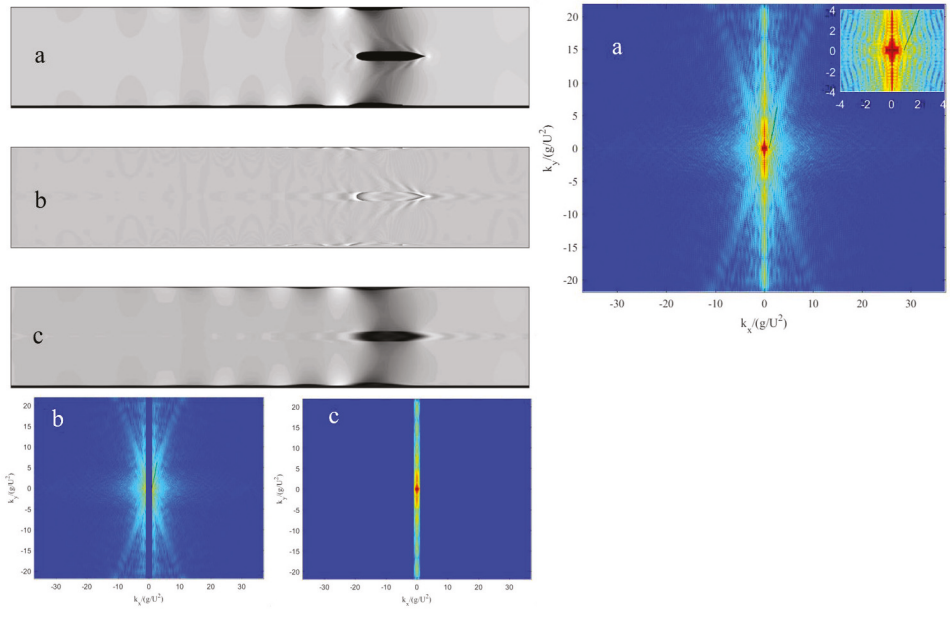

Figure 16. Free surface disturbance in the Suez Canal, $F_h = 0.57$; (**a**) Computed free surface. (**b**) Far-field and (**c**) near-field representations in the real and spectral space ($k_x^c = 9.5796$). Longitudinal extent: 13 m.

The lower speed investigated in the Suez Canal and the Fourier representation of its wave field are depicted in Figure 17. As expected, the disturbance generated by the ship at $F_h = 0.47$ is significantly smaller than that produced at $F_h = 0.57$ (Figure 16). The spectrum exhibits a similar structure to what was previously observed for $F_h = 0.57$. For both results shown in Figures 16 and 17, the near-field hydrodynamic response has caused bright parts of the spectrum, which are periodically broken. These correspond to what is identified as a near-field wave by the method, trapped at the lateral extents of the tank. This is primarily the case due to the relative size of these disturbances. Namely, their wavelength is of the order of magnitude of the ship itself. Whether this classification itself is correct probably requires further research. However, their effect on the Fourier representation is clearly visible, especially in Figure 16, where a high-intensity patch can be seen undulating along the ordinate.

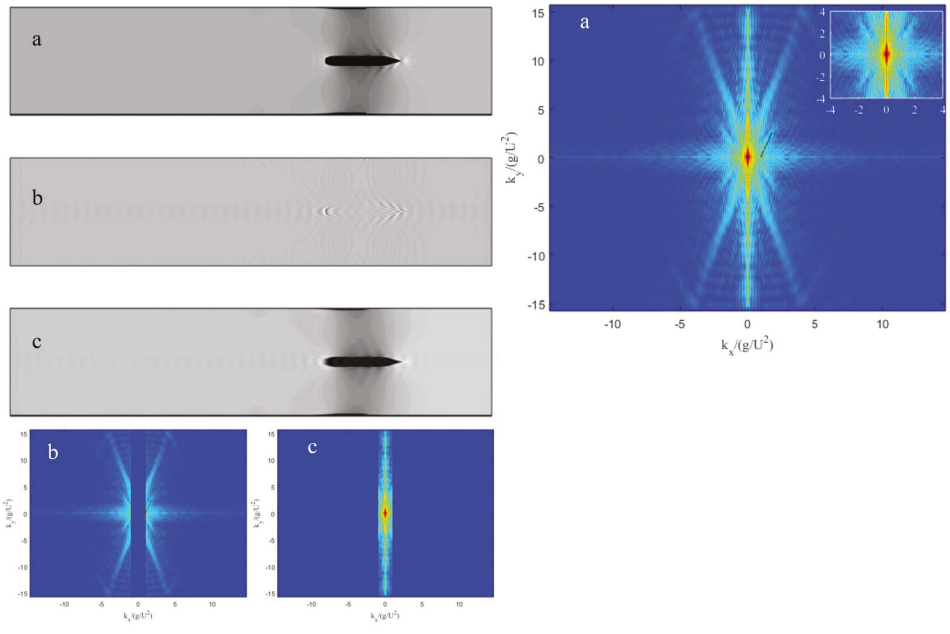

Figure 17. (**a**) Computed free surface in the Suez Canal, $F_h = 0.47$. Far-field (**b**) and near-field (**c**) representations in the real and spectral space ($k_x^c = 14.1833$). Longitudinal extent: 20 m.

5. Summary and Future Work

This paper presented a towing tank which does not make use of on the principle of Galilean relativity. This was accomplished via the overset method, which was used to actually 'tow' the KCS model in a virtual environment. The main benefits of adopting such an approach were identified in terms of the reduced number of assumptions needed to perform the analysis. Specifically, all boundaries (except those prescribed as symmetries or overset boundaries) are no-slip walls, which is more physically consistent than 'traditional' virtual towing tanks. Since the ship advances over a static fluid, the approach presented in this paper does not require the definition of inlet turbulent properties, as is usually the case. Thereby, one major source of modelling error and uncertainty is removed.

The adopted case studies numerically replicated recently published results in a rectangular canal and in the New Suez Canal [23]. The computed resistance of the ship was compared to the experimentally obtained values. Satisfactory agreement was found, although some discrepancy persisted in the highest speeds examined. The source of the difference between the experimental and numerical results is primarily attributed to the fixed sinkage and trim used in the virtual towing tank. The study was supplemented by a recently developed method to decompose the wave field and determine the Kelvin wake angle. In terms of the former, it was discovered that near-field disturbances propagate outwards towards the canal sides and are shed by the ship downstream. Their effect persisted over a significant distance. This is of practical interest, because near-field disturbances are typically linked with strong pressure variations. Thus, information extracted via the spectral decomposition method may be used to assess the optimum slope and positioning of canal sides to avoid excessive forces linked with bank erosion.

On the other hand, it was shown that it is difficult to identify the boundaries of the Kelvin wake in a narrow canal. Values for the half-angle computed via linear point-source methods were compared with those obtained by CFD. The effects of nonlinearity and interference of wave systems shed by the bow and stern were identified potential sources of discrepancy. The numerical (θ_{CFD} = 24.1°) and

theoretical (θ_{Theory} = 22.756°) Kelvin wake half-angles for $F_h = 0.77$ in the rectangular canal were found to compare reasonably well. However, the inflection point, which governs the value of the half-angle, was found to be in some disagreement. According to the theory, this should occur at approximately $k_x = 1.06$, whereas CFD suggests the inflection point is located at $k_x = 1.46$. The potential sources of this discrepancy likely pertain not only to limitations in terms of mesh size and time-step in CFD, but also, and likely more importantly, the theoretical assumptions.

One of the main conclusions drawn from this study is that the theoretical method used to predict the locus location has great potential for validation of numerical free surface problems. However, bounds of validity are yet to be determined. This forms the primary recommendation for future work. Specifically, a method should be devised to equip the practitioner with a number indicating how well the problem at hand is modelled. The answer to such a question can be found by performing a systematic experimental campaign, which should feature a variety of hull forms. These must ensure that the method is challenged with nonlinear forms to rigorously test its applicability. For example, these would include ships with high block coefficients, nonslender forms, as well as immersed transoms, where separation would be expected.

Another aspect requiring further attention is the manner in which the ship is accelerated up to the target velocity. In this study, the velocity changes linearly, inducing shocks onto the ship at the initial and target speeds. This results in longer times for convergence. To reduce the time taken to converge the result, different acceleration profiles must be compared, such as sinusoidal velocity changes. This is left as a piece of future work, alongside a turbulence dependence study and the relative impact of sinkage and trim.

Author Contributions: Conceptualization, M.T. and G.Z.; methodology, M.T. and G.Z.; software, M.T.; validation, M.T. and G.Z.; formal analysis, M.T. and G.Z.; investigation, M.T. and G.Z.; resources, T.T., Z.Y., A.I.; data curation, M.T. and G.Z.; writing—original draft preparation, M.T.; writing—review and editing, all authors; visualization, M.T. and G.Z.; supervision, T.T., Z.Y., A.I.; project administration, T.T., Z.Y., A.I.; All authors have read and agreed to the published version of the manuscript.

Funding: This research received no external funding.

Acknowledgments: Results were obtained using the ARCHIE-WeSt High-Performance Computer (www.archie-west.ac.uk) based at the University of Strathclyde. The work reported in this paper is drawn from the first author's PhD thesis. The first author gratefully acknowledges the scholarship provided by the Faculty of Engineering at the University of Strathclyde, which fully supports his PhD.

Conflicts of Interest: The authors declare no conflict of interest.

References

1. Bašić, J.; Degiuli, N.; Dejhalla, R. Total resistance prediction of an intact and damaged tanker with flooded tanks in calm water. *Ocean Eng.* **2017**, *130*, 83–91. [CrossRef]
2. Bechthold, J.; Kastens, M. Robustness and quality of squat predictions in extreme shallow water conditions based on RANS-calculations. *Ocean Eng.* **2020**, *197*, 106780. [CrossRef]
3. Farkas, A.; Degiuli, N.; Martić, I. Assessment of hydrodynamic characteristics of a full-scale ship at different draughts. *Ocean Eng.* **2018**, *156*, 135–152. [CrossRef]
4. Larsson, L.; Stern, F.; Visonneau, M. *Numerical Ship Hydrodynamics: An Assessment of the Gothenburg 2010 Workshop*; Springer: Berlin/Heidelberg, Germany, 2014. [CrossRef]
5. Razgallah, I.; Kaidi, S.; Smaoui, H.; Sergent, P. The impact of free surface modelling on hydrodynamic forces for ship navigating in inland waterways: Water depth, drift angle, and ship speed effect. *J. Mar. Sci. Technol.* **2018**, 1–22. [CrossRef]
6. Simonsen, C.D.; Otzen, J.F.; Joncquez, S.; Stern, F. EFD and CFD for KCS heaving and pitching in regular head waves. *J. Mar. Sci. Technol.* **2013**, *18*, 435–459. [CrossRef]
7. Toxopeus, S.L. Viscous-flow calculations for KVLCC2 in deep and shallow water. *Comput. Methods Appl. Sci.* **2013**, *29*, 151–169. [CrossRef]
8. Longo, J.; Stern, F. Effects of drift angle on model ship flow. *Exp. Fluids* **2002**, *32*, 558–569. [CrossRef]

9. Tahara, Y.; Longo, J.; Stern, F. Comparison of CFD and EFD for the Series 60 C B = 0.6 in steady drift motion. *J. Mar. Sci. Technol.* **2002**, *7*, 17–30. [CrossRef]
10. Kundu, P.; Cohen, I.M.; Dowling, D.R. *Fluid Mechanics*; Elsevier: Cambridge, MA, USA, 2012.
11. Wang, Z.Z.; Xiong, Y.; Shi, L.P.; Liu, Z.H. A numerical flat plate friction line and its application. *J. Hydrodyn.* **2015**, *27*, 383–393. [CrossRef]
12. Lopes, R.; Eca, L.; Vaz, G. On the Numerical Behavior of Rans-based Transition Models. *J. Fluids Eng.* **2019**, *142*, 1–14. [CrossRef]
13. Lopes, R.; Eca, L.; Vaz, G. *On the Decay of Free-stream Turbulence Predicted by Two-Equation Eddy-Viscosity Models*; NuTTS-2017: Wageningen, The Netherlands, 2017; pp. 1–6.
14. Wackers, J.; Koren, B.; Raven, H.C.; van der Ploeg, A.; Starke, A.R.; Deng, G.B.; Queutey, P.; Visonneau, M.; Hino, T.; Ohashi, K. Free-Surface Viscous Flow Solution Methods for Ship Hydrodynamics. *Arch. Comput. Methods Eng.* **2011**, *18*, 1–41. [CrossRef]
15. Perić, R.; Abdel-Maksoud, M. Reliable damping of free-surface waves in numerical simulations. *Ship Technol. Res.* **2016**, *63*, 1–13. [CrossRef]
16. Durbin, P.A.; Pettersson Reif, B.A. *Statistical Theory and Modelling for Turbulent Flow*, 2nd ed.; Wiley: Hoboken, NJ, USA, 2011.
17. Havelock, T. The Propagation of Groups of Waves in Dispersive Media, with Aplication to Waves on Water produced by a Travelling Disturbance. *Proc. R. Soc. London. Ser. A, Math. Phys. Sci.* **1933**, *140*, 359–377. [CrossRef]
18. Sorensen, R.M. Prediction of Vessel-Generated Waves with Reference to Vessels Common to the Upper Mississippi River System, US Army Corps of Engineers, Waterways Experiment Station, ENV Report 4; 1997. Available online: https://pdfs.semanticscholar.org/6ea7/49e2817a7e9d262e30ba3b5d07a9554a7f1b.pdf (accessed on 3 March 2020).
19. Soomere, T. Nonlinear components of ship wake waves. *Appl. Mech. Rev.* **2007**, *60*, 120–138. [CrossRef]
20. Caplier, C.; Rousseaux, G.; Calluaud, D.; David, L. Energy distribution in shallow water ship wakes from a spectral analysis of the wave field. *Phys. Fluids* **2016**, *28*, 107104. [CrossRef]
21. Fourdrinoy, J.; Caplier, C.; Devaux, Y.; Rousseaux, G.; Isae, C.U.D.P.; Jouteur, I.; Poitiers, U.; De France, F.; Martin, P.; Montpellier, U.; et al. The naval battle of actium and the myth of the ship-holder: The effect of bathymetry. *arXiv* **2019**, arXiv:1905.13024.
22. Gomit, G.; Rousseaux, G.; Chatellier, L.; Calluaud, D.; David, L. Spectral analysis of ship waves in deep water from accurate measurements of the free surface elevation by optical methods. *Phys. Fluids* **2014**, *26*. [CrossRef]
23. Elsherbiny, K.; Tezdogan, T.; Kotb, M.; Incecik, A.; Day, S. Experimental analysis of the squat of ships advancing through the New Suez Canal. *Ocean Eng.* **2019**, *178*, 331–344. [CrossRef]
24. Tunaley, J.K.E. *Ship Wakes in Shallow Waters*; LRDC Report: Pittsburgh, PA, USA, 2014; pp. 6–9.
25. Yang, R.; Shugan, I.V.; Fang, M. Kelvin ship wake in the wind and waves field and on the finite sea depth. *Environment* **2011**, *27*, 71–77. [CrossRef]
26. Suez Canal Authority. Suez Canal Rules of Navigation. 2019. Available online: https://www.suezcanal.gov.eg/English/Navigation/Pages/RulesOfNavigation.aspx (accessed on 6 January 2020).
27. Lee, B.W.; Lee, C. Equation for ship wave crests in the entire range of water depths. *Coast. Eng.* **2019**, *153*, 103542. [CrossRef]
28. Siemens. *Star-CCM+ User Guide Version 13.04*; Siemens: Munich, Germany, 2018.
29. Ferziger, J.H.; Peric, M. *Computational Methods for Fluid Dynamics*; Springer: Berlin/Heidelberg, Germany, 2002.
30. Wilcox, D.C. Formulation of the k-w Turbulence Model Revisited. *AIAA J.* **2008**, *46*, 2823–2838. [CrossRef]
31. Terziev, M.; Tezdogan, T.; Incecik, A. Application of eddy-viscosity turbulence models to problems in ship hydrodynamics. *Ships Offshore Struct.* **2019**. [CrossRef]
32. Pettersson Reif, B.A.; Mortensen, M.; Langer, C.A. Towards sensitizing the nonlinear v 2-f model to turbulence structures. *Flow Turbul. Combust.* **2009**, *83*, 185–203. [CrossRef]

33. Hirt, C.W.; Nichols, B.D. Volume of fluid (VOF) method for the dynamics of free boundaries. *J. Comput. Phys.* **1981**, *39*, 201–225. [CrossRef]
34. Muzaferija, S.; Peric, M. Computation of free-surface ows using interface- tracking and interface-capturing methods. In *Chapter 2, Nonlinear Water Wave Interaction, Computational Mechanics Publications*; Mahrenholtz, O., Markiewicz, M., Eds.; WIT Press: Southampton, UK, 1999.
35. Elsherbiny, K.; Terziev, M.; Tezdogan, T.; Incecik, A.; Kotb, M. Numerical and experimental study on hydrodynamic performance of ships advancing through different canals. *Ocean Eng.* **2019**, 106696. [CrossRef]
36. International Towing Tank Conference. *ITTC–Recommended Procedures and Guidelines-Practical guidelines for ship CFD Applications, 7.5-03-02-03 (Revision 01), ITTC–Recomm. Proced. Guidel. 19*; ITTC: Zürich, Switzerland, 2014.
37. Oberkampf, W.L.; Blottner, F.G. Issues in computational fluid dynamics code verification and validation. *AIAA J.* **1998**, *36*, 687–695. [CrossRef]
38. Yuan, Z.M. Ship Hydrodynamics in Confined Waterways. *J. Sh. Res.* **2019**, *63*, 1–14. [CrossRef]
39. Yuan, Z.M.; Zhang, X.; Ji, C.Y.; Jia, L.; Wang, H.; Incecik, A. Side wall effects on ship model testing in a towing tank. *Ocean Eng.* **2018**, *147*, 447–457. [CrossRef]
40. International Towing Tank Conference. *ITTC–Recommended Procedures and Guidelines Uncertainty Analysis, Example for Resistance Test*; ITTC: Zürich, Switzerland, 2002.
41. Roy, C.J. Review of code and solution verification procedures for computational simulation. *J. Comput. Phys.* **1997**, *205*, 131–156. [CrossRef]
42. Stern, F.; Wilson, R.; Shao, J. Quantitative V&V of CFD simulations and certification of CFD codes. *Int. J. Numer. Methods Fluids* **2006**, *50*, 1335–1355. [CrossRef]
43. Celik, I.B.; Ghia, U.; Roache, P.J.; Freitas, C. Procedure for Estimation and Reporting of Uncertainty Due to Discretization in CFD Applications. *J. Fluids Eng.* **2008**, *130*, 078001. [CrossRef]
44. Roache, P.J. Quantification of Uncertainty in Computational Fluid Dynamics. *Annu. Rev. Fluid Mech.* **1997**, *29*, 123–160. [CrossRef]
45. Eca, L.; Hoekstra, M. Evaluation of numerical error estimation based on grid refinement studies with the method of the manufactured solutions. *Comput. Fluids* **2009**, *38*, 1580–1591. [CrossRef]
46. Arnold-Bos, A.; Martin, A.; Khenchaf, A. Obtaining a ship's speed and direction from its Kelvin wake spectrum using stochastic matched filtering. In Proceedings of the International Geoscience and Remote Sensing Symposium (IGARSS), Barcelona, Spain, 23–27 July 2007; pp. 1106–1109.
47. Wu, Z. On the Estimation of a Moving Ship's Velocity and Hull Geometry Information from its Wave Spectra. Ph.D. Thesis, University of Michigan, Ann Arbor, MI, USA, 1992.
48. Lighthill, M.J. *Waves in Fluids*; Cambridge University Press: Cambridge, UK, 1990.
49. Carusotto, I.; Rousseaux, G. *The Cerenkov Effect Revisited: From Swimming Ducks to Zero Modes in Gravitational Analogues In Analogue Gravity Phenomenology*; Springer: Berlin/Heidelberg, Germany, 2013; pp. 109–144.
50. Crapper, G.D. Surface waves generated by a travelling pressure point. *Proc. R. Soc. London. Ser. A. Math. Phys. Sci.* **1964**, *282*, 547–558. [CrossRef]
51. Nakos, D.E.; Sclavounos, P.D. On steady and unsteady ship wave patterns. *J. Fluid Mech.* **1990**, *215*, 263. [CrossRef]
52. Tuck, E.O. Sinkage and Trim in Shallow Water of Finite Width. *Schiffstechnik* **1967**, *14*, 92–94.
53. Tuck, E.O. Shallow-Water Flows Past Slender Bodies. *J. Fluid Mech.* **1966**, *26*, 81–95. [CrossRef]
54. Jachowski, J. Assessment of ship squat in shallow water using CFD. *Arch. Civ. Mech. Eng.* **2008**, *8*, 27–36. [CrossRef]
55. Pena, B.; Muk-Pavic, E.; Ponkratov, D. Achieving a high accuracy numerical simulations of the flow around a full scale ship. In Proceedings of the International Conference on Offshore Mechanics and Arctic Engineering-OMAE, Scotland, UK, 9–14 June 2019; pp. 1–10. [CrossRef]
56. Whitham, G.B. *Linear and Nonlinear Waves*; Wiley-Interscience: Hoboken, NJ, USA, 2011.
57. Ma, C.; Zhu, Y.; He, J.; Zhang, C.; Wan, D.; Yang, C.; Noblesse, F. Nonlinear corrections of linear potential-flow theory of ship waves. *Eur. J. Mech. B/Fluids* **2018**, *67*, 1–14. [CrossRef]
58. Chen, X.; Zhu, R.; Ma, C.; Fan, J. Computations of linear and nonlinear ship waves by higher-order boundary element method. *Ocean Eng.* **2016**, *114*, 142–153. [CrossRef]

59. Wu, H.; Wu, J.; He, J.; Zhu, R.; Yang, C.J.; Noblesse, F. Wave profile along a ship hull, short farfield waves, and broad inner Kelvin wake sans divergent waves. *Phys. Fluids* **2019**, *31*. [CrossRef]
60. Noblesse, F.; He, J.; Zhu, Y.; Hong, L.; Zhang, C.; Zhu, R. Why can ship wakes appear narrower than Kelvin's angle? *Eur. J. Mech. -B/Fluids* **2014**, *46*, 164–171. [CrossRef]

Journal of
Marine Science and Engineering

MDPI

Article

Comparative Study of Air Resistance with and without a Superstructure on a Container Ship Using Numerical Simulation

Jun Seok [1] and Jong-Chun Park [2,*]

[1] Research Institute of Medium & Small Shipbuilding, Kangseo-gu, Busan 46757, Korea; jseok@rims.re.kr
[2] Department of Naval Architecture and Ocean Engineering, Pusan National University, Geumjeong-gu, Busan 46241, Korea
* Correspondence: jcpark@pnu.edu

Received: 16 March 2020; Accepted: 6 April 2020; Published: 9 April 2020

Abstract: This study investigated the resistance performance of ships, using the air resistance correction method. In general, air resistance is calculated using an empirical formula rather than a direct calculation, as the effect of air resistance on the total resistance of ships is relatively smaller than that of water. However, for ships with large superstructures, such as container ships, LNG (liquefied natural gas) carriers, and car-ferries, the wind-induced effects might influence the air resistance acting on the superstructure, as well as cause attitude (trim and sinkage) changes of the ship. Therefore, this study performed numerical simulations to compare the total resistance, trim, and sinkage of an 8000 TEU-class container, ship with and without superstructures. The numerical simulation conditions were verified by comparing them with the study results of the KCS (KRISO Container Ship) hull form. In addition, the differences in the above values between the two cases were compared using the coefficients calculated by the empirical formula to identify the effects on the air resistance coefficient.

Keywords: air resistance; container ship; superstructure; numerical simulation; trim

1. Introduction

Shipyards and ship design engineering companies are continuously making numerous efforts to improve the performance of their ships, to satisfy the requirements of clients and meet various environmental regulations.

The performance of a ship is determined by various factors, such as speed, fuel oil consumption (FOC), and deadweight. In particular, speed is the major indicator of a ship's performance and is one of the performance aspects that are guaranteed, through a sea trial after construction.

Although there are various methods, including attaching an appendage to improve the ship's speed, the most basic method is to improve the resistance performance by optimizing the hull form of a ship. Therefore, shipyards and ship design engineering companies continue to invest heavily in improving the existing hull forms or developing new hull forms. In addition, various methods are used to reliably estimate the resistance performance of newly developed ships.

Traditionally, model test using a basin has been employed to estimate the resistance performance of ships. However, with the recent developments in computer technologies, numerical simulations using computational fluid dynamics (CFD) have attracted attention as a replacement for experimental methods.

In the beginning, analysis using numerical simulations was performed only on the sub-surface portion of the ship, without considering the free surface. Since then, the analysis methods have evolved to consider other aspects, such as the free surface and variation in the ship's attitude for accurate performance estimation. In addition, full-scale numerical simulation [1–3] of a ship, which is

difficult to perform with the latest experimental methods, numerical simulation considering the hull roughness [4,5], and various other studies are underway.

In general, the estimation of resistance of a full-scale ship, through numerical simulations, is performed in the same method as in the experiment. First, a numerical simulation is performed for a model ship, which is a downsized model of a full-scale ship, and the total resistance value obtained from this simulation is used to estimate the resistance of the full-scale ship.

While estimating the resistance performance of a full-scale ship in the experimental method, as well as in the numerical simulation method, the air resistance acting on the superstructure, which has a relatively smaller effect on resistance performance than water, is estimated using an empirical formula without directly considering the superstructure [6].

However, for ships with large superstructures, such as container ships, LNG carriers, and car ferries, wind could not only affect the resistance acting on the superstructure but could also cause variation in the ship's attitude.

The variation in the ship's attitude is one of the factors that can directly affect the resistance performance [7–9]. As the resistance acting on the ship can increase or decrease according to the ship's attitude, an analysis that considers the superstructure is required for an accurate estimation of resistance performance.

Therefore, in this study, the effects of the presence or absence of the superstructure were evaluated by analyzing the resistance performance in two different cases; a model ship of an 8000 TEU-class container ship, with superstructures and without superstructures.

2. Model-Ship Correlation Method

2.1. Details of the 8000 TEU-Class Container Ship

The ship used for the analysis of resistance performance was an 8000 TEU-class container ship with 322.6-m L.B.P. (length between perpendiculars), 45.6-m breadth, and 24.6-m depth. The details are as provided in Table 1. The model ship for numerical simulations was set to 7.279 m, which was the same size as the KCS (3600 TEU KRISO Container ship).

In order to consider the superstructure, the ship was modeled with the containers loaded, as shown in Figure 1a, and the container was designed in a simple rectangular shape. In addition, breakwater, hatch cover, and accommodation were included in the modeling, whereas the lashing structures for the containers were omitted. Figure 1b shows a ship without superstructures, generally used for experiment in basin and numerical simulations.

Table 1. Principal dimensions of the 8000 TEU-class container ship (center of gravity means, from A.P. (Aft Perpendicular) to F.P. (Forward Perpendicular), centerline, from baseline to upward).

Item	Full Scale	Model Scale
Scale ratio	1:1	1/44.322
L.B.P (m)	322.6	7.279
Breadth (m)	45.6	1.029
Depth (m)	24.6	0.555
Draft (m)	13.0	0.293
Volume of displacement (m^3)	112,693.0	1.294
Wetted surface area (m^2)	16644.0	8.473
Center of gravity (m)	154.487, 0.0, 7.237	3.486, 0.0, 0.163
k_{xx}/Breadth	0.4	
k_{yy}/L.B.P, k_{zz}/L.B.P	0.25	

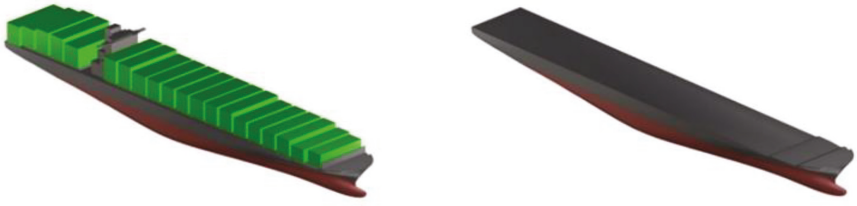

(a) (b)

Figure 1. Modeling of the 8000 TEU-class container ship. (**a**) Design of model with superstructure. (**b**) Design of model without superstructure.

2.2. Full-Scale Prediction Method

In the full-scale prediction method, the total resistance coefficient (C_{TS}) was calculated by a two-dimensional method, as the sum of the frictional resistance coefficient (C_F), residuary resistance coefficient (C_R), correlation allowance (C_A), and air resistance coefficient (C_{AA}), as shown in Equation (1). C_F is calculated according to the ITTC-1957 (International Towing Tank Conference-1957) frictional correlation line, C_A is calculated by the Harvald formulation, and C_{AA} is calculated by the ITTC method [6].

$$C_{TS} = C_F + C_R + C_A + C_{AA} \tag{1}$$

$$C_F = \frac{0.075}{(\log R_N - 2)^2} \tag{2}$$

$$C_R = C_{TM} - C_{FM} \tag{3}$$

$$C_A = \frac{0.5\log(\Delta) - 0.1(\log(\Delta))^2}{10^3} \tag{4}$$

$$C_{AA} = C_{DA}\frac{\rho_A \cdot A_{VS}}{\rho_S \cdot S_S} \tag{5}$$

where Δ is the displacement in ton, R_N is the Reynolds number, and C_{DA} is the air drag coefficient of the ship above the water line that can be determined through the wind tunnel testing or calculations. Typically, 0.8 can be used as the default value of C_{DA} in the range 0.5–1.0 if the specific value is not known [6]. ρ_A is the density of air, ρ_S is the density of seawater, A_{VS} is the projected area of the ship above the water line to the transverse plane, and S_S is the wetted surface area of the ship. The subscript M signifies the model and S signifies the full-scale ship.

3. Numerical Simulation

In this study, the commercial software Star-CCM+ was used to perform the numerical simulation. The governing equations were the continuity equation and momentum equation for three-dimensional unsteady incompressible viscous flow, shown in Equations (6) and (7) [10].

$$\frac{\partial U_i}{\partial x_i} = 0 \tag{6}$$

$$\frac{\partial U_i}{\partial t} + U_j\frac{\partial (U_i)}{\partial x_j} = -\frac{1}{\rho}\frac{\partial p}{\partial x_i} + \frac{1}{\rho}\frac{\partial}{\partial x_j}\left(\mu\frac{\partial U_i}{\partial x_j} - \rho\overline{u_i' u_j'}\right) + B \tag{7}$$

where U is the average velocity vector, x is the coordinate system, t is the time, ρ is the density, p is the pressure, and μ is the coefficient of viscosity. $\rho\overline{u_i' u_j'}$ is the turbulent shear stress that is determined using a turbulence model, and B is the body force. In this study, a realizable k-ϵ model was used for the turbulence model.

The governing equations mentioned above were discretized using the finite volume method (FVM). The convection and diffusion terms were discretized with the second-order upwind scheme. The second-order implicit scheme was used for temporal discretization.

The semi-implicit method for a pressure-linked equations (SIMPLE) algorithm was used for velocity-pressure coupling. The volume of fluid (VOF) method with a high-resolution interface capturing (HRIC) algorithm was used to define the water and air area of the free surface.

Equation (8) related to the translation of the center of mass of the body, and Equation (9) related to the rotation of the body, formulated with the origin at the center of mass of the body.

$$m\frac{dv}{dt} = f \tag{8}$$

$$M\frac{d\vec{\omega}}{dt} + \vec{\omega} \times M\vec{\omega} = \mathrm{n} \tag{9}$$

where m is the mass of the body, f is the force acting on the body, v is velocity of the center of mass, M is the tensor of the inertia moments, $\vec{\omega}$ is the angular velocity of the rigid body, and n is the moment acting on the body.

3.1. Initial Conditon and Boundary Condition

In the numerical simulation, the length, breadth, and height directions were set as 4.0 L, 1.5 L, and 2.5 L, as shown in Figure 2a. Here, L is the L.B.P. of the ship.

As shown in Figure 2b, velocity inlet, pressure outlet, symmetry, no-slip wall of the ship, and free-slip wall conditions were used for each boundary. To limit the calculation time, only half the breadth of the ship was modeled and the symmetry boundary condition was applied. Heave and pitch motion were considered by using the dynamic body fluid interaction (DFBI) method for the translation and rotation of the entire domain. The total calculation time of the numerical simulation was 90 s and the time increment was 0.02 s.

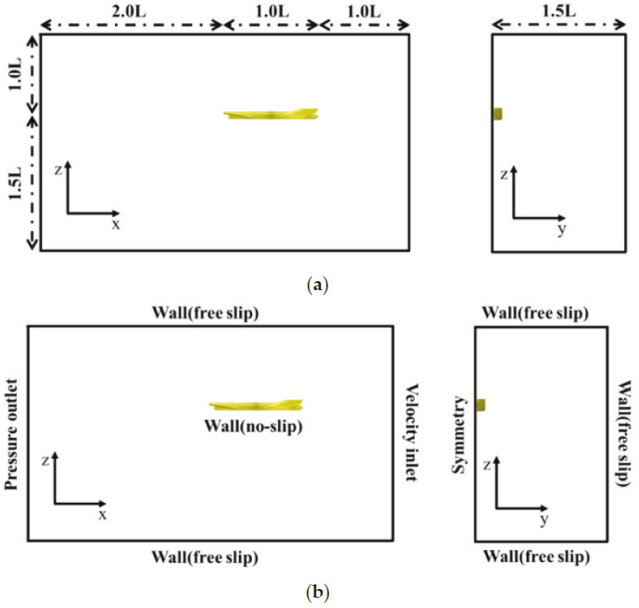

Figure 2. Computational domain and boundary conditions for numerical simulation; (**a**) computational domain and (**b**) boundary condition.

The above conditions were verified by conducting numerical simulations using the KCS hull form. KCS is a popular hull form like KVLCC (KRISO Very Large Crude-Oil Carrier) and DTMB (David Taylor Model Basin) it is often used to verify the conditions of numerical simulation through comparisons with experimental data [11–14]. Table 2 shows the main particulars of the KCS hull form; numerical simulation was performed for the model scale.

Table 2. Principal dimensions of KCS (center of gravity means (from A.P. to F.P., centerline, from baseline to upward)).

Item	Model Scale
Scale ratio	1/31.599
L.B.P (m)	7.279
Breadth (m)	1.019
Depth (m)	0.601
Draft (m)	0.342
Volume of displacement (m^3)	1.649
Wetted surface area (m^2)	9.544
Center of gravity (m)	3.532, 0.0, 0.230
k_{xx}/Breadth	0.4
k_{yy}/L.B.P, k_{zz}/L.B.P	0.25

3.2. Grid System

The grid system for the numerical simulation consisted of approximately 1.5 million cells, as shown in Figure 3. It was created using surface re-mesher, prism layer, and trimmer grid, which are auto-meshing methods provided by Star-CCM+. Five layers were generated in the normal direction to the hull, to consider the viscous flow field. In addition, we arranged the grid more closely around the free surface, to consider the wave generated by the hull. The minimum size of a cell was set to 1.0×10^{-2} m and Y^+ was less than 100 for the entire area of the hull, as shown in Figure 4. Additional numerical simulation was performed to validate the grid sensitivity of the 8000 TEU container ship, with the superstructure, as shown in Table 3.

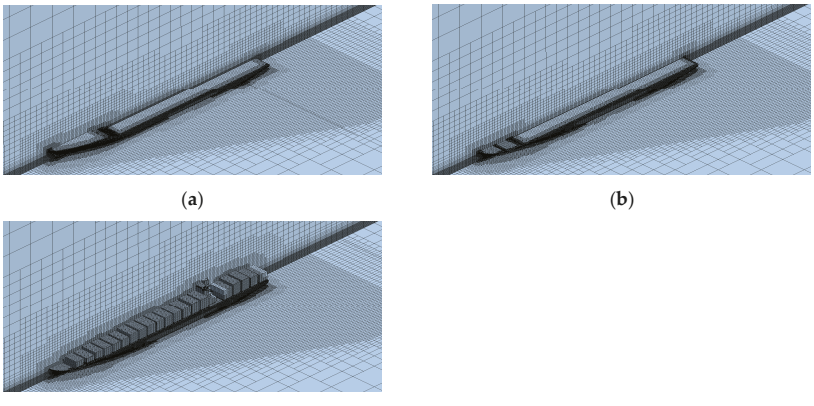

(**a**) (**b**) (**c**)

Figure 3. Grid system for numerical simulation. (**a**) KCS, (**b**) 8000 TEU-class container ship without superstructure, and (**c**) 8000 TEU-class container ship with superstructure.

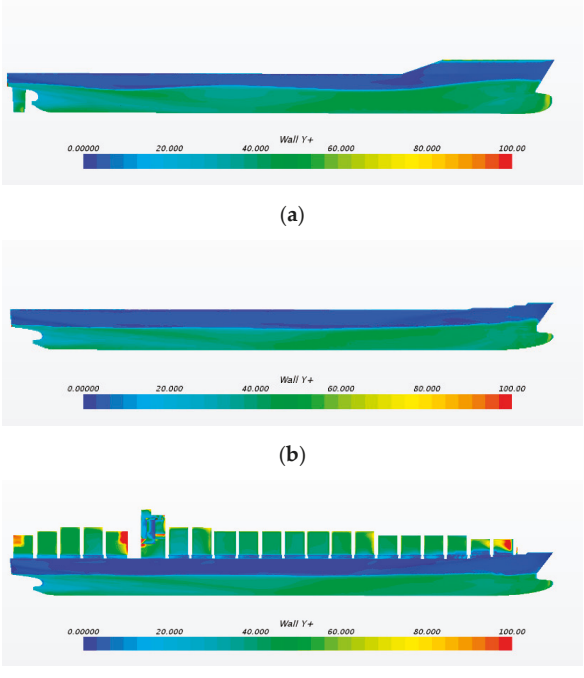

Figure 4. Y^+ entire area of the hull. (**a**) KCS, (**b**) 8000 TEU-class container ship without superstructure, and (**c**) 8000 TEU-class container ship with superstructure.

Table 3. Results of the grid dependency test of the 8000 TEU container ship, with superstructure.

F_N	$C_{TM} \times 10^3$		
	Coarse (Approx. 1.0 million)	**Medium (Approx. 1.5 million)**	**Fine (Approx. 2.0 million)**
0.274	3.823	3.771	3.750

As the number of grids increased from coarse to fine, C_{TM} tended to converge. In particular, since the difference in C_{TM} between the medium and the fine grid system was less than 1%, so the medium grid was applied to reduce the calculation time in numerical simulation.

4. Results of the Numerical Simulation

4.1. Validation Study

Numerical simulations were conducted under six different speed conditions (Froude number (F_N) of 0.108, 0.152, 0.195, 0.227, 0.260, 0.282) for validation of the simulation conditions. The results are as shown in Figure 5.

As shown in Figure 5a, the sinkage tended to increase as the speed increased. As shown in Figure 5b, the trim by stern tended to increase as speed increased, when F_N was at or below 0.269 and decreased when F_N exceeded 0.269. Overall, under the six speed conditions, the results for trim and sinkage were quantitatively similar to the experimental simulation results [11], when compared with the numerical simulation results of Villa et al. [14]. However, a quantitative difference from the experiment results was observed for the trim when F_N was less than 0.15 or more than 0.28, and for

the sinkage when F_N was 0.16 or below. A difference of approximately 3% was observed from the experimental value of the total resistance coefficient, at the low speed of F_N = 0.108. Overall, the results were quantitatively similar to the experimental results under all the six speed conditions. It was also relatively more consistent with the experimental results than the numerical simulation results of Villa et al. [14], as shown in Figure 5c.

Therefore, as the accuracy of the numerical simulations for the ship's attitude appeared to be relatively low in the low-speed range (F_N < 0.16) or in the high-speed range (F_N > 0.28), the numerical simulations of the 8000 TEU-class container ship were conducted in the F_N range of 0.16–0.27.

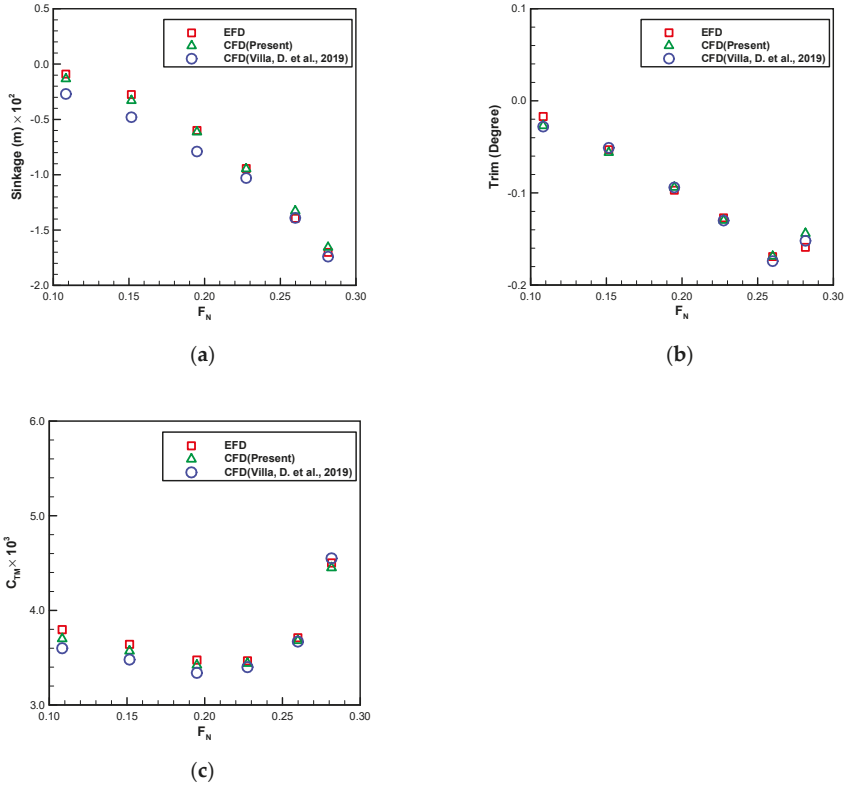

Figure 5. Comparison of KCS simulation results between EFD (Experimental Fluid Dynamics) and computational fluid dynamics (CFD) (a positive trim value was defined bow up and positive sinkage value was defined upward). (**a**) Sinkage; (**b**) trim; and (**c**) total resistance coefficient.

4.2. 8000 TEU-Class Container Ship

Numerical simulations were conducted under five different speed conditions (Froude number (F_N) 0.165, 0.192, 0.219, 0.247, and 0.274) for validation of the simulation conditions in a model scale. The results are as shown in Table 4 and Figure 6.

Similar to the KCS hull form, the sinkage tended to increase as the speed increased, and trim by head tended to increase as speed increased, when F_N was 0.247 or below and decreased when F_N was above 0.247. Sinkage was observed at a significant level in all cases where the superstructures were absent, and varied by approximately 3% to 9% between cases with superstructures. However, even as the speed increased, the quantitative difference remained consistent at approximately 0.0004. Trim was

observed at a significant level at F_N of 0.2 or below when the superstructures were considered and at F_N of 0.2 or above when the superstructures were not considered.

Table 4. Comparison of the simulation results with and without a superstructure (RD—relative difference).

F_N	Sinkage (m) × 10^2			Trim (Degree)		
	With Superstructure	Without Superstructure	RD (%)	With Superstructure	Without Superstructure	RD (%)
0.165	−0.393	−0.433	9.2	−0.035	−0.032	−9.4
0.192	−0.558	−0.597	6.5	−0.055	−0.050	−10.0
0.219	−0.763	−0.807	5.5	−0.067	−0.069	2.9
0.247	−1.030	−1.070	3.7	−0.078	−0.082	4.9
0.274	−1.350	−1.400	3.6	−0.062	−0.065	4.6

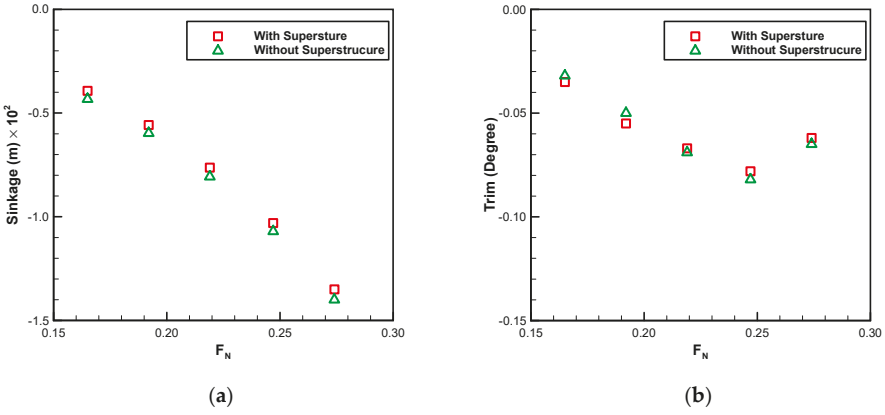

Figure 6. Comparison of simulation results with and without superstructures (a positive trim value was defined bow up and positive sinkage value was defined upwards). (**a**) Sinkage and (**b**) trim.

Wave patterns tended to become similar as the speed increased, with the biggest difference observed at the lowest speed (F_N 0.165) in Figure 7. Here, the vector distribution around the ship according to the presence or absence of the superstructure is shown in Figure 8.

C_{TM} differed by a maximum of approximately 2%, under five different speed conditions, with and without the superstructures, as shown in Figure 9a. When F_N was 0.2 or less, the resistance was higher in the case without superstructure and when F_N was 0.2 or above it showed opposite results. This showed a typical tendency where the trim by head had a relatively lower resistance, compared to the even conditions, or the trim by stern [15,16].

To analyze the effects of the presence or absence of superstructures on the resistance, the resistance performance of the full-scale ship was estimated using Equations (1)–(5). Here, C_{AA} obtained from Equation (5) was calculated using the coefficient in Table 5, for the case without the superstructure and C_{AA} was set to 0, when the superstructure was considered.

Table 6 and Figure 9b show that depending on whether C_{AA} is considered or not, C_{TS} differs by approximately 1% to 5%, under the six speed conditions and the difference was significant at approximately 5% when F_N was relatively low at 0.192 or below.

This indicated that calculation using an empirical formula could lead to over-estimation of the resistance performance of a full-scale ship, compared to a direct numerical interpretation, when considering the superstructures.

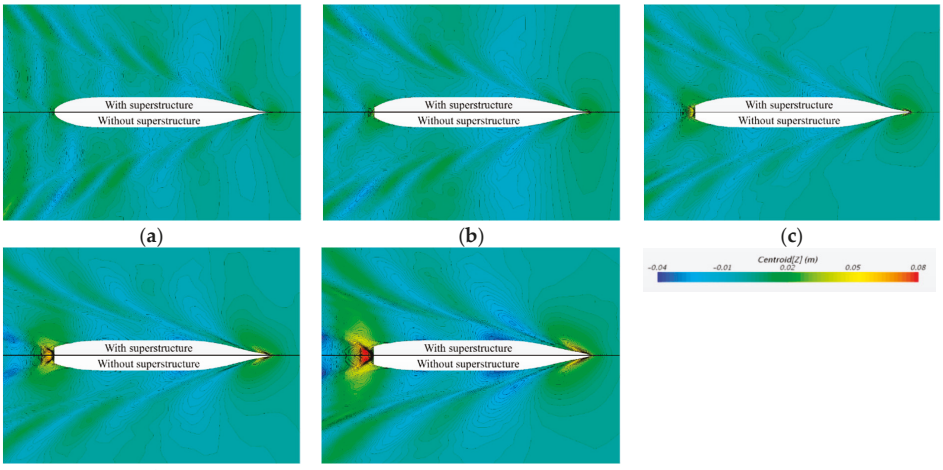

Figure 7. Comparison of wave pattern between the 8000 TEU container ship with superstructure and without superstructure. (**a**) F_N 0.165, (**b**) F_N 0.192, (**c**) F_N 0.219, (**d**) F_N 0.247, and (**e**) F_N 0.274.

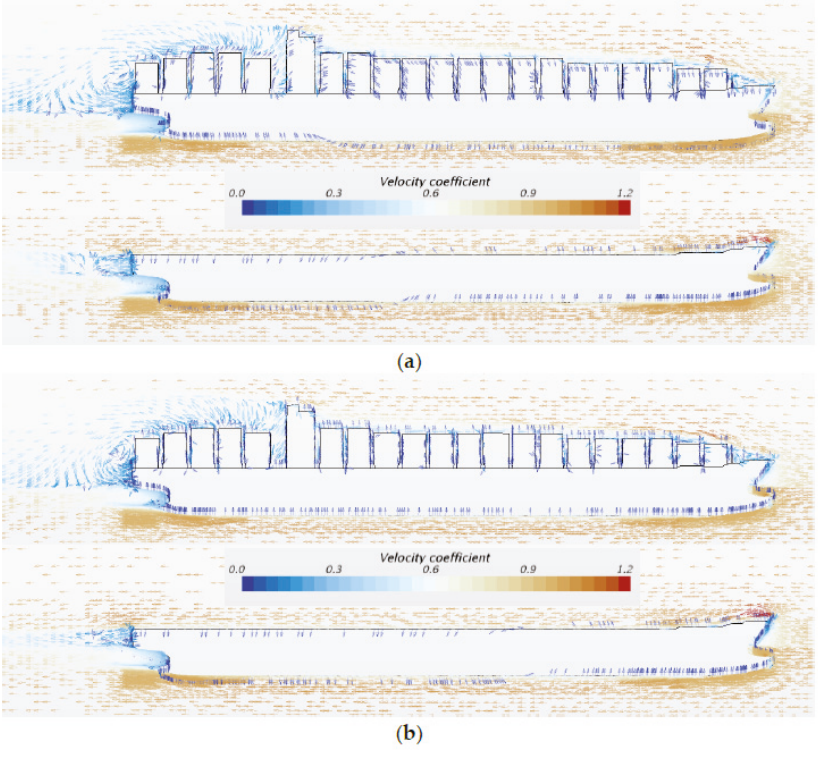

Figure 8. Velocity vector around the 8000 TEU-class container ship (velocity coefficient was defined as velocity divided by the inlet velocity). (**a**) F_N 0.165 and (**b**) F_N 0.274.

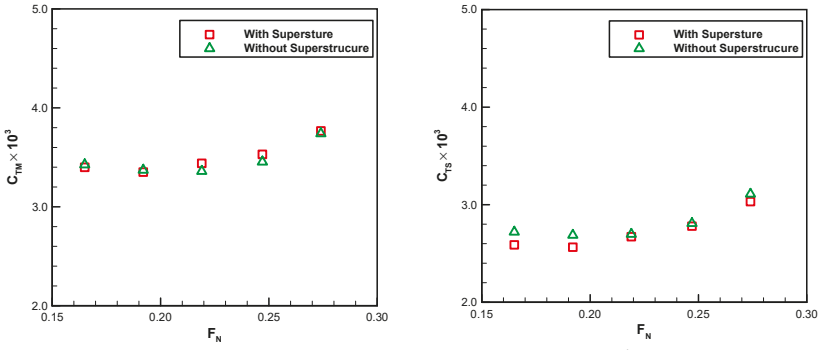

Figure 9. Comparison of total resistance coefficient for ships, with and without a superstructure. (**a**) Model scale and (**b**) full scale.

To analyze the effects of overestimating the C_{AA}, the default value of C_{DA} by ITTC was compared with the C_{AA} for a container ship, calculated by Kristensen and Lützen [17] and the result of the equations proposed by Fujiwara et al. [18].

The C_{AA} proposed by Kristensen and Lützen [17] estimates the air resistance coefficient according to the loading capacity of a container ship, as shown in Equation (10), and is not more than 0.09.

$$C_{AA} \cdot 1000 = 0.28 \cdot TEU^{-0.126} \text{ less than } 0.09 \tag{10}$$

Table 5. Factors for calculating the air resistance coefficient.

C_{DA}	ρ_A	ρ_S	A_{VS}	S_S
0.8	1.23 kg/m^3	1025.9 kg/m^3	1742.1 m^2	16644.0 m^2

Table 6. Comparison of resistance coefficients with and without superstructure.

F_N	Condition	C_{TM} $\times 10^3$	C_{FM} $\times 10^3$	C_R $\times 10^3$	C_{FS} $\times 10^3$	C_A $\times 10^3$	C_{AA} $\times 10^3$	C_{TS} $\times 10^3$
0.165	With superstructure	3.403	2.153	1.249	1.369	−0.026	-	2.593
	Without superstructure	3.430		1.276			0.1	2.720
	RD (%)	0.8	-	2.1	-		-	4.7
0.192	With superstructure	3.355	2.105	1.250	1.345		-	2.568
	Without superstructure	3.375		1.269			0.1	2.688
	RD (%)	0.6	-	1.5	-		-	4.5
0.219	With superstructure	3.443	2.065	1.377	1.324		-	2.676
	Without superstructure	3.363		1.298			0.1	2.697
	RD (%)	−2.4	-	−6.1	-		-	0.8
0.247	With superstructure	3.534	2.030	1.504	1.307		-	2.784
	Without superstructure	3.457		1.427			0.1	2.808
	RD (%)	−2.2	-	−5.4	-		-	0.9
0.274	With superstructure	3.771	2.000	1.771	1.291		-	3.036
	Without superstructure	3.744		1.743			0.1	3.109
	RD (%)	−0.7	-	−1.6	-		-	2.3

The Fujiwara formula [18], which is mainly used for resistance correction in sea trials, is shown in Equations (11)–(14). The value of each parameter used in the calculation is provided in Table 7; Table 8. Figure 10 shows the profile of the 8000 TEU-class container ship used to calculate the coefficient values.

$$C_{DA} = C_{LF}\cos\varphi_{WR} + C_{XLI}\left(\sin\varphi_{WR} - \frac{1}{2}\sin\varphi_{WR}\cos^2\varphi_{WR}\right)\sin\varphi_{WR}\cos\varphi_{WR} + C_{ALF}\sin\varphi_{WR}\cos^3\varphi_{WR} \quad (11)$$

$$C_{LF} = \beta_{10} + \beta_{11}\frac{A_{YV}}{L_{OA}B} + \beta_{12}\frac{C_{MC}}{L_{OA}} \quad (12)$$

$$C_{XLI} = \delta_{10} + \delta_{11}\frac{A_{YV}}{L_{OA}h_{BR}} + \delta_{12}\frac{A_{XV}}{Bh_{BR}} \quad (13)$$

$$C_{ALF} = \varepsilon_{10} + \varepsilon_{11}\frac{A_{OD}}{A_{YV}} + \varepsilon_{12}\frac{B}{L_{OA}} \quad (14)$$

Here, A_{OD} is the lateral projected area of the superstructures, A_{XV} is the area of the maximum transverse section exposed to the wind, A_{YV} is the projected lateral area above the waterline, B is the ship breadth, L_{OA} is the overall length, C_{MC} is the horizontal distance from the mid-ship section to the center of the lateral projected area, h_{BR} is the height of the top of the superstructure, and φ_{WR} is the relative wind direction (0 indicates the wind heading). The values of the non-dimensional parameters (β_{ij}, δ_{ij}, ε_{ij}) are listed in Table 8.

The calculation results of C_{DA} are as shown in Table 9. Here, C_{AA} was calculated using the method proposed by Kristensen and Lützen [17], which is shown in Equation (10). The ITTC value was the counter-calculated value of C_{DA}, using Equation (5). The value of 0.67 calculated by the Fujiwara formula was the same result as the C_{DA} value of the 6800 TEU-class container ship, with containers in the laden condition, provided by ITTC [19]. The result indicated that ships with typical forms, such as a container ship, would show similar results.

The C_{DA} value was 16% lesser with the Fujiwara formula and 10% lesser with the method proposed by Kristensen and Lützen [17] than the ITTC value of 0.8, which was the default value of C_{DA}.

The results of estimating the total resistance coefficient by applying the C_{DA} calculated by the respective methods are shown in Table 10 and Figure 11. All three methods over-estimated the resistance values when compared with the numerical simulations in the case where the superstructures were considered, but the quantitative differences were reduced by using a C_{DA} value lower than the default value. For the Fujiwara formula, which used the lowest C_{DA} value, the difference was approximately at a 4%lower speed of F_N at 0.192 or below, but decreased to 2% or below at higher F_N.

Table 7. Parameters for calculating the Fujiwara formula.

A_{OD}	A_{XV}	A_{YV}	L_{OA}	B	C_{MC}	h_{BR}	φ_{WR}
4774.0 m^2	1742.1 m^2	8806.1 m^2	339.4 m	45.6 m	−10.8 m	45.0 m	0°

Table 8. Non-dimensional parameters for calculating the Fujiwara formula.

Parameter	i	j		
		0	**1**	**2**
β_{ij}	1	0.922	−0.507	−1.162
	2	−0.018	5.091	−10.367
δ_{ij}	1	−0.458	−3.245	2.313
	2	1.901	−12.727	−24.407
ε_{ij}	1	0.585	0.906	−3.239
	2	0.314	1.117	-

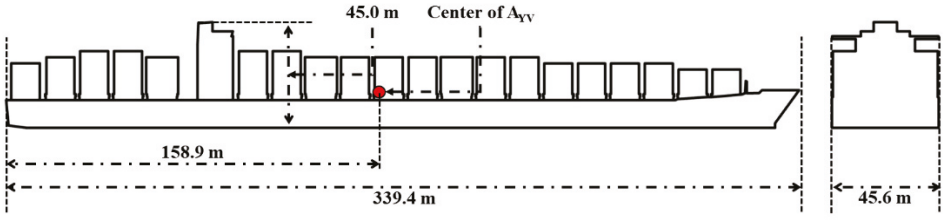

Figure 10. Schematic profile above the waterline for calculating the Fujiwara formula.

Table 9. Comparison of C_{DA} through different calculating methods.

Coefficient	ITTC (Default)	Fujiwara Formula	Kristensen and Lützen (2013)
C_{DA}	0.8	0.67	0.72
$C_{AA} \times 10^3$	0.100	0.084	0.090

Table 10. The total resistance coefficient according to C_{DA}.

F_N	$C_{TS} \times 10^3$			
	With Superstructure	Without Superstructure	Fujiwara Formula	Kristensen and Lützen (2013)
0.165	2.593	2.720	2.704	2.710
0.192	2.568	2.688	2.672	2.678
0.219	2.676	2.697	2.681	2.686
0.247	2.784	2.808	2.792	2.797
0.274	3.036	3.109	3.092	3.098

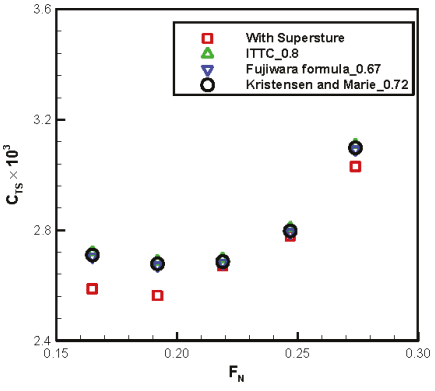

Figure 11. Comparison of total resistance coefficient by C_{DA}.

5. Conclusions

In this study, a numerical simulation was conducted on the 8000 TEU-class container ship to study the variation in resistance performance, according to the presence or absence of superstructures on a ship. Prior to the numerical simulation for the 8000 TEU-class container ship, numerical simulations using the KCS hull form were conducted to verify the numerical simulation conditions. The numerical simulation results of the KCS hull form for total resistance acting on the ship, showed a similar tendency as that observed for the experimental results, with a quantitative difference of approximately less than 3%. However, in the case of trim and sinkage, as excessive quantitative differences were observed at low and high speeds, numerical simulations for the 8000 TEU-class container ship was conducted at the F_N range of 0.16–0.27. The results of the study are summarized below:

- Trim

Trim tended to increase in volume as the speed increased at F_N of 0.247 or below and decreased at F_N above 0.247. Trim was significant with superstructures when F_N was 0.2 or below and without superstructures when F_N was 0.2 or above.

- Sinkage

Sinkage tended to increase as the speed increased. In the absence of superstructures, sinkage was significant with a difference of approximately 3% to 9% in the cases with superstructures. However, even as the speed increased, the quantitative difference remained consistent at approximately 0.0004.

- Total resistance coefficient

Under the five speed conditions, C_{TM} differed by a maximum of approximately 2% between ships, with and without superstructures. Here, when F_N was 0.2 or less, the resistance was higher in the case without superstructure and when F_N was 0.2 or above it showed the opposite results.

C_{TS} differed by approximately 1% to 5%, under the six speed conditions. The difference increased to approximately 5%, when F_N was at a relatively low speed of 0.192 or below. Overall, using an empirical formula overestimated the resistance performance of a full-scale ship in comparison to direct numerical analysis, when considering superstructures.

- Air resistance

To identify the effects of C_{DA}, C_{AA} was calculated using the method proposed by Kristensen and Lützen [17] and the Fujiwara formula [18]. The total resistance of the full-scale ship was estimated by incorporating the above result.

Both methods showed similar results as those of the numerical simulations that considered superstructures, when compared with the results obtained with C_{DA} of 0.8, which was the ITTC-proposed default value. However, a difference of approximately 4% was observed at the low speed of F_N = 0.192 or below. It is believed that the resistance performance of a full-scale ship could be more accurately estimated by calculating and using the C_{DA} obtained through wind tunnel testing, empirical formulas, and numerical analysis, rather than using the default value suggested by ITTC.

In addition, significant differences observed at low speeds were considered to be caused by the use of identical C_{AA} at all speeds. This is because C_{DA} was calculated in the high-speed range where the effects of the Reynolds number was absent through the Reynolds effect test, in the wind tunnel test or numerical simulation. Therefore, it might have led to errors in estimating the resistance performance of the ship at low speeds.

As mentioned above, it showed the difference in resistance performance between empirical methods and CFD with superstructure. This is because it was calculated only for the wind resistance, using the area of the superstructure and the wind load coefficient in the empirical methods. Thus, it did not consider the increase in resistance due to a change in the attitude of the ship in the empirical methods. Therefore, it was thought that a numerical simulation including superstructure for increasing accuracy about estimation of resistance performance should be performed. Especially, it was expected to be more useful for ships such as automobile ferries and LNG carriers, with a constant superstructure under ballast conditions. However, it was deemed necessary to conduct further studies on the methods of calculating air resistance, in relation to the presence or absence of superstructures and on various types of ships with large superstructures, in order to accurately estimate the resistance performance of a full-scale ship.

Author Contributions: J.S.; writing—original draft preparation; J.-C.P.; writing—review and editing. All authors have read and agreed to the published version of the manuscript.

Funding: This work was supported by the Technology Innovation Program (20000721, Development of Autopilot applicated collision avoidance technology for medium and large vessel) funded by the Ministry of Trade, Industry & Energy (MOTIE, Korea).

Conflicts of Interest: The authors declare no conflict of interest

References

1. Tezdogan, T.; Demirel, Y.K.; Kellett, P.; Khorasanchi, M.; Incecik, A.; Turan, O. Full-scale unsteady RANS CFD simulations of ship behaviour and performance in head seas due to slow steaming. *Ocean Eng.* **2015**, *97*, 186–206. [CrossRef]
2. Tezdogan, T.; Incecik, A.; Turan, O. Full-scale unsteady RANS simulations of vertical ship motions in shallow water. *Ocean Eng.* **2016**, *123*, 131–145. [CrossRef]
3. Wang, C.; Sun, S.; Li, L.; Ye, L. Numerical prediction analysis of propeller bearing force for full-scale hull–propeller–rudder system. *Int. J. Naval Archit. Ocean Eng.* **2016**, *8*, 589–601. [CrossRef]
4. Demirel, Y.K.; Turan, O.; Incecik, A. Predicting the effect of biofouling on ship resistance using CFD. *App. Ocean Res.* **2017**, *62*, 100–118. [CrossRef]
5. Song, S.; Demirel, Y.K.; Atlar, M. An investigation into the effect of biofouling on the ship hydrodynamic characteristics using CFD. *Ocean Eng.* **2019**, *175*, 122–137. [CrossRef]
6. ITTC. ITTC. ITTC Recommended Procedures and Guidelines. In *1978 ITTC Performance Prediction Method*; ITTC: Zurich, Switzerland, 2017.
7. Islam, H.; Soares, G. Effect of trim on container ship resistance at different ship speeds and drafts. *Ocean Eng.* **2019**, *183*, 106–115. [CrossRef]
8. Seo, D.W.; Park, H.S.; Han, K.M. Analysis of resistance performance for various trim conditions on container ship using CFD. *J. Ocean Eng. Technol.* **2015**, *29*, 224–230. [CrossRef]
9. Sun, J.; Tu, H.; Chen, Y.; Xie, D.; Zhou, J. A study on trim optimization for a container ship based on effects due to resistance. *J. Ship Res.* **2016**, *60*, 30–47. [CrossRef]
10. CD-Adapco. *STAR-CCM+ User Guide, Version 9.02*; CD-Adapco: Melville, NY, USA, 2014.
11. Kim, W.J.; Van, S.H.; Kim, D.H. Measurement of flows around modern commercial ship models. *Exp. Fluids* **2001**, *31*, 567–578. [CrossRef]
12. Bakica, A.; Gatin, I.; Vukčević, V.; Jasak, H.; Vladimir, N. Accurate assessment of ship-propulsion characteristics using CFD. *Ocean Eng.* **2019**, *175*, 149–162. [CrossRef]
13. Park, D.W.; Lee, S.B. The sensitivity of ship resistance to wall-adjacent grids and near-wall treatments. *Int. J. Naval Archit. Ocean Eng.* **2018**, *10*, 683–691. [CrossRef]
14. Villa, D.; Gaggero, S.; Gaggero, T.; Tani, G.; Vernengo, G.; Viviani, M. An efficient and robust approach to predict ship self-propulsion coefficients. *Appl. Ocean Res.* **2019**, *92*, 101862. [CrossRef]
15. Park, D.W.; Lee, S.B.; Chung, S.S.; Seo, H.W.; Kwon, J.W. Effects of trim on resistance performance of a ship. *J. Soc. Naval Archit. Korea* **2013**, *50*, 88–94. [CrossRef]
16. Han, K.M.; Park, H.S.; Seo, D.W. Study on Resistance Component of Container Ship According to Trim Conditions. *J. Ocean Eng. Technol.* **2015**, *29*, 411–417. [CrossRef]
17. Kristensen, H.O.; Lützen, M. *Prediction of Resistance and Propulsion Power of Ships*; Project No. 2010-56; Emissionsbeslutningsstøttesystem Work Package 2, Report No. 04; Technical University of Denmark and University of Southern Denmark: Copenhagen, Denmark, 2013.
18. Fujiwara, T.; Ueno, M.; Ikeda, Y. A new estimation method of wind forces and moments acting on ships on the basis of physical component models. *J. Japan Soc. Naval Archit. Ocean Eng.* **2005**, *2*, 243–255. [CrossRef]
19. ITTC. *ITTC Recommended Procedures and Guidelines: Preparation, Conduct and Analysis of Speed/Power Trials*; ITTC: Zurich, Switzerland, 2017.

Journal of
Marine Science and Engineering

MDPI

Article

Numerical Simulation and Validation in Scrubber Wash Water Discharge from Ships

Yong-Seok Choi [1] and Tae-Woo Lim [2,*]

[1] Division of Marine System Engineering, Korea Maritime and Ocean University, Busan 49112, Korea; choiys@kmou.ac.kr
[2] Division of Marine Engineering, Korea Maritime and Ocean University, Busan 49112, Korea
* Correspondence: kyunlim@kmou.ac.kr

Received: 12 March 2020; Accepted: 7 April 2020; Published: 10 April 2020

Abstract: A regulation on the sulfur emissions of ships sailing in global sea areas has been enforced since 1 January 2020. In this new regulation, ships are required to use low-sulfur fuel oils or to install an after-treatment equipment, such as a scrubber. Open and hybrid scrubbers wash the exhaust gas using seawater and then discharge the wash water overboard. According to the regulation promulgated by the International Maritime Organization (IMO) Marine Environment Protection Committee (MEPC), the wash water must have a pH of 6.5 or higher at 4 m from the discharge point. Wash water is generally acidic, with a pH of 2.5–3.5, whereas seawater is alkaline, with a pH of approximately 8.2. The wash water is dispersed after being discharged overboard through a nozzle, and its pH is restored through dilution with the surrounding seawater. In this study, the pH was calculated by using a theoretical chemical reaction model, and then the dispersion of wash water was analyzed using CFD simulation. This study describes the process of selecting the appropriate turbulent Schmidt number in a wide range of nozzle diameters. Finally, the appropriate nozzle diameter was determined based on the initial pH of the discharged scrubber wash.

Keywords: CFD; dispersion; pH; turbulent Schmidt number; scrubber; wash water

1. Introduction

In January 2020, the International Maritime Organization (IMO) enforced a regulation stipulating that the sulfur content of fuel used by ships sailing in the global sea area should be reduced from 3.5% to 0.5% [1,2]. In the future, it is expected that much attention will be given on regulations on emissions from ships. Shipping companies have searched for measures to comply with this new regulation on SOx emission. The most popular measure is the use of low-sulfur fuel oil (LSFO). For most ships that do not use LSFO, a scrubber was installed instead to remove SOx. Besides using LSFO or a scrubber, another option is to use alternative fuels, such as liquefied natural gas [3,4].

A scrubber is a washing system for exhaust gas. Scrubbers are classified into open-loop system, closed-loop system, and hybrid system, which combines the first two systems [5]. The open-loop system washes the exhaust gas using alkaline seawater and discharges the wash water overboard. This system has the simplest structure and is the most advantageous in terms of economic operation cost compared with the other types of scrubber [6]. The closed-loop system washes the exhaust gas using fresh water and then recycles the wash water using NaOH. The open-loop system and the hybrid system wash the exhaust gas using seawater, and discharge the wash water off-board because it is difficult to keep a large volume of wash water on-board.

However, there has been a discussion on the harmful effects of scrubber wash water [7,8], and some European sea areas and U.S. coastal areas prohibit the discharge of scrubber wash water. The number of sea areas where the discharge of scrubber wash water is restricted may increase in the future. Thus, shipping companies must install a closed-loop system scrubber or a hybrid scrubber to comply

with the SOx regulations; when they opt to use an open-loop scrubber system, they must use LSFO in sea areas where wash water discharge is restricted.

The current regulations stipulate that when stationary ships discharge scrubber wash water, the wash water at 4 m from the discharge point must have a pH of 6.5 or higher. Compliance to this regulation must be verified through experiments or through other equivalent scientifically proven methods, including numerical analysis, and must be certified by a classification society. Then the report must be kept on board [1].

Üplre et al. [9] theoretically and experimentally investigated the discharge of acidic turbulent jets in an alkaline environment. Their chemical model matched well with their titration experiment results. They introduced an empirical model of turbulent jets and integrated it with chemistry and fluid flow models. Also, Ülpre and Eames [10] conducted a physical and chemical research on the discharge of scrubber wash water from ships. To comply with the IMO's regulation on scrubber wash water discharge from ships, they developed a procedure for the use of multiple ports.

Turbulent jets have long been investigated because they are applied in various industries [11–13]. Studies in this field mainly focused on the velocity and concentration distributions of turbulent jets. With the development of numerical analysis, efforts have been made to match the experimental values with numerical analysis results. Pani et al. [14] proposed a point-source method to predict the velocity field of turbulent jets, and they found that their result agreed well with the CFD simulation. By considering the effect of buoyancy, Robinson et al. [15] conducted a numerical analysis on the mixing and dispersion of turbulent jets. They performed CFD simulation of two cases, namely, horizontal and angled jets, and then compared their result with published experimental results. In their numerical analysis, they applied the k-ε turbulence model and the Smagorinsky LES model, and they used adaptive mesh. Different results were obtained depending on the mesh quality. The simulation predicted the buoyant jet well, but it overestimated dispersion in a near field of the source.

Choi et al. [16] determined, through CFD, the discharge velocity and dilution ratio under different discharge velocities and nozzle diameters. The discharge velocity from the turbulent jets exerted little effect on dilution. However, in the study, the CFD validation process was insufficient, so the dilution ratio according to the nozzle diameter seems to have a low reliability.

In this study, the pH according to the dilution ratio of wash water and seawater was calculated through a theoretical chemical reaction model, and the volume fraction of wash water in the wash water-seawater mixture was calculated through CFD simulation. In addition, the pH was calculated by combining the dilution ratio, which was calculated using the theoretical chemical reaction model, and the volume fraction that was determined through CFD simulation. Furthermore, this paper details the accurate simulation method for turbulent jet flow under various nozzle diameters. Generally, the simulation of two-phase flow is implemented by using mixture model or volume of fluid (VOF) model. These models require a lot of time to calculate and are difficult to validate. In this study, the process in which the scrubber wash water is discharged and dispersed into the sea water is simulated solving the transport equation, and this method is highly dependent on the turbulent Schmidt number. Although studies that investigated the effect of Schmidt number on the flow have already been published, it is difficult to find a study that increases the reliability of the analysis by selecting the appropriate turbulent Schmidt number in the field of ship's scrubber technology. Therefore, we propose herein the use of appropriate turbulent Schmidt numbers according to the nozzle diameter. This study proposes an accurate and easy-to-access approach to calculate the pH of scrubber wash water discharged from ships. Results of this study are expected to be useful to scrubber manufacturers, to ship-building companies, and to classification societies.

2. Theoretical Analysis

2.1. Chemistry Reaction

In this study, modeling was based on the acid-weak alkali reaction reported in the works of Ülpre et al. [9] and Ülpre [17]. These chemical reactions are detailed in said references. Seawater is a weak base buffer solution. A buffer solution is a solution that absorbs hydrogen ions even when a small amount of acid is added and thus causes almost no change in pH. The buffer capacity of seawater is mainly determined by the HCO_3^- and CO_3^{2-} ions [9,18].

The chemical equilibrium of the acid HA and the base MOH is expressed as follows:

$$\left[H^+\right] + \left[M^+\right] = [OH^-] + [A^-] \tag{1}$$

The mass of acid (a) and base (b) are conserved by Equations (2) and (3):

$$C_a V_a = [A^-](V_a + V_b) \tag{2}$$

$$C_b V_b = \left([MOH] + \left[M^+\right]\right)(V_a + V_b) \tag{3}$$

where C indicates concentration and V indicates volume.

When Equation (1) is substituted in Equation (2), the following equation is obtained:

$$C_a V_a = \left(\left[H^+\right] + \left[M^+\right] - [OH^-]\right)(V_a + V_b) \tag{4}$$

Furthermore, when Equation (4) is substituted in Equation (3), Equation (5) is obtained, and Equation (5) can be summarized as Equation (6).

$$C_b V_b = \left([MOH] + \frac{C_a V_a}{V_a + V_b} - \left[H^+\right] + [OH^-]\right)(V_a + V_b) \tag{5}$$

$$V_a\left(C_a - \left[H^+\right] + [OH^-]\right) = V_b\left(C_b + \left[H^+\right] - [OH^-]\right) - [MOH](V_a + V_b) \tag{6}$$

The ionization constants of water, acid, and base are defined as follows:

$$K_w = [OH^-]\left[H^+\right] \tag{7}$$

$$K_a = \frac{[H^+][A^-]}{[HA]} \tag{8}$$

$$K_b = \frac{[M^+][OH^-]}{[MOH]} = \frac{K_w}{K_a} \tag{9}$$

When Equation (9) is substituted in Equation (3), the following equation is obtained:

$$[MOH](V_a + V_b) = C_b V_b - \left(\frac{C_b V_b}{\frac{[OH]}{K_b} + 1}\right) \tag{10}$$

When Equations (10) and (8) are substituted in Equation (6), the following standard acid-alkali titration equation is obtained:

$$\frac{V_b}{V_a} = \frac{C_a - [H^+] + \frac{K_w}{[H^+]}}{\frac{C_b}{1 + K_w/([H^+]K_b)} + [H^+] - \frac{K_w}{[H^+]}} \tag{11}$$

In weak base reaction, Equation (11) can be expressed as:

$$\frac{V_b}{V_a} = \frac{C_a - [H^+] + \frac{K_w}{[H^+]}}{\frac{C_b K_b}{K_w/[H^+]} + [H^+] - \frac{K_w}{[H^+]}} \text{for } \frac{K_w}{[H^+]} \gg K_b \tag{12}$$

In addition, the reaction of diprotic acid can be expressed as:

$$\frac{V_b}{V_a} = \frac{\frac{C_a(K_{a1}[H^+]+2K_{a1}K_{a2})}{([H^+]^2+K_{a1}[H^+]+K_{a1}K_{a2})-[H^+]+K_w/[H^+]}}{\frac{C_b}{(1+K_w/([H^+]K_b))} + [H^+] - K_w/[H^+]} \tag{13}$$

The constants used in this study are as follows [9,19]: $K_w = 10^{-14}$, $K_{a1} = 1$, $K_{a2} = 1.2 \times 10^{-2}$, $K_b = 2.3 \times 10^{-8}$. K_w is the ionization constant of water, K_{a1}, K_{a2} and K_b are the ionization constants of H_2SO_4 and HCO_3^-, respectively.

2.2. Turbulent Jets

Pani et al. [14] proposed the following velocity distribution correlation and concentration distribution correlation in circular turbulent jets:

$$\frac{u}{u_0} = 6.2\left(\frac{Z}{D}\right)^{-1} \tag{14}$$

$$\frac{C}{C_0} = 5.26\left(\frac{Z}{D}\right)^{-1} \tag{15}$$

where u is the velocity; u_0 is the initial velocity at the discharge point; Z and D denote the axial distance and nozzle diameter, respectively; and C and C_0 denote the concentration and initial concentration at the discharge point, respectively.

Furthermore, Hodgson et al. [20] suggested the following concentration distribution correlation in circular turbulent jets:

$$\frac{C}{C_0} = 5.34\left(\frac{Z}{D}\right)^{-1} \tag{16}$$

Equation (16) predicts a higher concentration than Equation (15), and a higher concentration indicates poor dilution. Thus, we adopted harsh conditions to minimize risks in this study. To verify the numerical analysis results, we compared the numerical analysis result with Equation (16).

3. Numerical Modeling

Using the chemical reaction model described in Section 2, the pH based on the dilution ratio of wash water and seawater can be calculated. Hence, the dilution ratio can be calculated by analyzing wash water dispersion without considering the chemical reaction in the numerical analysis. In the present study, CFD simulation was performed to simulate the discharge and dispersion process of wash water in seawater. Since the chemical reaction between wash water and seawater was assumed to occur within a considerably short period of time (10^{-9} s) compared with the physical mixing process [21], it was assumed that the chemical reaction does not affect the physical mixing. In addition, since the wash water is mostly composed of seawater, we used the properties of the latter. However, wash water and seawater are assumed to be totally different fluids, and the concentration of wash water was calculated in the same manner as the volume fraction of wash water. In this study, the commercial code ANSYS-CFX V13.0 was used for CFD simulation.

Since many studies have already reported that the k-ε model is appropriate for flow analysis in order to simulate turbulent jets [15,22,23], our study also used the k-ε model. In this model, k and ε are expressed in their respective transport equations as follows [23,24]:

$$\frac{\partial}{\partial x_j}\left(\rho u_j k\right) = \frac{\partial}{\partial x_j}\left[\left(\mu + \frac{\mu_t}{\sigma_k}\right)\frac{\partial k}{\partial x_j}\right] + P_k - \rho\varepsilon + P_{kb} \tag{17}$$

$$\frac{\partial}{\partial x_j}\left(\rho u_j \varepsilon\right) = \frac{\partial}{\partial x_j}\left[\left(\mu + \frac{\mu_t}{\sigma_\varepsilon}\right)\frac{\partial \varepsilon}{\partial x_j}\right] + \frac{\varepsilon}{k}(C_{\varepsilon 1}P_k - C_{\varepsilon 2}\rho\varepsilon + C_{\varepsilon 1}P_{\varepsilon b}) \tag{18}$$

P_{kb} is defined by an equation for Sc_t, as follows:

$$P_{kb} = \frac{\mu_t}{Sc_t}\beta g_i \frac{\partial T}{\partial x_i} \tag{19}$$

where k and ε denote the turbulence kinetic energy and turbulence eddy dissipation, respectively; μ_t, β, and g_i denote the turbulence viscosity, thermal expansion coefficient, and gravity vector, respectively. The constant values are as follows: $C_{\varepsilon 1} = 1.45$, $C_{\varepsilon 2} = 1.9$, $\sigma_k = 1.0$, $\sigma_\varepsilon = 1.3$.

Here, Sc_t is a turbulent Schmidt number, and the default value provided by ANSYS-CFX is 0.9. Sc_t is a major parameter that affects dispersion in the k-ε turbulence simulation [22,25] and is mainly obtained experimentally. Oliver et al. [22] suggested that Sc_t is approximately 0.7 when buoyancy is not considered, whereas it is 0.6 when buoyancy is considered. However, the appropriate Sc_t value is dependent on the nozzle diameter and shape and on the working fluid type. In this study, CFD was validated through the selection of the appropriate Sc_t which is dependent on the nozzle diameter.

The objective of CFD simulation was to verify the volume fraction, which changes according to the dispersion of wash water. Therefore, the transport equation was solved by applying the volume fraction to the transport equation, defined as Equation (20), by using the volume fraction (vf) as an additional variable without considering the complex detailed model of the two-phase flow [26]. The volume fraction of the wash water discharged from the nozzle was set as 1. Thus, the volume fraction of wash water in the initial external seawater of the nozzle is zero.

$$\frac{\partial(\rho vf)}{\partial t} + \nabla\cdot(\rho uvf) = \nabla\cdot\left(\left(\rho\alpha + \frac{\mu_t}{Sc_{add}}\right)\nabla vf\right) + S \tag{20}$$

In Equation (20), Sc_{add}, α, and S denote the turbulent Schmidt number, kinematic diffusivity, and source term of the additional variable, respectively.

3.1. Boundary Conditions

The nozzle length was set as 20 times the nozzle diameter to simulate the fully developed flow of wash water discharged from the nozzle. A study [16] showed that the discharge velocity from a turbulent jet flow exerts almost no effect on dilution. In the present study, the dispersion of wash water according to the change in nozzle diameter was verified through CFD, and the CFD model was validated based on the existing literature. For the CFD simulation, nozzles with a diameter of 0.05–0.40 m were used. The discharge velocity of wash water from the nozzle is 1 m/s, and the opening condition was used for the exterior of the total domain. In actual flows, buoyancy can be generated by the temperature and density differences between the wash water and seawater, but buoyancy was ignored in this study. Compared with the results of studies that considered buoyancy, the present result showed that risk was minimized because the prevailing condition within 4 m from the discharge point is disadvantageous for dilution.

3.2. Mesh

The quality of mesh used in CFD numerical analysis exerts a decisive effect on the result. In this study, hexahedral meshes were generated using ANSYS ICEM-CFD. Dense meshes were generated

using the O-grid method for areas where the gradient of velocity and transport variables were expected to be large. In addition, mesh dependence was reviewed using approximately 180,000, 1.5 million, 3.3 million, and 4.8 million nodes for a nozzle diameter of 0.05 m.

Figure 1 shows the dimensionless velocity according to the axial distance of discharge for different numbers of nodes. Dimensionless velocity is the local velocity divided by the maximum velocity. As the distance from the discharge point increased, variation in the results also increased depending on the number of meshes. At the point where the wash water is discharged from the nozzle, a rapid velocity gradient occurs due to the interaction of the wash water with the surrounding stagnant fluid. Hence, a sufficient number of meshes is required to simulate the dispersion phenomenon in this area. Therefore, 4.8 million meshes were selected based on the nozzle diameter of 0.05 m in this study. Figure 2 shows the hexahedral meshes used in this study.

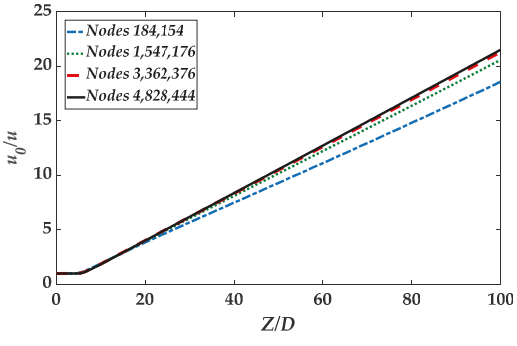

Figure 1. Mesh independence on the number of nodes.

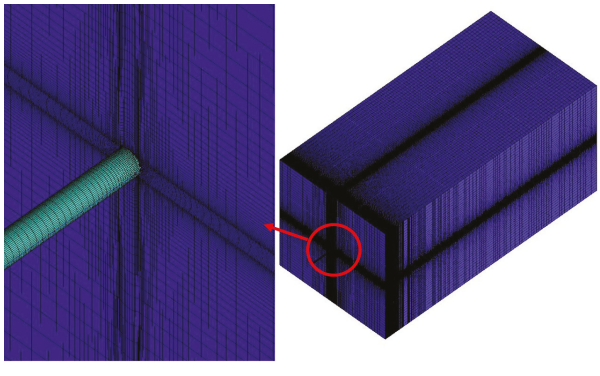

Figure 2. Hexahedral mesh for CFD simulations.

4. Results

4.1. Titration Curves

Figure 3 shows the titration curves of the chemical reaction model described in Section 2.1; this model describes the variations in pH as a function of the dilution ratio (V_b/V_a) of wash water at an alkalinity of 1800, 2200, and 2600 μmol/kg, and at an initial pH of 2.5–3.5. When the seawater alkalinity was 2200 μmol/kg, the initial pH of 2.5 increased to 6.5 at a dilution ratio of approximately 3.81, and the initial pH of 3.5 increased to 6.5 at a dilution ratio of approximately 0.35. Table 1 outlines the volume fractions ($V_a/(V_a + V_b)$) of the dilution ratio and wash water to achieve a pH of 6.5 based on the initial pH. When the seawater alkalinity was 1800 μmol/kg, dilution ratios of 4.66 and 0.42, respectively, should

be provided for the initial pH 2.5 and 3.5 to be pH of 6.5. For the dilution ratios, 4.66 and 0.42 are converted to volume fraction of wash water of 0.18 and 0.70, respectively. When the seawater alkalinity was 2600 µmol/kg, the volume fractions of the wash water for the initial pH of 2.5 and 3.5 to be pH of 6.5 are 0.24 and 0.77 respectively. This means that a relatively large amount of sea water is required to recover the wash water to pH of 6.5 at low alkalinity compared to high alkalinity. On the other hand, a low initial pH of wash water requires a large amount of sea water to recover to pH of 6.5.

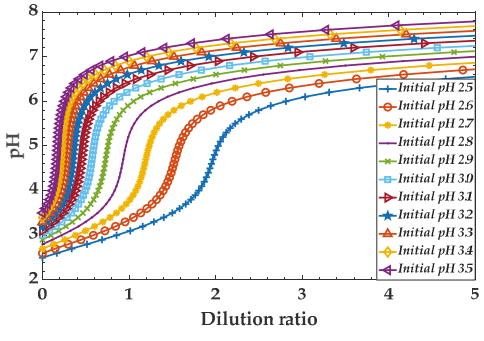

(**a**) Alkalinity: 1800 µmol/kg.

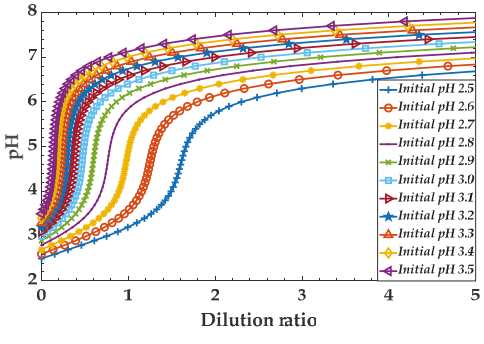

(**b**) Alkalinity: 2200 µmol/kg.

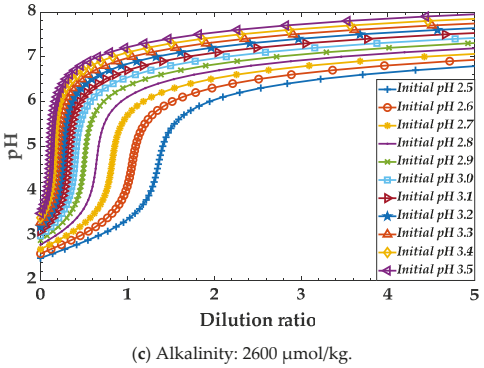

(**c**) Alkalinity: 2600 µmol/kg.

Figure 3. Titration curves obtained by the theoretical chemical reaction model.

Table 1. Required dilution ratio and volume fraction depending on the initial pH of scrubber wash water under different seawater alkalinity values.

Initial pH	Alkalinity 1800 μmol/kg		Alkalinity 2200 μmol/kg		Alkalinity 2600 μmol/kg	
	Dilution Ratio	Volume Fraction	Dilution Ratio	Volume Fraction	Dilution Ratio	Volume Fraction
2.5	4.66	0.18	3.81	0.21	3.23	0.24
2.6	3.63	0.22	2.97	0.25	2.51	0.28
2.7	2.83	0.26	2.32	0.30	1.96	0.34
2.8	2.22	0.31	1.82	0.36	1.54	0.39
2.9	1.74	0.36	1.43	0.41	1.21	0.45
3.0	1.37	0.42	1.12	0.47	0.95	0.51
3.1	1.08	0.48	0.88	0.53	0.75	0.57
3.2	0.85	0.54	0.70	0.59	0.59	0.63
3.3	0.67	0.60	0.55	0.64	0.47	0.68
3.4	0.53	0.65	0.44	0.70	0.37	0.73
3.5	0.42	0.70	0.35	0.74	0.29	0.77

4.2. CFD Validations

Figure 4 shows the variations in the dimensionless velocity (u_0/u) according to Equation (14), which is the correlation reported by Pani et al. [14]; it also shows the change in Sc_t. In Figure 4, the x-axis represents the dimensionless distance (Z/D). Equation (14) is a simple model that has a linear relationship between the dimensionless velocity and the dimensionless distance. Therefore, it is not possible to make accurate predictions at the initial discharge, that is, at a low dimensionless distance. The results of CFD simulation can be compared to Equation (14) only in the region with linearity as the dimensionless distance increases. In this study, only the total length of 5 m was considered for analysis, because the focus is on the flow variable at the 4 m point. It can be seen that Sc_t is a major parameter in the turbulent jet flow. As Sc_t increased, the dimensionless velocity also increased, whereas the axial local velocity (u) decreased. At a diameter of 0.05 m, a Sc_t value of approximately 0.54 was found to match best with the correlation reported by Pani et al. [14]; at a diameter of 0.40 m, the Sc_t value of 0.75 matched best with the said correlation. Figure 5 shows the Sc_t values that match best with Pani et al.'s [14] correlation for each nozzle diameter. The nozzle diameter and Sc_t displayed a nearly linear relationship, which can be linearly interpolated as follows:

$$Sc = 0.619D + 0.5007 \tag{21}$$

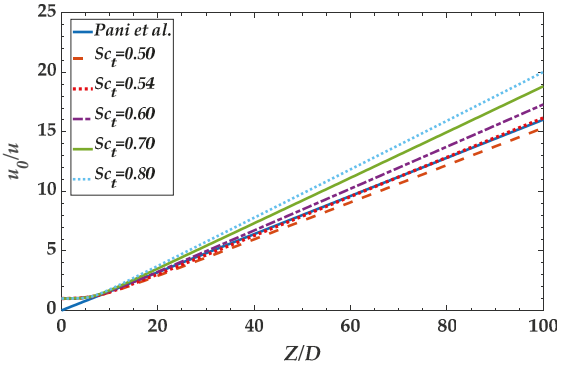

(**a**) D = 0.05 m.

Figure 4. *Cont.*

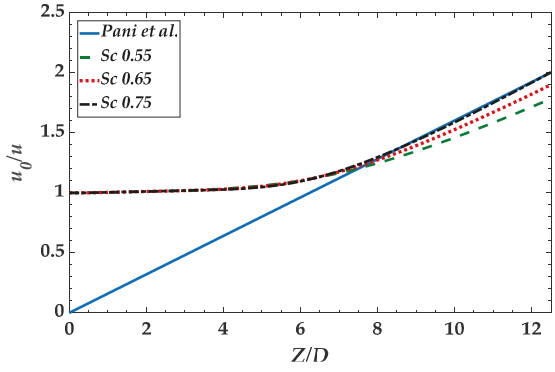

(**b**) D = 0.40 m.

Figure 4. Relationship between dimensionless velocity (u_0/u) and dimensionless distance (Z/D) under different turbulent Schmidt numbers.

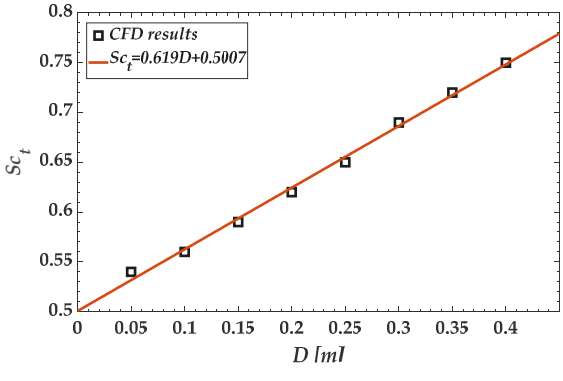

Figure 5. Relationship between valid turbulent Schmidt number and the nozzle diameter.

It should be noted that the Sc_t derived by Equation (21) is valid only when the working fluid is seawater, when the nozzle diameter is 0.05–0.40 m, and when the distance from the discharge point is less than 5 m.

Figure 6 shows the inverse of the volume fraction according to Equation (20), which is the correlation reported by Hodgson et al. [20]; it also shows the variation in Sc_{add}. As with the above velocity distribution, only the total length of 5 m was considered for analysis. As the Sc_{add} increased, the inverse of volume fraction decreased, and the volume fraction increased. In other words, at low Sc_{add}, dispersion and mixing actively occur. At a diameter of 0.05 m, the Sc_{add} of 0.71 matched best with the correlation reported by Hodgson et al. [20]; at a diameter of 0.40 m, the Sc_{add} of 0.63 matched best with the said correlation. Figure 7 shows the Sc_{add} values that match best with the correlation reported by Hodgson et al. [20] for each nozzle diameter. It can be linearly interpolated as follows:

$$Sc_{add} = -0.238D + 0.724 \quad (22)$$

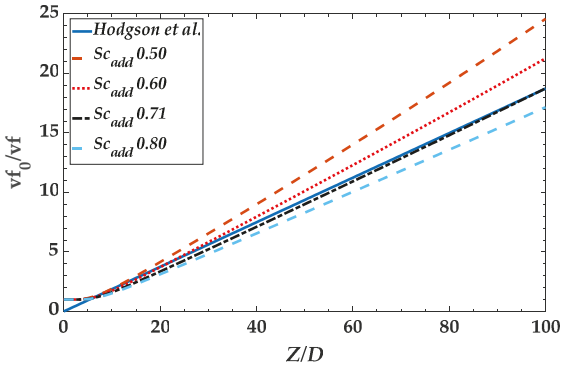

(**a**) D = 0.05 m.

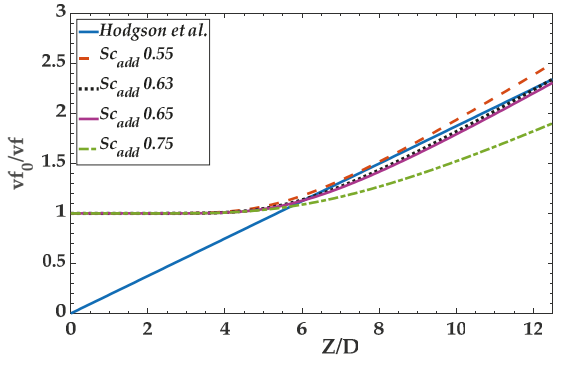

(**b**) D = 0.40 m.

Figure 6. Relationship between volume fraction ratio (vf_0/vf) and dimensionless distance (Z/D) under different turbulent Schmidt numbers of additional variable.

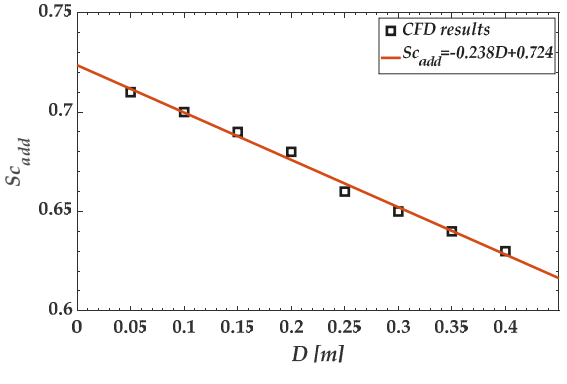

Figure 7. Relationship between valid turbulent Schmidt number and nozzle diameter of additional variable.

Finally, numerical analysis was performed by setting the optimal Sc_{add} for each nozzle diameter. Figure 8 shows the comparison between the volume fraction result of Hodgson et al. [20] at 4 m from the discharge point and the result of the numerical analysis. It was found that the numerical analysis result matched well with the result obtained by Hodgson et al. [20]. However, the Sc_t and

Sc_{add} proposed in this study must be used under limited conditions. It should be noted that they are valid only when buoyancy is not considered, when the working fluid is seawater, when the nozzle diameter is 0.05–0.40 m, and when the distance from the discharge point is less than 5 m. The CFD post processing data is detailed in Appendix A.

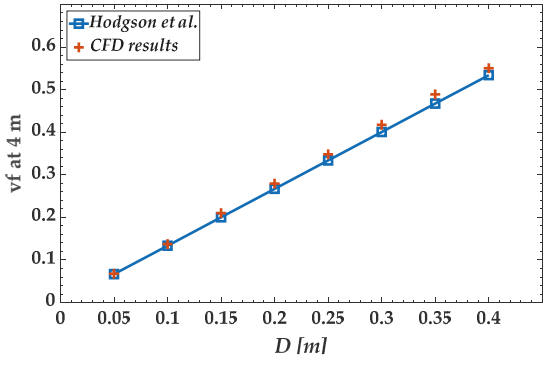

Figure 8. Comparison between existing correlation and CFD results.

The CFD results were compared with experimental data available in the literature for validation. Papanicolaou and List [27] conducted the experimental study on the vertical turbulent buoyant jets using lase-Doppler anemometry. They verified the velocity and concentration decay experimentally, and calculated the momentum fluxes using dimensionless parameters. Figure 9 shows the comparison between the CFD results and the experimental results obtained by Papanicolaou and List [27]. It was found that the simulation predicts well the results from Papanicolau and List [27].

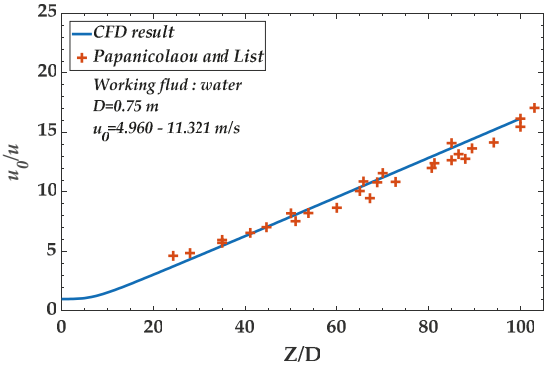

Figure 9. Comparison between the CFD results and the experimental data* (* reproduced from the work of Papanicolaou and List (1988) [27]).

4.3. pH Calculations

The volume fraction of wash water to achieve a pH of 6.5 in the wash water-seawater mixture can be determined based on the titration curves obtained in Section 4.1 and presented in Table 1. To achieve a pH of 6.5 by mixing with seawater that has an alkalinity of 2200 µmol/kg, a volume fraction of 0.21 is required when the wash water has an initial pH of 2.5, and a volume fraction of 0.74 is required when the initial pH is 3.5. The volume fraction at 4 m from the discharge point was calculated through the CFD numerical analysis described above.

Figure 10 shows the diameter required to achieve a pH of 6.5 at 4 m from the discharge point depending on the initial pH. Moreover, it shows the relationship between pH and nozzle diameter at different alkalinity values of seawater. At a low alkalinity, a large amount of seawater is required to restore the pH of the wash water, so the nozzle diameter must be small to facilitate dispersion. The nozzle diameter should be less than 0.34 m at the initial pH of 3.0 and alkalinity of 2200 μmol/kg and less than 0.30 m at alkalinity of 1800 μmol/kg to satisfy the regulation. Scrubber manufacturers can measure the pH of wash water and can roughly calculate the nozzle diameter for wash water discharge, based on the information shown in Figure 10. If the diameter is too small to discharge enough wash water, multiple ports should be considered. The wash water discharged from multiple ports should not interfere with each other, and research on this characteristic will be conducted as a future plan.

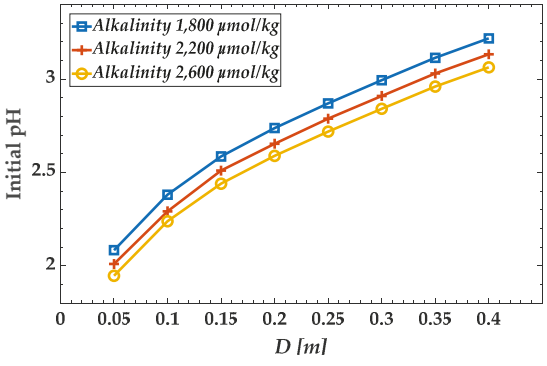

Figure 10. Variation in the treatable initial pH with the designed nozzle diameter under different seawater alkalinity values.

5. Conclusions

Theoretical and numerical analysis was conducted to comply with the regulation on the scrubber wash water discharge from ships. In the theoretical chemical models, the pH was calculated based on the initial pH and dilution ratio [9,17]. The volume fraction at 4 m from the discharge point was calculated through dispersion analysis of the turbulent jet flow. The results of this study are summarized as follows:

1. To simulate the dispersion phenomenon in turbulent jet flow, we solved the transport equation by applying the volume fraction. Simulation was performed for nozzle diameters ranging from 0.05 m to 0.40 m. The turbulent Schmidt number is a critical parameter that exerts a significant effect on dispersion. An appropriate turbulent Schmidt number must be selected according to the nozzle diameter. The appropriate turbulent Schmidt numbers of the transport equations were calculated by comparing them with the existing correlations. The simulation results obtained within 5 m from the discharge point by using the calculated turbulent Schmidt numbers matched well with the results obtained by Pani et al. [14] and Hodgson et al. [20].
2. The volume fraction at 4 m from the discharge point was calculated through simulation, and titration curves were obtained by the theoretical chemical reaction model. The pH value at 4 m can be derived from the initial pH by applying the calculated volume fraction or dilution ratio to the titration curves.
3. When the wash water has a low pH, a small diameter nozzle is required to restore the pH to 6.5 at 4 m from the discharge point. When the seawater in the surrounding sea area has a low alkalinity, a large amount of seawater is required. Hence, a small diameter nozzle must be used to promote dispersion. At the initial pH of 3.0 and alkalinity of 2200 μmol/kg, the nozzle diameter should be less than 0.34 m, and at the initial pH of 3.0 and alkalinity of 1800 μmol/kg, it should be less than 0.30 m.

4. For future research, we will improve the accuracy of the chemical reaction model through titration experiments by using wash water and seawater obtained from the scrubber of actual ship engines. Moreover, we intend to improve the reliability of the CFD simulation through comparison with correlations derived from more varied turbulent jet flows.

Author Contributions: Conceptualization, Y.-S.C. and T.-W.L.; software, Y.-S.C.; validation, Y.-S.C. and T.-W.L.; formal analysis, Y.-S.C. and T.-W.L.; investigation, Y.-S.C. and T.-W.L.; resources, Y.-S.C. and T.-W.L.; data curation, Y.-S.C. and T.-W.L.; writing—original draft preparation, Y.-S.C.; writing—review and editing, Y.-S.C. and T.-W.L.; visualization, Y.-S.C. and T.-W.L.; supervision, T.-W.L.; project administration, Y.-S.C. and T.-W.L. All authors have read and agreed to the published version of the manuscript.

Funding: This research received no external funding.

Conflicts of Interest: The authors declare no conflict of interest.

Appendix A CFD Post Processing Data

Figure A1 shows the calculation result for the volume fraction distribution of wash water using the Sc_t and Sc_{add} proposed above for each nozzle diameter. As shown in the figures, dispersion rapidly occurs when the nozzle diameter is small, and the volume fraction of wash water was relatively low at 4 m compared to when the nozzle diameter is large. It was found that the dispersion of wash water was greatly dependent on nozzle diameter.

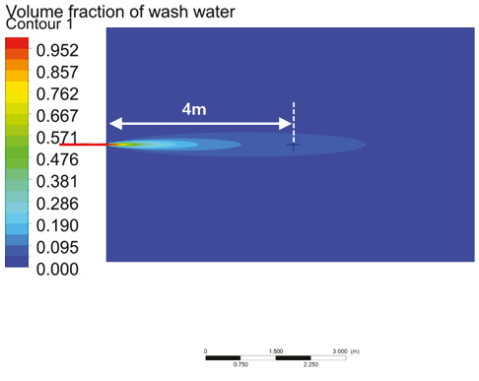

(**a**) D = 0.05 m.

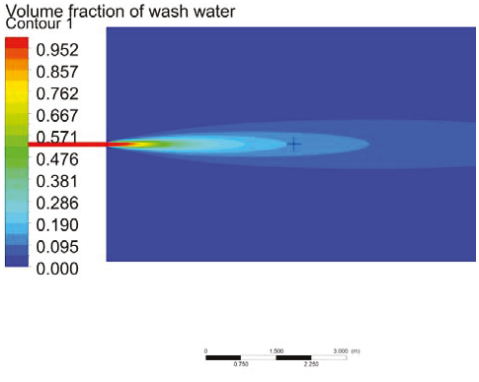

(**b**) D = 0.10 m.

Figure A1. *Cont.*

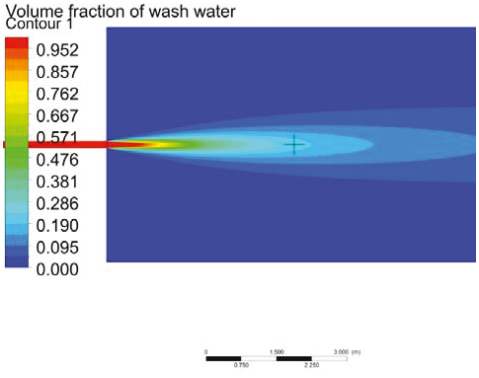

(**c**) D = 0.15 m.

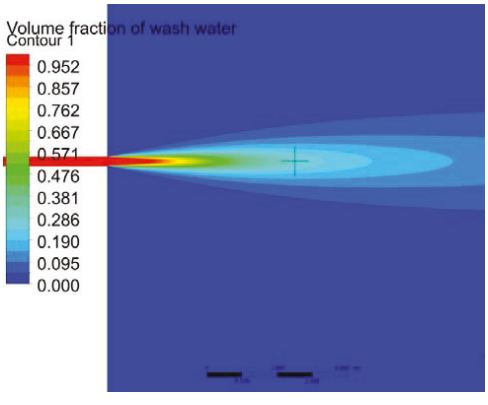

(**d**) D = 0.20 m.

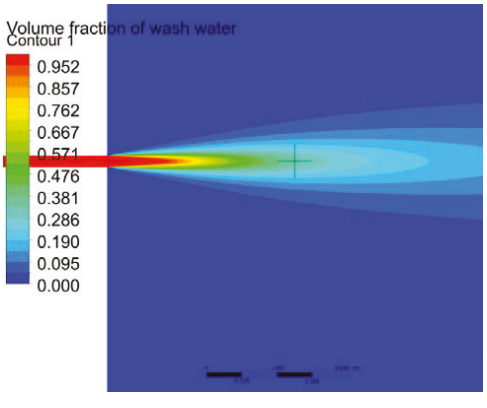

(**e**) D = 0.25 m.

Figure A1. *Cont*.

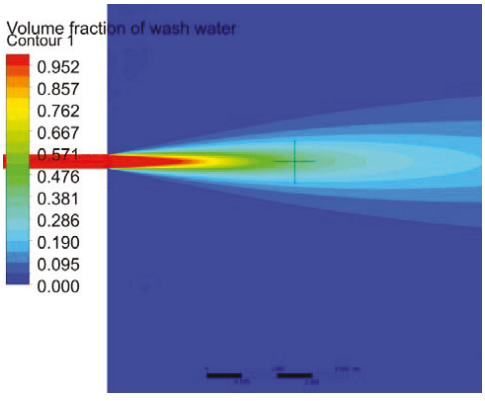

(**f**) D = 0.30 m.

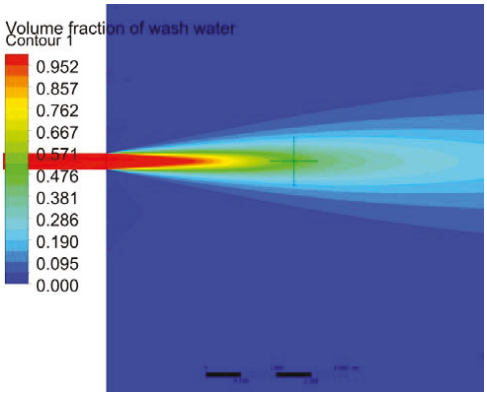

(**g**) D = 0.35 m.

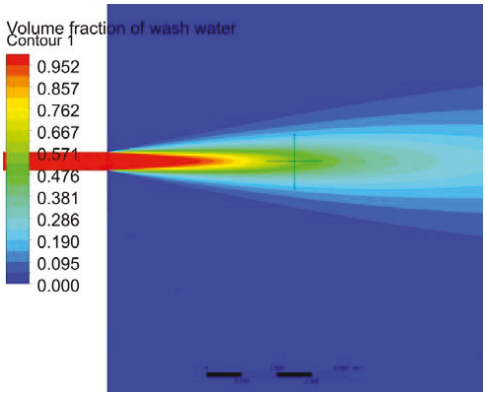

(**h**) D = 0.40 m.

Figure A1. Volume fraction distributions of wash water under different nozzle diameters.

References

1. IMO MEPC 70/18/Add.1 ANNEX6. Effective Date of Implementation of the Fuel Oil Standard in Regulation 14.1.3 of MARPOL ANNEX VI 2016. Available online: http://www.imo.org (accessed on 9 April 2020).
2. Van, T.C.; Ramirez, J.; Rainey, T.; Ristovski, Z.; Brown, R.J. Global impacts of recent IMO regulations on marine fuel oil refining processes and ship emissions. *Transp. Res. Part D Transp. Environ.* **2019**, *70*, 123–134. [CrossRef]
3. Cheenkachorn, K.; Poompipatpong, C.; Gyeung, C. Performance and emissions of a heavy-duty diesel engine fuelled with diesel and LNG (liquid natural gas). *Energy* **2013**, *53*, 52–57. [CrossRef]
4. Armellini, A.; Daniotti, S.; Pinamonti, P.; Reini, M. Evaluation of gas turbines as alternative energy production systems for a large cruise ship to meet new maritime regulations. *Appl. Energy* **2018**, *211*, 306–317. [CrossRef]
5. Tang, X.; Li, T.; Yu, H.; Zhu, Y. Prediction model for desulphurization efficiency of onboard magnesium-base seawater scrubber. *Ocean Eng.* **2016**, *76*, 98–104. [CrossRef]
6. Ammar, N.R.; Seddiek, I.S. Eco-environmental analysis of ship emission control methods: Case study RO-RO cargo vessel. *Ocean Eng.* **2017**, *137*, 166–173. [CrossRef]
7. Koski, M.; Stedmon, C.; Trapp, S. Ecological effects of scrubber water discharge on coastal plankton: Potential synergistic effects of contaminants reduce survival and feeding of the copepod Acartia tonsa. *Mar. Environ. Res.* **2017**, *129*, 374–385. [CrossRef] [PubMed]
8. Ytreberg, E.; Hassellöv, I.M.; Nylund, A.T.; Hedblom, M.; Al-Handal, A.Y.; Wulff, A. Effects of scrubber washwater discharge on microplankton in the Baltic Sea. *Mar. Pollut. Bull.* **2019**, *145*, 316–324. [CrossRef] [PubMed]
9. Ülpre, H.; Eames, I.; Greig, A. Turbulent acidic jets and plumes injected into an alkaline environment. *J. Fluid Mech.* **2013**, *734*, 253–274. [CrossRef]
10. Ülpre, H.; Eames, I. Environmental policy constraints for acidic exhaust gas scrubber discharges from ships. *Mar. Pollut. Bull.* **2014**, *88*, 292–301. [CrossRef]
11. Lipari, G.; Stansby, P.K. Review of experimental data on incompressible turbulent round jets. *Flow Turbul. Combust.* **2011**, *87*, 79–114. [CrossRef]
12. Panchapakesan, N.R.; Lumley, J.L. Turbulence Measurements in Axisymmetric Jets of Air and Helium. Part 2. Helium Jet. *J. Fluid Mech.* **1993**, *246*, 225–247. [CrossRef]
13. Boersma, B.J.; Brethouwer, G.; Nieuwstadt, F.T.M. A numerical investigation on the effect of the inflow conditions on the self-similar region of a round jet. *Phys. Fluids* **1998**, *10*, 899–909. [CrossRef]
14. Pani, B.S.; Lai, A.C.H.; Wong, C.K.C. Turbulent Jets: Point-Source and CFD Simulation Results. *J. Environ. Res. Dev.* **2011**, *5*, 952–959.
15. Robinson, D.; Wood, M.; Piggott, M.; Gorman, G. CFD modelling of marine discharge mixing and dispersion. *J. Appl. Water Eng. Res.* **2016**, *4*, 152–162. [CrossRef]
16. Choi, Y.S.; Cha, M.H.; Kim, M.; Lim, T.W. Design of nozzle diameter based on the IMO regulation for discharging scrubber wash-water. *J. Korean Soc. Mar. Eng.* **2019**, *43*, 285–291. [CrossRef]
17. Ülpre, H. Turbulence Acidic Discharges into Seawater. Ph.D. Thesis, University College London, London, UK, 2015.
18. Frankignoulle, M. A complete set of buffer factors for acid / base CO_2 system in seawater. *J. Mar. Syst.* **1994**, *5*, 111–118. [CrossRef]
19. Brown, T.E.; Lemay, H.E.; Bursten, B.E.; Murphy, C.; Woodward, P.; Stoltzfus, M.E. *Chemistry: The Central Science*, 13th ed.; Pearson: London, UK, 2014.
20. Hodgson, J.E.; Moawad, A.K.; Rajaratnam, N. Concentration field of multiple circular turbulent jets. *J. Hydraul. Res.* **1999**, *37*, 249–256. [CrossRef]
21. Eigen, M. Methods for investigation of ionic reactions in aqueous solutions with half-times as short as 10–9 sec Application to neutralization and hydrolysis reactions. *Discuss. Faraday Soc.* **1954**, *17*, 194–205. [CrossRef]
22. Oliver, C.J.; Davidson, M.J.; Nokes, R.I. *k-ε* Predictions of the initial mixing of desalination discharges. *Environ. Fluid Mech.* **2008**, *8*, 617–625. [CrossRef]
23. Shirzadi, M.; Mirzaei, P.A.; Naghashzadegan, M. Aerodynamics Improvement of k-epsilon turbulence model for CFD simulation of atmospheric boundary layer around a high-rise building using stochastic optimization and Monte Carlo Sampling technique. *J. Wind Eng. Ind. Aerodyn.* **2017**, *171*, 366–379. [CrossRef]
24. *ANSYS CFX-Theory Guide*; V13.0.; Ansys Inc.: Canonsburg, PA, USA, 2010.

25. He, G.; Guo, Y.; Hsu, A.T. The Effect of Schmidt Number on Turbulent Scalar Mixing in a Jet-in-Crossflow. *Int. J. Heat Mass Transf.* **1999**, *42*, 3727–3738. [CrossRef]
26. Nguyen, V.T.; Nguyen, T.C.; Nguyen, J. Numerical Simulation of Turbulent Flow and Pollutant Dispersion in Urban Street Canyons. *Atmosphere* **2019**, *10*, 683. [CrossRef]
27. Papanicolaou, P.N.; List, E.J. Investigations of Round Vertical Turbulent Buoyant Jets. *J. Flud Mech.* **1988**, *195*, 341–931. [CrossRef]

Journal of
Marine Science and Engineering

MDPI

Article

CFD Simulation of Ship Seakeeping Performance and Slamming Loads in Bi-Directional Cross Wave

Jialong Jiao * and Songxing Huang

School of Civil Engineering and Transportation, South China University of Technology, Guangzhou 510641, China; 201820107670@mail.scut.edu.cn
* Correspondence: jiaojl@scut.edu.cn; Tel.: +86-139-2514-6963

Received: 10 April 2020; Accepted: 28 April 2020; Published: 29 April 2020

Abstract: Accurate prediction of ship seakeeping performance in complex ocean environment is a fundamental requirement for ship design and actual operation in seaways. In this paper, an unsteady Reynolds-averaged Navier–Stokes (RANS) computational fluid dynamics (CFD) solver with overset grid technique was applied to estimate the seakeeping performance of an S175 containership operating in bi-directional cross waves. The cross wave is reproduced by linear superposition of two orthogonal regular waves in a rectangle numerical wave tank. The ship nonlinear motion responses, bow slamming loads, and green water on deck induced by cross wave with different control parameters such as wave length and wave heading angle are systemically analyzed. The results demonstrate that both vertical and transverse motion responses, as well as slamming pressure of ship induced by cross wave, can be quite large, and they are quite different from those in regular wave. Therefore, ship navigational safety when suffering cross waves should be further concerned.

Keywords: ship hydrodynamics; ship motions; green water on deck; slamming; cross wave; CFD

1. Introduction

The majority of existing ship seakeeping investigations are concerned with ship motion behavior in uni-directional or long-crested waves [1]. As a result, a lot of effort, which includes potential flow, computational fluid dynamics (CFD) and model test methods, is being dedicated to predicting ship motions in 2D regular or even irregular waves in the past few decades [2]. However, realistic sea states are multi-directional or short-crested, with wave components propagating in different directions. Therefore, an in-depth understanding of the multi-directional wave interactions with ship is essential in accurate prediction of ship hydrodynamics in realistic sea wave conditions.

In some places, e.g., the popular tourist destination of the Isle of Rhe, cross wave can be often observed due to the complex and extreme patterns of weather (see Figure 1a). The cross wave can be regarded as the superposition of wind or swell waves coming from two orthogonal directions. An example of the cross wave phenomenon in the ocean is shown in Figure 1. Until now, the problem for the interaction of a ship with a cross wave is not clear and has not been investigated, although people realize that the cross wave may pose a great threat to the safety of the passing ship. Therefore, this paper aims at investigating ship seakeeping behavior in wind-driven bi-directional cross sea waves.

(a) (b)

Figure 1. Phenomenon of cross sea wave: (**a**) swell wave; (**b**) wind wave.

Some researchers have investigated the interaction of multi-directional wave with fixing offshore structures [3–5]. However, studies on the seakeeping behavior of free running ships or other floating structures in multi-directional wave are quite limited. Renaud et al. [6] investigated the effect of wave directionality on second-order slow-drift loads and motion response of a Liquefied Natural Gas (LNG) carrier in regular cross waves by a potential flow code and tank model test. Chen et al. [7] numerically investigated ship motions in long-crested and short-crested irregular waves by 3D time domain potential flow theory. Jiao et al. [8] comparatively studied the wave-induced ship motion and load responses in long- and short-crested irregular waves by theoretical and experimental methods. To summarize, the existing investigations on the hydrodynamic behavior of ships in multi-directional waves are mainly conducted by potential flow theory or model experiments, while related investigation by CFD has not been found.

In recent years, CFD, which captures most complexities of the fluid physics with few assumptions, has been widely used as a potential tool in ship design and evaluation [9–11]. Although tremendous advances have been made in the CFD simulations of ship motion responses in uni-directional wave [12–14], CFD investigations on ship motions induced by multi-directional waves are rarely seen. Recently, fundamental work of multi-directional wave simulation by CFD tool has been conducted by some researchers. For example, Wang et al. [15] simulated 3D directional irregular wave by open-source CFD model REEF3D. Cao and Wan [16] developed a multi-directional nonlinear numerical wave tank by Naoe-FOAM-SJTU solver. Wang et al. [17] calculated the wave forces on a large cylinder in multi-directional irregular waves using a CFD tool. These works focus on the simulation of multi-directional wave and also provide some foundations for the research of ship seakeeping behavior in multi-directional waves using CFD.

This paper focuses on investigating ship seakeeping behavior in bi-directional cross progressive waves by the CFD method, which will also provide some insights into ship motion behavior in multi-directional waves. For this purpose, a cross progressive wave is simulated in a rectangular numerical wave tank, and corresponding ship hydrodynamic behavior are estimated by solving Unsteady Reynolds Averaged Navier–Stokes (URANS) equations. Ship motion response and slamming pressure behavior under different cross wave states are analyzed. This study also provides some useful guidance for the safe operation of a ship when sailing in bi-directional cross seas.

The structure of the rest of this paper is arranged as follows: The description of the adopted S175 containership model, CFD numerical scheme, and calculation conditions are reported in Section 2. In Section 3, the characteristics of a cross wave are analyzed and also demonstrated by CFD simulation results. The seakeeping behavior of a ship in different cross wave conditions are systematically analyzed and discussed in Section 4. The slamming behavior of a ship in typical cross wave conditions is analyzed in Section 5. Finally, the main conclusions and future perspectives are reported in Section 6.

2. Numerical Model Setup

2.1. Ship Model and Geometry

The ship motion simulations in cross wave were applied to a 1:40 scaled S175 containership model without the rudder, propeller, or bilge keels appended. The main particulars of the ship and model are presented in Table 1. Body plan of the ship is shown in Figure 2. A 3D view of the ship hull modeled using STAR-CCM+ software's pre-processing module is shown in Figure 3.

Table 1. Main properties of the S175 containership.

Item	Full-Scale	Model
Scale	1:1	1:40
Length between perpendiculars (L)	175 m	4.375 m
Breadth (B)	25.4 m	0.635 m
Depth (D)	19.5 m	0.488 m
Draft (T)	9.5 m	0.238 m
Displacement (Δ)	23,711 t	370 kg
Block coefficient (C_B)	0.562	0.562
Midship section coefficient (C_M)	0.990	0.990
Prismatic coefficient (C_P)	0.568	0.568
Longitudinal centre of gravity (LCG) from after perpendicular	84.980 m	2.125 m
Vertical centre of gravity (KG) from base line	8.5 m	0.213 m
Transverse radius of gyration	9.652 m	0.241 m
Longitudinal radius of gyration	42.073 m	1.052 m

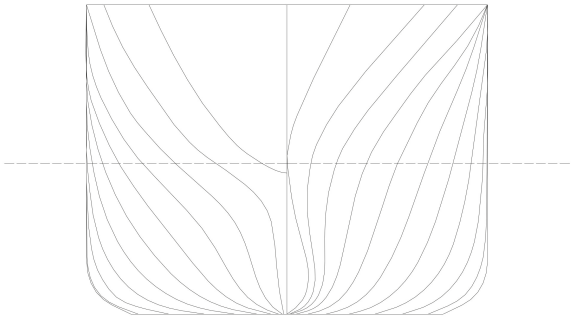

Figure 2. Body plan of the S175 hull.

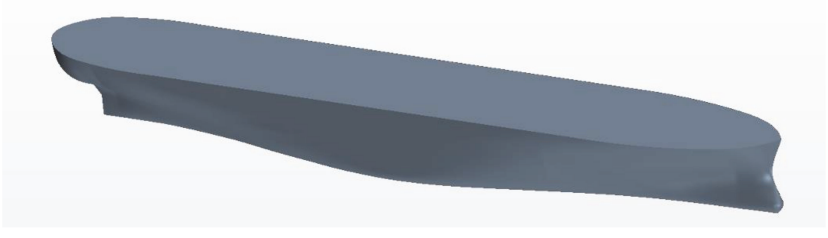

Figure 3. A 3D view of the model hull.

For the investigation of asymmetric impact loads on a ship when sailing in cross waves, an array of 17 pressure sensors were arranged on both the port and starboard sides of the ship bow area. The exact location of the pressure sensors is depicted in Figure 4. The gauges are positioned in the vertical level of baseline, 0.2 m, 0.3 m, or 0.4 m waterline. P1–P3 are located at the centerline of front bow from top

to bottom. P4–P7 (or P8–P11) are located at the intersection of cross-section at 19.5th station (or 19th station) with the 0.4 m, 0.3 m, 0.2 m waterline, and the keel. Note that the P4–P6 and P8–P10 exist in both the port and starboard sides of ship, while the P7 and P11 singly locate on the centerline of bow bottom.

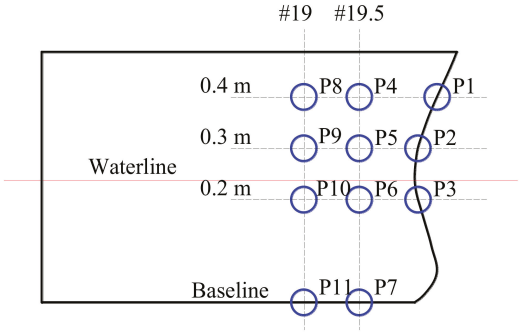

Figure 4. Arrangement of pressure sensors.

2.2. Numerical Scheme

The CFD numerical calculations were performed by the finite volume method (FVM) based STAR-CCM+ software, which use the URANS and Volume of Fluid (VOF) model. The realizable k-ε turbulence model, which provides a good compromise between robustness, computational cost, and accuracy, was used in this study [18,19]. The realizable k-ε turbulence model has more advantages in the simulation of separation flow and flow with larger streamline curvature, which is helpful for the simulation of the flow around hull. A second-order convection scheme was used throughout all simulations to accurately capture sharp interfaces between the two phases of air and water. Convection terms in the RANS formulae were discretised by applying a second-order upwind scheme. The overall solution procedure was obtained according to a SIMPLE-type algorithm. The rigid ship model was free to move in three degrees of freedom (3-DoF), i.e., heave, pitch, and roll, which is realized by the dynamic fluid body interaction (DFBI) model. The motion at ship's center of gravity (CoG) was monitored and used for analysis.

The origin of the coordinate system is located at the intersection of the free surface of calm water, symmetry plane, and cross section at the after perpendicular of the ship. The positive of ox, oy, and oz axes point to the bow, port side, and sky, respectively. A numerical wave tank for the entire fluid domain without symmetry plane was established to simulate the fluid flow. The extents of the computational domain are $-2.3\ L < x < 2.7\ L$, $-2.3\ L < y < 2.3\ L$, and $-2.3\ L < z < 1.1\ L$. For the generation of a multi-directional wave, the boundary conditions of the numerical wave tank were set in the following style: the four sidewalls and bottom of the fluid domain were set as the velocity inlet boundary; the top of the fluid domain was set as the pressure outlet; and the hull body surface was set as the no-slip wall. General view of the fluid domain and the ship model and the notations of boundary conditions are shown in Figure 5.

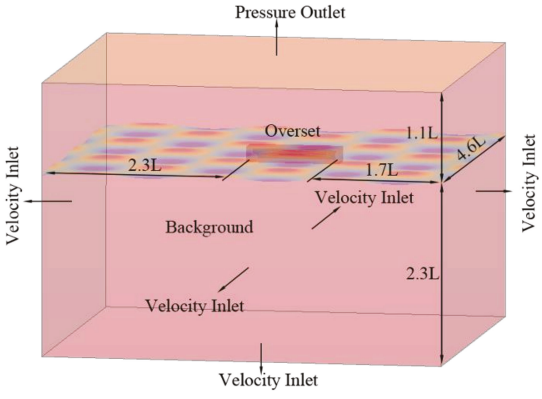

Figure 5. Overview of the fluid domain.

As shown in Figure 6, the fluid domain includes a background region and an overset region. Mesh generation was conducted by the automatic meshing facility in STAR-CCM+. A trimmed cell mesher was employed to produce a high-quality grid for complex mesh-generating problems. The ensuing mesh was formed primarily of unstructured hexahedral cells with trimmed cells adjacent to the surface. The computation mesh has areas of progressively refined mesh size in the area immediately around the hull, as well as the expected free surface, to ensure that the complex flow features were appropriately captured. The refined mesh density in these zones was achieved using volumetric controls applied to these areas. Local mesh was refined around the free surface. At least 16 cell layers are contained within the vertical range of wave height. The horizontal range of per wave length includes 45−150 cell layers for regular waves with wave length ranging from λ/L = 0.6 to 2.0 as a linear ratio scheme. As a result, approximately 4 million cells in total were generated, which turned out to be sufficient for the simulation of the cross wave and ship rigid-body motion responses. Figure 7 shows the refined grid near the free surface and hull body. As shown in Figure 8, the overlapping region consisted of five cell layers of boundary layer mesh near the hull surface (the normalized wall distance $y+$ value lies in the range of 30−60).

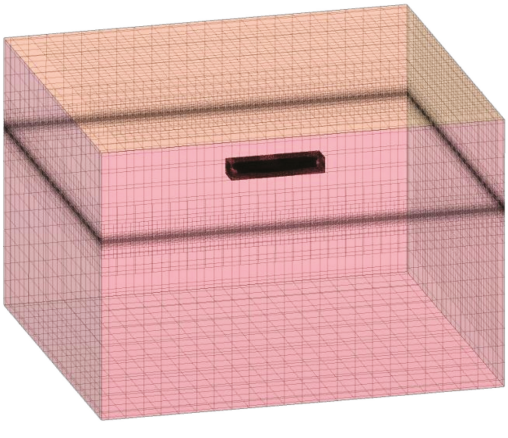

Figure 6. General view of meshes in fluid domain.

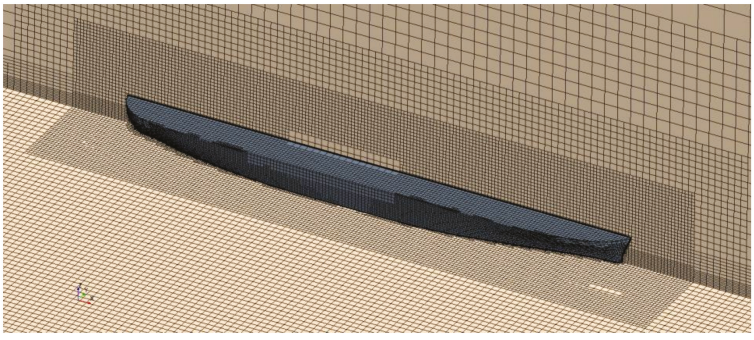

Figure 7. Refined grid near the free surface and hull.

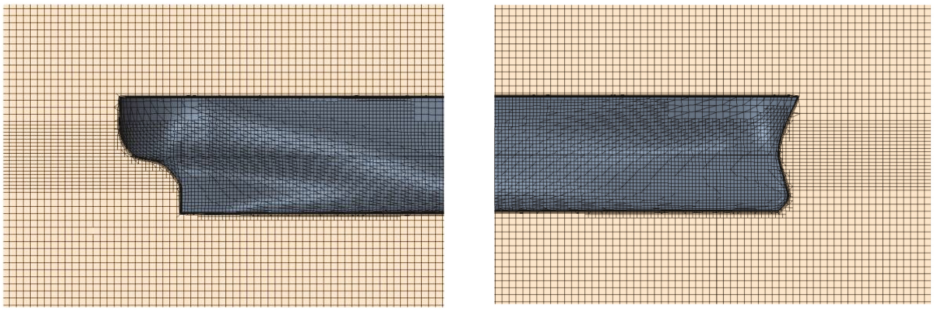

(**a**) (**b**)

Figure 8. Boundary layer mesh around hull surface at bow and stern: (**a**) stern; (**b**) bow.

The bi-directional cross wave can be obtained by the superposition of linear regular Airy waves coming from two orthogonal directions. The momentum source-term wave generating method was adopted to formulate the cross wave [20]. This kind of wave generating method can reduce the size of the computational domain and thus reduce the computing effort while not compromising the accuracy and reliability of the solution. Forcing region was applied near the four sidewalls of fluid domain to force the pattern of cross wave [21]. An example of the simulated cross wave field is shown in Figure 9, which shows the wave surface elevation. The figure confirmed that the cross wave simulation was well achieved, and the simulated cross waves are uniformly distributed throughout the tank.

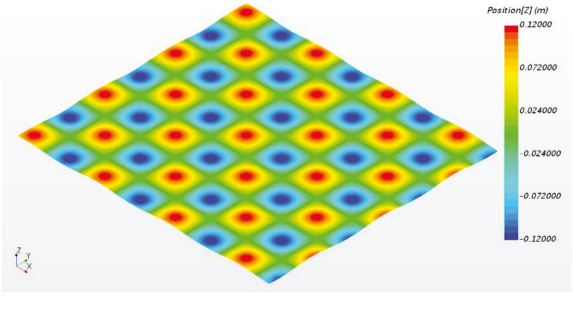

Figure 9. Example of the simulated cross wave field.

2.3. Simulation Conditions

The CFD numerical simulations of ship operating in cross waves have been carried out for different conditions. The involved conditions are summarized in Table 2. For the cross waves involved in this study, the wave lengths (and wave heights) of the two component regular waves are assumed to be identical and they are coming from two directions separated by 90°, i.e., only the monochrome cross wave is involved in this study. Moreover, different wave heading angles with respect to the ship are investigated. The head wave corresponds to 0°, and it increases clockwise, i.e., 90°, 180°, and 270°, corresponding to the starboard beam wave, following wave, and port beam wave, respectively. The ship forward speed is set at Froude's number of Fn = 0.25 for all cases. In the CFD calculations, for different simulation cases, the ship course angle was unchanged, while different wave heading angle was realized by changing the wave propagation direction of incident waves, which is shown in Figure 10.

Table 2. Numerical simulation conditions.

Case ID	Wave Heading, β_1/β_2 (°)	Resultant Wave Heading β (°)	Wave length, λ/L	Wave Height, H (mm)	Phase Difference, ε (rad)	Ship Speed, Fn
1–8	45/315	0	0.6, 0.8, 0.9, 1.0, 1.1, 1.2, 1.5, 2.0	120	0	0.25
9	0/90	45	1.0	120	0	0.25
10	45/135	90	1.0	120	0	0.25
11	90/180	135	1.0	120	0	0.25
12	135/225	180	1.0	120	0	0.25

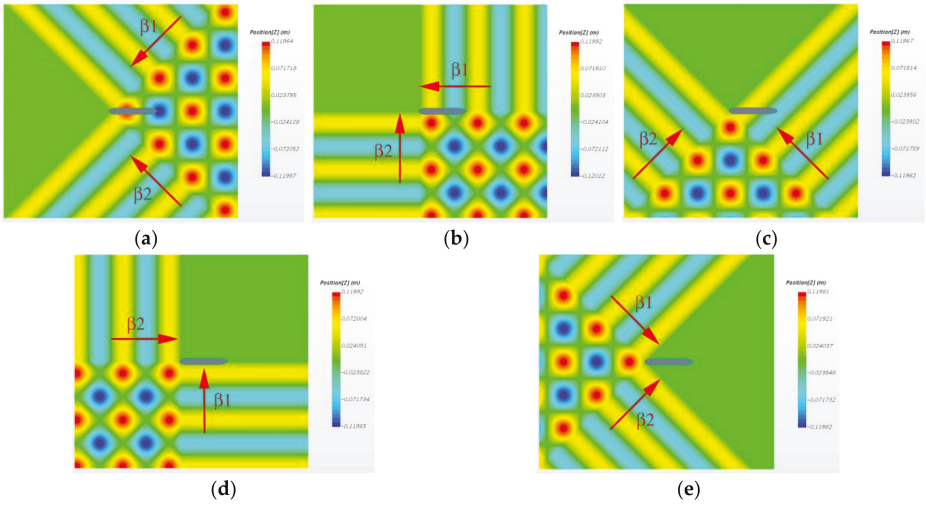

Figure 10. The initialized cross wave for different ship wave headings: (**a**) 45°/315° (Case 4); (**b**) 0°/90° (Case 9); (**c**) 45°/135° (Case 10); (**d**) 90°/180° (Case 11); (**e**) 135°/225° (Case 12).

The CFD simulations were performed using a computer with Intel Core i-9 CPU, 3.0 GHz, 18 core processors, 64 GB RAM, and 1 TB SSD disk for data writing. The majority of the conditions focus on calculating ship rigid-body motion responses; thus, the time step was set at 0.005 s, which was determined per the Courant number. On average, each of the simulation case took around three days to obtain sufficient time series of ship model's motions of 16 s. The slamming pressures were involved for calculation only in some typical calculation conditions due to the heavy calculation burden. In these conditions, the time step was set at 0.001 s, which is much smaller than other conditions, in order to

capture the impact pressure peak. The mesh was also refined with a total number of over 6 million cells for the slamming involved conditions. Higher mesh resolutions and smaller time step used for slamming pressure study took longer hours. On average, each simulation case took around 30 days for the same simulation period of 16 s.

The iterative convergence of CFD simulation was mainly judged by the residuals and behavior of the simulated signals. In the calculation procedure, the residual decreases gradually and oscillates periodically within a certain range. Moreover, the wave elevation and ship motion signals were also monitored for auxiliary judgment. For example, once the simulation converged, the wave elevation will be consistent with the theoretical value without any signal pollution.

3. Analysis of Cross Waves

The temporal and spatial distributional characteristics of the cross wave are analyzed in this section, which is fundamental for the subsequent ship seakeeping analysis. Due to the orthogonal property of the two component regular waves, the time series of surface elevation of resultant cross wave at any specific point follows a sine function, and it has a same frequency with the component regular wave. The wave amplitude at any specific point within the cross wave field is constant which falls in the closed interval of 0–2A, where A denotes the amplitude of component regular wave. It is noted that in the spatial field of cross wave there are stagnation points where the wave elevation remains zero and time-invariant.

However, the ship encounter wave is quite different from the in situ measurement result, and it depends on ship forward speed, course angle and navigational route. In the numerical wave tank, a wave probe was arranged in front of and with a distance of L/6 away from the ship bow to measure the incoming wave. The measured surface elevation of encounter wave includes the effects of radiation and diffraction due to the present of ship is summarized in Figure 11. This figure includes the cases for ship sailing in different wave headings at constant speed Fn = 0.25 in the same wave field with a wave length of λ/L = 1.0. The theoretical surface elevations of incident wave are also presented in the figures for comparison. As can be seen from the results, the measured data coincide well with the theoretical data of incident wave apart from the surface elevation at crest and trough peaks due to the radiation and diffraction waves in front of the advancing ship. The largest difference between the measured and theoretical value divided by wave amplitude (120 mm) are 16.72%, 13.64%, 14.00%, 10.87%, and 13.87% for the cases of wave heading 45°/315°, 0°/90°, 45°/135°, 90°/180°, and 135°/225°, respectively.

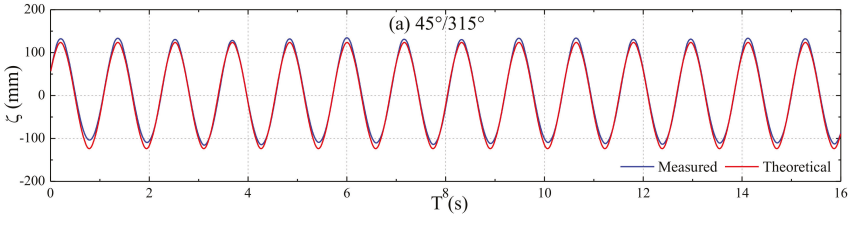

(**a**)

Figure 11. *Cont.*

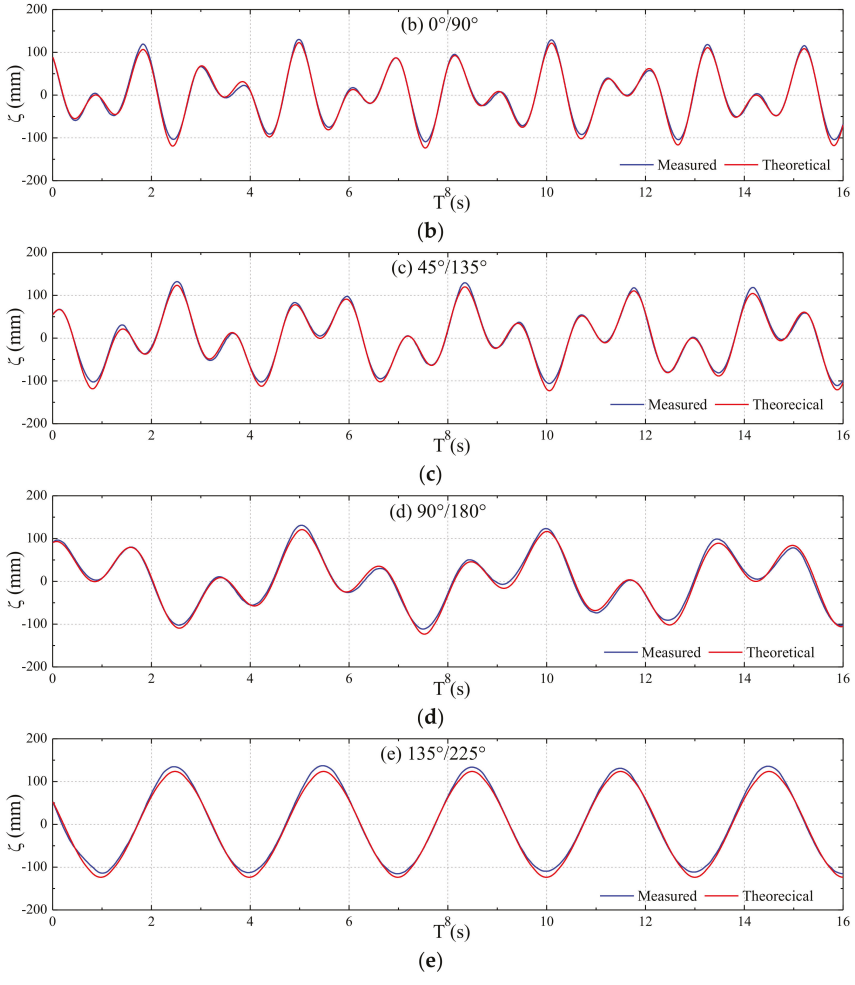

Figure 11. Surface elevation of ship encounter wave: (**a**) 45°/315° (Case 4); (**b**) 0°/90° (Case 9); (**c**) 45°/135° (Case 10); (**d**) 90°/180° (Case 11); (**e**) 135°/225° (Case 12).

It can be found that the time series of the encounter wave for ship advancing with wave heading 45°/315° or 135°/225° are monochromatic and sinusoidal, while the time series for the remaining three wave heading cases (0°/90°, 45°/135°, 90°/180°) are bichromatic and irregular. This can be explained by the fact that the ship encounter wave can be regarded as the superposition of two encounter component waves. For the cases of wave heading 45°/315° or 135°/225°, the encounter frequencies of the two component waves are identical; for the remaining three cases, the encounter frequencies of the two component waves are not identical. The encounter frequency of component wave can be obtained by

$$\omega_e = \omega\left(1 + \frac{U\omega\cos\beta}{g}\right), \tag{1}$$

where ω denotes wave frequency, ω_e denotes wave encounter frequency, U denotes ship speed, β denotes wave heading angle, and g denotes acceleration of gravity.

The frequency domain results of the ship encounter wave obtained by applying fast Fourier Transformation (FFT) of the time series data for different wave heading cases are summarized in Figure 12. The peak frequency can be identified from the vertical auxiliary red lines. As is seen from the curves, the peak frequency of encounter wave coincides well between the curves for different wave headings. The peak value of the curve for 45°/315° or 135°/225° that induced by two symmetric component waves is approximately double of the response peak value induced by asymmetric component wave due to the linear superposition effect of component waves. Moreover, a comparison of the peak frequency in Figure 12 against the encounter frequency obtained by Equation (1) is summarized in Table 3. The results indicate that the difference increases from 1.44% to 5.83% with the decrease of encounter frequency. The reason is that, in the case of head wave 180°, the ship speed is consistent with the wave propagation direction. Thus, the incident waves get superposed with the more diffraction wave, radiation wave, and ship steady wave, which affects the peak frequency of the incoming wave.

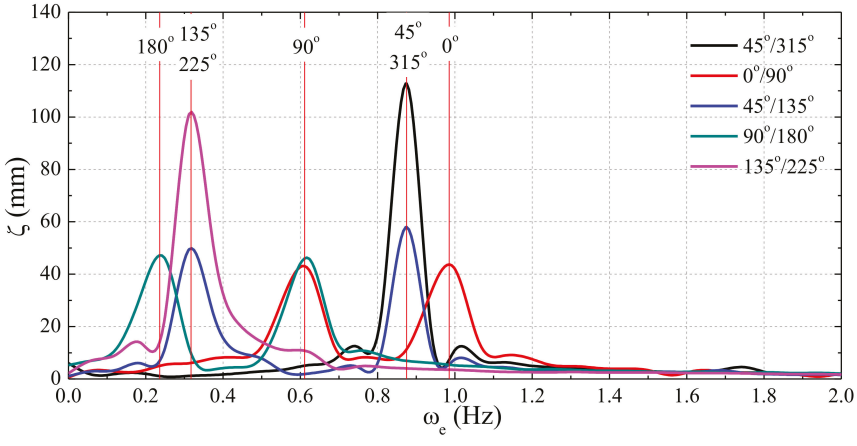

Figure 12. Frequency domain results of ship encounter wave.

Table 3. Comparison of the peak frequency with encounter frequency.

Wave Heading (°)	Peak Frequency (Hz)	Encounter Frequency (Hz)	Difference
0	0.985	0.971	1.44%
45/315	0.875	0.862	1.51%
90	0.611	0.597	2.35%
135/225	0.317	0.333	4.80%
180	0.236	0.223	5.83%

A band-pass filter was used to separate the component waves from the measured total cross wave for the three asymmetric wave heading cases. The cut-off frequency was set at 0.8 Hz, 0.6 Hz, and 0.4 Hz to divide the low- and high-frequency component wave for the cases of wave heading 0°/90°, 45°/125° and 90°/180°, respectively. As shown from the results in Figure 13, all the component waves show regular behavior with nearly the same amplitude of 60 mm. The results confirm that the cross wave can be regarded as the linear superposition of two component regular waves.

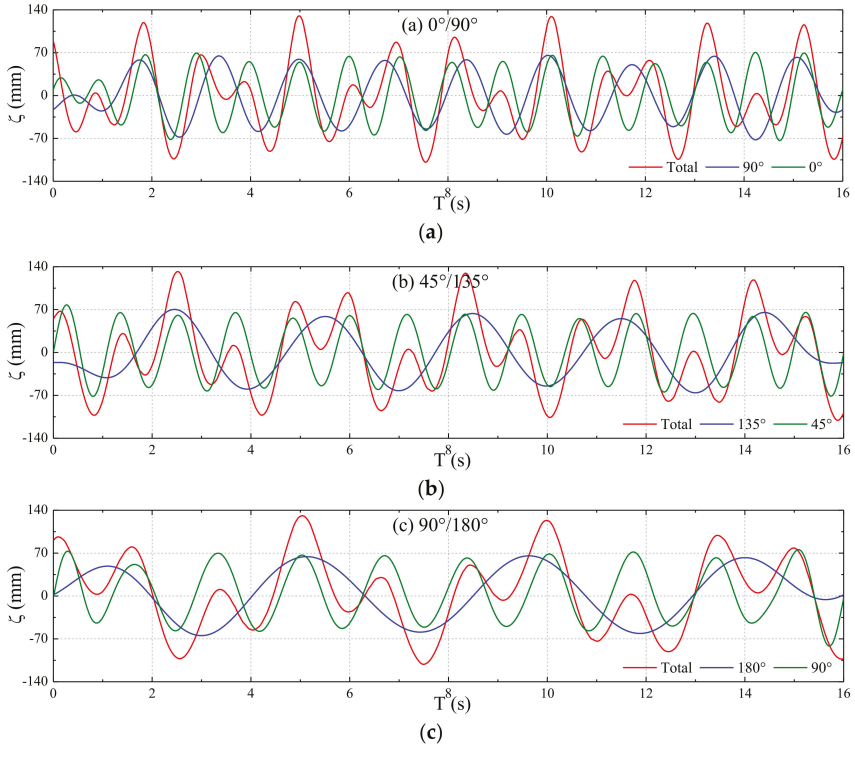

Figure 13. Wave components filtered from the measured cross wave: (**a**) 0°/90° (Case 9); (**b**) 45°/135° (Case 10); (**c**) 90°/180° (Case 11).

4. Analysis of Ship Seakeeping Behavior

Ship seakeeping behavior in the cross wave is systemically analyzed in this section. The CFD algorithm is preliminarily validated by comparing with experimental data of ship vertical motions in head regular waves. Then, ship motion responses and green water on deck in different cross wave fields are systemically analyzed. The impact pressure on the bow area induced by cross waves in typical conditions is also analyzed by the calculation results of the refined grid scheme. The results also indicate that ship motion response in a cross wave can be quite large, which is different from that induced by a uni-directional regular wave. It is worth mentioning that a comparative study on the ship's motion behavior in uni- and bi-directional waves has been conducted and reported in the authors' recently published paper [22].

4.1. Validation of the CFD Numerical Model

Some worldwide state-of-the-art wave basins are equipped with a two-side wave maker, which can be used for the generation of a cross wave. However, until now, ship seakeeping test in a cross wave has not been conducted or reported. Therefore, in this section, the developed CFD algorithm for ship seakeeping prediction is validated by comparison with some existing experimental data of ship motions in head regular waves presented by Fonseca and Guedes Soares [23].

The tests were conducted at the Laboratory of Ship Dynamics of the El Pardo Model Basin in Madrid, Spain, which is 150 m long by 30 m wide by 5 m deep. The experimental S175 ship model has the same dimensions as the numerical model used in this study. The ship speed Fn = 0.25 and wave amplitude 60 mm are selected in both the experiment and numerical simulation for the sake

of consistence. The ship heave and pitch motions in regular waves at different wave length range conditions are compared. It is worth mentioning that the numerical details including the mesh generation, wave making, and ship motion simulation methods in the regular wave cases are consistent with those in the cross wave cases. An example of the CFD simulated regular wave interaction with ship in a head wave case is shown in Figure 14.

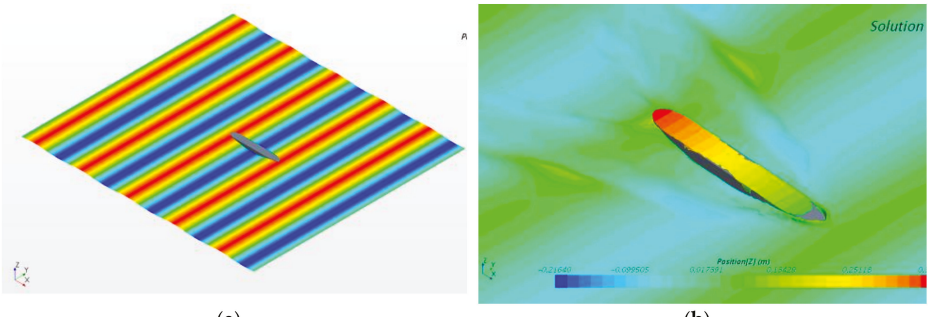

(**a**) (**b**)

Figure 14. Numerical simulation of ship motion in head regular wave: (**a**) overview of initial state; (**b**) green water on deck.

The comparative response amplitude operators (RAOs) of heave and pitch for the ship sailing in the head regular wave by experiment and numerical simulation are shown in Figure 15. As seen from the curves, the results confirmed that the ship motion responses predicted by the CFD solver coincide well with the experimental data even though there exist small difference near the peaks of the curve. The CFD numerical result overestimates the heave value by 4.25% at the peak of curve (at λ/L = 1.2). The experimental pitch value is slightly greater than the numerical data for the cases of λ/L > 1.2 and the largest difference 6.39% occurred at the peak of curve (around λ/L = 1.4).

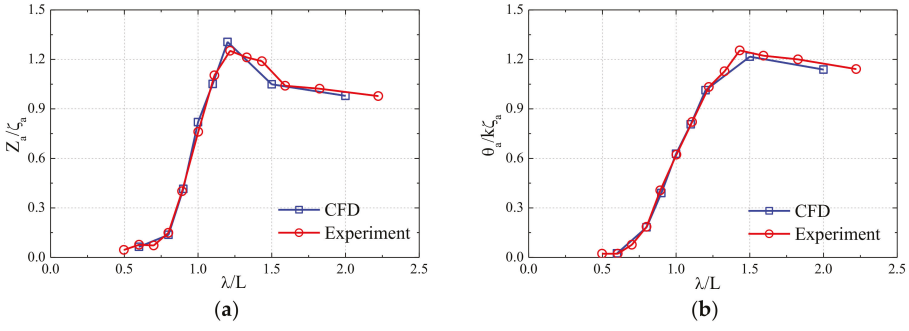

Figure 15. Comparison of experimental and numerical ship motions in head regular waves: (**a**) heave; (**b**) pitch.

4.2. Influence of Wave Heading on Ship Motions

The simulated time series of heave, pitch, and roll motions for the ship sailing in the cross wave field (λ/L = 1.0) at speed Fn = 0.25 at different wave headings (45°/315°, 0°/90°, 45°/135°, 90°/180°, and 135°/225°) are shown in Figures 16 and 17.

As can be seen from the results, the heave motion signal for ship sailing at wave headings 0° (45°/315°) and 180° (135°/225°) is regular or sinusoidal. Both the amplitude and frequency of the heave signal at wave heading angle 0° (45°/315°) is much greater than that of 180° (135°/225°). On the

other hand, the heave signal of the ship sailing at wave headings 45° (0°/90°), 90° (45°/135°), and 135° (90°/180°) is irregular and bichromatic. However, the bichromatic behavior of the ship sailing at wave heading 135° (90°/180°) is weak since the following component wave of 180° contributes less to the total heave response and the heave is mainly induced by the beam component wave of 90°.

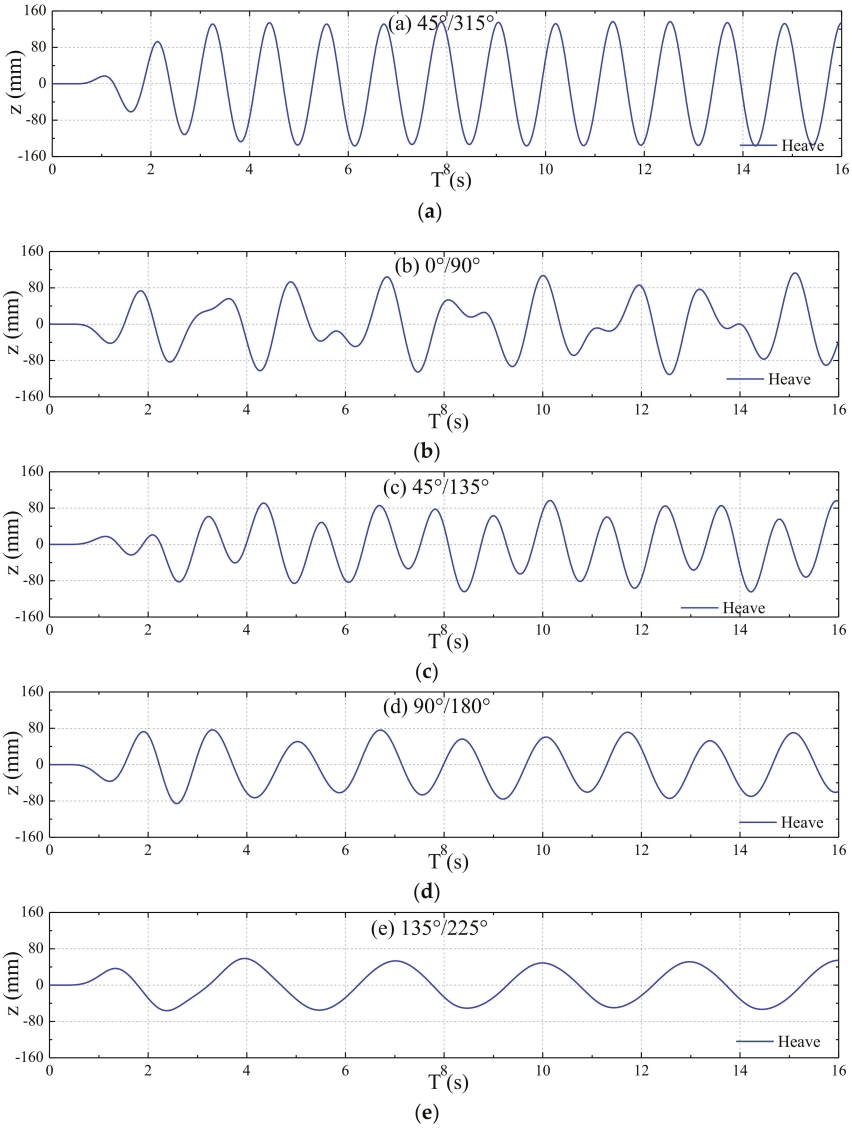

Figure 16. Time series of ship heave motion in different wave headings: (**a**) 45°/315° (Case 4); (**b**) 0°/90° (Case 9); (**c**) 45°/135° (Case 10); (**d**) 90°/180° (Case 11); (**e**) 135°/225° (Case 12).

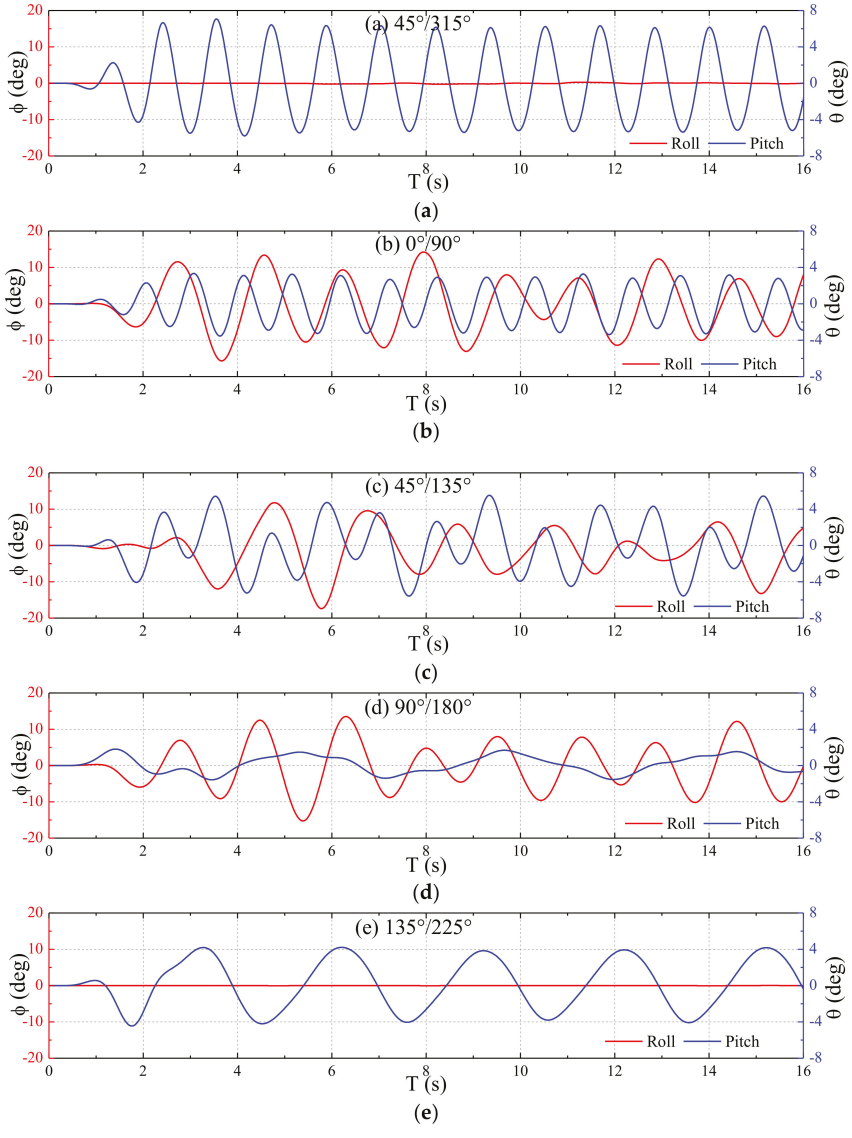

Figure 17. Time series of ship roll and pitch motions in different wave headings: (**a**) 45°/315° (Case 4); (**b**) 0°/90° (Case 9); (**c**) 45°/135° (Case 10); (**d**) 90°/180° (Case 11); (**e**) 135°/225° (Case 12).

Moreover, due to the symmetry of the incident wave, the roll motion is zero when the ship is sailing at wave heading 0° (45°/315°) or 180° (135°/225°), while the corresponding heave and pitch motion are regular. However, the roll and pitch motions for ship sailing at wave headings 45° (0°/90°), 90° (45°/135°), and 135° (90°/180°) are irregular or bichromatic, and the peak value of the roll is generally much larger than the pitch value for each case. The pitch response is small, with the largest value of 1.81° in the case of wave heading 135° (90°/180°) since the encounter frequency is far from its natural frequency. It is noted that the roll motion does not show steady behavior within the 16 s period. This is because the natural period of roll motion is relatively large, but the cycle period of roll

encountered by the ship within 16 s is limited. Since the CFD simulation time is not long enough due to computational cost limitation in this study, a longer simulation will be performed in future work to obtain more insightful conclusions.

The largest crest and trough peak values and the root mean square (RMS) of time series of ship motions within the 16 s varying with different resultant wave headings are summarized in Figure 18. Note that the polar angle in the polar coordinate denotes resultant wave heading of two component waves. As seen from the results, the largest heave and pitch response occur at resultant wave heading 0° (45°/315°). The second largest response values for heave and pitch occur at resultant wave heading 45° (0°/90°) and 90° (45°/135°), respectively. The lowest heave and pitch responses occur at resultant wave heading 180° (135°/225°) and 135° (90°/180°), respectively. The roll response value remains zero for the symmetrical wave heading case of resultant wave heading 0° (45°/315°) and 180° (135°/225°). The roll motion time series is not as steady as the pitch motion signal. The difference among the roll response statistical values in the three cases of resultant wave heading 45° (0°/90°), 90° (45°/135°), and 135° (90°/180°) is relatively small, and the largest peak (MAX) value lies in the narrow range of 15.25°–17.39°.

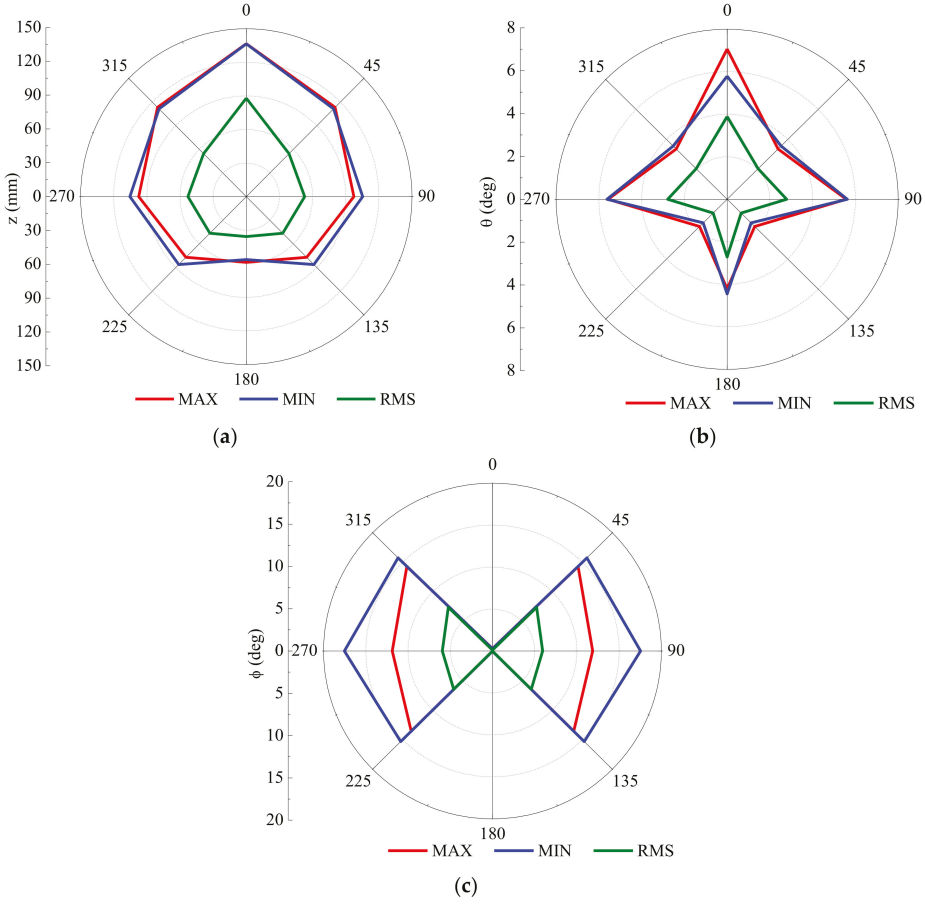

Figure 18. Response statistical values at different resultant wave heading: (**a**) heave; (**b**) pitch; (**c**) roll.

The severest vertical motion of the ship occurs in the resultant head wave condition 0° (45°/315°). The RMS value of heave and pitch for a ship sailing at the wave heading 0° (45°/315°) is, respectively, about three and two times as large as the value for the wave heading 180° (135°/225°). For a better understanding of the ship wave interaction problem, a comparison of the large amplitude longitudinal motion and green water on deck for a ship in the two symmetric wave conditions is shown in Figure 19. The figure includes two phases of ship motion state, which are bow up and bow down motions. As can be seen from the figures, severe green water on deck occurred when the ship was sailing in the wave heading 0° (45°/315°), and the water even overtopped and scoured the whole deck from bow to stern. However, due to the relatively small pitch and heave motion, only slight green water occurred when the ship was in a bow down motion phase at the wave heading 180° (135°/225°).

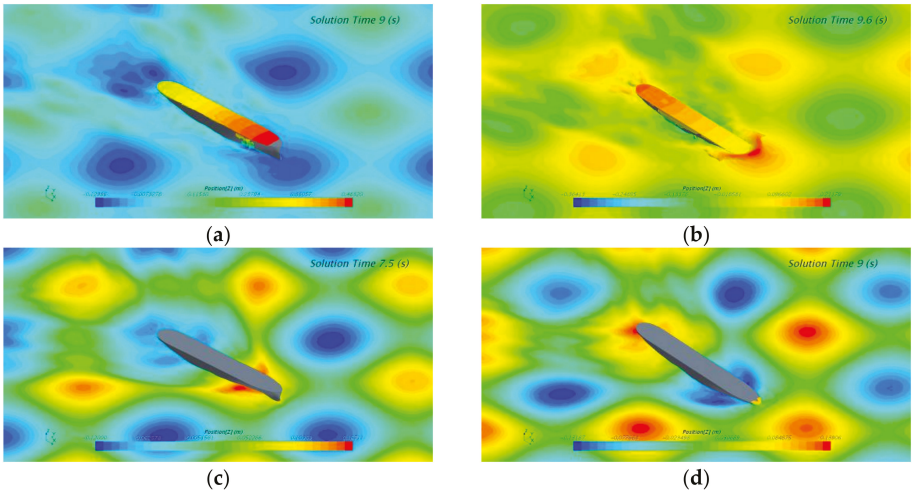

(**a**) (**b**) (**c**) (**d**)

Figure 19. Comparative view of ship green water on deck at bow emergence and down phases: (**a**) 0° (45°/315°) at t = 9 s; (**b**) 0° (45°/315°) at t = 9.6 s; (**c**) 180° (135°/225°) at t = 7.5 s; (**d**) 180° (135°/225°) at t = 9 s.

To be different from the large amplitude vertical motion of ship in the symmetrical waves, significant roll motion would occur for a ship sailing in the asymmetrical waves. The large amplitude roll motion procedure of a ship sailing in the wave heading 90° (45°/135°) is depicted in Figure 20. It can be observed that the water scoured onto the deck from the port side and ran out from the starboard side due to the coupled effect of pitch and roll motions. The green water for a ship in the wave heading 90° (45°/135°) is not as severe as that in the head wave condition 0° (45°/315°), and the reason is twofold: first, the vertical acceleration on deck is lower for ship in the wave heading 90° (45°/135°); second, the roll period is much larger than pitch period even though the roll amplitude is relatively large. Thus, the large roll will not result in so violent a flow on deck as that of the pitch motion.

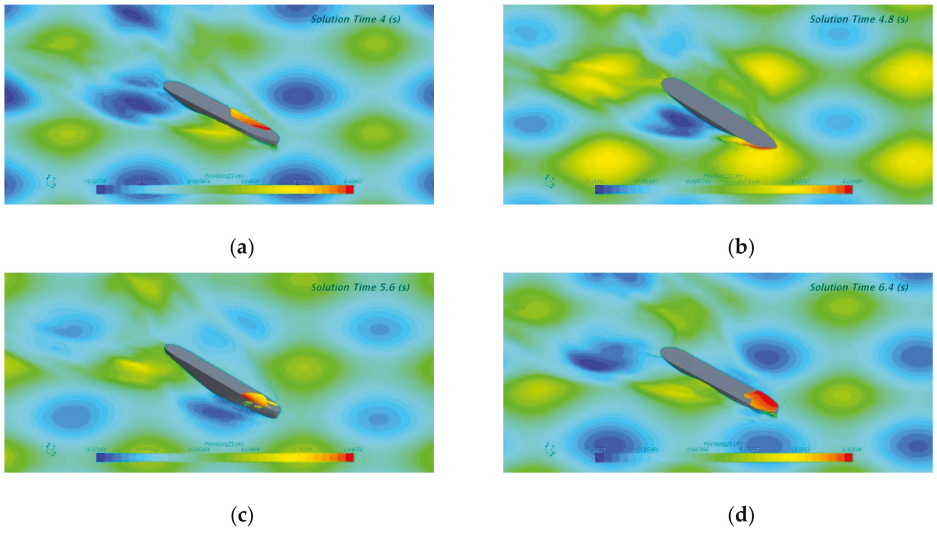

Figure 20. Ship large amplitude roll motion process at wave heading 90° (45°/135°): (**a**) t = 4 s; (**b**) t = 4.8 s; (**c**) t = 5.6 s; (**d**) t = 6.4 s.

4.3. Influence of Wave Length on Ship Motions

As concluded from the above analysis, the severest heave and pitch motions generally occur when ship sailing at the wave heading 45°/315°. The time series of ship heave and pitch motions at different wave lengths λ/L = 0.6–2.0 for wave heading 45°/315° and ship speed Fn = 0.25 are summarized in Figure 21. As it is seen from the time series, the vertical motion signals are generally regular and sinusoidal, with different amplitudes and different encounter frequencies.

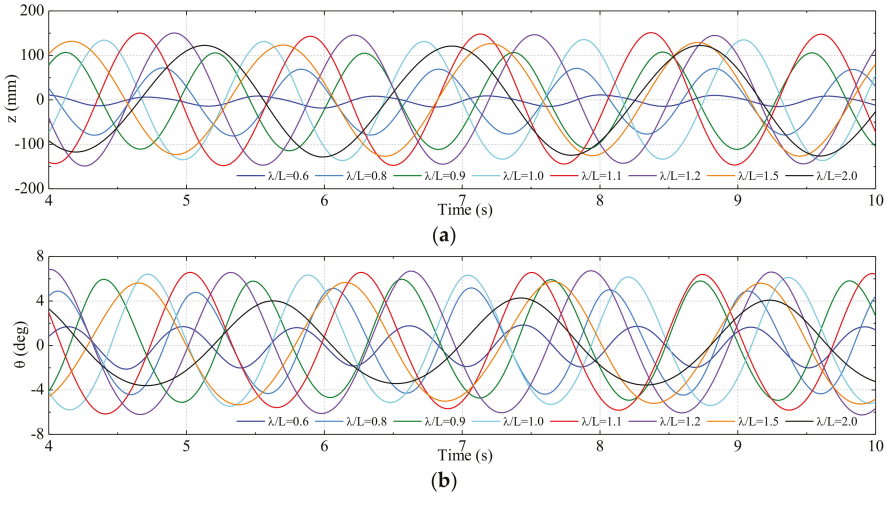

Figure 21. Time series of ship vertical motion at different wave lengths: (**a**) heave; (**b**) pitch.

The amplitude of ship vertical motions in different wave lengths λ/L = 0.6–2.0 at the wave heading 45°/315° is summarized in Figure 22. The results indicate that the heave increases from λ/L = 0.4 to 1.0 almost linearly, and the largest heave amplitude of 146.7 mm appears at λ/L = 1.1. The heave

amplitude trends steadily with a same value of the wave amplitude 120 mm when λ/L is greater than 1.5. The largest pitch amplitude 6.71° occurs at λ/L = 1.2 and decreases rapidly with the increasing λ/L. To summarize, the largest vertical motion response occurs when the encounter frequency is at or near the natural frequency of ship. The forward speed also contributes to the vertical motion especially for the cases around the peak.

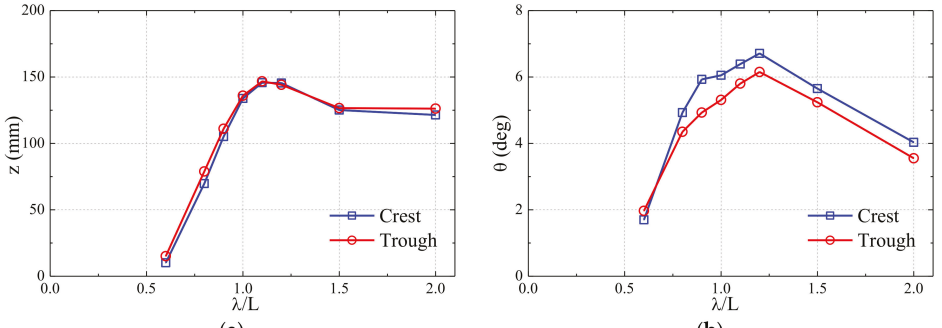

Figure 22. Ship vertical motion amplitude value at different wave lengths: (**a**) heave; (**b**) pitch.

The green water on deck phenomenon for ship sailing in the wave heading 45°/315° at four typical wave lengths of λ/L = 0.8, 1.2, 1.5, and 2.0 is compared in Figure 23. The figures reveal that the severest green water occurred in the case of λ/L = 1.2. This can be explained by the fact that a severe slamming event and green water on deck occurred when the encounter frequency is at or near the ship motion's resonant frequency. The green water on deck in the cases of λ/L = 0.8 and 1.2 is quite harsh. The heave and pitch motion response in the range of λ/L = 0.8–1.2 are also relatively high (see Figure 22), which results in the severe slamming and green water on deck. Only slight deck wetness occurred in the case of λ/L = 1.5, and no green water occurred in the case of λ/L = 2.0.

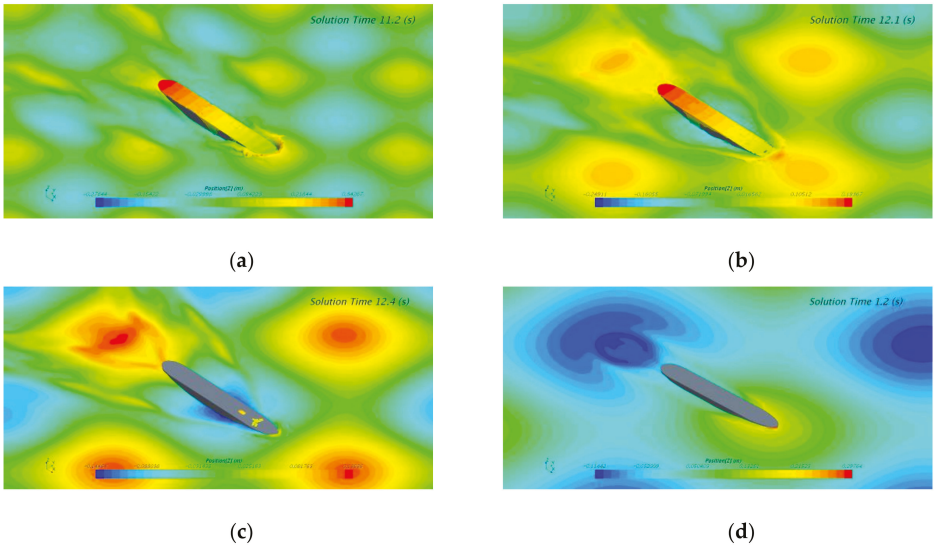

Figure 23. Green water on deck for ship in different wave length: (**a**) λ/L = 0.8; (**b**) λ/L = 1.2; (**c**) λ/L = 1.5; (**d**) λ/L = 2.0.

In addition, a view of ship slamming and green water procedure within one encounter period for ship sailing in the wave condition of $\lambda/L = 1.2$ is shown in Figures 24 and 25. The figures reveal that the water overtopped and scoured the whole deck from bow to stern. These figures also clearly reveal that the breaking waves and the splashing water have been successfully captured by the CFD simulation.

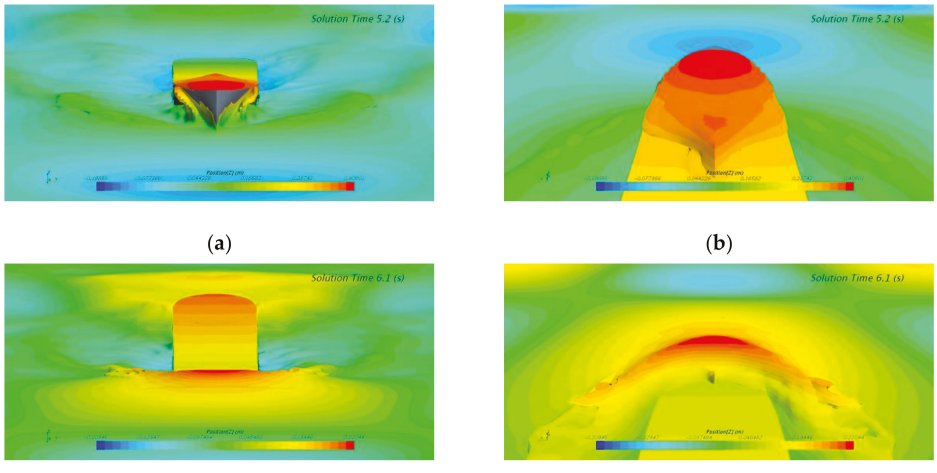

Figure 24. Front and deck view of wave impact and green water on deck ($\lambda/L = 1.2$): (**a**) front view ($t = 5.2$ s); (**b**) deck view ($t = 5.2$ s); (**c**) front view ($t = 6.1$ s); (**d**) deck view ($t = 6.1$ s).

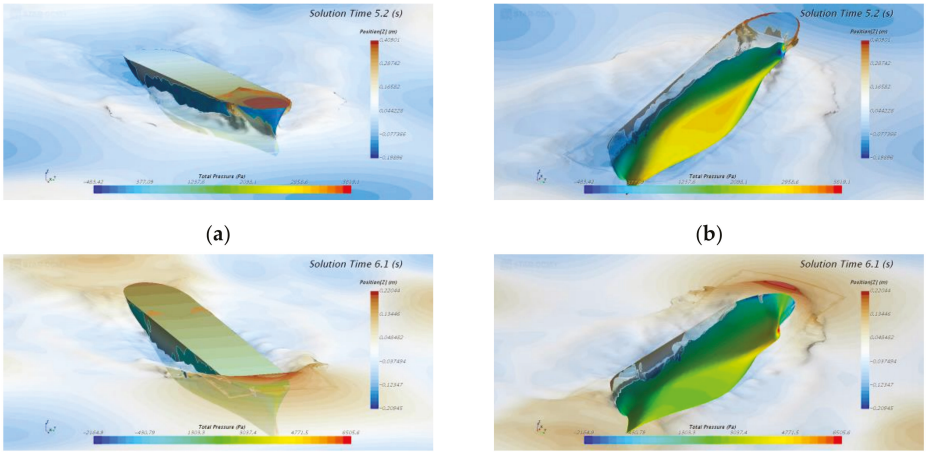

Figure 25. Starboard side view of wave impact and green water on deck ($\lambda/L = 1.2$): (**a**) top view ($t = 5.2$ s); (**b**) bottom view ($t = 5.2$ s); (**c**) top view ($t = 6.1$ s); (**d**) bottom view ($t = 6.1$ s).

5. Slamming Pressure on Ship Bow Area

The distribution of wave impact pressure on the bow area for the ship sailing in a cross wave is investigated in this section. Two typical conditions including the ship sailing in both symmetric and asymmetric cross wave fields are selected for investigation.

The time series of ship bow impact pressure in the severest wave condition ($\lambda/L = 1.2$, wave heading 45°/315° and ship speed $Fn = 0.25$) is summarized in Figure 26. In the figure, only the pressure data on the port side and the centerline of bow are presented due to the symmetry of the ship motion response and pressure distribution. Generally, the peak value of impact pressure decreases from the bottom to the deck and also from the bow to the stern. For example, the pressure peak value decreases from P7 to P3 (or from P11 to P8) and also decreases from P1 to P8 (or from P2 to P9, from P3 to P10). The largest impact pressure peak occurred at pressure sensor P7, which is mounted on bow bottom area. The peak of the pressure signal is very sharp for the measurement in the upper locations, and the peak of the curve becomes much smoother for the measurement downward. This is affected by the contact time and velocity of the hull surface with respect to the water wave and the dead rise angle of geometry. The sharpness of the pressure signal increases with the increasing of velocity of water entry and with the decreasing of the dead rise angle.

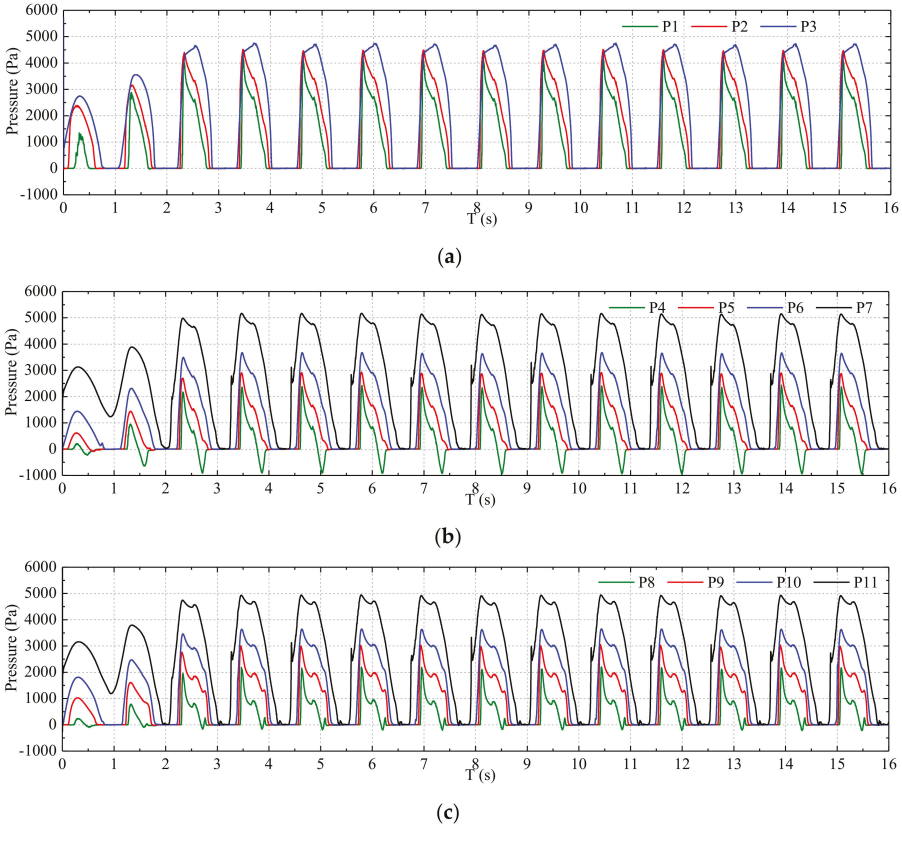

Figure 26. Impact pressure for the case of ship sail in symmetric wave field: (**a**) sensors at centerline of bow; (**b**) sensors at cross-section of #19.5 station; (**c**) sensors at cross-section of #19 station.

The asymmetric impact pressure acting on ship bow in the case of wave condition (λ/L = 1.2, wave heading 0°/90° and ship speed Fn = 0.25) is shown in Figure 27. Five typical pressure positions

are involved for illustration, which include P1–P3 at centerline and two symmetric P5 points at both the port and starboard sides. The pitch and roll motion are also presented together with the pressure curves for reference. As seen from the results, the pressure peak for the measurements of P1–P3 at centerline occurred almost simultaneously when the ship was in a bow down motion phase. Their slamming peak values fluctuate in a small range. However, due to the large roll motion, the pressure signal P5 at the bow side area is unsteady, and the large peak value alternates between the port and starboard sides. Their slamming peak values fluctuate in a relatively large range. View of the ship wave interaction in the asymmetric wave field at $t = 4$ s from different visual angles are presented in Figure 28, which corresponds to the moment of largest impact peak at P5 of port side.

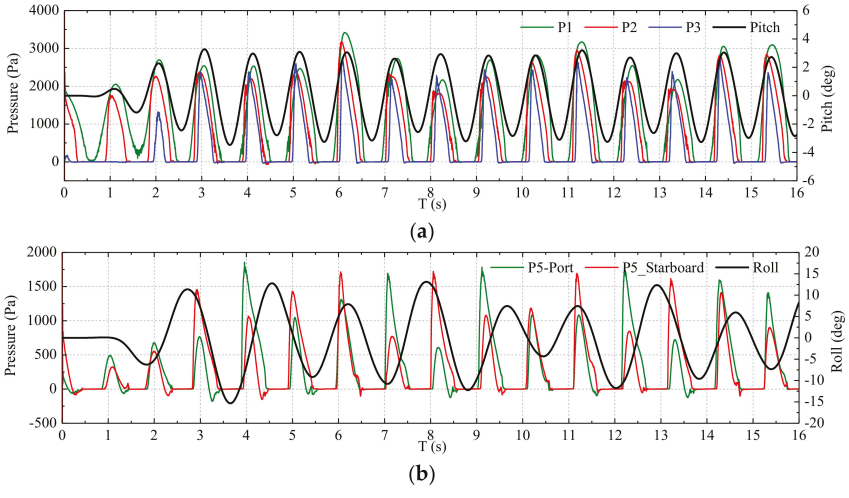

Figure 27. Impact pressure and pitch & roll for the case of ship sail in asymmetric wave field: (**a**) sensors at centerline of bow; (**b**) sensors at P5.

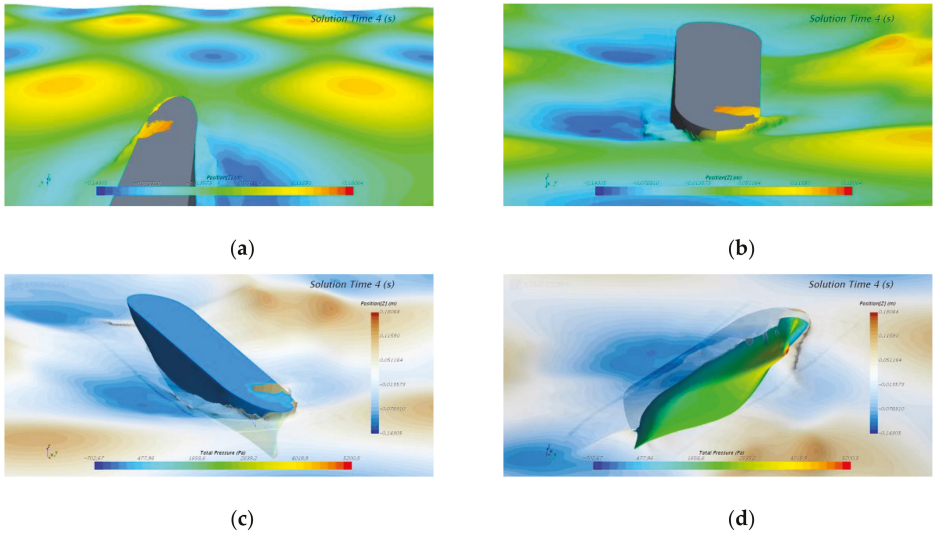

Figure 28. View of ship wave interaction in the asymmetric wave field ($t = 4$ s): (**a**) deck view; (**b**) front view; (**c**) top view; (**d**) bottom view.

The largest peak values of slamming pressure monitored by different sensors in the two conditions are summarized in Table 4. It can be found that a small difference (below 1%) can be observed at the corresponding sensors of the port and starboard sides even in the symmetric wave 0° (45°/315°) case. This was caused by the error introduced in geometric modeling and grid generating and the strongly randomicity and uncertainty of the slamming signal. The peak pressure at each sensor positions in the symmetric wave 0° (45°/315°) case are all greater than in the asymmetric wave 45° (0°/90°) case. For ship sailing in the asymmetric wave 45° (0°/90°) case, the peak pressure on the starboard side are generally greater than the port side since the resultant wave heading is starboard quarter wave. For both of the two conditions, the largest impact pressure peak occurred at pressure sensor P7, which is mounted on bow bottom area, and the smallest pressure peak occurred at P8 due to its lowest velocity of water entry.

Table 4. Summary of the largest peak values at bow area (in kPa).

Sensor ID		P1	P2	P3	P4	P5	P6	P7	P8	P9	P10	P11
Symmetric case 0° (45°/315°)	Port	4.40	4.49	4.75	2.41	2.92	3.68	5.17	2.18	3.03	3.65	4.94
	Starboard				2.39	2.91	3.67		2.16	3.03	3.64	
Asymmetric case 45° (0°/90°)	Port	2.72	3.18	3.42	1.51	1.84	2.56	3.89	1.42	1.97	2.56	3.79
	Starboard				1.71	1.74	2.49		1.71	2.07	2.71	

According to the above analysis, ship will probably encounter large amplitude vertical or transverse motion and severe slamming and green water on deck when sailing in cross waves. The cross wave will pose a threat to the navigational safety of a ship. Therefore, it is of great importance to provide some insightful strategies for the operational guidance of a ship when suffering a cross wave. As concluded from the wave analysis section, in the cross wave field, there exist stagnation lines where the wave elevation remains zero and time-invariant. The ship will experience the lowest wave if it travels along the stagnation lines. The motions of ship sailing along the stagnation line have been investigated in our recent work [24]. The lowest vertical motion responses can be realized when the ship sails along the stagnation lines at a wave heading of 0° (45°/315°).

6. Conclusions

This paper presents a numerical study on the seakeeping and slamming behavior of a S175 ship sailing in cross waves by CFD-based software STAR-CCM+. An URANS solver, which uses VOF and overset grid techniques, was developed in the framework of CFD to predict ship seakeeping behavior. This study also sheds some light on ship motion and slamming behavior in multi-directional or short-crested waves.

The numerical simulation results reveal that the cross wave can be approximately regarded as the linear superposition of two component regular waves. The surface elevation at a specific location within a monochromatic cross wave field follows the sine function with stagnation points existing in the wave field. The encounter wave is regular when the ship sails at a symmetrical wave heading with respect to the cross wave. However, the encounter wave is irregular and bi-chromatic when the ship sails at an asymmetrical wave heading with respect to the cross wave.

The ship heave and pitch motion is sinusoidal and regular, whereas the roll motion remains zero when the ship wave heading is symmetric with respect to the cross wave. The ship will experience the severest vertical motion when sailing at wave heading 45°/315°. The ship roll motion is generally large in addition to the pronounced vertical motions when the ship wave heading is asymmetric with respect to the cross wave. Ship vertical motion behavior in a cross wave is quite different from that in a regular wave, and the coupled effect of vertical and transverse motions of a ship in the cross wave should be of concern for the safety of ship.

For a ship advancing in a symmetric cross wave, the peak value of impact pressure decreases from the bottom to the deck and also from the bow to the aft. The peak of pressure signal is very

sharp for the measurement in the upper locations, and the curve peak becomes much smoother for the measurement downwards. For ship advancing in an asymmetric cross wave, the pressure signal at bow side area is unsteady and the large peak value alternates between port and starboard sides due to the large roll motion.

Although the CFD model was preliminary validated by the experimental data of ship motion in uni-directional head regular wave from tank measurement, the tank experiments for ship operating in cross wave have not been conducted or reported. Future work will focus on the experimental investigation of ship motion behavior in a cross wave and the validation of the CFD numerical method using experiment data. Moreover, comprehensive analysis of ship motions and slamming loads in different cross waves (i.e., various wave lengths, wave heights, wave heading angles, and phase differences, and even bichromatic cross waves) will be undertaken in our future studies.

Author Contributions: J.J. and S.H. contributed equally to this paper. J.J. and S.H. designed the research scheme, S.H. conducted the CFD computation, J.J. analyzed the data, and J.J. wrote the paper. All authors have read and agreed to the published version of the manuscript.

Funding: This research was supported by the National Natural Science Foundation of China (No. 51909096), the Pre-Research Field Foundation of Equipment Development Department of China (No. 61402070106), and the Guangdong Basic and Applied Basic Research Foundation (No. 2020A1515011181).

Conflicts of Interest: The authors declare no conflict of interest. The funders had no role in the design of the study; in the collection, analyses, or interpretation of data; in the writing of the manuscript, or in the decision to publish the results.

References

1. Zheng, W.T.; Miao, Q.M.; Zhou, D.C.; Kuang, X.F. Difference between motions in 3D and 2D waves. *J. Ship Mech.* **2009**, *13*, 184–188. (In Chinese)
2. Hirdaris, S.E.; Bai, W.; Dessi, D.; Ergin, A.; Gu, X.; Hermundstad, O.A.; Huijsmans, R.; Iijima, K.; Nielsen, U.D.; Parunov, J.; et al. Loads for use in the design of ships and offshore structures. *Ocean Eng.* **2014**, *78*, 131–174. [CrossRef]
3. Song, H.; Tao, L. Short-crested wave interaction with a concentric porous cylindrical structure. *Appl. Ocean Res.* **2007**, *29*, 199–209. [CrossRef]
4. Ji, X.; Liu, S.; Bingham, H.B.; Li, J. Multi-directional random wave interaction with an array of cylinders. *Ocean Eng.* **2015**, *110*, 62–77. [CrossRef]
5. Wang, L.Q. The Study of 3D and 3D Random Waves Acting on a Semicircular Breakwater. Ph.D. Thesis, Dalian University of Technology, Dalian, China, 2006. (In Chinese).
6. Renaud, M.; Rezende, F.; Waals, O.; Chen, X.B.; Dijk, R.V. Second-order wave loads on a LNG carrier in multi-directional waves. In Proceedings of the ASME 27th International Conference on Offshore Mechanics and Arctic Engineering, Estoril, Portugal, 15–20 June 2008; pp. 1–8.
7. Chen, J.P.; Wei, J.F.; Zhu, D.X. Numerical simulations of ship motions in long-crested and short-crested irregular waves by a 3D time domain method. *Chin. J. Hydrodyn.* **2011**, *26*, 589–596. (In Chinese)
8. Jiao, J.; Chen, C.; Ren, H. A comprehensive study on ship motion and load responses in short-crested irregular waves. *Int. J. Nav. Archit. Ocean Eng.* **2019**, *11*, 364–379. [CrossRef]
9. ITTC. The Seakeeping Committee, Final report and recommendations to the 26th ITTC. In Proceedings of the 26th ITTC, Vol. I, Rio de Janeiro, Brazil, 28 August–3 September 2011.
10. ITTC. The Seakeeping Committee, Final report and recommendations to the 27th ITTC. In Proceedings of the 27th ITTC, Vol. I, Copenhagen, Denmark, 31 August–5 September 2014.
11. ITTC. The Seakeeping Committee, Final Report and Recommendations to the 28th ITTC. In Proceedings of the 28th ITTC, Vol. I, Wuxi, China, 18–22 September 2017.
12. Hashimoto, H.; Yoneda, S.; Omura, T.; Umeda, N.; Matsuda, A.; Stern, F.; Tahara, Y. CFD prediction of wave-induced forces on ships running in irregular stern quartering seas. *Ocean Eng.* **2020**, *239*, 106277. [CrossRef]
13. Guo, B.J.; Steen, S.; Deng, G.B. Seakeeping prediction of KVLCC2 in head waves with RANS. *Appl. Ocean Res.* **2012**, *35*, 56–67. [CrossRef]

14. Chen, S.; Hino, T.; Ma, N.; Gu, X. RANS investigation of influence of wave steepness on ship motions and added resistance in regular waves. *J. Mar. Sci. Technol.* **2018**, *23*, 991–1003. [CrossRef]
15. Wang, W.; Bihs, H.; Kamath, A.; Arntsen, Ø.A. Multi-directional irregular wave modelling with CFD. *Lecture Notes Civil Eng.* **2019**, *22*, 521–529.
16. Cao, H.J.; Wan, D.C. Development of multidirectional nonlinear numerical wave tank by Naoe-FOAM-SJTU solver. *Int. J. Ocean Syst. Eng.* **2014**, *4*, 49–56. [CrossRef]
17. Wang, W.; Kamath, A.; Bihs, H. CFD simulations of multi-directional irregular wave interaction with a large cylinder. In Proceedings of the 37th International Conference on Ocean, Offshore and Arctic Engineering (OMAE), Madrid, Spain, 17–22 June 2018.
18. Tezdogan, T.; Incecik, A.; Turan, O. Full-scale unsteady RANS simulations of vertical ship motions in shallow water. *Ocean Eng.* **2016**, *123*, 131–145. [CrossRef]
19. Pereira, F.S.; Eça, L.; Vaz, G. Verification and Validation exercises for the flow around the KVLCC2 tanker at model and full-scale Reynolds numbers. *Ocean Eng.* **2017**, *129*, 133–148. [CrossRef]
20. CD-adapco. *User Guide STAR-CCM+ Version 14.02*; CD-adapco: Melville, NY, USA, 2019.
21. Li, D.Q.; Li, G.H.; Dai, J.J.; Zhang, Y.L.; Li, P. Numerical prediction of the added resistance and motions of ship in head waves based on overset mesh method. *Ship Sci. Technol.* **2018**, *40*, 13–20. (In Chinese)
22. Huang, S.X.; Jiao, J.L.; Chen, C.H. Comparative study on ship motions in uni- and bi-directional waves by CFD. In Proceedings of the 30th International Ocean and Polar Engineering Conference (ISOPE-2020), Shanghai, China, 12–16 October 2020.
23. Fonseca, N.; Guedes Soares, C. Experimental investigation of the nonlinear effects on the vertical motions and loads of a containership in regular waves. *J. Ship Res.* **2004**, *48*, 118–147.
24. Jiao, J.L.; Huang, S.X.; Chen, C.H. Numerical investigation of ship motions in cross waves using CFD. *Appl. Ocean Res.* **2020**, (Under Review).

Journal of
Marine Science and Engineering

MDPI

Article

Numerical Investigation of Unsteady Cavitation Dynamics over a NACA66 Hydrofoil near a Free Surface

Tiezhi Sun [1,2], Qingmo Xie [1], Li Zou [1,2,3,*], Hao Wang [4] and Chang Xu [5]

[1] School of Naval Architecture, Dalian University of Technology, Dalian 116024, China; suntiezhi@dlut.edu.cn (T.S.); alvinxqm@mail.dlut.edu.cn (Q.X.)
[2] State Key Laboratory of Structural Analysis for Industrial Equipment, Dalian 116024, China
[3] Collaborative Innovation Center for Advanced Ship and Deep-Sea Exploration, Shanghai 200240, China
[4] China Institute of Water Resources and Hydropower Research, Beijing 100038, China; wanghao@iwhr.com
[5] Department of Ocean Engineering, Texas A&M University, College Station, TX 77843, USA; xuchang@tamu.edu
* Correspondence: lizou@dlut.edu.cn; Tel.: +86-0411-84706373

Received: 21 April 2020; Accepted: 8 May 2020; Published: 11 May 2020

Abstract: Cavitation is a typical and unavoidable phenomenon for small waterline ships and high-speed vehicles. It creates a highly complex multiphase flow near the free surface and is primarily represented by the free surface-cavitation interaction. In this paper, the large-eddy method and Schnerr-Sauer cavitation model are combined to address the effects of a free surface on the cavitation dynamics of a NACA66 hydrofoil. The numerical method is validated by comparing the cavitation morphology and pressure with available experimental data. The results show that the presence of a free surface affects the cavitation evolution and hydrodynamic load characteristics. Compared with the non-free surface case for the same cavitation number, the free surface suppresses the cavitation intensity and increases the frequency of cavitation shedding. Furthermore, an improved dynamic mode decomposition method is applied to investigate the unsteady cavitation flow features. The results show a correlation between the characteristic mode and the flow state. Meanwhile, the presence of a free surface is found to reduce the energy content in each order mode and results in smaller scale of the coherent structure in higher-order modes. Moreover, with increasing distance from the hydrofoil to the free surface, the cavitation intensity increases, as well as the average lift and drag coefficients. In particular, significant free-surface unsteady fluctuations are observed in the wake region.

Keywords: near free surface; unsteady cavitation dynamics; NACA66 hydrofoil; dynamic mode decomposition

1. Introduction

Cavitation is a complex phenomenon that occurs when the local pressure in a liquid drops below the local saturated vapor pressure. This pressure drop always occurs around a rapidly moving object and is generated at the internal or liquid-solid interface of the liquid [1,2]. Cavitation can cause performance degradation, corrosion, vibration, and noise in hydraulic machinery, and is a major factor in fluid instability [3–5]. Particularly for the underwater region of a high-speed vehicle located near a free surface, free surface-cavity interactions render the flow field more complicated [6].

Unsteady cavitation flows are an important problem for ocean engineering [7–9]. Knapp [10] observed and analyzed cloud-cavitation flows, demonstrating that the re-entrant flow starting from the closed position of the cavitation causes the cloud cavitation to break off. Kubota et al. [11] measured

the flow structure of cloud cavitation using a laser Doppler anemometer (LDA) and compared it with the results obtained by a high-speed camera. The authors found a maximum of vorticity in the center of the cloud cavitation. Kawanami et al. [12] studied the nature of cavitation flow instability and found that cloud-like cavitations are closely related to retroreflective flows in a closed bubble. Reissman et al. [13] studied cloud-like cavitation around an oscillating hydrofoil using high-speed cameras and pressure sensors, and investigated the mechanism of transient pressure pulses near the detached cavitation. Arndt et al. [14] studied the flow of an NACA0015 hydrofoil from flaky cavitation to cloud cavitation by combining experimental and numerical methods. The authors observed two competing cavitation shedding induction mechanisms: re-entrant flow and a shock wave with the cavitating flow; moreover, they presented the dominant conditions for these two mechanisms. Gopalan et al. [15] proposed that the vortex generation and collapse are important characteristics of a cavitation flow. Leroux et al. [16,17] observed the cavitation flow of a NACA66 hydrofoil and proposed that the re-entrant flow is the primary cause of cavitation shedding. Passandideh-Fard and Roohi [18] used a modified VOF method to capture the gas-liquid interface of a two-dimensional cavitation flow field. The results show that the modified VOF method has higher calculation efficiency and calculation accuracy. Ganesh et al. [19] used wedges to study the transformation from sheet cavitation to cloud cavitation. Pendar and Roohi [20] used large eddy simulation to study cavitation around a sphere and compared with non-cavitation flow field. The result shows that cavitation suppresses instability near wake region and delays 3D decomposition of the vortex. Capurso et al. [21] simulated the hydrofoil with a passive control system. Their study indicated that passive control system suppress the cavitation effectively, which provides an effective solution to avoid the influence of cavity erosion on hydrofoil. Cheng et al. [22,23] used large-eddy simulations (LES) to capture an unstable tip leakage cavitation flow, and the spatial evolution of the tip leakage cavitation flow was divided into three stages. The results revealed how cavitation affects vorticity and turbulence. Researchers have performed numerous studies on cavitating flows at an infinite water depth; however, studies on cavity dynamics near free surface are limited.

Dawson [24] observed supercavitation near a free surface; however, the cavitating flow in the experiments was generated by ventilation under low-velocity restriction in a tunnel. Theoretical analysis and numerical simulations are the primary research methods used at present [25–28]. Faltinsen [29] proposed a theoretical model for free surface effects of hydrofoil cavitation. Kinzel et al. [30] simulated the supercavitation of the hydrofoil under a free surface and proved that using time accurate multiphase Navier-Stokes CFD method to simulate cavitation near the free surface is feasible. Wang et al. [31] performed experiments and simulations on the cavitation of a revolving body near a free surface. It has been proposed that the free surface will reduce the re-evaporation of the cavitation, and that the cavitation will become more stable as it approaches the free surface. Based on Wang's result, a multiphase flow solver for simulating near-free-surface cavitation flows has been proposed and validated [32,33]. The numerical simulation has been proven to be capable of analyzing the effect of unsteady cavitation flows near a free surface. However, the cavitation flow field evolution and cavitation dynamics under near-free-surface condition remain unclear.

Due to the limitations of experimental measurement techniques, increasingly more scholars have begun to use numerical methods to study cavitation flow phenomena. Due to the strong instability of the flow near the cavitation, the simulation method plays an important role in the numerical calculation. Most previous simulations used the Reynolds average Navier-Stokes (RANS) method for cavitation calculations due to its low computational complexity and high computational efficiency [34,35]. However, this method overestimates the turbulent eddy viscosity and the peak pressure pulsation of the cavitation [36]. With recent advances in computational power, LESs have arisen as a superior choice for simulating cavitation flows [37]. Pendar and Roohi [38] studied the cavities length and diameter of hemispherical heads and cone cavitators under different cavitation numbers by using different turbulence models and cavitation models. As a result, the combination of different turbulence models and cavitation models on the surface has different predictions of cavitation

shapes. Sedlar et al., [39] used an NACA2412 hydrofoil to simulate cavitation flows under different turbulence models. The results showed that the pressure pulsation and shedding cycle frequency obtained by the LES are similar to the experimental values. The LES model can predict the unstable nature of the flow, accurately capture small-scale vortices, forecast the flow field, and provides insight into the flow details [40–42]. Therefore, the cavitation-flow LES model has been used to predict multiscale turbulent vortex characteristics.

For complex cavitation-vortex interactions in cavitating flow, it is important to study the coherent structure of turbulence. In recent years, modal decomposition techniques have been gradually applied to computational fluid dynamics. These techniques are considered as important analytical tools for assessing nonlinear fluctuation data. Intrinsic mode decomposition (POD) and dynamic mode decomposition (DMD) are the two primary methods of modal decomposition. However, the POD method may contain multiple frequency components in single modality; thus, the frequency information of each coherent mode cannot be provided [43,44]. The DMD method sorts the components according to the frequency, with single-frequency modalities that show strong advantages in the analysis of flow characteristics. The standard DMD method is based on the Koopman analysis of nonlinear dynamical systems, which was originally proposed by Schmid et al. [45]. Vinha et al. [46] used the DMD method to analyze the jet pulsation behavior and cavitation flow caused by different jet shapes. Prothin et al. [47] and Liu et al. [5] combined POD with the DMD method to study the development of hydrofoil cavitation under a high Reynolds number. The cavitation flow field modes of two different positions of the hydrofoil were analyzed, and it was proposed that the DMD method can more accurately extract the frequency characteristics.

At present, most studies on unsteady cavitating flows over a hydrofoil have been performed for an infinite water depth. However, study on cavitation flows near the free surface is still limited, especially the mechanism of interaction between free surface and cavitation is unclear. This paper presents a numerical study of the unsteady cavitation dynamics over a NACA66 hydrofoil near the free surface. Section 2 introduces the numerical framework, including basic governing equations, cavitation models, turbulence models, numerical setup and validations. Section 3 presents the effects of the free surface on the unsteady cavitation. An improved DMD method is applied to investigate the unsteady cavitating flows fealtures. Finally, Section 4 summarizes the main conclusions.

2. Numerical Methods

2.1. Governing Equations

The volume fraction of phase n is:

$$\alpha_n = \frac{V_n}{V} \tag{1}$$

where V_n is the volume of phase n and V is the total volume.

The governing equations of the mixture model are:

$$\frac{\partial \rho}{\partial t} + \frac{\partial \left(\rho u_j\right)}{\partial x_j} = 0 \tag{2}$$

$$\frac{\partial (\rho u_i)}{\partial t} + \frac{\partial \left(\rho u_i u_j\right)}{\partial x_j} = -\frac{\partial p}{\partial x_i} + \frac{\partial}{\partial x_j}\left(\mu \frac{\partial u_i}{\partial x_j}\right) \tag{3}$$

where p is the pressure, and u_i is the velocity along the i-th direction.

The mixture density ρ is:

$$\rho = \alpha_l \rho_l + (1 - \alpha_l)\rho_v \tag{4}$$

where α_l is the liquid volume fraction, ρ_l is the liquid density and ρ_v is the vapor density.

2.2. Large-Eddy Simulation Model

The LES model can divide the vortices in a turbulent flow into large-scale vortices and small-scale vortices by using a filtering function. Direct numerical calculations are used to solve the large-scale vortices, and small-scale vortices are calculated via a connection with large-scale vortices. The LES governing equations are:

$$\frac{\partial \rho}{\partial t} + \frac{\partial \left(\rho \overline{u}_j\right)}{\partial x_j} = 0 \tag{5}$$

$$\frac{\partial (\rho \overline{u}_i)}{\partial t} + \frac{\partial \left(\rho \overline{u}_i \overline{u}_j\right)}{\partial x_j} = -\frac{\partial \overline{p}}{\partial x_i} + \frac{\partial}{\partial x_j}\left(\mu \frac{\partial \overline{u}_i}{\partial x_j}\right) - \frac{\partial \left(\rho \tau_{ij}\right)}{\partial x_j} \tag{6}$$

where τ_{ij} is the nonlinear sub-grid scale (SGS) stress tensor, which is defined as:

$$\tau_{ij} = \rho \overline{u_i u_j} - \overline{u}_i \overline{u}_j \tag{7}$$

The product of the fluid strain rate, $\overline{S}_{ij}$ and an assumed sub-grid viscosity v_{SGS} is used to describe the tensor, which is based on the Boussinesq hypothesis:

$$\tau_{ij} - \frac{1}{3}\tau_{kk}\delta_{ij} = -2v_{SGS}\overline{S}_{ij} \tag{8}$$

The SGS model used in this work is the WALE model [48], which is given as:

$$v_{SGS} = \rho L_s^2 \frac{\left(S_{ij}^d S_{ij}^d\right)^{3/2}}{\left(\overline{S}_{ij}\overline{S}_{ij}\right)^{5/2} + \left(S_{ij}^d S_{ij}^d\right)^{5/4}} \tag{9}$$

$$\overline{S}_{ij} = \frac{1}{2}\left(\frac{\partial \overline{u}_i}{\partial x_j} + \frac{\partial \overline{u}_j}{\partial x_i}\right) \tag{10}$$

$$S_{ij}^d = \frac{1}{2}(\overline{g}_{ij}^2 + \overline{g}_{ji}^2) - \frac{1}{3}\delta_{ij}\overline{g}_{kk}^2, \overline{g}_{ij} = \frac{\partial \overline{u}_i}{\partial x_j} \tag{11}$$

where L_s is the length or grid-filter width, which is given as:

$$L_s = \min(kd, C_w V^{1/3}) \tag{12}$$

Here, k is von Karman's constant, d is the distance to the closest wall, V is the cell volume, and C_w is a model coefficient which is set to 0.5.

2.3. Cavitation Model

Cavitation models generally consist of transport equations. These models are usually obtained by simplifying and improving the Rayleigh-Plesset cavity dynamics equation [49,50]. The processes of evaporation and condensation can be expressed by inserting a source term into the transport equation to describe the phase transition rate. The Schnerr-Sauer model is used as the cavitation model [49], and the transfer equation is:

$$\frac{\partial (\rho_v \alpha_v)}{\partial t} + \frac{\partial (\rho_v \alpha_v u_j)}{\partial x_j} = \dot{m}^+ - \dot{m}^- \tag{13}$$

where a_v is the vapor volume fraction. The source terms $\dot{m}^+$ and $\dot{m}^-$ describe the evaporation and condensation which can be solved as:

$$\dot{m}^+ = \frac{\rho_v \rho_l}{\rho} \alpha_v (1 - \alpha_v) \frac{3}{R_b} \sqrt{\frac{2}{3} \frac{\max(p_v - p, 0)}{\rho_l}} \tag{14}$$

$$\dot{m}^- = \frac{\rho_v \rho_l}{\rho} \alpha_v (1 - \alpha_v) \frac{3}{R_b} \sqrt{\frac{2}{3} \frac{\max(p - p_v, 0)}{\rho_l}} \tag{15}$$

where $\dot{m}^+$ is the evaporation term, $\dot{m}^-$ is the condensation term, and p_v is the saturation vapor pressure at the local temperature. R_b is the cavity radius which can be solved as:

$$R_b = \left(\frac{\alpha_v}{1 - \alpha_v} \frac{3}{4\pi} \frac{1}{N_b} \right)^{\frac{1}{3}} \tag{16}$$

where N_b is the density of cavity number. According to Schnerr and Sauer [51], $N_b = 10^{13}$.

2.4. Numerical Setup and Validation

For all the numerical simulations in the present study the Star-CCM+ software was used. A NACA66 hydrofoil was used in this work, which has a chord length $C = 0.15$ m and a span of 0.192 m. The angle of attack of the hydrofoil is 8°. The computational domain is shown in Figure 1. The velocity inlet of the computational domain is approximately 4C from the leading edge of the hydrofoil and the inflow velocity is $V_\infty = 5.33$ m/s, with a Reynolds number of $Re = 0.8 \times 10^6$. The outlet pressure can control the reference pressure of the flow field to adjust the cavitation number. The cavitation number is defined as:

$$\sigma = (p - p_v) / (0.5 \rho_l V_\infty^2) \tag{17}$$

where p is the far field pressure, which is set by the outlet boundary conditions. In order to be consistent with the experimental conditions [16], σ is set to 1.25 in this work. The saturated vapor pressure of water is $p_v = 2367$ Pa for a flow-field temperature of 20 °C. To capture the effect of cavitation on the tail of the free surface, the pressure outlet was set to 20C downstream of the leading edge.

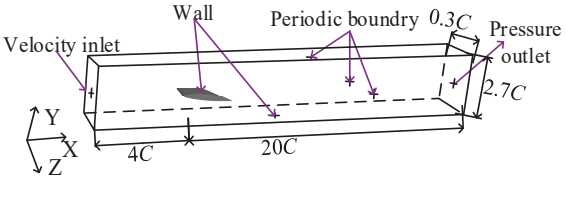

Figure 1. Computational domain and boundary condition.

Figure 2a shows the mesh of the computational domain. The mesh is generated by the Star-CCM+ auto trimmed mesher and prism layer mesher. Transition area between prism layer mesh and trimmed mesh is unstructured type, and structured mesh is generated in other regions. The total number of mesh elements is approximately 3×10^6 and the y+ < 1 over the hydrofoil surface to meet quality criterion requirements for LES, as shown in Figure 2b.The time step for the calculation is set to $\Delta t = 2.5 \times 10^{-5}$ to ensure stability in the numerical calculation.

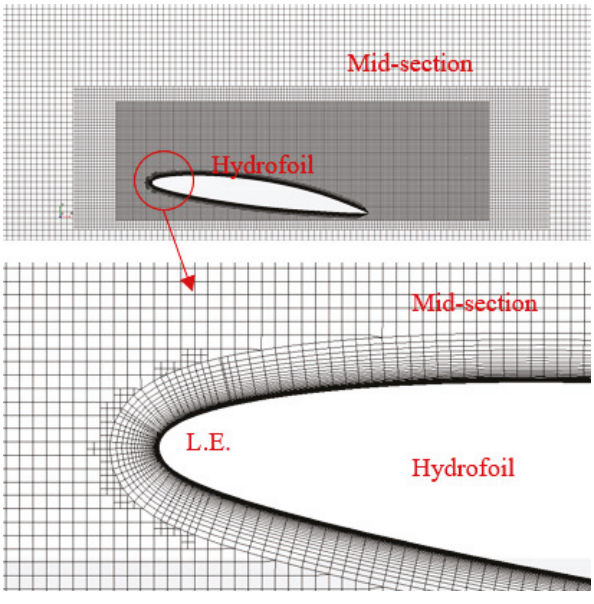

(a)

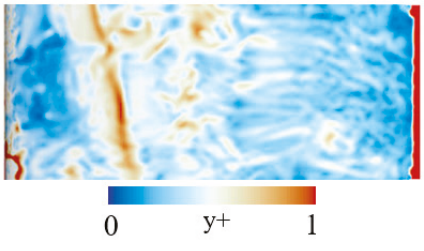

(b)

Figure 2. Mesh generation and y+ at $t = 0.566$ s around the hydrofoil. (**a**) Mesh generation at Mid-section and a visualization close to the profile, (**b**) y+ at $t = 0.566$ s.

Three pressure-monitoring points were set on the mid-section of the hydrofoil, as shown in Figure 3.

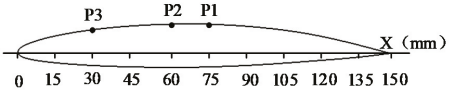

Figure 3. Locations of monitoring points.

The middle section along the spanwise length of the flow field is shown in Figure 4. The zero point of the primary coordinate system, XOY, is located at the leading edge of the hydrofoil. To represent the shape of the free surface, a local coordinate system, X_1OY_1, is established at the free surface of the velocity inlet.

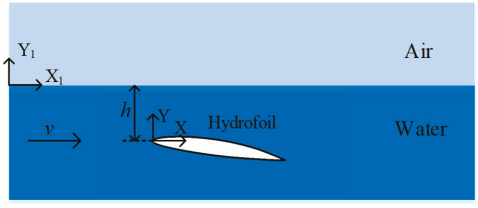

Figure 4. Definition of the coordinate systems in the computational domain.

In this paper, six working conditions are set under different depth conditions including the absence of a free surface condition and h = 1.25C, 1C, 0.75C, 0.5C, and 0.25C. In addition to the difference in depth from the free surface, the reference pressure also changes with the depth of the hydrofoil to keep the cavitation number at a constant.

To validate the numerical model, results from the numerical simulation and a previous experiment [16] were compared. In this experiment, numerical videos were used to record the cavitating flow, numbers of piezo-resistive transducers were used to measured pressure. Figure 5 shows the cavitation shape for a single cavitation cycle. T represents the period of cavity shedding. The numerical simulation accurately captured the periodic characteristics of the hydrofoil cavitation, such as the growing, shedding and collapsing processes. The cavitation shape is also well predicted by the numerical simulation. It shows that the numerical cavitation shape matches well with the experimental cavitation shape.

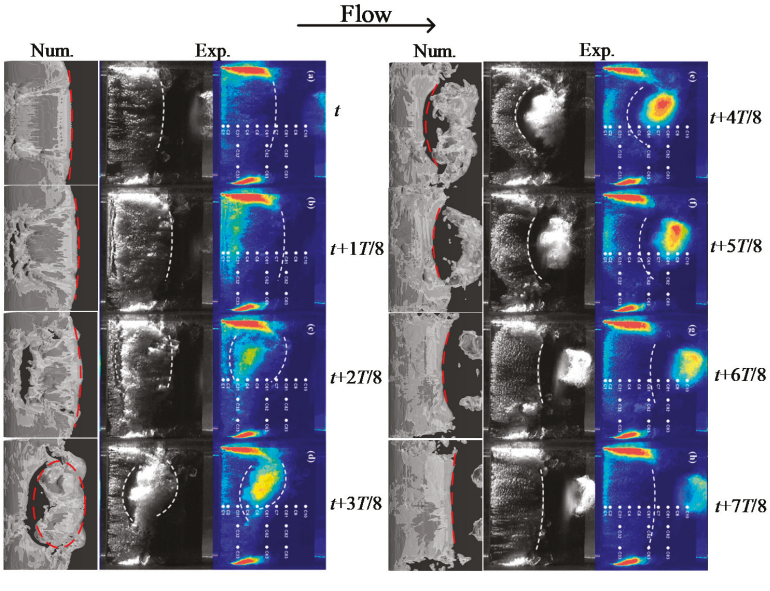

Figure 5. Numerically predicted cavity evolution compared with experimental results [16].

A collapse of the cavitation can lead to dramatic fluctuations in pressure. Thus, the dynamic pressure is difficult to predict. Numerical predictions of the pressure fluctuations at points P1 and P2 are plotted in Figure 6. As indicated by the experimental measurements, the pressure fluctuations caused by the cavitation collapse and the periodicity of the cloud cavitation flow are well predicted. The numerical prediction of cavitation shape and pressure results are highly consistent with experimental results indicating that the numerical method can effectively predict the unsteady cavitation dynamics.

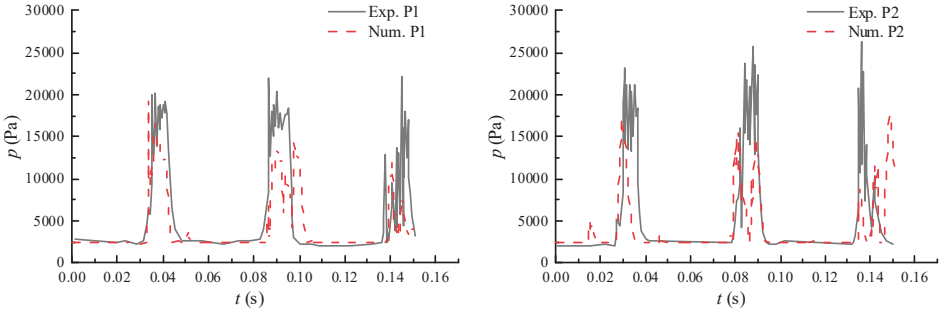

Figure 6. Pressure fluctuation on the suction surface of the hydrofoil at P1 and P2.

3. Results and Discussion

3.1. Effect of a Free Surface on the Dynamic Cavity Evolution and Hydrodynamic Load

To evaluate the effect of a free surface on cavitating flows, Figure 7 shows the cavity shapes at eight typical times in one cycle for the cases of without free surface and near the free surface (h = 0.25C), where T_0 and T_1 represent the evolution cycles of without and with free surfaces, respectively.

It can be seen that the overall characteristics of cavitation evolution in a cycle in both cases are similar, including cavitation development (from t_0 to t_0 + 4T_0/8), shedding (from t_0 + 5T_0/8 to t_0 + 6T_0/8) and collapsing (from t_0 + 6T_0/8 to t_0 + 7T_0/8). However, it is noted that the maximum length of the attached cavity for the near free surface condition is significantly shorter and the scale of cloud cavitation is smaller. Hence, the existence of free surfaces suppresses the cavitation intensity.

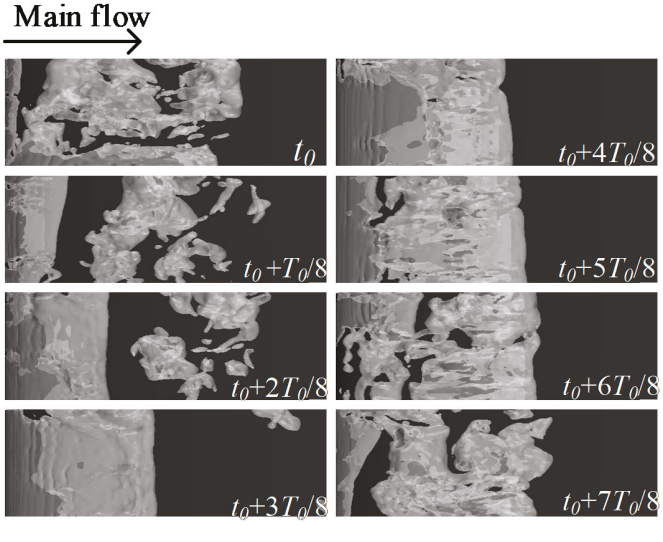

(**a**)

Figure 7. *Cont.*

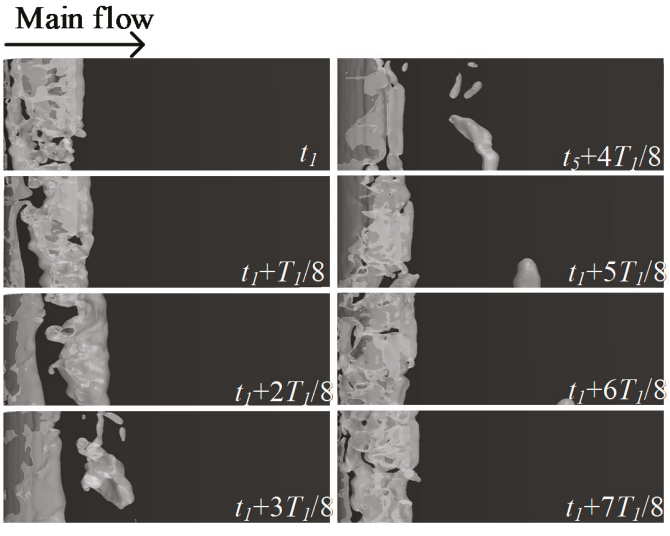

(**b**)

Figure 7. Comparison of the cavity evolution for a typical cycle for no free surface case and near the free surface case (h = 0.25C). (**a**) Cavity evolution in a typical cycle for the no free surface case, (**b**) Cavity evolution in a typical cycle for the near free surface case (h = 0.25C).

To explain the effect of free surface on the intensity of cavitation, we introduce the local cavitation numbers, which is defined as:

$$\sigma_{\text{local}} = (p_{\text{local}} - p_v)/(0.5\rho_l V_\infty^2) \tag{18}$$

where σ_{local} is the local cavitation number and p_{local} is the local absolute pressure.

Figure 8a shows the local cavitation number and Figure 8b shows the local velocity field on the mid-section plane of the computational domain. The local cavitation number near the cavitation zone is close to zero. As the distance from cavitation increases, the local cavitation number increases, indicating that a cavitation is more difficult to produce. Changes in the cavitation number represent changes in absolute pressure. It can be seen from the corresponding local velocity field that the high speed area under no free surface condition is larger than near free surface condition. This indicates that the existence of the free surface reduces the velocity of the flow field around the hydrofoil and resulting in a weaker cavitation intensity. Two straight lines L_1 and L_2 are set along the y-direction at x/C = 0.2 and 0.3. The pressure value of L_1 and L_2 as the x coordinates, and the vertical distance from the hydrofoil head is the y coordinate, as shown in Figure 8b. When the value of y is small, the pressure is small due to the cavitation. The pressure increases as y increases. When y = 0.05 m, the pressure under the near-free surface condition is larger than no free surface condition. The results show that the pressure increases faster near free surface. Near the suction surface of the hydrofoil, the free surface makes the pressure change more drastic, which leads to a larger local cavitation number. Subsequently, it is difficult to generate a cavitation, and the cavity length is reduced.

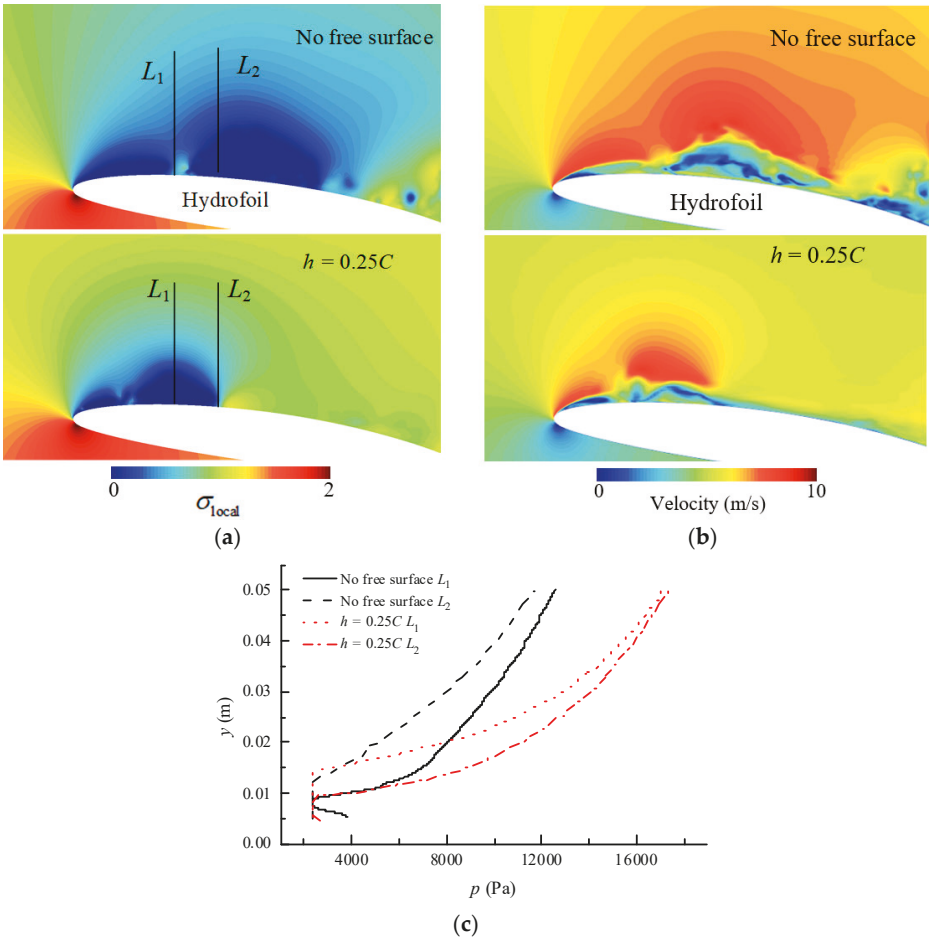

Figure 8. Comparison of the local cavitation number (**a**) and local velocity field (**b**) on the mid-section plane without free surface and with the free surface, (**c**) vertical pressure distribution in hydrofoil cavitation region.

The effect of the free surface and the cavitation is also reflected in the pressure fluctuation on the hydrofoil surface, as shown in Figure 9a. As the cavitation develops, the pressure is equal to the saturated vapor pressure, and the pressure is stable. When the cavities begin to break off, the cloud cavitation produces a dramatic pressure fluctuation, which causes the pressure to increase.

This feature is reflected in the periodic fluctuations of the pressure curve. The cavitation shedding frequency for the near free surface condition is approximately twice that of the no free surface condition. Figure 9b,c show the power spectral density (PSD) of the pressure curve for the two cases. The PSD curve indicates that the dominant frequency of periodic cavitation shedding is approximately 17.35 Hz in the absence of a free surface and approximately 35.75 Hz near the free surface. This difference is due to the reduced cavity length that occurs near a free surface and the time required for the cavities to develop and collapse which leads to an increased cavitation cycle frequency.

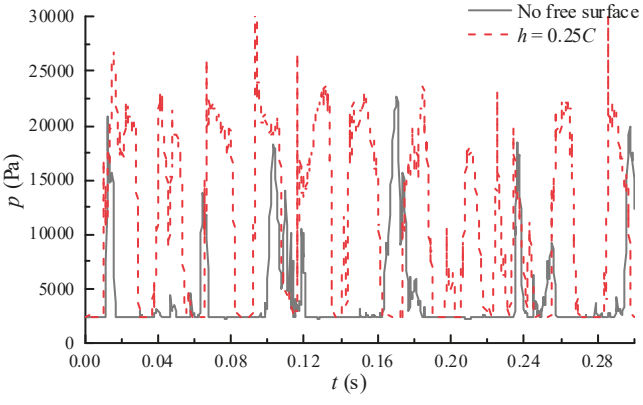

(**a**)

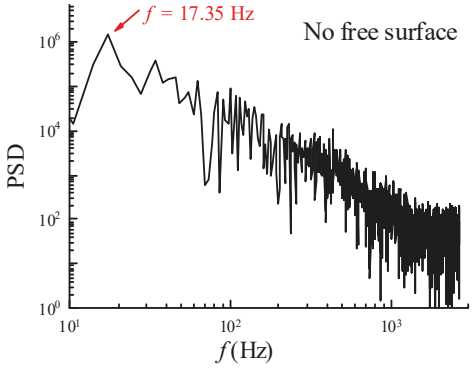

(**b**)

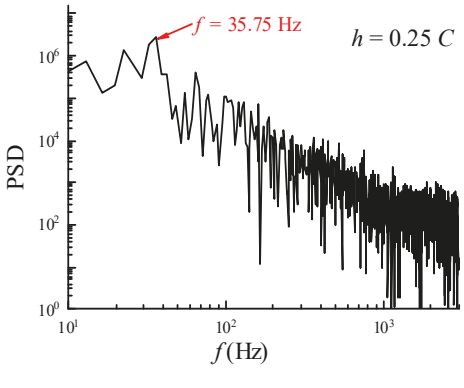

(**c**)

Figure 9. Pressure fluctuations and the corresponding PSD at P3. (**a**) Pressure fluctuation on the suction surface of the hydrofoil at P3; (**b**) PSD of the pressure fluctuation at P3 for the no free surface case; (**c**) PSD of pressure fluctuation at P3 for the near free surface case.

Figure 10 shows fluctuations in the lift and drag coefficients, which are defined as:

$$C_L = \frac{\text{Lift}}{0.5\rho \times V_\infty^2 \times C \times \text{Span}} \tag{19}$$

$$C_D = \frac{\text{Drag}}{0.5\rho \times V_\infty^2 \times C \times \text{Span}} \tag{20}$$

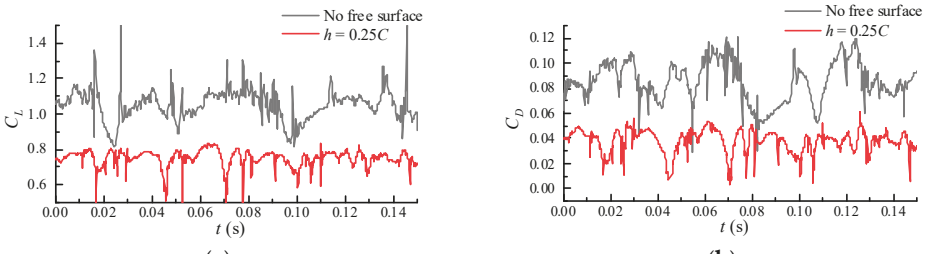

Figure 10. Comparison of the lift and drag coefficient fluctuations for the no free surface case and the near free surface case. (**a**) Lift coefficient; (**b**) Drag coefficient.

Due to the periodic fluctuations in pressure, the fluctuations in the lift and drag coefficients over time also appear cyclical. However, due to the strong instability of the cavitation flow, the periodic fluctuations of the lift and drag coefficients are not obvious.

Comparison shows that both coefficients are smaller under the near free surface case than under the no free surface case, which indicates that the free surface weakens the lift and drag of the hydrofoil by reducing the cavity length. Both the lift and drag coefficients have the same influencing factors: free surface and cavitation. The lift and drag coefficients increase with the increase in submergence ratio h/C [29]. Another influencing factor is that the low-pressure region of the hydrofoil suction surface is also reduced due to the reduction in the length of the cavitation. As the length of the cavity decreases, the pressure difference between the suction and pressure plane of the hydrofoil decreases. Hence, the existence of free surfaces reduces the lift and drag coefficients compared with the case of no free surface.

3.2. Analysis of the Flow Structure Based on the DMD Method

When the cloud cavity breaks off, a strong vortex is generated. The analysis of vortex structures is an important component in studying cavitation flows. The DMD method can effectively extract the modal information of each order in the cavitation flow field, and can analyze the vortex structure of each mode. For details on the standard DMD method, we refer the reader to previous publications [45]. It is assumed that the total number of snapshots is N and the time-space flow field of an unsteady flow can be represented as a matrix $\boldsymbol{V_1^N}$:

$$\boldsymbol{V_1^N} = [\boldsymbol{v_1}, \boldsymbol{v_2}, \ldots, \boldsymbol{v_N}] \tag{21}$$

where the column vector $\boldsymbol{v_i}$ represents the i-th snapshot of the flow field. Next, A is defined as an approximation of the nonlinear mapping, indicating the evolution of the matrix from one timepoint to the next, which is expressed by:

$$\boldsymbol{v_{i+1}} = \boldsymbol{A v_i} \tag{22}$$

Then, the dynamic flow system is represented by the mapping matrix $\boldsymbol{A}$. Matrix $\boldsymbol{V_1^N}$ can be defined as:

$$\boldsymbol{V_1^N} = \left[\boldsymbol{v_1}, \boldsymbol{A v_1}, \boldsymbol{A^2 v_1}, \ldots, \boldsymbol{A^{N-1} v_1}\right] \tag{23}$$

Assuming that a_i are coefficients of $\boldsymbol{A}$, the last snapshot $\boldsymbol{v}_N$ can be formulated by the previous $N-1$ vectors:

$$\boldsymbol{v_n} = a_1\boldsymbol{v}_1 + a_2\boldsymbol{v}_2 + \cdots + a_{N-1}\boldsymbol{v_{N-1}} + \boldsymbol{r} \tag{24}$$

or:

$$\boldsymbol{A}\boldsymbol{V}_1^{N-1} = \boldsymbol{V}_1^{N-1}\boldsymbol{S} + \boldsymbol{r}\boldsymbol{e}_{N-1}^{T} \approx \boldsymbol{V}_1^{N-1}\boldsymbol{S} \tag{25}$$

where $\boldsymbol{r}$ is the residual vector, $\boldsymbol{e}_{N-1}^{T}$ is the $(N-1)$-th unit vector and matrix $\boldsymbol{S}$ is formed as:

$$\boldsymbol{S} = \begin{bmatrix} 0 & & & & & a_1 \\ 1 & 0 & & & & a_2 \\ & \ddots & \ddots & & & \vdots \\ & & & 1 & 0 & a_{N-2} \\ & & & & 1 & a_{N-1} \end{bmatrix} \tag{26}$$

when the residual $\boldsymbol{r}$ is small, the eigenvalue of $\boldsymbol{S}$ approximates the eigenvalue of $\boldsymbol{A}$. The $\boldsymbol{S}$ matrix can be regarded as a low-dimensional form of matrix $\boldsymbol{A}$; therefore, the eigenvalue of $\boldsymbol{S}$ can represent the main eigenvalues in matrix $\boldsymbol{A}$. Eigenvalue decomposition is performed on matrix $\boldsymbol{S}$:

$$\boldsymbol{S} = \boldsymbol{P}\boldsymbol{N}\boldsymbol{P}^{-1}, \boldsymbol{N} = diag(\mu_1, \cdots, \mu_{N-1}) \tag{27}$$

where $\boldsymbol{P}$ is the matrix of the eigenvectors of matrix $\boldsymbol{S}$.

The dynamic mode $\boldsymbol{\varphi}$ can be formed as follows:

$$\boldsymbol{\varphi} = \boldsymbol{V}_1^{N-1}\boldsymbol{A} \tag{28}$$

The first m flow field snapshots can represent the flow field snapshot at any time:

$$\boldsymbol{v_i} = \sum_{j=1}^{m} \mu_j{}^{i-1}\boldsymbol{\varphi_j} \tag{29}$$

where m is the number of DMD modes and $\boldsymbol{\varphi_j}$ is the column vector of the matrix $\boldsymbol{\varphi}$.

The standard DMD method is not suitable for the convergence of strong unsteady flows such as cavitation [43]. Thus, in this paper, the raw velocity data are first processed, and then, DMD decomposition is performed.

The Hilbert-Huang transform is performed on the original velocity data [52]. For real-valued functions, $f(t), t \in (-\infty, \infty)$, the Hilbert transform is defined as a convolution of $f(t)$ with $1/t$:

$$H[f(t)] = \frac{1}{\pi}\int_{-\infty}^{+\infty} \frac{f(\tau)}{t-\tau} d\tau \tag{30}$$

$$H[f(t)] = \left|H[f(t)]\right| e^{j\phi(\omega)} \begin{cases} -j & \omega > 0 \\ +j & \omega < 0 \end{cases} \tag{31}$$

where:

$$\phi(\omega) = \begin{cases} -\frac{\pi}{2} & \omega > 0 \\ +\frac{\pi}{2} & \omega < 0 \end{cases} \tag{32}$$

By performing a Hilbert transform on a real number function, the imaginary part of the function can be obtained, and the complex function can then be constructed.

Although the Hilbert transform can convert a real function into a complex function, its conditions are highly demanding, requiring the input signal to be linearly stable. In practical applications, it is difficult for most signals to meet such conditions; thus, the Hilbert transform cannot be directly used. Huang's empirical mode decomposition (EMD) can be used to decompose the signal into several

intrinsic mode functions (IMFs) and residual signals. When the residual signal is a monotonic function or lacks a maximum or minimum, the EMD ends. Here, we have:

$$\xi(t) = \sum_{i=1}^{K} IMF_i(t) + r_K(t) \tag{33}$$

where $\xi(t)$ is the original signal, $IMF_i(t)$ is the eigenmode function, and r_K is the residual. Now all IMFs meet the linear steady-state requirements and can be Hilbert transforms. Finally, the transformed IMF is superimposed with the residual, that is, the original signal is converted into a complex signal. The Hilbert Huang transform is applied to the velocity field data at each timepoint as the initial data of the DMD method, and then, the standard DMD is performed.

Generally, to select a suitable mode for analysis, the modes must be sorted according to the energy. The energy of a dynamic mode can be denoted by the norm, which is defined as follows:

$$\|\boldsymbol{\varphi_i}\| = \sqrt{\sum_{i=1}^{n} |\boldsymbol{\phi_i}|^2} \tag{34}$$

where $\boldsymbol{\phi_i}$ is the velocity matrix of the i-th mode.

Figure 11 shows an energy spectrum of the dynamic modes. Mode 1 corresponding to a frequency of zero contains most of the energy of the flow field. Mode 2 contains the second greatest amount of energy in the flow field, and the corresponding frequency is close to the cavitation shedding frequency (35.75 Hz and 17.35 Hz) obtained in the previous section. The frequencies corresponding to mode 3 and mode 4 are close to two and three times of mode 2. Due to the strong instability of the cavitation flow field, the frequencies for mode 3 and 4 are not strictly two or three times the dominant frequency, which is acceptable. As shown in Figure 10a,b, for the near free surface case, the modes except for mode 1 contain significantly less energy than the no free surface case. This result indicates that the free surface inhibits the cavitation flow, which may explain why the length decreases for the near free surface cavitation case.

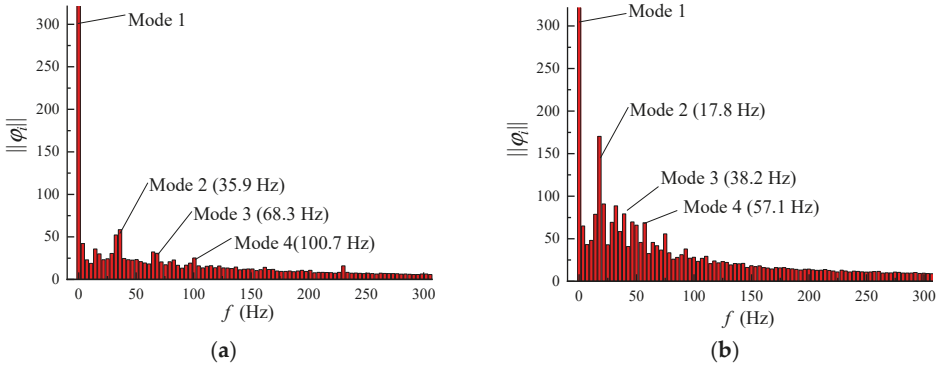

Figure 11. Comparison of the energy spectrum of the dynamic modes with free surface and without free surface. (**a**) Near free surface (h = 0.25C); (**b**) No free surface.

Figure 12a,b show the distributions of the real part of the dynamic modes on the mid-section plane. Mode 1 corresponds to an average flow field with a frequency of zero. The real part is negative only near the hydrofoil. The region of negative values is similar to the sheet cavitation region, and most other areas exhibit positive values. The positive and negative values alternately appear in couples for modes 2–4, reflecting the coherent structure of the turbulence. This phenomenon is due to the periodic development of the hydrofoil cavitation, which is caused as the vortex rolls up and sheds

off. As the frequency increases, the scale of the coherent structure becomes smaller. Compared with the case shown in Figure 11a in the absence of a free surface, the dynamic mode scale is larger near the free surface, as shown in Figure 11b, and the coherent structure regions have a larger range. This phenomenon may arise because the turbulence generated by the hydrofoil near the free surface is not fully developed due to the influence of the free surface. Moreover, the energy contained in modes 2–4 is less when it is near the free surface.

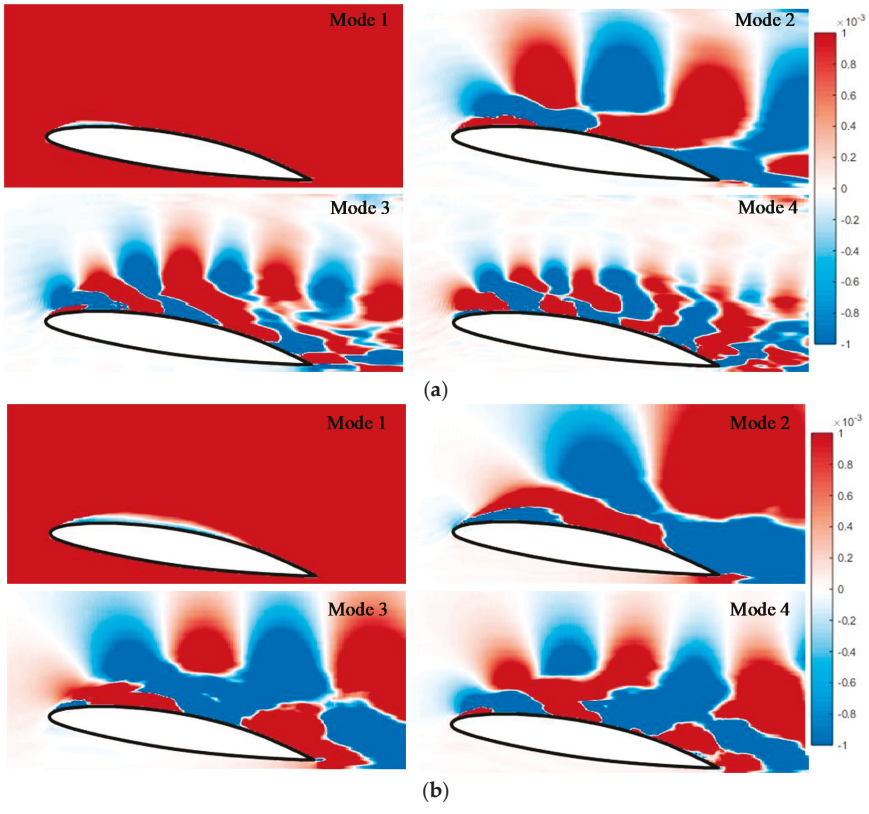

Figure 12. Comparison of the dynamic modes on mid-section plane with free surface and without free surface. (**a**) Dynamic mode near the free surface (h = 0.25C); (**b**) Dynamic mode without free surface.

Reconstruction with different modes can result in flow patterns at different characteristic frequencies. In this way, the vortex motion characteristics of the flow field at different frequencies can be analyzed. Figure 13a shows the reconstructed flow field velocity vector over a single cavitation cycle near a free surface. The first column presents the numerical simulation results, and the second column displays the flow field reconstructed by all modes, which reflects the true state of the flow field. The flow field matches the numerical simulation results, demonstrating the effectiveness of the improved DMD method. Because mode 1 corresponds to a frequency of zero and it has no periodicity, it is not analyzed here. The third and fourth columns present the reconstructed flow fields for mode 2 and mode 3, respectively. It can be seen that in addition to mode 1, the coherent structure of the single-order mode is embodied as a vortex in the reconstructed flow field. Over a single period, a vortex structure is observed inside the sheet cavitation on the suction side of the hydrofoil. As the cavitation sheds off and transitions to cloud cavitation, the tails of the sheet cavitation form new vortices and move downstream. The scale of the vortex decreases as the dynamic mode increases, similar to the

mode coherent structure. When there is no free surface, as shown in Figure 13b, the reconstructed flow fields of all modes are also similar to the numerical simulation results, which express the true state of the flow field. Compared with the near free surface case, in addition to the difference from the real flow field, the reconstructed flow fields for mode 2 and mode 3 exhibit significant deviations. In the absence of a free surface, the vortex formed by the shedding cavitation appears at a position further downstream, and the scale is larger than that near the free surface. This phenomenon indicates that the free surface has an inhibitory effect on the vortex generated by the cavitation, resulting in a reduced vortex scale.

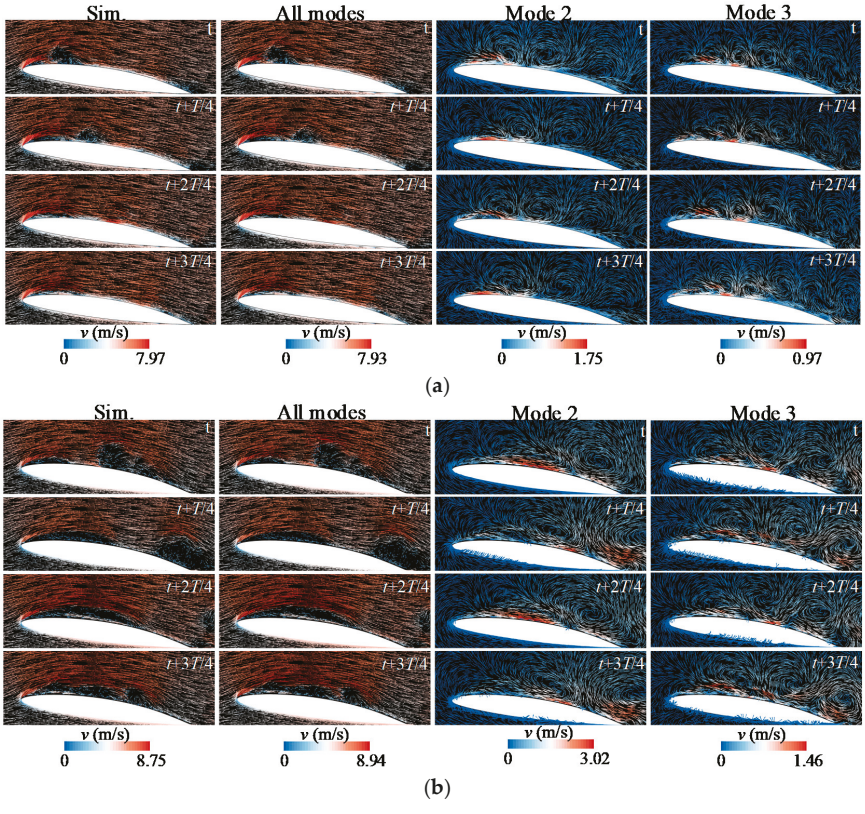

Figure 13. Comparison of the velocity vector of the reconstruction flow field for the near free surface case and no free surface case. (**a**) Velocity vector of the reconstruction flow field for the near free surface case (h = 0.25C); (**b**) The velocity vector of the reconstruction flow field for the no free surface case.

3.3. Free Surface-Cavitation Interaction at Different Water Depths

In the previous section, the effect of a cavitation near a free surface was analyzed. For high-speed vehicles, the distance between the underwater component and the free surface is constantly changing during movement, and the effect of the free surface on the cavitation flow varies at different depths. To study the effect of depth on the cavitation, we carried out the cavitating flows over the hydrofoil at five different water depths.

Figure 14 shows the cavity evolution for a typical cycle at five different depths. Similar typical cavitation characteristics can be observed in all cases: At t_1, the sheet cavitation begins to develop downstream of the leading edge of the hydrofoil. Also, the cloud cavitation reaches its maximum.

From t_1 to $t_1 + 3T_1/6$, the sheet cavitation develops and reaches its maximum at $t_1 + 3T_1/6$. The cloud cavitation moves downstream and becomes smaller because of collapsing.

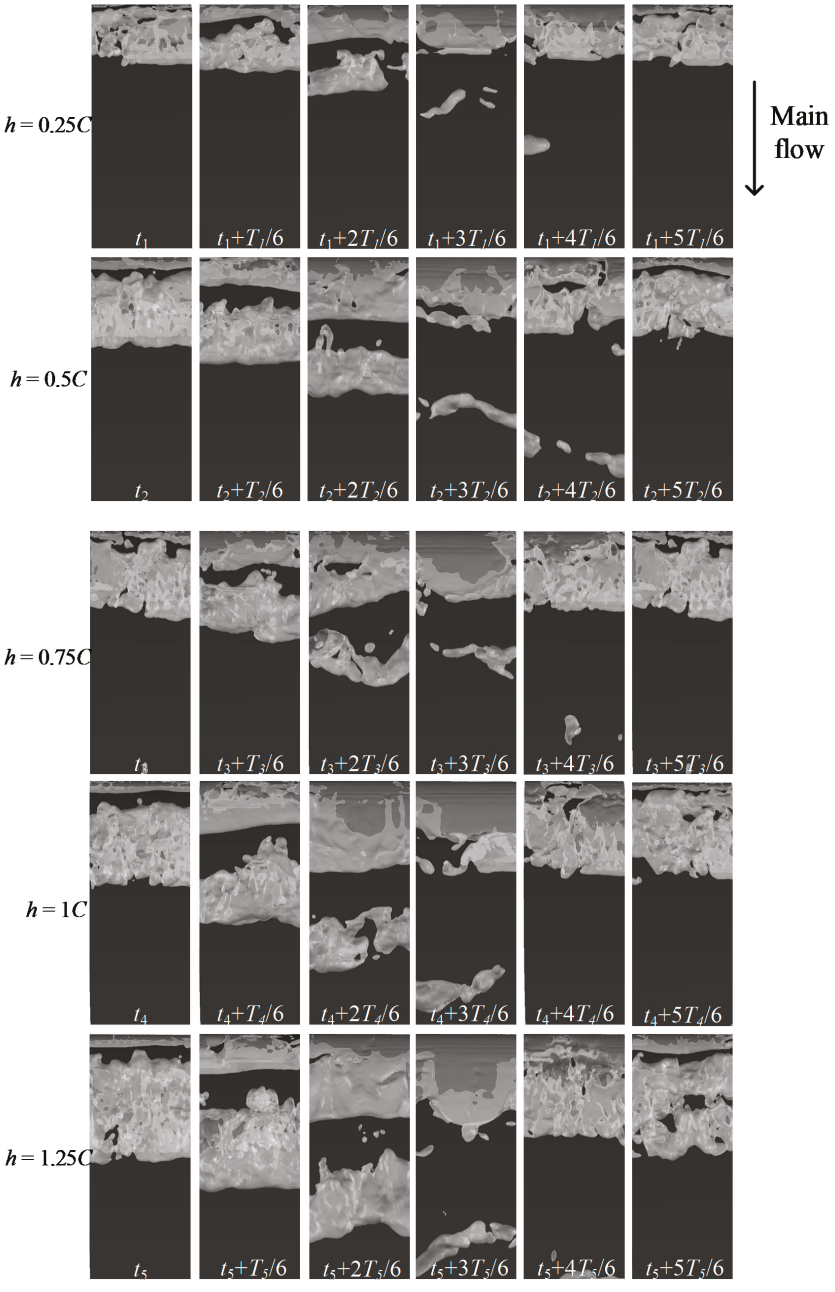

Figure 14. Comparison of cavity evolution in one typical cycle compared at five different water depths.

From $t_1 + 4T_1/6$ to $t_1 + 5T_1/6$, sheet cavitation begins shedding with the effect of the re-entrant flow, and then the next cycle begins. These characteristics are the same in the other four cases, where T_2, T_3, T_4, and T_5 represent different cycles for different cases.

The previous section described the influence on cavitation near a free surface, which shows a certain regularity at different depths. As the hydrofoil moves to greater depths, the cloud cavitation at the maximum size (t_i) increases, and the sheet cavitation at the maximum size ($t_i + 3T_i/6$) shows the same trend. Thus, the increase in water depth can promote the cavitation intensity at the same cavitation number.

The cavity volume fluctuations proved the above conclusion, which is shown in Figure 15. Five complete cycles have passed before the results are recorded, and the results are convergent. The peaks of periodic fluctuations under the same working conditions are different, indicating that cavity evolution is a strong unsteady phenomenon. Although it exhibits a certain periodicity, the flow characteristics of each cycle are not exactly the same. The cavity volume increases with increasing depth from the free surface, indicating that the effect of the free surface on cavitation decreases as the depth from the free surface increases. As the depth from the free surface increases, the fluctuations of the cavity volume become more obvious. It indicates that the volume of the cavitation shedding is larger, which is consistent with the conclusion obtained in Figure 14. Hence, the free surface inhibits the development of cavitation, leading to a reduction in cavitation volume.

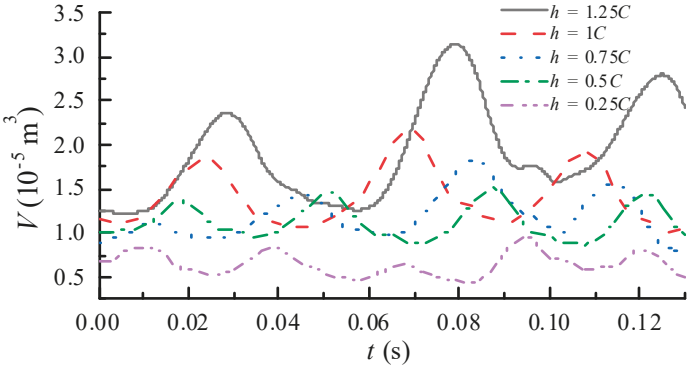

Figure 15. Comparison of the cavity volume fluctuations for five different water depths.

As mentioned above, the depth from the free surface affects the shape of the cavitation, and changes in cavitation shape alter the fluctuation characteristics of the pressure. Based on the pressure fluctuations of case 2 ($h = 0.25C$) shown above, Figure 16 presents the pressure fluctuation on the suction surface of hydrofoil at P3 with the other cases. Since the cavitation phenomenon is highly unstable, the pressure fluctuations obtained by numerical simulation are not stable at the peak. The fluctuation of the pressure is generated when the sheet cavitation is cut off by the re-entrant flow. When the sheet cavitation breaks off, and the cavitation again covers the monitoring point, the pressure value will be smooth close to the saturated vapor pressure. Moreover, the fluctuation of the pressure curves expresses the different frequencies of the cavitation cycle. It can be seen that as the depth of the hydrofoil increases, the frequency of the cavity shedding decreases, gradually approaching the frequency of the cavity shedding when there is no free surface. This result further demonstrates that the free surface inhibits the evolution of the cavity and increases the frequency of cavitation shedding.

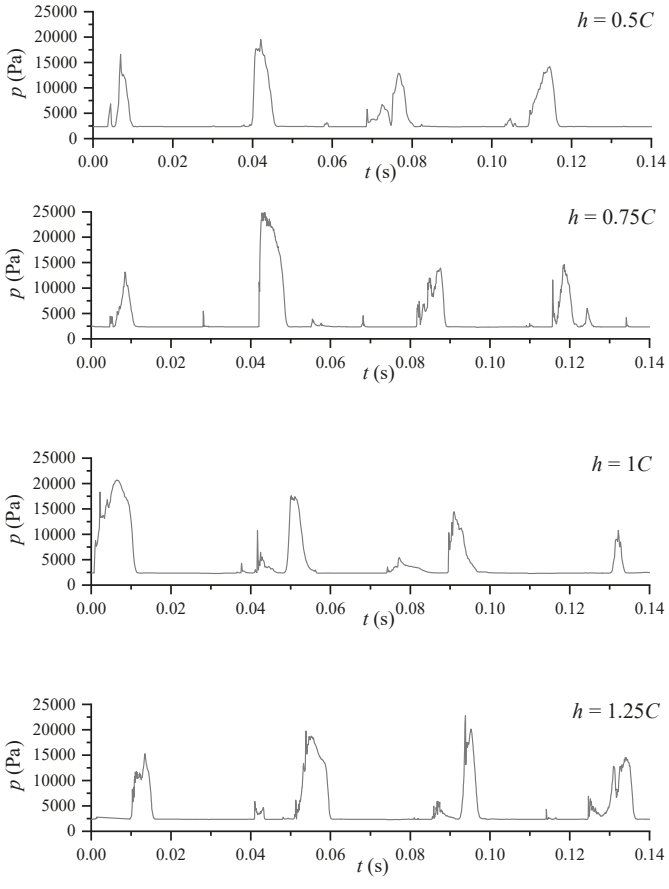

Figure 16. Comparison of the pressure fluctuation on the suction surface of hydrofoil at P3 in different water depth condition.

The corresponding PSD is shown in Figure 17. The maximum value of the curve represents the frequency of the cavity shedding. The pressure fluctuations in Figure 16 show that the duration of a cavitation period increases as the depth below the free surface increases, and thus, the frequency decreases, as verified by Figure 17. The frequency of the cavitation shedding period was extracted for each case. It can be seen that as the depth of the hydrofoil increases, the frequency of cavitation shedding decreases. This result may be attributed to the near free surface condition, the reduced cavitation length, and the reduced time required for development and shedding.

The effect of the free surface on the hydrofoil cavitation length also affects the lift resistance of the hydrofoil, which is an important factor for assessing the extent to how the free surface affects the cavitation and hydrofoil. Figure 18a shows the lift coefficient of the hydrofoil. It can be seen that the lift coefficient exhibits periodic fluctuations, consistent with the cavitation shedding period. The coefficient also shows strong instability, which is related to the unsteadiness of cavitation. To study the relationship between the different depth and the lift coefficient, the average lift coefficients for each operating condition is shown in Figure 18b. It can be seen that the average value of the lift coefficient decreases as the depth from the free surface decreases, which results that the relationship between lift coefficient and depth is linear.

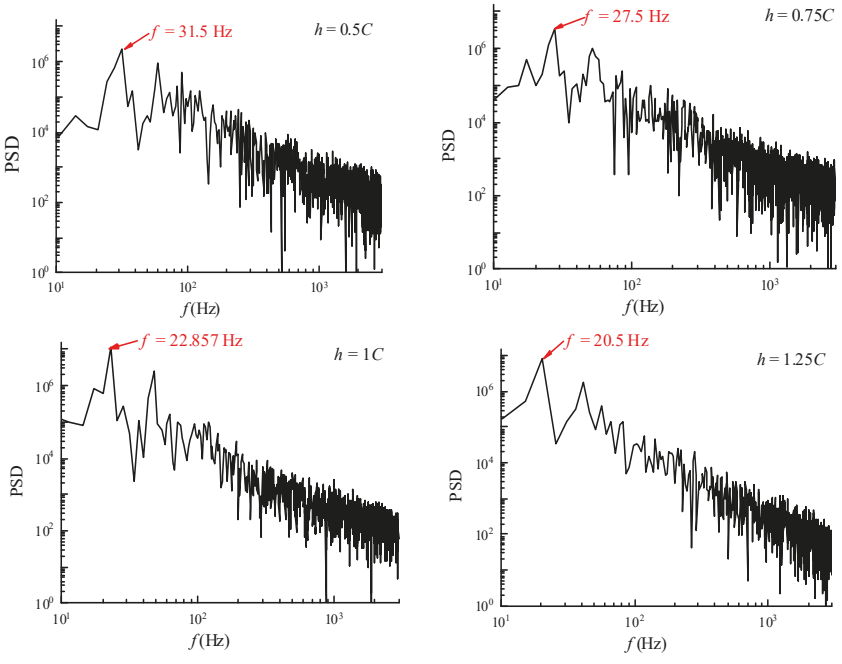

Figure 17. Comparison of the power spectral density of pressure fluctuations in different water depths.

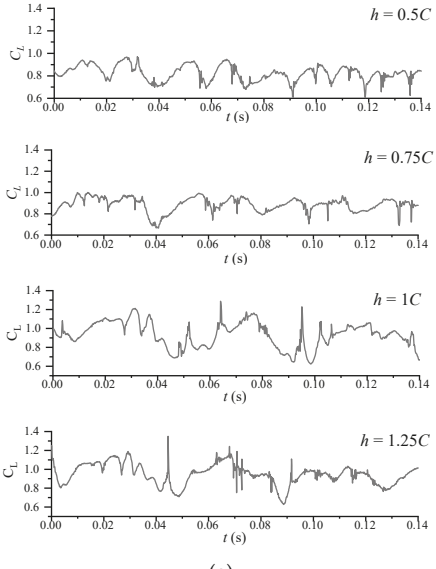

(**a**)

Figure 18. *Cont.*

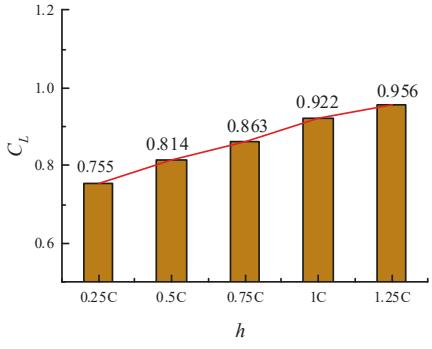

(**b**)

Figure 18. Comparison of the lift coefficient fluctuation and the average value at different water depth. (**a**) Lift coefficient fluctuations at different water depths; (**b**) Average lift coefficient at different water depths.

Figure 19a shows the drag coefficient of the hydrofoil at different water depths. The drag coefficient exhibits a cyclical trend similar to that of the lift coefficient curve, although the drag coefficient is much smaller than the lift coefficient. The average drag coefficient for different depths is shown in Figure 19b. As observed for the lift coefficient, the average drag coefficient increases with the increasing depth. Also the average drag coefficient has a linear development as the depth increasing.

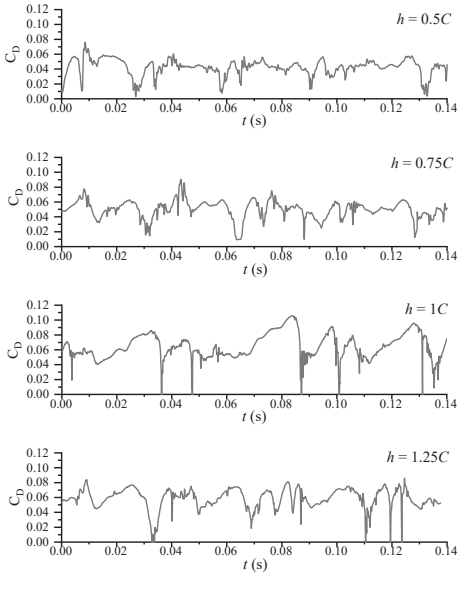

(**a**)

Figure 19. *Cont.*

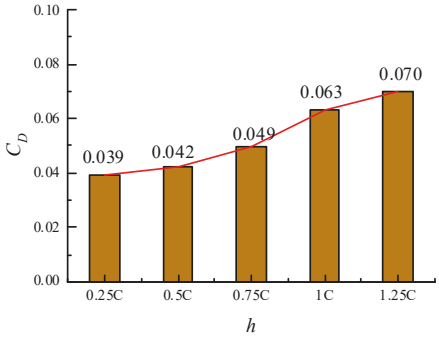

Figure 19. Comparison of the drag coefficient fluctuation and the average value at different water depths. (**a**) Drag coefficient fluctuations at different water depths; (**b**) Average drag coefficient at different water depths.

The effect of free surface on hydrofoil cavitation was analyzed above. Similarly, the cavitation of the hydrofoil near a free surface will also affect the free surface and form a wave. Figure 20 presents a water volume fraction scalar of the cross-section in the direction of the hydrofoil span of the hydrofoil at the same cavitation cycle stage. The shape of the free surface affected by the hydrofoil is shown in the figure. As the distance from the free surface increases, the influence of the hydrofoil on the free surface gradually decreases, and the liquid surface gradually becomes flat. In addition to the wave above the hydrofoil, the free surface behind the hydrofoil exhibits fluctuations, corresponding to the rectangular portion outside the dotted circle. As shown in Figure 20, as the depth of the hydrofoil increases, the turbulence at the hydrofoil tail also decreases. At the same time, the fluctuation of the free surface behind the hydrofoil is weakened. Hence, free surface evolution due to hydrofoil cavitation occurs not only above the hydrofoil, but also behind the hydrofoil.

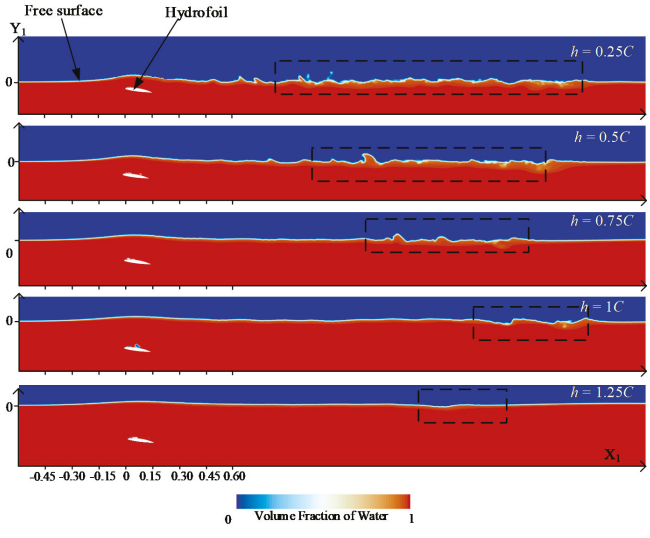

Figure 20. Volume fraction of water on the mid-section plane for different depths at the same cavitation cycle stage.

Positional information for the free surface was extracted from Figure 19 and is shown in Figure 21. The hydrofoil in the figure indicates the relative position of the hydrofoil under various working conditions and does not reflect the true depth. It can be seen that the wave height of the free surface above the hydrofoil decreases as the depth from the free surface increases. For h = 0.25C, 0.5C, 0.75C and 1C, the wavelength increases with increasing depth. However, for h = 1.25C, the wavelength is shorter than that for h = 1C. We speculate that there may be a transition point of the wavelength between h = 1C and h = 1.25C. At this point, the wavelength reaches a maximum above the hydrofoil. As a result, the effects of hydrofoil cavitation on the wave height are uniformly changed and there is a maximum wave length between h = 1.25C and h = 1C cases. We will carry out more detailed work in the future to study the mechanism of this situation.

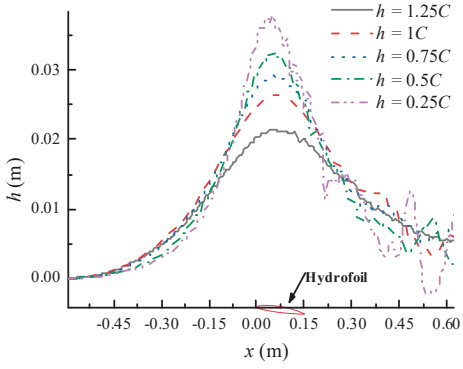

Figure 21. Free surface change caused by hydrofoil cavitation near the free surface in different depth at the same cavitation cycle stage.

4. Conclusions

In this paper, the unsteady cavitation dynamics over a NACA66 hydrofoil near free surface is investigated using the LES method coupled with the Schnerr-Sauer cavitation model. The interaction between free surface and cavitation is evaluated by analyzing cavity evolution, pressure pulsation, hydrodynamic loads and dynamic mode. The main conclusions are as follows:

(1) The existence of the free surface significantly affects the cavitation evolution and hydrodynamic load characteristics over the hydrofoil. Compared with non-free surface conditions, the free surface suppresses the cavitation intensity and accelerates the cavitation evolution. The specific feature is that the period of cavitation development, break-off, shedding and collapse becomes smaller. Meanwhile, both lift and drag are reduced due to the effects of the free surface.

(2) A close relationship is found that between the characteristic mode and the flow field by an improved dynamic mode decomposition method. The existence of free surfaces reduces the energy content in each order mode and results in smaller scale of the coherent structure in higher-order modes. Moreover, compared with the free surface, the reconstructed higher-order flow field indicates that the cavitation flow field is accompanied by a smaller scale and a larger number of vortices for the free surface case.

(3) The distance of the hydrofoil from the free surface has a significant effect on cavitation intensity, pressure pulsation, lift, drag and the wake region. For the same cavitation number, as the distance from the hydrofoil to the free surface increases, the cavitation intensity is promoted, the oscillating frequency of pulsating pressure decreases, the average lift and drag coefficients become larger. Furthermore, it is worth noting that the free surface in the wake region fluctuates more violently at small water depths cases.

Author Contributions: The manuscript was written by T.S. and Q.X.; all authors discussed the original idea; conceptualization, T.S. and L.Z.; methodology, T.S.; software, Q.X.; validation, T.S., Q.X. and L.Z.; formal analysis, T.S.; investigation, H.W.; resources, C.X.; data curation, Q.X.; writing—original draft preparation, T.S.; writing—review and editing, T.S.; visualization, C.X.; supervision, L.Z.; project administration, L.Z.; funding acquisition, L.Z. All authors have read and agreed to the published version of the manuscript.

Funding: This research was funded by the National Natural Science Foundation of China (grant number 51709042), the China Postdoctoral Science Foundation (2019T120211, 2018M631791), the Natural Science Foundation of Liaoning Province of China (20180550619), the Liao Ning Revitalization Talents Program (XLYC1908027).

Conflicts of Interest: The authors declare no conflict of interest.

References

1. Sun, T.; Zhang, X.; Xu, C.; Zhang, G.; Jiang, S.; Zong, Z. Numerical modeling and simulation of the shedding mechanism and vortex structures at the development stage of ventilated partial cavitating flows. *Eur. J Mech. B Fluids* **2019**, *76*, 223–232. [CrossRef]
2. Vahaji, S.; Han, J.; Cheung, S.C.; Yeoh, G.H.; Tu, J. Numerical investigation on the bubble size distribution around NACA0015 hydrofoil. *Ocean Eng.* **2019**, *172*, 59–71. [CrossRef]
3. Sun, T.Z.; Zong, Z.; Zou, L.; Wei, Y.J.; Jiang, Y.C. Numerical investigation of unsteady sheet/cloud cavitation over a hydrofoil in thermo-sensitive fluid. *J. Hydrodynam. B* **2017**, *29*, 987–999. [CrossRef]
4. Wu, Q.; Wang, Y.; Wang, G. Experimental investigation of cavitating flow-induced vibration of hydrofoils. *Ocean Eng.* **2017**, *144*, 50–60. [CrossRef]
5. Liu, M.; Tan, L.; Cao, S. Dynamic mode decomposition of cavitating flow around ALE 15 hydrofoil. *Renew. Energy* **2019**, *139*, 214–227. [CrossRef]
6. Faltinsen, O.M. *Hydrodynamics of High-speed Marine Vehicles*; Cambridge University Press: Cambridge, UK, 2005.
7. Furness, R.A.; Hutton, S.P. Experimental and theoretical studies of two-dimensional fixed-type cavities. *J. Fluids Eng.* **1975**, *97*, 515–521. [CrossRef]
8. Arndt, R.E. Cavitation in fluid machinery and hydraulic structures. *Annu. Rev. Fluid Mech.* **1981**, *13*, 273–326. [CrossRef]
9. Sun, T.; Zhang, X.; Xu, C.; Zhang, G.; Wang, C.; Zong, Z. Experimental investigation on the cavity evolution and dynamics with special emphasis on the development stage of ventilated partial cavitating flow. *Ocean Eng.* **2019**, *187*, 106140. [CrossRef]
10. Knapp, R.T. Recent investigations of the mechanics of cavitation and cavitation damage. *Trans. ASME* **1955**, *77*, 1045–1054.
11. Kubota, A.; Kato, H.; Yamaguchi, H.; Maeda, M. Unsteady structure measurement of cloud cavitation on a foil section using conditional sampling technique. *J. Fluids Eng.* **1989**, *111*, 204–210. [CrossRef]
12. Kawanami, Y.; Kato, H.; Yamaguchi, H.; Tanimura, M.; Tagaya, Y. Mechanism and control of cloud cavitation. *J. Fluids Eng.* **1997**, *119*, 788–794. [CrossRef]
13. Reisman, G.E.; Wang, Y.C.; Brennen, C.E. Observations of shock waves in cloud cavitation. *J. Fluid Mech.* **1998**, *355*, 255–283. [CrossRef]
14. Arndt, R.E.; Song, C.C.S.; Kjeldsen, M.; He, J.; Keller, A. Instability of partial cavitation: A numerical/experimental approach. In Proceedings of the Twenty-Third Symposium on Naval Hydrodynamics, Val de Reuil, France, 17–22 September 2000.
15. Gopalan, S.; Katz, J. Flow structure and modeling issues in the closure region of attached cavitation. *Phys. Fluids* **2000**, *12*, 895–911. [CrossRef]
16. Leroux, J.B.; Astolfi, J.A.; Billard, J.Y. An experimental study of unsteady partial cavitation. *J. Fluids Eng.* **2004**, *126*, 94–101. [CrossRef]
17. Leroux, J.B.; Coutier-Delgosha, O.; Astolfi, J.A. A joint experimental and numerical study of mechanisms associated to instability of partial cavitation on two-dimensional hydrofoil. *Phys. Fluids* **2005**, *17*, 052101. [CrossRef]
18. Passandideh-Fard, M.; Roohi, E. Transient simulations of cavitating flows using a modified volume-of-fluid (VOF) technique. *Int. J. Comput. Fluid Dyn.* **2008**, *22*, 97–114. [CrossRef]
19. Ganesh, H.; Mäkiharju, S.A.; Ceccio, S.L. Bubbly shock propagation as a mechanism for sheet-to-cloud transition of partial cavities. *J. Fluid Mech.* **2016**, *802*, 37–78. [CrossRef]

20. Pendar, M.R.; Roohi, E. Cavitation characteristics around a sphere: An LES investigation. *Int. J. Multiph. Flow* **2018**, *98*, 1–23. [CrossRef]
21. Capurso, T.; Lorusso, M.; Camporeale, S.M.; Fortunato, B.; Torresi, M. Implementation of a passive control system for limiting cavitation around hydrofoils. In *IOP Conference Series: Earth and Environmental Science*; IOP Publishing: Bristol, UK, 2019; Volume 240, p. 032025.
22. Cheng, H.; Long, X.; Ji, B.; Peng, X.; Farhat, M. LES investigation of the influence of cavitation on flow patterns in a confined tip-leakage flow. *Ocean Eng.* **2019**, *186*, 106115. [CrossRef]
23. Cheng, H.Y.; Bai, X.R.; Long, X.P.; Ji, B.; Peng, X.X.; Farhat, M. Large eddy simulation of the tip-leakage cavitating flow with an insight on how cavitation influences vorticity and turbulence. *Appl. Math. Model.* **2020**, *77*, 788–809. [CrossRef]
24. Dawson, T.E. An Experimental Investigation of a Fully Cavitating Two-dimensional Flat Plate Hydrofoil Near a Free Surface. Ph.D. Thesis, California Institute of Technology, Pasadena, CA, USA, 1959.
25. Roohi, E.; Zahiri, A.P.; Passandideh-Fard, M. Numerical simulation of cavitation around a two-dimensional hydrofoil using VOF method and LES turbulence model. *Appl. Math. Model.* **2013**, *37*, 6469–6488. [CrossRef]
26. Karim, M.M.; Prasad, B.; Rahman, N. Numerical simulation of free surface water wave for the flow around NACA 0015 hydrofoil using the volume of fluid (VOF) method. *Ocean Eng.* **2014**, *78*, 89–94. [CrossRef]
27. Oguchi, K.; Enoki, M.; Hirata, N. Numerical simulation for cavitation bubble near free surface and rigid boundary. *Mater. Trans.* **2015**, *56*, 534–538. [CrossRef]
28. Prasad, B.; Hino, T.; Suzuki, K. Numerical simulation of free surface flows around shallowly submerged hydrofoil by OpenFOAM. *Ocean Eng.* **2015**, *102*, 87–94. [CrossRef]
29. Faltinsen, O.M.; Semenov, Y.A. The effect of gravity and cavitation on a hydrofoil near the free surface. *J. Fluid Mech.* **2008**, *597*, 371–394. [CrossRef]
30. Kinzel, M.P.; Lindau, J.W.; Kunz, R.F. Free-surface proximity effects in developed and super-cavitation. In Proceedings of the 2008 DoD HPCMP Users Group Conference, Seattle, WA, USA, 14–17 July 2008; pp. 25–34.
31. Wang, Y.; Wu, X.; Huang, C.; Wu, X. Unsteady characteristics of cloud cavitating flow near the free surface around an axisymmetric projectile. *Int. J. Multiph. Flow* **2016**, *85*, 48–56. [CrossRef]
32. Ye, B.; Wang, Y.; Huang, C.; Huang, J. Numerical study of the pressure wave-induced shedding mechanism in the cavitating flow around an axisymmetric projectile via a compressible multiphase solver. *Ocean Eng.* **2019**, *187*, 106179. [CrossRef]
33. Zhou, H.; Xiang, M.; Zhao, S.; Zhang, W. Development of a multiphase solver for cavitation flow near free surface. *Ocean Eng.* **2019**, *188*, 106236. [CrossRef]
34. Sun, T.; Wei, Y.; Zou, L.; Jiang, Y.; Xu, C.; Zong, Z. Numerical investigation on the unsteady cavitation shedding dynamics over a hydrofoil in thermo-sensitive fluid. *Int. J. Multiph. Flow* **2019**, *111*, 82–100. [CrossRef]
35. Capurso, T.; Lopez, M.; Lorusso, M.; Torresi, M.; Pascazio, G.; Camporeale, S.M.; Fortunato, B. Numerical investigation of cavitation on a NACA0015 hydrofoil by means of OpenFOAM. *Energy Procedia* **2017**, *126*, 794–801. [CrossRef]
36. Huang, B.; Ducoin, A.; Young, Y.L. Physical and numerical investigation of cavitating flows around a pitching hydrofoil. *Phys. Fluids* **2013**, *25*, 102109. [CrossRef]
37. Long, X.; Cheng, H.; Ji, B.; Arndt, R.E.; Peng, X. Large eddy simulation and Euler–Lagrangian coupling investigation of the transient cavitating turbulent flow around a twisted hydrofoil. *Int. J. Multiph. Flow* **2018**, *100*, 41–56. [CrossRef]
38. Pendar, M.R.; Roohi, E. Investigation of cavitation around 3D hemispherical head-form body and conical cavitators using different turbulence and cavitation models. *Ocean Eng.* **2016**, *112*, 287–306. [CrossRef]
39. Sedlar, M.; Ji, B.; Kratky, T.; Rebok, T.; Huzlik, R. Numerical and experimental investigation of three-dimensional cavitating flow around the straight NACA2412 hydrofoil. *Ocean Eng.* **2016**, *123*, 357–382. [CrossRef]
40. Ji, B.; Luo, X.W.; Arndt, R.E.; Peng, X.; Wu, Y. Large eddy simulation and theoretical investigations of the transient cavitating vortical flow structure around a NACA66 hydrofoil. *Int. J. Multiph. Flow* **2015**, *68*, 121–134. [CrossRef]
41. Lidtke, A.K.; Humphrey, V.F.; Turnock, S.R. Feasibility study into a computational approach for marine propeller noise and cavitation modelling. *Ocean Eng.* **2016**, *120*, 152–159. [CrossRef]

42. Movahedian, A.; Pasandidehfard, M.; Roohi, E. LES investigation of sheet-cloud cavitation around a 3-D twisted wing with a NACA 16012 hydrofoil. *Ocean Eng.* **2019**, *192*, 106547. [CrossRef]
43. De Giorgi, M.G.; Fontanarosa, D.; Ficarella, A. Characterization of cavitating flow regimes in an internal sharp-edged orifice by means of Proper Orthogonal Decomposition. *Exp. Therm. Fluid Sci.* **2018**, *93*, 242–256. [CrossRef]
44. Prothin, S.; Djeridi, H.; Billard, J.Y. Coherent and turbulent process analysis of the effects of a longitudinal vortex on boundary layer detachment on a NACA0015 foil. *J. Fluids Struct.* **2014**, *47*, 2–20. [CrossRef]
45. Schmid, P.J. Dynamic mode decomposition of numerical and experimental data. *J. Fluid Mech.* **2010**, *656*, 5–28. [CrossRef]
46. Vinha, N.; Meseguer-Garrido, F.; De Vicente, J.; Valero, E. A dynamic mode decomposition of the saturation process in the open cavity flow. *Aerosp. Sci. Technol.* **2016**, *52*, 198–206. [CrossRef]
47. Prothin, S.; Billard, J.Y.; Djeridi, H. Image processing using proper orthogonal and dynamic mode decompositions for the study of cavitation developing on a NACA0015 foil. *Exp. Fluids* **2016**, *57*, 157. [CrossRef]
48. Nicoud, F.; Ducros, F. Subgrid-scale stress modelling based on the square of the velocity gradient tensor. *Flow Turbul. Combust.* **1999**, *62*, 183–200. [CrossRef]
49. Rayleigh, L. VIII. On the pressure developed in a liquid during the collapse of a spherical cavity. *Lond. Edinb. Dublin Philos. Mag. J. Sci.* **1917**, *34*, 94–98. [CrossRef]
50. Plesset, M.S. The dynamics of cavitation bubbles. *J. Appl. Mech.* **1949**, *16*, 277–282. [CrossRef]
51. Schnerr, G.H.; Sauer, J. Physical and numerical modeling of unsteady cavitation dynamics. In Proceedings of the Fourth International Conference on Multiphase Flow, New Orleans, LA, USA, 27 May–1 June 2001.
52. Huang, N.E.; Wu, M.L.; Qu, W.; Long, S.R.; Shen, S.S. Applications of Hilbert–Huang transform to non-stationary financial time series analysis. *Appl. Stoch. Models Bus. Ind.* **2003**, *19*, 245–268. [CrossRef]

Journal of
Marine Science and Engineering

MDPI

Article

Viscous Damping Identification for a Wave Energy Converter Using CFD-URANS Simulations

Marco Fontana *,†, Pietro Casalone *,†, Sergej Antonello Sirigu †, Giuseppe Giorgi †, Giovanni Bracco † and Giuliana Mattiazzo †

Department of Mechanical and Aerospace Engineering, Polytechnic of Turin, C.so Duca degli Abruzzi, 24, 10129 Turin, Italy; sergej.sirigu@polito.it (S.A.S.); giuseppe.giorgi@polito.it (G.G.); giovanni.bracco@polito.it (G.B.); giuliana.mattiazzo@polito.it (G.M.)

* Correspondence: marco_fontana@polito.it (M.F.); pietro.casalone@polito.it (P.C.)

† These authors contributed equally to this work.

Received: 19 April 2020; Accepted: 14 May 2020; Published: 17 May 2020

Abstract: During the optimization phase of a wave energy converter (WEC), it is essential to be able to rely on a model that is both fast and accurate. In this regard, Computational Fluid Dynamic (CFD) with Reynolds Averaged Navier–Stokes (RANS) approach is not suitable for optimization studies, given its computational cost, while methods based on potential theory are fast but not accurate enough. A good compromise can be found in boundary element methods (BEMs), based on potential theory, with the addition of non-linearities. This paper deals with the identification of viscous parameters to account for such non-linearities, based on CFD-Unsteady RANS (URANS) analysis. The work proposes two different methodologies to identify the viscous damping along the rotational degree of freedom (DOF) of pitch and roll: The first solely involves the outcomes of the CFD simulations, computing the viscous damping coefficients through the logarithmic decrement method, the second approach solves the Cummins' equation of motion, via a Runge-Kutta scheme, selecting the damping coefficients that minimize the difference with CFD time series. The viscous damping is mostly linear for pitch and quadratic for roll, given the shape of the WEC analysed.

Keywords: wave energy; computational fluid dynamics; identification; viscous damping; URANS

1. Introduction

Developing efficient, cost competitive and survivable wave energy converters (WECs), has proven, in the last years, to be a challenging task [1–3]. Fluid dynamic analyses are fundamental at every design stage to evaluate the behaviour of the WEC [4], so different methods for simulating the fluid forces and the interaction between waves and semi-submerged bodies have been developed, with increasing levels of fidelity and associated computational cost. Solving the complete set of Navier–Stokes Equations (NSE) for offshore engineering applications is expensive and not advised because the computational cost is too high compared to the accuracy desired [5]. Therefore, the NSE are simplified to obtain a linear equivalent potential flow theory (PF), where the solution is obtained through linearization, thanks to assumptions of inviscid fluid and irrotational, incompressible flow. In this way, one of the most complex set of equations is transformed into a Laplace problem. Under such hypotheses, the Boundary Element Method (BEM) can be implemented, which is a numerical approach for the solution of linear partial differential equations, expressed as integral equations. BEM represents a valid alternative to Reynolds Average Navier–Stokes (RANS) simulation: Being three (or more) orders of magnitude faster [6], BEM is used in many industrial and research applications, especially when computational resources are limited and accuracy is not of primary importance. Linear approaches produce satisfactory results when modelling linear waves and the WEC is moving around the operative point. In fact, non linearities of fluid forces are less important when oscillations

are small and smooth. The success of linear models is justified by their many perks, which include, but not limited to, extreme simplicity, compliance with the superposition principle and great flexibility that makes them compatible with a vast array of mathematical tools. The linearization is always referred to the operating point. In many applications this is a reasonable assumption, since the working condition is not far respect a specific setpoint; in contrast, in the case of wave energy conversion, the objective is to drive the system as far away from equilibrium as possible, in order to maximize the produced energy. This is likely to excite nonlinear dynamics, resulting in non-representative linear models, which usually underestimate energy losses and overestimate the productivity of the WEC [7].

Two main assumptions must be satisfied when using BEMs:

1. The maximum wave steepness should be less than 1/30.
2. The oscillations around the equilibrium point should be small.

The better these hypotheses are met, the higher the accuracy of the results obtained with the linear model [8]. Although linear PF methods have been used successfully in many offshore engineering applications, the linearizing assumptions are often challenged by realistic WEC behaviour, where large amplitude motions result in viscous drag, flow separation, vortex shedding and other nonlinear hydrodynamic effects [5]. In order to improve the linear time domain model of a WEC, described by the Cummins' equation [9], it is possible to include a viscous damping term as an external force, without significantly increment the computational time required to run the model. In this paper, a notional un-coupled linear and quadratic dependence of the viscous force on the velocity is assumed, hence considering two additive terms. It follows that two viscous drag coefficients should be identified, one for the linear contribution and one for the quadratic contribution. The addition of such non-linear damping force is necessary to avoid divergence in simulations under certain conditions: for example, the model of a forced, undamped system, is likely to explode into very large, non-realistic motion close to resonance conditions. Diverging behaviour can happen without a proper extinction coefficient and is not possible to model some of the conditions the WEC will face at sea [10].

A way to determine damping coefficients is to conduct an experimental campaign, analysing the free decay motion of the WEC [11,12]. For each degree of freedom (DOF), the WEC is released from a set of initial conditions in order to highlight when non-linearities become important; this test is usually performed to identify the roll damping for ships [13]. In order to consider only the significant kinematics of the free decay, the analysed time trace usually covers a few oscillations before the transient elapses; for different starting conditions, the resulting angular acceleration, velocity and rotation angle are post-processed to estimate damping parameters. However, experimental campaigns [14] are expensive and usually not affordable in the early design stage of a WEC. Such a critical obstacle can be overcome by using the use of a CFD Numerical Wave Tank (CNWT). CFD is a Hi-Fi approach to the problem that makes the inclusion of all non-linearities possible. However, CFD is so computationally expensive that it cannot be used for extensive analysis or study of operative conditions: Its most common use is when large non-linearities are expected (survivability, large motion) or for tuning and validating lower-fidelity models, or investigating behaviour of related devices such as tuning tanks [15]. Furthermore, turbulence is a critical feature to handle. There are mainly three techniques to deal with it: Direct Numerical Simulations (DNS), in such simulations, all of the motions contained in the flow are resolved, Large Eddy Simulations (LES) in which NSEs are filtered over the space, finally RANS in which flow quantities are split into the mean value and the perturbation. The resulting equations of LES and RANS are essentially identical, the difference is that in LES most of the turbulence energy is resolved [16]. The URANS approach is chosen because it is the best cost-efficient method considering accuracy and solver time (which could increase easily by several orders of magnitude from RANS to LES and DNS).

The aim of this paper is to define a CFD setup able to emulate a real tank experiment and to describe a methodology to identify the viscous damping coefficients along the two rotational DOFs of a WEC, namely pitch and roll. In particular, the WEC is a prismatic pitching platform that extracts energy from

the pitching motion. On the one hand, viscous losses in pitch are detrimental for power extraction, since they increase the dissipation in the DOF exploited to harvest energy; on the other hand, roll response to oblique or short-crested waves is also detrimental, since it absorbs part of the incoming energy, hence decreasing the energy available to the pitch DOF. Therefore, it is important to obtain a reliable prediction of both pitch and roll responses. The goal of this paper is to increase the fidelity of models based on the potential flow theory by adding the effect of viscous non-linearities. It is worthwhile to remark that most of the literature in the wave energy field is concerned with the identification of viscous losses in the DOF used for energy extraction only (usually a smooth surfaces), while ancillary DOFs are often neglected (with sharp edges in the case study herein considered). Hence, this paper also purports to discuss specific challenges and intrinsic differences between different DOFs, despite using the same test-case and identification technique. Results carried out from simulations are consistent with expectations based on the shape of the hull: the linear term of the damping force prevails in the pitch free decay analysis while the quadratic term, that models the viscous non-linearities, is predominant in the roll DOF.

This paper is organized as follows. After a brief presentation of the device considered in Section 2, the mathematical model of the methodology presented in this paper is discussed in Section 3. The CFD simulation and its setup is explained in Section 4 with emphasis on damping techniques to avoid wave reflections and overset mesh. In the final part of CFD section the mesh convergence study is presented and discussed. Results of simulations are shown in Section 5, firstly as regards CFD scenes, then kinematics and finally the application of methodology discussed in the mathematical section. Ultimately the conclusions of Section 6 involve the analysis of the previously shown outcomes and a last post-processing phase by solving the equation of motion in the time domain, including the non-linear damping effect and the optimization of coefficient identification through the goodness of fit.

2. Device

The present case considers the WEC shown in Figure 1. Such device, so-called Inertial Sea Wave Energy Converter (ISWEC), is a pitching gyroscope-based WEC, designed for the Mediterranean Sea. ISWEC absorbs wave energy through a floating hull, that drives a gyroscope within contained by means of reacting inertial effects. In particular, waves force the hull into pitching motion, which is transmitted to the gyroscopic system located on a platform inside the floater; the reaction is due to the gyroscopic effects on the spinning flywheel, which induces a torque that is transformed by the power take off (PTO) into electrical energy.

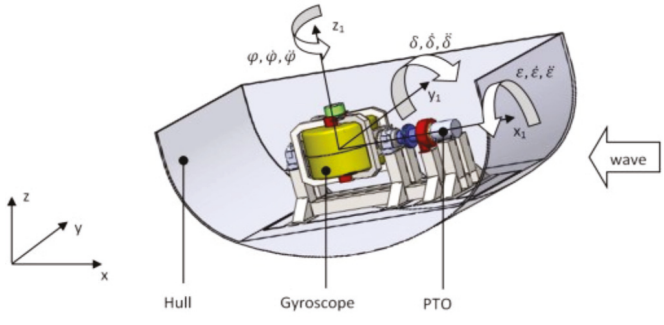

Figure 1. Schematic representation of the Inertial Sea Wave Energy Converter (ISWEC) device hull, gyroscope, power take off (PTO) and reference system with respect to the incoming wave.

The hull considered in this work has length L_H equals to 10m and width $W_H = 5\,\mathrm{m}$.

3. Mathematical Model and Identification Method

The time domain linear model of a floating WEC is based on the Cummins' equation [9].

$$(M + A_\infty)\ddot{X}(t) + \int_0^t h_r(t-\tau)\dot{X}(t)d\tau + KX(t) = F_w(t) \tag{1}$$

where the terms of Equation (1) are:

- A_∞ is the matrix of added mass at infinite frequency
- M is the mass matrix
- F_w is the external force
- K is the stiffness matrix
- h_r is the radiation impulse response function

The convolution term represents, along with A_∞, the effect of wave radiation in an ideal fluid and it is often referred to as fluid memory effect, because it considers the energy of the radiated waves due to the past motion of the body.

The hydrodynamic parameters in Equation (1) are computed via BEM-based software (e.g., NEMOH [17] and ANSYS Aqwa [18]). It is worth noting that in Equation (1) there are no linearity limitations on the external forces, hence the model is potentially capable to deal with non-linear contributions. Viscous effects are modelled via the addition of a nonlinear term to the right-hand side of Equation (1), divided into linear and quadratic dependence on the pitching velocity $\dot{\delta}$.

The identification of such damping parameter is conducted using the logarithmic-decrement decay method [11,12,19], which considers the rate of decay of oscillation starting from a non-equilibrium position. During a free decay test, the system oscillates, for each DOF, at its single natural frequency, thus it is possible to determine both the natural period and the hydrodynamic damping. The non-linear equation for free decay pitch motion is:

$$(I_{55} + A(\omega_\delta))\ddot{\delta}(t) + F^{\mathrm{NL}}_{\mathrm{vis},55} + K_{55}\delta(t) = 0 \tag{2}$$

where the subscript 55 refers to the pitching DOF, δ is the pitch angle and the frequency-dependent added mass A is calculated at the natural frequency of the system (ω_δ). $F^{\mathrm{NL}}_{\mathrm{vis},55}$ is the nonlinear viscous force, defined as

$$F^{\mathrm{NL}}_{\mathrm{vis},55} = B_{55,1}\dot{\delta} + B_{55,2}\dot{\delta}|\dot{\delta}| \tag{3}$$

where $B_{55,1}$ is the coefficient for linear dissipation, and $B_{55,2}$ is the coefficient for quadratic dissipation. Note that $B_{55,1}$ accounts for both linear viscous damping and radiation damping. Equation (3) can be directly included in a non-linear time domain model, with the coefficients $B_{55,1}$ and $B_{55,2}$ identified as the ones that minimize the error between a fidelity-benchmark (CFD, for instance) and the time-domain model. However, it is often crucial to preserve the linear structure of the lower-fidelity model, for example to retain the ability to simulate the model in the frequency domain. Therefore, it is useful to linearize Equation (3), while preserving the ability to discriminate between linear and quadratic contributions. According to [20], it is possible to assume that for each half-cycle, the oscillation is reasonably sinusoidal. Under such an assumption, the non-linear (quadratic) term of Equation (3) can be linearized using the Fourier series expansion:

$$\dot{\delta}|\dot{\delta}| = \frac{8}{3\pi}\omega_\delta\delta_i\dot{\delta} \tag{4}$$

where δ_i and ω_δ are the amplitude and the frequency of oscillation of the i-th oscillation cycle, respectively. Consequently, the linearized damping force can be defined as:

$$F^{\mathrm{L}}_{\mathrm{vis},55} = B_{55,\mathrm{tot}}\dot{\delta} = \left(B_{55,1} + \frac{8}{3\pi}\omega_\delta\delta_i B_{55,2}\right)\dot{\delta} \tag{5}$$

With the inclusion of $F^{L}_{vis,55}$ and dividing Equation (2) by the equivalent inertia $(I_{55} + A(\omega_\delta))$, it is possible to obtain the non-dimensional linear equation of motion in the canonical form:

$$\ddot{\delta} + 2\alpha_{eq}\dot{\delta} + \omega_\delta^2 \delta = 0 \tag{6}$$

where

$$\alpha_{eq} = \alpha + \frac{4}{3\pi}\omega_\delta \delta_i \beta \tag{7}$$

with $\alpha = \frac{B_{55,1}}{2(I_{55}+A(\omega_\delta))}$ and $\beta = \frac{B_{55,2}}{(I_{55}+A(\omega_\delta))}$. Equation (6) describes a linear underdamped system, for which the envelope curve of a decay starting from δ_0 is defined as:

$$\delta = \delta_0 e^{\alpha_{eq} t} \tag{8}$$

Applying Equation (8) for two consecutive peaks i and $i+1$ of the decay curve, it is possible to calculate the logarithmic decay:

$$\frac{\delta_i}{\delta_{i+1}} = e^{\alpha_{eq}(t_{i+1} - t_i)} \tag{9}$$

Thus, identifying the equivalent linear extinction coefficient:

$$\alpha_{eq} = \frac{1}{t_{i+1} - t_i} \ln\left(\frac{|\delta_i|}{|\delta_{i+1}|}\right) \approx \alpha + \frac{4}{3\pi}\omega_\delta \delta_{mean,i} \beta \tag{10}$$

where

$$\delta_{mean,i} = \frac{|\delta_i| + |\delta_{i+1}|}{2} \tag{11}$$

and the damped natural pitch frequency can be calculated as:

$$\omega_{\delta_0} = \sqrt{\omega_\delta^2 + \alpha_{eq}^2} \tag{12}$$

This method allows to calculate the extinction curve of the α_{eq} as a function of the mean amplitude δ_{mean} for each cycle. To exploit all the available experimental data and obtain a more accurate estimation, it is possible to calculate α_{eq} and δ_{mean} for each oscillation cycle, considering both maxima and minima peaks and grouping the informations of all the decay tests for the specific DOF. The linear regression fit is then performed on the calculated points, with respect to the curve expression:

$$\alpha_{eq} = a\delta_{mean} + b \tag{13}$$

which allows to identify the linear and quadratic extinction coefficients:

$$\alpha \equiv b \tag{14}$$

$$\beta \equiv \frac{3\pi}{4\omega_\delta} a \tag{15}$$

4. CFD Model

The analysis has been carried out on the commercial software Star-CCM+ from Siemens [21] and a Unsteady Reynold Average Navier–Stokes (URANS) approach has been used. Particular attention should be paid to the setup of the CFD simulation environment, since different fluid interfaces, fluid-structure interaction and large solid body motion present numerical problems of challenging resolution. Under such conditions, reliable results can only be achieved by an appropriate and comprehensive model definition. The following subsections detail the most relevant aspects to take under consideration when performing pitch and roll free decay tests of a floating pitching platform as the one considered in this paper.

4.1. Domain, Boundary Conditions and Damping Length

Due to its oscillation, the floater generates radiated waves that propagate towards the boundaries of the domain, effectively dissipating energy. In order to correctly represent the amount of energy that is subtracted from the floater due to wave generation, it is crucial to capture the wave pattern generated by the hull during the oscillations. In this regard, the domain needs to be large enough to contain the most energetic part of the wave pattern, freely propagating in each direction. Considering L_H and W_H, respectively length and width of the hull, domain overall length is $20\,L_H$ and its width $10\,W_H$. Since the wave are generated by the hull of length L_H, depth of domain is set to $2.5\,L_H$ in order to respect the deep water approximation Depth/Wave Length > 0.5.

The choice of the dimensions of the domain also depends on wave reflection phenomena, which are a critical problem in both real and numerical tanks. In fact, reflected waves modify the wave field and ultimately affect the dynamics of the floater; Furthermore, it is difficult, if not impossible, to accurately separate the contribution of radiated and reflected waves, leading to improper measures, in case of real experiments, and to numerical noise and simulation crash, in case of numerical tanks. A possible solution consists in adding a damping zone at the boundaries of the domain in order to decrement the energy and the height of waves before they reach the frontier of the domain. Therefore, damping zones hinder the generation of reflected waves, leaving fluid domain perturbed mainly by the radiated waves for the whole duration of the significant decay.

The damping zone should have an appropriate length (at least twice the wavelength [21]) and intensity of the damping [22]. Damping waves is possible by introducing an additional resistance term S_z as a source into the momentum equation relative to the vertical motion w, according to [22]:

$$S_z = \rho\left(f_1 + f_2|w|\right)\frac{e^k - 1}{e - 1}w \tag{16}$$

$$k = \left(\frac{x - x_{sd}}{x_{ed} - x_{sd}}\right)^n \tag{17}$$

where:

- x_{sd} is the starting point for wave damping (along x-axis direction)
- x_{ed} is the end point (i.e., the boundary)
- ρ is the water density
- w is the vertical velocity component
- f_1, f_2 and n are parameters of the damping model of Choi et al. [22].

In this particular case, considering a wavelength (λ) comparable to the hull's length, considering the results of Peric et al. [23] and after a trial-and-error evaluation stage, based on estimation of the simulation's residuals, the following values have been imposed:

$$f_1 = 0; \qquad f_2 = \frac{10^2\pi}{\lambda}; \qquad n = 2 \tag{18}$$

Bearing this in mind, the waves reflection phenomenon has been addressed imposing a damping factor k in Equation (17) within a distance of 20 m from the boundaries as shown in Figure 2, that represents a top-view of the sea surface of the simulation.

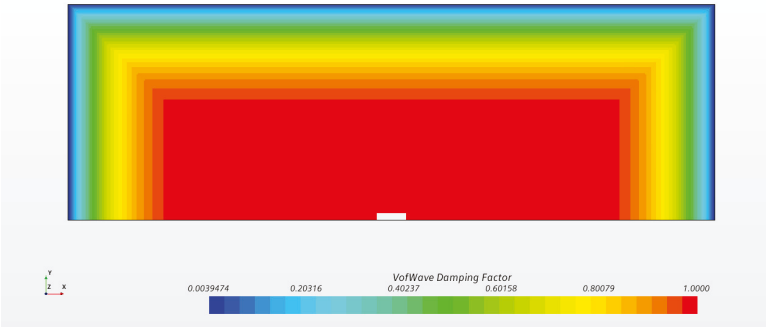

Figure 2. VOF Damping Factor k.

The boundaries conditions are shown in Figure 3. With respect to the boundaries named *top* and *bottom*, they are set as *velocity inlet*, because a unique phase, air and water, respectively, with zero-velocity is imposed. At *side*, *right* and *left*, the boundary conditions are set as *pressure outlet*, and the pressure is forced to be the atmospheric one for the air section and the hydrostatic one for the water part.

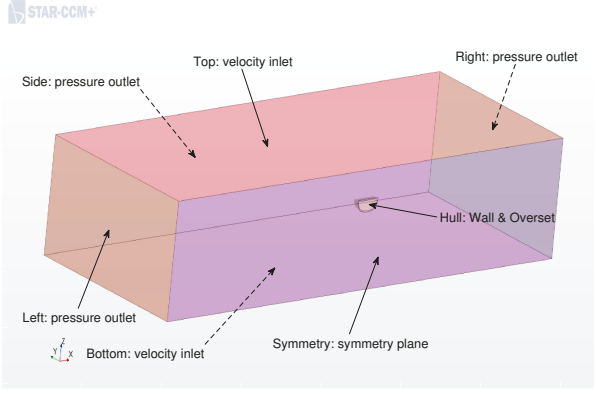

Figure 3. Domain boundary conditions.

Being the domain a function of wavelength, a parametric approach has been used: For the different free decay tests and different initial conditions the wave produced are quite various and so the domain and mesh refinements, to maximize efficiency of the simulation.

4.2. Mesh Generation

In CFD there are two ways to deal with moving bodies: Mesh morphing/remeshing techniques are best when the movement of the body is very small, while they are too computationally expensive and potentially unstable with large displacements of the floater, since the mesh morphing task becomes a significant portion of the overall computational burden. Alternatively, when large motions are expected, overset methods should be preferred [24,25]. Thus the overset approach has been chosen for this study and the domain is split in two different overlapped parts: background and overset. The overset is the one moving with the body, while the background is fixed. With the overset approach,

no remesh operation is needed because the mesh never deforms nor its quality decreases, since it moves with the body and remains unaltered. The overset and background separate regions exchange information due to an overlapping area consisting of some cells, called donor and acceptor, where the solution is interpolated trough Chimera Interpolation techniques according to [26,27]. Equations are solved separately in these different areas and bound together only at the interface between the two zones.

While the dimensions of the background are function of the wavelength, the dimensions of the overset region are constant for all the tests because they are referred to the hull and not to the wave pattern. Another important volumetric refinement is the one around the overset which ensures that, in the zone where information are exchanged, cells belonging to overset and background have the same volume, in order to reduce discretization and interpolation errors. When dealing with trimmed block mesh, it is is important to bear in mind that cells can increase their size only by double.

4.2.1. Tank

A trimmed mesh has been chosen due to the possibility to create anisotropic cells which provide a predominantly hexahedral mesh with minimal cell skewness, it results as the best discretization at the interface between the two fluids. It is worthwhile to remark that wave reflection can occur also when the mesh size suddenly changes. To avoid this problem, usually three different volumetric sea surface refinements are used in order to gradually coarsen the mesh, as shown from a prospective-side view in Figure 4 and side-view in Figure 5.

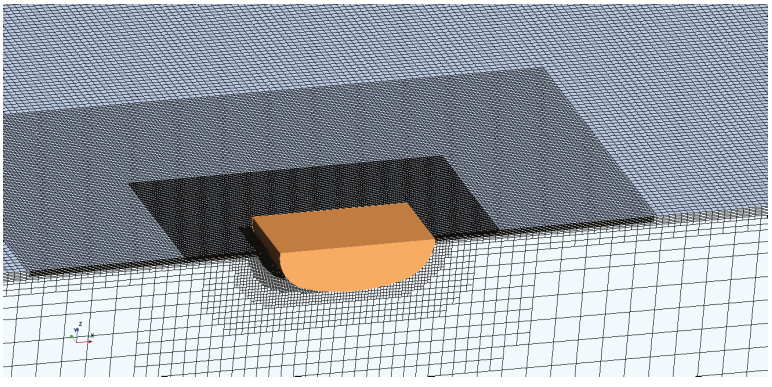

Figure 4. Sea surface refinements in prospective view.

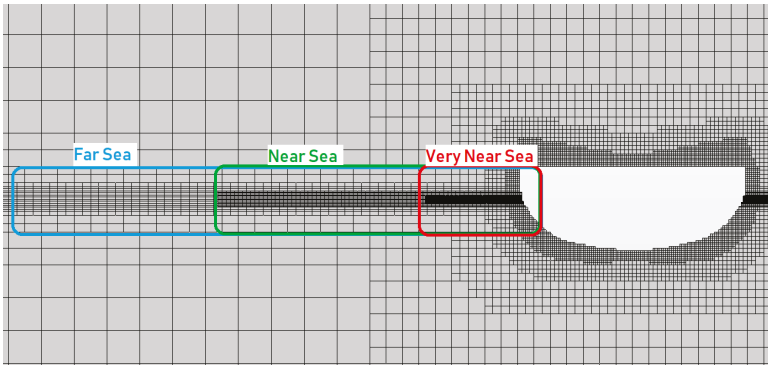

Figure 5. Sea surface refinements in side-view.

The wave damping should start before the coarsest grid level is reached since such a change in cell size is a potential source of reflection that should be included in the damping zone [28].

4.2.2. Overset Region

Two main factors influence the overset's dimensions:

- Overset does not have to be too large, otherwise the extremities will move too much when it rotates, generating interpolation errors and requiring a lower time step
- Neither too small, because cells need space to grow from the wall to the interfaces; Moreover this guarantees that the strongest gradients are solved within the overset and not in the zone where information is exchanged.

For the overset sea refinement, we used the shape displayed in Figure 6 and isotropic cells because, otherwise, when the region rotates, the anisotropic sea refinement at the water line will rotate along with the hull.

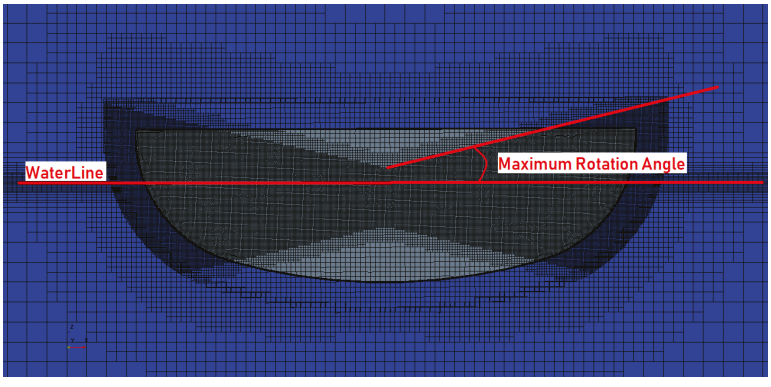

Figure 6. Hull mesh refinement based on maximum rotation angle.

4.3. Volume of Fluid

The Volume of Fluid (VOF) Multiphase model is an Eulerian numerical model suited to simulate flows of several immiscible fluids on numerical grids, capable of resolving the interface between the different phases [29]. The spatial distribution of each phase at a given time is defined in terms of a variable that is called the volume fraction. A method of calculating such distributions is to solve a transport equation for the phase volume fraction. The method uses the STAR-CCM+ Segregated Flow model which solves each of the momentum equations in turn. The VOF Multiphase model is the standard model to deal with marine environment and wave generation in a RANS simulation [21].

4.4. Turbulence, Wall Treatment, Y+

K-Epsilon is a two-equations model that solves transport equations for the turbulent kinetic energy and the turbulent dissipation rate in order to determine the turbulent eddy viscosity. Such model provides a good compromise between robustness, computational cost and accuracy and are well suited for external flows and when gradients at wall are not too strong [30,31]. In our case a Realizable Two layer K-Epsilon Model is used [32]. This model contains a new transport equation for the turbulent dissipation rate with respect to standard K-Epsilon. In addition, the turbulent viscosity is expressed as a function of mean flow and turbulence properties, rather than assumed to be constant as in the standard model. A two-layer wall treatment is adopted: this method solves for but prescribes and turbulent viscosity algebraically with distance from the wall in the viscosity-dominated near-wall flow regions. In this approach, the boundary layer is divided into two layers. The values specified in the near-wall layer

are blended smoothly with the values computed from solving the transport equation far from the wall. The equation for the turbulent kinetic energy is solved across the entire flow domain. The two-layer approach, which resolves correctly for both low and high y_+, using respectively standard wall function and blended wall function according to Reichardt's law [33], fits perfectly with the free decay problem: after few oscillations the velocities are smaller and y_+ value decreases during the numerical experiment. Based on such considerations, a target value of $y_+ = 1$ has been chosen, since the aim of this work is to define damping coefficient accounting for non-linear effects, thus it is important to describe properly the boundary layer zone where viscous stress, separation or vortex shedding that occur. The value of $y_+ = 1$ is obtained considering the flat-plate boundary layer theory [34], obtaining a first cell height of $4.222 \cdot 10^{-4}$ m, considering a reasonable total thickness of 3 cm and using a number of 10 layers, which guarantee a smooth grow rate of the cells.

4.5. Time Step

In Star-CCM+ the multiphase VOF model requires the use of an implicit unsteady approach. A second order time-marching discretization has been chosen since the first order is numerically dissipative and the property of the wave may not be transported correctly. First order time discretization is the only model unconditionally stable, but it has a drawback: the leading term of the truncation error of convective flux resembles a diffusive flux. This numerical, or artificial, diffusion that is introduced in the solution is magnified in multidimensional problems if the flow is oblique to the grid. A very fine grid would be necessary to obtain accurate solutions. On the other hand, since a second order approach does not require such a refined mesh-discretization, it is faster and more accurate than a first-order time-discretization. Time step is limited by two different conditions:

- The courant number at the interface between the two fluids has to be at least less than 1 (required by the VOF model), although it is suggested to keep it less than 0.5 in order to have a clean separation of the two fluids.
- The movement of the overset cells at the interface between the two regions must be less than half the minimum cell size, when using a second order temporal scheme, in order to prevent overset mesh problems due to the exchange of information.

The more severe limitation on the time step comes from the latter condition; therefore, it is convenient to change the time step according to the different initial conditions: since the oscillation period is always the same, the further away from equilibrium is the initial displacement, the smaller the time step needs to be in order to maintain the same courant number.

4.6. Mesh Convergence Study

In order to support the goodness of the numerical scheme created, a grid independence analysis has been carried out. This process proves the stability of the numerical method and ensures that solution does not change when refining the mesh. This convergence study is based on the number of cells used to discretize the wave height that is generated by the oscillations of the hull. In the wave pattern there is the energy lost by the device during the free decay and it is fundamental to capture it accurately. Moreover, prism layer properties are base size independent and computed as absolute values, thus base size has little influence in the overall mesh. The number of layers that are necessary to discretize the wave is very dependent on wave steepness; according to [5], at least 10 layers are suggested and even more for a sharp interface between fluids. Not using enough cells some information may be lost and wave transport and generation may be inaccurate, resulting in overly-damped or magnified waves. Cells count is very dependent on the number of layers of sea refinement because most of the cells come from this mesh control and from the overset zone, as confirmed by results presented in Figure 7.

In order to choose the appropriate mesh sizes CPU time is considered, as shown in Figure 8: passing from 15 cells to 20 means an increase of about 115%. So the configuration of 20 cells per wave height has been excluded because of the prohibitive computational time.

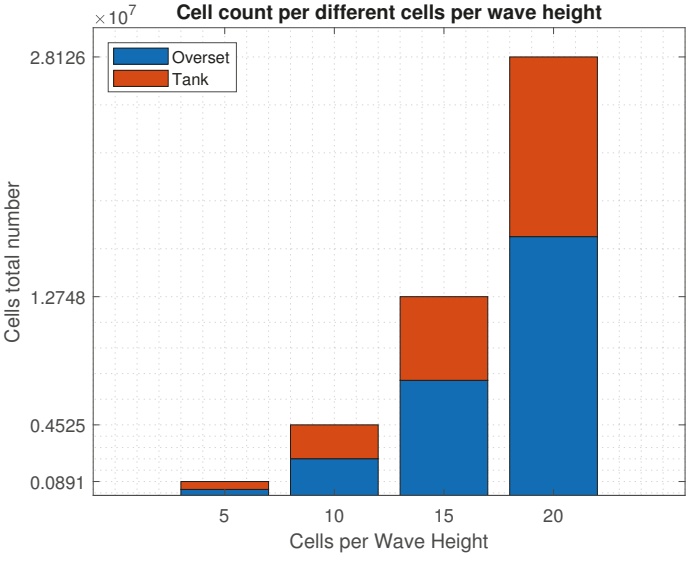

Figure 7. Number of total cell varying the cells per wave height.

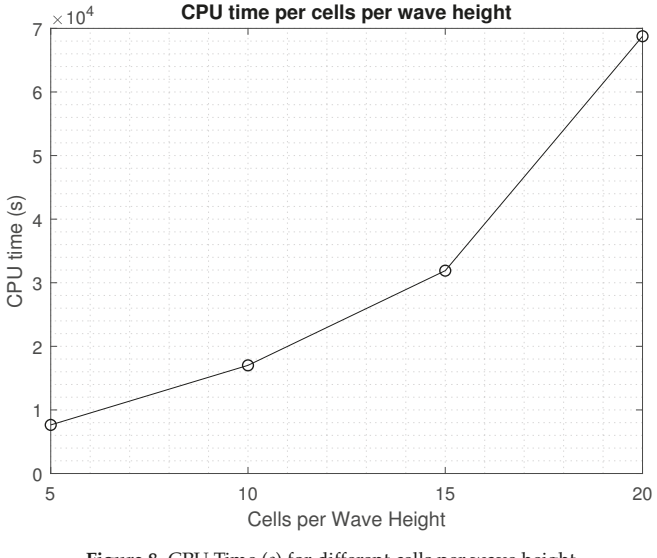

Figure 8. CPU Time (*s*) for different cells per wave height.

The cells count of the overset is related with the size of the sea refinement, because cells at the interface between background and overset must have same volume, especially at sea surface. Convergence study is done on the kinematics of the free decay with respect to Figure 9, which is also the data used for the post-processing and evaluation of damping coefficients.

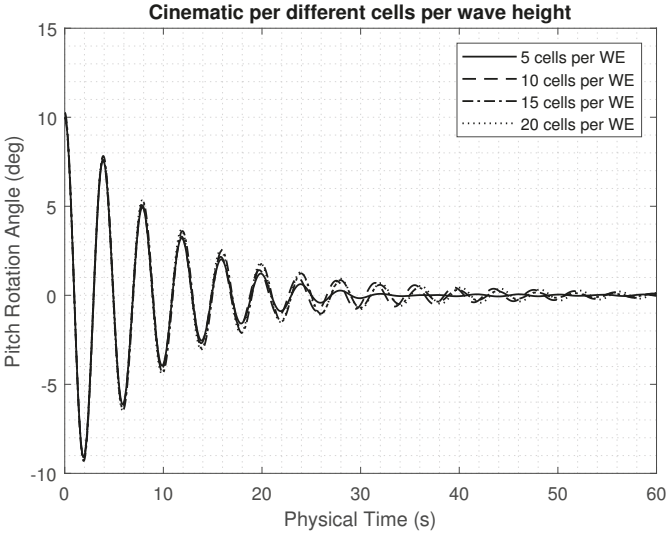

Figure 9. Different kinematics in terms of pitch angle for various cells per wave height.

The wave height with several probes has also been monitored in order to understand the impact of mesh resolution in areas far from the floater.

The coarsest mesh setups have been compared to the finest ones corresponding to 20 cells in terms of relative errors and the associated root-mean-square as shown in Figures 10 and 11.

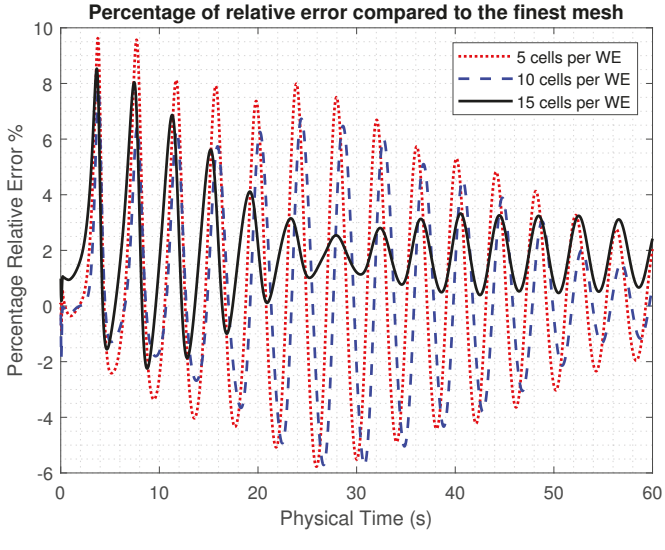

Figure 10. Relative error for different meshes.

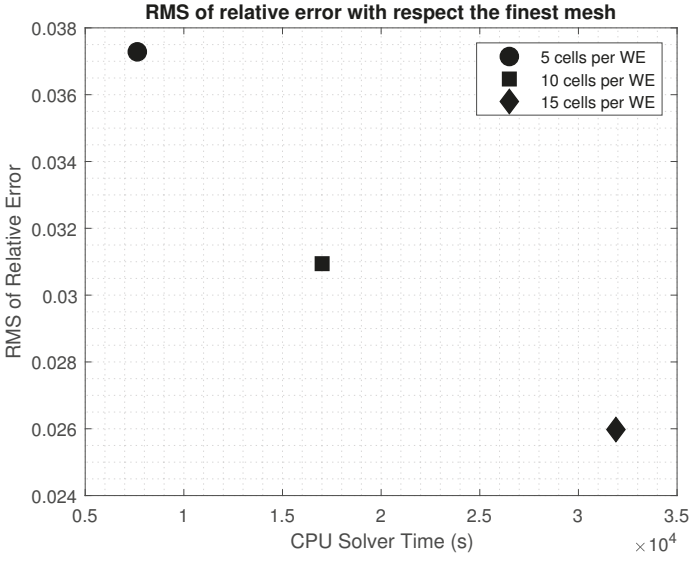

Figure 11. RMS of error compared to 20 cells per wave height.

Finally, 15 cells per wave height have been chosen, in order to ensure a good compromise between wave capturing and computational cost specially considering the trend of errors in Figure 10, the low related rms (Figure 11) and its computational cost in terms of time (Figure 8).

5. Results

5.1. CFD Scenes

In this section, results are presented in terms of scalar and vector scenes in order to show the validity and the reliability of the conducted CFD simulations for pitch and roll free decay motions. An example of the wave pattern generated by the pitching motion is shown in Figure 12, starting from a non-equilibrium angle equal to 10°. The outcomes are consistent with the physical phenomenon.

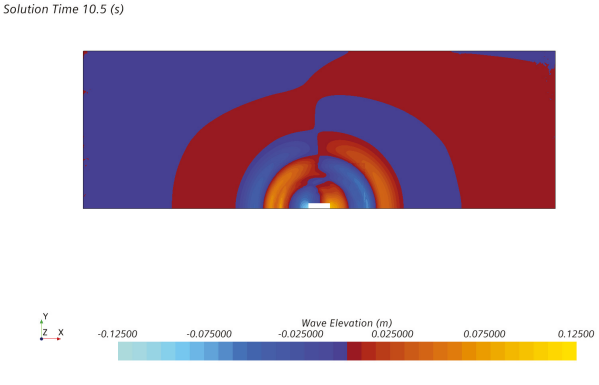

Figure 12. Wave pattern for a pitching free decay simulation, starting from a 10° initial displacement.

The hydrostatic pressure referred to the waterline is well defined as shown in the example of a roll simulation in Figure 13.

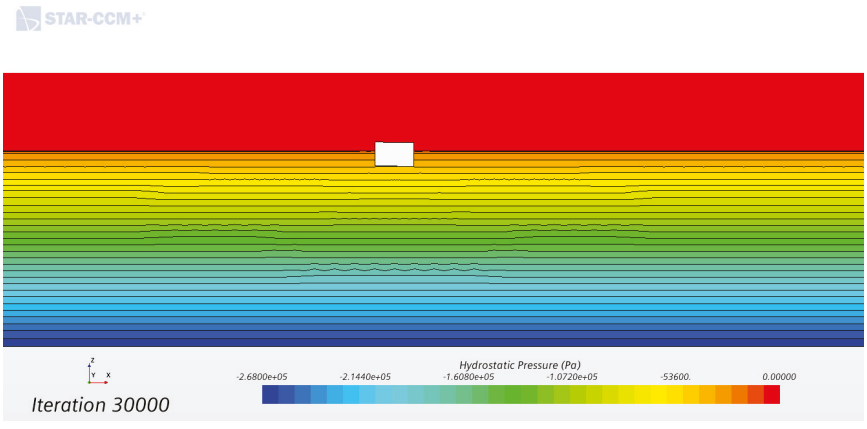

Figure 13. Hydrostatic pressure referred to the waterline.

The interface is smooth and well-captured, as shown in Figure 14, where the line convolution integral (LIC) of velocity is presented. Such a visualization tends to show a texture where points along the same streamline have the same colour; Displaying LIC of velocity is more computationally efficient the actual streamline scene which the latter is very expensive in terms of computational costs. Generally this technique [35] involves convoluting a white noise image along streamlines computed from the vector field. In the resulting image, the streamlines cover the entire domain of the vector field. This technique has the advantage of being able to visualize large and detailed vector fields in a reasonable display area. Compared with simpler integration-type approaches, which entail following the flow vector at each point to produce a line, LIC produces a whole image at every step.

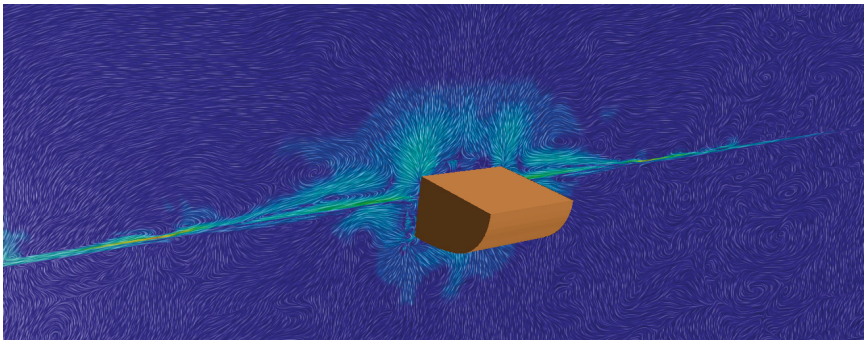

Figure 14. Line Integral Convolution of velocity in roll simulation.

Lastly, the target value of $y_+ = 1$ on the wet surface of the hull, on average, has been correctly obtained, as shown in Figure 15. The scene in Figure 15 refers to an intermediate time step and proves an adequate mesh sizing within the scope of capturing a low value of y_+ which results into an accurate interpolation by the solver in terms of wall stresses and frictional velocity.

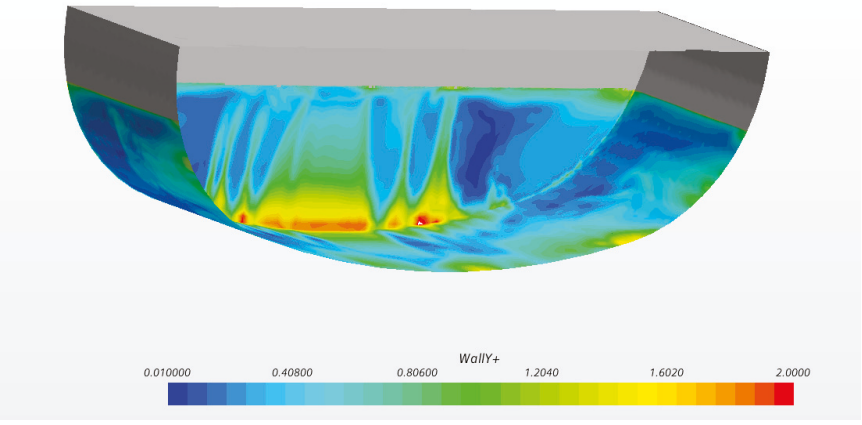

Figure 15. Wall Y+ on wet surface, grey color refers to the surface in air.

5.2. Post-Processing and Damping Coefficients Identification

The kinematics of pitch and roll motion versus physical time are presented in Figures 16 and 17, respectively. In order to graphically represent and evaluate the importance of non-linearities, each free decay time trace has been normalized with respect to the initial displacement, as reported in Figures 18 and 19, respectively for pitch and roll. While the pitch normalized responses significantly overlap, suggesting linearity, roll normalized responses are diverse, showing a clear nonlinear behaviour. In particular, the larger the initial displacement, the faster the decaying rate, suggesting a higher content of non-linearity. This is hereafter quantified through the identification of the nonlinear damping coefficient β, as discussed in Section 3.

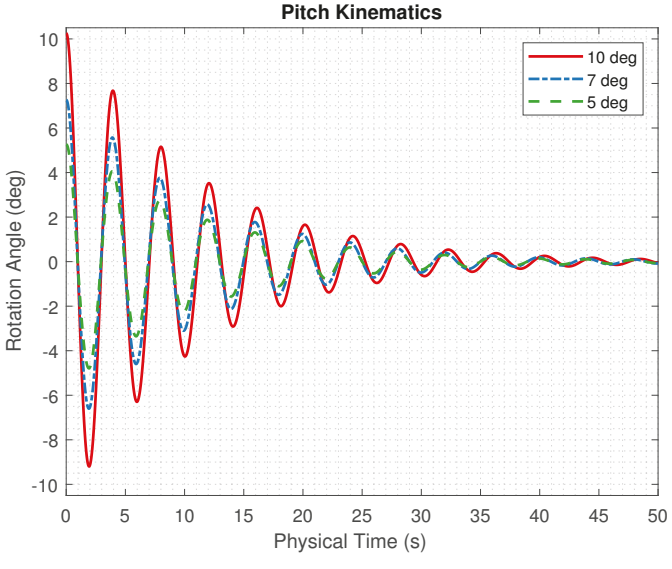

Figure 16. Pitch kinematic.

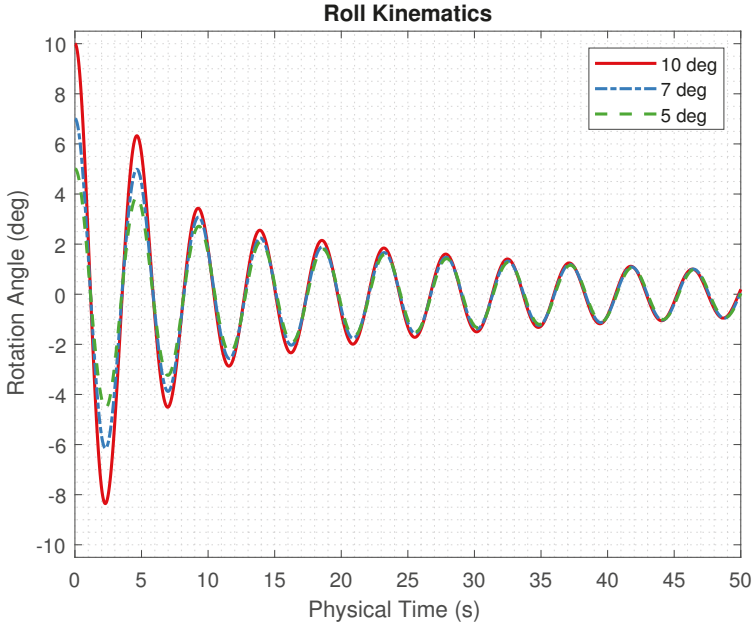

Figure 17. Roll kinematic.

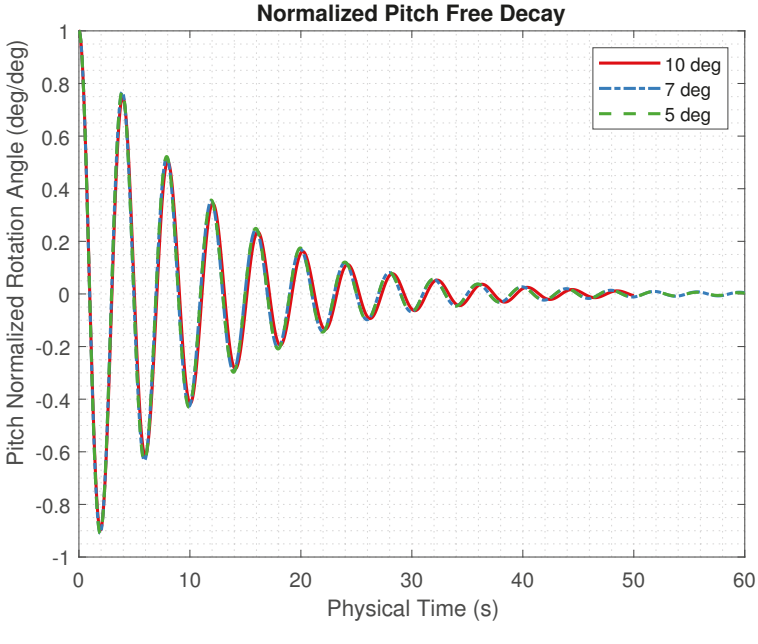

Figure 18. Normalized Pitch kinematic.

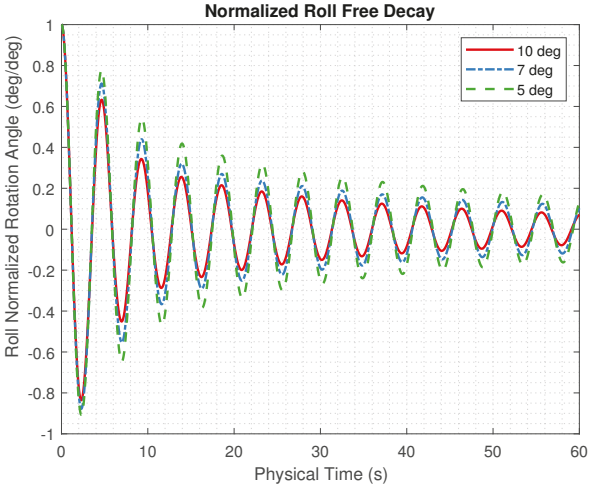

Figure 19. Normalized Roll kinematic.

The different behaviour of pitch and roll in terms of damping is clearly presented in kinematics figures, and the roll motion results less damped than pitch. This behaviour is justified considering the radiation curves related to the hull of this work, shown in Figure 20 where the pitch motion has a more significant value with respect to roll damping, on a point of detail greater than roll of about two orders of magnitude. When oscillations become small and non-linearities less important, roll needs more time to reduce the amplitude of motion. Anyway, roll is strongly damped at the beginning, when oscillations are big because the quadratic part, i.e., proportional to the square of velocity, is predominant in roll viscous damping while the linear part is almost negligible.

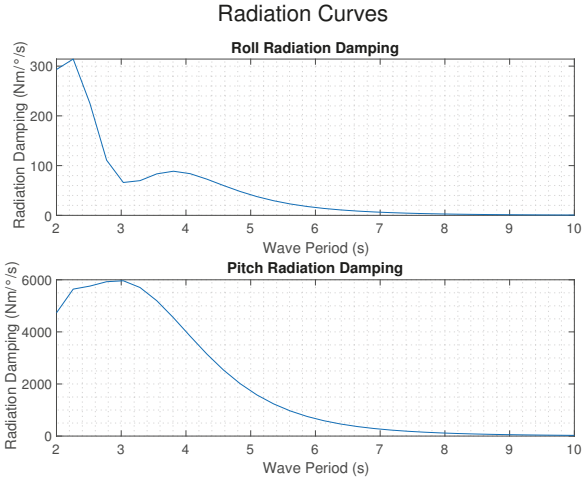

Figure 20. Radiation curves.

Each pair of consecutive peaks (considering both maxima and absolute values of minima) defines a α_{eq} and a $\delta_{mean,i}$, according to Equations (10) and (11), respectively. Such parameters are shown in Figures 21 and 22 for pitch and roll responses, respectively.

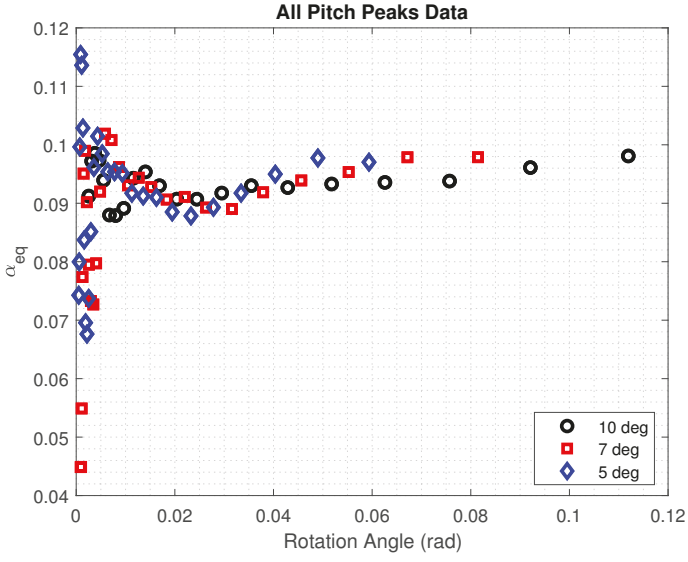

Figure 21. All pitch peaks data.

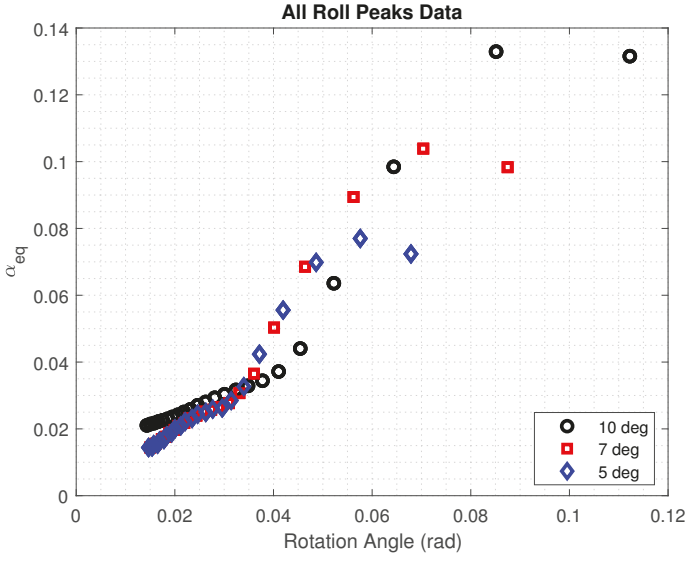

Figure 22. All roll peaks data.

As regards peaks data in Figures 21 and 22, the wide spread in pitch data at low angles is justified by oscillations around the equilibrium point. Such low angles measurements are negligible as far as the identification of viscous damping coefficient is concerned and thus will be neglected.

About the roll motion the previous spread is absent because it is overall less damped; In addition two trends are clear (Figure 22), one until about 2°, the other one afterwards. This behaviour is possibly related to the linearization assumptions done in order to define and obtaine α_{eq}.

Therefore, the identification regards only the left side of the plot, where points are well aligned and so the linearization appears to be more valid.

Taking into account the Equation (10) and also referring to the plots in Figures 23 and 24, the more non-linear behaviour of roll is confirmed. Indeed, considering Equation (10), if α represents the intercept and β the slope, it is clear the different pattern both in pitch and roll motion. Pitch kinematics are more damped than the roll one, but the first has a linear behaviour instead of the second one which results less damped, but mainly quadratic. With regards to roll data in Figure 24, points corresponding to $\delta_0 = 10°$ differ from the 5° and 7° because the first case involves much larger angles and consequently a more non-linear behaviour.

Numerical results are summarized in Table 1 in terms of coefficient of determination R^2 of the linear fit, the period of oscillations T and finally α and β respectively corresponding to intercept and slope of the linear regression, or in a more physical meaning, the linear and quadratic damping terms.

The computation of values of α and β throughout the logarithmic decrement here proposed can be considered as a starting step for solving Equation (6). Taking into account the previous outcomes, the equation is solved with a Runge-Kutte scheme (RK) of 4th-order accuracy with an adaptative time step [36].

Furthermore, this technique has been enriched considering a parametrization of 100 values α and β centred on the outcomes computed through the linear regression and shown in Table 1. For each value, the goodness of fit has been computed with the cost function Normalized Mean Square Error:

$$\text{fit} = 1 - \frac{||x_{ref} - x||^2}{||x_{ref} - \text{mean}(x_{ref})||^2} \tag{19}$$

where x_{ref} and x represents respectively the reference time history (i.e., the one obtained from CFD) and the one computed through RK-solver, the goodness of fit equals to 1 means a perfect match of results. By way of example and for sake of brevity, outcomes are presented in a visual way through plot in Figures 25 and 26, considering pitch and roll free decay with an initial condition of 10°, showing CFD results, Equation (6) solved with values in Table 1 and finally with α and β corresponding to the maximum of goodness of fit (GoF).

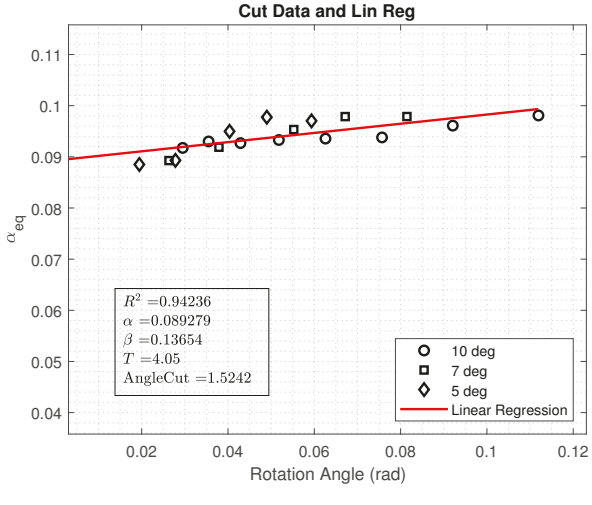

Figure 23. Cut pitch data and outcomes.

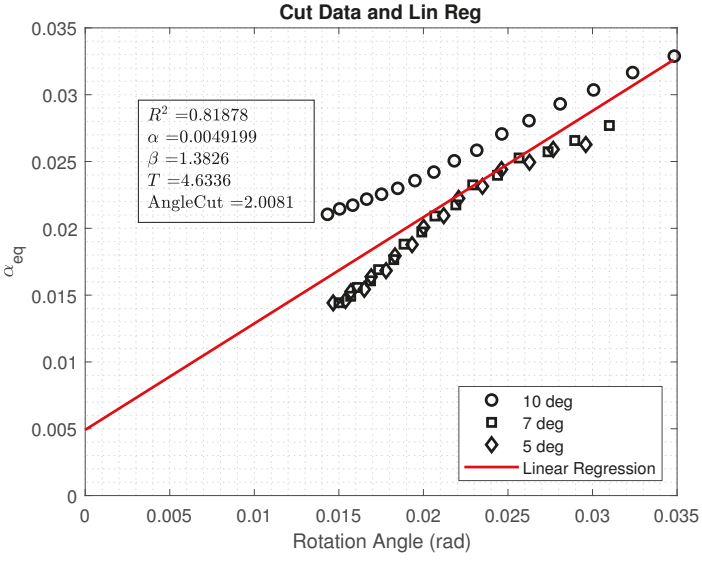

Figure 24. Cut roll data and outcomes.

Table 1. Numerical results for pitch and roll motion post-processing.

	R^2	T (s)	α	β
Pitch	0.92	4.05	0.089	0.136
Roll	0.82	4.63	0.005	1.38

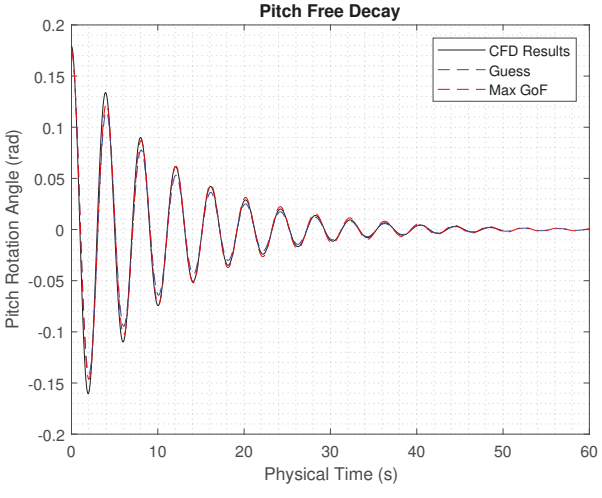

Figure 25. Pitch results.

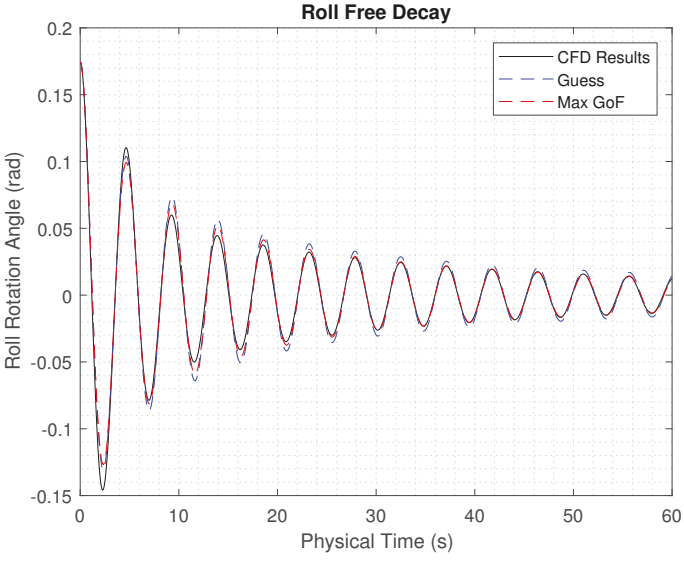

Figure 26. Roll results.

For clarity's sake, zoomed portions of plot are presented in Figures 27 and 28 as far as the first oscillations where large amplitude occur and Figures 29 and 30 as regards the final tail.

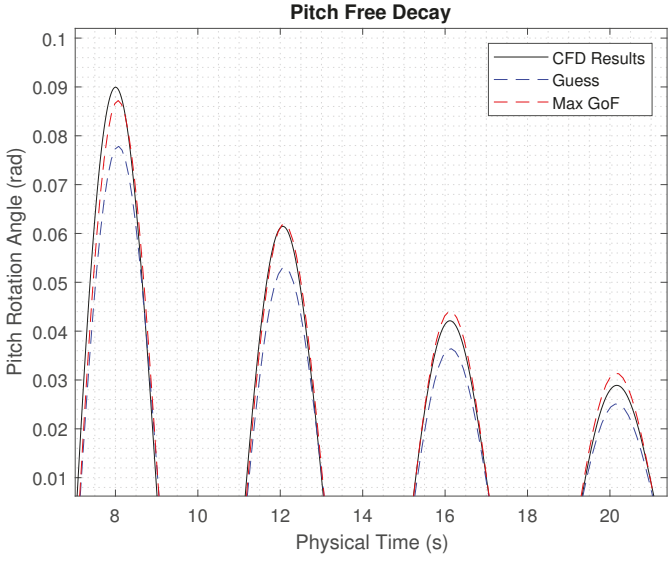

Figure 27. Large oscillations in pitch.

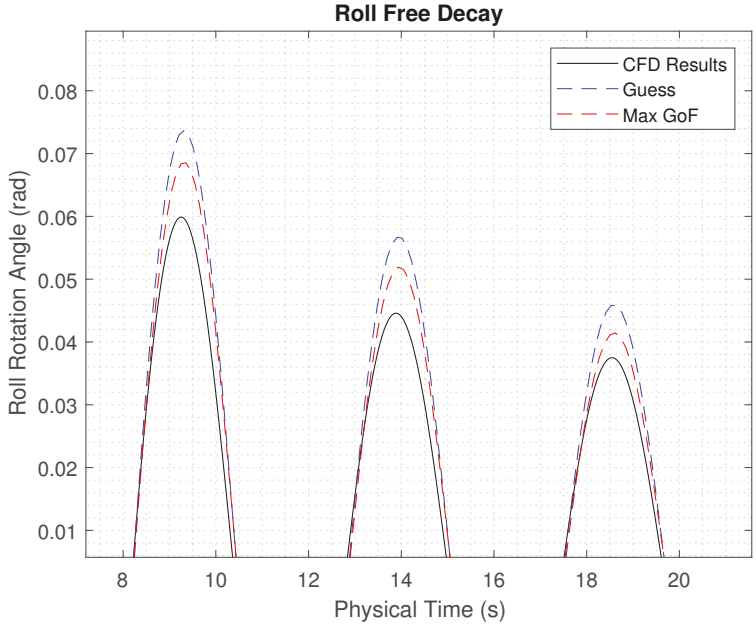

Figure 28. Large oscillations in roll.

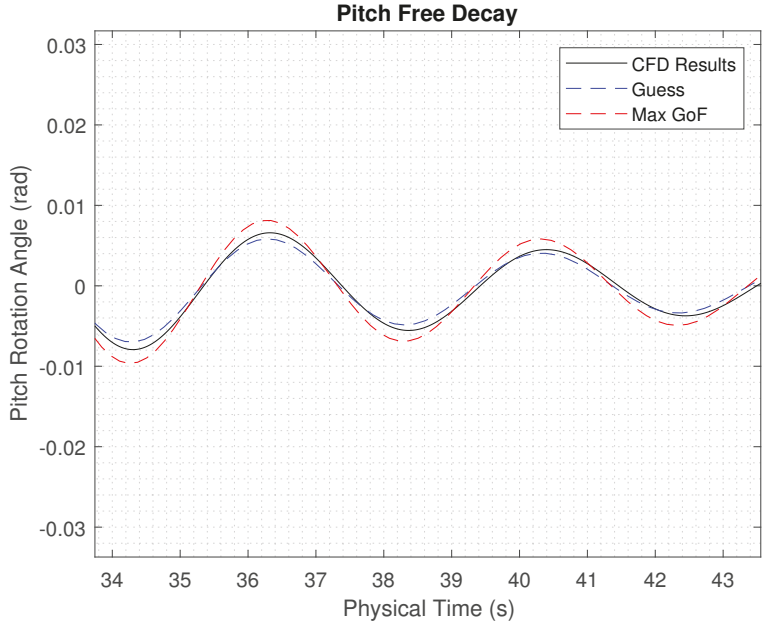

Figure 29. Tail pitch results.

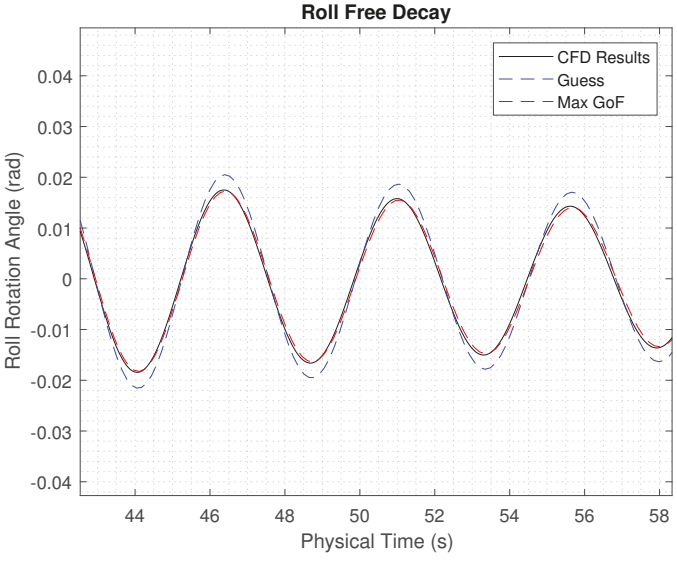

Figure 30. Tail roll results.

A different behaviour of the optimization of α and β is observed as regards pitch and roll. Concerning the first, the maximization of GoF tends to a best fit of larger oscillations as shown in Figure 27 and a poorest fit of the final tail of the decay (Figure 29); The opposite behaviour is evident concerning the roll motion, where the largest amplitudes are not perfectly fitted by the optimal values of α and β (Figure 28), even if the fit is nevertheless better than the guess value of Table 1. The explanation of such trend is analogous to the considerations about the cloud of data in Figures 21 and 22. Results are summarized in Tables 2 and 3, respectively for pitch and roll motion.

Table 2. Outcomes for pitch free decay motion.

	Runge-Kutta			Linear Regression		
δ_0 (deg)	α	β	GoF	α	β	R^2
10	0.0818	0.0341	0.9869	0.0897	0.1026	0.8877
7	0.0805	0.0387	0.9640	0.0898	0.1281	0.8652
5	0.0791	0.0384	0.9615	0.9153	0.1538	0.4568 *
All data	N.A. †	N.A. †	N.A. †	0.0894	0.1102	0.9436

* Low value due to the small amout of points after the angle cut. † The solution of differential equation can not be performed considering all the initial conditions.

Table 3. Outcomes for roll free decay motion.

	Runge-Kutta			Linear Regression		
δ_0 (deg)	α	β	GoF	α	β	R^2
10	0.0088	1.495	0.9873	0.0121	1.0356	0.9968
7	0.0087	1.5368	0.9919	0.0124	1.3962	0.9968
5	0.0051	1.5577	0.9961	0.0014	1.568	0.9810
All data	N.A.[2]	N.A.[2]	N.A.[2]	0.0049	1.3826	0.8188

where

- δ_0 is the initial condition for the decay in degrees
- α and β are the linear and quadratic terms of the equivalent extinction coefficient α_{eq} in Equation (10)
- GoF is the the goodness of fit defined in Equation (19)
- R^2 is the ordinary coefficient of determination of the linear fit model

6. Conclusions

In conclusion, in this work we propose an affordable methodology with the aim of the identification of non-linear viscous damping parameters. Results obtained are in line with the expectations and consistent with the physics and experience about the WEC device considered. The hi-fi CFD techniques could be performed one-time considering few cases (in this work three different initial conditions for the free decay). This first investment in terms of computational costs and effort can lead to the evaluation of those non-linear coefficients, related to significant physical phenomena. This identification provides an important enrichment of low-order models used for next design and analysis steps.

Author Contributions: Conceptualization, M.F. and P.C.; data curation, M.F., P.C., S.A.S. and G.G.; formal analysis, M.F. and P.C.; funding acquisition, G.B. and G.M.; investigation, M.F. and P.C.; methodology, M.F., P.C., S.A.S. and G.G.; project administration, S.A.S., G.G., G.B. and G.M.; resources, M.F., P.C., G.B. and G.M.; software, M.F. and P.C.; supervision, S.A.S., G.G., G.B. and G.M.; validation, M.F., P.C., S.A.S. and G.G.; visualization, M.F. and P.C.; writing—original draft, M.F. and P.C.; writing—review and editing, M.F., P.C., S.A.S. and G.G. All authors have read and agreed to the published version of the manuscript.

Funding: This research received no external funding.

Acknowledgments: Computational resources provided by hpc@polito (http://hpc.polito.it).

Conflicts of Interest: The authors declare no conflict of interest. The funders had no role in the design of the study; in the collection, analyses, or interpretation of data; in the writing of the manuscript, or in the decision to publish the results.

References

1. Mattiazzo, G. State of the Art and Perspectives of Wave Energy in the Mediterranean Sea: Backstage of ISWEC. *Front. Energy Res.* **2019**, *7*, 114. [CrossRef]
2. Pozzi, N.; Bonetto, A.; Bonfanti, M.; Bracco, G.; Dafnakis, P.; Giorcelli, E.; Passione, B.; Sirigu, S.; Mattiazzo, G. PeWEC: Preliminary design of a full-scale plant for the mediterranean sea. In Proceedings of the NAV International Conference on Ship and Shipping Research, Trieste, Italy, 20–22 June 2018; pp. 504–514. [CrossRef]
3. van Rij, J.; Yu, Y.H.; Edwards, K.; Mekhiche, M. Ocean power technology design optimization. *Int. J. Mar. Energy* **2017**, *20*. [CrossRef]
4. Sirigu, A.S.; Gallizio, F.; Giorgi, G.; Bonfanti, M.; Bracco, G.; Mattiazzo, G. Numerical and Experimental Identification of the Aerodynamic Power Losses of the ISWEC. *J. Mar. Sci. Eng.* **2020**, *8*, 1–25. [CrossRef]
5. Windt, C.; Davidson, J.; Ringwood, J.V. High-fidelity numerical modelling of ocean wave energy systems: A review of computational fluid dynamics-based numerical wave tanks. *Renew. Sustain. Energy Rev.* **2018**, *93*, 610–630. [CrossRef]
6. Giorgi, G.; Ringwood, J.V. Analytical Formulation of Nonlinear Froude-Krylov Forces for Surging-Heaving-Pitching Point Absorbers. In Proceedings of the ASME 37th International Conference on Ocean, Offshore and Arctic Engineering, Madrid, Spain, 17–22 June 2018.
7. Davidson, J.; Giorgi, S.; Ringwood, J.V. Linear parametric hydrodynamic models for ocean wave energy converters identified from numerical wave tank experiments. *Ocean. Eng.* **2015**, *103*, 31–39. [CrossRef]
8. Penalba, M.; Giorgi, G.; Ringwood, J.V. Mathematical modelling of wave energy converters: A review of nonlinear approaches. *Renew. Sustain. Energy Rev.* **2017**, *78*, 1188–1207. [CrossRef]
9. Cummins, W. *The Impulse Response Function and Ship Motions*; Technical Report; David Taylor Model Basin: Washington, DC, USA, 1962.
10. Passione, B. Hydrodynamic Analysis and Mooring Design of a Floating Pitching Wave Energy Converter. Ph.D. Thesis, Politecnico di Torino, Torino, Italy, 2018.

11. Begovic, E.; Bertorello, C.; Prpic Orsic, J. Roll damping coefficients assessment and comparison for round bilge and hard chine hullforms. In Proceedings of the ASME 32nd International Conference on Ocean, Offshore and Arctic Engineering, Nantes, France, 9–14 June 2013.
12. Begovic, E.; Mancini, S.; Day, A.; Incecik, A. Applicability of CFD methods for roll damping determination of intact and damaged ship. In *High Performance Scientific Computing Using Distributed Infrastructures: Results and Scientific Applications Derived from the Italian PON ReCaS Project*; World Scientific: Singapore, 2017; pp. 343–359.
13. Begovic, E.; Day, A.H.; Incecik, A.; Mancini, S.; Pizzirusso, D. Roll damping assessment of intact and damaged ship by CFD and EFD methods. In Proceedings of the 12th International Conference on the Stability of Ships and Ocean Vehicles, Glasgow, UK, 14–19 June 2015; pp. 13–19.
14. Sirigu, S.A.; Bonfanti, M.; Begovic, E.; Bertorello, C.; Dafnakis, P.; Bracco, G.; Mattiazzo, G. Experimental Investigation of Mooring System on a Wave Energy Converter in Operating and Extreme Wave Conditions. *J. Mar. Sci. Eng.* **2020**, *8*, 1–31. [CrossRef]
15. Sirigu, S.; Bonfanti, M.; Dafnakis, P.; Bracco, G.; Mattiazzo, G.; Brizzolara, S. Pitch Resonance Tuning Tanks: A novel technology for more efficient wave energy harvesting. In Proceedings of the OCEANS 2018 MTS/IEEE Charleston, Charleston, SC, USA, 22–25 October 2018. [CrossRef]
16. Ferziger, J.H.; Perić, M. *Computational Methods for Fluid Dynamics*; Springer: Berlin/Heidelberg, Germany, 2002. [CrossRef]
17. Penalba, M.; Kelly, T.; Ringwood, J. Using NEMOH for modelling wave energy converters: A comparative study with WAMIT. In Proceedings of the 12th European Wave and Tidal Energy Conference, Cork, Ireland, 27 August–2 September 2017.
18. Ansys, A. *Theory Manual*; ANSYS® Academic Research; ANSYS: Canonsburg, PA, USA, 2014.
19. Zhao, W.; Efthymiou, M.; McPhail, F.; Wille, S. Nonlinear roll damping of a barge with and without liquid cargo in spherical tanks. *J. Ocean. Eng. Sci.* **2016**, *1*, 84–91. [CrossRef]
20. Chakrabarti, S.K. *Offshore Structure Modeling*; World Scientific: Singapore, 1994; Volume 91994.
21. CD-adapco, S. *STAR CCM+ User Guide Version 12.04*; CD-Adapco: New York, NY, USA, 2017.
22. Choi, J.; Yoon, S.B. Numerical simulations using momentum source wave-maker applied to RANS equation model. *Coast. Eng.* **2009**, *56*, 1043–1060. [CrossRef]
23. Perić, R.; Abdel-Maksoud, M. Reliable damping of free-surface waves in numerical simulations. *Ship Technol. Res.* **2016**, *63*, 1–13. [CrossRef]
24. Windt, C.; Davidson, J.; Chandar, D.; Ringwood, J. On the importance of advanced mesh motion methods for WEC experiments in CFD-based numerical wave tanks. In Proceedings of the VIII International Conference on Computational Methods in Marine Engineering, Gothenburg, Sweden, 13–15 May 2019.
25. Davidson, J.; Karimov, M.; Szelechman, A.; Windt, C.; Ringwood, J. Dynamic mesh motion in openfoam for wave energy converter simulation. In Proceedings of the 14th OpenFOAM Workshop, Duisburg, Germany, 23–26 July 2019.
26. Meakin, R.L. Composite overset structured grids. In *Handbook of Grid Generation*; CRC Press: Boca Raton, FL, USA, 1999; pp. 1–20.
27. Petersson, N.A. Hole-cutting for three-dimensional overlapping grids. *SIAM J. Sci. Comput.* **1999**, *21*, 646–665. [CrossRef]
28. Field, A. How the Wave Damping Length Influences the Domain and Wake Refinements in a Hull Performance Analysis. 2017. Available online: https://thesteveportal.plm.automation.siemens.com/articles/en_US/FAQ/How-the-Wave-Damping-Length-can-influence-the-mesh-domain-and-the-wake-refinement-sizes-in-a-Hull-performances-analysis (accessed on 14 May 2020).
29. Hirt, C.W.; Nichols, B.D. Volume of fluid (VOF) method for the dynamics of free boundaries. *J. Comput. Phys.* **1981**, *39*, 201–225. [CrossRef]
30. Menter, F. Zonal two equation kw turbulence models for aerodynamic flows. In Proceedings of the 23rd Fluid Dynamics, Plasmadynamics, and Lasers Conference, Orlando, FL, USA, 6–9 July 1993; p. 2906.
31. Menter, F.R. Two-equation eddy-viscosity turbulence models for engineering applications. *AIAA J.* **1994**, *32*, 1598–1605. [CrossRef]
32. Shih, T.H.; Liou, W.W.; Shabbir, A.; Yang, Z.; Zhu, J. A new k-epsilon eddy viscosity model for high Reynolds number turbulent flows: Model development and validation. In *NASA Technical Reports Server*; Document ID: 19950005029; NASA: Washington, DC, USA, 1994.

33. Reichardt, H. Vollständige Darstellung der turbulenten Geschwindigkeitsverteilung in glatten Leitungen. *ZAMM J. Appl. Math. Mech* **1951**, 31, *208–219*. [CrossRef]
34. White, F. *Fluid Mechanics*; McGraw-Hill International Editions; McGraw-Hill: New York, NY, USA, 2003.
35. Cabral, B.; Leedom, L.C. Imaging vector fields using line integral convolution. In Proceedings of the 20th Annual Conference on Computer Graphics and Interactive Techniques, Anaheim, CA, USA, 2–6 August 1993; pp. 263–270.
36. Dormand, J.R.; Prince, P.J. A family of embedded Runge-Kutta formulae. *J. Comput. Appl. Math.* **1980**, *6*, 19–26. [CrossRef]

Journal of
Marine Science and Engineering

MDPI

Article

Unsteady RANS CFD Simulations of Sailboat's Hull and Comparison with Full-Scale Test

Pietro Casalone *,†, Oronzo Dell'Edera *,†, Beatrice Fenu, Giuseppe Giorgi, Sergej Antonello Sirigu and Giuliana Mattiazzo

Polytechnic of Turin, Department of Mechanical and Aerospace Engineering, C.so Duca degli Abruzzi, 24, 10129 Turin, Italy; Beatrice.fenu.pst@gmail.com (B.F.); Giuseppe.giorgi@polito.it (G.G.); Sergej.sirigu@polito.it (S.A.S.); Giuliana.mattiazzo@polito.it (G.M.)

* Correspondence: Pietro.casalone@polito.it (P.C.); Oronzo.delledera.pst@gmail.com (O.D.)

† These two authors contributed equally to the work described.

Received: 15 April 2020; Accepted: 27 May 2020; Published: 29 May 2020

Abstract: The hydrodynamic investigation of a hull's performance is a key aspect when designing a new prototype, especially when it comes to a competitive/racing environment. This paper purports to perform a fully nonlinear unsteady Reynolds Averaged Navier-Stokes (RANS) simulation to predict the motion and hydrodynamic resistance of a sailboat, thus creating a reliable tool for designing a new hull or refining the design of an existing one. A comprehensive range of speeds is explored, and results are validated with hydrodynamic full-scale tests, conducted in the towing tank facility at University of Naples Federico II, Italy. In particular, this work deals with numerical ventilation, which is a typical issue occurring when modeling a hull; a simple and effective solution is here proposed and investigated, based on the phase-interaction substitution procedure. Results of the computational fluid dynamic (CFD) campaign agree with the experimental fluid dynamic (EFD) within a 2% margin.

Keywords: computational fluid dynamic; experimental fluid dynamic; sailboat; hull; towing tank test; numerical ventilation; overset; volume of fluid (VOF), hydrodynamic; Polito Sailing Team (PST)

1. Introduction

The design of a new sailboat prototype is complex and requires time, experience, and resources. It is important to draw several hull shapes and understand which behaves better at sea, as well as to consider the complexity of the boat system and meteorological conditions.

Experience and computer-aided design (CAD) software help the engineer to explore several promising concepts and forms; however, quantitative evaluation of the performance requires tests, either numerical or physical, by means of towing tank tests (TTTs) [1].

The hydrodynamic testing of a new hull is a mandatory step, requiring considerable resources, in terms of time and economic capital, since different prototype models must be built and tested in the tank [2]. Tests can take up to weeks or even months considering all phases involved, from transportation, setup, and calibration, to the actual test and post-processing.

Moreover, most of the time, it is not possible to simulate the real-scale experiment because the cost of realizing a full-scale model is usually prohibitive and, most importantly, towing tanks have limitations for the maximum beam, length, and velocity that can be tested in order to avoid blockage effects and wave reflection [3]. This means that once the analysis is completed, results must be scaled, potentially introducing errors [4].

On the other hand, in the last decades, numerical tanks have become quite popular: The main reason is the cheap availability of computational power, which is now accessible to many designers, researchers, and even students. The widespread use of computational fluid dynamics (CFD) for naval

and marine application [5] has also provided the community of users with a set of best practices and state-of-the-art modeling techniques [6,7], which allow the engineers to obtain better results from their CFD towing tank (CTT) and reduce the need for real test validation [8].

At the current stage of development, CFD cannot entirely replace real tests, which are still necessary when realizing a new boat; however, based on the several advantages of CFD over physical experiments and an increasing confidence in CFD setup and results [9,10], numerical simulation will tend to supplant real tests. A fast, cheap, and high-fidelity method, CFD is now used in almost every study of the hydrodynamics of sailboats, or ships in general [11].

An important advantage of numerical tests is flexibility, which makes it possible to easily change the model characteristics (e.g., shape, wetted surface, trim angle, fixed and moving mass distribution), which is crucial at the design stage.

This paper deals with the definition of a CFD setup for a numerical towing tank test and the comparison of the model with a full-scale experimental test. Moreover, a case with numerical ventilation, which is likely to occur when simulating a hull [7,12,13], even for low speeds, is analyzed and two different techniques to solve the problem are presented.

The scope of this numerical and experimental campaign is to mimic real tank tests and to evaluate the drag and the best trim angle for the hull in order to optimize the distribution of the moving weight on board. To gain a greater insight into the non-linear behavior of the hull, three different speeds were tested: 1, 2, and 3 m/s, which correspond respectively to a Froude number of 0.1488, 0.2977, and 0.4465, since the length of water line (LWL) does not change over the three speeds tested and is equal to 4.60 m.

The first two velocities correspond to a displacing mode, the latter to a semi-planing asset.

The towing tank test was carried out at University of Naples Federico II during the Midwinter Indoor Race, a spin-off from the 1001Vela Cup competition.

The 1001Vela Cup is an international competition where students from different universities design, build, and race their own skiff (a kind of sailboat, "sail, keep it fast and flat") prototype. The class rules of this regatta are wide open and allow the designer to explore a huge selection of boat concepts with different hulls, sail plans, or even foil. These rules are defined by R3 class regulation and allow a maximum hull length of 4.60 m and a maximum beam of 2.1 m.

Thus, it is fundamental to model the hull, appendix, and sail geometry in accordance with marine conditions expected during the regatta, which every year is held in a different place; in this regard, CFD represents a useful tool to test with accuracy all the design options [14].

During the Midwinter Indoor Race, the hulls of the competitors is tested to evaluate which hull produces less drag for the whole set of speeds; during this race, designers can evaluate and compare the behavior and performance of different hulls and, most importantly, can validate the results of the hydrodynamic models they developed.

A special thanks goes to University of Napoli for providing free towing tank tests for all participants in the competition, thus providing the students with the opportunity to validate their work.

This paper is organized as follows. Section 2 gives a brief review of the skiff and its properties, as well as describing the Federico II towing tank facility. In Section 3, the numerical setup of the CFD model is explained, with details provided in the subsections. Section 4 concerns the presentation of the results and the comparison with the experimental fluid dynamics (EFD). Finally, in Section 5, conclusions are shown.

2. Materials and Model

2.1. Properties of Atka during the Midwinter Race

In this section, the characteristics of the hull of Atka (name of the boat) as it was tested are reported (see Figure 1).

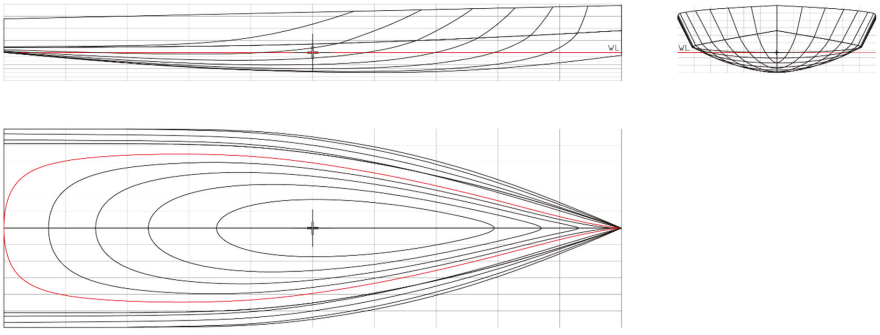

Figure 1. Atka's hull profile.

Mass and inertia values are accounting for the two sailors that were on board during the regatta and for the full rig of the boat. In order to reproduce the real mass distribution during the experiment, the rig and the sailors were replaced with 18 small blocks of 9.722 kg. A schematic representation of the hull and its mass distribution is shown in Figure 2.

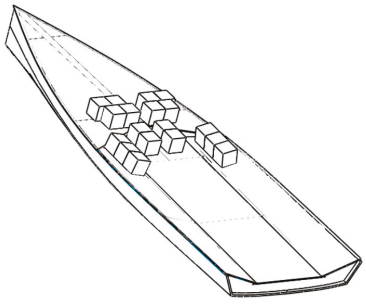

Figure 2. Distribution of moving mass simulating the weight and position of the sailors and the rig.

It is a good and widespread practice to place the reference system in the bottom part of the stern, with the x axis pointing to the bow, the y axis pointing inside the domain, and the z axis pointing to the top [1].

Atka's hull properties are shown in Table 1, and all the measurements are in accordance with the laboratory coordinate system just defined:

Table 1. Properties of Atka's hull.

Displacement with Rig and Two Sailors (kg)	**265**
Center of Gravity (m)	(2.21259, 0.0, 0.28274)
Inertia Moments (kg × m^2)	(38.464, 158.549, 183.495)
Water Line Height (m)	0.0442
Length Water Line (m)	4.60
Max Beam (m)	1.480

2.2. *The Towing Tank of Naples University*

The tank of Federico II is the largest in Europe supplied to a university and has the following dimensions: 136.74 × 9.00 × 4.25 m (length, width, depth), and on its sides, it has the sliding rails of a dynamometric carriage. At the end, an absorbing "beach" is present, which can reduce the amplitude

of the incident waves by up to 95% for wavelengths between 5 and 7 m. The beach consists of a steel structure of appropriate curvature, 6 m long in the longitudinal direction, covered with PVC.

During the test, the boat is hooked up to the dynamometric carriage through two guides on the axis of the boat, one at the bow and the other at the stern, which restrict the boat in the y-direction and make it move forward in the x-direction, at the speed of test. These guides guarantee free motion along the two degrees of freedom of heave and pitch as shown in Figure 3.

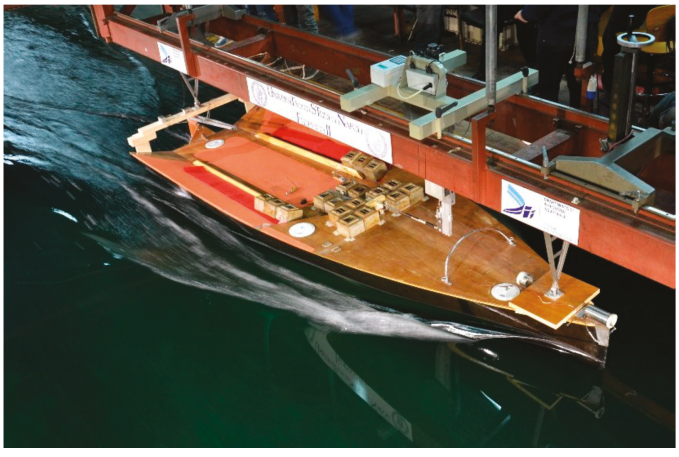

Figure 3. Atka during the 3 m/s test.

Before each test starts, the acquisition system measures the hydrostatic conditions which will be used as a reference offset for the measurement of pitch and heave values. Then, the carriage is launched, and only after the transient acceleration phase, when the condition of uniform motion is reached, does the acquisition of running data begin.

In data acquisition, all measurements are temporal variables and therefore the basics of statistics are applied to obtain a summary of the data.

The dynamometric carriage is equipped with all the instruments necessary to measure dimensional quantities such as drag forces, motions, accelerations, speeds, inclinations, and temperatures. All these quantities are evaluated through the use of sensors which are in direct interaction with the measured system and transform the input signal into an electrical signal.

3. CFD Model

The analysis was carried out on the commercial software Star-CCM+ 2019.1 from Siemens [15]. The simulation setup was quite complex since the problem involved multiphysics and dealt with dynamic body motion. We used an Unsteady Reynolds Averaged Navier Stokes (URANS) CFD approach, which is considered to be an appropriate compromise between accuracy and computational cost for naval applications, according to consultancy companies and relevant bibliographies [16–18]. A time advancing approach was used in this work, even though the final solution was stationary, because the dynamic equilibrium position that the hull reached under different speeds was not known a priori, and the trim angle changed for the three different tests [19].

3.1. Domain, Boundary Condition, and Damping Factor

In fluid dynamic simulations of a towing tank test, it is not advised to use the real dimensions of the towing tank for the computational domain. In fact, it is only required that the boundary conditions do not influence the physics within the domain; thus, using the real tank for sizing the domain would be a waste of resources that would bring no benefit on accuracy [20].

However, the domain's dimensions do have an important impact on the fluid dynamics and are linked to the speed of the test. It is fundamental to capture the wave pattern reasonably well, in order to evaluate the amount of energy that is subtracted from the boat. In this regard, the domain needs to be large enough to contain about 6 wavelengths behind the hull; in this way, it is possible to accurately compute the contribution to the total drag due to the perturbation of the wave field after the transition of the hull, usually referred to as wave-making resistance [13,14].

Another important aspect that influences the domain's dimensions is wave reflection, which is undesirable and should be avoided.

The reflection problem is of crucial importance in both real towing tanks and numerical tanks. It is not possible to produce accurate and meaningful measurements when the tank or the computational domain is perturbed with reflected waves coming from all directions. This leads to bad measuring in real cases and/or simulation crash in the case of numerical tanks.

A simple approach is used to solve this issue in real and in CFD tanks: A large damping zone is introduced at the boundaries of the tank in order to absorb most of the energy of the incoming waves before they are reflected, hence leaving the domain undisturbed from reflection. In numerical simulations, the length and the intensity of this damping zone must be related with the domain dimensions, wavelength, and wave height. For our case, a damping zone of two times wavelength is enough to prevent wave reflection at boundaries [21–23].

At this point, it is clear that a parametric approach represents the best choice in order to save computational time, where domain length, mesh refinement, damping zone, and other important parameters are functions of the wavelength and thus of the speed of test. In this regard, a reference length (RL), which is the longer length between hull-length and wavelength, was chosen, and the domain's dimensions are a function of the reference length, as shown hereafter and in Figures 5 and 6:

(1) Two hull-lengths (HL) in front of the boat;
(2) Two reference lengths (RF) for the side;
(3) Four reference lengths behind;

It is worth noting that the dimension in front of the boat is not parametric but fixed because waves do not propagate in that direction.

A damping zone of two wavelengths acting on outlet and side boundaries was added to these dimensions; intensity and length of damping was evaluated in accordance with [24].

Following bibliography and the Star-CCM+ guidelines, boundary conditions were set as follows [20,25], and are shown in Figure 4:

(1) Top and front are velocity inlets;
(2) bottom and back are pressure outlets;
(3) both sides are symmetry planes.

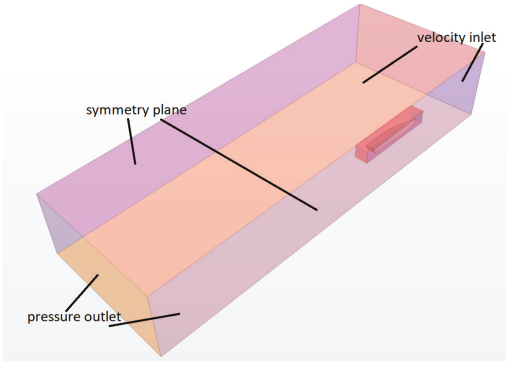

Figure 4. Boundary conditions.

Figures 5 and 6 show the dimensions of the overset and background regions:

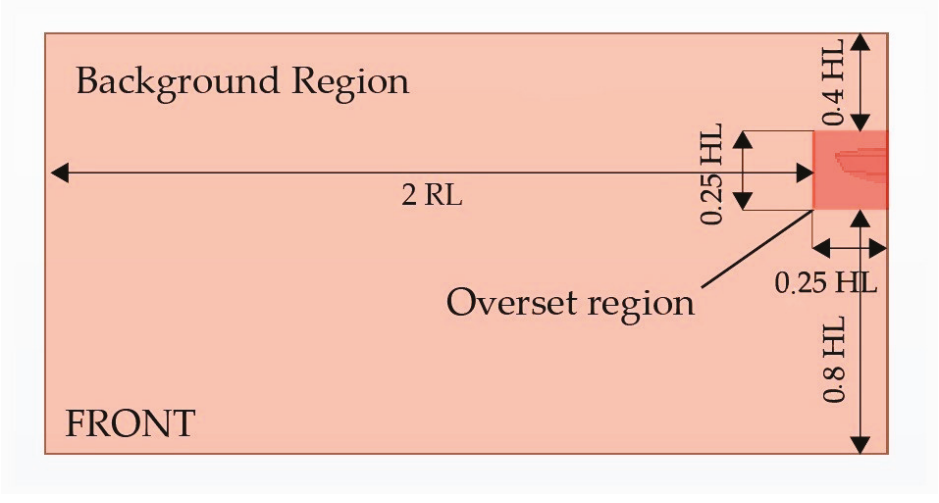

Figure 5. Front view of the domain.

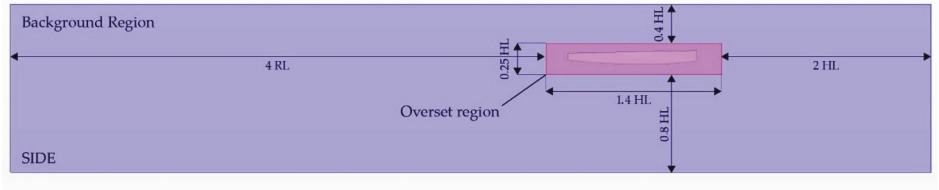

Figure 6. Side view of the domain.

3.2. Mesh Generation

The model deals with a moving body, because the final dynamic equilibrium position the hull reached under different velocities was not known a priori. In CFD, there are two ways to deal with a moving body: Mesh morphing/remeshing and overset mesh. Mesh morphing is better when the movements of the body are very small, so the cell quality does not decrease and few remeshing operations are needed. Overset mesh is used if, when dealing with large motion, a mesh morphing approach becomes unstable and too time-consuming due to several remeshing operations required. Using the overset approach, no re-mesh operation is needed because the mesh never deforms, nor does its quality decrease, since it moves with the body and remains unaltered [24,25].

A mesh morphing approach suited the application under consideration well, since the dynamic equilibrium was not far from the static one and there were incoming no waves that would induce large movements of the hull.

On the other hand, in order to deal with a head sea, the overset approach became necessary due to the large expected motion of the hull. Therefore, although there was no incoming wave in this study, an overset motion was implemented since the same CFD model can be used for further analysis to also comprise incoming waves [26].

The domain was thus divided into two separate regions: Background tank and overset.

The overset contained the moving part of the problem and allowed the boat to translate and rotate while the background remained fixed and unaltered. Equations were solved separately in the two regions and the solution was interpolated in an overlapping area consisting of cells called donors and

acceptors, where information is exchanged. A linear interpolation scheme was used, even though it required a higher computational effort in respect to the other methods available, because it minimized interpolation errors and guaranteed better convergence and a more accurate solution.

While the dimension of the tank changed as a function of the test speed, the dimension of the overset was constant in all the simulations, because it referred to the moving body.

The meshing algorithm used in the two regions was different, as discussed in Sections 3.2.1 and 3.2.2 for the tank and overset regions, respectively.

3.2.1. Tank

A trimmed block mesh was chosen due to the possibility to create anisotropic cells which best discretize the interface between the two fluids.

It is worthwhile to remark that wave reflection can occur, not only at boundaries, but also when the mesh size changes too abruptly [23,27]. To solve this problem, usually 2 or 3 different volumetric refinements are used to gradually coarsen the mesh at sea surface, from the near wall zone to the far field. The artificial damping of waves should start before the coarsest grid starts, since such a change in cell size is a potential source of reflection that has to be included in the damping zone. Therefore, wave damping should start where the mesh is still fine, but not too close to the hull, in order to avoid any influence on the wave pattern [23]. The mesh refinement regions, as well as the damping zone, are shown in Figure 7.

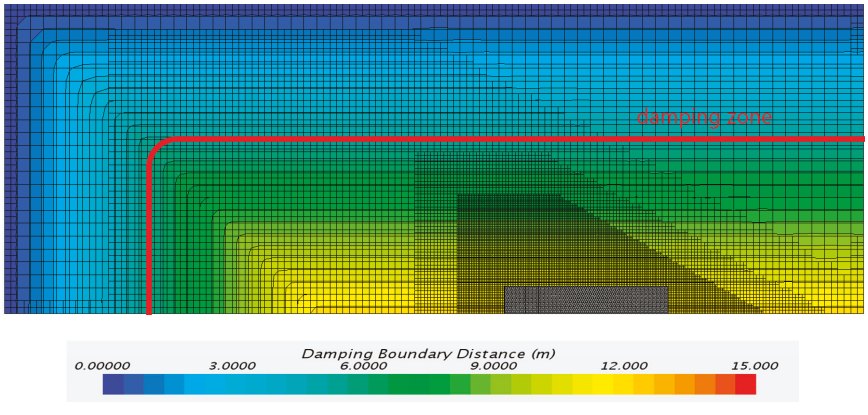

Figure 7. Damping zone and mesh refinements.

When dealing with trimmed mesh in Star-CCM+, it is important to bear in mind that cells can only double or half their size; so, starting from the inner and finer volumetric control for the sea surface and doubling up dimensions, we used this distribution of cells: 20 cells to discretize the wave produced by the hull, with an aspect ratio between x/y and z dimensions of 4:1 (because the waves were not too steep) [28,29].

Moreover, to prevent wave reflection at the interface between the overset and background mesh, cells at the interface had an aspect ratio of 2 in order to facilitate communication between the two regions. The volume of the cells at the interface had to be comparable to obtain good results and prevent a simulation crash.

3.2.2. Overset

A polyhedral mesh was chosen for the overset region, as shown in Figure 8, due to the possibility to change the volume of cells gradually and prevent wave reflection near the boat where the strongest gradients are solved.

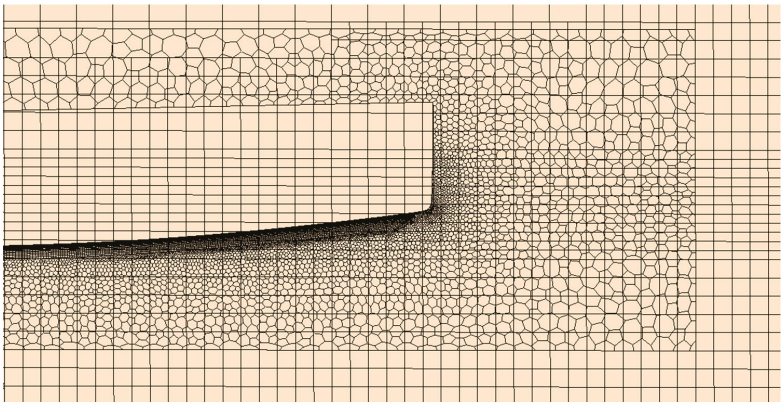

Figure 8. Overset polyhedral mesh.

To better capture the pressure gradients and wave generation at the bow and stern, volumetric refinement controls were applied in order to reduce mesh size in these areas: A control at the bow with very fine cells was used to avoid numerical ventilation [30], and a control for the stern guaranteed the correct flux under the hull.

When deciding for the overset dimensions, two main aspects should be considered:

(1) Overset does not have to be excessively large, otherwise even small rotations may induce large movements and increase the probability of interpolation errors;
(2) neither should it be too small, because cells need some space to grow from the wall to a decent size in order to maintain a low element count.

3.3. Volume of Fluid

The volume of fluid (VOF) multiphase model is a simple multiphase model. It is used to solve problems involving immiscible fluid mixtures, free surfaces, and phase contact. Figure 9 represents the elevation of the free surface in respect to the laboratory reference system, and shows how the VOF model is able to track difference phases and thus define the wave pattern behind the hull.

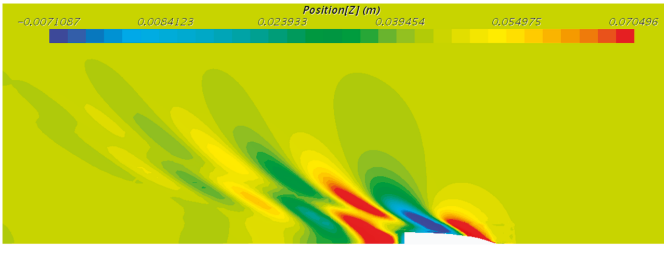

Figure 9. Wave pattern behind the hull for 3 m/s.

Due to its numerical efficiency, the model is suited for simulations of flows wherein each phase constitutes a large structure, with a relatively small total contact area between phases [31].

The spatial distribution of each phase at a given time is defined in terms of a variable that is called the volume fraction. A method of calculating such distributions is to solve a transport equation for the phase volume fraction. The method uses the STAR-CCM+ segregated flow model [32].

By default, the VOF free surface calculation is performed during the same time step as the other calculations. To ensure simulation stability, at free surface the value of CFL (Courant–Friedrichs–Lewy

number) must be limited to 1, and better results with a sharp resolution of the two phases are obtained with a CFL around 0.5 [28,29]. However, such a limitation is overly restrictive, as other physics calculations with implicit solvers can run at a much larger CFL number. This reduces the computational efficiency of VOF free surface simulations.

The multi-stepping feature removes this limitation on the CFL number; this option applies temporal sub-cycling to the transport of volume fraction and can improve the resolution of the interface between two phases; however, multi-stepping cannot be used with second order time discretization in Star-CCM+.

To maintain the accuracy that only a second order time scheme can guarantee, the multi-stepping feature has been disabled; thus, the value of CFL at the interface between phases represents a real and strong limitation for the time step of the model.

3.4. Dynamic Fluid Body Interaction (DFBI)-6DoF Solver

The dynamic fluid body interaction (DFBI) module simulates the motion of a rigid body in response to forces exerted by the physic continuum.

The 6-DoF (degree of freedom) solver computes fluid forces, moments, and gravitational forces on a 6-DoF body; pressure and shear forces are integrated over the surfaces.

For time integration, the 6-DoF solver employs a trapezoidal scheme of second order accuracy. This is independent of the order of accuracy of the implicit unsteady solver for the momentum and continuity equations.

When working with body motion, it is convenient to provide a smoothing ramp, so that forces on the hull are released meekly and not impulsively.

If no ramp is set up, abrupt impulses generate both physical and numerical transients and oscillations that affect the kinematics of the floater, which damp out several seconds after the beginning of the simulation [30,31,33].

Therefore, although the additional ramp time must be added to the simulation, the computational time is shorter due to a faster and cleaner convergence.

We decided on a release time of one second and a ramp time of two seconds: The moving body remained fixed in all DoFs for the first second of the simulation, in order to allow the fluid field around the floater to assume more realistic values in respect to initialization with a constant speed all over the domain; then from seconds 1 to 3, all the forces were smoothly applied to the body until the full value was used when ramp time ended at 3 s. The simulation results converged 6 seconds after the end of the ramp time; thus, the total time simulated was 9 s, which was enough to fully develop the wave pattern behind the boat and to stabilize drag and trim reports to constant values.

3.5. Turbulence and Law of the Wall

The flux around the hull was fully turbulent since the Reynolds number was in the order of millions; thus, turbulence had to be modeled to accurately compute forces acting on the boat.

The K-epsilon model is recommended in VOF simulations as the computational cost is low and the accuracy in the discretization of the interface between the two phases is good enough [31,34].

In the present case, a realizable K-Epsilon model was used, which represented an upgrade of the standard model: A new transport equation was used for the turbulent dissipation rate; moreover, the turbulence viscosity was expressed as a function of mean flow and turbulence properties instead of being constant.

A two-layer wall treatment was used in combination with the realizable K-Epsilon model.

In this approach, the turbulence quantities were computed as a function of the wall distance in the near wall region, and evaluated solving the transport equation in the far field; values were smoothly blended between these two zones.

The two-layer approach allowed the use of different values for $Y+$ because it applied wall treatment when the mesh could not accurately solve the boundary layer, and solved without wall functions when the mesh was fine enough to discretize the sub-viscous layer near the wall.

The hull is designed with a hydrodynamic shape in order to disturb the flow around it as little as possible; thus, phenomena like vortex shedding and fluid vein detachment do not occur, at least not for the range of speeds tested. This made it possible to discretize the region near the hull with a coarse mesh. In fact, if the fluid remained attached to the wall, there was no need to finely mesh the sub-viscous layer; however, values of $Y+$ around 50 (first cell in the logarithm layer zone) or more could be used (Figure 10) [35].

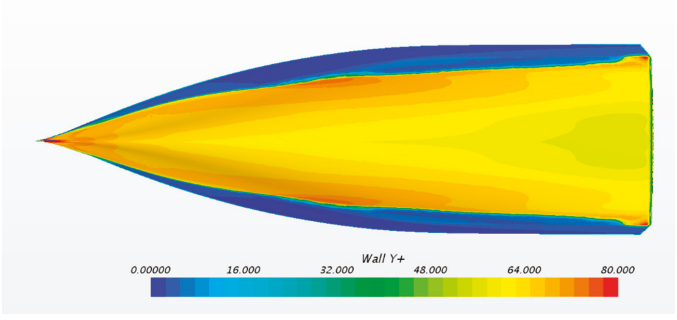

Figure 10. Wall $Y+$ under the hull.

The discretization that guaranteed these $Y+$ values was the following: Thickness of the first cell for the 3 m/s simulation was 1 mm; 12 layers were used with a smooth growth factor of 1.2.

The thickness of the first cell near the wall changed for every simulation, in order to always aim for the same $Y+$ values when the speed changed.

3.6. Time Discretization

In Star-CCM+, the multiphase VOF solver requires an implicit time scheme and is not available when an explicit time scheme is used. Thus, a second order implicit time discretization was chosen because the first order was numerically diffusive, and the property of the waves was not transported correctly [32,33]. As a consequence, if a first order is used, waves behind the hull are significantly damped out a few meters behind the boat and the wave pattern results are much smaller than in real experience.

Time step for an implicit time scheme can be high because implicit is unconditionally stable; the CFL factor can be up to 10 and even more, while for an explicit approach, the CFL factor has to be below 1, otherwise the method becomes unstable. Nevertheless, when dealing with multiphase models and overset technology, two additional limitations must be satisfied:

(1) The CFL number at the interface between the two fluids has to be at least less than 1 and it is suggested to keep it less than 0.5 in order to have a clean separation of the two fluids and a sharp interface [28,29];
(2) the movement of the overset cells at the interface between the two regions must be less than half of the minimum cell size to prevent overset mesh crash errors due to the exchange of information [36].

The second condition is very important when simulating a hull in head sea and when deciding about the overset dimensions. The more severe limitation on the time step comes from the former, so the time step is a function of the speed of the test in order to aim for the same CFL at the sea

surface. The time step goes from 0.01 s for 1 m/s test, to 0.0033 s for the 3 m/s test, and it scales linearly with speed.

3.7. Numerical Ventilation

In the case of planing hulls, for very high speeds, phenomenon of ventilation can occur: A thin film of air gets caught between the hull and the water, drastically reducing the drag. This is a well-known phenomenon often exploited to improve the design of high-speed planing motor yachts to reduce the viscous drag with water. Ventilation requires a speed of an order of magnitude greater than the speeds tested; therefore, it was not tested in the real experiment, nor will the sailboat ever experiment with it.

However, the numerical model can suffer from numerical ventilation [7,8,37], even for low speed such as 3 m/s (Froude number = 0.4465), for particular hull shapes or trimming angle, especially if the bow is not piercing the sea surface but lies over it [12,13], as shown in Figure 11.

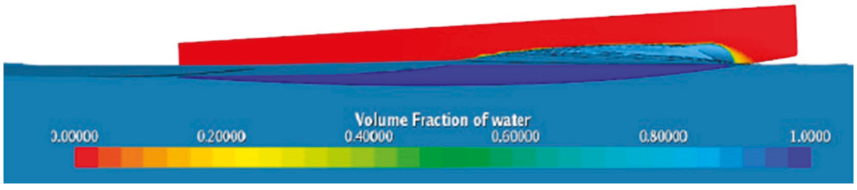

Figure 11. Bow is lying on the surface and not piercing it for high speeds.

When implementing a dual phase simulation, due to the numerical interpolation method in the VOF model, it is possible that a fraction of air gets caught and remains trapped under the hull, creating a mixture of phases [30], as shown in Figure 12. Air usually undergoes the hull at the bow and travels down to the stern, establishing a steady flux. As a consequence, the wall friction drag is underestimated. It is worth remarking that the contribution of the form drag to the overall drag is not affected by numerical ventilation.

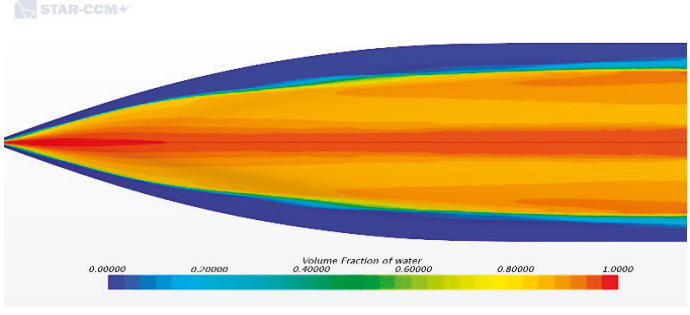

Figure 12. Ventilated hull at 3 m/s, bottom view.

In order to solve numerical ventilation related problems, in this work, two approaches are used:

(1) The first approach is related to the refinement of the mesh near the interface between water and air in the aft part of the bow. Here, an isotropic mesh is also used for the sea surface because an anisotropic mesh is more subject to numerical ventilation. This treatment works best when paired with the high-resolution interface capturing (HRIC) scheme designed to mimic the convective transport of immiscible fluid components, and is thus suited for tracking sharp interfaces [37].

This approach requires the CFL number in the target region to remain low; therefore, the computational cost increases because a very small time step is required. Furthermore, increasing

the number of inner iterations in the implicit time-stepping scheme can reduce the likelihood of numerical ventilation; however, this numerical phenomenon remains dependent on the shape of the hull, trim angle, and speed of test, and may not be completely solved with this approach:

(2) The second method, used to completely resolve the numerical ventilation problem, is the phase-interaction substitution procedure. After the simulation is converged to a certain draft and trim angle and the wave pattern is well established around the hull, a phase interaction is applied which substitutes all fluid zones that contain mixed phases with water.

This procedure consists of the following steps:

(a) A scalar-user field function aiming to calculate all zones in the domain with a volume fraction of water higher than 0.5 is created;
(b) the phase-interaction procedure is applied setting the user field function created at preceding point as the input; and the mixed phase is replaced with water;
(c) the first order time accuracy must be set (because VOF phase replacement is not compatible with the second order time scheme);
(d) only a single time step can be running to obtain the final result after the substitution procedure. If more steps are run, the water level keeps rising for each iteration because at sea surface there is never a sharp separation between phases; thus, a step after the other, the water occupies more and more volume. This also explains why it is important that the simulation is already converged to final values.

The correct shear stress was computed, and the real wetted surface was used without changing the physics of the problem. This technique allowed for a higher time step and a coarser mesh, especially at the wall in the bow part. Numerical ventilation was solved and all the forces acting on the hull were computed correctly, as shown in Figure 13. The second approach was preferred because it worked well in a calm sea simulation and granted a faster solution than that of the first method.

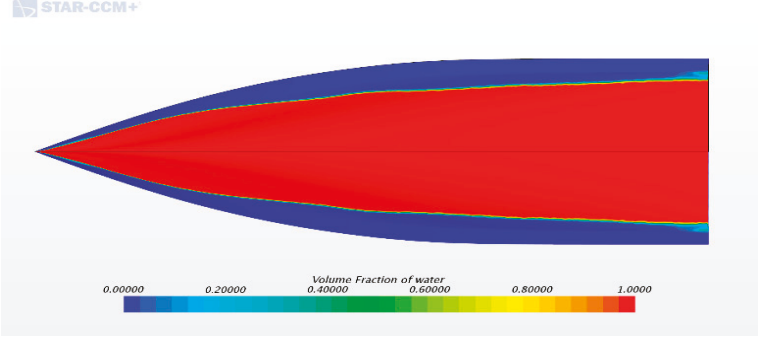

Figure 13. Ventilation solved after the phase-interaction substitution procedure.

3.8. Convergence Study

Convergence study has key importance in every CFD simulation. This process proves that the discretization error has small influence on the result and that the solution will not change when refining the mesh. Convergence study allows the analyst to choose the best cell size, which represents an appropriate compromise between accuracy and computational speed; thus, it represents an opportunity to quantify the increment with an accuracy that a finer model would obtain, and compare it with the increase in central processing unit (CPU) hours required, as shown in Table 1.

Four different base sizes (the parametric value with which all the mesh is scaled) are investigated, associated with different cells' count: Halving the base size generates a number almost 2^3 times higher,

since 3D volume cells are considered. When investigating grid convergence, it is important not to change other models and parameters, otherwise it would be impossible to discern what caused the different behavior in the simulation. This means scaling the time step for every different mesh size in order to maintain a constant CFL number. Similar considerations apply to the $Y+$ value, which must remain constant in all the simulations.

Therefore, a fixed value for the thickness of the first cell near the wall is used (when changing base size, not when changing the speed of the test), and the time step is scaled to maintain the same CFL for all the grids tested [38]. It is important to notice that simulation time increases significantly using the finest grid. This is not only due to the higher number of cells, but also to the smaller time step.

Table 2 presents the different base sizes used, the associated number of cells, the relative errors, and the corresponding CPU time of the simulation. The physical quantities that were monitored in this convergence study are the total drag experienced by the hull, the translation along the z axis, and the trim angle. The obtained total drag and vertical translations are shown in Figures 14 and 15, respectively. The benchmark used to build the error metrics is the dataset from the EFD. The method used for the analysis is the Richardson extrapolation, with the correction based on the total number of cells [39]. In this regard, the base size had to have a constant increment; in order to keep the cell count low, we decided for 1.5 as the multiplier for the base size.

Table 2. Convergence study and comparison with experimental data for the 3 m/s test.

Base Size	Cell Count (Millions)	Total Drag (Half Hull) (N)	ΔTrim (Degrees)	ΔTranslation z (mm)	Relative Error Drag	Relative Error ΔTranslation z	Relative Error ΔTrim	Computational Time
Experimental Data	-	66	0.878	18.6	0	0	0	-
0.667	2.2	65.34	0.871	18.8	1.00%	1.08%	0.80%	36 h × 16 CPU
1	1.01	65.24	0.892	19.103	1.15%	2.70%	1.59%	12 h × 16 CPU
1.5	0.62	64.94	0.901	19.846	1.61%	6.70%	2.62%	6 h × 16 CPU
2.25	0.5	60.5	0.935	20.01	8.33%	7.58%	6.49%	4 h × 16 CPU

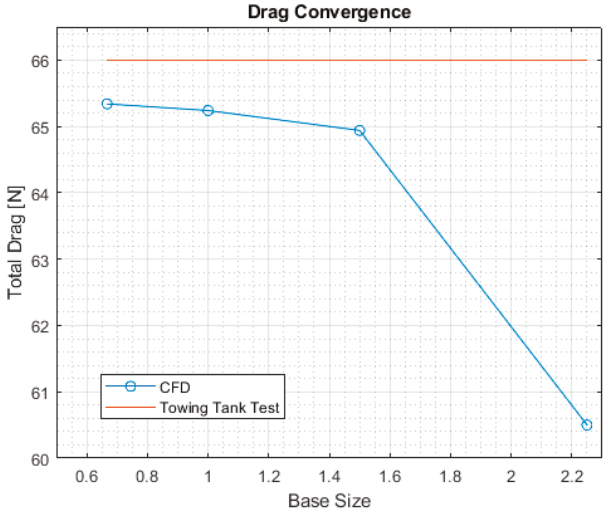

Figure 14. Drag convergence.

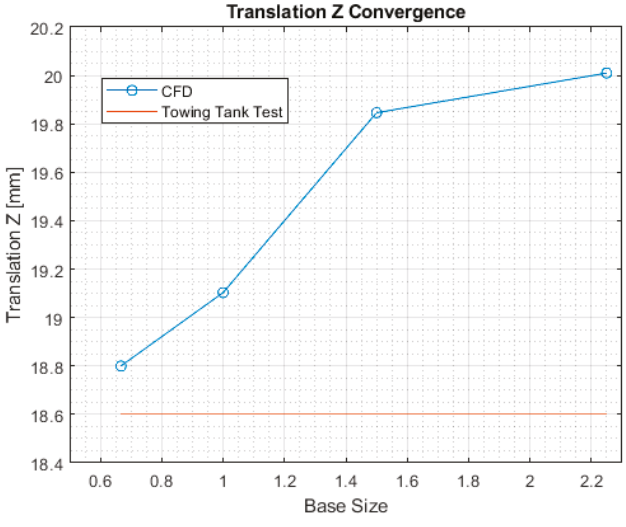

Figure 15. Translation z convergence.

As shown in Table 2, the mesh resulting from the base size equal to one was chosen, since it achieved errors similar to the finest mesh, while computing 3 times faster. Further refinement of the mesh would not significantly increase the accuracy of the simulation but would make it more expensive.

4. Results: Comparison between CFD and EFD

Results in Table 3 are obtained from the postprocessing of CFD simulations and are presented in Figures 16 and 17. The main objective of this work was to validate the numerical model through comparison with experimental data. Furthermore, it is interesting to compare results with and without correction for numerical ventilation in order to evaluate the benefit of the numerical strategy herein proposed. Values of ΔTrim angle were positive when the bow was lifted up.

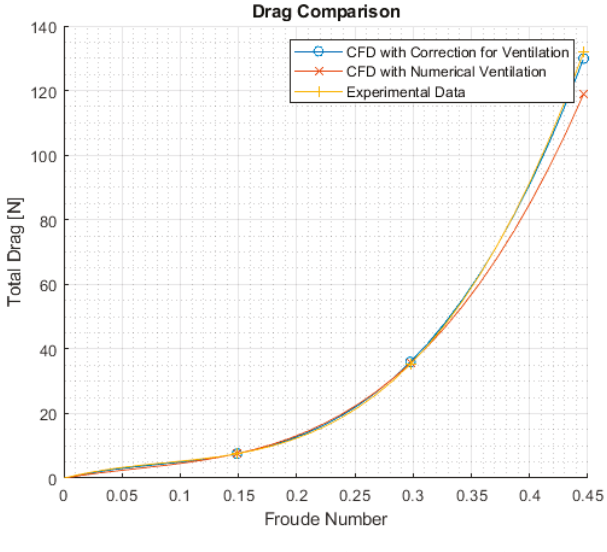

Figure 16. Total resistance curve: EDF vs. ventilated CFD vs. CFD with ventilation correction.

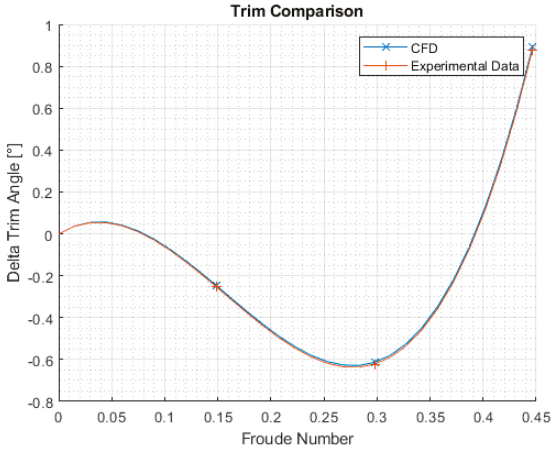

Figure 17. Δ Trim, CFD vs. EFD.

Table 3. Comparison between experimental fluid dynamic (EFD), computational fluid dynamic (CFD) with numerical ventilation, and CFD after correction.

Froude Number	Velocity [m/s]	CFD Drag (Numerically Ventilated) (N)	CFD Drag Post Correction (N)	TTT Drag (N)	Relative Error (Corrected Drag vs. EFD)	ΔTrim Angle CFD (°)	TTT ΔTrim Angle (°)	Relative Error (CFD ΔTrim vs. EFD ΔTrim)
0.1488	1	7.58	7.60	7.55	0.61%	−0.248	−0.254	2.3%
0.2977	2	35.6	36.0	35.3	1.94%	−0.613	−0.622	1.4%
0.4465	3	119	130.48	132	1.13%	0.892	0.878	1.5%

As clearly shown in Figure 16, experimental results are better approximated when the numerical ventilation correction is applied. This method increased the total advancing drag of the hull and guaranteed a reduction of the relative error with respect to the experimental data; the error of the numerical model after correction was between 0.61% and 1.94% for drag, below the 2% threshold. The difference after ventilation correction was noticeable only for 3 m/s because for the other two speeds tested the numerical ventilation under the hull was practically absent. Moreover, it is important notice that the ventilation correction did not influence the trim angle at all, leaving it unchanged.

5. Conclusions

Considering the results that emerged from this work, the advantages of the CFD model have been confirmed. Numerical RANS simulation represents an accurate mean for the test of a new hull and can be useful during the boat design and testing process. This work aimed to group all the best practices that should be implemented during a CFD study of a hull in calm sea conditions, and represents the starting point for future studies regarding motion in head sea. Two different methodologies dealing with numerical ventilation, which can also occur for low speeds such as 3 m/s, were presented in this paper. The goal of having a fast and accurate simulation, and of solving the numerical ventilation problem, was achieved using the second methodology proposed, which fits perfectly for cases in which speed is low and no real ventilation occurs. It is worth noting that the phase substitution procedure cannot be used when the ventilation is both real and numerical because this method completely removes air from the bottom of the hull; therefore, the technique proposed here should not be used for high-speed planing crafts.

Author Contributions: Conceptualization, P.C., O.D., and G.M.; data curation, P.C., B.F., and G.G.; formal analysis, P.C. and O.D.; funding acquisition, P.C., O.D., and G.M.; investigation, P.C., O.D., and B.F.; methodology, P.C., O.D., G.G., and S.A.S.; resources, P.C., O.D., and G.M.; software, P.C., O.D., and B.F.; supervision, G.G., S.A.S., and

G.M.; validation, P.C., O.D., S.A.S.; visualization, P.C.; writing—original draft, P.C. and O.D.; writing—review and editing, P.C., G.G. and S.A.S. All authors have read and agreed to the published version of the manuscript.

Funding: This research received no external funding.

Acknowledgments: We would like to thank the Polito Sailing Team, especially all the members of the fluid dynamic area who contributed to carrying out the tests in the naval tank, and, most importantly, to the development of the numerical model presented here. Without their fundamental contribution this work would not have been possible. A special thanks goes to University of Napoli for providing free towing tank tests for all participants in the competition, providing the students with the opportunity to validate their work.

Conflicts of Interest: The authors declare no conflict of interest.

References

1. Eliasson, R.; Larsson, L.; Orych, M. *Principles of Yacht Design*; A&C Black: Edinburgh, London, 2014.
2. Fossati, F. *Aero-Hydrodynamics and the Performance of Sailing Yachts: The Science behind Sailing yachts and Their Design*; A&C Black: Edinburgh, London, 2009.
3. Gad-el-Hak, M. The water towing tank as an experimental facility. *Exp. Fluids* **1987**, *5*, 289–297. [CrossRef]
4. Min, K.-S.; Kang, S.-H. Study on the form factor and full-scale ship resistance prediction method. *J. Mar. Sci. Technol.* **2009**, *15*, 108–118. [CrossRef]
5. Xia, M.; Mao, M.; Niu, Q. Implementation and comparison of the recent three-dimensional radiation stress theory and vortex-force formalism in an unstructured-grid coastal circulation model. *Estuar. Coast. Shelf Sci.* **2020**, *240*, 106771. [CrossRef]
6. Quality Systems Group of the 28th ITTC. *Recommended Procedures and Guidelines*. 25th ITTC 09/2008. Available online: https://ittc.info/media/8372/index.pdf (accessed on 29 May 2020).
7. De Marco, A.; Mancini, S.; Miranda, S.; Scognamiglio, R.; Vitiello, L. Experimental and numerical hydrodynamic analysis of a stepped planing hull. *Appl. Ocean Res.* **2017**, *64*, 135–154. [CrossRef]
8. Mancini, S.; De Luca, F.; Ramolini, A. Towards CFD guidelines for planing hull simulations based on the Naples Systematic Series. In Proceedings of the VII International Conference on Computational Methods in Marine Engineering MARINE 2017, Nantes, France, 15–17 June 2017; pp. 15–17.
9. Tezdogan, T.; Demirel, Y.K.; Kellett, P.; Khorasanchi, M.; Incecik, A.; Turan, O. Full-scale unsteady RANS CFD simulations of ship behaviour and performance in head seas due to slow steaming. *Ocean Eng.* **2015**, *97*, 186–206. [CrossRef]
10. ITTC Resistance Committee. *Uncertainty Analysis in CFD: Verification and Validation Methodology and Procedures*; ITTC: Fukuoka, Japan, 2008.
11. Silverberg, J.P.; Miller, P.H. *A Comparison of Parametric Analysis, Tank Testing and CFD Methods as Part of An Advanced Sailboat Velocity Prediction Program*; United States Naval Academy: Annapolis, MD, USA, 2020.
12. Viola, I.M.; Flay, R.G.J.; Ponzini, R. CFD analysis of the hydrodynamic performance of two candidate America's Cup AC33 hulls. *Int. J. Small Cr. Technol.* **2012**, *154*, 1–12.
13. De Luca, F.; Mancini, S.; Miranda, S.; Pensa, C. An extended verification and validation study of CFD simulations for planing hulls. *J. Ship Res.* **2016**, *60*, 101–118. [CrossRef]
14. Peri, D.; Rossetti, M.; Campana, E.F. Design optimization of ship hulls via CFD techniques. *J. Ship Res.* **2001**, *45*, 140–149.
15. Available online: https://www.plm.automation.siemens.com/global/it/products/simcenter/STAR-CCM.html (accessed on 13 April 2020).
16. Kim, Y.-C.; Kim, K.S.; Kim, J.; Kim, Y.; Park, I.-R.; Jang, Y.-H. Analysis of added resistance and seakeeping responses in head sea conditions for low-speed full ships using URANS approach. *Int. J. Nav. Arch. Ocean Eng.* **2017**, *9*, 641–654. [CrossRef]
17. Li, A.; Li, Y. Numerical and experimental study on seakeeping performance of a high-speed trimaran with t-foil in head waves. *Pol. Marit. Res.* **2019**, *26*, 65–77. [CrossRef]
18. Yang, C.; Huang, F. An overview of simulation-based hydrodynamic design of ship hull forms. *J. Hydrodyn.* **2016**, *28*, 947–960. [CrossRef]
19. Weymouth, G.D.; Wilson, R.V.; Stern, F. RANS computational fluid dynamics predictions of pitch and heave ship motions in head seas. *J. Ship Res.* **2005**, *49*, 80–97.

20. Windt, C.; Ringwood, J.V.; Davidson, J.; Ransley, E.J.; Jakobsen, M.; Kramer, M. Validation of a CFD-based numerical wave tank of the Wavestar WEC. In Proceedings of the 3rd International Conference on Renewable Energies Offshore (RENEW 2018), Renewable Energies Offshore, Lisbon, Portugal, 8–10 October 2018; p. 439.
21. Choi, J.; Yoon, S.B. Numerical simulations using momentum source wave-maker applied to RANS equation model. *Coast. Eng.* **2009**, *56*, 1043–1060. [CrossRef]
22. Perić, R.; Abdel-Maksoud, M. Reliable damping of free-surface waves in numerical simulations. *Ship Technol. Res.* **2016**, *63*, 1–13. [CrossRef]
23. Field, A. *How the Wave Damping Length Influences the Domain and Wake Refinements in a Hull Performance Analysis*. Steve Portal: 10/30/2017. Available online: https://www.reddit.com/r/CFD/comments/fmcxop/accessing_steve_portal/ (accessed on 29 May 2020).
24. Mucha, P. *How to Determine Coefficients for the Wave Damping Model?* Steve Portal: 2019. Available online: https://www.reddit.com/r/CFD/comments/fmcxop/accessing_steve_portal/ (accessed on 29 May 2020).
25. Jacobsen, N.G.; Fuhrman, D.R.; Fredsoe, J. A wave generation toolbox for the open-source CFD library: OpenFoam®. *Int. J. Numer. Methods Fluids* **2011**, *70*, 1073–1088. [CrossRef]
26. Windt, C.; Davidson, J.; Chandar, D.; Ringwood, J. On the importance of advanced mesh motion methods for WEC experiments in CFD-based numerical wave tanks. In Proceedings of the VIII International Conference on Computational Methods in Marine Engineering, Gothenburg, Sweden, 13–15 May 2019.
27. Vichnevetsky, R.; Turner, L. Spurious scattering from discontinuously stretching grids in computational fluid dynamics. *Appl. Numer. Math.* **1991**, *8*, 289–299. [CrossRef]
28. Cholleti, P. *How do I Setup My Mesh to Best Capture VOF Waves?* Steve Portal: 2015. Available online: https://www.reddit.com/r/CFD/comments/fmcxop/accessing_steve_portal/ (accessed on 29 May 2020).
29. Connell, K.O.; Cashman, A. Development of a numerical wave tank with reduced discretization error. In Proceedings of the 2016 International Conference on Electrical, Electronics, and Optimization Techniques (ICEEOT), Chennai, India, 3–5 March 2016; pp. 3008–3012.
30. Gray-Stephens, A.; Tezdogan, T.; Day, S. Strategies to minimise numerical ventilation in CFD simulations of high-speed planing hulls. In Proceedings of the ASME 2019 38th International Conference on Ocean, Offshore and Arctic Engineering, Glasgow, UK, 9–14 June 2019.
31. Brizzolara, S.; Serra, F. Accuracy of CFD codes in the prediction of planing surfaces hydrodynamic characteristics. In Proceedings of the 2nd International Conference on Marine Research and Transportation, Ischia, Italy, 28–30 June 2007; pp. 147–159.
32. *Star-ccm+ User Guide*. Siemens. 2015. Available online: https://www.scribd.com/doc/193836790/Star-CCM-User-Guide (accessed on 29 May 2020).
33. Caponnetto, M. Practical CFD simulations for planing hulls. Process Second Int. EuroConference High Perform. *Mar. Veh.* **2001**, *HIPER'01*, 128–138.
34. Woolliscroft, M.; Maki, K. A fast-running CFD formulation for unsteady ship maneuvering performance prediction. *Ocean Eng.* **2016**, *117*, 154–162. [CrossRef]
35. Simpson, R.L.; Chew, Y.-T.; Shivaprasad, B.G. The structure of a separating turbulent boundary layer. Part 1. Mean flow and Reynolds stresses. *J. Fluid Mech.* **1981**, *113*, 23. [CrossRef]
36. Li, Y.; Paik, K.-J.; Xing, T.; Carrica, P.M. Dynamic overset CFD simulations of wind turbine aerodynamics. *Renew. Energy* **2012**, *37*, 285–298. [CrossRef]
37. Dashtimanesh, A.; Mancini, S.; Carlini, M.D.; Caterino, F.D.; Bilandi, R.N. A numerical way for a stepped planing hull design and optimization. In *Technology and Science for the Ships of the Future, Proceedings of NAV 2018: 19th International Conference on Ship & Maritime Research*; IOS Press: Amsterdam, The Netherlands, 2018; p. 220. [CrossRef]
38. Almohammadi, K.; Ingham, D.; Ma, L.; Pourkashan, M. Computational fluid dynamics (CFD) mesh independency techniques for a straight blade vertical axis wind turbine. *Energy* **2013**, *58*, 483–493. [CrossRef]
39. Roache, P.J. Perspective: A Method for Uniform Reporting of Grid Refinement Studies. *J. Fluids Eng.* **1994**, *116*, 405–413. [CrossRef]

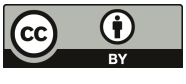

Journal of
Marine Science and Engineering

MDPI

Article

Numerical Simulation of Wave Interaction with Payloads of Different Postures Using OpenFOAM

Mingwei Yan [1], Xin Ma [1,*], Wei Bai [2], Zaibin Lin [2] and Yibin Li [1]

[1] Center for Robotics, School of Control Science and Engineering, Shandong University, Jinan 250061, China; yanmingwei1122@mail.sdu.edu.cn (M.Y.); liyb@sdu.edu.cn (Y.L.)
[2] Department of Computing and Mathematics, Manchester Metropolitan University, Chester Street, Manchester M1 5GD, UK; w.bai@mmu.ac.uk (W.B.); z.lin@mmu.ac.uk (Z.L.)
* Correspondence: maxin@sdu.edu.cn

Received: 10 May 2020; Accepted: 5 June 2020; Published: 12 June 2020

Abstract: A three-dimensional numerical wave tank (NWT) is established with Open Source Field Operation and Manipulation (OpenFOAM) software and waves2foam to investigate wave interaction with payloads with different postures in the process of offshore lifting or lowering. Numerical results of regular wave interaction with a vertically suspending cylinder are presented first for validation by comparison with the published data. A series of simulation experiments are carried out, and the forces and the moments exerted by the regular waves on a fixed suspending cylinder payload and a fixed suspending cuboid payload with different postures are presented. It can be concluded from the results that the rotating rectangular payload (cuboid and cylinder) suffers a drastically changed moment when it is initially vertically placed, and the projection area of payload vertical to the force affects the corresponding force. The simulation results also show how the forces and the moments change with different posture angles. With some certain posture, the suspending payload suffers minimum forces and moments. Parametric study for the cuboid payload is done in the case of normal incidence. The influence of the payload's size and wave parameters on forces and moments are analyzed. All of the numerical simulation results and conclusions provide the fundamentals for further research and safe control of offshore lifting or lowering.

Keywords: offshore crane; OpenFOAM; wave-payload interaction; NWT

1. Introduction

With ever-increasing marine exploration and subsea resource exploitation, offshore cranes which are mounted on vessels and carry out lifting/lowering have been widely used in marine operations. While working on the sea, offshore cranes suffer from persistent disturbances induced by ocean waves. During lifting or lowering, the payloads may be subject to large hydrodynamic forces, which could cause payload damages or cable breaks. This would further cause accidents and impair the safety of life and property [1].

In order to lift/lower payloads on the sea safely and efficiently, the capability to estimate the hydrodynamic loads on payloads is of vital importance. The hydrodynamic loads on stationary structures in waves have been studied for the safe and cost-effective design of coastal and offshore structures in the past decades. Compared to physical experiments, which need to establish scaled models, numerical modeling is more practical. The numerical models based on potential flow theory and Navier-Stokes (N-S) equations are two main categories for the simulation of wave-structure interactions.

The potential flow model is applied for wave interaction with large structures where viscous and turbulence effects can be ignored, such as the second-order potential flow theory model [2,3] and the fully nonlinear potential flow theory model [4]. With the assumption that the flow is inviscid and flow irrotational, it is challenging for the potential flow theory to capture the nonlinear free

surface correctly when wave breaking occurs. Computational Fluid Dynamics (CFD) based on Navier–Stokes (N–S) equations is used for highly nonlinear wave–structure interactions in the case of breaking wave impacts and evolution of vortices. Various methods or models have been considered for wave–structure interaction, such as the Institute of Environmental Hydraulics of Cantabria Field Operation and Manipulation (IHFOAM) model, which solves Volume-Averaged Reynolds-Averaged Navier–Stokes equations (VARANS) [5,6], the multiple-layer σ-coordinate model [7], the Immersed Boundary Method [8], the Smooth Particle Hydrodynamics method [9,10], and the Constrained Interpolation Profile method [11].

OpenFOAM, a free open-source C++ toolbox for the development of customized numerical solver (such as the naoe-FOAM-SJTU solver [12]) based on CFD, has been applied in coastal and offshore engineering recently. Regular wave interaction with two tandem cylinders is studied with OpenFOAM [13], and an improved model named IHFOAM is used to study wave interaction with porous coastal structures [14,15]. The performance of OpenFOAM for nonlinear wave interactions with offshore structures is assessed, with up to eighth order harmonics correctly modeled [16].

In addition to the normal incident wave interaction with structures, many researchers have also investigated the interaction of oblique waves with stationary structures, such as perforated caissons [17], bridge decks [18], and various other structures [19–24]. The stationary nature of the structure makes it hard to rotate around different axes, the above oblique papers only focus on the situation of one single posture angle. Compared with stationary structures, the payloads can move with much more freedom while lifting or lowering payloads on the sea. Here, we want to reach a general conclusion when considering different posture angles, and to the authors' knowledge, there has been no previous research about the general postures' study of the payload.

Importantly, the posture of the payload has an impact on the force and moment exerted by the wave; additionally, the force and moment can also change the posture. This paper focuses on studying the influence of different postures of the payloads on wave forces and moments exerted on the payloads; thus, we assume that the payload is fixed without linear motion and rotation. A cylinder payload and a cuboid payload, both fixed and suspended with different postures in regular waves, are investigated, respectively. By carrying out a series of simulations, the influence of the payloads' posture angles relative to the regular waves on the hydrodynamic forces and moments exerted on the payloads are analyzed. It can be concluded from the results that the rotating rectangular payload (cuboid or cylinder) suffers a drastically changed moment when it is initially vertically placed, and the direction of the moment is the same as axis' rotation except for one situation. The projection area of the payload vertical to the force affects the corresponding force. The analysis could provide help for developing control strategies for offshore cranes, such as choosing the appropriate payload posture during water entry, and then using a controller to keep the payload on a certain posture that suffers minimal forces or moments during water entry.

2. Numerical Methods

2.1. Governing Equations

In order to represent the payload's posture in the wave, two Cartesian frames are defined, as shown in Figure 1a. The world frame $(o_w - \mathbf{x}_w\mathbf{y}_w\mathbf{z}_w)$ defined based on the 3D NWT. o_w is the midpoint of the inlet. $o_w\mathbf{x}_w$ is the direction of wave propagation. $o_w\mathbf{z}_w$ points straight upwards. The body frame is fixed with the payload. As for the body frame $(o_b - \mathbf{x}_b\mathbf{y}_b\mathbf{z}_b)$ of the cuboid payload, o_b is the centroid of the payload, and the three axes follow the directions of the three edges of the cuboid, respectively. The cuboid payload's posture in the wave can be expressed by the three Euler angles θ, ϕ, ψ (pitch, roll, and yaw angles), which represent the pose relationship between the payload's body frame $(o_b - \mathbf{x}_b\mathbf{y}_b\mathbf{z}_b)$ and the world frame $(o_w - \mathbf{x}_w\mathbf{y}_w\mathbf{z}_w)$ as shown in Figure 1b.

Both air and water are assumed to be incompressible laminar fluid. The motion of the fluid continuum is described with the governing equations, i.e., the Navier–Stokes equations and the continuity equation [16],

$$\frac{\partial \rho}{\partial t} + \nabla \cdot (\rho \mathbf{U}) = 0 \tag{1}$$

$$\frac{\partial \rho \mathbf{U}}{\partial t} + \nabla \times (\rho \mathbf{U}\mathbf{U}) - \nabla \times (\mu \nabla \mathbf{U}) - \rho g = -\nabla p - f_\sigma \tag{2}$$

where $\mathbf{U}$ is the fluid velocity, ρ is the fluid density, p is the fluid pressure, μ is the dynamic viscosity, t is the time, g is the gravity acceleration, and f_σ is the surface tension. Only the laminar flow is considered in the study.

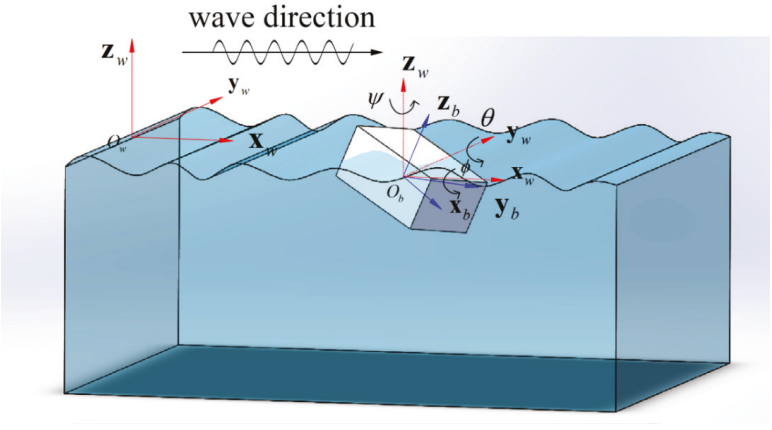

(**a**)

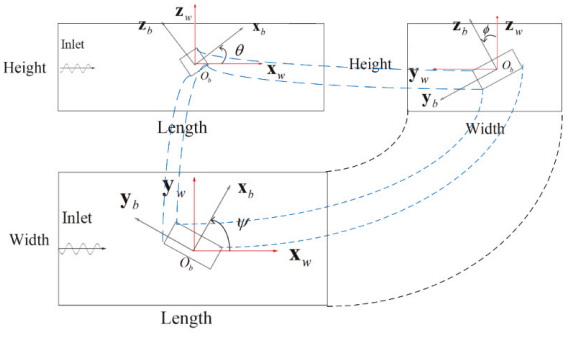

(**b**)

Figure 1. Two different descriptions of frames and the postures of the cuboid payload in the 3D numerical wave tank (NWT). (**a**) The overall description of two frames and a cuboid payload in the 3D NWT; (**b**) description of Euler angles in the top, side, and front view.

2.2. Free Surface Tracking

The Volume of Fluid (VOF) method is applied for tracking the free surface in OpenFOAM. In the VOF method, a phase function α is defined in each cell, which indicates the quantity of water in the cell. α is 1 if the cell is full of water, and it is 0 in empty cells. On the air-water interface, the value of α is between 0 and 1. The fluid density ρ and the dynamic viscosity μ in each cell are calculated with the equations,

$$\begin{aligned} \rho &= \alpha\rho_1 + (1-\alpha)\rho_2 \\ \mu &= \alpha\mu_1 + (1-\alpha)\mu_2 \end{aligned} \tag{3}$$

where the subscripts 1 and 2 mean the values of water and air, respectively. The phase function α can be determined by solving an advection equation,

$$\frac{\partial \alpha}{\partial t} + \nabla\cdot(\alpha\mathbf{U}) + \nabla\cdot(\alpha(1-\alpha)\mathbf{U}_\alpha) = 0 \tag{4}$$

where the last term on the left-hand side is an artificial compression term and $\mathbf{U}_\alpha$ is the relative compression velocity [25].

2.3. Waves2Foam Library and WaveFoam Solver

The library waves2Foam is used to generate regular waves. The boundary condition and solve procedures are listed below.

2.3.1. Waves2Foam Library

The library waves2Foam is a toolbox for generating and absorbing water waves [26]. Waves are generated at the inlet and absorbed at the outlet.

The velocities of regular waves are based on the linear Stokes' wave theory,

$$u(x,z,t) = \frac{gkA}{\omega}\frac{\cosh k(z+h)}{\cosh kh}\sin\varphi \tag{5}$$

$$w(x,z,t) = \frac{gkA}{\omega}\frac{\sinh k(z+h)}{\cos kh}\cos\varphi \tag{6}$$

where $u(x,z,t)$ is the horizontal velocity distribution, A is the wave amplitude, ω is the wave frequency, $\varphi = kx - \omega t$ and k is the wave number, h and is the water depth.

The relaxation zone technique is used to absorb waves at the outlet. The relaxation function is

$$\alpha_R(\chi_R) = 1 - \frac{\exp({\chi_R}^{3.5}) - 1}{\exp(1) - 1} \quad \text{for} \quad \chi_R \in [0:1] \tag{7}$$

It is applied into the relaxation zone as follows,

$$\lambda = \alpha_R\lambda_{\text{computed}} + (1-\alpha_R)\lambda_{\text{target}} \tag{8}$$

where λ is either $\mathbf{U}$ or α. The variation of α_R is the same as given in [27], and χ_R represents a certain point in the relaxation zone. The definition of χ_R is such that it is always 1 at the interface between the nonrelaxed part of the computational domain and the relaxation zone.

2.3.2. WaveFoam Solver and Boundary Conditions

1. Boundary conditions

The boundary name is just as shown in Figure 2. At the inlet of the 3D NWT, a specified boundary condition of fluid velocity **U** is set to *waveVelocity*, the boundary condition of the indicator phase function α is set to *waveAlpha*, and the boundary condition of the fluid pressure p is set to *zeroGradient*. At the top of the NWT, the velocity **U** is set to *pressureInletOutletVelocity*, which is a default boundary condition in OpenFOAM, the pressure p is set to *totalPressure*, and the phase function α is set to *inletOutlet*.

For the remaining parts of the NWT and the fixed suspending objects, the boundary conditions are considered as solid walls, where the fluid velocity **U** is set to a fixed value of zero, the fluid pressure p and the indicator phase function α are set to *zeroGradient*.

2. Solving procedure

The *waveFoam* solver starts with the preprocessor, which is used to set up wave properties and computational meshes. The meshes of the NWT are generated by using the built-in tool *blockMesh* and *snappyHexMesh*. The N–S equations are discretized into a set of algebraic equations by integrating the boundary conditions over the whole solution domain and time domain. The physical parameters of the whole domain like the fluid pressure p and the fluid velocity **U**, etc., are calculated and updated at each timestep by calling solver *waveFoam*.

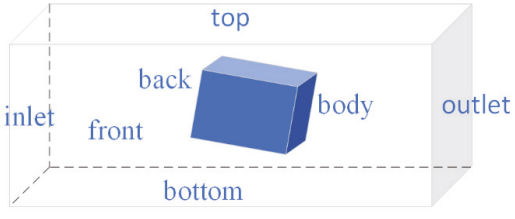

Figure 2. The boundary name of the NWT.

3. Comparison Against Published Data

A 3D numerical wave tank (NWT) is established with the above numerical methods of OpenFOAM and waves2foam. To validate the 3D NWT model, we compare the numerical results of wave interaction with a fixed and vertically suspended cylinder payload with the published data [16].

3.1. Numerical Wave Tank

A 3D numerical wave tank (NWT) is established, as shown in Figure 3. Its geometry has the outer dimensions 15 $m \times 4$ $m \times 1.2$ m with the water depth $h = 0.505$ m and the relaxation zone of 1.5 L, where L is the wavelength. A cylinder whose radius $a = 0.125$ m is stationary and vertical is suspended in the tank, leaving a 1 mm gap beneath to the bed of the tank. The length of the cylinder is 1 m. The cylinder is located at 7.5 m from the paddles in the center of the tank. A wave gauge WG2 is placed 2 mm in front of the upstream stagnation point of the cylinder to monitor the wave field around the cylinder, and a wave gauge WG1 is placed 0.77 m from the inlet to monitor the wave elevation.

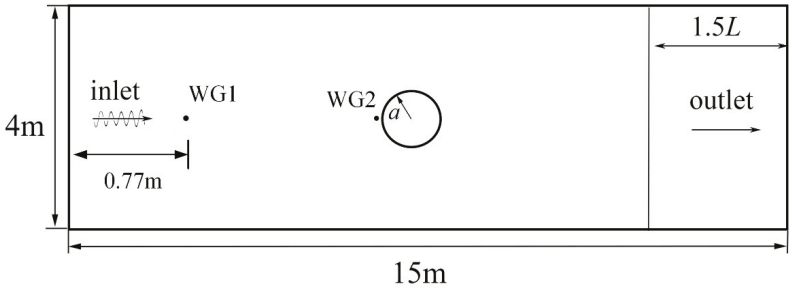

Figure 3. Layout of the numerical wave tank.

Two regular wave cases [16] R1 and R2 are reproduced with our 3D NWT. The wave parameters are shown in Table 1, where h is the water depth, k is the wavenumber, A is the wave amplitude, and T is the wave period.

Table 1. Parameters of regular wave for validation.

Regular Wave	A(m)	T(s)	kh	kA
R1	0.035	1.22	1.39	0.1
R2	0.06	1.63	0.86	0.1

h is the water depth, k is the wavenumber, A is the wave amplitude, and T is the wave period.

The mesh resolution in the computational domain affects the numerical solution. The built-in mesh generator *blockMesh* is used to generate meshes of hexahedral cells, then *snappyHexMesh* in OpenFOAM is used to generate the cylinder. The mesh consists of multilevel grids, as shown in Figure 4. In the areas around the payload, the grid cells have a resolution of Δx in the horizontal direction and Δz in the vertical direction, which are measured by the cells per wavelength and wave height.

Three different time steps are used here for the convergence examination. As shown in Figure 5, three cases are set to a fixed time-step, and the results are convergent. For each time-step, one, two, and three inner iterations (*nOuterCorrectors* in OpenFOAM) are used for convergence examination, the result is the same as Figure 5. For each inner iteration, the PIMPLE algorithm is called three times (*nCorrectors* in OpenFOAM). For the remaining cases in the paper, one *nOuterCorrectors* and three *nCorrectors* are used, the simulation time is 18 s, and the fixed time step is set to 0.005 s, the courant numbers during the simulation are all less than 0.1.

The time history of horizontal force F_x on the cylinder payload with three different mesh schemes for the regular waves are shown in Figure 6. From this grid convergence examination, it can be seen that the results of Mesh 2 and Mesh 3 are convergent and Mesh 2 uses much less time; thus, the intermediate Mesh 2 is selected in this paper. For the Mesh 2 scheme, multilevel grids are used just as Figure 4 shows: in total, 470 cells in the x-direction, 125 cells in the y-direction, and 100 cells in the z-direction. The mesh around the inlet, outlet, and object is dense, and the rest transitions smoothly. The mesh around the cylinder and free surface is uniform: 110 cells per wavelength and 110 cells in total are set in the x-direction, 30 cells per wave height, and 60 cells in total are set in the z-direction and 60 cells in total in 1 m are set in the y-direction.

The simulations are run on purchased Dell T7920 workstation with Intel Xeon (R)E5 2699v4 CPU, 128GB RAM, and 44 cores. The comparison of the computation cost, the total cell numbers, the number of cores, and the simulated time under three different mesh schemes are illustrated in Table 2.

Table 2. Mesh parameters and computation cost.

Mesh Scheme	$\Delta x = \Delta y$	Δz	Cell Number (Million)	Cores	Run Time (h)
1	$L/88$	$H/15$	2.04	24	3.15
2	$L/110$	$H/30$	5.88	24	12.54
3	$L/132$	$H/45$	16.88	24	55.4

L is the wavelength. H is the wave height.

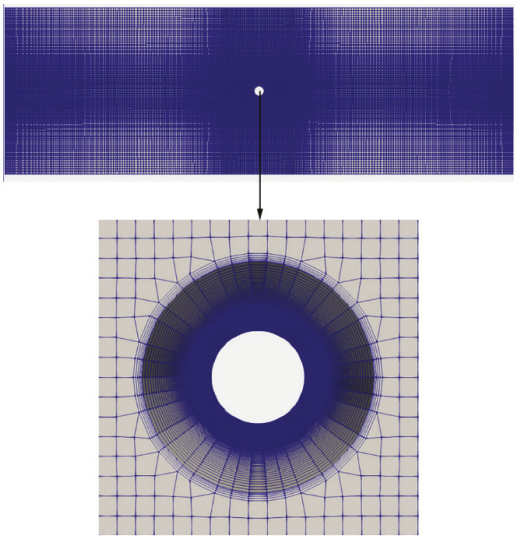

Figure 4. Mesh around the cylinder in the 3D NWT.

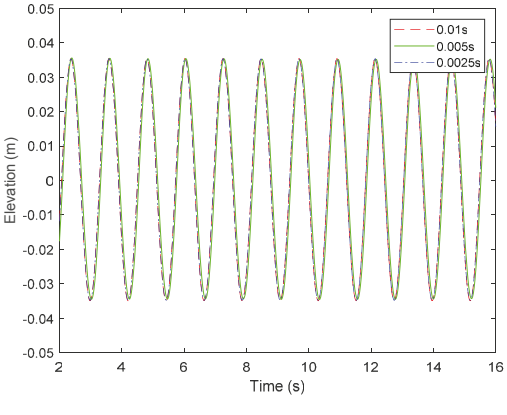

Figure 5. Time history of the surface elevation at WG1 for the wave R1 with three different time-steps.

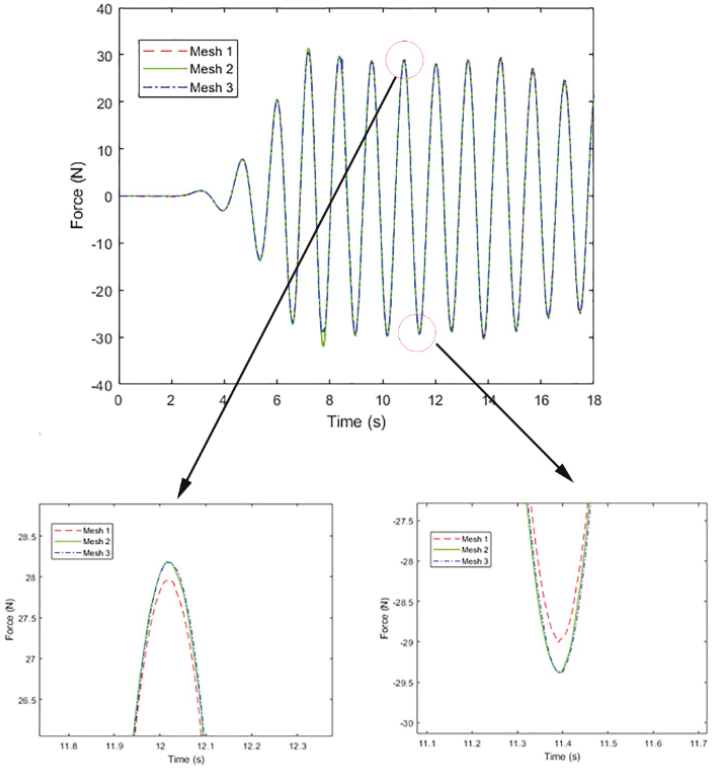

Figure 6. Time history of horizontal force F_x on the cylinder payload with three different mesh schemes for regular wave R1.

3.2. Comparison with the Published Data

Before the simulation, the surface elevation at WG1 for the wave R1 is compared with theory results, the result is as Figure 7 shows, the surface elevation agrees well with the theory. The free surface elevation and horizontal force are compared with published data. The time histories of the free surface elevation at WG2, and the corresponding amplitude spectra obtained by applying the FFT algorithm to the time histories are shown in Figure 8. The surface elevation is normalized by the wave amplitude A, and the time is normalized by the wave period t. The time series of the horizontal force on the cylinder and the corresponding amplitude spectra are presented in Figure 9. The force is normalized by $0.5\rho gAS$, where ρ is density of the water, and S is the cross-sectional area of the payload in the water perpendicular to the wave propagation direction. It can be seen that the results obtained with our NWT model match with the published data [16]. It is validated that our present 3D NWT numerical model can be used to calculate the wave load exerted on the payload with a reasonable degree of accuracy.

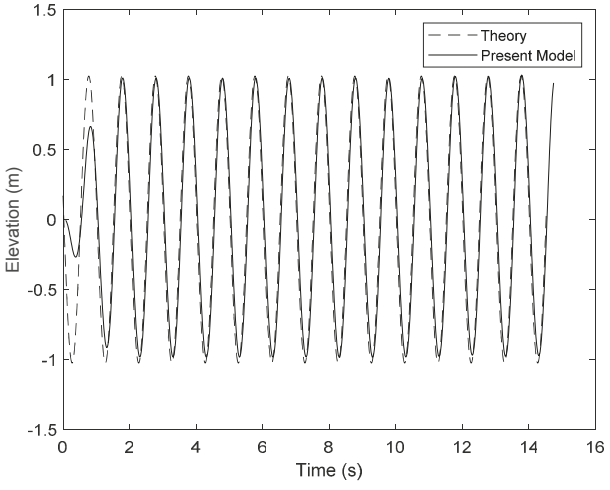

Figure 7. Surface elevation at WG1 for the wave R1 compared with theory result.

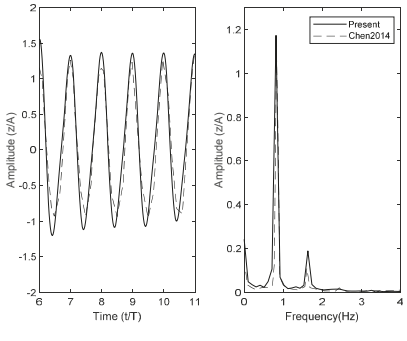

(**a**)

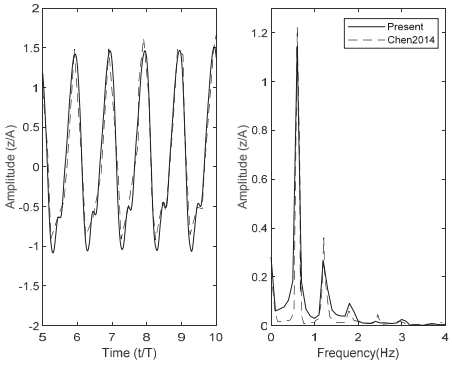

(**b**)

Figure 8. Time series of free surface elevation and amplitude spectra at WG2 for regular wave R1 and R2. (**a**) Results of R1; (**b**) results of R2.

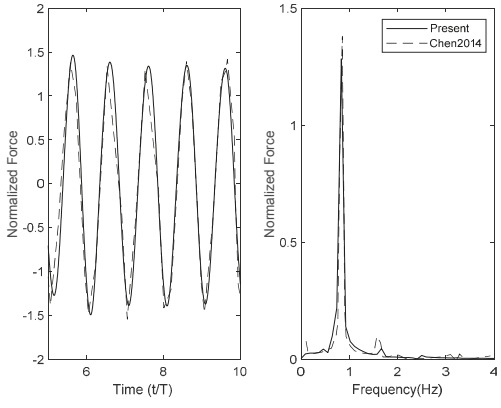

(**a**)

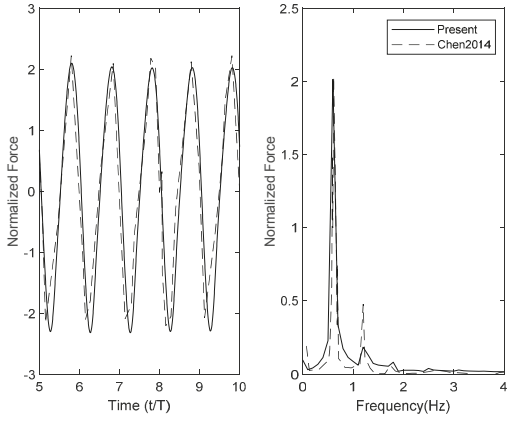

(**b**)

Figure 9. Time series of horizontal force on the cylinder and amplitude spectra for regular wave R1 and R2. (**a**) Results of R1; (**b**) results of R2.

4. Numerical Results

The 3D NWT established in Section 3 is applied in a series of simulation experiments in this section. Our study focuses on the influence of different postures of the payloads on wave forces and moments exerted on the payloads while suspending in the sea. We assume that the payloads are fixed and stationary while suspended in the sea without considering their translational and rotational motions caused by wave forces and rotational moments. A cylinder payload and a cuboid payload with different postures that are fixed and suspended in the regular wave R1 are simulated respectively. F_x, F_y, F_z three forces along the axes $o_b\mathbf{x}_w, o_b\mathbf{y}_w, o_b\mathbf{z}_w$, and M_x, M_y, M_z, three rotational moments about the axes are computed for two payloads. The influence of the postures of the payloads on wave forces and rotational moments exerted on the payloads are analyzed.

4.1. Case 1: A Cylinder Payload Fixed Suspending in the 3D NWT

The same cylinder payload in Section 3 is used here. In this subsection, in addition to the vertical suspension, several postures of the cylinder in the NWT are considered. The posture of the cylinder payload in the 3D NWT is shown in Figure 10. The wave condition is the same as the regular wave R1.

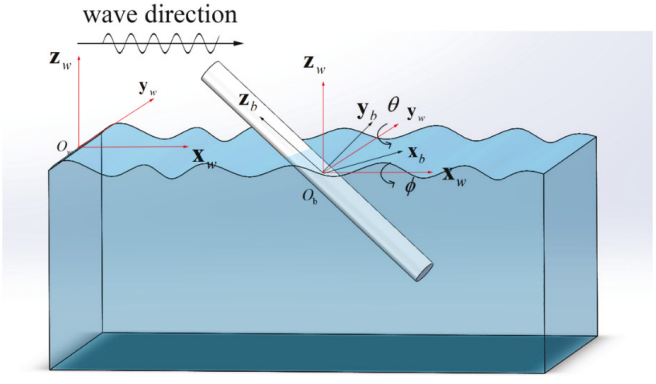

(**a**)

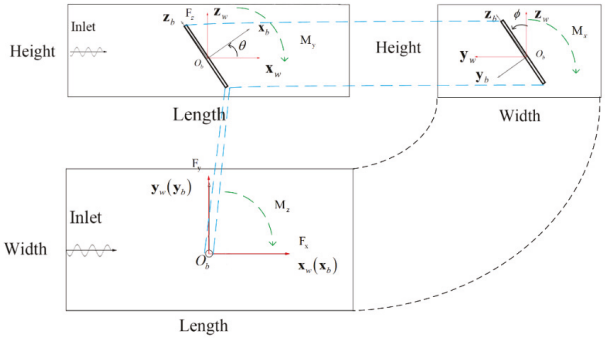

(**b**)

Figure 10. Two different descriptions of frames and the postures of the cylinder payload in the 3D NWT. (**a**) The overall description of two frames and a cylinder payload in the 3D NWT; (**b**) description of Euler angles in the top, side, and front view.

To validate the 3D NWT, the horizontal wave force F_x is compared with results computed by Morison's equation [27]

$$F_x = \rho C_m V \dot{u} + \frac{1}{2}\rho C_d S u|u| \tag{9}$$

where C_m is the added mass coefficient ($C_m = 1.15$), C_d is the drag coefficient ($C_d = 1$), V is the volume of the payload in the water, S is the cross-sectional area of the payload in the water perpendicular to the wave propagation direction, and $\dot{u}$ is the horizontal acceleration.

As shown in Figure 11, the normalized first-harmonic forces and moments are obtained by applying the FFT algorithm to the time histories. The first-harmonic forces are normalized by $0.5\rho gAS$ and the first-harmonic rotational moments are normalized by $\rho gdAS$ where d is the draft of the cylinder. In the latter study, the same normalization method is used for the forces and moments.

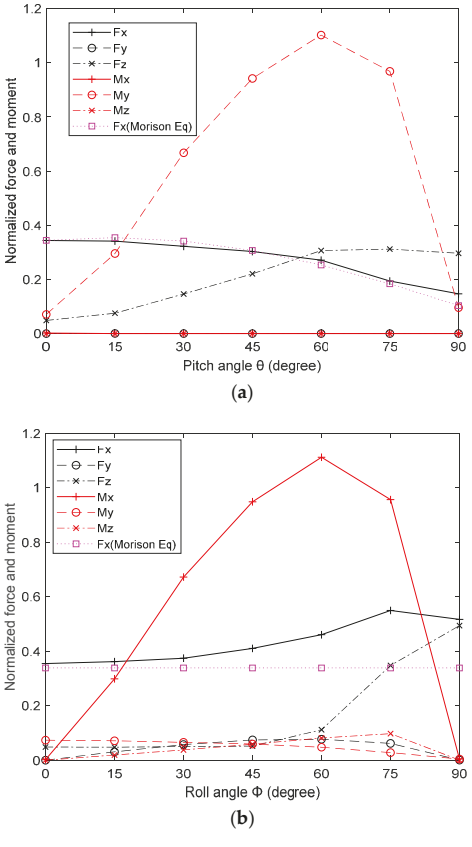

Figure 11. Normalized forces and moments on the cylinder payload versus a single posture angle. (**a**) the pitch angle θ; (**b**) the roll angle ϕ.

1. Pitch angle $\theta = (0°,\ 15°,\ 30°,\ 45°,\ 60°,\ 75°,\ 90°)$, roll angle $\phi = 0°$.

In Figure 11a, it can be seen that the horizontal force F_x obtained with the 3D NWT matches with that computed by Morison's equation. The horizontal force F_x decreases with the pitch angle and F_z increases with the pitch angle. This could be explained by the decrease of the projection area of the cylinder on the surface yoz and increase of the projection area of the cylinder on the surface xoy.

It is obvious that F_y, the lateral force, and M_y, M_z the rotational moments about x-axis and z-axis, are much less than the others, and can be neglected regardless of pitch angle θ. The numerical results match the physical phenomena and can be explained easily with the force analysis. In the case of $\psi = 0°, \phi = 0°$ the rotational moment M_y exerted on the cylinder about y-axis depends on the horizontal force F_x and the vertical force F_z. M_y increases with the increase of θ from 0° to 60°, then it decreases with the increase of θ from 60° to 90°. The maximum moment with $\theta = 60°$ is 10 times larger than that of vertical suspension.

2. Roll angle $\phi = (0°, 15°, 30°, 45°, 60°, 75°, 90°)$, pitch angle $\theta = 0°$.

In Figure 11b, it can be seen that the horizontal force F_x obtained from the 3D NWT matches with that computed with Morison's equation only for a limited range near to $\phi = 0°$. The reason is that the two coefficients C_m, C_d change with the increase of the roll angle ϕ. The values of C_m, C_d at $\phi = 0°$ no longer work with the increase of ϕ.

It can be seen that the lateral force F_y, the rotational moments M_y, M_z, about the y-axis and z-axis are not zero but small values. Both the horizontal force F_x and the vertical force F_z increase with the roll angle ϕ, but F_x decreases when the angle is 75°. The projection area of the cylinder on the surface xoy increases with the increase of θ from 0° to 90°, and the vertical force exerted on the cylinder also increases. The increase is quicker with the roll angel ϕ from 60° to 90°. The rotational moment M_x increases with the increase of ϕ from 0° to 60°, and then decreases with the increase of ϕ from 60° to 90°.

From the above simulations of the two cases, we can see that the changes of force could be explained by the change of the corresponding projection area. Additionally, the moment around a certain axis changes drastically with the change of angle. For example, when the cylinder rotates around the y-axis (pitch angle), the max value of M_y is 10 times larger than the initial value. For the vertical cylinder payload, there is no angle where all the forces and moments are minimal, but the initial posture could be an optimal selection.

4.2. Case 2: A Cuboid Payload Fixed Suspending in the 3D NWT

A cuboid payload is fixed and suspended in the 3D NWT as shown in Figure 1. The size of the cuboid is $1m \times 0.5m \times 0.5m$, and the draft is $d = 0.25m$. The cuboid's posture in the 3D NWT is represented by the three Euler angles. A series of simulations are done with different postures of the suspending cuboid in the 3D NWT.

1. Yaw angle $\psi = (0°, 15°, 30°, 45°, 60°, 75°, 90°)$, pitch and roll angle $\theta = 0°, \phi = 0°$.

The normalized forces and moments on the cuboid payload versus its yaw angle ψ are shown in Figure 12a. With the normal incident regular waves, the horizontal force F_x decreases with the increase of ψ from 0° to 90°. The projection area on the surface yoz is the biggest when $\psi = 0°$. The projection area on the surface yoz decreases with the increase of ψ from 0° to 90°. It can be seen only F_x changes drastically with the angle, which is not the same as the results of cylinder where the moment changes drastically.

2. Pitch angle $\theta = (0°, 15°, 30°, 45°, 60°, 75°, 90°)$, yaw and roll angle $\psi = 0°, \phi = 0°$.

The normalized forces and moments on the payload versus the pitch angle θ are shown in Figure 12b. It is obvious that both the lateral force F_y and the rotational moment M_x and M_z are near to zero no matter the pitch angle. The horizontal force F_x, the vertical force F_z.and the rotational moment M_y are all symmetrical around 45°. This could be easily explained by the change in the projection area. When the pitch angle θ increases from 0° to 45°, the horizontal force F_x decreases. Additionally, it increases when θ increases from 45° to 90°. At $\theta = 0°, 90°$, the regular waves which are normally incident to the cuboid's face with the largest surface area exert the maximum horizontal force on the cuboid. It can be seen that there is also not a drastically changed moment with the change of the angle.

3. Roll angle $\phi = (0°, 15°, 30°, 45°, 60°, 75°, 90°)$, pitch, yaw angle $\theta = 0°, \psi = 0°$.

The normalized forces and moments on the cuboid payload versus the roll angle ϕ are shown in Figure 12c. It can be seen that compared with M_x, the changes of other forces and moments are small, and M_x increases very quickly with the increase of ϕ from 0° to 30°, and decreases with ϕ from 30° to 90°. The phenomenon of a drastically changed moment is similar to the results of the cylinder.

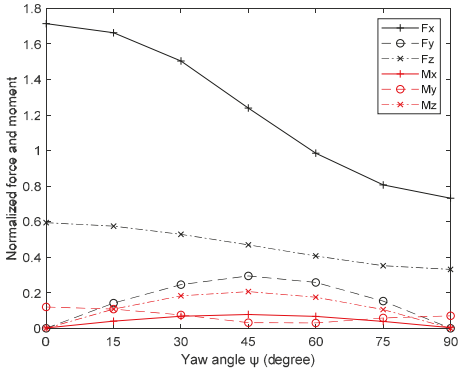

(**a**)

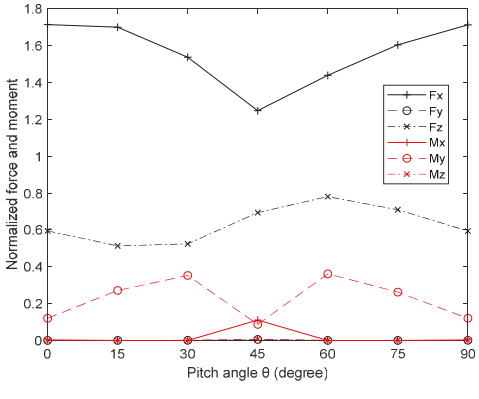

(**b**)

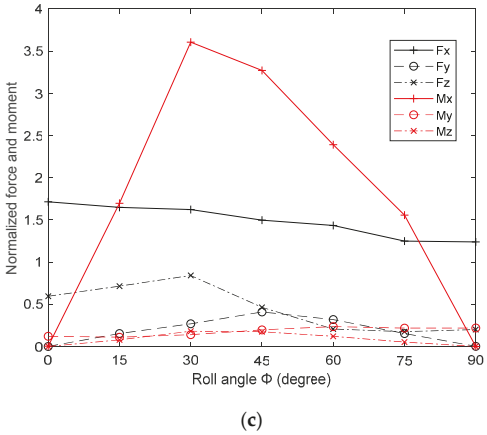

(**c**)

Figure 12. Normalized forces and moments on the cuboid payload versus a single posture angle. (**a**) the yaw angle ψ; (**b**) the pitch angle θ; (**c**) the roll angle ϕ.

For the two cases of the cylinder, the moment changes drastically with the angle. For the three cases of the cuboid payload, when the cuboid payload rotates around the x-axis (roll angle), the change of force and moment is similar to the cylinder cases. The changes of force could be explained by the change of the corresponding projection area, and the moment around a certain axis changes drastically with the change of angle. However, results when rotating around the z-axis (yaw angle) and y-axis (pitch angle) show no drastically changed moment.

To show that the difference could be brought by the initial posture, we plot the normalized forces and moments on the cylinder payload versus its yaw angle ψ when the roll angle $\phi = 90°$, just as Figure 13 shows. It can be seen that the result is similar to Figure 12a,b. When the roll angle $\phi = 90°$, the cylinder is horizontally placed, its length side along the y-axis. When this happens, the phenomenon of a drastically changed moment disappears.

For further study, we also plot the result when the vertically placed cuboid payload rotates around the y-axis and z-axis. Just as Figure 14 shows, the result is similar to Figure 12c. When the cuboid is vertically placed and the roll angle $\phi = 90°$, its long side along the z-axis. However, in Figure 14b, there is an exception, the drastically changed moment is not around the z-axis but the y-axis, other results are all as expected.

All three above figures show that the drastically changed moment is brought about by the initial posture. The moment around a certain axis changes drastically with the change of angle when the payload is vertically placed (which means the long side of the payload is vertical to the water surface) such as in Figure 14, and this phenomenon could happen when the horizontally placed payload changes to the vertical posture, such as in Figure 12c.

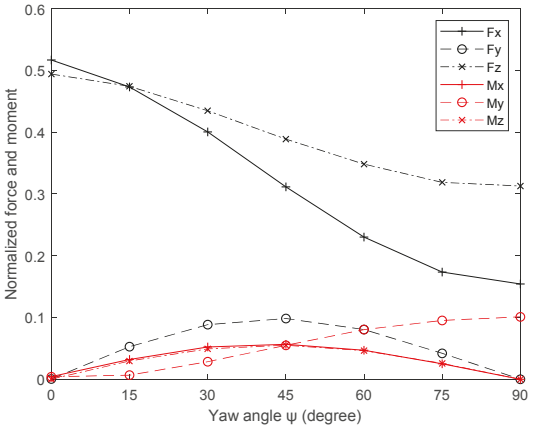

Figure 13. Normalized forces and moments on the cylinder payload versus its yaw angle ψ when the roll angle $\phi = 90°$.

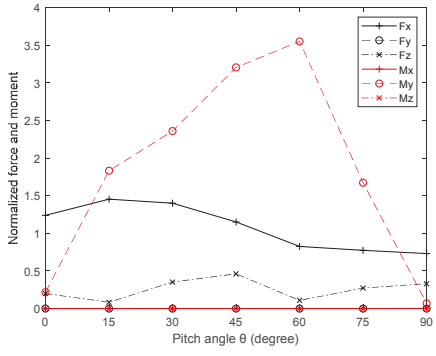

(**a**)

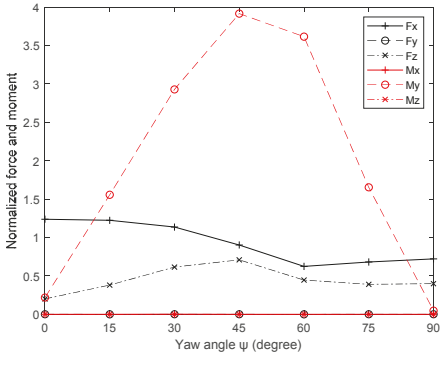

(**b**)

Figure 14. Normalized forces and moments on the cuboid payload versus a single posture angle when the roll angle $\phi = 90°$. (**a**) the pitch angle θ; (**b**) the yaw angle ψ.

4. Yaw ψ and roll ϕ concurrently change from 0° to 90°, pitch $\theta = 0°$.

The force and moment exerted on the cuboid versus the yaw angle ψ and the roll angle ϕ is shown in Figures 15 and 16. For the horizontal force F_x, it decreases with the yaw angle ψ regardless of the roll angle ϕ. When the roll angle is 0°, the cuboid is horizontally placed, with its long side vertical to the wave direction when the yaw angle is 0°. When the roll angle increases from 0° to 90°, the long side gradually changes to the vertically placed position; thus, the gradient along the yaw angle decreases with the increase of the roll angle. For the lateral force F_y, the result is symmetrical about yaw angle and roll angle.

The results of M_x could also be explained by the conclusion raised above. When the yaw angle is 0°, the roll angle increases to 90°, the cuboid changes from horizontally placed to be vertically placed, and the M_x changes drastically with the roll angle. When the yaw angle is 90°, the cuboid payload could not change to be vertically placed with the change of roll angle, and the phenomenon of a drastically changed moment disappears. When the yaw angle change from 0° to 90°, the phenomenon gradually disappears.

The result of M_y and M_z demonstrate the exceptional condition in Figure 14b. When the roll angle is 0°, the cuboid is horizontally placed, and there is no drastically changed moment. When the roll angle is 90°, the cuboid is vertically placed and the moment M_y, instead of M_z, drastically changes with

the yaw angle. There is also a transition when the roll angle increases from 0° to 90°. The amplitude of M_z is much less than the others, and can be neglected.

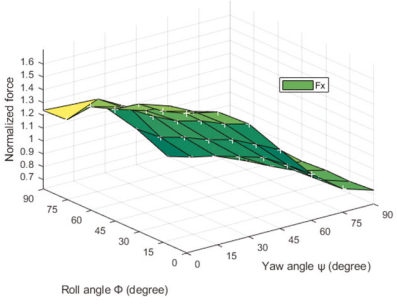

(**a**)

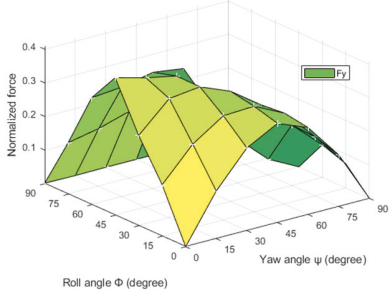

(**b**)

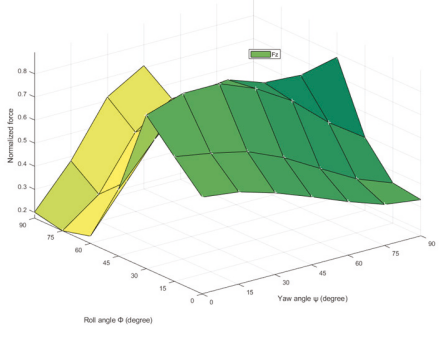

(**c**)

Figure 15. Normalized force on the cuboid payload versus yaw ψ and roll ϕ. (**a**) the horizontal force F_x; (**b**) the lateral force F_y; (**c**) vertical force F_z.

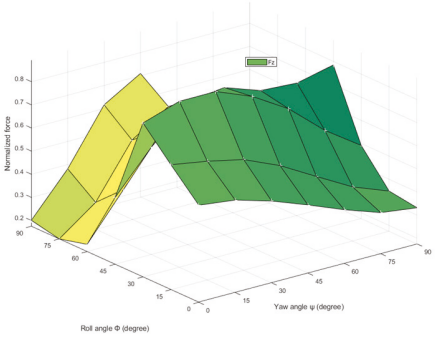

(**a**)

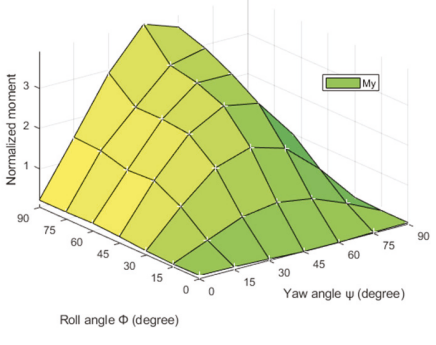

(**b**)

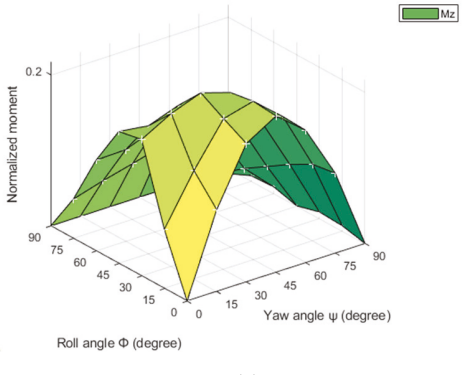

(**c**)

Figure 16. Normalized moment on the cuboid payload versus yaw ψ and roll ϕ. (**a**) the horizontal moment M_x; (**b**) the lateral moment M_y; (**c**) vertical moment M_z.

4.3. Parameter Studies

The parameter studies are done to analyze the effects of the cuboid's size and wave parameters on the forces and moments exerted on the cuboid payload. Here, in order to focus on the effects of cuboid's size and wave parameters, no posture angles are considered and the cuboid is horizontally placed.

1. Cuboid's size effects on forces and moments

The normalized forces and moments on the cuboid payload with different drafts, lengths, and widths are shown in Figure 17a–c. The results show that the horizontal force F_x increases with the increase of the payload draft and length. The vertical force F_z decreases slowly with the increase of the draft and increases with the length and width. The rotational moment M_y increases slowly with the increase of the payload draft d. The change of other forces and moments can be neglected.

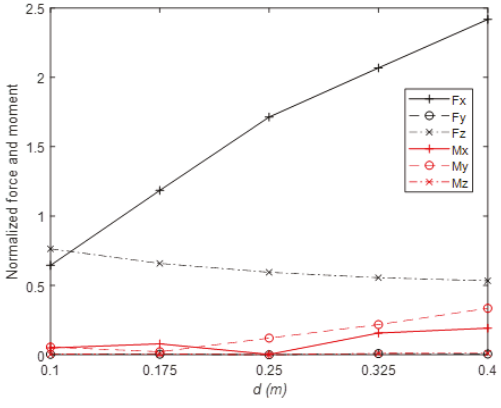

(**a**)

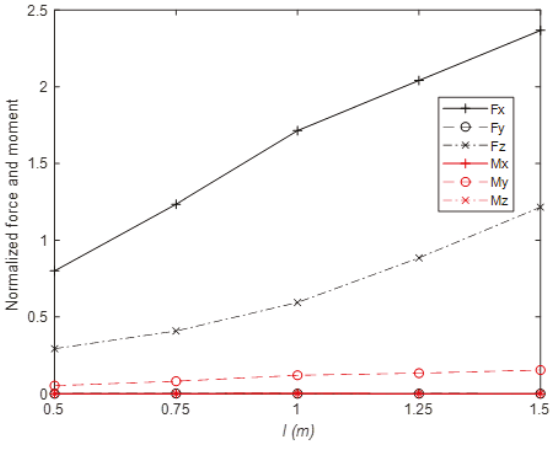

(**b**)

Figure 17. *Cont.*

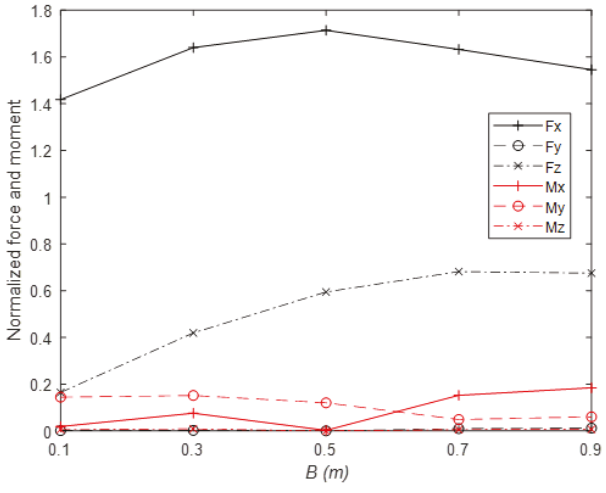

(**c**)

Figure 17. Normalized forces and moments on the cuboid payload with different size parameters. (**a**) with different drafts; (**b**) with different lengths; (**c**) with different widths.

2. Wave's parameters effects on forces and moments

The normalized forces and moments on the cuboid payload with different drafts, lengths, and widths are shown in Figure 18a,b. It can be seen that both the horizontal force F_x and the vertical force F_z increase with the increase of the wave amplitude and wavelength. The change of other forces and moments could be neglected.

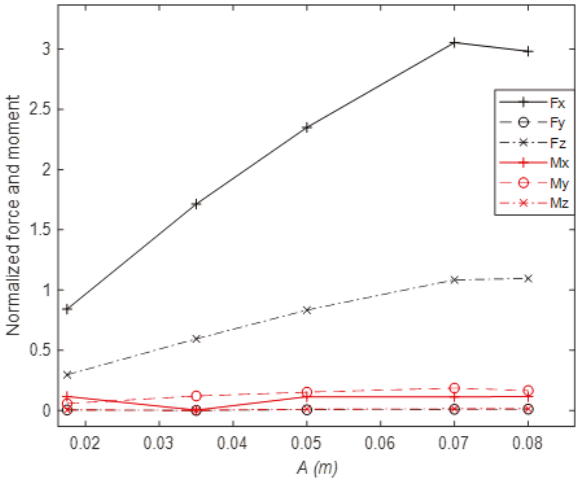

(**a**)

Figure 18. *Cont.*

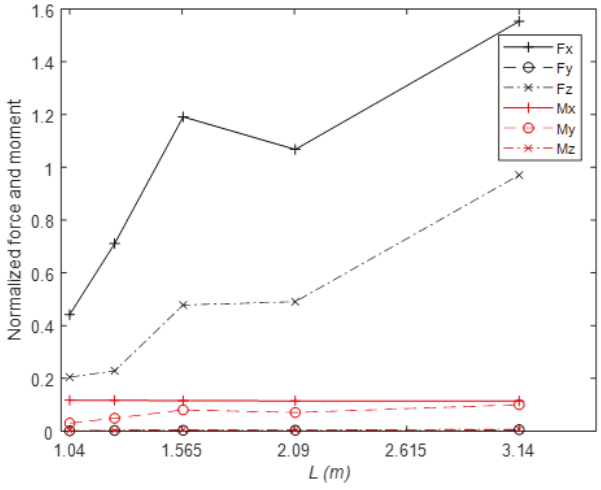

(**b**)

Figure 18. Normalized forces and moments on the cuboid payload with different wave parameters. (**a**) different wave amplitudes; (**b**) different wavelengths.

From the above parameter simulations, we can see that the horizontal force F_x and the rotational moment M_y exerted on the cuboid payload increase with the increase of its draft d, and its length l. The vertical force F_z and the rotational moment M_x increase with its width B. The increase of the wave amplitude A and wave length L cause the increase of the horizontal force F_x and the vertical force F_z.

5. Conclusions

In order to investigate regular wave interaction with a fixed suspending payload with different postures, a three-dimension NWT based on OpenFOAM and waves2foam is established. Regular wave interaction with a vertically suspended cylinder is investigated. The free surface elevation, horizontal wave force, as well as the corresponding amplitude spectra obtained by the FFT algorithm, are compared with the theory result and the results reported in [16] for validation. Then, the representation of the payload's posture in the regular wave is given. The forces and moments exerted on a suspended cylinder and a suspended cuboid with different postures are investigated separately. Finally, parameter studies in the case of payload's size wave parameters are considered.

It can be concluded that the moment around a certain axis changes drastically with the change of the same angle when the payload is initially vertically placed (which means the long side of the payload is vertical to the water surface). For example, the moment around the y-axis could change drastically when rotating around the y-axis. This phenomenon could also happen when the horizontally placed payload (which means the long side parallel to the sea level) changes to the vertical posture. There is an exception: when rotated around the z-axis, the drastically changed moment is not around the z-axis but the y-axis. Therefore, for the rectangular shape payload, it is better to keep the payload horizontally placed to prevent the drastic change of the moment. Additionally, the projection area of the payload vertical to the direction of force affects the corresponding force. It is better to keep the short side vertical to the incident direction of the wave; thus, a minimal horizontal force can be obtained. Through the simulations, some certain posture of the payload with the minimum forces and moments can be reached. It can guide the design of control strategies for the safe operation of offshore cranes, such as keeping the payload to a certain posture that suffers minimal force and moment or changing the controller weight of some forces and moments under specific circumstances.

Author Contributions: Conceptualization, M.Y. and X.M.; data curation, M.Y.; formal analysis, M.Y. and X.M.; funding acquisition, X.M.; investigation, M.Y.; methodology, M.Y.; project administration, X.M. and Y.L.; resources, M.Y.; Software, M.Y., W.B. and Z.L.; supervision, X.M.; validation, M.Y.; Visualization, M.Y.; writing—original draft preparation, M.Y.; writing—review and editing, M.Y., X.M. and W.B. All authors have read and agreed to the published version of the manuscript.

Funding: This research was funded by the Joint Fund of the National Nature Science Foundation of China and Shandong Province, grant number No. U1706228.

Conflicts of Interest: The authors declare no conflicts of interest.

References

1. DNV. *Modelling and Analysis of Marine Operations*; DNV Offshore Standards: Hovik, Norway, 2011.
2. Chau, F.; Taylor, R.E. Second-order wave diffraction by a vertical cylinder. *J. Fluid Mech.* **1992**, *240*, 571–599. [CrossRef]
3. Hunt, J.; Baddour, R. The diffraction of nonlinear progressive waves by a vertical cylinder. *Q. J. Mech. Appl. Math.* **1981**, *34*, 69–87. [CrossRef]
4. Bai, W.; Taylor, R.E. Numerical simulation of fully nonlinear regular and focused wave diffraction around a vertical cylinder using domain decomposition. *Appl. Ocean Res.* **2007**, *29*, 55–71. [CrossRef]
5. Del Jesus, M.; Lara, J.L.; Losada, I.J. Three-dimensional interaction of waves and porous coastal structures: Part I: Numerical model formulation. *Coast. Eng.* **2012**, *64*, 57–72. [CrossRef]
6. Lara, J.L.; del Jesus, M.; Losada, I.J. Three-dimensional interaction of waves and porous coastal structures: Part II: Experimental validation. *Coast. Eng.* **2012**, *64*, 26–46. [CrossRef]
7. Lin, P. A multiple-layer σ-coordinate model for simulation of wave–structure interaction. *Comput. Fluids* **2006**, *35*, 147–167. [CrossRef]
8. Kang, A.; Lin, P.; Lee, Y.J.; Zhu, B. Numerical simulation of wave interaction with vertical circular cylinders of different submergences using immersed boundary method. *Comput. Fluids* **2015**, *106*, 41–53. [CrossRef]
9. Ren, B.; Wen, H.; Dong, P.; Wang, Y. Numerical simulation of wave interaction with porous structures using an improved smoothed particle hydrodynamic method. *Coast. Eng.* **2014**, *88*, 88–100. [CrossRef]
10. Didier, E.; Martins, R.; Neves, M.G. Numerical and Experimental Modeling of Regular Wave Interacting with Composite Breakwater. *Int. Soc. Offshore Polar Eng.* **2013**, *23*, 9.
11. Ji, Q.; Dong, S.; Luo, X.; Soares, C.G. Wave transformation over submerged breakwaters by the constrained interpolation profile method. *Ocean Eng.* **2017**, *136*, 294–303. [CrossRef]
12. Wang, J.-H.; Zhao, W.-W.; Wan, D.-C. Development of naoe-FOAM-SJTU solver based on OpenFOAM for marine hydrodynamics. *J. Hydrodyn.* **2019**, *31*, 1–20. [CrossRef]
13. Liu, Z.H.; Wan, D.C.; Hu, C.H. Numerical investigation of regular waves interaction with two fixed cylinders in tandem arrangement. In Proceedings of the 37th ASME International Conference on Ocean, Offshore and Arctic Engineering, Madrid, Spain, 17–22 June 2018; ASME: New York, NY, USA, 2018.
14. Lara, J.; Higuera, P.; Maza, M.; del Jesus, M.; Losada, I.J.; Barajas, G. Forces induced on a vertical breakwater by incident oblique waves. In Proceedings of the 33rd Conference on Coastal Engineering, Santander, Spain, 1–6 July 2012; Coastal Engineering Proceedings: Santander, Spain, 2012.
15. Higuera, P.; Lara, J.L.; Losada, I.J. Three-dimensional interaction of waves and porous coastal structures using OpenFOAM®. Part I: Formulation and validation. *Coast. Eng.* **2014**, *83*, 243–258. [CrossRef]
16. Chen, L.; Zang, J.; Hillis, A.; Morgan, G.; Plummer, A. Numerical investigation of wave–structure interaction using OpenFOAM. *Ocean Eng.* **2014**, *88*, 91–109. [CrossRef]
17. Teng, B.; Zhang, X.; Ning, D. Interaction of oblique waves with infinite number of perforated caissons. *Ocean Eng.* **2004**, *31*, 615–632. [CrossRef]
18. Fang, Q.H.; Hong, R.C.; Guo, A.X.; Stansby, P.K.; Li, H. Analysis of hydrodynamic forces acting on submerged decks of coastal bridges under oblique wave action based on potential flow theory. *Ocean Eng.* **2018**, *169*, 242–252. [CrossRef]
19. Zheng, Y.-H.; Shen, Y.-M.; Ng, C.-O. Effective boundary element method for the interaction of oblique waves with long prismatic structures in water of finite depth. *Ocean Eng.* **2008**, *35*, 494–502. [CrossRef]
20. Abul-Azm, A.; Gesraha, M. Approximation to the hydrodynamics of floating pontoons under oblique waves. *Ocean Eng.* **2000**, *27*, 365–384. [CrossRef]

21. Gesraha, M.R. Analysis of Π shaped floating breakwater in oblique waves: I. Impervious rigid wave boards. *Appl. Ocean Res.* **2006**, *28*, 327–338. [CrossRef]
22. Zheng, Y.; Liu, P.; Shen, Y.; Wu, B.; Sheng, S. On the radiation and diffraction of linear water waves by an infinitely long rectangular structure submerged in oblique seas. *Ocean Eng.* **2007**, *34*, 436–450. [CrossRef]
23. Zheng, Y.; Shen, Y.; You, Y.; Wu, B.; Jie, D. Wave radiation by a floating rectangular structure in oblique seas. *Ocean Eng.* **2006**, *33*, 59–81. [CrossRef]
24. Song, H.; Tao, L. Wave Interaction with an Infinite Long Horizontal Elliptical Cylinder. In Proceedings of the 30th International Conference on Ocean, Offshore and Arctic Engineering, Rotterdam, The Netherlands, 19–24 June 2011; ASME: New York, NY, USA, 2011; pp. 589–597.
25. Weller, H.G.; Tabor, G.; Jasak, H.; Fureby, C. A tensorial approach to computational continuum mechanics using object-oriented techniques. *Comput. Phys.* **1998**, *12*, 620–631. [CrossRef]
26. Jacobsen, N.G.; Fuhrman, D.R.; Fredsøe, J. A wave generation toolbox for the open-source CFD library: OpenFoam®. *Int. J. Numer. Methods Fluids* **2012**, *70*, 1073–1088. [CrossRef]
27. Morison, J.; Johnson, J.; Schaaf, S. The force exerted by surface waves on piles. *J. Pet. Technol.* **1950**, *2*, 149–154. [CrossRef]

Journal of
Marine Science and Engineering

MDPI

Article

Numerical Prediction of the Vertical Responses of Planing Hulls in Regular Head Waves

Emre Kahramanoğlu, Ferdi Çakıcı * and Ali Doğrul

Department of Naval Architecture and Marine Engineering, Yıldız Technical University, 34349 Istanbul, Turkey; emrek@yildiz.edu.tr (E.K.); adogrul@yildiz.edu.tr (A.D.)
* Correspondence: fcakici@yildiz.edu.tr; Tel.: +90-212-383-2848

Received: 30 May 2020; Accepted: 19 June 2020; Published: 20 June 2020

Abstract: The evaluation of the hydrodynamic performance of planing vessels has always been one of the most attractive study fields in the maritime agenda. Resistance and self-propulsion studies have been performed using experimental and numerical methods by researchers for a long time. As opposed to this, the seakeeping performance of planing hulls is assessed with 2D approximation methods, but limitedly, while the experimental campaign is not cost-effective for several reasons. With this motivation, pitch and heave transfer functions and accelerations were obtained for a monohedral hull and a warped hull using a state of art commercial Reynolds-averaged Navier–Stokes (RANS) solver, in this study. Moreover, 2-DOF (degree of freedom) dynamic fluid–body interaction (DFBI) equations were solved in a coupled manner with an overset mesh algorithm, to find the instantaneous motion of the body. After verification, obtained numerical results at three different Froude numbers and a sufficiently large wave frequency range were compared with the experiments. The results showed that the employed RANS method offers a very accurate prediction of vertical motions and accelerations for planing hulls.

Keywords: CFD; overset mesh; planing hull; seakeeping; vertical motions

1. Introduction

Planing hulls have been widely used recently for commercial and military purposes in the naval architecture sector. Therefore, hydrodynamic calculations of planing hulls, in terms of resistance, seakeeping, and maneuvering, have become an important issue for marine applications. As is well known, the hydrodynamic investigation of planing hulls is relatively tougher compared to displacement type ships, due to several complex phenomena which are primarily caused by large motions of the body inside fluids. That is the main reason that the very first studies in this field were experimental and remained limited.

As a contribution to the experimental methods, the pioneered study was performed by Savitsky to discover the underlying physics in the planing regime [1]. He proposed an empirical approach that predicts the dynamic trim and total resistance of prismatic hull forms with a very simple algorithm. Several studies have been carried out after Savitsky's work. The most known experimental study was conducted by Fridsma [2], that covers the behaviors of the prismatic hull forms in both calm water and regular head waves. This study, especially the seakeeping part, is still accepted as a milestone benchmark case for researchers.

As the recent literature is reviewed, there are still many experimental studies carried out in order to explore planing hull hydrodynamics. For example, De Luca and Pensa [3] investigated the hydrodynamics of a warped chinned planing hull series, both in calm water and irregular head seas, experimentally [4]. Begovic et al. [5] studied a similar case by conducting model experiments in regular waves for their planing hull series. In another study, the irregular wave conditions of prismatic and

warped hull forms were also investigated by Begovic et al. [6], to find the best statistical approach to represent planing hull performance in the random sea. Santoro et al. [7] conducted a study on the prediction of pressure loads on a high speed planing hull with model experiments in regular waves.

Besides experimental studies, 2D methods based on potential flow theory were also developed by researchers, with many reasonable assumptions. The cornerstone research was conducted by Zarnick [8,9], where he proposed a mathematical model that predicts the vertical motions of planing hulls in regular and irregular head waves. This method simplifies the 3D problem into a 2D water entry problem, and then allows one to calculate the pitch and heave motions. Even though this method was proposed for the seakeeping performance of a planing hull, it can be used for calm water analysis with some reasonable assumptions. Akers [10] put forward a non-linear mathematical model based on Zarnick's theory and validated the results with the experiments of Fridsma [2]. Van Deyzen [11] also developed a mathematical method based on the theory of Zarnick and he implemented the modifications offered by Keuning [12]. Ghadimi et al. [13] developed another mathematical model which is based on Algarin and Tacson's studies [14,15] for the coupled heave and pitch motions of planing hulls at non-zero heel angle in regular head waves, and they validated the numerical results with the experimental data of several benchmark models. Tavakoli et al. [16] then used a similar method to calculate the hydrodynamic coefficients of a planing hull.

With the recent development in computational capability, CFD (computational fluid dynamics) solvers are widely used for the calculation of viscous flow around ships, including the planing hulls. Several studies revealing the calm water performance of planing vessels based on the Reynolds-averaged Navier–Stokes (RANS) approach have been carried out by researchers [17–20]. Thanks to this development, not only calm water characteristics, but also the seakeeping performance of the planing hulls, can be investigated by CFD solvers. Fu et al. [21] examined the hydrodynamic characteristics of a planing hull, both in calm water and head waves, numerically. In regular wave analyses, simulation results were in good agreement for the phases of heave and pitch motions, even though the amplitudes were over-predicted. Mousavariaad et al. [22] presented a comprehensive study about the planing hulls. In this study, they investigated the performance of the historical benchmark Fridsma hull in calm water in deep and shallow water conditions, with fixed and free to trim and sinkage cases. Moreover, their simulation conditions include the regular and irregular head waves in deep water. In regular head waves, they validated the simulation results with the available experimental data by transfer functions of heave and pitch motions and phases with a high order of accuracy. Masumi and Nikseresht [23] performed a numerical study to show the effect of finite depth to calm water resistance and added resistance. Although they investigated different head wave cases, they were only interested in the resistance of the planing hull. Judge et al. [24] made a comprehensive study of a high-speed deep-V planing hull form. They conducted model experiments and numerical simulations in both regular and irregular waves, and they focused on the slamming behavior of the planing hull. It is found that the largest slamming occurs in short and steep waves. The authors validated their numerical approach with vertical motions, accelerations and slamming pressures. Azcueta [25], Wang et al. [26] and Ling and Wang [27] utilized computational fluid dynamics approaches, so that the heave and pitch motions of a planing hull in regular head wave can be accurately predicted. Xiaosheng et al. [28,29] conducted numerical studies on the seakeeping performance of a planing vessel in a regular head wave. After validating the numerical results with the experimental data with a good accuracy, they used different designs to reach a better seakeeping performance.

According to recent literature, it might be said that there is still a room for a numerical investigation about the vertical motion prediction of planing vessels. In this study, URANS computations for a monohedral hull and a warped chine hull form were carried out by solving 2DOF dynamic fluid–body interaction (DFBI) equations with a commercial CFD solver (STAR CCM+) for regular head waves. A verification and validation study was carried out for one velocity and wave frequency for the heave motion. The computational domain was discretized using an overset mesh algorithm.

Three different Froude number cases were investigated by means of vertical motions (heave and pitch) and acceleration RAOs (response amplitude operator).

The paper is organized as follows: Section 2 depicts the geometric definition of the hull forms and numerical background, covering the solution procedure and the mesh algorithm. Section 3 gives information about the verification and validation processes. Section 4 gives the obtained numerical results with respect to the motion and acceleration RAOs. Finally, the concluding remarks were given in Section 5.

2. Methodology

2.1. Planing Hull Geometries

In this study, two different planing hull models were used for all simulations. One of them is a monohedral hull that has a constant deadrise angle and the other one is a warped hull (called W3 in [5]) whose deadrise angle changes from stern to bow. Both models belong to the study of Begovic et al. [5,30] The main particulars of these models are shown in Table 1. In Table 1, L_{OA} denotes the overall length of the model, B denotes the beam and Δ denotes the displacement of the model. LCG and VCG represent the longitudinal and vertical center of gravity, respectively. β, k_{yy}, T_{AP} and Fn_B depict the deadrise angle, gyration radius of the pitch motion, draught at the aft peak and the beam Froude number, respectively. Please note that $Fn_B = \frac{V}{\sqrt{gB}}$ where V denotes the forward speed, B denotes the breadth of the planing hull and g denotes the gravity constant.

Table 1. Main Particulars of Planing Hulls [5,30].

Main Particular	Mono	Warped
L_{OA} (m)	1.900	1.900
B (m)	0.424	0.424
Δ (N)	319.7	318.5
LCG (m)	0.697	0.586
VCG (m)	0.143	0.156
k_{yy} (m)	0.583	0.519
T_{AP} (m)	0.096	0.108
β (deg)	16.70	9.09–35.75
Fn_B (-)	1.67, 2.26, 2.82	

The 2D geometries of the monohedral and warped hull are shown in Figures 1 and 2, respectively. The L/B ratios are the same for both hull forms and equal to 4. The deadrise angle of the warped hull form is varied linearly from transom to 0.8 L, while the mono hull has constant deadrise angle. To avoid much spray and allow the transition to planing regime, the bow has been faired. Detailed information about the hull forms can be found in Begovic et al. [30]

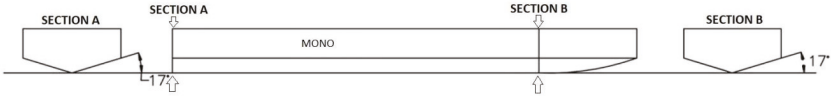

Figure 1. The 2D geometries of the mono hull.

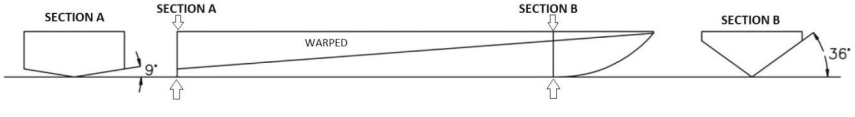

Figure 2. The 2D geometries of the warped hull.

2.2. Numerical Setup

2.2.1. Physics Modelling

The numerical analyses were conducted using a commercial CFD software, solving unsteady Reynolds-averaged Navier–Stokes (URANS) equations. The governing equations are the continuity equation and the momentum equations, considering that the flow is incompressible and turbulent. The continuity equation can be given as:

$$\frac{\partial U_i}{\partial x_i} = 0 \tag{1}$$

Velocity U_i can be derived as the mean velocity and the fluctuating velocity components, respectively.

$$U_i = \overline{U_i} + u_i' \tag{2}$$

The momentum equations can be written in tensor notation and Cartesian coordinates:

$$\frac{\partial U_i}{\partial t} + U_j \frac{\partial (U_i)}{\partial x_i} = \frac{1}{\rho}\frac{\partial P}{\partial x_i} + \frac{\partial}{\partial x_j}\left[\upsilon\left(\frac{\partial U_i}{\partial x_j} + \frac{\partial U_j}{\partial x_i}\right)\right] - \frac{\partial \overline{u_i' u_j'}}{\partial x_j} \tag{3}$$

Here, ρ is the fluid density, U_i is the velocity vector, and P is the pressure. The last two terms belong to the viscous stress tensor, while υ is the kinematic viscosity.

The solution procedure was based on a semi-implicit method for pressure-linked equations (SIMPLE) type algorithm. The turbulent flow was modeled using the k-ε turbulence model that is widely used in numerical ship hydrodynamics. Detailed information about this model can be found in Wilcox [31]. The hull was presumed to be free to only the heave and pitch motions. The dynamic fluid–body interaction (DFBI) method was implemented to represent 2-DOF (degree of freedom) motions accurately. With this implementation, the 2-DOF motion of the planing hull can be obtained by solving the linear and angular momentum equations:

$$\sum \vec{F} = m\vec{a} \tag{4}$$

$$\sum \vec{M_G} = I_G \vec{a_a} + \vec{\omega} \times I_G \vec{\omega} \tag{5}$$

In Equations (4) and (5), $\vec{F}$ represents the total force, m represents the mass and $\vec{a}$ represents the linear acceleration. $\vec{M_G}$, I_G, $\vec{a_a}$ and ω depict the total moment according to center of gravity, inertial mass moment, angular acceleration and angular speed, respectively.

Two different coordinate systems are defined. One of them is the earth fixed coordinate system, while the other one is fixed at the center of gravity of the hull. The fluids (water and air) are considered to flow in the negative x direction. The volume of fluid (VOF) approach [32] was utilized with high-resolution interface capturing (HRIC). The discretization orders and some other properties of the physical model are given in Table 2.

Table 2. Features of the Physical Modelling.

VOF scheme	Second-order
Convectional discretization	Second-order
Temporal discretization	First-order
Interpolation option	Linear
Iteration per one time-step	10

In the present work, the time step size was correlated with the encounter period and defined by considering ITTC [33] recommendations and another relevant study [22]. The time step sizes were calculated as follows:

$$\Delta t = \frac{T_e}{2^8} \tag{6}$$

2.2.2. Mesh Generation and Computational Domain

In this study, two different planing hulls were investigated numerically, to obtain the seakeeping performance in regular head waves. The computational domain was created to solve the viscous flow around the planing hulls, by taking the ITTC recommendations [33] into account. The computational domain created in the present study is shown in Figure 3. It should be noted that the computational domain and the mesh structure are set as identical, since these two models have the same length.

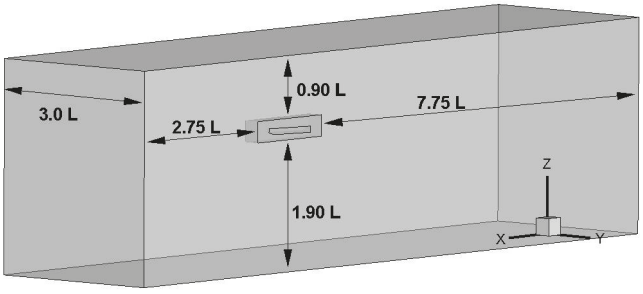

Figure 3. Computational domain dimensions.

In Figure 4, the boundary conditions are shown. As can be seen from this figure, the center lines of the model and the computational domain are aligned to be able to represent the symmetrical phenomena using only half of the domain. Therefore, the computational cost was reduced. The plane aligned with the centerline of the model was defined as the symmetry plane and the outlet plane was defined as the pressure outlet, while the other boundaries were set to be velocity inlet. The planing hull surfaces were defined as a no-slip wall to dictate that the normal component of the velocity is zero.

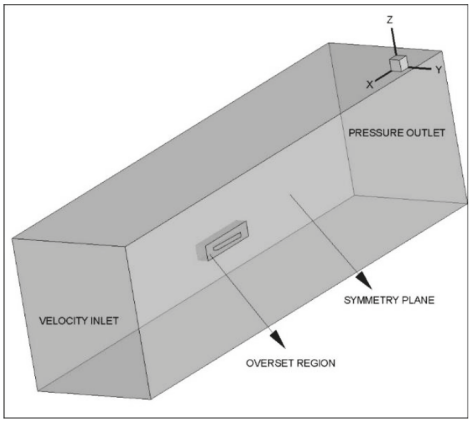

Figure 4. Boundary conditions.

The computational domain was discretized with hexahedral elements, based on the finite volume method. Since the overset mesh technique proved its perfection on high orientation and translation,

it was applied to represent the 2-DOF motions correctly. Therefore, two different mesh regions were created with fully hexahedral elements. The first one was the overset mesh region covering the planing hull, and its near region that is free to motion, in order to predict the vertical motions precisely. The second one was the outer region that the rigid mesh is employed. Trimmer mesh algorithm was employed in both overset and rigid mesh regions. Local mesh refinements were made, covering the free surface and Kelvin wave pattern. The prism layer mesh was applied near the hull geometry to model the flow in the near-wall region precisely, while keeping the wall y+ values between 30–300. Overlap refinements were used for good coupling between the overset and rigid mesh regions. The mesh structure and the refinements are given in Figure 5a,b.

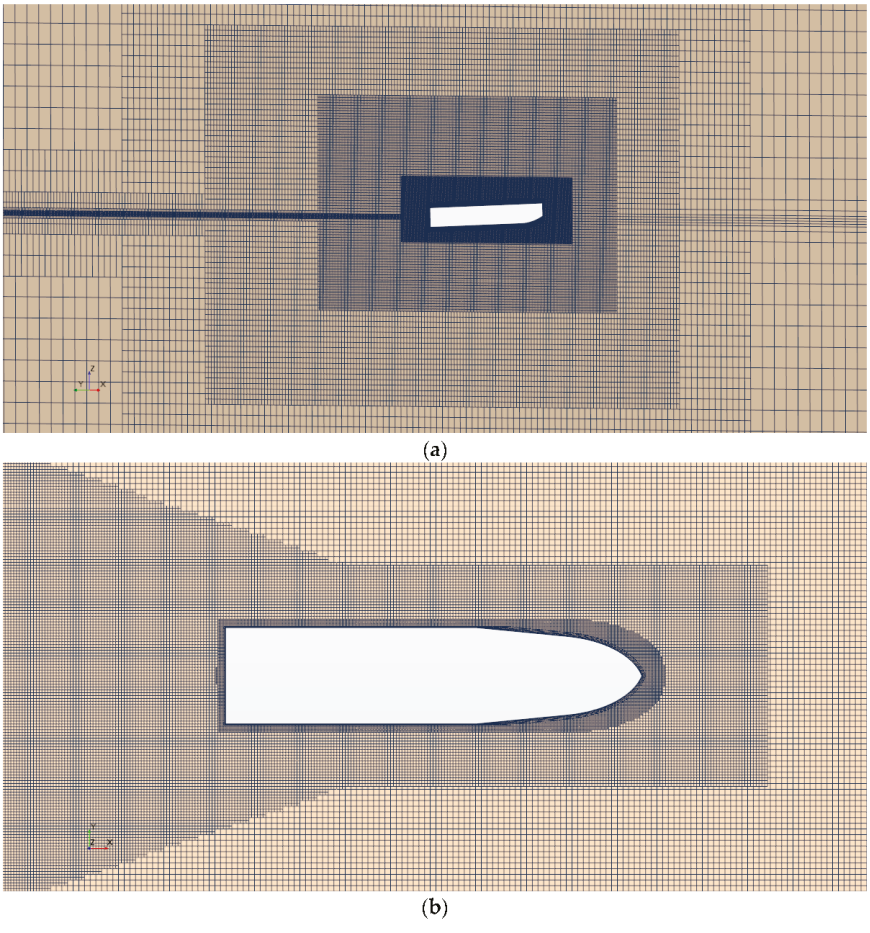

Figure 5. (**a**) Overset mesh structure around the hull. (**b**) Local refinements in the domain covering the free surface and the wave pattern.

3. CFD Verification Study

The verification study can be applied by reducing time-step and/or mesh sizes to show the convergence of the numerical approaches. In other words, it should show that any scalar value of the numeric solution would go a certain value, with an acceptable uncertainty when the mesh and/or time-step size is reduced. In this paper, the GCI (grid convergence index) method was used for

this purpose. This method, which is based on Richardson extrapolation [34], is proposed firstly by Roache [35] and modified by numerous studies [36–38]. The methodology presented by Celik et al. [39] was used to determine uncertainty with this technique, as numerous hydrodynamic studies from self-propulsion of submarines [40] to vertical motions of vessels [41].

Before starting the verification study, three different mesh and time-step sizes were determined with a constant refinement factor (r), which was selected as $\sqrt{2}$. After finishing all the analyses, the difference between any scalar values of the solutions can be calculated as follows:

$$\varepsilon_{21} = x_2 - x_1 \qquad \varepsilon_{32} = x_3 - x_2 \tag{7}$$

Here, x_1, x_2 and x_3 refer to the value of any scalar of fine, medium and coarse time-step or grid sizes, respectively. The convergence condition, which is the ratio of the difference between the solutions, has to be between 0 and 1 to have a monotonic convergence regime. It can be calculated as follows:

$$R = \frac{\varepsilon_{21}}{\varepsilon_{32}} \tag{8}$$

It also should be kept in mind that when a source of uncertainty (time step or mesh) is refined, the other one was kept constant and fine.

In Table 3, the uncertainties of the time step and grid size are in an applicable level. It should be kept in mind that, this mesh structure and time step size can be used for the other cases. It also should be noted that, since the relative difference between fine and medium time step size is around 2.5%, the medium time step size ($T_e/2^8$) is selected for all simulations similar to Mousavariaad et al. [22].

Table 3. Uncertainty Studies for Heave Transfer Functions (ωe = 7.59_Mono_V = 3.4 m/s).

Parameter	Grid Spacing	Time Step
R	$\sqrt{2}$	$\sqrt{2}$
X_1 (Fine)	1.080	1.109
X_2(Medium)	1.114	1.080
X_3 (Coarse)	1.184	1.022
R	0.49	0.51
GCI $_{FINE}$	3.90%	3.42%

4. Seakeeping Analyses

The seakeeping analyses are conducted for two different planing hull models, three different advance velocities and wide-range wave frequencies. The numerical cases are selected identically with the experimental ones [5], to ensure a reasonable comparison. It should be reported that the all numerical analyses took approximately 8–10 h of wall clock time in a 30-core processor with 128 GB RAM for five periods of simulations for each case.

The seakeeping analyses are conducted with the numerical cases listed in Table 4. The cases are named starting from C1 to C8. It has to be reminded that these cases are repeated for each Fn_B, and for each model, it means that the number of total case is $2 \times 3 \times 8 = 48$.

Table 4. Validation Study of Transfer Functions for the Selected Case.

Models	Fn_B (-)	Case Code	ω (rad/s)	k (rad/m)	λ (m)	A (m)	λ/L
Mono and Warped	1.67 2.26 2.82	C1	5.65	3.260	1.928	0.020	1.014
		C2	5.03	2.576	2.440	0.020	1.284
		C3	4.40	1.972	3.186	0.020	1.677
		C4	4.08	1.700	3.695	0.032	1.945
		C5	3.77	1.449	4.337	0.032	2.283
		C6	3.46	1.217	5.161	0.035	2.717
		C7	3.14	1.006	6.245	0.035	3.287
		C8	2.83	0.815	7.710	0.045	4.058

After observing a steady-state regime for each defined case, the time histories of heave and pitch motions are exported from the RANS solver, to be represented with sinusoidal curves. As there is a need to calculate the first harmonics (amplitude) of the motion for RAO, the trigonometric Fourier series expansion can be used. All the characteristics of a sinusoidal curve can be calculated as follows:

$$\eta_i(t) = \eta_{i,0} + \sum_{n=1}^{N} \eta_{i,n} \cos(\omega t + \beta_{i,n}) \quad n = 1, 2, 3 \ldots .. \qquad i = 3, 5 \tag{9}$$

$$a_{i,1} = \frac{2}{T} \int_0^T \eta_i(t) \sin(\omega t) dt \tag{10}$$

$$b_{i,1} = \frac{2}{T} \int_0^T \eta_i(t) \cos(\omega t) dt \tag{11}$$

$$\eta_{i,1} = \sqrt{a_{i,1}^2 + b_{i,1}^2} \tag{12}$$

$$\beta_{i,1} = \arctan\left(\frac{a_{i,1}}{b_{i,1}}\right) \tag{13}$$

Here, $\eta_{i,0}$ depicts the zeroth harmonic of the selected signal (heave or pitch), $a_{i,1}$ and $b_{i,1}$ depict the Euler coefficients; $\eta_{i,1}$ depicts the first harmonics of the selected motion, while $\beta_{i,1}$ depicts the phase angle. Since the motion can be represented by a single frequency that is encountered, the first harmonic of the motion signal is symbolized as η_i instead of $\eta_{i,1}$ for the simplicity. It should be noted that EFD (experimental fluid dynamics) represents the experimental results in all graphs.

4.1. Motion RAOs

In this subsection, the numerical results are compared with the available experimental data, in terms of RAOs of heave and pitch motions. The non-dimensional RAOs of vertical motions are indicated as follows:

$$\mathrm{RAO}_3 = \frac{\eta_3}{\mathrm{A}} \tag{14}$$

$$\mathrm{RAO}_5 = \frac{\eta_5}{\mathrm{Ak}} \tag{15}$$

where η_3, η_5, A and k depict the first harmonics of the heave and pitch motions, wave amplitude and wave number ($2\pi/\lambda$), respectively. Here, λ is the wavelength. It should be kept in mind that the wave amplitude (A) and wave number (k) are related to the sea surface state and those are listed in Table 4.

RAO graphs consist of three main regions, which are inertia, damping and hydrostatic dominated. The obtained results are discussed in this section by addressing these regions. The results obtained from the numerical study are given in Figure 6 for the mono hull, where the heave and pitch RAOs are compared with the available experimental data for $\mathrm{Fn_B}$ = 1.67. As clearly seen, the results in inertia region are generally in satisfactorily good agreement with experimental data for heave motion. At only one wave frequency, which remains in the hydrostatic region, CFD overestimates the heave motion compared to the experimental data. It is noted that the general trend for pitch motion at $\mathrm{Fn_B}$ = 1.67 follows the experimental data.

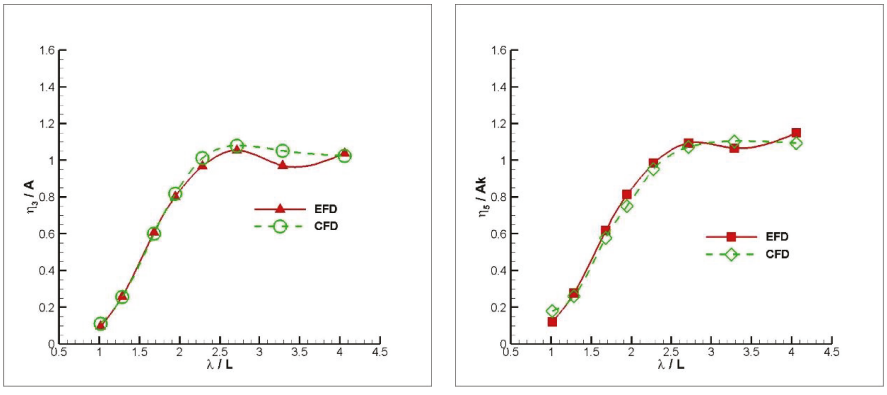

Figure 6. Heave (**left**) and Pitch (**right**) RAOs of the mono hull at Fn_B = 1.67.

In Figure 7, a similar comparison is made for Fn_B = 2.26 for the monohedral hull. Similar to lowest Fn_B, the discrepancies from the experimental data increase for the relatively larger wavelengths for the heave motion. Similar comments are valid for the pitch motions for the Fn_B = 2.26 case for the mono hull.

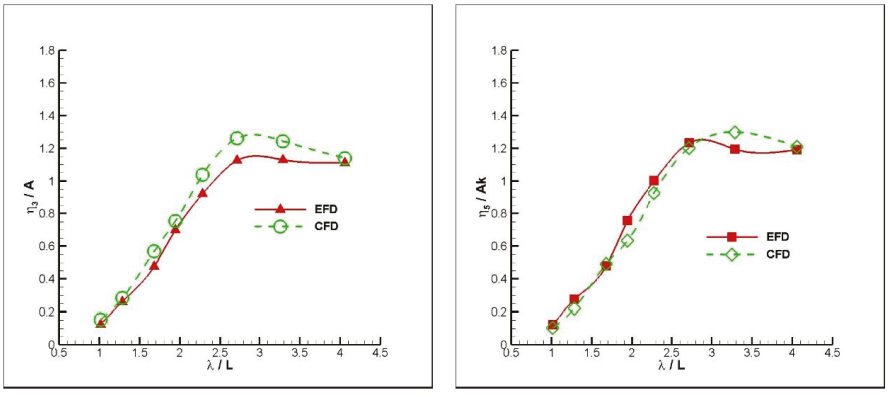

Figure 7. Heave (**left**) and Pitch (**right**) RAOs of the mono hull at Fn_B = 2.26.

Figure 8 reveals the investigation of RAO at the highest Fn_B case. It can be easily seen that CFD generally overestimates the heave motion while it underestimates the pitch motion. It is obvious that the results obtained from CFD are in satisfactorily good agreement with the available experimental data for both heave and pitch motions, for all advance velocities investigated in this study.

The results obtained from the numerical approach for the warped hull are compared with the experimental data in Figures 9–12. In Figure 9, the heave and pitch transfer functions are plotted against the experimental data for the Fn_B = 1.67. For relatively larger wavelength regions, the numerical method overestimates the heave motion expect for the largest wavelength. For the pitch motion, while the results of the numerical method are in good agreement with experiments, it can be concluded that it generally underestimates the pitch motion.

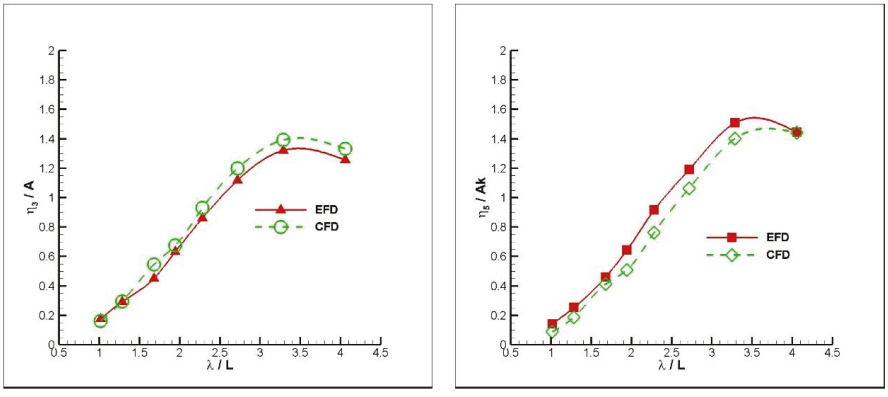

Figure 8. Heave (**left**) and Pitch (**right**) RAOs of the mono hull at Fn_B = 2.82.

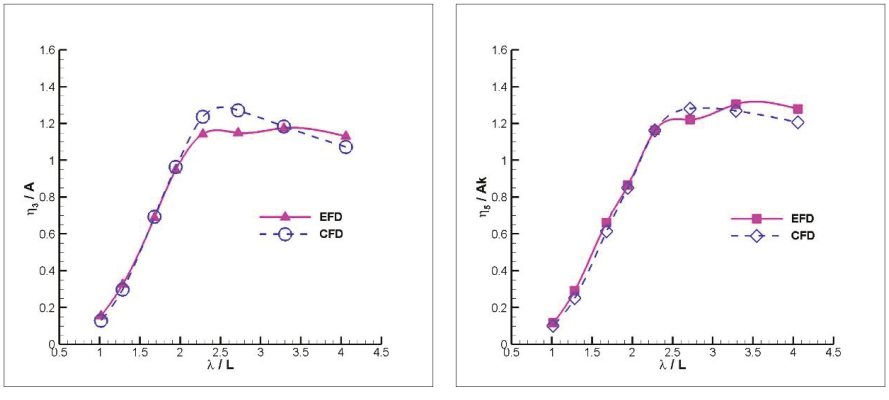

Figure 9. Heave (**left**) and Pitch (**right**) RAOs of the warped hull at Fn_B = 1.67.

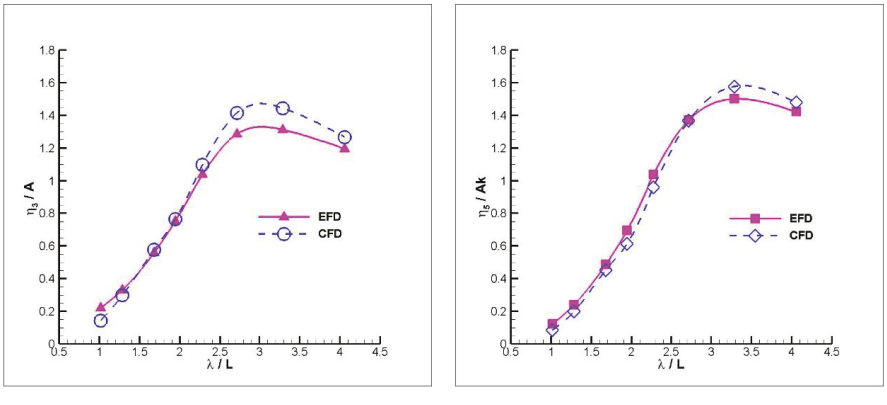

Figure 10. Heave (**left**) and Pitch (**right**) RAOs of the warped hull at Fn_B = 2.26.

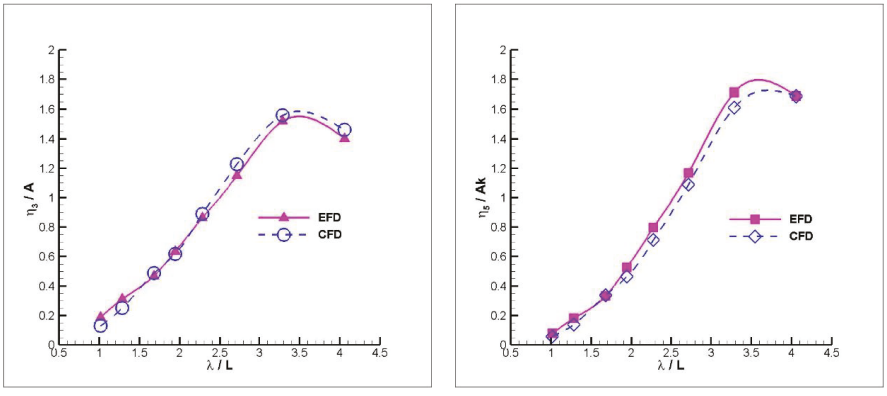

Figure 11. Heave (**left**) and Pitch (**right**) RAOs of the warped hull at Fn_B = 2.82.

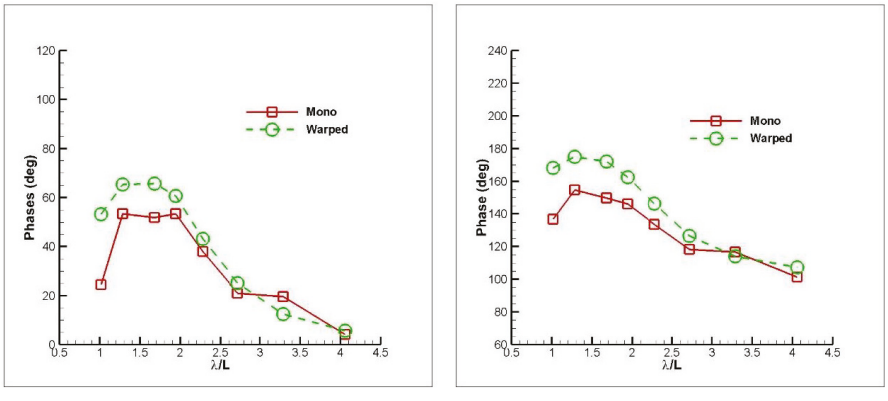

Figure 12. Phases of heave (**left**) and pitch (**right**) for both models at Fn_B = 1.67.

Similar to the mono hull case, it can be easily deduced from Figure 10 that the difference for the heave motion is getting higher for the relatively larger wavelengths for the Fn_B = 2.26 case. For the pitch motion, a better agreement than heave motion can be observed in this case as well.

Figure 11 represents the highest advance velocity case, Fn_B = 2.82. Even though CFD generally overestimates the heave motion, it underestimates the heave motion in the inertia region. However, it underestimates the pitch motion for the entire wavelength range.

For both planing hull types, more or less the same findings are obtained for vertical motions. Generally, CFD overestimates the heave motion, although it rarely underestimates the heave motion in the inertia region. A better agreement is observed for the pitch motion for all the Fn_B cases, although it mostly underestimates the pitch motion. Also, for both planing hull types, the largest deviation is detected in Fn_B = 2.26 case for the heave motion, at the hydrostatic region in particular. Figures 12–14 show the phase between the wave position at the fixed global coordinate system and heave and pitch motions for the mono and warped hull. The same trends in phases are observed, more or less, for both advance speeds and hull types.

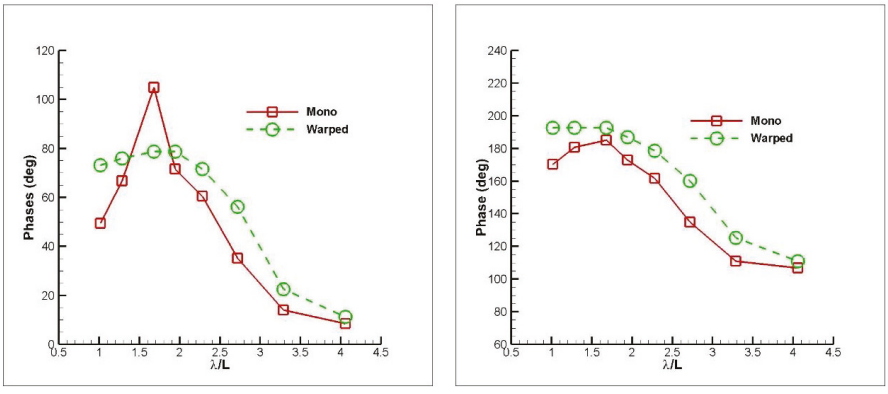

Figure 13. Phases of heave (**left**) and pitch (**right**) for both models at Fn_B = 2.26.

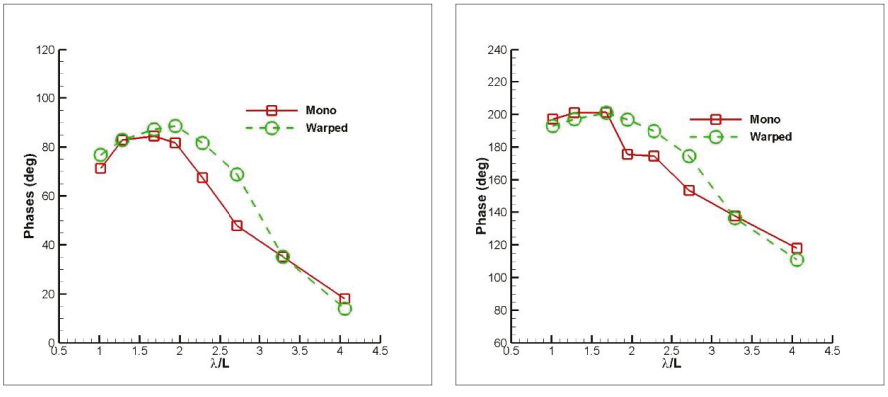

Figure 14. Phases of heave (**left**) and pitch (**right**) for both models at Fn_B = 2.8.

4.2. Acceleration RAOs

After obtaining the time histories of the accelerations at CoG (center of gravity) using CFD, bow accelerations are computed as follows:

$$a_{bow}(t) = a_{CoG,\ heave}(t) - x_{bow}a_{CoG,pitch}(t) \tag{16}$$

where, $a_{bow}(t)$ denotes the time series of bow accelerations, $a_{CoG,\ heave}(t)$ and $a_{CoG,\ pitch}(t)$ denote the time series of heave and pitch accelerations and x_{bow} represents the distance between center of gravity and bow. After reaching the steady state condition, instead of the Fourier series expansion, through to peak analysis, is used for the bow acceleration RAO that is non-dimensionalized by dividing to the gravity constant. The reason of using through to peak analysis is that there is more than one frequency in bow acceleration frequency plot, as opposed to the motion frequency plot that contains reasonable energy. More details will be given below.

The accelerations at bow for both models are shown in Figures 15–17. The accelerations at bow are compared for Fn_B = 1.67 for both models in Figure 15. For mono hull, the numerical results are in satisfactorily good agreement with the experimental data. The general tendency of the results for warped hull is quite remarkable with the experimental data, while there are larger deviations than mono hull.

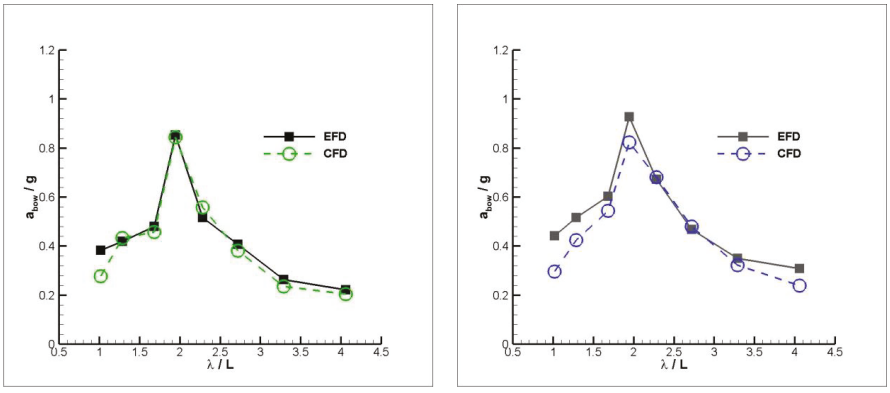

Figure 15. Bow accelerations for mono (**left**) and warped (**right**) hulls at Fn_B = 1.67.

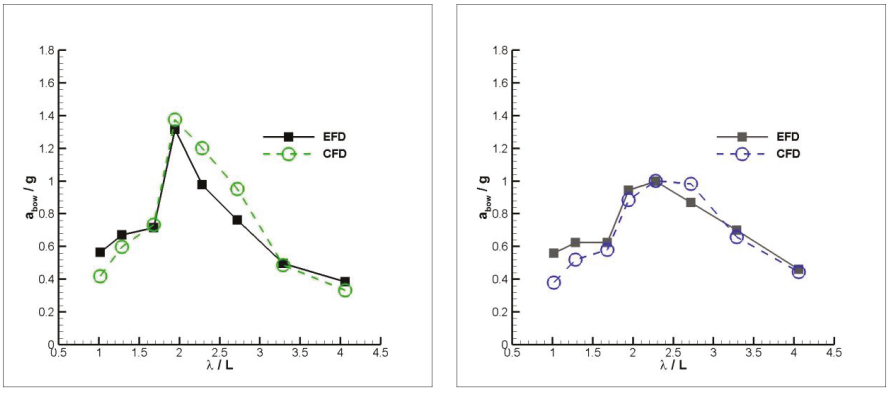

Figure 16. Bow accelerations for mono (**left**) and warped (**right**) hulls at Fn_B = 2.26.

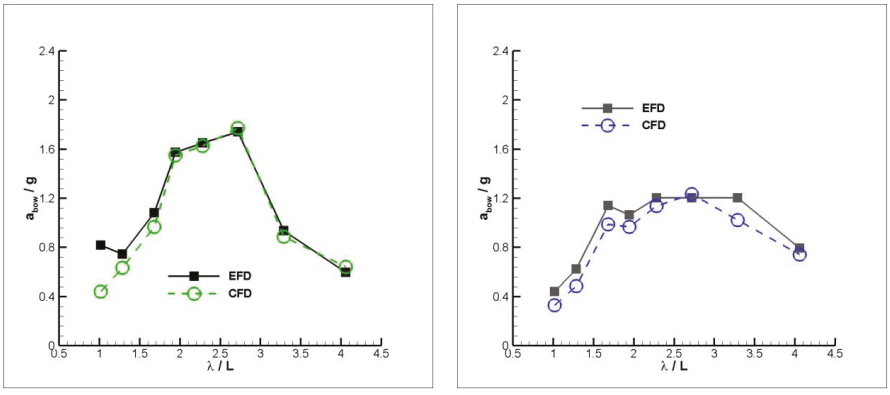

Figure 17. Bow accelerations for mono (**left**) and warped (**right**) hulls at Fn_B = 2.82.

In Figures 16 and 17, the same comparison is made for the higher Froude numbers. In these figures, the general tendency of the bow accelerations is similar with the experiments, although there are some differences for mono hull. However, the tendency is not similar for warped hull, even though the differences are not remarkably high, except for Fn_B = 2.82, λ/L = 1.677 case.

As is seen in Equation (16), the bow acceleration signal is composed of two signals: heave and pitch accelerations. The time histories of heave and pitch motions and their frequency domain response for the case C8 for Fn_B = 2.82 for the warped hull are given in Figures 18 and 19 as an example. As it is drawn from these figures, the only and dominant frequency for heave and pitch motions is the encounter frequency. Therefore, there is only one apparent peak in frequency domain response. It means that RAO can be easily calculated using Equations (9)–(15).

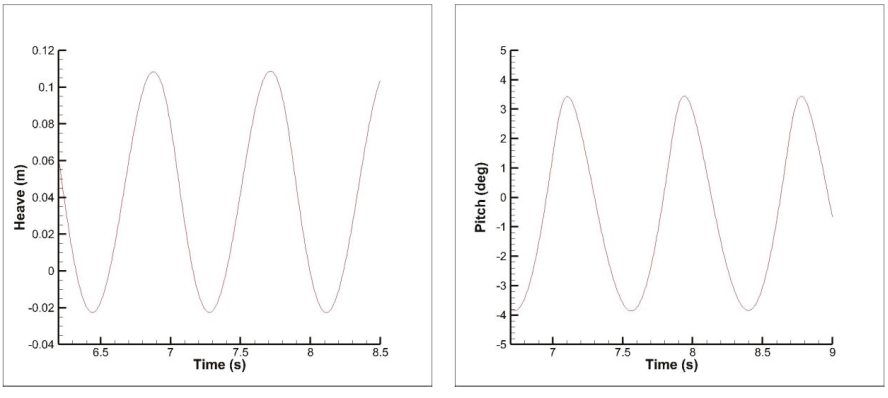

Figure 18. Time histories of heave (**left**) and pitch (**right**) motions for C7, Fn_B = 2.26, mono hull.

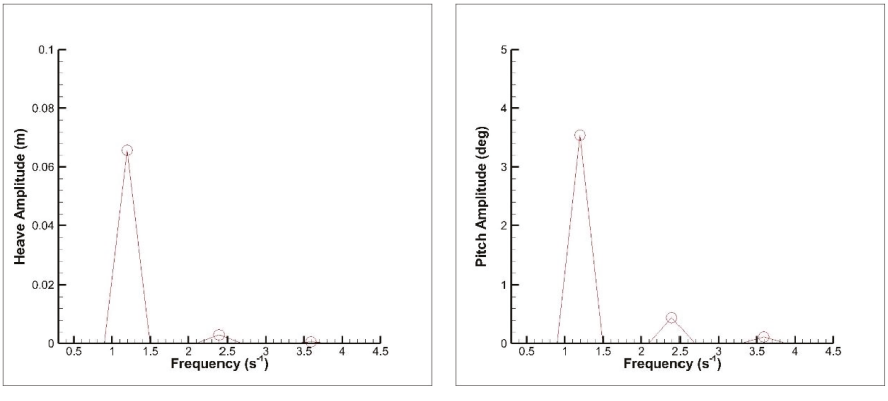

Figure 19. Frequency domain response of heave (**left**) and pitch (**right**) motions for C8, Fn_B = 2.82, warped hull.

On the other hand, the time histories of heave and pitch accelerations and their frequency domain responses for the same case are given in Figures 20 and 21. As is deduced from these figures, the heave and pitch acceleration signals do not consist of only encounter frequency; there are also other peaks. Therefore, through to peak analysis is used during the calculation of bow RAO.

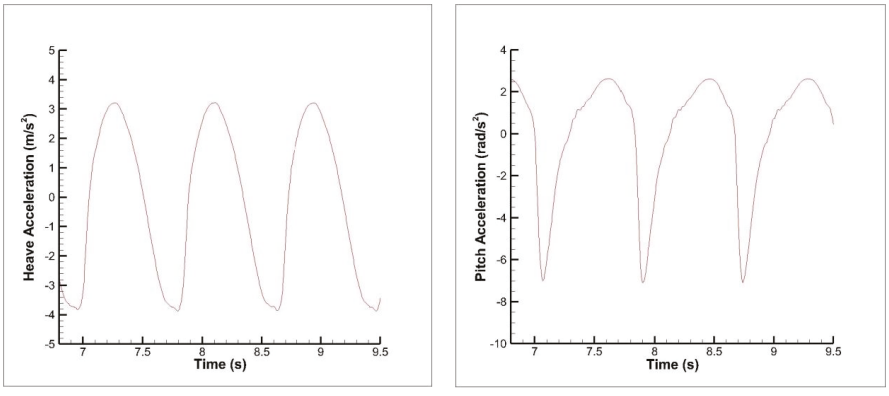

Figure 20. Time histories of heave (**left**) and pitch (**right**) accelerations for C8, Fn_B = 2.82, warped hull.

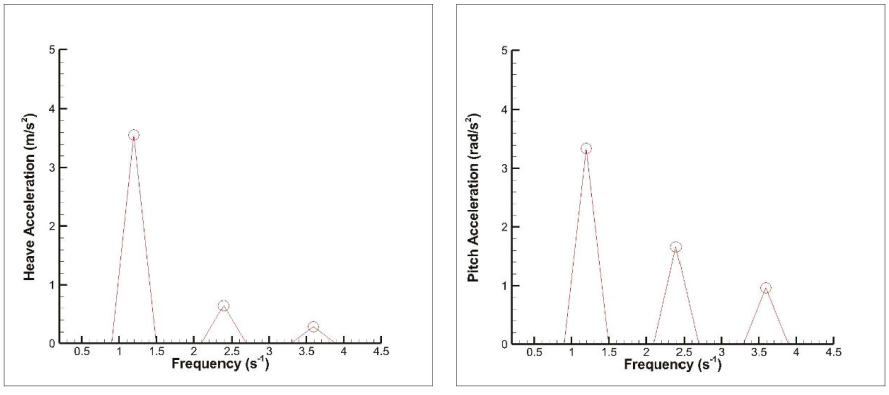

Figure 21. Frequency domain response of heave (**left**) and pitch (**right**) accelerations for C8, Fn_B = 2.82, warped hull.

5. Conclusions

Vertical motions of two different planing hull types under regular head waves are obtained using a commercial RANS solver in the present paper. After conducting a reliable verification study, the analyses are carried out at a sufficiently large frequency range and three different forward speeds. In accordance with the obtained results, the following comments can be made:

- An employed viscous solver is reliable in predicting heave and pitch motions in regular waves and bow accelerations for each case.
- In general, the heave motion is overestimated, while the pitch motion is underestimated at almost all frequencies and advance velocities for both hull forms.
- The deviations between the numerical and experimental results are getting larger with the increase in the wavelength, especially for the heave motion.
- The largest deviations are observed in the minimum wavelength cases (Case 1), for both models at all advance velocities. Since the motions are reasonably smaller in the inertia region, these deviations might be directly related to the measurement difficulties in the experiments.
- Similar to the experiments, more than one dominant frequency is observed in the accelerations. Therefore, the comparison of acceleration RAOs is made with through to peak analysis.

- Since there is more than one dominant frequency in the acceleration signal, the RAO calculation technique might cause a small variation in these results.

As a planned further work, the investigation of irregular wave characteristics for planing vessels will be carried out by the authors.

Author Contributions: Conceptualization, Methodology, Writing, Investigation, Verification and Software: E.K.; Conceptualization, Methodology, Writing, Investigation, Verification and Software: F.Ç.; Conceptualization, Methodology, Writing, Investigation, Verification and Software: A.D. All authors have read and agreed to the published version of the manuscript.

Funding: The first author is supported by the Scientific and Technological Research Council of Turkey (TÜBİTAK) during his PhD.

Acknowledgments: The authors would like to thank Ermina BEGOVIC for private discussions throughout the writing process of this paper.

Conflicts of Interest: The authors declare no conflict of interest.

References

1. Savitsky, D. Hydrodynamic Design of Planing Hulls. *Mar. Technol. SNAME News* **1964**, *1*, 71–95.
2. Fridsma, G. *A Systematic Study of the Rough-Water Performance of Planing Boats*; Stevens Inst of Tech Hoboken NJ Davidson Lab.: Hoboken, NJ, USA, 1969.
3. De Luca, F.; Pensa, C. The Naples warped hard chine hulls systematic series. *Ocean Eng.* **2017**, *139*, 205–236. [CrossRef]
4. De Luca, F.; Pensa, C. The Naples Systematic Series—Second part: Irregular waves, seakeeping in head sea. *Ocean Eng.* **2019**, *194*, 106620. [CrossRef]
5. Begovic, E.; Bertorello, C.; Pennino, S. Experimental seakeeping assessment of a warped planing hull model series. *Ocean Eng.* **2014**, *83*, 1–15. [CrossRef]
6. Begovic, E.; Bertorello, C.; Pennino, S.; Piscopo, V.; Scamardella, A. Statistical analysis of planing hull motions and accelerations in irregular head sea. *Ocean Eng.* **2016**, *112*, 253–264. [CrossRef]
7. Santoro, N.; Begovic, E.; Bertorello, C.; Bove, A.; De Rosa, S.; Franco, F. Experimental Study of the Hydrodynamic Loads on High Speed Planing Craft. *Procedia Eng.* **2014**, *88*, 186–193. [CrossRef]
8. Zarnick, E.E. A Nonlinear Mathematical Model of Motions of a Planing Boat in Regular Waves; David W Taylor Naval Ship Research and Development Center Bethesda Md Dtnsrdc-78/032, USA. 1978. Available online: https://apps.dtic.mil/docs/citations/ADA052039 (accessed on 18 March 2020).
9. Zarnick, E.E. A Nonlinear Mathematical Model of Motions of a Planing Boat in Irregular Waves; David W Taylor Naval Ship Research and Development Center Bethesda Md, Dtnsrdc/Spd-0867-91, USA. 1979. Available online: https://apps.dtic.mil/docs/citations/ADA052039 (accessed on 18 March 2020).
10. Akers, R.H. Dynamic Analysis of Planing Hulls in the Vertical Plane; Meeting of New England Section of SNAME. 1999, p. 19. Available online: https://d1wqtxts1xzle7.cloudfront.net/32221394/nes42999.pdf?1383459146=&response-content-disposition=inline%3B+filename%3DDynamic_Analysis_of_Planing_Hulls_in_the.pdf&Expires=1592664320&Signature=d7eiv564cfspF2x346l1qvXMyEZocxjwSCdcQydINtQAyJd5ISA2eRPai8ANcOt2Q1icLfbIlPmf~dAQFDLMiwzMB4PszT6BUnmzAlk3NR2t0KzKQPKTbV5DSA70UCG4S5hYmu9v75LUxL6g1ihBrjQOFzJ4~ortZYnkO3YTIRUMMAdJzKSaeEsEnnmnGKVFC1AUlJ1VYtk~8yrY7~T2t7udCkCIVqhR2USA4J7ZLNdg-06KakhDagZ2CmS5xeL~3o04FX8dMR98l~Hvl6~2q1RCqhVd1Xfkjr-1uOuJvPKiY7Os0r1HsNy4NXfw69dvv~dHaO8lLEZuPg2N8Qb9VG1g__&Key-Pair-Id=APKAJLOHF5GGSLRBV4ZA (accessed on 18 March 2020).
11. van Deyzen, A. A Nonlinear Mathematical Model of Motions of a Planing Monohull in Head Seas. In Proceedings of the HIPER08, Naples, Italy, 18–19 September 2008; p. 14.
12. Keuning, J.A. Non-Linear Behaviour of Fast Mono-Hulls in Head-Waves. Ph.D. Thesis, Delft University of Technology, Delft, The Netherlands, 1994.
13. Ghadimi, P.; Tavakoli, S.; Dashtimanesh, A. Coupled heave and pitch motions of planing hulls at non-zero heel angle. *Appl. Ocean Res.* **2016**, *59*, 286–303. [CrossRef]
14. Algarín, R.; Tascón, O. Hydrodynamic Modeling of Planing Boats with Asymmetry and Steady Condition. In Proceedings of the 9th Conference on High Sped Marine Vehicles, Naples, Italy, 26–27 May 2011.

15. Algarín, R.; Tascón, O. Analysis of Dynamic Stability of Planing Craft on the Vertical Plane. *Ship Sci. Technol.* **2014**, *8*, 35–43. [CrossRef]
16. Tavakoli, S.; Dashtimanesh, A.; Sahoo, P.K. Prediction of Hydrodynamic Coefficients of Coupled Heave and Pitch Motions of Heeled Planing Boats by Asymmetric 2D+T Theory. In Proceedings of the 37th International Conference on Ocean, Offshore & Arctic Engineering (OMAE2018), Madrid, Spain, 17–22 June 2018; p. V07AT06A009. [CrossRef]
17. De Luca, F.; Mancini, S.; Miranda, S.; Pensa, C. An Extended Verification and Validation Study of CFD Simulations for Planing Hulls. *J. Ship Res.* **2016**, *60*, 101–118. [CrossRef]
18. Mancini, S.; De Luca, F.; Ramolini, A. Towards CFD Guidelines for Planing Hull Simulations Based on the Naples Systematic Series. In Proceedings of the Computational Methods in Marine Engineering VII (Marine 2017), Nantes, France, 15–17 June 2017.
19. Sukas, O.F.; Kinaci, O.K.; Cakici, F.; Gokce, M.K. Hydrodynamic assessment of planing hulls using overset grids. *Appl. Ocean Res.* **2017**, *65*, 35–46. [CrossRef]
20. Judge, C.; Mousaviraad, M.; Stern, F.; Lee, E.; Fullerton, A.; Geiser, J.; Schleicher, C.; Merrill, C.; Weil, C.; Morin, J.; et al. Experiments and CFD of a high-speed deep-V planing hull—-Part I: Calm water. *Appl. Ocean Res.* **2020**, *96*, 102060. [CrossRef]
21. Fu, T.C.; Brucker, K.A.; Mousaviraad, S.M.; Ikeda, C.M.; Lee, E.J.; O'Shea, T.T.; Wang, Z.; Stern, F.; Judge, C.Q. An Assessment of Computational Fluid Dynamics Predictions of the Hydrodynamics of High-Speed Planing Craft in Calm Water and Waves. In Proceedings of the 30th Symposium on Naval Hydrodynamics, Tasmania, Australia, 2–7 November 2014.
22. Mousaviraad, S.M.; Wang, Z.; Stern, F. URANS studies of hydrodynamic performance and slamming loads on high-speed planing hulls in calm water and waves for deep and shallow conditions. *Appl. Ocean Res.* **2015**, *51*, 222–240. [CrossRef]
23. Masumi, Y.; Nikseresht, A.H. 2DOF numerical investigation of a planing vessel in head sea waves in deep and shallow water conditions. *Appl. Ocean Res.* **2019**, *82*, 41–51. [CrossRef]
24. Judge, C.; Mousaviraad, M.; Stern, F.; Lee, E.; Fullerton, A.; Geiser, J.; Schleicher, C.; Merrill, C.; Weil, C.; Morin, J.; et al. Experiments and CFD of a high-speed deep-V planing hull—Part II: Slamming in waves. *Appl. Ocean Res.* **2020**, *97*, 102059. [CrossRef]
25. Azcueta, R. Steady and Unsteady RANSE Simulations for Planing Craft. In Proceedings of the 7th Conference on Fast Sea Transportation FAST'03, Ischia, Italy, 7–10 October 2003.
26. Wang, S.; Su, Y.; Zhang, X.; Yang, J. RANSE simulation of high-speed planning craft in regular waves. *J. Mar. Sci. Appl.* **2012**, *11*, 447–452. [CrossRef]
27. Ling, H.; Wang, Z. Numerical prediction and analysis of motion response of high speed planing craft in regular waves. *J. Jiangsu Univ. Sci. Technol. Nat. Sci. Ed.* **2019**, *33*, 1–8.
28. Bi, X.; Shen, H.; Zhou, J.; Su, Y. Numerical analysis of the influence of fixed hydrofoil installation position on seakeeping of the planing craft. *Appl. Ocean Res.* **2019**, *90*, 101863. [CrossRef]
29. Bi, X.; Zhuang, J.; Su, Y. Seakeeping Analysis of Planing Craft under Large Wave Height. *Water* **2020**, *12*, 1020. [CrossRef]
30. Begovic, E.; Bertorello, C. Resistance assessment of warped hull form. *Ocean Eng.* **2012**, *56*, 28–42. [CrossRef]
31. Wilcox, D.C. *Turbulence Modeling for CFD*, 3rd ed.; DCW Industries: La Cãnada, CA, USA, 2006.
32. Hirt, C.W.; Nichols, B.D. Volume of fluid (VOF) method for the dynamics of free boundaries. *J. Comput. Phys.* **1981**, *39*, 201–225. [CrossRef]
33. 7.5-03-02-03 Practical Guidelines for Ship CFD Applications. In Proceedings of the ITTC—Recommended Procedures and Guidelines, Copenhagen, Denmark, 31 August–6 September 2014.
34. Richardson, L.F. The Approximate Arithmetical Solution by Finite Differences of Physical Problems Involving Differential Equations, with an Application to the Stresses in a Masonry Dam. *Philos. Trans. R. Soc. Lond.* **1910**, *210*, 307–357. [CrossRef]
35. Roache, P.J. Verification of Codes and Calculations. *AIAA J.* **1998**, *36*, 696–702. [CrossRef]
36. Stern, F.; Wilson, R.V.; Coleman, H.W.; Paterson, E.G. Comprehensive Approach to Verification and Validation of CFD Simulations—Part 1: Methodology and Procedures. *J. Fluids Eng.* **2001**, *123*, 793–802. [CrossRef]
37. Wilson, R.V.; Stern, F.; Coleman, H.W.; Paterson, E.G. Comprehensive Approach to Verification and Validation of CFD Simulations—Part 2: Application for Rans Simulation of a Cargo/Container Ship. *J. Fluids Eng.* **2001**, *123*, 803. [CrossRef]

38. Stern, F.; Wilson, R.; Shao, J. Quantitative V&V of CFD simulations and certification of CFD codes. *Int. J. Numer. Methods Fluids* **2006**, *50*, 1335–1355. [CrossRef]
39. Çelik, I.; Ghia, U.; Roache, P.; Fretias, C.J.; Coleman, H.; Raad, P.E. Procedure for Estimation and Reporting of Uncertainty Due to Discretization in CFD Applications. *J. Fluids Eng.* **2008**, *130*, 078001. [CrossRef]
40. Sezen, S.; Dogrul, A.; Delen, C.; Bal, S. Investigation of self-propulsion of DARPA Suboff by RANS method. *Ocean Eng.* **2018**, *150*, 258–271. [CrossRef]
41. Tezdogan, T.; Incecik, A.; Turan, O. Full-scale unsteady RANS simulations of vertical ship motions in shallow water. *Ocean Eng.* **2016**, *123*, 131–145. [CrossRef]

Journal of
Marine Science and Engineering

MDPI

Article

A Mesh Deformation Method for CFD-Based Hull form Optimization

Kwang-Leol Jeong [1] and Se-Min Jeong [2,*]

[1] Research Center, NEXTfoam Co., Ltd., Seoul 08512, Korea; kl.jeong@nextfoam.co.kr
[2] Department of Naval Architecture and Ocean Engineering, Chosun University, Gwangju 61452, Korea
* Correspondence: smjeong@chosun.ac.kr; Tel.: +82-62-230-7218

Received: 8 June 2020; Accepted: 24 June 2020; Published: 26 June 2020

Abstract: Computational fluid dynamics (CFD) is an effective tool for ship resistance prediction and hull form optimization. A three-dimensional volume mesh is essential for CFD simulation, and mesh generation requires much time and effort. Mesh deformation can reduce the time for mesh generation and simulation. The radial basis function (RBF) and inverse distance weighted (IDW) methods are well-known mesh deformation methods. In this study, the two methods are compared and a novel mesh deformation method for hull form optimization is proposed. For the comparison, a circular cylinder polyhedral mesh was deformed to the National Advisory Committee for Aeronautics (NACA) 0012 mesh. The results showed that the RBF method is faster than the IDW method, but the deformed mesh quality using the IDW method is better than that using the RBF method. Thus, the RBF method was modified to improve the deformed mesh quality. The centroids of the boundary layer cells were added to the control points, and the displacements of the centroids were calculated using the IDW method. The cells far from the ship were aligned to the free surface to minimize the numerical diffusion of the volume of fluid function. Therefore, the deformable region was limited by the deformed boundary, which reduced the time required for mesh deformation. To validate its applicability, the proposed method was applied for varying the bow shape of Japan Bulk Carrier (JBC). The resistances were calculated with the deformed meshes. The calculation time was reduced to approximately one-third using the result of the initial hull form as the initial condition. Thus, the proposed mesh deformation method is efficient and effective enough for CFD-based hull form optimization.

Keywords: mesh deformation; computational fluid dynamics (CFD); radial basis function (RBF) method; inverse distance weighted (IDW) method; hull form optimization

1. Introduction

Computational fluid dynamics (CFD) is one of the general tools for estimating the resistance of a ship in calm water. Naval architects iterate the hull form variation, grid generation, and CFD calculation to minimize the resistance. Even though the hull form variation is extremely localized and low, the grid must be regenerated. Many shipbuilding and design companies are exerting efforts to automate the procedure to reduce the time and cost. Moreover, many studies on CFD-based design optimization have been conducted. An optimization algorithm to minimize the iterations is the most important and the hull form variation method according to the design parameter is very essential.

Kim and Yang [1] applied two surface modification methods for hull form optimization. One was based on a radial basis function (RBF), while the other was based on a sectional area curve. Kim and Yang's [1] RBF method uses only 6 control points as design variables to minimize the resistance of Korea Research Institute for Ships and Ocean Engineering (KRISO) Container Ship (KCS) in three speeds. The resistance of the modified hull was evaluated using a method based on the Neumann–Michell

theory, which uses only a surface mesh. Kim et al. [2] applied the same method used by Kim and Yang [1] to improve the resistance and seakeeping performance of the US Navy surface combatant David Taylor Model Basin (DTMB) 5415. Mahmood and Huang [3] optimized a bulbous bow to minimize the total resistance using a genetic algorithm. They used ANSYS FLUENT and GAMBIT (Ansys, In., Canonsburg, PA, USA) for resistance calculation and mesh generation, respectively. A GAMBIT journal file was created to automate the hull form variation and volume mesh generation in accordance with the design parameters. Zhang et al. [4] proposed an improved particle swarm optimization algorithm, where Siemens STAR-CCM+ (Siemens Industry Software Ltd., Plano, TX, USA) was used for volume mesh generation and resistance calculation. The hull form was varied using an arbitrary shape deformation (ASD) technique proposed by Sun et al. [5]. The ASD technique is based on a B-spline and requires that the volume is set up outside the body with many control points and connections.

The volume mesh deforming method has been developed to simplify the optimization process and reduce the turnaround time as shown in Figure 1. Mesh deformation is much faster than grid generation, and the simulation with a deformed mesh uses the results of the original mesh as the initial condition. Successive calculation also reduces the calculation time. Morris et al. [6] developed a mesh deformation method based on the RBF method. The control points of the RBF method were used as design parameters. The method was independent of both the flow solver and grid generator. Morris et al. [6] applied a method for optimizing airfoils with feasible sequential quadratic programming. They concluded that the method was extremely fast and efficient, and the deformed mesh quality was very high. Sieger et al. [7] compared the classical free-form deformation (FFD), direct manipulation FFD, and RBF methods with each other. They concluded that the RBF method was much faster and more precise than the other two methods. Luke et al. [8] proposed a mesh deformation method based on inverse distance weighted (IDW) interpolation. Their method interpolated the translational displacement and rotational displacement using the IDW method. The parallelization of the algorithm was also described. They showed that the non-orthogonality of the boundary layer of the deformed mesh using the IDW method is better than that by the RBF method if the rotation of the body surface is high. He et al. [9] applied the IDW method to optimize an airfoil that starts with a circle. To show the robustness of the IDW method, a two-dimensional (2D) mesh for the circle was deformed to the mesh of NACA 0012. They concluded that the IDW method is better than the RBF method in terms of non-orthogonality of the boundary layer. TransFinite Interpolation (TFI) method is also a popular and efficient method for structured grid. However, the TFI method is difficult to apply to polyhedral mesh because of the irregular distribution of mesh points [10].

In this paper, Section 2 introduces the RBF, IDW and improved RBF methods. To compare the quality and time for deformation, a polyhedral mesh for circular cylinder are deformed to the mesh for NACA 0012. The results show that the RBF method have problem with non-orthogonality in boundary layer cell. The IDW method takes much longer time than that of the RBF method. The non-orthogonality of the improved RBF method is as good as IDW method and the turnaround time is shorter than any other methods. To check the applicability of the improved RBF method, the polyhedral mesh for Japan bulk carrier (JBC) resistance calculation is deformed and the mesh is calculated in Section 3. Because of the mesh topology is identical with the original mesh, the result of the original mesh is used as the initial condition of deformed mesh. Therefore, the time for solution converging is reduced by two-thirds.

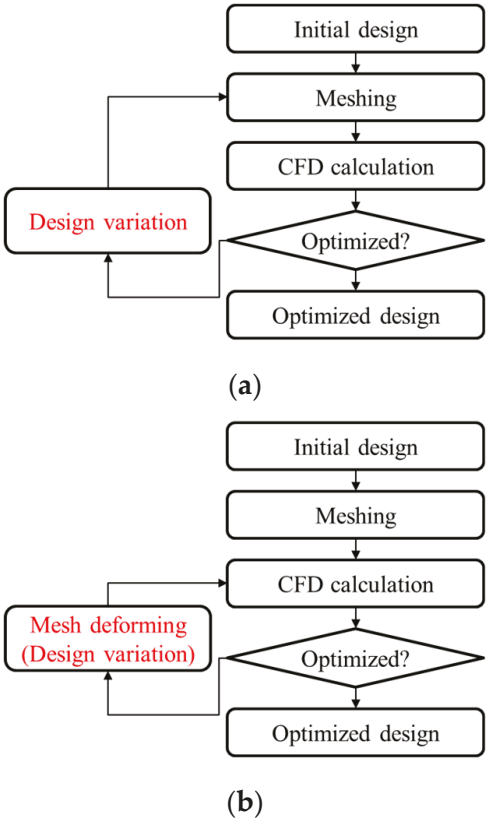

Figure 1. Procedure of computational fluid dynamics (CFD)-based optimization. (**a**) Re-meshing method. (**b**) Mesh deforming method.

2. Mesh Deformation Methods

In this section, the RBF and IDW methods are introduced and compared. In addition, an improved RBF method to remedy its shortcomings is proposed. A mesh for a circular cylinder was deformed to the mesh of NACA 0012 using the RBF, IDW, and proposed methods. The red points in Figure 2 denote the control points on the surface of the circle and the blue ones indicate the displaced points on the surface of NACA 0012. The number of control points is 256 and the points move only in the vertical direction. The vertical movements make the normal vectors of the boundary faces rotate.

The initial grid for the circular cylinder is shown in Figure 3. The grid is a polyhedral mesh generated using snappyHexMesh, a standard built-in utility of OpenFOAM (The OpenFOAM Foundation Ltd., London, U.K.). The number of cells is 103,160 and the thickness of first boundary layer cell is 1% of the cylinder diameter. The top, bottom, right, and left boundaries were set as fixed boundary conditions. The front and back boundaries were set as symmetric boundary conditions. To satisfy the fixed boundary condition, the grid points of the fixed boundary were added to the control points. The displacements of the fixed boundary were set as zero.

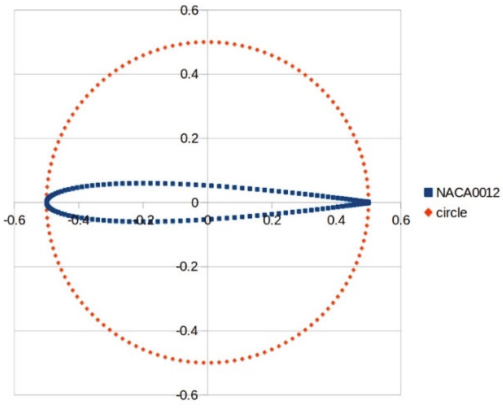

Figure 2. Control points (red) and displaced points (blue).

2.1. RBF Method

The RBF method is an interpolation method that uses the distance between the grid point and control points. It was proposed by Sieger et al. [7], Boer et al. [11], Botch and Kobbelt [12], Jakobsson and Amoignon [13], and Michler [14]. The basic formula for displacement is presented in Equation (1).

$$D(x, y, z) = a_1 + a_2 x + a_3 y + a_4 z + \sum w_i U(R_i) \tag{1}$$

$$R_i = \left|\left(x_i, y_i, z_i\right) - (x, y, z)\right| \tag{2}$$

Here, R_i is the distance between the grid point and the i-th control point, and U is a basis function. In this study, a thin plate spline (TPS) is applied as a basis function. The TPS provides a minimal and smooth displacement distribution. The details about basis functions can be found in [15].

$$\text{Thin plate spline}: \; U(R) = |R|^2 \log R \tag{3}$$

The unknowns of Equation (1), a_i and w_i, are obtained by calculating Equation (4). The partitioned matrix K is determined by the distance between the control points, and P is composed of coordinates of the control points. Column vector $\vec{v}$ contains the displacements of control points. Equation (4) is calculated with LU decomposition instead of an iterative method because the matrix is dense and small.

Because the size of the matrix in Equation (4) is proportional to the number of control points, every four points on the fixed boundary is added to the control points. Sheng and Allen [16] applied a greedy data reduction algorithm to reduce the matrix size and calculation time. Coulier and Darve [17] developed the inverse fast multipole method to reduce the computational time. After the mesh deformation, the normal component of displacement of the grid points on the symmetric plane is removed to satisfy the symmetric boundary condition.

$$\begin{bmatrix} K & P \\ P^T & O \end{bmatrix} \begin{bmatrix} \vec{w} \\ \vec{a} \end{bmatrix} = \begin{bmatrix} \vec{v} \\ \vec{o} \end{bmatrix} \tag{4}$$

$$K_{ij} = U\left(\left|(x_i, y_i, z_i) - \left(x_j, y_j, z_j\right)\right|\right) \tag{5}$$

$$P = \begin{bmatrix} 1 & x_1 & y_1 & z_1 \\ 1 & x_2 & y_2 & z_2 \\ \vdots & \vdots & \vdots & \vdots \\ 1 & x_p & y_p & z_p \end{bmatrix} \tag{6}$$

$$O = \begin{bmatrix} 0 & 0 & 0 & 0 \\ 0 & 0 & 0 & 0 \\ 0 & 0 & 0 & 0 \\ 0 & 0 & 0 & 0 \end{bmatrix} \tag{7}$$

$$\vec{w} = \begin{bmatrix} w_1 \\ w_2 \\ \vdots \\ w_p \end{bmatrix}, \vec{a} = \begin{bmatrix} a_1 \\ a_2 \\ a_3 \\ a_4 \end{bmatrix}, \vec{v} = \begin{bmatrix} \vec{D_1} \\ \vec{D_2} \\ \vdots \\ \vec{D_p} \end{bmatrix}, \vec{o} = \begin{bmatrix} 0 \\ 0 \\ 0 \\ 0 \end{bmatrix} \tag{8}$$

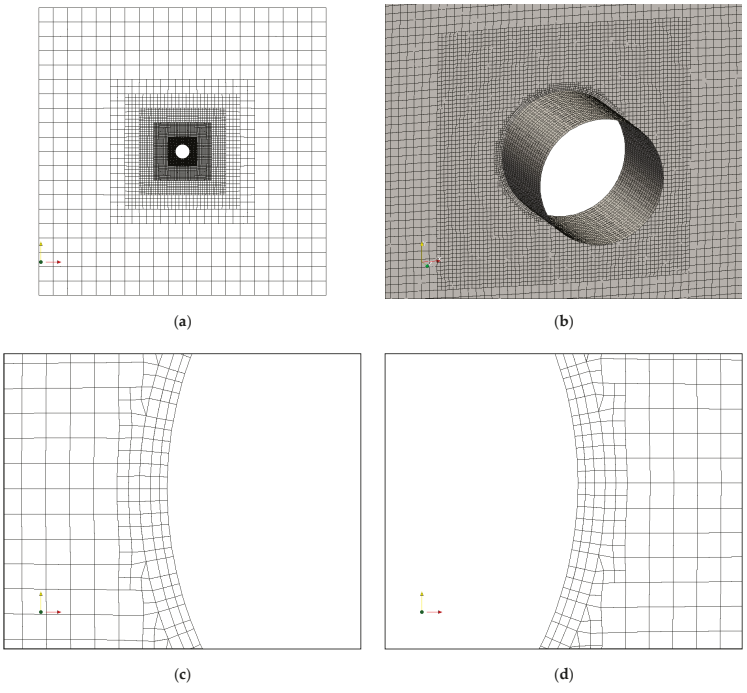

Figure 3. Initial grid shape for circular cylinder. (**a**) whole domain (side view), (**b**) surface mesh (perspective view), (**c**) around front part of the body (leading edge), (**d**) around rear part of the body (trailing edge).

The deformed mesh using the RBF method is illustrated in Figure 4. The overall domain is deformed smoothly, but the boundary layer is thinner than the initial grid and the non-orthogonality is worse than in the initial grid. The maximum skewness and maximum non-orthogonality are compared in Table 1. The mesh deformation takes approximately 45 s. The results are similar to those of He et al. [9], who conducted similar mesh deformation using the RBF and IDW methods with a 2D structured grid.

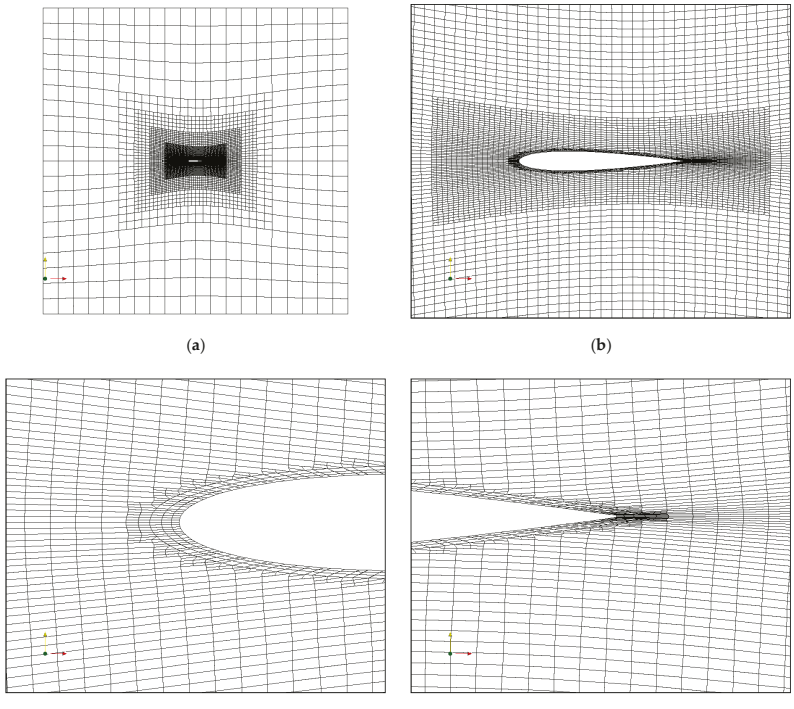

Figure 4. Deformed mesh using the radial basis function (RBF) method. (**a**) whole domain (side view), (**b**) near body (side view), (**c**) around leading edge (side view), (**d**) around trailing edge (side view).

Table 1. Quality of deformed mesh by the RBF method.

	Maximum Skewness	Average Non-Orthogonality	Maximum Non-Orthogonality	Turnaround Time (s)
Initial	0.376	7.233	50.435	-
RBF method	4.742	18.992	86.545	45

2.2. IDW Method

The IDW method is an interpolation method. The displacement of the grid points is calculated using Equation (9), where R_i denotes the distance as defined in Equation (3). M_i and T_i in Equation (10) are the rotation matrix and translation displacement of the boundary face, respectively. The weighting function is given by Equation (11). Luke et al. [8] suggested these values: $a = 3$, $b = 5$, and $\alpha = 0.25$. L_{def} is recommended as the maximum distance of mesh points, and A_i is the area of the boundary face. In this study, a, b, and α are set as 3, 0, and 0, respectively. Because of the irregular face area distribution of the boundaries, the thickness of the boundary layer becomes uneven. The calculation time is also reduced since the second term is not calculated.

$$D(x, y, z) = \frac{\sum w(R_i)s(R_i)}{\sum w\,(R_i)} \tag{9}$$

$$s(R_i) = M_i R_i + T_i - R_i \tag{10}$$

$$\mathrm{w}(R_i) = A_i \times \left[\left(\frac{L_{def}}{R_i}\right)^a + \left(\frac{\alpha L_{def}}{R_i}\right)^b\right] \tag{11}$$

Figure 5 depicts the deformed mesh using the IDW method. The non-orthogonality of the boundary cell is much better than that by the RBF method. The thickness of the boundary cell is almost equal to that of the initial grid except for the leading and trailing edges. The thickness around the leading and trailing edges is slightly larger than that of the initial grid. The displacements of grid points far from the deformed boundary are smaller than those by the RBF method. The grid quality of deformed mesh is compared with that of the initial grid in Table 2. The time for mesh deformation is approximately 115 s, which is ≈2.6 times larger than that by the RBF method.

Table 2. Quality of deformed mesh using the IDW method.

	Maximum Skewness	Average Non-Orthogonality	Maximum Non-Orthogonality	Turnaround Time (s)
Initial	0.376	7.233	50.435	-
IDW method	0.571	11.644	73.849	115

2.3. Improved RBF Method

The drawback of the RBF method is the non-orthogonality of the boundary layer. To reduce the non-orthogonality, the centroids of the first boundary cells are added as control points. The displacements of the new control points are calculated using the IDW method. To calculate the translational and rotational displacement, the RBF calculation is repeated twice. First, the boundary face is deformed with only the initial control points. The displacements of the centroids of the first boundary cells are calculated with the displacements of the deformed boundary face by the IDW method. Second, the displacements of the volume mesh grid points are calculated with the grid points of the deformed boundary and the centroids of the first boundary cells. To reduce the calculation time, every 4 points of the grid points and centroids is used as control points.

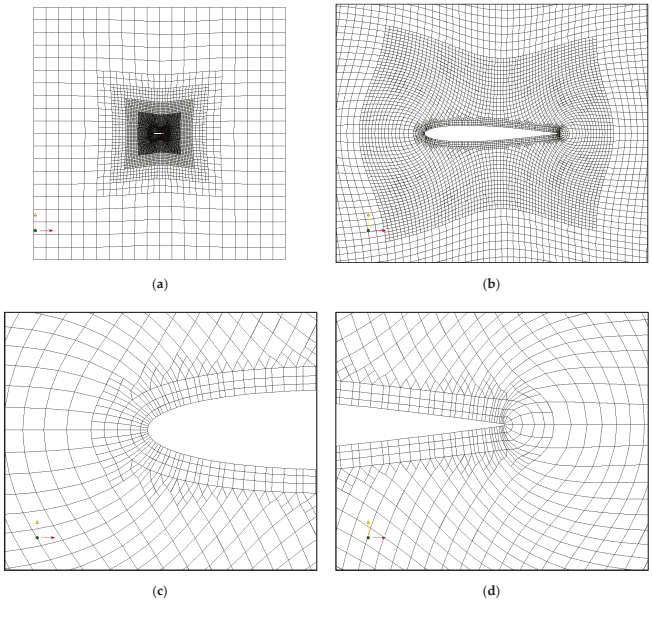

Figure 5. Deformed mesh using the inverse distance weighted (IDW) method. (**a**) whole domain (side view), (**b**) near body (side view), (**c**) around leading edge (side view), (**d**) around leading trailing (side view).

It is difficult to apply both the RBF and IDW methods to problems involving the free surface because the grid around the free surface has to be aligned to the free surface to minimize the numerical diffusion of the volume of fluid function (VOF). Therefore, the deformable region must be limited. The cells around the deformed boundary are designated as deformable cells, while those outside of the regions are set as frozen cells. The faces sheared by the deformable and frozen cells are designated as fixed faces. The points on the fixed faces are added to the fixed control points.

Figure 6 displays the deformed mesh. The non-orthogonality of the boundary cell is better than those by the RBF and IDW methods. The thickness of the boundary cells around the leading and trailing edges is well preserved. The cells in yellow circle are deformable cells.

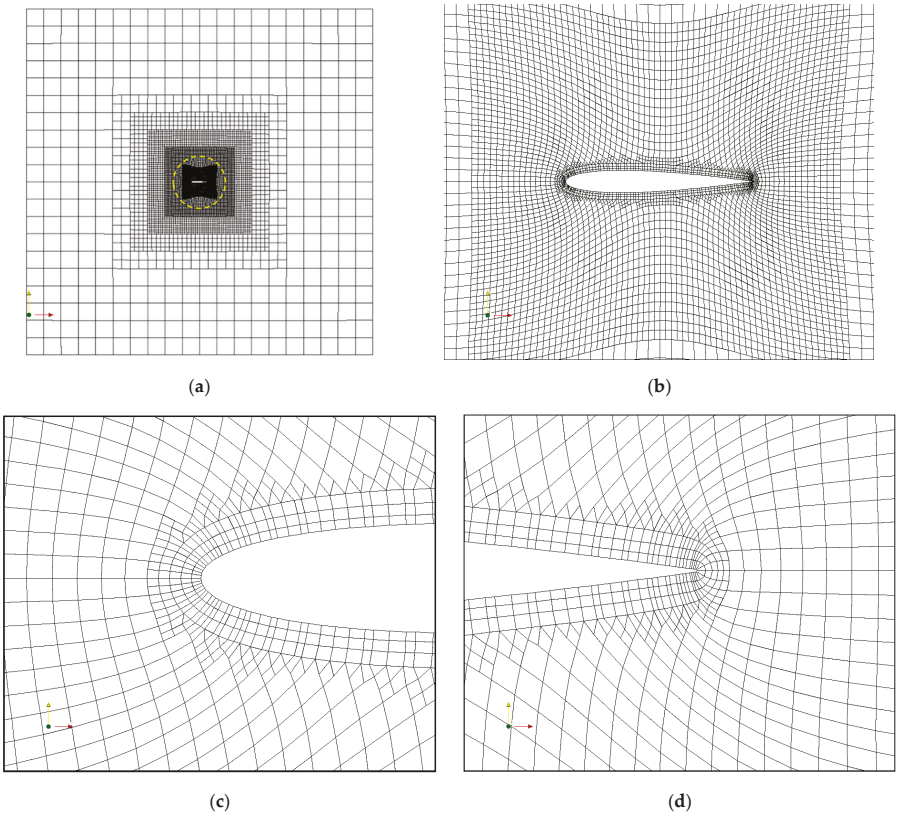

Figure 6. Deformed mesh using the RBF method with additional control points. (**a**) whole domain (side view), (**b**) near body (side view), (**c**) around leading edge (side view), (**d**) around trailing edge (side view).

The quality of the deformed mesh is compared with the initial mesh in Table 3. The deformed mesh quality using the proposed method is as good as that by the IDW method. Moreover, the proposed method is much faster than the others owing to the limited deformation region.

Table 3. Quality of the deformed mesh using the proposed method.

	Maximum Skewness	Average Non-Orthogonality	Maximum Non-Orthogonality	Turnaround Time (s)
Initial	0.376	7.233	50.435	-
Proposed method	0.782	12.141	74.920	13

3. Mesh Deformation for Hull Form Variation

The proposed mesh deformation method was applied to the mesh for ship resistance calculation to examine its applicability to CFD-based optimization. The ship used in the calculations is the JBC model. The scale ratio and the draft are 1:40 and 0.4125 m (16.5 m in full scale), respectively. The speed is 1.179 m/s (14.5 knots in the model).

The initial grid used for the JBC resistance calculation is illustrated in Figure 7. The number of cells is 2,402,361. The Y+ of first layer thickness is approximately 50 and the number of boundary layers is 4. The expansion ratio of the boundary layer is approximately 1.3. The running attitude of the ship is fixed as even keel condition. The simulation was conducted using interFoam, a standard solver of OpenFOAM. kOmegaSST and nutUSpaldingWallFunction were used as the turbulence model and wall function, respectively.

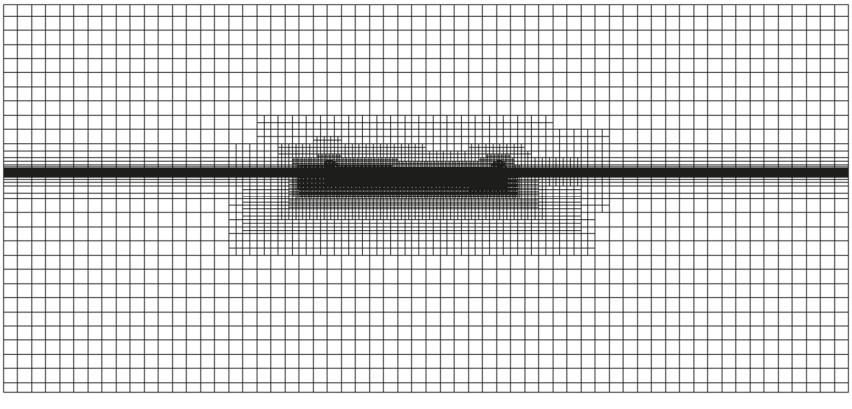

(**a**)

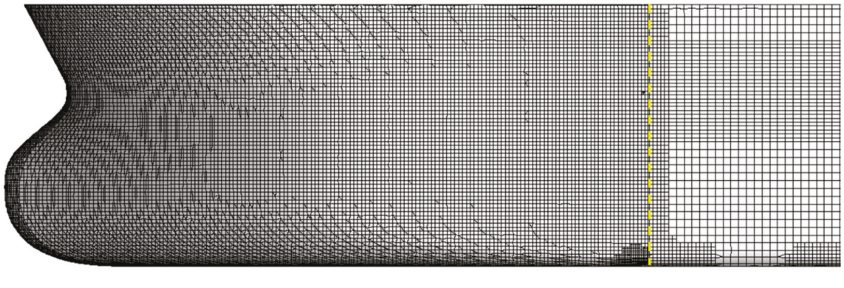

(**b**)

Figure 7. Grid shape for Japan bulk carrier (JBC) resistance calculation. (**a**) whole domain (side view), (**b**) surface mesh of fore body (side view).

Three points on the forward perpendicular (F.P.) line were moved by 5 mm (0.2 m in full scale) to make an alternative hull form. The hull surface is split by the yellow dashed line in Figure 8. The hull surface in front of the line was set as deformable patch, while that behind the yellow line was set as fixed patch.

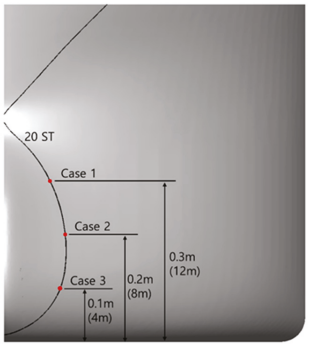

Figure 8. Definition sketch of control points for hull form variation.

The deformed hull is depicted in Figure 9. The red lines indicate the JBC station lines, whereas the blue lines denote the station lines of the deformed hull. Figure 10 displays a slice of the deformed mesh on the F.P. Because of the small deformation, the variation in mesh quality is small enough to be ignored. The time to deform a mesh with 2 million cells is approximately 118–120 s with a core of Intel Xeon CPU E5-2630 v3 2.4 GHz. The turnaround time is reasonably small. The mesh deformations and CFD simulations are conducted by shell script.

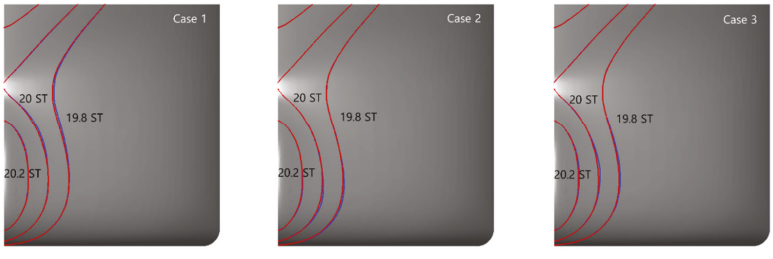

Figure 9. Deformed hull shapes.

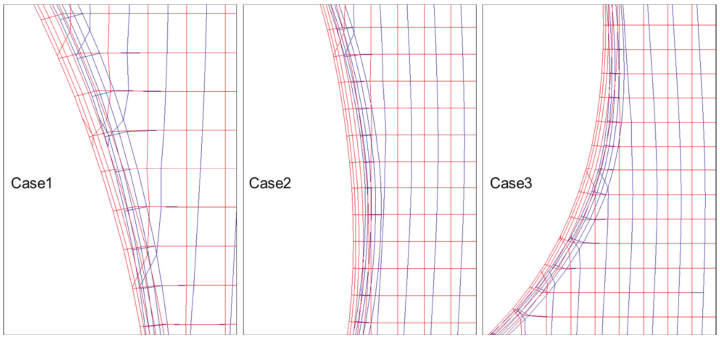

Figure 10. A slice of the deformed mesh at forward perpendicular forward perpendicular (F.P.) (red grid line: original mesh, blue grid line: deformed mesh).

The resistance histories of the JBC and deformed hulls are compared in Figure 11. The calculations of deformed hulls converged much faster than the JBC calculation because the result of the JBC calculation was used as the initial condition for the deformed hull resistance calculations. The calculation of the JBC resistance took approximately 60 s, whereas the calculation of deformed hulls took 20 s in flow time. The variations in the resistances are small because the hull form variation is small. The resistance coefficients are compared in Table 4.

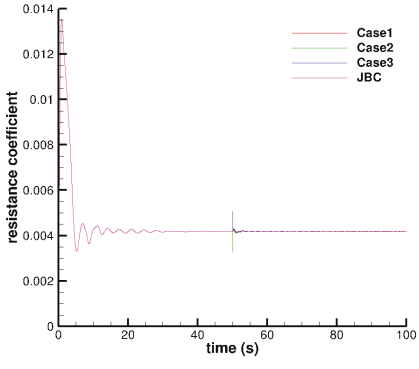

(**a**)

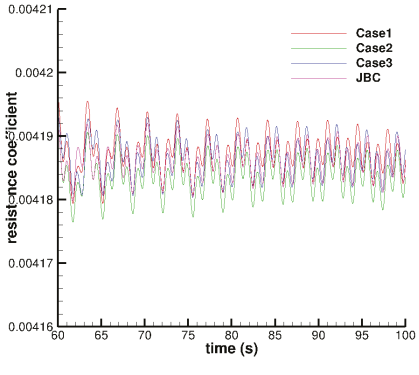

(**b**)

Figure 11. Comparisons of resistance convergence histories. (**a**) whole time, (**b**) zoomed.

Table 4. Comparison of resistances of the JBC and deformed hull.

	JBC	Case 1	Case 2	Case 3
Resistance coefficient	4.186×10^{-3}	4.187×10^{-3}	4.184×10^{-3}	4.186×10^{-3}

The pressure distributions and wave height contours are compared in Figures 12 and 13, respectively. It was found that the result of the initial hull form can be used as the initial condition for the deformed hull resistance calculation.

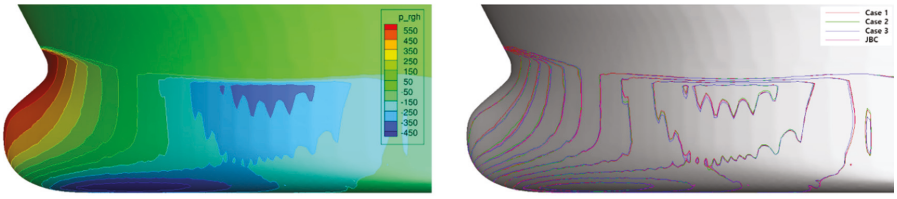

Figure 12. Comparison of pressure distributions around the bow (**left**: JBC only, **right**: JBC and deformed hull).

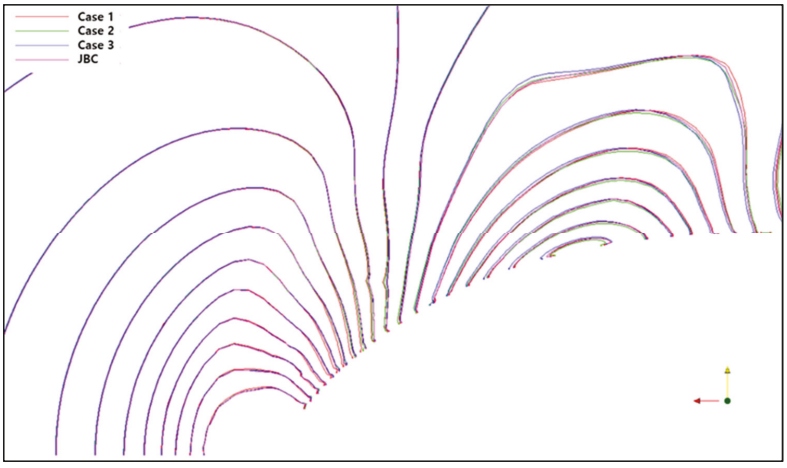

Figure 13. Comparison of wave height contour around the bow.

4. Conclusions

In this study, two methods for mesh deformation, namely, the RBF and IDW methods, were compared. Moreover, an improved RBF method was proposed for a largely deformed mesh. The RBF method was much faster than the IDW method, but the quality of the deformed mesh using the IDW method was better than that by the RBF method. The quality of the deformed mesh by the RBF method was improved by adding the centroids of boundary cells to the control points. The displacements of the centroids were calculated using the IDW method. The deformable region was limited for the problem involving the free surface. The limitation also reduced the calculation time.

The improved RBF method was applied to the mesh for the JBC resistance calculation to validate its applicability. The resistance was calculated by varying the bow shape with three control points. It took approximately 120 s for the mesh to deform, which is short enough to apply to practical problems. The calculation result of the initial hull form was used as the initial condition for the deformed hull form, which reduced the calculation time to approximately one-third of that of the initial hull form. Thus, the improved RBF method proposed in this study is effective and efficient for hull form variation.

In the future, the CFD-based hull form optimization will be conducted using the proposed mesh deformation method together with an optimization algorithm such as sequential quadratic programming or an adjoint variable method.

Author Contributions: Conceptualization, K.-L.J. and S.-M.J.; methodology, K.-L.J.; validation K.-L.J.; formal analysis, K.-L.J.; investigation, K.-L.J. and S.-M.J.; resources, K.-L.J. and S.-M.J.; writing—original draft preparation, K.-L.J. and S.-M.J.; writing—review and editing, S.-M.J.; visualization, K.-L.J.; supervision, K.-L.J. and S.-M.J.; and funding acquisition, S.-M.J. All authors have read and agreed to the published version of the manuscript.

Funding: This study was supported by a research fund from Chosun University (K207177004).

Conflicts of Interest: The authors declare no conflicts of interest.

References

1. Kim, H.; Yang, C.; Noblesse, F. Hull form optimization for reduced resistance and improved seakeeping via practical designed-oriented CFD tools. In Proceedings of the 2010 Conference on Grand Challenges in Modeling and Simulation, Ottawa, ON, Canada, 11–14 July 2010.
2. Kim, H.; Yang, C. A new surface modification approach for CFD-based hull form optimization. *J. Hydrodyn.* **2010**, *22*, 503–508. [CrossRef]
3. Mahmood, S.; Huang, D. Computational fluid dynamics based bulbous bow optimization using a genetic algorithm. *J. Martine Sci. Appl.* **2012**, *11*, 286–294. [CrossRef]
4. Zhang, S.; Zhang, B.; Tezdogan, T.; Xu, L.; Lai, Y. Computational fluid dynamics-based hull form optimization using approximation method. *Eng. Appl. Comput. Fluid Mech.* **2018**, *12*, 74–88. [CrossRef]
5. Sun, Z.X.; Song, J.J.; An, Y.R. Optimization of the head shape of the CRH3 high speed train. *Sci. China Technol. Sci.* **2010**, *53*, 3356–3364. [CrossRef]
6. Morris, A.M.; Allen, C.B.; Rendall, T.C.S. CFD-based optimization of aerofoils using radial basis functions for domain element parameterization and mesh deformation. *Int. J. Numer. Meth. Fluids* **2008**, *58*, 827–860. [CrossRef]
7. Sieger, D.; Menzel, S.; Botsch, M. *On Shape Deformation Techniques for Simulation–Based Design Optimization, In New Challenge in Grid Generation and Adaptively for Scientific Computing*; Springer Series: Cham, Switzerland, 2015; pp. 281–303.
8. Luke, E.; Collins, E.; Blades, E. A fast mesh deformation method using explicit interpolation. *J. Comput. Phys.* **2012**, *231*, 586–601. [CrossRef]
9. He, X.; Li, J.; Mader, C.A.; Yildirim, A.; Martins, J.R.R.A. Robust aerodynamic shape optimization-form a circle to an airfoil. *Aerosp. Sci. Technol.* **2019**, *87*, 48–61. [CrossRef]
10. Ding, L.; Lu, Z.; Guo, T. An efficient dynamic mesh generation method for complex multi-block structured grid. *Adv. Appl. Math. Mech.* **2014**, *6*, 120–134. [CrossRef]
11. Boer, A.; Van der Schoot, M.; Bijl, H. Mesh deformation based on radial basis function interpolation. *Comput. Struct.* **2007**, *85*, 784–795. [CrossRef]
12. Botch, M.; Kobbelt, L. Real-time shape editing using radial basis function. *Comput. Graph. Forum* **2005**, *24*, 611–621. [CrossRef]
13. Jakobsson, S.; Amoignon, O. Mesh deformation using radial basis functions for gradient-based aerodynamic shape optimization. *Comput. Fluids* **2007**, *36*, 1119–1136. [CrossRef]
14. Michler, A.K. Aircraft control surface deflection using RBF-based mesh deformation. *Int. J. Numer. Meth. Eng.* **2011**, *88*, 986–1007. [CrossRef]
15. Buhmann, M.D. *Radial Basis Functions: Theory and Implementations*; Cambridge University Press: Cambridge, UK, 2003; ISBN 978-0511040207.
16. Sheng, C.; Allen, C.B. Efficient mesh deformation using radial basis functions on unstructured meshes. *AIAA J.* **2013**, *51*, 707–720. [CrossRef]
17. Coulier, P.; Darve, E. Efficient mesh deformation based on radial basis function interpolation by means of the inverse fast multipole method. *Comput. Methods Appl. Mech. Eng.* **2016**, *308*, 286–309. [CrossRef]

Journal of
Marine Science and Engineering

MDPI

Article

Numerical Modelling of the Nearfield Longitudinal Wake Profiles of a High-Speed Prismatic Planing Hull

Angus Gray-Stephens *, Tahsin Tezdogan and Sandy Day

Department of Naval Architecture, Ocean and Marine Engineering, The University of Strathclyde, Glasgow G4 0LZ, UK; tahsin.tezdogan@strath.ac.uk (T.T.); sandy.day@strath.ac.uk (S.D.)
* Correspondence: angus.gray-stephens@strath.ac.uk; Tel.: +44-7979-262-357

Received: 10 June 2020; Accepted: 9 July 2020; Published: 14 July 2020

Abstract: This study investigates the level of accuracy with which Computational Fluid Dynamics (CFD) is capable of modelling the nearfield longitudinal wake profiles of a high-speed planing hull. It also looks to establish how various set-ups influence the accuracy, with a specific emphasis on turbulence modelling. It analyses a hull over a broad range of conditions to provide detailed insight into the strengths and limitations of CFD, comparing the numerical results to the experimental results previously generated by the authors. A quantitative comparison is made for the centreline (CL) and quarterbeam (QB) longitudinal wake profile plots. Following this, a qualitative comparison is made between photos of the flow pattern from the experimental testing and free surface elevation plots from CFD. The study concluded that CFD is an accurate and robust method of modelling the nearfield longitudinal wake profiles of a high-speed planning hull.

Keywords: planing hull; Computational Fluid Dynamics; Verification and Validation; nearfield wake pattern; longitudinal wake profile

1. Introduction

Whilst high-speed planing hulls have always been of interest to naval architects, substantially less time and resources have been invested into research surrounding the topic than larger, more commercially exploitable areas, such as shipping. In industry, a lot of the knowledge was developed from experience working in the field, and it was commonplace to employ a 'trial and error' based design process. Despite this, in recent years there has begun a steady progression in the available work researching high-speed hulls. Notably, in recent years, as is the case across the board with all topics relating to naval architecture, advancements in the power and availability of computational resources have led to an increase in numerical studies using Computational Fluid Dynamics (CFD) to model complex flow.

The use of CFD provides numerous advantages over conventional model testing. Perhaps the most notable of these is the enhanced post processing capabilities and the ability to extract data that is difficult to measure experimentally, such as pressure fields and flow patterns. Before CFD may be used as a design tool with a high level of confidence, it is first necessary to explore its applicability to a given problem, ensuring that it is capable of producing accurate results. While numerous studies have investigated CFD's capabilities in relation to high-speed vessels, few have looked to determine its ability in modelling the nearfield wake patterns. The nearfield wake region of a planning hull is of specific interest for a number of reasons. Primarily in the case of a planning hull, it may have implications over the choice of propulsion system. There may also be a number or operation specific requirements on the wake produced by a vessel that require analysis of this flow.

A variant of the traditional planning hull that is of particular interest to naval architects is the stepped hull, which aims to minimise the resistance of a vessel through a reduction in the wetted

surface area. It has been shown that the inclusion of steps is capable of producing a reduction of 10–15% in the hydrodynamic resistance and typically gives an increase in speed of 6–10 knots [1]. A stepped hull has one or more transverse discontinuities, or steps, behind each of which the hull elevation raises slightly. When the vessel is travelling at high speeds, air is drawn in through inlets, causing the flow to separate at each step. The forces generated by both the forebody and afterbody must combine to provide vertical equilibrium for a stepped vessel, as well being used to determine the resistance and trim. In order to determine the forces on the afterbody the nearfield wake profile of the forebody must be determined in order to calculate the intersection with the afterbody.

The study reported in this paper sets out to determine the accuracy of CFD in modelling the nearfield longitudinal wake profile through a comparison with physical testing. This will allow designers to use CFD as a tool for the analysis of wake of a planning hull with confidence. In addition to performing this validation, the paper will report on the systematic study of the CFD set up. This will ensure that the most accurate set up is established, as well as highlighting the effects that different set ups have on the accuracy of the simulation. Finally, the work will be used to justify whether CFD is capable of modelling the flow of a stepped hull as it separates from the forebody and interacts with the afterbody of the hull. Modelling the wake profiles without the presence of the afterbody changes the physics of the problem and simplifies it massively; however, it has previously been proposed for the analysis of stepped hulls by Savitsky and Morabito [2] and provides a good validation case for CFD being able to accurately model flow patterns. This simplification is necessary as experimentally extracting the wake profiles behind a step with anything other than photographs to compare is extremely challenging, and is something that has not been achieved by researchers to date. As such, there is no available validation data for cases where the afterbody is included.

The paper begins by presenting an in-depth literature review of previous numerical studies on the subject of planing hulls. Following this, the aims and the methodology are detailed before the numerical set up is outlined. Finally, the results are presented and discussed, before the work is rounded off with the concluding remarks.

2. Literature Review

There are few examples in literature of authors investigating the near-field longitudinal wake profiles using experimental, analytical or numerical means. A number of studies in the first half of the 20th century attempted to extract the longitudinal wake profiles of planing surfaces [3–6]; however, the focus of these studies is upon seaplane floats, and as such, the parameters are vastly different from those typical of planing hulls.

In the past 20 years, some work has been conducted upon the mid and far-field wake of planning hulls. Notably Thornhill et al. [7] conducted a series of bare hull resistance tests of a planing hull for a range of conditions in order to provide validation data for CFD using an array of capacitance probes. Following this, the same experimental strategy was employed by [8,9]. Callander [8] went on to use the measured experimental data to evaluate the MacPhail 2D + t method for application with planing hulls. His work concluded that the analytical method was able to model the trends of the experimental data; modification was required to improve its accuracy to a suitable level. De Luca [9] went on to use the data generated to evaluate the effectiveness of interceptors. He provided the profiles he obtained to carry out validation procedures. The experimental procedure followed by these researchers was unable to provide any data for the nearfield wake region due to the placement of the capacitance probes.

Savitsky and Morabito [2] conducted the first experimental investigation into the nearfield wake of planing hulls, developing empirical equations that quantitatively defined the longitudinal surface wake profiles at both the centreline (CL) and quarterbeam (QB). The authors found that the developed empirical formulae displayed good agreement with the experimental results; however, there is a noticeable scatter and it is clear that while an empirical equation may be capable of providing a good representation of the wake profiles they will not be entirely accurate for all cases. The work undertaken

by Stavisky was comprehensive and was published with the intention of aiding the designers of stepped hulls determine how the flow of the fore hull intersects with the aft hull.

The second example of an experimental investigation into the nearfield wake of a planing hull was conducted by Gray-Stephens et al. [10]. This paper set out to determine the accuracy of the empirical wake equations derived by [2] when they were employed out with their published range or applicability. The study also examined the accuracy of the Linear Wake Assumption, which is often employed by researchers when modelling stepped hulls in an attempt to evaluate its validity for this application. A further motivation behind this paper was to provide detailed experimental data to be used for the validation of CFD in modelling the flow in this region, as is being undertaken by the present study.

The number of available numerical studies investigating both planing and stepped hulls has been increasing rapidly in recent years. This has led to vast improvements in the level of accuracy that is reported by authors, with a mean prediction error of 10% being considered achievable by the International Towing Tank Conference (ITTC) [11]. This prediction error is for the calculation of forces and there is little information available to evaluate the accuracy CFD in modelling wake field.

Following a study of the available literature, the authors of this paper were unable to identify any examples of experimental data being used to validate or evaluate the performance of CFD in calculating the longitudinal wake profiles of a high-speed planing hull. A number of studies do however make use of Savitsky's Wake Equations in conjunction with numerical methods, primarily as one-off validation cases of the CFD. In 2014, Faison [12] used the Savitsky Wake Equations to compare the wake profiles of transverse steps with the CFD generated profiles of swept back and cambered steps. The study found there to be significant differences between the numerical and empirical profiles however the authors were unable to determine if the differences were solely accountable to the change in design, or due to the superior accuracy of one the methods employed. In 2015 Ghadimi et al. [13] used the Savitsky Wake Equations to validate a numerical computation modelling the CL wake profile. The authors went on to use the validated simulation to investigate how altering the transom stern may reduce the wakes rooster tail height. The paper shows the validation comparison to have reasonably good correlation, but, once again, the authors are not able to comment on the reasons behind this difference. Moreover, in 2015, Lotfi et al. [14] compared a numerically generated CL wake profile to the equivalent one calculated using the Savitsky Wake Equations. Similarly to [12] the two methods are not shown to have good correlation, featuring an average error of 20%. Most recently, in 2017 Bakhtiari and Ghassemi [15] were investigating the effect of a forward swept step angle on the performance of a planing hull through the use of CFD. They employed the results of the Savitsky Wake Equations as part of their validation procedure, showing that there is a reasonable level of agreement between the two methods, but that they do not exactly agree.

No examples of authors investigating the modelling of the nearfield wake profiles with CFD were found, aside from those using the Savitsky Wake Equations as a brief validation case. Those using the Savitsky Wake Equations to validate their CFD model often found discrepancies between the two methods, however, were not able to identify which of the methods was closer to the physical solution. The lack of investigation into this topic is in part due to the lack of experimental nearfield wake data available in the public domain, with only two sources of this being identified. Some studies have compared mid and far-field experimental wake cuts with CFD results for conventional displacement ships. Analysis of the work submitted to the Gothenburg 2010 Workshop revealed that wave cuts closest to the hull tend to be well predicted; however, as distance from the hull increases, the results varied considerably [16]. This workshop was for a KCS vessel, and it is well known that CFD is significantly more accurate when evaluating conventional displacement ships compared to planing hulls. An example of this comparison being made for planing hulls was undertaken by Mancini [17]. The study compared the numerical results for the wake field to the experimental mid and far field wave cuts of the Naples Systematic Series. It was found that CFD was able to model the trends in a

satisfactory manner; however, it was noted that there was differences in both the amplitudes and phase of the results.

3. Aims and Objectives

The primary aim of this study is to perform an in-depth investigation into the ability of CFD in modelling the near-field longitudinal wake profiles of a planing hull. An evaluation of both the CL and QB profiles will be made through a comparison with experimental data. Additionally, comments will be made upon the accuracy of CFD in comparison to Savitsky's Wake Equations and the Linear Wake Assumption. The secondary aim of the work is to investigate how the set-up of a CFD simulation may affect its accuracy, with the most accurate set up being presented in detail. Following this, the findings relating to the influence of a number of factors on the simulation results will be outlined so that their impact may be quantitatively understood. Throughout this study, there is a specific focus on turbulence modelling. In order to achieve these aims a number of objectifies have been identified:

(1) develop a CFD simulation that may be considered accurate;
(2) systematically investigate the identified factors to establish their influence;
(3) perform a Validation and Verification study to ensure a high confidence level in the CFD simulation;
(4) quantitatively evaluate the accuracy of CFD at modelling the nearfield longitudinal wake profiles of a planing hull through comparisons of the CL & QB profiles;
(5) qualitatively evaluate the accuracy of CFD at modelling the wake pattern of a planing hull through comparison of surface elevation plots with experimental pictures;
(6) comment on the set up deemed to be most accurate and make comparisons to other methods.

4. Methodology

The global methodology of the project was broken down into two stages. The experimental work as performed by [10] was to be used as validation data:

The first stage was to set up a CFD simulation capable of accurately modelling the longitudinal wake profiles. The simulations were tuned to ensure the best set up was achieved, with a number of factors being systematically varied to determine the effects on the predicted wake profile. Once an accurate simulation had been developed, an extensive Validation & Verification (V & V) study was undertaken. All numerical simulations were performed using the commercial software, Star CCM+ (12.04.011-R8), on the University of Strathclyde's Archie-WeST High Performance Computer.

The second stage was for all cases that were experimentally tested to be run using the CFD simulation, allowing a comparison to be made over a range of conditions. The results were then assessed both quantitatively and qualitatively to provide a detailed assessment of the accuracy of CFD. As the paper [10] from which the experimental data was obtained also investigated the accuracy of Savitsky's Wake Equations and the Linear Wake Assumption comments will also be made towards the accuracy of CFD in relation to other methods.

While it is possible to develop a robust and reliable numerical model based on either an overset grid or morphing mesh methodology that is capable of resolving the final attitude of a planing vessel these approaches were not utilised. Instead, the hull was fixed in both sinkage and trim. This methodology was chosen for two key reasons. Firstly, the experimental study had employed a hull that was fixed in sinkage and trim to give the researchers more control over the position for which the wake profile was being extracted, allowing a broad range of cases to be examined. Secondly, it is known that CFD is accurate in modelling the position of a planing vessel that is free to sink and trim, and it was not the place of this study to further evaluate this. In order to ensure an exact comparison between the experimental data and the numerical result and give a fair evaluation of CFDs capabilities it was important that the hull positioning was exactly the same in the experimental and numerical studies. Introducing the typical ~10% error in both sinkage and trim of the CFD simulation through a model that was not fixed would add uncertainty and taint the analysis of the wake profiles.

5. Experimental Set Up

The experimental results were obtained from [10]. Please refer to this paper for detailed discussion upon the experimental set up. This section will, however, briefly detail the experimental testing that was undertaken.

The experimental work used a simple prismatic hull form, featuring a constant deadrise. It was tested in the fully planing condition in calm water. The lines plan is presented by Figure 1.

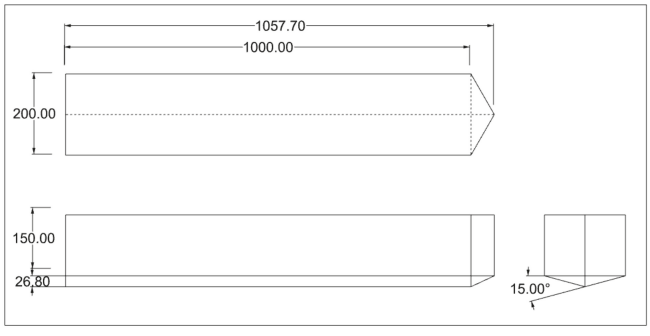

Figure 1. Lines Plan of Model (Linear Dimensions in mm).

The experimental test matrix was defined to cover a broad a range of hull positions, allowing a robust validation case for the CFD set up across a number of conditions. A total of 175 runs were completed, taking measurements for 12 test cases featuring three trim (τ) conditions and four speeds. The hull parameters for each test case are detailed in Table 1, where the draft given is the immersion of the transom once the model has been positioned correctly. Due to the speed limitations of the carriage, a small-scale testing methodology was employed.

Table 1. Hull Parameters.

τ [Deg]	Draft at Transom [mm]	Wetted Keel Length [mm]	Wetted Chine Length [mm]	Static Volume [cm^3]	Static Wetted Area [cm^2]
1.9	27	814	0	739.19	849.78
3	33	630	119	850.61	776.16
4	39	545	172	1004.93	742.16

The wake profiles was measured using sonic probes mounted on a gantry behind the model, as detailed in Figure 2. Additionally, the forces and moments were measured to allow further validation of the CFD simulation.

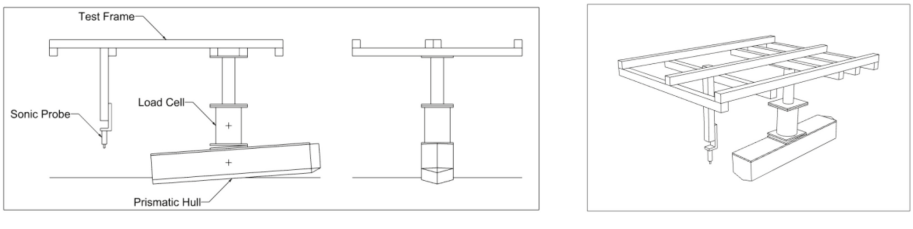

Figure 2. Gantry Step Up for One Sonic Probe.

6. Numerical Set Up

This section outlines the approach followed when developing the numerical simulation, giving the specific details of the final set up that was deemed the most appropriate for modelling this problem. Information regarding alternate set ups and the effect of these upon the simulations results is presented in the results section. Detailed information upon the inner numerical workings of the CFD code will not be discussed as the commercial solver Star CCM+ was used, and such details are not relevant to the scope of the work. Detailed information outlining the inner workings of a CFD solver can be found in [18]. The numerical set up was in the same scale and conditions as reported in the experimental study, ensuring that both the Froude and Reynolds numbers in both were identical.

6.1. Physics Modelling

It is commonplace to use a two-equation turbulence model for numerical studies into ship hydrodynamics, with [16] stating that they have been proven to give accurate predictions. Whilst more advanced models are available it was found by the ITTC following the analysis of entries to the Gothenburg 2010 Workshop, that there was no visible improvements to the accuracy of a resistance simulation when these are used.

The most widely used two-equation turbulence models for engineering application are $\kappa-\varepsilon$ and $\kappa-\omega$. Both are used when studying ship hydrodynamics; however, variants of $\kappa-\omega$ are far more prevalent, accounting for 80% of the submissions for the Gothenburg 2010 Workshop. When comparing the models the ITTC concluded that turbulence model selection has little impact upon the accuracy when analysing resistance [11]. A review of studies investigating planing hull performance through CFD found that there was no clear indication that one was more favourable than the other with both being used in a number of papers:

- $\kappa-\varepsilon$: ([14,19–23])
- $\kappa-\omega$ *SST*: ([24–27])

The $\kappa-\omega$ *SST* model is known to be more computationally expensive, with simulations taking up to 25% longer to run [28]. Despite this downside, studies have shown it to be superior when predicting separating flows and wake patterns [11,16]. Additionally, it has been shown to be the most prevalent turbulence model for use with marine hydrodynamics over the past two decades [29].

An investigation into turbulence model selection revealed that for low y^+ planing hull simulations turbulence model choice resulted in a notable variation in the calculated forces and moments. It was also shown to have reliable impact upon the accuracy of the calculated wake program. In this investigation $\kappa-\omega$ *SST* proved to be the most accurate, so this model was selected despite the fact that it is more computationally expensive.

The Volume of Fluid (VOF) method was used to model and track the position of the free surface. It is known for its numerical efficiency and is a simple-multiphase model that is well suited to simulating flows of immiscible fluids. The model introduces a 'volume fraction' variable, which is used to define the spatial distribution of each phase. A cell with a volume fraction of 0.5 contains a 50:50 mixture of air and water, and is used by the VOF method to define the free surface.

A known and documented problem when modelling planing hulls using the VOF method is that it can lead to Numerical Ventilation (NV), or Steaking, which may be considered one of the main sources of error in these numerical simulations [21,26] NV occurs when the free surface is not captured adequately and results in air falsely being introduced into the boundary layer flow adjacent to the hull. When NV occurs, it has a negative impact on the calculation of forces as it alters the fluid properties. Gray-Stephens et al. investigated a number of strategies to minimise NV [30]. All strategies that were found to be effective were employed in the setup of this simulation to ensure that NV did not affect its accuracy. Additionally, over the course of the current work it was found that including a surface tension model equal to 0.072 N/m helped to reduce NV further when used in conjunction with established methods.

The surface tension coefficient expresses how easily two fluids can be mixed, with a higher surface tension represents a stronger resistance to mixture. The coefficient itself is defined as the amount of work necessary to create a unit area of free surface [31]. For the most part the effects of surface tension are negligible with The ITTC Specialist Committee on Computational Fluid Dynamics stating that they may usually be neglected for ship hydrodynamics problems [32]. As this work adopted a small-scale testing approach, the surface tension forces are larger relative to the hydrodynamic forces than for a more conventional model size. It was thus necessary to determine if neglecting these forces was valid, or if they must be included in the simulations.

Including the surface tension model had a significant effect upon the forces calculated. This was achieved through a reduction in the level of NV (Figure 3), which changed the fluid properties in the near wall cells. It has been concluded a number of times that it is not possible to eradicate NV, however it is possible to reduce it to a level that is acceptable for engineering purposes [31,33]. This study presents a new viable strategy to reduce the levels of numerical ventilation. This is supported by [34], who investigated free surface flows with air entrainment and concluded that failure to include the surface tension model resulted in an increased level of air entrainment.

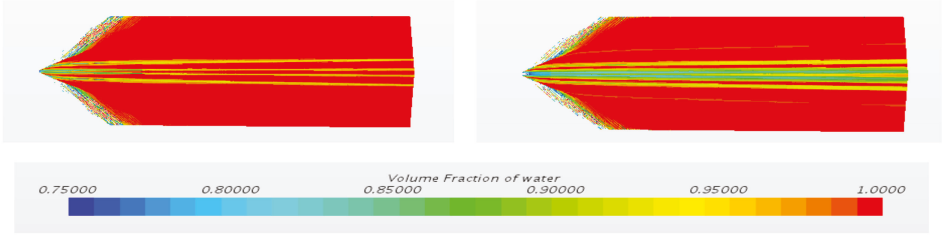

Figure 3. Numerical Ventilation (Left: Surface Tension On) (Right: Surface Tension Off).

All previous studies investigated planing hull hydrodynamics that were found over the course of the literature review followed a high y^+ approach, using wall functions to model turbulence. A low y^+ approach is desirable if an accurate prediction of the boundary layer velocity is required, for instance in drag calculations, and if the cell count and simulation time is not considered a critical issue [35]. Adopting a low y^+ approach almost doubled the cell count and increased the computational time required for convergence by a factor of three, however lead to a significant improvement in the accuracy of both the wake profile and forces.

As the cell count and simulation time were not considered critical issues the low y^+ approach was selected, primarily due to the improved the accuracy in calculating the wake profiles, however also as it reduced the comparison error in resistance to a more acceptable level. The low y^+ approach resolves the viscous sublayer and, as such, the simulation should be more representative of the physical phenomena occurring.

6.2. Timestep

A timestep may be selected to ensure that it satisfies the flow features of interest or that it satisfies the Courant–Friedrichs–Lewy (CFL) condition. For standard pseudo-transient resistance simulations, a timestep that satisfies the flow features of interest is usually selected when an implicit solver is employed. When the V & V study (as presented in Section 7) was performed, a number of timesteps were tested. The timestep study revealed that as the timestep was reduced by a factor of two, the calculated forces featured Monotonic convergence upon a solution. The average timestep convergence ratio for all forces was 0.27, and was as low as 0.016 for resistance. The selection of timestep was made to balance the computational run time against the accuracy of the solution. It was shown that when the timestep was reduced further there was no significant improvement in the results.

A timestep (Δt) that satisfactorily resolves the flow features as a function of the vessels speed (U) and the wetted length ($L_{K(m)}$) of the hull was selected, such that:

$$\Delta t = 0.02 \frac{L_{K(m)}}{U} \quad (1)$$

It was ensured that the selected timestep was within the range suggested by the ITTC for such simulations in all cases [36]. Satisfying the CFL condition for all cells resulted in an impractically small timestep that would result in an unjustifiable increase in computational time. It would also have a negligible impact upon the results over a timestep that was selected to ensure that the flow features of interest were satisfied through a timestep independence study. The verification study determined that a timestep defined by Equation (1) is capable of resolving the flow features of interest, suitably balancing accuracy against computational time.

6.3. Computational Domain

It is well documented that for a CFD simulation to be accurate the choice of domain size must be appropriate, such that the boundaries are placed sufficiently far away to ensure they have no effect upon the solution through interaction with the wake. The ITTC recommend that the inlet and exterior boundaries are located 1–2 Length between perpendiculars (L_{PP}) from the hull, with the outlet being placed 3–5 L_{PP} downstream [37]. It is also important to ensure that wake does not intersect with the side boundary as this can cause reflections that influence the solution. Due to the narrow wake associated with a planing hull this is of less concern than for a conventional displacement simulation. The sizing of the computational domain was chosen in accordance with ITTC recommendations and may be seen in Figure 4. To ensure the domain was robust and suitable for all possible trim conditions the overall length of the model was used rather length between perpendiculars, or wetted length.

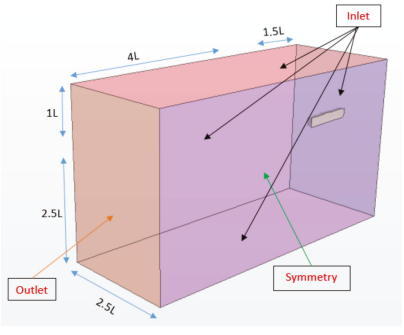

Figure 4. Domain Sizes and Boundary Conditions (L = Overall Length).

In addition to selecting an appropriately sized domain, the VOF Wave Damping option was enabled on the side and outlet boundaries to ensure that wave reflections did not impact the solution. The VOF Wave Damping option introduces a vertical resistance to vertical motion, and suppresses waves, and prevent them reflecting back into the simulation. A damping zone of one length overall (L) was chosen.

6.4. Boundary Conditions

The selection of appropriate boundary conditions is essential to ensure that the solution remains accurate whilst at the same time managing the computational costs of the simulation. The Dirichlet boundary condition was applied, simulating free flow. A common practice to reduce the size of the domain for calm water resistance simulations is to implement a symmetry condition on the x-z plane at

the centreline of the hull. The nature of the wake profile was shown to include symmetrical elements of flow that crossed the centreline and interact with one another. As such, prior to employing this strategy, tests were undertaken to determine if it influenced the calculated wake profiles. It was shown that there was negligible impact upon the results and, as such, the symmetry boundary condition was utilised, halving the computational demand.

If the simulation were to be an accurate representation of the physical tank, the walls of the domain would be modelled using no-slip walls, the top as an inlet, the front as an inlet, and the rear as a pressure outlet. The modelling of no-slip walls requires the inclusion of a prism layer mesh, and this in turn requires volume mesh refinements to ensure the interface between the volume mesh and the prism layer mesh is appropriate, maintaining an acceptable volume change between cells. Such a selection of boundary conditions is impractical due to the significant increase in cells. A simplification to avoid this is to model the sides and bottom of the domain as inlets. The inlet condition is reported to be the least computationally expensive, whilst the selection of any appropriate combination of boundary conditions has no significant affect upon the flow results, provided they are located suitably far from the vessels hull [28]. The physical tank walls were far enough from the hull as to have no influence upon it, while the depth was great enough to consider the scenario a deep-water problem. Similarly, the domain of the simulation is large enough that the boundaries are far enough away to have no impact upon the result.

Extra consideration was given to the deep-water assumption. Before employing this assumption for the CFD case, the following were checked for the experimental test regime:

- $d/\lambda > 0.5$ in all conditions [38] (where d is depth and λ is wavelength);
- the depth Froude number was below the critical value;
- all recommendations regarding depth and width outlined in [39] were adhered to.

6.5. Computational Grid

A planing hull is subject to larger variations in trim and sinkage than a conventional displacement hull. One of the greatest challenges when developing a numerical simulation modelling a planing hull is ensuring the mesh can accurately deal with these motions. For this test program, the physical model was fixed in sinkage and trim, removing the need for the mesh to be capable of modelling motion and allowing a rigid mesh to be used as opposed to morphing or overset grids.

To generate the mesh Star CCM+'s automated meshing capability was utilised [35], with the surface remesher, automatic surface repair, trimmed cell c and prism layer mesher selected. The 'trimmed cell mesher' was selected as it aligns the cells with the direction of the flow, minimising numerical diffusion. This feature relies upon the Cartesian cut-cell method. It allows for a large degree of control through the use of local surface and volumetric controls that allow the user to increase or decrease the mesh density. This method presents a robust and efficient method of producing a high-quality grid, predominantly made up of unstructured hexahedral cells with polyhedral cells next to the surface. The mesh is formed by constructing a template mesh from the target sizes input by the user, and then trimming as required, this using the input surfaces. Using a trimmer mesh enables the use of growth parameters that can be used to ensure there is smooth transitions within the mesh and help prevent the introduction of numerical errors.

Volumetric controls were used to progressively refine areas of the mesh in which flow features of interest occurred, ensuring that the mesh was capable of capturing the complex flow in these regions. The areas that were identified for progressive refinement were the free surface, the area surrounding the hull, and the wake region, with three layers of increasing refinement used for each. Additional refinements were included at the bow, the stern, and for the free surface upstream of hull. These further enhance the resolution where the largest flow gradients occurred, and to help prevent Numerical Ventilation. Figure 5 shows the computational grid and the refinements that it contains. It should be

noted that the mesh shown was for the coarsest studied in the mesh study as it shows the refinement zones clearly.

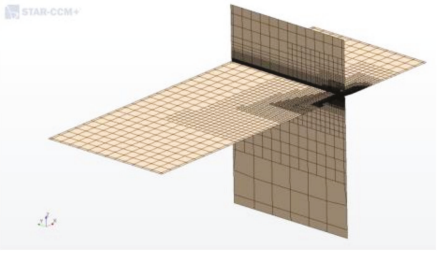

Figure 5. Computational Grid.

To allow the simulation to accurately resolve the high velocity gradients associated with the boundary layer flow the 'prism layer mesher' was used. This generates orthogonal prismatic cells adjacent to the hull. These are high-aspect ratio cells that are aligned with the local flow and are vital for the accuracy of the simulation. The thickness of the prism layer was calculated to be equal to the thickness of turbulent flow (δ) for a given Reynolds number (R_n) over a flat plate of the same wetted length (x), as calculated by [40]:

$$\frac{\delta}{x} = 0.38R_n^{-\frac{1}{5}} \tag{2}$$

After the simulation converged satisfactorily, a scalar plot of the Turbulent Viscosity Ratio was checked to ensure that the prism layer was thick enough. If the prism layer mesh is not thick enough then a non-trivial amount of turbulent viscosity would be present in the core mesh, indicating that part of the boundary layer has diffused into the core mesh region.

The first cell height of the prism layer was calculated to ensure that the y^+ value was below one. A stretching ratio of 1.2 as suggested by [37] was used to grow the prism layer until it reached the desired thickness. Care was taken to ensure that the outer layer of the prism layer mesh and the first layer of the core mesh were of comparable sizes to ensure that numerical errors were not introduced.

An additional volumetric refinement was included in the area in which the free surface met the hull. The prism layer thickness was reduced to 25% of the calculated thickness in this region as suggested in [30].This further reduces Numerical Ventilation as it decreases the numerical diffusion caused by the cells of the prism layer that are misaligned with the free surface.

A mesh study was undertaken to ensure that the mesh was fine enough, resulting in the final mesh consisting of around 20 million cells. The choice to follow a low y^+ approach significantly increased the cell count, however as the body was fixed this did not result in an impractical computational time to reach convergence. Simulations took between 7.5–27 h to run on the Archie-WeST High Performance Computer (HPC), equating to between 300–1080 core hours. The large variation in run time was caused by differences in the physical time the simulation had to run for to converge satisfactorily. Another factor effecting the run time was that some simulations required very large number of iterations in the early stages of the simulation to ensure that the large gradients associated with beginning a simulation did not cause divergence.

7. Verification and Validation of CFD

In most examples of planing hull simulations available in literature validation is conducted by a straightforward comparison of the simulated result and tank testing data. This approach is rather basic and may not be used to evaluate the true accuracy of the simulation. It is possible for numerical and experimental results to be very close; however, this may be by chance with the simulation containing considerable numerical uncertainties, which combine to give the correct result. Without conducting a

thorough Verification and Validation (V & V) study, there can be little confidence in any results as the accuracy and uncertainty of the simulation has not been evaluated. As such, one should be completed prior to generating any results for analysis. The ITTC has published guidelines on how best to perform a V & V study in relation to marine simulations [41]. The full V & V methodology and procedure that was followed is outlined in the aforementioned guidelines.

Before continuing, it is necessary to provide a brief definition of Validation and Verification:

- verification is the quantitative assessment of the numerical uncertainty (U_{SN}) and when conditions permit, estimating the sign and magnitude of the numerical error $\left(\delta^*_{SN}\right)$ and the uncertainty (U_{S_CN}) in that estimate. It is used to determine if a computational simulation accurately represents the conceptual model [42];
- validation is the assessment of the modelling uncertainty (U_{SM}) of the simulation through the use of experimental data, and if conditions permit, estimating the sign and magnitude of the modelling error (δ_{SM}). It is the process of determining whether a computational simulation represents the real world [42].

The ITTC recommendations [41] are based upon the work of [43]. This approach defines errors and uncertainties in a way that is consistent with experimental uncertainty analysis, where the simulation error (δ_S) is the difference between a simulations result (S) and the truth (T), and is made up of modelling (δ_{SM}) and numerical (δ_{SN}) errors.

$$\delta_S = T - S \tag{3}$$

$$\delta_S = \delta_{SM} + \delta_{SN} \tag{4}$$

The procedure relies upon the Richardson Extrapolation (RE) procedure [44], which is the basis for existing quantitative numerical uncertainty and error estimates for both grid and timestep convergence [45]. Following the method, the error is expanded in a power series, with integer powers of grid spacing or timestep taken as a finite sum. When it is assumed that the solutions lie within the asymptotic range it is acceptable that only the first term is considered, leading to a so-called triplet study.

The Correction Factor approach was employed. The first step of this approach is to assess the convergence condition using the convergence ratio (R_i), defined as the ratio between $\varepsilon_{i,21} = S_{i,2} - S_{i,1}$ and $\varepsilon_{i,32} = S_{i,3} - S_{i,2}$. Here $S_{i,k}$ refers to the solution obtained from the i^{th} input parameter using the k^{th} refinement. The solutions obtained by systematically coarsening the i^{th} parameter by the refinement ratio, r_k. Four convergence conditions may exist, as defined by [43]:

- Monotonic Convergence: $0 < R_i < 1$
- Oscillatory Convergence: $R_i < 0; |R_i| < 1$
- Monotonic Divergence: $R_i > 1$
- Oscillatory Divergence: $R_i < 0; |R_i| > 1$

For the first condition, Generalized Richardson Extrapolation is used to assess the uncertainty (U_i). The error and order of accuracy must be calculated:

$$\delta^*_{RE_{i,1}} = \frac{\varepsilon_{i,21}}{r_i^{P_i} - 1} \tag{5}$$

$$P_i = \frac{\ln\left(\frac{\varepsilon_{i,32}}{\varepsilon_{i,21}}\right)}{\ln(r_i)} \tag{6}$$

Using a correction factor approach provides a quantitative measure of defining how far from a solution is from the asymptotic range, and then approximately accounting for the effects of higher

order terms when making error and uncertainty estimates. It is based on verification studies for 1D wave and 2D Laplace equation analytical benchmarks. These showed that one-term RE error estimates are poor when not in the asymptotic range, but that multiplying them by a correction factor improved error and uncertainty estimates. The numerical error is defined as:

$$\delta_i^* = C_i \delta_{RE_{i,1}}^* = C_i \left(\frac{\varepsilon_{i,21}}{r_i^{P_i} - 1} \right) \tag{7}$$

The correction factor (C_i) is based upon replacing the observed order of accuracy with an improved estimate, which roughly accounts for the effects of higher order terms. This limits the order of accuracy of the first term as spacing size goes to zero and ensures that as the asymptotic range is reached (C_i) tends to zero [43].

$$C_i = \frac{\left(r_i^{P_i} - 1 \right)}{\left(r_i^{P_{est}} - 1 \right)} \tag{8}$$

Depending how close the numerical error (δ_i^*) is to the asymptotic range determines the expression that is used to evaluate the solution uncertainty:

$$U_i = \left[9.6(1 - C_i)^2 + 1.1 \right] \left| \delta_{RE_{i,1}}^* \right| \; |1 - C_i| < 0.125 \tag{9}$$

$$U_i = \left[2|1 - C_i| + 1 \right] \left| \delta_{RE_{i,1}}^* \right| \; |1 - C_i| \geq 0.125 \tag{10}$$

Validation is the process of assessing the simulations modelling uncertainty (U_{SM}) by using benchmark experimental data, and where possible the modelling error (δ_{SM}). The comparison error (E) is defined as the difference between the data (D) and the simulation solution (S).

$$E = D - S = \delta_D - (\delta_{SM} + \delta_{SN}) \tag{11}$$

Modelling error (δ_{SM}) can be decomposed into modelling assumptions and use of previous data. To determine if validation has been achieved the comparison error is compared to the validation uncertainty (U_V) as given by:

$$U_V^2 = U_D^2 + U_{SN}^2 \tag{12}$$

If the validation uncertainty is smaller than the comparison error then the combination of all of the errors in the experimental data and the numerical data is smaller than the validation uncertainty. This allows the simulation to be considered validated at the level of the validation uncertainty.

$$|E| < U_V \tag{13}$$

V & V Case

Having completed the setup of the simulation a V & V study was undertaken. Both grid and timestep studies were conducted, producing a triplet of results and allowing the analysis of the uncertainty attributable to both. For the grid study, a refinement ratio of $\sqrt{2}$ was selected, as recommended by the ITTC. For the timestep study, a refinement factor of 2 was selected. These refinements were previously used by [28], and shown to provide a strong validation case. The case for which the V & V was carried out for was a trim angle of 4° and a speed of 4 ms^{-1}.

The triplet of solutions for both the grid and timestep studies displayed monotonic convergence. Specific grid and timestep uncertainties were calculated following the Correction Factor approach. Prior to this, it was checked that the iterative uncertainty was negligible and would not contaminate the results. The calculated uncertainties, and whether each parameter has been validated, are shown in Tables 2 and 3, respectively.

Table 2. Grid Convergence Study.

Parameter	r_G	*EFD*	S_1	S_2	S_3	R_G	U_G	U'_G
Cell Count	-	-	18,696,864	9,043,490	4,397,783	-	-	-
F_X [N]	$\sqrt{2}$	4.503	4.906	5.022	5.198	0.661	0.448	9.14%
F_Z [N]	$\sqrt{2}$	15.602	17.188	17.578	18.141	0.692	1.854	10.78%
M_Y [Nm]	$\sqrt{2}$	2.646	3.220	3.334	3.567	0.485	0.121	3.77%

Table 3. Timestep Convergence Study.

Parameter	r_T	*EFD*	S_1	S_2	S_3	R_T	U_T	U'_T
Timestep [s]	-	-	2.86×10^{-3}	5.73×10^{-3}	1.15×10^{-2}	-	-	-
F_X [N]	2	4.503	4.906	4.909	5.120	0.016	0.002	0.04%
F_Z [N]	2	15.602	17.188	17.366	18.344	0.182	0.079	0.46%
M_Y [Nm]	2	2.646	3.220	3.262	3.330	0.619	0.176	5.48%

As can be seen, suitably small uncertainties exist for most parameters. Larger uncertainties for U_G were calculated for resistance and lift, showing that these parameters are reasonably sensitive to the grid resolution.

Following the calculation of the uncertainties it is possible to determine whether the simulation may be considered validated. The results for this are shown in Table 4. The validation uncertainty for both resistance and lift was found to be lower than the comparison error, deeming the simulation valid for both these parameters. The same cannot be said for trimming moment unfortunately. This however, was only included as a means of establishing the accuracy of the simulations and was not the primary focus of the study. As the simulation had been validated for both resistance and lift, it was deemed satisfactory to proceed.

Table 4. Validation Study.

Parameter	U_{SN}	U_D	U_V	$\|E\|$	$\|E\|<U_V$
F_X [N]	0.448	0.319	0.550	0.402	Yes
F_Z [N]	1.855	0.426	1.904	1.586	Yes
M_Y [Nm]	0.214	0.168	0.272	0.574	No

8. Results

The following section will compare and discuss the results. While only certain results are shown here, the full data set may be found in the Appendices. The results section first details the findings of the investigation into the impact of a number of parameters upon the accuracy of the CFD simulation. This attempts to highlight what may be considered vital when establishing a simulation that looks to accurately model the nearfield longitudinal wake field of a high-speed planning hull. It then goes on to discuss and compare the experimental and numerical resistance, lift and trimming moment results. This comparison is made to evaluate the accuracy of the CFD at modelling forces before investigating its ability at modelling wake profiles. Following this, the quantitative wake profile data from each method will be analysed, with qualitative wake profile data in the form of pictures. All graphs are presented with error bars as calculated in the Experimental Uncertainty and V & V sections.

The wake profile plots are presented in a format consistent with those as presented by [10], with the origin representing the point where the keel meets the transom and the horizontal axis in line with the keel, as seen in Figure 6. The distance aft of the transom, and height of the wake profile, have been nondimensionalised by beam on all figures.

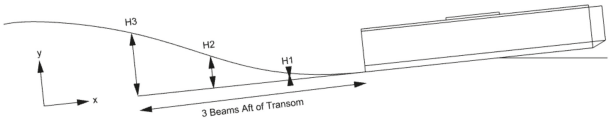

Figure 6. Results Reference Axis.

8.1. Parameters Affecting CFD Accuracy

A number of parameters that had the potential to impact the accuracy of the CFD simulation were identified to be systematically studied. The focus of this study was to establish what effect they had on the accuracy of the calculated wake profile; however, their effects on the calculated forces and moments are also noted. The purpose of presenting these results as opposed to only these of the final set up is to provide insight to other researchers working within the same field. Over the course of this work, tens of thousands of CPU hours were used to establish what set up produced the most accurate results.

During the systematic testing, as many factors as possible were held constant, with only the parameter under examination being varied in an attempt to isolate its impact upon the results. In the following discussion, the percentage differences given show the difference in comparison error with the experimental results, with a negative value indicating that the result was found to be further from the experimental data.

8.1.1. Use of the Symmetry Condition

It is common practice to employ a symmetry plane as a boundary condition on the centreline of the vessel when the computation is for a steady state simulation. This strategy halves the mesh count and allows for a significant reduction in computational demand. The ITTC [46] does note that this approach this may led to a loss of physics when transient flow occurs between port and starboard and recommends that if a Detached Eddy Simulation (DES) or Large Eddy Simulation (LES) approach is followed then a full domain should be modelled. When photos of the experimental study are examined elements of flow are seen to cross the centreline. It is, thus, necessary to establish whether the use of the symmetry boundary condition causes the wake field to be incorrectly calculated due to the lack of modelling of these elements.

The use of the symmetry condition was found to have no significant impact on the results of the simulation. A difference of 0.11% in resistance, −0.15% in lift, and −0.37% in trimming moment were found when it was employed, while both the centreline and quarterbeam longitudinal profiles were identical. A final check of the surface elevation plots revealed no significant differences in the wake field. The results of this suggest that a Reynolds-averaged Navier–Stokes (RANS) approach to modelling the flow does not provide enough resolution to capture the asymmetric elements of flow that are present. In order to accurately model these, it is suggested that the higher fidelity DES or LES approaches are employed.

8.1.2. Use of the Surface Tension Model

The inclusion of the surface tension model adds a tensile force tangential to the interface separating two fluids. This force works to keep the molecules of fluid that are at the free surface in contact with the rest of the fluid [47]. When the surface tension model is included in a simulation the Navier–Stokes equations are reformulated to contain an additional source term, which accounts for the momentum exchange across the interface due to the surface tension forces [48]. Surface tension may have a larger impact upon the hydrodynamic forces of a small-scale model due to the relative larger size of the surface tension forces. As it also effects the creation of the free surface, it is necessary to determine how its inclusion impacts both the calculated forces and wake profile.

When the surface tension model was included a difference of −1.68% in resistance, 2.87% in lift, and 11.68% in trimming moment were found. This shows that due to the small scale of the model the surface tension forces influence may be considered significant. This may in part be due to the reduction in the level of numerical ventilation as discussed in the CFD set-up section. When the centreline and quarterbeam profiles were examined, they were seen to be largely similar, with the surface tension model reducing the accuracy by a maximum of 1.51 mm. Despite the reduction in accuracy the inclusion of the surface tension model was deemed to be more physically representative.

8.1.3. Approach to Turbulence Modelling

In most flow problems, walls are a source of vorticity and as such accurately predicting the flow and turbulence parameters in the wall boundary layer is essential. The presence of the wall results in the gradients of the flow variables becoming very large and as the wall distance reduces to zero. The behaviour of the flow in this region near is a complex phenomenon that is made up the viscous sublayer (where the flow is dominated by viscous effects), the buffer layer (where viscous and turbulent stresses are of the same order), and the log-law layer (where turbulence stress dominates the flow). The concept of wall y+ is used to distinguish between these components, with its value being used to determine the characteristics of the flow.

Wall treatment models are a set of configurations and assumptions that are used by a CFD solver to model the near wall turbulence quantities such as the turbulence dissipation, turbulence production and the wall shear stress. These are categorised as high or low y^+ wall treatment, with each following a different approach to resolve the flow in the boundary layer.

If a low y^+ approach is chosen, the whole near wall turbulent boundary layer is resolved, including the viscous sublayer, the buffer layer, and the log-law region. There is no modelling used to predict the flow, with the transport equations being solved all the way to the wall cell and the wall shear stress being computed as in laminar flows. In order to resolve the viscous sublayer the mesh has to be suitably fine, with a y^+ value of one or less, ensuring that the centre of the wall cell located in the viscous sublayer. This approach can be very computationally expensive as a large number of prism layer cells may be required to ensure the wall cell is placed within the viscous sublayer [47].

The high y^+ approach models the viscous sub layer and the buffer layer using wall functions for the turbulence production, the turbulence dissipation and the wall shear stress. These are values are derived from equilibrium turbulent boundary layer theory. Using wall functions to model these means that the mesh is not required to resolve the viscous sublayer and the buffer layer and can therefore be far courser. For a high y^+ approach to be valid there should be y^+ that is larger than 30 to ensure that the wall cell is in the log-law region of the flow. There have been successful applications of a high y^+ approach using a y^+ value of up to 500 in marine and civil engineering applications, however best practice guides recommend an upper limit of 100 unless a thorough validation is carried out. Following a high y^+ approach results in a significant saving in computational time as far fewer prism layer cells are required [47].

The decision on whether to adopt a high or low y^+ approach is generally based upon the computational resources that are available. When the literature was reviewed in relation to planning hulls (both conventional and stepped), no examples of low y^+ approaches were found. However, for conventional marine CFD the wall function approach performs remarkably well at predicting the resistance and does not seem to compromise the quality of the solution [11].

Both a high y^+ of 40 and low y^+ of 1 were employed to assess their impact upon the results. The number of prism layers increased from 9 to 28, while the total thickness and stretching ratio remained constant. The change from high to low y^+ increased the cell count by 82% and increased the run time by 68%. It was found that changing to a low y^+ approach caused a 6.01% change in resistance, a −10.08% change in lift, and a −21.50% change in trimming moment. When the wake profiles were examined it was found that there was a maximum difference of 4.75 mm for the centreline wake profile,

and a maximum difference of 3.33 mm for the quarterbeam profile, where the low y^+ profiles were found to be more accurate.

The results show that the choice between a low and high y^+ approach is the numerical set up factor that has the single largest effect upon the accuracy of the solution. As the low y^+ approach resolves the viscous sublayer the calculation of forces should be more accurate, however it has been shown to be detrimental in terms of lift and trimming moment. Planning hulls clearly do not fall into the same category as displacement hulls where this selection has been shown to have little impact. A more comprehensive investigation into the effects of selecting a low y^+ approach over a range of speed and trim conditions is recommended in the future to gain a more detailed understanding.

8.1.4. Choice of Turbulence Model

Whilst it is possible for the exact turbulence solution in a simulation to be fully described by the Navier–Stokes Equations through Direct Numerical Simulation (DNS), it is impractical due to its requirement for massive computational resources. A commonly accepted alternative that is less computationally expensive is to solve for averaged (or filtered) quantities, and approximate the impact of small fluctuating structures. This is known as a Reynolds-averaged Navier–Stokes (RANS) approach, which utilises turbulence models. These models provide closure of the RANS equation and are approximate representation of the physical phenomena of turbulence [47].

The ITTC [36] states that the two-equation turbulence models have been shown to give accurate predictions in ship hydrodynamics. Larson [16] concluded from his analysis of the entries to Gothenburg 2010 Workshop that there was no visible improvement in accuracy for resistance prediction when turbulence models that are more advanced than the two-equation models were used. It found that $\kappa-\omega$ was by far the most applied with 80% of the submissions for the workshop using some form of variation of them. Other authors have also concluded that for resistance calculations the turbulence modelling has little effect on the prediction accuracy [32].

A review of other studies using CFD for planing hull performance prediction found that the majority of simulations use the $\kappa-\varepsilon$ [14,19–21,23] or the $\kappa-\omega$ *SST* [26,27,48–50] models. Despite both models being comparable in terms of resistance prediction it has been shown by [16] that the choice of turbulence model has a profound influence on the accuracy of the local flow in the stern region. It was found that the wake predicted by advanced turbulence models such as Reynolds Stress Model (RSM), Explicit Algebraic RSM (EARSM), and $\kappa-\omega$ *SST* clearly show better correlation with measured data. This is echoed by [36], who concluded that wake can be predicted fairly accurately using advanced models such as $\kappa-\omega$ *SST*.

The $\kappa-\varepsilon$ turbulence model is the baseline two-equation model, solving for the kinetic energy (k) and the turbulent dissipation (ε). This is one of the most commonly used turbulence models in industrial CFD and provides a good compromise between robustness, computational cost, and accuracy. This model is known to give good predictions for free flows with small pressure gradients [48]; however, performs poorly for complex flows with severe pressure gradients, separation, or strong streamline curvature.

The $\kappa-\omega$ *SST* turbulence model is a hybrid model that was developed by [51] in order to take advantage of the collective advantages of the $\kappa-\varepsilon$ and the $\kappa-\omega$ models. It was developed to address the sensitivity issue with the free stream sensitivity faced by the standard $\kappa-\omega$. The two models were combined into one using a blended function. This model uses the $\kappa-\omega$ model in the boundary layer, whilst the $\kappa-\varepsilon$ (formulated on $\kappa-\omega$) is used in the free flow [48]. The approach is accepted to have cured the biggest drawback of the $\kappa-\omega$ model when modelling practical flow simulations [47].

The two-layer approach allows the k-ε turbulence model to be applied to the viscous-affected layers. Following this approach, the computation is divided into two layers, where the standard turbulence model is used to turbulent kinetic energy for the whole domain and the turbulent dissipation away from the wall, while for the near wall layer the turbulent dissipation rate is calculated as a function of wall distance and local turbulent kinetic energy.

The realizable κ−ε model contains a new formulation to calculate the kinetic dissipation rate, and adds a variable damping function. This results in the model being substantially better than the standard κ−ε formulation for many applications, while the model can be relied upon to produce results that are at least as accurate as those of the standard model [47]. It is compatible with the two-layer approach, allowing it to resolve the viscous sublayer.

In the course of this study a four turbulence models were employed to gauge their effects on the calculation of forces and wake pattern. Where applicable, these were tested for both a low y^+ and high y^+ approach, resulting in seven test cases. The results showing the comparison error with the experimental data for all cases are detailed in Table 5.

Table 5. Turbulence Model Selection.

Turbulence Model	y^+	Resistance	Lift	Trimming Moment
κ−ε	40	17.91%	3.32%	5.19%
Standard κ−ε Two-Layer	40	17.62%	3.45%	5.57%
Realizable κ−ε Two-Layer	40	15.32%	3.30%	4.65%
$k-\omega$ *SST*	40	16.10%	3.25%	4.59%
Standard κ−ε Two-Layer	1	13.18%	15.24%	17.52%
Realizable κ−ε Two-Layer	1	14.66%	13.57%	28.26%
$k-\omega$ *SST*	1	10.09%	13.33%	26.09%

It is apparent that the choice of whether to employ wall functions or to resolve the viscous sub-layer remains the largest factor that effects the accuracy for all turbulence models. It is once again seen that following a low y^+ approach results in more accurate resistance prediction; however, less accurate lift and trimming moment prediction. It is seen that the choice of model has a larger effect on the results for the low y^+ cases, resulting in variations of a 4.75% in resistance, 1.91% in lift, and 10.74% in trimming moment. The variations for the high y^+ cases were significantly smaller with 2.59% in resistance, 0.20% in lift and 0.98% in trimming moment.

When the wake profile plots are examined it is found that the choice of turbulence model has no discernible impact upon the results, while the choice of turbulence modelling approach is once again seen to have some effect. For all high y^+ cases, the centreline wake profiles are almost identical, regardless of turbulence model, with a maximum difference of 0.21 mm. Low y^+ cases result in a the centreline wake profiles that is more accurate than the high y^+ results, but these are once again almost identical, regardless of turbulence model with a maximum difference of 0.15 mm. Similar trends were found for the quarterbeam profiles, where the low y^+ was seen to be more accurate. These profiles feature slightly more variation with a maximum variation of 0.58 mm for the high y^+ approach and 0.42 mm for low y^+.

It can be concluded from this study that while the choice of turbulence model clearly effects the boundary layer and the resultant forces that are calculated for the hull, it has little impact upon the flow and the wake pattern remains largely unchanged when different turbulence models are employed.

8.1.5. Spatial and Temporal Discretization

As is discussed in the V & V section the improper choice of the fineness of either the temporal or spatial discretization of the simulation space may result in inaccuracies. If the selected values for either are to large it will result in the simulation being incapable of capturing the phenomena that are occurring. The effects on the calculation of forces has been studied and discussed in the V & V section, where it was seen that the spatial discretization caused variations of 6.50% in resistance, 6.11% in lift and 13.10% in trimming moment. The temporal discretization was less influential however still caused variations of 1.33% in resistance, 1.55% in lift, and 2.17% in trimming moment.

While the discretization of the simulation space was seen have a large impact upon the calculation of forces, it was found to have negligible impact upon the wake profiles. As the data was extracted from the V & V study, all data variations for one factor were made with the finest selection of the other.

The spatial discretization was found to produce a maximum difference of 0.85 mm while the temporal discretization was found to produce a maximum difference of 0.38 mm.

8.1.6. Conclusions

From the study of factors effecting the accuracy of the CFD, it can be seen that the calculation of forces is far more sensitive than the calculation of the wake profiles. The approach to modelling turbulence was found to be the most influential on the calculation of the wake profile, with simulations where the laminar sub-layer is resolved found to be more accurate. The selection of the turbulence model itself was shown to have limited impact on the wake profile. The second most influential factor was found to be the inclusion of the surface tension model; however, further investigation is required to establish if this is the case for all simulations or it is accountable to the small scale testing approach that was employed and the scale of surface tension effects relative to the calculated values. The spatial and temporal discretization showed that the choice of grid refinement was more important than that of timestep to accurately predict the wake pattern; however, this study also showed relatively course set ups to be capable of modelling the wake with a surprising degree of accuracy. Finally, it was shown that for RANS simulations the use of a symmetry boundary condition on the centreline has no effect on the calculation of the wake profiles.

8.2. Resistance

The choice of hull positions was selected in order to provide a broad range of conditions for which the ability of CFD at predicting the wake profiles would be assessed. As such, there were no systematic changes between each of the conditions tested, and no real conclusions can be drawn from a comparison between the measured forces of each.

The comparison error in resistance varies between 4.63% and 19.74%, with an average value of 12.43%. The comparison error is made significantly worse by the results for trim condition 3°, which have an average error of 16.76% and is notably larger than for 4° & 1.9°, which have average comparison errors of 11.49% & 9.04%, respectively. The relatively large errors that are found by this study are likely attributable to issues arising from small scale testing, as outlined by [10]. The key points of this discussion were in relation to the fact that the effects of positioning errors were amplified for a small-scale model when compared to a larger, more conventional model, and also that a standard absolute error value becomes a larger percentage value for the smaller forces associated with a small model.

It is commonplace for CFD simulations of High Speed Vessels to achieve an error of 10% [11]. While the 1.9° and 4° were found to have an average error in this region it is expected that the accuracy of these simulations should have been higher due to the high cell number used, and the higher fidelity low y+ scheme that was employed. It is seen that for the 3°, which has a considerable higher average error. The errors in the resistance are caused predominantly by errors arising from the accuracy of the hull positioning. Accurately determining the position of the hull and measuring this relative to a known location was one of the main challenges outlined for small scale testing. It is likely the case the position of the models in the experiments does not exactly match the hull position in the CFD simulations due to this. A sensitivity study was undertaken determine the effect of a small positioning error, finding that a small change in position did have a large effect upon the results and confirming that the large errors were accountable to positioning errors.

The sensitivity study found that a 1 mm positioning alteration to sinkage caused a 3.27% change to resistance, a 0.55% change to lift, and a 8.45% change in trimming moment. A 0.1° alteration in trim produced respective changes of 7.96%, 5.10%, and 7.78%. Finally, a combined alteration of 1 mm in sinkage and 0.1° in trim caused respective changes of 11.21%, 6.50%, and 13.97%. This study goes some way to highlight the problems associated with small scale testing, showing how sensitive to plausible positioning errors the results are. When the wake profiles for all cases studied in the sensitivity study were examined; however, they were found to contain no significant changes. This allows a higher

degree of confidence in both the experimental and numerical results of the wake profiles that for the forces and moment.

Despite the errors, it can be seen in Figure 7 that for all cases the CFD results show relatively good agreement with the experimental results. It has been reported by [52] that once a hull is in the fully planning regime a linear trend between resistance crests may be expected. When a linear data is applied to the experimental results, an R^2 value of 0.99 is returned, indicating that the speed range studied is showing this linear trend between resistance crests. A linear data fit applied to the CFD results also returns an R^2 value of 0.99, showing CFD is modelling the same trend as is apparent in the experimental data.

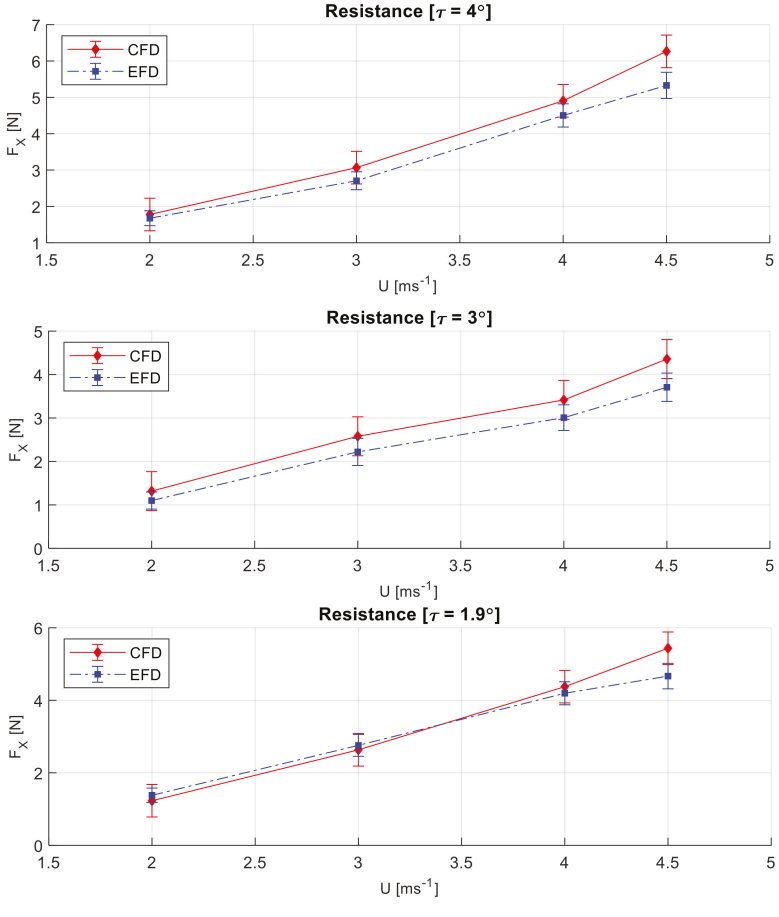

Figure 7. Numerical Resistance Results.

8.3. Lift

The experimental set up only measured dynamic lift, whereas the CFD measured both the buoyant and dynamic components. As such, the CFD results were corrected to dynamic lift by determining the buoyant contribution and subtracting it from the total lift. The results for the dynamic lift are shown in Figure 8.

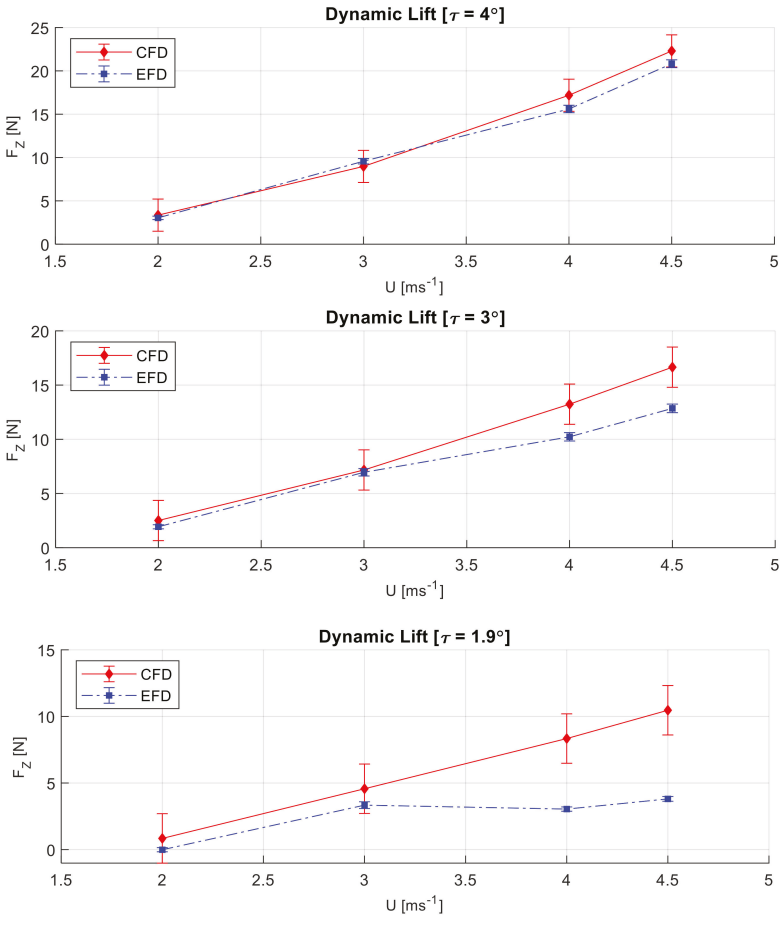

Figure 8. Numerical Lift Results.

For trim angles of 3° and 4°, the CFD results show good correlation with the experimental data, however at the higher speeds of 3° accuracy is lost a little. This can be seen to a lesser extend for 4° as well. For 1.9°, the CFD trend is very different from the experimental trend. The CFD trend remains linear, with an R^2 of 0.99, and does not plateau as the experimental data does. This fits more with what was expected for the lift, given that the experimental results of 3° & 4° are shown to vary linearly with speed.

8.4. Trimming Moment

Trimming moment is more closely linked to lift than resistance due to the larger moment arm, so as would be expected given that the CFD lift data shows good correlation with the experimental data, so too does the trimming moment. The results for the trimming moment can be seen in Figure 9. There is good correlation between the two methods for 3° & 4°, with linear fits returning R^2 values of 0.99 for all cases. Similar to the lift results, for 1.9°, the CFD trimming moment maintains a linear trend and does not feature the plateau of the experimental data as it is heavily influenced by the lift.

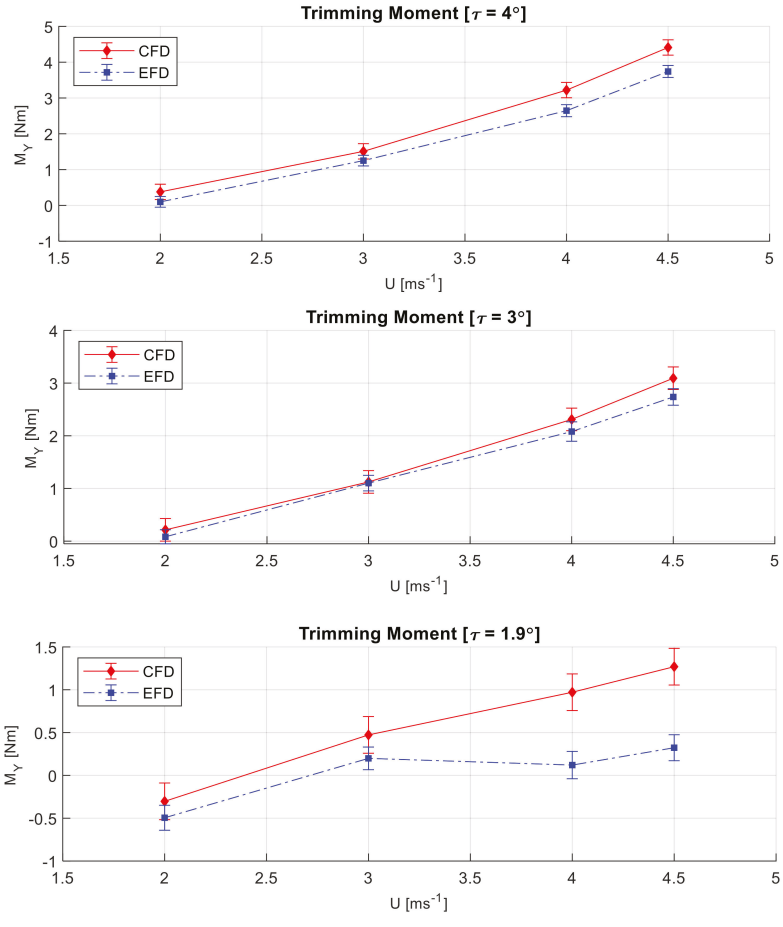

Figure 9. Numerical Trimming Moment Results.

8.5. Centreline Wake Profiles

This section presents the experimental and numerical results upon the same graphs, allowing an easy comparison to be made. The results of Savitsky's Wake Equations and the Linear Wake Assumption as calculated by [10] are not presented in this section, however they are included in the appendixes to allow for an easy comparison between methods. The results for all cases will not be presented here as to do so would require 20 individual graphs, which instead will be detailed in Appendix A. The data presented in this section has been selected to highlight key findings and trends in the results.

It should be noted that the experimental uncertainty in the measurements of the wake profile amplitudes was 0.56 mm. This uncertainty is not displayed as error bars on the graphs, as they are not visible due to the scale of the graphs. Unfortunately, it was not possible to determine the uncertainty in the CFD results. Following the mesh and timestep studies, the wake profiles were shown to be have insignificant differences between them so it can be assumed that the numerical uncertainty is negligible.

In all cases, the centreline wake profile as calculated by the numerical solution is shown to have good correlation with the experimental results. It shows CFD to be an accurate and robust method of calculating wake profiles across a range of speed and trim conditions. At the lower speeds of 2

and 3 ms^{-1}, the CFD results are seen to marginally under predict the amplitude of the wake profile; however, at the larger velocities of 4 and 4.5 ms^{-1} the opposite is true, with CFD being shown to slightly over predict the wake profiles.

Figure 10 shows what is considered the best-fit result when all cases are compared. As can be seen the CFD profile may be considered an extremely good fit with the experimental data, passing almost exactly through the data points from zero to −0.4 m. Following this there is a slight deviation, with a maximum difference of 2.56 mm, which has a corresponding comparison error of 3.83%. The best fitting point in this case has a deviation of 0.03 mm, or a corresponding comparison error of 0.04%.

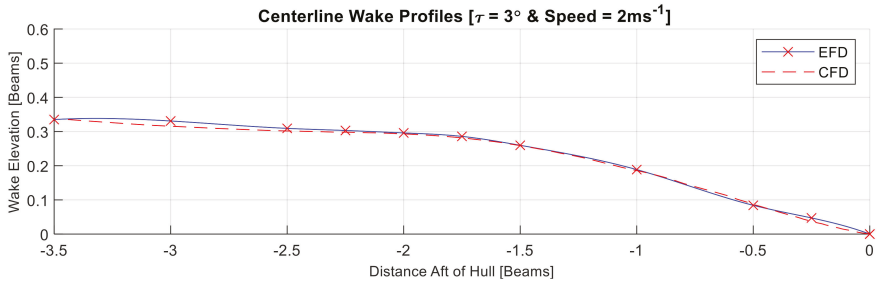

Figure 10. Best-Fit Computational Fluid Dynamics (CFD) Results.

Figure 11 shows what is considered the worst fit of CFD results to experimental data. Despite this there is still seen to be a very good correlation between the data. The maximum deviation is 4.72 mm, or a comparison error of 10.87%. When the other centreline cases are examined, it is found that the second worst deviation is 4.18 mm with a comparison error or 7.37%.

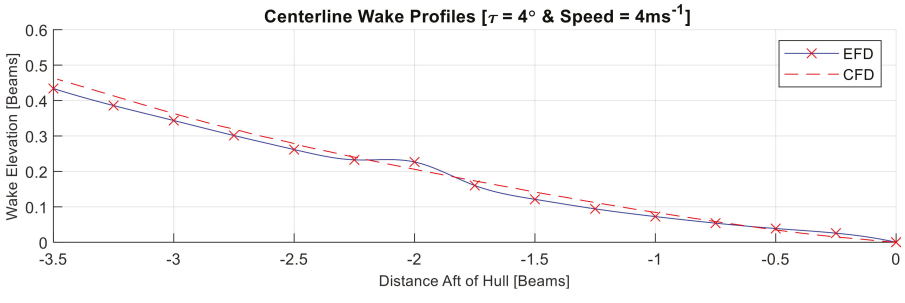

Figure 11. Best-Fit Computational Fluid Dynamics (CFD) Results.

The comparison of experimental centreline profiles to those calculated numerically validates the use of CFD in this application. The results are shown to have good correlation for all conditions, with the best and worst fit being discussed here. Whilst all the data points were not analysed, the best and worst have been, showing the CFD results to have a deviation of between 0.03 mm and 4.72 mm. When the results of Savitsky's Wake Equations and The Linear Wake Assumption are considered, the results generated through CFD are considerably more accurate. This method may be considered accurate and capable of modelling the nearfield longitudinal wake profiles of a high-speed planing hull.

8.6. Quarter Beam Wake Profiles

This section presents the numerical and experimental results, in the same manner as for the previous section whereby the results for all cases are not presented, instead being detailed in Appendix A. Similarly, the results of Savitsky's Wake Equations and the Linear Wake Assumption as calculated

by [10] are not presented in this section, however they are included in the appendixes to allow for an easy comparison between methods.

The ability of CFD to model the QB profiles is seen to be strongly related to the speed of the hull. Whilst the trim effects the shape of the wake, it does not appear to influence CFDs capabilities in calculating the profile, with the same trends being seen for both the 3° & 4° trim conditions. As the speed is shown to be influential, plots of QB profiles for all speeds in the 4° condition are displayed in Figure 12 and will be discussed in this section.

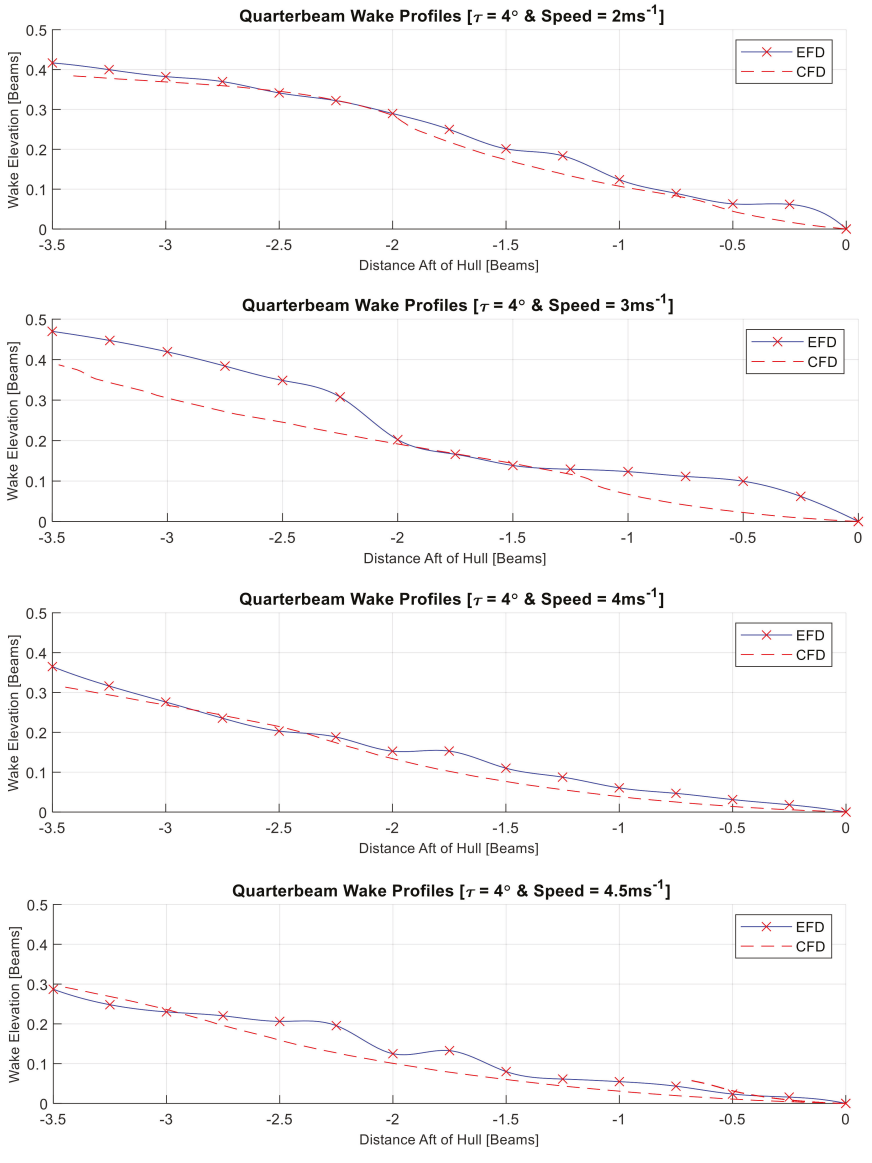

Figure 12. Quarterbeam Profiles [$\tau = 4°$].

Once again, CFD is shown to be relatively accurate for almost all cases. The case that features the best fit between CFD and the experimental data is 2 ms^{-1} where is a maximum difference of 6.54 mm, however for the most part the difference this is smaller than 3.34 mm.

As the speed increases the accuracy of the QB profiles decreases. As is discussed in the following wake pattern section, it appears that CFD set up as used in this work is incapable of modelling the feature lines that appear between the interacting aspects of flow. These feature lines are why the experimental QB wake profiles have disturbances, whilst the inability to model these feature lines is why the CFD wake profiles are smooth. Cases that have the largest disturbances (3 and 4.5 ms^{-1}) are seen to be the ones that CFD is least capable of modelling. This results in a maximum discrepancy of 12.9 mm in the 3 ms^{-1} case, where the CFD performs poorly for distances over 0.4 m from the hull. Despite this, for distances less than 0.4 m from the hull, the CFD result is still considered accurate.

Despite the fact that the CFD is unable to model the feature lines visible in the wake patterns at higher speeds, the quarter beam profiles are still shown to have relatively good correlation with the experimental data. CFD performs well in the region closer to the hull before the feature lines impact the profile; however, is still able to model the trends of the profiles where feature lines impact the results. When the results of Savitsky's Wake Equations and The Linear Wake Assumption are considered it is seen that neither of these methods are capable of modelling the feature lines either, and that the results generated through CFD are considerably more accurate.

8.7. Wake Pattern

One of the notable advantages in using CFD is that the post processing capabilities are significantly improved, and that analysis of the simulation offers far more possibilities. Experimental tests at 4.5 ms^{-1} provided only six seconds of run time. Measurements of certain parameters is made more difficult by this time restriction. In addition to this increased challenge, it is not always possible to acquire certain data from experimental testing, such as free surface elevation plots.

In addition to allowing a comparison of quantitative data in the form of wake profile plots, a qualitative comparison of photos taken during the tank testing is made with free surface contour plots from the CFD simulations. The wake profile plots give a far better measure of the accuracy of the CFD; however, comparing the wake patterns from both methods offers further insight. One of the key issues when comparing the photos and the elevation plots is that it is impossible to ensure that the views are at the same scale and perspective to allow a valid comparison. It is possible to ensure that the scale and angles are similar; however, engineering judgment must be employed when making visual comparisons.

Figures 13 and 14 show these comparisons for the trim angles 4°, 2°, and 4.5 ms^{-1}. As can be seen both cases show similar wake patterns, further validating the ability of CFD in calculating the longitudinal wake profiles and wave pattern of a planing hull. One of the notable differences is that the experimental photos show far more distinct feature lines, created by the interaction of different aspects of flow. Some of these are visible in the contour plots; however, they are far less clearly defined. It is thought to be the inability to accurately model these feature lines from the intersecting parts of flow that leads to the loss of accuracy in some of the quarter beam wake profiles, as mentioned previously. In general, aside from these pronounced feature lines the CFD is very capable of modelling the wake elevation.

Finally, it is possible to compare the spray patterns of the two methods. Once again, there is issues in ensuring that the comparison is made from the same angle and scale, and, as such, engineering judgment must once again be used. Figure 15 shows the sheet spray for 4 ° trim at 4.5 m/s. In order to visualise the spray the isosurface value must be changed from 0.5 to 0.99 as the spray is not considered to be a free surface, and instead is a mixture of air and water. As can be determined from the visual comparison the spray pattern appears to be well captured.

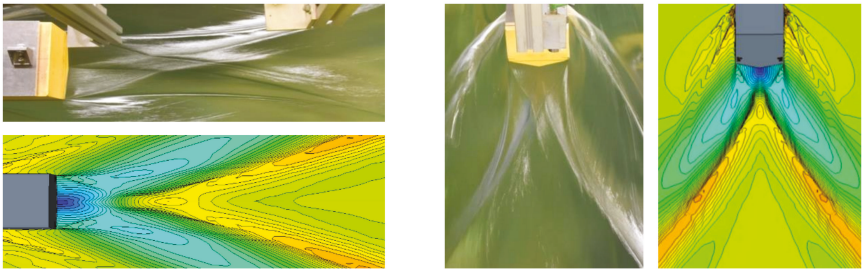

Figure 13. Wake Pattern Comparison [$\tau = 4°$ and *speed* = 2 ms^{-1}].

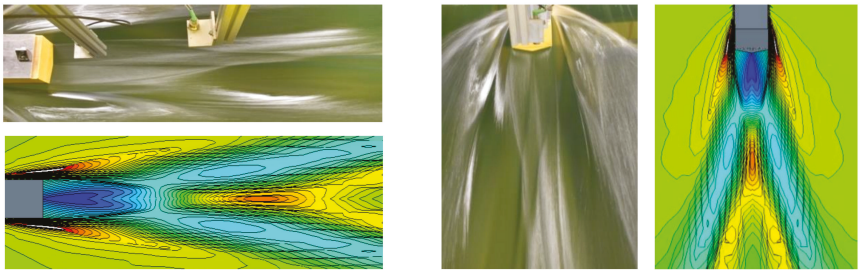

Figure 14. Wake Pattern Comparison [$\tau = 4°$ and *speed* = 4.5 ms^{-1}].

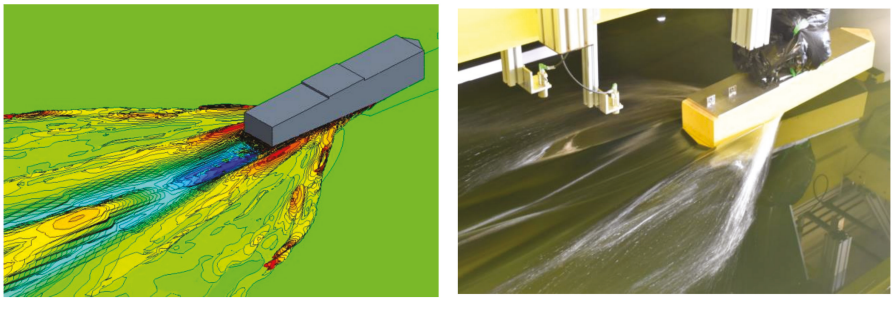

Figure 15. Spray Sheet [$\tau = 4°$ and *speed* = 4.5 ms^{-1}].

9. Concluding Remarks

This work has set out to evaluate the capabilities of CFD in modelling the nearfield longitudinal wake profile of a planing hull. It undertook a systematic study investigating what factors influenced a simulations accuracy in modelling the nearfield wake, with a particular emphasis on turbulence modelling approach and choice of turbulence model. Finally, it looked to verify whether CFD was able to model flow features of the nearfield wake region and the spray sheet. An extensive literature review revealed that there have been no previous studies looking to investigate the accuracy of CFD in modelling the nearfield longitudinal wake profile of a planing hull. A CFD simulation was set and a systematic study of a number of factors undertaken to ensure the presented set up was the most accurate. Following this, an in-depth validation and verification study was completed to ensure that the numerical results may be utilised with a high level of confidence. Following this experimental data was compared to the numerical results to make a judgment on the ability of CFD in modelling the nearfield longitudinal wake profile of a planing hull. A broad range of conditions was considered to ensure a thorough and robust validation case.

The study showed that CFD may be considered accurate and robust in this application. The numerical Centreline Profile results showed extremely good correlation with the experimental data, with a comparison error of between 0.03 mm and 4.72 mm. CFD was shown to be less capable at modelling the quarterbeam Profile, however there was still good correlation between the experimental and numerical results. Further analysis revealed that this is due to the inability of CFD to model the feature lines that are caused by different aspects of flow interacting with one another. The fact that the use of a symmetry plane on the centreline was found to have no impact on the resulting nearfield wake suggests that a RANS approach fails to model flow that is transient across the centreline. Higher fidelity methods such as LES of DES are suggested as an alternate approach to accurately model these features. A qualitative comparison of the entire nearfield wake pattern in the form of photos and free surface elevation plots confirmed CFD's ability to accurately model the wake pattern of a planing hull, excluding these feature lines.

The study also showed that the calculation of the wake profiles was far less sensitive to the set-up of the simulation than the calculation of forces. With this knowledge, it is safe to make the assumption that once a simulation is considered accurate at modelling the forces acting on a planning hull it may also be considered accurate in the modelling of the nearfield wake. The approach to modelling turbulence was shown to be the most influential in the accuracy of both the forces and the wake field.

This work increases the level of confidence with which CFD may be utilised when modelling stepped hulls, where calculating the nearfield wake region correctly is vital to determine the portion of the afterbody that will be wetted. Investigating the ability of CFD to model the longitudinal wake profile without the presence of the afterbody represents a large simplification of the problem; however, it does show CFD to be capable of accurately modelling the physics of a similar problem. This simplification was suggested by [2] and assumes the presence of the afterbody has no effect upon the flow pattern of the forebody. It is necessary as experimentally measuring this flow pattern with the presence of the afterbody is extremely challenging and is something that has not been achieved to date and, as such, no validation data exists. Having established that CFD provides an accurate and robust solution for the nearfield flow pattern of a planing hull the researchers plan to expand this research to extract and analyse the flow patterns associated with the steps of a stepped planing hull using a numerical methodology as part of their future research.

Author Contributions: Conceptualization, A.G.-S., T.T., and S.D.; Data curation, A.G.-S.; Formal analysis, A.G.-S.; Funding acquisition, S.D.; Investigation, A.G.-S.; Methodology, A.G.-S., T.T., and S.D.; Project administration, A.G.-S. and T.T.; Resources, T.T.; Supervision, T.T. and S.D.; Validation, A.G.-S.; Visualization, A.G.-S.; Writing—Original draft, A.G.-S.; Writing—Review & editing, T.T. All authors have read and agreed to the published version of the manuscript.

Funding: This research was funded by the EPSRC as part of the research project: "Shipping in Changing Climates" (EPSRC Grant no. EP/K039253/1).

Acknowledgments: Numerical Results were obtained using the ARCHIE-WeSt High Performance Computer (www.archie-west.ac.uk) based at the University of Strathclyde. The work presented in this paper is taken from the first authors Doctoral Thesis. The first author gratefully acknowledges the scholarship provided by the University of Strathclyde, which fully supports his PhD.

Conflicts of Interest: The authors declare no conflict of interest.

Data Statement: The underlying data in this paper is openly available from the University of Strathclyde's data repository at: https://doi.org/10.15129/35ef2762-5cd4-480a-90be-745b38ef1539.

Nomenclature

C_i	Correction Factor
D	Data
d	Depth
E	Comparison Error
$L_{K(m)}$	Wetted Keel Length [meters]
L	Length Overall [Meters]

L_{PP}	Length between Perpendiculars [Meters]
P_{est}	Estimated Order of Accuracy
P_i	Order of Accuracy
R_i	Convergence Ratio
r_i	Refinement Ratio
R_n	Reynolds Number
S_i	Simulation Result
T	Truth
Δt	Timestep [seconds]
U	Vessel Speed [Meters per Second]
U_D	Data Uncertainty
U_i	Solution Uncertainty (Absolute Value)
U_{i}	Solution Uncertainty (Percentage Value)
U_{SN}	Simulation Numerical Uncertainty
U_V	Validation Uncertainty
x	Wetted Length [Meters]
β	Deadrise [Degrees]
δ	Boundary Layer Thickness [Meters]
δ_i^*	Corrected Error
δ_S	Simulation Error
δ_{SM}	Modelling Errors
δ_{SN}	Numerical Errors
$\delta^*_{RE_{i,1}}$	Generalized RE Error Estimate
$\varepsilon_{i,21}$	Change between Course and Medium Solutions
$\varepsilon_{i,32}$	Change between Medium and Fine Solutions
λ	Wavelength
τ	Trim Angle [Degrees]

Appendix A

Appendix A.1. Centreline Near-Field Longitudinal Wake Profiles

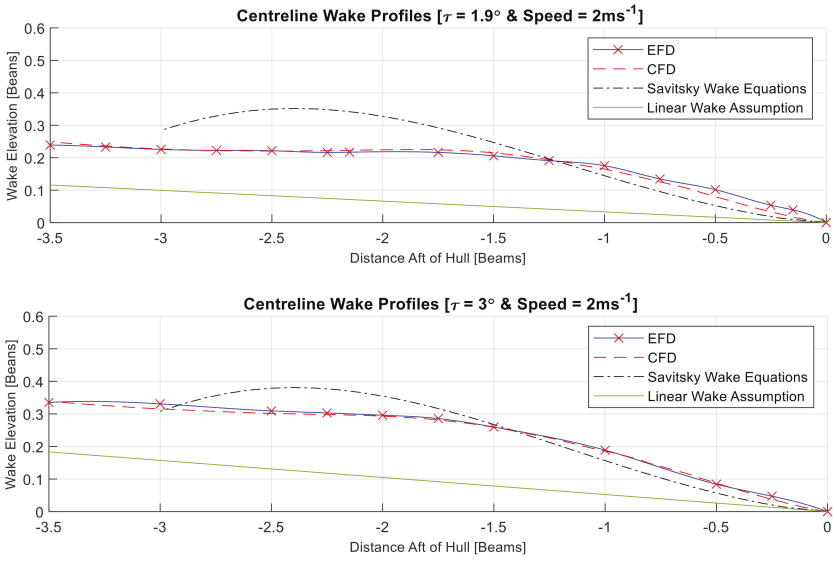

Figure A1. *Cont.*

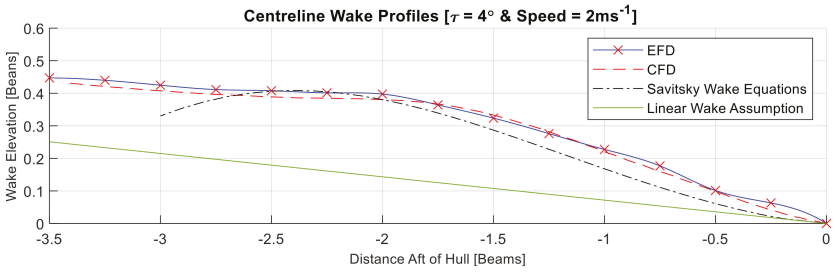

Figure A1. Centreline profiles for 2 ms^{-1} condition.

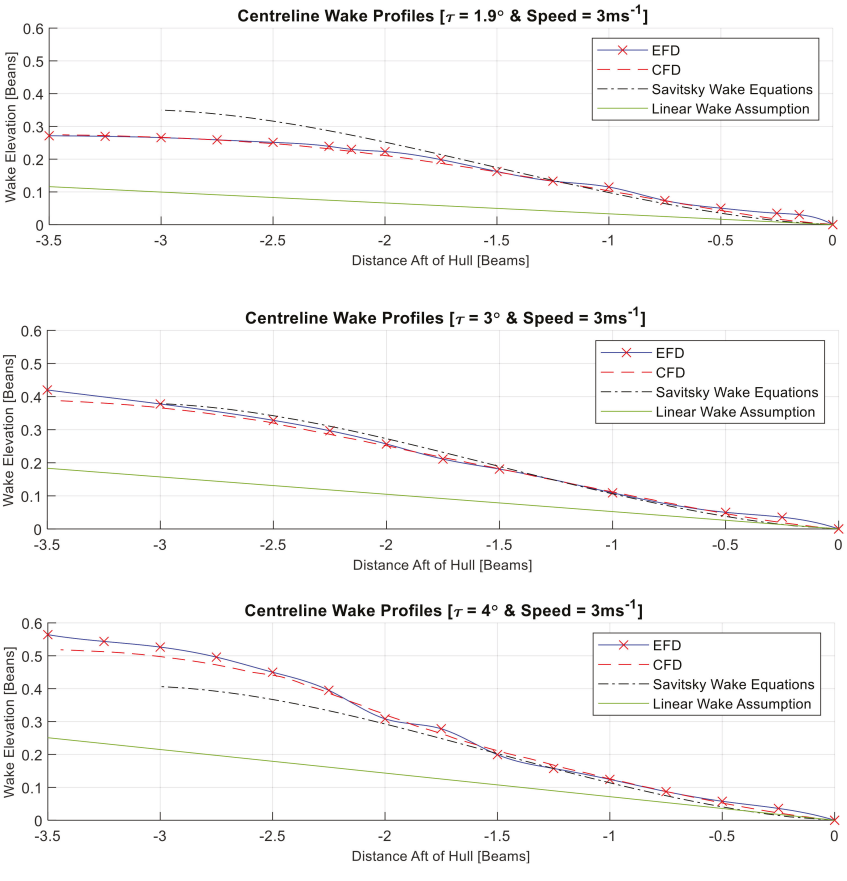

Figure A2. Centreline profiles for 3 ms^{-1} condition.

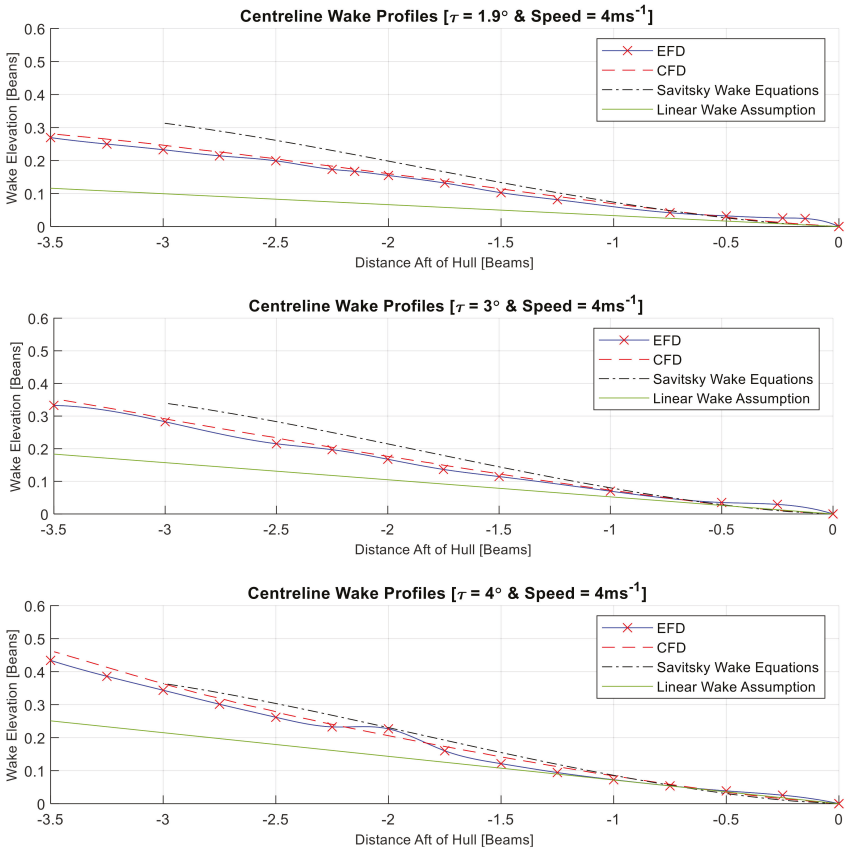

Figure A3. Centreline profiles for 4 ms^{-1} condition.

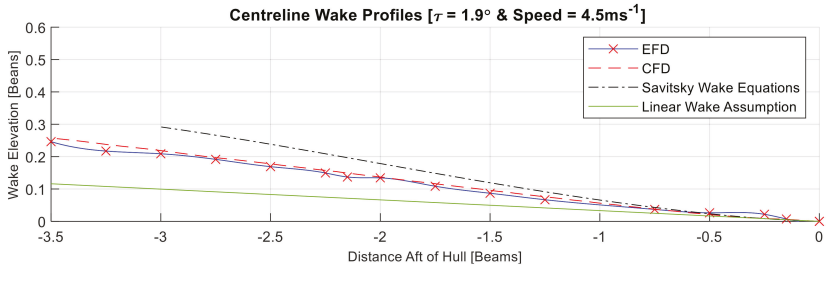

Figure A4. *Cont.*

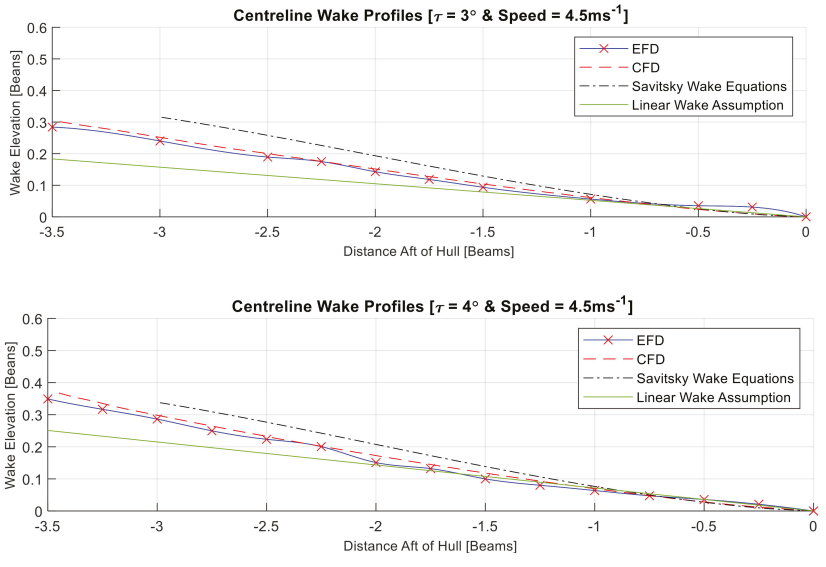

Figure A4. Centreline profiles for 4.5 ms^{-1} condition.

Appendix A.2. Quarterbeam Near-Field Longitudinal Wake Profiles

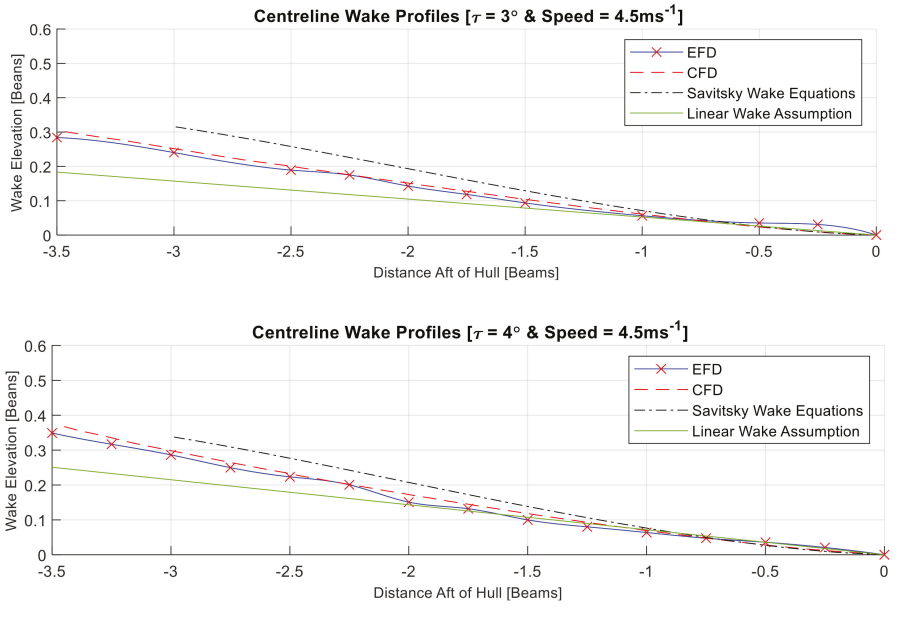

Figure A5. Quarterbeam profiles for 2 ms^{-1} condition.

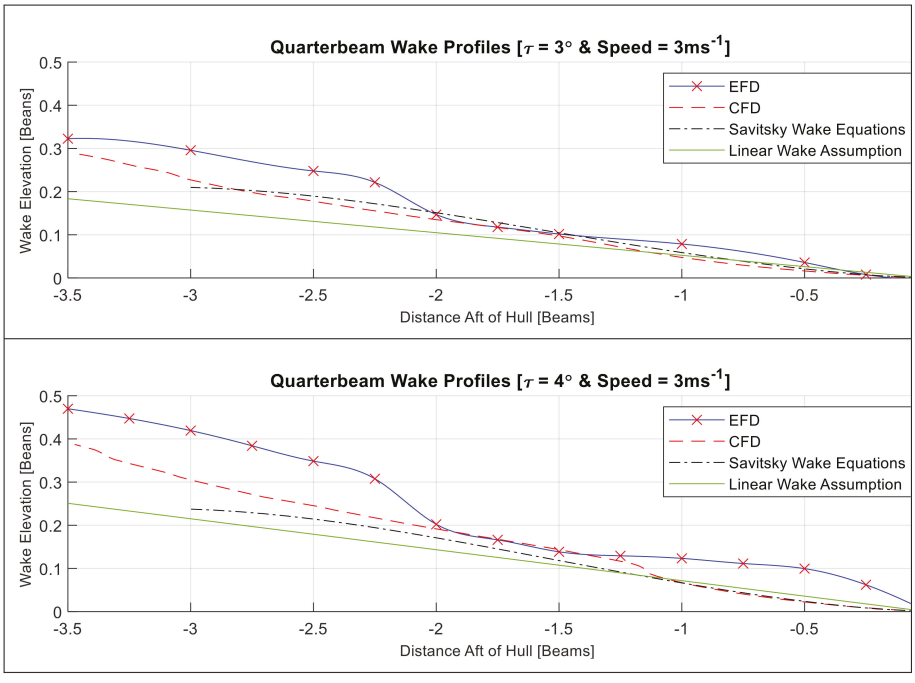

Figure A6. Quarterbeam profiles for 3 ms^{-1} condition.

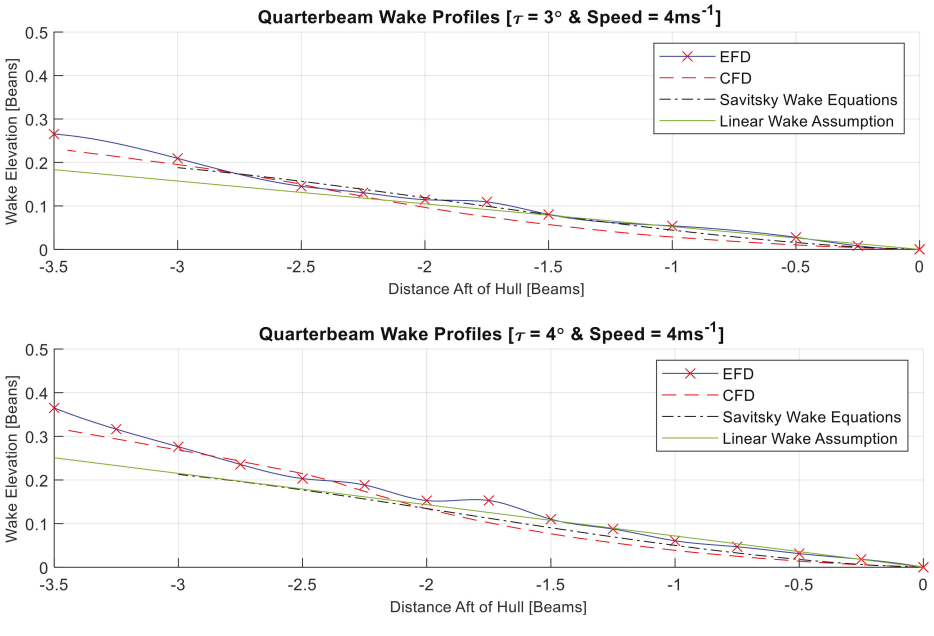

Figure A7. Quarterbeam profiles for 4 ms^{-1} condition.

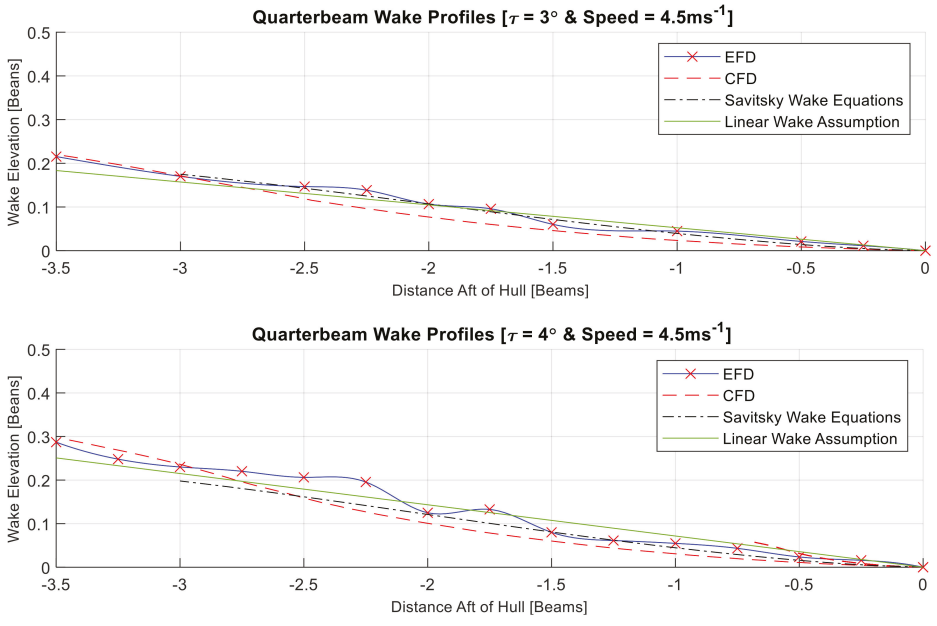

Figure A8. Quarterbeam profiles for 4.5 ms^{-1} condition.

References

1. Loni, A.; Ghadimi, P.; Nowruzi, H.; Dashtimanesh, A. Developing a Computer Program for Mathematical Investigation of Stepped Planing Hull Characteristics. *Int. J. Phys. Res.* **2013**, *1*. [CrossRef]
2. Savitsky, D.; Morabito, M. Surface Wave Contours Associated with the Forebody Wake of Stepped Planing Hulls. *Mar. Technol.* **2010**, *47*, 1–16.
3. Sottorf, W. *Experiments with Planing Surfaces*; Natl. Advis. Comm. Aeronaut. Tech. Memo. 661; National Advisory Committee for Aeronautics Technical Memorandums: Washington, DC, USA, 1932.
4. Korvin-Kroukovsky, B.; Savitsky, D.; Lehman, W. *Wave Contours in the Wake of a 20-Degree Deadrise Planing Surface*; Fairchild Publication Fund Report No. 337; Institute of the Aeronautical Sciences: New York, NY, USA, 1948.
5. Korvin-Kroukovsky, B.; Savitsky, D.; Lehman, W. *Wave Contours in the Wake of a 10-Degree Deadrise Planing Surface*; Fairchild Publication Fund Report No. 344; Institute of the Aeronautical Sciences: New York, NY, USA, 1948.
6. Korvin-Kroukovsky, B.; Savitsky, D.; Lehman, W. *Wave Profile of a VEE Planing Surface, Including Test Data on a 30- degree Deadrise Surface*; Fairchild Publication Fund Report No. 339; Institute of the Aeronautical Sciences: New York, NY, USA, 1949.
7. Thornhill, E.; Oldford, D.; Bose, N.; Veitch, B.; Liu, P. Planing Hull Model Tests for CFD Validation. *Int. Shipbuild. Prog.* **2003**, *50*, 5–18.
8. Callander, C.K. Wake prediction behind planing hulls. *Trans. Soc. Nav. Archit. Mar. Eng.* **2015**, *21*, 450–457.
9. De Luca, F.; Pensa, C. The Naples warped hard chine hulls systematic series. *Ocean Eng.* **2017**, *139*, 205–236. [CrossRef]
10. Gray-Stephens, A.; Tezdogan, T.; Day, S. Experimental Measurement of the Nearfield Longitudinal Wake Profiles of a High-Speed Prismatic Planing Hull. 2019; manuscript submitted to Ship Technolgy Research for publication.
11. ITTC Specialist Committee on CFD in Marine Hydrodynamics. Specialist Committee on CFD in Marine Hydrodynamics Final report and Recommendations to the 27 th ITTC. 2014. Available online: https://ittc.info/media/6097/sc-cfd.pdf (accessed on 11 December 2018).

12. Faison, L.A. Design of a High Speed Planing Hull with a Cambered Step and Surface Piercing Hydrofoils. Master's Thesis, Massachusetts Institute of Technology, Cambridge, MA, USA, 2014.
13. Ghadimi, P.; Dashtimanesh, A.; Zamanian, R.; Chekab, M.A.F.; Mirhosseini, S.H.R. Rooster tail depression by originating a modified transom stern form using a Reynolds averaged Navier Stokes solver. *Sci. Iran.* **2015**, *22*. [CrossRef]
14. Lotfi, P.; Ashrafizaadeh, M.; Esfahan, R.K. Numerical investigation of a stepped planing hull in calm water. *Ocean Eng.* **2015**, *94*, 103–110. [CrossRef]
15. Bakhtiari, M.; Ghassemi, H. Numerical study of step forward swept angle effects on the hydrodynamic performance of a planing hull. *Sci. J. Marit. Univ. Szczec.* **2017**, *51*, 35–42. [CrossRef]
16. Larson, L.; Stern, F.; Visonneau, M. *Numerical Ship Hydrodynamics—An Assesment of the Gothenburg 2010 Workshop*; Springer: Berlin, Germany, 2014; ISBN 978-94-007-7188-8.
17. Mancini, S. The problem of verification and validation processes of CFD simulations of planing hulls. 2015. Available online: https://core.ac.uk/reader/78395650 (accessed on 16 September 2019).
18. Ferziger, J.H.; Perić, M. *Computational Methods for Fluid Dynamics*, 3rd ed.; Springer: Berlin, Germany, 2002; ISBN 978-3-540-78091-5.
19. Brizzolara, S.; Villa, D. CFD SIMULATION OF PLANING HULLS. In Proceedings of the Seventh International Conference On High-Performance Marine Vehicles. 2010. Available online: https://s3.amazonaws.com/academia.edu.documents/32730317/Brizzolara_CFD_Planing-HullsV5.pdf?AWSAccessKeyId=AKIAIWOWYYGZ2Y53UL3A&Expires=1540308488&Signature=V%2FrE4Tvozubk8fc1RQ%2B%2FB54TLTw%3D&response-content-disposition=inline%3Bfilename%3DCFD_Simulat (accessed on 23 October 2018).
20. Bakhtiari, M.; Veysi, S.; Ghassemi, H. Numerical Modeling of the Stepped Planing Hull in Calm Water. *Int. J. Eng.* **2016**, *29*. [CrossRef]
21. De Luca, F.; Mancini, S.; Miranda, S.; Pensa, C. An Extended Verification and Validation Study of CFD Simulations for Planing Hulls. *J. Ship Res.* **2016**, *60*, 101–118. [CrossRef]
22. Dashtimanesh, A.; Esfandiari, A.; Mancini, S. Performance Prediction of Two-Stepped Planing Hulls Using Morphing Mesh Approach. *J. Sh. Prod. Des.* **2017**, *34*, 1–13. [CrossRef]
23. Sukas, O.F.; Kinaci, O.K.; Cakici, F.; Gokce, M.K. Hydrodynamic assessment of planing hulls using overset grids. *Appl. Ocean Res.* **2017**, *65*, 35–46. [CrossRef]
24. Castiglione, T.; Stern, F.; Bova, S.; Kandasamy, M. Numerical investigation of the seakeeping behavior of a catamaran advancing in regular head waves. *Ocean Eng.* **2011**, *38*, 1806–1822. [CrossRef]
25. Wang, T.; Yang, X.; Yao, X. Numerical wave tank for study seakeeping of amphibious vehicle. In Proceedings of the 2nd International Conference on Electronic and Mechanical Engineering and Information, EMEIT 2012, Shenyang, China, 7 September 2012; pp. 1676–1679.
26. De Marco, A.; Mancini, S.; Miranda, S.; Scognamiglio, R.; Vitiello, L. Experimental and numerical hydrodynamic analysis of a stepped planing hull. *Appl. Ocean Res.* **2017**, *64*, 135–154. [CrossRef]
27. Mancini, S.; De Luca, F.; Ramolini, A. Towards CFD guidelines for planing hull simulations based on the Naples Systematic Series. In Proceedings of the 7th International Conference on Computational Methods in Marine Engineering, MARINE 2017, Nantes, France, 15–17 May 2017.
28. Tezdogan, T.; Demirel, Y.K.; Kellett, P.; Khorasanchi, M.; Incecik, A.; Turan, O. Full-scale unsteady RANS CFD simulations of ship behaviour and performance in head seas due to slow steaming. *Ocean Eng.* **2015**, *97*, 186–206. [CrossRef]
29. Terziev, M.; Tezdogan, T.; Incecik, A. Application of eddy-viscosity turbulence models to problems in ship hydrodynamics. *Ships Offshore Struct.* **2019**, 1–24. [CrossRef]
30. Gray-Stephens, A.; Tezdogan, T.; Day, S. Strategies to Minimise Numerical Ventilation in CFD Simulations of High-Speed Planing Hulls. In Proceedings of the OMAE, Glasgow, UK, 9–14 June 2019; pp. 1–10.
31. Ubbink, O. Numerical Prediction of Two Fluid Systems with Sharp Interfaces. Ph.D. Thesis, University of London and Diploma of Imperial College, London, UK, January 1997.
32. Campana, E.F.; Hino, T.; Bull, P.; Carrica, P.; Kim, J.; Kim, S.E.; Li, D.Q.; Saisto, I.; Starke, B. The Specialist Committee on Coputational Fluid Dynamics—Final Report and Recommendations to the 26th ITTC. In Proceedings of the 26th ITTC—Volume II, Rio de Janeiro, Brazil, 28 August–3 September 2011; Volume 2, p. 41.

33. Böhm, C.; Graf, K. Advancements in free surface RANSE simulations for sailing yacht applications. *Ocean Eng.* **2014**, *90*, 11–20. [CrossRef]
34. Jesudhas, V. Modeling of Free-Surface Flows with Air Entrainment. Ph.D. Thesis, University of Windsor, Windsor, ON, Canada, 2016.
35. Siemens. *Siemens Star-CCM+ User Guide Version*; Siemens: Munich, Germany, 2018.
36. 26th ITTC Specialist Committee on CFD in Marine Hydrodynamics. Practical Guidelines for Ship CFD Applications. 2014. Available online: http://ittc.info/media/1357/75-03-02-03.pdf (accessed on 1 May 2018).
37. ITTC–Recommended Procedures and Guidelines. Practical Guidelines for Ship CFD. 2011. Available online: https://ittc.info/media/1357/75-03-02-03.pdf (accessed on 3 January 2019).
38. Lloyd, A.R.J.M. *Seakeeping: Ship Behaviour in Rough Weather*; E. Horwood: St John's, NL, Canada, 1989; ISBN 0470212322.
39. ITTC. *ITTC—Recommended Procedures and Guidelines—Testing and Extrapolation Methods High Speed Marine Vehicles—Resistance Testt, 7.5-02-05-01 (Revision 02)*. 2008. Available online: https://ittc.info/media/1279/75-02-05-01.pdf (accessed on 17 April 2019).
40. Çengel, Y.; Cimbala, J. *Fliud Mechanics: Fundamentals and Application*, 6th ed.; McGraw-Hill: New York, NY, USA, 2006.
41. Resistance Committee of 25th ITTC. Uncertainty Analysis in CFD Verification and Validation Methodology and Procedures. 2008. Available online: http://ittc.info/media/4184/75-03-01-01.pdf (accessed on 13 April 2019).
42. American Institute of Aeronautics and Astronautics. *AIAA Guide for the Verification and Validation of Computational Fluid Dynamics Simulations*; American Institute of Aeronautics and Astronautics, Inc.: Washington, DC, USA, 1998.
43. Stern, F.; Wilson, R.; Shao, J. Quantitative V&V of CFD simulations and certification of CFD codes. *Int. J. Numer. Methods Fluids* **2006**, *50*, 1335–1355. [CrossRef]
44. Richardson, L.F. The Approximate Arithmetical Solution by Finite Differences of Physical Problems Involving Differential Equations, with an Application to the Stresses in a Masonry Dam. *Philos. Trans. R. Soc. Math. Phys. Eng. Sci.* **1911**, *210*, 307–357. [CrossRef]
45. Xing, T.; Stern, F. Factors of safety for Richardson extrapolation. *J. Fluids Eng. Trans. ASME* **2010**, *132*, 0614031–0640313. [CrossRef]
46. ITTC-Recommended Procedures and Guidelines Practical Guidelines for RANS Cal-culation of Nominal Wakes. 2014. Available online: https://ittc.info/media/4202/75-03-03-02.pdf (accessed on 15 May 2019).
47. CD Adapco. Simcenter STAR-CCM+ Documentation. 2018. Available online: https://documentation.thesteveportal.plm.automation.siemens.com/starccmplus_latest_en/index.html#page/connect%2Fsplash.html (accessed on 7 January 2019).
48. Frisk, D.; Tegehall, L. *Prediction of High-Speed Planing Hull Resistance and Running Attitude. A Numerical Study Using Computational Fluid Dynamics*; Chalmers University of Technology: Gothenburg, Sweden, 2015.
49. Ghassemi, H.; Kamarlouei, M.; Veysi, S.T.G. A Hydrodynamic Methodology and CFD Analysis for Performance Prediction of Stepped Planing Hulls. *Pol. Marit. Res.* **2015**, *22*, 23–31. [CrossRef]
50. Dicaterino, F.; Bilandi, R.N.; Mancini, S.; Dashtimanesh, A.; Carlini, M.D. A Numerical Way for a Stepped Planing Hull Design and Optimization. In Proceedings of the NAV 2018: 19th International Conference on Ship and Maritime Research, Trieste, Italy, 21 June 2018; pp. 220–229.
51. Menter, F.R. Two-Equation Eddy-Viscosity Turbulence Models for Engineering Applications. *AIAA J.* **1994**, *32*. [CrossRef]
52. Ma, W.; Sun, H.; Zou, J.; Yang, H. Test research on the resistance performance of high-speed trimaran planing hull. *Pol. Marit. Res.* **2013**, *20*, 45–51. [CrossRef]

Journal of
Marine Science and Engineering

MDPI

Article

Distributed Propulsion Systems for Shallow Draft Vessels

Ladislav Illes [1], Tomas Kalina [2], Martin Jurkovic [2,*] and Vladimir Luptak [3]

[1] MULTI Engineering Services, The Faculty of Operation and Economics of Transport and Communications, University of Zilina, Dunajske nabrezie 4726, 94501 Komarno, Slovakia; ladislav.illes@multi.engineering
[2] The Faculty of Operation and Economics of Transport and Communications, University of Zilina, Univerzitna 1, 01026 Zilina, Slovakia; tomas.kalina@fpedas.uniza.sk
[3] Department of Transport and Logistics, Faculty of Technology, Institute of Technology and Business in Ceske Budejovice, 37001 Ceske Budejovice, Czech Republic; luptak@mail.vstecb.cz
* Correspondence: martin.jurkovic@fpedas.uniza.sk; Tel.: +421-903-869-308

Received: 13 July 2020; Accepted: 24 August 2020; Published: 29 August 2020

Abstract: The aim of this study was to investigate the impact of distributed propulsion systems used on inland and coastal navigation in shallow water. Five layouts were assessed by computational fluid dynamics (CFD) simulation. The hull/propulsion layout cases have been analyzed for discrete flow speed values in the range 0–6 m/s. All cases have been examined under restricted draft conditions in shallow water with a minimum of 0.3 m under keel clearance (UKC) and under unrestricted draft conditions in deep water. The results show that distributed propulsion consisting of 6 or 8 (in some cases, even more) units produces noticeable higher thrust effects in shallow water than the traditional layout. Under restricted conditions, the thrust increase between two distributed layouts with different numbers of propulsors is higher, in contrast to deep water, where differences in performance are not so significant.

Keywords: distributed propulsion; draft; shallow water; computational fluid dynamics

1. Introduction

A long-standing problem of inland waterways in Europe is the existence of bottlenecks related to the provision of the required navigation parameters. International agreements oblige individual European states to ensure the navigability of international waterways with required parameters [1]. Ensuring a minimum navigation depth of 250 cm for 300 days a year is particularly important for the Danube. Long-term forecasts of the impact of climate change [2,3] assume a further deterioration of the situation, which is mainly related to the phenomenon of drought. This problem directly and negatively affects the use of inland waterway transport. This limits the navigation period during the year. This also has a direct impact on the economics of operating shipping companies [4]. Another negative is the lower attractiveness, stability, and usability of the transport mode compared to others.

The draft of an inland ship can undoubtedly be included among the critical points that significantly affect its usability during the year. As the design of a ship and determination of the design draft are closely related to the tonnage of the ship, it is natural that the limitation of the draft will result in a reduction in the deadweight capacity of the ship. This is not the way.

Propulsion systems intended for inland or coastal navigation vessels are equipped with small propellers due to low under keel clearance (UKC). Due to their small size, it is necessary to operate at high rotational speeds for sufficient thrust of the propeller. In general, this fact results in relatively low efficiency of such systems (combination of small propeller diameter and high revolutions per minute).

Several possibilities to increase the efficiency of the propulsor are presented in [5]. One of the ways to increase propulsion efficiency is the application of half-submerged double propellers. The efficiency

of the propulsion can be increased by increasing the diameter of the propeller, taking into account the restricted draft and the reduction in its rotational speed. By using two counter-rotating semi-submerged propellers, their dimensions can be increased by a factor of approximately 2.5. Another way to increase efficiency is the installation of surface-cutting double propellers. This propulsion system increases propulsion efficiency by about 20–40% compared to conventional drives and does not require an independent steering (rudder) system [5].

Another way to increase the availability of inland waterway transport is to adapt the fleet to current and future navigation conditions. The solution may be the optimization of the hull shape. At limited water conditions, the flow around the hull changes compared to the flow in unrestricted water due to the influence of the bottom and banks of the waterway. This leads to increased backflow, stronger squat effects, and changes in the waveform created by the ship's motion. The lower the UKC, the sooner the backflow occurs. This leads to additional immersion, lowering the water level around the ship, and usually, to an increase in wave resistance (in some cases, it may decrease, see [6]) [7].

Several methods have been proposed to estimate the increased resistance in shallow water navigation [6,8–11]. In addition to resistance, the wake fraction and thrust deduction also change [12,13]. There are also additional effects in shallow water on the propeller compared to sailing at unlimited depth [14].

Optimization studies for wave resistance in shallow water have been published [15,16], but due to changes in the wake field and propulsive efficiency, attention should be paid to thrust force when optimizing for shallow water.

The Rotteveel study addresses the effect of water depth on inland ship rudder optimization. This represents the optimization of propulsion power for different water depths using parametric inland ship stern shape, computational fluid dynamics (CFD), and surrogate modeling. Using Pareto fronts, a compromise is proven: the driving force in shallow water can be reduced at the cost of increasing driving force in unrestricted water and vice versa. The results of the study show that the effects of shallow water on effective wake fraction are significant. In addition to the wake fraction and thrust deduction factors, relative rotational efficiency may also vary due to different behavior in shallow water. In the conclusions of this study, it is recommended to focus on the effects of shallow water on propulsion as resistance [7].

One of the solutions that could increase the throughput of the ship through critical sections is changing the propulsion system. Most inland ships are powered by conventional propellers, usually operating in synchronous dual mode [17]. Changing the propulsion system by distributing the propulsion equipment to other suitable locations may result in better throughput of the ship through critical points with restricted draft. With the traditional conventional stern propulsion method, a natural suction from the propellers occurs. This results in a reduction in UKC. Distribution of the propulsion to other places, or its extension, may result in a decrease in suction, which will ensure a greater margin under the hull [18].

This study describes an investigation process aimed at finding an efficient way to propel inland vessels for navigation at restricted draft conditions. It is based on a typical inland cargo vessel hull with dimensions suitable for the Rhine–Main–Danube waterway, which was used for all calculation cases in the CFD analyses.

The Methods section describes that in order to compare the thrust efficiency, four different symmetrical layouts of ideal propulsors were proposed along the hull, with 2, 4, 6, and 8 propulsion units. As a fifth case, the classical two-propeller stern arrangement for reduced draft was also analyzed. A series of CFD simulations was performed with identical conditions and with the same total pressure-generated force on the propulsors. During the calculation, the mass flow values in front of the plane, at the working plane, and behind the plane of the propulsors were recorded, and subsequently, the results were evaluated using Rankine's theory.

In the Results section, the results from numerous CFD analyses are processed and clearly visualized in the form of various comparative figures. In these figures, the differences in the total generated thrust and absorbed power values under the unrestricted and restricted water depth conditions can be seen.

The last two sections discuss and explain the results and provide conclusions, with possible guidance on how to proceed in further investigations.

2. Methods

The original axial momentum theory of Rankine is based on the axial motion of the water flowing through the propulsor (propeller) actuator disc. The geometry of the propulsor is irrelevant, and its rotational effects on the water flow are neglected. Therefore, this theory is suitable to describe and study the characteristics of water flow through an ideal propulsor (Figure 1) [19].

This theory is based on the following assumptions:

- The propulsor works in an ideal fluid without energy losses due to frictional drag.
- The propulsor can be replaced in calculation cases by a theoretical actuator disc.
- The propulsor is able to provide thrust without rotational effects on water flow.

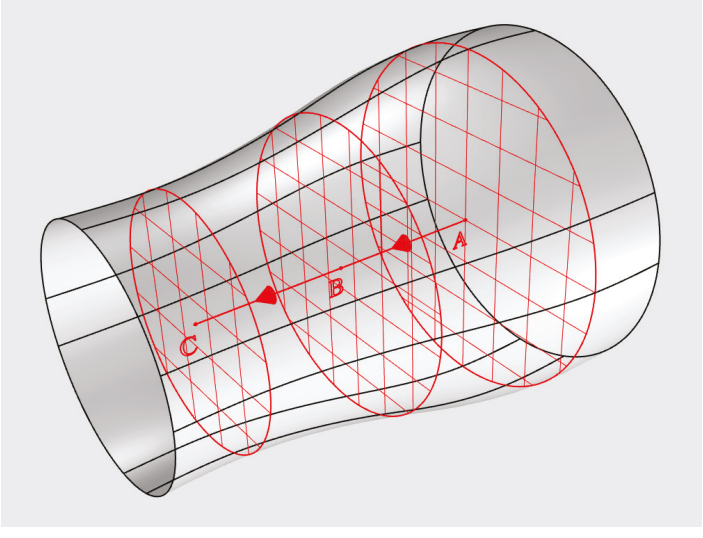

Figure 1. Stream tube of ideal propulsor based on the momentum theory. Source: Authors based on [19].

Three typical cross sections are introduced to study the acceleration of the flow between the upstream and the downstream caused by the pressure jump of the actuator disc:

- Station A—cross section located far upstream;
- Station B—section in the plane of the actuator disc;
- Station C—cross section located far downstream.

The power absorbed by the propulsor is given by:

$$P_D = \frac{\dot{m}_B}{2} \cdot \left({v_C}^2 - {v_A}^2 \right) \quad (1)$$

It is also equal to:

$$P_D = T_D \cdot v_B = T_D \cdot \frac{\dot{m}_B}{\rho \cdot A_B}. \quad (2)$$

The thrust generated by the propulsor is given by:

$$T_D = \dot{m}_B \cdot (v_C - v_A), \quad (3)$$

$$T_D = \frac{\dot{m}_B}{\rho} \cdot \left(\frac{\dot{m}_C}{A_C} - \frac{\dot{m}_A}{A_A} \right). \quad (4)$$

When examining fluid flow, the basic laws of physics can be applied, i.e., conservation law of mass, conservation law of momentum, and conservation law of energy. All these laws, as well as viscous phenomena in real (Newtonian) fluid, are reflected in the Navier–Stokes equations that describe both laminar and turbulent flow.

The Navier–Stokes partial differential equations are applicable for all unit actions on the fluid particle in three basic directions of space, i.e., weight, pressure, and friction and inertia. They can be simplified to the form:

$$\begin{aligned} X - \frac{1}{\rho} \cdot \frac{\delta p}{\delta x} + v \cdot \left(\frac{\delta^2 v_x}{\delta x^2} + \frac{\delta^2 v_x}{\delta y^2} + \frac{\delta^2 v_x}{\delta z^2} \right) &= a_x, \\ Y - \frac{1}{\rho} \cdot \frac{\delta p}{\delta y} + v \cdot \left(\frac{\delta^2 v_y}{\delta x^2} + \frac{\delta^2 v_y}{\delta y^2} + \frac{\delta^2 v_y}{\delta z^2} \right) &= a_y \, , \\ Z - \frac{1}{\rho} \cdot \frac{\delta p}{\delta z} + v \cdot \left(\frac{\delta^2 v_z}{\delta x^2} + \frac{\delta^2 v_z}{\delta y^2} + \frac{\delta^2 v_z}{\delta z^2} \right) &= a_z \, . \end{aligned} \quad (5)$$

These equations can be interpreted as the specific form of Newton's second law for the flow of viscous incompressible fluid per unit mass, on the right with the product of acceleration and weight and on the left with the sum of mass and surface (pressure and viscous) forces [20,21].

The CFD method is the most commonly used in computer modeling of fluid flow. Several mesh-based methods have been developed in this area, where the geometry under investigation is replaced by a 2D or 3D mesh and the flow problem is solved using the Navier–Stokes equations (Figure 2). The basic principle of CFD is to create a computational domain that consists of a geometric model of the actual and discretized form (mesh), a definition of boundary conditions, a set of physical properties and calculation methods, and possibly external geometry boundaries of the flow area (external flow).

In the CFD simulation of sailing, the geometry under investigation consists of the outer surface of the hull, surrounded by a flow area, mostly of hexahedral shape. This is a typical case of external flow where the flow takes place in the surrounding environment and not within the computational geometry. The investigated physical phenomena take place in a multiphase environment, at the boundary of two phases (water–air), which considerably increases the computational complexity of these tasks.

The most serious limitation in CFD analysis is the number of mesh elements (and nodes). In each iteration of the calculation, the hydrodynamic state of the elements is evaluated individually, and their excessive number can enormously increase computational complexity and machine time. For this reason, it is necessary to keep the number of elements as low as possible, but not to the detriment of the accuracy of the calculation.

We call it a quality mesh when the elements have the same size, are geometrically regular, and their distribution is also regular in the discretized area. A suitable choice of element size ensures that the hydrodynamic properties of the flow are captured, but velocities are decisive for dimensions [20,21].

Many numerical methods have been developed to address particular physical problems. Their application depends both on the suitability of the method for solving the issue and on the history of development.

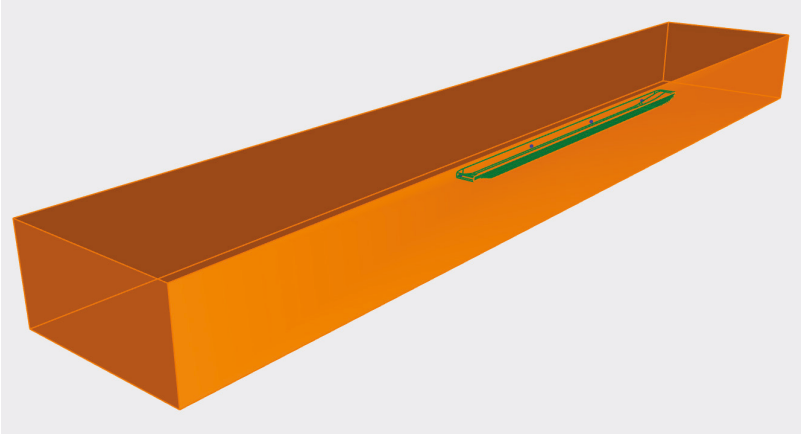

Figure 2. 3D geometry of a typical CFD domain (Layout E, deep water). Source: Authors.

By replacing the geometry of the examined area with a mesh of generated nodal points, the flow calculation domain is discretized, thus, allowing the flow equations to be converted into algebraic equations.

The finite volume method (FVM) is a method that, in a discretized form, retains very reliably the principles of conservation laws of balanced physical quantities in the control volume and is, therefore, the most widely used CFD simulation apparatus for solving the Navier–Stokes equations [22].

Numerical modeling of turbulent flows is still in the process of research and development, supported by the latest knowledge of mathematics, physics, and technical computational methods. However, there is no universal model of turbulence that is generally and effectively applicable in all cases. In order to choose the most suitable model for a particular calculation case, it is necessary to consider the possibilities and limitations of individual numerical models.

The time-averaging method (RANS—Reynolds-averaged Navier–Stokes equations), which has relatively low computational capacity requirements and provides acceptable accuracy, is becoming increasingly widespread in engineering simulations. It consists of parametric modeling of turbulent flow by time-averaged values of physical quantities using the Reynolds method. Several different RANS methods have been developed for various specific task types, which simplify the modeling of swirls using added transport equations [23].

For simulation purposes, a typical Danube cargo ship hull has been chosen with a pushed barge type bow (to be able to push barges) and with a simplified aftship suitable for all the examined layouts (Figure 3). The main particulars of the ship hull are shown in Table 1.

Table 1. Basic ship dimensions.

Length (L) [m]	Beam (B) [m]	Depth (H) [m]	Draft (T) [m]
110.0	11.4	2.5	1.5

The dimensions of the hexahedral calculation domain are shown in Table 2.

Table 2. Dimensions of the hexahedral calculation domain.

Length [m]	Width [m]	Height (Restricted) [m]	Height (Unrestricted) [m]	Water Depth (Restricted) [m]	Water Depth (Unrestricted) [m]
300.0	50.0	6.8	25.0	1.8	20.0

The layout cases of the CFD domains were designed as follows:

- One-half (SB) of the ship hull and the surrounding environment is modeled.
- Identical hull geometry is used for all the cases.
- Uniform pressure jump dp = 100,000 Pa is applied for all the actuator discs.
- Uniform total surface area (sum) of actuator discs is 1.2 m^2 on one side.
- Monitoring surfaces are assigned to every actuator disc on the upstream and the downstream sides with the same offset.

The CFD analyses have been performed with identical set-up parameters (Table 3). Only the boundary conditions and the initializing values vary from case to case.

Table 3. CFD set-up parameters.

Software	ANSYS Fluent v. 17.2.0
Solver	Pressure-based, transient
Model	Volume of fluid, multiphase, open channel wave BC
Eulerian phases	Air, freshwater
Viscous model	k-omega, SST
Mesh type 1	Prismatic, 3 layers at the hull boundary, aspect ratio 10-7
Mesh size 1	min. 50 mm; max. 125 mm; curvature and proximity controlled
Mesh type 2	Pyramidal, transition zone between prismatic and hexahedral mesh
Mesh size 2	Automatic
Mesh type 3	Hexahedral, filling out the rest of the exterior CFD domain
Mesh size 3	min. 50 mm—near zones; max. 1000 mm—far zones
Mesh refinement 3	Hull zone—a box enclosing the hull, max. mesh size 125 mm Wave zone—a layer of thickness 1000 mm at the free surface level; max. mesh size 250 mm
Report	Mass flow rate through the actuator discs and their monitoring surfaces

The following hull/propulsion layout cases have been analyzed for discrete flow speed values taken from the vessels working in the range 0–6 m/s:

- A: Traditional 2 stern-mounted propulsors (twin-screw) layout (without tunnel and fins);
- B: 2 side propulsion units mounted in the aft hull zone (symmetrically);
- C: 4 side propulsion units mounted in the aft and fore hull zones (2 + 2, symmetrically);
- D: 6 side propulsion units mounted in the aft, mid, and fore hull zones (2 + 2 + 2, symmetrically);
- E: 8 side propulsion units mounted evenly along the ship hull (2 + 2 + 2 + 2, symmetrically).

The actuator disc was simulated using a fan boundary condition in the ANSYS Fluent CFD package. A boundary condition was applied on a circular surface whose diameter was set so that the total area of the propellers was constantly 2.4 m^2. Diameters and locations of actuator disk centers in individual layouts are shown in Table 4.

Table 4. Actuator disc parameters.

	Disc Diameter	Center, off Centerline	Center, above Baseline
Layout A:	1236 mm	4000 mm	675 mm
Layout B:	1236 mm	6437 mm	675 mm
Layout C:	874 mm	6437 mm	675 mm
Layout D:	714 mm	6437 mm	675 mm
Layout E:	618 mm	6437 mm	675 mm

Special attention has been paid to cases C, D, and E because they can be considered as distributed ship propulsion systems, which were the main focus of interest.

For comparison reasons, all the studied cases have been examined under restricted draft conditions in shallow water, keeping a minimum of 0.3 m UKC, and also, under unrestricted draft conditions in deep water.

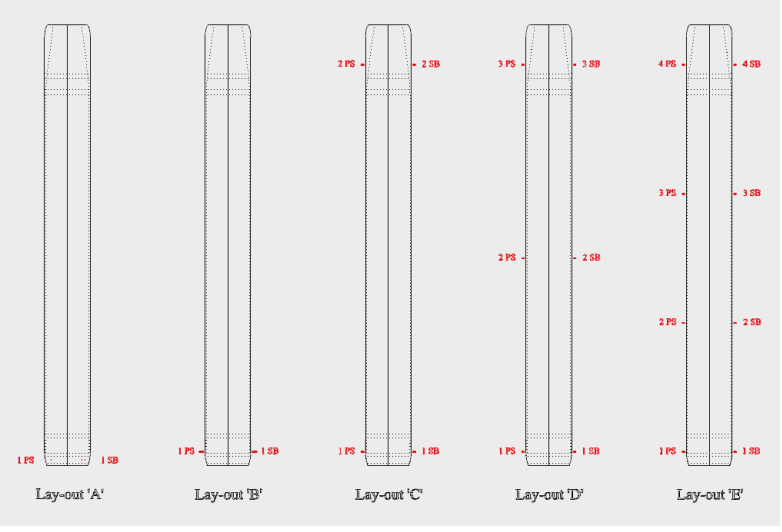

Figure 3. Different hull/propulsion layouts examined by CFD analyses. Source: Authors.

A total of 50 CFD flow analyses have been performed for unrestricted and restricted draft conditions. The mass flow rate values recorded for the actuator disc and the upstream/downstream monitors at every propulsion position have been used in Equation (4) of the Rankine momentum theory to obtain the increase in thrust generated by the propulsor. The power absorbed by the propulsors has been calculated by means of Equation (2) from the already known thrust value.

A visual check of the water flow field around the ship hull and the propulsors, the free surface of the water, and the wave pattern is possible in the graphical output generated by the CFD system (Figure 4). Some special variations in the values of the reported hydrodynamic quantities can be easier understood in this simple way (Figure 5).

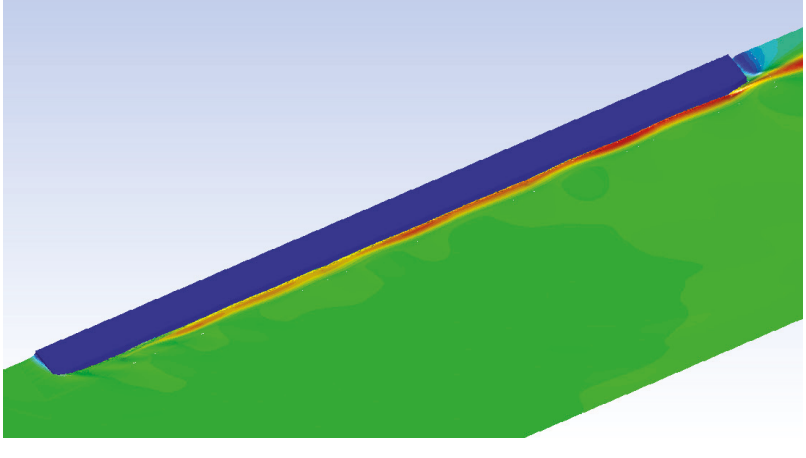

Figure 4. Velocity magnitude on the free water surface (Layout E, deep water). Source: Authors.

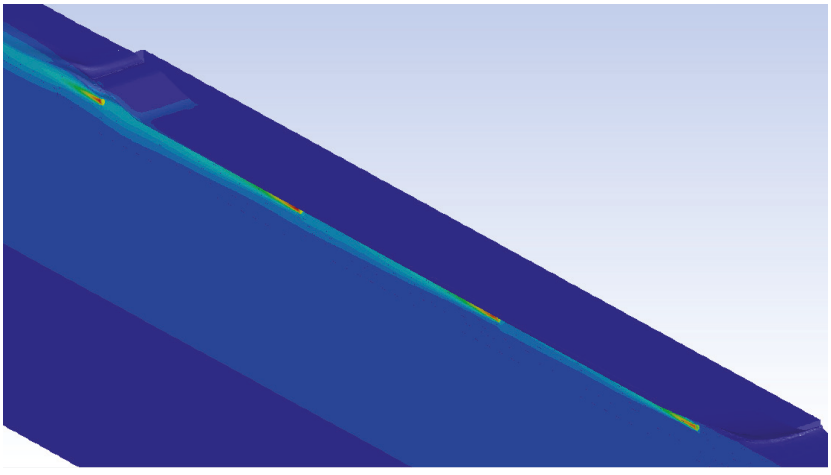

Figure 5. Dynamic pressure at the propulsors' center plane (Layout E, deep water). Source: Authors.

3. Results and Discussion

The resulting values of mass flow increase, generated thrust, and absorbed power are shown in Figures 6–11, where their relative values are represented for an easier comparison and evaluation.

In the following comparative line graphs, the resulting total values are shown, where every curve represents a specific hull/propulsion layout. The absolute values of layout A in deep water at a mean speed of 4 m/s have been chosen as the reference unity values to calculate the relative values.

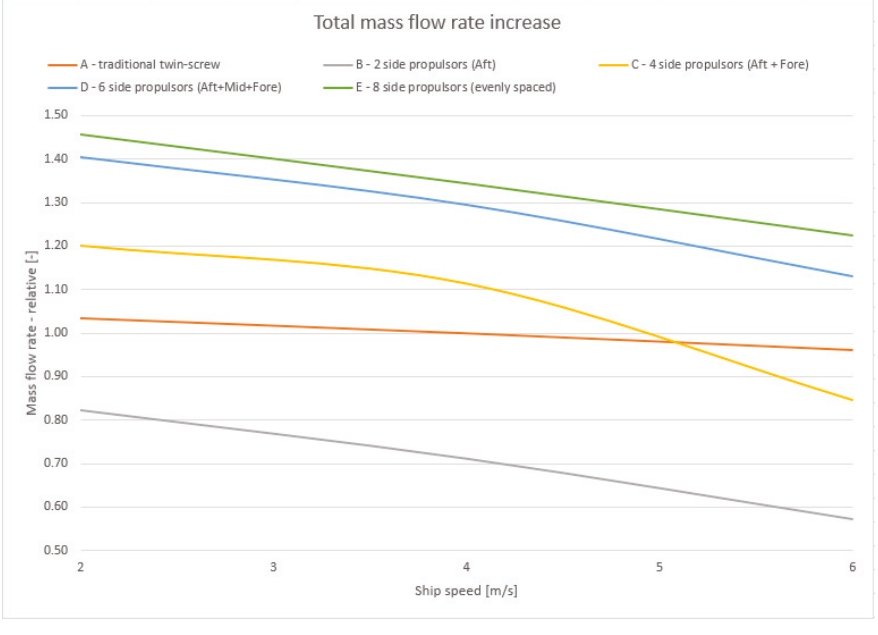

Figure 6. Total mass flow rate, deep water (comparison). Source: Authors.

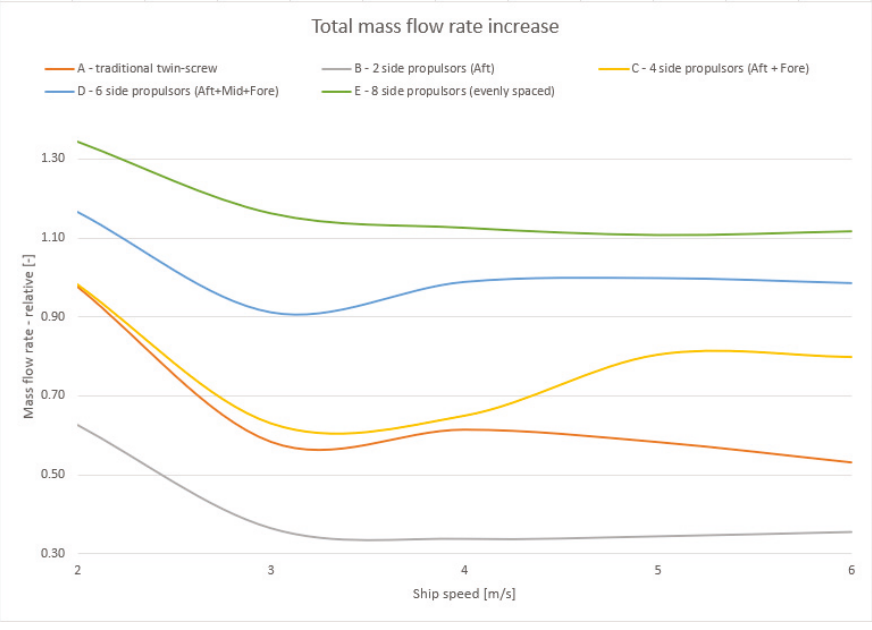

Figure 7. Total mass flow rate, shallow water (comparison). Source: Authors.

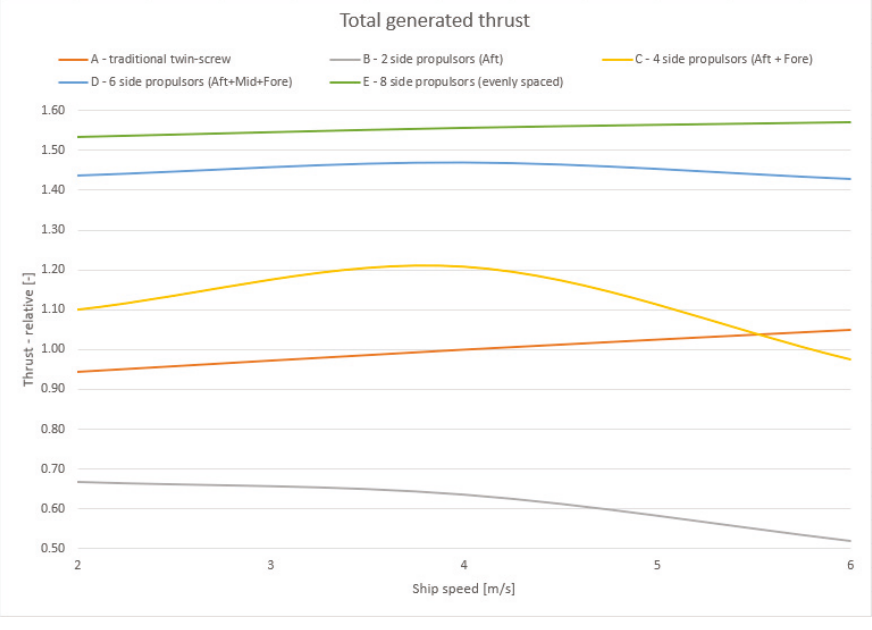

Figure 8. Total generated thrust, deep water (comparison). Source: Authors.

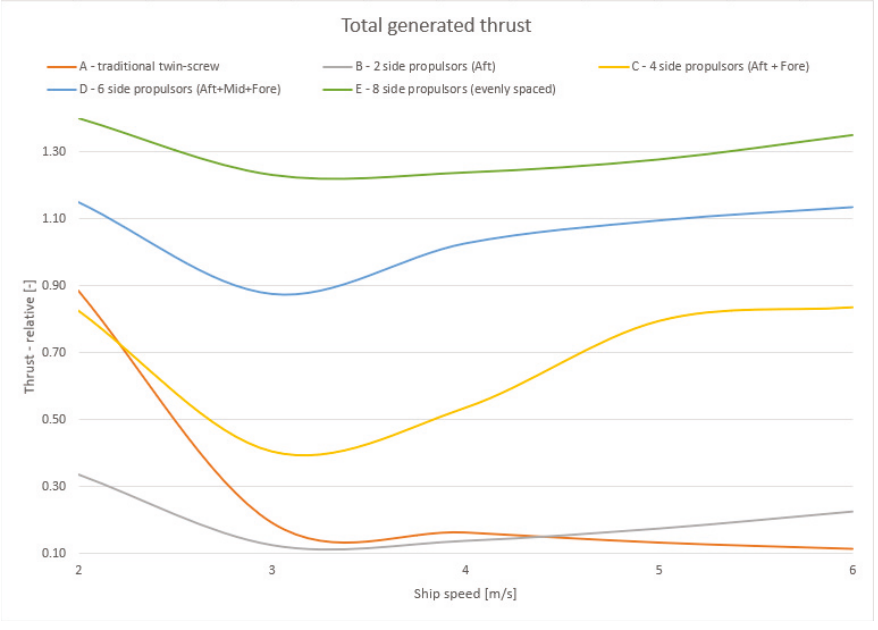

Figure 9. Total generated thrust, shallow water (comparison). Source: Authors.

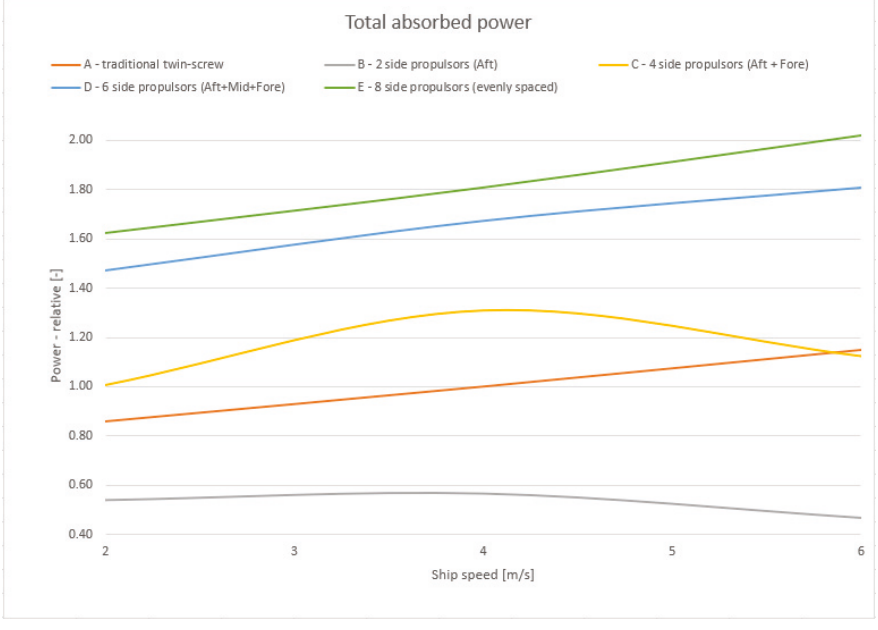

Figure 10. Total absorbed power, deep water (comparison). Source: Authors.

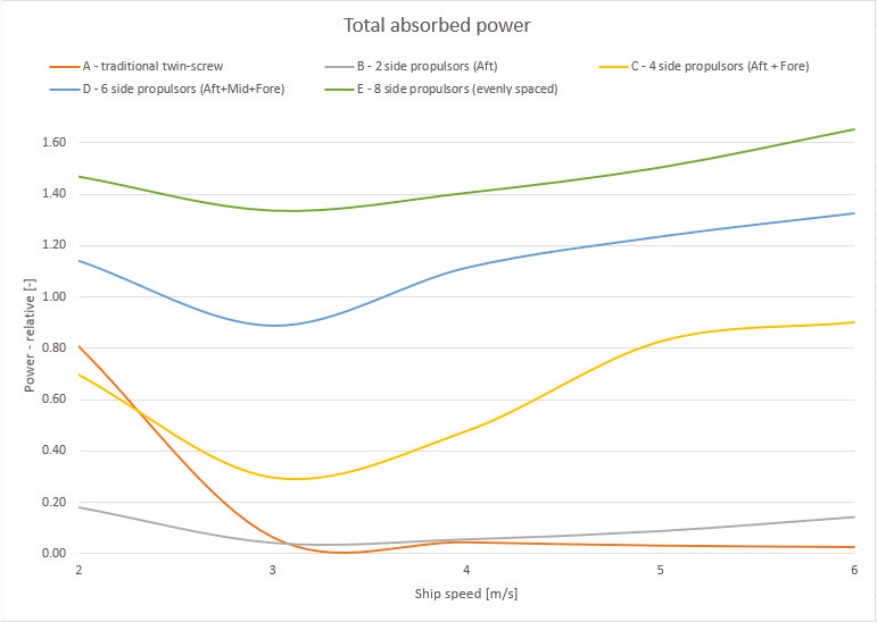

Figure 11. Total absorbed power, shallow water (comparison). Source: Authors.

Rapid changes and some problematic areas can be identified easily in these graphs. In general, a significant fall in performance indicates intensive air intake into the propulsor. The occurrence of such ventilation can be checked visually in the graphical output from the CFD analysis.

In the figures showing the restricted water conditions, a special region can be localized around the sailing speed of 3 m/s. All the curves have a "wave trough" at this area, and this is a hot candidate for a speed value characteristic for this specific hull and water flow field.

It can also be seen that the absence of the propulsion tunnel (and fins) has a much more significant impact on the performance of hull/propulsion layout A (traditional twin-screw) under the restricted sailing conditions.

To show which propulsion locations are prone to have a strong air intake from the free water surface, a different type of figure has been introduced.

The examples in Figures 12 and 13 represent the resulting generated trust and absorbed power values for hull/propulsor layout E (8 propulsors) on a per-propulsor basis. For these two special graphs, the absolute values of the aftmost propulsor at speed 2 m/s in shallow water have been chosen as the reference unity values.

In this example case, the critical propulsor position is No. 1, which is located in the aftship zone of the hull (aftmost side propulsors, see Figure 14). Intensive ventilation of the propulsion is typical for this location also in other layouts. The performance of propulsor No. 4, located in the foreship zone (foremost side propulsors), seems to be quite unstable; in some layouts, air intake is also present.

Both propulsion positions are typically located at the curved (shaped) hull endings, where the water flow speeds up quickly, causing a pressure drop and a wave trough. Therefore, the air intake occurs much easier in these locations than in the straight and long midship area.

The following comparative figures (Figures 15 and 16) show the thrust and power curves of three distributed propulsion layouts (C, D, E) in restricted and unrestricted water depth conditions. The thrust and power of layout A at mean speed 4 m/s in deep water have been used as unity values.

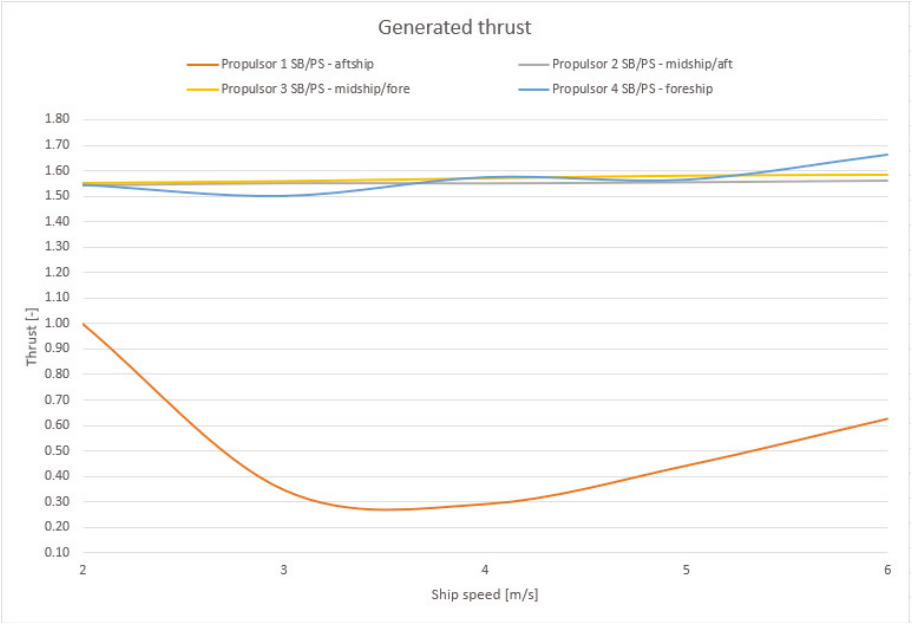

Figure 12. Propulsion thrust, shallow water (layout E). Source: Authors.

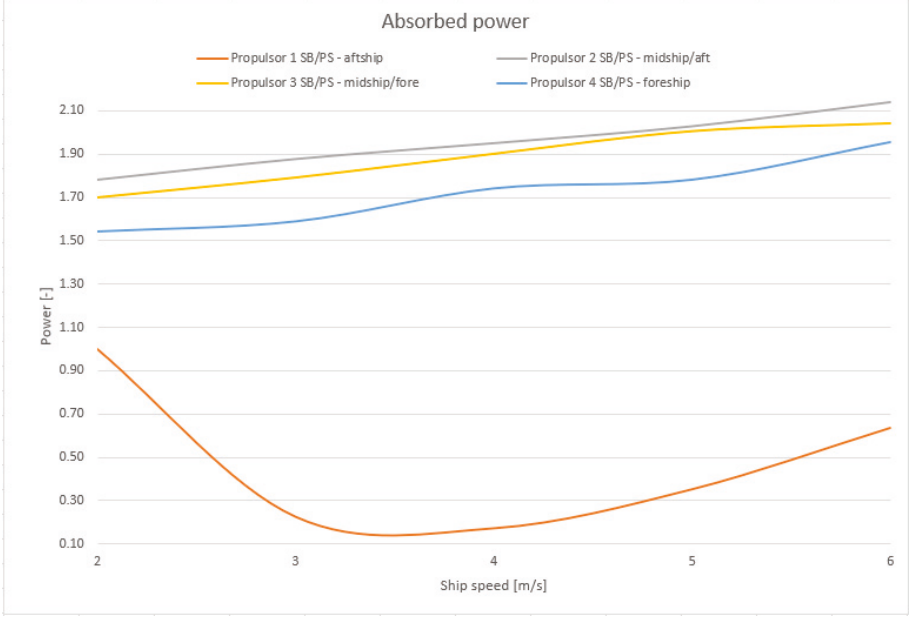

Figure 13. Propulsion power, shallow water (layout E). Source: Authors.

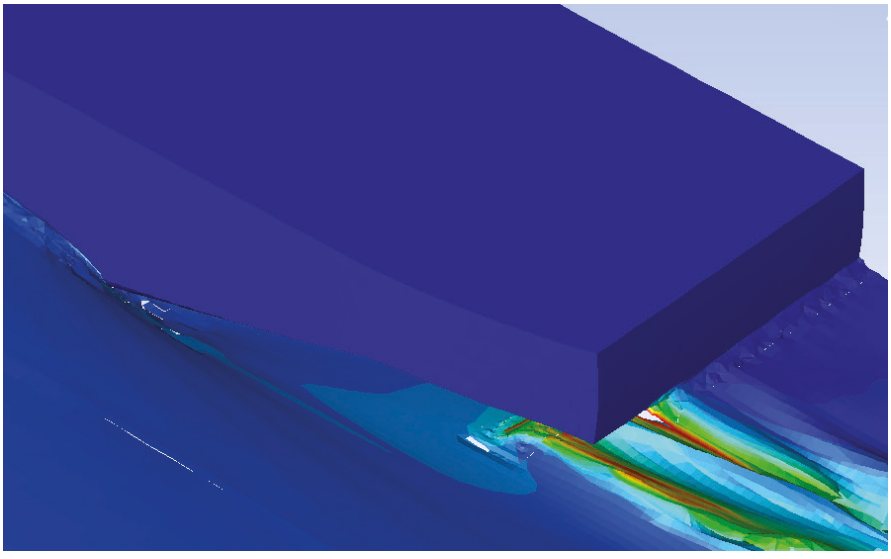

Figure 14. View of the aftship air intake zone (Layout A, shallow water). Source: Authors.

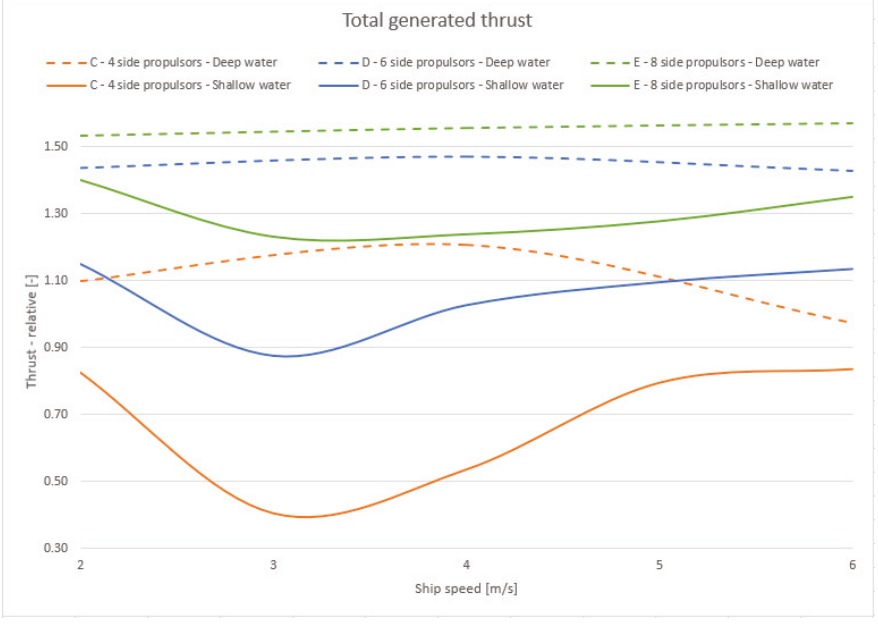

Figure 15. Thrust of distributed systems in deep and shallow water conditions. Source: Authors.

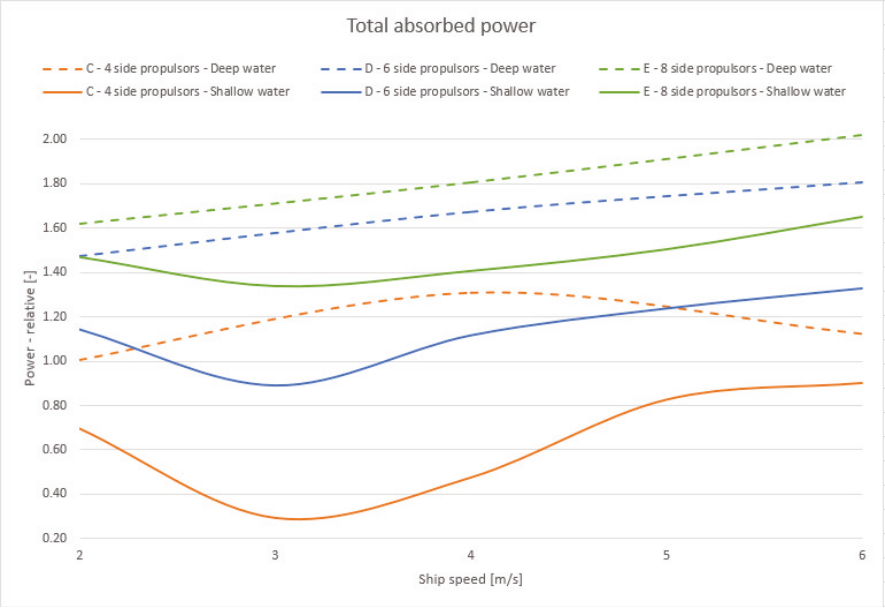

Figure 16. Power of distributed systems in deep and shallow water conditions. Source: Authors.

Generally, after comparing the hydrodynamical performance in Figures 6–11, 15 and 16 of ideal propulsors under both water depth conditions, it can be stated that the distributed propulsion systems consisting of 4+ (preferably 6 or 8 or more) units produce noticeably higher thrust effects in shallow water sailing than the traditional aft end layouts. Under restricted conditions, the thrust increase between two distributed layouts with a different number of propulsors is higher in contrast to deep water sailing, where differences in performance are not so significant.

The aim of this investigation was not to evaluate the absolute values of hydrodynamic quantities obtained from CFD analyses, but rather, to find new ways and possible principal solutions for shallow water propulsion systems. Due to the large number of CFD simulations to be performed, some simplifications had to be made on the computational domain in order to keep the computing time at a reasonable level. For the same reasons, the real propulsion units have been represented with ideal propulsors (actuator discs).

However, the accuracy reached in this way by CFD calculations is sufficient only if the relative quantity values are needed for comparison purposes. The resulting main performance parameters of all the examined propulsion layouts have been compared properly, so it was possible to filter out the most promising solutions. The comparison of the results from the restricted and unrestricted water depth conditions has clearly shown the differences in the courses of their graphs.

To determine the effect of mesh quality, a dependence study has been performed for case E in shallow water. For the new analyses, the CFD mesh of the entire computational domain has been refined by halving the average element sizes. With these several times larger amounts of elements, the interval of sailing speeds from 2 to 6 m/s has been analyzed and the results have been compared with the values obtained from the original coarser mesh. The result of this comparison is shown in Figure 17 as percentage difference of the new values from the reference values. The graph shows that in the operating range of the vessel, the maximum difference value is close to 2.5%, which is fully acceptable for comparison purposes.

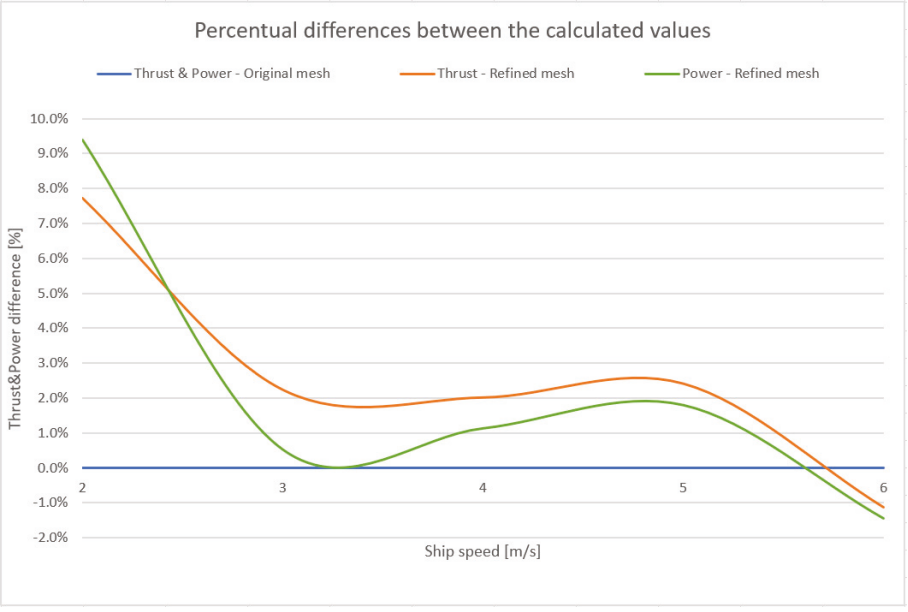

Figure 17. Percentual comparison of the original and the refined mesh results. Source: Authors.

In the technical literature, the expressions "distributed propulsion system" or "multiple propeller ship" refer to ships which are equipped with more than three propulsors (propellers) in general, located in the aftship area and arranged in different geometric patterns. Based on the lack of available publications concerning side-mounted propulsions, it can be assumed that we have given a new meaning to the expression "distributed propulsion".

Similar R&D and experiments have been performed in the past for another reason, i.e., for better longitudinal distribution of thrust power in terms of the propeller load and cavitation. The best-known cases are overlapping propellers and tandem propellers (their modern versions are twin propeller azimuths and pods), which have also been implemented on experimental ships. Overlapping propellers each have their own shaft line, while the tandem system is mounted on a single common shaft. However, all these propulsions are located in a traditional place under the stern part of the ship (aft end layout), which is a significant difference from the distribution along the side of the ship that we have investigated. In addition, these systems tend to appear as integrated propulsion units due to their small distance from each other. Based on the significant differences and the poor documentation of the above listed cases, they have not been mentioned in the work as reference cases or comparative bases.

For a final validation of the working method, it was not possible to make a comparison of our CFD-based results with other published results from earlier investigations either made by computer simulations or by model tests made in towing tanks. No usable publication reporting a similar approach studying longitudinal distribution of propulsion units has been found up to now.

4. Conclusions

The analysis results have confirmed that shallow water vessels driven by distributed (side-mounted) propulsion systems can be operated efficiently, eliminating the unwelcome side effects of the traditional stern-mounted propeller systems. The preliminary assumptions have been substantiated, at least at the simulation level.

Technical implementation of the propulsors was beyond the scope of this work. Standard propeller-based propulsion units are probably not usable because of their tendency to take in the air from near the free

water surface. Rather, different, more suitable propulsors should be employed, or a completely new concept should be developed for this special purpose.

This was the first step of investigations around distributed propulsion systems, bringing purely principal solutions to the problem. In the next step, the most promising hull/propulsion layouts should be further examined at a higher level by performing a series of complex and demanding CFD analyses. The most appropriate are layouts E and D (8 and 6 units), but for shorter ship hulls, layout C (4 units) could be useful as well. In this phase, a new side-mounted type of propulsion unit should be preliminarily designed. The purpose of the third phase should be the validation of the results from the previous two phases. Preferably, a towing tank test should be performed, examining the real hull-propulsion interactions.

The main contribution of this work is that it shows a possible way how the more efficient vessels of the future intended for restricted navigation depth could be developed. Such vessels could also operate on waterways where the ships with a traditional hull and propulsion can no longer do so, either for technical or economic reasons. Further R&D tasks should lead to the development of special propulsors and hulls optimized for their best interaction in restricted but also in unrestricted conditions of navigation.

Author Contributions: Conceptualization, L.I., T.K. and M.J.; methodology, L.I. and M.J.; software, L.I.; validation, L.I., T.K. and M.J.; formal analysis, M.J.; investigation, L.I., T.K., M.J. and V.L.; resources, M.J. and V.L.; data curation, T.K.; writing—original draft preparation, L.I.; writing—review and editing, M.J.; visualization, T.K. and V.L.; supervision, T.K. and M.J.; project administration, T.K and M.J.; funding acquisition, T.K. and M.J. All authors have read and agreed to the published version of the manuscript.

Funding: This research was funded by Institutional research of the Grant system of the Faculty of Operation and Economics of Transport and Communications, University of Zilina. This research is also the result of the Project VEGA No. 1/0128/20: Research on the Economic Efficiency of Variant Transport Modes in the Car Transport in the Slovak Republic with Emphasis on Sustainability and Environmental Impact, Faculty of Operation and Economics of Transport and Communications, University of Zilina, 2020–2022.

Conflicts of Interest: The authors declare no conflict of interest.

References

1. David, A.; Madudova, E. The Danube river and its importance on the Danube countries in cargo transport. In Proceedings of the 13th International Scientific Conference on Sustainable, Modern and Safe Transport, TRANSCOM 2019, High Tatras, Slovakia, 29–31 May 2019.
2. Danube River Basin Climate Change Adaptation, Final Report. Department of Geography, Chair of Geography and Geographical Remote Sensing, Ludwig-Maximilians-Univesitat Munich, Germany. 2018. Available online: https://www.icpdr.org/main/sites/default/files/nodes/documents/danube_climate_adaptation_study_2018.pdf (accessed on 15 June 2020).
3. Alberto, P.; Hylke, B.; Bernard, B.; Emiliano, G.; Carlo, L.; Janos, F. Water scenarios for the Danube River Basin: Elements for the assessment of the Danube agriculture-energy-water nexus. *JRC Tech. Rep.* **2016**. [CrossRef]
4. Stopka, O.; Simkova, I.; Konecny, V. The quality of service in the public transport and shipping industry. *Nase More* **2015**, *62*, 126–130. [CrossRef]
5. Buchler, D.; Luck, R.; Markert, M. Propulsion and control system for shallow water ships based on surface cutting double Propellers. In Proceedings of the 8th IFAC Conference on Control Applications in Marine Systems, Rostock-Warnemunde, Germany, 15–17 September 2010.
6. Raven, H. A new correction procedure for shallow-water effects in ship speed trials. In Proceedings of the 13th International Symposium on PRActical Design of Ships and Other Floating Structures PRADS' 2016, Copenhagen, Denmark, 4–8 September 2016.
7. Rotteveel, E.; Hekkenberg, R.; Ploeg, A. Inland ship stern optimization in shallow water. *Ocean. Eng.* **2017**, *141*, 555–569. [CrossRef]
8. Schlichting, O. Schiffwiderstand auf beschränkter wassertiefe: Widerstand von seeschiffen auf flachem wasser. *Jahrb. Schiffbautech. Ges.* **1934**, *35*, 127.
9. Lackenby, H. The effect of shallow water on ship speed. *Shipbuild. Mar. Eng.* **1963**, *70*, 446–450.

10. Tuck, E. Hydrodynamic problems of ships in restricted waters. *Annu. Rev. Fluid Mech.* **1978**, *10*, 33–46. [CrossRef]
11. Ferreiro, L.D. The effects of confined water operations on ship performance: A guide for the perplexed. *Nav. Eng. J.* **1992**, *104*, 69–83. [CrossRef]
12. Rotteveel, E.; Hekkenberg, R. The influence of shallow water and hull form variations on inland ship resistance. In Proceedings of the 12th International Marine Design Conference (IMDC), Tokyo, Japan, 11–14 May 2015.
13. Raven, H. A computational study of shallow-water effects on ship viscous resistance. In Proceedings of the 29th Symposium on Naval Hydrodynamics, Gothenburg, Sweden, 26–31 August 2012.
14. Harvald, S.A. Wake and thrust deduction at extreme propeller loadings for a ship running in shallow water. *RINA Suppl. Pap.* **1977**, *119*, 20–21.
15. Zhao, L. Optimal ship forms for minimum total resistance in shallow water. *Schriftenreihe Schiffbau* **1984**, *445*. [CrossRef]
16. Saha, G.K.; Suzuki, K.; Kai, H. Hydrodynamic optimization of ship hull forms in shallow water. *J. Mar. Sci. Technol.* **2004**, *9*, 51–62. [CrossRef]
17. Galierikova, A.; Sosedova, J. Environmental aspects of transport in the context of development of inland navigation. *Ekol. Bratisl.* **2016**, *35*, 279–288. [CrossRef]
18. Sugalski, K.; Skrucany, T. Grid type impact on the results of the volume of fluid method in the free surface flow calculations around ship hull. In *New Trends in Production Engineering*; De Gruyter: Warsaw, Poland, 2018; Volume 1, pp. 151–157.
19. Carlton, J. *Marine Propellers and Propulsion*, 4th ed.; Butterworth-Heinemann: Oxford, UK, 2019.
20. Ganco, M. *Fluid Mechanics*; ALFA: Bratislava, Slovakia, 1983.
21. Douglas, J.F.; Gasiore, J.M.; Swaffield, J.A.; Jack, L.B. *Fluid Mechanics*, 5th ed.; Pearson: Harlow, UK, 2005.
22. Molnar, V. *Computational Fluid Dynamics—Interdisciplinary Approach with CFD*; University of Technology in Bratislava (STU): Bratislava, Slovakia, 2011.
23. Kudelas, D. *Basic of Computer Flow Modelling and Visualization*; Faculty of Mining, Ecology, Process Control and Geotechnologies: Kosice, Slovakia, 2017.

Journal of
Marine Science and Engineering

MDPI

Article

A New Systematic Series of Foil Sections with Parallel Sides

Antonio Saporito [1,*], Adam Persson [2,3], Lars Larsson [2] and Antonio Mancuso [1]

[1] Department of Engineering, University of Palermo, 90128 Palermo, Italy; antonio.mancuso@unipa.it
[2] Department of Mechanics and Maritime Sciences, Chalmers University of Technology, 412 96 Gothenburg, Sweden; adam.persson@sspa.se (A.P.); lars.larsson@chalmers.se (L.L.)
[3] SSPA Sweden AB, 400 22 Gothenburg, Sweden
* Correspondence: antonio.saporito@unipa.it; Tel.: +39-3208289026

Received: 12 August 2020; Accepted: 26 August 2020; Published: 3 September 2020

Abstract: Parallel-sided foil sections are used for centerboards and rudders in sailing dinghy classes and also for struts placed in a fluid flow. The objective of this work is to create a systematic series of parallel-sided sections to be used under different conditions, with an emphasis on the sailing dinghies 470, 420 and Optimist. The loss, and surprisingly the gain, in performance relative to 4-digit NACA sections are also investigated. A 2D Reynolds-averaged Navier–Stokes solver is used with the k-ω SST turbulence model and the gamma transition criterion. A verification study is carried out based on four grids of systematically varied density, and results compared with experimental data on a NACA 64-006 section. The parallel-sided sections are modeled with rational Bézier curves whose geometrical parameters permit to link the shape of the profile to physical variables, which are systematically varied. Three Reynolds numbers and two angles of attack are investigated. Systematic plots show the influence of the trailing edge angle and nose radius for the different section families, and the optimum combination is presented in a table. Physical explanations of the trends, and of the exceptions, are given in the paper, using flow visualizations as well as pressure and friction plots.

Keywords: parallel-sided; NACA; CAD; systematic investigation; low Reynolds number; sailing; centerboard; Bézier curves; gamma transition criterion

1. Introduction

The purpose of airfoils is to produce lift with minimum drag. To obtain this result, aerodynamic sections are carefully designed. Very common, in a wide range of fields such as airplanes, ships, sports cars, and sailboats, are the NACA sections [1]. Over the years, many studies have been conducted of these profiles to optimize their shape and also to guide the designers in their choice of the best profile for a certain application. Parallel-sided sections are a particular family of airfoils where the main part of the section has parallel sides, while only the front and aft parts are streamlined. They find applications for sailing dinghies, such as 470, 420 and Optimist, where class rules [2–4] define how the centerboard must be built. Other applications are supporting struts in a fluid flow, and a wind-tunnel application was presented by Pollock [5]. This is the only investigation on parallel-sided sections known to the authors, and the objective of the present work is to fill this knowledge gap, with an emphasis on sailing boats. For this reason, the parameter ranges are taken from the class rules of the dinghies mentioned. The investigation includes two different conditions: upwind (lift coefficient equal to 0.4) and downwind (angle of attack equal to 0.0°). The upwind case is of interest for all three classes, while the downwind case is of less interest for the 470 and the 420, since they hoist the centerboard while sailing downwind in most wind speeds. For the Optimist, the centreboard is partly hoisted. However, since this type of section can be found in other fields than sailing, the authors are interested in showing the results of both cases.

By far, the most common tools for designing airfoils over the years have been potential flow/boundary layer methods. Even today, the most widely used software for this purpose: XFOIL [6], is based on these theories. However, airfoil design depends crucially on the prediction of separation, both at the leading and trailing edges, and this is a weak point of boundary layer theory. Furthermore, the viscous/inviscid interaction is difficult to model accurately for thick and separated boundary layers. To increase accuracy, less approximate methods based on the Navier-Stokes equations are preferable, and the only realistic possibility, if thousands of computations are to be carried out, is the Reynolds-averaged Navier–Stokes (RANS) method.

Another critical feature of the numerical method is the transition prediction. By designing sections with its pressure minimum far aft, the laminar boundary layer may be maintained over the main part of the foil, reducing the frictional resistance considerably. This is the feature of the so-called laminar sections in the 6-series of the NACA sections [1], but transition is not only important for the friction. There is a crucial dependence of separation on transition, as laminar boundary layers separate more easily than turbulent ones, where the turbulent mixing transports external flow momentum to the inner parts of the boundary layer. This is important, both for separation bubbles at the leading edge, and for the open separation further back on the foil. The latter effect will be seen very clearly in the results below. For a thorough discussion on the effects of transition and separation on airfoil performance, see Larsson et al. [7].

In order to predict these critical features, attention should be paid to both the numerical and physical modelling of the flow [8]. The former should be addressed through a numerical verification study. In the present work, this is performed through a systematic grid variation. Since the method used is based on the RANS equations, a turbulence model is needed, and the choice may have a significant influence on the separation prediction. The motivation for the present choice is given below. Reasons for the choice of transition model are also given.

The numerical method with its parameter settings is described in Section 2. In Section 3, the verification study is presented, including a systematic grid variation and a numerical uncertainty assessment. Section 4 deals with the validation of the method against a NACA 64-006 section, for which measured data are available in [1], and in Section 5 the systematic investigation is presented. Results are shown in Section 6, and the final conclusions are drawn in Section 7.

2. Numerical Method

2.1. Equations

In the present project, STAR CCM+ [9] is used for the CFD computations. The Reynolds-averaged Navier–Stokes equations are solved together with the k-ω SST turbulence model [10]. This is by far the most popular turbulence model for hydrodynamic computations, see e.g., Larsson et al. [11] and Hino et al. [12] It is based on the original k-ω model developed for boundary layers in adverse pressure gradients by Wilcox [13], but improved by Menter [10] to avoid the unphysical influence of the external turbulence. The k-ω SST model is recommended for computations of the present kind in the STAR CCM+ Manual [9].

In STAR CCM+, two transition models are available: the two equation Gamma ReTheta model and the one equation Gamma model. The former has been widely used in aerodynamic and turbomachinery applications [14], but has a few drawbacks, and therefore the more modern Gamma model was developed [15]. Since the drawbacks are eliminated in this model, it was selected for the present investigation.

2.2. Boundaries

Figure 1 shows the computational domain and the related boundary conditions applied for the validation case (NACA64-006) and for the systematic investigation of the parallel-sided sections (the zero angle of attack and the constant lift).

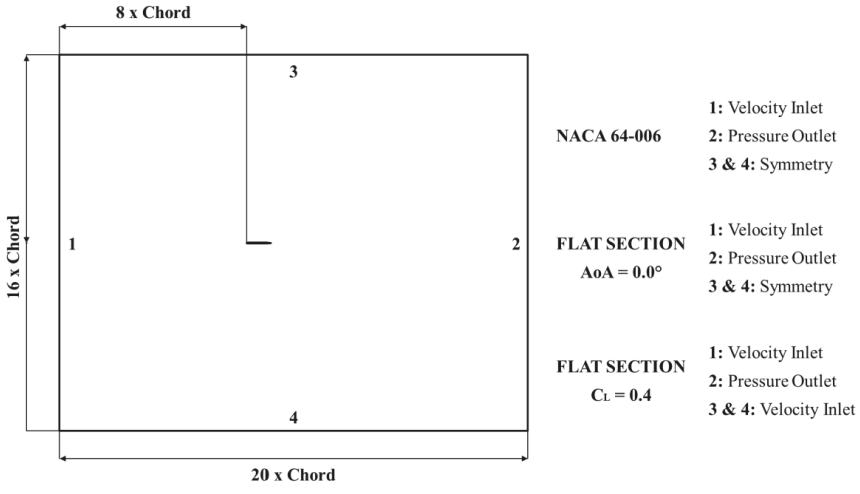

Figure 1. Boundary definition.

For the NACA 64-006 section, the ambient turbulence intensity, defined as a fraction of the free stream velocity, is 0.006, taken from the wind tunnel specification in [16]. For the systematic investigation, an estimation of the turbulence level in the sea, presented in [17], is adopted. This value is 0.0025. The turbulence viscosity ratio is the ratio between the turbulent and laminar viscosities, and determines the turbulence length scale. Note that, to maintain the ambient turbulence level throughout the domain, source terms are added to the kinetic energy equation; see [9]. This is an important possibility in STAR CCM+. Tests were done without these source terms, and numerical diffusion caused the turbulence to die out rapidly behind the inlet. There was then zero turbulence level at the position of the foil, and this caused the solution to become more unstable. The inner boundary condition is no-slip.

2.3. Discretization

For the discretization, the finite volume discretization method is used with a segregated flow solver (SIMPLE algorithm). All computations presented in this paper are carried out in steady mode.

2.4. Grid Settings

The same grid settings are used for the test case and the systematic investigations. Polygonal and prism layer meshes, with the number of prism layers equal to 100 and prism layer stretching equal to 1.0678, are selected. y+ is set to 0.125. The mesh is generated directly in 2D. In Figure 2, the grid close to the test foil, with close-ups at the leading and trailing edges, is presented. With the present transition model, it turned out that a fluctuating laminar separation bubble occurred on the suction side of the nose (lift case) for all tested grids with 50,000 to 400,000 cells. This bubble disappeared for all finer grids, and is therefore assumed to be unphysical. The transition model thus poses strong requirements on the grid density; 400,000 cells is very much for a 2D case. The presented grid settings were the best configuration obtained after the test case analyses, and for this reason, they were also adopted for the systematic investigation.

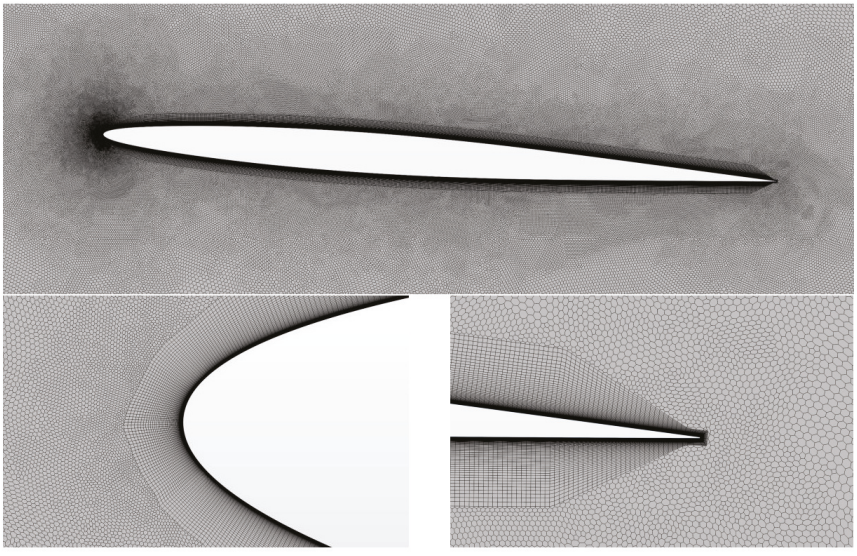

Figure 2. View of the mesh surrounding the test case section, and close-ups of leading and trailing edges. For the test case, the angle of attack is achieved by rotation of the foil, while for the systematic computations the direction of the inflow is varied to obtain the requested lift coefficient (0.4).

3. Verification

Once the coarsest grid for a stable solution is identified, the verification process to identify the numerical uncertainty is carried out. Two methods are recommended by the ITTC [18]: the factor of safety method by Xing and Stern [19], and the least square root (LSR) method by Eça and Hoekstra [20]. The advantage of the LSR method is that it takes numerical scatter into account by considering solutions from more than three grids. For more details, see [20]. Therefore, this method is selected. Note that only grid uncertainty is considered. Since iterative convergence is achieved by reducing the residuals by 4–5 orders of magnitude, the iterative error can be neglected

Four different grids, the largest one with 6.5 million cells, are created to perform the verification process with the least square root method [20]. Table 1 and Figure 3 show the results. H_i is the linear cell size ratio between a specific grid (i) and the finest one, U is the numerical uncertainty, and U ($\%C_L$) is the uncertainty in percent of the coefficient.

Table 1. Numerical uncertainty of lift and drag coefficient for the test case at different grid densities.

Nr. Cells	H_i	C_L	U (C_L)	U ($\%C_L$)	C_D	U	U ($\%C_D$)
6.5 M	1	0.4354	0.00187	0.5	0.00850	0.000102	1.2
3.6 M	1.34	0.4337	0.00411	0.9	0.00849	0.000060	0.7
1.6 M	2	0.4346	0.00237	0.5	0.00848	0.000106	1.3
0.4 M	4.03	0.4342	0.00606	1.4	0.00862	0.000301	3.5

The very high number of cells for this 2D study leads to very low levels of uncertainty for the finer grids. However, the coarsest grid, with 0.4 million cells, is chosen for further computations. This decision is taken considering the number of simulations that must be performed during the systematic investigation. Although the numerical uncertainty is larger for this grid (1.4% and 3.5% respectively for lift and drag), the difference between the grids in terms of drag coefficients is very small, as can be seen in Figure 4, where the coarse mesh (0.4 million cells) is compared with a finer

one (1.6 million cells). In this comparison, a family of parallel-sided sections with small thickness (T1), long leading edge (LE2) and long trailing edge (TE2) is taken as an example (see Section 5 for the nomenclature). The angle of attack is equal to zero, and five configurations with the same nose radius, but varying trailing edge angles, are evaluated for both the coarse and the fine grid.

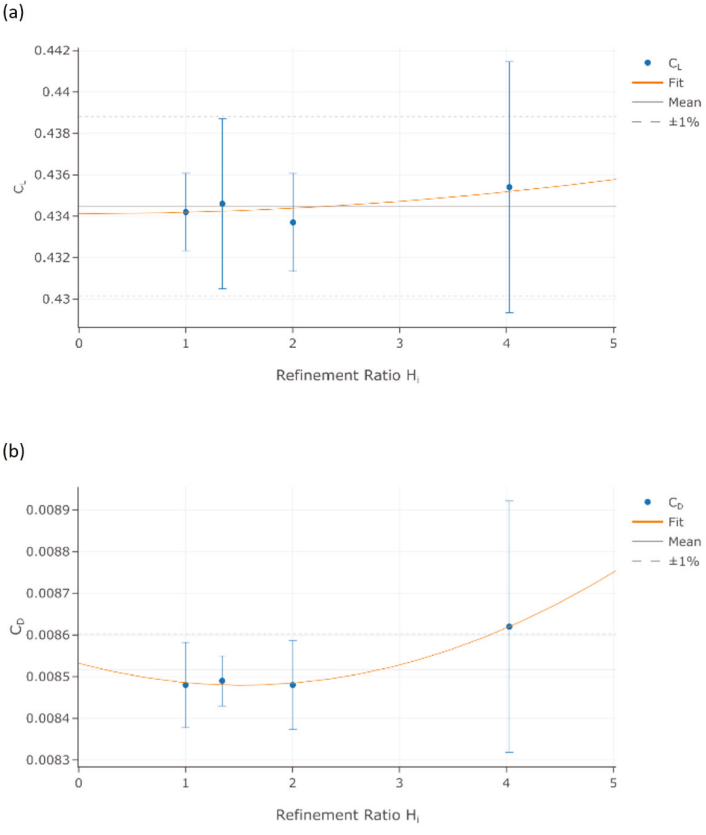

Figure 3. Regression curve of lift coefficient (**a**) and drag coefficient (**b**).

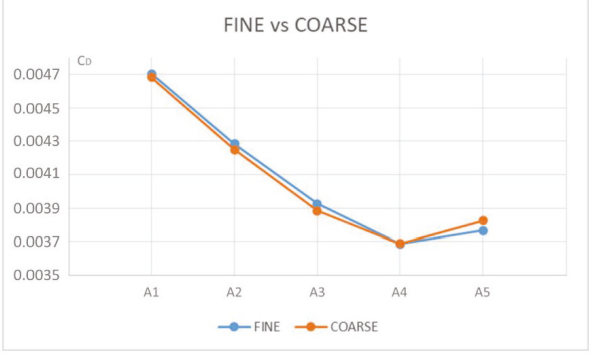

Figure 4. Comparison of drag coefficients for the coarse grid and a finer one. The independent variable is the trailing edge angle (see below).

4. Validation Case

To validate the numerical model, an effort was made to find a suitable test case in the literature. The aim was to find a thin section at a relevant Reynolds number. However, although there are several such cases reported, even with detailed flow data, none appeared to present accurate force measurements. Therefore, a NACA 64-006 section is selected as a test case [1]. The lowest Reynolds number in the NACA tests is 3,000,000, while in the present systematic computations the Reynolds number varies from 300,000 to 1,500,000. The results from the validation simulation are compared with the experimental data for angles of attack between 0.0° and 4.0° in Figure 5 and Table 2. Apparently, the transition model is not accurate enough to predict the width of the drag bucket, but since this study is carried out for 0° and approximately 4°, the less perfect match of results between 1.5° and 2.0° should not influence the systematic investigation.

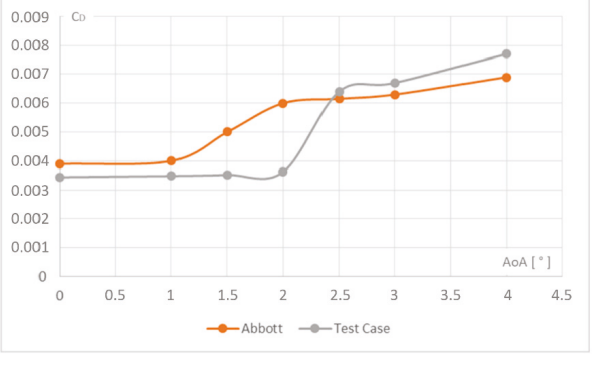

Figure 5. Comparison between numerical and experimental results. Reynolds number 3,000,000.

Table 2. Numerical and experimental results for different angle of attack.

Angle of Attack	Test Case	Abbott
α	C_D	C_D
0.0	0.00344	0.0039
1.0	0.00348	0.0040
1.5	0.00352	0.0050
2.0	0.00362	0.0060
2.5	0.00640	0.0062
3.0	0.00670	0.0063
4.0	0.00770	0.0069

It should be stressed that this is not a formal validation (see, for instance, [18]). For this to be possible the experimental uncertainty is required, and this is not available in [1]. Therefore, this is merely a comparison with experimental data.

5. Systematic Investigation

The authors are mainly interested in 470, 420 and Optimist centerboards, so the variable ranges are chosen according to the rules of each class [2–4] and their respective typical sailing conditions. However, these values are reasonable for other applications of these sections. Table 3 shows the limits for the Reynolds number (based on chord length and typical speed for each boat), thickness, leading edge length and trailing edge length.

Table 3. Ranges of Reynolds numbers, thicknesses, leading edge lengths, trailing edges lengths of 470, 420 and Optimist dinghies.

Boat	Reynolds Number	Thickness (% Chord)	Leading Edge (% Chord)	Trailing Edge (% Chord)
Optimist	280,000	5.52	21.43	21.43
	290,000	7.14	20.69	20.69
420	830,000	3.76	25.30	25.30
	850,000	4.82	24.71	24.71
470	910,000	4.26	18.08	35.49
	1,500,000	7.89	11.70	22.97

Table 4 summarizes the setup of the systematic investigation, to cover as closely as possible all cases for the three sailboats, and considering the time to perform the entire investigation. Three Reynolds numbers are chosen, as well as two sailing conditions, two thicknesses, two leading edge lengths, two trailing edge lengths, five nose radii and five trailing edge angles. The latter are defined in terms of a reference angle A_{REF}, where

$$A_{REF} = \arctan\left(1.5\frac{\mathrm{T}}{\mathrm{TE}}\right) \quad (1)$$

Table 4. Values and codes for the systematic investigation of Parallel-Sided sections.

Reynolds Number	Sailing Condition	Thickness (% Chord)	Leading Edge (% Chord)	Trailing Edge (% Chord)	Nose Radius (% Thickn.)	Trailing Edge Angle [°]
300,000	AoA = 0.0°	T1 = 4%	LE1 = 10%	TE1 = 20%	R1 = 40%	A1 = A_{REF}
900,000	C_L = 0.4	T2 = 8%	LE2 = 20%	TE2 = 40%	R2 = 20%	A2 = $\frac{4}{5}A_{REF}$
1,500,000	-	-	-	-	R3 = 10%	A3 = $\frac{3}{5}A_{REF}$
-	-	-	-	-	R4 = 5%	A4 = $\frac{2}{5}A_{REF}$
-	-	-	-	-	R5 = 2%	A5 = $\frac{1}{5}A_{REF}$

For more details, see Appendix A. With all these variables, a set of 200 shapes is generated, and in total, 1200 cases are investigated, considering the combination of the three Reynolds numbers and the two sailing conditions.

For the upwind sailing condition, the angle of attack is not defined. A target value of lift (C_L = 0.4) is set instead, so the angle of attack is slightly different between the cases. It is the given side force from the sails that should be balanced, and this will be achieved at different leeway angles for the different sections. The authors choose a lift coefficient equal to 0.4 as a target value after conducting a study of typical leeway angles of the 470 and Optimist dinghies using a velocity prediction program (VPP). For 420 and 470, the 0° case may not be relevant, since the centerboard is hoisted while sailing downwind. For the Optimist, the centerboard is usually only partly hoisted during the downwind leg, so the 0° case can be useful for this type of dinghy. Furthermore, the 0° case for this type of sections is of interest in other fields than sailing, where the angle of attack is often 0°.

6. Results

In the following figures, the computed results are presented. To enhance readability, only the best case for each family of thickness (T), leading edge length (LE) and trailing edge length (TE) is represented, since the trend is the same inside each family, and the results are very close. In particular, for 0° angle of attack, the nose radius has a very small effect on the drag, and the same is true for the trailing edge angle at constant lift. By presenting the results in this way, the authors believe that it is

easier to compare the results and draw conclusions. The drag coefficient for the cases with a Reynolds number of 300,000 are averaged over the last 1000 iterations, due to a slightly oscillating solution.

First, the results of all families are presented. Figures 6–8 show the results for the Reynolds numbers 300,000, 900,000 and 1,500,000, respectively. The top left plot in each figure is for the thin sections (4%) at 0° angle of attack, while the top right figure shows the corresponding results for the thick sections (8%). The two lower figures show the results for the C_L = 0.4 case.

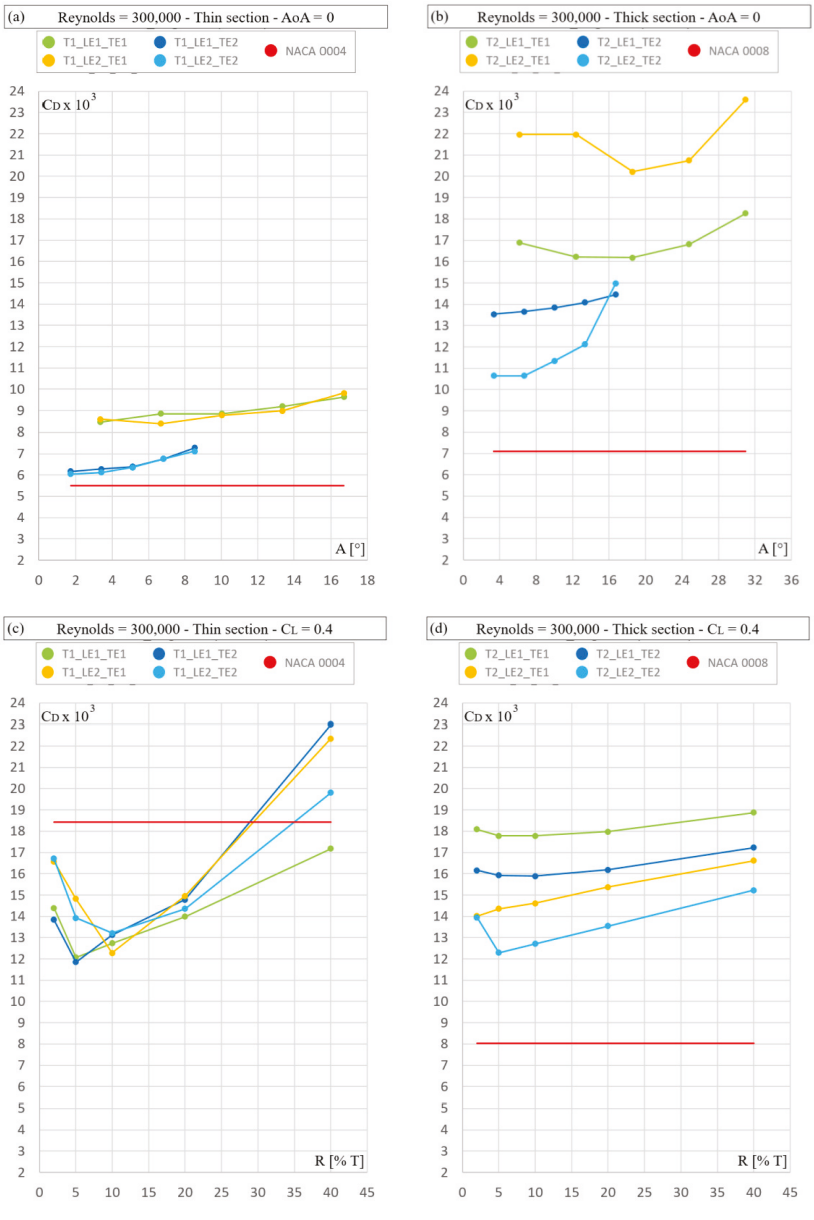

Figure 6. Drag coefficient ($C_D \times 10^3$) for Reynolds number 300,000. Independent variable: trailing edge angle (**a**,**b**); nose radius (**c**,**d**).

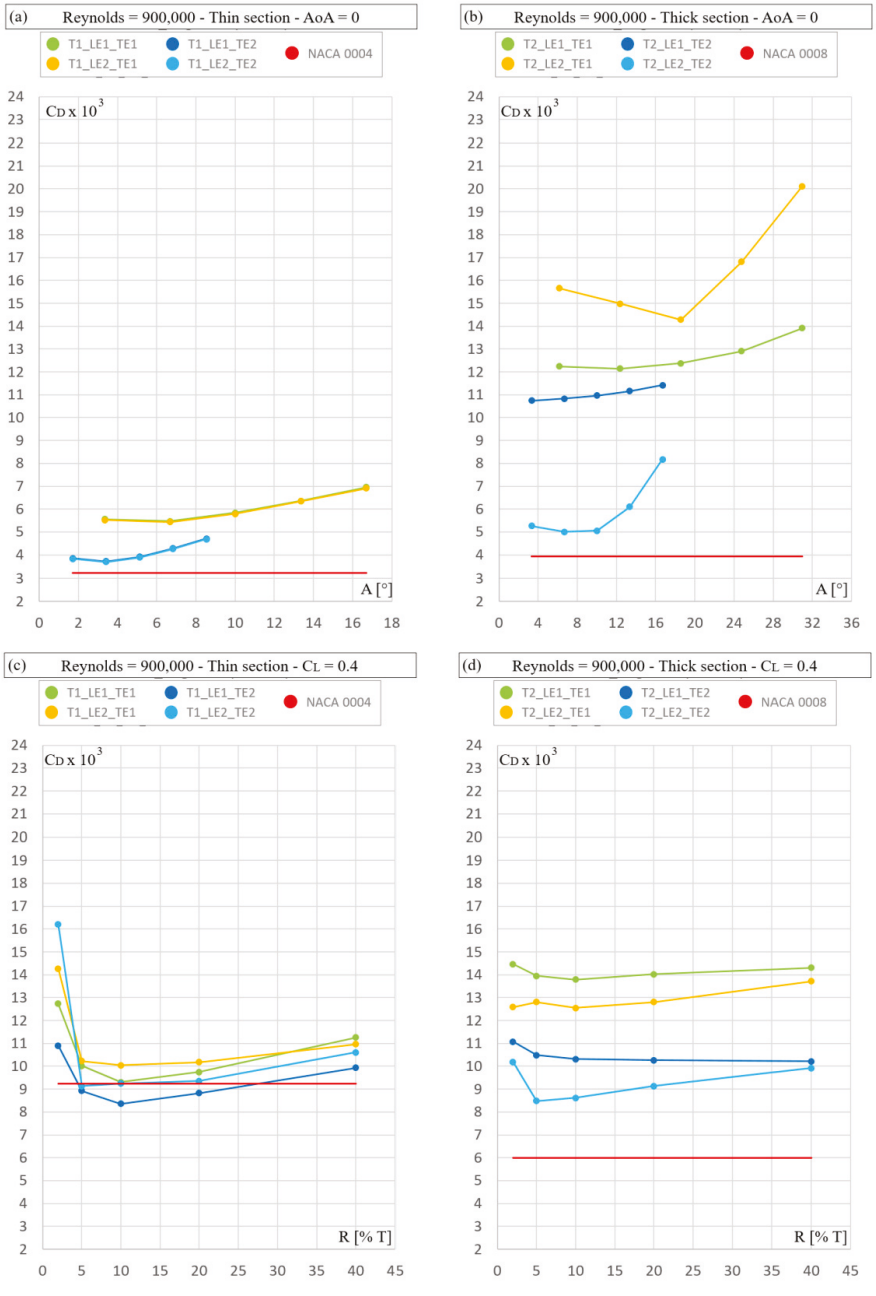

Figure 7. Drag coefficient ($C_D \times 10^3$) for Reynolds number 900,000. Independent variable: trailing edge angle (**a**,**b**); nose radius (**c**,**d**).

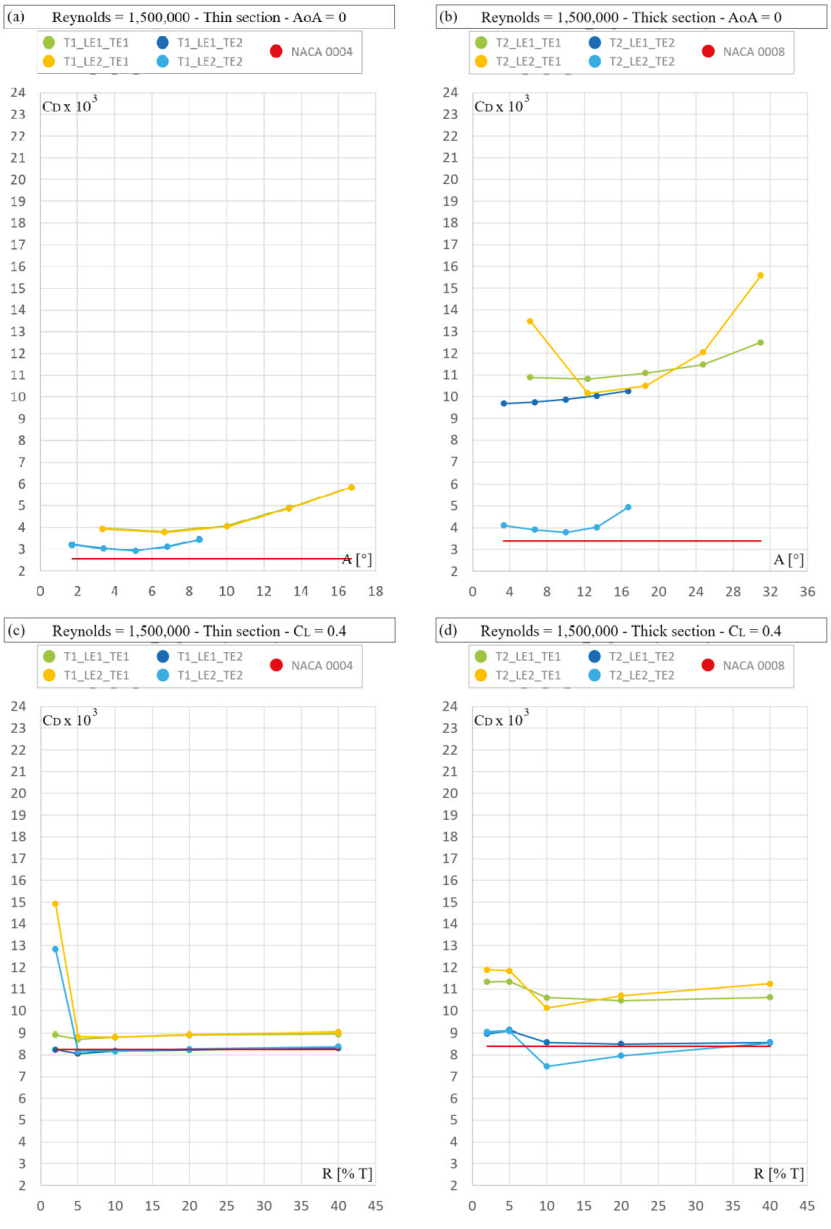

Figure 8. Drag coefficient ($C_D \times 10^3$) for Reynolds number 1,500,000. Independent variable: trailing edge angle (**a**,**b**); nose radius (**c**,**d**).

Having presented the results for all families of sections, the results will now be analyzed and commented on. In Section 6.1 results for zero angle of attack are discussed, while in Section 6.2 the results for $C_L = 0.4$ are considered. In order to explore the physics, field plots of the axial velocity are presented, together with line plots of the pressure or friction variation along the section on the two

sides. To identify regions of separation, the lower limit of the axial velocity is set to zero, such that negative velocities, i.e., separations, are indicated by a white color.

6.1. Zero Angle of Attack

It is obvious from Figures 6–8 that the thinner sections have considerably lower drag than the thick ones at zero angle of attack. A comparison is made in Figure 9, where the thicker profile exhibits separation (white area) at the trailing edge. This causes a reduced pressure in the build-up region between X/L from 0.6 to 0.9. The reduced pressure in this region increases drag, although the pressure is higher at the trailing edge. T2 has a lower pressure also further forward, but this is mostly in the parallel part and has a small effect on the pressure drag.

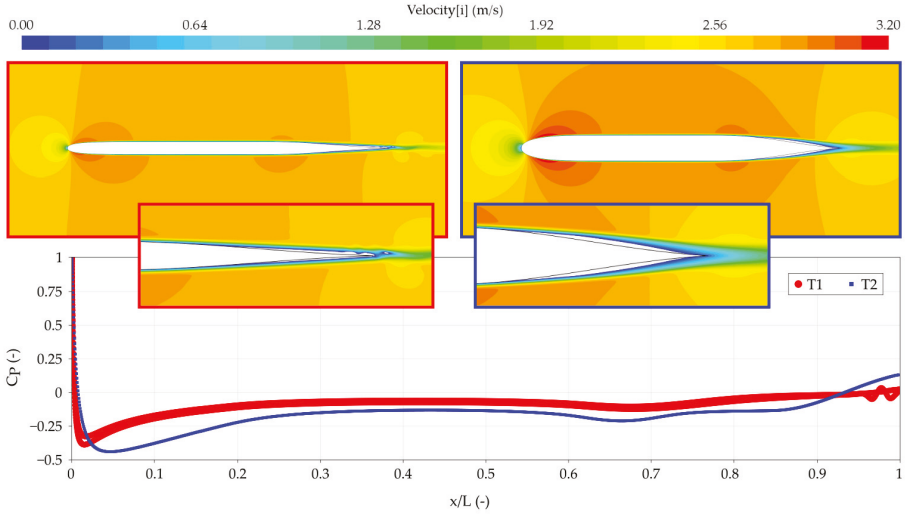

Figure 9. Plots of axial velocity (upper) and pressure distribution (lower) for a thin and a thick section.

As it appears from Figures 6–8, the length of the leading edge is unimportant for thin sections. For thick sections, it is important in some cases. Figure 10 shows that the profile with a short leading edge performs better than the one with the longer leading edge. This is due to the different nature of the boundary layers. As can be seen in the figure, the skin friction coefficient for the short leading edge is much larger than for the other case. This indicates that the flow on the short leading edge section is turbulent, while it is laminar on the other section. The reason for this is that the pressure minimum at the forward shoulder is much lower for the short leading edge, causing a large positive pressure gradient behind the minimum, thus promoting both transition and separation. Although the laminar flow gives less friction, the drag of the section is high, since a larger (unsteady) separation zone is created at the trailing edge of this foil. A laminar boundary layer separates much more easily than a turbulent one, where energy is transferred through the boundary layer due to the stirring effect of the turbulence. Note that the separated region on the short leading edge foil between X/L = 0.1 and 0.2 has negative friction, indicating a small separation bubble in this region. Since this separation is on the parallel part, it does not increase drag. The long leading edge has an unsteady separation, so the figures show instantaneous results.

Figures 6–8 show that the trailing edge should be as long as possible. As can be seen in Figure 11, the short trailing edge has massive separation, while no separation can be seen on the long trailing edge. The separation reduces the pressure from about X/L = 0.7 and backwards, which results in larger drag.

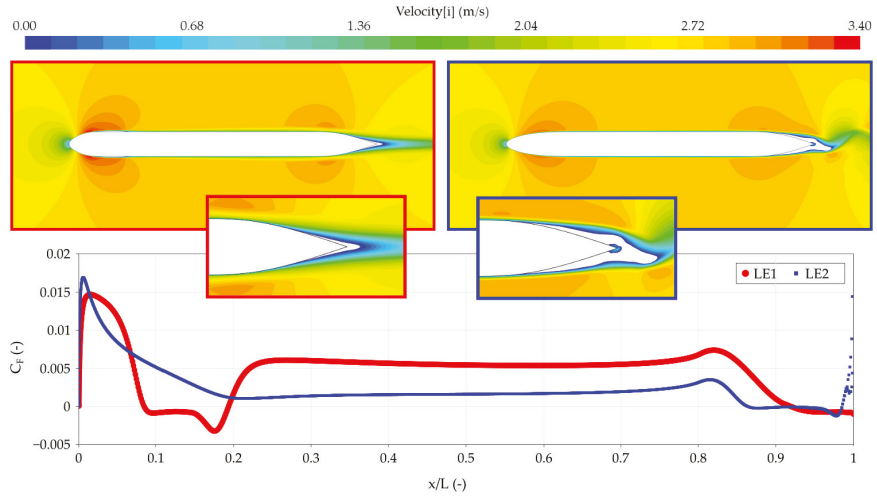

Figure 10. Velocity plot and skin friction coefficient of short leading edge length (**left**) and long leading edge length (**right**).

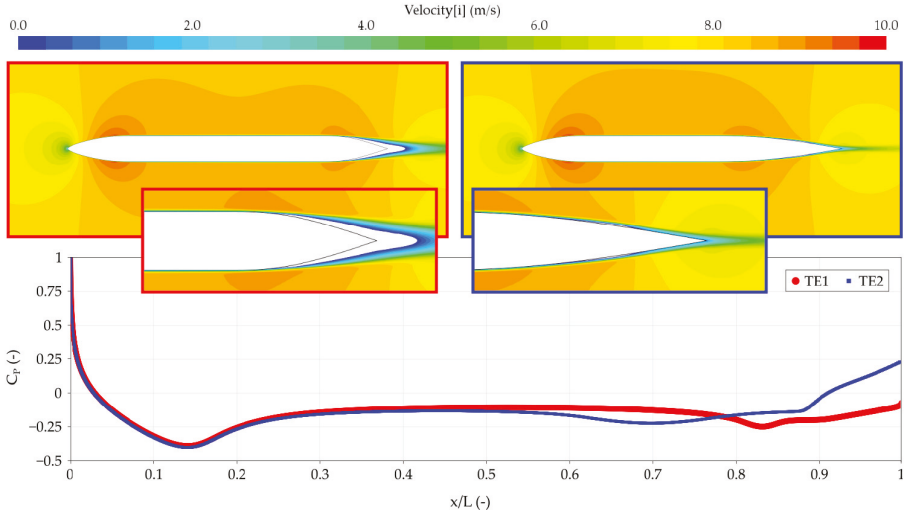

Figure 11. Velocity plot and pressure plot of short trailing edge (**left**) and long trailing edge (**right**) sections.

The nose radius has a very small effect on the drag. An example is given in Figure 12, where the drag for all thin sections with long leading and trailing edges are shown for the intermediate Reynolds number. Plotting drag versus trailing edge angle, it can be seen that the curves for all five nose radii collapse.

The trailing edge angle should be small for the thin sections. For the thick sections, this is also true, however with one exception: the family with a short trailing edge. In this case, the optimum solution is not obtained with the smallest trailing edge angle, but with a medium angle. Figure 13 shows results for three trailing edge angles. The flow for all three cases is laminar over the entire profile, so when it gets close to the trailing edge, it separates. When the angle is large (figure to the

left), there is a large curvature at the aft shoulder which promotes (unsteady) separation, and when the angle is small (figure on the right), the aft end exhibits an inflexion, which causes a large curvature slightly more forward. This again promotes separation. The smallest curvature is obtained for an intermediate angle (middle figure), which has a slightly smaller separated area and a smaller drag. Note that the separation is unsteady, so the plots show results at one time instant.

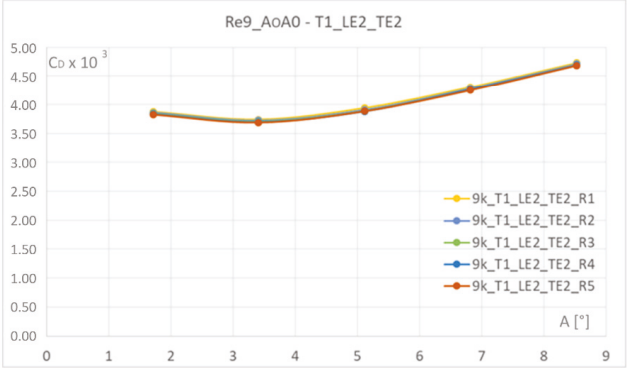

Figure 12. Five different radii are compared. x-axis trailing edge angle, y-axis drag coefficient times 10^3.

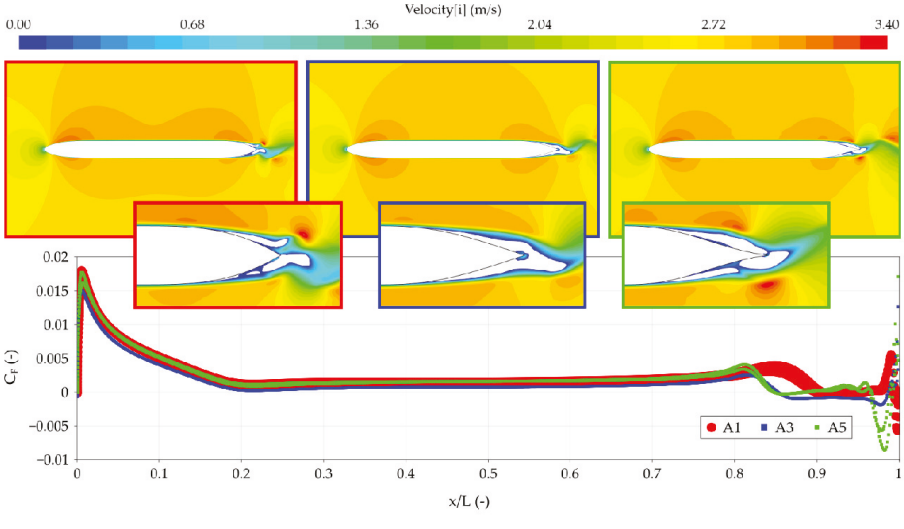

Figure 13. Velocity plot and skin friction coefficient of large (**left**), medium (**center**) and small (**right**) trailing edge angle sections.

The best thin parallel-sided sections have on average 13% higher drag than the four-digit NACA section with the same thickness ratio. For the thick sections, the average drag increase is 30%.

6.2. Lift Coefficient 0.4

For the case with lift, thin and thick sections have surprisingly equal drag. Exceptions are sections with a short trailing edge at medium and high Reynolds numbers where the thick sections have higher drag. As can be seen in Figure 14, the thin section does not exhibit separation, but the thick section

separates at the trailing edge. The separation is on the pressure side of the airfoil; this phenomenon will be explained in more detail below.

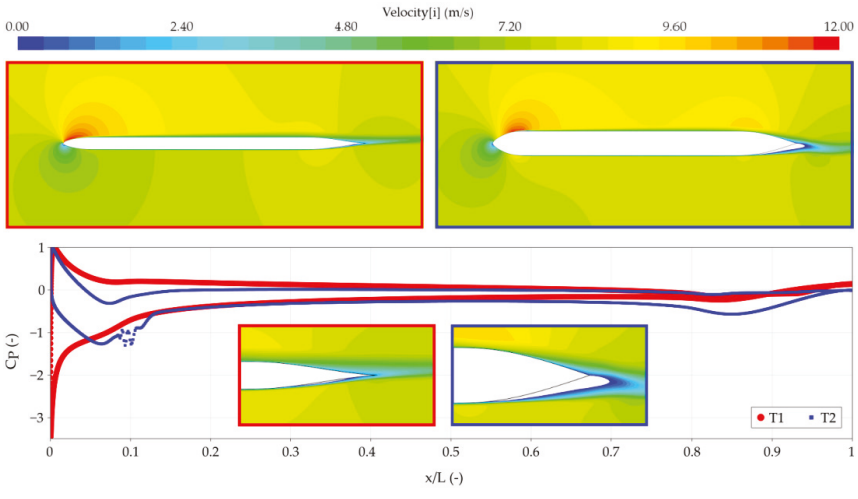

Figure 14. Velocity plot and pressure plot of thin (**left**) and thick (**right**) sections.

Generally, sections with long leading and trailing edges are the best, while sections with short leading and trailing edges are the worst. The performance of other combinations depends on the Reynolds number. As can be seen in Figures 15 and 16, an interesting phenomenon occurs. For the shape with short trailing edge, there is large steady separation on the pressure side of the section. This is due to the laminar flow over the pressure side, as the plot of the friction coefficient shows in Figure 15. On the suction side, the boundary layer is turbulent, and, as explained above, the turbulent boundary layer is much more resistant to separation.

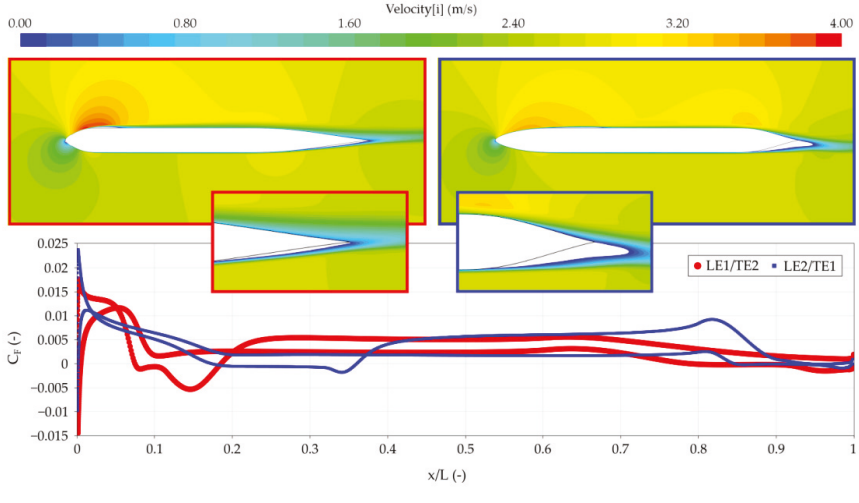

Figure 15. Velocity plot and skin friction coefficient of short leading edge and long trailing edge (**left**) and long leading edge and short trailing edge (**right**) sections.

The asymmetric separation causes an interesting flap effect, as seen in Figure 16 Here the streamlines are shown for the short trailing edge. This asymmetry increases the lift of the section.

The trailing edge angle has a very small effect on the drag, as can be seen in Figure 17, where five different trailing edges are compared.

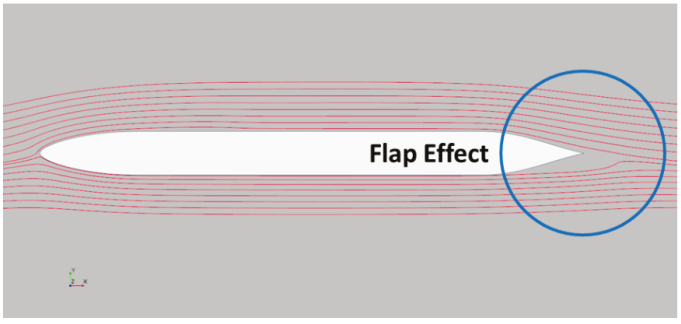

Figure 16. Streamlines of long leading edge and short trailing edge section.

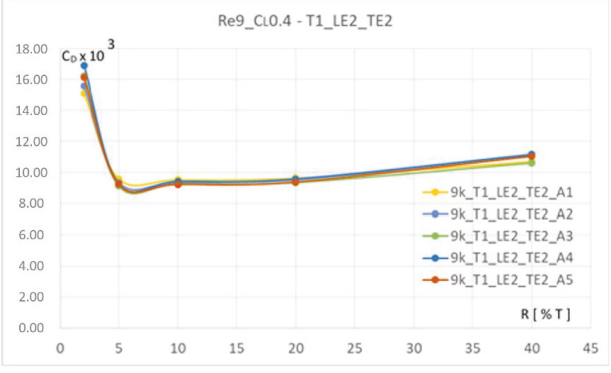

Figure 17. Five different trailing edge angles are compared, *x*-axis nose radius, *y*-axis drag coefficient times 10^3.

Apparently, a rather small (but not too small) leading edge radius is the best for the thin sections. The same is true for the thick sections, however with one exception at high Reynolds number and short leading edge. This result can be related to the different ways the outline of the section approaches the maximum thickness. For the short leading edge, the thickness increases faster, since there is less space to reach the zone with constant thickness. On the other hand, with the long leading edge length, the nose radius gets too small. As can be seen in Figure 18, the section with a long leading edge has a thicker boundary layer, resulting in a larger drag coefficient. The thicker boundary layer is caused by the earlier transition, which is very close to the nose for this section.

The thin parallel-sided sections at the smallest Reynolds number are better than the NACA sections by about 10%. For the intermediate and high Reynolds number, they are about equal. The thick sections have, on average, 35% higher drag than the NACA sections. Especially at low Reynolds number (300,000) and for thin sections, some parallel-sided profiles perform better than NACA0004 profile. The nose radius of the NACA0004 is very close to R4, so this effect cannot be related to the nose radius. One cause of this behavior can be the length of the leading edge, since the two best shapes have the short leading edge length and the NACA profile has the longest leading edge. The main contribution to the drag coefficient for the NACA section is the pressure and not the friction.

These results confirm the conclusion made by Pollok (1987), who affirms "There are many situations where parallel-sided aerofoil sections with leading and trailing edge fairings of limited chord wise extent have advantages over conventional sections."

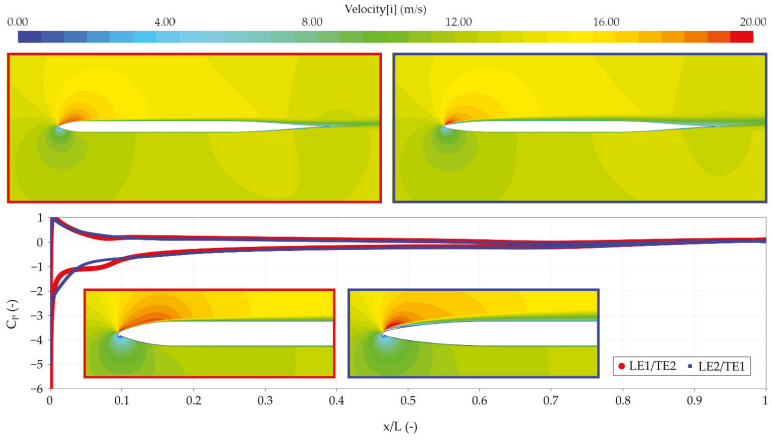

Figure 18. Velocity plot and pressure plot of short leading edge (**left**) and long leading edge (**right**) sections.

7. Conclusions

The objective of the present work has been to develop a series of 2D foil sections with partly parallel sides. Such sections are found on many dinghy centerboards. Starting from 7 design variables, 200 sections and 1200 cases are systematically investigated. Trends are found between different solutions, and the exceptions are explained. Six tables with the best shapes are created to help the designers to choose the optimal profile for a specific application. These tables are found in Appendix B.

The general conclusions from the study may be summarized as follows:

Zero angle of attack:

- The thinner sections have considerably lower drag than the thick ones.
- The length of the leading edge is unimportant for thin sections. For thick sections, it is important in some cases, but not all. The reasons are explained above.
- The trailing edge should be as long as possible.
- The nose radius has a very small effect on the drag.
- The trailing edge angle should be very small for the thin sections. For the thick sections, this is also true, with one exception that is explained above.
- The best thin parallel-sided sections have, on average, 13% higher drag than the four-digit NACA section with the same thickness ratio. For thick sections, the average drag increase is 30%.

Lift coefficient 0.4:

- The thin and thick sections have surprisingly equal drag. Exceptions are sections with a short trailing edge at medium, and high Reynolds numbers where the thick sections have higher drag. This effect is explained above.
- Generally, sections with long leading and trailing edges are the best, while sections with short leading and trailing edges are the worst. The performance of other combinations depends on the Reynolds number.
- The trailing edge angle has a very small effect on the drag.

- A rather small (but not too small) leading edge radius is the best for the thin sections. The same is true for the thick sections. There is however an exception at high Reynolds number and short leading edge.

The thin parallel-sided sections at the smallest Reynolds number are in fact better than the NACA sections by about 10%. For the intermediate and high Reynolds number, they are about equal. The thick sections have on average 35% higher drag than the NACA sections.

Optimizing wing sections using CFD is a difficult task, since it relies on the accurate prediction of two important physical phenomena: transition and separation. The latter depends strongly on the accuracy of the turbulence model. In the text above, we have tried to give motivations for the use of the models adopted, which have been validated in the literature for a very large number of cases, and are recommended by the developers of the software used. A formal validation of the present computations is unfortunately not possible, due to the lack of information about experimental accuracy. Estimates are however made of the numerical uncertainty, which is low, due to the very high grid density.

Author Contributions: The four authors of the paper, A.S., A.P., L.L. and A.M. contributed as follows. Conceptualization, L.L. and A.P.; methodology, L.L., A.P. and A.S.; software, A.P. and A.S.; validation, A.S., L.L. and A.P.; formal analysis, A.S., A.P., L.L. and A.M.; investigation, A.S.; resources, L.L.; data curation, A.S.; writing—original draft preparation, A.S.; writing—review and editing, L.L., A.P. and A.M.; visualization, A.S.; supervision, L.L. and A.M.; project administration, A.S., L.L. and A.M.; funding acquisition, L.L. All authors have read and agreed to the published version of the manuscript.

Funding: This study received funding from the Chalmers University of Technology Foundation for the Strategic Research project Hydro- and Aerodynamics. It was also partly funded by Hugo Hammar's fund for international research in shipping, project number HHS280. The computations were performed on resources at Chalmers Centre for Computational Science and Engineering (C3SE) provided by the Swedish National Infrastructure for Computing (SNIC).

Acknowledgments: The first author gratefully acknowledges the invitation by Chalmers University of Technology and SSPA and the help and contributions by the staff duringhis six months' visiting period as a PhD student of the University of Palermo.

Conflicts of Interest: The authors declare no conflict of interest.

Nomenclature

Symbol	Definition
C_D	Drag Coefficient
C_L	Lift Coefficient
α	Angle of Attack
Hi	Refinement Ratio
U	Numerical Uncertainty
$C(t)$	Parametric Curve
$B(t)$	Bernstein polynomials
$k(t)$	Curvature
w	Weight of a Control Point
T	Thickness
LE	Leading Edge Length
TE	Trailing Edge Length
R	Nose Radius
A	Trailing Edge Angle
A_{REF}	Trailing Edge Angle (Reference)

Appendix A. Parametric Section Design

A rational Bézier curve can be defined [21] as shown in Equation (A1):

$$C(t) = \frac{\sum_{i=0}^{n} w_i B_{i,n}(t) P_i}{\sum_{i=0}^{n} w_i B_{i,n}(t)}, \quad t = 0, \ldots, 1 \tag{A1}$$

where n is the degree of the curve, P_i are the coordinates of $n+1$ control points, w_i are the weights of the control points and $B_{(i,n)}(t)$ are the Bernstein polynomials over the parametric abscissa, t, whose definition is given in Equation (A2):

$$B_{i,n}(t) = \frac{n!}{i!(n-i)!} t^i (1-t)^{n-i}, \quad i = 0, 1, \ldots, n \tag{A2}$$

In the case of third- and fourth-degree curves, Equation (A2) gives:

$\boldsymbol{B_{i,3}(t)}$	$\boldsymbol{B_{i,4}(t)}$
$B_{0,3}(t) = (1-t)^3$	$B_{0,4}(t) = (1-t)^4$
$B_{1,3}(t) = 3\,t\,(1-t)^2$	$B_{1,4}(t) = 4\,t\,(1-t)^3$
$B_{2,3}(t) = 3\,t^2\,(1-t)$	$B_{2,4}(t) = 6\,t^2\,(1-t)^2$
$B_{3,3}(t) = t^3$	$B_{3,4}(t) = 4\,t^3\,(1-t)$
	$B_{4,4}(t) = t^4$

A cubic curve ($n = 3$) is selected to define the shape of the leading edge of the profile. There are two reasons leading to this choice: the needs to assure G2 continuity of the profile between the leading edge and the flat zone, and the control of the curvature at the beginning of the profile. The G2 continuity is obtained by assuring that the two neighboring curves have the same tangent line and also the same center of curvature at their common boundary. The control of the curvature at the beginning of the profile is obtained with the following Equation (A3):

$$k(t_0) = \frac{w_0 w_2}{w_1^2} \frac{n-1}{n} \frac{h}{a^2} \tag{A3}$$

where $k(t_0)$ is the curvature, while h and a are defined in Figure A1.

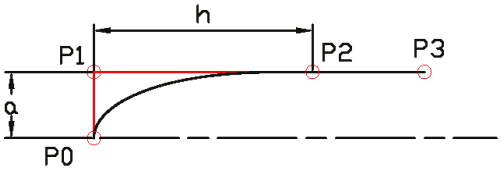

Figure A1. Leading edge designed with a rational cubic Bézier curve.

In this specific case, $k(t_0) = \frac{1}{R}$, $a = y_{P1}$ and $h = y_{P2}$. Equation (A3) can be solved to obtain the correct value of the weight w_1 of the control point P_1, according to Equation (A4).

$$w_1 = \sqrt{\frac{2\,R\,x_{P2}\,w_{P0}\,w_{P2}}{3\,{y_{P2}}^2}} \tag{A4}$$

Table A1 shows the values of the coordinates of each control point of the leading edge and the corresponding weights.

Table A1. Coordinates and weights of leading edge control points.

Leading Edge			
Control Point	**x**	**y**	**Weight**
P0	0	0	1
P1	0	$\frac{T}{2}$	$\sqrt{\frac{2\,R\,x_{P2}\,w_{P0}\,w_{P2}}{3\,{y_{P2}}^2}}$
P2	$\frac{2\,LE}{3}$	$\frac{T}{2}$	1
P3	LE	$\frac{T}{2}$	1

A fourth-degree ($n = 4$) curve is selected to define the shape of the trailing edge of the profile. In the same way as the leading edge, the G2 continuity is assured. A higher degree is needed to control the trailing edge angle at the end of the profile without violating the G2 continuity. The shape of the trailing edge can be seen in Figure A2, while Equation (A5) shows how to properly obtain the value of the trailing edge angle.

Figure A2. Trailing edge designed with a rational Bézier curve.

$$\mathrm{A} = \arctan\left(\frac{y_{P7}}{x_{P8} - x_{P7}}\right) \tag{A5}$$

Table A2 shows the values of the coordinates of each control point of the trailing edge and the corresponding weights.

Table A2. Coordinates and weights of trailing edge control points.

Trailing Edge			
Control Point	**x**	**y**	**Weight**
P4	0	$\frac{\mathrm{T}}{2}$	1
P5	$\frac{x_{P6}}{2}$	$\frac{\mathrm{T}}{2}$	1
P6	$\frac{\mathrm{TE}}{2.5}$	$\frac{\mathrm{T}}{2}$	1
P7	$\frac{2\,\mathrm{TE}}{3}$	$(x_{P8} - x_{P7})\tan(A)$	1
P8	TE	0	1

In Figure A3, the whole flat section is shown. It is obtained by translating the values of the coordinate points of the trailing edge by a quantity equal to the leading edge length plus the length of the flat zone of the profile.

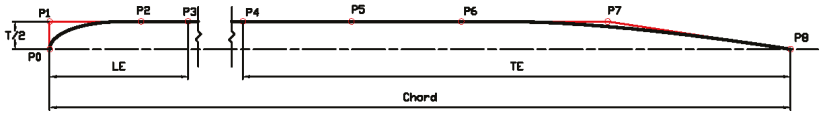

Figure A3. Flat section designed with three rational Bézier curves.

A reference value for the trailing edge angle is A_{REF}, defined by Equation (A5) for $y_{P7} = \frac{\mathrm{T}}{2}$, i.e., it may be computed as

$$A_{REF} = \arctan\left(\frac{\frac{\mathrm{T}}{2}}{\mathrm{TE} - \frac{2\mathrm{TE}}{3}}\right) = \arctan\left(1.5\frac{\mathrm{T}}{\mathrm{TE}}\right) \tag{A6}$$

To define the profile of a parallel-sided section, rational Bézier curves are defined and linked to the geometrical variables of the problem: thickness (T), leading edge length (LE), trailing edge length (TE), nose radius (R) and trailing edge angle (A). T, LE, TE are expressed in percent of the chord, and R is expressed in percent of the thickness. A is expressed as a fraction of A_{REF}. The shape of the profile is completely parameterized, so it is possible to automatically generate all 200 shapes needed for the present study. Since this technique is very versatile, it can easily be implemented in different cases from the one presented here. A code, developed in Excel VBA, starts from the values of the design variables, processes this information to define the geometry of each curve, and saves the data for each of the sections in a neutral CAD format (e.g., IGES, CSV). Figure A4 shows the geometry of one section. As can be seen, it has been divided into three main zones: leading edge, flat zone, trailing edge. The length of each zone is related to the class rules of each dinghy. The red dots represent the control points of the curve, while the blue ones represent the points of the curves whose internal spacing can be modified to better follow the shape.

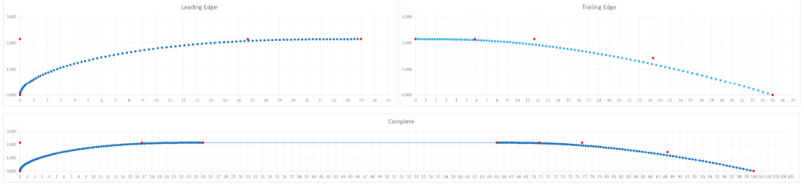

Figure A4. An example of the shape of a Parallel-Sided section.

Appendix B. Selection of the Best Shape

Tables A3–A5 show the best shapes for each Reynolds number. These can be useful for designers that can enter the desired values of thickness (T), leading edge length (LE) and trailing edge length (TE) and see what radius (R) and trailing edge angle (A) to use for minimizing the drag coefficient. Note that T, LE, TE are given in percent of the chord length, R is expressed in percent of the thickness and A as a fraction of A_{REF}. If there are many possibilities, the tables can be useful to compare all the possible solutions and design the best one for the specific application. The best LE, TE, R and A combination for each combination of thickness, angle of attack and Reynolds number is given in bold.

Table A3. Best shapes for Reynolds number 300,000.

Re 300,000 − AoA = 0.0°						**Re 300,000 − CL = 0.4**					
T	**LE**	**TE**	**R**	**A**	$\mathbf{C_D \times 10^3}$	**T**	**LE**	**TE**	**R**	**A**	$\mathbf{C_D \times 10^3}$
4	10	20	20	$\frac{1}{5}A_{REF}$	8.46	4	10	20	5	$\frac{4}{5}A_{REF}$	12.06
4	10	40	20	$\frac{1}{5}A_{REF}$	6.18	**4**	**10**	**40**	**5**	$\boldsymbol{\frac{1}{5}A_{REF}}$	**11.85**
4	20	20	2	$\frac{2}{5}A_{REF}$	8.38	4	20	20	10	$\frac{1}{5}A_{REF}$	12.28
4	**20**	**40**	**10**	$\boldsymbol{\frac{1}{5}A_{REF}}$	**6.05**	4	20	40	10	A_{REF}	13.21
8	10	20	20	$\frac{3}{5}A_{REF}$	16.18	8	10	20	10	$\frac{2}{5}A_{REF}$	17.78
8	**10**	**40**	**20**	$\boldsymbol{\frac{1}{5}A_{REF}}$	**13.52**	8	10	40	10	$\frac{4}{5}A_{REF}$	15.89
8	20	20	10	$\frac{3}{5}A_{REF}$	20.21	8	20	20	2	$\frac{2}{5}A_{REF}$	14.01
8	20	40	2	$\frac{1}{5}A_{REF}$	10.64	**8**	**20**	**40**	**5**	$\boldsymbol{\frac{1}{5}A_{REF}}$	**12.29**

Table A4. Best shapes for Reynolds number 900,000.

Re 900,000 − AoA = 0.0°						**Re 900,000 − CL = 0.4**					
T	**LE**	**TE**	**R**	**A**	$\mathbf{C_D \times 10^3}$	**T**	**LE**	**TE**	**R**	**A**	$\mathbf{C_D \times 10^3}$
4	10	20	5	$\frac{2}{5}A_{REF}$	5.47	4	10	20	10	$\frac{1}{5}A_{REF}$	9.30
4	10	40	5	$\frac{2}{5}A_{REF}$	3.71	**4**	**10**	**40**	**10**	$\boldsymbol{\frac{1}{5}A_{REF}}$	**8.36**
4	20	20	2	$\frac{2}{5}A_{REF}$	5.43	4	20	20	10	$\frac{4}{5}A_{REF}$	10.05
4	**20**	**40**	**2**	$\boldsymbol{\frac{2}{5}A_{REF}}$	**3.69**	4	20	40	5	$\frac{3}{5}A_{REF}$	9.13
8	10	20	40	$\frac{2}{5}A_{REF}$	12.14	8	10	20	10	$\frac{3}{5}A_{REF}$	13.79
8	10	40	40	$\frac{1}{5}A_{REF}$	10.74	8	10	40	40	$\frac{1}{5}A_{REF}$	10.22
8	20	20	20	$\frac{3}{5}A_{REF}$	14.28	8	20	20	10	$\frac{3}{5}A_{REF}$	12.55
8	**20**	**40**	**2**	$\boldsymbol{\frac{2}{5}A_{REF}}$	**5.01**	**8**	**20**	**40**	**5**	$\boldsymbol{\frac{2}{5}A_{REF}}$	**8.48**

Table A5. Best shapes for Reynolds number 1,500,000.

Re 1,500,000 − AoA = 0.0°						**Re 1,500,000 − CL = 0.4**					
T	**LE**	**TE**	**R**	**A**	$\mathbf{C_D \times 10^3}$	**T**	**LE**	**TE**	**R**	**A**	$\mathbf{C_D \times 10^3}$
4	10	20	5	$\frac{2}{5}A_{REF}$	3.80	4	10	20	5	$\frac{1}{5}A_{REF}$	8.71
4	10	40	2	$\frac{3}{5}A_{REF}$	2.94	**4**	**10**	**40**	**5**	$\boldsymbol{\frac{1}{5}A_{REF}}$	**8.06**
4	20	20	10	$\frac{2}{5}A_{REF}$	3.78	4	20	20	10	$\frac{1}{5}A_{REF}$	8.83
4	**20**	**40**	**2**	$\boldsymbol{\frac{3}{5}A_{REF}}$	**2.93**	4	20	40	10	$\frac{1}{5}A_{REF}$	8.17
8	10	20	40	$\frac{2}{5}A_{REF}$	10.81	8	10	20	20	$\frac{2}{5}A_{REF}$	10.47
8	10	40	40	$\frac{1}{5}A_{REF}$	9.68	8	10	40	20	$\frac{2}{5}A_{REF}$	8.50
8	20	20	20	$\frac{2}{5}A_{REF}$	10.15	8	20	20	10	$\frac{1}{5}A_{REF}$	10.12
8	**20**	**40**	**2**	$\boldsymbol{\frac{3}{5}A_{REF}}$	**3.79**	**8**	**20**	**40**	**10**	$\boldsymbol{\frac{2}{5}A_{REF}}$	**7.48**

With the information presented in the tables, it is possible to find a good set of parameters for a given dinghy. For example, as seen in Table 3, the Optimist centerboard has a Reynolds number near 300,000, so Table A3 should be used. The maximum trailing edge length is 21.43% of the chord, so TE2 cannot be used. Considering the upwind condition ($C_L = 0.4$), the best computed configuration is: T = 4, LE = 10, TE = 20, R = 5, A = $\frac{4}{5}A_{REF}$. For the downwind condition (AoA = 0.0), the best computed configuration is: T = 4, LE = 20, TE = 20, R = 2, A = $\frac{2}{5}A_{REF}$. It is important to consider the fact that, during the downwind leg of a regatta, it is common practice to partially hoist the centreboard in order to reduce the wetted surface, so the designer should give more importance to the upwind configuration.

References

1. Abbott, I.H.; von Doenhoff, A.E. *Theory of Wing Sections*; Dover Publications INC.: New York, NY, USA, 1959.
2. World Sailing Class Association. *International 470 Class Rules*; World Sailing Class Association: Paris, France, 2017.
3. World Sailing Class Association. *International 420 Class Rules*; World Sailing Class Association: Paris, France, 2017.
4. International Optimist Dinghy Association. *International Optimist Class Rules*; International Optimist Dinghy Association: Paris, France, 2018.
5. Pollok, N.A. *Note on the Aerodynamic Design of Thin Parallel-Sided Aerofoil Sections*; Aerodynamics NACA Technical Memorandum 388; Aeronautical Research Labs: Melbourne, Australia, 1987.
6. Drela, M. XFOIL Subsonic Airfoil System. Available online: https://web.mit.edu/drela/Public/web/xfoil/ (accessed on 31 May 2019).
7. Larsson, L.; Eliasson, R.E.; Orych, M. *Principles of Yacht Design*; Adlard Coles Nautical Ltd.: London, UK, 2014.
8. Larsson, L.; Raven, H. *Ship Resistance and Flow*; Principles of Naval Architecture Series; SNAME: Hoboken, NJ, USA, 2010.
9. Siemens. *Simcenter STAR-CCM+ Documentation, Version 2020.1*, 2020.
10. Menter, F.R. Two-equation eddy-viscosity turbulence models for engineering applications. *AIAA J.* **1994**, *32*, 1598–1605. [CrossRef]
11. Larsson, L.; Stern, F.; Visonneau, M. *Numerical Ship Hydrodynamics—An Assessment of the Gothenburg 2010 Workshop*; Springer: Doordrecht, Germany, 2014.
12. Hino, T.; Stern, F.; Larsson, L.; Visonneau, M.; Hirata, N.; Kim, J. *Numerical Hydrodynamics—An Assessment of the Tokyo 2015 Workshop*; Springer: Cham, Switzerland, 2020.
13. Marvin, J.G. Book review turbulence modeling for CFD. *AIAA J.* **1994**, *32*, 1339. [CrossRef]
14. Menter, F.R.; Langtry, R.B.; Likki, S.R.; Suzen, Y.B.; Huang, P.G.; Völker, S.A. Correlation-based transition model using local variables—Part I: Model formulation. *J. Turbomach.* **2006**, *128*, 413–422. [CrossRef]
15. Menter, F.R.; Smirnov, P.E.; Liu, T.; Avancha, R. A one-equation local correlation-based transition model. *Flow Turbul. Combust.* **2015**, *95*, 583–619. [CrossRef]
16. Von Doenhoff, A.E.; Albert, E.; Abbott, F.T., Jr. *The Langley Two-Dimensional Low-Turbulence Pressure Tunnel*; NACA TN No. 1283; NASA Langley Research Center: Hampton, VA, USA, 1947.
17. Remmlinger, U. *The Factors that Trigger the Transition to Turbulent Flow on the Keel of a Sailing Yacht*, 2013; unpublished.
18. ITTC. *Uncertainty Analysis in CFD Verification and Validation Methodology and Procedures*, International Towing Tank Conference. 2017.
19. Xing, T.; Stern, F. Closure to Discussion of 'Factors of Safety for Richardson Extrapolation'. *ASME J. Fluids Eng.* **2011**, *133*, 115502. [CrossRef]
20. Eça, L.; Hoekstra, M. A procedure for the estimation of the numerical uncertainty of CFD calculations based on grid refinement studies. *J. Comput. Phys.* **2014**, *262*, 104–130. [CrossRef]
21. Sederberg, T.W. *Computer Aided Geometric Design; Computer Aided Geometric Design Course Notes*; BYU Scholars Archive, 2012.

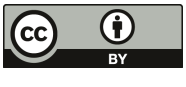

Journal of
Marine Science and Engineering

MDPI

Article

Numerical Simulation of the Ship Resistance of KCS in Different Water Depths for Model-Scale and Full-Scale

Dakui Feng, Bin Ye *, Zhiguo Zhang and Xianzhou Wang

Key Laboratory of Ship and Ocean Hydrodynamics of Hubei Province, School of Naval Architecture & Ocean Engineering, Huazhong University of Science and Technology, Wuhan 430074, China; feng_dk@hust.edu.cn (D.F.); zzg@hust.edu.cn (Z.Z.); wqzwn@126.com (X.W.)
* Correspondence: binye@hust.edu.cn

Received: 27 August 2020; Accepted: 23 September 2020; Published: 26 September 2020

Abstract: Estimating ship resistance accurately in different water depths is crucial to design a resistance-optimized hull form and to estimate the minimum required power. This paper presents a validation of a new procedure used for resistance correction of different water depths proposed by Raven, and it presents the numerical simulations of a Kriso container ship (KCS) for different water depth/draught ratios. Model-scale and full-scale ship resistances were predicted using in-house computational fluid dynamics (CFD) code: HUST-Ship. Firstly, the mathematical model is established and the numerical uncertainties are analyzed to ensure the reliability of the subsequent calculations. Secondly, resistances of different water depth/draught ratios are calculated for a KCS scaled model and a full-scale KCS. The simulation results show a similar trend for the change of model-scale and full-scale resistance in different water depths. Finally, the correction procedure proposed by Raven is briefly introduced, and the CFD resistance simulation results of different water depth/draught ratios are compared with the results estimated using the Raven method. Generally, the reliability of the HUST-Ship solver used for predicting ship resistance is proved, and the practicability of the Raven method is discussed.

Keywords: restricted channel; resistance correction; CFD

1. Introduction

The shallow-water effect refers to the situation that the hydrodynamic performance of a ship clearly changes when the water depth is less than a certain critical value. For a channel that produces the shallow water effect, we divide it into two categories: (1) one is the channel that only considers the limited water depth and its effect on the hydrodynamic performance of the ship, which is called the shallow water channel; and (2) the other is the channel in which both the water depth and the width are limited, causing an effect on the hydrodynamic performance of the ship, which is called the restricted channel. The hydrodynamic characteristics of ships in navigation will change and differ significantly when encountering restricted channels versus shallow water channels. Generally, the effects of shallow water can be summarized into the following three aspects: (1) the change of attitude manifested as the change of trim and sinkage; (2) the increase of ship resistance; and (3) worse maneuverability of the ship. For some high-speed vessels, the water depth needs to be rather deep to avoid the influence of shallow water, which cannot always be guaranteed. Especially in recent years, the shallow-water effect of vessels becomes more and more evident with the increase in tonnage of ships. The obvious sinkage of vessels in shallow water is caused by many bottom touching accidents, which makes it difficult for the safe navigation of vessels encountering shallow-water channels. In addition, the obvious increase of ship resistance in shallow water leads to a worse speed–power

characteristic, which directly affects the operational efficiency of the vessel. An accurate prediction of ship resistance in shallow or confined water is crucial. Model tests are the most common way to predict the resistance of a ship, and the resistance of the full-scale ship can be obtained utilizing extrapolation. Even though much practice has proved the reliability of the extrapolation approach, the Reynolds number similarity between the ship model and the full-scale ship cannot be achieved, which results in significant differences between the model-scale and full-scale ship flow. The ITTC-57 correlation line [1] used to build a relationship between the resistance of a scaled model and the full-scale ship may not be accurate in shallow water. Zeng et al. [2] mentioned in their paper "This is probably due to the backflow and/or a different wetted surface". Raven [3] also suggested considering the scale effect in the extrapolation. The rapid development of computational performance and numerical methods promotes the development of computational fluid dynamics (CFD) [4], and the Unsteady Reynolds Average Navier-Stokes equation (URANS) CFD solver is becoming another practical tool used for predicting the hydrodynamic characteristics of ships. In addition to saving time and money, another advantage of using a CFD solver is that it is easier to obtain the local flow characteristics. URANS simulations were conducted for a KCS [5]; the effective power and the increase of resistance in a series of designed head waves are predicted. In addition, the effect of speed loss on the reduction of effective power is explained. Yang et al. [6] presented a study on the air cavity under a stepped planing hull based on the finite volume method (FVM), and a mesh convergence study was conducted to ensure the accuracy of the simulation. Cucinotta et al. [7,8] analyzed the performance of a multi stepped air cavity planing hull using URANS CFD code. Duy et al. [9] investigated the stern flow field for several transom configurations of a KCS using a viscous CFD solver. Jachowski et al. [10] predicted the squat of a KCS scaled model in shallow water using the CFD method; the results show quite good agreement with the empirical method of Hooft [11]. Numerical prediction of the resistance of a barge ship with different calculation velocities at different water depth-to-ship draft ratios (T/H) was conducted [12]. It can be seen in the study that the increase of resistance becomes increasingly obvious with the decrease of water depth and the increase of velocity, which means that the increase of resistance is related to both velocity and water depth. JI et al. [13] conducted a 3D numerical simulation to research the relationship of the sediment movement induced by the compounding effects of ship-generated waves, water flow due to ship propellers, and the influence of ship and channel characteristics. Linde et al. [14] proposed a 3D hydrodynamic numerical model to predict ship resistance and sinkage of an inland ship in restricted waterways; the results showed that the ship resistance is more sensitive to water depth than channel width. Du et al. [15] studied inland vessels in the fully-confined waterway, and the characteristics of resistance and waves were analyzed. CFD simulations of the pure sway tests in a shallow water towing tank were conducted for the DTC container ship model using URANS solver [16]. From the study, the ability of URANS CFD solver to simulate the pure sway tests in a shallow water towing tank was proved by comparing with the test data. Researchers also conducted the maneuvering tests of a scaled ship model with different water depths and speeds [17], the results show that the shallow water effect has an adverse effect on ship maneuverability, which is manifested by the increase of turning diameter and the decrease of course stability. Simulations of straightforward, turning and zig-zag motions for a cargo ship were carried out [18]; as the depth–draft ratio decreases, the ship's resistance increases and the maneuverability becomes worse.

Furthermore, some researchers proposed methods for resistance correction in different water depths. The earliest method that can be found for correcting shallow water resistance was proposed by Schlichting [19]. A further method of Lackenby [20] was proposed by the reanalysis of Schlichting's method, which was recommended by the International Towing Tank Conference in 2014 [21]. Methods proposed at that time was based on less experimental data due to limited resources. In recent years, with the development of numerical methods and experimental technology, researchers derived some new methods based on numerical calculations and experimental data. Jiang introduced a mean effective speed, which can be calculated by the mean sinkage, ship speed, and water depth [22]. In his study, Jiang found that the model resistance is almost a unit function of the effective speed and independent

of the water depth. Raven [23] proposed a new method to correct the resistance in shallow water after theoretical analysis and numerical calculations, which was recommended by the ITTC in 2017 [24].

For the great importance of estimating ship resistance in different water depths, it is significant to predict the hydrodynamic characteristics of a ship in different water depths. The existing relevant literature mainly focuses on the very shallow water; most of their water depths/draft ratios are less than 2. However, the limited water depths of a larger value play a very important role in reality. This paper studied the influence of water depth on ship resistance; several large limited water depths were chosen to conduct the towed resistance simulations for a Kriso container ship (KCS). Resistance and attitude in different water depths for the scaled model and the full-scale KCS were calculated. Before performing the calculation at different water depths, analysis of numerical uncertainties was carried out. For model scale, the sensitivity of grid spacing from the bottom of the ship to the tank bottom was also studied. Numerical tanks with large width were established to ignore the influence of limited width. The chosen water depths were slightly larger to match the constraints of Raven's method. The in-house CFD solver HUST-Ship was employed to carry out the calculations. The simulation results were compared with the predicted results of Raven's model.

2. Mathematical Model

2.1. Governing Equations and Turbulence Model

The in-house CFD code HUST-Ship, based on the finite difference method (FDM), is employed to solve the unsteady incompressible RANS equations coupled with the continuity equation:

$$\frac{\partial u_i}{\partial x_i} = 0, \quad (i = 1, 2, 3) \tag{1}$$

$$\frac{\partial u_i}{\partial t} + u_j \frac{\partial u_i}{\partial x_j} + \frac{\partial \hat{p}}{\partial x_i} - \frac{1}{R_e} \frac{\partial^2 u_i}{\partial x_j{}^2} - \frac{\partial}{\partial x_j}\left(-\overline{u_i{}' u_j{}'}\right) = 0, \quad (i, j = 1, 2, 3) \tag{2}$$

where $\overline{u_i{}' u_j{}'}$ is the Reynolds stress with turbulent pulsation; $u_i{}'$ is the fluctuating velocity, $\hat{p} = \left(\frac{p - p_\infty}{\rho U_0{}^2} + \frac{z}{F_r{}^2}\right)$ is the dynamic pressure coefficient, $\overline{u_i{}' u_j{}'}$ is Reynolds stress tensor, and R_e is the Reynolds number.

The Froude number and Reynolds number are defined as:

$$F_r = \frac{u_0}{\sqrt{g L_{pp}}}, \; R_e = \frac{u_0 L_{pp}}{\nu} \tag{3}$$

where ν is the fluid viscosity coefficient, g is the acceleration of gravity, and u_0 and L_{pp} are the ship service speed and the length between perpendiculars, respectively.

The turbulent equation uses an SST (shear–stress transport) equation turbulence model to close the governing equation. The equations for turbulent flow energy k and turbulent dissipation rate ω are:

$$\frac{\partial}{\partial t}(\rho k) + \frac{\partial}{\partial x_j}(\rho k u_i) = \frac{\partial}{\partial x_j}\left(\Gamma_k \frac{\partial k}{\partial x_j}\right) + G_k - Y_k + S_k \tag{4}$$

$$\frac{\partial}{\partial t}(\rho \omega) + \frac{\partial}{\partial x_j}(\rho \omega u_i) = \frac{\partial}{\partial x_j}\left(\Gamma_\omega \frac{\partial k}{\partial x_j}\right) + G_\omega - Y_\omega + S_\omega + D_k \tag{5}$$

where Γ_k and Γ_ω are the diffusion ratios of k and ω, respectively; Y_k and Y_ω are the turbulent diffusion terms for k and ω, respectively; G_k is the turbulent kinetic energy generated by the average velocity gradient; G_ω is the production term of the ω equation; and S_k and S_ω are the custom source terms for the k and ω equations respectively.

2.2. Coordinate System and 6-DOF Equations

In the process of the towing simulation, the attitude (pitch and heave) of a KCS always changes with the pressure distribution on the hull surface, hence the need for the 6-DOF equations [25].

The equations involve a time item; therefore, the unsteady RANS equation was solved with the 6-DOF system integrated into the solution program. Figure 1 shows the coordinate system of the HUST-Ship program. The 6-DOF equations can be written as:

$$m\left[\dot{u} - vr + wq\right] = X \tag{6}$$

$$m\left[\dot{v} - wp + ur\right] = Y \tag{7}$$

$$m\left[\dot{w} - uq + vp\right] = Z \tag{8}$$

$$I_x\dot{p} + \left[I_z - I_y\right]qr = K \tag{9}$$

$$I_y\dot{q} + [I_x - I_z]rp = M \tag{10}$$

$$I_z\dot{r} + \left[I_y - I_x\right]pq = N \tag{11}$$

in which, I_x, I_y and I_z are the components of moment of inertia with respect to the gravity center; X, Y, Z and K, M, and N are the components of external forces and moments acting on the hull, respectively. The ship position is described in an earth fixed coordinate system with X pointing south, Y pointing east, and Z pointing upward. The origin of the ship local coordinate system is set at the intersection of the design waterline and the bow. The velocities for 6-DOF motions (u, v, w, p, q, r) are reported in a ship local coordinate system with the x-axis positive toward stern, the y-axis positive toward starboard and the z-axis positive upward. The 6-DOF motions of the ship are reported at the center of gravity.

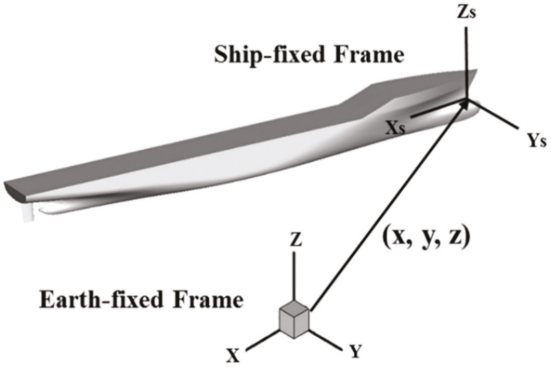

Figure 1. The coordinate system of HUST-Ship.

To obtain the trim angle and sinkage of a KCS, only 2-DOF motion related to pitching and heaving are solved in this paper.

2.3. Level-Set Method

HUST-Ship can capture the change of free surface based on the single-phase level-set [26] method. The level-set method is a general calculation method for tracking interface motion, which was widely used in the field of numerical simulation; the free surface was thought of as an interface. The term φ is the distance from a point of the field to the free surface. It is always the case that φ = 0 represents all points on the position of the free surface, a positive value of φ represents a particle in air and a negative value represents a point in water. Compared with the classical multi-phase level-set method and the volume of fluid (VOF) method [27], the discrepancy of single-phase level-set method is very small as

it ignores the effects of air since the influence of air on free-surface ships is very small. The level-set function [28] is:

$$\frac{\partial \varphi}{\partial t} + V\nabla\varphi = 0 \tag{12}$$

where V is the vector of the velocity within the domain and only the flow of water would be solved in the area of $\varphi \leq 0$. The position of the free surface ($\varphi = 0$) can be obtained using interpolation. The boundary condition for the velocity at the interface can be defined as:

$$\nabla V \cdot n_j = 0 \tag{13}$$

in which n_j is the normal vector and can be defined as:

$$n_j = \frac{\frac{\partial \varphi}{\partial x_i}}{\left|\frac{\partial \varphi}{\partial x_i}\right|} \tag{14}$$

The main advantage of the level-set method is that the quality of the grid is stable and easy to control.

2.4. Wall Function

For the calculations of full-scale vessels, the high Reynolds number led to a need for a smaller boundary layer thickness, which increased the grid quantity. Therefore, a wall function is introduced to deal with the near-wall situation, and a multi-layer wall function of a two-point model is adopted, wherein the velocity of the first node far away from the wall can be obtained from the following equation:

$$\frac{U}{u_\tau} = lny^+ + B - \Delta B \tag{15}$$

where $u_\tau = \sqrt{\frac{\Gamma_\omega}{\rho}}$ is the tangential velocity; Γ_ω is the wall shear stress; and $y^+ = \frac{u_\tau y}{\nu}$ is the dimensionless wall distance. The constant values are $\kappa = 0.41$ and $B = 5.1$; ΔB is a correction term considering wall friction and thinning of the logarithmic layer, which is defined as:

$$\Delta B = \kappa^{-1} \ln(1 + \varepsilon^+) - 3.5 \tag{16}$$

where $\varepsilon^+ = \frac{u_\tau \varepsilon}{\nu}$ is dimensionless surface roughness and ε is the surface roughness. For full-scale calculations, the Tokyo 2005 workshop carried out the model-scale self-propulsion computations of the KCS using the dimensionless skin friction correction factor $SFC^* = 1.3294 \times 10^{-3}$, from which the value of the surface roughness ε for the KCS scaled model can be derived to be 32 μm according to the literature [29], while ε=0 is assumed for model-scale calculations.

The value of y^+ is controlled by giving the first wall thickness of the boundary layer Δs as [30]:

$$\Delta s = 8.6 y^+ L R_e^{-(\frac{13}{14})} \tag{17}$$

in which, L is the input length of the ship, for the HUST Ship solver, all input parameters are nondimensionalized by the characteristic length L_{pp} and the service ship speed u_0, so the input length of the ship is 1. In this study, the target values of the wall y^+ are 1 and 30 for model scale and full scale respectively.

2.5. Overset Grid Technology

The overall flow field is usually divided into a system of grids which overset one another by one or more grid cells. As shown in Figure 2, the points of mesh 1 that fall into the solid surface of mesh 2 are marked as hole points which do not participate in the calculation of the flow field. The points adjacent to the hole points in grid 1 are hole boundary points. These points accept the flow field information

transmitted from mesh 2 through interpolation. Correspondingly, the outer boundary points of mesh 2 would also receive the flow field information transmitted from mesh 1 through interpolation, which is obtained by the trilinear interpolation method. The area between the hole boundary point of mesh 1 and the interpolation point of the mesh 2 outer boundary is the overset area.

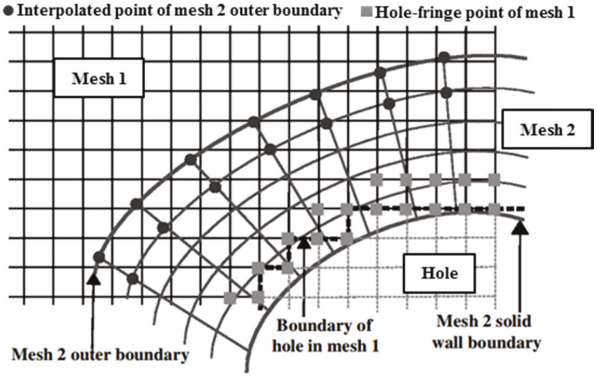

Figure 2. Details of the overset mesh.

Three steps are required for the overset approach: hole cutting, the identification of interpolation points, and the identification of donor cells. The purpose of hole cutting is to remove unnecessary cells before calculation. The cutting face will be set in the area which needs to be removed, and then the grid points that fall into cutting face will be identified and discarded in the CFD computation process. The hole mapping method is employed for the hole-cutting process. The interpolation point identification identifies two types of interpolation points, as illustrated in Figure 2: hole-fringe points and outer boundary points. The hole-fringe points, as any point near a hole point, are easily identified. The outer-boundary point is any point that lies on the boundary of a computational mesh. The donor cells identification identifies the hexahedral donor cells with the interpolation points as the vertex. The simplest and most reliable way to find donor cells is to traverse the entire mesh domain until the correct cells are found. However, the efficiency of this method is the lowest and the use of an excellent data structure can improve the seeking speed. The attribute distributed tree (ADT) approach is employed for the donor search process.

3. Problem Setup

3.1. HUST-Ship Solver

Based on solving the dimensionless conservation equations of mass and momentum, HUST-Ship adopted the SST k-ω turbulence model to simulate the turbulent flow and multibody and multi-coordinates were employed to solve the 6DOF motion of ships. The structured overset grid technology was used for grid discretization, coupled with the single-phase level-set method to capture the change of the free surface. As a mature CFD solver applicable in the domain of ship hydrodynamics, much previous work has proved the ability of HUST-Ship [31,32].

The whole workflow is shown in Figure 3.

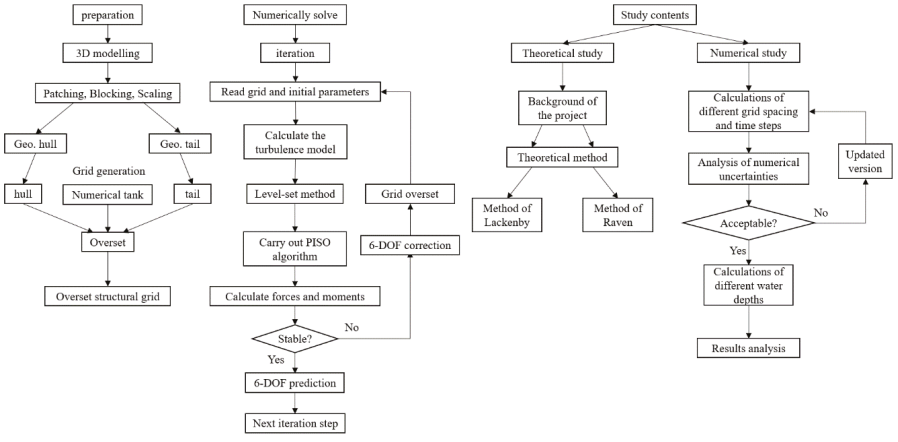

Figure 3. The workflow flowchart.

3.2. Ship Geometry

The principle parameters of the KCS are given in Table 1.

Table 1. Main parameters of ship geometry.

Main Particulars of KCS	Model-Scale	Full-Scale
Length (L_{PP})	7.2786 m	230 m
Beam (B_{WL})	1.019 m	32.2 m
Depth (D)	0.6013 m	19.0 m
Design draft (T)	0.3418 m	10.8 m
Displacement (∇)	1.649 m^3	52030 m^3
Wetted surface area (S)	9.4379 m^2	19556.1 m^2
Block coefficient (C_B)	0.6505	0.6505
Longitudinal center of buoyancy (%L_{PP}), fwd+	–1.48	–1.48
Moment of inertia (K_{xx}/B)	0.4	0.4
Moment of inertia (K_{yy}/L_{PP}, K_{zz}/L_{PP})	0.25	0.25

All the parameters were nondimensionalized by the characteristic length L_{PP} and the service ship speed v before the calculation was conducted. A complete geometry database of the ship is provided by Tokyo 2015 CFD workshop website [33].

3.3. Computational Domain and Boundary Conditions

The prismatic rectangular computational domain was generated to simulate the flow around the KCS. For full-scale calculations, a larger Reynolds number resulted in the need of thinner boundary layers, which increased the number of mesh cells. Due to the symmetry of the ship geometry and the 2DOF ship motion, the hydrodynamic characteristics of the ship obtained by half of the computational domain and the whole computational domain are the same, so only half of the ship and domain were used for full-scale calculations to reduce the number of mesh cells.

Figures 4 and 5 show the computational domains and the boundary conditions of the model scale and full scale respectively. The upstream is the "Inlet" boundary condition and the downstream is the "Exit" boundary condition; the Y = 0 plane of full-scale calculations is set as the symmetrical plane boundary condition "X-axis symmetry"; the side of the tank is set as a constant velocity boundary condition "Zero gradient"; the top of the domain is a far-field boundary condition "Farfield#2"; for limited water depths, the bottom of computational domains are set as the impermeable boundary

"Impermeable slip, no force", on which the force will not be calculated by the solver, while it is usually set as a "Farfield#1" boundary condition in deep water simulations.

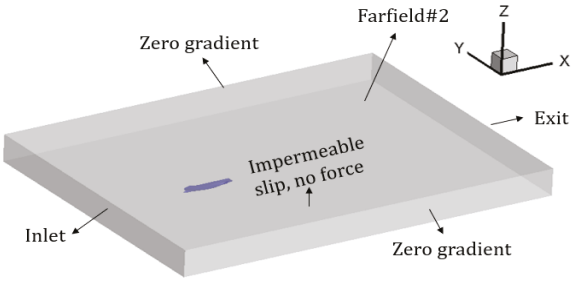

Figure 4. The computational domain for the model-scale calculations.

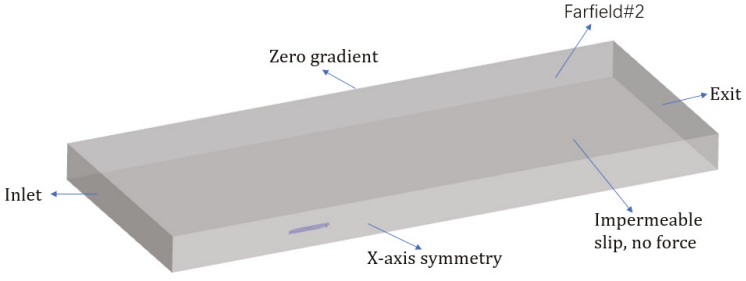

Figure 5. The computational domain for the full-scale calculations.

Table 2 shows the mathematical description of the boundary conditions listed above.

Table 2. The mathematical description of boundary conditions.

	Φ	***p***	**U**	**V**	**W**
Inlet	$\phi = -z$	$\frac{\partial p}{\partial n} = 0$	-	-	-
Exit	$\frac{\partial \phi}{\partial n} = 0$	$\frac{\partial p}{\partial n} = 0$	$\frac{\partial^2 U}{\partial n^2} = 0$	$\frac{\partial^2 V}{\partial n^2} = 0$	$\frac{\partial^2 W}{\partial n^2} = 0$
Far field #1	$\frac{\partial \phi}{\partial n} = 0$	$\frac{\partial p}{\partial n} = 0$	$\frac{\partial U}{\partial n} = 0$	$\frac{\partial V}{\partial n} = 0$	$\frac{\partial W}{\partial n} = 0$
Zero gradient	-	-	$\frac{\partial U}{\partial n} = 0$	$\frac{\partial V}{\partial n} = 0$	$\frac{\partial W}{\partial n} = 0$

To simulate the different water depths of the towing tank, computational domains of different sizes are established. Since only the effect of water depth is of concern in this study, i.e., the effect of the tank wall should be ignored, so a series of computational domains that are of sufficient length and width are used. Table 3 shows the size of the full-scale computational domains.

Table 3. The CFD computational domain size of the full-scale (half hull).

Upstream to the Hull	**3L_{PP}**
Downstream to the hull	10L_{PP}
Tank wall to the midsection	40B_{WL}
The height of the top surface from the waterline	0.5L_{PP}

Table 4 shows the size of the model-scale domains.

Table 4. The CFD computational domain size of the model-scale (full hull).

Upstream to the Hull	$2L_{PP}$
Downstream to the hull	$5L_{PP}$
Tank wall to the midsection	$3L_{PP}$
The height of the top surface from the waterline	$0.4L_{PP}$

Figures 6 and 7 give the grid of hull surface and the distribution of the overset grid of the whole computational domain respectively. Figure 8 shows the transverse and longitudinal mesh sections of the overset domain near the hull respectively.

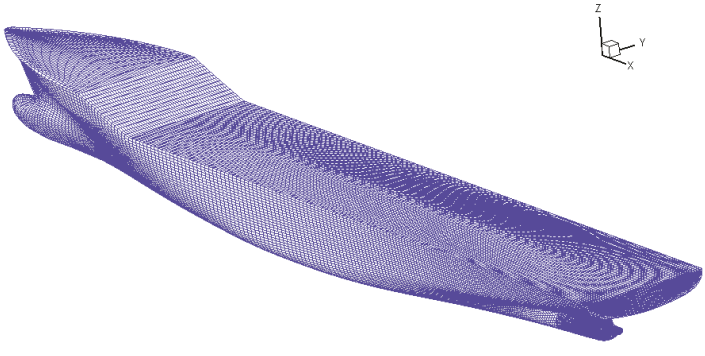

Figure 6. The grid of the hull surface.

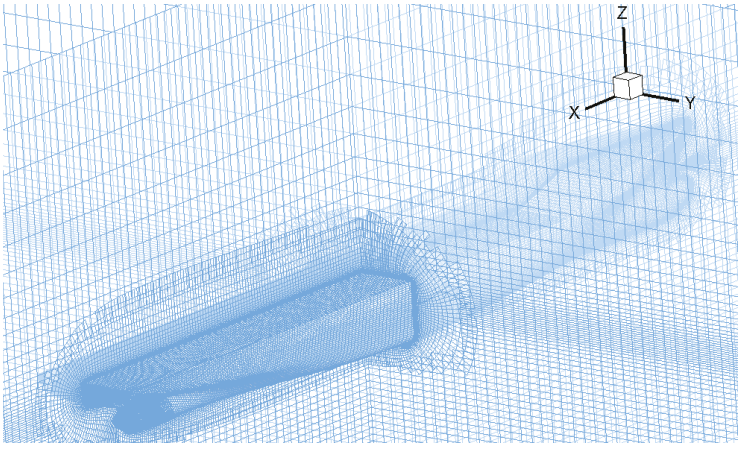

Figure 7. The overset grid of the computational domain.

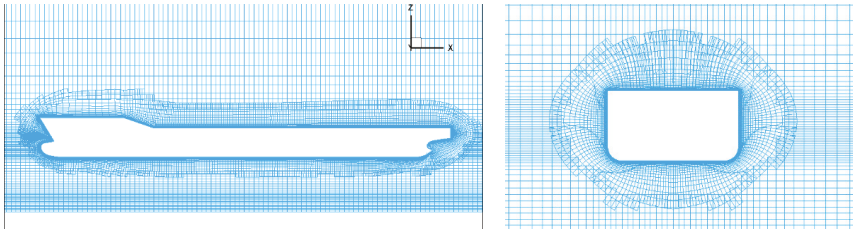

(**a**) (**b**)

Figure 8. 2D mesh sections: (**a**) midsection in the Y = 0 plane and (**b**) midsection in the X = 0.5L_{PP} plane.

3.4. Estimation of Numerical Uncertainties

Verification and validation of the numerical method for calculations of the bare hull resistance have been carried out. ITTC V & V (Verification and Validation) 2008 [34] A validation procedure was used to estimate the uncertainties of the numerical method.

In general, the numerical uncertainty U_{SN} includes the following aspects: uncertainty of iteration steps U_I, the uncertainty of the grid space U_G, the uncertainty of the time step U_T and the other parameters uncertainty U_P. For URANS solver HUST-Ship, U_I, and U_P could be ignored utilizing lots of iterations. For the specific computation in this study, U_G and U_T are of the most concern. Therefore, the numerical uncertainty U_{SN} can be expressed as follows:

$$U_{SN}{}^2 = U_G{}^2 + U_T{}^2 \tag{18}$$

Systematic grid-spacing and time-step studies were carried out using the generalized Richardson extrapolation method according to the literature [35].

At first, the uniform parameter refinement ratio r_k between solutions is assumed as:

$$r_k = \frac{\Delta x_2}{\Delta x_1} = \frac{\Delta x_3}{\Delta x_2} \tag{19}$$

in which Δx_1, Δx_2, and Δx_3 are the space of the coarse grid, medium grid, and fine grid or time step, respectively. S_1, S_2, and S_3 are the calculation results obtained by fine, medium and coarse grid spacing or time step, respectively. $\varepsilon_{21} = S_2 - S_1$ and $\varepsilon_{32} = S_3 - S_2$ are the differences between solutions of medium-fine and coarse-medium grid spacings, respectively. The convergence ratio R is defined as:

$$R = \frac{\varepsilon_{21}}{\varepsilon_{32}} \tag{20}$$

There are three possible conditions:

- Monotonic convergence (MC): $0 < R < 1$
- Oscillatory convergence (OC): $R < 0$
- Divergence (D): $R > 1$

When monotonic convergence is achieved, the Richardson extrapolation method can be used. The estimated numerical error δ_{RE} and order of accuracy P_{RE} can be calculated as:

$$\delta_{RE} = \frac{\varepsilon_{21}}{r_k^{P_{RE}} - 1} \tag{21}$$

$$P_{RE} = \frac{\ln(\varepsilon_{32}/\varepsilon_{21})}{ln\ r_k} \tag{22}$$

The correction factor C_G is defined as:

$$C_G = \frac{r_k^{P_{RE}}-1}{r_k^{P_{TH}}-1} \tag{23}$$

where P_{th} is an estimated value for the limiting order of accuracy as the spacing size goes to zero; generally, $P_{th} = 2$. The numerical error δ_{SN}, benchmark result S_C and uncertainty $U_{G,T}$ can be estimated from:

$$\delta_{SN} = C_G \cdot \delta_{RE} \tag{24}$$

$$S_C = S - \delta_{SN} \tag{25}$$

$$U_{G,T} = \begin{cases} \left(2.4(1-C_G)^2 + 0.1\right)|\delta_{RE}|, & |1-C_G| < 0.25 \\ |1-C_G||\delta_{RE}|, & |1-C_G| \geq 0.25 \end{cases} \tag{26}$$

When C_G is significantly less than or greater than 1, which means the solutions are far away from the asymptotic range, the numerical uncertainty $U_{G,T}$ can be calculated from:

$$U_{G,T} = \begin{cases} \left(9.6(1-C_G)^2 + 1.1\right)|\delta_{RE}|, & |1-C_G| < 0.125 \\ (2\,|1-C_G| + 1)|\delta_{RE}|, & |1-C_G| \geq 0.125 \end{cases} \tag{27}$$

4. Results

The directions of the drag force, trim angle, and sinkage are defined as shown in Figure 9.

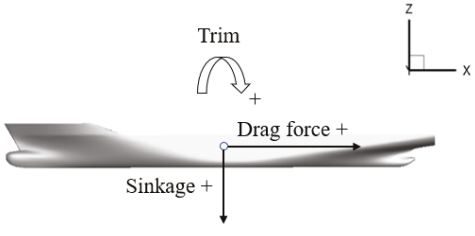

Figure 9. The directions of the drag force, trim angle and sinkage.

4.1. Verification and Validation

To ensure the reliability of numerical simulation, verification and validation study is conducted for the model-scale ship and the full-scale ship, in deep-water condition.

4.1.1. Model Scale (Fr = 0.26, Re = 1.477e+7)

In the previous work [32], the sensitivity of grid spacing and time step was studied for a KCS scaled model. The velocity of the scaled model is 2.197 m/s and the length between perpendiculars is 7.2786. Three grid cases and three time-step schemes were conducted for the KCS scaled model, as a preparation step; it is a key step to ensure the accuracy of the results. Table 5 shows the results obtained by the different grid cases and Table 6 shows the results obtained for different time step cases. Table 7 shows the results of numerical uncertainty of the KCS scaled model. Three different grids were generated with a grid refinement ratio $\sqrt{2}$ and three time-step schemes were generated with a refinement ratio of 2.

Table 5. Total resistance coefficients of different grid cases of the 1:31.6 scaled model.

Case	Cell (M)	$C_t/10^{-3}$	Diff.
Coarse	1.29	3.92	10.42%
Medium	3.66	3.67	3.38%
Fine	9.72	3.53	−0.56%
EFD	-	3.55	-

Table 6. The total resistance coefficients of different time steps of the 1:31.6 scaled model.

Case	Δt/s	$C_t/10^{-3}$	Diff.
Coarse	0.0331	3.74	5.35%
Medium	0.0165	3.67	3.38%
Fine	0.0083	3.66	3.10%
EFD	-	3.55	-

Table 7. The numerical uncertainties of resistance of the 1:31.6 scaled model.

	r_k	R	Convergence Conditions	CG	$U_{G,T}$ (%Sc)	U_{SN} (%Sc)
Grid (G)	$\sqrt{2}$	0.560	MC	1.366	1.984	1.984
Time-step (T)	2	0.143	MC	1.538	0.025	

For both grid-spacing and time-step, the convergence factor R was between 0 and 1, which meant that monotonic convergence was achieved and the generalized Richardson extrapolation method could be used. From Table 7, it can be observed that the uncertainties of the grid and time-step for the total resistance coefficient of the 1:31.6 scaled model were 1.984% S_C and 0.025% S_C, respectively, where S_C is the bench mark experimental data obtained from Equation (25) and the total numerical uncertainty is 1.984% S_C.

4.1.2. Full Scale (Fr = 0.26, Re = 2.84e+9)

Three grid cases and three time-step schemes were conducted for the full-scale KCS ship. Table 8 shows the results obtained for different grid cases and Table 9 shows the results obtained for different time step cases. Table 10 shows the results of numerical uncertainty. Three different grids were generated with a constant refinement ratio $\sqrt[3]{2}$ and three time-step schemes were generated with a constant refinement ratio $\sqrt{2}$. The reference EFD value comes from the literature [29].

Table 8. The total resistance coefficients of different grids of the full-scale KCS.

Case	Cell (M)	$C_t/10^{-3}$	Diff.
coarse	3.40	2.317	4.32%
medium	4.81	2.262	1.85%
fine	6.81	2.234	0.59%
EFD	-	2.221	-

Table 9. The total resistance coefficients of the different time steps of the full-scale KCS.

Case	Δt/s	$C_t/10^{-3}$	Diff.
coarse	0.132	2.321	4.50%
medium	0.093	2.262	1.85%
fine	0.065	2.245	1.08%
EFD	-	2.221	-

Table 10. The numerical uncertainties of the total resistance coefficients of the full-scale KCS.

	r_k	R	Convergence Conditions	CG	$U_{G,T}$ (%D)	U_{SN} (%D)
Grid (G)	$\sqrt[3]{2}$	0.509	MC	4.565	4.926	5.012
Time-step (T)	$\sqrt{2}$	0.288	MC	4.078	0.924	

For both grid-spacing and time-step, the convergence factor R was between 0 and 1, which meant that monotonic convergence was achieved and the generalized Richardson extrapolation method could be used. From Table 10, it can be observed that the uncertainties of grid and time-step for the total resistance coefficient of the 1:31.6 scaled model were 4.926%S_C and 0.924%S_C, respectively, where S_C is the bench mark experimental data obtained from Equation (25) and the total numerical uncertainty is 5.012%S_C.

4.1.3. Grid Spacing Sensitivity

For ships passing through the shallow-water channels, the flow parameters under the keel can change significantly, so the grid spacing between the bottom of the tank and the keel may significantly affect the calculation results.

As a reference for subsequent calculations, the grid spacing of the model scaled at H/T = 4 is chosen to study. Tables 11 and 12 show the results of the convergence study.

Table 11. The grid spacing convergence analysis.

Case	Grid Spacing/LPP	$C_t/10^{-3}$	$C_f/10^{-3}$
coarse	0.0113	4.267	2.926
middle	0.0075	4.192	2.925
fine	0.0050	4.158	2.925

Table 12. The numerical uncertainties of the grid spacing under the keel.

	r_k	R	Convergence Conditions	CG	U_G (%D)	U_{SN} (%D)
Grid (G)	1.5	0.453	MC	1.541	0.371	0.371

Since the calculated resistance coefficients of the middle and fine grid spacing are very close, the subsequent calculations are carried out using the middle spacing to ensure accuracy and to reduce the number of grid cells for computation processing.

4.1.4. Validation Based on EFD data

Assuming that the benchmark experimental value is D, the comparison error E can be defined as:

$$E = D - S_C \tag{28}$$

in which, S_C is the benchmark numerical result from Equation (25).

The validation uncertainty U_V is given by:

$$U_V{}^2 = U_D{}^2 + U_{SN}{}^2 \tag{29}$$

Where, $U_D = 1\%$ is the uncertainty of the experimental data provided for the KCS towed resistance. The results of the validation study are given in Table 13.

Table 13. Validation study.

	U_{SN} (%D)	U_D (%D)	U_V (%D)	E (%D)
Full-scale	5.012	1.00	5.11	1.85
1:31.6 model	1.984	1.00	2.22	3.38

4.2. Force and Attitude

4.2.1. Model Scale (Fr = 0.26, Re = 1.26e + 7)

The velocity of the scaled model is 2.197 m/s and the length between perpendiculars is 7.2786 m, which are same as presented with the previous cases of uncertainty analysis. The only difference is that the experimental kinematic viscosity leads to a slightly different Reynolds number from previous studies, however, previous studies can still be used to prove that the selected grid and time step are appropriate. As shown in Figure 10 and Table 14, the total resistance coefficient increases with a decrease of water depth; the increase of ship resistance in shallow water is shown intuitively. With the decrease of water depth, the total resistance coefficient increases gradually, but the total resistance coefficient of the three calculation cases with draft ratios H/T = 6, H/T = 8, and H/T = 10 does not increase significantly compared with the deep-water resistance measured in the model test. According to the International Towing Tank Conference (ITTC), the water depth H which can ignore the shallow water effect shall meet the following requirements:

$$H > 3\sqrt{BT} \tag{30}$$

$$H > 2.75\frac{V^2}{g} \tag{31}$$

where B is the maximum width of the ship; T is the draft; V is the ship speed; and g is the acceleration of gravity.

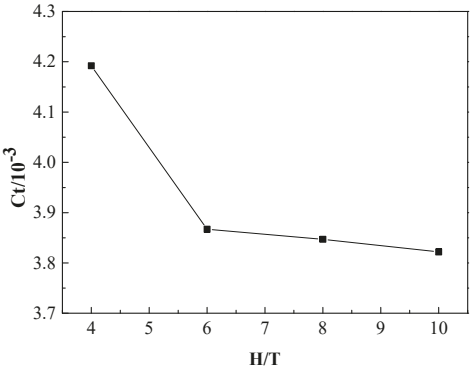

Figure 10. The total resistance coefficients of the KCS scaled model with different depth/draft ratios (H/T).

Table 14. The results of resistance, sinkage and trim.

H/T	Ct/10^{-3}	Sinkage/10^{-3}Lpp	Trim Angle/10^{-3}rad
4	4.192	2.847	−3.259
6	3.867	2.084	−3.128
8	3.847	1.849	−2.983
10	3.822	1.758	−2.913
EFD (deep water)	3.711	-	-

A further calculation shows that the calculation cases of H/T = 6, H/T = 8, and H/T = 10 are in this range, which indicates that the shallow-water effect is not so obvious.

Table 14 shows the detailed data of the resistance coefficients, sinkage, and trim in different calculation cases. The experimental fluid dynamics (EFD) value is obtained from the Tokyo 2015 workshop website.

As shown in Figure 11, the sinkage of the KCS increases monotonically with the decrease of H/T. There are many empirical formulas for predicting sinkage and the calculation results were compared with Raven's method in the following section. Figure 12 shows the changing trend of the trim angle in different water depths; the negative value means trim by the bow. As the H/T decreases, the trim angle gradually becomes larger.

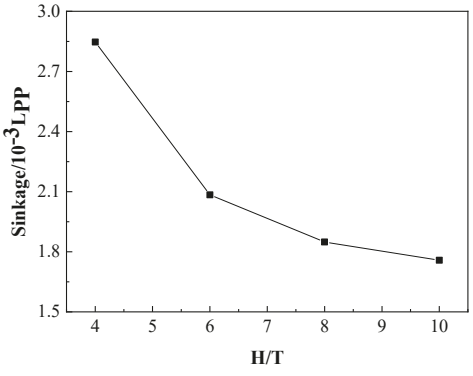

Figure 11. The dimensionless sinkage of the KCS scaled model with different depth/draft ratios (H/T).

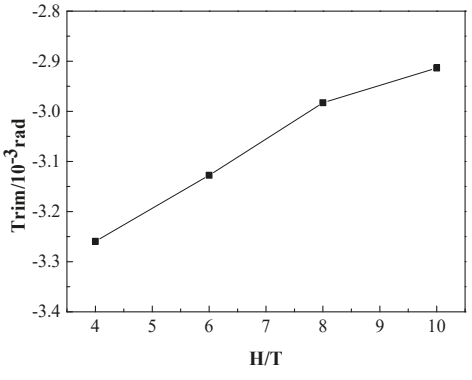

Figure 12. The trim angle with different depth/draft ratios of KCS scaled model (H/T).

4.2.2. Full Scale (Fr = 0.26, Re = 2.84e + 9)

As shown in Figure 13, the total resistance coefficient increases with the decrease of water depth; the increase of ship resistance in shallow water is shown intuitively. For a KCS, with the decrease of water depth, the total resistance coefficient increases gradually, but the total resistance coefficient of the two working conditions with draft ratio H/T = 6.7 and H/T = 10 does not increase significantly compared with the deep-water working condition (H/T = 21.3), for which the water depth is equal to the length between perpendiculars of the KCS.

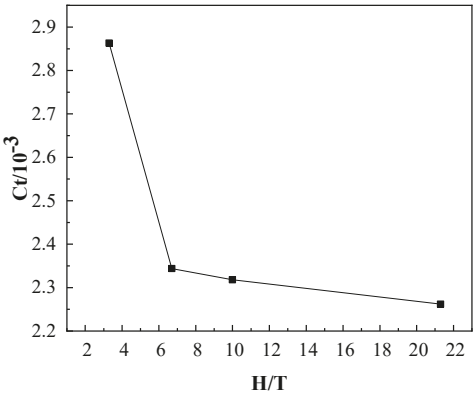

Figure 13. Total resistance coefficients of the full-scale KCS with different depth/draft ratios (H/T).

4.2.3. Comparison with the Existing Experimental Results

Some calculations were conducted for a 1:75 KCS scaled model to compare with the experimental study of Khaled Elsherbiny [36]; a low-speed point (F_{nH} = 0.32) and a high-speed point (F_{nH} = 0.8) are chosen for comparison. The comparison results of the total resistance coefficient and sinkage are given in Table 15. The EFD value is obtained from the results in the literature by interpolation.

Table 15. The comparison with the experimental value.

	$Ct/10^{-3}$	Diff./%	$Sinkage/10^{-3}Lpp$	Diff./%
F_{nH} = 0.32 (CFD)	5.735	3.11	0.769	6.3624
F_{nH} = 0.32 (EFD)	5.562	-	0.723	-
F_{nH} = 0.8 (CFD)	19.2	3.448	14.2	−1.183
F_{nH} = 0.8 (EFD)	18.56	-	14.37	-

4.3. Wave Properties

As we know, the dispersion relation for limited water depth is:

$$c = \sqrt{\frac{g\lambda}{2\pi}\tanh\left(\frac{2\pi h}{\lambda}\right)} \tag{32}$$

or

$$\frac{c}{\sqrt{gh}} = \sqrt{\frac{\lambda}{2\pi h}tanh\frac{2\pi h}{\lambda}} \tag{33}$$

Evidently, for a larger λ/h, the factor introduces a dependence on the ratio of wavelength to water depth. When the water depth h further decreases and the ratio λ/h becomes large, as Equation (27) shows, the propagation speed of waves will reach a limiting value of $c = \sqrt{gh}$. This indicates that there is an upper limit to the wave propagation speed in shallow water.

The different propagation speeds of waves in different water depths led to the differences in wave properties among the calculation cases. To show the wave properties, the nondimensionalized wave height on the hull surface and the Y = 0.1509 Lpp section are extracted.

4.3.1. Model Scale

As shown in Figure 14, the wave height curves for the cases of H/T = 6, H/T = 8, and H/T = 10 almost coincide, while for the H/T = 4 case, there is a clear departure from the other curves. It can also be seen that the wave height distribution characteristics on the Y = 0.1509 Lpp section are very similar to those on the hull surface, but tend to be flat on the whole. The further away from the ship, the more

horizontal the free surface becomes, because the kinetic energy of the wave gradually changes into potential energy in the process of propagation.

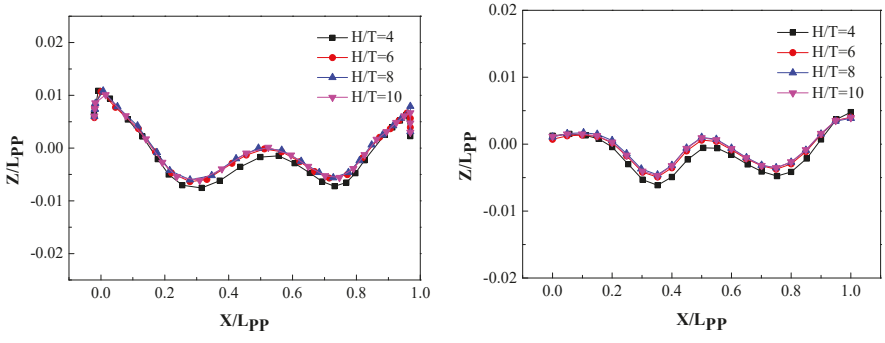

Figure 14. The model-scale wave profiles at different water depths: (**a**) on the hull surface and (**b**) on the Y = 0.1509 Lpp section.

4.3.2. Full Scale

It can be seen from Figure 15 that the wave height distribution characteristics of the full-scale ship are very similar to the wave properties of the scaled model.

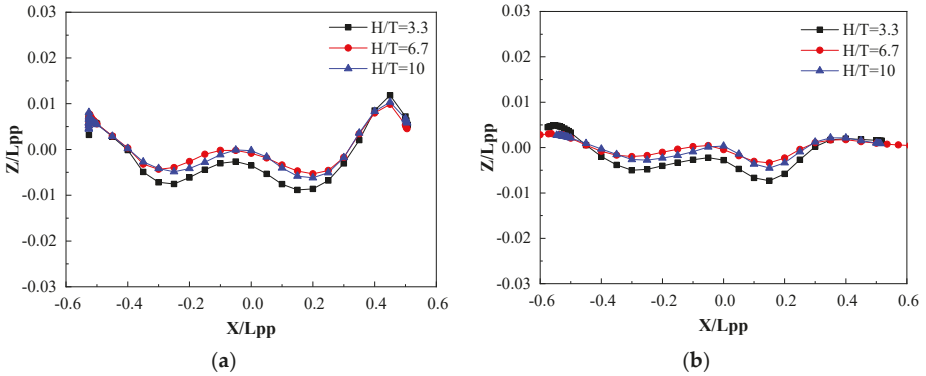

Figure 15. The full-scale wave profiles at different water depths: (**a**) on the hull surface and (**b**) on the Y = 0.1509 Lpp section.

4.4. Comparison with the Method of Raven

To get a proportion of viscous resistance, the estimation method of the form factor is introduced in this study.

According to the literature, "the most popular empirical formula for determining the form factor is attributed to Watanabe" [37].

$$k = -0.095 + 25.6 \cdot \frac{C_B}{\left(\frac{L}{B}\right)^2 \sqrt{\frac{B}{T}}} \tag{34}$$

The calculated value of KCS is close to 0.1.

4.4.1. Correction Process

After studying the effect of shallow water on viscous resistance, Raven began to do further research on the shallow water effect. A complete set of shallow water resistance correction procedures was proposed in his paper [38]. The correction steps are following as:

1. The correction of the viscous resistance coefficient is

$$r_{vfac} = 1 + 0.57\left(\frac{T}{H}\right)^{1.79} \tag{35}$$

in which T represents the draft; H represents the water depth; and r_{vfac} represents the ratio of shallow-water viscous resistance coefficient to deep-water viscous resistance coefficient.

2. No correction of wave resistance in the range of the critical Froude number $F_{nH} < 0.65$. After analyzing many numerical results and a large amount of test data, Raven thought that the change of wave resistance could be ignored when the Froude depth number is under the critical value 0.65 in Raven's study.
3. Estimate additional sinkage A good prediction formula was first proposed in the 1960s [39]; then Hooft [11] made a small change on it. The estimation formula of additional sinkage is derived from the formula proposed by Hooft; Ankudinov's [40] idea was used by Raven for reference in the process.

$$\frac{d_{sinkage}}{L} = max\left\{1.46\frac{\nabla}{L^3}\left[\frac{{F_{nH}}^2}{\sqrt{1-{F_{nH}}^2}} - \frac{{F_{nHD}}^2}{\sqrt{1-{F_{nHD}}^2}}\right], 0\right\} \tag{36}$$

in which L is the ship length, $\nabla = LBTC_B$ is the displacement volume; and $F_{nHD} = \frac{V}{\sqrt{0.3gL}}$ is the Froude depth number.

4. Estimate the resistance increase due to additional sinkage

$$r_{sink} = (1 + \delta\nabla)^{\frac{2}{3}} \tag{37}$$

in which r_{sink} is the factor that represents the effect of the sinkage increase caused by shallow water and $\delta\nabla = \frac{d_{sinkage} \cdot Awp}{\nabla}$ is the additional displacement volume due to additional sinkage.

5. The total resistance coefficient increase factor caused by shallow water is

$$r_{tfac} = \left[r_{visc} \cdot r_{vfac} + (1 - r_{visc}) \cdot r_{wfac}\right] \cdot r_{sink} \tag{38}$$

in which r_{tfac} is the correction factor of total resistance; r_{visc} is the relative contribution of viscous resistance in deep water at the same ship speed with a computational case; and $r_{wfac} = 1$, which restricts the use of this method to the case where $F_{nH} < 0.65$.

6. Range of applicability

- $F_{nH} < 0.65$, the Froude depth number should be less than 0.65. Otherwise, a significant increase of wave-making resistance will occur.
- $\frac{T}{H} < 0.5$, the ratio of the draft to the water depth T/H should be less than 0.5. For a higher value, the viscous resistance could not be accurately estimated using a simple formula.
- $\delta\nabla < 5\%$, the increase of displacement volume $\delta\nabla$ should be no more than 5%, otherwise, a better method may be needed to estimate the effect of the draft difference.

4.4.2. Model Scale

Table 16 gives the brief process of resistance correction using Raven's method and compares the results with CFD results; a maximum difference of 5.8771% appears when H/T = 4.

Table 16. The difference of total resistance coefficients between Raven's method and CFD results.

H/T	4	6	8	10
$r_{vfac} = 1 + 0.57 * (T/H)^{1.79}$	1.0477	1.0231	1.0138	1.0092
$F_{nH} = V/(gH)^{0.5}$	0.6128	0.5004	0.4333	0.3876
$F_{nHD} = V/(0.3gL)^{0.5}$	0.4747	0.4747	0.4747	0.4747
$r_{sink} = (1 + \delta\Delta)^{2/3}$	1.0247	1.0038	1.0000	1.0000
Ct-Prediction	0.0040	0.0038	0.0038	0.0037
Ct-CFD	0.0042	0.0039	0.0039	0.0038
Diff. (%)	5.8771	1.8867	2.5380	2.1305

As shown in Figure 16, the calculation results show quite good agreement with Raven's method when the water depths are deeper, but as the Froude depth number becomes larger with the decreasing of water depth h, a larger difference between the estimation and calculation occurs. In the case of the shallowest water depth, there is a maximum difference, and we find the Froude number, in this case, is close to the critical value 0.65. In Raven's correction method, the increase of wave resistance was ignored when $F_{nH} < 0.65$, however, a significant increase in wave resistance may occur when $F_{nH} > 0.65$, which could be the reason why a small difference is observed.

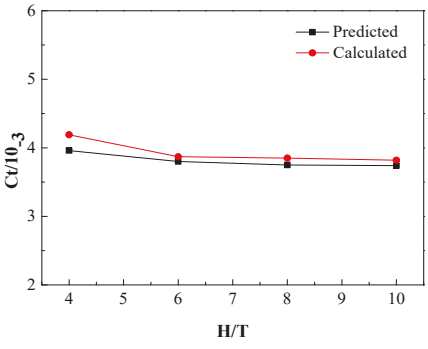

Figure 16. The comparison of the model-scale total resistance coefficients, estimated from Raven's equations (**Black**) and computed by CFD code (**Red**).

As can be seen in Figure 17, a clear difference appears in the case of H/T = 4: we cannot make sure here whether it is caused by a deficiency of the CFD simulation or a deficiency of the empirical formula. However, when considering the resistance increase caused by an additional sinkage, Raven adopted the method of constant admiralty coefficient, which can be defined as:

$$\frac{\Delta_1^{\frac{2}{3}} \cdot u_0{}^3}{P_1} = \frac{\Delta_2^{\frac{2}{3}} \cdot u_0{}^3}{P_2} \tag{39}$$

in which, Δ_1 and Δ_2, P_1 and P_2 are the displacement and effective power at different water depths. As we know, the effective power can be expressed as a product of resistance and ship speed, i.e., $P_{1,2} = R_{1,2}u_0$. As a result, the ratio of ship resistance at the same speed in different water depths can be derived as:

$$\frac{R_1}{R_2} = \left(\frac{\Delta_1}{\Delta_1}\right)^{\frac{2}{3}} \tag{40}$$

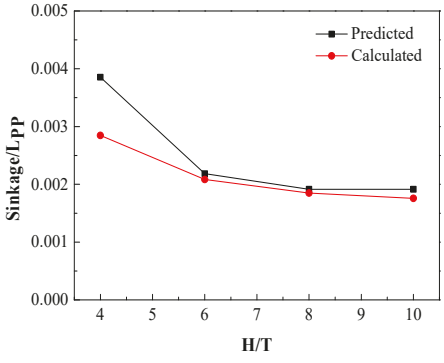

Figure 17. The comparison of model-scale dimensionless sinkage between the predicted value obtained by Raven's formula (**Black**) and the calculated value obtained by CFD simulations (**Red**).

Assumed R_1 is the resistance at a finite water depth and R_2 is the resistance in unrestricted water, Equation (31) can be derived.

Although the difference between the predicted sinkage and the value calculated by the CFD code is up to 26%, the value can as low as 0.5% when comparing the r_{sink}, which means it has little influence on estimating the increase of total resistance.

4.4.3. Full Scale

Table 17 gives the brief process of resistance correction using the Raven method and compares the results with the CFD results; a maximum difference of 20.942% appears when H/T = 3.3.

Table 17. The difference of total resistance coefficients between Raven's method and CFD results.

H/T	3.3	6.7	10
r_{vfac} = 1 + 0.57 * (T/H)1.79	1.0673	1.0189	1.0092
F_{nH} = V/(gH)0.5	0.6569	0.4645	0.3793
F_{nHD} = V/(0.3gL)0.5	0.4747	0.4747	0.4747
r_{sink} = (1 + δΔ)2/3	1.0356	1.0000	1.0000
Ct-Prediction	2.3671	2.2084	2.1928
Ct-CFD/10–3	2.8631	2.3442	2.3181
Diff. (%)	20.941	6.1421	5.7107

As shown in Table 11, the difference between the CFD results and the prediction results are within the acceptable range at the water depth to draft ratios H/T = 6.7 and H/T = 10, but an unacceptable difference occurs when H/T = 3.3.

Even though the comparison differences between the CFD results and the prediction results are larger than the model-scale comparison differences, a similar trend is observed: the largest difference occurs in the case of the minimum water depth to draft ratio. Actually, with the increase of the Froude depth number, the increase of wave resistance in shallow water may be significant, however, it was ignored in the process of resistance correction, which may cause an underestimate of the total resistance coefficient. In addition, there is no experimental data of full-scale trials, so the reference value is extrapolated using the value measured in model test, which may further increase the differences between the CFD and prediction results.

5. Discussion

5.1. Shallow-Water Effect on Ship Resistance

5.1.1. Viscous Resistance

According to fluid dynamics, when encountering a channel of limited water depth, the flow velocity between the tank bottom and the ship keel will increase significantly. As a result, the static pressure of particles will decrease, which results in the dynamic sinkage of ships, as well as the increase of frictional resistance. In addition, the increase of the relative velocity between the ship and the water results in an increase of the pressure gradient, which increases the viscous pressure resistance.

Figure 18 shows the model-scale dimensionless flow velocity in the x-axis direction between the ship keel and the tank bottom. The number marked on the figure represents the overspeed ratio γ, which is defined as:

$$\gamma = \frac{U}{\hat{u_0}} \tag{41}$$

where U represents the dimensionless flow velocity in the x-axis, and $\hat{u_0}$ is the nondimensionalized ship speed, i.e., $\hat{u_0} = 1$. As a result, $\gamma = U$ can be derived.

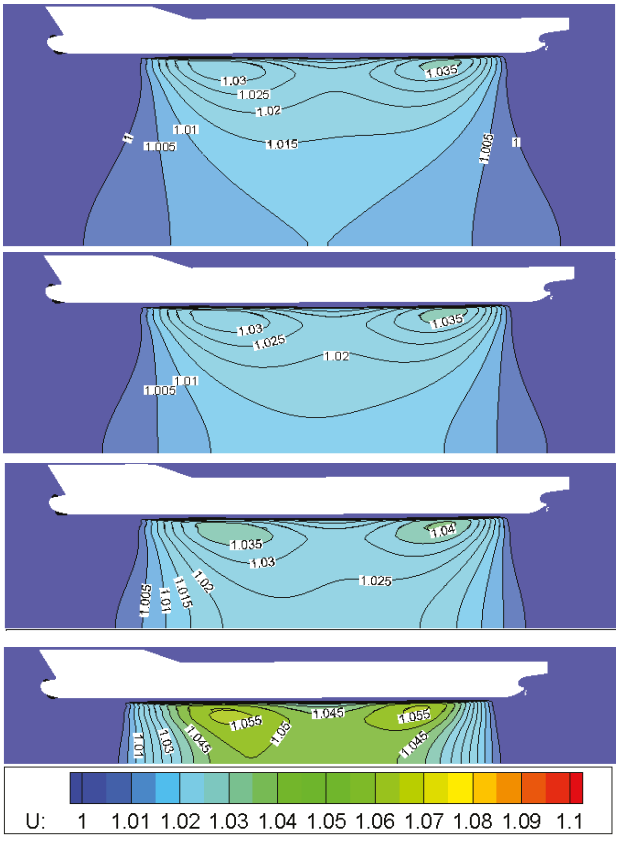

Figure 18. The overspeed ratios at different water depths for the 1:31.6 scaled model of the KCS (water depth decreases from top to bottom, corresponding to H = 4T, H = 6T, H = 8T, H = 10T respectively).

It is evident from the figure that both the peak value of the overspeed ratio and the gradient of flow velocity increases with a decrease of water depth, which is in line with the above analysis.

5.1.2. Wave Resistance

The influence factor of wave resistance is the Froude depth number F_{nH}. The critical value of the Froude depth number is $F_{nH} = 1$, where $F_{nH} < 1$ represents the interval of subcritical speed, and $F_{nH} > 1$ corresponds to the interval of supercritical speed.

According to the wave theory, the wave resistance increases significantly with the increase of the Froude depth number in the subcritical interval. However, the wave resistance decreases abnormally with the increase of F_{nH} after the ship speed exceeds the critical value.

Figure 19 shows the wave patterns of the full-scale simulations. It can be seen from the figure that a higher Froude depth number indicates a higher wave height contour density. It also means that a higher Froude depth number indicates a larger wave resistance.

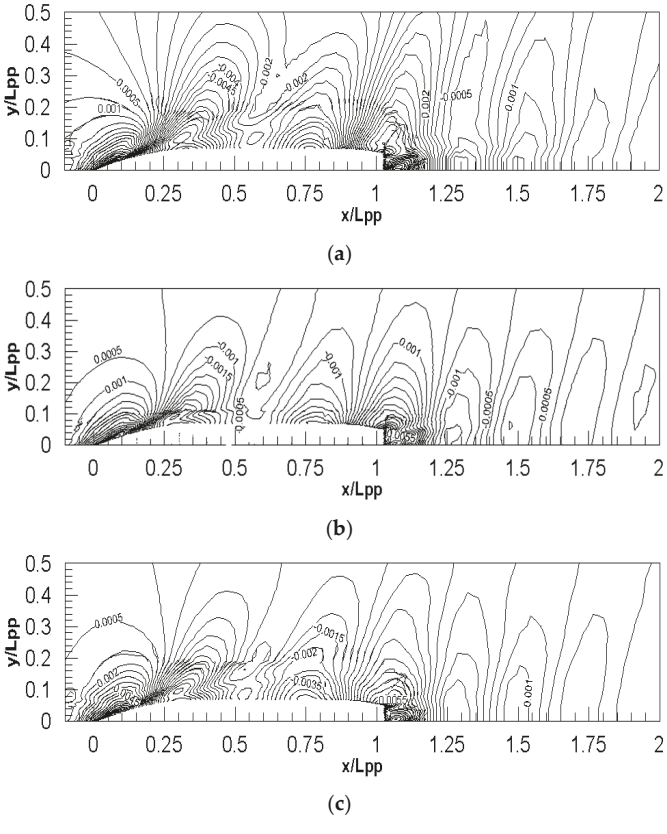

Figure 19. The wave patterns of full-scale simulations for different Froude depth numbers: (**a**) $F_{nH} = 0.66$, (**b**) $F_{nH} = 0.47$ and (**c**) $F_{nH} = 0.38$.

6. Conclusions

Taking the full-scale and model-scale KCS as study objects, numerical simulations were conducted to calculate the ship resistance at different water depth/draft ratios. The hydrodynamic force, sinkage, trim angle, and wave properties at different water depths are presented and discussed. The in-house URANS CFD solver, based on the finite difference method (FDM), is used for this study.

Two right-handed Cartesian coordinate systems are established to predict the 2-DOF motion of the forward ship and the single-phase level-set method is used to capture the change of the free surface. Lots of previous applications of HUST-Ship show quite a good accuracy. All results of resistance, trim angle, sinkage, and wave patterns show differences among different water depths, which indicates that the HUST-Ship solver can well express the effect of shallow water.

Verification study in terms of grid and time step sensitivity was performed to make sure that the numerical method was reliable; the Richardson extrapolation method was used in the process. A validation study was then conducted to judge the availability of the numerical results. Furthermore, the sensitivity of the grid spacing between the keel and the bottom of the towing tank was studied to obtain a proper grid spacing of the computational domain.

The results of total resistance coefficients and dynamic sinkage obtained by the CFD simulations were compared with the predicted value obtained by Raven's method. The comparison indicates that the differences between the CFD results and Raven's estimation results are extremely small in larger water depths. When the water depth becomes shallower, the differences between CFD and Raven's estimation increased rapidly. As Raven claimed in his paper, the increase of wave resistance can be ignored when $F_{nH} < 0.65$, however, some classical literatures support different critical values. As the results of this paper show, a lower critical value of F_{nH} may be more appropriate, since the difference between the estimation and the CFD goes up to 20% when F_{nH} is over 0.65 (0.66) in the full-scale simulation, and a maximum difference of 5.8771% occurs in the model-scale simulation when the F_{nH} is close to 0.65 (0.61). Comparing the model-scale simulation results with the full-scale simulation results, a similar trend for the change of resistance and altitude with a decrease of water depths is evident.

Even though the conclusion can be roughly obtained, the drawback of this paper is that only the designed speed of the KCS is considered, and the important impact index F_{nH} can only be controlled by changing the water depth. Future works will contain the simulation of different Froude numbers to get a more persuasive conclusion.

Author Contributions: D.F.: methodology, investigation, resources, writing–original draft, funding acquisition. B.Y.*: software, data curation, visualization, validation, formal analysis. Z.Z.: writing–review and editing, Project administration, funding acquisition. X.W.: supervision, funding acquisition. All authors have read and agreed to the published version of the manuscript.

Funding: This research received no external funding.

Acknowledgments: The research work comes from the ITTC workshop in 2019. This research was sponsored by the Advanced Research Common Technology Project of CHINA CMC (41407010401, 41407020502). The essential support is greatly acknowledged.

Conflicts of Interest: The authors declare no conflict of interest.

List of Symbols

x, y, z	Direction of the independent coordinates
u_0	Ship service speed, incoming velocity
L_{pp}	Length between perpendiculars
ρ	Density of water
ν	Kinematic viscosity
H	Water depth
T	Draft of the ship
$F_{nH} = u_0/\sqrt{gH}$	Froude depth number
$\hat{p} = \left(\frac{p-p_\infty}{\rho U_0^2} + \frac{z}{Fr^2}\right)$	Dynamic pressure coefficient
$\overline{u_i' u_j'}$	Reynolds stress
k	Turbulent kinetic energy
I_x, I_y, I_z	Components of moment of inertia with respect to the gravity center
X, Y, Z	Components of external forces acting on the hull
K, M, N	Components of external moments acting on the hull
φ	Distance from any point in the flow field to the free surface
Δt	Time step
EFD	Results obtained by experimental fluid dynamics
MC	Monotonic convergence

References

1. Sezen, S.; Cakici, F. Numerical prediction of total resistance using full similarity technique. *China Ocean. Eng.* **2019**, *33*, 493–502. [CrossRef]
2. Zeng, Q.; Hekkenberg, R.; Thill, C.; Rotteveel, E. A numerical and experimental study of resistance, trim and sinkage of an inland ship model in extremely shallow water. In Proceedings of the International Conference on Computer Applications in Shipbuilding, Singapore, 26–28 September 2017; pp. 26–28.
3. Raven, H.C. A computational study of shallow-water effects on ship viscous resistance. In Proceedings of the 29th Symposium on Naval Hydrodynamics, Gothenburg, Sweden, 27 August 2012.
4. Choi, J.; Min, K.-S.; Kim, J.; Lee, S.; Seo, H. Resistance and propulsion characteristics of various commercial ships based on CFD results. *Ocean. Eng.* **2010**, *37*, 549–566. [CrossRef]
5. Tezdogan, T.; Demirel, Y.K.; Kellett, P.; Khorasanchi, M.; Incecik, A.; Turan, O. Full-scale unsteady RANS CFD simulations of ship behaviour and performance in head seas due to slow steaming. *Ocean. Eng.* **2015**, *97*, 186–206. [CrossRef]
6. Yang, D.; Sun, Z.; Jiang, Y.; Gao, Z. A Study on the Air Cavity under a Stepped Planing Hull. *J. Mar. Sci. Eng.* **2019**, *7*, 468. [CrossRef]
7. Cucinotta, F.; Guglielmino, E.; Sfravara, F.; Strasser, C. Numerical and experimental investigation of a planing Air Cavity Ship and its air layer evolution. *Ocean. Eng.* **2018**, *152*, 130–144. [CrossRef]
8. Cucinotta, F.; Guglielmino, E.; Sfravara, F. A critical CAE analysis of the bottom shape of a multi stepped air cavity planing hull. *Appl. Ocean. Res.* **2019**, *82*, 130–142. [CrossRef]
9. Duy, T.-N.; Hino, T.; Suzuki, K. Numerical study on stern flow fields of ship hulls with different transom configurations. *Ocean. Eng.* **2017**, *129*, 401–414. [CrossRef]
10. Jachowski, J. Assessment of ship squat in shallow water using CFD. *Arch. Civ. Mech. Eng.* **2008**, *8*, 27–36. [CrossRef]
11. Hooft, J.P. *The Influence of Nautical Requirements on the Dimensions and Layout of Entrance Channels and Harbours*; Proc. International Course Modern Dredging: The Hague, The Netherlands, 1977.
12. Pacuraru, F.; Domnişoru, L. Numerical investigation of shallow water effect on a barge ship resistance. *IOP Conf. Series Mater. Sci. Eng.* **2017**, *227*, 012088. [CrossRef]
13. Ji, S.; Ouahsine, A.; Smaoui, H.; Sergent, P. 3D Numerical Modeling of Sediment Resuspension Induced by the Compounding Effects of Ship-Generated Waves and the Ship Propeller. *J. Eng. Mech.* **2014**, *140*, 04014034. [CrossRef]
14. Linde, F.; Ouahsine, A.; Huybrechts, N.; Sergent, P. Three-Dimensional Numerical Simulation of Ship Resistance in Restricted Waterways: Effect of Ship Sinkage and Channel Restriction. *J. Waterw. Port. Coastal. Ocean. Eng.* **2017**, *143*, 06016003. [CrossRef]
15. Du, P.; Ouahsine, A.; Sergent, P.; Hu, H. Resistance and wave characterizations of inland vessels in the fully-confined waterway. *Ocean. Eng.* **2020**, *210*, 107580. [CrossRef]
16. Liu, Y.; Zou, Z.; Zou, L.; Fan, S. CFD-based numerical simulation of pure sway tests in shallow water towing tank. *Ocean. Eng.* **2019**, *189*, 106311. [CrossRef]
17. Xu, H.; Hinostroza, M.; Wang, Z.; Soares, C.G. Experimental investigation of shallow water effect on vessel steering model using system identification method. *Ocean. Eng.* **2020**, *199*, 106940. [CrossRef]
18. Tang, X.; Tong, S.; Huang, G.; Xu, G. Numerical investigation of the maneuverability of ships advancing in the non-uniform flow and shallow water areas. *Ocean. Eng.* **2020**, *195*, 106679. [CrossRef]
19. Schlichting, O. *Schiffwiderstand auf beschränkter wassertiefe: Widerstand von seeschiffen auf flachem wasser. Jahrbuch der Schiffbautechnischen Gesellschaft*; Springer: Hanburg, Germany, 1934; Volume 35, p. 127.
20. Lackenby, H. The Effect of Shallow Water on Ship Speed. *Nav. Eng. J.* **1964**, *76*, 21–26.
21. ITTC. Speed and Power Trials, Part 2, Analysis of Speed/Power Trial Data. In Proceedings of the 25th ITTC, Copenhagen, Denmark; 2014. Available online: https://ittc.info/media/4210/75-04-01-012.pdf (accessed on 21 January 2020).
22. Jiang, T. *A New Method for Resistance and Propulsion Prediction of Ship Performance in Shallow Water*; Elsevier: Amsterdam, The Netherlands, 2001; pp. 509–515.
23. Raven, H.C. A new correction procedure for shallow-water effects in ship speed trials. In Proceedings of the 13th International Symposium on Practical Design of Ships and Other Floating Structures, Copenhagen, Denmark, 4–8 September 2016.

24. ITTC. Procedures and Guidelines. In Proceedings of the 28th ITTC, Wuxi, China; 2017.
25. Guo, L.; Yu, J.; Chen, J.; Jiang, K.; Feng, D. Unsteady Viscous CFD Simulations of KCS Behaviour and Performance in Head Seas. In *International Conference on Offshore Mechanics and Arctic Engineering*; American Society of Mechanical Engineers: New York, NY, USA, 2018; Volume 51210, p. V002T08A040. [CrossRef]
26. Carrica, P.M.; Wilson, R.V.; Noack, R.W.; Stern, F. Ship motions using single-phase level set with dynamic overset grids. *Comput. Fluids* **2007**, *36*, 1415–1433. [CrossRef]
27. Ji, S.C.; Ouahsine, A.; Smaoui, H.; Sergent, P. 3-D Numerical Simulation of Convoy-Generated Waves in a Restricted Waterway. *J. Hydrodyn.* **2012**, *24*, 420–429. [CrossRef]
28. Burg, C.O.E. Single-phase level set simulations for unstructured incompressible flows. In Proceedings of the 17th AIAA Computational Fluid Dynamics Conference, Toronto, ON, Canada, 6–9 June 2005.
29. Castro, A.M.; Carrica, P.M.; Stern, F. Full scale self-propulsion computations using discretized propeller for the KRISO container ship KCS. *Comput. Fluids* **2011**, *51*, 35–47. [CrossRef]
30. Hu, K. Near-Wall Treatment. Available online: http://url.cn/jbbb6MO5 (accessed on 20 January 2020).
31. Wang, X.; Liu, L.; Zhang, Z.; Feng, D. Numerical study of the stern flap effect on catamaran' seakeeping characteristic in regular head waves. *Ocean. Eng.* **2020**, *206*, 107172. [CrossRef]
32. Feng, D.; Yu, J.; He, R.; Zhang, Z.; Wang, X. Free running computations of KCS with different propulsion models. *Ocean. Eng.* **2020**, *214*, 107563. [CrossRef]
33. Tokyo 2015 CFD Workshop. Available online: https://t2015.nmri.go.jp/ (accessed on 15 January 2020).
34. ITTC, Uncertainty Analysis in CFD, Part 1, Verification and Validation Methodology and Procedures. In Proceedings of the 25th ITTC, Fukuoka, Japan, 14–20 September 2008; Available online: https://ittc.info/media/4184/75-03-01-01.pdf (accessed on 22 January 2020).
35. Stern, F.; Wilson, R.V.; Coleman, H.W.; Paterson, E.G. Comprehensive Approach to Verification and Validation of CFD SimulationsMethodology and Procedures. *J. Fluids Eng.* **2001**, *123*, 793–802. [CrossRef]
36. Elsherbiny, K.; Tezdogan, T.; Kotb, M.; Incecik, A.; Day, S. Experimental analysis of the squat of ships advancing through the New Suez Canal. *Ocean. Eng.* **2019**, *178*, 331–344. [CrossRef]
37. Larsson, L.; Raven, H.C. *Ship Resistance and Flow*; The Society of Naval Architects and Marine Engineers: Jersey City, NJ, USA, 2010; p. 103.
38. Raven, H.C. A method to correct shallow-water model tests for tank wall effects. *J. Mar. Sci. Technol.* **2018**, *24*, 437–453. [CrossRef]
39. Tuck, E.O. Shallow-water flows past slender bodies. *J. Fluid Mech.* **1966**, *26*, 81. [CrossRef]
40. Ankudinov, V.; Daggett, L.; Huval, C.; Hewlett, C. Squat predictions for maneuvering applications. In Proceedings of the International Conference on Marine Simulation and Ship Maneuverability MARSIM'96, Copenhagen, Denmark, 9–13 September 1996; pp. 467–495.

Journal of
Marine Science and Engineering

MDPI

Article

Impact of Hard Fouling on the Ship Performance of Different Ship Forms

Andrea Farkas [1], Nastia Degiuli [1,*], Ivana Martić [1] and Roko Dejhalla [2]

[1] Faculty of Mechanical Engineering and Naval Architecture, University of Zagreb, Ivana Lučića 5, 10000 Zagreb, Croatia; andrea.farkas@fsb.hr (A.F.); ivana.martic@fsb.hr (I.M.)
[2] Faculty of Engineering, University of Rijeka, Vukovarska ulica 58, 51000 Rijeka, Croatia; roko.dejhalla@riteh.hr
* Correspondence: nastia.degiuli@fsb.hr; Tel.: +38-516-168-269

Received: 3 September 2020; Accepted: 24 September 2020; Published: 26 September 2020

Abstract: The successful optimization of a maintenance schedule, which represents one of the most important operational measures for the reduction of fuel consumption and greenhouse gas emission, relies on accurate prediction of the impact of cleaning on the ship performance. The impact of cleaning can be considered through the impact of biofouling on ship performance, which is defined with delivered power and propeller rotation rate. In this study, the impact of hard fouling on the ship performance is investigated for three ship types, keeping in mind that ship performance can significantly vary amongst different ship types. Computational fluid dynamics (CFD) simulations are carried out for several fouling conditions by employing the roughness function for hard fouling into the wall function of CFD solver. Firstly, the verification study is performed, and the numerical uncertainty is quantified. The validation study is performed for smooth surface condition and, thereafter, the impact of hard fouling on resistance, open water and propulsion characteristics is assessed. The differences in the impact of biofouling on the ship performance are noticed amongst different ship forms. They are mainly influenced by the portion of viscous resistance in the total resistance, relative roughness, roughness Reynolds number and advance coefficient for the self-propulsion point.

Keywords: biofouling; ship performance; container ship; oil tanker; bulk carrier; CFD

1. Introduction

Although recognized as an efficient mode of transport that has steadily enhanced safety, as well as environmental performance, over the past few decades, the maritime transport industry is transforming. Lately, in order to fulfil the new regulatory requirements and market needs, ship operators and ship owners have to improve capability of their ships to enable innovative, relevant and efficient services. Several technical and operational measures are adopted for increasing energy efficiency [1], however, it is crucial to accurately measure their effects. Namely, new regulations demand an increasing level of environmental performance, while ship operators and ship owners are faced with mounting pressure to keep up the competitiveness of their ships. As a result of this, ship operators and ship owners often hesitate to implement measure for increasing the energy efficiency due to the lack of reliable data on their effect [2,3]. The optimization of the maintenance schedule related to hull and propeller cleaning presents an important operational measure for increasing energy efficiency as ship operator or ship owner has large degree of control over it [4]. The successful optimization of maintenance schedule relies on accurate prediction of the impact of cleaning on the ship performance. The presence of biofouling on ship hull and propeller is causing an increase in roughness, which leads to an increase in ship resistance and if the ship speed is kept constant, an increase in the fuel consumption [5]. The biofouling occurrence is mostly prevented through the application of antifouling (AF) coatings, while hull and propeller cleaning are usually performed in drydock. It should be noted that both of those measures are

costly [6]. Consequently, an accurate assessment of the impact of biofouling on the ship performance is required for the proper selection of AF coatings and scheduling of hull cleaning [7].

There are different approaches for the assessment of this impact which can be classified into statistical studies, performance monitoring and approaches, based on the wall similarity hypothesis [8]. Approach based on the wall similarity hypothesis allows estimation of the fouling effect if the drag characterization of certain fouling type is performed. Drag characterization of a rough surface implies assessing the velocity decrement caused by the frictional drag of the surface as a function of the roughness Reynolds number (k^+). This velocity decrement, i.e., downward shift of the mean velocity in the log-law region of turbulent boundary layer (TBL) is called the roughness function (ΔU^+). There is no universal roughness function, however, once ΔU^+ for a certain fouling type is assessed, it can be used for the determination of frictional drag of any arbitrary body covered with that fouling type [9]. Over the last few decades, Granville similarity law scaling method has been imposed for the assessment of the impact of biofouling on the ship resistance with $\Delta U^+ = f(k^+)$ known and it has been widely used in the literature [10–14]. Nevertheless, this method has several important drawbacks, as claimed by [15]. Namely, this method can be used for the prediction of the frictional resistance coefficient of the fouled flat plate having the same length as an investigated ship, and other resistance components of fouled ship are considered to be the same as for smooth ship. What is more, this method assumes only one k^+ value and thus one ΔU^+ value over the entire flat plate. Since the k^+ value depends on friction velocity (u_τ), this assumption may lead to certain errors, as, even on a flat plate u_τ, it is not constant over the entire plate. Lastly, using Granville similarity law scaling method only increase in effective power can be estimated. As shown in [16], due to the presence of biofilm the increase in the delivered power is significantly higher than the increase in effective power.

Recently, there have been an increasing number of studies using a computational fluid dynamics (CFD) approach based on the implementation of certain ΔU^+ model within the wall function [17–20]. This approach can calculate u_τ for each discretized cell and, in that way, can obtain the distribution of u_τ values along the investigated surface. Consequently, k^+ distribution along the investigated surface will be obtained, and various ΔU^+ values will be used along the surface. Furthermore, the fouling effects on the other resistance components can be investigated, as well as the impact of biofouling on the open water and propulsion characteristics. This approach for the assessment of the impact of hull roughness on the ship's total resistance has been recently validated within [21]. Namely, within [21], it was demonstrated that CFD wall function approach can precisely determine not only the impact of roughness on the skin friction, but on the total resistance of 3D hull as well. The investigations related to the impact of barnacle and biofilm fouling on the ship propulsion performance have been presented in [8,22]. These studies demonstrated the impact of biofouling on the propulsion characteristics using CFD approach. However, both studies were performed on the example of Kriso Container Ship (KCS). Since ship resistance and propulsion characteristics can significantly vary amongst different ship forms, it would be beneficial to investigate the fouling effect on the ship performance of different ship forms.

In this study, the impact of biofouling on the ship performance of three merchant ships is analyzed. As already noted, the obtained increases due to the presence of biofouling in effective and delivered power are not equal. Therefore, it is more accurate to study the impact of biofouling on the ship performance through the analysis of the increase in delivered power and propeller rotation rate, than through analysis of the increase in effective power solely. To the best of the authors' knowledge, the impact of biofouling on the ship performance of different hull forms is investigated in this paper for the first time. This investigation is performed utilizing the CFD simulations and a Colebrook-type ΔU^+ of Grigson which is implemented within the wall function of CFD solver. Drag characterization study of hard fouling was performed by Schultz [12]. CFD model for the assessment of the impact of hard fouling on the ship resistance has been proposed in [16], where the CFD model is validated. This study can be considered as a continuation of study [16]. A verification study is carried out in order to assess grid and temporal uncertainty. A validation study for smooth surface conditions is performed, by comparing the numerically obtained results with the extrapolated towing tank results.

Finally, the detail investigation of the impact of hard fouling on the ship resistance and propulsion characteristics is performed for six different fouling conditions. The obtained results show the impact of hard fouling on the resistance and propulsion characteristics amongst different ship types, as well as on the increase in delivered power and propeller rotation rate.

2. Materials and Methods

2.1. Governing Equations

In this study Reynolds-averaged Navier–Stokes (RANS) and averaged continuity equations are used as governing equations, and they read:

$$\frac{\partial(\rho\overline{u}_i)}{\partial t} + \frac{\partial}{\partial x_j}\left(\rho\overline{u}_i\overline{u}_j + \rho\overline{u'_i u'_j}\right) = -\frac{\partial\,\overline{p}}{\partial x_i} + \frac{\partial\overline{\tau}_{ij}}{\partial x_j} \tag{1}$$

$$\frac{\partial(\rho\overline{u}_i)}{\partial x_i} = 0 \tag{2}$$

where ρ is the density, $\overline{u}_i$ is the averaged velocity vector, $\rho\overline{u'_i u'_j}$ is the Reynolds stress tensor, $\overline{p}$ is the mean pressure and $\overline{\tau}_{ij}$ is the mean viscous stress tensor, given as:

$$\overline{\tau}_{ij} = \mu\left(\frac{\partial\overline{u}_i}{\partial x_j} + \frac{\partial\overline{u}_j}{\partial x_i}\right) \tag{3}$$

where μ is the dynamic viscosity coefficient.

In order to close Equations (1) and (2), $k-\omega$ SST turbulence model with wall functions is applied. For the discretization of governing equations, the finite volume method (FVM) is utilized, and the volume of fluid (VOF) method with high resolution interface capturing (HRIC) is utilized for tracking and locating the free surface. After the discretization, Equations (1) and (2) are solved in a segregated manner, the second order upwind convection scheme is used for the discretization of convective terms, while temporal discretization is performed using the first order scheme.

As already noted, the impact of roughness, i.e., biofouling, can be noticed as a downward shift of the mean velocity profile within the log-law region of TBL:

$$U^+ = \frac{1}{\kappa}\ln y^+ + B - \Delta U^+ \tag{4}$$

where κ is the von Karman constant, U^+ is the non-dimensional mean velocity, y^+ is the non-dimensional normal distance from the wall and B is the smooth wall log-law intercept.

The drag characterization of a certain roughness or fouling type means finding the relation between ΔU^+ and k^+, where k^+ is defined as:

$$k^+ = \frac{k u_\tau \rho}{\mu} \tag{5}$$

where k is the roughness length scale, which cannot be directly measured.

Schultz has proposed following scaling for the hard fouling [12]:

$$k = 0.059 R_t \sqrt{\%SC}, \tag{6}$$

where R_t is the height of the largest barnacles, while $\%SC$ is the percentage of the surface covered with barnacles.

Using Equation (6), Schultz has demonstrated excellent collapse for the obtained results with the Grigson roughness function, which is given with following equation:

$$\Delta U^+ = \frac{1}{\kappa} \ln\left(1 + k^+\right) \tag{7}$$

It should be noted that Schultz has proposed Equation (6) based on the assumption that the height of the larger barnacles has the dominant influence on drag and that the effect of increase in $\%SC$ is larger for lower $\%SC$ and smaller for higher $\%SC$, and these assumptions were deduced from the obtained results, pipe flow experiments [23] and the observations from [24] for typical roughness types.

An explanation of the approach for the determination of the impact of biofilm on the ship resistance and propulsion characteristics is presented in [8,18] and is applied within this study. Firstly, an experimental study related to towing tank measurements of fouled flat plates was carried out within [12]. Based on the obtained results, Schultz has proposed Equation (6) for the determination of roughness length scale and Equation (7) as a ΔU^+ model for hard fouling. This ΔU^+ model was implemented within the wall function of CFD solver and CFD model was validated with the comparison of the numerically obtained frictional resistance coefficients for fouled flat plates [16] with the experimentally measured ones [12]. Additionally, CFD simulations for fouled full-scale plates representing two merchant ships were carried out, and the obtained results were compared with the results obtained using Granville similarity law scaling method [16]. Once the CFD model is validated, it can be utilized for the assessment of the impact of hard fouling on the resistance and propulsion characteristics. The impact of hard fouling on the ship resistance characteristics for two merchant ships is studied in [16] using CFD simulations of a towed ship. In this paper, the impact of hard fouling on the propeller performance in open water conditions is assessed through implementation of ΔU^+ model for hard fouling within wall function of CFD solver and by performing CFD simulations of the open water test (OWT). CFD simulations of OWT are performed using the moving reference frame (MRF) method, and CFD simulations are performed as steady simulations. More details regarding this method can be found within [25]. The impact of hard fouling on ship propulsion characteristics is assessed utilizing the proposed ΔU^+ model within CFD simulations of the self-propulsion test (SPT). It should be noted that CFD simulations of SPT are performed using the body force method and more details regarding this method can be found in [25]. The change in certain hydrodynamic characteristic is calculated as follows:

$$\Delta\varphi = \frac{\varphi_R - \varphi_S}{\varphi_S} \cdot 100\% \tag{8}$$

where φ_R represents certain hydrodynamic characteristic for fouled condition and φ_S represents certain hydrodynamic characteristic for smooth surface condition.

The impact of hard fouling on the ship performance is studied for six different fouling conditions presented in Table 1. The presented fouling conditions are investigated considering certain fouling condition present both at the hull and propeller.

Table 1. Studied fouling conditions.

Fouling Condition	R_t, μm	$\%SC$, %	k, μm
R1	7000	25	2065
R2	5000	25	1475
R3	7000	5	923.5
R4	5000	5	659.64
R5	7000	1	413
R6	5000	1	295

2.2. Resistance, Open Water and Propulsion Characteristics

The total resistance coefficient can be decomposed as follows:

$$C_T = (1+k)C_F + C_W \tag{9}$$

where k represents the form factor, C_F represents the frictional resistance coefficient and C_W represents the wave resistance coefficient. It should be noted that C_T is obtained by dividing total resistance (R_T) with $\frac{1}{2}\rho v^2 S$ (where v is the ship speed and S is the wetted surface) and in that way, the non-dimensional form is obtained.

Effective power (P_E) can be obtained as a product of R_T and v. Most studies related to the impact of biofouling on ship performance investigate the effect of biofouling on effective power. However, the fuel consumption and greenhouse gas (GHG) emission can be related to delivered power (P_D) and propeller rotation rate (n). The quasi-propulsive efficiency coefficient defines relation between P_E and P_D as follows:

$$\eta_D = \frac{P_E}{P_D} = \eta_H \eta_O \eta_R \tag{10}$$

where η_H is the hull efficiency, η_O is the open water efficiency and η_R is the relative rotative efficiency. These efficiencies are defined as follows:

$$\eta_H = \frac{1-t}{1-w} \tag{11}$$

$$\eta_O = \frac{J}{2\pi}\frac{K_{TO}}{K_{QO}} \tag{12}$$

$$\eta_R = \frac{K_{QO}}{K_Q} \tag{13}$$

where t is the thrust deduction coefficient, w is the wake fraction coefficient, J is the advance coefficient, K_{TO} is the thrust coefficient in open water conditions, K_{QO} is the torque coefficient in open water conditions and K_Q is the torque coefficient obtained in SPT.

Delivered power can be obtained as follows:

$$P_D = 2\pi\, \rho K_Q n^3 D^5 \tag{14}$$

where D is the propeller diameter.

3. Computational Model

3.1. Case Study

Within this paper, the impact of hard fouling on the ship performance is presented on the example of three commercial ships: containership, oil tanker and bulk carrier. The portion of CO_2 emission from containerships, bulk carriers and tankers in total CO_2 emission from international shipping is significantly higher than for other ship types and accounts for almost 62% of CO_2 emission from international shipping [26]. The Kriso Container Ship (KCS) was designed with an aim to represent a modern panamax container ship with a bulbous bow [27]. The Korea Research Institute for Ships and Ocean Engineering (KRISO) carried out an extensive towing tank experiments, in order to determine resistance, mean flow data and free surface waves [27]. Self-propulsion tests were performed at the Ship Research Institute (now the National Maritime Research Institute, NMRI) in Tokyo, and the obtained results were reported in the Proceedings of the CFD Workshop Tokyo in 2005 [28]. Kriso Very Large Crude-oil Carrier 2 (KVLCC2) was designed with the aim to represent a large oil tanker that can transport 300,000 t of crude oil, and it represents the second variant of KRISO tanker with more U-shaped stern frame lines in comparison with KVLCC. KRISO carried out resistance and self-propulsion tests,

as well as towing tank measurements for the determination of mean flow data and wave profile elevations [27]. Bulk Carrier (BC) represents a typical handymax bulk carrier. Extensive towing tank experiments, including resistance tests, self-propulsion tests, as well as nominal wake measurements were performed in Brodarski institute [29]. It should be noted that KCS, KVLCC2 and BC were only designed as models, i.e., full-scale ships have never been built. The geometry of the investigated ships is presented in Figure 1.

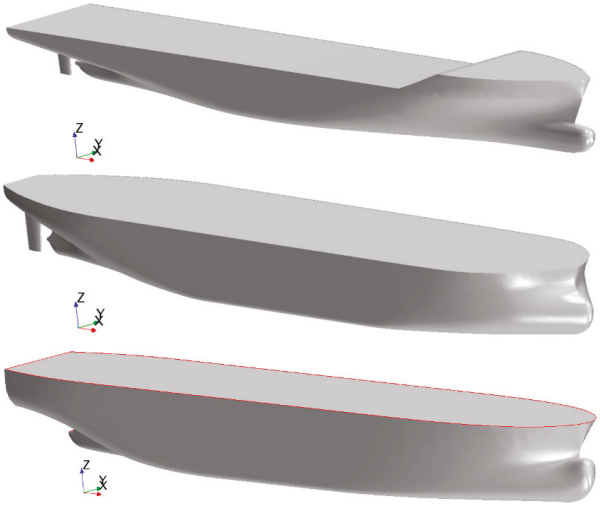

Figure 1. Geometry of the Kriso Container Ship (KCS) (**upper**), Kriso Very Large Crude-oil Carrier 2 (KVLCC2) (**middle**) and Bulk Carrier (BC) (**lower**).

From Figure 1. it is evident that all three ships have bulbous bow and transom stern. KCS has more slender form than BC and KVLCC2. The main particulars of the investigated ships are presented in Table 2.

Table 2. The main particulars of KCS, KVLCC2 and BC.

Parameter	KCS	KVLCC2	BC
length between perpendiculars, L_{pp}	230 m	320 m	175 m
waterline length, L_{wl}	232.5 m	325.5 m	182.69 m
breadth, B	32.2 m	58 m	30 m
draft, T	10.8 m	20.8 m	9.9 m
Displacement, Δ	53,382.8 t	320,750 t	41,775 t
Displacement volume, ∇	52,030 m^3	312,622 m^3	40,716 m^3
Wetted surface, S	9645 m^2	27,467 m^2	7351.9 m^2
Block coefficient, C_B	0.6505	0.8098	0.7834
Froude number, Fn	0.26	0.1423	0.2026
Design speed, V	24 kn	15.5 kn	16.32 kn
Propeller center, longitudinal location from FP $\left(x/L_{pp}\right)$	0.9825	0.9797	0.9800
Propeller center, vertical location from WL $(-z/T)$	0.62037	0.72115	0.6800

SPT were performed using the KP505 for KCS, the KP458 for KVLCC2 and one stock propeller from the Wageningen series (WB) for BC, and their geometry is shown in Figure 2. The main particulars of the investigated propellers are given in Table 3. Towing tank tests for all three investigated propellers are performed at Reynolds numbers (Rn) higher than $Rn = 2 \cdot 10^5$ as prescribed by ITTC [30], and the obtained results are given in [29,31,32].

Figure 2. KP505 (**left**), KP458 (**middle**) and Wageningen series (WB) (**right**) propeller.

Table 3. The main particulars of KP505, KP458 and WB.

Propeller	KP505	KP458	WB
propeller diameter, D	7.900 m	9.860 m	6.199 m
propeller pitch, P	7.505 m	7.085 m	5.294 m
number of blades, Z	5	4	4
chord length, c	2.844 m	2.233 m	1.633 m
maximum thickness of profile, t	0.132 m	0.131 m	0.168 m
Hub ratio, d/D	0.180	0.155	0.179

3.2. Computational Domain and Boundary Conditions

In this study, the impact of hard fouling on resistance, open water and propulsion characteristics is investigated using CFD simulations of resistance, open water and self-propulsion tests. It should be noted that the impact of hard fouling on resistance characteristics of KCS and KVLCC2 is already investigated in [16]. Therefore, within this paper, the impact of hard fouling on ship resistance characteristics is only briefly presented as it is important for further discussion. R_T of a ship is determined using CFD simulations which include free surface effects, i.e., free surface simulations (FSS). Viscous resistance (R_V) is obtained using double body simulations (DBS), which do not take free surface effects into account. In DBS, the flow around deeply immersed double body ship is simulated and thus the obtained R_T is equal to R_V. The frictional resistance (R_F) is obtained by integrating the tangential stresses over the wetted surface, while viscous pressure resistance (R_{VP}) is obtained by integrating the pressure over the wetted surface in DBS. Once R_V and R_F are determined, $1+k$ is determined as a ratio between R_V and R_F. Wave resistance (R_W) is obtained as difference between R_T obtained in FSS and R_V obtained in DBS. For more details regarding the performed CFD simulations of resistance tests, reference may be given to [16]. It should be noted that CFD simulations of resistance tests for BC are performed using the same computational domain and boundary conditions as in [16]. CFD simulations of OWT are performed using the cylindrical computational domain. The domain boundaries are placed sufficiently far from the investigated propeller and appropriate boundary conditions are applied in order to prevent their impact on the obtained solution, Figure 3. The computational domain for CFD simulations of SPT is the same as for CFD simulations of resistance test, however within CFD simulations of SPT symmetry condition is not applied, i.e., the whole computational domain is generated (Figure 4). In Figure 4, the applied boundary conditions are presented as well. It should be noted that the same boundary conditions are applied in CFD simulations of the resistance test, except for the symmetry boundary condition, which is applied at the symmetry plane within CFD simulations of resistance test. Possible occurrence of wave reflection is prevented by applying VOF wave damping at the inlet, outlet and side boundaries. More details regarding the applied damping function can be found in [33], and the VOF wave damping length is set to L_{pp}.

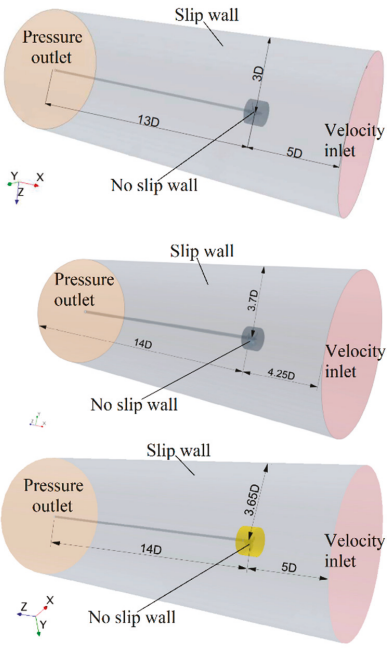

Figure 3. Computational domain for the open water test (OWT): KP505 (**upper**), KP458 (**middle**) and WB (**lower**).

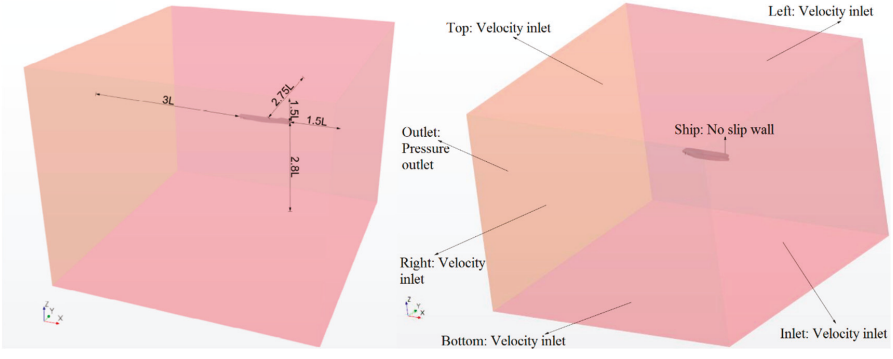

Figure 4. Computational domain (**left**) and the applied boundary conditions (**right**) within computational fluid dynamics (CFD) simulations of the self-propulsion test (SPT).

3.3. Discretization of Computational Domain and Computational Setup

Cut-cell grids with prism layer mesh on the walls were made utilizing the surface remesher, prism layer mesher and trimmer mesher within STAR-CCM+. The unstructured hexahedral mesh is refined locally in the critical regions. Thus, within DBS and FSS of resistance test, as well as in CFD simulations of SPT, mesh is refined near the hull surface, near the bow and stern and hull surface is discretized very fine, i.e., the cell size at the hull surface is set to 1/1000 L_{pp}. Within CFD simulations including free surface effects, mesh is refined in the region where free surface is expected, as well as in order to capture Kelvin wake around free surface. Additionally, mesh for CFD simulations of SPT is refined in the region where virtual disk is located. It should be noted that refinements are made in the same way within [8,25,34]. The mesh for CFD simulations of OWT is refined in the region around the propeller.

Additionally, mesh is particularly refined along the leading and trailing edges of propeller in order to allow proper demarcation between the suction and pressure sides. The thickness of the first cell on the wall surfaces within all CFD simulations is chosen in a way that y^+ values are higher than 30 and k^+ values, as recommended by [15]. As a result of this, near wall mesh for smooth and fouled surfaces is not the same since investigated surface conditions represent very severe fouling conditions with high k values. The obtained mesh for CFD simulations of OWT is presented in Figure 5, while the obtained mesh for CFD simulations of SPT is shown in Figure 6. Within these two figures, the above mentioned refinements can be seen.

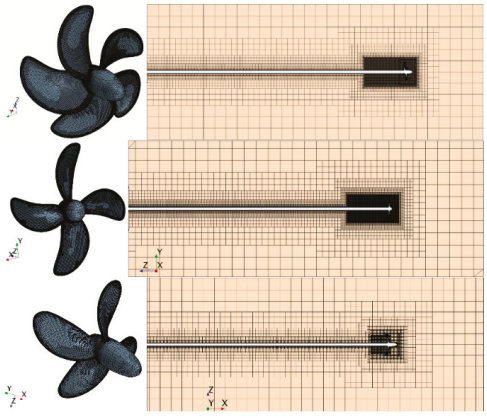

Figure 5. Propeller surface (**left**) and profile view (**right**) cross section of the volume mesh for KP505 (**upper**), KP458 (**middle**) and WB (**lower**).

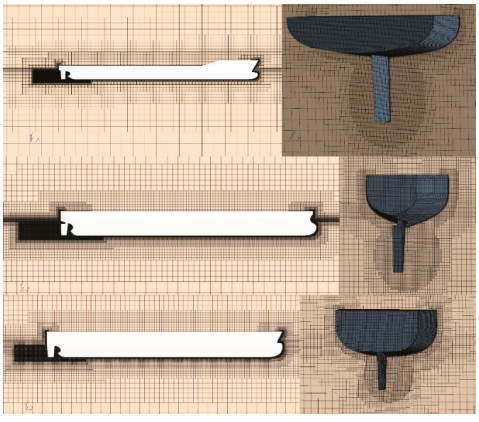

Figure 6. The profile view cross-section of the domain for KCS (**upper left**), KVLCC2 (**middle left**) and BC (**lower left**) and mesh refinement in stern region of KCS (**upper right**), KVLCC2 (**middle right**) and BC (**lower right**).

CFD simulations of OWT are performed for full-scale KP505, KP458 and WB in a way that $n = 1.5$ rps is kept constant and advance velocity varies with J. CFD simulations for KP505 are performed for range of J from 0.1 to 0.8, with a step equal to 0.1, for KP458 for range of J from 0.1 to 0.7 with step equal to 0.1 and for WB for range of J from 0.08 to 0.88 with step equal to 0.08. CFD simulations of SPT are performed without discretization of propeller geometry, as the body force method is applied. Therefore, a virtual disk model is placed at the propeller location with the inner

radius of the virtual disk set to the propeller hub radius and the outer radius set to the propeller radius (R). Thickness of virtual disk model is set as propeller thickness, the inflow plane radius is set as $1.1R$ and the inflow plane offset is set as $2.2R$ towards the bow from the half of virtual disk thickness.

CFD simulations without free surface effects, i.e., DBS of resistance test and CFD simulations of OWT, are performed as steady simulations. The remaining CFD simulations include free surface effect, and they are performed with time step equal to $T/200$, where T is the ratio between L_{pp} and ship speed (v). FSS of resistance test and CFD simulations of SPT are stopped once R_T and thrust (T) force became steady, i.e., once they oscillate around averaged value with oscillation amplitude lower than 0.5% of R_T or T value.

4. Verification and Validation Study

4.1. Verification Study

A verification study is carried out in order to estimate sufficient grid spacings and adequate time steps. This study is carried out using three different meshes and three different time steps. Verification study for grid size is made with fine time step and verification study for time step is made with fine mesh. Thereafter, numerical uncertainty, which is consisted of both spatial and temporal uncertainties, is calculated using the grid convergence index (GCI) method. This method is recommended by the American Society of Mechanical Engineers, as well as by the American Institute of Aeronautics and Astronautics for the assessment of grid uncertainty (U_G) [35], but can be used for the assessment of temporal uncertainty (U_T) as well [35–37]. More details regarding the GCI method and numerical uncertainty can be found in [18].

For the purposes of verification study three meshes are generated for smooth surface condition and fouling condition R1. Since all mesh parameters, except prism layer mesh, are set to be relative to cell base size, mesh is refined by changing cell base size. It should be noted that all remaining CFD simulations, i.e., for the fouling conditions R2, R3, R4, R5 and R6 are performed using fine mesh. In Table 4, the number of cells used in the verification study is shown. Three different time steps, i.e., $T/50$, $T/100$ and $T/200$ are used in the verification study for time step.

Table 4. Number of cells within CFD simulations.

Smooth Surface Condition			
Simulation	KCS/KP 505	KVLCC2/KP 458	BC/WB
	Coarse/Medium/Fine	Coarse/Medium/Fine	Coarse/Medium/Fine
OWT	3.50/5.10/7.10 Million	2.40/3.30/5.30 Million	2.20/3.50/5.00 Million
SPT	2.12/4.19/8.47 Million	1.23/2.74/5.25 Million	0.96/2.20/5.06 Million
Fouling Condition R1			
Simulation	KCS/KP 505 Coarse/Medium/Fine	KVLCC2/KP 458 Coarse/Medium/Fine	BC/WB Coarse/Medium/Fine
OWT	2.30/3.50/5.30 Million	1.80/2.30/3.90 Million	1.60/2.40/3.40 Million
SPT	1.89/3.83/7.54 Million	1.14/2.54/4.86 Million	0.89/2.01/4.61 Million

It should be noted that the verification study for CFD simulations of resistance tests of KCS and KVLCC2 is carried out in [16]. Numerical uncertainties in the prediction of R_F and R_V consisted of grid uncertainties solely, and R_T consisted of grid and temporal uncertainties, which are calculated using the GCI method. The obtained numerical uncertainties in the prediction of R_F were below 1.3% for both ships and for all analyzed fouling conditions (Table 1). Numerical uncertainties in the prediction of R_V were slightly higher, however, the highest obtained numerical uncertainty was equal to 2.86%. Finally, the highest numerical uncertainties are obtained for the prediction of R_T. Nevertheless, these grid and time step uncertainties were relatively low, i.e., the highest obtained grid uncertainty in the

prediction of R_T was equal to 2.99%, while the highest time step uncertainty in the prediction of R_T was equal to 0.1%. Within this paper, the numerical uncertainty in the prediction of K_{TO} and $10K_{QO}$ from CFD simulations of OWT are calculated for one J value and the obtained results are presented in Tables 5 and 6. Additionally, numerical uncertainty in the prediction of P_D, n, T and J from CFD simulations of SPT are calculated.

Table 5. The verification study for K_{TO}.

Propeller	J	ϕ_3	ϕ_2	ϕ_1	ϕ_{ext}^{21}	$GCI_{fine'}^{21}$, %
KP505 S	0.7	0.18068	0.18047	0.18058	0.18071	0.092
KP458 S	0.5	0.18513	0.18576	0.18478	0.18264	1.443
WB S	0.56	0.17468	0.17338	0.17250	0.16758	3.565
KP505 R1	0.6	0.20722	0.20665	0.20668	0.20668	0.001
KP458 R1	0.4	0.15868	0.15883	0.15725	0.15698	0.217
WB R1	0.4	0.20876	0.20855	0.20878	0.21098	1.317

Table 6. The verification study for K_{QO}.

Propeller	J	ϕ_3	ϕ_2	ϕ_1	ϕ_{ext}^{21}	$GCI_{fine'}^{21}$, %
KP505 S	0.7	0.29436	0.29386	0.29387	0.29387	0.000
KP458 S	0.5	0.21219	0.21268	0.21169	0.21045	0.729
WB S	0.56	0.24312	0.24120	0.23910	0.23372	2.815
KP505 R1	0.6	0.40234	0.40168	0.40249	0.40615	1.136
KP458 R1	0.4	0.22703	0.22713	0.22533	0.22512	0.115
WB R1	0.4	0.32578	0.32591	0.32531	0.32524	0.024

As can be seen from Tables 5 and 6, relatively low numerical uncertainties are obtained, and are in line with numerical uncertainties of other CFD studies regarding open water tests [38,39]. Thus, the highest U_G in the prediction of K_{TO} and $10K_{QO}$ is obtained for the WB propeller with smooth surface condition, and it is equal to 3.565% and 2.815%, respectively. It should be noted that numerical uncertainties obtained for smooth and fouled propellers are relatively close, i.e., numerical uncertainty has not raised due to the roughness effects.

From the results of verification study of SPT, Tables 7–9, it can be concluded that U_T are lower than U_G. Generally, the obtained U_G related to the prediction of P_D for smooth and fouled ships are slightly higher than for the other investigated key variables and the highest GCI_{fine}^{21} for KCS is equal to 3.123%, for KVLCC2 is equal to 1.174% and for BC is equal to 7.318%. The obtained U_T related to the prediction of P_D for smooth and fouled ships are lower and the highest GCI_{fine}^{21} for KCS is equal to 1.366%, for KVLCC2 is equal to 1.502% and for BC is equal to 3.390%. The obtained U_G related to the prediction of n for smooth and fouled ships are the lowest amongst investigated key variables and the highest GCI_{fine}^{21} for KCS is equal to 0.255%, for KVLCC2 is equal to 0.164% and for BC is equal to 1.661%. Interestingly, the obtained U_T values related to the prediction of n for smooth and fouled ships are higher than U_G values and the highest U_T for KCS is equal to 0.401%, for KVLCC2 is equal to 0.701% and for BC is equal to 2.909%. The obtained U_G values related to the prediction of T for smooth and fouled ships are low and the highest GCI_{fine}^{21} for KCS is equal to 3.273%, for KVLCC2 is equal to 1.478% and for BC is equal to 4.717%. The obtained U_T values related to the prediction of T for smooth and fouled ships are lower or similar to U_G and the highest GCI_{fine}^{21} for KCS is equal to 0.807%, for KVLCC2 is equal to 1.529% and for BC is equal to 3.499%. Finally, the obtained U_G values related to the prediction of J for smooth and fouled ships are low and the highest GCI_{fine}^{21} for KCS is equal to 0.452%, for KVLCC2 is equal to 1.257% and for BC is equal to 2.041%. The obtained U_T values related to the prediction of J for smooth and fouled ships are low as well, and the highest GCI_{fine}^{21} for KCS is equal to 0.451%, for KVLCC2 is equal to 0.703% and for BC is equal to 2.719%.

Table 7. The obtained grid uncertainties in the prediction of P_D, n, T and J.

P_D							
Ship	**Surface Condition**	ϕ_3, **MW**	ϕ_2, **MW**	ϕ_1, **MW**	ϕ_{ext}^{21}, **MW**	GCI_{fine}^{21}, **%**	U_G, **MW**
KCS	S	26.744	25.321	24.624	24.009	3.123	0.769
	R1	67.008	65.429	64.807	64.361	0.860	0.558
KVLCC2	S	20.172	17.325	17.850	18.017	1.174	0.209
	R1	58.651	55.524	55.940	56.036	0.214	0.120
BC	S	7.384	7.267	6.725	6.573	2.825	0.190
	R1	20.778	21.326	20.301	19.112	7.318	1.486
n							
Ship	**Surface Condition**	ϕ_3, **rpm**	ϕ_2, **rpm**	ϕ_1, **rpm**	ϕ_{ext}^{21}, **rpm**	GCI_{fine}^{21}, **%**	U_G, **rpm**
KCS	S	100.982	99.686	99.341	99.225	0.146	0.145
	R1	118.374	117.672	117.376	117.137	0.255	0.299
KVLCC2	S	73.068	70.484	70.858	70.951	0.164	0.117
	R1	95.356	93.902	93.963	93.968	0.007	0.006
BC	S	101.830	101.580	99.541	99.251	0.364	0.362
	R1	130.805	132.033	131.120	128.345	1.661	2.160
T							
Ship	**Surface Condition**	ϕ_3, **kN**	ϕ_2, **kN**	ϕ_1, **kN**	ϕ_{ext}^{21}, **kN**	GCI_{fine}^{21}, **%**	U_G, **kN**
KCS	S	1903.77	1877.34	1810.89	1763.46	3.273	59.281
	R1	3669.43	3630.48	3605.91	3557.73	1.670	60.226
KVLCC2	S	2276.43	2015.69	2009.71	2009.41	0.019	0.374
	R1	4557.62	4308.72	4390.60	4442.50	1.478	64.872
BC	S	829.63	813.35	763.94	739.27	4.037	30.839
	R1	1616.88	1644.82	1592.13	1532.04	4.717	75.107
J							
Ship	**Surface Condition**	ϕ_3	ϕ_2	ϕ_1	ϕ_{ext}^{21}	GCI_{fine}^{21}, **%**	U_G
KCS	S	0.7196	0.7215	0.7293	0.7319	0.452	0.0033
	R1	0.5476	0.5442	0.5452	0.5456	0.094	0.001
KVLCC2	S	0.4428	0.4603	0.4573	0.4564	0.248	0.0011
	R1	0.3066	0.3128	0.3099	0.3068	1.257	0.0039
BC	S	0.5160	0.5209	0.5328	0.5414	1.997	0.0106
	R1	0.3593	0.3580	0.3591	0.3649	2.041	0.0073

The obtained U_T, U_Q, U_n, U_{P_D} and U_J, which consist of both U_G and U_T, are shown in Table 9. As can be seen from Table 9, the lowest U_{SN} values for smooth and fouled ships are obtained for KCS, which was expected, since U_G values are higher than U_T values and the mesh for KCS had more cells than for KVLCC2 and BC. The highest U_{SN} is obtained for the prediction of U_{P_D} for BC fouled with R1 and it is equal to 7.421% and other obtained U_{SN} values are lower than 5.5%. Higher U_{P_D} were expected, since, for the prediction of P_D, both n and the propeller torque should be determined. It should be noted that the obtained U_{P_D} are in line with the previously published studies [8,25]. From Table 9, it can be seen that higher numerical uncertainties are obtained for the prediction of P_D and T, than for n and J, which was also obtained in [8]. Additionally, it can be seen that U_{SN} in the prediction of key variables for R1 are mostly below U_{SN} for smooth surface condition. Higher U_{SN} obtained for R1 than for smooth surface condition can be ascribed to the lower cell number used in CFD simulations of SPT for rough surface condition (Table 4). Therefore, it can be concluded that the implementation of ΔU^+ within the wall function did not cause higher uncertainties in the prediction of the key variables.

Table 8. The obtained temporal uncertainties in the prediction of P_D, n, T and J.

P_D							
Ship	**Surface Condition**	ϕ_3, **MW**	ϕ_2, **MW**	ϕ_1, **MW**	ϕ_{ext}^{21}, **MW**	GCI_{fine}^{21}, **%**	U_T, **MW**
KCS	S	25.058	24.918	24.624	24.355	1.366	0.336
	R1	65.020	65.198	64.807	64.479	0.633	0.410
KVLCC2	S	17.413	17.256	17.850	18.064	1.502	0.268
	R1	56.335	55.490	55.940	56.454	1.147	0.642
BC	S	6.813	6.903	6.725	6.542	3.390	0.228
	R1	20.546	20.458	20.301	20.101	1.233	0.250
n							
Ship	**Surface Condition**	ϕ_3, **rpm**	ϕ_2, **rpm**	ϕ_1, **rpm**	ϕ_{ext}^{21}, **rpm**	GCI_{fine}^{21}, **%**	U_T, **rpm**
KCS	S	99.697	99.577	99.341	99.094	0.311	0.309
	R1	117.477	117.628	117.376	116.999	0.401	0.471
KVLCC2	S	70.490	70.249	70.858	71.255	0.701	0.496
	R1	94.492	93.715	93.963	94.079	0.154	0.145
BC	S	99.638	100.066	99.541	97.225	2.909	2.896
	R1	130.805	130.529	130.073	129.374	0.672	0.874
T							
Ship	**Surface Condition**	ϕ_3, **kN**	ϕ_2, **kN**	ϕ_1, **kN**	ϕ_{ext}^{21}, **kN**	GCI_{fine}^{21}, **%**	U_T, **kN**
KCS	S	1833.25	1827.69	1810.89	1802.58	0.574	10.388
	R1	3611.92	3621.12	3605.91	3582.67	0.807	29.104
KVLCC2	S	2025.11	2018.75	2009.71	1988.26	1.334	26.816
	R1	4371.42	4347.51	4390.60	4444.32	1.529	67.146
BC	S	774.04	784.54	763.94	742.56	3.499	26.730
	R1	1609.60	1597.42	1592.13	1588.07	0.319	5.077
J							
Ship	**Surface Condition**	ϕ_3	ϕ_2	ϕ_1	ϕ_{ext}^{21}	GCI_{fine}^{21}, **%**	U_T
KCS	S	0.7269	0.7279	0.7293	0.7319	0.451	0.0033
	R1	0.5457	0.5442	0.5452	0.5466	0.335	0.0018
KVLCC2	S	0.4596	0.4600	0.4573	0.4569	0.114	0.0005
	R1	0.3107	0.3116	0.3099	0.3082	0.703	0.0022
BC	S	0.5312	0.5276	0.5328	0.5444	2.719	0.0145
	R1	0.3590	0.3590	0.3591	0.3591	0.007	0.0000

Table 9. The obtained simulation uncertainties (U_{SN}) in the prediction of P_D (U_{P_D}), n (U_n), T (U_T) and J (U_J).

Ship	**KCS**		**KVLCC2**		**BC**	
Surface condition	U_{P_D}, MW	U_{P_D}, %	U_{P_D}, MW	U_{P_D}, %	U_{P_D}, MW	U_{P_D}, %
S	0.839	3.409	0.340	1.906	0.297	4.413
R1	0.692	1.068	0.653	1.167	1.506	7.421
Surface condition	U_n, rpm	U_n, %	U_n, rpm	U_n, %	U_n, rpm	U_n, %
S	0.341	0.343	0.510	0.720	2.918	2.932
R1	0.558	0.475	0.145	0.154	2.331	1.791
Surface condition	U_T, kN	U_T, %	U_T, kN	U_T, %	U_T, kN	U_T, %
S	60.185	3.323	26.819	1.334	60.185	3.323
R1	66.890	1.855	93.365	2.126	66.890	1.855
Surface condition	U_J	U_J, %	U_J	U_J, %	U_J	U_J, %
S	0.0047	0.638	0.0012	0.273	0.0180	3.374
R1	0.0019	0.348	0.0045	1.440	0.0073	2.041

4.2. Validation Study

Relative deviations between numerically obtained and extrapolated results are calculated using the following equation:

$$RD = \frac{\phi_{\mathrm{CFD}} - \phi_{\mathrm{EX}}}{\phi_{\mathrm{EX}}} \cdot 100\% \quad (15)$$

where ϕ_{CFD} is the certain hydrodynamic characteristic obtained using CFD and ϕ_{EX} is the certain hydrodynamic characteristic obtained using the ITTC 1978 Performance Prediction Method (PPM) and experimental results [30].

The obtained C_T for full-scale KCS and KVLCC2 is validated within [16] through comparison of the obtained numerical results with extrapolated values using original ITTC 1978 PPM, based on Equation (9). Within ITTC 1978 PPM, C_F is determined using the ITTC 1957 model-ship correlation line. In Table 10, the validation of the numerically obtained C_T for the smooth surface condition is presented. As can be seen from Table 10, the obtained results are in satisfactory agreement with the extrapolated results, i.e., the highest RD is obtained for BC and it is equal to −4.338%.

Table 10. The validation study for C_T.

Ship	C_T		RD, %
	CFD	EX	
KCS [16]	2.081	2.053	1.376
KVLCC2 [16]	1.795	1.724	4.107
BC	2.197	2.296	−4.338

The numerically obtained open water characteristics for all three propellers have been validated, with the towing tank results published in the literature [29,31,32]. It should be noted that CFD simulations of OWT are performed in full-scale, while experimental OWT are performed in model scale. Towing tank tests for all three investigated propellers are performed at Rn above $Rn = 2 \cdot 10^5$, as prescribed by ITTC [30]. In Figure 7, the comparison between the numerically and experimentally obtained open water characteristics is presented. From this figure, it can be seen that numerically obtained K_{TO}, $10K_{QO}$ and η_O are in satisfactory agreement with the experimentally obtained ones. Slightly higher RD between numerically and experimentally obtained K_{TO} and especially $10K_{QO}$ is obtained at lower J values, however, at higher J values, these RD are significantly lower.

The obtained results of the validation study for P_D and n are presented in Table 11, from which it can be concluded that satisfactory agreement is obtained. The highest obtained RD between numerical and extrapolated P_D is obtained for KVLCC2 and it is equal to −5.701%, while the highest obtained RD for n is obtained for BC and it is equal to −1.786%. The validation study for ship propulsion characteristics is presented in Table 12. From Table 12, it can be seen that the obtained RD for $1 - t$ are lower than 3.7%, for $1 - w$ are lower than 7.4% and for η_H are lower than 5.6% for all analyzed ships. It should be noted that slightly higher RD for $1 - w$ is obtained only for BC, and this can be attributed to the application of body force method. However, this RD is in line with previously published studies dealing with CFD simulations of SPT where the virtual disk model is applied [40,41]. The obtained RD for η_O are lower than 3.1%, for propeller efficiency behind ship (η_B) are lower than 3.8%, for η_R are lower than 2.9% and for η_D is lower than 6.2%. It should be noted that slightly higher RD for η_D is obtained only for KCS. However, in [42] where the authors carried out full-scale SPT for KCS using discretized propeller, η_D was equal to 0.766, which is also lower than the extrapolated result. From this result, the obtained η_D in this paper has RD equal to −3.394%. In Table 12, the validation for the obtained J, K_T and K_Q for self-propulsion point is shown as well. It can be seen that the obtained RD for J are lower than 5.7%, for K_T are lower than 4.1% and for K_Q are lower than 3.4% for all analyzed ships. Generally, the obtained RD presented in Tables 11 and 12 can be ascribed to different reasons. For example, insufficiently precise assessment of the nominal wake, as well as the

propeller performance in OWT can be related to the inaccurate assessment of J for self-propulsion point, which then leads to inaccurate assessment of other propulsion characteristics. In addition to this, the modelling error should also be taken into account, as, in the body force method, the effect of propeller is modelled, rather than propeller itself. Furthermore, there is a numerical error as well, which is related to the applied mesh and time step. Lastly, there are also aspects regarding the applied PPM for the extrapolation of towing tank results. Namely, in [25] four different PPM are compared, and it was shown that extrapolated values can significantly vary with respect to the applied PPM. Thus, it was shown that for BC, extrapolated value of P_D can vary up to 1.5%, for n up to 0.4%, for $1-t$ up to 0.5%, for $1-w$ up to 6.3%, for η_R up to 1.1% and for η_B up to 2.6%. In addition to these variations, experimental uncertainty should also be considered. Considering all above mentioned aspects, it can be concluded that satisfactory agreement is achieved for P_D, n and all propulsion characteristics.

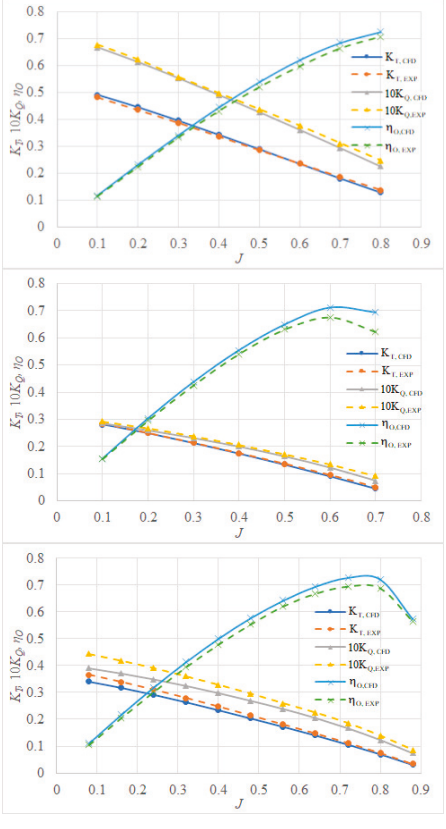

Figure 7. The validation study for open water characteristics of KP505 (**upper**), KP458 (**middle**) and WB (**lower**).

Table 11. The validation study for self-propulsion point.

Ship	n_{CFD}, rpm	n_{EX}, rpm	RD, %	$P_{D,CFD}$, MW	$P_{D,EX}$, MW	RD, %
KCS	99.341	100.359	−1.014	24.624	25.511	−3.476
KVLCC2	70.858	71.417	−0.784	17.850	18.929	−5.701
BC	99.541	101.351	−1.786	6.725	6.961	−3.392

Table 12. The validation study for propulsion characteristics.

Propulsion Characteristic	KCS		KVLCC2		BC	
	EX	CFD (*RD*,%)	EX	CFD (*RD*,%)	EX	CFD (*RD*,%)
$1-t$	0.853	0.867 (1.613)	0.810	0.820 (1.199)	0.794	0.764 (−3.722)
$1-w$	0.803	0.773 (−3.476)	0.695	0.668 (−3.904)	0.705	0.653 (−7.418)
η_H	1.062	1.122 (5.596)	1.165	1.227 (5.310)	1.126	1.171 (3.992)
η_O	0.690	0.700 (1.485)	0.620	0.600 (−3.146)	0.623	0.622 (−0.112)
η_B	0.698	0.702 (0.565)	0.623	0.600 (−3.752)	0.642	0.623 (−2.964)
η_R	1.011	1.002 (−0.906)	1.005	0.998 (−0.626)	1.030	1.000 (−2.855)
η_D	0.741	0.787 (6.193)	0.726	0.736 (1.359)	0.722	0.729 (0.910)
J	0.750	0.729 (−2.786)	0.472	0.457 (−3.145)	0.565	0.533 (−5.734)
K_T	0.161	0.165 (2.954)	0.155	0.149 (−4.055)	0.179	0.183 (2.312)
$10K_Q$	0.275	0.274 (−0.477)	0.187	0.180 (−3.449)	0.251	0.250 (−0.609)

5. The Impact of Hard Fouling on the Ship Performance

Within this section, the impact of hard fouling on the resistance, open water and propulsion characteristics is presented for three investigated ships. While detail investigation of the impact of hard fouling on resistance characteristics for KCS and KVLCC2 is presented in [16], within this study this impact is only briefly mentioned as emphasis is given to the impact of hard fouling on the ship performance, which is defined by propeller operating point.

5.1. The Impact of Hard Fouling on Resistance Characteristics

As demonstrated within [16,18] the impact of biofouling on each resistance component is different. Thus, the presence of biofouling causes the increase in C_F, decrease in C_W, while the impact of biofouling on $1+k$ value is almost negligible. Consequently, it is valuable to study the increase in R_T, due to the presence of hard fouling through analysis of decomposed R_T and the portion of each resistance component in R_T for certain fouling condition. In Figure 8, decomposition of R_T for three investigated ships and fouling conditions is presented. Additionally, within Figure 8 the portions of R_F, R_{VP} and R_W in R_T are given. From Figure 8, it is clear that, for all analyzed ships, the portion of R_F in R_T increases, due to the presence of hard fouling, and this increase is the highest for KCS, which can be attributed to the ship speed. Namely, KCS is investigated at the highest speed and therefore u_τ values along the KCS hull are higher than u_τ values along the KVLCC2 and BC hulls. Since k^+ values and consequently ΔU^+ values for given fouling condition and fluid properties depend only on u_τ values, those values are higher for KCS than for KVLCC2 and BC resulting in higher increases in C_F [16]. Additionally, C_F for rough surface condition at high Rn value depends solely on k/L value, i.e., relative roughness [16]. The portion of R_{VP} in R_T due to the presence of hard fouling has increased for KCS and BC, while for KVLCC2 this portion has decreased. Regardless of this, from Figure 8, it is clear that the absolute value of R_{VP}, due to the presence of hard fouling, has increased, which is expected, since the impact

of biofouling on $1 + k$ value is minimal [16]. Finally, the portion of R_W in R_T due to the presence of hard fouling decreases for all analyzed ships and this decrease is the highest for KCS, which can be also attributed to ship speed. What is more, from Figure 8 it is clear that absolute values of R_W due to the presence of hard fouling have decreased for all analyzed ships [16]. Generally, KVLCC2 is the most affected, due to the presence of hard fouling in terms of the increase in R_T, which can be seen from Figure 9. Thus, the increase in R_T due to the presence of hard fouling for KVLCC2 ranges from 63.8% (R6) to 120.9% (R1), for BC ranges from 59.5% (R6) to 114.6% (R1) and for KCS ranges from 49.9% (R6) to 95.8% (R1). This can be mostly attributed to the portion of R_V in R_T, since, due to the presence of biofouling R_V, significantly increases. The portion of R_V in R_T is the highest for KVLCC2 and for smooth surface condition this portion is equal to 99.46%, as R_W of KVLCC2 is negligible [28]. However, beside the portion of R_V in R_T, the ship speed also affects the increase in R_T, as already explained. Thus, the increase in R_T due to the presence of hard fouling is only slightly lower for BC than for KVLCC2 and the portion of R_V in R_T for smooth surface condition is equal to 83.6%. It should be noted that the significantly lower increase in R_T is obtained for KCS, as KCS has relatively large portion of R_W in R_T (for smooth surface condition this portion is equal to 24.7%). Due to the presence of hard fouling, R_W decreases, and, therefore, the increase in R_T for KCS is lower.

Figure 8. Decomposition of R_T for KCS (**upper**), KVLCC2 (**middle**) and BC (**lower**) for smooth and fouled surface condition.

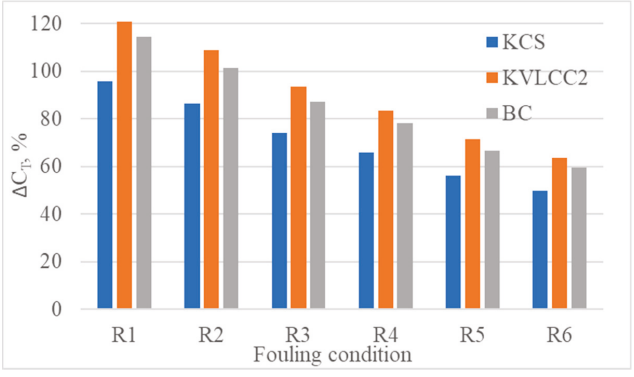

Figure 9. The impact of hard fouling on C_T.

5.2. The Impact of Hard Fouling on Open Water Characteristics

The impact of hard fouling (R1) on the propeller performance in open water conditions is presented in Figure 10. The obtained changes in K_{TO}, K_{QO} and η_O, due to the presence of hard fouling, are presented in Table 13. As can be seen from Figure 10 and Table 13, due to the presence of hard fouling K_{TO} has decreased and K_{QO} has increased resulting in significant reduction in η_O. As fouling severity increases (i.e., from R6 to R1), fouling penalties related to decrease in K_{TO} and increase in K_{QO} increase as well. Additionally, at higher J the fouling penalty related to decrease in η_O is higher. Therefore, it can be concluded that the ships operating at higher J values will experience a greater reduction in η_O, i.e., propeller fouling penalty on the ship performance will be greater. Thus, due to the presence of hard fouling ΔK_{TO} values for KP505 at $J = 0.6$ range from −6.22% (R6) to −12.05% (R1), for KP458 at $J = 0.4$ range from −7.44% (R6) to −14.45% (R1) and for WB at $J = 0.48$ range from −7.86% (R6) to −12.09% (R1). An increase in ΔK_{QO} values for KP505 at $J = 0.6$ range from 4.66% (R6) to 11.37% (R1), for KP458 at $J = 0.4$ range from 2.59% (R6) to 7.46% (R1) and for WB at $J = 0.48$ range from 3.77% (R6) to 11.19% (R1). Fouling penalties on the propeller performance in open water conditions can be ascribed to fouling impact on the skin friction and the pressure field. Thus, due to the presence of hard fouling on propeller surfaces wall shear stress (τ_w) increases, while the pressure difference between pressure and suction sides of propeller is reduced, which can be seen from Figures 11 and 12. In Figure 11, the obtained τ_w distributions at KP505 surface at $J = 0.7$ for both smooth and R1 surface condition are shown. It is clear that due to the presence of hard fouling τ_w values at KP505 surface are significantly increased resulting in increase in drag coefficient of the blade section and consequently in K_{QO}. In Figure 12 the obtained pressure distribution shown as distribution of pressure coefficient (C_P), which is defined as a ratio between pressure and $\frac{1}{2}\rho v_A^2$, at KP505 surface is presented. Since the magnitudes of C_P at both pressure and suction sides of fouled KP505 are significantly reduced, the pressure difference between pressure and suction sides is reduced as well, resulting in a decrease in the lift coefficient of the blade section and, consequently, in K_{TO}.

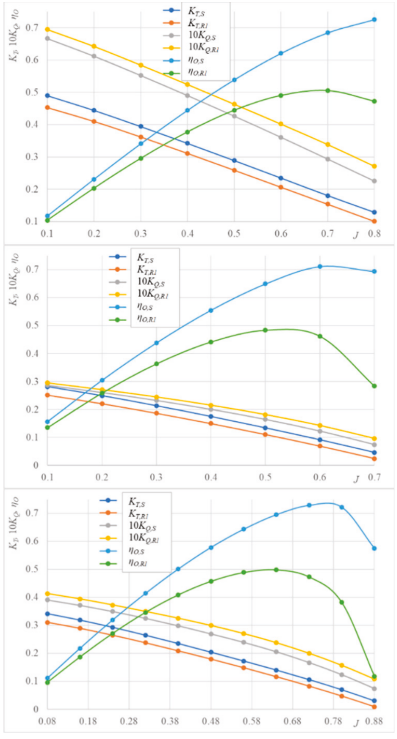

Figure 10. The impact of hard fouling (R1) on KP505 (**upper**), KP458 (**middle**) and WB (**lower**) performance in OWT.

Table 13. The obtained changes in K_{TO}, K_{QO} and η_O due to the presence of hard fouling.

Propeller	KP505			KP458			WB		
	$J = 0.6$			$J = 0.4$			$J = 0.48$		
Surface Condition	ΔK_{TO}, %	ΔK_{QO}, %	$\Delta\eta_O$, %	ΔK_{TO}, %	ΔK_{QO}, %	$\Delta\eta_O$, %	ΔK_{TO}, %	ΔK_{QO}, %	$\Delta\eta_O$, %
R1	−12.05	11.37	−21.03	−14.45	7.46	−20.39	−12.09	11.19	−20.93
R2	−10.77	9.56	−18.55	−12.81	6.11	−17.83	−11.18	9.75	−19.07
R3	−9.24	7.66	−15.69	−11.66	4.69	−15.62	−10.10	7.65	−16.49
R4	−8.13	6.49	−13.73	−9.72	3.81	−13.03	−9.39	6.34	−14.79
R5	−6.85	5.30	−11.54	−8.20	2.99	−10.87	−8.47	4.75	−12.62
R6	−6.22	4.66	−10.39	−7.44	2.59	−9.77	−7.86	3.77	−11.21

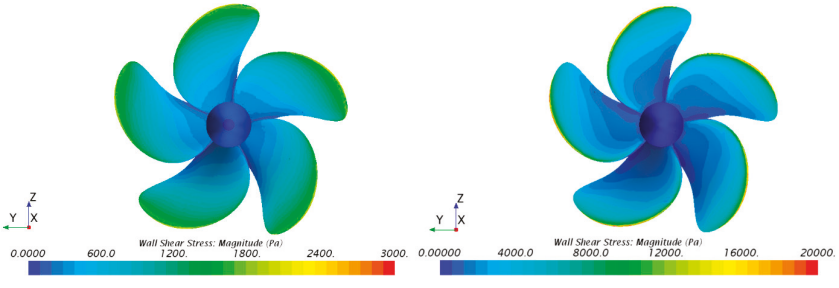

Figure 11. The obtained τ_w distribution for smooth (**left**) and R1 (**right**) surface condition for KP505.

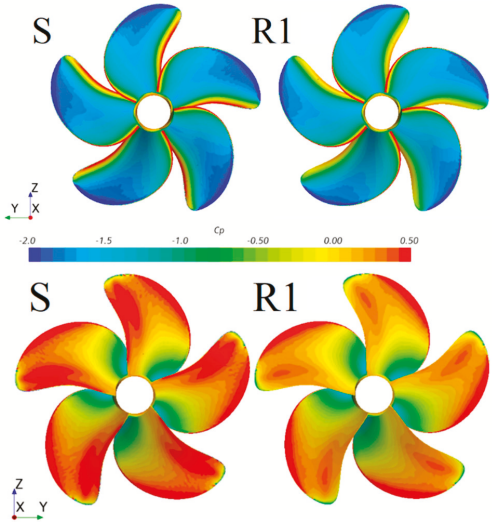

Figure 12. The obtained C_P distribution on KP505 surface for suction (**upper**) and pressure (**lower**) side of propeller.

5.3. The Impact of Hard Fouling on Propulsion Characteristics

After CFD simulations of resistance and open water tests are carried out, CFD simulations of SPT for smooth and fouled ships are performed. As said before, the fouling penalty on the ship performance should be considered through the change in P_D and n. The obtained increases in P_D and n due to the presence of hard fouling are presented in Figure 13. From this figure, it is clear that for surface conditions R1, R2 and R3 KVLCC2 is most affected due to the presence of hard fouling, while for surface conditions R4, R5 and R6 the fouling penalties for KVLCC2 and BC are almost the same and higher than fouling penalties for KCS. The obtained increases in P_D due to the presence of hard fouling for KVLCC2 range from 90.7% (R6) to 213.4% (R1), for BC range from 90.6% (R6) to 201.9% (R1) and for KCS range from 75.0% (R6) to 163.2% (R1), while the obtained increases in n for KVLCC2 range from 16.7% (R6) to 32.6% (R1), for BC range from 16.6% (R6) to 30.7% (R1) and for KCS range from 9.4% (R6) to 18.2% (R1). It is clear that the obtained increases in P_D are significantly higher than the obtained increases in P_E due to the presence of hard fouling, which can be related with the decrease in η_D. This highlights the importance of the assessment of the impact of biofouling on P_D rather than on P_E. The increase in P_D due to the presence of biofouling is dependent on many parameters. Thus, besides the portion of R_V in R_T, k/L and ship speed, which are important for the increase in P_E, it is also important at which J propeller operates and the way the propeller loading defined with K_T/J^2 is affected due to the presence of hard fouling. Namely, due to change in propeller loading, J value at which propeller operates changes as well. Thus, the change in J at which propeller operates as well as the absolute value of J is important, as, for ships which operate at higher J values, the fouling penalty on the propeller performance is higher.

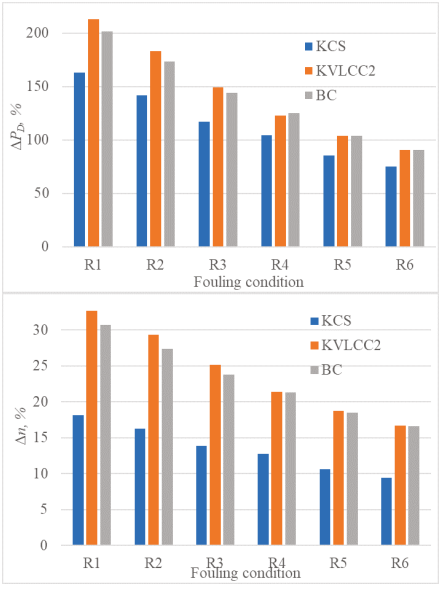

Figure 13. The obtained increases in P_D (**upper**) and n (**lower**) due to the presence of hard fouling.

In order to study the differences in the obtained fouling penalties more detailly, the impact of hard fouling on propulsion characteristics should be investigated. Within Tables 14–16, the obtained impact of hard fouling on propulsion characteristics is presented. From the obtained results, it is clear that most of the propulsion characteristics are affected by the presence of hard fouling on the hull and propeller surfaces. However, from Tables 14–16, it is clear that the impact of hard fouling on η_R is minimal, i.e., it is lower than 0.45% for all analyzed fouling conditions and ships. What is more, the impact of hard fouling on $1 - t$ is present, however, it is relatively low. Thus, due to the presence of hard fouling, the $1 - t$ value for KCS and KVLCC2 decreases, while for BC, it increases. It should be noted that the $1 - t$ value depends on many different parameters, i.e., on the fouling penalty related to increase in R_T, to propeller performance, as well as hull and propeller interaction. Obviously, the assessment of the effect of biofouling on $1 - t$ value is very complex. It should be noted that the obtained impact of hard fouling on $1 - t$ is within the obtained numerical uncertainty in the assessment of R_T and T. Additionally, within the assessment of $1 - t$, a modelling error is present as well, and it is related to turbulence modelling, modelling of the effect of ship propeller with body force method etc. Consequently, in order to assess this impact more accurately, numerical uncertainty as well as modelling error should be reduced through the application of more dense grids and lower time steps, as well as through the discretization of the propeller itself. Thus, a more accurate prediction of the impact of biofouling on $1 - t$ would be assessed. Therefore, based on the obtained results, it can be concluded that the impact of hard fouling on $1 - t$ is present, however, it is minimal. On the other hand, the impact of hard fouling on $1 - w$ is significant and detrimental, since it causes a decrease in the $1 - w$ value. Due to the presence of hard fouling, the obtained decreases in $1 - w$ values range from −6.99% (R6) to −11.7% (R1) for KCS, from −6.29% (R6) to −10.1% (R1) for KVLCC2 and from −8.46% (R6) to −12.0% (R1) for BC. The decrease in $1 - w$ can be attributed to slower flow around the propeller location for fouled ship, due to thicker boundary layer. The decrease in $1 - w$ has beneficial effect on η_H (Equation (11)). Thus, due to the presence of hard fouling the obtained $\Delta\eta_H$ values range from 6.13% (R6) to 11.3% (R1) for KCS, from 6.11% (R6) to 10.2% (R1) for KVLCC2 and from −11.3% (R6) to 16.9% (R1) for BC. Regardless of the fact that the decrease in $1 - w$ has beneficial effect on η_H, in general, the decrease in $1 - w$ has detrimental effect on η_D and P_D. Namely, the decrease in $1 - w$ points out

that the flow around propeller is slower and consequently propeller operating point is changed when compared with the smooth hull surface. Additionally, due to the presence of hard fouling, the nominal wake field behind the fouled ship is more inhomogeneous than nominal wake field behind the smooth ship, and because of this, the operating point is changed as well. Therefore, J for self-propulsion point decreases since v_A is lower. What is more, J for self-propulsion point decreases because of the increase in n as well. Due to the presence of hard fouling the obtained ΔJ values for self-propulsion point range from −15.0% (R6) to −25.3% (R1) for KCS, from −19.7% (R6) to −32.2% (R1) for KVLCC2 and from −21.5% (R6) to −32.6% (R1) for BC. The decrease in the J value is unfavorable, as KP 505, KP 458 and WB operate at J lower than J, for which the η_O function has a maximum value, which is common for all marine propellers. Consequently, due to the decrease in J value, η_O value decreases as well. The decrease in η_O value is related to the detrimental impact of hard fouling on the propeller performance in open water conditions. Thus, the obtained decreases in η_O values are higher than the obtained increases in η_H values. Due to the presence of hard fouling the obtained $\Delta\eta_O$ values range from −19.2% (R6) to −32.9% (R1) for KCS, from −21.1% (R6) to −37.3% (R1) for KVLCC2 and from −24.9% (R6) to −39.2% (R1) for BC. The obtained decreases in η_B values are similar to the ones obtained for η_O values, as the impact of hard fouling on η_R value is negligible. The presence of hard fouling, therefore, has two detrimental effects on η_O, because of detrimental effect on the open water characteristics and on the propeller operating point. These two effects can be equally meaningful. The importance of the impact of hard fouling on the propeller operating point can be seen from the obtained impact of biofouling on K_T values. Even though the presence of hard fouling on the propeller surfaces causes the decrease in K_T, due to the impact of hard fouling on the propeller operating point, K_T increases as J for self-propulsion point of fouled ship is lower than J for self-propulsion point of smooth ship. The obtained ΔK_T values due to the presence of hard fouling range from 26.8% (R6) to 42.6% (R1) for KCS, from 18.2% (R6) to 24.2% (R1) for KVLCC2 and from 15.1% (R6) to 22.1% (R1) for BC. The presence of hard fouling on hull and propeller surfaces causes an increase in K_Q due to two reasons. Firstly, due to the presence of hard fouling on propeller surfaces K_Q values in open water conditions are higher, and secondly due to the change in J for self-propulsion point K_Q value increases. The obtained increases in K_Q values due to the presence of hard fouling range from 33.6% (R6) to 59.6% (R1) for KCS, from 20.0% (R6) to 34.4% (R1) for KVLCC2 and from 20.2% (R6) to 35.3% (R1) for BC. Finally, from Tables 14–16, it is clear that the presence of hard fouling on the hull and propeller surfaces causes a significant decrease in η_D, since decreases in η_B are higher than increases in η_H. The obtained decreases in η_D values due to the presence of hard fouling range from −14.4% (R6) to −25.6% (R1) for KCS, from −16.1% (R6) to −31.0% (R1) for KVLCC2 and from −16.3% (R6) to −28.9% (R1) for BC. Since the impact of biofouling on η_D value is not negligible, the increases in P_E and P_D are not the same, and it is therefore necessary to investigate the impact of biofouling on P_D rather than on P_E. It should be noted that the results presented in this subsection are obtained for the presence of biofouling on both propeller and hull surfaces. For clean propeller surfaces and fouled ship hull the obtained results, i.e., trends may not be the same. Thus, Song et al. [22], have obtained slight increases in η_D values due to the presence of barnacles at hull surfaces, i.e., with a clean propeller. This can be attributed to the fact that the authors have obtained higher increases in η_H due to the presence of barnacles than decreases in η_B due to change in operating point. As a result of all this, the analysis of the impact of biofouling on propulsion characteristics is very important, i.e., the assessment of biofouling on the resistance characteristics and P_E is not sufficient.

Table 14. The obtained impact of hard fouling on the propulsion characteristics for KCS.

Propulsion Characteristic	S	R1	R2	R3	R4	R5	R6
$1-t$	0.867	0.852 −1.67%	0.857 −1.15%	0.858 −1.07%	0.858 −1.06%	0.856 −1.28%	0.856 −1.29%
$1-w$	0.773	0.682 −11.7%	0.690 −10.8%	0.699 −9.56%	0.707 −8.54%	0.714 −7.64%	0.719 −6.99%
η_H	1.122	1.249 11.3%	1.243 10.8%	1.227 9.39%	1.214 8.19%	1.199 6.89%	1.191 6.13%
η_O	0.700	0.470 −32.9%	0.489 −30.2%	0.514 −26.6%	0.527 −24.8%	0.553 −21.1%	0.566 −19.2%
η_R	1.002	0.998 −0.40%	1.000 −0.16%	0.999 −0.29%	1.000 −0.18%	1.001 −0.11%	1.000 −0.16%
η_D	0.787	0.585 −25.6%	0.607 −22.8%	0.630 −19.9%	0.639 −18.8%	0.663 −15.7%	0.674 −14.4%
J	0.729	0.545 −25.3%	0.560 −23.3%	0.579 −20.6%	0.592 −18.9%	0.609 −16.5%	0.620 −15.0%
K_T	0.165	0.236 42.6%	0.231 39.6%	0.224 35.6%	0.218 32.0%	0.214 29.3%	0.210 26.8%
$10K_Q$	0.274	0.436 59.6%	0.420 53.7%	0.402 47.0%	0.390 42.7%	0.374 36.9%	0.365 33.6%

Table 15. The obtained impact of hard fouling on the propulsion characteristics for KVLCC2.

Propulsion Characteristic	S	R1	R2	R3	R4	R5	R6
$1-t$	0.820	0.812 −1.00%	0.812 −0.91%	0.813 −0.88%	0.813 −0.79%	0.814 −0.66%	0.815 −0.56%
$1-w$	0.668	0.600 −10.1%	0.608 −9.02%	0.613 −8.19%	0.616 −7.75%	0.620 −7.17%	0.626 −6.29%
η_H	1.227	1.352 10.2%	1.337 8.91%	1.325 7.96%	1.320 7.55%	1.313 7.01%	1.302 6.11%
η_O	0.600	0.377 −37.3%	0.397 −34.0%	0.421 −29.9	0.448 −25.4%	0.461 −23.3%	0.474 −21.1%
η_R	0.998	0.997 −0.10%	1.002 0.35%	0.998 −0.02%	0.998 −0.02%	1.003 0.44%	1.001 0.28%
η_D	0.736	0.508 −31.0%	0.531 −27.8%	0.557 −24.4%	0.590 −19.8%	0.607 −17.6%	0.618 −16.1%
J	0.457	0.310 −32.2%	0.322 −29.7%	0.336 −26.6%	0.348 −24.0%	0.357 −21.8%	0.367 −19.7%
K_T	0.149	0.185 24.2%	0.183 23.4%	0.181 21.7%	0.182 22.4%	0.178 20.1%	0.176 18.2%
$10K_Q$	0.180	0.242 34.4%	0.236 31.0%	0.230 27.4%	0.225 24.7%	0.220 21.8%	0.216 20.0%

From the results presented in Tables 14–16, it can be concluded that the impact of hard fouling on the propulsion characteristics is the most pronounced for BC. Namely, the obtained changes in $1-t$, $1-w$, J, η_H, η_O and η_B due to the presence of hard fouling are largest for BC. What is more, the obtained changes in η_D due to the presence of hard fouling for fouling conditions R4, R5 and R6 are the largest for BC as well. However, for fouling conditions R1, R2 and R3 the obtained decreases in η_D are larger for KVLCC2 than for BC. For these fouling conditions, larger increase in η_H which is obtained for BC has surpassed the larger decrease in η_B, which has also been obtained for BC and because of this the obtained decreases in η_D are larger for KVLCC2. The largest changes in ΔK_T and ΔK_Q are obtained for KCS and this can be attributed to the fact that KCS operates at a higher J value than KVLCC2 and BC. The largest decrease in the ratio between K_T and K_Q has been noticed, due to the presence of hard fouling for KCS as well. Nevertheless, amongst the investigated ships, the decrease in η_O is the lowest, which can be attributed through the lowest obtained decrease in J for KCS. Namely, J for self-propulsion point decreases due to the increases in n and $1-w$. As can be seen from Figure 13,

the obtained increases in n due to the presence of hard fouling are significantly lower for KCS than for KVLCC2 and BC, while increases in $1 - w$ due to the presence of hard fouling are relatively similar for all analyzed ships, Tables 14–16.

Table 16. The obtained impact of hard fouling on the propulsion characteristics for BC.

Propulsion Characteristic	S	R1	R2	R3	R4	R5	R6
$1-t$	0.764	0.787 2.95%	0.785 2.76%	0.782 2.31%	0.781 2.22%	0.779 1.95%	0.779 1.88%
$1-w$	0.653	0.575 −12.0%	0.579 −11.3%	0.583 −10.7%	0.590 −9.68%	0.595 −8.89%	0.598 −8.46%
η_H	1.171	1.369 16.9%	1.356 15.8%	1.341 14.5%	1.325 13.2%	1.310 11.9%	1.303 11.3%
η_O	0.622	0.378 −39.2%	0.396 −36.4%	0.416 −33.1%	0.436 −30.0%	0.456 −26.8%	0.468 −24.9%
η_R	1.000	1.000 −0.03%	0.999 −0.09%	1.001 0.10%	0.999 −0.14%	0.999 −0.15%	1.001 0.10%
η_D	0.729	0.518 −28.9%	0.536 −26.4%	0.559 −23.4%	0.577 −20.8%	0.596 −18.2%	0.61 −16.3%
J	0.533	0.359 −32.6%	0.371 −30.3%	0.384 −27.8%	0.397 −25.6%	0.410 −23.1%	0.418 −21.5%
K_T	0.183	0.224 22.1%	0.221 20.8%	0.219 19.3%	0.217 18.4%	0.213 16.4%	0.211 15.1%
$10K_Q$	0.250	0.338 35.3%	0.331 32.5%	0.321 28.6%	0.314 26.0%	0.306 22.5%	0.300 20.2%

5.4. The Impact of Hard Fouling on the Flow Around Fouled Ship

The impact of hard fouling on the ship performance is investigated for three ships at their design speeds presented in Table 2. This resulted in different τ_w distributions for smooth surface condition, Figure 14. From this figure it is clear that the highest τ_w values are obtained for KCS, followed by BC and KVLCC2, which was expected as KCS is investigated at the highest design speed. As a result of this, the highest k^+ values are also obtained along the KCS hull, which can be seen from Figure 15. The obtained k^+ distributions for R1 fouling condition along the KCS, KVLCC2 and BC hull are shown. Since the highest k^+ values are obtained along the KCS hull, the highest ΔU^+ values are present as well, which resulted in more significant increase in τ_w and C_F for KCS than for BC and KVLCC2. The obtained τ_w distributions for R1 fouling condition along the KCS, KVLCC2 and BC hull are presented in Figure 16.

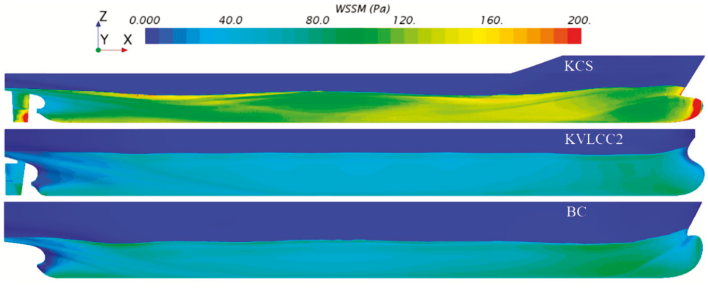

Figure 14. The obtained τ_w distributions for smooth surface condition along the KCS (**upper**), KVLCC2 (**middle**) and BC (**lower**) hull.

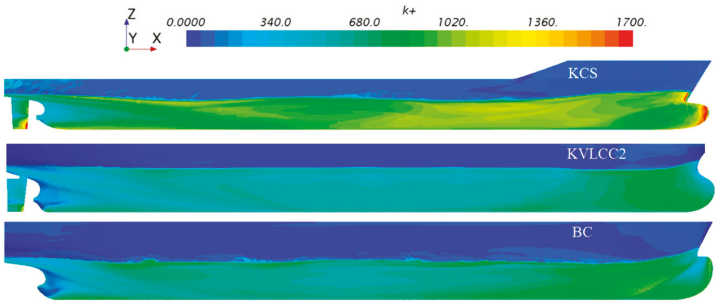

Figure 15. The obtained k^+ distributions for R1 fouling condition along the KCS (**upper**), KVLCC2 (**middle**) and BC (**lower**) hull.

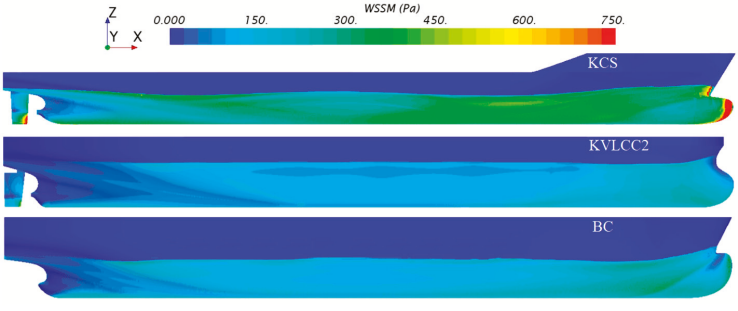

Figure 16. The obtained τ_w distributions for R1 fouling condition along the KCS (**upper**), KVLCC2 (**middle**) and BC (**lower**) hull.

The increase in τ_w along the hull causes a decrease in the velocity in the turbulent boundary layer, i.e., turbulent boundary layer thickness increases due to the presence of roughness, which can be seen from Figure 17. In this figure, boundary layers, which are defined as the distance between the hull surface and the point where the axial velocity magnitude of the flow reaches the proportion of 0.99 of the ship speed, are shown for smooth and R1 surface condition. The boundary layers for KCS are given at locations x = 30 m and x = 50 m, for KVLCC2 at locations x = 50 m and x = 70 m and for BC at x = 17.5 m and x = 35 m. The obtained increases in the boundary layer thickness, due to the presence of biofouling or roughness, is in line with previously published experimental results in the literature [43,44].

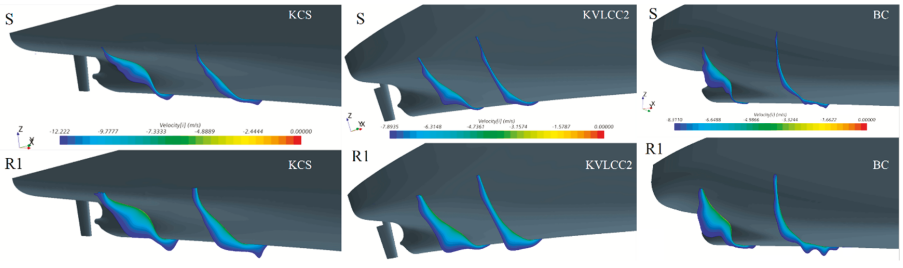

Figure 17. The obtained boundary layers for smooth ships (**upper**) and fouled ships with fouling condition R1 (**lower**).

As the boundary layer thickness increases it is obvious that the presence of hard fouling will cause the change in the nominal wake distribution. In Figure 18, the obtained contours of $1 - w_N$ for

smooth and fouled ships (R1) in the propeller disc plane are shown. It should be noted that $1 - w_N$ is calculated as the ratio between axial velocity and ship speed [45]. From this figure, it is clear that the presence of hard fouling causes the significant reduction of the flow in the propeller disc plane for all three investigated ships. This reduction causes the change of J for self-propulsion point and in that way, it affects propeller efficiency, as already explained.

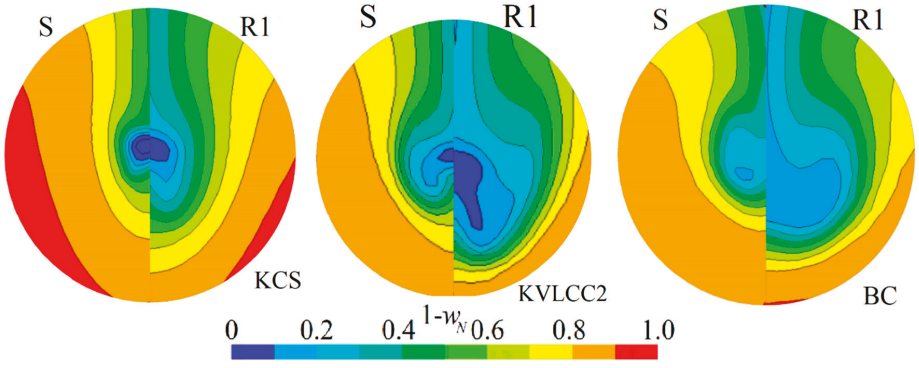

Figure 18. The obtained contours of $1 - w_N$ for smooth and fouled KCS (**left**), KVLCC2 (**middle**) and BC (**right**) with fouling condition R1 in the propeller disc plane.

In addition to the impact of hard fouling on τ_w values, the presence of hard fouling causes the change in pressure distribution along the hull. However, this change mainly occurs in the area near the stern of fouled ship [16]. In Figure 19, the obtained C_P distributions are presented for the area near the stern of investigated ships for smooth and R1 fouling conditions within CFD simulations of SPT. It should be noted that C_P is obtained as a ratio between pressure and $\frac{1}{2}\rho v^2$. From this figure, it is clear that due to the presence of hard fouling pressure recovery at the stern is reduced and because of this R_{VP} increases. Additionally, the impact of hull and propeller fouling on C_P distribution at the rudder can be noticed, i.e., C_P values at the rudder surface are slightly reduced.

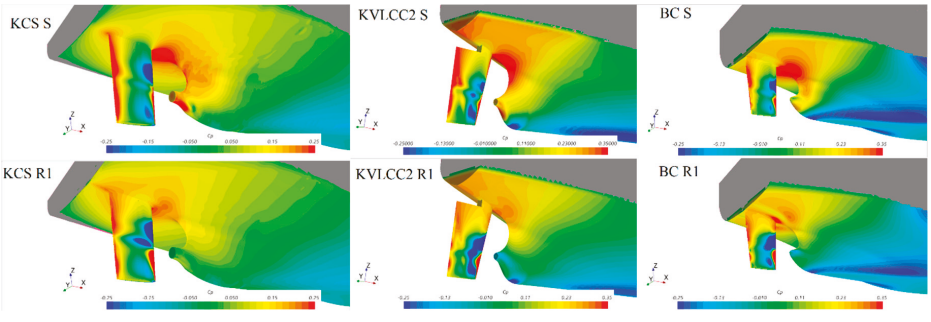

Figure 19. The impact of hard fouling on C_P distribution for the area near the stern.

In Figure 20, the obtained wave patterns around the hulls of the investigated ships for smooth surface condition and R1 fouling condition from CFD simulations of resistance tests are presented. From the comparison between wave pattern for smooth KCS and BC and wave pattern for KCS and BC fouled with R1, it can be noticed that due the presence of hard fouling wave elevations are reduced. On the other hand, wave elevations for KVLCC2 are almost the same for smooth and R1 fouling condition. The similar finding is noticed within [16,20]. Reductions of wave elevations and consequently R_W, due to the presence of hard fouling can be related to the increase in viscosity [15].

It can be concluded that the impact of hard fouling on the wave elevations is in agreement with the obtained decreases in R_W, i.e., for KCS and BC this impact is relevant, while for KVLCC2 this impact is negligible.

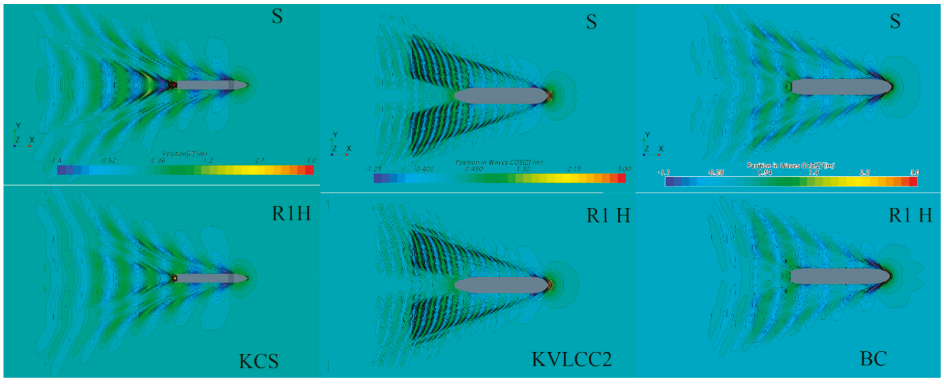

Figure 20. The obtained wave patterns around KCS (**left**), KVLCC2 (**middle**) and BC (**right**).

6. Conclusions

In this paper, the impact of hard fouling on ship performance for three different ship types is investigated. This impact is investigated using the CFD simulations of resistance, open water and self-propulsion tests. The impact of hard fouling is represented through the modification of wall function, i.e., through the implementation of the Grigson ΔU^+ model in the wall function within CFD solver. The verification study for grid size and time step is carried out, and grid and temporal uncertainties are estimated using GCI method. The verification study is performed for several key variables, i.e., K_{TO} and K_{QO} for open water test and for P_D, n, T and J for self-propulsion test. Relatively low simulation uncertainties are obtained for all key variables. Thereafter, the obtained results of the performed CFD simulations for smooth surface condition are validated with the extrapolated towing tank results using the ITTC 1978 Performance Prediction Method. Satisfactory agreement is achieved for all resistance, open water and propulsion characteristics. After the verification and validation study, the impact of hard fouling on the ship performance is studied in terms of the impact on resistance, open water and propulsion characteristics. The obtained results demonstrated the significant impact of hard fouling on the increase in frictional resistance and viscous resistance, as well for all three ships. It should be noted that the viscous resistance of KCS is mostly affected due to the presence of hard fouling, which is ascribed to the fact that KCS is investigated at the highest speed. As a result of this, friction velocity along the KCS hull is higher than along the KVLCC2 and BC hulls. Higher ΔU^+ values are obtained along the KCS hull in comparison with KVLCC2 and BC hulls, since the roughness Reynolds number and therefore ΔU^+ are dependent on the friction velocity. However, wave resistance has decreased for KCS and BC, due to the presence of hard fouling, while for KVLCC2, it is almost negligible, and has remained almost the same as for smooth surface condition. The impact of hard fouling on the wave resistance is in agreement with the impact of hard fouling on the wave elevations, i.e., wave elevations for KCS and BC due to the presence of hard fouling are decreased, while for KVLCC2, it remained the same as for the smooth surface condition. Therefore, the most affected ship due to the presence of hard fouling, related to the fouling penalty on the ship resistance, is KVLCC2. Obviously, beside the ship speed the portion of viscous resistance in total resistance is very important for the estimation of the fouling penalty on the ship resistance, as well as the ratio k/L. Significant detrimental effects due to the presence of hard fouling on the propeller performance in open water conditions are found. Thus, due to the presence of hard fouling on the propeller surfaces, K_{TO} decreases and K_{QO} increases, which results in a significant decrease in η_O. Namely, due to the

presence of hard fouling drag coefficient of propeller blade section increases, causing the increase in K_{QO}, and lift coefficient decreases, causing the decrease in K_{TO}. The impact of hard fouling on the ship performance is best reflected through the impact on the delivered power and propeller rotation rate. From the obtained results, it is clear that increases in the delivered power are significantly larger than increases in the effective power, due to the presence of hard fouling for all three investigated ships. Therefore, the impact of hard fouling on propulsion efficiency must not be neglected, especially for fouled ship and propeller. The impact of hard fouling on the delivered power and propeller rotation rate is most pronounced for KVLCC2 for fouling conditions R1, R2 and R3, while for R4, R5 and R6, the obtained changes in the ship performance due to hard fouling are similar for BC and KVLCC2. This can be attributed to different impact of hard fouling on propulsion characteristics, as the fouling penalty on effective power for R4, R5 and R6 fouling conditions is higher for KVLCC2 than for BC. Namely, the additional important parameter that affects the impact of biofouling on the ship performance is the value of advance coefficient for self-propulsion point, since it is demonstrated that ships which operate at higher values of advance coefficient will be more affected in terms of propeller performance in open water conditions than ships which operate at lower values of advance coefficient. The impact of hard fouling on propulsion characteristics is presented for all three ships. From the obtained results it can be seen that propulsion characteristics of BC are mostly affected due to the presence of hard fouling, as the obtained changes in $1-t$, $1-w$, J, η_H, η_O and η_B due to the presence of hard fouling are largest for BC. Additionally, the obtained changes in η_D due to the presence of hard fouling for fouling conditions R4, R5 and R6 are the largest for BC as well, while, for R1, R2 and R3, they are the largest for KVLCC2. The largest change in K_T and K_Q values due to the presence of hard fouling are obtained for KCS, which is expected as KCS operate with the highest advance coefficient. Finally, the impact of hard fouling on the flow around fouled ship is studied through the analysis of the impact on wall shear stress distribution, boundary layer thickness, nominal wake distributions, wave elevations and pressure distributions.

The paper provided several valuable insights related to the impact of hard fouling on the ship performance amongst different ship forms. Future study will be focused on investigations related to the impact of biofouling for systematic series of certain ship at different speeds, which will allow more comprehensive insight into the impact of biofouling on the ship performance will be assessed. In this paper, the investigations related to the impact of hard fouling on the ship performance are performed for the presence of hard fouling on both propeller and hull surfaces. If analyzed per unit area, the impact of propeller fouling condition on the ship performance is significantly more important than the impact of hull fouling condition. Therefore, the future studies will be also focused on the investigations related to the impact of solely propeller cleaning on the ship performance. Thus, relatively cheap and effective practice for achieving significant energy saving will be demonstrated. The optimization of maintenance schedule is an important operational measure for reducing ship emissions and the successful application of this measure relies on the accurate assessment of the impact of cleaning, i.e., the impact of biofouling on the ship performance. Currently, these predictions are carried out using performance monitoring. However, performance monitoring has several important drawbacks [8], and the approach presented in this paper presents another way for this assessment. The important benefit of the proposed approach over the performance monitoring is that fouling effects on the ship performance can be analyzed independently of all other additional resistances, which may occur during sailing. However, since drag characterization studies are performed only for limited number of fouling conditions, CFD approach based on the modified wall function approach is limited to these fouling conditions. For more comprehensive assessment there is a need for further drag characterization studies. Additionally, the investigations performed in this paper are carried out for hull surface, which is treated as a uniformly rough surface with certain roughness length scale determined using Equation (6), as done in most of the conventional CFD studies dealing with biofouling. Since the fouling pattern along the immersed surface is not uniform, future studies will be focused on the investigations of the influence of fouling settlement on the ship performance. The locations of niche

areas along the hull surface will be found from the literature and in that areas, wall function model for certain fouling condition will be implemented within the wall function of CFD solver. In that way, more realistic fouling conditions will be analyzed, and the investigations regarding the partial cleaning of the ship hull will be performed as well. Based on that, the proposed method can be used for the assessment of fouling penalties on the ship performance, after the fouling condition of the hull and propeller are determined by divers in the port.

Author Contributions: Conceptualization, A.F. and N.D.; methodology, A.F., N.D., I.M. and R.D.; software, A.F.; validation, A.F.; formal analysis, A.F.; investigation, A.F., N.D. and I.M.; resources, A.F.; writing—Original draft preparation, A.F., N.D., I.M. and R.D.; writing—Review and editing, A.F., N.D., I.M. and R.D.; visualization, A.F.; supervision, N.D. All authors have read and agreed to the published version of the manuscript.

Funding: This research received no external funding.

Conflicts of Interest: The authors declare no conflict of interest.

Abbreviations

AF	antifouling
CFD	Computational Fluid Dynamics
GCI	Grid Convergence Index
GHG	Greenhouse Gas
ITTC	International Towing Tank Conference
MRF	Moving Reference Frame
PPM	Performance Prediction Method
OWT	Open Water Test
RANS	Reynolds Averaged Navier-Stokes
RD	Relative Deviation
R1-R6	fouling conditions
S	Smooth surface condition
SPT	Self-Propulsion Test
VOF	Volume Of Fluid
HRIC	High Resolution Interface Capturing
FVM	Finite Volume Method
SST	Shear Stress Transport
KCS	Kriso Container Ship
KVLCC2	Kriso Very Large Crude Carrier 2
BC	Bulk Carrier
B	breadth (m)
B	smooth wall log-law intercept (-)
C_B	block coefficient (-)
C_F	frictional resistance coefficient (-)
C_P	pressure coefficient (-)
C_T	total resistance coefficient (-)
C_W	wave resistance coefficient (-)
c	chord length at radius $0.75R$ (m)
D	propeller diameter (m)
d	shaft diameter (m)
Fn	Froude number (-)
J	advance coefficient (-)
k	roughness length scale (μm)
k	form factor (-)
k^+	roughness Reynolds number (-)
K_T	thrust coefficient (-)
K_Q	torque coefficient (-)
K_{TO}	thrust coefficient in open water conditions (-)

K_{QO}	torque coefficient in open water conditions (-)
L_{pp}	length between perpendiculars (m)
L_{wl}	length of waterline (m)
n	propeller rate of revolution (rpm)
S	wetted surface area (m^2)
P	propeller pitch (m)
$\overline{p}$	mean pressure (Pa)
P_E	effective power (W)
P_D	delivered power at propeller (W)
Rn	Reynolds number (-)
R	propeller radius (m)
R_F	frictional resistance (N)
R_T	total resistance (N)
R_t	height of the largest barnacle (μm)
R_V	viscous resistance (N)
R_{VP}	viscous pressure resistance (N)
T	thrust (N)
T	time interval calculated as the ratio between ship length and speed (s)
T	draught (m)
t	thrust deduction fraction (-)
t	maximum thickness at radius $0.75R$ (mm)
$\overline{u}_i$	averaged velocity vector (m/s)
U^+	non-dimensional mean velocity (-)
U_G	grid uncertainty (-)
U_J	numerical uncertainty in the prediction of J (-)
U_n	numerical uncertainty in the prediction of n (-)
U_{P_D}	numerical uncertainty in the prediction of P_D (-)
U_T	time step uncertainty (-)
U_T	numerical uncertainty in the prediction of T (-)
u_τ	friction velocity (m/s)
v	speed (m/s)
V	ship design speed (kn)
y^+	non-dimensional wall distance (-)
w	wake fraction coefficient (-)
Z	number of blades (-)
$\%SC$	percentage of the surface coverage (-)
Δ	displacement (t)
ΔU^+	roughness function (-)
$\Delta\phi$	change in certain hydrodynamic characteristic (-)
∇	displacement volume (m^3)
η_B	propeller efficiency behind ship (-)
η_D	quasi-propulsive efficiency coefficient (-)
η_H	hull efficiency (-)
η_O	propeller efficiency in open water (-)
η_R	relative rotative efficiency (-)
κ	von Karman constant (-)
μ	dynamic viscosity coefficient (Pas)
ρ	fluid density (kg/m^3)
$\rho\overline{u'_i u'_j}$	Reynolds stress tensor (N/m^2)
$\overline{\tau}_{ij}$	mean viscous stress tensor (N/m^2)
τ_w	wall shear stress (N/m^2)
ϕ	certain hydrodynamic characteristic (-)
ϕ_{ext}^{21}	extrapolated value (-)
EXP	experimental

EX	extrapolated
M	ship model
R	fouled surface
S	smooth surface
1	fine grid/time step
2	medium grid/time step
3	coarse grid/time step

References

1. Bouman, E.A.; Lindstad, E.; Rialland, A.I.; Stromman, A.H. State-of-the-art technologies, measures, and potential for reducing GHG emissions from shipping—A review. *Transp. Res. D Transp. Environ.* **2017**, *52*, 408–421. [CrossRef]
2. Corbett, J.J.; Wang, H.; Winebrake, J.J. The effectiveness and costs of speed reductions on emissions from international shipping. *Transp. Res. D Transp. Environ.* **2009**, *14*, 593–598. [CrossRef]
3. Poulsen, R.T.; Johnson, H. The logic of business vs. the logic of energy management practice: Understanding the choices and effects of energy consumption monitoring systems in shipping companies. *J. Clean. Prod.* **2016**, *112*, 3785–3797. [CrossRef]
4. Adland, R.; Cariou, P.; Jia, H.; Wolff, F.C. The energy efficiency effects of periodic ship hull cleaning. *J. Clean. Prod.* **2018**, *178*, 1–13. [CrossRef]
5. Farkas, A.; Degiuli, N.; Martić, I. Towards the prediction of the effect of biofilm on the ship resistance using CFD. *Ocean Eng.* **2018**, *167*, 169–186. [CrossRef]
6. Schultz, M.P.; Bendick, J.A.; Holm, E.R.; Hertel, W.M. Economic impact of biofouling on a naval surface ship. *Biofouling* **2011**, *27*, 87–98. [CrossRef] [PubMed]
7. Uzun, D.; Demirel, Y.K.; Coraddu, A.; Turan, O. Time-dependent biofouling growth model for predicting the effects of biofouling on ship resistance and powering. *Ocean Eng.* **2019**, *191*, 106432. [CrossRef]
8. Farkas, A.; Song, S.; Degiuli, N.; Martić, I.; Demirel, Y.K. Impact of biofilm on the ship propulsion characteristics and the speed reduction. *Ocean Eng.* **2020**, *199*, 107033. [CrossRef]
9. Yeginbayeva, I.A.; Granhag, L.; Chernoray, V. Review and historical overview of experimental facilities used in hull coating hydrodynamic tests. *Proc. Inst. Mech. Eng. Part M J. Eng. Marit. Environ.* **2019**, *233*, 1240–1259. [CrossRef]
10. Uzun, D.; Ozyurt, R.; Demirel, Y.K.; Turan, O. Does the barnacle settlement pattern affect ship resistance and powering? *Appl. Ocean Res.* **2020**, *95*, 102020. [CrossRef]
11. Demirel, Y.K.; Uzun, D.; Zhang, Y.; Fang, H.C.; Day, A.H.; Turan, O. Effect of barnacle fouling on ship resistance and powering. *Biofouling* **2017**, *33*, 819–834. [CrossRef] [PubMed]
12. Schultz, M.P. Frictional resistance of antifouling coating systems. *J. Fluids Eng.* **2004**, *126*, 1039–1047. [CrossRef]
13. Demirel, Y.K.; Song, S.; Turan, O.; Incecik, A. Practical added resistance diagrams to predict fouling impact on ship performance. *Ocean Eng.* **2019**, *186*, 106112. [CrossRef]
14. Schultz, M.P. Effects of coating roughness and biofouling on ship resistance and powering. *Biofouling* **2007**, *23*, 331–341. [CrossRef]
15. Demirel, Y.K.; Turan, O.; Incecik, A. Predicting the effect of biofouling on ship resistance using CFD. *Appl. Ocean Res.* **2017**, *62*, 100–118. [CrossRef]
16. Farkas, A.; Degiuli, N.; Martić, I. An investigation into the effect of hard fouling on the ship resistance using CFD. *Appl. Ocean Res.* **2020**, *100*, 102205. [CrossRef]
17. Song, S.; Demirel, Y.K.; Atlar, M. An investigation into the effect of biofouling on the ship hydrodynamic characteristics using CFD. *Ocean Eng.* **2019**, *175*, 122–137. [CrossRef]
18. Farkas, A.; Degiuli, N.; Martić, I. Impact of biofilm on the resistance characteristics and nominal wake. *Proc. Inst. Mech. Eng. Part M J. Eng. Marit. Environ.* **2020**, *234*, 59–75. [CrossRef]
19. Andersson, J.; Oliveira, D.R.; Yeginbayeva, I.; Leer-Andersen, M.; Bensow, R.E. Review and comparison of methods to model ship hull roughness. *Appl. Ocean Res.* **2020**, *99*, 102119. [CrossRef]
20. Song, S.; Demirel, Y.K.; Muscat-Fenech, C.D.M.; Tezdogan, T.; Atlar, M. Fouling effect on the resistance of different ship types. *Ocean Eng.* **2020**, *216*, 107736. [CrossRef]

21. Song, S.; Demirel, Y.K.; Atlar, M.; Dai, S.; Day, S.; Turan, O. Validation of the CFD approach for modelling roughness effect on ship resistance. *Ocean Eng.* **2020**, *200*, 107029. [CrossRef]
22. Song, S.; Demirel, Y.K.; Atlar, M. Penalty of hull and propeller fouling on ship self-propulsion performance. *Appl. Ocean Res.* **2020**, *94*, 102006. [CrossRef]
23. Leer-Andersen, M.; Larsson, L. An Experimental/Numerical Approach for Evaluating Skin Friction on Full-Scale Ships with Surface Roughness. *J. Mar. Sci. Technol.* **2003**, *8*, 26–36. [CrossRef]
24. Bradshaw, P. A Note on "Critical Roughness Height" and "Transitional Roughness". *Phys. Fluids* **2000**, *12*, 1611–1614. [CrossRef]
25. Farkas, A.; Degiuli, N.; Martić, I. Assessment of hydrodynamic characteristics of a full-scale ship at different draughts. *Ocean Eng.* **2018**, *156*, 135–152. [CrossRef]
26. IMO. *Third IMO GHG Study 2014*; International Maritime Organization (IMO): London, UK, 2014.
27. Kim, W.J.; Van, S.H.; Kim, D.H. Measurement of flows around modern commercial ship models. *Exp. Fluids* **2001**, *31*, 567–578. [CrossRef]
28. Hino, T.; Kenkyujo, K.G.A. *Proceedings of CFD Workshop Tokyo 2005*; National Maritime Research Institute: Tokyo, Japan, 2005.
29. Brodarski Institute. *Report 6389-M. Technical Report*; Brodarski Institute: Zagreb, Croatia, 2014.
30. ITTC. Recommended procedures and guidelines. In *1978 ITTC Performance Prediction Method*; ITTC: Bournemouth, UK, 1999.
31. Larsson, L.; Stern, F.; Visonneau, M.; Hino, T.; Hirata, N.; Kim, J. *Proceedings, Tokyo 2015 Workshop on CFD in Ship Hydrodynamics*; NMRI: Tokyo, Japan, 2015.
32. SIMMAN. 2008. Available online: http://www.simman2008.dk/ (accessed on 1 September 2020).
33. Farkas, A.; Degiuli, N.; Martić, I. Numerical investigation into the interaction of resistance components for a series 60 catamaran. *Ocean Eng.* **2017**, *146*, 151–169. [CrossRef]
34. Farkas, A.; Degiuli, N.; Martić, I.; Ančić, I. Performance prediction method for fouled surfaces. *Appl. Ocean Res.* **2020**, *99*, 102151. [CrossRef]
35. Tezdogan, T.; Demirel, Y.K.; Kellett, P.; Khorasanchi, M.; Incecik, A.; Turan, O. Full-scale unsteady RANS CFD simulations of ship behaviour and performance in head seas due to slow steaming. *Ocean Eng.* **2015**, *97*, 186–206. [CrossRef]
36. Terziev, M.; Tezdogan, T.; Incecik, A. Application of eddy-viscosity turbulence models to problems in ship hydrodynamics. *Ships Offshore Struct.* **2020**, *15*, 511–534. [CrossRef]
37. Terziev, M.; Tezdogan, T.; Oguz, E.; Gourlay, T.; Demirel, Y.K.; Incecik, A. Numerical investigation of the behaviour and performance of ships advancing through restricted shallow waters. *J. Fluid Struct.* **2018**, *76*, 185–215. [CrossRef]
38. Owen, D.; Demirel, Y.K.; Oguz, E.; Tezdogan, T.; Incecik, A. Investigating the effect of biofouling on propeller characteristics using CFD. *Ocean Eng.* **2018**, *159*, 505–516. [CrossRef]
39. Song, S.; Demirel, Y.K.; Atlar, M. Propeller performance penalty of biofouling: Computational fluid dynamics prediction. *J. Offshore Mech. Arct.* **2020**, *142*. [CrossRef]
40. Choi, J.E.; Min, K.S.; Kim, J.H.; Lee, S.B.; Seo, H.W. Resistance and propulsion characteristics of various commercial ships based on CFD results. *Ocean Eng.* **2010**, *37*, 549–566. [CrossRef]
41. Gaggero, S.; Villa, D.; Viviani, M. An extensive analysis of numerical ship self-propulsion prediction via a coupled BEM/RANS approach. *Appl. Ocean Res.* **2017**, *66*, 55–78. [CrossRef]
42. Castro, A.M.; Carrica, P.M.; Stern, F. Full scale self-propulsion computations using discretized propeller for the KRISO container ship KCS. *Comput. Fluids* **2011**, *51*, 35–47. [CrossRef]
43. Schultz, M.P.; Flack, K.A. The rough-wall turbulent boundary layer from the hydraulically smooth to the fully rough regime. *J. Fluid Mech.* **2007**, *580*, 381. [CrossRef]
44. Flack, K.A.; Schultz, M.P.; Connelly, J.S. Examination of a critical roughness height for outer layer similarity. *Phys. Fluids* **2007**, *19*, 095104. [CrossRef]
45. Farkas, A.; Degiuli, N.; Martić, I.; Dejhalla, R. Numerical and experimental assessment of nominal wake for a bulk carrier. *J. Mar. Sci. Technol.* **2019**, *24*, 1092–1104. [CrossRef]

Journal of
Marine Science and Engineering

MDPI

Article

A Discrete-Forcing Immersed Boundary Method for Moving Bodies in Air–Water Two-Phase Flows

Haixuan Ye *, Yang Chen and Kevin Maki

Department of Naval Architecture and Marine Engineering, University of Michigan, Ann Arbor, MI 48109, USA; chanyang@umich.edu (Y.C.); kjmaki@umich.edu (K.M.)

* Correspondence: hxye@umich.edu

Received: 24 September 2020; Accepted: 13 October 2020; Published: 19 October 2020

Abstract: For numerical simulations of ship and offshore hydrodynamic problems, it is challenging to model the interaction between the free surface and moving complex geometries. This paper proposes a discrete-forcing immersed boundary method (IBM) to efficiently simulate moving solid boundaries in incompressible air–water two-phase flows. In the present work, the air–water two-phase flows are modeled using the Volume-of-Fluid (VoF) method. The present IBM is suitable for unstructured meshes. It can be used combined with body-fitted wall boundaries to model the relative motions between solid walls, which makes it flexible to use in practical applications. A field extension method is used to model the interaction between the air–water interface and the immersed boundaries. The accuracy of the method is demonstrated through validation cases, including the three-dimensional dam-break problem with an obstacle, the water exit of a circular cylinder, and a ship model advancing with a rotating semi-balanced rudder. The flow field, free-surface profile and force on the immersed boundaries (IBs) are in good agreement with experimental data and other numerical results.

Keywords: immersed boundary method; air–water two-phase flows; VoF method; OpenFOAM; finite volume method

1. Introduction

Incompressible air–water two-phase flows are of practical interest in the ship and offshore industries. When complex geometries are involved, such simulations are challenging because it is non-trivial to generate high quality meshes near the geometries, especially when there is relative motion between boundaries of the domain. Techniques such as deforming meshes, sliding meshes, overset meshes and IBMs are commonly used to simulate both single-phase and two-phase flows around moving boundaries.

The identifying feature of IBMs is that the grid lines do not need to conform the solid boundaries. The governing equations are solved on the background meshes, and the effects of the solid boundaries are introduced into the governing equations through interpolation. As a result, the effort to generate high-quality body-fitted meshes is not required. The quality of meshes with respect to non-orthogonality and skewness is also well preserved for arbitrary body motions.

The IBM is first proposed by Peskin [1] to simulate the blood flow in the heart, in which the IBM is used to represent the elastic heart walls. Since then, IBMs have become increasingly popular for the simulations of single-phase flows around boundaries with complex shapes at relatively low Reynolds numbers. Attempts are successfully made to simulate elastic boundaries [2–4] and rigid boundaries [5–7] on both structured and unstructured meshes.

Compared with body-fitted meshes, one of the most notable disadvantages of IBMs is that the near-wall cell spacing is difficult to control. For body-fitted meshes, prism layers with large aspect ratios can be used in the near-wall region to resolve the boundary layer which is especially thin at high

Reynolds numbers. Whereas, IBMs have to refine the near-wall cells in all directions to achieve the similar cell spacing in the wall-normal direction as its body-fitted counterpart. This disadvantage is one of the main reasons why IBMs are more developed for low-Reynolds-number flows. Fadlun [8] extends Mohd-Yusof's work [7] to three dimensions and successfully simulates the turbulent flow inside an axisymmetric piston-cylinder assembly. For high Reynolds-number applications, large eddy simulations (LES) is one favourable choice for the implementation of the IBMs, since the requirement of the near-wall mesh resolution for LES is inline with the IBMs. Balaras [9] proposes a discrete-forcing IBM to couple with a LES solver to simulate the turbulent flows inside a channel with a wavy bottom. Very good agreement is achieved with other numerical data. Choi et al. [10] proposes to reconstruct the wall normal and tangential components of velocity separately near the IB surfaces for turbulent-flow simulations. A power-law function is used for the tangential component to represent the near-wall velocity profile at high Reynolds numbers. Good agreement with other computational and experimental results is reported. However, the choice of the constants in the power-law function is case specific. Reynolds-Averaged Navier-Stokes (RANS) simulations is another commonly used technique for turbulent flows. Since the near-wall mesh resolution is not always enough to fully resolve the boundary-layer flow for a RANS simulation, a wall function can be used to predict the correct wall shear stress on the immersed boundary. Kalitzin et al. [11] couples an IBM into a RANS solver with both the Spalart–Allmaras and $k-\omega$ SST turbulence models. Wall functions are used to alleviate the requirement of the near-wall cell spacing. The surface pressure and skin friction on the T106 turbine blade passage in turbulent flows are well predicted. Capizzano [12] proposes a two-layer approach to simulate various 2D and 3D airfoils. In his approach, the numerical result is composed of the solution via a boundary-layer equation in the near-wall region, and the solution in the outer region via the compressible RANS equations.

In recent years, an increasing amount of research has been conducted on the implementation of IBMs for air–water two-phase flows. Dommermuth et al. [13] develops an approach combining a penalty method and a VoF [14,15] method to simulate breaking waves around ships and the resulting hydrodynamic forces. A free-slip boundary condition is imposed on the hull surface, which leads to solutions with smaller velocity gradient near the slip boundary. Although the boundary condition is sufficient for many marine flows, it is not appropriate for cases where the no-slip hull boundary condition is important.

Sanders et al. [16] presents a level-set two-phase flow solver employing a finite difference IBM. The solver is validated by solving the decay of the heave motion of a buoyant cylinder and the roll motion of a box in 2D. It seems that the method has not been extended to 3D or complex geometries.

Shen and Chan [17] propose a methodology that combines a discrete-forcing IBM and the VoF method to simulate flow interactions between free-surface waves and submerged solid bodies in 2D. Good agreement of the free-surface profile is presented. However, no additional boundary condition of the volume fraction on the IB needs to be considered since the solid bodies are fully submerged.

Yang and Stern [18] present a combined sharp interface IB/level-set Cartesian grid method for the LES simulations of 3D free-surface flows. The contact angle boundary condition on the IB is implemented to enforce the boundary condition of the level-set function ϕ, which requires the linear interpolation of ϕ in the vicinity of the IB. A series of simulations, including flows around simple geometries and ship hulls, are performed. The capability of the solver is demonstrated through the comparison of the flow field and the free-surface profile.

Sun and Sakai [19] present a numerical model that combines an IBM and the VoF method for simulating the two-phase flow in a twin screw kneader, which has two counter-rotating screw elements. The free-surface boundary condition of the volume fraction near the IB is enforced by either a simple dilation method, or by solving an additional "extension" equation introduced by Sussman [20].

Calderer et al. [21] proposes a new level-set IBM for solving 3D fluid-structure interaction problems. The spatially-filtered N-S equations are used as governing equations, and they are solved using the fractional step method on curvilinear grids. The boundary conditions on the IBs are enforced

through interpolation and enforcement of the velocity in the cells in the vicinity of the IBs. A Neumann boundary condition is applied to the level set function at the IB. A two-step approach is proposed to compute the force and moment on the IB by projecting the pressure and the viscous stress to a set of grid faces that encloses the IB. The accuracy of the solver is demonstrated by a series of test cases including water entry and exit of a horizontal circular cylinder, free roll decay of different floating geometries, and wedge impact on the free-surface.

In view of the previous work, the combined usage of IBM and air–water two-phase flow solvers especially for ship hydrodynamic flows is not explored as much as the application of IBMs for single-phase flows. Most of the methods are focused on using Cartesian grids, and require the interpolation for either the level-set function or the volume fraction in a similar way for the enforcement of the velocity boundary condition on the IBs. In addition, the benefit of the combined usage of unstructured body-fitted meshes and IBMs has not been well explored. In the previous work [22], we have proposed a complete development of a second-order IBM for single-phase applications of both laminar and turbulent flows. Careful verification and validation are carried out to demonstrate the capability of the method. In this paper, we aim to extend our previous work for the simulations of air–water two-phase flows. The flow field is governed by the RANS equations and the Spalart–Allmaras turbulence model. The VoF method is used to track the air–water interface. The dilation method introduced in [19] is adopted to deal with the intersection between the air–water interface and IBs. The goal of the implementation is to develop a solver that is suitable and efficient for ship hydrodynamic applications with minimal modification from the IB single-phase solver. It should be noted that for many ship hydrodynamic applications where turbulent flow separation important, there are other choices, such as detached-eddy simulations (DES) or LES, that may better resolve the flow. However, RANS simulations are still widely used in both academic and industrial fields because of the balance of computational cost and accuracy.

The paper is structured as follows: the numerical methods are introduced in Section 2, including the governing equations and coupling of the IBM with the two-phase flow solver. The results of the validation cases are presented in Section 3, including the 3D dam-break problems with an obstacle, water exit of a circular cylinder and a KRISO container ship (KCS) model advancing with a rotating rudder. Comparisons as for the flow field, free-surface profile and force on the IBs are made with experimental data and other numerical results. Specifically, for the simulation of the KCS model, unstructured body-fitted mesh is used for the hull and the fixed rudder horn, and the IBM is used to represent only the rotating rudder blade. Thereby, the benefit of the present IBM for combined usage with unstructured body-fitted approaches is demonstrated.

2. Numerical Methods

2.1. Governing Equations

In this work, the air–water two-phase incompressible turbulent flows are simulated by the RANS equations:

$$\nabla \cdot \mathbf{u} = 0 \tag{1}$$

$$\frac{\partial \rho \mathbf{u}}{\partial t} + \nabla \cdot (\rho \mathbf{u}\mathbf{u}) = \nabla \cdot \left[\rho \nu_{\text{eff}} \left(\nabla \mathbf{u} + \nabla \mathbf{u}^T \right) \right] - \nabla p_{\text{rgh}} - \mathbf{g} \cdot \mathbf{x} \nabla \rho + \mathbf{f} \tag{2}$$

in which, $\mathbf{u}$ is the velocity; $\nu_{\text{eff}} = \nu + \nu_t$ is the effective viscosity; ν and ν_t are the kinematic viscosity and turbulent viscosity, respectively; $p_{\text{rgh}} = p - \rho \mathbf{g} \cdot \mathbf{x}$ is the dynamic pressure; p is the total pressure; $\mathbf{g}$ is the gravitational vector; $\mathbf{x}$ is the position vector; $\mathbf{f}$ is the body force term introduced via the IBM to enforce proper boundary conditions on the IB surfaces. The calculation of $\mathbf{f}$ is discussed later.

2.2. Air–Water Two Phase Flow Modelling

The VoF method is applied to solve the air–water flows. The fluid volume fraction α is introduced to represent the different fluids. The transport equation for α is written as:

$$\frac{\partial \alpha}{\partial t} + \nabla \cdot (\mathbf{u}\alpha) + \nabla \cdot [\mathbf{u}_r(1-\alpha)\alpha] = 0 \tag{3}$$

in which, $\mathbf{u}_r$ is a compression velocity, and its value at face centers $\mathbf{u}_{r,f}$ is calculated by:

$$\mathbf{u}_{\mathrm{r,f}} = \mathbf{n}_f \min\left\{C_\alpha \frac{|\phi|}{|\mathbf{S}_f|}, \max\left(\frac{|\phi|}{|\mathbf{S}_f|}, 1\right)\right\} \tag{4}$$

in which $\mathbf{S}_f$ is the face area vector and its direction is the face normal direction. ϕ is the velocity flux, C_α is the compression coefficient, and $\mathbf{n}_f$ is the interface normal vector. Larger values of C_α permit greater compression of the smeared layer at the interface, but it can result in the decreasing accuracy for the calculation of the surface curvature. For all the simulations in this article C_α is set to be 1.5.

The last term in Equation (3) represents an artificial compression term, and only appears near the air–water interface to confine the smearing of α. As a result, the method numerically represents the air–water interface as a thin layer instead of a sharp boundary.

The different fluid phases (air or water) are indicated by different values of α, as shown in Equation (5).

$$\begin{cases} \alpha = 0, & \text{air} \\ \alpha = 1, & \text{water} \\ 0 < \alpha < 1, & \text{near the interface} \end{cases} \tag{5}$$

The boundary condition of α at the intersection of the interface and the solid wall is provided through the contact-angle boundary condition:

$$\mathbf{n}_f \cdot \mathbf{n}_B = \cos\theta \tag{6}$$

in which, $\mathbf{n}_f$ is the air–water interface normal vector pointing from air to water; $\mathbf{n}_B$ is the normal vector on the wall pointing from the fluid phase to the solid phase; θ is the contact angle.

$\mathbf{n}_f$ is calculated using the gradient of α at the air–water interface as:

$$\mathbf{n}_f = \frac{(\nabla\alpha)_f}{|(\nabla\alpha)_f + \delta|} \tag{7}$$

in which, δ is a small number used to stabilize the simulations.

In the present work, a neutral contact angle $\theta = \pi/2$ is assumed. Substitution of Equation (7) into Equation (6) yields the homogeneous Neumann boundary condition of α on the wall:

$$\mathbf{n}_f \cdot \mathbf{n}_B = \frac{(\nabla\alpha)_f}{|(\nabla\alpha)_f + \delta|}\mathbf{n}_B = 0 \qquad \nabla_n \alpha = 0 \tag{8}$$

Subsequently, the density and viscosity fields in the momentum equation Equation (2) is calculated as:

$$\rho = \alpha\rho_w + (1-\alpha)\rho_a \quad \text{and} \quad \nu = \alpha\nu_w + (1-\alpha)\nu_a \tag{9}$$

where the subscript w and a represent water and air, respectively.

2.3. Immersed Boundary Formulation

The IBM developed in our previous work [22] is adopted for the calculation of the body force term $\mathbf{f}$ in the momentum equation. The first step is to divide into three domains with respect to

the IB surface $\mathcal{S}$, which are the solid domain, forcing domain and the fluid domain. The resultant computation domain for a circular boundary is shown in Figure 1 as an example.

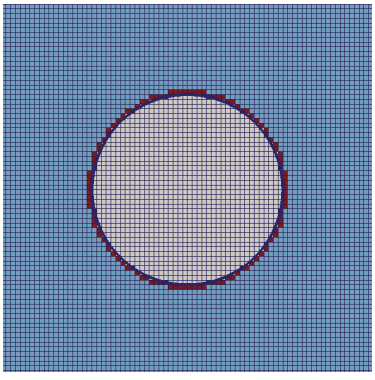

Figure 1. Categories of domains: a. *solid* domain: white cells; b. *forcing* domain: red cells; c. *fluid* domain: blue cells.

The body force term $\mathbf{f}$ will then be imposed in the forcing and solid domains to represent the proper boundary conditions on the IB surface. Similar to the method for single-phase flows, $\mathbf{f}$ is calculated by:

$$\mathbf{f} = \frac{\partial \rho \mathbf{u}^*}{\partial t} + \nabla \cdot (\rho \mathbf{u}^* \mathbf{u}^*) - \nabla \cdot \left[\rho \nu_{\text{eff}} \left(\nabla \mathbf{u}^* - \nabla \mathbf{u}^{*T} \right) \right] + \nabla p_{\text{rgh}} + \mathbf{g} \cdot \mathbf{x} \nabla \rho \tag{10}$$

where,

$$\mathbf{u}^* = \begin{cases} \mathcal{L}(\mathbf{u}), & \text{forcing domain} \\ \mathbf{u}_{\text{body}}, & \text{solid domain} \end{cases} \tag{11}$$

in which, the operator $\mathcal{L}(*)$ denotes the interpolation of the velocity near the IB surface. The interpolation is based on the solution of the governing equations and the velocity boundary conditions on the IB surface. The second-order Laplacian interpolation is used in the present work. The detailed descriptions and a series of verification and validation tests can be found in [22].

Different from the IBM used in the single-phase flow, the additional gradient of density in the momentum equation due to buoyancy is challenging for the IBM. Since the fluid inside the solid domain is unphysical, the volume fraction α and the density field are not properly determined at this stage. By examining Equation (9), one can find that without a proper setup of the volume fraction α near the IB surface, the calculation of the density field is problematic in that region. In addition, considering the density ratio between air and water, large error will be introduced to the calculation of the gradient of density near the IB surface, leading to an incorrect solution of the momentum equation.

In the current work, the dilation method proposed by Sun and Sakai [19] is adopted. At the end of each time step, the volume fraction field is extended into the solid domain as follows:

1. Mark all solid cells and store in a list $\mathcal{M}$.
2. Loop through all marked cells in $\mathcal{M}$.

   (a) Check all the cells that share nodes with the marked cell i, and store the indices of all unmarked cells. The volume fraction α of these cells is used to interpolate the α in cell i.

   (b) After storing all the unmarked cells, use the inverse square distance method to interpolate α_i as

$$\alpha_i = \frac{\sum_j w_j \alpha_j}{\sum_j w_j} \tag{12}$$

where

$$w_j = \frac{1}{d^2} \tag{13}$$

where d is the distance between the cell centers of i and j. j is the cell index of each unmarked cell.

(c) Store the cell index i into a temporary list $\mathcal{S}$.

(d) Go to next marked cell $i + 1$.

3. Remove all cells in $\mathcal{S}$ from $\mathcal{M}$.
4. Go back to the beginning of Step. 2.

The number of iterations in Step. 2 determines how many layers of solid cells α are extended inside the IB surface. Note that this extension is naturally a good approximation of the Neumann boundary condition. In practice, we find that five layers are good enough for both cases with both static and moving IB surfaces. It should be noted that this process of extension changes the fluid volume in the solid domain solely to enforce the Neumann boundary condition of α on the IB. Therefore, it changes the total fluid volume in the whole domain. However, since the velocity boundary condition is imposed on the IB, there is no velocity flux across the IB boundaries. Change of the fluid volume in the solid domain serves the sole purpose to impose the correct boundary condition of α on the IB, and does not affect the total volume in the fluid domain.

The effect of the field extension operation is demonstrated by the canonical 2D dam-break problem. In this case, the dam walls are modeled using IB surfaces, which do not coincide with the grid lines, as shown in Figure 2a. In Figure 2, the color represents the value of the volume fraction α, where red represents water $\alpha = 1$, and blue represents air $\alpha = 0$. The IB surfaces are denoted as white dots.

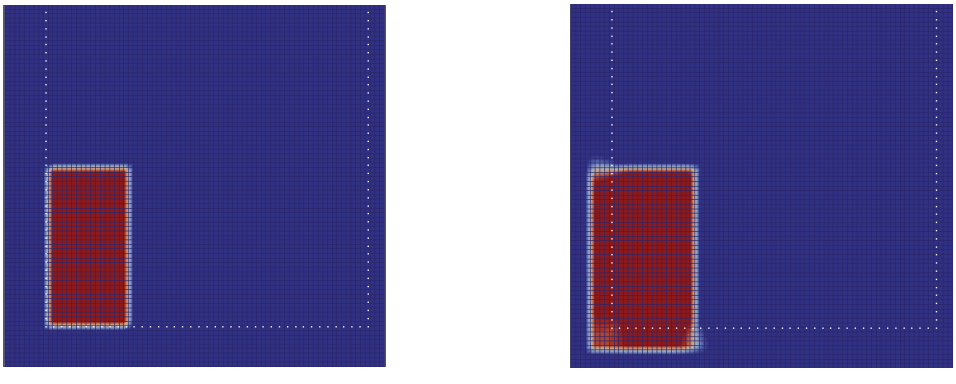

(**a**) Original α field (**b**) α field after the extension

Figure 2. Extension of α into the solid region. The IB surfaces are denoted as white dots.

Figure 3 shows the comparison of the shape of the air–water interface between the present IBM and the results on the body-fitted mesh with the same mesh resolution after the dam is released. The shape of the air–water interface, especially at the water front along the tank bottom, is not correctly predicted without the field extension. Inaccurate simulation of the water volume will cause a poor prediction of the momentum of the water body, leading to an inaccurate simulation of the development of fluid field and the impact force.

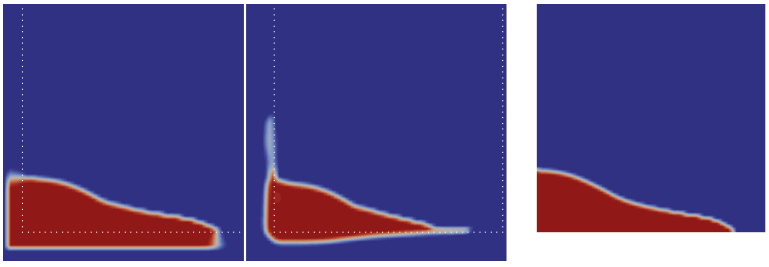

Figure 3. Comparison of the shape of the water volume. **Left**: Field extension; middle: no enforcement of the α BC; **Right**: body-fitted mesh.

2.4. Turbulence Modelling

Following our previous work [22], the Spalart–Allmaras turbulence model is used in the current work. Previous results of flows in an asymmetric diffuser and behind a KVLCC2 ship model demonstrate that moderate flow separation can be well handled with decent accuracy. It should be noted that for many marine hydrodynamic applications where massive separation effects are important, more advanced turbulence modelling techniques can offer additional accuracy, such as DES or LES.

In the Spalart–Allmaras turbulence model, the turbulent viscosity ν_t is calculated by solving the transport equation of the modified turbulent viscosity $\tilde{\nu}$:

$$\begin{aligned}\frac{D}{Dt}\tilde{\nu} =& \frac{1}{\sigma_{\nu_t}}\nabla\cdot((\nu+\tilde{\nu})\nabla\tilde{\nu}) + \frac{C_{b2}}{\sigma_{\nu_t}}|\nabla\tilde{\nu}|^2 + C_{b1}\tilde{S}\tilde{\nu}(1-f_{t2}) \\ &- (C_{w1}f_w - \frac{C_{b1}}{\kappa^2}f_{t2})\frac{\tilde{\nu}^2}{\tilde{d}^2} + S_{\tilde{\nu}}\end{aligned} \tag{14}$$

with the wall boundary condition $\tilde{\nu}_{\text{wall}} = 0$. Detailed description of the model and the default model coefficients can be found in [23]. The near-wall distance $\tilde{d}$, which is essential for the correct modelling of the destruction of the turbulence, is calculated taking into account the IB surfaces. As proposed in our previous work, the IB wall function is also used to relax the requirement of the near-wall cell spacing. The wall function provides a universal velocity profile from the outer edge of the logarithmic layer down to the IB surface. The wall tangential component of the velocity in the forcing cell is corrected based on the velocity profile. $\tilde{\nu}$ in the forcing cell is directly calculated based on a linear profile as follows:

$$\tilde{\nu}^+ = \kappa y^+ \tag{15}$$

in which $\tilde{\nu}^+ = \tilde{\nu}/\nu$; $\kappa = 0.41$ is the Von Karman constant; $y^+ = yu_\tau/\nu$; u_τ is the friction velocity determined from the Spalding's velocity profile:

$$y^+ = u^+ + \frac{1}{E}\left[e^{\kappa u^+} - 1 - \kappa u^+ - \frac{1}{2}(\kappa u^+)^2 - \frac{1}{6}(\kappa u^+)^3\right] \tag{16}$$

3. Numerical Results

3.1. 3D Dam-Break with an Obstacle

In this section, the canonical problems of dam-break are investigated. Two different setups are considered to validate the solver from different aspects including the flow velocity, development of the air–water interface and the impact on the obstacle.

3.1.1. Dam-Break No.1

This section discusses the interaction between a vertical square cylinder and a single large wave caused by the dam break. The flow velocity in front of the obstacle and the impact force on the square cylinder are examined. The experimental data is found in [24] provided by Profs. Catherine Petroff and Harry Yeh. Numerical results are also provided in [24] using their three-dimensional Eulerian-Lagrangian marker and micro-cell method.

Figure 4 illustrates the setup of the numerical simulation. The dimensions of the tank are 1.6 m $\times$ 0.61 m $\times$ 0.75 m. A volume of water with the size 0.4 m $\times$ 0.61 m $\times$ 0.3 m is initially placed at the left end of the tank. The dimensions of the vertical obstacle are 0.12 m $\times$ 0.12 m $\times$ 0.75 m. It is placed downstream of the volume of water with center of the bottom of the obstacle at $(0.96, 0, 0)$. As reported by Petroff and Yeh, the bottom of the tank was not completely drained in the physical experiment. Therefore, a thin layer of water with 0.01 m in depth is setup in the present simulation as shown in Figure 4.

It should be noted the way that the water is released in the present simulation is different from how the experiment was conducted. In the physical experiment, the water is blocked by a gate that is lifted vertically with finite speed at the beginning of the test, whereas in the simulation the water is released instantaneously. Lin and Chen [25] discuss the influence of the opening speed of the gate on the time history of the impact force on the obstacle. Their results show that the peak of the impact force is delayed as the finite opening speed of the gate decreases.

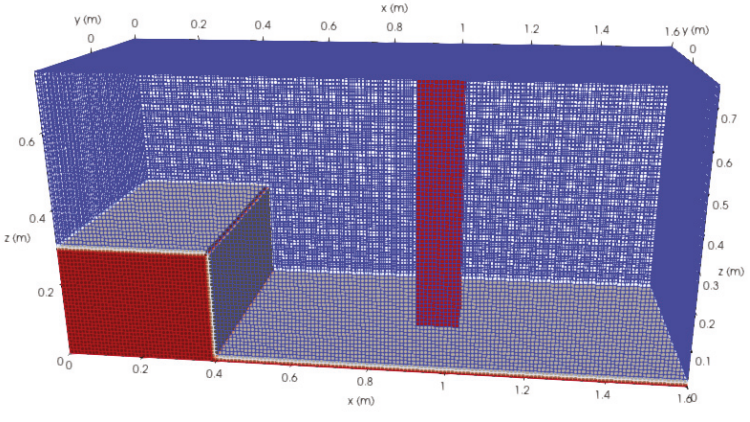

Figure 4. Case setup of Dam-Break No.1.

In the present simulations, the walls of the tank are represented by the body-fitted wall boundaries as shown in Figure 4. The solid walls of the vertical obstacle are represented by an IB surface. A set of three background meshes with a refinement ratio of $\sqrt{2}$ in each direction is used to validate the solver. The total numbers of cells of the background meshes are 114 $\times$ 43 $\times$ 53, 161 $\times$ 61 $\times$ 75 and 228 $\times$ 86 $\times$ 106, respectively. The position of the IB in the tank is shown in Figure 5.

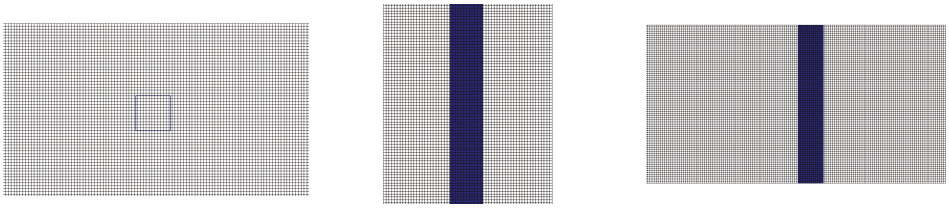

(**a**) top view (**b**) front view (**c**) side view

Figure 5. Relative position between the IB and the medium background mesh.

The density and viscosity are $\rho_w = 1000\ \mathrm{kg/m^3}$, $\nu_w = 1 \times 10^{-6}\ \mathrm{m^2/s}$ for the water, and $\rho_a = 1\ \mathrm{kg/m^3}$, $\nu_a = 1 \times 10^{-5}\ \mathrm{m^2/s}$ for the air. The gravitational acceleration is $g = 9.81\ \mathrm{m/s^2}$. In the simulations, the time step size is adjusted automatically to keep the Courant number less than 1.0.

A probe is used to record the flow velocity at a location in front of the obstacle at $(0.754, 0, 0.026)$. In addition, the impact force on the obstacle is calculated.

Figure 6 shows the wave propagation and its interaction with the obstacle at different time instants. It provides a general idea of what the critical phases of the dam-break problem look like. At $t = 0$ s, the water is released. After the water hits the front side of the obstacle, it runs up along the front wall and causes a large impact force. Afterwards, the water that travels around the obstacle joins together behind the obstacle, travels to the end of the tank, and hits the back side of the obstacle after being reflected by the end wall of the tank. It causes a second impact in the opposite direction compared to the first peak of impact. The second impact force is expected to be weaker than the first one because the velocity of the front of the wave is decreasing in general.

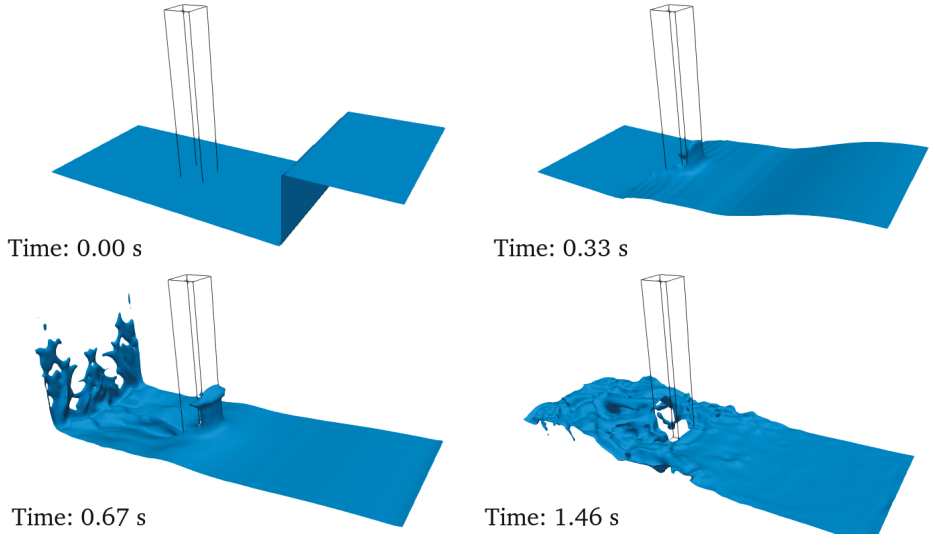

Figure 6. Simulation of the 3D dam-break problem with a vertical square obstacle.

To further evaluate the accuracy of the solver, Figure 7 shows the x-component of the velocity at the velocity probe using all three background meshes. The data is shifted in time such that $t = 0$ s in the figure is the moment when the water first reaches the probe. Specifically, $t = 0$ s in the figure corresponds to 0.238 s after the water is released. The experimental data is plotted together for the

purpose of comparison. The gaps in the experimental data at $0.6 < t < 0.85$ s and $t > 1.5$ s are due to the presence of bubbles in the water as explained in [24]. The velocity at $t = 0$ s is slightly overpredicted by the medium and fine meshes, which means the water moves faster in present simulations than in the experiment. It should be noted that in the simulations, the floor is set to be covered by a thin layer of water of thickness 0.01 m. The layer of water is used to mimic the wet floor in the experiment. However it cannot perfectly reproduce the experimental environment. Another reason is that the gate in front of the water is released with finite speed in the experiment, which reduces the velocity at the water front near the floor. A similar conclusion is drawn in [25] by investigating the influence of the release speed of the gate. The medium and fine meshes correctly predict the decrease in the velocity of the water (e.g., $0 < t < 1.5$ s) due to the blockage of the obstacle. After $t = 1.5$ s, the wave is reflected from the tank wall at $x = 1.6$ m, and it is further blocked by the back side of the obstacle. The water near the bottom floor in front of the obstacle is almost stationary. This can be confirmed from Figure 7 that the velocity at the probe drops to almost zero after $t = 1.5$ s.

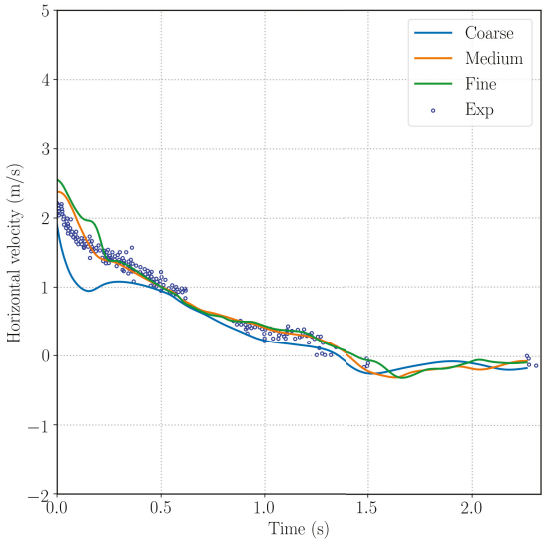

Figure 7. Time history of the horizontal velocity in front of the obstacle at $(0.754, 0, 0.026)$ using different background meshes.

Figure 8 shows the impact force on the obstacle. It is worth pointing out that $t = 0$ s in this figure corresponding to the time when the simulation starts, which explains the zero impact force at about $t < 0.25$ s. The different background meshes predict a consistent start time of the impact. Compared with the experimental data, it can be seen that the first impact happens earlier than in the experiment, which is consistent to the behavior of the horizontal velocity at the velocity probe discussed before. Figure 8 shows that the numerical results slightly underpredict the positive peak value at around $t = 0.4$ s. Afterwards, the impact force decreases gradually to zero around $0.4 < t < 1.5$ s, which is consistent with experimental data. At $t \approx 1.5$ s, the wave reflected from the end the tank arrives and impacts on the back side of the obstacle causing a negative peak of the impact force. During the last phase of the dam break, the impact force decreases to zero again.

In summary, the accuracy of the solver is demonstrated via the comparisons between the numerical solutions and the experimental data for the impact force and the horizontal velocity in the front of the obstacle.

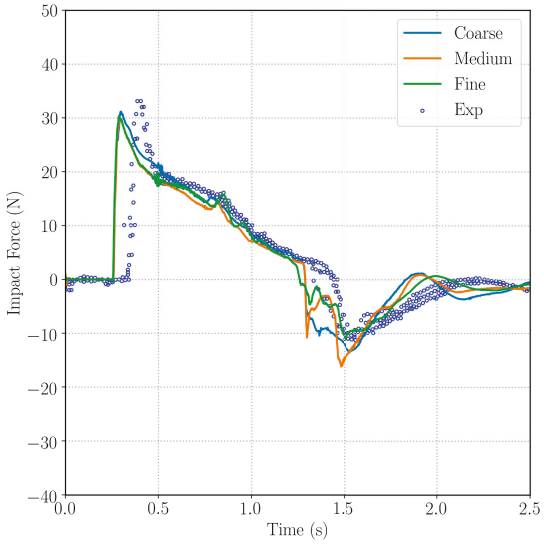

Figure 8. Time history of the impact force on the obstacle using different background meshes.

3.1.2. Dam-Break No.2

In the previous section, the discussion is focused on the velocity of the water and the total impact force, which is an integrated variable. It is equally important to investigate the local pressure during the impact, as well as the water elevation at different places. To fulfill this goal, a different setup of the 3D dam-break problem with an obstacle is used in this section. The height of the obstacle is much smaller than in the previous case, which means the water also flows over the top of the obstacle. The physical experiment was carried out by the Maritime Research Institute Netherlands (MARIN, [26]) to investigate the phenomenon of green water on the deck of a ship. Local pressure at different positions of the obstacle, and the water elevation at different locations of the tank were recorded in the experiment. The results of numerical simulations are also provided in [26].

Figure 9 shows the computational domain and the numerical setup. The dimensions of the tank are 3.22 m $\times$ 1 m $\times$ 1 m. At the beginning of the simulation, the volume of water with the size 1.22 m $\times$ 1 m $\times$ 0.55 m is located at the end of the tank from $x = 2$ m. A rectangular obstacle is placed in front of the dam to represent a container on the deck of the ship. The dimensions of the obstacle are 0.16 m $\times$ 0.4 m $\times$ 0.16 m with its front side (the side which faces the dam) positioned at $x = 0.83$ m. The water elevation is monitored at two places along the vertical plane $y = 0$ m, which are $x = 1.0$ m and 2.66 m. Eight sensors are used to record the local pressure on the top and front sides of the obstacle, and the locations are listed in Table 1. The numerical results of the time histories at the pressure sensors P1, P3, P5 and P7 are compared with the experimental data. The locations of these four sensors are illustrated in Figure 10. The sensors P1 and P3 are on the side facing to the initial volume of water. The blue solid line represents the plane $y = 0$ m as a reference.

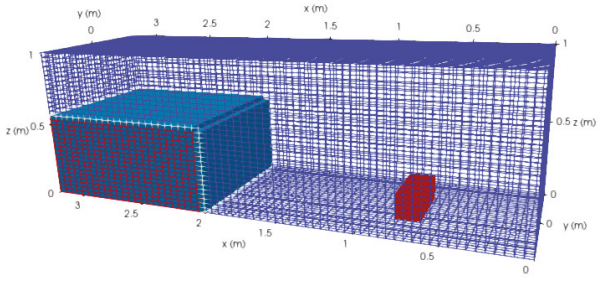

Figure 9. Case setup of the 3D dam-break problem with an obstacle: Problem No.2.

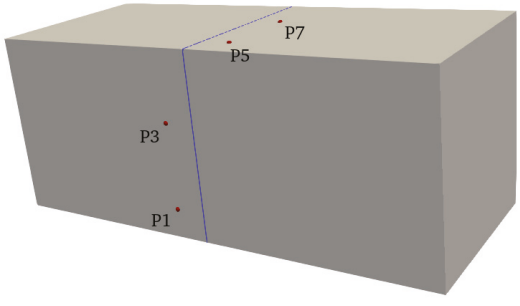

Figure 10. Locations of the pressure sensors P1, P3, P5 and P7.

The density and viscosity of the water are $\rho_w = 998.2$ kg/m^3, $\nu_w = 1 \times 10^{-6}$ m^2/s, and $\rho_a = 1$ kg/m^3, $\nu_a = 1.48 \times 10^{-5}$ m^2/s for the air. The gravitational acceleration is $g = 9.81$ m/s^2. Similar to the previous section, a set of three background meshes with a refinement ratio of $\sqrt{2}$ in each direction is used. The number of cells of the background meshes are $64 \times 32 \times 32$, $90 \times 46 \times 46$ and $128 \times 64 \times 64$, respectively. All the sides of the tank are represented by the body-fitted boundary conditions as no-slip walls, and the obstacle is modeled with an IB. The time step size is adjusted automatically to keep the global Courant number less than 0.75 and the Courant number near the free surface less than 0.3.

Table 1. Locations of the pressure sensors in the 3D dam-break problem No.2.

Sensor	Location
P1	$(0.83, -0.026, 0.025)$
P2	$(0.83, -0.026, 0.063)$
P3	$(0.83, -0.026, 0.099)$
P4	$(0.83, -0.026, 0.136)$
P5	$(0.806, 0.026, 0.16)$
P6	$(0.769, 0.026, 0.16)$
P7	$(0.733, 0.026, 0.16)$
P8	$(0.696, 0.026, 0.16)$

Figure 11 shows the time histories of the water elevation at the locations $x = 2.66$ m and 1.0 m, which are inside the initial position of the dam and in front of the obstacle, respectively. During the initial part of the time series the comparison between the experiment and simulation is very close. At about $t = 2.5$ s and 1.8 s, the water reflected from the wall of the tank at $x = 0$ m arrives to the two probes, and causes a random unsteady and high frequency response. For the second part of the time histories, there are differences between the numerical results and the experimental data with regard to

the high frequency part, yet the mean elevation is in very close agreement. For example in the probe at $x = 1$ m, the front of the water arrives at around $t = 4.5$ s, and the numerical results accurately capture the instant when the air–water interface starts to rise in accordance with the experiments.

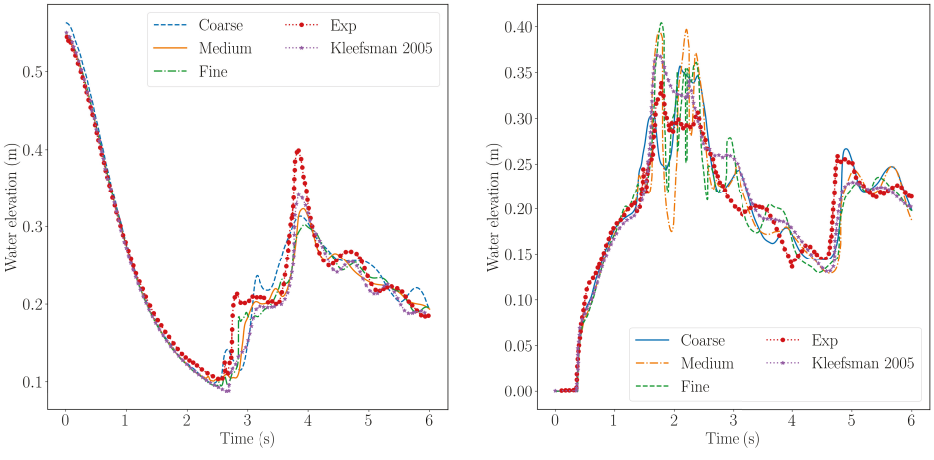

(**a**) $x = 2.66$ m (**b**) $x = 1$ m

Figure 11. Time histories of the water elevation at different locations.

As shown in Figure 12, the time histories of the local pressure at four different sensors are selected to compare with the experimental data. The present numerical simulation captures the behavior when the water first impacts the sensors, especially for the ones on the front side of obstacle. The peak pressure at P1 matches with the experimental data very well, while the peak pressure at P3 is underpredicted by the fine mesh. At around $2 < t < 4$ s, the pressure at both sensors drops gradually.

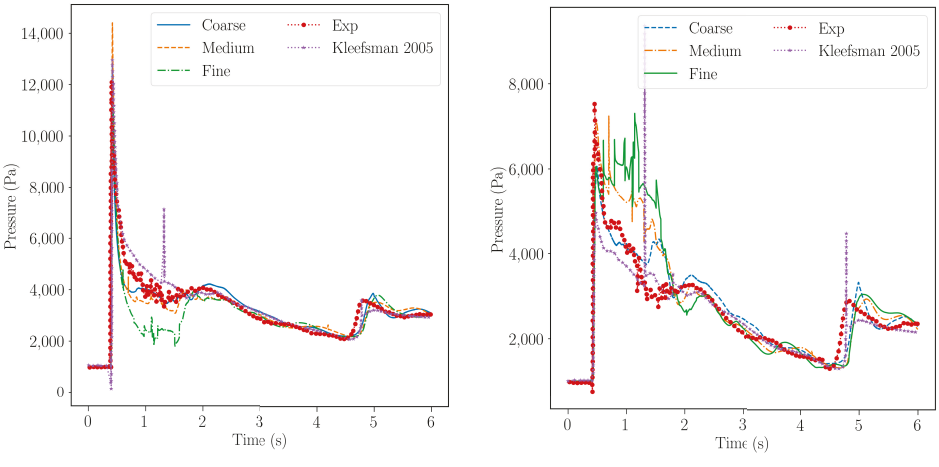

(**a**) P1 (**b**) P3

Figure 12. *Cont.*

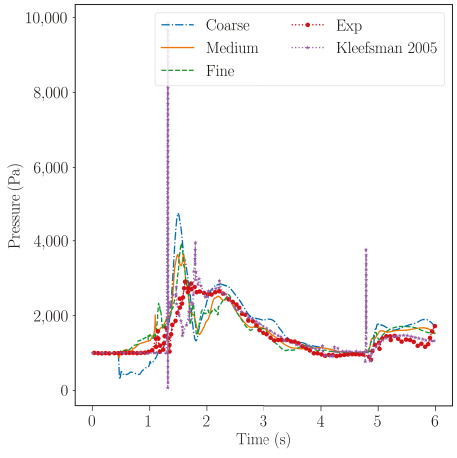

(**c**) P5

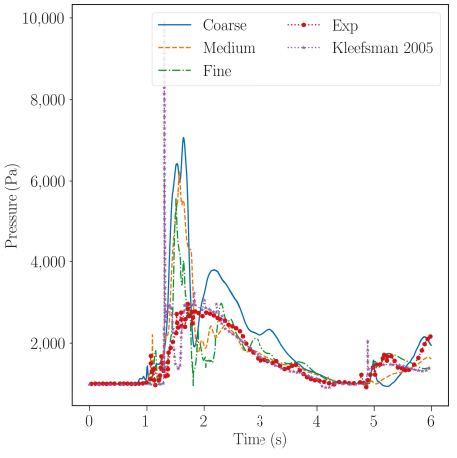

(**d**) P7

Figure 12. Time histories of the pressure at different locations.

For the numerical results at P5 and P7, which are on the top surface of the obstacle, the numerical results show a large oscillation. It is because when the water flow over the obstacle, the large vertical velocity of the water causes the water to detach from the surface of the obstacle. Subsequently, air is entrapped when the water starts to impact on the top the obstacle. However, the effect of air compressibility is not considered in the current solver. Figure 13 shows the profile of the air–water interface around the pressure sensor P7 at around $t = 1.1$ s. It can be clearly seen that the air is entrapped and a bubble is formed around P7. As a result, the large oscillation appears in the numerical results at P5 and P7 in the limitations of the current numerical framework.

Overall, the results demonstrate that the present IBM solver can handle the problems of wave interaction with solid walls with respect to the evolution of the air–water interface, velocity of the water, force on the obstacle and the local pressure due to the impact.

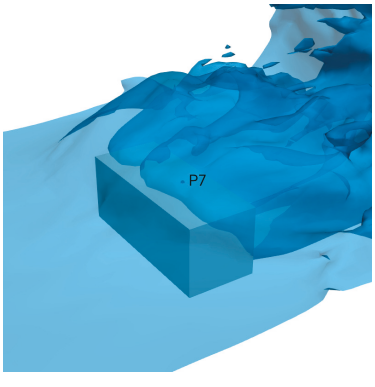

Figure 13. Air entrapped on the top of the obstacle in the dam-break problem No.2.

3.2. Water Exit of a Circular Cylinder

In this section, the IBM is used to simulate a moving surface in the air–water two-phase flow to further demonstrate its capability. The test case is the water exit of a 2D circular cylinder with constant vertical velocity. The physical experiments were conducted by Miao [27]. The results of the numerical

simulations carried out by Zhu et al. [28] are also presented as a reference. The numerical simulations use the Constrained Interpolation Profile (CIP) method.

The computational domain and the initial position of the cylinder with the radius of $R = 0.0625$ m are shown in Figure 14. The domain is 1 m wide and the water depth is $h = 0.5$ m. At the beginning of the simulation, the cylinder accelerates upwards from rest and gradually reaches the final constant velocity v. Eventually, the cylinder exits the water until the water fully dropped from the surface the cylinder. In the present simulations, the cylinder is represented using the IB, and a uniform structured mesh is used as the background mesh with the cell size $\Delta x = \Delta y = 0.04R$.

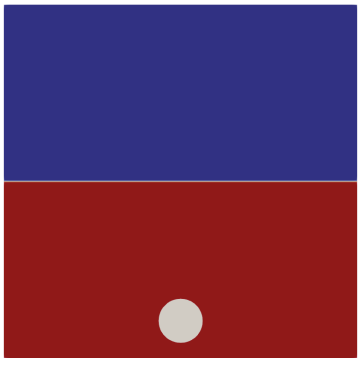

Figure 14. Computational domain and the initial condition of the water exit of a circular cylinder.

In the experiment, the dimensionless time $vt/R = 0$ corresponds to the time instant when the top of the cylinder touches the air–water interface. $vt/R = -5.5$ and -5 correspond to the time instants where the cylinder starts to move and reaches the final velocity v, respectively. The prescribed motion of the cylinder is described by the position of the center of the cylinder with respect to time:

$$y(t) = \begin{cases} \frac{1}{2}v(t - \frac{t_0}{\pi}\sin(\frac{\pi t}{t_0})), & t < t_0 \\ v(t - \frac{1}{2}t_0), & t \geq t_0 \end{cases} \tag{17}$$

where t_0 is the time of ramping up the velocity. It should be noted that in the simulations, $t = 0$ s corresponds to the time instant when the cylinder starts to move.

Two numerical tests are carried out with different final velocity v as listed in Table 2.

Table 2. Parameters for the water exit tests.

Test	Fr	v(m/s)	t_0(s)
No.1	0.4627	0.5124	0.0610
No.2	0.6903	0.7644	0.0409

The time step size is automatically adjusted to keep the global Courant number less than 1.0 and the Courant number near the free surface less than 0.3.

Figure 15 shows the time histories of the exit coefficient C_e for the two test cases. The time $t = 0$ of the present simulations is shifted to compare with the experimental data. The exit coefficient C_e is defined as:

$$C_e = \frac{F}{\rho v^2 R} \tag{18}$$

where ρ is the density of water and F is the vertical hydrodynamic force on the cylinder.

For both test cases, the present numerical results show good agreement with the experimental data. In general, C_e shows similar trend for both exit speeds. Before the dimensionless time $vt/R < -5$,

the cylinder starts to accelerate from its initial position. It results in a large negative peak in force, which is captured by all the three results for both cases. For the time range $-5 < vt/R < 0$, the cylinder moves upward with a constant speed. As the cylinder approaches the surface of the water, C_e gradually decreases with a nearly constant rate of change. In addition, the vertical speed of the cylinder does not have much influence on the rate of decrease of C_e. When the cylinder starts to exit from the water at $vt/R = 0$, the hydrodynamic force drops significantly, and eventually becomes zero when the cylinder is drained after it completely leaves the water.

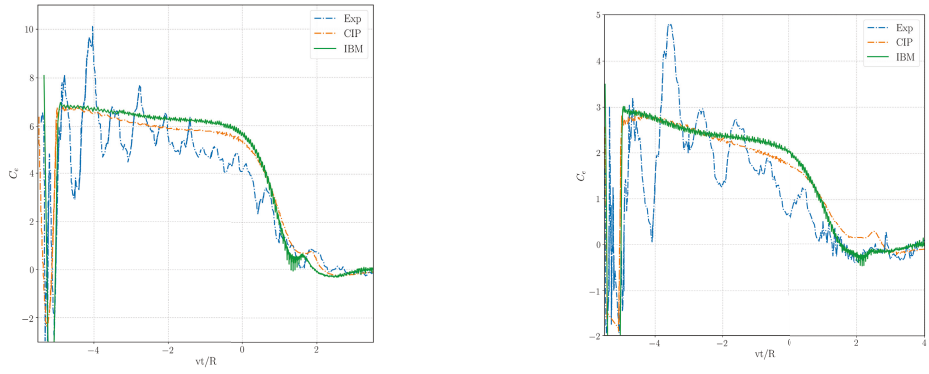

(**a**) Test No.1 (**b**) Test No.2

Figure 15. Time histories of the exit coefficient C_e for the water exit tests.

Figure 16 shows the comparison of the profile of the air–water interface with the numerical solutions of Zhu et al. [28] at different time instants. The present results show overall good agreement with the other numerical results with respect to the hydrodynamic force on the cylinder with different exit velocities. When the cylinder exits the water after $vt/R = 0$, the present results capture the thin layer of water on top of the cylinder. The present results also predict the deformation of the air–water interface when the layer of water starts to fall down along the surface of the cylinder at $vt/R > 1$.

In summary, for both vertical speeds of the cylinder, the present IBM quantitatively captures the unsteady behavior of the hydrodynamic force at different phases of the two water-exit tests. In addition, the deformation of the air–water interface, especially due to the interaction between the IB surface and the air–water interface is accurately modeled.

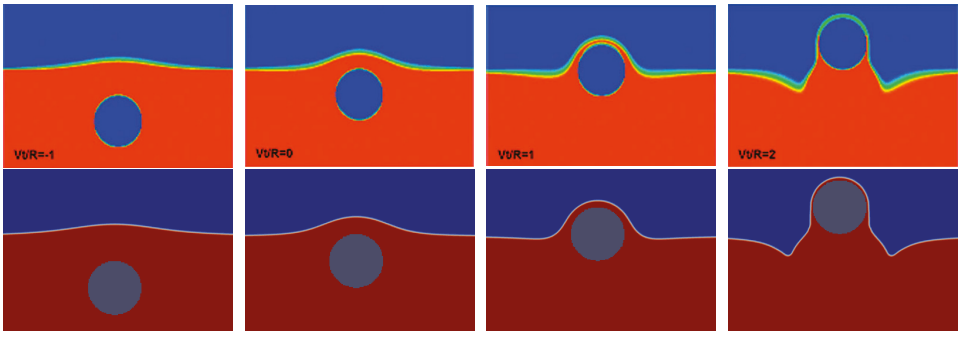

Figure 16. Comparison of the profiles of the air–water interface at different time instants in Case No.1. Top row:zhu et al. [28]; bottom row: Present.

3.3. KCS Model Advancing with a Rotating Rudder

To fully demonstrate the flexibility and the accuracy the present IBM. A combined usage of IB surfaces and unstructured body-fitted approach is considered in this section, which is a KCS ship model advancing with a rotating rudder. More specifically, the computational domain is drawn using unstructured mesh with body-fitted boundary on the ship hull and the fixed rudder horn. The rotating rudder blade is modeled using an IB surface.

In this simulation, the equations are written in a coordinate system that moves with the constant velocity of the ship hull. In addition, the boundary layer flow is more well defined on the ship hull than in the wake where the rudder operates, due the high Reynolds number. For such a case, using an unstructured grid and body-fitted approach on the ship hull is more efficient than IBMs. If an IB is used to represent the entire ship hull, it will require many more cells to achieve similar accuracy since it requires resolution in the boundary layer cells in all directions. Whereas, if the body-fitted approach is applied to the rotating rudder blade, a huge amount of time and effect is required to properly design the mesh to achieve satisfying mesh quality near the tip of the blade, and in the gap between the blade and the rudder horn. Additional attention is also required to design the mesh topology such that the mesh quality is preserved due to the rotation of the blade. In comparison, using an IB to represent the rotating rudder blade completely avoids mesh motion and also saves the effort of designing the mesh. A novel capability of our approach is to combine the benefits of unstructured grid, body-fitted approach and an IBM Therefore, the present IBM, which can be used together with body-fitted boundaries on unstructured grids, is more flexible and efficient than other IBMs, where all boundaries are represented by IBs and structured background grids are used.

The ship model and the rudder are shown in Figure 17. in which, the propeller is not considered. The main particulars of the model-scaled KCS and the rudder are listed in Tables 3 and 4, respectively.

In the simulations, the ship model is fixed in the even-keel condition without considering the vertical motions. Whereas the experimental ship model is free to sink and trim in the experiments. The forward speed of the ship model is $V_{\text{model}} = 1$ m/s, corresponding to $Fr = 0.216$ and 19.9 knots in full scale. The Reynolds number is 1.72×10^6. Four rudder angles are tested, which are $\delta = -5^\circ, -10^\circ, -15.1^\circ$ and -20.1°, respectively.

Table 3. Main Particulars of the model-scaled KCS.

Main Particulars	Symbol	Value
Scale	λ	105
Length between perpendiculars	$L_{\text{pp}}(m)$	2.19
Length of waterline	$L_{\text{wl}}(m)$	2.2143
Width	$B_{\text{wl}}(m)$	0.3067
Depth	$D(m)$	0.1810
Draft	$T(m)$	0.1029
Displacement	Δ (m^3)	0.0449
Wetted area without rudder	S (m^2)	0.8644
Longitudinal center of buoyancy (fwd+)	LCB ($\%L_{\text{pp}}$)	–1.48
Vertical center of gravity	KG (m)	0.118
Moment of inertia	$K_{\text{yy}}/L_{\text{pp}}$	0.25

Table 4. Main Particulars of the model-scaled rudder.

Main Particulars	Value
Scale	105
Type	Semi-balanced horn rudder
Area of rudder (m^2)	0.0104
Lateral Area of rudder (m^2)	0.0049

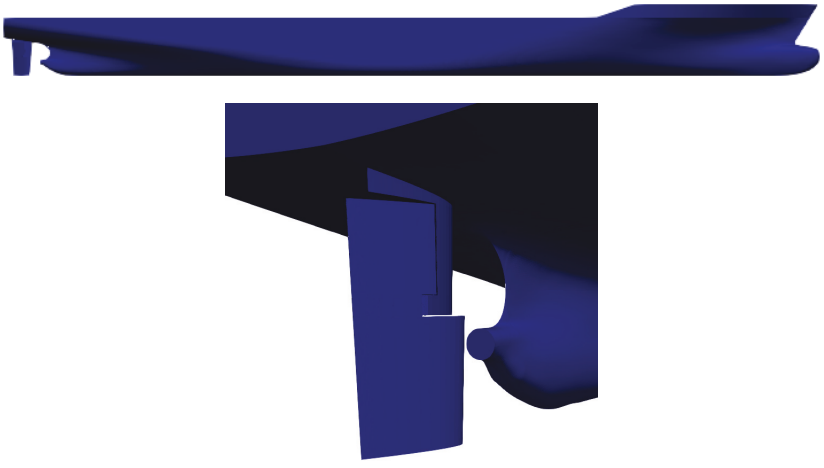

Figure 17. Geometry of the KCS ship model and the rudder.

Since the ship hull and the rudder horn are fixed, it is reasonable to use body-fitted mesh to represent these parts to efficiently resolve the boundary layer. The moving part of the rudder is modeled using an IB to take full advantage of the IBM for modeling moving geometries. The numerical solutions are compared with the experimental data [29] to demonstrate the capability of the present IBM. Since the accuracy is limited by not only the IBM, but also the underlying solver and discretization schemes, the RANS simulations with the rudder at fixed deflection angles are also carried out using body-fitted meshes as a comparison. Three sets of simulations are carried out to systematically show the capability of the solver as listed in Table 5. In the first set, a mesh convergence study is conducted by using body-fitted meshes to find an appropriate resolution of the background mesh to balance the accuracy and computational cost. In the second set, the simulations of the rudder at fixed deflection angles are carried out on body-fitted meshes. The body-fitted results represent the baseline of the accuracy of the solver that the present IBM combined with. The simulation with the hybrid method at the maximum deflection angle $\delta = -20.1^\circ$ is also carried out to validate the IBM. In addition, a simulation without the IB wall function is carried out using the hybrid method at the maximum deflection angle to examine the effect of the IB wall function. In the third set, the simulation of a rotating rudder is conducted with the hybrid method. The results demonstrate that, with the help of the present IBM, the single-run procedure can be applied to this problem to predict the hydrodynamic forces accurately and efficiently.

Table 5. Summary of the simulations of a ship model advancing with a deflected rudder.

Case No.	Mesh Refinement	Mesh Type	Symmetric	$\delta(^\circ)$	WF	RR
1	C	BF	Y	0	Y	N
2	M	BF	Y	0	Y	N
3	F	BF	Y	0	Y	N
4	M	BF	N	–5	Y	N
5	M	BF	N	–10	Y	N
6	M	BF	N	–15.1	Y	N
7	M	BF	N	–20.1	Y	N
8	M	Hybrid	N	–20.1	Y	N
9	M	Hybrid	N	–20.1	N	N
10	M	Hybrid	N	-	Y	Y

C: coarse, M: medium, F: fine. BF: body-fitted. Symmetric: symmetric boundary condition on the centerline. WF: wall function. RR: rotating rudder.

3.3.1. Mesh Convergence Study

In this section, the simulation with the rudder at $\delta = 0°$ is carried out. A set of three body-fitted meshes with a constant refinement ratio is used to test the spatial convergence and to find an appropriate background mesh for the following simulations by the IBM. The meshes are generated by snappyHexMesh, an automatic mesh generation utility provided by OpenFOAM. The meshes are systematically refined by refining the background meshes with a refinement ratio of $\sqrt{2}$ in each direction. In addition, the mesh is further refined near the ship hull, the rudder and the air–water interface. Only half of the ship is used in the simulations with a symmetric boundary condition applied on the centerline to accelerate the simulation. The total number of cells of each mesh is listed in Table 6.

Table 6. Number of cells for the mesh convergence study.

Mesh Name	Coarse	Medium	Fine
Number of cells	518,640	1,220,948	2,382,616

Figure 18 shows the computational domain and the local mesh refinement around the ship. The dimensions of the computational domain are $4L_{\mathrm{pp}} \times L_{\mathrm{pp}} \times 1.5L_{\mathrm{pp}}$. The boundary conditions are summarized in Table 7, where the bottom and the far field of the domain are both included in the inlet boundary.

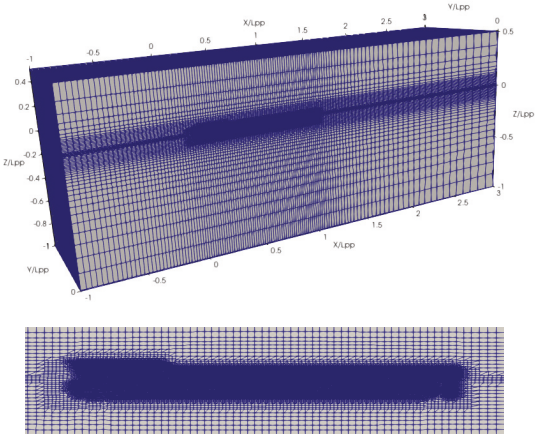

Figure 18. Computational domain and the local mesh refinement.

Table 7. Summary of the boundary conditions for the mesh convergence study.

Boundary Names	α	U	p_{rgh}
Inlet	waveAlpha	waveVelocity	zeroGradient
Outlet	zeroGradient	zeroGradient	fixedValue
Top	inletOutlet	pressureInletOutletVelocity	totalPressure
Centerline	symmetryPlane	symmetryPlane	symmetryPlane
Hull and rudder	zeroGradient	movingWallVelocity	fixedFluxPressure
Boundary Names	$\tilde{\nu}$	ν_t	
Inlet	fixedValue 5.871×10^{-6}	fixedValue 1.27×10^{-6}	
Outlet	zeroGradient	zeroGradient	
Top	zeroGradient	calculated	
Centerline	symmetryPlane	symmetryPlane	
Hull and rudder	fixedValue 0	nutUSpaldingWallFuntion	

The viscous pressure drag coefficient C_p, the frictional drag coefficient C_v, and the total drag coefficient C_T are defined as:

$$C_p = \frac{F_p}{\frac{1}{2}\rho U^2 LT} \quad C_v = \frac{F_v}{\frac{1}{2}\rho U^2 LT} \quad C_T = \frac{F_T}{\frac{1}{2}\rho U^2 LT} \tag{19}$$

where F_p, F_v and F_T are the viscous pressure drag, frictional drag and the total drag on the ship hull and the rudder. Table 8 shows the mesh convergence results of the drag coefficients on different meshes. The total drag coefficient C_T shows that the numerical solutions converge with satisfying agreement.

Table 8. Results of the drag coefficients in the mesh convergence study.

Mesh Name	C_p	C_v	C_T	Exp [29]	Error
Coarse	0.00272	0.01682	0.01954	0.0178	9.8%
Medium	0.00237	0.01686	0.01924	0.0178	8.1%
Fine	0.002244	0.01696	0.01921	0.0178	7.9%

Figure 19 shows the profile of the air–water interface on the ship hull extracted with the volume fraction $\alpha = 0.5$. It can be seen that the medium and fine meshes agree closely with each other, while the coarse mesh misses the short wave near the bow. In the following sections, the medium mesh is used for all the simulations considering a balance of accuracy and efficiency.

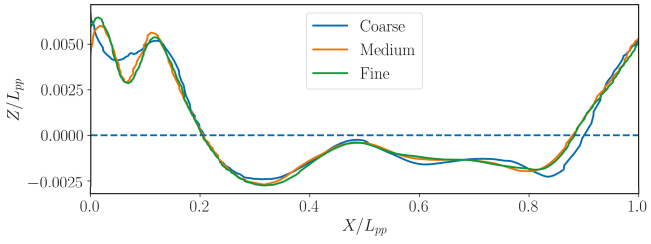

Figure 19. Free-surface profile on the ship hull with $\alpha = 0.5$.

3.3.2. Simulations with the Rudder at Fixed Deflection Angles

The accuracy of the IBM solver relies on not only the additional operations introduced by the IBM, but also the underlying RANS solver and numerical discretization schemes as discussed in the previous chapters. In this section, the simulations with the rudder at fixed deflection angles using pure body-fitted meshes are carried out. Therefore, the accuracy of the underlying RANS solver and numerical schemes can be evaluated. As a comparison, the case with the rudder at the maximum deflection angle $\delta = -20.1^\circ$ is also simulated using the IBM with a fixed IB. Comparisons of the surge coefficient X', sway coefficient Y' and the normal force coefficient FN' of the rudder with the experimental data are made to validate the solver. The coefficients are defined in Equation (20) as:

$$X' = \frac{X}{\frac{1}{2}\rho U^2 LT} \quad Y' = \frac{F_v}{\frac{1}{2}\rho U^2 LT} \quad FN' = \frac{FN}{\frac{1}{2}\rho U^2 LT} \tag{20}$$

where X and Y are the surge and sway forces on the ship including the rudder, respectively. FN is the force on the moving part of the rudder in the direction normal to the rudder mid plane.

Since the ship hull with the deflected rudder is not symmetric, the medium mesh used in the previous section is mirrored with respect to its centerline. The total number of cells used by both the body-fitted mesh and the IBM is listed in Table 9.

Table 9. Total number of cells for the simulations of the rudder at fixed deflection angles.

Mesh Name	Body-Fitted	Hybrid
Number of cells	2,441,378	2,499,112

Figures 20–22 show the results of the force coefficients X', Y' and FN', respectively. In the figures, "BF" represents the results of cases No. 4–7 in Table 5. It should be noted that in the experiments tests were carried out at $\delta = \pm 5°, \pm 10°, \pm 15.1°$ and $\pm 20.1°$. The numerical results generated for positive deflection angles, but are reflected accordingly with respect to the y axis to compare with the full range of experimental data.

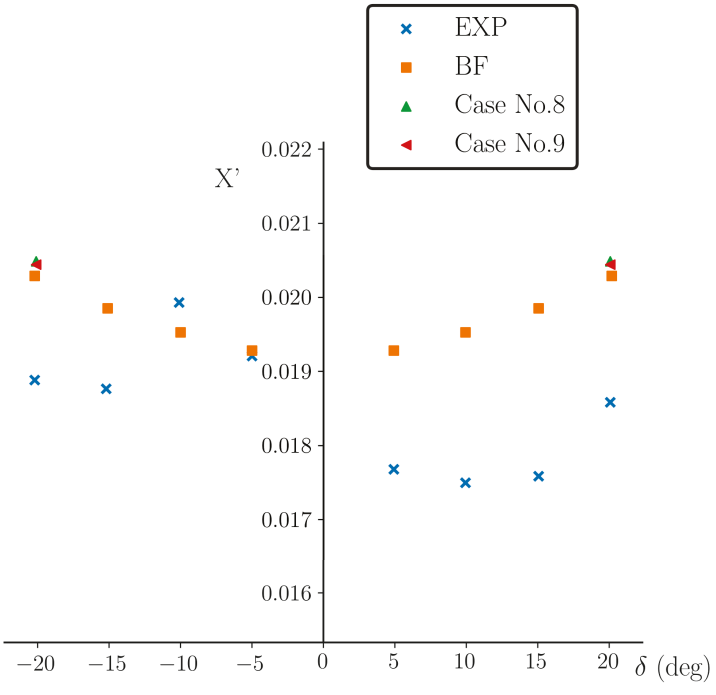

Figure 20. Surge force coefficient X' predicted at the fixed deflection angles.

Inspection of the experimental data highlights some of the challenges in measuring and predicting rudder forces at model scale. At this model scale Reynolds number, fully turbulent flow may be difficult to maintain along the length of the hull, and the flow patterns in the stern and on the rudder are very sensitive to any asymmetry in the model geometry and setup in the tank. For example, without a propeller, it is expected that a positive and negative rudder angle of the same degree would produce the same drag, whereas this is not exactly the case in the experiments. Likewise, the sway force should pass through zero as the rudder is in its zero position, and again there is a slight positive sway force in the experiments. Figure 20 shows that when $\delta > -15°$, the total drag is well predicted by OpenFOAM. However, when $\delta \leq -15°$ the numerical results overpredict the drag. It is because when the deflection angle is large, the flow massively separates from the surface of rudder. The Spalart–Allmaras turbulence model used in the current simulation is not fully capable of capturing the massive flow separation on the rudder. In addition, the wall function that is used in the IBM is based on the near-wall velocity profile in an attached turbulent flow, which does not hold true when

the deflection angle is large. Compared between the results of Cases No.8 and No.9, it shows that the usage of the wall function does not have notable impact on the total drag. It may because that the rudder is in the region of the wake flow, where the boundary layer effect is not as significant as on the ship hull.

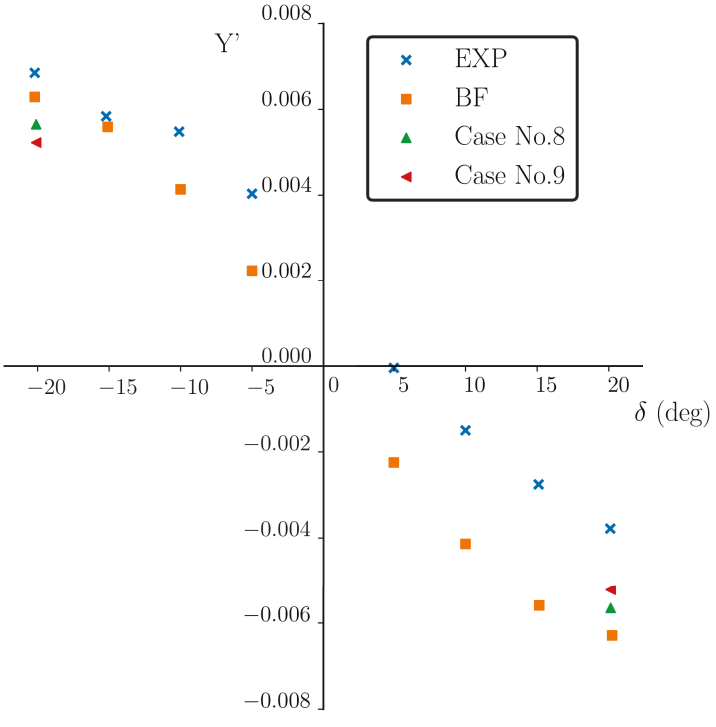

Figure 21. Sway force coefficient Y' predicted at the fixed deflection angles.

Figure 21 shows that the numerical prediction of the sway force matches well with the experimental data at all deflection angles. The sway force increases consistently with the increase of the deflection angle. It makes sense since the dominant contribution of the sway force comes from the lift force on the rudder, and the lift force increases with the increase of the deflection angle. The prediction of the IBM at the maximum rudder angle is less than the results on the body-fitted mesh, while both results fall into the uncertainty region of the experimental data. In addition, the IB wall function used in the IBM has no notable influence on the sway force.

Figure 22 shows the force on the moving part of the rudder in the direction normal to the rudder mid plane. Again, the numerical predictions match well at all deflection angles. The results at the maximum deflection angle obtained by the body-fitted mesh and the IBM agree well with each other, which again validates the accuracy of the IBM. The result without using the IB wall function underpredicts the normal force on the rudder. In the circumstance of simulating turbulent flows at high Reynolds numbers, it is almost unavoidable for the IBM to have similar near-wall resolution as the body-fitted mesh if the total number of cells is similar. Although due to the fact that the rudder is in the wake flow, the boundary layer effect is not as significant as on the ship hull. Using the IB wall function still improves the overall accuracy, especially when it only slightly increases the computational time.

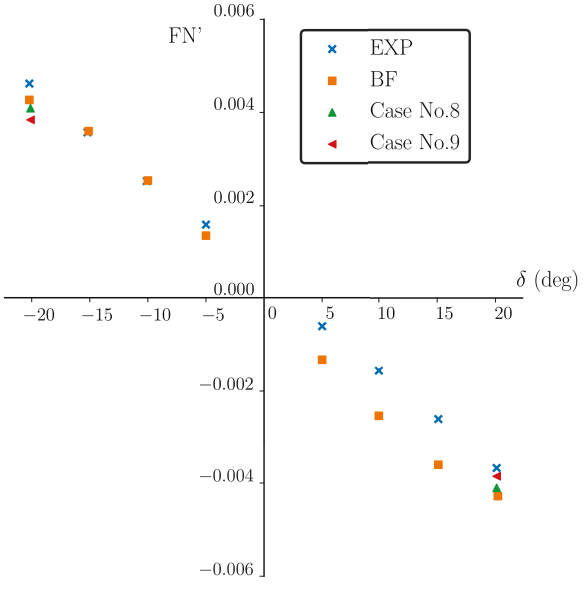

Figure 22. Normal force coefficient of the rudder FN' predicted at the fixed deflection angles.

Finally, Figures 23 and 24 show the velocity and dynamic pressure at $z = -0.065$ m when $\delta = -20.1°$, respectively. The velocity field shows the flow separation happens at this deflection angle, which confirms the discussion about the forces on the rudder in the previous paragraphs. For both the velocity and the pressure, the results of the IBM match closely with the body-fitted results.

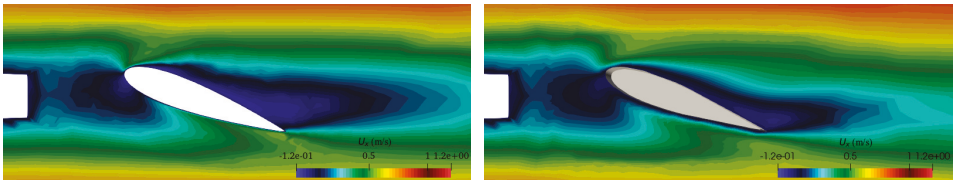

(**a**) Body-fitted mesh (**b**) IB mesh

Figure 23. Comparison of the velocity at $z = -0.065$ m when $\delta = -20.1°$.

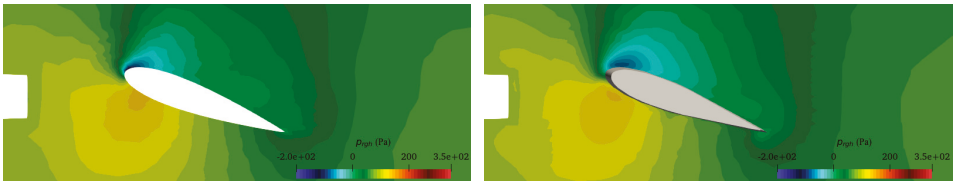

(**a**) Body-fitted mesh (**b**) IB mesh

Figure 24. Comparison of the dynamic pressure at $z = -0.065$ m for $\delta = -20.1°$.

4. Conclusions

In this paper, we extended our work of single-phase IBM for RANS simulations of fixed and moving objects in air–water two-phase turbulent flows. The VoF method with a compression term

was used to simulate the air–water interface. Compared with the simulations of single-phase flows, the momentum equation for two-phase flows has the gradient of density term because of buoyancy. Due to the large ratio of density between air and water, a correct density distribution near the IB surface is necessary to represent the homogeneous Neumann wall condition of density on body-fitted boundaries. This is satisfied indirectly by setting the homogeneous Neumann boundary condition of the volume fraction α, and it corresponds to a neutral contact angle boundary condition $\theta = \pi/2$. In the present work, the volume fraction α is extended into the solid domain by a field extension operation. The process involves interpolation of α one layer a time into the solid domain using the inverse square distance method. For turbulence modeling, the same methodology in our previous work is adopted, i.e., the Spalart–Allmaras turbulence model with an IB wall function.

A series of test cases are presented to evaluate the accuracy of the IBM. The cases consider both fixed and moving IB. Various aspects are carefully investigated, including the deformation of the air–water interface, the flow fields and the forces on the IB surfaces. Comparisons between the present results and other resourses demonstrate that the proposed IBM is capable of simulating the interaction between the air–water interface and the solid boundaries. Finally, we investigate the simulation of a KCS ship model advancing with a rotating rudder. The accuracy and flexibility of the IBM is fully demonstrated via the combined usage of the IB surfaces with unstructured body-fitted approach.

Author Contributions: Conceptualization, H.Y. and K.M.; methodology, H.Y.; software, H.Y. and Y.C.; validation, H.Y., Y.C. and K.M.; formal analysis, H.Y.; investigation, H.Y., Y.C., and K.M.; resources, H.Y. and K.M.; data curation, H.Y.; writing—original draft preparation, H.Y.; writing—review and editing, Y.C. and K.M.; visualization, H.Y.; supervision, K.M.; project administration, K.M.; funding acquisition, K.M. All authors have read and agreed to the published version of the manuscript.

Funding: This research was funded by Ford Motor Company and the United States Office of Naval Research.

Acknowledgments: The authors gratefully acknowledge the financial support of Ford Motor Company and the United States Office of Naval Research.

Conflicts of Interest: The authors declare no conflict of interest. The funders had no role in the design of the study; in the collection, analyses, or interpretation of data; in the writing of the manuscript, or in the decision to publish the results.

References

1. Peskin, C.S. Flow patterns around heart valves: A numerical method. *J. Comput. Phys.* **1972**, *10*, 252–271. [CrossRef]
2. Saiki, E.; Biringen, S. Numerical simulation of a cylinder in uniform flow: Application of a virtual boundary method. *J. Comput. Phys.* **1996**, *123*, 450–465. [CrossRef]
3. Beyer, R.P.; LeVeque, R.J. Analysis of a one-dimensional model for the immersed boundary method. *SIAM J. Numer. Anal.* **1992**, *29*, 332–364. [CrossRef]
4. Lai, M.C.; Peskin, C.S. An immersed boundary method with formal second-order accuracy and reduced numerical viscosity. *J. Comput. Phys.* **2000**, *160*, 705–719. [CrossRef]
5. Goldstein, D.; Handler, R.; Sirovich, L. Modeling a no-slip flow boundary with an external force field. *J. Comput. Phys.* **1993**, *105*, 354–366. [CrossRef]
6. Khadra, K.; Angot, P.; Parneix, S.; Caltagirone, J.P. Fictitious domain approach for numerical modelling of Navier–Stokes equations. *Int. J. Numer. Methods Fluids* **2000**, *34*, 651–684. [CrossRef]
7. Mohd-Yusof, J. Combined immersed-boundary/B-spline methods for simulations of ow in complex geometries. *Annu. Res. Briefs NASA Ames Res. Cent. Stanf. Univ. Cent. Turbul. Res. Stanf.* **1997**, *161*, 317–327.
8. Fadlun, E.; Verzicco, R.; Orlandi, P.; Mohd-Yusof, J. Combined immersed-boundary finite-difference methods for three-dimensional complex flow simulations. *J. Comput. Phys.* **2000**, *161*, 35–60. [CrossRef]
9. Balaras, E. Modeling complex boundaries using an external force field on fixed Cartesian grids in large-eddy simulations. *Comput. Fluids* **2004**, *33*, 375–404. [CrossRef]
10. Choi, J.I.; Oberoi, R.C.; Edwards, J.R.; Rosati, J.A. An immersed boundary method for complex incompressible flows. *J. Comput. Phys.* **2007**, *224*, 757–784. [CrossRef]

11. Kalitzin, G.; Iaccarino, G. Turbulence modeling in an immersed-boundary RANS method. *Annu. Res. Briefs* **2002**, 415–426. Available online: https://ctr.stanford.edu/annual-research-briefs-2002 (accessed on 24 September 2020)
12. Capizzano, F. Turbulent wall model for immersed boundary methods. *AIAA J.* **2011**, *49*, 2367–2381. [CrossRef]
13. Dommermuth, D.G.; O'Shea, T.T.; Wyatt, D.C.; Ratcliffe, T.; Weymouth, G.D.; Hendrikson, K.L.; Yue, D.K.; Sussman, M.; Adams, P.; Valenciano, M. An application of cartesian-grid and volume-of-fluid methods to numerical ship hydrodynamics. In Proceedings of the 9th International Conference Numerical Ship Hydrodynamics, Ann Arbor, MI, USA, 5–8 August 2007.
14. Hirt, C.W.; Nichols, B.D. Volume of fluid (VOF) method for the dynamics of free boundaries. *J. Comput. Phys.* **1981**, *39*, 201–225. [CrossRef]
15. Hibiki, T.; Ishii, M. One-dimensional drift-flux model and constitutive equations for relative motion between phases in various two-phase flow regimes. *Int. J. Heat Mass Transf.* **2003**, *46*, 4935–4948. [CrossRef]
16. Sanders, J.; Dolbow, J.E.; Mucha, P.J.; Laursen, T.A. A new method for simulating rigid body motion in incompressible two-phase flow. *Int. J. Numer. Methods Fluids* **2011**, *67*, 713–732. [CrossRef]
17. Shen, L.; Chan, E.S. Numerical simulation of fluid–structure interaction using a combined volume of fluid and immersed boundary method. *Ocean Eng.* **2008**, *35*, 939–952. [CrossRef]
18. Yang, J.; Stern, F. Sharp interface immersed-boundary/level-set method for wave–body interactions. *J. Comput. Phys.* **2009**, *228*, 6590–6616. [CrossRef]
19. Sun, X.; Sakai, M. Numerical simulation of two-phase flows in complex geometries by using the volume-of-fluid/immersed-boundary method. *Chem. Eng. Sci.* **2016**, *139*, 221–240. [CrossRef]
20. Sussman, M. An adaptive mesh algorithm for free surface flows in general geometries. In *Adaptive Method of Lines*; Chapman and Hall/CRC: Boca Raton, FL, USA, 2001; pp. 227–252.
21. Calderer, A.; Kang, S.; Sotiropoulos, F. Level set immersed boundary method for coupled simulation of air/water interaction with complex floating structures. *J. Comput. Phys.* **2014**, *277*, 201–227. [CrossRef]
22. Ye, H.; Chen, Y.; Maki, K. A discrete-forcing immersed boundary method for turbulent-flow simulations. *Proc. Inst. Mech. Eng. Part M J. Eng. Marit. Environ.* **2020**. [CrossRef]
23. Spalart, P.; Allmaras, S. A one-equation turbulence model for aerodynamic flows. In Proceedings of the 30th Aerospace Sciences Meeting and Exhibit, Reno, NV, USA, 6–9 January 1992; p. 439.
24. Raad, P.E.; Bidoae, R. The three-dimensional Eulerian–Lagrangian marker and micro cell method for the simulation of free surface flows. *J. Comput. Phys.* **2005**, *203*, 668–699. [CrossRef]
25. Lin, S.Y.; Chen, Y.C. A pressure correction-volume of fluid method for simulations of fluid–particle interaction and impact problems. *Int. J. Multiph. Flow* **2013**, *49*, 31–48. [CrossRef]
26. Kleefsman, T. Water impact loading on offshore structures-a numerical study. Ph.D. Thesis, University of Groningen, Groningen, The Netherlands, November 2005.
27. Miao, G. Hydrodynamic Forces and Dynamic Response of Circular Cylinders in Wave Zones. Ph.D. Thesis, University of Trondheim, Trondheim, Norway, 1989.
28. Zhu, X.; Faltinsen, O.M.; Hu, C.; Straub, D.; Faber, M.H.; Morris-Thomas, M.T.; Irvin, R.J.; Thiagarajan, K.P.; Storhaug, G.; Moe, E.; et al. Water Entry and Exit of a Horizontal Circular Cylinder. *J. Offshore Mech. Arct. Eng.* **2007**, *129*, 253–264. [CrossRef]
29. Yoshimura, Y.; Fukui, H.Y.; Yano, H. Mathematical Model for Manoeuvring Simulation including Roll motion. Conference Proceedings The Japan Society of Naval Architects and Ocean Engineers. *Jpn. Soc. Nav. Archit. Ocean. Eng.* **2013**, *16*, 17–20.

Journal of
Marine Science and Engineering

MDPI

Article

Interaction Effect between Hull and Accommodation on Wind Drag Acting on a Container Ship

Ngo Van He [1,*], Ngo Van Hien [1,*], Van-Thuan Truong [1,*] and Ngoc-Tam Bui [2,3,*]

[1] School of Transportation Engineering, Hanoi University of Science and Technology, Hanoi 10000, Vietnam
[2] School of Mechanical Engineering, Hanoi University of Science and Technology, Hanoi 10000, Vietnam
[3] College of Systems Engineering and Science, Shibaura Institute of Technology, Tokyo 135-8548, Japan
* Correspondence: he.ngovan@hust.edu.vn (N.V.H.); hien.ngovan@hust.edu.vn (N.V.H.); thuan.truongvan@hust.edu.vn (V.-T.T.); tambn@shibaura-it.ac.jp (N.-T.B.)

Received: 3 October 2020; Accepted: 9 November 2020; Published: 16 November 2020

Abstract: In this paper, we present our research on applying the commercial Computational Fluid Dynamics (CFD) code to investigate interaction effect between hull and accommodation on wind drag acting above the water hull surface of a full scale 1200 TEU container ship. With this purpose, aerodynamic performances and wind drag acting on the ship hull with and without accommodations have been computed. Analyzing the obtained CFD results, the interaction effect between hull and accommodation on aerodynamic performances and wind drag acting on the ship have been found. Various new accommodation shapes have been proposed for the original ship to reduce the interaction effect on wind drag. A drastic reduction in the interaction effect between hull and accommodation on wind drag acting on the ship has been achieved and the obtained results have been shown in this paper.

Keywords: CFD; interaction effect; wind drag; container ship; aerodynamic

1. Introduction

Nowadays, research on reducing wind resistance acting on ship hull to save fuel consumption and improve economic efficiency is still an attractive topic in the field of marine transportation. This is especially true for container ships with a large windward area, due to their high above-water superstructure and multi-external forms, resulting from the position of containers on the deck, where wind drag accounts for a large percentage of the total resistance. Therefore, researchers around the world are of the opinion that research on reducing wind drag acting on container ships as well as the ships with high superstructure and or large windward areas is more and more important.

It goes without saying that in recent years, a large number of studies on the reduction in wind drag acting on ships' hulls as well as on optimal aerodynamic hull forms, the effect of side covers and domes on wind drag, the interaction effect between hull and accommodation, the effect of strong wind on resistance, the safety of the ship in strong wind, and so on, have been published. A comprehensive review is given as follows:

There are many studies on applying commercial Computational Fluid Dynamics (CFD) to solve the aerodynamic performances of the ships. The most important point of the research is that: the CFD has been a popular and useful tool to solve ships' aerodynamic problems with fairly good accuracy. Using CFD modelling, various types of modified hull shapes with reduced wind drag acting on the ship have been developed [1–7].

Janssen, W.D. et al. (2017) presented a study on using both the commercial CFD code and wind tunnel model test to study aerodynamic performances and wind drag acting on a container ship hull. The 3D steady Reynolds Averaged Navier Stokes (RANS) CFD simulation method was used to solve the problem. The author concluded that CFD results were in good agreement with the experimental

ones and that the CFD could be used to develop a new hull shape with reduced wind drag acting on the ship. The average absolute difference of wind drag obtained in CFD simulation and tunnel test ranged from 37.9% for a box shaped representation of the ship to only 5.9% for a more detailed model. Modelling the spaces in between container stacks decreased the average total wind load considerably. The average absolute difference of total wind load was 10.4%. Using a slender ship hull instead of a blunt ship one decreased total wind load by up to 5.9%. Taking into account wind tunnel blockage following the approach of the engineering science data showed an underestimation of up to 17.5% for the lateral wind load, as shown by comparing the CFD results obtained in the narrow domain with those of the wider domain [1].

Andersen, I.M.V. (2013) presented a study that investigates the influence of the container configuration on the deck of a 900TEU container ship on wind drag by wind tunnel test with scale model of 1:450. The author concluded that the results serve as an indication that the magnitude of wind force acting on a large container ship depends on the container configuration on deck rather than the purpose of assessing the full scale wind resistance of a given container ship. For the reduced longitudinal force in relative wind, it was advantageous to make the container configuration as smooth as possible and streamlining could reduce the force in the head wind. However, streamlining of the configuration on the aft deck was a trade-off as it increased the yaw moment compared to full load on the aft deck. The high container stacks in the configuration appeared to increase the longitudinal force more than the low or empty container bays in the configuration. The transverse force of concern in beam wind depends largely on the side area of the ship, and for a fully loaded ship it could be reduced by reducing the stacking height of the outermost stacks. The yaw moment in relative wind could be reduced by achieving full load on the aft of the ship, and it is possible to reduce the resistance through a combination of drift and increased rudder angle. Moreover, the author gave a general recommendation that the external form of the ship should be made as smooth as possible. In addition, it is important that the center of gravity of the side area was as far from the aft as possible [2].

Fujiwara, T. et al. (2009) presented an experimental investigation on wind force for a container ship with various external forms due to different positions of containers on the desk, in order to study aerodynamic specifications. Based on the obtained experimental results, an estimation method for wind load acting on the container ship has been proposed. In the tunnel experiment, a scale model of 1.5 m long, a mean wind velocity of 25 m/s and a Reynolds number of about 2.4×10^6 have been selected. Under these conditions, the flow field was turbulent and the drag coefficients were independent of the Reynolds number. The authors have shown that a good agreement between their proposed estimation method the tunnel experimental test has been obtained. They also showed that the new method is important for the calculation of speed as well as other characteristics in the operation stage of container ships [3].

In a study presented by Kim, Y. et al. (2015), several design concepts and devices on the superstructure of a container ship have been suggested and tested in a wind tunnel to estimate the wind drag reduction. The authors have also used CFD with the RANS simulation method to estimate wind drag acting on the ship. The results show that the gap protectors between container stacks and visors in front of upper deck have been found to be the most effective means for reducing wind drag acting on the ship. The CFD results agreed with the experimental measurements in the wind tunnel, and the wind drag acting on the modified ships could be reduced by up to 56% in the wind direction angle from 0 to 50 degrees [4]. Other researchers [5–7] also presented results on using CFD and experimental tests to develop a modified hull shape with reduced wind drag acting on a container ship. The authors have proposed modified hull shapes with attached side covers, a center wall, a "T" center wall and a dome at the bow deck of the container ship to reduce wind drag. By using side covers and a center wall, the container ship could reduce wind drag by up to 40% in the head wind direction. A dome at the bow of the ship could reduce the total wind drag acting on the container ship by up to 30% at wind direction angles of less than 30 degrees.

Other available studies focused on the aerodynamic performances and wind drag acting on different types of ships and offshore using both the wind tunnel measurement and CFD simulation. Jun, S. et al. (2020) investigated the resistance performance of ships, using the air resistance correction method [8]. Wnęk, A.D. et al. (2011, 2015) focused on the wind load acting on a LNG carrier with a specific geometrical hull shape [9,10]. Saydam, A.Z. et al. (2018) conducted an evaluation of wind load acting on ships by CFD analysis [11]. He, N.V. et al. (2013, 2016, 2019) presented research on the interaction effect between hull and accommodation on aerodynamic performances and wind drag acting on a wood chip carrier hull [12–14]. Sugata, K. et al. (2010) studied the reduction in wind drag acting on the hull of a Non Ballast water Ship (NBS) [15], and so on [16–19].

The mesh of computed domain effects on the CFD results of a ship has been reported in many previous published works. Viola, I.M. et al. (2009) tested two different mesh numbers of 1 million and 6.5 million tetrahedral elements. The obtained CFD results, i.e., the wind forces, have been compared with those of the experimental ones. It has been observed that the wind forces computed by the turbulent viscous model Realizable k-ε was in good agreement with the experimental results and the differences between computed results in the two mesh numbers were lower than 5% [20]. Wnęk, A.D. et al. (2011, 2015) used two models of a floating LNG platform and an LNG carrier in the 1:400 scale to conduct an experimental tunnel test and CFD computation to investigate the wind forces acting on the models. The turbulent viscous model k-ω SST and three different mesh generation techniques, which were CFD hexa (y+ = 5), CFD tetra (no prism) and CFD tetra y+ (y+ = 0.1), were used for CFD computation. The CFD results of CFD tetra (y+ = 0.1) showed the best agreement with the experimental data obtained in the wind tunnel test and the tetrahedral mesh was shown to be of good quality for the meshing of complex geometric shapes [9,10]. Saydam, A.Z. et al. (2017) used the mesh numbers from 1 million to 5 million elements of unstructured tetrahedral mesh to test CFD results independent of mesh number for computed wind forces acting on the ships. It has been shown that the CFD results were in good agreement with the experimental data obtained in wind tunnel test, and mesh independence of wind forces was up to more than 2 million elements [11]. Watanabe, I. et al. (2016) and Trieu, N.V. et al. (2017a, 2017b) used unstructured tetrahedral mesh with three mesh numbers of 2.2 million, 2.6 million and 3.8 million elements, with y+ of less than 25, to test CFD results independent of mesh. They showed that the CFD results given were in good agreement with the experimental data, and about 2% of the wind drag coefficient was different from the mesh number [5,7,21]. In our previous paper [12–14], we used the same unstructured tetrahedral mesh to investigate the wind drag acting on a wood chip carrier. It has been shown that the CFD results were in good agreement with those of the experimental data obtained in the towing tank test conducted at Osaka Prefecture University, Japan.

In this paper, a commercial CFD code ANSYS-Fluent has been used to investigate the interaction effect between the hull and accommodation of a container ship on wind drag. By applying the CFD, aerodynamic performances and wind drag acting on a 1200 TEU container ship have been computed for two different cases, namely the hull with and without accommodation on its deck, to determine the interaction effect between the hull and accommodation of the ship. From the obtained results, several new hull shapes and frontal accommodation shapes, with reduced interaction effects between hull and accommodation on wind drag acting on the ship, have been proposed in this paper.

2. Original Model and Computed Domain

2.1. Model Ship Used for Computation

The full scale 1200 TEU container ship, which is designed with an accommodation located at the aft, has been used as the reference model for computation. The principal particulars of the ship are given in Table 1, and Figure 1 shows the designed hull form of the original model.

Table 1. Principal dimensions of the 1200TEU container ship.

Name	Description	Value	Unit
L	Length	176.20	m
B	Breadth	24.90	m
H	Depth	13.70	m
d	Draft	8.30	m
$A_{F(x)}$	Frontal projected area	541.29	m^2
$A_{F(y)}$	Lateral projected area	2483.23	m^2
C_b	Block coefficient	0.68	-
α	Wind attack angle	0	degree
V	Wind velocity	12–18	knot
R_e	Reynolds number	$(5.8–8.7) \times 10^7$	-

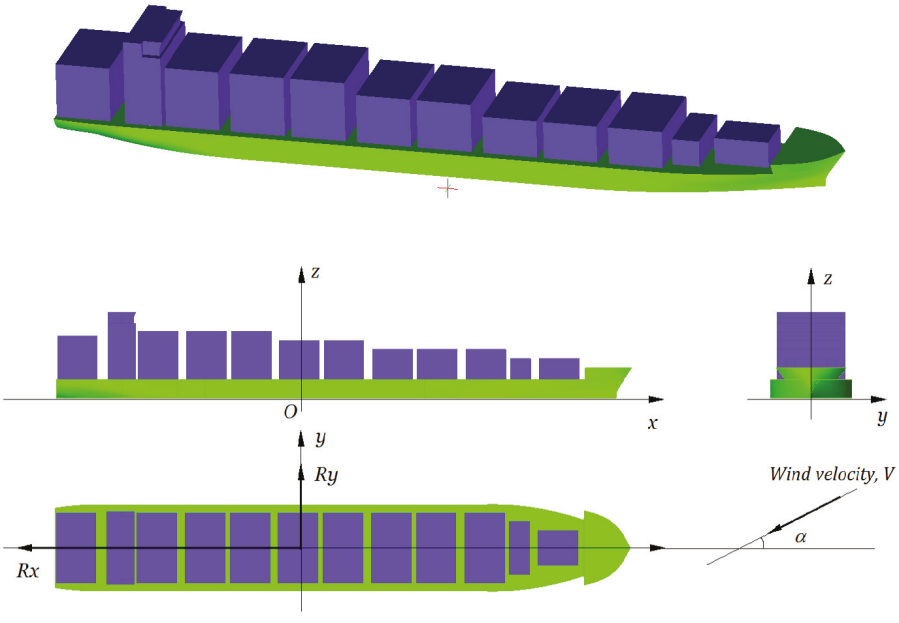

Figure 1. Model of the ship and coordinate system.

2.2. Computational Domain and Boundary Conditions

In this research, all steps for the designed simulation domain, meshing and setting of the boundary conditions have been done as per the user guide published by the International Towing Tank Conference (ITTC) manual for using CFD, [22–26] and our previous publications [12–14]. In this study, the computational domain has been designed with 6.5 L, 2.2 L and 0.75 L instead of 1200 m length, 450 m breadth and 150 m height. Mesh of the computed domain has been used as unstructured mesh with a triple prism layer and y+ has been taken to be less than 5. The popular turbulent viscous model k-ε for unsteady flow has been used. The velocity inlet is given at the inlet as the wind velocity, the pressure outlet is given at the outlet of the computed domain. The bottom, top and sides are given at the walls. To meet realistic case pressure, the outlet makes the open air condition possible, the limited dimension of the computed domain must be designed to be large enough. However, the dimensions of the computed domain has an effect on the mesh number and also an effect on running time. If the top and side of the domain is far enough, the effects on the CFD result become small. Therefore, we must design an appropriate domain and boundary condition. In computation, the time size step is of 0.005 s and

6000 time steps. All cases have been done by an Intel Xeon Gold 6138 2.0 GHz computer, with 3.7 GHz Turbo, 20 C with 64 GB of RAM. Figure 2 shows computed domain and mesh used for simulation.

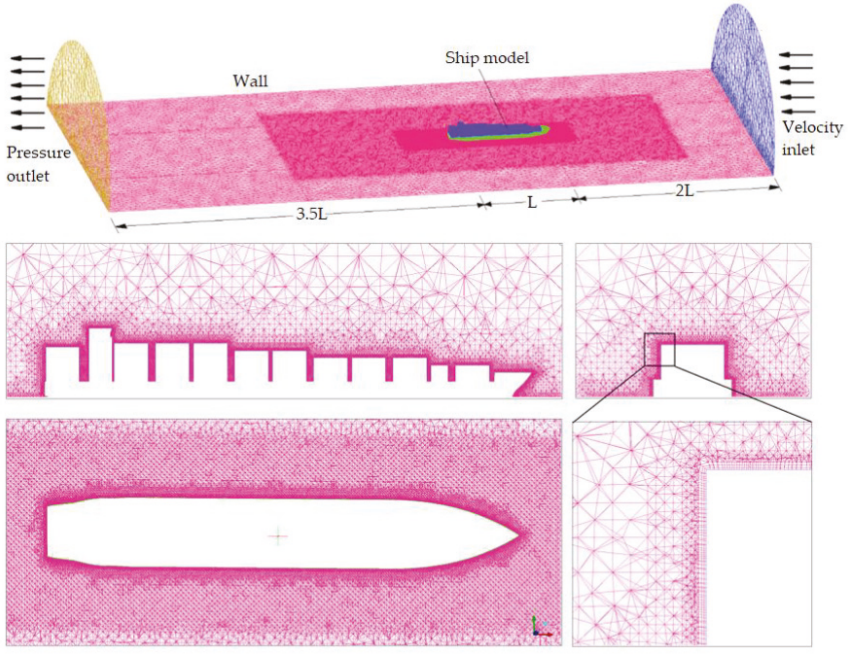

Figure 2. Computational domain and mesh.

2.3. Covegence of Mesh Using for Computation

In this research, the effect of mesh numbers generated in the computed domain on aerodynamic performance and wind drag acting on the original container ship has been investigated. The computed domain is shown in Figure 2, where twelve different mesh numbers have been used. The mesh numbers are from 0.05 to 21.52 million elements and value of y+ is taken from 1.08 to 502.49, respectively. The meshes have been used to compute the aerodynamic performances of the ship under the same conditions. Analyzing the obtained CFD results, the effect of mesh numbers on aerodynamic performances and wind drag as well as the state of independence of mesh numbers have been found. The computation was done in head wind condition at a wind velocity of 14 knot instead of a Reynolds number of 6.73×10^7. Table 2 shows a detailed mesh of the computed domain.

Table 2. The detailed meshes used in computation.

No.	y+	Total Elements ($\times 10^6$)	Minimum Face Area, m^2 ($\times 10^{-2}$)	Maximum Face Area, m^2 ($\times 10^2$)	Minimum Volume, m^3 ($\times 10^{-3}$)	Maximum Volume, m^3 ($\times 10^3$)
1	502.49	0.0575	64.3907	3.1801	414.689	1.3602
2	358.92	0.1504	29.3068	2.3441	117.371	0.9033
3	215.35	0.2267	2.3832	2.0662	6.66706	0.8561
4	143.57	0.3881	2.9348	4.6849	4.32068	2.8079
5	71.78	1.0761	0.2197	3.6252	0.08926	1.8030
6	50.25	1.6178	0.5163	2.6564	0.49978	0.9891
7	35.89	2.4881	0.9272	3.0937	0.99869	2.1242
8	21.54	3.4288	1.1114	1.4511	0.81512	0.6278

Table 2. *Cont.*

No.	y+	Total Elements ($\times 10^6$)	Minimum Face Area, m^2 ($\times 10^{-2}$)	Maximum Face Area, m^2 ($\times 10^2$)	Minimum Volume, m^3 ($\times 10^{-3}$)	Maximum Volume, m^3 ($\times 10^3$)
9	14.36	5.4566	0.0548	4.8017	0.01296	2.7449
10	7.18	8.9854	0.0121	1.0236	0.00326	0.6128
11	3.59	12.3683	0.0092	1.2763	0.00163	0.7629
12	1.08	21.5228	0.0016	2.0125	0.00032	0.6293

Tables 3 and 4 show detailed results of wind drag, and the interaction effect of the mesh number on wind drag acting on the ship. Figure 3 shows the curve of the effect of the mesh number on wind drag, as well as the state of the mesh number becoming independent of the wind drag acting on the ship obtained in the computation.

Table 3. Wind drag acting on the original container ship in the different mesh numbers.

Total Elements ($\times 10^6$)	Wind Drag, R_x (N)			Wind Drag Coefficient, C_d		
	Acc	Hull	Total	Acc	Hull	Total
0.0575	13,464.3	3081.8	16,546.1	0.7829	0.1792	0.9621
0.1504	13,181.5	2910.2	16,091.7	0.7665	0.1692	0.9357
0.2267	13,350.4	2180.2	15,530.6	0.7763	0.1268	0.9031
0.3881	13,328.6	2025.4	15,353.9	0.7750	0.1178	0.8928
1.0761	13,245.9	1917.1	15,163.0	0.7702	0.1115	0.8817
1.6178	13,210.3	1880.2	15,090.5	0.7682	0.1093	0.8775
2.4881	13,115.6	1878.3	14,993.9	0.7627	0.1092	0.8719
3.4288	13,144.7	1837.1	14,981.7	0.7644	0.1068	0.8712
5.4566	13,142.3	1842.1	14,984.4	0.7642	0.1071	0.8713
8.9854	13,040.1	1798.4	14,838.5	0.7583	0.1046	0.8628
12.3683	13,001.2	1792.8	14,794.0	0.7560	0.1043	0.8603
21.5228	13,012.0	1778.1	14,790.1	0.7566	0.1034	0.8600

Table 4. Effect of mesh number on wind drag acting on the ship, at Re = 6.73×10^7, in head wind.

Total Elements ($\times 10^6$)	Different of Wind Drag, ΔR_x, %			Different of Wind Drag Coefficient, ΔC_d, %		
	Acc	Hull	Total	Acc	Hull	Total
0.0575	3.36	42.30	10.61	3.36	42.30	10.61
0.1504	1.29	38.90	8.09	1.29	38.90	8.09
0.2267	2.53	18.44	4.77	2.53	18.44	4.77
0.3881	2.37	12.21	3.67	2.37	12.21	3.67
1.0761	1.77	7.25	2.46	1.77	7.25	2.46
1.6178	1.50	5.43	1.99	1.50	5.43	1.99
2.4881	0.79	5.34	1.36	0.79	5.34	1.36
3.4288	1.01	3.21	1.28	1.01	3.21	1.28
5.4566	0.99	3.48	1.30	0.99	3.48	1.30
8.9854	0.22	1.13	0.33	0.22	1.13	0.33
12.3683	0.08	0.82	0.03	0.08	0.82	0.03
21.5228	0.00	0.00	0.00	0.00	0.00	0.00

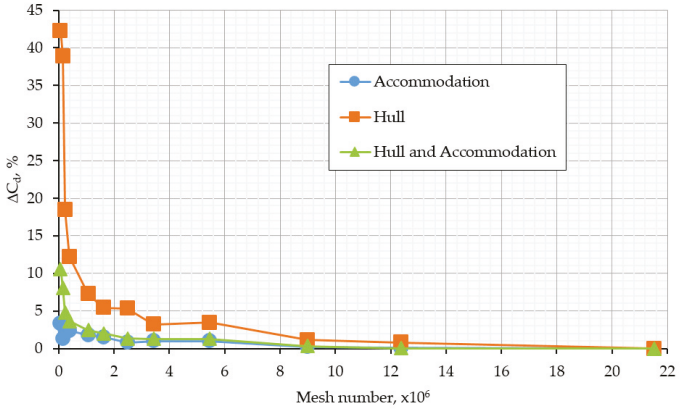

Figure 3. Effect of mesh number on wind drag acting on the ship in head wind, at $R_e = 6.73 \times 10^7$.

Tables 3 and 4 clearly show wind drag acting on the original ship in the different computed mesh numbers, where the wind drag acting on the ship is defined by the following equation [27,28].

$$C_d = \frac{R_x}{0.5\rho A_{F(x)} V^2} \quad (1)$$

where:

C_d is the wind drag coefficient.
R_x is the wind drag acting on the hull, N.
$A_{F(x)}$ is the frontal projected area, m^2.
V is the ship velocity, m/s.

The results given in the Tables 3 and 4 show that the wind drag acting on the ship decreases slowly with increasing mesh number, although the wind drag is slightly different when the y+ is less than 50 and retains the same value when the y+ less than 7. The effect of mesh number on wind drag acting on the ship decreases with the increasing of the mesh number. The difference of wind drag is around 5% when the y+ is less than 50 and the same value when y+ is less than 7. When the y+ increases to over 50 but continues to be less than 500, the difference in wind drag increases by up to 42%, as shown. This is important in studying aerodynamic performances using the CFD tool. Apart from paying attention to calculating the wind drag acting on the ship, it is very useful to get a clear pattern of pressure distribution around the hull to understand how the flow has an effect on the hull, as well as factors affecting the wind drag, and so on.

Figure 3 shows the effect of mesh number on wind drag acting on the ship as well as the mesh convergence curve obtained in computation. From the results shown, it can be seen that when the mesh number increases to over two million instead of a y+ of less than 50, the effect of the mesh number on total wind drag acting on the ship drastically reduces and becomes zero when the y+ is less than 7, as shown. The obtained result is useful in the application of CFD to investigate aerodynamic performances of the ship.

3. Interaction Effect between Hull and Accommodation

In this section, aerodynamic performances of the ship have been computed in two different cases, namely the hull with and without accommodation on its deck. Analyzing the obtained CFD results for the two cases, the interaction effect on aerodynamic performances of the hull and accommodation in

head wind has been obtained. Figure 4 shows the pressure distribution around the ship in the two computed cases at a Reynolds number of 6.73×10^7 in head wind.

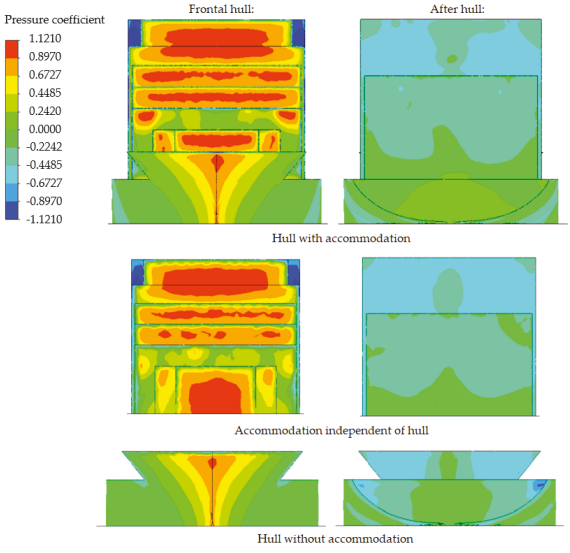

Figure 4. Pressure coefficient distribution over the hull surface of the model in the two computed cases at a Reynolds number of 6.73×10^7, in head wind.

Analyzing the results as shown in Figure 4, the red and yellow regions show high pressure and the blue region shows lower pressure acting on the model. Hence, the effect of hull and accommodation on pressure distribution over the hull surface of the ship could be evaluated. The interaction effect between hull and accommodation may also be determined by comparison of the wind drag acting on the hull and accommodation in both of the computed cases, as shown.

In this research, interaction effect between hull and accommodation on wind drag acting on the ship has been determined by the following Equation (2) [12–14]:

$$\Delta C_d, \% = \frac{C_d(\text{Hull with Acc}) - C_d(\text{Independent Hull and Acc})}{C_d(\text{Independent Hull and Acc})} 100\% \quad (2)$$

where:

ΔC_d, % is the interaction effect between hull and accommodation.
C_d (Hull with Acc) is wind drag coefficient acting on the hull with accommodation.
C_d (Independent Hull and Acc) is total wind drag coefficient acting on hull without accommodation and independent accommodation.

Tables 5–7 show, in detail, the wind drag acting on the hull, the accommodation, and the interaction effect between the hull and accommodation on the wind drag of the ship in head wind.

Analyzing the results shown in the Tables above, the wind drag acting on hull part and accommodation part in the case of the hull with accommodation is less than that of the case of accommodation independent of hull, by up to 42%. The total wind drag acting on the ship in the case of hull with accommodation is also less than that of the independent hull by up to 10%. For the wind drag acting on the hull part and the accommodation part, the interaction effect is about 42% for the hull part and 4% for the accommodation part. The interaction effect between the hull and accommodation on wind drag is around 10%, as shown.

Table 5. Wind drag acting on the hull with accommodation.

	Wind Drag, R_x (N)			Wind Drag Coefficients, C_d		
$R_e \times 10^7$	Acc	Hull	Total	Acc	Hull	Total
5.77	9906.00	1438.69	11,344.69	0.7844	0.1139	0.8983
6.73	13,021.11	1793.28	14,814.39	0.7572	0.1043	0.8614
7.69	17,125.29	2417.25	19,542.54	0.7622	0.1076	0.8697
8.65	22,089.69	3052.63	25,142.32	0.7766	0.1073	0.8839

Table 6. Wind drag acting on an independent hull and independent accommodation.

	Wind Drag, R_x (N)			Wind Drag Coefficients, C_d		
$R_e \times 10^7$	Acc	Hull	Total	Acc	Hull	Total
5.77	10,321.21	2329.01	12,650.22	0.8173	0.1844	1.0017
6.73	13,128.19	3100.13	16,228.31	0.7638	0.1804	0.9442
7.69	17,162.62	4012.14	21,174.76	0.7643	0.1787	0.9429
8.65	22,398.21	5051.24	27,449.45	0.7879	0.1777	0.9656

Table 7. Interaction effect between hull and accommodation on wind drag.

	Different Wind Drag, ΔR_x, %			Difference, ΔC_d, %		
$R_e \times 10^7$	Acc	Hull	Total	Acc	Hull	Total
5.77	4.02	38.23	10.32	4.02	38.23	10.32
6.73	0.82	42.15	8.71	0.87	42.19	8.77
7.69	0.22	39.75	7.71	0.28	39.79	7.76
8.65	1.38	39.57	8.41	1.44	39.60	8.46

4. Reduced Interaction Effect on Wind Drag Acting on the Container Ship

4.1. Proposed Accommodation Shape for the Ship

The original container ship has been designed with an accommodation located at the aft of the ship. In this section, three new hull forms with an accommodation located at the frontal part of ship have been proposed. Three models with frontal accommodation, named N1, N2 and N3, have been used for computation to determine the interaction effect on aerodynamic performances of the proposed streamlined hull shapes. The dimensions of the models are the same ones as those of the original ship shown in Table 1. The computation for all ships have also been done under the same conditions as shown in the Section 2. Figure 5 shows the proposed new models N1, N2 and N3.

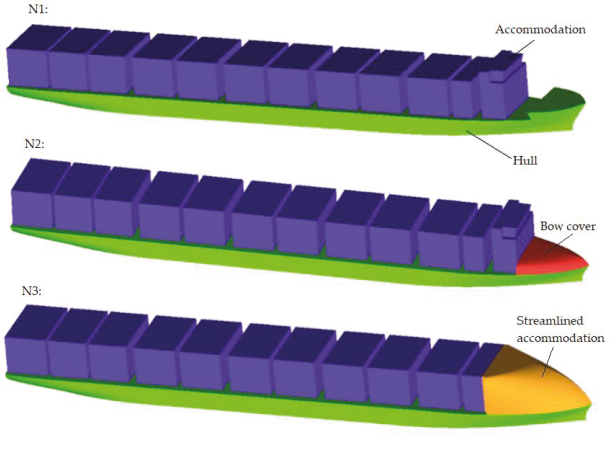

Figure 5. Newly proposed shapes for the ship with frontal accommodation N1, N2 and N3.

In the proposed models, the N1 has the same accommodation shape of the original ship but is located at frontal hull, the N2 has a streamlined bow cover, and the N3 has a streamlined accommodation shape and it is located at frontal hull. Computation has been done for all the models under the same conditions to investigate the aerodynamic performances of the ships.

4.2. Reduced Interaction Effect of the New Hull Shapes on Pressure Distribution

In this section, the effect of the streamlined hull shapes on aerodynamic performances of the proposed container ships have been investigated by the CFD. Figures 6–11 show pressure distribution around and over the hull surface of the ships. Analyzing the obtained CFD results of pressure distribution around and over hull surfaces of the ships, the reasons for the increasing interaction effect between hull and accommodation have been clearly found.

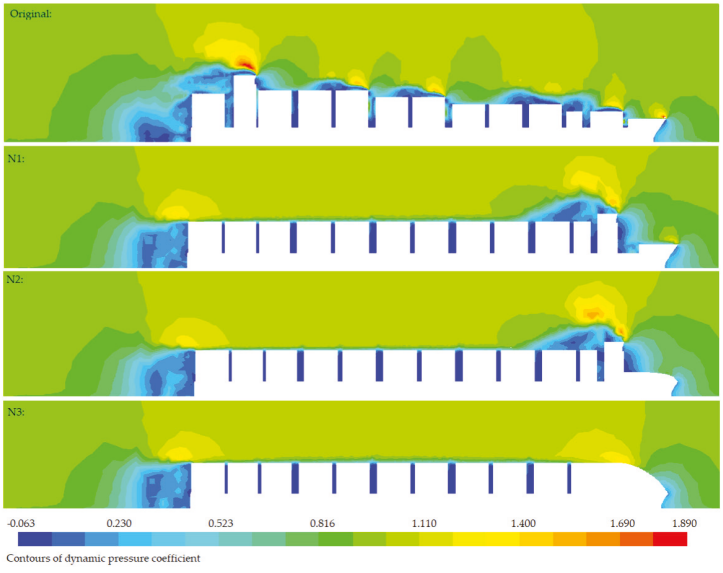

Figure 6. Dynamic pressure coefficient distribution around the ships at the center plane (y/L = 0) in head wind, at $R_e = 6.73 \times 10^7$.

In the above results, the blue region shows low dynamic pressure and, consequently, high static pressure acting on the ship. The results, as shown in Figure 6, clearly show reduced separation flow at the lower dynamic pressure region (blue color region) around the streamlined hull shape N3. Figure 7 shows dynamic pressure distribution around the ships at several horizontal planes of the computed domain.

The results, as shown in Figure 7, clearly show the effects of the accommodation shapes on the dynamic pressure distribution around the ships. The separation flow regions at the low dynamic pressure regions (blue color regions) at the aft of the accommodation N2 and N3 have been drastically reduced, as shown. Figure 8 shows the dynamic pressure distribution around several cross sections of the computed domain of the ships.

The results obtained in the above figures clearly show differences of dynamic pressure distribution around the ships. A drastic reduction in low dynamic pressure region (blue color) could be seen around the hull shapes of N2 and N3, as shown. These results clearly show the reduced interaction effect on ship aerodynamic performance of streamlined accommodation shapes which are located at

frontal hull of the ship. There is a reason why a suitable frontal accommodation should be installed to reduce wind drag acting on the ship hull.

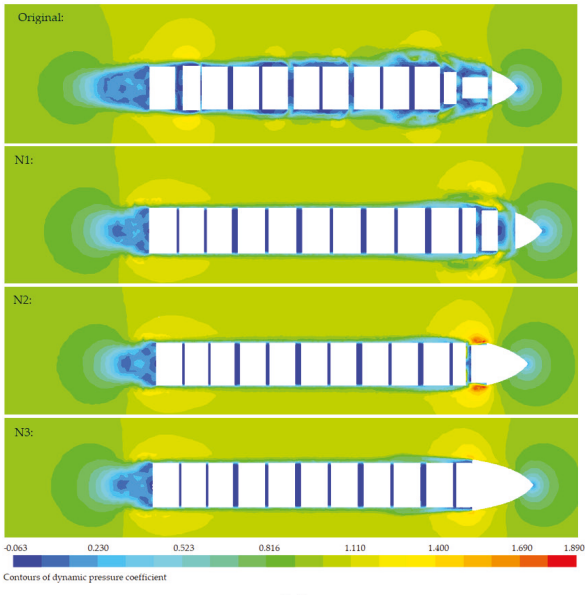

(**a**)

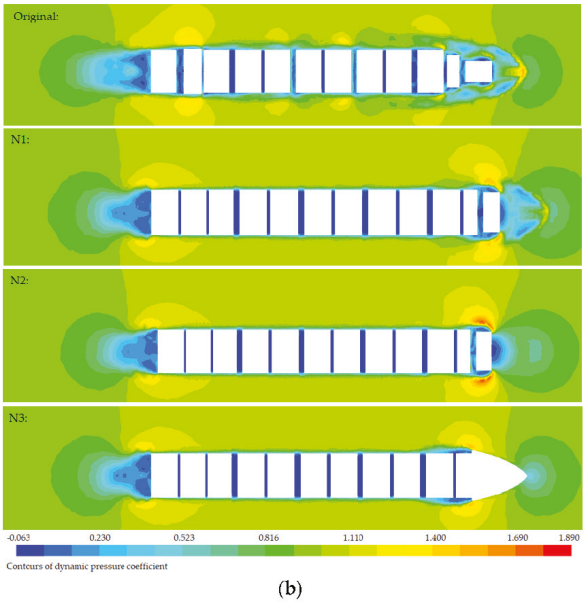

(**b**)

Figure 7. Dynamic pressure coefficient distribution around the ships at the horizontal plane in head wind, at $R_e = 6.73 \times 10^7$. (**a**) z/L = 0.08 and (**b**) z/L = 0.11.

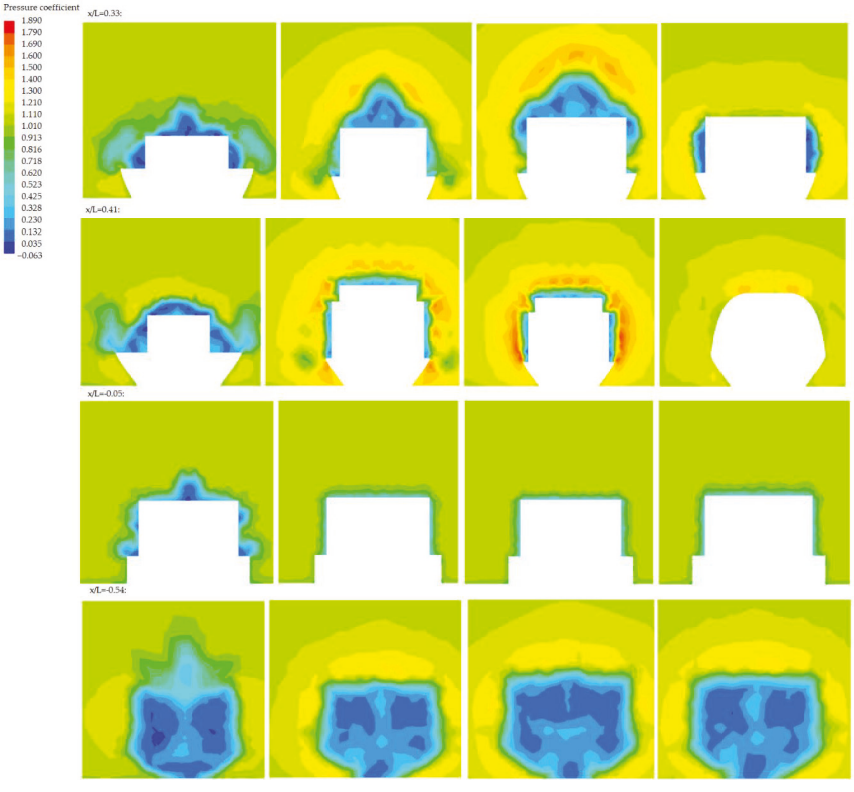

Figure 8. Dynamic pressure coefficient distribution around the ships at various cross sections of the computed domain in head wind, at $R_e = 6.73 \times 10^7$.

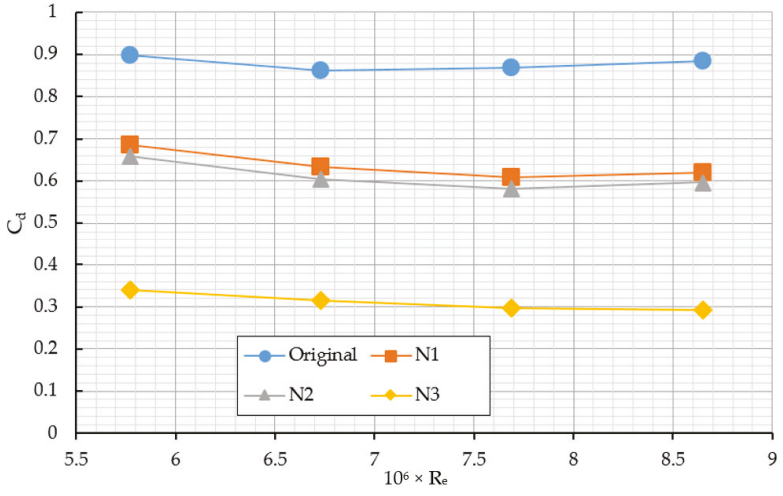

Figure 9. Wind drag acting on the ships with different frontal accommodation shapes in head wind.

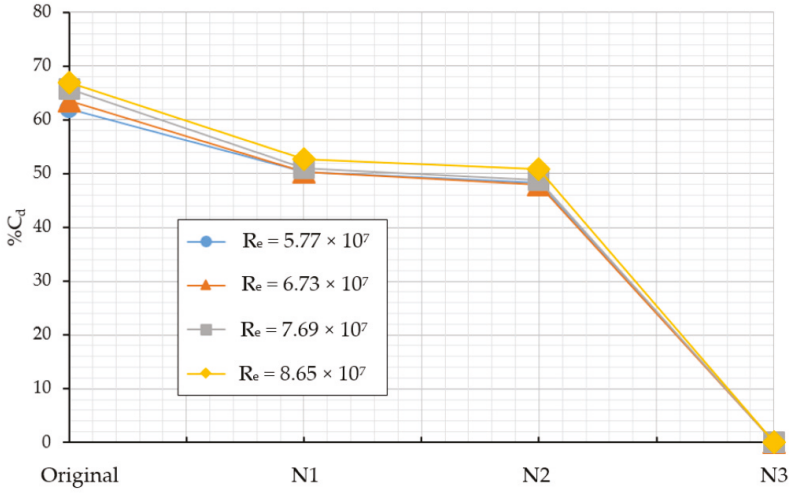

Figure 10. Different wind drag coefficients acting on the ships due to the developed frontal streamlined accommodations.

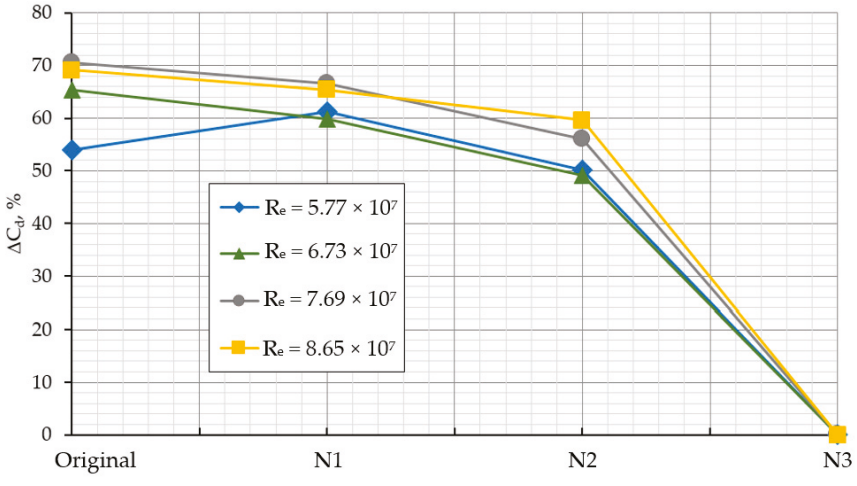

Figure 11. Comparison of interaction effect on wind drag acting on the ship with different frontal accommodation shapes.

4.3. Interaction Effect between Hull and Accommodation on Wind Drag

In this section, wind drag acting on hull of the ship with and without accommodation has been investigated. By comparison, the obtained results of wind drag acting on hull of the ship in two different computed cases, namely hull with and without accommodation, interaction effect between hull and accommodation on wind drag acting on hull, have been found. Moreover, by comparison with the obtained results of wind drag acting on the ship with different accommodation shapes on the deck, the effect of accommodation shapes on wind drag has also been found. Figure 9 shows wind drag acting on the ships with different accommodation shapes on their decks in head wind. A detailed comparison of wind drag acting on the ships is shown in Table 8.

Table 8. Wind drag acting on hull with different frontal accommodation shapes.

	Wind Drag, R_x (N)			Wind Drag Coefficients, C_d		
$R_e \times 10^7$	N1	N2	N3	N1	N2	N3
5.77	8667.38	8326.23	4298.26	0.6863	0.6593	0.3404
6.73	10,881.60	10,387.23	5406.22	0.6328	0.6040	0.3144
7.69	13,678.13	13,093.17	6692.28	0.6087	0.5827	0.2978
8.65	17,611.17	16,966.34	8328.29	0.6191	0.5965	0.2928

The results, as shown in Figure 9, show wind drag coefficients acting on the ship with different frontal accommodation shapes. The results show drastically reduced wind drag acting on the ship by developed frontal accommodations N2 and N3. Table 9 and Figure 10 show detailed differences of wind drag acting on the ship in comparison with those of the original one.

Table 9. Effect of accommodation shape on wind drag acting on the hull of the ship.

	Different Wind Drag, R_x, %			Difference, C_d, %		
$R_e \times 10^7$	N1	N2	N3	N1	N2	N3
5.77	23.60	26.61	62.11	23.60	26.61	62.11
6.73	26.55	29.88	63.51	26.55	29.88	63.51
7.69	30.01	33.00	65.76	30.01	33.00	65.76
8.65	29.95	32.52	66.88	29.95	32.52	66.88

The results given in Table 9 and Figure 10 show drastically reduced wind drag acting on the ships; a reduction of up to 66.88% of the total wind drag has been obtained by developed frontal accommodation shape N3. The frontal box shape accommodation N1 and N2 are also smaller wind drag models, with a reduction of up to 33% of wind drag, as shown. The results of wind drag acting on the ships are in good agreement with the obtained pattern of pressure distribution around and over the hull surface of the ship.

Analyzing the pressure distribution around the ships is a useful tool for finding the reason behind the effects on the wind drag acting on the ship hull. Moreover, the results of the interaction effect between the hull and accommodation on wind drag are highly important from the marine container transportation point of view. Tables 10–12 show the results of the interaction effect between hull and accommodation on wind drag acting on the ship with the different frontal accommodation shapes.

Table 10. Wind drag acting on the hull with accommodation.

	Wind Drag, R_x (N)			Wind Drag Coefficients, C_d		
$R_e \times 10^7$	Acc	Hull	Total	Acc	Hull	Total
			Model N1:			
5.77	7524.57	1142.81	8667.38	0.5958	0.0905	0.6863
6.73	9398.81	1482.79	10,881.60	0.5465	0.0862	0.6328
7.69	12,049.96	1628.17	13,678.13	0.5363	0.0725	0.6087
8.65	15,623.23	1987.94	17,611.17	0.5492	0.0699	0.6191
			Model N2:			
5.77	6796.24	1529.99	8326.23	0.5382	0.1212	0.6593
6.73	8376.86	2010.37	10,387.23	0.4871	0.1169	0.6040
7.69	10,695.20	2397.97	13,093.17	0.4760	0.1067	0.5827
8.65	13,869.29	3097.05	16,966.34	0.4876	0.1089	0.5965
			Model N3:			
5.77	3271.08	1027.18	4298.26	0.2590	0.0813	0.3404
6.73	4083.03	1323.19	5406.22	0.2374	0.0769	0.3144
7.69	5106.26	1586.02	6692.28	0.2273	0.0706	0.2978
8.65	6575.66	1752.63	8328.29	0.2312	0.0616	0.2928

Table 11. Wind drag acting on independent hull and accommodation.

	Wind Drag, R_x (N)			Wind Drag Coefficients, C_d		
$R_e \times 10^7$	Acc	Hull	Total	Acc	Hull	Total
			Model N1:			
5.77	7162.61	2329.01	9491.62	0.5672	0.1844	0.7516
6.73	9011.22	3100.13	12,111.35	0.5240	0.1803	0.7043
7.69	10,987.28	4012.14	14,999.42	0.4890	0.1786	0.6675
8.65	14,406.12	5051.24	19,457.36	0.5064	0.1776	0.6840
			Model N2:			
5.77	7264.60	2109.13	9373.73	0.5752	0.1670	0.7423
6.73	8905.23	3019.18	11,924.41	0.5178	0.1756	0.6934
7.69	10,985.50	3827.16	14,812.66	0.4889	0.1703	0.6592
8.65	14,063.60	5016.12	19,079.72	0.4944	0.1763	0.6707
			Model N3:			
5.77	3432.35	2109.13	5541.48	0.2718	0.1670	0.4388
6.73	4220.22	3019.18	7239.40	0.2454	0.1756	0.4210
7.69	5263.25	3827.16	9090.41	0.2342	0.1703	0.4046
8.65	6456.65	5016.12	11,472.77	0.2270	0.1763	0.4033

Table 12. Interaction effect between hull and accommodation on wind drag.

	Wind Drag, ΔR_x, %			Difference, ΔC_d, %		
$R_e \times 10^7$	Acc	Hull	Total	Acc	Hull	Total
			Model N1:			
5.77	5.05	50.93	8.68	5.05	50.93	8.68
6.73	4.30	52.17	10.15	4.30	52.17	10.15
7.69	9.67	59.42	8.81	9.67	59.42	8.81
8.65	8.45	60.64	9.49	8.45	60.64	9.49
			Model N2:			
5.77	6.45	27.46	11.17	6.45	27.46	11.17
6.73	5.93	33.41	12.89	5.93	33.41	12.89
7.69	2.64	37.34	11.61	2.64	37.34	11.61
8.65	1.38	38.26	11.08	1.38	38.26	11.08
			Model N3:			
5.77	4.70	51.30	22.43	4.70	51.30	22.43
6.73	3.25	56.17	25.32	3.25	56.17	25.32
7.69	2.98	58.56	26.38	2.98	58.56	26.38
8.65	1.84	65.06	27.41	1.84	65.06	27.41

The results shown in Tables 10–12 clearly show wind drag acting on the ship with the different accommodation shapes in two computed cases, namely the hull with and without accommodation in head wind. The interaction effect between hull and accommodation on wind drag acting on the ship is drastically reduced due to the developed frontal accommodation shapes, as shown. The interaction effect on wind drag acting on the accommodation part is less than 10% and up to 65% of the hull part. The interaction effect on the total wind drag is about 10% of the frontal box shape accommodations N1 and N2, and up to 27% for the streamlined accommodation N3. Figure 11 shows a comparison of the interaction effects on wind drag acting on the ship with different frontal accommodation shapes.

The results show a drastically reduced interaction effect between hull and accommodation on wind drag of the model N3. The interaction effect between hull and accommodation of the original ship is higher than that of the model N3, by up to 70%, as shown. The obtained results are very useful to develop a new accommodation shape with reduced interaction effect and wind drag acting on the ship hull as little as possible.

For a streamlined accommodation shape like the proposed model N3, the interaction effect between hull and accommodation on wind drag has been drastically reduced, as shown. Most researchers are of the opinion that the streamlined accommodation is the best shape to reduce wind drag acting on the

ship when in operation. However, the huge streamlined accommodation shape is difficult to be made and will also require a very high cost. Therefore, an accommodation shape which is simply made of only plat plates but still capable of producing a reduced wind drag could be a good choice for the ship building industry.

5. Conclusions

In this paper, aerodynamic performances of a container ship in head wind have been simulated by CFD. From the obtained results, the interaction effect between hull and accommodation has been investigated. Furthermore, the obtained results in this paper have shown that the newly proposed frontal accommodation shapes can be used to considerably reduce wind drag acting on the container ships, leading to more economic fuel consumption in marine transportation. The main conclusions are summarized as follows:

- The effect of mesh number on aerodynamic performances of the reference container ship has been determined. The obtained results show that the effect of mesh number on wind drag acting on the container ship is about 10% when the value of y+ is less than 50 and the same value when y+ is less than 7.
- The CFD results for the two computed cases, namely the original ship hull with and without accommodation, have been obtained. The effect of the hull on the wind drag is as high as 42%, while the interaction effect between hull and accommodation of the container ship on the total wind drag has been evaluated and is only about 10%.
- The newly proposed frontal accommodation shapes' effect on aerodynamic performance as well as wind drag acting on hull of the ship. It has been shown that the developed frontal accommodation shapes affect both the pressure distribution around the ship hull and the separation regions around the accommodation. Hence, a suitable shape of the frontal accommodation could be installed to greatly reduce the total wind drag.
- The effect of accommodation shapes on wind drag acting on hull of the ship has been investigated. Using the proposed frontal accommodation shapes, up to 30% of the total wind drag in head wind (N1), and up to 66.88% of the total wind drag acting on the hull at a Reynolds number of 8.65×10^7 in head wind (N3), could be reduced.
- The interaction effect between the hull and accommodation of the ship, with different accommodation shapes, has been investigated. Drastically reduced interaction effects on wind drag acting on the hull, using the accommodation shape N2 (up to 49%) and using the accommodation shape N3 (up to 70%), have been shown.

Author Contributions: Conceptualization, N.V.H. (Ngo Van He), N.V.H. (Ngo Van Hien), V.-T.T. and N.-T.B.; methodology, N.V.H. (Ngo Van He), N.V.H. (Ngo Van Hien), V.-T.T. and N.-T.B.; software, N.V.H. (Ngo Van He), N.V.H. (Ngo Van Hien) and V.-T.T.; validation, N.V.H. (Ngo Van He), N.V.H. (Ngo Van Hien), V.-T.T. and N.-T.B.; writing—original draft preparation, N.V.H. (Ngo Van He), N.V.H. (Ngo Van Hien) and V.-T.T.; writing—review and editing N.V.H. (Ngo Van He), N.V.H. (Ngo Van Hien), V.-T.T. and N.-T.B.; supervision, N.V.H. (Ngo Van Hien); project administration, N.V.H. (Ngo Van He). All authors have read and agreed to the published version of the manuscript.

Funding: Vietnam National Foundation for Science and Technology Development (NAFOSTED).

Acknowledgments: This research is funded by Vietnam National Foundation for Science and Technology Development (NAFOSTED) under the grant number 107.03-2019.302. The authors would like to warmly express their thanks for the support.

Conflicts of Interest: The authors declare no conflict of interest.

References

1. Janssen, W.; Blocken, B.; van Wijhe, H. CFD simulations of wind loads on a container ship: Validation and impact of geometrical simplifications. *J. Wind Eng. Ind. Aerodyn.* **2017**, *166*, 106–116. [CrossRef]

2. Andersen, I.M.V. Wind loads on post-panamax container ship. *Ocean Eng.* **2013**, *58*, 115–134. [CrossRef]
3. Fujiwara, T.; Tsukada, Y.; Kitamura, F.; Sawada, H. Experimental Investigation and Estimation on Wind Forces for a Container Ship. In Proceedings of the Nineteenth International Offshore and Polar Engineering Conference, Osaka, Japan, 21–26 July 2009; pp. 555–562.
4. Kim, Y.; Kim, K.-S.; Jeong, S.-W.; Jeong, S.-G.; Van, S.-H.; Kim, Y.-C.; Kim, J. Design and performance evaluation of superstructure modification for air drag reduction of a container ship. In Proceedings of the Twenty-Fifth International Ocean and Polar Engineering Conference, Kona, HI, USA, 21–26 June 2015.
5. Van Nguyen, T.; Kinugawa, A. Development of Practical Gap Covers to Reduce Air Resistance Acting on Deck Containers of a Ship. In Proceedings of the 23th conference Japan Society of Naval Architects and Ocean Engineers, Hiroshima, Japan, 2017; pp. 211–216.
6. Van Nguyen, T. Vortex Control in Gap Flow by Small Appendages to Reduce Air Resistance Acting on Deck Containers of a Ship. In Proceedings of the 24th Conference Japan Society of Naval Architects and Ocean Engineers, Tokyo, Japan, 26 May 2017; pp. 335–338.
7. Watanabe, I.; Van Nguyen, T.; Miyake, S.; Shimizu, N.; Ikeda, Y. A study on reduction of air resistance acting on a large container ship. *Proc. APHydro* **2016**, *2016*, 321–330.
8. Seok, J.; Park, J.-C. Comparative Study of Air Resistance with and without a Superstructure on a Container Ship Using Numerical Simulation. *J. Mar. Sci. Eng.* **2020**, *8*, 267. [CrossRef]
9. Wnęk, A.; Soares, C.G. Numerical Analysis of the Shadow Effect of an LNG Floating Platform on an LNG Carrier under Wind Conditions. In *Sustainable Maritime Transportation and Exploitation of Sea Resources*; Taylor & Francis Group: London, UK, 2012.
10. Wnęk, A.; Soares, C.G. CFD assessment of the wind loads on an LNG carrier and floating platform models. *Ocean Eng.* **2015**, *97*, 30–36. [CrossRef]
11. Saydam, A.Z.; Taylan, M. Evaluation of wind loads on ships by CFD analysis. *Ocean Eng.* **2018**, *158*, 54–63. [CrossRef]
12. He, N.V.; Ikeda, Y. A Study on Interaction Effects between Hull and Accommodation on air Resistance of a Ship. In Proceedings of the Conference Japan Society of Naval Architects and Ocean Engineers, Fukuoka, Japan, 27–28 May 2013; pp. 281–284.
13. Van He, N.; Mizutani, K.; Ikeda, Y. Reducing air resistance acting on a ship by using interaction effects between the hull and accommodation. *Ocean Eng.* **2016**, *111*, 414–423. [CrossRef]
14. Van He, N.; Mizutani, K.; Ikeda, Y. Effects of side guards on aerodynamic performances of the wood chip carrier. *Ocean Eng.* **2019**, *187*, 106217. [CrossRef]
15. Sugata, K.; Iwamoto, Y.; Ikeda, Y.; Nihei, Y. Reduction of Wind Force Acting on Non Ballast Ship. In Proceedings of the 5th Asia Pacific Workshop on Marine Hydrodynamics-APHydro2010, Osaka, Japan, 1–4 July 2010; pp. 1–4.
16. Du, L.; Lin, Z.; Jiang, Y.; Li, P.; Dong, Y. Numerical Investigation on the Scale Effect of a Stepped Planing Hull. *J. Mar. Sci. Eng.* **2019**, *7*, 392. [CrossRef]
17. Schmitt, P.; Windt, C.; Davidson, J.; Ringwood, J.V.; Whittaker, T. The efficient application of an impulse source wavemaker to cfd simulations. *J. Mar. Sci. Eng.* **2019**, *7*, 71. [CrossRef]
18. Zalesny, V.; Agoshkov, V.; Aps, R.; Shutyaev, V.; Zayachkovskiy, A.; Goerlandt, F.; Kujala, P. Numerical modeling of marine circulation, pollution assessment and optimal ship routes. *J. Mar. Sci. Eng.* **2017**, *5*, 27. [CrossRef]
19. Feng, D.; Ye, B.; Zhang, Z.; Wang, X. Numerical Simulation of the Ship Resistance of KCS in Different Water Depths for Model-Scale and Full-Scale. *J. Mar. Sci. Eng.* **2020**, *8*, 745. [CrossRef]
20. Viola, I.M. Downwind sail aerodynamics: A CFD investigation with high grid resolution. *Ocean Eng.* **2009**, *36*, 974–984. [CrossRef]
21. Nguyen, T.; Shimizu, N.; Kinugawa, A.; Tai, Y.; Ikeda, Y. Numerical studies on air resistance reduction methods for a large container ship with fully loaded deck-containers in oblique winds. In Proceedings of the VII International Conference on Computational Methods in Marine Engineering, MARINE, Gothenburg, Sweden, 13–15 May 2019; pp. 1040–1051.
22. Ittc, R. *Procedures and Guidelines: Practical Guidelines for Ship CFD Applications, 7.5*; ITTC: London, ON, Canada, 2011; pp. 1–18.
23. Celik, I.B.; Ghia, U.; Roache, P.J.; Freitas, C.J. Procedure for estimation and reporting of uncertainty due to discretization in CFD applications. *J. Fluids Eng. Trans. Asme* **2008**, 1–130.

24. Collie, S.; Gerritsen, M.; Jackson, P. *A Review of Turbulence Modeling for Use in Sail Flow Analysis*; Report; University of Auckland's Faculty of Engineering: Auckland, New Zealand, 2001.
25. Xia, M.; Jiang, L. Application of an unstructured grid-based water quality model to Chesapeake Bay and its adjacent coastal ocean. *J. Mar. Sci. Eng.* **2016**, *4*, 52. [CrossRef]
26. Windt, C.; Davidson, J.; Schmitt, P.; Ringwood, J.V. On the assessment of numerical wave makers in CFD simulations. *J. Mar. Sci. Eng.* **2019**, *7*, 47. [CrossRef]
27. Bertram, V. *Practical Ship Hydrodynamics*; Elsevier: Amsterdam, The Netherlands, 2011.
28. Murdock, J.W. *Fundamental Fluid Mechanics for the Practicing Engineer*; CRC Press: Boca Raton, FL, USA, 1993.

Journal of
Marine Science and Engineering

MDPI

Article

Numerical Analysis of the Rudder–Propeller Interaction

Diego Villa *, Andrea Franceschi and Michele Viviani

Department of Electrical, Electronic and Telecommunications Engineering and Naval Architecture (DITEN), University of Genova, 16126 Genova, Italy; andrea.franceschi@edu.unige.it (A.F.); michele.viviani@unige.it (M.V.)

* Correspondence: diego.villa@unige.it; Tel.: +39-010-335-2345

Received: 10 November 2020; Accepted: 3 December 2020; Published: 4 December 2020

Abstract: The proper evaluation of the Rudder–Propeller interactions is mandatory to correctly predict the manoeuvring capability of a modern ship, in particular considering the commonly adopted ship layout (rudder often works in the propeller slipstream). Modern Computational Fluid Dynamics (CFD) solvers can provide, not only the performance of the whole system but also an insight into the flow problem. In the present paper, an open-source viscous flow solver has been validated against available literature experimental measurements in different conditions. After an extensive analysis of the numerical influence of the mesh arrangement and the turbulent quantities on the rudder provided forces, the study focused its attention on the forces generated by the rudder varying the propeller loading conditions and the mutual position between the two devices. These analyses give a hint to describe and improve a commonly-used semi-empirical method based on the actuator disk theory. These analyses also demonstrate the ability of these numerical approaches to correctly predict the interaction behaviour in pre-stall conditions with quite reasonable computational requests (proper also for a design stage), giving additional information on the sectional forces distribution along the span-wise rudder direction, useful to further develop a new semi-empirical rudder model.

Keywords: Reynolds Average Navier–Stokes (RANS); rudder–propeller interactions; validations and verification; actuator disk theory; rudder sectional forces

1. Introduction

The rudder is the most common steering device adopted to control the ship track. It is a lifting surface positioned, normally, in the stern ship region which, generating a lateral force, guarantees to perturb the ship direction. The correct design of its performance is mandatory to be able to control the ship's route and to obtain good manoeuvring and course-keeping ability of the ship, in particular, when auto-pilot or dynamic positioning capability are of interest ([1] or [2]). For safety reasons, at the beginning of the century, the International Maritime Organization (IMO) ([3,4]) required to satisfy mandatory manoeuvrability criteria for new ship constructions.

From a hydrodynamic point of view, it is a fairly simple device. It is a finite wing completely submerged (for big ships) with simple shapes. Despite its simplicity, in modern ships, in most cases it works in the propeller slipstream. This poses several issues in terms of predictability of hydrodynamic performance because its developed forces are not only correlated with the rudder characteristics (such as rudder span or chord size) but also with the propeller size and its working conditions (see [5]). Often, due to the complexity of the problem (further increased by the presence of the ship wake), traditional approaches based on semi-empirical mathematical models are still fashionable in the preliminary design stage, mainly due to their low computational demands ([6]). These approaches nowadays start to be overcome by fully viscous CFD codes which, however, are characterised by very high computational costs (see for instance [7]). In light of this, the traditional manoeuvrability

methods based on semi-empirical mathematical models ([8–10]) require not only a correct hull forces description ([11,12]) but also a complete and accurate model of rudder performance, able to provide their forces starting from kinematic quantities and known propeller settings.

In the past, several researchers worked on this topic using both experimental (among the others [13–16]) and numerical approaches. Different numerical approaches have been adopted in the reference literature, ranging from simpler potential ones (see for instance [17–21]) up to more demanding ones based on the complete flow equations ([7,22–24]). Particular attention should be paid also to hybrid methods, which try to merge the benefits of both approaches, consequently reducing the overall computational costs (among the others [5,25,26]).

The researchers who adopted numerical codes have focused their attention on different flow problems, ranging from the isolated rudder condition, often with peculiar rudder shapes ([14,15]) or when it interacts with a propeller ([27,28]). Others, on the contrary, considered the more complex problem which includes the mutual interactions of the complete system, i.e., rudder–propeller–hull (as in [24]).

This paper starts with a general overview of the numerical approach here adopted in Section 2, followed by a description of the reference rudder and the test conditions considered (Section 3). Then, after the description of the used propeller model and an in-depth comparison with the actuator disk theory in Section 4, the open-water rudder performances are compared with available experimental measurements (Section 5) focusing attention on the influence on the simulation results caused by the mesh arrangement and the turbulent quantities. These preliminary results provide the basic model set-up for the successive numerical and experimental comparisons when the rudder operates behind the propeller in different reciprocal positions (Section 6). These results provide the key to analyse and update a widely-used mathematical model for predicting the rudder forces behind a propeller (Section 7). Section 8 shows further analyses extracted by the CFD results analysing the rudder sectional forces, these can be used to better describe how the rudder–propeller interactions occur. Finally, some conclusions are presented in the last section.

2. Numerical Background

Several viscous codes are nowadays available to assess the performance of a moving finite wing immersed in a fluid. In the present paper, the open-source CFD library OpenFOAM has been considered as flow solver. This code has been demonstrated to be able to tackle marine problems with high quality results (see for instance [29–31]). It is designed to solve the flow field characteristics by adopting a general polyhedral mesh with a finite volume approach. The classical Navier–Stokes equations, which are here presented in time-varying form for an incompressible flow (see Equation (1)), are used taking advantage of the classical Reynolds decomposition to account for the turbulent effects.

$$\begin{cases} \nabla \cdot U = 0 \\ \rho \dfrac{\partial U}{\partial t} + \rho(U \cdot \nabla U) = -\nabla p + \mu \nabla^2 U + \nabla T^{Re} + S \end{cases} \tag{1}$$

where ρ and μ are the average density and molecular viscosity of the fluid, respectively, which, for the present case, have been considered constant in time and space, therefore, under the incompressibility assumption. U and p are the main flow characteristics: respectively velocity and pressure fields. These quantities have been averaged following the Reynolds decomposition, which adds in the momentum equation a turbulent stress tensor (T^{Re}) properly defined to account for the turbulent effects on the mean flow fields. The present equation form further includes a momentum source term (S), which is devoted to adding external mass forces into the motion equations. The latter term, commonly considered to include gravitational forces, is one of the key features here adopted to consider the propeller effect in the viscous simulations, without completely discretising its geometry.

The propeller effect has been, therefore, simulated following the same procedure already proposed in [5,32]. Instead of including the real blade geometry, which consequently requires a very dense

mesh in that region and a proper solver able to consider the propeller revolution rate (as sliding or overlapping mesh approaches), a simple force field can be considered in place of the propeller disc. This approach mimics the well-known immersed-boundary method (IB first proposed by [33]) further avoiding to resolve also the blade forces. As demonstrated in previous works (see [5]), although the local force unsteadiness (mainly due to the blade vortices interacting with the rudder, see also [34,35]) is out of the aim of the study (as for this case), only a reliable mean force distribution is required to reproduce the mean flow field behind the propeller correctly. Regarding the numerical set-up for the rudder performance evaluations (see Figure 1), a box domain with the same cross-section of the experimental wind-tunnel facility (see next section) is used. The inlet and outlet surfaces have been positioned sufficiently far enough (2.2 m upstream and 3.8 m downstream the rudder position) to avoid unwanted influences, and a symmetry condition has been imposed for the far-field boundaries (red surfaces in Figure 1). A prescribed velocity and pressure field have been imposed at the inlet and outlet, respectively, and for all the other wall surfaces (rudder and lower surface, in yellow in the figure), a wall condition is imposed. A mesh of about 1.5 million cells has been obtained. Further details, together with the mesh dependence analysis are reported in a previous work [5], and not repeated here for the sake of brevity.

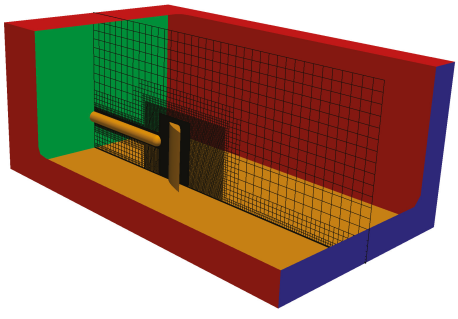

Figure 1. Sketch of the adopted mesh for the rudder with propeller simulation.

3. Test Cases

A considerable amount of experimental data is available in the literature dealing with the forces experienced by rudders. The most complete ones are the experimental measurements performed by [16,36]) at the Southampton low-speed wind tunnel over several years. They adopted a simple spade rudder characterized by a constant sectional profile defined by the NACA 4 digit series (NACA0020). The rudder dimensions were 1 m span and a constant chord of 0.667 m (see Table 1). Therefore, a rectangular rudder longitudinal profile was considered. Even if this shape is far from real rudder shapes nowadays used for ships, thanks to the extensive measurements performed by different authors, this series is an excellent numerical benchmark.

Table 1. Rudder main data (named N.2 in the original paper).

Data	Value	Unit
Section	NACA 0020	-
Span	1	m
Chord	0.667	m
Effective A.R.	3	-
t/c	0.2	-
Taper Ratio	1	-

The rudder was mounted in tandem with a propeller (as depicted in Figure 2). This particular experimental setup adopted allows to explore several rudder/propeller configurations (for instance varying their relative positions).

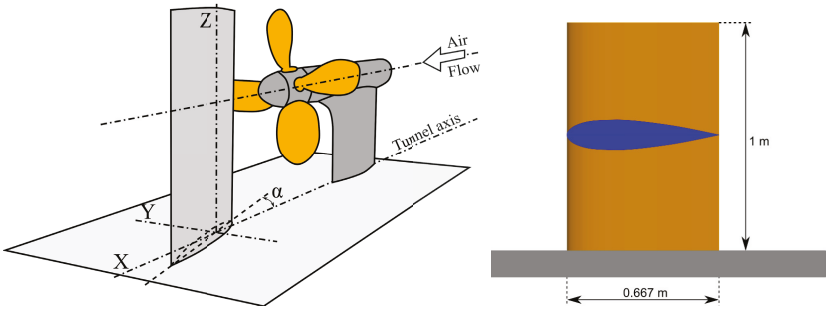

(**a**) Sketch of the Experimental setup (**b**) Plan view of the rudder (CFD model)

Figure 2. Rudder overview and main data.

The propeller was a modified Wageningen B4-40 propeller made of fibre-glass (see Table 2), more details can be found in reference literature [37]. The experimental measurements covered two flow speeds (10 and 20 m/s, equivalent to 4.4×10^5 and 8.8×10^5 Reynolds number respectively) and a wide range of angles of attack in a wind tunnel with a rectangular test section of about 3.5×2.5 m.

Table 2. Propeller main data (Modified Wageningen B4.40 Series).

Data	Value	Unit
N. blades	4	-
Diameter	0.80	m
Hub Diameter	0.20	m
P/D	0.95	-
Rake	0	-

4. Analysis of the Effectiveness of the Propeller Approach

When a rudder operates in the propeller slipstream (the usual arrangement for modern ships), its performances is strongly related to the propeller working point. For this reason, as a first step, it is mandatory to show the propeller model capability and accuracy here adopted. As mentioned previously, the time-averaged flow field generated by the propeller has been included in the viscous simulations via a body force approach. This approach guarantees to correctly reproduce the flow acceleration generated by the propeller (if the correct force distribution is considered) with a minimal increase of computational requests. This model, to correctly work, must be fed with the blade load distribution obtained by preliminary CFD open-water results. Different numerical methods (in some cases simplified and not very time consuming) can be used to generate the correct blade load, see for instance the ones based on the potential theory (lifting lines, lifting surfaces or Boundary Element Methods) or the ones based on the blade element momentum theory. All these approaches require a small additional computational effort (compared to a viscous solver), so they could also be applied for extensive analysis at all ship design stages. A fast and accurate viscous flow solver has been adopted here. Its numerical set-up can be found in previous works (see for instance [38,39]), not here reported for brevity. Through this type of solver, a quite wide range of advance coefficients ($J = \frac{V}{n \cdot D}$) can be easily computed with adequate confidence.

Figure 3 shows the comparison of the computed non-dimensional thrust, torque and load ($\frac{K_T}{J^2}$) coefficients with respect to all the measurements reported in [16] for the here adopted propeller.

All the EFD data come from different tests (different revolution rates and flow speeds), consequently, showing also the uncertainty range of the measurements. An overall good agreement between the predictions and the measurements can be highlighted from the figure, demonstrating the reliability of the proposed CFD simulations. Only the torque shows a slight underestimation, mainly due to the small Reynolds number adopted in the experiments. Anyway, for the sake of completeness, the torque values are not so correlated with the propeller/rudder interaction effects in term of lift as shown in last part of this work; therefore, these discrepancies can be neglected. In light of these considerations, the blade load distribution, defined as the sectional longitudinal and tangential forces provided by the blades, has been extracted from the simulations. Three characteristic working conditions, the design one (about $J = 0.5$) and two off design ones (about $J = 0.3$ and 0.9), have been considered. The obtained distributions are depicted in Figure 4, reporting both the longitudinal and tangential contribution with respect to the sectional forces generated by the blades.

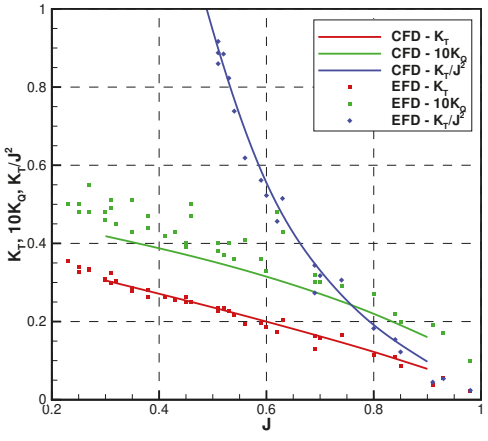

Figure 3. Numerical and experimental comparison of thrust and load coefficients.

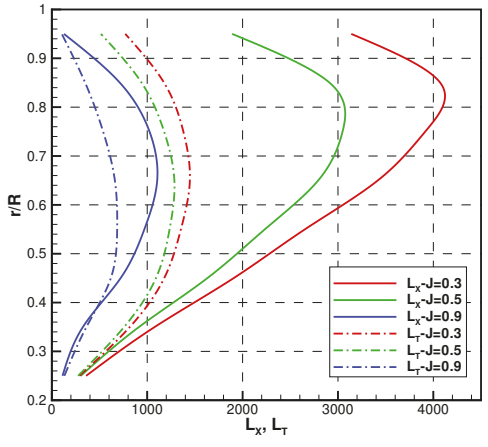

Figure 4. Longitudinal (solid) and tangential (dashed) sectional forces at three advance coefficients with high (J = 0.3), low (J = 0.9) and medium (J = 0.5) loads.

Figure 4 clearly shows that decreasing the advance coefficient, the load distribution increases, shifting its maximum upward (in the radial direction). Ref. [5] already showed this effect, where, for the same propeller, the bollard pull condition was considered. In that case, the maximum load value was positioned almost at the blade tip. Similar behaviour also involves the tangential component (the one which generates the torque experienced by the propeller), which, differently from the axial component, is often characterized by a peak positioned nearer to the hub (at about half the blade span).

In the literature, the overall propeller effect on the flow field is normally represented by the actuator disk theory. Based on this theory, the flow acceleration index a (defined as the ratio between the induced velocity in the propeller disk and the inflow speed) provided by a propeller is a function (see Equation (3)) of the thrust coefficient defined in (2).

$$C_T = \frac{T}{1/2\rho(\pi R^2)V^2} \tag{2}$$

$$a = \frac{1}{2}(\sqrt{1+C_T} - 1) \tag{3}$$

where R stands for the propeller radius and T and V are respectively the propeller thrust and the average in-flow velocity to the propulsor. These increased velocities can be found inside the tube flow generated by the propeller disk. The shape of this tube, and the average velocities inside it, can be approximated by the following Equations (4) and (5) respectively.

$$D(x) = D\sqrt{\frac{1+a}{1+K_P \cdot 2a}} \tag{4}$$

$$U(x) = V(1 + K_P \cdot 2a) \tag{5}$$

where a is the acceleration index computed in Equation (3), D is the propeller diameter and V is the undisturbed speed. Their behaviours are therefore proportional to the K_P coefficient, dependent upon the non-dimensional distance (x) between the propeller and the rudder with respect to the propeller radius. The coefficient K_P ranges between 0 for $x \to -\infty$ and 1 for $x \to \infty$. Moreover, it assumes the value of 0.5 for $x = 0$. A possible approximation of the variation of K_P with the longitudinal position is:

$$K_P(x) = 0.5 + 0.36 \times \tanh(0.98x) + 0.11 \times \tanh(15x) \tag{6}$$

Other formulations exist for these quantities like the one proposed by Brix in [40], which generates (only for the propeller slip-stream region) a quite similar behaviour.

The experimental activities focus their attention on three propeller working conditions characterized by different propeller loads ($K_T/J^2 = 0.05, 0.88, 2.3$). In light of this, a simple simulation with only the propeller, represented via the body force approach, has been carried out imposing the corresponding thrust and torque. These simulations have been carried out considering the rudder domain, but excluding the rudder surface. Each simulation adopts the proper thrust and torque radial distribution previously mentioned. Figure 5 shows the computed velocities (made non-dimensional by means of the acceleration index a times the inflow speed) in the propeller disk for the three loads considered. These behaviours qualitatively well match the flow measurements reported in [41,42] that show, for different propeller shapes at high load conditions, the radial distributions of velocities in the propeller slipstream. Two considerations need to be exposed: first the obtained velocities in the propeller plane due to the body forces, well match with the actuator disk theory globally (the three curves match one each other); second, the different adopted load distributions slightly change the radial velocity distributions generated by the models. In fact, when higher load is considered, also the velocity behaviour shows its peak slightly shifted to the higher radii as expected. In the range between $r/R = \pm 0.25$, due to the presence of the hub, the data has been forced to zero value. In addition, an overall velocity reduction can be seen out of the propeller disk, mainly due to the 3-dimensional

effects of the body force approach. For the sake of completeness, it has to be kept in mind that this particular model can only reproduce the overall propeller effect, not its flow details (as tip or hub vortex or similar features), as for instance, the induced axial velocity due to the flow swirl.

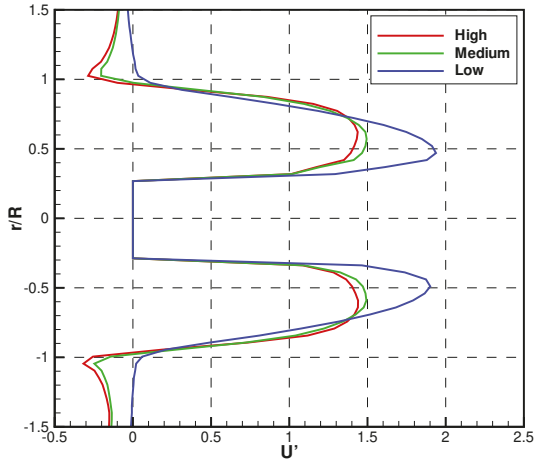

Figure 5. Non-dimensional induced velocity distributions in the propeller plane for the propeller body force simulations at three considered loads.

As mentioned previously, the two theoretical tube flow behaviours can be compared to the one extracted from the CFD simulations. The CFD values have been obtained evaluating the mass flow rate in correspondence of the propeller plane (where the diameter is known), then, imposing its conservation, for each section at a different longitudinal position, the diameter and the average speed can be easily obtained. Figure 6 reports this comparison for the three loads adopted, showing that all the approaches (mathematical models and CFD ones) well describe the typical wake contraction and consequently, due to the conservation of the mass flow rate, the mean velocities increasing accordingly. Moreover, this comparison shows two important aspects: first as expected, the computed flow behaviour is not exactly the same as the two proposed formulations: the CFD simulations predict faster diameter contraction than the ones proposed by Brix; second, in the down-stream region the diameter does not become constant but slightly increases. This latest effect can be ascribed partially to the presence of the hub wake, and partially to a diffusion effect (also connected with the turbulent mixing effect) whose importance increases proportionally with the velocity jump between inside and outside the tube. This latter effect, already mentioned by Brix in [40], is well visible in Figure 7, where the longitudinal computed velocities at different positions (from 0.75 to $2x/D$) are depicted together with the tube flow characteristics. Moving to the propeller slipstream, the velocity jump from the propeller accelerated flow field to the external undisturbed flow tends to diffuse, making the tube diameter slightly bigger than the theoretical one (reported as dashed and doted lines). For the sake of completeness, it has to be pointed out that the reported numerical results, with respect to the theoretical ones, are affected by a small blockage effect due to the ratio between the propeller area and the cross-section of the virtual tunnel. Following the well-known Glauert Correction [43], the flow speed variation is estimated less than 3% for the higher load considered; therefore, it can be considered negligible.

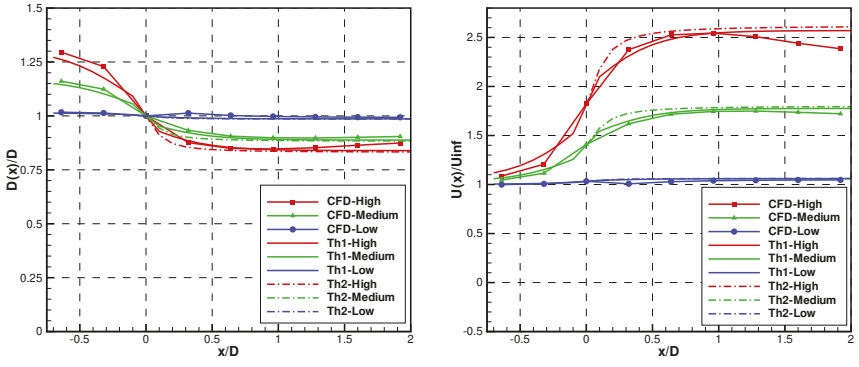

(**a**) Diameter (**b**) Average Velocity

Figure 6. Comparison of the CFD non-dimensional tube flow quantities versus the longitudinal distance for the three loads versus two theoretical formulations (solid line from reported equations and dashed lines from Brix formulation).

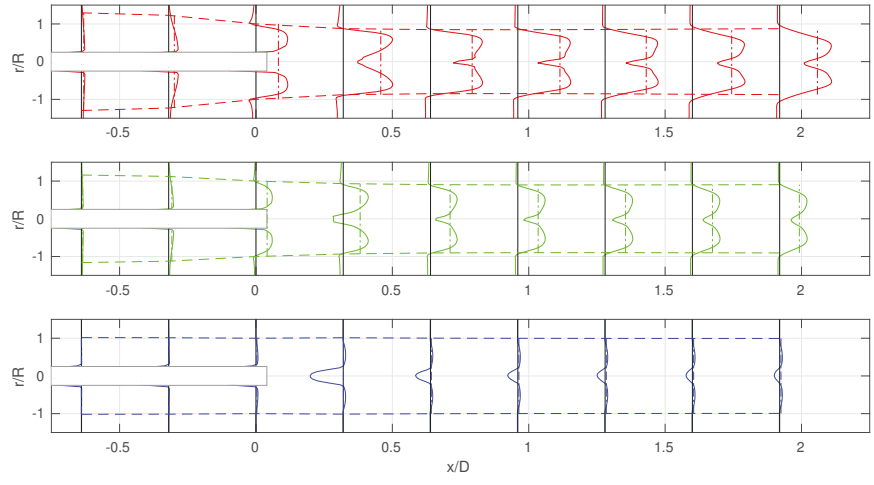

Figure 7. Non-dimensional longitudinal velocity distributions for the propeller body force simulations.

5. Open-Water Rudder Analysis

A preliminary validation of the CFD viscous code's ability to correctly predict the rudder open-water characteristics under different flow conditions has been already shown in [5]. Here, to enlarge that analysis, some additional simulation parameters have been investigated: the inflow turbulence and the near-wall treatment. The main drawback highlighted in previous research was related with the ability of the CFD simulations to correctly predict the stall inception occurrence. Even though several studies can be found on the rudder forces, most of them do not focus their attention on the stall inception angle. Considering that the stall phenomenon is due to a flow instability, which detaches the near wall stream line from the rudder back profile, it is difficult to be numerically predicted due to its intrinsic unstable nature. In addition, from an experimental point of view, some hysteresis effects, strongly connected to the inflow turbulence, can occur (see [44]), making the rudder force evaluation at higher radii subject to significant variations. Often, particular numerical approaches are used to consider this effect, but they are mainly based on complex experimental calibrations. To elaborate on this topic using numerical calculations, some systematic analyses have

been carried out on two numerical aspects: the influence of the inflow turbulence and the first-cell wall-layer treatment. The simulations adopted here are based on the well-known SST $k-\omega$ turbulence model. This model is widely adopted for external flows characterized by both attached and separated flow conditions. From a physical point of view, when an external flow is considered, it is mandatory to prescribe realistic inflow turbulence quantities. The reference literature shows that the turbulent quantities at the inlet influence most of the usually used turbulent models. Among all the possible choices, the Turbulent Intensity (I) and the Eddy Viscosity Ratio (E) are here considered. The first one represents the amount of mean velocities fluctuations with respect to the mean flow speed. Depending on the physical conditions considered, it can assume several values: ranging from 5% to 20% for flows in complex geometries and less than 1% if a very stable inflow field is considered (almost absent inflow turbulence). Regarding the here considered simulations, values between 1% and 10% can be expected: lower values inside the wind tunnel and higher ones behind a ship wake. The second parameter, the Eddy Viscosity Ratio, estimates the effects of the turbulent viscosity with respect to the molecular one. This value is hard to estimate, and generally, its value can range from one to one thousand. These quantities, therefore, can be used to estimate the inflow turbulent model parameters via the typical literature Equation (7) with respect to the means inflow speed U.

$$k = \frac{3}{2}(IU)^2 \quad \text{and} \quad \omega = \frac{k}{\nu E} \tag{7}$$

Considering that no experimental measurements have been reported in the reference literature, neither in the wind tunnel nor behind a ship, for these quantities, several simulations have been carried out to explore the sensitivity of the proposed numerical model to a quite wide range of these parameters. Two different types of simulations have been considered: the first one adopts a boundary layer mesh designed in order to take advantage of the wall-functions in the first near-wall cells, therefore its $Y+$ value (the non-dimensional distance of the first cell from the wall) is about 30; the second one, on the contrary, adopts a wall-resolved boundary layer, so with a $Y+$ value always lower than 1.

Figure 8 shows the two adopted meshes. The one which models the boundary layer has only 4 layers of cells characterized by a quite low aspect ratio; on the contrary, the wall-resolved one has 10 layers with a quite high grading (about 1.6). From a hydrodynamic point of view, both the meshes follow state-of-the-art for the solution of the boundary layer problem.

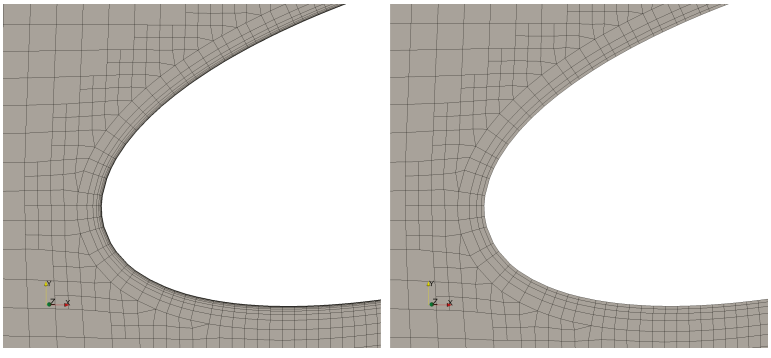

Figure 8. Details of the boundary layer mesh arrangement for the two types of simulations: wall-modelled (**Right**), wall-resolved (**Left**).

Figure 9 shows the simulation results for the two mesh arrangements compared with the experimental values. Regarding the EFD data, not only the simulated flow speed (10 m/s) is reported but also the higher one (20 m/s) for comparison. These two sets of data can give an overview of the expected experimental uncertainty also concerning the turbulent quantities. In the linear region,

the two measures show almost identical values, but when the stall occurs, the two data differ significantly. Analysing the obtained results, it is evident that the CFD predictions give the same results in the pre-stall region. Only when very high values of turbulence (I = 10% and E = 1000) are considered, a slightly over-prediction of the lift occurs. When the rudder stalls the two meshes work differently. The wall-modelled one abruptly anticipates the stall inception (of about 5 degrees) for all the turbulence parameters here adopted. Moreover, the turbulent parameters slightly affect the lift behaviour also after the stall, showing a maximum standard deviation among the series of 0.026. Differently, accurately predicting the boundary layer characteristics, a better agreement can be observed between the CFD and EFD results also in terms of stall inception. In fact, the predicted stall inception angle is shifted towards 20 degrees.

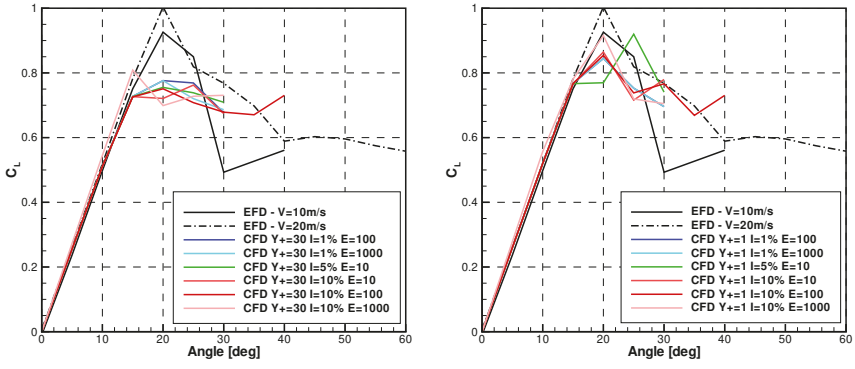

(**a**) Wall-modelled simulations ($Y+$ = 30) (**b**) Wall-resolved simulations ($Y+$ = 1)

Figure 9. Non-dimensional lift force predicted at 10 m/s vs. EFD measurements.

Considering the previously mentioned conclusion related to the high turbulence values, a systematic analysis of their effect on the stall inception has been performed on the wall resolved mesh arrangement. To better analyse the problem, the results have been refined every 2.5 degrees in the range between 15 to 25 degrees. Figure 10 collects the systematic results varying the turbulent viscosity ratio from 1% to 10% and the turbulent intensity from 1 to 10. These results show again that the proposed model well predicts the force behaviour in the pre-stall zone (from 0 to 15 degrees) but, when the stall occurs (15 to 25 degrees), a great force variability is found. Moreover, again, no clear correlation between the force behaviour and the turbulence parameters can be drawn from these figures. Among all the results, the simulation which best approximates the EFD measurements (compared with the value at the same flow speed of 10 m/s) is the one with turbulent values equal to $I = 2\%$ and $E = 10$. Therefore, these values have been selected for all the following analyses.

In conclusion, the wall-resolved model better predicts the stall inception but with a quite significant sensitivity on the turbulent parameters. In other words, if the pre-stall region is of interest, both the approaches (wall-resolved and wall-modelled) give the same accuracy with the only constraints to avoid too high turbulent values (maybe unfeasible) of the inflow. For the sake of completeness, two aspects should be considered: first, all the here reported simulations are steady, consequently, the post-stall region can not be accurately computed because the transient effects are neglected; second, in the previous activity ([5]), also the mesh density had been varied showing the inability of this numerical approach to capture the post-stall phenomena also with a finer mesh. Considering that the main aim of the present paper was to investigate the interactions between the propeller and the rudder for manoeuvring purposes, the here reported results can be considered adequate enough. The following reported simulations adopt the wall-resolved model, which proves to be able to capture the physics of the problem better.

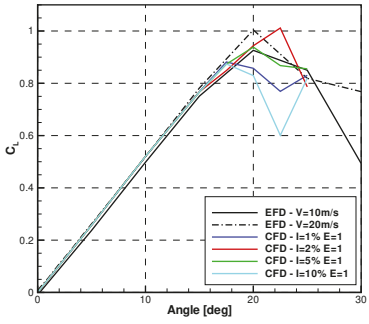

(**a**) Fixed Eddy Viscosity Ratio (E=1)

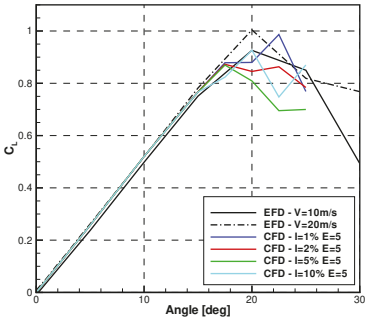

(**b**) Fixed Eddy Viscosity Ratio (E=5)

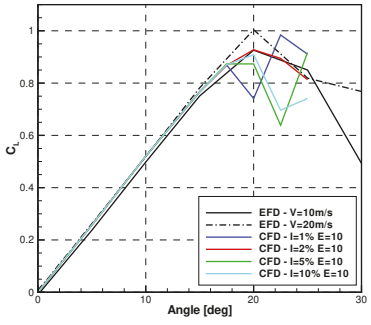

(**c**) Fixed Eddy Viscosity Ratio (E=10)

Figure 10. Numerical influence of the turbulent parameters on the non-dimensional lift.

6. Rudder behind Propeller

Starting from the previously mentioned analyses concerning the adopted propeller model and the rudder numerical set-up, some additional simulations varying the interaction parameters (the propeller load and the rudder/propeller positions) have been carried out and compared with the available experimental measurements ([16,36]).

6.1. Propeller Load Effect

Figure 11 shows, for three considered loads, the comparison between the EFD measurements and the CFD predictions. The measurements were performed at three revolution rates, 800, 1460 and 2100 RPM, with a common value of the velocity in the tunnel, thus varying propeller load, with values of $K_T/J^2 = 0.05, 0.88, 2.3$. Knowing the adopted propeller load, a fixed thrust and torque can be obtained from the propeller open-water curves together with their radial force distributions (as shown in the previous section). Analysing the results collected in Figure 11, a good agreement between the CFD data and the EFD measurements for a wide range of angles is present. As previously, the stall inceptions do not correspond to the experimental ones, even if the tendency is well captured, with stall postponed in correspondence to higher propeller loadings. This further confirms the inability of the proposed method to correctly account this particular aspect. On the contrary, the increase of the lift force due to the propeller interaction is accurately reproduced for all the loads. Some minor discrepancies can be highlighted for the negative range of angles of attack, mainly due to the swirl effect induced by the propeller. In fact, due to the propeller revolutions, some tangential flow components are generated in the propeller slipstream which make the rudder force behaviour not completely

symmetrical with respect to the angle of attack. This effect seems sightly more evident for the EFD measurements instead of the CFD data. In order to have a complete analysis, another aspect has to be considered. The adopted thrust, and consequently the torque, for each simulation has been assumed considering the propeller open-water diagram. Therefore, no interactions of the rudder on the propeller forces has been considered. From the experimental data, at the prescribed revolution rate, also the propeller forces were measured for each rudder angle, thus allowing to have an insight into the possible interactions.

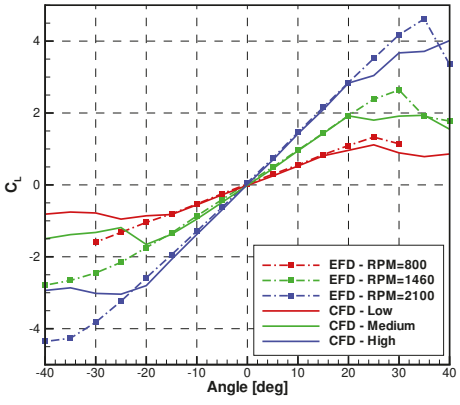

Figure 11. EFD and CFD comparison of rudder lift behind propeller at three loads: equivalent to 800, 1460 and 2100 RPM.

Table 3 summarises the theoretical (the ones computed by the open-water diagram) and the effective (the mean one measured) thrust and torque provided by the propeller. It is evident that the rudder interacts with the propeller force modifying the expected behaviour in open water. In particular, a higher thrust is always experienced by the propeller. It is interesting, on the contrary, that the proposed model correctly predicts the rudder force behaviour imposing the theoretical thrust not the effective one. This could be due to the fact that the two devices interact by means of a pressure field and not velocities, i.e., the rudder overpressure generates an additional propeller force without significantly modifying its inflow velocity field. Further numerical and experimental analysis in this direction are needed to confirm this conclusion. Anyway, this consideration could be important, because, if the rudder forces are of interest, the numerical model can neglect this additional effect. Differently, in the manoeuvring perspective, this aspect assumes quite a low impact.

Table 3. Rudder effect on the propeller forces.

	n (rpm)	K_T/J^2 (-)	T (N)	Q (Nm)
Theoretical	800	0.05	3.92	0.85
	1460	0.88	68.99	8.32
	2100	2.30	180.32	20.23
Measured	800	0.05	7.30	1.25
	1460	0.88	72.12	8.50
	2100	2.30	221.67	23.91

6.2. Propeller Position Effect

Additionally, the relative position between the rudder and the propeller has been investigated (Figure 12). Considering the small variations included in the experimental activities (which amplitude can be extracted from the legends of Figure 12), a wider range of the parameters has been numerically considered. Three parameters were considered: the longitudinal, lateral and vertical propeller position. The first, expressed as X/D, represents the distance of the propeller plane from the leading edge of the rudder at zero-angle. This parameter, from a theoretical point of view (following the actuator disk theory), changes the accelerated flow which is experienced by the rudder. Farther from the propeller plane, the flow tube becomes faster and narrower, as seen in the previous section. The second one is the lateral position, defined by the distance of the propeller axis from the rudder plane at zero-angle (Y/D). This parameter influences the rudder force due to the different portion of the accelerated tube flow which hits the rudder. Increasing the lateral shift reduces the portion of the accelerated flow that affects the rudder. Moreover, due to the propeller tangential components, this effect is asymmetrical with respect to both the rudder angle of attack and to the direction of the lateral shift. Finally, the vertical position, defined as the distance of the propeller axis from the rudder root plane (Z/D), generates a similar effect as the lateral shift. Together with the CFD predictions, also the EFD results have been reported as reference.

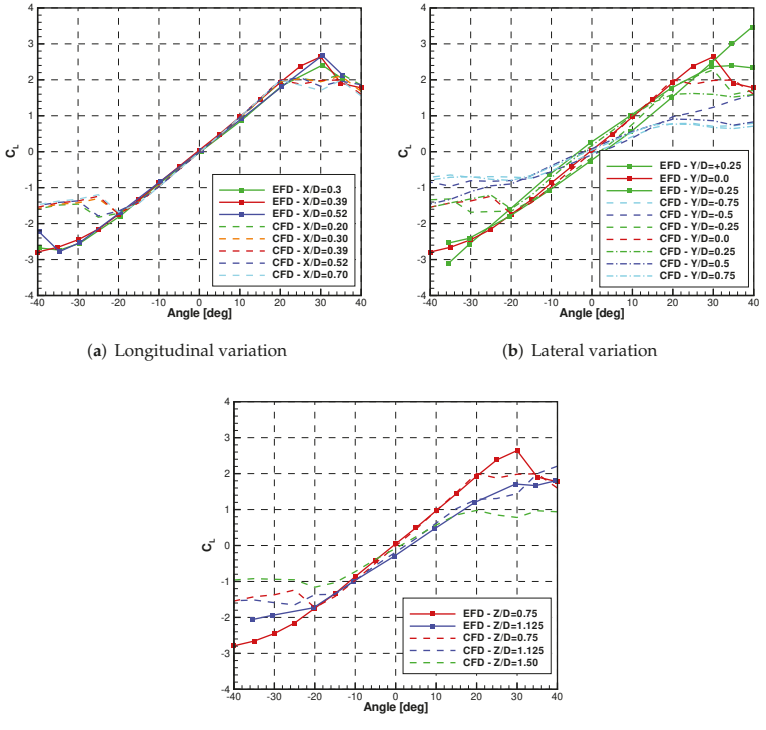

(**a**) Longitudinal variation (**b**) Lateral variation

(**c**) Vertical variation

Figure 12. EFD–CFD results varying the relative positions between the rudder and the propeller.

Figure 12a shows the effect of the longitudinal position. Both the CFD and EFD results show that the distance between the rudder and the propeller has a negligible effect on the linear part of the data. Some minor effects can be seen only in the stall inception. This is a very interesting aspect. Even though, due to the propeller wake contraction in the range between 0.2 and $0.7X/D$, the tube

area decreases by about 10%, with a corresponding increase of speed, the rudder forces do not change. In the reference literature, this is ascribed to a cancellation effect between the wake contraction and the increased propeller thrust. In the CFD results, considering that a constant thrust is imposed, some effects should be visible. Therefore, in the light of the CFD results obtained, at least for the present cases, another flow mechanism should underlay this insensitivity to the longitudinal distance. For instance because the energy produced by the propeller wake is constant along the tube and proportional to the power delivered by the propeller (or the actuator disc for these simulations). Further analyses are certainly needed to confirm this and the authors plan to continue this study in this direction.

In contrast, Figure 12b shows a strong effect of the lateral position with respect to the rudder provided forces. The CFD behaviour is confirmed by the experimental measurements. Two different effects can be seen. First, the rudder force decreases with increasing lateral shift. This effect is strongly non linear, mainly due to the portion of the rudder hit by the propeller slipstream.

Figure 13 highlights this aspect, showing how the portion of the rudder involved by the accelerated flow of the propeller changes with the lateral shift. These pictures clearly highlight that the expected propeller effect is maximum for the smallest lateral shift ($Y/D = 0; \pm 0.2$) and it strongly decreases (up to zero) for the larger shifts ($Y/D = \pm 0.4; \pm 0.6$). Similar considerations can be seen in the rudder force behaviour: for small shifts, the force does not significantly change, differently, for larger shifts, the rudder works almost as in open-water condition. The second aspect shown by these data concerns the loss of symmetry of the forces. In both the measurements and calculations the rudder lift, at zero angle of attack, assumes values different from zero and proportional to the shift values. This is due to the swirl effect induced by the propeller. The magnitude of this effect is again well captured by the CFD prediction with respect to the literature EFD measurements. Figure 12c again confirms the accuracy of the proposed model. Here, it is well visible as the combined effects, reduction of the rudder portion affected by the accelerated flow and the propeller swirl effect, are well captured by the CFD simulations. It is also interesting to note as the effect of the vertical position is again strongly non linear, despite of the linearity of the interaction area (see Figure 14).

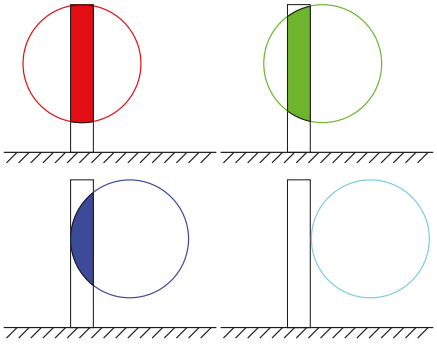

Figure 13. Interaction area varying the lateral position between rudder and propeller. From left to right and top to bottom, respectively, $Y/D = 0; 0.2; 0.4; 0.6$.

This can be mainly due to the radial distribution of the velocities in the flow tube induced by the propeller rotation. In fact, shifting upward the centre of the disk by only about one third of the diameter, its effect on the rudder forces is strongly reduced.

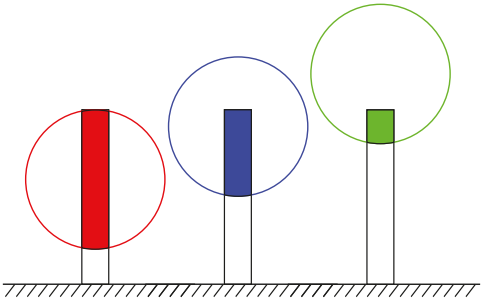

Figure 14. Interaction area varying the vertical position between rudder and propeller. From right to left and top to bottom, respectively, $Z/D = 0.75; 1.125; 1.50$.

7. Rudder–Propeller Model

In the previous section, the ability of the proposed CFD procedure to accurately predict (at least in the pre-stall region) the rudder force, also when it interacts with a propeller, has been demonstrated. In the manoeuvring research field, this aspect is fundamental to correctly predict the manoeuvring ability of a ship, because the rudder is the main device that controls the ship route.

The reference literature adopts a quite crude, but effective, approach. Starting from the knowledge of the rudder performance in free-flow condition, it evaluates the rudder interaction with the propeller by means of the actuator disk theory. First, the propeller accelerated flow to the rudder is evaluated using Equation (5); then, considering that only a portion of the rudder will be affected by the propeller slipstream, the mean flow field to the rudder (U_{Rad}) can be obtained by averaging the two speeds (the accelerated one U_R and the undisturbed one U_S) proportionally to the interested rudder areas (Equation (8)). A sketch of the considered areas can be seen in Figure 15.

$$U_{Rad} = \sqrt{U_R^2 \left(\frac{A_P}{A_R}\right) + U_S^2 \left(1 - \frac{A_P}{A_R}\right)} \tag{8}$$

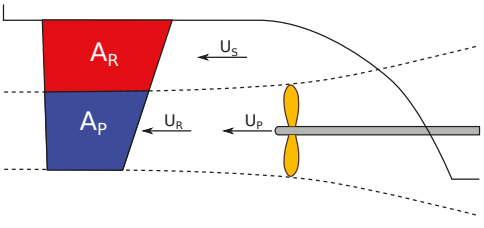

Figure 15. Rudder model quantities.

As extensively reported in literature (see for instance [45] or [46]), the flow acceleration at the rudder section needs to be strongly reduced to some extent (about 40% considering the present experiments), obtaining a new rudder speed given by the Equation (9).

$$U_R^* = k(U_R - U_S) + U_S \tag{9}$$

The meaning of this experimentally tuned coefficient is not completely clear. In addition, its value is strongly connected with the relative size between the rudder and the propeller and slightly also with the distance between the rudder and the propeller. Figure 16 shows the numerical non-dimensional lift force of the rudder at a prescribed angle of attack (15 degrees), varying the propeller size and its load separately. The red lines show the force behaviour applying the original semi-empirical model,

keeping the k coefficient fixed. It is easily seen that its values do not follow the numerically predicted forces, with errors up to 13%.

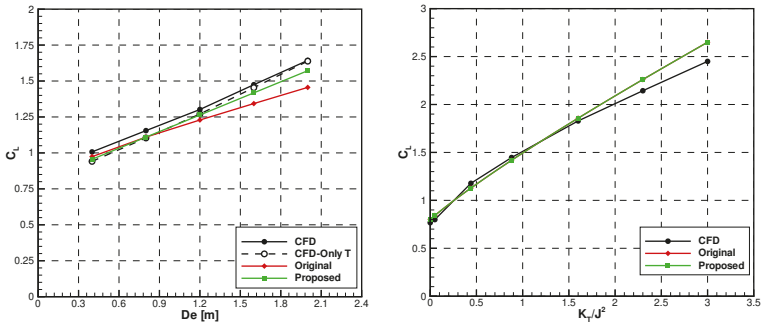

(**a**) with fixed propeller load (**b**) with fixed propeller diameter

Figure 16. Comparison of the original and proposed rudder–propeller models for a single pre-stall angle (15 degrees) versus the CFD results (solid line: complete propeller model; dashed line: only thrust, no torque).

Therefore, a new method has been proposed to increase the trustworthiness of this general approach. Instead of correcting the accelerated flow generated by the propeller at the rudder section, the increased velocity at the propeller section is used. Consequently, the mean flow speed at the rudder can be obtained by the new expression (10):

$$U_{Rad} = \sqrt{U_P^2 \left(\frac{A_P}{A_R}\right) + U_S^2 \left(1 - \frac{A_P}{A_R}\right)} \tag{10}$$

where U_P is the average speed at the propeller plane. In contrast to the original model, also the rudder area affected by the accelerated flow depends only on the propeller diameter. The effectiveness of this new approach is easily seen in Figure 16 (green lines). When a different propeller size is considered, with the same rudder, the new method shows a better agreement with the CFD predictions (the agreement is further increased compared with a pure actuator disk, no torque: dashed line). At the same time (as reported in the lower part of the figure), this proposed approach provides the same results of the original model with respect to a change in propeller load (the two lines are overlapped), without including any experimental corrections. Furthermore, the longitudinal propeller-rudder distance results mathematically irrelevant, as demonstrated by the numerical and experimental data previously reported. For the sake of completeness, the original model is only slightly affected by this longitudinal distance. Figure 17 enlarges the comparison showing how the new model works for all the rudder angles calculated using the three analysed loads.

In conclusion, apparently, at least in the considered cases, the proposed model may be adopted without the need of experiments (or CFD data), fitting better experimental results. It has to be pointed out that this is only a first result, which needs further tests. Therefore, to increase the trustworthiness on this new model, a broader numerical and experimental campaign should be conducted for different rudder shapes and propeller arrangements.

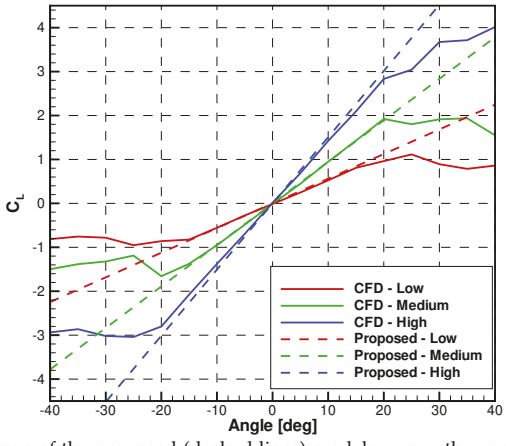

Figure 17. Comparison of the proposed (dashed lines) models versus the computed rudder forces (solid lines).

8. Rudder Sectional Force Analysis

To further enlarge the understanding of the rudder–propeller interaction, additional analyses have been considered focusing the attention on the rudder force distribution. Thanks to the significant amount of data within a CFD simulation, also the rudder force distribution in span-wise direction can be extracted and analysed.

A new rudder shape and test conditions are used to gain a better insight into the problem (Figure 18 shows a sketch). A doubled span characterises the adopted rudder compared to the original one with the same chord length. In addition, the sidewall has been eliminated. These simplifications generate to obtain a rudder which experiences a similar force of the original one (almost the same effective aspect ratio) but with more available space to interact with different propeller sizes. In light of this, a simpler actuator disk with a constant load radial distribution has been considered, positioned in the middle of the rudder span. These simplifications further reduce the extremities effects, to better show how the load changes with respect to the rudder/propeller interaction. With this set-up, five propeller diameters have been explored ranging from 0.4 m up to 2 m (equivalent to 0.2–1.0 in terms of diameter/span ratio). Each propeller provides the same total load, so both the thrust and the torque have been varied accordingly.

Figure 19 shows the non-dimensional force distributions for three angles: 15, 0 and −15 degrees along the rudder span. They were obtained by integrating the stress fields (pressures and wall shear stresses) on different rudder sections, thus obtaining the sectional contribution to the total lift. These selected angles, within the linear region, are able to show how the rudder force distributions change due to the non-symmetrical effect of the flow induced by the torque. As a reference, with a black line, also the rudder load without propeller effect has been included. When the rudder angle is zero, even if the rudder does not provide any lift force, its load is characterised by a significant effect induced by the tangential components generated by the propeller. The same effect is well visible also for the other two analysed conditions, which makes the force distribution strongly non-symmetrical. In the same way, Figure 20 shows the rudder force distribution in the previous condition (limited for only 15 degrees) but neglecting the torque component in the actuator disks (continuous line). Comparing the two figures, it is evident that the two effects (loads induced by to the thrust and the torque) can be linearly superimposed. To further support this conclusion, in Figure 20, with the dashed lines, the previous force distributions subtracting those zero degrees (which are only affected by the tangential components) are reported. Except for a small effect near the propeller hub (most evident for the smallest diameter), the two distributions are in good agreement. These considerations demonstrate

why the mathematical model, though completely neglecting the torque effect, maintains a good agreement with the measurements. Consequently, it is evident by the proposed results that the torque has a small effect on the lift generation (at least in the pre-stall functioning region). On the other hand, it becomes important if other aspects are of interest, for instance cavitation effects or other local effects.

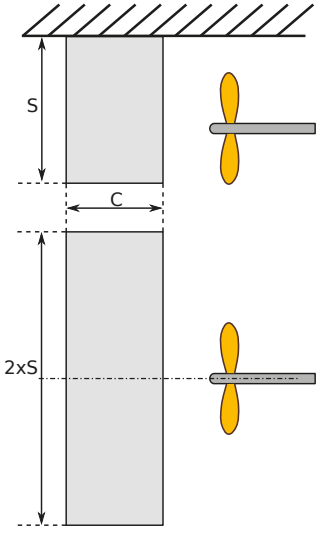

Figure 18. Sketch of the two rudder arrangements.

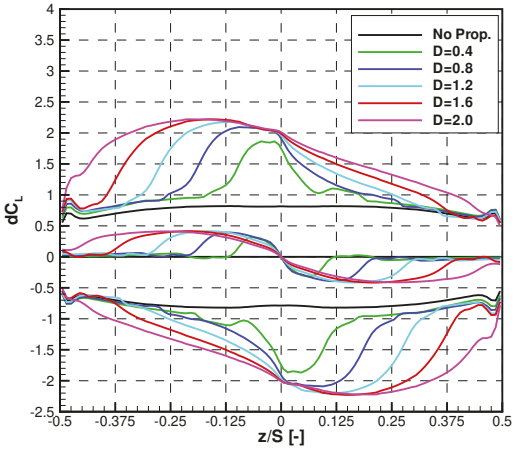

Figure 19. Rudder span-wise force distribution with complete propeller model at three angles of attack: ± 15 and 0 degrees.

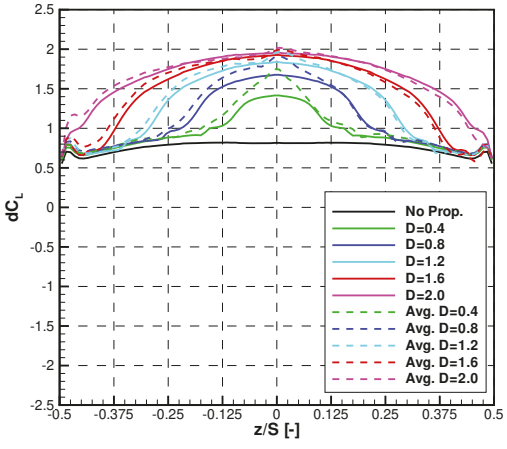

Figure 20. Comparison of the rudder span-wise force distributions without torque (solid lines) and the average force distributions with the complete model (dashed lines) at 15 degrees of rudder angle.

9. Conclusions

This work shows the application of an open-source CFD numerical procedure to predict the interaction between a propeller and a rudder positioned in its slip-stream, considering typical operative conditions during the ship life. Different aspects have been considered to define properly the code ability to tackle this particular problem.

Preliminarily, the flow field generated by the viscous solver, which adopts the body force approach to include the propeller effect in an efficient way, has been compared with classical actuator disk theory, showing its ability to provide more information with respect to this simplified approach. The tube contraction and the expected velocities distribution well match with the theoretical ones.

Then an extensive analysis of the influence of the mesh set-up (in term of wall boundary layer description and turbulent inlet quantities) on the expected numerical results for a wide range of angle of attacks has been considered. These simulations demonstrate that the wall-resolved model better predicts the stall inception but with a quite significant sensitivity on the turbulent parameters. Differently, if the pre-stall region is of interest, both the approaches (wall-resolved and wall-modelled) give the same accuracy with the only constraints to avoid too high turbulent values of the inflow field. Comparing the results with the available measurements, optimal values of turbulent intensity and Eddy Viscosity have been selected obtaining a better CFD/EFD agreement.

Selecting the proper simulations set-up parameters, a systematic analysis of the interactions between the rudder and the propeller varying the propeller load and their mutual position have been carried out comparing the results with respect to the measurements. A very good agreement was found showing that most of the interaction effects are well captured by the CFD predictions. Two are the main additional considerations drawn by the data. First, varying the longitudinal distance between the two devices, the rudder force increment due to the propeller is constant, in contrast with the classical actuator disk theory. Second, the propeller forces seem to vary due to an additional pressure field generated by the rudder, not for a different working condition of the propeller itself. Therefore, if only the rudder forces are of interests, this additional interaction can be neglected without losing accuracy.

Thanks to all these data, a new simplified mathematical model has been developed based on the one typically adopted in the manoeuvring field. Compared to the original one, it does not depends on the longitudinal distance by the propeller and the rudder (as demonstrated by the numerical and experimental measurements) and it works also for different propeller sizes without requiring any calibration parameters.

Finally, analysing the rudder sectional forces when it operates behind propellers with different diameters, the load generated by the accelerated flow (due to the propeller thrust) can be linearly superimposed to the load generated by the tangential flow components (due to the propeller torque). Therefore, if the rudder performances are of interest, the propeller torque can be neglected; differently, if local flow quantities are important, as for cavitation, it has to be included in the analyses.

Author Contributions: Conceptualization, D.V., A.F. and M.V.; methodology, D.V. and A.F.; software, D.V.; validation, D.V.; formal analysis, D.V. and M.V.; investigation, D.V., A.F.; resources, D.V. and M.V; data curation, D.V.; writing–original draft preparation, D.V.; writing–review and editing, M.V.; visualization, D.V.; supervision, M.V. All authors have read and agreed to the published version of the manuscript.

Funding: This research received no external funding.

Conflicts of Interest: The authors declare no conflict of interest.

Abbreviations

The following abbreviations are used in this manuscript:

CFD	Computational Fluid Dynamics
EFD	Experimental Fluid Dynamics
RANS	Reynolds Average Navier–Stokes

References

1. Martelli, M.; Figari, M. Real-Time model-based design for CODLAG propulsion control strategies. *Ocean Eng.* **2017**, *141*, 265–276. [CrossRef]
2. Alessandri, A.; Donnarumma, S.; Luria, G.; Martelli, M.; Vignolo, S.; Chiti, R.; Sebastiani, L. Dynamic positioning system of a vessel with conventional propulsion configuration: Modeling and simulation. In *Maritime Technology and Engineering, Proceedings of the MARTECH 2014: 2nd International Conference on Maritime Technology and Engineering, Lisbon, Portugal, 15–17 October 2014*; Taylor & Francis Group: London, UK, 2015; pp. 725–734. [CrossRef]
3. International Maritime Organization. *Explanatory Notes to the Standards for Ship Manoeuvrability*; MSC/Circ.1053 Adopted 16 December 2002; International Maritime Organization: London, UK, 2002.
4. International Maritime Organization. *Standards for Ship Manoeuvrability*; Resolution MSC. 137 (76); International Maritime Organization: London, UK, 2002.
5. Villa, D.; Viviani, M.; Tani, G.; Gaggero, S.; Bruzzone, D.; Podenzana, C. Numerical Evaluation of Rudder Performance Behind a Propeller in Bollard Pull Condition. *J. Mar. Sci. Appl.* **2018**, *17*, 153–164. [CrossRef]
6. Martelli, M.; Villa, D.; Viviani, M.; Donnarumma, S.; Figari, M. The use of computational fluid dynamic technique in ship control design. *Ships Offshore Struct.* **2019**. [CrossRef]
7. Muscari, R.; Dubbioso, G.; Viviani, M.; Di Mascio, A. Analysis of the asymmetric behavior of propeller–rudder system of twin screw ships by CFD. *Ocean Eng.* **2017**, *143*, 269–281. [CrossRef]
8. Piaggio, B.; Martelli, M.; Viviani, M.; Figari, M. Manoeuvring model and simulation of the non-linear dynamic interaction between tethered ship and tug during escort. In Proceedings of the Maritime Transportation and Harvesting of Sea Resources, Lisbon, Portugal, 9–11 October 2017; Volume 1, pp. 95–104.
9. Figari, M.; Martinelli, L.; Piaggio, B.; Enoizi, L.; Viviani, M.; Villa, D. An all-round design-to-simulation approach of a new Z-drive escort tug class. *J. Offshore Mech. Arct. Eng.* **2020**, *142*, 031107. [CrossRef]
10. Piaggio, B.; Viviani, M.; Martelli, M.; Figari, M. Z-Drive Escort Tug manoeuvrability model and simulation. *Ocean Eng.* **2019**, *191*, 106461. [CrossRef]
11. Villa, D.; Viviani, M.; Gaggero, S.; Vantorre, M.; Eloot, K.; Delefortrie, G. CFD-based analyses for a slow speed manoeuvrability model. *J. Mar. Sci. Technol.* **2019**, *24*, 871–883. [CrossRef]
12. Bruzzone, D.; Ruscelli, D.; Villa, D.; Vivani, M. Numerical prediction of hull force for low velocity manoeuvring. In Proceedings of the 18th International Conference on Ships and Shipping Research (NAV 2015), Lecco, Italy, 24–26 June 2015; pp. 284–295.
13. Suzuki, R.; Tsukada, Y.; Tsujimoto, M.; Muraoka, E.; Ueno, M. A study on high-lift rudder performance in adverse weather based on model tests under high propeller load. *Ocean Eng.* **2017**, *136*, 152–167. [CrossRef]

14. Shin, Y.J.; Kim, M.C.; Lee, J.H.; Song, M.S. A numerical and experimental study on the performance of a twisted rudder with wavy configuration. *Int. J. Nav. Archit. Ocean Eng.* **2019**, *11*, 131–142. [CrossRef]
15. Seo, D.W.; Oh, J.; Jang, J. Performance analysis of a horn-type rudder implementing the Coanda effect. *Int. J. Nav. Archit. Ocean Eng.* **2017**, *9*, 177–184. [CrossRef]
16. Molland, A.; Turnock, S. *Wind Tunnel Investigation of the Influence of Propeller Loading on Ship Rudder Performance*; Project Report; University of Southampton: Southampton, UK, 1991; ISSN 0140-3818.
17. Li, D.Q. A non-linear method for the propeller-rudder interaction with the slipstream deformation taken into account. *Comput. Methods Appl. Mech. Eng.* **1996**, *130*, 115–132. [CrossRef]
18. He, L.; Kinnas, S.A. Numerical simulation of unsteady propeller/rudder interaction. *Int. J. Nav. Archit. Ocean Eng.* **2017**, *9*, 677–692. [CrossRef]
19. Li, D.Q. *Investigation on Propeller-Rudder Interaction by Numerical Methods*; Chalmers University of Technology: Göteborg, Sweden, 1994.
20. Nakatake, K.; Koga, T.; Yamazaki, R. On the Interaction between Screw Propeller. In *Transactions of the West-Japan Society of Naval Architects*; The Japan Society of Naval Architects and Ocean Engineers: Tokyo, Japan, 1981.
21. Turnock, S. Prediction of ship rudder-propeller interaction using a panel method. In Proceedings of the 19th WEGEMT School on Numerical Simulation of Hydrodynamics: Ships and Offshore Structures, Propeller and Lifting Surfaces, Nantes, France, 20–24 June 1993.
22. Badoe, C.E.; Phillips, A.B.; Turnock, S.R. Influence of drift angle on the computation of hull–propeller–rudder interaction. *Ocean Eng.* **2015**, *103*, 64–77. [CrossRef]
23. Liu, J.; Quadvlieg, F.; Hekkenberg, R. Impacts of the rudder profile on manoeuvring performance of ships. *Ocean Eng.* **2016**, *124*, 226–240. [CrossRef]
24. Guo, H.P.; Zou, Z.J.; Liu, Y.; Wang, F. Investigation on hull-propeller-rudder interaction by RANS simulation of captive model tests for a twin-screw ship. *Ocean Eng.* **2018**, *162*, 259–273. [CrossRef]
25. Phillips, A.B.; Turnock, S.R.; Furlong, M. Accurate Capture of Propeller-Rudder Interaction using a Coupled Blade Element Momentum-RANS Approach. *Ship Technol. Res.* **2010**, *57*, 128–139. [CrossRef]
26. Calcagni, D.; Bellotto, F.; Broglia, R.; Salvatore, F.; Bensow, R. Comparative analysis of the hydrodynamic performance of untwisted and twisted rudders using a hybrid RANSE/BEM model. In Proceedings of the International Offshore and Polar Engineering Conference, Busan, Korea, 15–20 June 2014.
27. Van Nguyen, T.; Ikeda, Y. Development of fishtail rudder sections with higher maximum lift coefficients. In Proceedings of the Twenty-Fourth International Ocean and Polar Engineering Conference, Busan, Korea, 15–20 June 2014.
28. Liu, J.; Quadvlieg, F.; Hekkenberg, R. Impacts of rudder profiles on ship manoeuvrability. In Proceedings of the International Conference on Marine Simulation and Ship Maneuverability, Newcastle upon Tyne, UK, 8–11 September 2015.
29. Ferrando, M.; Gaggero, S.; Villa, D. Open source computations of planing hull resistance. *Trans. R. Inst. Nav. Archit. Part Int. J. Small Craft Technol.* **2015**, *157*, 83–98. [CrossRef]
30. Piaggio, B.; Villa, D.; Viviani, M. Numerical analysis of escort tug manoeuvrability characteristics. *Appl. Ocean. Res.* **2020**, *97*. [CrossRef]
31. Piaggio, B.; Villa, D.; Viviani, M.; Figari, M. Numerical analysis of escort tug manoeuvrability characteristics—Part II: The skeg effect. *Appl. Ocean. Res.* **2020**, *100*, 102199. [CrossRef]
32. Villa, D.; Gaggero, S.; Gaggero, T.; Tani, G.; Vernengo, G.; Viviani, M. An efficient and robust approach to predict ship self-propulsion coefficients. *Appl. Ocean. Res.* **2019**, *92*, 101862. [CrossRef]
33. Peskin, C.S. Flow patterns around heart valves: A numerical method. *J. Comput. Phys.* **1972**, *10*, 252–271. [CrossRef]
34. Hu, J.; Zhang, W.; Sun, S.; Guo, C. Numerical simulation of Vortex–Rudder interactions behind the propeller. *Ocean Eng.* **2019**, *190*, 106446. [CrossRef]
35. Gaggero, S.; Gaggero, T.; Tani, G.; Vernengo, G.; Viviani, M.; Villa, D. Ship self-propulsion performance prediction by using OpenFOAM and different simplified propeller models. In *Progress in Maritime Technology and Engineering, Proceedings of the 4th International Conference on Maritime Technology and Engineering, (MARTECH), Lisbon, Portugal, 7–9 May 2018*; Taylor & Francis Group: London, UK, 2018; pp. 195–206. [CrossRef]

36. Molland, A.; Turnock, S. *Further Wind Tunnel Tests on the Influence of Propeller Loading On Ship Rudder Performance*; Project Report; University of Southampton: Southampton, UK, 1992; ISSN 0140-3818.
37. Molland, A.; Turnock, S. *Wind Tunnel Test Results for a Model Ship Propeller Based on A Modified Wageningen b4.40*; Project Report; University of Southampton: Southampton, UK, 1990; ISSN 0140-3818.
38. Gaggero, S.; Villa, D. Cavitating Propeller Performance in Inclined Shaft Conditions with OpenFOAM: PPTC 2015 Test Case. *J. Mar. Sci. Appl.* **2018**, *17*, 1–20. [CrossRef]
39. Villa, D.; Gaggero, S.; Tani, G.; Viviani, M. Numerical and experimental comparison of ducted and non-ducted propellers. *J. Mar. Sci. Eng.* **2020**, *8*, 257. [CrossRef]
40. Brix, J. *Manoeuvring Technical Manual*; Schiff und Hafen; The National Academies of Sciences, Engineering, and Medicine: Washington, DC, USA, 1987; ISSN 0036-603X.
41. Wei, M.; Chiew, Y.M. Impingement of propeller jet on a vertical quay wall. *Ocean Eng.* **2019**, *183*, 73–86. [CrossRef]
42. Felli, M.; Falchi, M.; Fornari, P.; Pereira, F.J.A. PIV Measurements on an Impinging Swirl Jet in a Large Cavitation Tunnel. In Proceedings of the 14th International Symposium on Applications of Laser and Imaging Techniques to Fluid Mechanics (LISBON'08), Lisbon, Portugal, 7–10 July 2008.
43. Glauert, H. *The Elements of Aerofoil and Airscrew Theory*; Cambridge Science Classics, Cambridge University Press: Cambridge, UK, 1983. [CrossRef]
44. Ahn, T.; Kim, C.; Rho, O.H. Dynamic-stall control based on an optimal approach. *J. Aircr.* **2004**, *41*, 1106–1116. [CrossRef]
45. Yasukawa, H.; Yoshimura, Y. Introduction of MMG standard method for ship maneuvering predictions. *J. Mar. Sci. Technol.* **2014**, *20*, 37–52. [CrossRef]
46. Martelli, M. *Marine Propulsion Simulation*; Walter de Gruyter GmbH: Berlin, Germany, 2015; pp. 1–104.

Journal of *Marine Science and Engineering*

MDPI

Article

Numerical Study on Wave-Ice Interaction in the Marginal Ice Zone

Tiecheng Wu [1,2], Wanzhen Luo [1,2,*], Dapeng Jiang [1,2], Rui Deng [1,2] and Shuo Huang [1,2]

[1] School of Marine Engineering and Technology, Sun Yat-Sen University, Zhuhai 518000, China; wutch7@mail.sysu.edu.cn (T.W.); jiangdp5@mail.sysu.edu.cn (D.J.); dengr23@mail.sysu.edu.cn (R.D.); huangsh97@mail.sysu.edu.cn (S.H.)
[2] Southern Marine Science and Engineering Guangdong Laboratory (Zhuhai), Zhuhai 519000, China
* Correspondence: luowzh5@mail.sysu.edu.cn; Tel.: +86-188-4642-1436

Abstract: The effect of waves on ice sheet is critical in the marginal ice zone (MIZ). Waves break large sea ice into small pieces and cause them to collide with each other. Simultaneously, the interaction between sea ice and waves attenuates these waves. In this study, a numerical research is conducted based on a computational fluid dynamics (CFD) method to investigate the response of single ice floe to wave action. The obtained results demonstrate that the sea ice has a violent six degree of freedom (6DoF) motion in waves. Ice floes with different sizes, thicknesses, and shapes exhibit different 6DoF motions under the action of waves. The heave and surge response amplitude operator (RAO) of the sea ice are related to wavelength. Furthermore, the overwash phenomenon can be observed in the simulation. The obtained results are compared with the model test in the towing tank based on artificial ice, and they agree well with test results.

Keywords: marginal ice zone; sea ice; wave; six degree of freedom (6DoF) motion; CFD

Citation: Wu, T.; Luo, W.; Jiang, D.; Deng, R.; Huang, S. Numerical Study on Wave-Ice Interaction in the Marginal Ice Zone. *J. Mar. Sci. Eng.* **2021**, *9*, 4. https://dx.doi.org/10.3390/jmse9010004

Received: 27 November 2020
Accepted: 17 December 2020
Published: 22 December 2020

1. Introduction

The marginal ice zone (MIZ) is the area between open water and level ice sheet that is directly affected by waves. The sea ice in this area mainly exists as crushed ice due to the action of waves. With the increase in global warming, the marginal ice zone has garnered more attention. The coupling effect of sea ice and wave influences the safety and navigation performance of ships sailing in this area, and hence the need to research on the interaction between sea ice and waves before moving ahead to study the ship–wave–ice interaction in the MIZ.

The research methods of wave–ice interaction include theoretical research, model tests, and numerical simulations. At the beginning of the research, field observation and theoretical study were carried out to observe the attenuation of waves, the fracture mechanism, and movement form of sea ice in the MIZ. In 1983, a special research team was setup in the MIZ field. After that, researchers studied the sea ice changes near the MIZ of Greenland and Beaufort Seas [1–4]. Marchenko A et al. [5] carried out a field observation and test on the wave–sea ice interaction process in the MIZ of Barents Sea, and they determined that the high-frequency wave will be significantly damped when propagating under the sea ice. The frequency of energy wave decreases when it is far away from the MIZ. Kovalev P D et al. [6] observed the wave–sea ice interaction process in the south eastern coastal zone of Sakhalin Island, and obtained the interaction relationship between the generation of wave–sea ice and the dissipation process. Squire V A et al. [7] studied the wave motion and the breaking process of sea ice in the MIZ. Toyota T et al. [8] studied and analysed the distribution characteristics of the size and shape of sea ice in the Antarctic marginal ice zone at the end of winter. Zhang J et al. [9] conducted theoretical and experimental research and analyses on the size and thickness distribution of ice floes in the MIZ, and to explicitly simulate the evolution of the size and thickness of ice floes, the

obtained results are combined with the thickness theory of ice floes by Thorndike et al. [10]. Gupta M [11] observed the complex environment in the MIZ. Williams T D et al. [12] carried out numerical simulations of sea ice–wave interaction in the MIZ. Additionally, the results obtained from these studies provide a better understanding of the MIZ in the early stage.

There are three main research strategies for ice–wave interaction, namely theoretical research, numerical simulation, and experimental research. Concerning theoretical research, sea ice is regarded as an elastic or viscoelastic continuum, and there are mainly three theoretical models: mass loading, thin elastic plate, and viscous layer models. The mass loading model is mainly suitable for the discontinuous pancake ice area, the thin elastic plate model is best suited for the continuous ice sheet area, and the viscous layer model is mainly suitable for the grease ice area. The mass load model was first proposed and developed by Peters A S et al. [13] and Weitz and Keller [14]. To establish the numerical model of the wave dispersion relationship in the ice area, the ice floes were assumed as a series of discrete mass points that were not related to each other. The elastic sheet model [15] assumes that the ice sheet is a thin but uniform elastic plate, such that the elastic plate bending theory can be adopted. The viscous layer model, first derived by Keller J B [16], assumed that sea ice is viscous fluid while sea water was assumed to be a non-viscous fluid. By matching the vertical velocity with stress at the interfaces of sea ice, water, and air, the boundary condition of the dispersion relationship interface of the wave is obtained. Against this backdrop, Carolis D G [17] developed a two-layer viscous fluid model considering the viscosity of sea water. In 2010, Wang R and Shen H H [18] developed a viscoelastic model and generalized the already mentioned three models to predict wave propagation under different sea ice types in the MIZ.

With the development of model test and numerical calculation methods, researchers have conducted some experimental and numerical investigations on wave–ice interaction. Newyear K and Martin S [19] carried out wave propagation experiments with grease ice in a small, refrigerated water channel in Washington University. The results obtained from the experiment show that wave attenuation varies exponentially with distance, relative to frequency. Sakai S and Hanai K [20] studied the influence of the ice size, its thickness, and elastic modulus on the wavelength in a water channel. The obtained results exhibit an insignificant difference between the two ice-thickness models. When the ice length is short, the propagation speed is approximate to that in open water. Based on experiments and numerical simulations, Dai M et al. [21] studied the thickness of sea ice accumulated under wave action. In this experiment, a plastic ice model and a three-dimensional discrete element model were used to simulate the movement of ice floes under wave action. The results obtained from the experiments and numerical simulation are consistent with the theoretical calculation. Parra S M et al. [22] carried out an ice–wave interaction experiment in a wave tank and described the wave propagation along the ice sheet. Three types of ice were used in the experiment, including ice sheet, crushed ice, and grease ice. Additionally, the wave dispersion and attenuation characteristics under different ice and wave properties were studied in this experiment. The obtained results show that the wave attenuation is most robust in the ice row, and it is related to the surface wave orbital velocity. The results also show that the attenuation degree of waves is the largest in the ice sheet, which is related to the surface wave orbital velocity. Huang L et al. [23] applied the hydro-elastic wave–ice interaction method based on OpenFOAM to predict the wave propagation and ice motion in the ice–wave interaction process. Based on an unstructured grid surface-wave model, Zhang Y et al. [24] studied the wave attenuation and propagation characteristics triggered by sea ice and simulated the evolution trend of the wave–sea ice interaction process. The simulation results agree well with the mechanism of sea ice–wave generation and dissipation.

In this research, a numerical study is conducted based on the computational fluid dynamics (CFD) method to investigate the response of single ice floe under wave action. This study mainly focuses on the six degree of freedom (6DoF) motion of sea ice under

different ice parameters. The calculation results are compared with the model test results in the towing tank.

2. CFD Numerical Simulation

2.1. Governing Equations

The motion of incompressible Newtonian fluid satisfies the continuity and momentum conservation equations, which can be expressed as [25]:

$$\frac{\partial u_i}{\partial x_i} = 0 \tag{1}$$

$$\frac{\partial u_i}{\partial t} + \frac{\partial u_j u_i}{\partial x_j} = \frac{\partial}{\partial x_j}(\mu \frac{\partial u_i}{\partial x_j}) - \frac{1}{\rho}\frac{\partial p}{\partial x_i} + S_j \tag{2}$$

where u_i and u_j (i, j = 1, 2, 3), p, ρ and S_j represent the time-averaged values of velocity components, time-averaged pressure, fluid density, and source term, respectively. The fluid density was assumed constant for incompressible Newtonian fluids.

2.2. Turbulence Model and Free-Surface Treatment

The finite-volume computational method was combined with a segregated flow solver and used to analyse the interaction between ice floes and waves. An implicit pseudo-time-marching scheme was adopted to attain convergence. To solve the resulting discrete linear system of equations during each iteration, a point-implicit (Gauss–Seidel) linear system solver with algebraic multigrid acceleration was adopted. The shear stress transport (SST) k-ω turbulence model was employed for numerical simulations. The free-surface of the ocean was modelled using the two-phase volume-of-fluid (VOF) technique with the high-resolution interface capturing (HRIC) scheme [26].

2.3. Numerical Wave Tank

The STAR-CCM+ commercial software package was used to perform numerical wave simulations. Wave generation in the STAR-CCM+ solver was realized via the inlet and outlet boundaries, at which incident–wave boundary conditions were enforced. Specifically, this approach, referred to as the boundary velocity input method, sets a velocity profile over the water depth of waves at the inlet boundary. A fifth order wave was modelled by approximating the fifth order to the Stokes theory of waves as the numerical wave type in this study. The wave generated by the fifth order is more similar to a real wave than that generated by the first order method. The wave profile, including the wave phase velocity, depends on the water depth, wave height, and current. A detailed description of fifth order VOF waves can be found in the studies conducted by Fenton J D [27].

In the simulation, the length, width, and water depth of the calculation domain are 15, 4, and 4.5 m, respectively. Due to the symmetricity of the calculation model, only half of the computational domain is calculated. Regular waves were generated at the velocity inlet, the position of the floating ice was 5 m away from the inlet, and the wave elimination function was opened near the outlet. To better ascertain the flow characteristics near the floating ice, the mesh near the ice surface and ice movement area is refined, as shown in Figure 1.

The Euler overlay method (EOM) [28] was adopted to address the reflections of surface waves at boundaries. The illustration of the Euler overlay method is shown in Figure 2. As the principal solution of this method, the simulation domain contains three zones: the inner CFD, overlay, and outer Euler wave zones.

The overlay zone located between the outer Euler and inner CFD zones gradually blends the CFD and Euler solutions, applying source terms to VOF and momentum equations. The reflections of surface waves are addressed via the forcing solution of the discretized Navier–Stokes equations towards another solution (such as a theoretical

solution or simplified numerical solution) over a specified distance, which reduces the computing efficiency due to its use of a reduced-size solution domain.

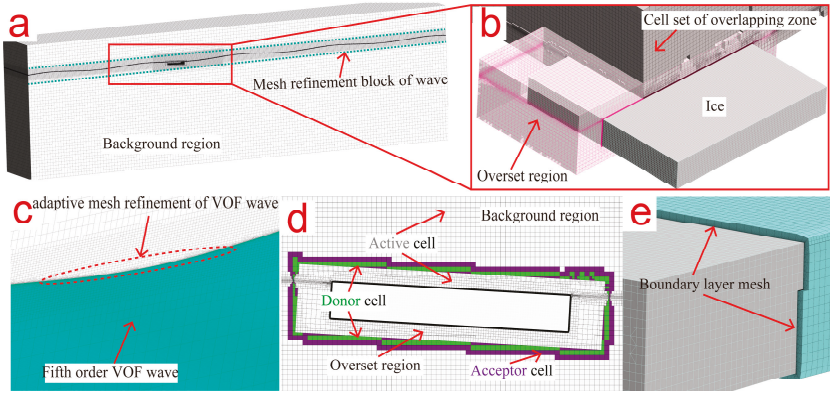

Figure 1. Computational mesh. (**a**) Overall of the mesh; (**b**) Mesh around the ice floe; (**c**) Adaptive mesh refinement of VOF wave; (**d**) Overset mesh; (**e**) Boundary layer mesh.

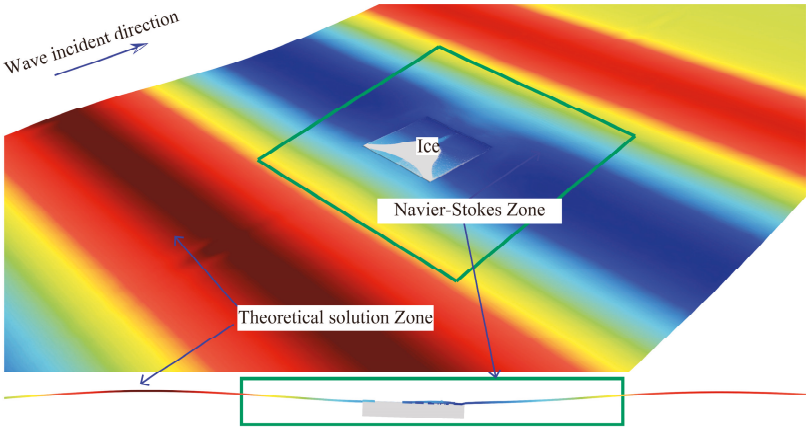

Figure 2. Illustration of the Euler overlay method.

Wave forcing is achieved by adding a source term to the transport (momentum) equations expressed as:

$$q_\phi = -\gamma\rho(\phi - \phi^*) \tag{3}$$

where γ, ρ, ϕ, and ϕ^* represent the forcing coefficient, fluid density, current solution of the transport equation, and value towards which the solution is forced, respectively.

The forcing coefficient varies smoothly from zero at the inner edge of the forcing zone to the maximum value γ at the boundary (the outer edge of the forcing zone). x^* is the relative coordinate within the forcing zone.

$$\gamma = -\gamma_0 \cos^2(\pi x^*/2) \tag{4}$$

The volume coupling can be either one-way or two-way because the forcing zones usually do not coincide.

2.4. Numerical Model Ice

Three model ice shapes, square, circular and triangular, were used in the numerical calculation, as illustrated in Figure 3. Table 1 presents the parameters of model ice.

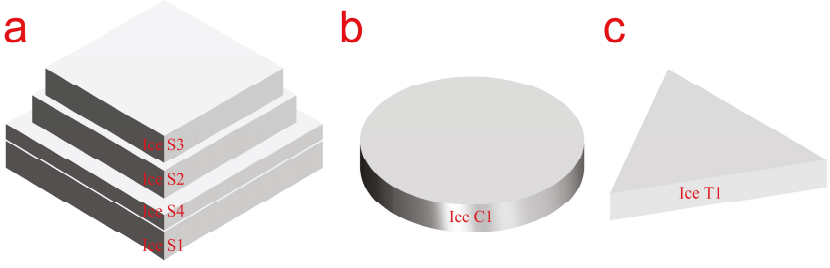

Figure 3. Model ice shapes. (**a**) Square ice floe; (**b**) Circle ice floe; (**c**) Triangle ice floe.

Table 1. Model ice parameters.

Model Ice Type	Symbol	Length of Side/Diameter (cm)	Thickness (cm)
Square	S1	60	9
	S2	50	9
	S3	45	9
	S4	60	5
Circle	C1	60	9
Triangle	T1	60	9

3. Description of Wave–Ice Model Test

The wave–ice model test was performed in the towing tank of Harbin Engineering University [29]. The length, width, and depth of the towing tank are 108, 7, and 3.5 m, respectively. The tank takes the structure of reinforced concrete while the maximum velocity of the carriage is 6.5 m/s. The wave maker used in this experiment is a three-dimensional wave maker with eight push plates imported from Denmark, which can generate regular two-dimensional waves, as well as irregular waves. The wave making period ranges from 0.4 to 4 s, and the maximum value of the regular wave height can be 0.4 m. The wave gauges are in the range of 0–10 m, the maximum permitted error of the wave height is $\pm$(0.2 + 5% of measurement value) m, the calibration error is $\leq$2 cm, the sampling frequency is 4 HZ, and the sampling time is in the range of 17–20 min.

In the test, paraffin was used as the model ice. The density of sea ice was in the range of 840–910 kg/cm^3 in the first year, and 720–910 kg/cm^3 in the following years. The paraffin model ice had an average thickness of 20 mm, and an approximate relative density of 900 kg/cm^3, which is very similar to that of sea ice.

The Qualisys track manager (QTM) system is used to capture the movement of ice. The QTM system mainly consists of the following parts: high speed video motion capture camera, QTM tracking management software, calibration equipment, marking sensitive spheres, and equipment fixtures. The system can realize 2/3/6-DOF (degree of freedom) motion capture and collect 2D (two dimensional) mark data in real-time before converting it to 3D/6D (3 dimensional/ 6 dimensional) data. The QTM system mainly applies the optical principle to position three sensitive spheres at three points of the ice model, as shown in Figure 4. Additionally, it employs two high-speed camera devices to capture the real-time dynamic positions of these three spheres, which are transformed into dynamic positions at the centre of the model by calculations.

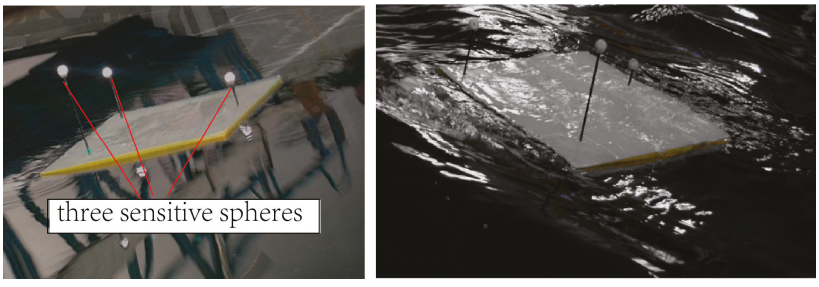

Figure 4. Model ice with sensitive spheres in wave condition. (**Left**: Three sensitive spheres; **Right**: Overwash in the test).

4. Results and Discussion

4.1. Wave Accuracy Verification

Before the calculation, the regular waves with wavelength and wave height of 3.4 and 0.08 m, respectively, were simulated, and the obtained results were compared with the theoretical solutions to verify the accuracy of the solver. To record the change in water surface, a wave height detection point was set at the centre of floating ice, as shown in Figure 5a. The comparison of free surface is presented in Figure 5b. The red and green curves represent the numerical and theoretical calculation results, respectively. It can be observed from Figure 5b that the form of the wave can stabilized, and also the wave height, as well as its phase, can be consistent with the theoretical solution. Figure 6 presents the comparison of wave velocity distribution. Figure 6a,b demonstrates the velocity distribution in the X direction, U and Z direction, W direction, respectively. Figure 6c illustrates the distribution of the wave velocity vector. The left and right sides represent the theoretical and numerical calculation results, respectively. The simulation results of the velocity distribution in the numerical wave tank agree well with the theoretical velocity distribution of the waves. Therefore, the reliability of the method used in this study is verified.

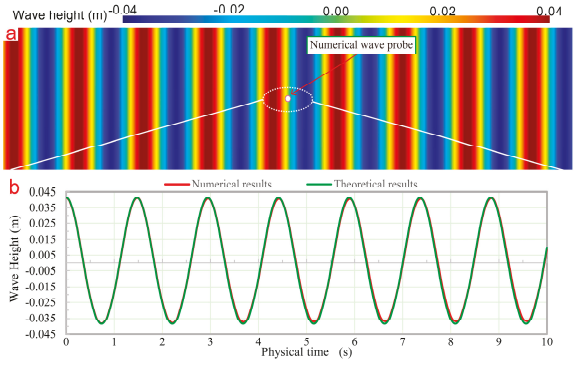

Figure 5. Comparison and verification of free surface wave height. (**a**) Waveform and wave height detection point; (**b**) Comparison of free surface wave height.

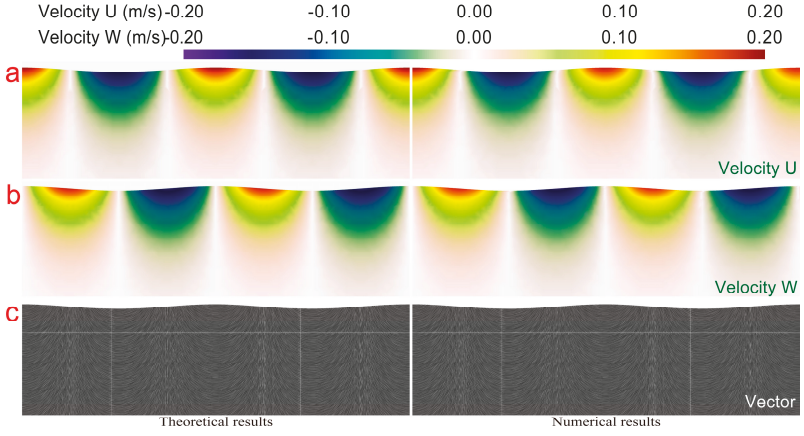

Figure 6. Comparison of wave velocity distribution. (**a**) Velocity distribution in the X direction; (**b**) Velocity distribution in the Z direction; (**c**) Distribution of the wave velocity vector.

4.2. Influence of Wavelength on x, y, and z Motions

The objects floating on the water will move in 6DoF under the influence of waves, which can be roughly divided into two types: translational and rotational waves. The motion coordinates of floating ice and the wave are shown in Figure 7.

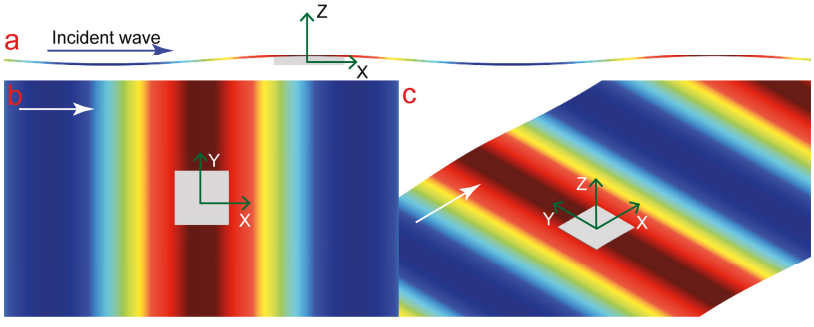

Figure 7. Motion coordinates of ice floe and waves. (**a**) Coordinates of floating ice and the wave in side view; (**b**) Coordinates of floating ice and the wave in top view; (**c**) Coordinates of floating ice and the wave in 3 dimensional view.

A wave is mainly determined by two parameters: wavelength (λ) and wave height (h). Wave steepness is the ratio of wave height to wavelength (h/λ), which is defined as a parameter used to represent the average slope of the fluctuation. The response amplitude operator (RAO) was defined as a dimensionless variable and used to describe the heave amplitude. The RAO value (z) is defined as: z = heave/h, where heave is the measured amplitude of heave motion.

Taking ice floe S1 as the simulation model, six conditions are presented in Table 2. The wave heights of all six conditions is 0.08 m while the wavelengths at these wave heights are 1.4, 1.8, 2.2, 2.6, 3.0, and 3.4 m, respectively. The RAO values under six different conditions are shown in Figure 8. When the wave height is fixed, with an increase in the wavelength, the RAO value first rises and then tends to be stable, which is mainly caused by the diffraction and scattering of waves. When the wavelength reaches a certain value, the RAO of the model ice is maximum. Then, the existence of the model ice no longer affects the wave, and the motion of ice floe follows the motion law of fluid particles.

Table 2. Test and simulation conditions.

Condition Number	Model Ice Type	Wavelength (m)	Wave Height (m)
1	S1	1.4	0.08
2	S1	1.8	0.08
3	S1	2.2	0.08
4	S1	2.6	0.08
5	S1	3.0	0.08
6	S1	3.4	0.08

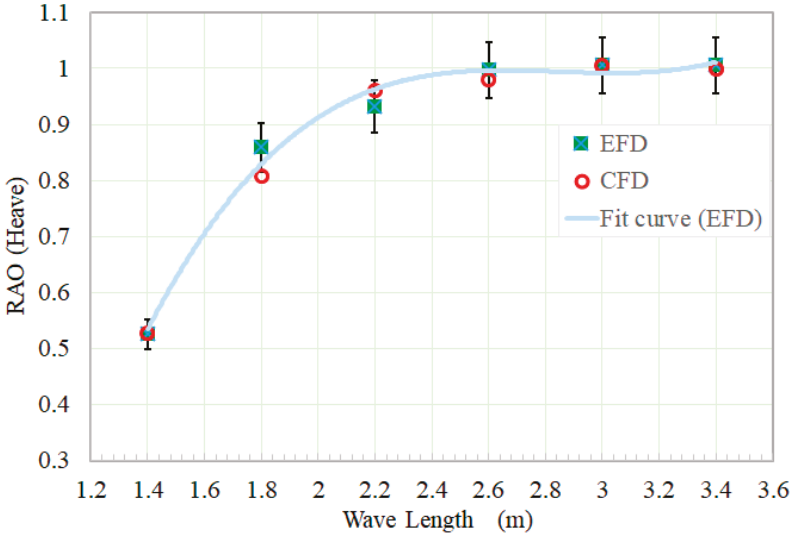

Figure 8. Variation of the response amplitude operator (RAO) with wavelength at constant wave height.

The motion of ice floes along the x, y, and z directions with a fixed wave height and varied wavelength is shown in Figure 9. The wave heights are all at 0.08 m and the wavelengths at these heights are 1.4, 1.8, 2.2, 2.6, 3.0, and 3.4 m, respectively. Under the action of waves, the ice floe moves forward continuously. The motion in the x direction is divided into two parts: oscillating surge and drift motions. Drift motion is mainly caused by the second-order drift force of waves. Figure 9a shows the drift motion along the x direction. From Figure 9a, it can be observed that the drift displacement along the x-axis is closely related to the wavelength. The wavelengths in numerical simulation are larger than the characteristic length of ice floe. The trajectory of the floating ice drifting along the x-axis is in a periodic reciprocating motion, and it gradually moves away from the initial position along the positive direction of the x-axis. Figure 9b shows the time history curve of ice floe rotating along the y-axis, and Figure 9c presents the time history curve of ice floe translation along the z-axis. Both the rotational and translational motions along the y- and z-axes, respectively, are periodic. It can be observed from Figure 9b that when the wavelength is small, the rotation amplitude along the y-axis is large, and with the increase in the wavelength, the rotation amplitude along the y-axis decreases. Figure 9c shows that the translational reciprocating motion along the z-axis is steady when the wavelength is small but intensified when the wavelength is increased.

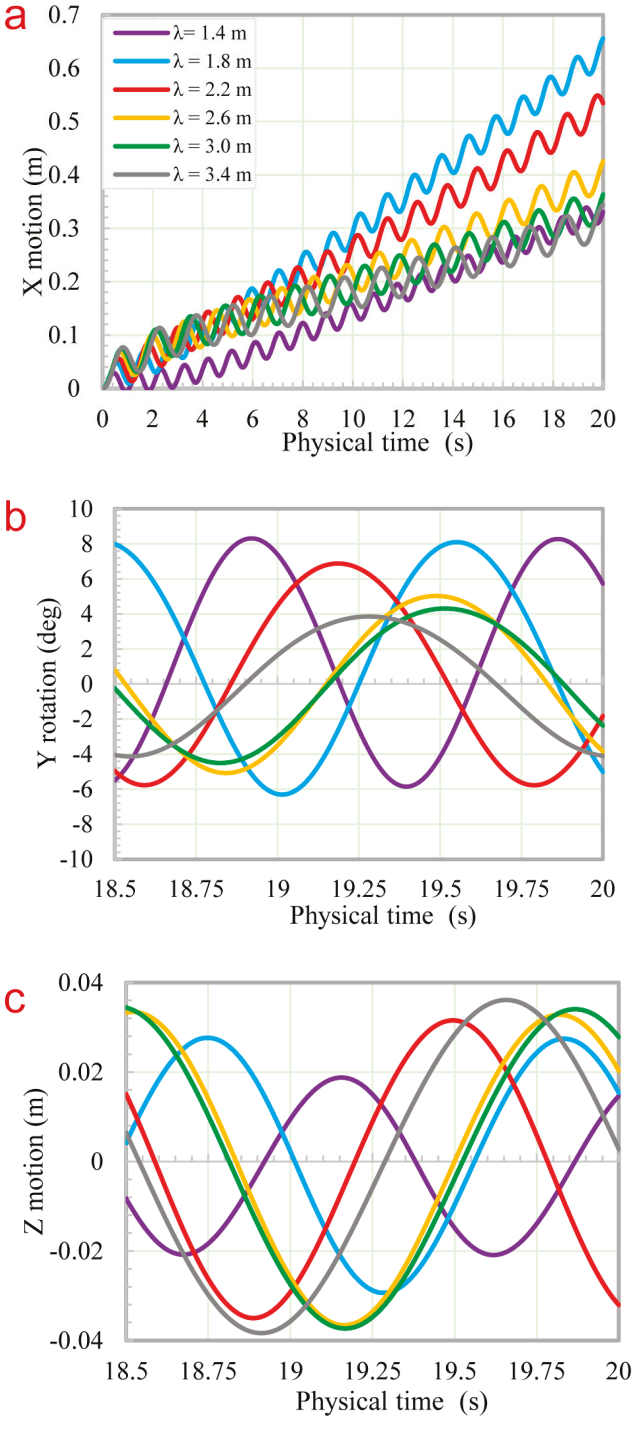

Figure 9. Ice floe motions along x, y, and z directions at different wavelengths. (**a**) X motion of ice floe; (**b**) Y rotation of ice floe; (**c**) Z motion of ice floe.

4.3. Influence of Ice Shape on x, y, and z Motions

In this section, the influence of ice shape on the motion of ice floes along the x, y, and z directions is discussed. The wave height is at 0.08 m and the wavelength is 3.4 m. The ice floe models employed here are S1, C1, and T1, respectively, as shown in Table 1. From Figure 10a, it can be observed that the trajectory of floating ice drifting along the x-axis under the action of waves is in a periodic reciprocating motion, as it gradually moves away from the initial position along the positive direction of the x-axis. The drift distance of ice floe C1 along the x-axis is the longest, followed by that of ice floe T1, with ice floe S1 as the closest. Figure 10b presents the time history curve of the ice floe rotating along the y-axis, and Figure 10c shows the time history curve of the ice floe translation along the z-axis. The rotational and translational motions along the y- and z-axes, respectively, are periodic in different shapes, and the shape has no obvious effect on the motions of the y- and z-axes.

4.4. Influence of Ice Thickness on x, y, and z Motions

In this section, the influence of ice thickness on the motion of ice floes along the x, y, and z directions is discussed. The square ice floes S1 and S4 with thicknesses of 9 and 5 cm, respectively, are used as the calculation model. The wave height and wavelength are 0.08 and 3.4 m, respectively. As shown in Figure 11, the rotational and translational motions along the y- and z-axes, respectively, are periodic in different ice thicknesses, therefore, thickness has no significant effect on the motions of the y- and z-axes. The motion along the x-axis is a periodic reciprocating motion, which gradually moves away from the initial position, and the drift distance of the ice with a smaller thickness is longer.

4.5. Influence of Ice Size on x, y, and z Motion

In this section, S1, S2, and S3 (Table 1) are used as the calculation models to discuss the influence of ice size on the motion of ice floes along the x, y, and z directions. As shown in Figure 12a, ice floe S3 with the smallest size has the farthest drift distance along the x axis, followed by ice floe S2, whereas ice floe S1 has the closest drift distance. Ice floes of different sizes have no significant effect on the rotational and translational motions of the y- and z-axes, respectively.

4.6. Overwash

In the wave–ice floe interaction process, an obvious phenomenon called overwash can be observed. Nelli F et al. [30] used a numerical model to simulate the transmission of regular water waves by a thin floating plate. The phenomenon of waves overwash is especially studied. Tran-Duc T et al. [31] investigated the phenomena of overwash with a flexible elastic plate under wave action. Overwash is a nonlinear phenomenon in which water flows over the top of floating ice under the action of waves [32]. Figure 13 shows the wave elevation at different times after the wave–ice floe interaction. T_0 represents the wave period, and Figure 13a–c show the wave elevation at $T = 0.2\ T_0$, $T = 0.4\ T_0$, $T = 0.6\ T_0$, $T = 0.8\ T_0$ and $T = T_0$ with ice floe S1, C1 and T1, respectively. Due to the symmetricity of the computational domain and model, only half of the results are presented.

At the point $T = 0.2\ T_0$, it can be observed that the wave is at its peak and overwash is negligible at this time. From $T = 0.4\ T_0$ to $T = T_0$, we can observe a significant overwash phenomenon. At $T = 0.4\ T_0$, the wave elevation on the surface of the floating ice is at the wave's peak. At $T = 0.6\ T_0$, the wave elevation on the surface of the floating ice decreases. At $T = 0.8\ T_0$, the wave elevation on the floating ice is at the wave trough. Finally, at $T = T_0$, the wave elevation increases gradually and begins to change in the next cycle.

Figure 14 illustrates the velocity distribution of the fluid around the ice floes in different shapes, in which the upper and lower parts represent the velocity field and streamline distributions, respectively. Figure 14a–c illustrate the velocity distribution of the fluid around S1, T1, and C1 ice floes at $T = 0.2\ T_0$, $T = 0.4\ T_0$, $T = 0.6\ T_0$, $T = 0.8\ T_0$ and $T = T_0$, respectively.

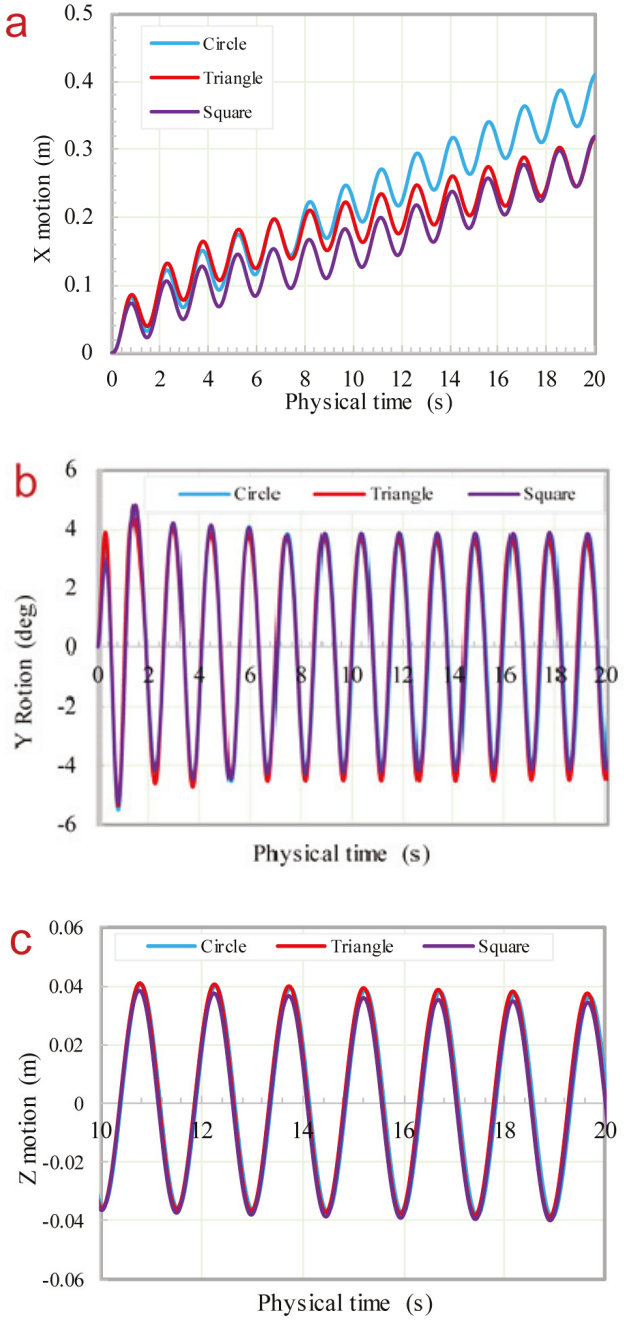

Figure 10. Motions of ice floes along x, y, and z directions in different shapes. (**a**) X motion of ice floe; (**b**) Y rotation of ice floe; (**c**) Z motion of ice floe.

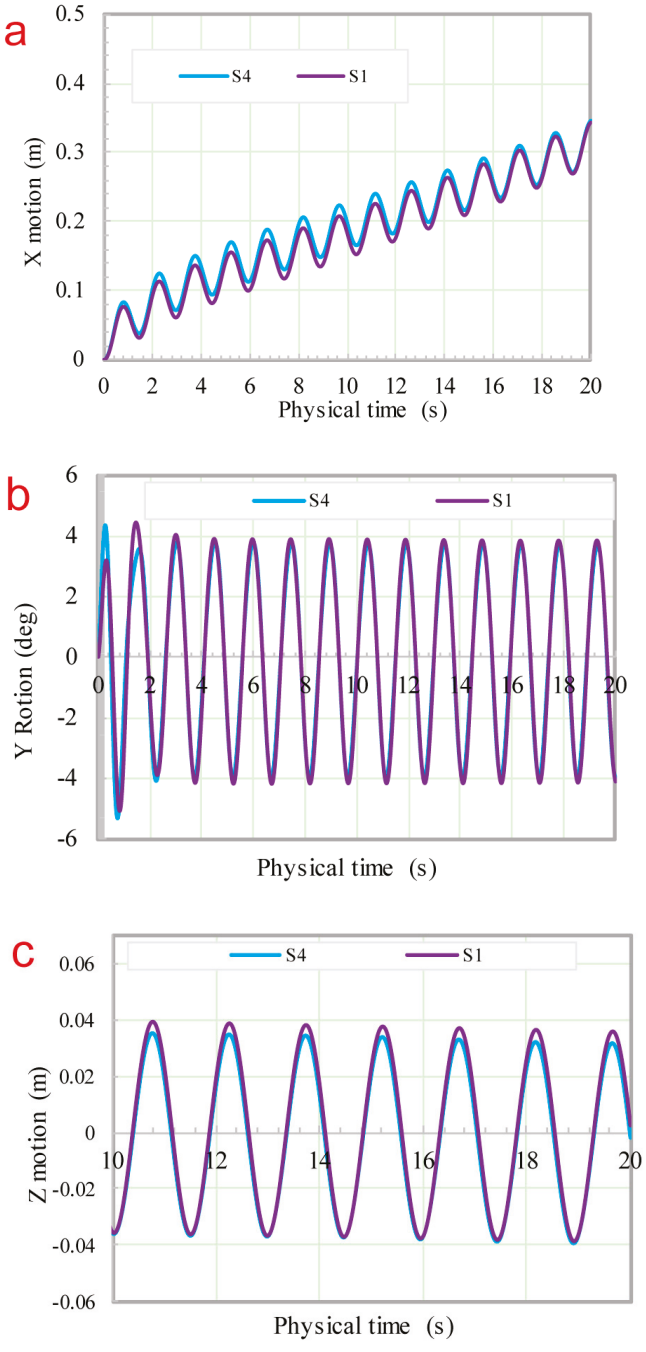

Figure 11. Motions of ice floes along x, y, and z directions in different ice thicknesses. (**a**) X motion of ice floe; (**b**) Y rotation of ice floe; (**c**) Z motion of ice floe.

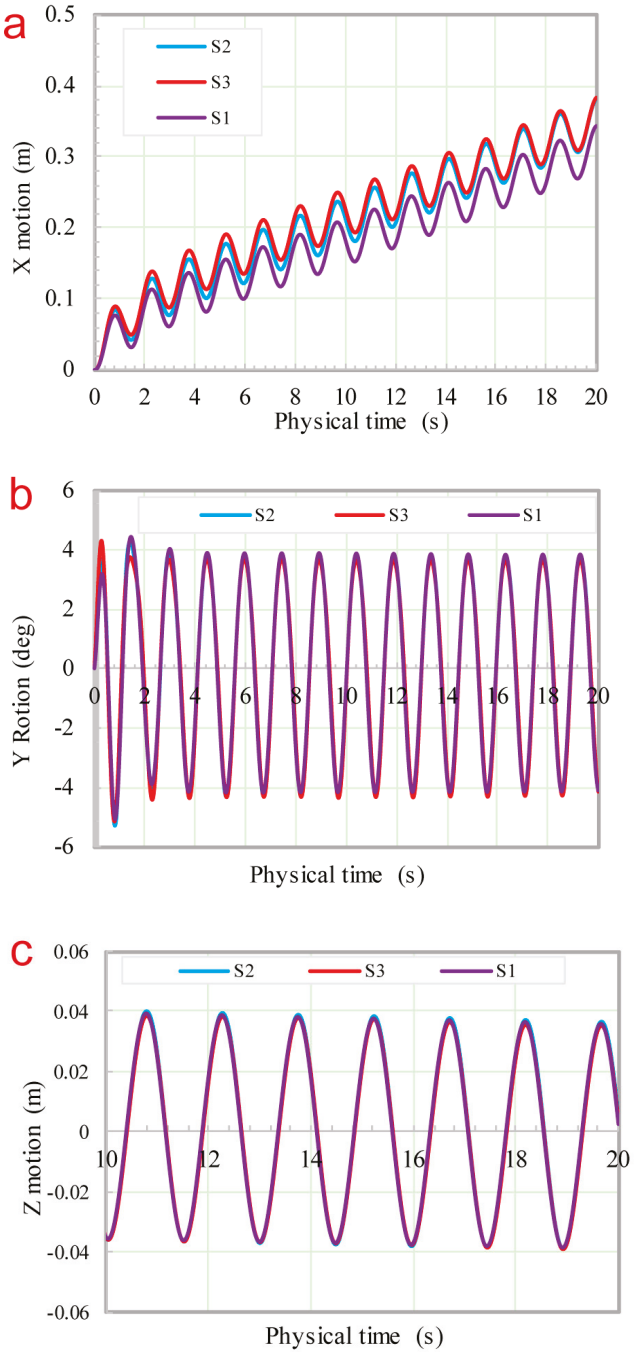

Figure 12. Motions of ice floes along x, y, and z directions in different ice sizes. (**a**) X motion of ice floe; (**b**) Y rotation of ice floe; (**c**) Z motion of ice floe.

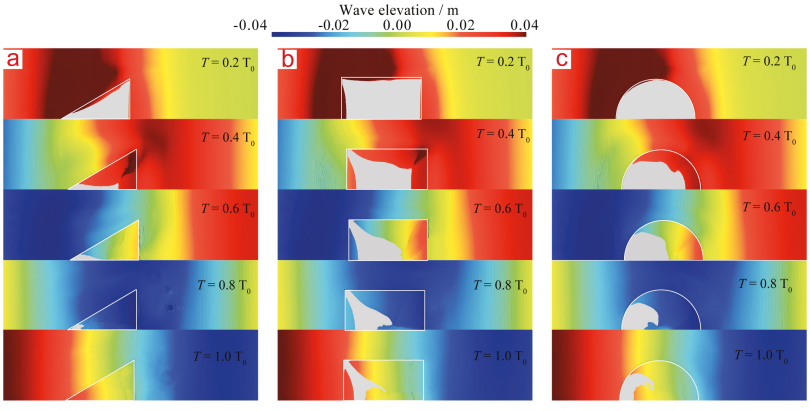

Figure 13. Wave elevation at different times (T) after wave–ice floe interaction. (**a**) Triangle ice floe; (**b**) Square ice floe; (**c**) Circle ice floe.

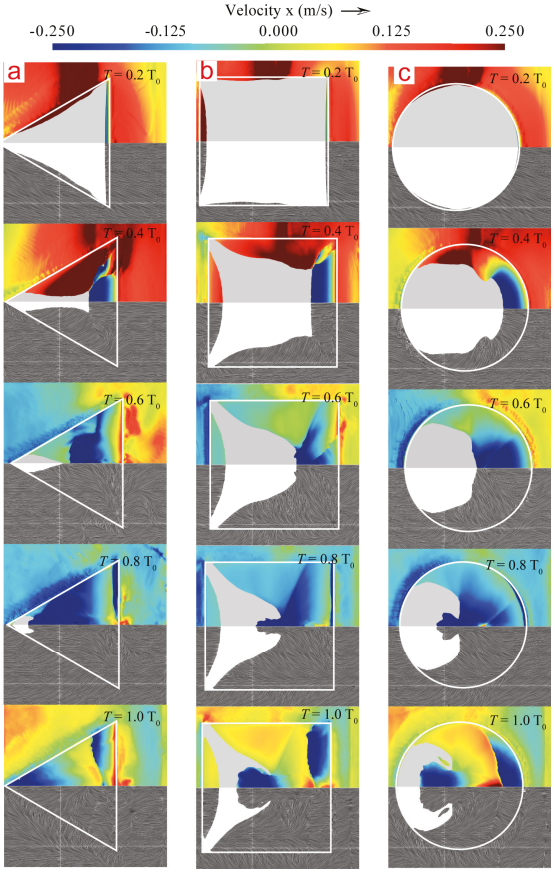

Figure 14. Distribution of fluid velocity around ice floes. (**a**) Triangle ice floe; (**b**) Square ice floe; (**c**) Circle ice floe.

When the wave acts on the edge of the ice floe, the fluid around the ice floe takes a velocity direction that is consistent with the wave propagation direction at T = 0.2 T_0 and T = 0.4 T_0. At T = 0.6 T_0, the wave slows down due to the opposite force of the propagation direction of the wave on the edge of the floating ice; the fluid velocity around the ice decreases, and even produces a velocity that is opposite to the wave propagation direction. The streamline in the lower half of Figure 14 represents the flow direction of the fluid. The overwash phenomenon on the surface of floating ice can be clearly observed in Figure 14. The exposed white area in the figure indicates a non-overwash area. It can be inferred that the overwash phenomenon is most significant at T = T_0.

Figure 15 presents the motion attitude of ice floe S1 and its drift position in the x direction at T = 20 s. The drift distance is the longest when the wavelength is 1.8 m, but decreases with the increase in the wavelength from 2.2 to 3.4 m. The drift distance of ice floes reflects the drift velocity along the x-axis at different wavelengths.

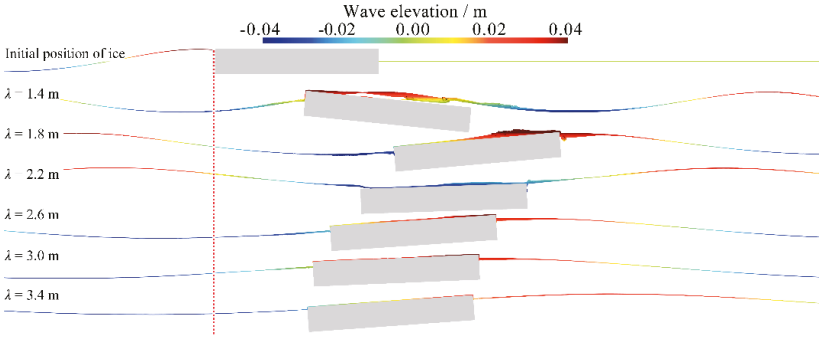

Figure 15. Floating ice attitude at T = 20 s.

5. Conclusions

A numerical study was conducted based on the CFD method to investigate the response of a single ice floe under wave actions. The simulation results obtained were compared with the model scale test in a towing tank while the calculated values agreed well with experimental results. The conclusions drawn from this study are summarized as follows:

(1) After comparing the CFD and EFD (experimental fluid dynamics) results of RAO at different wavelengths, it is inferred that the numerical results agree optimally with the experimental results. Under the action of wave diffraction and scattering, the RAO value initially increased and then stabilized with an increase in wavelength.

(2) Under the action of waves, ice floes produced a violent motion. In different conditions, the longitudinal translation, vertical heave, and pitch motions were significant and maintained a certain consistency. The motion of ice floes along the x-, y-, and z-axes is related to wavelength, ice size, ice thickness, and ice shape. When the wavelength was greater than 1.8 m, the drift distance along the x-axis decreased with an increase in wavelength. The ice floes rotated periodically along the y-axis and the rotation amplitude along the y-axis decreased as the wavelength increased. The translational motion along the z-axis was steady when the wavelength is small, but the reciprocating motion along the z-axis was intensified as the wavelength increased.

(3) Under the same wave parameters, the circular floating ice C1 exhibited the longest drift distance along the x-axis, followed by the triangular floating ice T1; however, the square floating ice exhibited the closest drift distance. The shape of the ice has no significant influence on the motions of the y- and z-axes. The ice thickness exerted a negligible influence on the motions of the x, y, and z directions. The ice floes with the

smallest sizes exhibited the longest offset distance along the x-axis, and the motion difference of the y- and z-axes, relative to size, was insignificant.

(4) In this study, the overwash of different shapes of floating ice was analysed at different times. It was inferred that the overwash phenomenon was the most significant at $T = T_0$ for any shape of floating ice, and the overwash changes with the wave period.

Author Contributions: Conceptualization, T.W. and W.L.; methodology, T.W.; software, W.L.; validation, R.D. and S.H.; formal analysis, W.L.; investigation, D.J.; resources, T.W.; data curation, W.L.; writing—original draft preparation, T.W., W.L. and D.J.; writing—review and editing, W.L.; visualization, S.H.; supervision, D.J. and R.D.; project administration, D.J.; funding acquisition, R.D. and D.J. All authors have read and agreed to the published version of the manuscript.

Funding: This research was funded by the Guangdong Basic and Applied Basic Research Foundation (2019A1515110721), the China Postdoctoral Science Foundation (No. 2019M663243); the Fundamental Research Funds for the Central Universities (No.20lgpy52); the Foundation of Pre-research on Military Equipment of the Chinese People's Liberation Army (No.6140241010103; JZX7Y20190252032901); the Aeronautical Science Foundation of China (No. 201723P6001).

Institutional Review Board Statement: Not applicable.

Informed Consent Statement: Not applicable.

Data Availability Statement: Data is contained within the present article.

Conflicts of Interest: The authors declare no conflict of interest. The funders had no role in the design of the study; in the collection, analyses, or interpretation of data; in the writing of the manuscript, or in the decision to publish the results.

References

1. Lee, C.M.; Cole, S.; Doble, M.; Freitag, L.; Hwang, P. *Marginal Ice Zone (MIZ) Program: Science and Experiment Plan*; Technical Report; Washington University Seattle Applied Physics Lab: Seattle, WA, USA, 2012.
2. Kohout, A.L.; Meylan, M.H. An elastic plate model for wave attenuation and ice floe breaking in the marginal ice zone. *J. Geophys. Res. Oceans* **2008**, *113*. [CrossRef]
3. Dumont, D.; Kohout, A.; Bertino, L. A wave-based model for the marginal ice zone including a floe breaking parameterization. *J. Geophys. Res.* **2011**, *116*, 241–253. [CrossRef]
4. Toyota, T.; Kohout, A.; Fraser, A. Formation processes of floe size distribution in the marginal ice zone (Invited). *Blood* **1998**, *92*, 1297–1307.
5. Marchenko, A.; Wadhams, P.; Collins, C.; Rabault, J.; Chumakov, M. Wave-ice interaction in the north-west barents sea. *Appl. Ocean Res.* **2019**, *90*, 101861. [CrossRef]
6. Kovalev, P.D.; Squire, V.A. Ocean wave/sea ice interactions in the south-eastern coastal zone of Sakhalin Island. *Estuar. Coast. Shelf Sci.* **2020**, *238*, 106725. [CrossRef]
7. Squire, V.A.; Dugan, J.P.; Wadhams, P.; Rottier, P.J.; Liu, A.K. Of ocean waves and sea ice. *Annu. Rev. Fluid Mech.* **1995**, *27*, 115–168. [CrossRef]
8. Toyota, T.; Haas, C.; Tamura, T. Size distribution and shape properties of relatively small sea-ice floes in the Antarctic marginal ice zone in late winter. *Deep Sea Res. Part II Top. Stud. Oceanogr.* **2011**, *58*, 1182–1193. [CrossRef]
9. Zhang, J.; Schweiger, A.; Steele, M.; Stern, H. Sea ice floe size distribution in the marginal ice zone: Theory and numerical experiments. *J. Geophys. Res. Oceans* **2015**, *120*, 3484–3498. [CrossRef]
10. Thorndike, A.S.; Rothrock, D.A.; Maykut, G.A.; Colony, R. The thickness distribution of sea ice. *J. Geophys. Res.* **1975**, *80*, 4501–4545. [CrossRef]
11. Gupta, M. Various remote sensing approaches to understanding roughness in the marginal ice zone. *Phys. Chem. Earth Parts Abc* **2015**, *83–84*, 75–83. [CrossRef]
12. Williams, T.D.; Bennetts, L.G.; Squire, V.A.; Dumont, D.; Bertino, L. Wave–ice interactions in the marginal ice zone. Part 1: Theoretical foundations. *Ocean Model.* **2013**, *71*, 81–91. [CrossRef]
13. Peters, A.S. The effect of a floating mat on water waves. *Commun. Pure Appl. Math.* **1950**, *3*, 319–354. [CrossRef]
14. Weitz, M.; Keller, J.B. Reflection of water waves from floating ice in water of finite depth. *Commun. Pure Appl. Math.* **1950**, *3*, 305–318. [CrossRef]
15. Wadhams, P. The seasonal ice zone. In *The Geophysics of Sea Ice*; Springer: Boston, MA, USA, 1986; pp. 825–991.
16. Keller, J.B. Gravity waves on ice covered water. *J. Geophys. Res. Oceans* **1998**, *103*, 7663–7669. [CrossRef]
17. Carolis, D.G.; Desiderio, D. Dispersion and attenuation of gravity waves in ice: A two-layer viscous fluid model with experimental data validation. *Phys. Lett. A* **2002**, *305*, 399–412. [CrossRef]

18. Wang, R.; Shen, H.H. Gravity waves propagating into an ice-covered ocean: A viscoelastic model. *J. Geophys. Res. Oceans* **2010**, *115*. [CrossRef]
19. Newyear, K.; Martin, S. A comparison of theory and laboratory measurements of wave propagation and attenuation in grease ice. *J. Geophys. Res. Oceans* **1997**, *102*, 25091–25099. [CrossRef]
20. Sakai, S.; Hanai, K. Empirical formula of dispersion relation of waves in sea ice. Ice in the Environment. In Proceedings of the 16th IAHR International Symposium on Ice, Dunedin, New Zealand, 1–6 December 2002; pp. 327–335.
21. Dai, M.; Shen, H.H.; Hopkins, M.A.; Ackley, S.F. Wave rafting and the equilibrium pancake ice cover thickness. *J. Geophys. Res. Oceans* **2004**, *109*. [CrossRef]
22. Parra, S.M.; Sree, D.K.; Wang, D.; Rogers, E.; Lee, J.H.; Collins, C.O., III; Law, A.W.K.; Babanin, A.V. Experimental study on surface wave modifications by different ice covers. *Cold Reg. Sci. Technol.* **2020**, 103042. [CrossRef]
23. Huang, L.; Ren, K.; Li, M.; Tuković, Ž.; Cardiff, P.; Thomas, G. Fluid-structure interaction of a large ice sheet in waves. *Ocean Eng.* **2019**, *182*, 102–111. [CrossRef]
24. Zhang, Y.; Chen, C.; Beardsley, R.C.; Perrie, W.; Gao, G.; Zhang, Y.; Qi, J.; Lin, H. Applications of an unstructured grid surface wave model (FVCOM-SWAVE) to the Arctic Ocean: The interaction between ocean waves and sea ice. *Ocean Model.* **2020**, *145*, 101532. [CrossRef]
25. Wilcox, D.C. *Turbulence Modeling for CFD*; DCW Industries, Inc.: La Canada, CA, USA, 1994; pp. 15–19.
26. Muzaferija, S. Computation of free surface flows using interface-tracking and interface-capturing methods. In *Nonlinear Water-Wave Interaction*; Computational Mechanics: Southampton, UK, 1998.
27. Fenton, J.D. A Fifth-Order Stokes Theory for Steady Waves. *J. Waterw. Port Coast. Ocean Eng.* **1985**, *111*, 216–234. [CrossRef]
28. Kim, J.W.; Jang, H.; Baquet, A.; O'Sullivan, J.; Lee, S.; Kim, B.; Read, A.; Jasak, H. Technical and Economic Readiness Review of CFD-Based Numerical Wave Basin for Offshore Floater Design. In Proceedings of the Offshore Technology Conference, Houston, TX, USA, 2–5 May 2016.
29. Wang, C.; Song, M.; Guo, C.; Wang, S.; Tian, T.; Luo, W. Experimental Study of Sea Ice Motion in Waves. *J. Cold Reg. Eng.* **2020**, *34*, 04020010. [CrossRef]
30. Nelli, F.; Bennetts, L.G.; Skene, D.M.; Toffoli, A. Water wave transmission and energy dissipation by a floating plate in the presence of overwash. *J. Fluid Mech.* **2020**, 889. [CrossRef]
31. Tran-Duc, T.; Meylan, M.H.; Thamwattana, N.; Lamichhane, B.P. Wave Interaction and Overwash with a Flexible Plate by Smoothed Particle Hydrodynamics. *Water* **2020**, *12*, 3354. [CrossRef]
32. Skene, D.M.; Bennetts, L.G.; Meylan, M.H.; Toffoli, A. Modelling water wave overwash of a thin floating plate. *J. Fluid Mech.* **2015**, *777*. [CrossRef]

Journal of *Marine Science and Engineering*

MDPI

Article

Inhibition and Hydrodynamic Analysis of Twin Side-Hulls on the Porpoising Instability of Planing Boats

Jiandong Wang, Jiayuan Zhuang *, Yumin Su and Xiaosheng Bi

National Key Laboratory of Science and Technology on Autonomous Underwater Vehicle, Harbin Engineering University, Harbin 150001, China; jdwang_heu@163.com (J.W.); suyumin@hrbeu.edu.cn (Y.S.); xyyan_heu@163.com (X.B.)

* Correspondence: zhuangjiayuan@hrbeu.edu.cn

Abstract: A comparative analysis of the hydrodynamic performance of a planing craft in the monomer-form state (MFS) and trimaran-form state (TFS) was performed, and the inhibition mechanism of twin side-hulls on porpoising instability was evaluated based on the numerical method. A series of drag tests were conducted on the monomer-form models with different longitudinal locations of the center of gravity (L_{cg}); the occurrence of porpoising and the influence of L_{cg} on porpoising by the model was discussed. Then, based on the Reynolds-averaged Navier–Stokes (RANS) solver and overset grid technology, numerical simulations of the model were performed, and using test data, the results were verified by incorporating the whisker spray equation of Savitsky. To determine how the porpoising is inhibited in the TFS, simulations for the craft in the MFS and TFS when porpoising were performed and the influence of side-hulls on sailing attitudes and hydrodynamic performance at different speeds were analyzed. Using the full factor design spatial sampling method, the influence of longitudinal and vertical side-hull placements on porpoising inhibition were deliberated, and the optimal side-hull location range is reported and verified on the scale of a real ship. The results indicate that the longitudinal side-hull location should be set in the ratio (a/L_m) range from 0.1 to 0.3, and vertically, the draft ratio (D_d/T_m) should be less than 0.442. Following these recommendations, porpoising instability can be inhibited, and lesser resistance can be achieved.

Keywords: planing craft; twin side-hulls; porpoising instability; model tests; numerical simulation; inhibition mechanism; optimal location

Citation: Wang, J.; Zhuang, J.; Su, Y.; Bi, X. Inhibition and Hydrodynamic Analysis of Twin Side-Hulls on the Porpoising Instability of Planing Boats. *J. Mar. Sci. Eng.* **2021**, *9*, 50. https://doi.org/10.3390/jmse9010050

Received: 2 December 2020
Accepted: 31 December 2020
Published: 5 January 2021

1. Introduction

Stability problems associated with high-speed planing crafts have long been a notable research focus for designers, even in calm waters. It is well known that due to the existence of longitudinal or transverse instability, many kinds of dangerous accidents may occur [1]. The abrupt variation of trim causes the self-induced heave and pitch oscillations, which has been named porpoising [2]. In severe cases, the bow even suffers a violent attack and generates greater resistance in fast vessels, which threatens the safety of on-board personnel and equipment. The transverse instability causes the sudden emergence of large heeling, leads to a loss of course-keeping ability, and facilitates chine walking [3].

Considering the reasons outlined above and the associated adverse situations, it is important for engineers to control the longitudinal and transverse instability of high-speed crafts. In terms of the longitudinal instability, since the porpoising was observed during the test conducted by Clement and Blount [4], Blount and Codega [5] analyzed the dynamic instability problem, focusing on the nonlinear vibration of the planing craft through the test method, and the suggested criterion conditions for the unstable motion were given. Katayama and Yoshiho [6] conducted a series of performance tests on planing crafts, concretely involving accelerated longitudinal motion and porpoising instability, which provides crucial comparative data for many scholars. In recent years, porpoising theory has been applied in some studies based on established numerical methods [7] and Savitsky's

work [8,9]; those studies were primarily concerned with the inhibition of trim instability by appendages such as interceptors, trim tabs, and wedges [10–12]. The interceptor is a thin vertical plate protruding from the stern that is installed at the bottom edge. Mehran et al. [13] ascertained that the inhibition mechanism of the interceptor on porpoising in the planing boat, and Mansoori et al. [14,15] further analyzed the influence of boundary layer thickness, interceptor height, and span on the inhibition of porpoising and navigation resistance, and demonstrated that the combination of trim tab and interceptor with the same size is more beneficial to control the trim and reduce the resistance than the single interceptor. In addition, to develop a craft design utilizing an interceptor that included six heights at distinct positions of the stern bottom, Ahmet and Baris [16] tested resistance and sailing attitudes and reported that for the same-size interceptor, the effect of drag reduction and porpoising inhibition was gradually reduced when installed at the interval from keel to bilge line. Hongjie et al. [17] and Hanbing et al. [18] calculated the porpoising of a planing boat in a uniform incoming flow, indicating that moving forward of the center of gravity could reduce the resistance peak value, which is beneficial to avoid porpoising.

Regarding transverse instability research, owing to the interference of many nonlinear factors and high calculation costs, most studies merely involved model test and improving the calculation method, as discussed in Refs. [19–25]. This research is not involved in the transverse stability of the planing boat because the installing of twin side-hulls widens the transverse weight distribution of the vessel, the transverse righting moment increases, which makes the transverse stability of the craft better than that of the monomer-form.

However, well-known porpoising instability restrains the maximum speed of high-speed planing crafts, but it can be controlled by using external devices, such as trim tabs, interceptors, side-hulls, etc. The doctoral thesis of Yi [26] indicated that a high-speed trimaran planing craft was beneficial to improve longitudinal stability, but it increased the resistance at lower speeds. So a conceptual planing boat, capable of freely retracting and releasing the twin side-hulls, is proposed in this research. At lower speeds, it maintains the monomer-form state (MFS), and at higher speeds, it expands into the trimaran-form state (TFS) to inhibit the porpoising and improve the longitudinal stability. But due to the strong interference of nonlinear factors and the high test cost, there are no or few studies analyzing the inhibition of twin side-hulls on porpoising.

Therefore, the hydrodynamic performance of twin side-hulls and their inhibiting effect on the porpoising instability in high-speed planning crafts were analyzed in this research. And a series of tests were conducted on the monomer-form models with different longitudinal locations of the gravity center (L_{cg}), and the influence of the L_{cg} on porpoising was determined. Then, based on the comparisons of the numerical (CFD) setup, simulations of the test model were performed, and the calculated results were verified using the whisker spray equation of Savitsky [27]. Further, the inhibition mechanism of the side-hulls on porpoising was ascertained, and a comparative analysis of the hydrodynamics of the planing craft in the MFS and TFS was performed. Finally, the influence of longitudinal and vertical side-hull locations on inhibiting porpoising was determined, and the optimal location range is provided.

2. Experimental Setup

2.1. Model Design

This study took a 1:2.5-scale test model of an actual planing hull with twin position-adjustable side-hulls as a research object. The twin side-hulls can be synchronously placed in any longitudinal, horizontal, and vertical positions of the ship broadsides within a certain scale range by the variable-structure link bridge. When on a relatively stable seas, the craft will pack up the twin side-hulls and sail forward quickly in the monomer-form state (MFS), as shown in Figure 1a. When encountering high sea conditions, it will put down the twin side-hulls and sail stably in the TFS, as shown in Figure 1b. Main geometric details of the planing hull in different navigation states are listed in Table 1.

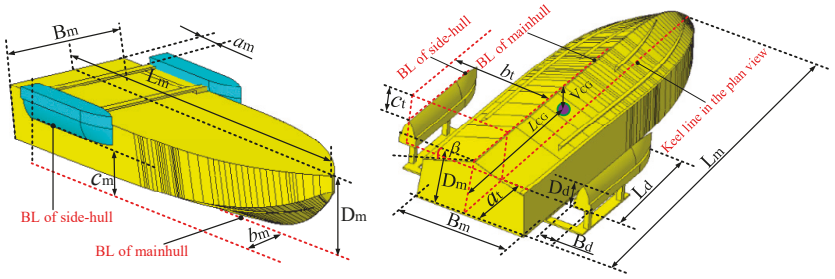

Figure 1. Main geometric characteristics of the hull in different navigation states: (**a**) monomer-form state (MFS) and (**b**) trimaran-form state (TFS).

Table 1. Primary geometric details of the planing hull at each navigation state.

Main Feature	Symbol	Value
Monomer-form state (MFS)		
Main hull length (m)	L_m	2.3
Main hull breadth (m)	B_m	0.702
Main hull depth (m)	T_m	0.357
Main hull draft (m)	D_m	0.168
Design waterline length (m)	L_{wl}	2.201
Original fixed location of side-hull in the longitudinal, horizontal and vertical direction (m)	a_m b_m c_m	0.23 0.38 0.26
Main hull deadrise angle (°)	θ_m	18
Displacement of main hull (kg)	Δ_m	122.4/137.3
Inertia tensor of main hull (kg·m^2)	I_{ym}	40.2 (Test model)
Longitudinal location of center of gravity (CG) (m)	L_{cg}	0.94/0.882/0.83
Vertical location of CG (m)	V_{cg}	0.23
Trimaran-form state (TFS)		
Side-hull length (m)	L_d	0.72
Side-hull breadth (m)	B_d	0.104
Side-hull depth (m)	T_d	0.155
Side-hull draft (m)	D_d	0.098
Initial design location of the released side-hulls in longitudinal, horizontal and vertical direction (m)	a_t b_t c_t	0.23 0.548 0.07
Draft of TFS (m)	D_t	0.168
Displacement of trimaran (kg)	Δ_t	137.3
Inertia tensor of trimaran (kg·m^2)	I_{yt}	49.43
Longitudinal location of CG (m)	L_{cg}	0.882/0.83
Vertical location of CG (m)	V_{cg}	0.23

The hard chine test model (main hull), built-in wood, was square-tailed and non-stepped, had a larger knuckle line width, a plurality of spray deflectors with variant dimensions were symmetrically installed at the main hull bottom to improve its seakeeping and reduce resistance in calm water. The twin side-hulls were arranged at both broadsides of the main hull by a link bridge, were thin and sharp in cross-section, slender in whole and vertical in the bilge, provide bare buoyancy and hydrodynamic lift but improved directional stability. The molded lines of the main hull and side-hulls are presented in Figure 2. For convenient adjustment to the center of gravity (CG) position in the TFS and making the model easier to slide, the twin side-hulls were initially designed on both sides of the rear of the main hull as shown in Figure 1b, and the specific location is listed in Table 1.

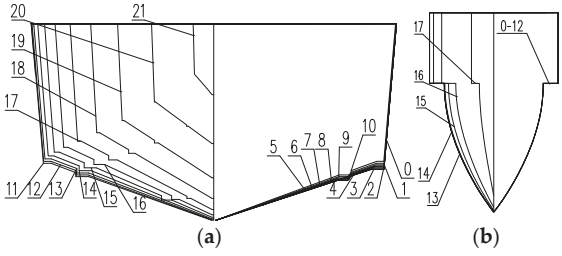

Figure 2. Molded lines of the model: (**a**) main hull; (**b**) side-hull.

2.2. Model Test

All model tests were conducted in the towing tank (510 m × 6.5 m × 6.8 m) of the High-speed Hydrodynamic Laboratory of Special Aircraft Research Institute of China. Owing to the higher test cost, only the towing tests of the model in the MFS were completed, and considering that the twin side-hulls were far higher than the waterline when packed up in the MFS, both were not installed in the test process, the schematic diagram of the experimental setup is presented in Figure 3.

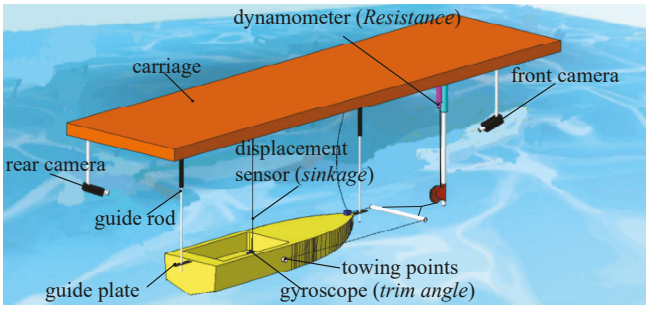

Figure 3. Schematic diagram of the experimental setup.

The model was attached to a carriage (0.1%), and two guide robs were also fixed in the carriage, separately inserted into the guide plates of the bow and stern to prevent yaw and roll motion; the towing points were located at the broadside and aligned with the center of gravity (CG). The cable-extension displacement sensor (0.01 mm) and the gyroscope (0.01°) were fixed at the CG to measure the sinkage and dynamic trim, the electronic dynamometer (0.02 kg) was mounted on the carriage, pulled the tow bar for measuring the resistance, and the accuracy of the above measuring instruments is presented in the corresponding brackets. Moreover, the front and rear cameras were fixed on the forward and aft of the carriage to capture the flow phenomena of the model sailing in calm water.

In the model tests, aimed at the two displacements and three longitudinal positions of the CG, four conditions were designed, as shown in Table 2. The towed speeds of the model were 3–13 m/s (length Froude numbers Fr = 0.63–2.72) or until porpoising occurred. The wave surface condition around the model and the stern wake in the distance were clearly captured, as presented in Figure 4, which shows the photographs from various perspectives of the model at Fr = 1.26 under condition two, and subsequently, a Longitudinal location of CG/Main hull length (L_{cg}/L_m) ratio of 0.38 occurred under condition two.

Table 2. Model test conditions in calm water.

Condition	Δ_m (kg)	L_{cg} (m)	L_{cg}/L_m	τ_0 (°)
One	137.3	0.94	0.41	−0.4
Two	137.3	0.882	0.38	0.6
Three	137.3	0.83	0.35	1.6
Four	125.4	0.882	0.38	0.6

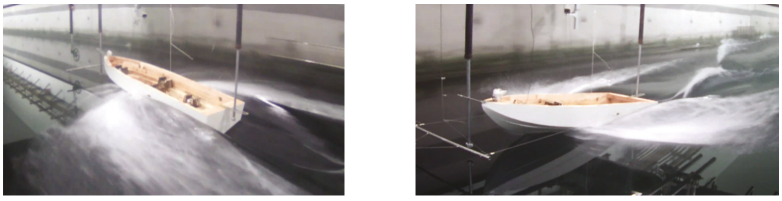

Figure 4. Photographs of the monomer-form model.

2.3. Experimental Results

The measured parameters mainly include total resistance R_T, sinkage Z_{cg}, and trim angle τ when sailing stably; the R_T was treated into the dimensionless form of R_T/Δ. The test results on the R_T, Z_{cg}, and τ of the monomer-form model under different conditions are shown in Figure 5.

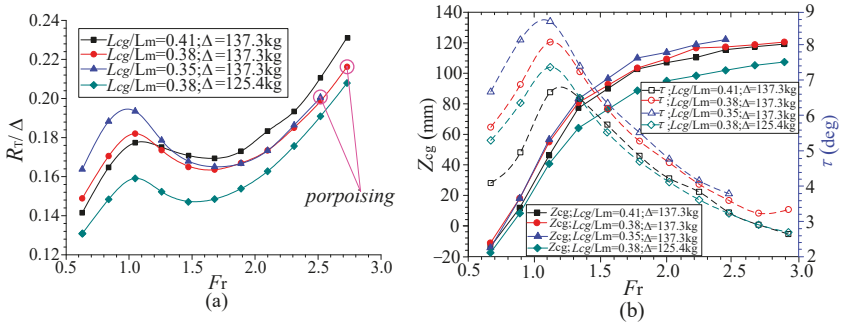

Figure 5. Test results of the monomer-form model: (**a**) total resistance; (**b**) sinkage and trim angle.

Combing test phenomena and results, we found that at low speeds ($Fr < 1.05$), the bow was gradually lifted upwards as the speed increased. At the semi-planing state ($Fr = 1.05$), the sinkage and trim angle increased significantly. When crossing the resistance peak, entering the planing regime ($Fr > 1.05$), the R_T appeared to be notably reduced; however, after descending to a certain threshold, the R_T rose and exceeded the previous peak as the speed further increased. When $Fr > 2.31$, the Z_{cg} increased slowly, but the τ always reduced as the speed increased during the planing stage.

For the model with equal displacement during the semi-planing state, as the L_{cg} moved backward, the resistance peak increased. When $Fr > 1.05$, as speed further increased, the more the L_{cg} moves backward within a certain scale, the more the R_T decreased, but the Z_{cg} and τ increased. In addition, when the L_{cg} remained at the same and speed increased, the R_T, Z_{cg}, and τ of the small-displacement boat were all less than those of the large-displacement boat, especially for the small-displacement boat, R_T is lesser when crossing the resistance peak.

The porpoising of the model under conditions two and three occurred at $Fr = 2.73$ ($v = 13$ m/s) and 2.52 ($v = 12$ m/s), respectively. From the videos recorded in the experiment, we observed that the coupled heave and pitch oscillation amplitudes under condition three were extremely larger compared with condition two, which shows that when L_{cg} becomes

increasingly backward, porpoising occurs more easily, and the oscillation amplitudes are even larger it limits the maximum speed.

3. CFD Setup

3.1. The Numerical Method

To simulate the viscous flow field around the sailing vessel, the governing equations of viscous incompressible fluid were introduced, and that were solved based on the Finite Volume Method (FVM) described in Ref. [28]; the main CFD solver is the platform of Star-CCM+, the Reynolds-averaged Navier–Stokes (RANS) and continuity equations jointly constitute the governing equations, and as follows

$$\frac{\partial(\rho u_i)}{\partial t} + \frac{\partial}{\partial x_i}(\rho u_i u_j) = -\frac{\partial p}{\partial x_i} + \frac{\partial}{\partial x_j}\left(\mu\frac{\partial u_i}{\partial x_j} - \rho\overline{u_i' u_j'}\right) + S_i \tag{1}$$

$$\frac{\partial \rho}{\partial t} + \frac{\partial(\rho u_i)}{\partial x_i} = 0 \tag{2}$$

where u_i and u_j are the time mean of the velocity component, (i, j = 1, 2, 3), p is the pressure mean, ρ is the fluid density, μ is the coefficient of dynamic viscosity, $\rho\overline{u_i' u_j'}$ is the Reynolds stress term, S_i represents the generalized source term.

To close the governing equations, the Shear Stress Transport turbulence (SST) k–ω model [29] was adopted to calculate the Reynolds stress term in this research. Despite the existence of the strong adverse pressure gradient, the RANS model has been shown to be inaccurate and has some limitations as discussed in Refs. [30–32], but the SST k–ω turbulence model is still widely used to deal with high Reynolds number flow problems and has higher precision on solving the flow field around the high-speed planing craft [33].

Moreover, the volume of fluid (VOF) method, proposed by Nichols and Hirt [34,35] in 1981, was also used to track the change of the free surface in this research. In the VOF method, the most critical aspect is obtaining the volume ratio function (F) of the specified fluid occupancy in a grid cell. When the calculation of the F values in each grid cell is completed, the motion interface of the liquid-gas, two-phase flow can be tracked.

Then, to acquire the hull position, based on velocity and pressure in the flow field, the centroid motion theorem and centroid moment of motion theorem were used as follows

$$\begin{array}{l} \frac{d\vec{B}}{dt} + \vec{\Omega} \times \vec{B} = \vec{F} \\ \frac{d\vec{K}}{dt} + \vec{\Omega} \times \vec{K} + \vec{V} \times \vec{B} = \vec{M} \end{array} \tag{3}$$

where $\vec{B}$ is the momentum of the model, $\vec{\Omega}$ (p, q, r) is the angular velocity, $\vec{F}$ (X, Y, Z) is the combined force, $\vec{K}$ is the momentum moment relative to the CG, $\vec{V}$ (u, v, w) is the speed and $\vec{M}$ (L, M, N) is the combined moment.

$\vec{F}$ and $\vec{M}$ can be solved as below

$$\vec{F} = \int_S ([\tau] - P[I])\cdot\vec{n}\,ds - \vec{G} \tag{4}$$

$$\vec{M} = \int_S \left(\vec{r} - \vec{r}_G\right) \times ([\tau] - P[I]) \cdot \vec{n}\,ds \tag{5}$$

where $[\tau]$, $P[I]$ and $\vec{G}$ are the shear stress, pressure, and gravity, respectively. S is the hull surfaces. $\vec{r}$ is the displacement of mesh nodes, and $\vec{r}_G$ is the displacement of CG.

The overset-grid method, as described in Ref. [36], was adopted due to the complex hull motion. The solver procedure of the numerical method is shown in Figure 6.

When variations of the forces and moments were less than the tolerance (ε) or the total iteration time (T) reaches, the calculation was terminated.

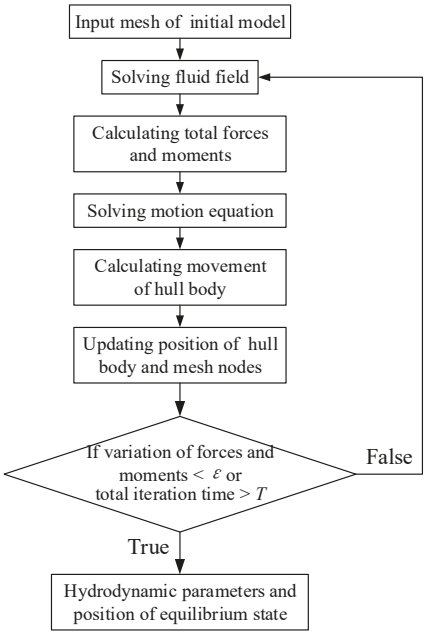

Figure 6. Solver procedure of the numerical method.

In the post-processing, the pressure, shear force, unit node coordinates at each unit are known; thus, the longitudinal moment of the side-hulls to CG can be calculated by integrating the element moments to the CG, and the dimensionless form as follows

$$C_{M_d} = \frac{\iint\limits_{S_d}\left[P\cdot\vec{I}\cdot\vec{n}\right]ds + \iint\limits_{S_d}\left[\tau\cdot\vec{I}\cdot\vec{n}\right]ds}{\Delta g \mathrm{L_m}} \tag{6}$$

where $\vec{I}$ and $\vec{n}$ are the local normal vector of the grid element and the displacement relative to the CG, respectively, S_d represents the surface area of twin side-hulls.

Likewise, adopting the same integral strategy, the dimensionless forms of the resistance and lift for the twin side-hulls are acquired as follows:

$$C_{R_d} = \frac{\iint\limits_{S_d}[\tau]ds}{\Delta g} \tag{7}$$

$$C_{N_d} = \frac{\iint\limits_{S_d}[P]ds}{\Delta g} \tag{8}$$

3.2. Computational Domains and Boundary Conditions

To prevent the reflection of waves in the computational domain and obtain a better precision, the domain should be no less than five times the hull length ($\mathrm{L_m}$) [37]; thus, it was designed to a cuboid region with dimensions of 7.5 $\mathrm{L_m}$ × 2 $\mathrm{L_m}$ × 2.6 $\mathrm{L_m}$, and its specific dimensions and the boundary conditions were depicted in Figure 7. Considering

the symmetry of the model and flow field, only half a domain of the model was established to reduce the simulation duration.

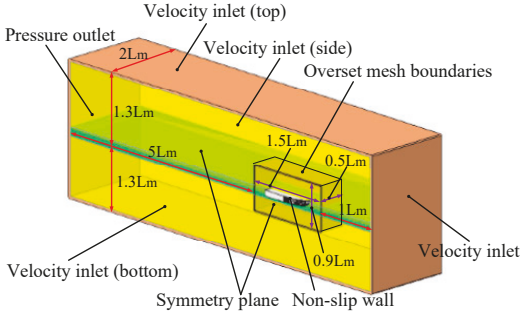

Figure 7. Dimensions and boundary conditions in the domain.

To obtain a better simulation on the sailing attitudes of model, the overset region was embedded in the background region; the boundary conditions were set as follows: The background region, incoming-flow inlet, top, bottom, and side were all set to the velocity inlet, the outlet was the pressure outlet, and the middle longitudinal section was a symmetry plane; for the overset region, the mid-ship section was still a symmetry plane, the ambient planes were set to the overset mesh boundaries, and the hull body was defined as the non-slip wall.

3.3. Mesh Generation

The grids in the background and overset region were automatically generated, as shown in Figure 8, and the grids of the two regions defined as follows: The cutting hexahedron grids were mainly used to discretize the background region, both the cutting hexahedron grids and the prismatic layer grids were selected to fill the overset region due to the complex geometrical details of the hull body. To obtain the more accurate flow field around the hull, the circumambience of the hull was refined by the smaller hexahedron grids in the volume control region; for the grids around the free surfaces in the two regions, that were set to more than twenty layers in the vertical direction to clearly capture the change of free surface; and the boundary layer grids were imposed on the surface of hull body.

3.4. Wall Non-Dimensional Distance of the First Layer Grid (y+) and Time Step Set-Up

To obtain the accurate stress and pressure of the flow field around the hull, wall functions, and boundary layer grids were required, referred to the Ref. [37]. The $y+$ value was ascertained as below

$$y^+ = \frac{y}{v}\sqrt{\frac{1}{2}U^2\frac{0.074}{\mathrm{Re}_L^{\frac{1}{5}}}} \tag{9}$$

where $y+$ and y separately represent the non-dimensional distance and the height of the first layer grid, U is the speed of vessel, L is the waterline length of the vessel, v is the fluid viscosity coefficient and Re represents the Reynolds number.

In this research, five boundary layers were adopted with a grid growth rate of 1.3. The generated boundary layer grids on the hull body are presented in Figure 8d. The details of when the $y+ = 250$, the y values, and total boundary layer grid reached thicknesses Δh at different speeds are shown in Figure 9.

In addition, considering the time step of iteration (Δt) depends on flow characteristics in the implicit unsteady simulation, as discussed in Ref. [38], the range of Δt is initially defined as follows:

$$\Delta t = (0.005 \sim 0.01) \cdot \mathrm{Lm}/U \tag{10}$$

The maximum number of internal iterations and total calculation time were set to five times and 15 s, respectively.

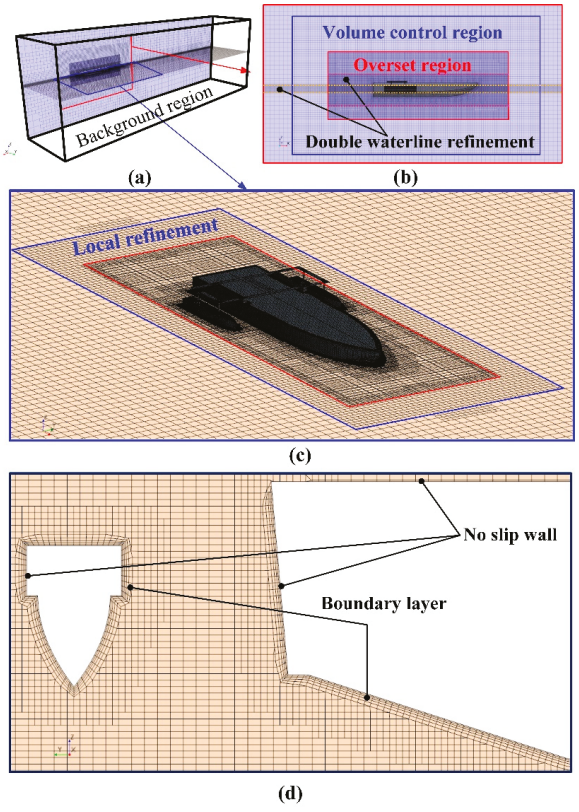

Figure 8. Detailed grid partition of the entire computational domain: (**a**) axis view; (**b**) front view; (**c**) vertical view; (**d**) partial view.

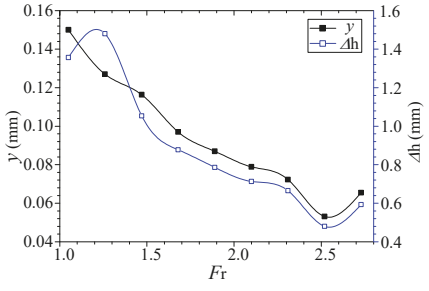

Figure 9. The height of the first layer grid (y) values and total thicknesses of the boundary layer grid at different speeds.

4. Numerical Simulation Verification

4.1. Grid Parameters

To verify the convergence of the grid, four grids were designed, whose sizes on the hull surface and in the background region were the same, but the grid sizes in the overset region, volume control region, and around the free surface increased with the refinement

ratio ($r = \sqrt{2}$, L_g = 1 m), the grid parameters of four grids are shown in Table 3, and the grids around the hull and the free surface are presented in Figure 10. Then, the sailing of the model in calm water was simulated, and the results of resistance were compared with the test. The numerical setting is consistent with the Section 3, and the towing speed Fr = 1.26 (v = 6 m/s) was selected for verification.

Table 3. Parameters of the four grids.

Grid Parameters	Detailed Description	Grid 4	Grid 3	Grid 2	Grid 1
Mesh number	Entire calculation domain (k)	238	524	788	1550
Overset region grid size	Relative minimum size (%L_g)	2.828	2	1.414	1
	Relative target size (%L_g)	5.656	4	2.828	2
Volume control region grid size	Relative grid size in the x, y, z direction (%L_g)	11.31	8	5.656	5
		11.31	8	5.656	5
		11.31	8	5.656	5
Grid size around the free surface	Relative grid size in the x, y, z direction (%L_g)	28.28	20	14.14	10
		28.28	20	14.14	10
		2.828	2	1.414	1

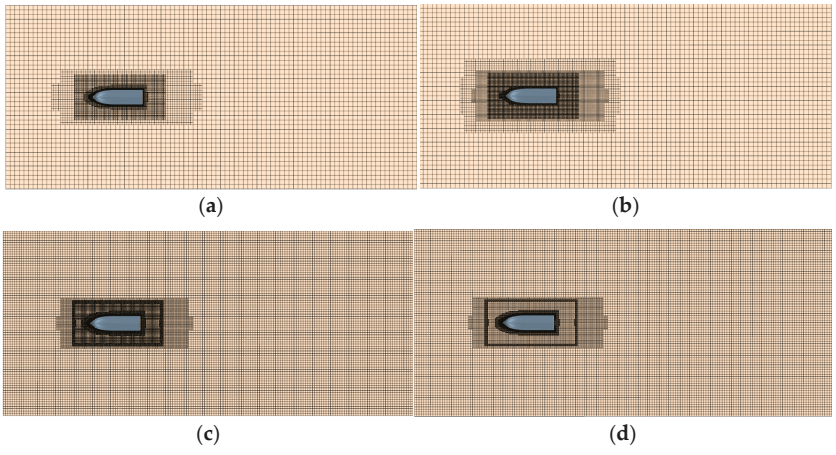

Figure 10. The four designed grids: (**a**) grid 4, (**b**) grid 3, (**c**) grid 2, (**d**) grid 1.

Table 4 and Figure 11 indicate that the resistance curves of the four grids have good convergence; comparing the numerical results of the four grids, the coarse grid 4 had a larger deviation compared with test results, and as the grid was refined, the deviation gradually decreased. However, when the grid was fine enough (grid 2), the further refinement of grid 1 did not greatly improve the simulation accuracy; inversely, the calculation efficiency dropped significantly due to too many grids.

Table 4. Resistance comparisons of the test (EFD) and numerical (CFD) results for different grids.

Grid	Resistance (N)		Deviation (%)
	EFD	CFD	
4	233.436	202.616	−13.203
3	233.436	214.535	−8.097
2	233.436	224.45	−3.849
1	233.436	224.754	−3.719

Summing up the above, considering the high accuracy and the less computing time at the same time, the parameters of grid 2 were selected to be the more suitable grid input setting, and subsequent grid settings were all based on grid 2.

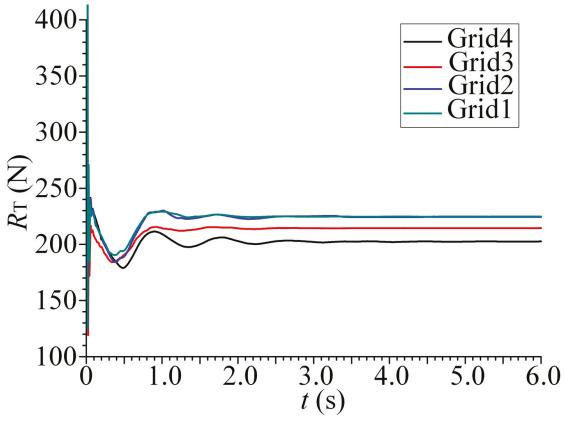

Figure 11. Resistance curves of the different grids.

4.2. Y+ Values

In general, the value of $y+$ has a profound influence on the calculation accuracy. In 2005, Wang et al. [39] analyzed the influence of y+ on the turbulence problem, indicating that the $y+$ value near the hull should be restrained between 30 and 300. Thus, to ascertain the influence of $y+$ value on the calculation accuracy, six different $y+$ values of 50, 100, 150, 200, 250, and 300 were selected, and as in the previous CFD set up, simulations of different $y+$ values were conducted, and the wall $y+$ and resistance after calculation were obtained, which are shown in Figure 12 and Table 5, respectively.

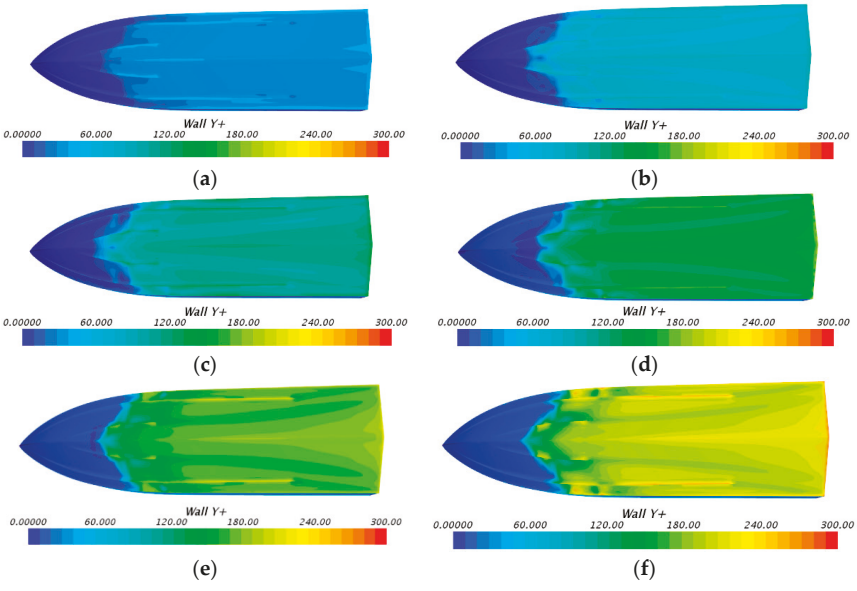

Figure 12. Wall non-dimensional distance of the first layer grid ($y+$) after calculation: (**a**) $y+ = 50$; (**b**) $y+ = 100$; (**c**) $y+ = 150$; (**d**) $y+ = 200$; (**e**) $y+ = 250$; (**f**) $y+ = 300$.

Figure 12 indicates that the setting of boundary layer under different $y+$ values was reasonable, and the amount waterline of the vessel arose changed due to the increase of the trim angle; the reduction of the waterline length made the $y+$ value less than the theoretical value.

Table 5 and Figure 13 indicate that the resistance curves of different $y+$ values had the same convergence. However, a smaller $y+$ value made the calculation deviation larger due to the sharp reduction of the waterline length. When $y+ = 250$, the deviation was smallest, so subsequently, the $y+$ value of 250 was adopted in this research.

Table 5. Resistance comparisons of the test and numerical results at different $y+$ values.

$y+$	Resistance (N)		Deviation (%)
	EFD	CFD	
50	233.436	203.321	−12.901
100	233.436	209.901	−10.082
150	233.436	212.742	−8.865
200	233.436	221.456	−5.132
250	233.436	224.45	−3.849
300	233.436	223.521	−4.247

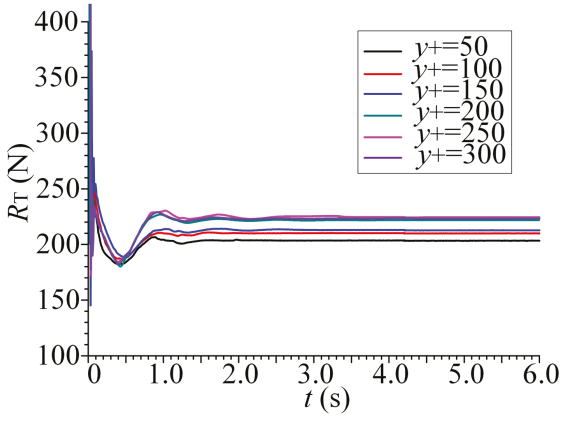

Figure 13. Resistance curves of the different $y+$.

4.3. Time Step of Iteration

The determination of time step (Δts) is usually based on the incoming flow characteristics, and it must satisfy not less than the distance of the designed minimum grid at the same time. Thus, with the aim of high accuracy and solution efficiency, the influence of the Δts on the deviation was analyzed in this section.

To ascertain the appropriate value of Δts, five values of 0.01 s, 0.008 s, 0.006 s, 0.004 s, 0.002 s were used to compute the resistance, and the numerical results of different Δts values were compared with the test, and are presented in Table 6 and Figure 14.

Table 6. The numerical results of resistance at different determination of time steps (Δts).

Δts	Resistance (N)		Deviation (%)
	EFD	CFD	
0.01	233.436	214.902	−7.94
0.008	233.436	221.478	−5.123
0.006	233.436	224.45	−3.849
0.004	233.436	225.509	−3.396
0.002	233.436	229.033	−1.886

Table 6 and Figure 14 shows that the five resistance curves had the same convergence trend, the larger Δts (0.01 s) had a weaker calculation accuracy, and the deviation became smaller with the shortening of the time step, which indicates a smaller time interval is

conducive to improve the solution precision. However, when the Δ*ts* was less than 0.004 s, further reducing the Δ*ts* value greatly increased the convergence duration, which caused a waste of calculation efficiency, so the time step Δ*ts* = 0.004 s was adopted because of its higher accuracy and lesser calculation duration.

Summing up the above, the influences of the grid parameters, *y*+ values, and time step on the calculation accuracy and efficiency were verified. The results show that the numerical method had good convergence, high accuracy, and appropriate efficiency in simulating the navigation of the model in calm water.

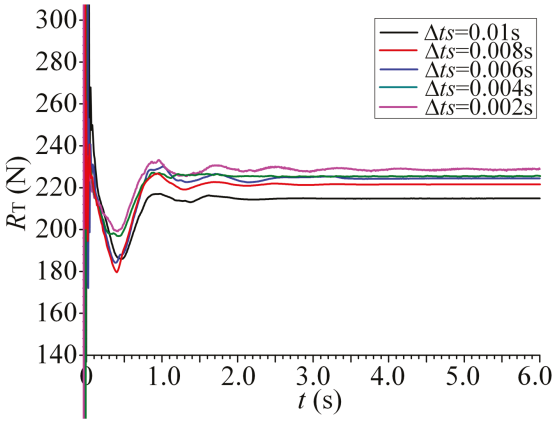

Figure 14. Resistance curves of the different time steps.

4.4. Comparison of Numerical and Experimental Results

As in the aforementioned CFD setup, simulations were performed for the model at *Fr* = 0.63–2.52 or until the porpoising appears when L_{cg}/L_m = 0.38 (condition two) and 0.35. The comparison between experimental data and simulated values for total resistance (R_T), sinkage Z_{cg}, and trim angle τ are shown in Figure 15, and the deviations are listed in Table 7.

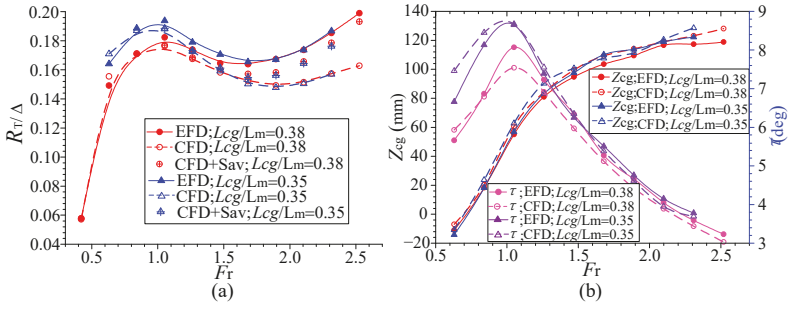

Figure 15. Comparison between EFD and CFD results for (**a**) total resistance R_T and the R_T added to the whisker spray resistance, (**b**) sinkage and trim angle.

Whether the ratio L_{cg}/L_m was 0.38 or 0.35, the changing trend of the CFD results for the R_T, Z_{cg}, and τ with speed was consistent with the test, as shown in Figure 15. During the planing stage (*Fr* ≥ 1.05), for the Z_{cg} and τ when L_{cg}/L_m = 0.38, the maximum deviations were 10.06% and −6.6%, respectively; when L_{cg}/L_m = 0.35, the maximum deviations were 10.42% and −4.87%, respectively, most deviations of the remaining were below 10%, as shown in Table 6, that indicates the CFD setup could accurately forecast the sailing attitudes (Z_{cg} and τ) of the model in the planing regime. But for the Z_{cg} and τ in

the draining state ($Fr < 1.05$), the deviations of Z_{cg} were relatively larger, the deviations of τ were smaller, controlled at approximately 12% or lower.

In addition, for the computation of R_T in the draining and semi-planing state ($Fr \leq 1.05$), the deviations were controlled below 5%, which implies that the CFD setup had better forecast precision for the R_T at that stage. However, when entering the planing state, as speed increased, the deviations of R_T under the two conditions got larger, especially at $Fr = 2.52$ when $L_{cg}/L_m = 0.38$, the maximum deviation attained was 18.15%, which indicates the numerical method could weakly forecast the R_T of the model during the high-speed planing stage ($Fr > 2.1$). In this stage, the spray resistance accounted for a large proportion of the total resistance, but the size of the refined mesh was unable to finely capture the tiny splash and jet. Concurrently, the nonlinear factors such as splash and jet were not effectively solved by the turbulence model, which caused the forecast precision to descend.

To obtain more accurate results of the R_T during the high-speed planing stage, based on the trim angle obtained by the CFD method and combining the whisker spray equation reported by Savitsky [27], the spray resistance (R_S) was computed and further added to the R_T solved by the CFD method, the amendatory R_T are summarized in the brackets of the third column in Table 7 and Figure 15a. Comparing the amendatory R_T with test results, the maximum deviation was −6.53% at $Fr = 1.89$ when $L_{cg}/L_m = 0.35$, which proves the calculated results of the R_T could be remarkably improved after the correction of the whisker spray equation of Savitsky [27].

In addition, under conditions two and three, porpoising respectively occurred at v = 13 m/s and 12 m/s in the simulation process, which accorded with the observed phenomena during the test. In brief, the combination of the CFD method and the whisker spray equation of Savitsky [27] achieved good forecasting of the total resistance and sailing attitude of the vessel during the high-speed planing stage.

Table 7. The comparisons of total resistance (R_T), sinkage (Z_{cg}), and trim angle (τ).

Fr	R_T (kg·F)			Z_{cg} (mm)			τ (deg)		
	EFD	**CFD (+Sav)**	**Deviation (%)**	**EFD**	**CFD**	**Deviation (%)**	**EFD**	**CFD**	**Deviation (%)**
0.42	7.94	7.85	−1.12	-	-	-	-	-	-
0.63	20.44	21.30	4.21	−11	−7.01	−36.27	5.66	5.93	4.70
0.84	23.41	23.46	0.20	18.3	20.33	11.09	6.87	6.79	−1.11
1.05	24.98	24.16 (24.24)	−3.27 (−2.95)	55.1	60.65	10.06	8.07	7.54	−6.60
1.26	23.82	22.95 (23.08)	−3.67 (−3.09)	81	84.07	3.79	7.23	6.91	−4.45
1.47	22.54	21.68 (22.0)	−3.81 (−2.42)	94.8	99.59	5.06	6.34	5.97	−5.82
1.68	22.45	20.86 (21.54)	−7.09 (−4.04)	103.6	109.26	5.46	5.27	5.12	−2.94
1.89	22.92	20.45 (21.67)	−10.76 (−5.44)	109.5	114.17	4.27	4.66	4.43	−4.90
2.10	23.8	20.75 (22.70)	−12.81 (−4.60)	116.7	119	1.97	4.05	3.89	−3.95
2.31	25.39	21.57 (24.47)	−15.06 (−3.62)	117.3	123.15	4.99	3.59	3.44	−4.18
2.52	27.26	22.31 (26.46)	−18.15 (−2.95)	118.8	128.12	7.85	3.23	3.03	−6.19

(a) Fr = 0.42–2.52; L_{cg}/L_m = 0.38; when Fr = 2.73 (v = 13 m/s), the porpoising occurs.

Fr	R_T (kg·F)			Z_{cg} (mm)			τ (deg)		
	EFD	**CFD (+Sav)**	**Deviation (%)**	**EFD**	**CFD**	**Deviation (%)**	**EFD**	**CFD**	**Deviation (%)**
0.63	22.48	23.43	4.20	−14.2	−10.82	−23.8	6.66	7.46	12.01
0.84	25.84	25.63	−0.84	18.2	23.59	18.72	8.13	8.45	3.94
1.05	26.55	25.78 (25.83)	−2.91 (−2.71)	56.8	62.72	10.42	8.65	8.67	0.23
1.26	24.51	23.64 (23.75)	−3.53 (−3.1)	83.4	90.28	8.25	7.39	7.55	2.17
1.47	23.37	21.82 (22.09)	−6.65 (−5.5)	97.6	100.65	3.13	6.25	6.35	1.54
1.68	22.66	20.59 (21.20)	−9.15 (−6.44)	110.1	107.61	−2.26	5.51	5.38	−2.36
1.89	22.88	20.25 (21.39)	−11.51 (−6.53)	113.8	111.38	−2.13	4.76	4.62	−2.88
2.10	23.79	20.62 (22.53)	−13.32 (−5.3)	118.9	120.43	1.29	4.15	3.95	−4.87
2.31	25.58	21.51 (24.14)	−15.91 (−5.65)	122.2	128.44	5.1	3.78	3.69	−2.32

(b) Fr = 0.63–2.31; L_{cg}/L_m = 0.35; when Fr = 2.52 (v = 12 m/s), the porpoising occurs.

5. Results and Discussion

5.1. Side-Hulls Inhibition of Porpoising Instability in High-Speed Crafts

To verify that the release of side-hulls can inhibit porpoising instability in high-speed crafts, simulations for the initial designed TFS (Table 1) advancing in calm water at Fr = 2.73

(condition two) and 2.52 (condition three) were performed, and the oscillation curves with time of τ and R_T were attained. Based on the previous computations of the MFS, the oscillation comparisons of the τ and R_T in the MFS and TFS were conducted; the results under condition two are presented in Figure 16.

The τ and R_T of the TFS exhibited minimal oscillation, but that of the MFS was significant, which indicates that the side-hulls could effectively inhibit porpoising instability.

To ascertain why porpoising occurs, the pressure distributions of the hull bottom in the MFS and the TFS were compared, and results are shown in Figure 17. A weak pressure area arose at the fore of hull bottom in the MFS, indicating that the fore moment M_f (Figure 18) was relatively less than that of the rear moment M_r, and due to the high trim angle (Figure 16a) and low lift coefficient, porpoising occurred, the specific cause of this are explained in Figure 19.

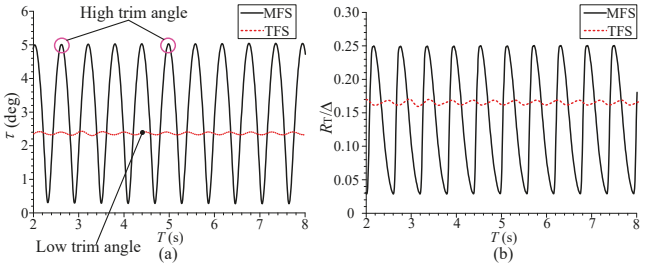

Figure 16. Oscillation comparisons when L_{cg}/L_m = 0.38: (**a**) trim angle; (**b**) total resistance.

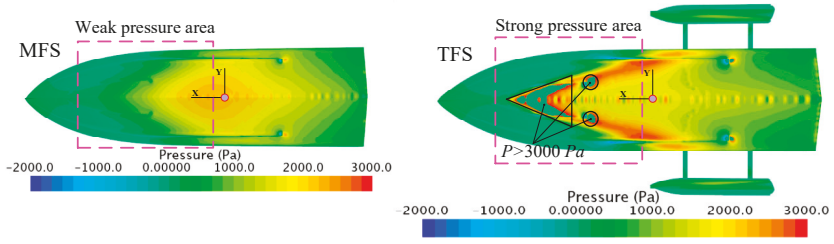

Figure 17. Comparisons of the hull bottom pressure in the MFS and TFS when L_{cg}/L_m = 0.38.

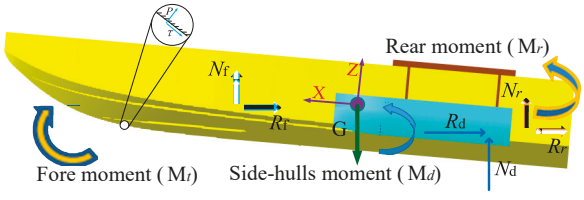

Figure 18. Forces and moment acted on the hull surface in the TFS.

When porpoising occurred, releasing the twin side-hulls into water caused them to acquire more lift and longitudinal moment M_d to the CG, which is equivalent to increasing the lift of hull bottom and the rear longitudinal moment M_r to the CG; thus, the higher trim angle was decreased (Figure 16a). A strong pressure area arises at the fore of the hull bottom, so the porpoising was inhibited, the detailed explanation is shown in Figure 20.

When porpoising occurs in the MFS and TFS, the pressure from stern to bow on the keel line was acquired by using probe technology; the results are summarized in Figure 21. For the MFS, the maximum pressure mainly concentrated near the CG; when the location ratio l/L_m exceeded 0.5, the pressure at the fore area reduced sharply, which led to porpoising. Conversely, for the TFS, most of the maximum pressure was located in the fore area (l/L_m

> 0.5), and the pressure at the CG and rear was relatively lower, which further explains the inhibition of the side-hulls on porpoising.

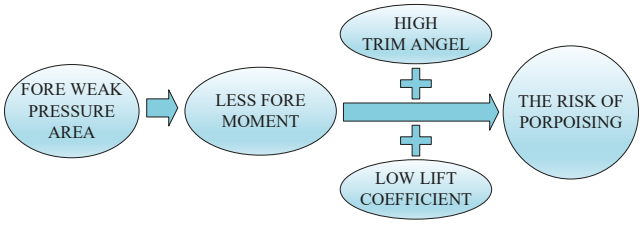

Figure 19. Why porpoising occurs.

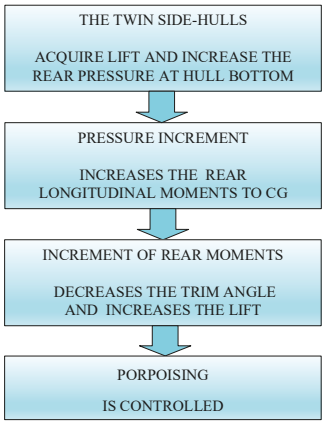

Figure 20. How side-hulls inhibit porpoising.

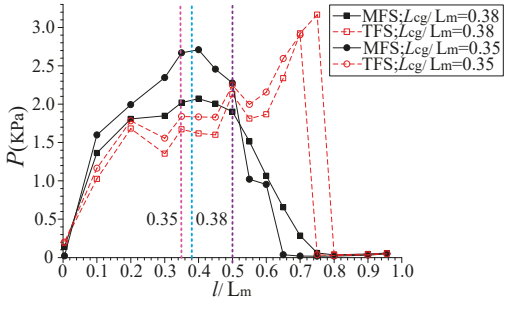

Figure 21. Pressure distribution from stern to bow on keel line in the MFS and TFS.

5.2. Influence of Side-Hulls on Sailing Attitudes and Hydrodynamic Performance at Different Speeds

In this section, adopting the same CFD setup and the whisker spray equation of Savitsky [27], computations for the initial designed TFS (Table 1) sailing at different speeds were carried out, and the influence of the side-hulls on sailing attitudes and hydrodynamic performance were analyzed. The dimensionless resistance ($C_T = R_T/\Delta$) and sailing attitudes at different speeds in the MFS and TFS when $L_{cg}/L_m = 0.38$ are shown in Figure 22.

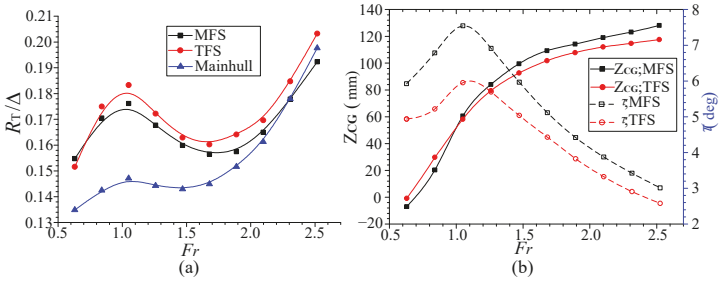

Figure 22. Change in total resistance and sailing attitudes with speed when L_{cg}/L_m = 0.38: (**a**) total resistance; (**b**) sinkage and trim angle.

Figure 22a shows that the R_T of the boat in the TFS was larger when crossing the resistance peak, and during the high-speed planing stage, the R_T in the TFS was relatively larger than that in the MFS at an equal speed, indicating releasing the side-hulls into the water could bring more resistance when porpoising. For the main hull resistance R_M in the TFS, the changing trend with increasing speed was similar to the MFS, and when $Fr > 1.89$, the R_M even surpassed its previous resistance peak value.

In addition, Figure 22b shows in any navigation stage, the trim angle in the TFS was smaller than that of the MFS at equal speeds, especially during the draining stage, the discrepancy was more obvious. The sinkage of TFS in the draining stage was larger compared with the MFS; however, during the planing stage, the sinkage of the MFS was relatively larger. This was mainly because most of the volume of the side-hulls was submerged into the water during the draining stage; the side-hulls could acquire more lift and lead to the further lifting of the CG. When entering the planing stage, the side-hulls were gradually lifted out of the water with increasing speed, as shown in Figure 23; the reduction of side-hulls immersion volume made them acquire less lift, which is mainly used to generate more rear moment to adjust the trim angle; only a fraction of the lift is used to raise the CG of craft.

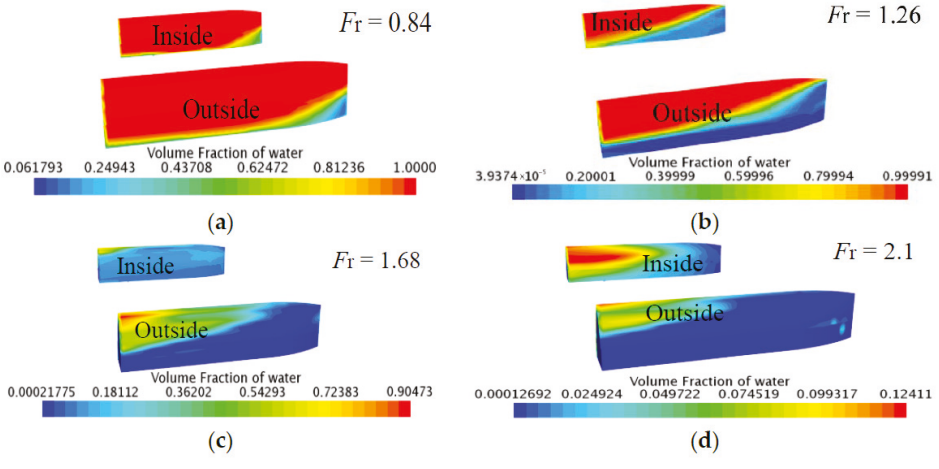

Figure 23. Volume fraction of water for the twin side-hulls at different speeds: (**a**) Fr = 0.84; (**b**) Fr = 1.26; (**c**) Fr = 1.68; (**d**) Fr = 2.1.

Figure 24a presents the change with speed of the side-hulls resistance (R_d) and the moment of side-hulls to the CG (M_d), which shows the R_d and M_d gradually increased with the increase of speed during the draining stage, but when entering the planing stage,

both the R_d and the M_d had a significant decline due to the reduction of the side-hulls immersion volume; but when $Fr > 1.89$ the M_d increased as speed further increased, indicating porpoising could be inhibited by the side-hulls.

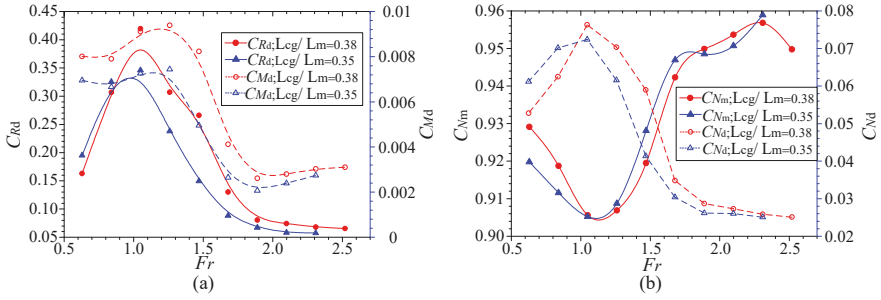

Figure 24. Forces and moment acted on the hull in the TFS at different speeds: (**a**) resistance and moment of the side-hulls; (**b**) lift of the side-hulls and the main hull.

Moreover, Figure 24b shows that the changing trend of the side-hulls lift (C_{Nd}) was consistent with that of the C_{Md}. For the main hull lift (C_{Nm}) in the TFS, with the increase of speed the C_{Nm} reduced during the draining stage; but when entering the planing stage, the C_{Nm} exhibited an obvious rise; when $Fr > 1.89$, the upward trend gradually slowed.

Figure 25 shows the free surface of the vessel in the TFS when porpoising; we observed that the main hull was lifted very high due to the strong hydrodynamic lift during the high-speed planing stage. At the same time, only the rear part of the side-hulls was slightly immersed in the water, so the interference influence on the side-hulls, caused by the ship traveling wave of the main hull, was lesser, the wave surface change mainly concentrated on the stern wake.

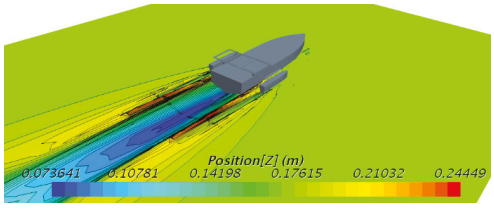

Figure 25. The free surface of the vessel in the TFS when porpoising.

Based on the attained Z_{cg} and τ values, the waterline surfaces (WS) of the two navigation states at different speeds were intercepted and compared utilizing the Creo software; the results are shown in Figure 26. As the speed increased, the root of the WS gradually moved backward to the stern, and the WS became sharper and longer; the area of WS also decreased, causing porpoising. However, the release of side-hulls delayed the backward movement of the root, lengthened the WS, and the stagnation points moved forward even far beyond the MFS, which further enhanced the longitudinal stability during high-speed navigation.

5.3. Influence of Longitudinal and Vertical Side-Hull Locations on Inhibiting Porpoising

The longitudinal and vertical locations of the side-hulls had a profound impact on porpoising instability. To simulate the location adjustments of twin side-hulls in the two directions, we chose the TFS, whose side-hulls were installed at $a_t = 0.23$ m, $b_t = 0.548$ m and $c_t = 0.07$ m (No. 3 in Table 8) as the basic research object.

5.3.1. Location Adjustments of the Twin Side-Hulls

Figure 27 shows the side-hulls adjustment mode of the longitudinal location. The ratio a/Lm was adjusted and the longitudinal location of side-hulls, the Lcg, and the longitudinal inertia tensor (I_{yt}) of the TFS were changed. Then, six different longitudinal locations of the side-hulls are designed and shown in Figure 28a, corresponding to the NOs. 1–6, as listed in Table 8. Besides, for condition two, the L_{cg} and I_{yt} of the TFS after adjustment was measured by utilizing the Creo software, presented in Table 8.

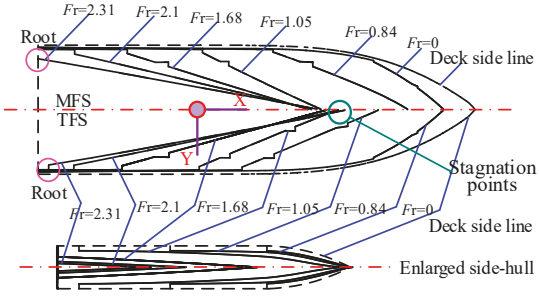

Figure 26. Waterline surface comparisons of the two navigation states when $L_{cg}/L_m = 0.35$.

Table 8. Six longitudinal locations of side-hulls in the TFS.

No.	Δ_t (kg)	Δ_d/Δ_t	*a* (m)	*b*/L_m	*a*/L_m	L_{cg} (m)	I_{yt} (kg·m^2)
1	137.3	0.047	−0.23	0.8	−0.1	0.864	53.079
2	137.3	0.047	0	0.8	0	0.873	50.979
3	137.3	0.047	0.23	0.8	0.1	0.882	49.430
4	137.3	0.047	0.46	0.8	0.2	0.891	48.612
5	137.3	0.047	0.69	0.8	0.3	0.901	48.362
6	137.3	0.047	0.92	0.8	0.4	0.910	48.735

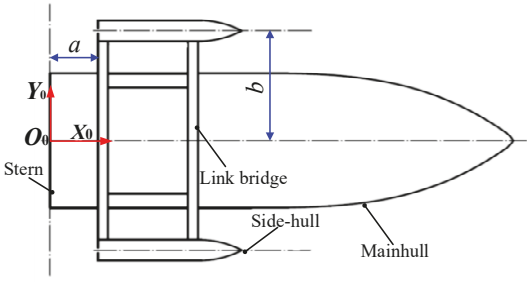

Figure 27. Longitudinal adjustment mode of the twin side-hulls.

Figure 29 shows the vertical adjustment mode of the twin side-hulls, in which the solid and dashed lines separately represent the two positions before and after adjustment, *d* represents the waterline position relative to the Base line (BL) of the main hull, *c* is the distance between main hull BL and demihull BL, Δ_{dh} represents the variation of BL position for the main hull before and after adjustment. Six different vertical locations of the side-hulls were obtained, shown in Figure 28b, corresponding to the six draft ratios D_d/T_m (NOs. 1–6) listed in Table 9, where S_m and S_d represent the waterline (WL) areas of the main hull and twin side-hulls, respectively.

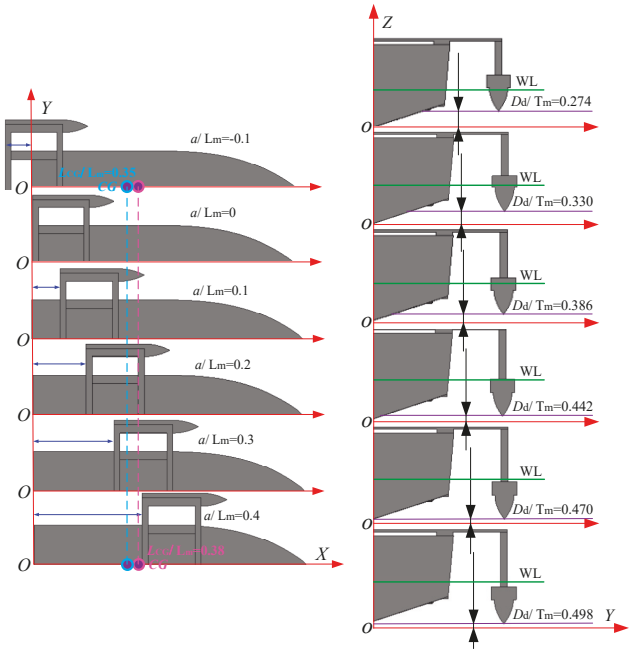

Figure 28. Different (**a**) longitudinal locations; (**b**) vertical locations of the side-hulls in the TFS.

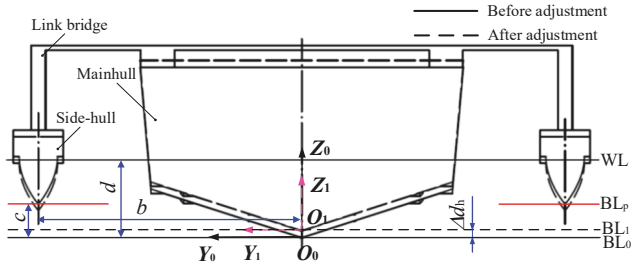

Figure 29. Vertical adjustment mode of the twin side-hulls.

Table 9. Six vertical locations of the side-hulls in the TFS.

No. Number	Δ_t (kg)	Δ_d/Δ_t	b/L_m	c (m)	D_d/T_m	D_m (m)	S_m (m^2)	S_d (m^2)	V_{cg} (m)	I_{yt} (kg·m^2)
1	137.3	0.047	0.8	0.07	0.274	0.168	1.251	0.051	0.2301	49.430
2	137.3	0.067	0.8	0.05	0.330	0.166	1.248	0.068	0.2292	49.441
3	137.3	0.086	0.8	0.03	0.386	0.164	1.246	0.068	0.2285	49.455
4	137.3	0.104	0.8	0.01	0.442	0.162	1.245	0.068	0.2277	49.473
5	137.3	0.113	0.8	0	0.470	0.161	1.244	0.068	0.2273	49.484
6	137.3	0.122	0.8	−0.01	0.498	0.160	1.243	0.068	0.2269	49.495

5.3.2. The Optimal Range of Side-Hull Locations on Porpoising Instability

To achieve the inhibition of porpoising at the cost of lower resistance, the R_T and τ in the TFS with different side-hulls longitudinal and vertical locations were computed, and the positive location ranges are presented in this section. Moreover, to evaluate the inhibition effect on porpoising, the dimensionless oscillation amplitude of trim angle ($C_\tau = |\tau-\tau_{av}|/\tau_{av}$) and

the average resistance ($C_{Ra} = R_{av}/\Delta$) were introduced. As shown in Figure 30, for the C_τ prescribing that when the side-hulls were at the optimal location ($C_\tau < 2\%$), the porpoising was completely inhibited; at the weak location ($2\% < C_\tau < 10\%$), the craft was regarded as achieving the stable navigation; at the unfit location ($C_\tau > 10\%$), porpoising occurred; for the C_{Ra} prescribing when $C_{Ra} < C_{Ra\_m}$ (R_{av_m}/Δ), the side-hulls were at the optimal location, here the R_{av_m} is the average resistance of the MFS when porpoising; when $C_{Ra\_m} < C_{Ra} < 1.5\ C_{Ra\_m}$ the craft suffered more navigation resistance; when $C_{Ra} > 1.5\ C_{Ra\_m}$, sailing forward in the TFS required too much thrust and was uneconomical.

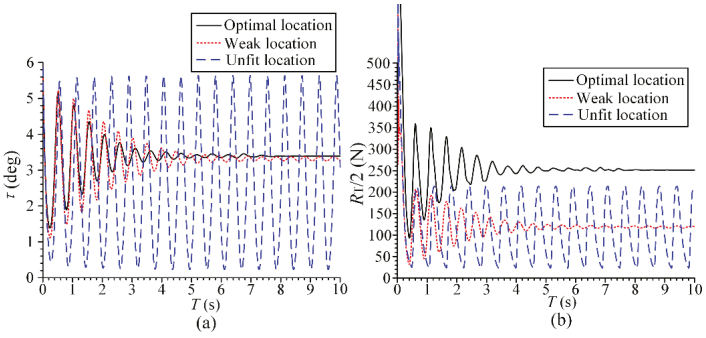

Figure 30. The optimal, weak, and unfit locations: (**a**) trim angle; (**b**) half total resistance.

According to the six longitudinal locations (Nos. 1–6 in Table 8) and the six vertical locations (Nos. 1–6 in Table 9) of side-hulls in the TFS, adopting the spatial sampling method of full factor design [40], simulations for the TFS with 36 different side-hull locations under condition two were performed, and the results are shown in Table 10.

Table 10. Influence of side-hull longitudinal and vertical locations on the inhibition of porpoising instability and total resistance.

Symbol		a/L_m											
		−0.1		0		0.1		0.2		0.3		0.4	
D_d/T_m	0.274	✓	✓	○	✓	✓	✓	○	✓	✓	✓	⊘	✓
	0.330	○	○	✓	○	○	○	✓	✓	○	✓	○	✓
	0.386	✓	○	✓	○	○	○	✓	○	○	○	○	✓
	0.442	✓	⊘	✓	⊘	✓	○	○	○	⊘	○	⊘	○
	0.470	✓	⊘	✓	⊘	✓	⊘	○	○	⊘	○	⊘	○
	0.498	✓	⊘	✓	⊘	✓	⊘	○	○	⊘	○	⊘	○
												$C\tau$	C_{Ra}

Condition two ○ Weak location ✓ Optional location ⊘ Unfit location

Table 10 shows with the backward movement of side-hulls, the probability that porpoising could be entirely suppressed increased. However, when the side-hulls were too backward ($a/L_m = -0.1$–0.1), along with an increasing draft, the average resistance R_{av} also increased, and when draft ratio D_d/T_m exceeded 0.442, the craft frequently suffered too much resistance, which inversely consumes more thrust. In addition, when side-hulls were relatively forward ($a/L_m = 0.2$–0.4) and the draft ratio exceeded 0.442, the probability that porpoising would occur, increased significantly. The more forward location ($a/L_m = 0.4$) is not recommended owing to the significant risk of porpoising. Considering the C_τ and C_{Ra}, the draft of the side-hulls is not recommended to exceed the ratio (D_d/T_m) of 0.442.

Summing up the above, the positive range of the side-hull location was $-0.1 \leq a/L_m \leq 0.3$ and $0.274 \leq D_d/T_m \leq 0.386$. As shown in Figure 31, in the preferred area, the craft could bear slightly more resistance and sail stably, while in the optimal area, porpoising was suppressed, and the boat could sail in the sea with lesser resistance.

Figure 32a shows that side-hulls being placed relatively forward ($a/L_m = 0.4$) was not conducive to inhibiting porpoising. For the side-hulls, when backward relative to the CG of the main hull, the deeper the draft in the vertical direction, and the greater the total resistance (Figure 32b), then the side-hulls resistance and the ratio of R_d to R_T also increased when porpoising.

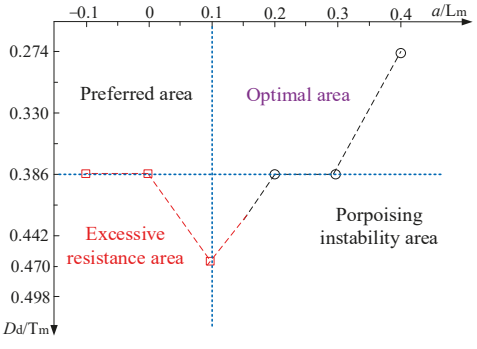

Figure 31. Optimization of longitudinal and vertical side-hull locations on porpoising instability inhibition and resistance reduction.

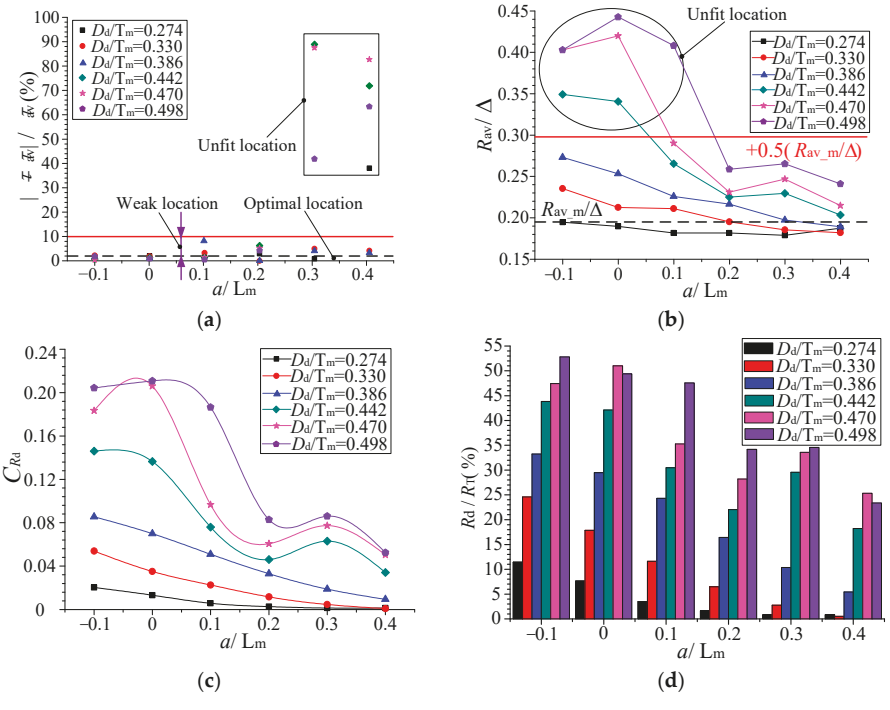

Figure 32. *Cont.*

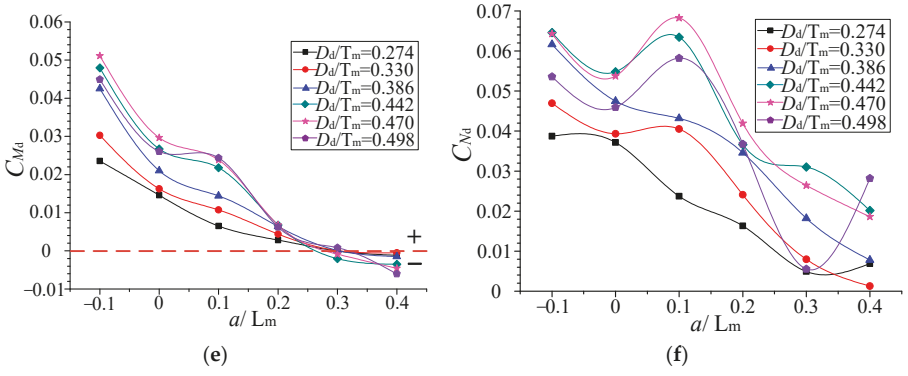

Figure 32. Influence of the longitudinal and vertical side-hull locations on (**a**) C_τ, (**b**) C_{Ra}, (**c**) C_{Rd}, (**d**) R_d/R_T, (**e**) C_{Md}, and (**f**) C_{Nd}.

Figure 32e shows that when $a/L_m > 0.3$, the C_{Md} becomes negative, porpoising occurs at the unfit location (Figure 32a); as the side-hulls move backward, there was an obvious increase in C_{Md}, which further proves the previous analysis.

Figure 32f shows the more backward locations of the side-hulls relative to the CG of the main hull was more conducive to the increase of the side-hulls lift due to the planing attitudes; however, the influence of the side-hull draft on its lift was somewhat messy.

5.4. Inhibition of the Side-Hulls on the Porpoising of Real Ship with Scale Effect

To determine the impact at the scale of a real ship (RS) of the side-hulls being located in the positive range on restraining porpoising with a lesser resistance cost, the RS model (scaling $\lambda = 2.5$) in the MFS and TFS (cases 1–4 in Table 11) when porpoising were simulated, and the total resistance R_T, effective power P_w curves with speed increasing of the RS were also offered in this section.

Table 11. The main geometric parameters of the real-scale MFS and cases 1–4 under condition two.

Cases	Δ_t (kg)	a/L_m	b/B_m	D_d/T_m	L_{cg} (m)	V_{cg} (m)	I_{yt} (kg·m^2)
MFS	2200	0.1	0.8	0	2.205	0.521	4827
Case 1	2200	0	0.8	0.330	2.183	0.573	4978
Case 2	2200	0.1	0.8	0.274	2.205	0.575	4827
Case 3	2200	0.2	0.8	0.330	2.228	0.573	4747
Case 4	2200	0.3	0.8	0.274	2.253	0.575	4723

Considering higher solution cost caused by enlarged computational domain and the model, the grid parameters in Section 4.1 were enlarged in proportion to the λ, and boundary layer grids were further refined to ensure the consistency of $y+$ on the hull surface. Then, as in the previous CFD setup, computations for the MFS and cases 1-4 were completed.

The oscillation comparisons of τ and Z_{cg} are shown in Figure 33, further processing the results, the dimensionless oscillation amplitudes of trim angle and sinkage ($C_Z = |Z_{cg} - Z_{av}|/Z_{av}$) were attained, and based on the acquired τ_{av}, τ (maximum), and the whisker spray equation of Savitsky [27], the total resistance (R_{av}) including R_S, the maximum resistance (R_{am}) and the percentage of resistance increment ($PRI = (R_{av} - R_{av\_m})/R_{av\_m}\%$) on releasing side-hulls when porpoising were solved and listed in Table 12.

Figure 33 shows that on the scale of a real ship, releasing the side-hulls in the positive range could significantly reduce the pitch and heave oscillation when porpoising, and the oscillation amplitudes of the more forward side-hulls placement (case 4) were larger compared with cases 1–3. Table 12 further shows the more backward side-hulls placement brought a greater resistance increment, especially for case 1, the *PRI* attained was 27.04%,

so to avoid increasing too much resistance of RS, longitudinally, it is recommended not to have a ratio less than $a/L_m = 0.1$.

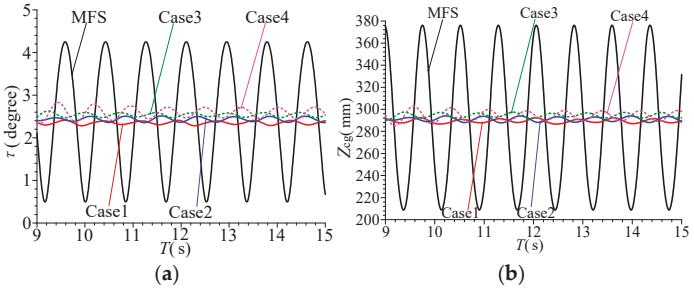

Figure 33. Oscillation comparisons of (**a**) τ and (**b**) Z_{cg} when porpoising under condition 2.

Table 12. The comparisons of the dimensionless oscillation amplitude of trim angle ($C\tau$), dimensionless oscillation amplitudes of sinkage (C_Z), total average resistance (R_{av}), maximum resistance (R_{am}), and percentage of resistance increment (*PRI*) under condition two.

Cases	C_τ	C_Z	R_{av} (N)	*PRI* (%)	R_{am} (N)
MFS	0.790	0.273	4288	0	4529
Case 1	0.022	0.008	5078	18.43	5169
Case 2	0.025	0.011	4369	1.89	4460
Case 3	0.024	0.009	4450	3.78	4515
Case 4	0.045	0.015	4203	−1.97	4310

In addition, through the deliberation to C_τ, $R_{av,}$ and R_{am} in Table 12, case 2 was chosen as the better side-hulls placement. And utilizing the verified CFD method and the whisker spray equation of Savitsky [27], R_T and P_W of the RS in the MFS and TFS (cases 2) at different speeds were computed, the R_T and P_W curves with speed increasing under conditions two and three, are shown in Figure 34, which can provide a sufficient reference for the overall design of planing boats with this concept.

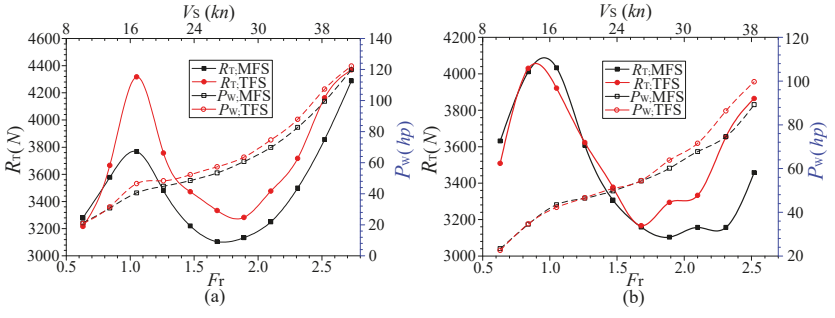

Figure 34. The R_T, power (P_W) curves of the real ship in the MFS and TFS under (**a**) condition two, (**b**) condition 3.

6. Conclusions

In this study, the hydrodynamics of twin side-hulls and their inhibiting effect on the porpoising of planing boats were analyzed. Based on the CFD method, the whisker spray equation of Savitsky [27], and the test, a comparative analysis was conducted on the hydrodynamic performance of the vessel in the MFS and TFS. The optimal location range of the side-hulls for porpoising inhibition and lesser resistance was also provided.

The CFD setup can accurately forecast the sailing attitudes of the model during the planing regime, but the forecastability of the total resistance during the high-speed planing stage was weaker. The application of the whisker spray equation of Savitsky [27] allowed the deviations of amendatory resistance to be controlled within 7%, which indicates the calculation method utilized in this research could effectively forecast the total resistance, including spray resistance and sailing attitude of the vessel during the high-speed planing stage.

The weak pressure area at the fore of hull bottom in the MFS causes the fore moment to be lesser than the rear moment, coupled with the existence of high trim angle and the low lift coefficient, porpoising occurs. Releasing the side-hulls in the water increased the total lift of the hull bottom and the rear longitudinal moment; thus, the high trim angle could be decreased, and a strong pressure area at the fore inhibited porpoising instability.

The comparisons of the MFS and TFS show that releasing the side-hulls into the water was conducive to inhibiting porpoising, but sailing in the TFS yields more navigation resistance when crossing the resistance peak and during the high-speed planing stage. In addition, at any stage, the trim angle of TFS was smaller compared with the MFS at equal speeds, and the sinkage of the TFS in the draining stage was larger, but during the planing stage, that of the MFS is relatively larger.

Side-hull longitudinal locations exceeding the ratio of $a/\mathrm{Lm} = 0.3$ are not recommended, and vertically, the draft ratio ($D_\mathrm{d}/\mathrm{T_m}$) is suggested not to exceed 0.442. The positive range of side-hull locations is $-0.1 \leq a/\mathrm{L_m} \leq 0.3$ and $0.274 \leq D_\mathrm{d}/\mathrm{T_m} \leq 0.386$, and in the optimal area, porpoising could be suppressed; the boat can also then sail with lesser resistance. In addition, at the scale of a real ship, longitudinally, the side-hull locations are recommended not to be less than the ratio $a/\mathrm{L_m} = 0.1$ to avoid increasing resistance.

Author Contributions: Conceptualization, Y.S. and J.W.; methodology, J.W.; software, J.W. and X.B.; validation, X.B., J.W. and Y.S.; formal analysis, J.W.; investigation, J.W.; resources, J.Z.; data curation, X.B.; writing—original draft preparation, J.W.; writing—review and editing, J.W. and J.Z.; visualization, J.Z.; supervision, Y.S.; project administration, Y.S.; funding acquisition, J.Z. All authors have read and agreed to the published version of the manuscript.

Funding: The research reported here was supported by the National Natural Science Foundation of China (Grant No. 52071100). The authors would like to express their gratitude to all the test participants for their suggestions and observations that helped in improving the present research.

Data Availability Statement: Data is contained within the article.

Conflicts of Interest: The authors declare no conflict of interest.

References

1. Yasin, M.; Amir, H.N. Drag Optimization of a planing vessel based on the stability criteria limits. *China Ocean Eng.* **2019**, *33*, 365–372.
2. Yasin, M.; Amir, H.N. Comparison of numerical solution and semi-empirical formulas to predict the effects of important design parameters on porpoising region of a planing vessel. *Appl. Ocean Res.* **2017**, *68*, 228–236.
3. Shuo, W.; Yumin, S.; Yongjie, P.; Huanxing, L. Numerical study on longitudinal motions of a high speed planing craft in regular waves. *J. Harbin Eng. Univ.* **2014**, *35*, 45–52.
4. Clement, E.P.; Blount, D. Resistance tests of systematic series of planing hull forms. *Trans. Soc. Nav. Archit. Mar. Eng.* **1963**, *71*, 491–561.
5. Blount, D.L.; Codega, L.T. Dynamic stability of planing boats. *Mar. Technol.* **1992**, *29*, 4–12.
6. Katayama, T.; Teshima, A.; Ikeda, Y. A Study on transverse proposing of a planning craft in drifting motion. *J. Mar. Sci. Appl.* **2001**, *236*, 181–190.
7. Payam, L.; Mahmud, A.; Reza, K.E. Numerical investigation of a stepped planning hull in calm water. *Ocean Eng.* **2015**, *94*, 103–110.
8. Reza, K.E.; Mohammad, A.R.; Sajad, H. Hydrodynamic evaluation of a planing hull in calm water using RANS and Savitsky's method. *Ocean Eng.* **2019**, *187*, 106–221.
9. Savitsky, D. Chapter IV planning craft of modern ships and craft. *Naval Eng.* **1985**. Special Edition.
10. Najafi, A.; Siamak, A.; Mohammad, S.S. RANS simulation of interceptor effect on hydrodynamic coefficients of longitudinal equations of motion of planing catamarans. *J. Braz. Soc. Mech. Sci. Eng.* **2015**, *37*, 1257–1275. [CrossRef]

11. Jokara, H.; Zeinali, H.; Tamaddondar, M.H. Planing craft inhibition using pneumatically driven trim tab. *Math. Comput. Simul.* **2020**, *178*, 439–463. [CrossRef]
12. Sayyed, M.S.; Parviz, G. Experimental and numerical analyses of wedge effects on the rooster tail and porpoising phenomenon of a high-speed planing craft in calm water. *J. Mech. Eng. Sci.* **2019**, *233*, 4637–4652.
13. Mehran, M.; Antonio, C.F. The interceptor hydrodynamic analysis for inhibition the porpoising instability in high speed crafts. *Appl. Ocean Res.* **2016**, *57*, 40–51.
14. Mansoori, M.; Fernandes, A.C.; Ghassemi, H. Interceptor design for optimum trim inhibition and minimum resistance of planing boats. *Appl. Ocean Res.* **2017**, *69*, 100–115. [CrossRef]
15. Mansoori, M.; Fernandes, A.C. Interceptor and trim tab combination to prevent interceptor's unfit effects. *Ocean Eng.* **2017**, *134*, 140–156. [CrossRef]
16. Ahmet, G.A.; Baris, B. An experimental investigation of interceptors for a high speed hull. *Int. J. Nav. Archit. Ocean Eng.* **2019**, *11*, 256–273.
17. Hongjie, L.; Zhidong, W. Real-time numerical prediction method of dolphin motion in high-speed planing crafts. *J. Shanghai Jiaotong Univ.* **2014**, *48*, 106–110.
18. Hanbing, S.; Yumin, S.; Jin, Z.; Kexin, Z.; Jiayuan, Z. Longitudinal navigation performance test of high-speed unmanned boat. *J. Shanghai Jiaotong Univ.* **2013**, *47*, 278–283.
19. Katayama, T.; Yoshiho, I. Hydrodynamic forces acting on porpoising craft at high speed. *J. Ship Ocean Tech.* **1999**, *3*, 17–26.
20. Katayama, T.; Fujimoto, M.; Ikeda, Y. A study on transverse stability loss of planning craft at super high forward speed. *Int. Shipbuilding Pro.* **2007**, *54*, 365–377.
21. Sasan, T.; Abbas, D. Mathematical simulation of planar motion mechanism test for planing hulls by using 2D+T theory. *Ocean Eng.* **2018**, *169*, 651–672.
22. Parviz, G.; Sasan, T.; Abbas, D.; Zamanian, R. Steady performance prediction of a heeled planing boat in calm water using asymmetric 2D+T model. *J. Eng. Mar. Environ.* **2017**, *231*, 234–257.
23. Parviz, G.; Sasan, T.; Abbas, D. Coupled heave and pitch motions of planing hulls at non-zero heel angle. *Appl. Ocean Res.* **2016**, *59*, 286–303.
24. Shuo, W.; Yumin, S.; Zhaoli, W.; Xuguang, Z.; Huanxing, L. Numerical and experimental analyses of transverse static stability loss of planing craft sailing at high forward speed. *Eng. App. Comput. Fluid Mech.* **2014**, *8*, 44–54.
25. Abbas, D.; Sasan, T.; Ahmadreza, K.; Khosravani, R. Numerical study on a heeled one-stepped boat moving forward in planing regime. *Appl. Ocean Res.* **2020**, *96*, 102–117.
26. Yi, J. Hybrid Hydro-Aerodynamic Characteristics Investigation on High-Speed Planing Hull under the Coupling Effect of Step and Tunnel. Doctoral Thesis, Harbin Engineering University, Harbin, China, 2018.
27. Savitsky, D.; Delorme, M.F.; Datla, R. Inclusion of whisker spray drag in performance prediction method for high-speed planing hulls. *Mar. Technol.* **2007**, *44*, 35–56.
28. Yi, J.; Hanbing, S.; Jin, Z.; Ankang, H.; Jinglei, Y. Experimental and numerical investigations on hydrodynamic and aerodynamic characteristics of the tunnel of planning trimaran. *Appl. Ocean Res.* **2017**, *63*, 1–10.
29. Florian, R.; Menter, P. Improved two-equation turbulence models for aerodynamic flows. *NASA Tech. Memo.* **1992**, *103*, 103975.
30. Mireille, B.F.; Carlos, F.L.; Arman, H.; Fleck, B.A. Performance of turbulence models in simulating wind loads on photovoltaics modules. *Energies* **2019**, *12*, 3290.
31. Menter, F.R. Two-equation eddy-viscosity turbulence models for engineering applications. *AIAA* **1994**, *32*, 1598–1605. [CrossRef]
32. Ghasemi, E.; Mceligot, D.M.; Nolan, K.P.; Crepeau, J.; Siahpush, A.; Budwig, R.S.; Tokuhiro, A. Effects of adverse and favorable pressure gradients on entropy generation in a transitional boundary layer region under the influence of free stream turbulence. *Int. J. Heat Mass Transfer.* **2014**, *77*, 475–488. [CrossRef]
33. Shuo, W.; Yumin, S.; Yongjie, P.; Xi, Z. Study on the accuracy in the hydrodynamic prediction of high-speed planing crafts of CFD method. *J. Ship Mech.* **2013**, *17*, 1107–1114.
34. Hirt, C.W.; Nichols, B.D. Volume of Fluid (VOF) method for the dynamics of free boundary. *J. Comput. Phys.* **1981**, *39*, 201–225. [CrossRef]
35. Scardovelli, R.; Zaleski, S. Direct numerical simulation of free-surface and interfacial flow. *Annu. Rev. Fluid Mech.* **1999**, *31*, 567–603. [CrossRef]
36. Xiaosheng, B.; Hailong, S.; Jin, Z.; Yumin, S. Numerical analysis of the influence of fixed hydrofoil installation position on seakeeping of the planing craft. *Appl. Ocean Res.* **2019**, *90*, 101863.
37. Xiaosheng, B.; Jiayuan, Z.; Yumin, S. Seakeeping Analysis of Planing Craft under Large Wave Height. *Water Res.* **2020**, *12*, 1020. [CrossRef]
38. Yumin, S.; Jianfeng, L.; Dagang, Z.; Chao, W.; Chunyu, G. Review of numerical simulation methods for full-scale ship resistance and propulsion performance. *Shipbuild. China* **2020**, *61*, 229–239.
39. Wang, F. *Book Computational Fluid Dynamics Analysis-Theory and Application of CFD Software*; Tsinghua University Press: Beijing, China, 2005; pp. 23–49.
40. Guay, M. Uncertainty estimation in extremum seeking inhibition of unknown static maps. *IEEE Inhib. Syst. Lett.* **2021**, *5*, 1115–1120.

Journal of *Marine Science and Engineering*

MDPI

Article

Verification and Validation of CFD Based Form Factors as a Combined CFD/EFD Method

Kadir Burak Korkmaz [1,2,*], Sofia Werner [1] and Rickard Bensow [2]

[1] SSPA SWEDEN AB, Chalmers Tvärgata 10, Box 24001, SE 400 22 Göteborg, Sweden; sofia.werner@sspa.se
[2] Department of Mechanics and Maritime Sciences, Chalmers University of Technology, SE 412 96 Göteborg, Sweden; rickard.bensow@chalmers.se
* Correspondence: burak.korkmaz@sspa.se

Abstract: Predicting the propulsive power of ships with high accuracy still remains a challenge. Well established practices in the 1978 ITTC Power Prediction method have been questioned such as the form factor approach and its determination method. This paper investigates the possibility to improve the power predictions by the introduction of a combined CFD/EFD Method where the experimental determination of form factor is replaced by double body RANS computations. Following the Quality Assurance Procedure proposed by ITTC, a best practice guideline has been derived for the CFD based form factor determination method by applying systematic variations to the CFD set-ups. Following the verification and validation of the CFD based form factor method in model scale, the full scale speed-power-rpm relations between large number of speed trials and full scale predictions using the CFD based form factors in combination with ITTC-57 line and numerical friction lines are investigated. It is observed that the usage of CFD based form factors improves the predictions in general and no deterioration is noted within the limits of this study. Therefore, the combination of EFD and CFD is expected to provide immediate improvements to the 1978 ITTC Performance Prediction Method.

Keywords: ship resistance; form factor; best practice guidelines; numerical friction line; combined CFD/EFD methods

Citation: Korkmaz, K.B.; Werner, S.; Bensow, R. Verification and Validation of CFD Based Form Factors as a Combined CFD/EFD Method. *J. Mar. Sci. Eng.* **2021**, *9*, 75. https://doi.org/10.3390/jmse9010075

Received: 27 December 2020
Accepted: 8 January 2021
Published: 13 January 2021

1. Introduction

During the design process of ships, power predictions are of utmost importance because the speed attained at a certain power consumption in a trial run, so called the contract speed, is specified at the contract of a new ship order. If the speed does not meet the specifications, the yard is forced to pay a penalty depending on the terms in the contract. Therefore, designers are under a pressure of being just in the limits. The dilemma for the designer and the yard as stated by Larsson and Raven [1] is that too optimistic predictions might end up in a big burden for the yard while too conservative predictions will be a lost order. In addition to increasing competitiveness of the market, legal authorities have also been taking steps towards further improvement of the energy efficiency of ships due to environmental concerns IMO [2]. Therefore, the importance of the power predictions and the required accuracy are increasing ever more.

The towing tank testing and extrapolation procedures have been used for more than a century to predict the performance of a ship in deep and calm water. The efforts to standardize and improve the early towing tank testing and extrapolation practices resulted in the foundation of the International Towing Tank Committee (ITTC) in 1933. The extrapolation of full scale ship resistance evolved in time, starting from a rather simple William Froude's method and going through several major revisions: adoption of using both Froude and Schoenherr lines in ITTC [3]; adoption of ITTC 1957 model to ship correlation lines [4]; recommendation of the Prohaska method [5] following the introduction of the form factor concept of Hughes [6]; adoption of the Bowden and Davison [7] formula in ITTC [8]; and

confirmation and integration of the previous concepts and formulas [4–7] via comparison of approximately one thousand sea trials to model test predictions in the formulation of the ITTC 1978 Power Prediction Method [9]. The roughness allowance was updated by replacing the previous formulation with Townsin and Dey [10] and introducing a new correlation allowance formulation in the ITTC Report of Power Performance Committee [11], and the calculation of air resistance was modified in the Revision 03 of the 1978 ITTC Performance Prediction Method [12]. The extrapolation procedures and towing tank tests are still considered as the last step of the performance prediction considering the current commercial tendencies and the evaluations such as EEDI calculations as enforced by IMO [2] where the applicable ships must go through the pre-verification by model testing during the design phase of a new ship.

Even though towing tank testing and extrapolation methods have been improved over many decades, there are inherent and well known shortcomings mainly because the Froude and Reynolds similarities cannot be fulfilled simultaneously, i.e., scale effects. Therefore, towing tank facilities must rely on experience obtained from large databases of model tests and sea trials. Computational fluid dynamics (CFD), however, can handle these scale effects and have been under development for more than a century as the advent of computational hydrodynamics dates back to 1898 by the work of Michell [13]. However, it was in 1980s when the "numerical methods to started to become really useful in ship design" Larsson [14] (p. 2). The development of the Reynolds Averaged Navier–Stokes (RANS) methods have been evaluated since 1980 [15] and the verification and validation (V&V) of CFD methods in model scale is now a well established practice. According to the statistics presented in Hino et al. [16], the mean absolute comparison error of JBC is around 2% for the towed cases (resistance) and 3% for the self-propulsion, while the standard deviation is approximately 2% and 4%, respectively. It is noticeable that no further reductions neither in comparison error nor in scatter were obtained at the 2015 Workshop [16] compared to the 2010 Workshop [15]. Unlike in model scale, the accuracy of CFD on prediction of full scale performance is still under concern mainly due to scarcity of the full scale validation data in the literature and limited CFD studies. Recently, studies presented by Sun et al. [17] and Niklas and Pruszko [18] showed that full scale simulations can predict the power similar to or better than the towing tank tests. On the other hand, the results of Lloyd's Register workshop on ship scale hydrodynamics [19] indicated that differences between the numerical setups can lead to very diverse predictions on both power and propeller turning rate.

Instead of choosing between towing tank testing (EFD) and computational hydrodynamics (CFD), a combination of the two methods can be a feasible solution to increase the accuracy of the power predictions. As identified by the ITTC Specialist Committee on the Combined CFD/EFD Methods, if a part of the model testing or extrapolation procedure causes higher uncertainty than the numerical uncertainty and modeling errors of the CFD applications, the accuracy is expected to increase. In the 1978 ITTC Performance Prediction method [20], the form factor approach is identified as a major uncertainty source due to its determination method, i.e., the Prohaska Method [5], and the scale effects when the ITTC-57 model to ship correlation line is used [21–28]. The study performed by Wang et al. [29] showed that when the Prohaska Method is replaced by CFD based form factors in the ITTC-78 Power Prediction Method, the sea trials correlated better for a ship. As it is the case for the direct full scale CFD predictions, the CFD/EFD combined methods were applied to only a limited number of cases. Therefore, this paper aims to address this issue by investigating the verification and validation of the CFD based form factor approach in model scale and by comparing large number predictions using combined CFD/EFD methods to sea trials.

Verification and validation of CFD codes and methods are essential measures not only for the improvement of the CFD methods, but also the quality assurance of the CFD applications. It requires significant computational resources and validation data with an experimental uncertainty at hand. Since the derived uncertainty levels are only valid for a

unique case and condition, each test case should be subjected to V&V studies in order to ensure the quality of the CFD application. However, thorough verification studies cannot be performed for each commercial application for practical reasons and experimental uncertainty analysis is not available in advance. This raises the question on whether a V&V result is valid for a similar case and also if it is required to be done only once. Therefore, a practical procedure is needed for the organizations that regularly perform CFD predictions for similar cases. To respond to this need, two ITTC committees jointly proposed a new procedure for the quality assurance comprised of the following parts: (1) requirement of an organization's Best Practice Guideline (BPG), (2) Quality Assessment (QA) of the BPG methodology, and (3) demonstration of quality. This paper will follow the proposed Quality Assurance Recommended Procedures when demonstrating the application of the CFD based form factors. For the first time in the literature, the practicality and usefulness of the proposed QA procedure will be tested for the quality assurance of CFD based form factor method and are presented in the following steps:

1. Detailed explanation of the flow solver, numerical methods, boundary conditions, grid generation, and computational conditions are presented in Section 3 and the derivation of the BPG for the SHIPFLOW code by systematically varying the CFD set-up such as grid dependence studies in Section 5.1, y^+ in Section 5.1.1, additional grid refinements in Section 5.1.2, domain size in Section 5.1.3, model scale speed in Section 5.1.4, and turbulence models in Section 5.1.5.
2. Verification and validation of the CFD based form factors of six test cases in model scale is presented in Section 5.1.6.
3. Comparison of up to 78 sea trials to the predictions made by combined CFD/EFD methods is presented in Section 6.

Through these steps, the following research questions are aimed to be answered by this study:

- Can the proposed quality assurance procedure be used to to ensure the predicted form factors are suitable for full scale predictions?
- Can CFD based form factors introduce immediate improvements to the existing ITTC-78 method?
- Can there be further improvements to the full scale predictions by further modification of ITTC-78 method such as the change of the friction line in combination with CFD based form factors?

2. Extrapolation of Model Tests to Full Scale

In this study, the procedure recommended by ITTC [20] is used to extrapolate the towing tank test results to full scale. According to the 1978 ITTC Performance Prediction Method [20], the resistance of the full scale ship is calculated as

$$C_T = (1+k)C_{FS} + \Delta C_F + C_A + C_R + C_{AAS}, \quad (1)$$

where k is the form factor, C_{FS} is the frictional resistance coefficient in full scale (the subscript 'S' signifies the full scale ship), C_R is the residual resistance coefficient, ΔC_F represents the roughness allowance, C_A is the correlation allowance, and C_{AAS} is the air resistance coefficient.

According to the recommended procedure [20], the form factor is obtained by the Prohaska method [5] in model scale. The residual resistance, which is assumed to be the same in model and full scale, is then obtained as

$$C_R = C_{TM} - (1+k)C_{FM}, \quad (2)$$

where C_{TM} is the total resistance coefficient (the subscript 'M' signifies the model). C_{TM} is measured at each speed in the towing tank, and C_{FM} is obtained from the friction lines. In the study, two form factors were obtained from the Prohaska method and CFD based

form factor determination methods. The latter method follows the assumptions of [6] and is derived using the relation:

$$(1+k) = \frac{C_F + C_{PV}}{C_{FM}} = \frac{C_V}{C_{FM}}, \quad (3)$$

where the frictional resistance coefficient (C_F) and viscous pressure coefficient (C_{PV}) are obtained by the double body CFD simulation. C_{FM} in the denominator of Equation (3) is the equivalent flat plate resistance in two-dimensional flow obtained from the same Reynolds number as the computations. When the CFD based form factor determination is used, C_{FM} in Equation (3), C_{FM} in Equation (2) and C_{FS} in Equation (1) are derived from the same friction line.

The frictional resistance coefficients of the ship, C_{FM} and C_{FS}, are obtained by using three different friction lines: the ITTC-57 model-ship correlation line [4], and two numerical friction lines for EASM and $k-\omega$ SST turbulence models, respectively, proposed by Korkmaz et al. [30].

Correlation factors for the extrapolation were separated from the roughness allowance by ITTC [11] and the formulation of Bowden and Davison [7] is replaced by Townsin and Dey [10]. The correlation allowance recommended by the 19th ITTC is

$$C_A \approx (\Delta C_F)_{Bowden} - (\Delta C_F)_{Townsin} = 5.68 - 0.6\log(Re) \times 10^{-3}, \quad (4)$$

where $(\Delta C_F)_{Bowden}$ is the roughness allowance proposed by Bowden and Davison [7], and $(\Delta C_F)_{Townsin}$ [10] is the recommended roughness allowance in the present recommended procedures [20]. Note that, if the recommended C_A in Equation (4) is used for the extrapolation, summation of $(\Delta C_F)_{Townsin}$ and C_A is essentially the same as using the old formulation of roughness allowance proposed by Bowden and Davison [7], i.e., the original 1978 ITTC method. As an option, it was recommended in the ITTC Report of Power Performance Committee [11] that each institution maintains their own C_A formulations. However, a certain reluctance can be expected from towing tanks to change the C_A value since it would require a substantial amount of work and risk-taking to derive new model-full scale correlations that are derived from a consistent model testing and extrapolation practices. Therefore, in the context of this study, C_A used for the extrapolations is the recommended correlation factor in Equation (4). As explained in Section 6, C_A is omitted in calculation of the full scale resistance when the numerical friction lines are used as $(\Delta C_F)_{Bowden}$ "is suitable when extrapolating resistance using the 1957 ITTC line on a form factor basis..." Bowden and Davison [7].

For the cases when a flow separation is observed in model scale CFD computations, an additional computation has been performed also in full scale. The extrapolation method is slightly altered to mitigate the adverse effect of the flow separation which causes an overestimation of the full scale viscous resistance. In the altered method, the residual resistance is obtained by using the model scale form factor as in Equation 2, but the viscous resistance of the full scale ship ($(1+k) \times C_{FS}$) is calculated by the form factor obtained from the full scale double body computations.

3. Flow Solver, Grid Generation, Computational Domain, and Boundary Conditions

The XCHAP module of SHIPFLOW 6.5 is used for solving the steady state viscous flow [31]. Reynolds Averaged Navier–Stokes (RANS) equations are solved with a finite volume method. The first order accurate Roe scheme is used for discretization of the convective terms and a flux correction is applied explicitly in order to increase the order of accuracy. The equations are solved with a Krylov solver (adopted from PETSc) which implements the Generalized Minimal Residual method (KSPGMRES). Two turbulence models are available in XCHAP solver: EASM as described by Deng and Visonneau [32] and $k-\omega$ SST as described by Menter [33]. Both turbulence models are used in this study.

The viscous flow solver XCHAP can only handle structured grids, which can be in H-H, H-O, or O-O topologies. Although it is possible to import external grids to the

solver, the grid generator of SHIPFLOW, XGRID, is used for the study. The coarsest body fitted grid used for the study is presented in Figure 1. The parametrized nature of grid generation with XGRID ensures almost identical grid distribution in the longitudinal and circumferential directions for the most conventional hulls simulated. However, the grid distribution in the normal direction to the hull varies between different hulls as the *Re* differs; therefore, different first cell sizes in the normal direction to the wall and cell growth ratios are obtained to achieve (nearly) the same y^+ values. The overlapping grid technique is used to model the flow around the rudders [34] and to apply refinement on the single block of structured grid. As can be seen in Figure 1b, a refinement is applied to the region within the black line boundaries. The refinement does not improve the geometry resolution but only divides the existing cells into two or more pieces in desired directions [31]. In this study, the refinements are applied in all directions and the cells are divided in two. All simulations in this study were performed as double body computations with rudders that are integrated into the flow domain with an overlapping grid technique as seen in Figure 1b.

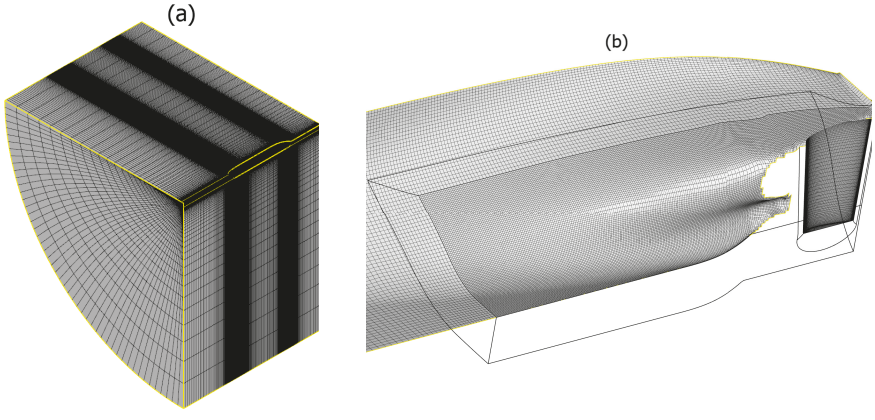

Figure 1. (**a**) Grid distribution of the coarsest grid, (**b**) grid refinement at the stern and the rudder as overlapping grids.

The computational domain is shaped as a quarter of a cylinder that consists of six boundaries where the center plane of the ship is set as the symmetry boundary condition. By default, the distance between inlet and fore-perpendicular (FP) is $0.5L_{PP}$, outlet plane is located at $0.8L_{PP}$ behind the aft-perpendicular, and the radius of the cylindrical outer boundary is $3L_{PP}$.

Two boundary conditions are used: Dirichlet and Neumann conditions. Boundary types employed in XCHAP are noslip, slip, inflow, outflow, and interior. Inlet boundary condition sets a fixed uniform velocity (U_∞), the estimated turbulent quantities and a zero pressure gradient normal to the inlet boundary. The turbulent quantities, specific turbulent dissipation rate, and turbulent kinetic energy at the inlet are estimated as

$$\omega_{inlet} = \lambda U_\infty / L \,, \tag{5}$$

$$k_{inlet} = \mu \omega_{inlet} C_i / \rho \,, \tag{6}$$

where the factor of proportionality, λ, is set to $\lambda = 10$, L is the reference length, μ represents the dynamic viscosity, and ρ is the water density and constant $C_i = 1 \times 10^{-4}$. Outflow condition only consists of a Neumann boundary condition that sets the gradient of velocity, turbulent kinetic energy, and pressure to zero, normal to the outflow plane. Slip condition is similar to a symmetry condition where the normal velocity and normal gradient of other variables are set to zero. No-slip condition specifies the velocities components, turbulent

kinetic energy, and normal pressure component as zero at the wall. The ω on the wall for a smooth surface is specified as described by Hellsten [35]:

$$\omega_w = \frac{u_\tau^2}{\nu} \times \left(\frac{50}{4.3(y^+)^{0.85}} \right)^2, \quad (7)$$

where u_τ is the friction velocity and ν is the kinematic viscosity. Since no wall-functions are used in XCHAP, all simulations were performed with the wall resolved approach.

4. Test Cases and Computational Conditions

Fourteen common cargo vessels having a model test and full scale speed trial results are used as test cases. As the speed trials of some vessels were carried out at more than one loading condition, the total number of tests cases are 18. The L_{PP} of the vessels are ranging from 200 m to 355 m, block coefficients (C_B) vary between 0.5 and 0.84, and the Froude numbers (the achieved speed at 75% MCR) are covering the range of 0.14 to 0.23. The vessels are built in series and speed trials were performed for each sister ship. The data set consists of 78 sea trials in total. The trial measurements were conducted by the yards and analyzed by SSPA with an in-house software according to ITTC Recommended Procedures and Guidelines for Preparation, Conduct and Analysis of Speed/Power Trials [36] and ISO Ships and marine technology—Guidelines for the assessment of speed and power performance by analysis of speed trial data [37]. The trials fulfill the ISO 15016/ITTC limits on weather condition. The corresponding model tests were conducted at SSPA.

The model tests corresponding to the speed trials were performed at SSPA's towing tank (260 m long, 10 m wide and 5 m deep). The models were made of the plastic foam material Divinycell, and they were manufactured with a 5-axis CNC milling machine at SSPA. A trip wire is mounted at 5% of L_{PP} aft from the fore perpendicular for the turbulence stimulation. All hull models are equipped with a dummy propeller hub and a rudder (two rudders for twin skeg hulls) for the resistance tests. The computational conditions for each test case are replicating the same conditions as in the corresponding towing tank tests such as the non-dimensional quantities, Re and Fn, loading condition, and geometrical features.

5. Best Practice Guidelines and the Quality Assurance of the CFD Based Form Factor Methodology

The proposed ITTC QA procedure consists of three steps, the first one being derivation of a Best Practice Guideline. In this section, the derivation of a best practice guideline for the CFD based form factors will be presented. Considering the plethora of numerical methods and possible CFD set-ups, it is not possible to formulate a general standard procedure for CFD-work that is generally applicable to all codes and cases [28]. Instead, each organization is required to formulate their own process (BPG) and assess its suitability for a specific application.

In order to derive the best practice guidelines for the determination of form factor using the SHIPFLOW code, CFD setups were varied systematically and verification and validation of the predicted form factors were performed. Since the validation is a key factor for the evaluations, the hulls were selected on the basis that experimentally determined form factors are suitable for the Prohaska method (i.e., C_T/C_{FM} values are fairly linear as presented in Section 5.1.6). The analysis is based on 300 double body simulations of the six test cases consisting of four hulls (H1, H2, H3, and H4) out of which one is in three different loading conditions (indicated as H2-b, H2-d, H2-s). The variations applied to the CFD set-ups are explained in Sections 5.1.1–5.1.6.

5.1. Grid Dependence Study

Grid dependence studies were performed to quantify the numerical uncertainty (U_{SN}). Four geometrically similar grids were generated for each test case. The simulations were performed in double precision in order to eliminate the round-off errors. The iterative uncertainties were quantified by the standard deviation of the force in percent of the

average force over the last 10% of the iterations. Iterative uncertainty for C_F and C_{PV} were kept below 0.01% and 0.20% for all simulations except two computations where mild separation is observed at the stern, and standard deviations are 3 to 4 times higher than the rest of the simulations. Considering the small standard deviations in both resistance components, it was assumed that the numerical errors are dominated by the discretization errors and both iterative errors and round-off errors are neglected. The procedure proposed by Eça and Hoekstra [38] was used to predict the grid uncertainties which are presented for the finest grid as a ratio of the computed value ($U_{SN}\%S_1$) in Table 1.

Table 1. Estimated numerical uncertainties of SHIPFLOW in model scale for EASM and $k-\omega$ SST turbulence models, in a percentage of the computed result of the finest grid, S_1.

$U_{SN}\%S_1$	Turb. Model	H1	H2-b	H2-d	H2-s	H3	H4
C_F	EASM	1.2	0.6	1.3	1.1	1.1	4.5
	$k-\omega$ SST	1.5	0.7	0.5	1.2	1.3	1.0
C_{PV}	EASM	37.2	4.1	52.6	20.1	7.8	13.2
	$k-\omega$ SST	61.2	4.1	52.9	20.7	9.1	8.2
C_V	EASM	6.9	1.1	10.6	4.7	2.2	6.0
	$k-\omega$ SST	10.2	1.1	9.5	4.8	2.5	2.2

Numerical uncertainty of the viscous resistance is predicted by a combination of the frictional and viscous pressure resistance components ($U_{C_V} = U_{C_F} + U_{C_{PV}}$) as C_V is not directly computed. As seen in Table 1, grid uncertainties on C_F mostly vary between 0.6 to 1.5 percent of the computed result of S_1. The grid uncertainty on C_{PV} varies greatly between different hulls. As a result of the large fluctuations in the C_{PV}, the grid uncertainty on the viscous resistance coefficient varies between 1.1% and 10.2%. The reason for the large fluctuation in the grid uncertainties is explained by the scatter in the computed values which strongly penalizes the estimated uncertainties [38]. Computed values for C_F, C_{PV} and C_V are presented in Figure 2 in a percentage of the result of the finest grid which has approximately 10M cells (N_{grid}). As seen in Figure 2, a majority of the C_F and C_{PV} values shows somewhat oscillatory behavior, which is observed significantly more for the latter. The fluctuations stems mostly from the grid generation strategy, which is a structured grid with a stair-step profile in the stem and stern profiles. As the curvature around the bulb changes rapidly, the structured grid that captures the profile of the bulb changes abruptly with changing grid. As a result, the computed quantities are influenced by the such variations. Considering the tip of the bulb where the stagnation point is often situated and followed by a steep pressure gradient, it is expected that C_{PV} will be influenced more than C_F as observed in Figure 2.

The estimated numerical uncertainties shown in Table 1 do not indicate a particular trend for a specific ship type or loading condition. Even though U_{SN} varies significantly between the test cases due to the drawbacks of the grid generation, its reflection on C_V is limited and the variation on the predicted form factors is rather small, especially between the finest two grids. Therefore, the g_2 grid settings have been chosen as a baseline for the rest of the BPG investigation since the grid cell count were reduced to approximately 7 million, and computational time was shortened compared to the finest grid.

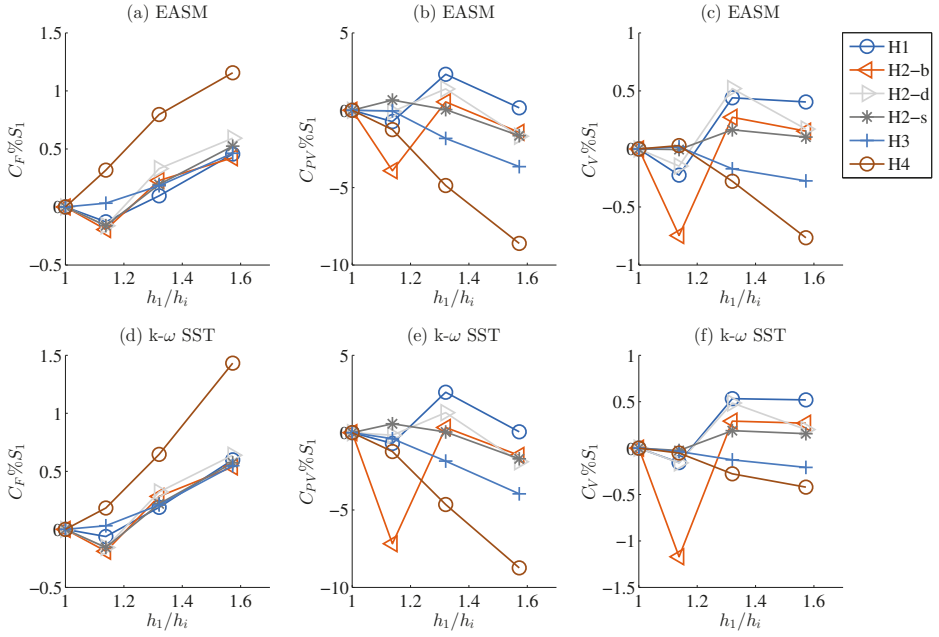

Figure 2. Computed values for (**a**) C_F, (**b**) C_{PV} and (**c**) C_V with the EASM model and (**d**) C_F, (**e**) C_{PV} and (**f**) C_V with the $k-\omega$ SST model vs. grid refinement ratio, $h_1/h_i = \sqrt[3]{N_{grid_1}/N_{grid_i}}$.

5.1.1. Variation of the First Cell Size Normal to the Wall, i.e., y^+ Variation

It is essential to calculate the wall shear stresses accurately as the resistance of a ship at model scale is often dominated by the frictional resistance component. Previous studies performed with SHIPFLOW and other codes [28,39,40] showed that computation of the frictional resistance component is rather sensitive to the turbulence model, and the first cell size normal to the wall. In order to investigate both of them, the second finest grid (g_2) is selected as a reference point since the differences between the g_1 (finest grid) and g_2 in C_V were less than 0.2% (except for one hull). Keeping the same number of cells as g_2 in all directions and the position of no-slip grid points identical in longitudinal and circumferential directions, the height of the first cell in the normal direction to the wall was varied. These variations were performed for all test cases using EASM and $k-\omega$ SST turbulence models.

The height of the first cell normal to the wall is non-dimensionalized as $y^+ = (u_* y)/\nu$, where y is the height of the first cell and ν is the kinematic viscosity. In SHIPFLOW, the average y^+ is calculated by arithmetic mean

$$(y^+)_{avg} = \frac{1}{N_{grid}} \sum_{i=1}^{N_{grid}} y_i^+ . \tag{8}$$

The height of the first cells for all test cases are adjusted to cover a wide range of $(y^+)_{avg}$ including the values exceeding the recommended $y^+ < 1$ for the wall resolved approach. The results of the y^+ variations are presented in Figure 3 as the comparison error of form factors

$$E\%D = (D - S)/(D + 1) \times 100 \tag{9}$$

where D is the experimentally determined form factor (using the Prohaska method), and S denotes the CFD based form factor based on the ITTC-57 line. The comparison error

shows a consistent ±2.5% of spread throughout the $(y^+)_{avg}$ range of 0.1 to 1.5. When the fitted curve to all the computed results (dashed black line) is considered, the average $E\%D$ converges to zero as the $(y^+)_{avg}$ gets smaller, and it is nearly constant for the simulations performed where $(y^+)_{avg} < 0.5$. The mean comparison error for the computations where $(y^+)_{avg} \approx 1.5$ is the largest, as expected, since the non-dimensional height y^+ is required to be lower than 1 for the wall resolved approach. However, the $E\%D$ of the simulations with $(y^+)_{avg} \approx 0.75$ and $(y^+)_{avg} \approx 1$ are also in an increasing trend. As presented in Figure 4, the histogram of the acquired y^+ values for the six different first cell heights for the H3 hull reveals that achieving $(y^+)_{avg} < 1$ does not guarantee that all (or most) of the y^+ values will be also below 1. As seen in Figure 4, 3%, 35% and 60% of the no-slip cells have y^+ values are higher than 1 for the simulations that resulted in $(y^+)_{avg}$ of 0.5, 0.73, and 0.95, respectively. Considering the histogram plots of y^+ values of the other test cases as well, it is recommended that the target $(y^+)_{avg}$ should be smaller than 0.5 in order make sure that nearly all the y^+ values will be smaller than 1.

As observed in Figure 3, CFD based form factors are heavily dependent on the choice of the turbulence model. The form factors obtained by the $k-\omega$ SST model are consistently 1.5 to 2.5 percent higher than what is achieved with EASM, mainly as a result of the calculated C_F being approximately 3% higher with the $k-\omega$ SST model than the EASM for the same grid. These trends are noticeably consistent within the range of $0.1 < (y^+)_{avg} < 1$. Therefore, if the $(y^+)_{avg}$ is smaller than 0.5, the modeling error is dominated by the choice of turbulence model.

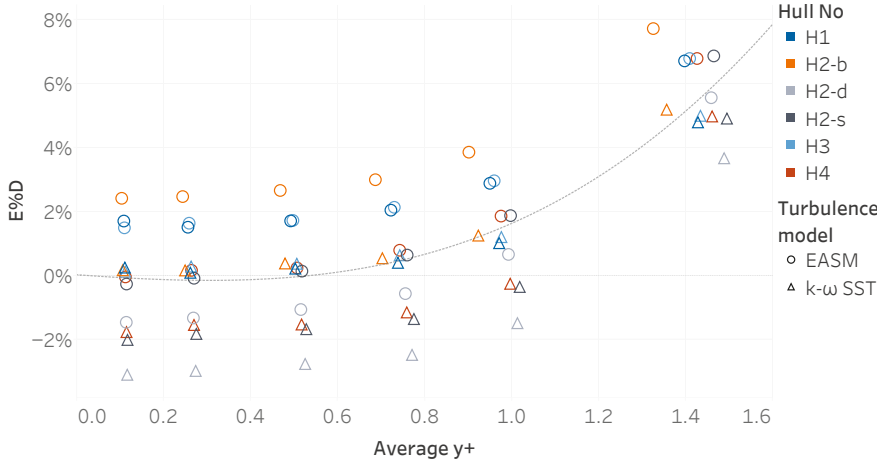

Figure 3. Comparison error of all test cases for average y^+ variation.

5.1.2. Variation of Refinement Region

Using the overlapping grid technique, the single block grid describing the flow domain can be effectively refined as explained in Section 3. As shown in Figure 5, three geometrically similar refinement regions (R1, R2, and R3) are determined for all test cases. The refinements are applied to the g_2 grid of each test case presented in Section 5.1. The starting and ending boundaries of the refinement regions are positioned at the same longitudinal position (with respect to L_{PP} of each hull) relative to the aft perpendicular. The smallest refinement limits in the circumferential and normal directions are determined with respect to the propeller diameter to be able to encapsulate the *nominal wake*, i.e., flow field at the propeller plane without the presence of the propeller.

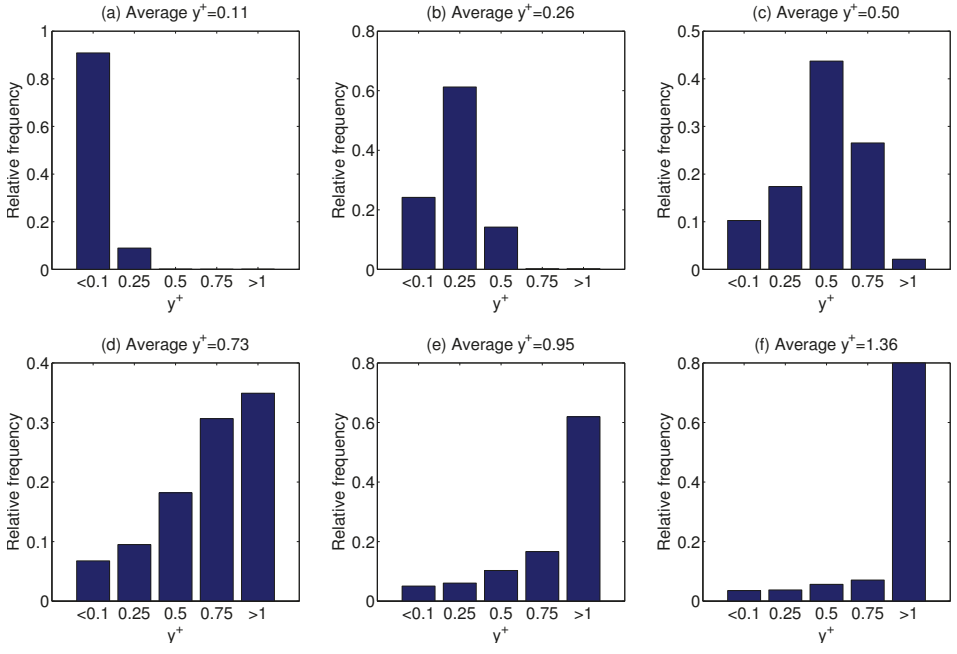

Figure 4. The histogram of the acquired y^+ values for the H3 hull for the average (**a**) $y^+ = 0.11$, (**b**) $y^+ = 0.26$, (**c**) $y^+ = 0.50$, (**d**) $y^+ = 0.73$, (**e**) $y^+ = 0.95$ and (**f**) $y^+ = 1.36$.

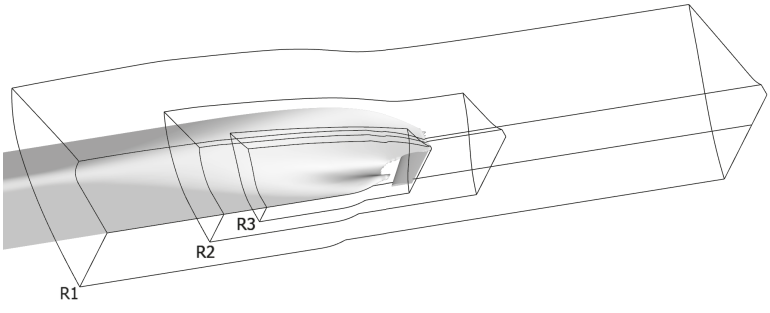

Figure 5. Systematic refinement variation in three steps for R1, R2, and R3 regions.

As observed in Figure 6, the comparison error of the form factor remains relatively unchanged between the grids without refinement (computations with 7M grid cells) and the grids with different refinement regions (shown in Figure 5). The regression lines are fitted to computations of each test case. As seen in Figure 6, the steepest line belongs to the H4 hull where a mild flow separation at the bilge of the gondola (i.e., lower part of the stern bulb) is observed. In this case, the varying refinement regions had a somewhat noticeable effect on the local flow as well as the computed resistance components. However, the variations in C_F, C_{PV} and C_V are well within the grid uncertainties reported in Table 1 for all hulls. Therefore, it is concluded that, for the purpose of obtaining CFD based form factors, g_2 (the baseline) is fine enough for all test cases, and no further grid refinements are required.

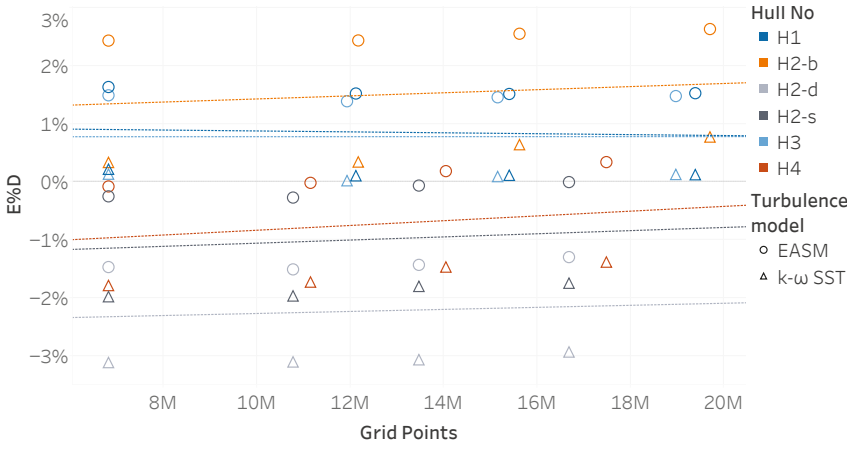

Figure 6. Comparison error of all test cases for the refinement region variation.

5.1.3. Domain Size Variation

The size of the domain was varied from the default settings where the distance between inlet and fore-perpendicular (FP) is $0.5L_{PP}$ (denoted as U/L_{PP}), outlet plane is located at $0.8L_{PP}$ behind the aft-perpendicular (denoted as W/L_{PP}), and the radius of the cylindrical outer boundary is $3L_{PP}$ (denoted as N/L_{PP}). The default domain size is increased in two steps by changing the distance of only one part (either U/L_{PP}, W/L_{PP} or N/L_{PP}) and keeping the rest the same. When a part of the domain is changed (for example U/L_{PP}), the number of cells are also changed with the same ratio in that region (e.g., number of cells are doubled when the distance is doubled), while the rest of the domain (in this example W/L_{PP} or N/L_{PP}) parameters and the grid cells within the coverage of the unchanged domain are kept identical. In this way, errors due to the discretization is aimed to be kept similar to the baseline grid (g_2).

The distance between the outlet plane and the aft-perpendicular (W/L_{PP}) is varied between 0.8 and 2.4. The variations of C_F due to changing W/L_{PP} are smaller than 0.03% which is more than one order smaller than the numerical uncertainties shown in Table 1. The calculated viscous pressure resistance component increased up to 2% with respect to the base line. Investigations in the modified part of the flow domain showed that the traces of the wake of the hulls are reaching the outlet boundary in most of the test cases. However, when the outlet boundary moved further away from the hull (W/L_{PP} = 1.6 and 2.4), the wake almost completely dissipated and diffused into the free stream. The difference in C_V for all test cases varied between 0.1 to 0.4%, and, therefore, it is concluded that the Neumann boundary condition at the outlet boundary worked satisfactorily to handle the wake reaching the outlet plane. The resulting changes can be seen in Figure 7b where the predicted form factors are rather insensitive to the W/L_{PP} change regardless of the turbulence model used.

The radius of the cylindrical domain varied between $N/L_{PP} = 3$ to 5. Similar to the W/L_{PP} variations, the change in the frictional resistance component is limited (up to 0.2%) and approximately one order smaller than the numerical uncertainties on Cf. The change in the C_{PV} and C_V is also comparable for N/L_{PP} and W/L_{PP} variations. Considering the insignificant variation in form factor predictions as seen in Figure 7c and already having much smaller blockage effect (ratio between mid-sectional area of the hulls and the towing tank section area) in CFD compared to towing tank, the domain size of the baseline grid (N/L_{PP} = 3) is found to be large enough.

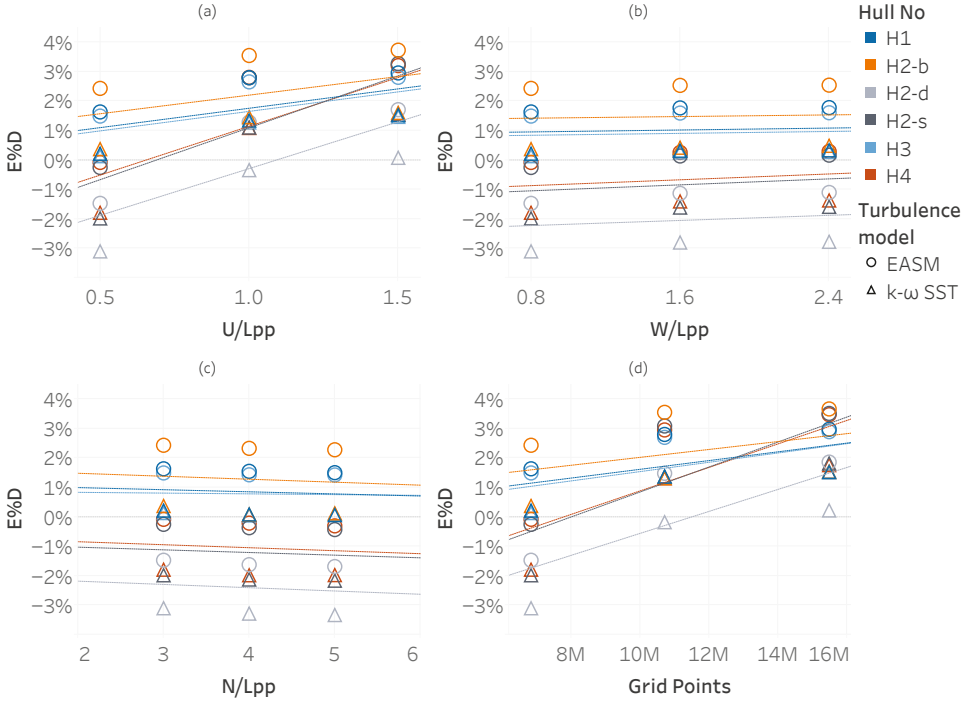

Figure 7. Comparison error of all test cases for the domain size variations: (**a**) U/L_{PP}, (**b**) W/L_{PP}, (**c**) N/L_{PP}, (**d**) in all directions.

The distance between the inlet and the fore-perpendicular (U/L_{PP}) is varied between 0.5 and 1.5. Contrary to the previously mentioned parts of the domain (N/L_{PP} and W/L_{PP}), the choice of the inlet plane location had prominent implications both on the local flow and the resistance components. The analysis performed on all test cases indicated that the significant changes between different U/L_{PP} values are mainly due to the differing turbulence intensity reaching the hull. As explained in Section 3, the specific turbulent dissipation rate and turbulent kinetic energy (TKE) are set at the inlet plane for each hull regardless of the distance between inlet boundary and the FP (see Equations (6) and (7)). As a result, the TKE reaching the hulls decreased since the TKE is dissipated more by traveling greater distances with the increasing U/L_{PP}. The reduced turbulence intensity in the free stream arriving to the hulls caused a significant drop in C_V varying between 1.3% to 3.5%. The contribution of the frictional and viscous pressure resistance to the reduced viscous resistance is nearly equal for all cases. As seen in Figure 7a, the comparison errors in form factors are highly dependent on the U/L_{PP}.

In addition to commonly known modeling errors such as turbulence modeling, the transition from laminar to turbulent flow is also considered for this study. Contrary to the common perception, the flow in a typical model scale RANS computation with a wall resolved approach is *not* fully turbulent in the boundary layer even with the commonly used turbulence models (i.e., without transition models). The analysis performed on infinitely thin 2D flat plates by Eça and Hoekstra [39] and Korkmaz et al. [30] indicated that, even though the correct position of the transition could not be predicted using ordinary turbulence models such as k-omega SST [33] and EASM [32], the transition occurs qualitatively rather accurately. In order to show if this is the case also for the hulls, local skin friction coefficient, C_f is calculated for baseline grid of each test case as

$$C_f = \frac{\mu\left(\frac{\partial u_x}{\partial y}\right)_{y=0}}{\frac{1}{2}\rho U_\infty A}, \tag{10}$$

where $\left(\frac{\partial u_x}{\partial y}\right)_{y=0}$ is the velocity gradient at the wall and A is the wetted surface of the hull. The velocity gradients of the cells in the same x-position were summed, and all no-slip cells are included in the calculation of the local skin friction coefficient.

In Figure 8, the local skin friction coefficient of all test cases are presented together with the Blasius solution [41] for the reference of the friction coefficient of the laminar flow, Prandtl–Schlichting formula [41] for the fully turbulent flat plate skin friction coefficient, and the numerical friction line [30] for the EASM turbulence model derived using SHIPFLOW.

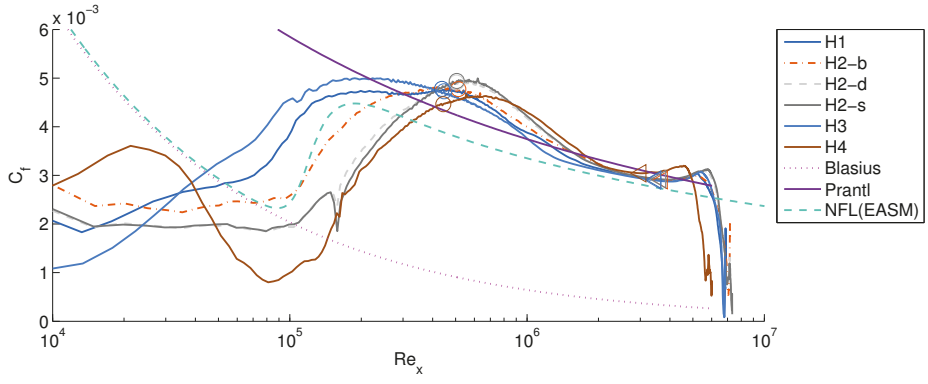

Figure 8. Local skin friction resistance coefficients for all hulls versus Reynolds number.

As seen in Figure 8, C_f of all test cases are even below the Blasius line before $Re < 4 \times 10^4$. However, C_f values are steeply increasing approximately between $Re = 7 \times 10^4$ and $Re = 1.5 \times 10^5$ where the numerical friction line is also showing remarkably similar increase from laminar regime towards turbulent. The C_f values of each test case are expected to have some quantitatively and qualitatively differences both among themselves and the friction lines (Blasius, Prandtl–Schlichting, and NFL) since each hull shape is unique and the flow is not under zero-pressure-gradient. However, it can be argued that the flow is not fully turbulent in all parts of the hull in the computations as it may be also the case for the towing tank tests. To make sure that turbulent flow is achieved in the model tests, turbulence simulators are attached to the hull. The model tests used for all the test cases in this study also utilized turbulence stimulators placed at 5% of the L_{PP} from the fore perpendicular. In Figure 8, these locations are marked with circles. It is ensuring to observe that the flow in CFD transitioned into turbulent flow before the position of the turbulence stimulators. In the previous studies with flat plates [30,39], the Reynolds number where transition occurred was found to be dependent on the choice of turbulence model and turbulence intensities. Additionally, different CFD solvers (SHIPFLOW and FINEMARINE) using the same grid also led to not only different transition behaviors but also significantly different C_f values in the turbulent region [30]. Therefore, it is recommended to adjust the turbulence intensities for each code and the turbulence model when the wall resolved approach is used for making sure the flow characteristics are similar in CFD to the experiments.

In order to investigate the effect of varying turbulence intensities, the local skin fiction coefficient of the H1 hull is presented in Figure 9a for U/L_{PP} = 0.5, 1 and 1.5. C_f of all U/L_{PP} values seem to be nearly identical in Figure 9a except where the C_f is steeply increasing, i.e., transition of the flow. In order to visualize the differences in more detail,

C_f of the U/L_{PP} = 1 and 1.5 are plotted relative to C_f of the baseline domain. As seen in Figure 9b, the C_f[%] values are differing the most at the position where transition from laminar to turbulent flow occurs. In the laminar and turbulent regions, C_f values are nearly uniformly 0.7% and 0.8% less for U/L_{PP} = 1 and 1.5 compared to U/L_{PP}=0.5. The local viscous pressure resistance component also decreased with the lower turbulence intensity but not as uniformly as is the case for C_f. The local viscous pressure resistance coefficient, C_{pv}, of U/L_{PP} = 1 and 1.5 was predominantly lower in the laminar parts of the hull and at the stern region that is covered by the boundary layer.

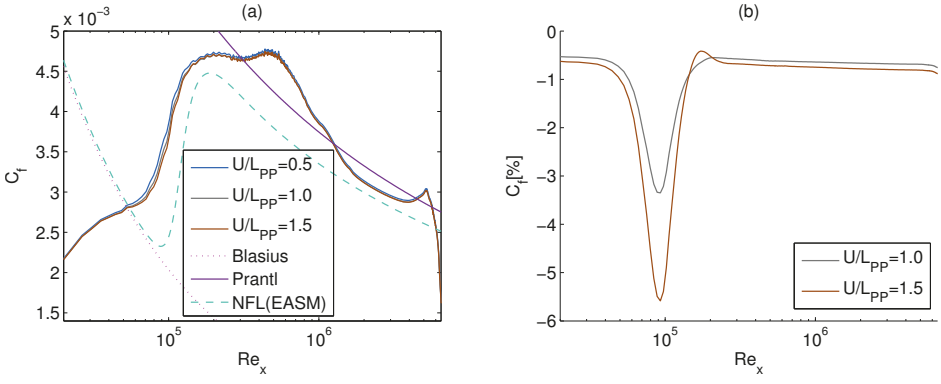

Figure 9. (**a**) Comparison of the local frictional resistance coefficients of H1 hull for the domain size variation in U/L_{PP} and (**b**) comparison of C_f of H1 hull relative to U/L_{PP} = 1.

In the final step, the domain size is varied in all directions (U/L_{PP}, N/L_{PP} and W/L_{PP}) at the same time in two steps. Starting from the baseline grid (U/L_{PP} = 0.5, W/L_{PP} = 0.8 and N/L_{PP} = 3), the boundaries in all directions are first moved to U/L_{PP} = 1.0, W/L_{PP} = 1.6 and N/L_{PP} = 4 and then U/L_{PP} = 1.5, W/L_{PP} = 2.4 and N/L_{PP} = 5 for all test cases. The number of cells are also increased proportionally in the region where the domain size is enlarged. As seen in Figure 7d, the resulting form factors due to varying the domain size in all directions are nearly the same with the domain size variation only in U/L_{PP} as seen in Figure 7a. As a result, the turbulence intensities are playing a more significant role in terms of modeling errors than the wake reaching the outlet plane and the blockage effect. The default domain size gives the smallest comparison error on average, and it is concluded that further enlarging the domain is not necessary.

5.1.4. Variation of the Model Scale Speed

The previous CFD studies presented by Raven et al. [42], Wang et al. [25], Dogrul et al. [26], Korkmaz et al. [27], Terziev et al. [24], Van et al. [43], and Korkmaz et al. [28] supported the existence of speed dependency for the form factors even though this should not be the case according to the hypothesis of Hughes [6]. Therefore, regardless of the choice of the CFD code, numerical methods, and settings, the choice of speed that the double body computations are performed for will have a significant impact on the CFD based form factors when the ITTC-57 model to ship correlation line is used. The towing tank tests are also not immune to the variation of form factors with changing the scale factor of the model as shown by García Gómez [21], Toki [22] and Van et al. [43].

The baseline grid, g_2, of each test case is simulated in three different speeds: the lowest speed tested in the towing tank, the design speed of the vessel, and an interim speed between the two speeds. The average non-dimensional first cell height, y^+, and other CFD settings are kept the same for all speeds. As can be seen in Figure 10a, all test cases indicate a definitive trend for the comparison error of factors which is based on the ITTC-57 line. As also explained in the earlier studies [22,28,42], the ITTC-57 line is the main reason for

form factors increasing with increasing Reynolds number due to its excessive steepness in model scale Reynolds numbers.

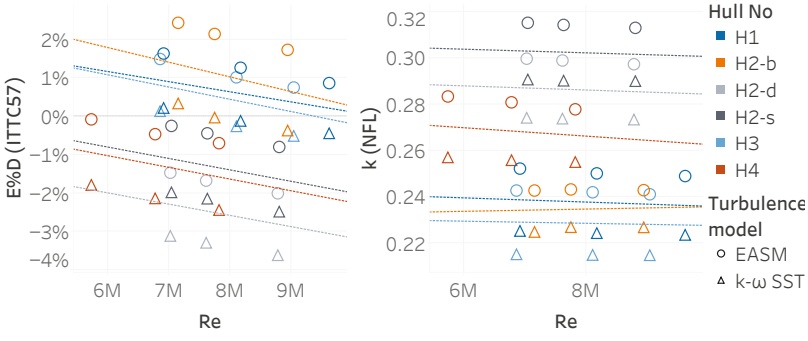

Figure 10. Comparison error of all test cases for the speed variations, (**a**) using the ITTC-57 line and (**b**) using the NFL.

Using the results of the same simulations but changing the friction line from the ITTC-57 line to a numerical friction line (NFL) [30] of the same CFD code and turbulence model reduced, and, in some cases nearly eliminated, the speed dependency of CFD based form factors, as can be seen in Figure 10b. As there is no experimental comparison point with the NFL, the form factors are directly plotted in Figure 10b. Contrary to other test cases, the H4 hull shows a decreasing trend with Reynolds number. The investigation in the local flow highlighted that the trend observed in H4 is due to the existence of mild flow separation at the stern. The separation is noticeably larger in the computations with the EASM than with the $k-\omega$ SST turbulence model. As Reynolds number is increased, the separation diminishes in intensity; therefore, the form factor is reduced as expected. Note that, according to the form factor hypothesis of Hughes [6], there should not be any flow separation in the model tests nor in the CFD. In such cases, the CFD simulations are recommended to be performed at higher Reynolds number until the separation is vanished. Except for the case with flow separation, the smallest average comparison error is observed at the slowest model tow speed. Therefore, it is recommended to perform the CFD simulations at the lower end of the model speed interval. However, such a conclusion may as well be different for other codes, numerical methods, or the size of the model used in towing tank tests.

5.1.5. Turbulence Model

The systematic variations applied to the CFD set-ups have been performed with the $k-\omega$ SST and EASM turbulence models. The conclusions regarding the other CFD settings: the non-dimensional cell height normal to the wall, additional grid refinement at the stern, domain size, and model scale speed, are valid for both turbulent models. The form factor predictions of all test cases using the $k-\omega$ SST model are approximately 10% higher than the computations with EASM using the same grid. As a result of this consistent difference between the form factors from different turbulence models, the full scale viscous resistance ($C_{VS} = (1+k)C_{FS}$) predictions using the $k-\omega$ SST model will be higher while the residual resistance (see Equation (2)) predictions will be lower than the predictions from EASM when the ITTC-57 line is used.

When the comparison error of the form factors is presented for each turbulence model with respect to the loading conditions, a certain prediction pattern is observed as presented in Figure 11. Computations at ballast, design, and scantling loading conditions are stacked in separate columns where box-and-whisker plots are placed with markers. The box plot can be identified with the gray color and sized with the lower and upper quartiles. Lines extending from the boxes (whiskers) extend to the data within 1.5 times the interquartile

range (IQR). The markers are colored with the test cases and sized according to the number of cells. The computational results from the finest two grids (original g_1 and g_2 from Section 5.1), from average $y^+ \leq 0.5$ presented in Section 5.1.1 and all grid refinements presented in Section 5.1.2 are presented in Figure 11. The form factor predictions from the $k-\omega$ SST model at ballast loading condition corresponds better to the experimentally determined form factors than the EASM turbulence model. However, the opposite trend is true for the design and scantling loading conditions. When the results are considered regardless of the loading condition, the average comparison error is 0.75% and −0.9% for the EASM and the $k-\omega$ SST turbulence models, respectively. Therefore, the absolute mean comparison error of the two turbulence models is similar.

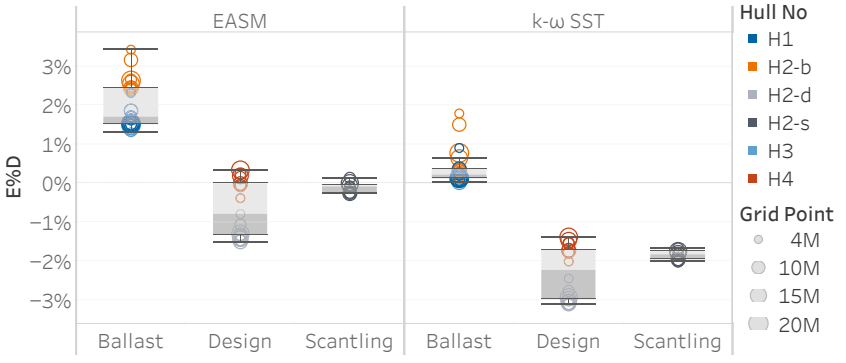

Figure 11. Comparison error of form factors for different loading conditions for the EASM and the $k-\omega$ SST turbulence models.

5.1.6. Validation in Model Scale

In order to complete the verification and validation study, experimental uncertainty needs to be determined [44]. As the experimental data used in this study were obtained through routine towing tank testing, thorough uncertainty analyses according to ITTC [45] could not be performed but instead the simplified implementation of this procedure as presented in ITTC [46] was used.

Using the standard uncertainty of calibration (SEE) for routine tests and the SSPA database of the repeatability of resistance tests, the uncertainties in resistance measurement [46] (without repeat tests) are calculated for each measurement point of each test case. However, the combined uncertainty of measured resistance, $u_c(R_T)$, cannot be used as direct indicatives of the uncertainties related to the form factors. Therefore, an additional step is required to consider the uncertainties due to the data reduction process of the form factor, i.e., the linear regression in the Prohaska method. The regression lines in Figures 12 and 13 are obtained by using the measurement uncertainties for the 95% confidence interval ($k_P = 2$) and applying the method explained in [47], which considers the experimental uncertainties in the regression progress and predicts the uncertainties in the form factor as well. The resulting regression line is indicated as York's method in Figures 12 and 13, where the uncertainty on the form factor is illustrated with magenta colored error bar at $Fn^4/C_F = 0$, and the measurement uncertainties are shown as the blue colored error bars. The uncertainty of the form factors, U_D, for the 95% confidence interval are varying between 0.015 and 0.023, which corresponds to 1.3% and 2.0% of the $(1 + k)$.

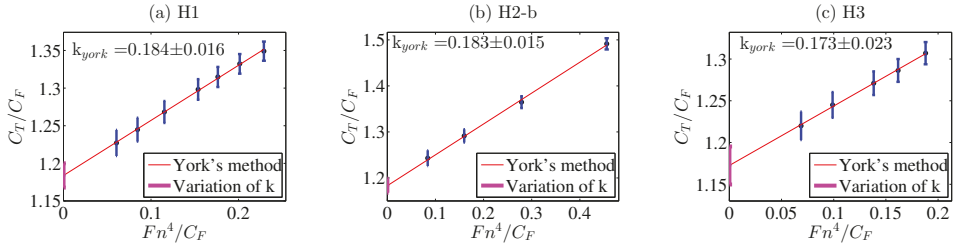

Figure 12. Prohaska plot of test cases in ballast loading condition: (**a**) H1, (**b**) H2-b, (**c**) H3.

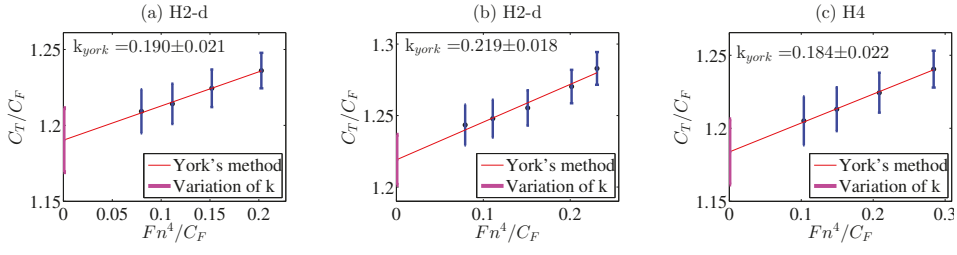

Figure 13. Prohaska plot of test cases in design and scantling loading conditions: (**a**) H2-d, (**b**) H2-d, (**c**) H4.

The numerical uncertainty, U_{SN}, of the CFD based form factors is calculated similar to form factor calculation in Equation (3),

$$U_{SN}(k) = \frac{U_{SN}(C_V)}{C_{FM}}, \tag{11}$$

where C_{FM} is the equivalent flat plate resistance in two-dimensional flow obtained from the same Reynolds number as the computations and obtained from the ITTC-57 line [4]. The validation uncertainty is calculated as $U_V = \sqrt{{U_{SN}}^2 + {U_D}^2}$.

The numerical and experimental uncertainties, absolute comparison error, and the validation uncertainties for the baseline grids (g_2) of all test cases are presented in Table 2 in percent of $(1 + k)$ where the form factor from the Prohaska method is used. The validation uncertainty, U_V, is bigger than the absolute comparison error for all test cases with the $k - \omega$ SST turbulence model. Except the H2-b test case with the EASM, all other test cases are also $|E| < U_V$; validation is achieved at U_V level, i.e., the comparison error is below the noise level. However, it should be noted that the U_V of H1 and H2-d test cases are exceptionally high due to very large numerical uncertainties as explained in Section 5.1. When only U_D and E are compared, the form factor predictions made with the $k - \omega$ SST are within the experimental uncertainty for the same number of test cases as the EASM turbulence model.

Table 2. Validation of the CFD based form factors.

Form Factor	Turb. Model	H1	H2-b	H2-d	H2-s	H3	H4
U_{SN}%D	EASM	7.6	2.0	11.7	5.4	2.9	7.0
	$k - \omega$ SST	11.2	2.5	10.7	5.6	3.2	3.2
U_D%D	-	1.3	1.3	1.8	1.5	2.0	1.8
$\|E\|$%D	EASM	1.6	2.4	1.1	0.3	1.5	0.1
	$k - \omega$ SST	0.2	0.3	2.8	2.0	0.1	1.8
U_V%D	EASM	7.7	2.4	11.9	5.7	3.5	7.2
	$k - \omega$ SST	11.2	2.8	10.8	5.8	3.8	3.7

The required uncertainty, U_{reqd}, is determined based on the typical $U_{SN}\%D$ and $U_D\%D$ values observed in Table 2. The numerical uncertainties of 2.5% to 3.5% and the experimental uncertainties of 1.3% to 1.8% were considered satisfactory levels in consideration of the U_{reqd}. The combination of $U_{SN}\%D$ and $U_D\%D$ indicates that $U_{reqd}\%D$ should be approximately 4%. This required uncertainty level results in approximately $\pm 4\%$ variation in the full scale power predictions. It can be seen in Table 2 that $U_{reqd}\%D = 4\%$ is larger than the comparison error of all test cases with a considerable margin. The comparison of $U_{reqd}\%D$ and $U_V\%D$ for H2-b, H3, and H4 (only with the $k-\omega$ SST) shows that required uncertainty is larger than the validation uncertainty, and, therefore, the validation of these cases is successful for a programmatic standpoint [44]. The rest of the test cases $U_{reqd}\%D$ is smaller than $U_V\%D$ due to substantial numerical uncertainties.

It should be noted that the experimental determination of the form factor, i.e., the Prohaska method [5], is not a direct measurement but obtained as a result of data reduction. The Prohaska method is solely an approximation to obtain the form factor described by Hughes [6]. Therefore, the comparison error of the form factor should be interpreted with care since the experimental form factors may not always represent the true value.

6. Demonstration of Quality by Comparison of Full Scale Predictions

In the final step of the proposed quality assurance procedure, full scale speed-power-rpm relations between speed trials and full scale predictions based on model tests carried out at SSPA are compared. In order for such comparisons to be meaningful, a large number of sea trials are required since the uncertainty of each trial is large. The combination of the precision and bias limits of single speed trial result in approximately 10% of total uncertainty as indicated by Werner and Gustafsson [48] and Insel [49].

Correlation of model test power predictions to the speed trials are quantified with the *correlation factors* which are also used as "correction for any systematic errors in model test and powering prediction procedure, including any facility bias" [50] in the 1978 Power Prediction method [20]. There are three different schemes of correlation factors that can be used: C_A, $C_P - C_N$ and $\Delta C_{FC} - \Delta w_C$. In this study, the correlation scheme of $C_P - C_N$ coefficients are applied. In order to obtain these coefficients, the correlation of each individual speed trial, $C_P^{'}$ and $C_N^{'}$, are calculated as

$$C_P^{'} = \frac{P_{D\ trial}}{P_{D\ tank}} \quad \text{and} \quad C_N^{'} = \frac{n_{trial}}{n_{tank}} \tag{12}$$

where the $P_{D\ trial}$ and n_{trial} are the power and propeller turning rate from a speed trial, while $P_{D\ tank}$ and n_{tank} represent the corresponding predictions based on the model test. The power, P_D, is derived from the faired speed-power curve at the design speed. After $C_P^{'}$ and $C_N^{'}$ are calculated for a large number of sea trials, an assembled correlation factor for C_P and C_N are determined by taking the median of $C_P^{'}$ and $C_N^{'}$ of all trials of sufficient quality [48]. In this study, assembled correlation factors are not disclosed, but the probability density functions (PDFs) of $C_P^{'}$ and $C_N^{'}$ are presented by shifting the median of PDFs to 1, i.e., normalizing the correlation factors.

In the determination of the ITTC 1978 Power Prediction Method, the standard deviation of normalized $C_P^{'}$ and $C_N^{'}$ were used as the main measure to rank different extrapolation methods. In this study, the same approach is adopted, and reduced scatter of the normalized $C_P^{'}$ and $C_N^{'}$ is interpreted as an improvement for the extrapolation methods explained in Sections 6.1 and 6.2.

6.1. Comparison of the Standard ITTC-78 Method and CFD Based Form Factors Using the ITTC-57 Line

Correlation of the speed trials to model test power predictions is quantified by using three different sources of form factors: the Prohaska method, CFD based form factors using EASM, and $k-\omega$ SST turbulence models. The ITTC-78 method [20] is used for all predictions with the ITTC-57 model to ship correlation line [4] and the correlation allowance

stated in Equation (4). A special wake scaling suggested in the ITTC 1999 method [51] is applied to the vessels with a pre-swirl stator type of device ahead of the propellers. All predictions used the same model test data, but only the source of the form factor is changed. The difference in the form factors among predictions leads to a change in the residual resistance as calculated in Equation (2) and the viscous resistance of the full scale ship ($(1+k) \times C_{FS}$) as calculated by using Equation (1). As a result of the change in C_{TS}, the predicted delivered power and propeller rate of revolution vary.

The probability density functions (PDFs) of the normalized correlation factors, $C_P^{'}$ and $C_N^{'}$, are calculated for the speed trials that have an uncertainty index less than eight using the different sources of the form factors. The uncertainty index, u, is an in-house developed index that quantifies the trustworthiness of each speed trial by summarizing the largest error sources and weighting them according to their impact on the results. In addition to the PDF curves, the standard deviations (σ) of $C_P^{'}$ and $C_N^{'}$ are also presented in Figure 14. The comparison of the standard deviations for the power predictions (C_P) indicates that the scatter is reduced considerably when the CFD based form factors from the EASM turbulence model are used compared to the Prohaska method. The PDF curve of CFD based form factors from EASM suggests that the frequency of predictions that are within $\pm$5% of the sea trials is increased, while the predictions that are off more than 10% are slightly reduced. The PDF curve of CFD based form factors from $k-\omega$ SST for the power prediction remained nearly the same as the standard ITTC-78 method. The propeller rate of revolution predictions remained the same with EASM but slightly worsened by the predictions with CFD based form factors with $k-\omega$ SST model when the standard deviation is considered. It should be noted that the reduction of scatter in the power predictions is a more significant measure than the propeller turning rate since the scatter in power prediction is much larger than the prediction of rps. Hence, it can be concluded that the usage of CFD based form factors with ITTC-57 line improves the predictions in general or at least do not deteriorate them.

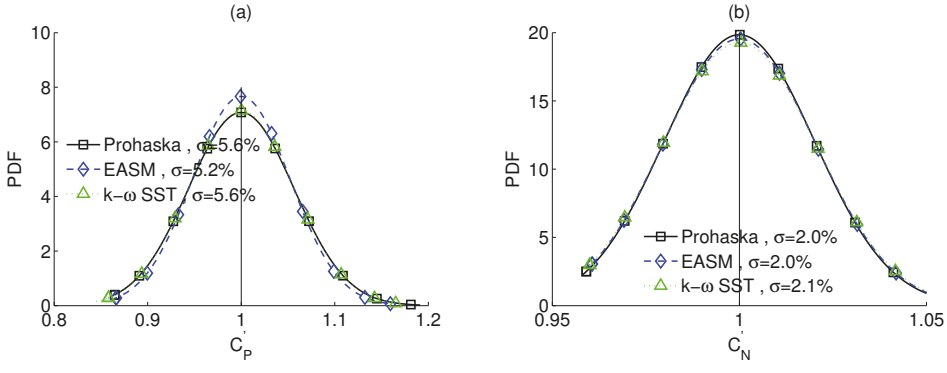

Figure 14. The probability density functions (PDFs) of the normalized correlation factors for the standard ITTC-78 method and using CFD-based form factors with two different turbulence models. (**a**) $C_P^{'}$ and (**b**) $C_N^{'}$.

6.2. Comparison of the CFD Based Form Factors Using the ITTC-57 Line and Numerical Friction Lines

To investigate if the predictions can be further improved by modifying the standard ITTC-78 method, the ITTC-57 model to ship correlation line is replaced by the numerical friction lines [30]. The CFD based form factor of each hull is recalculated using the same simulation results as in Section 6.1 for EASM and $k-\omega$ SST turbulence models using the corresponding numerical frictional line as explained in Section 2. Similar to the previous section (Section 6.1), the correlation of the speed trials to model test power predictions is

quantified using four different sources of form factors; CFD based form factors for EASM and $k-\omega$ SST using ITTC-57 line and NFLs.

The same population of the speed trials presented in the Section 6.1 are used for generating the PDFs of the normalized $C_P^{'}$ and $C_N^{'}$. As can be seen in Figure 15, the standard deviation of the predictions with the CFD based form factors is lower with the application of NFL compared to using the ITTC-57 line, while the scatter of $C_N^{'}$ increased slightly. Another distinctive result of using the NFLs is the reduced difference between the turbulence models. The previous studies [27,28] indicated that, when the numerical friction lines are used, the full scale viscous resistance ($C_{VS} = (1+k)C_{FS}$) is nearly the same regardless of using EASM and $k-\omega$ SST turbulence models for the derivation of the form factor. However, the residual resistance varies with regard to the turbulence model, and, therefore, leading to the different full scale total resistance (see Equation (1)). As observed in Figure 15, the form factors from using the EASM turbulence model and its numerical friction line correlates better than when using the $k-\omega$ SST model. In addition, the CFD based form factors using numerical friction lines considerably reduced the frequency of the predictions that differ from the speed trials more than 10%, which is the level of the total uncertainty of a speed trial [48,49].

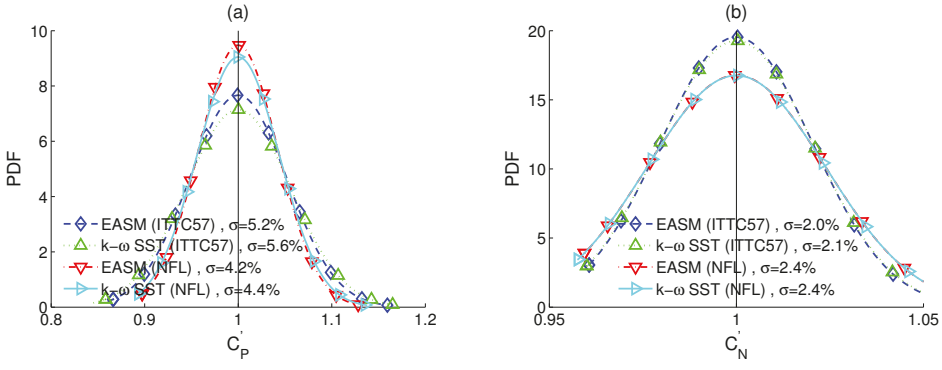

Figure 15. The probability density functions (PDFs) of the normalized correlation factors using the CFD based form factors with the ITTC-57 and the numerical friction lines. (**a**) $C_P^{'}$ and (**b**) $C_N^{'}$.

6.3. Analysis of the Extrapolation Methods and Speed Trials

The full scale speed-power-rpm relations between speed trials and full scale predictions using different extrapolation methods have been presented in Sections 6.1 and 6.2. It is important to make sure that the conclusions are not biased for a specific population of speed trials and also the speed trials with large error sources are excluded when general conclusions are made. Therefore, the statistical analysis on the $C_P^{'}$ is repeated for the speed trials with varying maximum uncertainty indexes. As presented in Table 3, three different levels of maximum uncertainty index, u, are used. In practice, the cut off uncertainty index should be as low as possible since the larger u index value of a speed trial indicates the existence of larger error or uncertainty sources such as large wave and wind corrections due to adverse weather conditions. However, the number of sea trials with very low uncertainty is limited and, as a result, the danger of drawing conclusions from small number of speed trials arise.

In Table 3, the statistics of different populations of speed trials with maximum cut off values of u varying between 4 and 8 are presented. The number of speed trials is 46 for the cut off value of $u = 4$. A lower u cut off value for the uncertainty index is not preferred since the size of the population decreases significantly. The comparison of the standard deviations between the corresponding u index shows that σ increases slightly with the increasing u index as there are more speed trials with lower quality in the larger

populations. However, the ranking of the magnitude of the standard deviations among each extrapolation method remains consistent. The scatter of the standard ITTC-78 method, where the form factors are obtained from the Prohaska method, is higher than all other extrapolation methods where the form factor is obtained from CFD except when $k-\omega$ SST is used with the ITTC-57 line. The standard deviations when using CFD based form factors with the ITTC-57 line are slightly in favor of the EASM turbulence model and also the percentage of the predictions with less than a 5% error are consistently higher when the EASM is used, while the predictions that differ from the speed trials more than 10% remained similar to the $k-\omega$ SST with the ITTC-57 line. The replacement of the ITTC-57 line with the numerical friction lines in combination with the CFD based form factors shows promising and consistent improvements towards not only reduction in the scatter but also decline in the number of speed trials where the prediction error is larger than 10% for both turbulence models. The correlation between the predictions and the speed trials is improved the most when the EASM turbulence model is used in combination with NFL.

Table 3. Statistics of the power predictions compared to speed trial.

u<	Number Speed Trials	Quantitiy	Standard ITTC-78	CFD Based k, ITTC-57 Line with EASM	CFD Based k, ITTC-57 Line with $k-\omega$ SST	CFD Based k, NFL with EASM	CFD Based k, NFL with $k-\omega$ SST
4	46	σ	4.9%	4.7%	5.0%	4.3%	4.3%
		5% < Error <10%	19%	15%	19%	13%	13%
		10% < Error	7%	9%	9%	4%	4%
6	69	σ	5.8%	5.3%	5.7%	4.4%	4.6%
		5% < Error <10%	21%	19%	24%	18%	19%
		10% < Error	9%	9%	9%	4%	4%
8	78	σ	5.6%	5.2%	5.6%	4.2%	4.4%
		5% < Error <10%	20%	20%	24%	11%	16%
		10% < Error	9%	8%	9%	4%	5%

The relatively large standard deviations observed in Table 3 are mainly due to the scatter in the speed trials of the sister ships. In order to illustrate this, an ideal prediction scenario has been prepared. Ideal case means if the model test prediction is fully correct compared to the speed trial. In theory, it would mean that the mean $C_P^{'}$ of a series of sisters would be 1. The resulting $C_P^{'}$ values are presented in Figure 16 together with the standard deviations of each ship series. As observed in Figure 16, the standard deviations among the sister ship series are varying between 2% to 6%. The standard deviation of all the $C_P^{'}$ values in the ideal prediction case is 3.6%, which is only marginally smaller than the predictions made with the CFD based form factor with the EASM turbulence model and NFL as shown in Table 3. Additionally, the percentage of predictions within 5% and the predictions that differ from the speed trials more than 10% are also nearly the same with the ideal prediction case and the predictions made with the CFD based form factors with the NFL. This indicates that it is hardly possible to achieve a better accuracy than this, unless the uncertainty of the speed trials become lower.

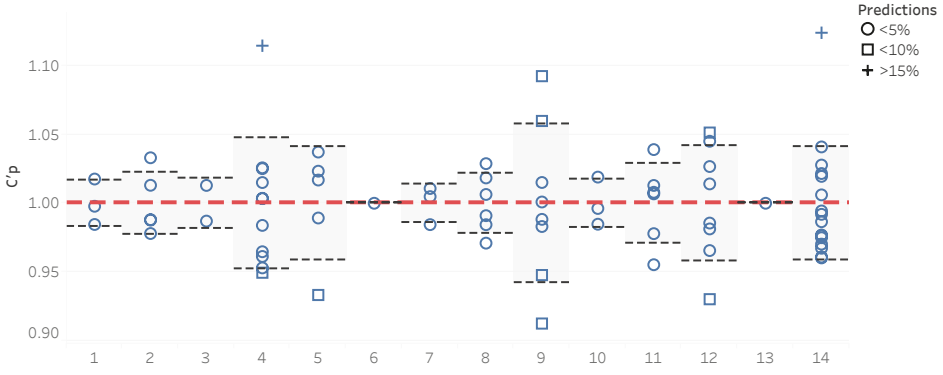

Figure 16. Illustration of the speed trial spread between sister ships for 14 ship series. $C_P^{'}$ values normalized to the mean of each series. Dashed black lines indicates the standard deviation.

6.4. Discussion

The analysis of the model test power predictions is further deepened by grouping the vessels based on their main dimensions, operational conditions, and general characters. Four main groups have been identified:

1. full block, large vessels ($L_{WL} > 320$ m) operating at $Fn < 0.16$;
2. full block, medium size vessels (220 m < $L_{WL} < 280$ m) operating at $0.15 < Fn < 0.17$;
3. medium block, large vessels (280 m < $L_{WL} < 330$ m) operating at $0.17 < Fn < 0.20$;
4. low block, medium size vessels (200 m < $L_{WL} < 240$ m) operating at $0.22 < Fn < 0.23$.

The comparison error of the predictions to the speed trials on a group level is calculated as

$$P\%T = (\overline{C_P^{'}} - 1) \times 100 \tag{13}$$

where P represents predictions, T is the speed trials, and $\overline{C_P^{'}}$ is the average normalized $C_P^{'}$ of each group. $P\%T$ values are calculated for the five different extrapolation methods presented in Sections 6.1 and 6.2. The $P\%T$ values from CFD based form factor methods (Section 6.2) are compared to the $P\%T$ of the standard ITTC-78 method. This comparison, $\Delta P\%T$, is calculated by subtracting the absolute $P\%T$ values of the CFD based form factor methods from the absolute $P\%T$ values of the standard ITTC-78 method. As a result, the $\Delta P\%T = 0$ indicates that the prediction accuracy with the CFD based form factors remained the same as the standard ITTC-78 method, positive values $\Delta P\%T$ indicate improvement and negative values point out that the predictions are worsened for the corresponding prediction method relative to the predictions from the standard ITTC-78 method. $\Delta P\%T$ of CFD based form factor methods are presented in Figure 17 for the four groups. In order to give an indication of the uncertainty of the speed trials for each group, the standard deviation of the $C_P^{'}$ values from the standard ITTC-78 method is combined with the bias limit of 4% as estimated by Insel [49]. The resulting total uncertainties ($\sqrt{\sigma^2 + U_{bias}^2}$) are indicated in Figure 17 as error bars for each group. It should be noted that the total uncertainties of trials for the each group are larger than the corresponding comparison error from the standard ITTC-78 method, i.e., $P\%T$ is below the noise level. Therefore, the improvements (if any) as a result of using the CFD based form factors will be within the noise levels caused by the uncertainty of the trials. However, the changes in the accuracy of predictions, $\Delta P\%T$, are considered statistically valid as the number of speed trials are rather large.

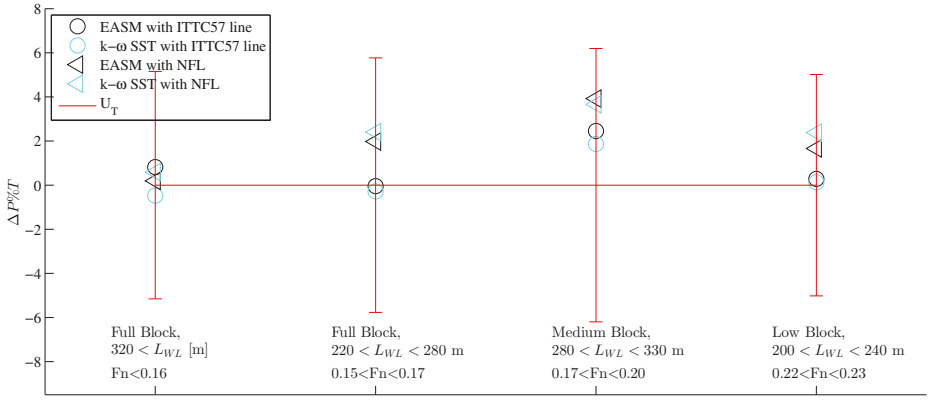

Figure 17. Relative change of the accuracy of the predictions, $\Delta P\%T = 0$, made with the CFD based form factors compared to the predictions with the standard ITTC-78 method, based on 18 test cases and 78 trials.

Starting with the extrapolations based on the CFD based form factors using the ITTC-57 line, there is no significant change in the accuracy of predictions for the full block and slow speed ($Fn < 0.17$) vessels. This outcome is expected since the form factor determination with the Prohaska method often functions well for such vessels and the CFD based form factors predict similar form factors to the Prohaska method as discussed in Section 5.1.6. As a result of obtaining nearly the same form factors from EFD and CFD while using the same friction line, the correlation between the predictions and speed trials remained nearly the same. However, it should be noted that the usage of $k-\omega$ SST turbulence model with the ITTC-57 line led to negative or too small C_R values in some test cases as a result of over-prediction of form factors which was also the observation in validation in the model scale (see Figure 11).

The accuracy of predictions for the low block vessels also remain nearly the same when the CFD based form factors are used in combination with the ITTC-57 line. This group of vessels are equipped with large protruding bulbous bows where the Prohaska method does not work in most cases. Therefore, the CFD based form factors are expected to introduce improvement to the predictions. The analysis performed on each vessel in this group showed that the CFD based form factors were up to 60% lower than the EFD based form factors. This caused the full resistance predictions to increase just enough to be predicted with similar accuracy but making it an over prediction on average instead of under prediction as it was the case for the standard ITTC-78 method.

The medium block and medium speed group are another group of vessels where a significant improvement is expected because the bulbous bow designs of these ships and typical loading condition for which the speed trials are performed for these vessels are not ideal for the Prohaska method. The CFD based form factors with the ITTC-57 line are predicted 25% to 50% lower than the form factors based on the Prohaska method. As can be seen in Figure 17, the predictions are in fact improved by implementation of the CFD based form factor for the both turbulence models.

The analysis is also performed for the CFD based form factors with the numerical friction lines. As can be seen in Figure 17, nearly all groups of vessels are predicted better than the standard ITTC-78 method and also the CFD form factors with the ITTC-57 line. The accuracy of the predictions for the full block vessels with LWL $>$ 320 m remained nearly the same as the predictions from the standard ITTC-78 method were already in good agreement with the speed trials. The improvement in the predictions for the medium block and medium speed vessels are doubled on average and the low block vessel indicates a gain in accuracy when the CFD based from factors with NFL are used compared to using the ITTC-57 line.

The full block vessels with 220 m < LWL < 280 m are also predicted better on average with the numerical friction line than other extrapolation methods. Considering that the form factors for the vessels in this group are nearly the same for EFD and CFD when the ITTC-57 line is used, it is significant to investigate why such an improvement is observed. When the CFD based form factors are obtained for the ITTC-57 line and the NFL, the same computation is used for a test case and turbulence model. This leads to variations in the full scale resistance predictions even when the same turbulence model is used. The origin of such variations is explained by the difference

1. between the form factor predictions as the C_{FM} values are significantly different in model scale between the friction lines [30].
2. in the model scale viscous resistance, C_{VM}, except at the *Rn* for which the simulation is performed and the form factors are obtained from. Note that C_{VM} at the model scale are calculated as $C_{VM} = (1 + k)C_{FM}$ and the slope of the ITTC-57 line and the numerical friction lines are different.
3. in the residual resistance (see Equation (2)) due to different C_{VM} values.
4. in the full scale viscous resistance of the smooth hull since it is calculated as $C_{VS} = (1 + k)C_{FS}$, where the form factors are substantially different for different friction lines, but the C_{FS} values are highly similar for the ITTC-57 line and the numerical friction lines in full scale as demonstrated in Korkmaz et al. [30].
5. in the correlation allowance (see Equation (4)) which is only included in the calculation of full scale resistance when ITTC-57 line as explained in Section 2.

The full scale resistance components explained above in the items 3 to 5 have varying effects on the final predictions as the main dimensions of each hull and its operational conditions such as *Re* and *Fn* are different. In Figure 18a, the difference between the full scale resistance predictions using the CFD based form factors with the EASM turbulence model but with different friction lines are presented. This difference is calculated as $((C_{TS}(NFL)/C_{TS}(ITTC57) - 1)*100)$ where the friction line used for the prediction of C_{TS} is indicated in brackets. In order to simplify the visualization and evaluation, the speed C_{TS} curve of each test case is averaged. As seen in Figure 18a, the difference between the average total resistance of the predictions made with the NFL and the ITTC-57 shows a linear trend when plotted against L_{WL}. At around $L_{WL} = 240$ m, the total resistance predictions of both friction lines intersect, the vessels shorter than 240 m are under-predicted, and the ships longer than 240 m are over predicted up to 6% by the application of the numerical friction lines compared to using the ITTC-57 line.

Among the possible sources of the trend observed in the total resistance predictions, the full scale viscous resistance (the roughness and correlation allowances summed with $(1 + k)C_{FS}$) is identified as the main contributor. The comparison of C_{VS} for the rough hulls are calculated in a similar fashion to the C_{TS} comparison and presented in Figure 18b. It can be noticed that the trends for the difference between the predictions made with the NFL and the ITTC-57 line are highly similar for C_{TS} and C_{VS}, which is by far the biggest resistance component when combined with roughness and correlation allowances. The comparison between Figure 18b,c also suggests that the difference in the C_R when NFL and ITTC-57 line are used indeed has a noticeable effect on the total resistance, but it is limited when compared to the contribution of the viscous resistance.

The full scale viscous resistance for the smooth hull ($C_{VS} = (1 + k)C_{FS}$) could not have been the reason behind the trend observed in Figure 18b,c because the slope of C_{FS} curves for NFL and ITTC-57 line are highly similar at the Reynolds numbers that most of the conventional ships operate. Following this statement and the previous arguments, no other part of the extrapolation is left but the roughness allowance [10] and the correlation allowance as in Equation (4). In Figure 18c, the proportion of the $\Delta C_F + C_A$ and ΔC_F in the full scale total resistance of the each test case are presented for the predictions with the ITTC-57 line and the NFL, respectively. The contribution of the roughness allowance to the total resistance varies between 4% to 7% when NFL is used. However, the usage of the ITTC-57 line led 7% to 11.5% of the total resistance to be constituted by $C_F + C_A$.

The formulation of the C_A in Equation (4) is dependent on *Re* and clearly explains the trends observed in Figure 18c. The relationship observed in Figure 18b for the full scale viscous resistance including the roughness and correlation allowance is a direct result of the contribution of the C_A in Equation (4), which propagated into the full scale total resistance seen in Figure 18c.

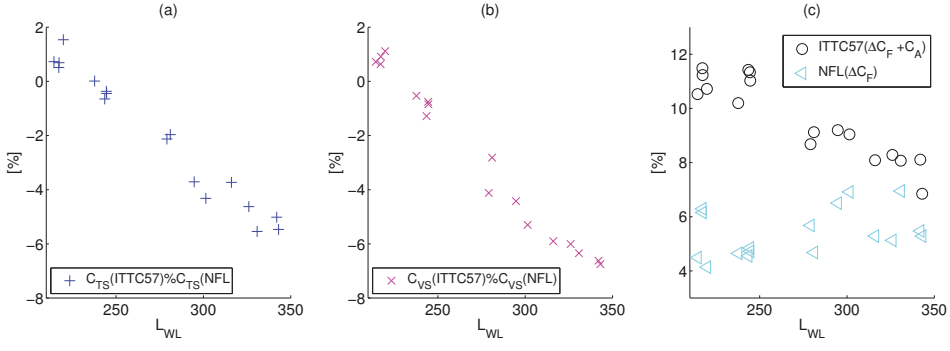

Figure 18. Difference between the (**a**) C_{TS}, (**b**) C_{VS} (including $\Delta C_F + C_A$), and (**c**) $\Delta C_F + C_A$ predictions using the CFD based form factors with the EASM turbulence model and different friction lines.

Going back to the discussion on correlation of the predictions and the speed trials for the full block vessels with 220 m < LWL < 280 m, it can be stated that the full scale resistance predictions vary 0 to 2% as a result of using different friction lines with CFD based form factors. Therefore, the improvement due to using NFL as presented in Figure 17 is arguably due to the combination of the changes in resistance predictions and also as a result of the overall changes in the whole population (shift in the median of the $C_P^{'}$ of all speed trials).

As explained in this section, the full scale speed-power-rpm relations between speed trials and full scale predictions using CFD based form factors can be improved compared to the standard ITTC-78 prediction method. This conclusion is confirmed for the different populations of speed trials where the trials were filtered through varying uncertainty indices as shown in Table 3. Using the numerical friction lines derived by Korkmaz et al. [30], correlation between the predictions and the speed trials are further improved in general. The difference in the predictions when the NFL and the ITTC-57 line is used with the CFD based form factors largely originates from the correlation allowance recommended by ITTC [20]. The correlation allowance was omitted when the numerical friction lines were used in the extrapolations since it is only fit to be used in combination with the ITTC-57 line. As a result of omitting the C_A term, the predictions are significantly improved for the 18 test cases. However, this may not be the case for the ships that are shorter than the test cases considered in this study because of the way the C_A term [20] is formulated. Since the C_A is a logarithmic function of the Reynolds number, the contribution of C_A increases rapidly with decreasing *Re*, i.e., the shorter vessels. At lower Reynolds numbers than the ones investigated in this study, it may be desirable to have new C_A in combination with the roughness allowance derived for the numerical friction lines to sustain the improvements. Therefore, the conclusions regarding the CFD based form factor method explained in this study is limited to the ships with $1.05 \times 10^9 < Re$ and 200 < L_{WL}.

7. Conclusions

In order to respond to the need for a practical procedure for the organizations that regularly perform CFD predictions on similar cases, a new procedure of quality assurance has been proposed by the ITTC Specialist Committee of Combined CFD and EFD Methods. This study serves as an example of how the procedure can be applied in practice to a problem: CFD based form factors. The quality assurance of this practical problem is

demonstrated in three parts: the content of the Best Practice guidelines of the specific CFD code used in this study as explained in Sections 3 and 5.1.1–5.1.5, the quality Assessment of the BPG methodology through verification and validation studies presented in Section 5.1.6, and finally the demonstration of quality by the comparisons of 78 speed trials to the predictions made by combined CFD/EFD methods explained in Section 6.

In order to investigate and derive a best practice guideline for CFD based form factors, systematic variations have been applied to the CFD set-ups. The non-dimensional cell height normal to the wall, additional grid refinement at the stern, domain size, and model scale speed were analyzed in Sections 5.1.1–5.1.4 and the following observations and recommendations were made:

- Mainly as a result of grid generation strategy of SHIPFLOW, monotonic convergence of the computed resistance coefficients may not always be possible, and, therefore, sometimes leading to excessive numerical uncertainties. However, the variation of C_V between all the grids is limited and less than 1% may be indicating that non-monotonic behavior is overly penalized by the numerical uncertainty determination method in this study.
- The differences between the two finest grids are less than 0.2% except one case where the viscous pressure resistance coefficient varies significantly more compared to other test cases due to an abrupt change of grid cell formation near the stagnation point at the bulb. This indicates that, even though the grid generator of the CFD code used in this study may occasionally introduce errors, the fine grids are of good quality for CFD based form factor determination.
- In order to make sure that nearly all no-slip cells are $y^+ < 1$, the target for the average y^+ should be maximum 0.5 for the SHIPFLOW code. Due to the curvature and the boundary layer growth of conventional hulls, y^+ is likely to vary significantly when fixed first cell height is applied for all CFD codes. Therefore, similar exercises are recommended for other codes when a wall resolved approach is used.
- Additional refinements added to the stern region of all the test cases had no significant impact on the predicted form factor. Therefore, additional refinements are redundant when the initial grid is fine enough.
- The variation of the domain size had extensive consequences on the computed resistance coefficients for SHIPFLOW. However, other CFD codes are expected to experience similar issues as the main reason was identified as the change in the turbulence quantities when the distance between the inlet boundary and the fore-perpendicular of the hull is increased.
- The investigations on the local skin friction coefficient, C_f, indicated that the flow is not all fully turbulent. The transition of flow in CFD occurred not later than the location where the turbulence stimulators are fitted in the model tests, making sure that the modeling errors due to different flow characteristics between CFD and EFD are negligible. Since the numerical methods, types of boundary conditions, and initial turbulence quantities (turbulent dissipation rate, turbulence kinetic energy) vary for each code, it is recommended that similar investigations should be performed for each code.
- The speed dependency of the form factors with the ITTC-57 line can be clearly observed for all test cases. Similar trends are expected by all CFD codes as the main reason for the dependency is the ITTC-57 line rather than the numerical methods. Considering that the experimental form factor determination is not immune to the scale effects (geosim models having different form factors with the ITTC-57 line), the model tow speed for CFD computations should be chosen with respect to the typical model sizes of the validation data.
- The application of numerical friction lines of the same code and turbulence model to the CFD based form factor determination, the speed dependency is nearly eliminated in all cases but one that is exhibiting mild flow separation. As the *Re* is increasing, the separation region is reduced; hence, the form factor changes as expected. According

to the form factor approach of Hughes [6], there shall be no flow separation to ensure its validity. Therefore, for the cases where flow separation is observed, higher *Re* numbers should be used for the simulations regardless of the friction line used.
- The turbulence modeling is the largest source of modeling error for the form factor determination. The form factor predictions of all test cases from the $k-\omega$ SST model are approximately 10% higher than the EASM with the same grid.
- All variations to the CFD setting were performed for both turbulence models ($k-\omega$ SST and EASM). The conclusions regarding to the other CFD settings are valid for both turbulent models.

In the second step of the proposed quality assurance procedure, verification and validation of the CFD based form factor method were performed. Experimental uncertainties of the six test cases were determined and the uncertainties on the form factors were derived. The following conclusions were made for the verification and validation studies:

- The validation in model scale indicated that the comparison error is below the noise level for all test cases with the $k-\omega$ SST turbulence model. Except for one test case with EASM, validation is achieved at the U_V level for simulations using the EASM turbulence model. However, these findings are rather inconclusive due to very large numerical uncertainties in two test cases.
- The comparison between experimental uncertainty and the comparison error of CFD based form factors showed that the form factor predictions made with the $k-\omega$ SST model are within the experimental uncertainty for the same number of test cases as with the EASM turbulence model, but the $k-\omega$ SST model is better at predicting the ballast loading condition while EASM is better for the design and scantling loading conditions.

The last step of the of the proposed quality assurance procedure, demonstration of quality, was performed by investigating the full scale speed-power-rpm relations between the speed trials and the full scale predictions based on different extrapolation methods but using the same model test data. In total, 18 test cases were simulated using the best practice guidelines presented in this study and CFD based form factors were determined. The conclusions regarding the comparison of the full scale predictions and speed trials are that:

- The sample size of the sea trials is large enough to rank the extrapolation methods as varying the population of speed trials led to the same conclusions.
- The scatter of the correlation factors for the power prediction, $C_P^{'}$, is higher with the standard ITTC-78 method, where the form factors are obtained from the Prohaska method, than the extrapolation methods where the form factor is obtained from CFD with the EASM turbulence model and with the $k-\omega$ SST in combination with the NFL. The opposite trend is observed for the shaft rate. However, the prediction accuracy of the correlation factors for the propeller turning rate is significantly higher than $C_P^{'}$ and the increase in the scatter of $C_N^{'}$ is smaller than the gains in power predictions when CFD based form factors are used.
- Compared to the standard ITTC-78 method, the standard deviation of the normalized $C_P^{'}$ is lower when the CFD based form factors are used with the EASM turbulence model.
- The CFD based form factors from the $k-\omega$ SST model led to negative or too small C_R values in some test cases as a result of the over-predicted form factors. Additionally, the scatter of $C_P^{'}$ are higher when the $k-\omega$ SST model is used in comparison with the EASM turbulence model.
- The usage of CFD based form factors with the EASM turbulence model in combination with the ITTC-57 line improves the predictions for the medium block, medium speed hulls noticeably, while the prediction accuracy remained the same for the other types of ships in comparison with the prediction from the standard ITTC-78 method.

- The most promising method out of the five investigated extrapolation methods is the CFD based form factors using the EASM turbulence model and the NFL. It reduces the standard deviation of $C_P^{'}$ and decreases the number of predictions with larger errors than 10%, while the number of predictions with errors less than 5% are increased significantly.
- The main contributor of the standard deviation of $C_P^{'}$ originates from the scatter of the speed trials among the sister ships. The standard deviation of $C_P^{'}$ is close to the minimum value that could be obtained from the speed trial data set when the CFD based form factors are used with the EASM turbulence model and the NFL.
- The group of vessels that improved most in prediction accuracy are the medium block and medium speed ($0.17 < Fn < 0.20$) ships which are typical difficult cases for the form factor determination using the Prohaska method.

Following the proposed quality assurance procedure, the CFD based form factor method has been investigated. As a result of the systematic variations applied to the CFD settings, a best practices guideline was derived for the CFD based form factor method. Using the BPG, form factor predictions have been made for a variety of ship types. The investigation on the correlations between the full scale power predictions and speed trials showed that the CFD based form factors can be considered as an alternative or supplementary method to the Prohaska method. As explained, the selection of friction lines in combination with CFD based form factors played a prominent role towards reducing the scatter between the predictions and trials. However, the change of the friction line would also require altering the well accustomed correlation factors.

It is worth remembering the statement of Gilbert Dyne who was the mastermind behind the ITTC 1978 Power Prediction Method: "It is ... relatively easy to criticise the different details of the...ITTC method. It is much more difficult to find an alternative which gives better power and RPM predictions" Lindgren and Dyne [52] (p. 14).

As stated by Dr. Dyne, there are still shortcomings with full scale resistance predictions. However, the combination of EFD and CFD is expected to provide immediate improvements to the 1978 ITTC Performance Prediction Method. Further studies should be performed with many more test cases to be used for the comparison of speed trials and power predictions with the CFD based form factors as the uncertainty of the speed trials are rather large.

Author Contributions: Conceptualization, K.B.K., S.W., and R.B.; methodology, K.B.K., S.W., and R.B.; validation, K.B.K.; formal analysis, K.B.K.; investigation, K.B.K., S.W., and R.B.; data curation, K.B.K.; writing—original draft preparation, K.B.K.; writing—review and editing, K.B.K., S.W., and R.B.; visualization, K.B.K.; supervision, S.W. and R.B.; project administration, S.W.; funding acquisition, S.W. All authors have read and agreed to the published version of the manuscript.

Funding: This research was funded by VINNOVA, the Swedish Governmental Agency for Innovation Systems, grant 2017-02953, and the computational resources provided by Chalmers Center for Computational Science and Engineering (C3SE).

Conflicts of Interest: The authors declare no conflict of interest. The funders had no role in the design of the study; in the collection, analyses, or interpretation of data; in the writing of the manuscript, or in the decision to publish the results.

References

1. Larsson, L.; Raven, H.C. *Ship Resistance and Flow*; The Society of Naval Architects and Marine Engineers: Jersey City, NJ, USA, 2010.
2. IMO. *Annex 19: Resolution MEPC.203(62)*; International Maritime Organization: London, UK, 2011.
3. ITTC. *D. Skin Friction*; International Conference of Ship Tank Superintendents: London, UK, 1948.
4. ITTC. *Subjects 2 and 4 Skin Friction and Turbulence Stimulation*; International Towing Tank Conference: Madrid, Spain, 1957.
5. Prohaska, C.W. A Simple Method for the Evaluation of the Form Factor and Low Speed Wave Resistance. In Proceeding of the 11th ITTC, Tokyo, Japan, 11–20 October 1966.

6. Hughes, G. *Friction and Form Resistance in Turbulent Flow, and a Proposed Formulation for Use in Model and Ship Correlation*; National Physical Laboratory: London, UK, 1954; Volume 96.
7. Bowden, B.S.; Davison, N.J. *Resistance Increments Due to Hull Roughness Associated with form Factor Extrapolation Methods*; National Physical Laboratory: London, UK, 1974.
8. ITTC. *Report of Performance Committee*; International Towing Tank Conference: Ottawa, ON, Canada, September 1975.
9. ITTC. *Report of Performance Committee*; International Towing Tank Conference: Hague, The Netherlands, 3–10 September 1978.
10. Townsin, R.L.; Dey, S.K. The Correction of Roughness Drag with Surface Characteristics. In Proceedings of the International Workshop on Marine Roughness and Drag, RINA, London, UK, 29 March 1990.
11. ITTC. Report of Power Performance Committee. In Proceedings of the International Towing Tank Conference, Madrid, Spain, 16–22 September 1990.
12. ITTC. *1978 ITTC Performance Prediction Method*; ITTC: Copenhagen, Denmark, 2014.
13. Michell, J. The wave resistance of a ship. *Philos. Mag.* **1898**, *45*, 106–123. [CrossRef]
14. Larsson, L. Will Computational Fluid Dynamics Completely Take the Role of Model Testing? In Proceedings of the 11th WEMT International Conference: The West European Maritime Industry in the Global Challenge of the Next, Century, Rotterdam, The Netherlands, 12–14 May 1998.
15. Larsson, L.; Stern, F.; Visonneau, M. *Numerical Ship Hydrodynamics: An Assessment of the Gothenburg 2010 Workshop*; Springer: Dordrecht, The Netherlands, 2014. [CrossRef]
16. Hino, T.; Stern, F.; Larsson, L.; Visonneau, M.; Hirata, N.; Kim, J. *Numerical Ship Hydrodynamics: An Assessment of the Tokyo 2015 Workshop*; Springer International Publishing: New York, NY, USA, 2020. [CrossRef]
17. Sun, W.; Qiong, H.; Jia, S.; Jie, X.; Jinfang, W.; Guofu, H. Numerical Analysis of Full-Scale Ship Self-Propulsion Performance with Direct Comparison to Statistical Sea Trail Results. *J. Mar. Sci. Eng.* **2020**, *8*, 24. [CrossRef]
18. Niklas, K.; Pruszko, H. Full-Scale CFD Simulations for the Determination of Ship Resistance as a Rational, Alternative Method to Towing Tank Experiments. *Ocean. Eng.* **2019**, *190*. [CrossRef]
19. Ponkratov, D. 2016 Workshop on Ship Scale Hydrodynamic Computer Simulation. In Proceedings of the Loyd's Register Workshop on Ship Scale Hydrodynamics, Southampton , UK, 25 October 2016.
20. ITTC. *1978 ITTC Performance Prediction Method*; ITTC: Wuxi, China, 17–22 September 2017.
21. García Gómez, A. On the Form Factor Scale Effect. *Ocean. Eng.* **2000**, *26*, 97–109. [CrossRef]
22. Toki, N. Investigation on Correlation Lines through the Analyses of Geosim Model Test Results. *J. Jpn. Soc. Nav. Archit. Ocean. Eng.* **2008**, *8*, 71–79. [CrossRef]
23. Pereira, F.S.; Eça, L.; Vaz, G. Verification and Validation Exercises for the Flow around the KVLCC2 Tanker at Model and Full-Scale Reynolds Numbers. *Ocean. Eng.* **2017**, *129*, 133–148. [CrossRef]
24. Terziev, M.; Tezdogan, T.; Incecik, A. A Geosim Analysis of Ship Resistance Decomposition and Scale Effects with the Aid of CFD. *Appl. Ocean. Res.* **2019**, *92*. [CrossRef]
25. Wang, Z.Z.; Xiong, Y.; Shi, L.P.; Liu, Z, H. A Numerical Flat Plate Friction Line and Its Application. *J. Hydrodyn.* **2015**, *23*, 383–393. [CrossRef]
26. Dogrul, A.; Song, S.; Demirel, Y.K. Scale effect on ship resistance components and form factor. *Ocean. Eng.* **2020**, *209*, 107428. [CrossRef]
27. Korkmaz, K.B.; Werner, S.; Bensow, R. Investigations for CFD Based Form Factor Methods. In Proceedings of the Numerical Towing Tank Symposium (NuTTS 2019), Tomar, Portugal, 29 September–1 October 2019.
28. Korkmaz, K.B.; Werner, S.; Sakamoto, N.; Queutey, P.; Deng, G.; Yuling, G.; Guoxiang, D.; Maki, K.; Ye, H.; Akinturk, A.; et al. CFD Based Form Factor Determination Method. *Ocean. Eng.* **2021**, *220*, 108451. [CrossRef]
29. Wang, J.B.; Yu, H.; Feng, Y. Feasible Study on Full-Scale Delivered Power Prediction Using CFD/EFD Combination Method. *J. Hydrodyn.* **2019**, *31*. [CrossRef]
30. Korkmaz, K.B.; Werner, S.; Bensow, R. Numerical Friction Lines for CFD Based Form Factor Determination Method. In Proceedings of the VIII International Conference on Computational Methods in Marine Engineering MARINE 2019, Göteborg, Sweden, 13–15 May 2019.
31. Broberg, L.; Regnström, B.; Östberg, M. *SHIPFLOW Users Manual*; FLOWTECH International AB: Gothenburg, Sweden, 2014.
32. Deng, G.; Visonneau, M. Evaluation of eddy-viscosity and second-moment turbulence closures for steady flows around ships. In Proceedings of the 21st ONR Symposium on Naval Hydrodynamics,Trondheim, Norway, 24–28 June 1996; pp. 453–469.
33. Menter, F.R. Two-equation eddy-viscosity turbulence models for engineering applications. *AIAA J* **1994**, *32*, 1598–1605. [CrossRef]
34. Regnström, B. *Introduction to Overlapping Grids in SHIPFLOW*; FLOWTECH International AB: Gothenburg, Sweden, 2008.
35. Hellsten, A. Some improvements in Menter's k-omega SST turbulence model. In Proceedings of the 29th AIAA, Fluid Dynamics Conference, Albuquerque, NM, USA, 15–18 June 1998. [CrossRef]
36. ITTC. *Preparation, Conduct and Analysis of Speed/Power Trials*; ITTC: Wuxi, China, 17–22 September 2017.
37. ISO. *Ships and Marine Technology—Guidelines for the Assessment of Speed and Power Performance by Analysis of Speed Trial Data*; ISO: Geneva, Switzerland, 2015.
38. Eça, L.; Hoekstra, M. A procedure for the estimation of the numerical uncertainty of CFD calculations based on grid refinement studies. *J. Comput. Phys.* **2014**, *262*, 104–130. [CrossRef]
39. Eça, L.; Hoekstra, M. The Numerical Friction Line. *J. Mar. Sci. Technol. Mar. Sci. Technol.* **2008**, *13*, 328–345. [CrossRef]

40. Eça, L.; Pereira, F.S.; Vaz, G. Viscous flow simulations at high Reynolds numbers without wall functions: Is $y^+ \simeq 1$ enough for the near-wall cells? *Comput. Fluids* **2018**, *170*, 157–175. [CrossRef]
41. Schlichting, H.; Gersten, K. *Boundary-Layer Theory*; Springer: Berlin/Heidelberg, Germany, 2000.
42. Raven, H.C.; van der Ploeg, A.; Starke, A.R.; Eça, L. Towards a CFD-based prediction of ship performance—Progress in predicting full-scale resistance and scale effects. *Int. J. Marit. Eng.* **2008**, *150*, 31–42.
43. Van, S.H.; Ahn, H.; Lee, Y.Y.; Kim, C.; Hwang, S.; Kim, J.; Kim, K.S.; Park, I.R. Resistance Characteristics and Form Factor Evaluation for Geosim Models of KVLCC2 and KCS. In Proceeding of 2nd International Conference on Advanced Model Measurement Technology for EU, Newcastle upon Tyne, UK, 4–5 April 2011, pp. 282–293.
44. ITTC. *Uncertainty Analysis in CFD Verification and Validation Methodology and Procedures*; ITTC: Wuxi, China, 17–22 September 2017.
45. ITTC. General Guideline for Uncertainty Analysis in Resistance Tests. In Proceedings of the ITTC—Recommended Procedures and Guidelines, 7.5–02.02–02, Revision 02, Copenhagen, Denmark, 31 August–5 September 2014.
46. ITTC. Practical Guide for Uncertainty Analysis of Resistance Measurement in Routine Tests. In Proceedings of the ITTC—Recommended Procedures and Guidelines, 7.5–02.02–02.2, Revision 00, Copenhagen, Denmark, 31 August–5 September 2014.
47. York, D.; Evensen, N.; Ló, M.; Nez, M.; De, J.; Delgado, B. Unified equations for the slope, intercept, and standard errors of the best straight line. *Am. J. Phys.—Am. Phys.* **2004**, *72*. [CrossRef]
48. Werner, S.; Gustafsson, L. Uncertainty of Speed Trials. In Proceedings of the HullPIC 2020, Hamburg, Germany, 26–28 October 2020.
49. Insel, M. Uncertainty in the analysis of speed and powering trials. *Ocean. Eng.* **2008**, *35*, 1183–1193. [CrossRef]
50. ITTC. Guidelines on the determination of model-ship correlation factors. In Proceedings of the ITTC—Recommended Procedures and Guidelines, 7.5-04-05-01, Revision 0, Wuxi, China, 17–22 September 2017.
51. ITTC. *Report of Propulsion Committee*; ITTC: Seul, Korea; Shanghai, China, 5–11 September 1999.
52. Lindgren, H.; Dyne, G. Ship Performance Prediction. In Proceedings of the International Symposium on Advances in Marine Technology, Trondheim, Norway, June 1979.

Journal of *Marine Science and Engineering*

MDPI

Article

Numerical Investigation on Hydrodynamic Characteristics of Immersed Buoyant Platform

Jinjiang Yao, Xingwei Zhen *, Yi Huang and Wenhua Wang

School of Naval Architecture and Ocean Engineering, Dalian University of Technology, Dalian 116024, China; yjj294980436@163.com (J.Y.); huangyi@dlut.edu.cn (Y.H.); wangwenhua0411@163.com (W.W.)
* Correspondence: zhenxingwei@dlut.edu.cn

Abstract: The Next Generation Subsea Production System (NextGen SPS) is considered as a competitive alternative system used for offshore petroleum production in ultra-deep sea based on the artificial seabed technology. The Immersed Buoyant Platform (IBP), which is located at a constant depth below the free surface of the water to minimize wave loading, provides a buoyant stable platform for supporting the well completion equipment. Therefore, the hydrodynamic characteristics of IBP in the currents play an essential role in determining the global responses of NextGen SPS. In this paper, aiming at acquiring an optimum structural form of IBP, the hydrodynamic characteristics of the flow past the cylindrical IBP with different height-to-diameter ratios are systematically investigated by use of the large eddy simulation (LES) approach. The simulations with fifteen different height-to-diameter ratios (H/D) are investigated. The Reynolds numbers are ranged from 0.94×10^6 to 3.45×10^6. It can be verified that the separated fluid reattaches on the surface of the cylinder when the aspect ratio is between 0.1 and 0.4. Due to the specific shape ratio and obvious 3D effect of the cylindrical IBP, no significant vortex shedding has been clearly observed when the aspect ratio is between 0.1 and 0.4. In the case of $0.4 \leq H/D \leq 5.0$, a series of regular and alternating vortex street shedding appear behind the circular cylinder. The simulation results also show that the recirculation region length behind the cylindrical IBP can be significantly reduced with the decreasing aspect ratio. It can be concluded that the cylindrical IBP performs the best hydrodynamic characteristics when the aspect ratio is between 0.3 and 0.4. The research findings will be of great significance to providing valuable reference and foundation to determine the optimum form of underwater structures, such as the buoyancy cans of the hybrid riser system.

Keywords: next generation subsea production system; Immersed Buoyant Platform; hydrodynamic characteristics; ultra-deep sea

Citation: Yao, J.; Zhen, X.; Huang, Y.; Wang, W. Numerical Investigation on Hydrodynamic Characteristics of Immersed Buoyant Platform. *J. Mar. Sci. Eng.* **2021**, *9*, 168. https://doi.org/10.3390/jmse9020168

Academic Editor: Yigit Kemal Demirel
Received: 31 December 2020
Accepted: 2 February 2021
Published: 6 February 2021

1. Introduction

1.1. Background

Currently, offshore oil exploration is gradually developing into ultra-deep sea. Therefore, innovative ocean engineering equipment are naturally required to deal with the great challenges brought by extreme depth and severe environment in ultra-deep sea. In this scenario, Zhen et al. [1,2] put forward the NextGen SPS concept, which can be used to conduct as the Subsurface Well Completion (SWC) system for offshore petroleum production in ultra-deep sea. IBP as the key equipment of this system provides a buoyant stable platform, which is located at 300 m below the mean water level to minimize direct wave loading. Thus, the form of the IBP has an critical effect on the hydrodynamic loads that act on the IBP from current. The initial form of the IBP is circular cylinder. However, it is widely believed that the aspect ratio of the circular cylinder has the main impact on the vortex shedding and the forces acting on cylinders. The drag force, lift force and Strouhal number, which define the hydrodynamic characteristics, vary with the aspect ratio.

NextGen SPS [3] is an innovative concept that can be used to implement the extraction and exporting of subsea oil. This system mainly consists of the following four parts:

the IBP that is tethered perpendicularly, SWC equipment, flexible jumpers and rigid risers, as shown in Figure 1. The IBP supplies a buoyant stable platform for carrying the SWC equipment and rigid risers. The IBP [4] is located at a constant depth below the free surface of the water to minimize wave loading and reduce the influence of surface flow field. In addition, the IBP is jointed to the Floating Production Unit (FPU) through flexible jumpers. Flexible jumpers play the role of decoupling the IBP from the motion of FPU with the shape of catenary.

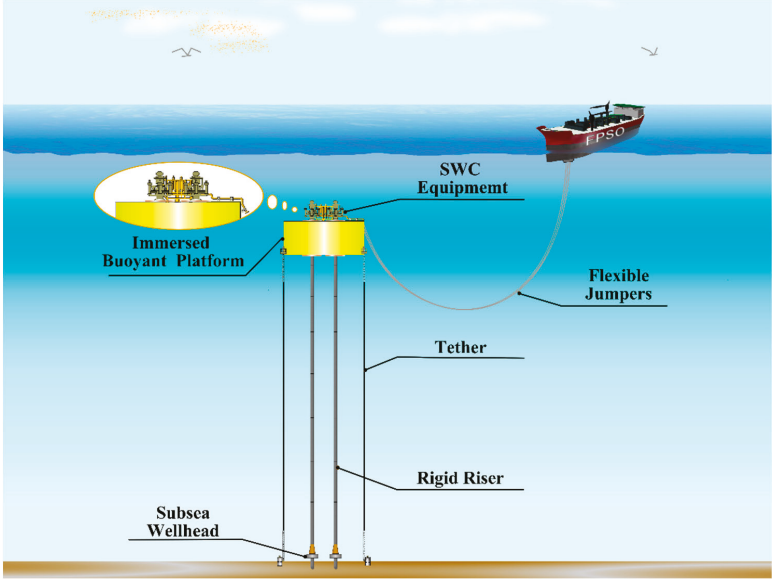

Figure 1. Sketch of the NextGen SPS.

The mooring system [5] of NextGen SPS consists of four vertically tensioned mooring ropes, which are fixed in the seabed by suction piles. The mooring system provides the stability of the IBP and reduces the tension forces on rigid risers.

As mentioned above, the NextGen SPS offers specific advantages as follows:

(1) The presence of the IBP takes up the huge riser loads and reduces the dynamic loads and the main dimensions of FPU.

(2) The IBP is located at a constant depth below the free surface of the water to circumvent the surface wave and flow.

(3) The joint production of multiple wells on the seabed can be implemented.

(4) The existence of the flexible jumpers reduces the fatigue damage of the structure.

(5) The SWC is mounted on the IBP, which reduces the requirements of the capability for the SWC.

(6) Under extreme sea conditions, the FPU can be disengaged from the IBP quickly to enhance the security of production.

As we can see, the IBP is the most important part of the NextGen SPS. The structural form of the IBP has great influence on the hydrodynamic performance of the system. With regard to the best hydrodynamic behavior of such novel concept, the IBP has been developed featuring cylindrical shape. However, the height-to-diameter ratio of the cylindrical buoy needs to be ascertained and investigated, because the height-to-diameter ratio of the circular cylinder will affect the distribution of wake field and the forces acting on the cylinder. With this background, there is a strong need to study the hydrodynamic behavior of the circular cylinders with different aspect ratios in order to acquire the optimum structural form of the IBP.

1.2. Relevant Research Works and Objective

There are many factors that affect the wake of the circular cylinder, vortex shedding is one of the most significant characteristics which can affect the vibration of the structures. Many researchers have done lots of studies to explore the mechanism of vortex shedding and the wake characteristics. Naudascher and Wang [6] classified and defined vortex shedding generated behind the structures as three types when the direction of the incident flow was zero. However, the aspect ratio of the circular cylinder is the most predominant factor affecting the vortex shedding and the distribution of pressure on the surface of cylinder. In experiments, one of the most important experiments was conducted by Adaramola et al. [7] to study the wake field of circular cylinders with four different aspect ratios. They found that the characteristics of wake were similar when the aspect ratio was 9, 7 and 5, respectively. However, in the case of the aspect ratio of the cylinder was 3, the wake structure was apparently different. Krajnović [8] studied the near wake flow, far wake flow and vortex shedding of the circular cylinder with aspect ratio of 6. He found that the vortices formed behind the cylinder were unstable, and their shape changed as time went on. Okamoto and Yagita [9] measured the surface pressure distributions in order to gain the drag coefficient, by varying the aspect ratio from 1 to 12.5. It is found that the position of the separation point forwarded as the aspect ratio decreased. In addition, the drag coefficient changed greatly when H/D varied from 6 to 7 because a vortex street did not appear at $H/D \leq 6$. The frequency of the vortex shedding was depended on both H/D and Reynolds number. Sakamoto and Arie [10] described experimentally the vortex shedding of the rectangular prism and the circular cylinder to study the impact of the aspect ratio on these two structures. They observed that the shape of the vortex shedding changed when the aspect ratio reached a critical value. Okamoto and Sunabashiri [11] carried out experiments to study the drag coefficient, type of vortices and the recirculation region of circular cylinders with aspect ratios of 0.5, 1, 2, 4, 7 and 23.75. The results indicated that the drag coefficient increased with the increasing aspect ratio. The vortices generated behind the circular cylinder were symmetrical when the aspect ratio was in the case of 1 and 2. It was shown that the length of the recirculation region enlarged with the increasing aspect ratio of cylinder.

At present, there are large amount of studies that are conducted to investigate the factors affecting the patterns of vortex behind the cylinder, such as the aspect ratio, the effect of free end surface and the effect of boundary layer. Wang and Zhou [12] investigated the flow structure of near wake of the square cylinder by experimental method. The aspect ratio of the cylinder ranged from 3 to 7. The results indicated that the vortex shedding behind the cylinder was greatly affected by the downwash and upwash of the free end. In addition, the length of the recirculation region varied with the aspect ratio of the cylinder. Wang et al. [13] investigated the impact of the aspect ratio on the drag force of the cylinder under two different states of subcritical and critical. They found that the drag coefficient and the Strouhal number reduced with the decreasing aspect ratio, especially when the aspect ratio was greater than 5. Tsutsui [14] studied the surface pressure distribution, flow visualization and fluid force of a cylindrical structure, by varying the aspect ratio from 0.125 to 1.0. The experimental results gave the empirical formulas of the drag coefficient and the lift coefficient by considering the boundary layer thickness and the aspect ratio.

Afgan et al. [15] investigated the velocity distribution, pressure distribution and the drag and lift forces of the cylinder when the aspect ratio was in the case of 6 and 10. They found that the influence of the downwash became more apparent when the aspect ratio was smaller. In addition, the downwash changed the pressure distribution behind the cylinder, which in turn changed the drag and lift forces of the cylinder. Gonçalves et al. [16,17] carried out experiments to show the force measurements and PIV measurements of the circular cylinders with eight different aspect ratios. It is found that the drag coefficient and the Strouhal number reduced as the aspect ratio decreased. The oscillation force caused by the vortex shedding could no longer be observed when the aspect ratio was less than 0.2. In addition, they conducted other experiments which studied the response amplitudes of the

circular cylinders with several different aspect ratios and mass ratios. They found that the transverse response reached its maximum value when the aspect ratio was 2.0 and reduced as the aspect ratio decreased. Zhao and Cheng [18] studied the effect of the aspect ratio on the response amplitude and response frequency of circular cylinders of H/D = 1, 2, 5, 10, and 20 numerically. They found that the vortex shedding was no longer observed when the aspect ratio was in the case of 1 and 2. In addition, the flow characteristics of circular cylinders with aspect ratios of 5, 10, and 20 changed a lot along the downstream direction. Yu and Kareem [19] conducted a study to analysis the velocity field and pressure field of rectangular prisms by numerical method. It was demonstrated that the reattachment of the flow occurred when the aspect ratio was in the case of 1:3 and 1:4. Yeon et al. [20] also focused on numerical method to investigate the mean flow field and instantaneous flow field of the circular cylinder. In their research, the instantaneous flow field performed more complicated for the high aspect ratio (H/D = 8). The mean flow field became messy and no vortex shedding was observed for the low aspect ratio (H/D = 2). They also found that the main reason for the variation of the drag force was the redistribution of the pressure on the surface of cylinder. Vakil and Green [21] carried out computer simulations to study the drag and lift coefficients of circular cylinders of H/D = 2, 5, 10, and 20. The results indicated that the lift coefficient increased and the drag coefficient decreased with the increasing aspect ratio when this ratio was less than 10. Rostamy et al. [22] established the PIV method to study the upstream flow field and the near wake flow field of circular cylinders of H/D = 3, 5, 7, and 9. They found that the position of reattachment of the separated flow on the surface of the cylinder varied with the aspect ratio. In addition, significant recirculation zone was observed behind the cylinder for all four aspect ratios. Lee et al. [23] modeled the flow around a cylinder with high aspect ratio and another cylinder with low aspect ratio to study the flow characteristics. The simulation results showed that the intensity of the downwash and the vortex shedding behind the high aspect ratio cylinder was much stronger than that of the low aspect ratio cylinder. Palau-Salvador et al. [24] also presented the vortex shedding, the time averaged flow and the instantaneous flow around the circular cylinder with two aspect ratios. They found that the vortex shedding was observed along the whole length of the high aspect ratio cylinder while for the low aspect ratio cylinder this phenomenon occurred only near the ground.

Although there are abundant previous works on the flows around circular cylinders with different aspect ratios, the optimal value of the aspect ratio has not been studies as yet. Few studies have been done to investigate the flow structure of the circular cylinders with excessive low aspect ratio varies from 0 to 1.0. Therefore, it is necessary to investigate the determination of the optimal value of the aspect ratio. In this scenario, the destination of this paper is to study the hydrodynamic characteristics of the circular cylinders based on NextGen SPS concept to acquire an optimum structural form of the IBP.

1.3. Arrangement of Paper

This article consists of the following parts: Section 1 presents the components and the specific advantages of NextGen SPS. Section 2 describes the numerical model and method which are used in this article in detail. In Section 3, several cases are simulated with different mesh densities for the purpose of ensuring that the mesh independent is achieved, and a comparison between the simulations of this article and the results of previous experiments is made to examine the computational accuracy. The average quantities, the vortex shedding, the flow visualization and the recirculation region length are discussed in Section 4. The main conclusions are summarized in the last section.

2. Numerical Model and Method

2.1. Governing Equations

In this work, the LES is used for the numerical simulation. In the LES approach, the large scale turbulences are spatially computed, while the small scale turbulences are

solved by the SGS model. The Navier–Stokes equations for the incompressible viscous flow can be described as:

$$\frac{\partial \overline{u_i}}{\partial t} + \frac{\partial}{\partial x_j}(\overline{u_i u_j}) = -\frac{1}{\rho}\frac{\partial \overline{p}}{\partial x_i} + \nu \frac{\partial^2 \overline{u_i}}{\partial x_j \partial x_j} - \frac{\partial \tau_{ij}}{\partial x_j} \tag{1}$$

$$\frac{\partial \overline{u_i}}{\partial x_i} = 0 \tag{2}$$

In the equations, i, j =1,2,3, ρ is the water density, t is the time, ν is the kinematic viscosity, x_i represents the streamwise direction, transverse direction and vertical direction when i is 1, 2 and 3, respectively, $\overline{u_i}$ is the velocity vector, $\overline{p}$ is the pressure, τ_{ij} represents the non-resolvable subgrid stress.

Equations (1) and (2) are the results of filtering of the Navier–Stokes equations. The filtering coefficient G is written as:

$$\overline{f}(x_i) = \int_{-\infty}^{+\infty} f(x_i')G(x_i, x_i')dx_i' \tag{3}$$

$$G(x_i, x_i') = \begin{cases} \frac{1}{V}, & x_i' \in V \\ 0, & x_i' \notin V \end{cases} \tag{4}$$

where f stands for (u, p, etc. ...), V is the size of geometric space occupied by the control volume.

The quantity $\tau_{ij}(= \overline{u_i u_j} - \overline{u_i}\,\overline{u_j})$, called subgrid scale (SGS) stress tensor, quantifies the effect of the small-scale eddies. In order to model the SGS stress tensor, the Boussinesq approximation is used:

$$\tau_{ij} - \frac{1}{3}\delta_{ij}\tau_{kk} = -2\nu_{sgs}\overline{S_{ij}} \tag{5}$$

where δ_{ij} is the Kronecker delta function and ν_{sgs} is the SGS viscosity. The τ_{kk} takes into account the pressure term. The strain rate tensor $\overline{S_{ij}}$ can be written as:

$$\overline{S_{ij}} = \frac{1}{2}\left(\frac{\partial \overline{u_i}}{\partial x_j} + \frac{\partial \overline{u_j}}{\partial x_i}\right) \tag{6}$$

where $|\overline{S}| = \sqrt{2\overline{S_{ij}}\,\overline{S_{ij}}}$.

The SGS viscosity ν_{sgs} is modeled by the following expressions:

$$\nu_{sgs} = l^2|\overline{S}| \tag{7}$$

$$l = \min(k_v y, C_s\overline{\Delta}) \tag{8}$$

$$\overline{\Delta} = (\Delta x \Delta y \Delta z)^{1/3} \tag{9}$$

where l is the mixing length for the SGS model, k_v is the von Karman constant ($k_v = 0.42$), y is the minimum distance to the wall, C_s is the Smagorinsky constant, $\overline{\Delta}$ is the filtering grid scale. The value of the Smagorinsky constant C_s is found to vary from 0.1 to 0.12 for good results of a wide range of flows. In this work of simulation, C_s was selected as 0.1 for LES of turbulence. Equations (3)–(9) mentioned above are all dimensionless. The Reynolds number is defined as $\mathrm{Re} = \rho v D/\mu$, where D is the characteristic length of the cylinder. A total of fifteen different aspect ratios of circular cylinders have been simulated in this paper. During this process, the volume of the circular cylinder remains constant. Therefore, these cylinders have different characteristic lengths and hence different Reynolds numbers. The Reynolds numbers are ranged from 0.94×10^6 to 3.45×10^6.

2.2. Numerical Scheme

In this article, the finite volume method (FVM) is used to discretize the differential equations. The PISO algorithm is proposed to correct the velocity terms and the pressure terms to guarantee the conservation of mass. The method which used for spatial discretization is the bounded central differencing scheme. The least squares cell based algorithm is used for gradient terms. In addition, the pressure and the momentum terms are second order and second order upwind, respectively. All of the schemes mentioned above remain second order accuracy. The time terms are integrated by using the implicit scheme based on the bounded second order accuracy. The bounded central differencing is used for convective terms. The convective terms in Equations (1) and (2) need to be discretized on a spatial scale. The bounded central differencing scheme is to use linear interpolation formula to calculate the physical quantity on the interface; that is, to take the arithmetic average value of the upstream and downstream nodes. This method is based on the normal variable database (NVD) and convective boundedness criterion (CBC). It is a hybrid scheme which includes pure central differencing scheme and second order upwind scheme. The PISO algorithm is proposed to correct the velocity terms and the pressure terms to guarantee the conservation of mass. Equations (1) and (2) are discretized using a finite volume method (FVM) for solving the incompressible Navier–Stokes equations. In this method, the whole computing domain is decomposed into non-overlapping control volumes, and each grid node is guaranteed to have an adjacent control body. Then, the differential equations for each control volume are solved to obtain the discrete equations. Once the governing equations have been discretized by the method described above, they can be calculated. The method which used to calculate the equation is Pressure Implicit with Splitting of Operators (PISO). The principle of this method is that in the unsteady flow calculation, when the time step is very small and the change of the value of solution at two adjacent time points is also very small, the influence of nonlinear lag can be ignored, and the coupling effect of pressure and velocity is mainly considered. The PISO algorithm including one forecast and two corrections, is a process of "forecast—correction—revising", and this method takes into account the effect of the value of revised speed of neighboring points. The results of the first revision are revised again, and the velocity field and pressure field obtained by solving the pressure correction item twice could better satisfy the continuity equation and momentum equation.

During this process, the Courant number is always remained below 0.2. The simulation flow domain is arranged as $-4 \leq x/D \leq 8$, $-2.5 \leq y/D \leq 2.5$ and $-2.5 \leq z/H \leq 2.5$, the center of gravity of the cylinder is located at $x = y = z = 0$, as shown in Figure 2a,b. A uniform flow field with the same velocity of the incoming flow is given as the initial condition of the calculation. The inflow and outflow are specified as the velocity inlet and outflow boundary conditions, respectively. No slip conditions are applied on the cylinder surface by referring to the vortex particle methods to handle the no-slip boundary conditions [25,26]. In order to guarantee the computational accuracy of the boundary layer, the grid near the surface of the cylinder is greatly refined, as shown in Figure 3a–c.

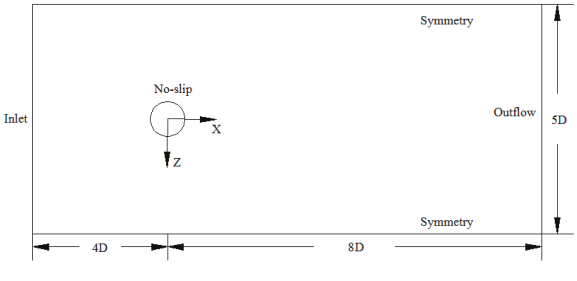

(a)

Figure 2. *Cont.*

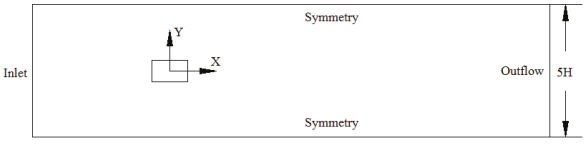

(**b**)

Figure 2. Simulation flow domain: (**a**) Top view; (**b**) Front view.

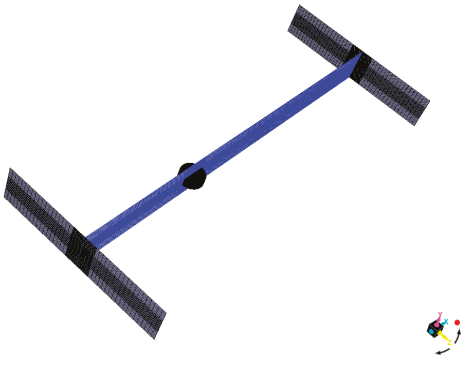

(**a**)

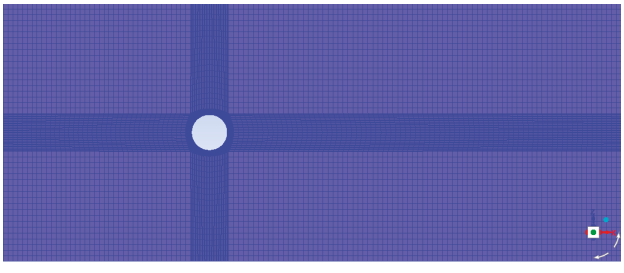

(**b**)

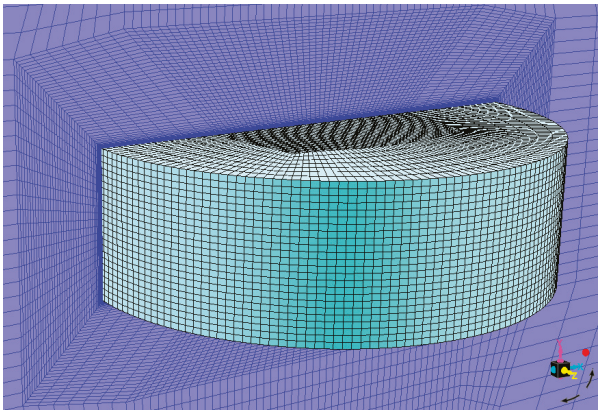

(**c**)

Figure 3. (**a**) The computational mesh; (**b**) Top view; (**c**) Detail of mesh near cylinder.

3. Mesh Independence and Validation

3.1. Mesh Independence

The definitions of the drag coefficient and lift coefficient are:

$$C_D = \frac{F_D}{\frac{1}{2}\rho U_\infty{}^2 LD} \tag{10}$$

$$C_L = \frac{F_L}{\frac{1}{2}\rho U_\infty{}^2 LD} \tag{11}$$

In the equations, D is the diameter of the cylinder, L is the length of the cylinder, U_∞ is the velocity, F_D is the drag force, F_L is the lift force.

Several cases were simulated with different mesh densities for the purpose of ensuring that the mesh independent was achieved. Five different cases were simulated with mesh numbers of approximately 150,000, 300,000, 600,000, 1,200,000 and 2,400,000. The simulated results which include computational time, comparison of the time averaged drag coefficient between simulations and experiments [27,28], relative error are exhibited in Table 1, Figures 4 and 5.

Table 1. Comparison of the computational time, the mean drag coefficient and the relative error.

Grid	Node	Computational Time (h)	$\overline{Cd}$		
			Simulation $\overline{Cd}$	Ref. [27]	Relative Error (%)
150,000	166784	54	0.513	0.56	−8.39%
300,000	322096	87	0.516	0.56	−7.86%
600,000	668376	136	0.527	0.56	−5.89%
1,200,000	1253696	192	0.538	0.56	−3.93%
2,400,000	2460496	278	0.544	0.56	−2.86%

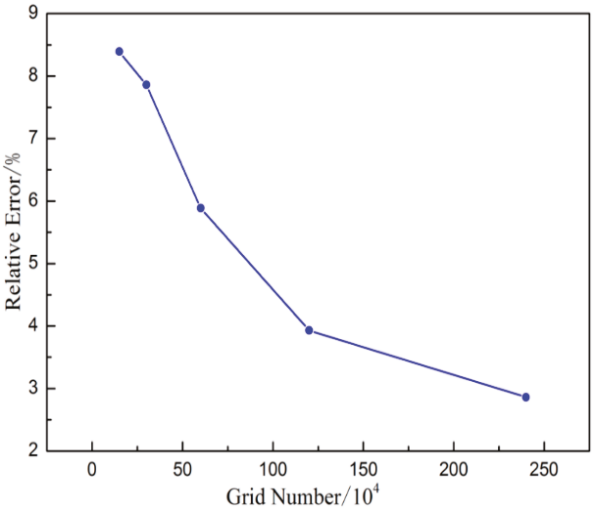

Figure 4. Effect of the grid number on computational error.

The results demonstrate that the relative error decreases as the mesh number increases, while the computational time increases significantly with increasing mesh number. As usual, the computational accuracy increases as the number of mesh increases, but the difference between the relative error of the simulation which is computed with 1.2 million mesh numbers and those computed with larger numbers of mesh is within 1.2%. Further-

more, the simulation needs to expend bigger computational costs and computational time with increasing mesh number. Therefore, the number of the mesh used in the simulations is determined between 1.2 and 2 million by considering the computational accuracy and computational time.

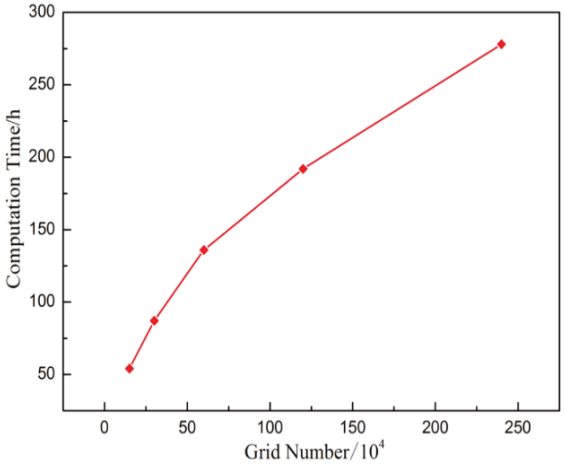

Figure 5. Effect of the grid number on computational time.

3.2. Verification

The mean drag coefficient of the circular cylinder with different Reynolds numbers was calculated in the previous literatures. For the purpose of examining the performance of the numerical simulation for circular cylinders, a comparison between the numerical results of this article and the results of previous experiments is made in Figure 6. In order to compare the difference between our numerical results and previous simulations and experiments more intuitively, the mean drag coefficients were plotted with respect to various Re numbers. The numerical results and the relative error between simulations and experiments are showed in Table 2.

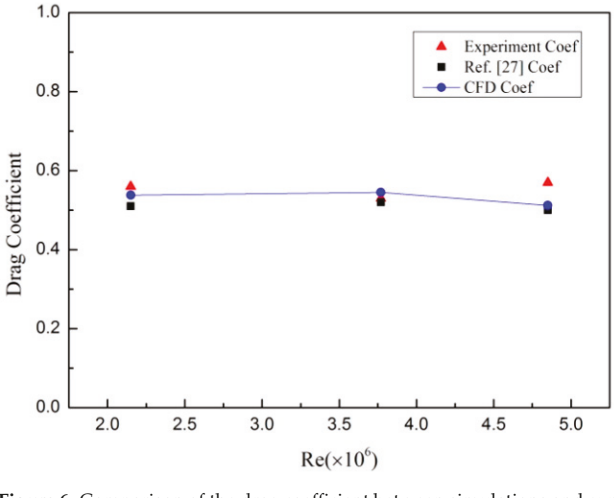

Figure 6. Comparison of the drag coefficient between simulations and experiments and previous simulations.

Table 2. Comparison of the drag coefficient between simulations and experiments and previous simulations.

$Re(\times 10^6)$	Experiments	Ref. [27]	CFD	Relative Error (%)	
				Ref. [27]	CFD
2.15	0.56	0.51	0.538	−8.93%	−3.93%
3.77	0.53	0.52	0.545	−1.89%	2.83%
4.85	0.57	0.5	0.512	−12.28%	−10.18%

In order to ensure the second order accuracy, mesh independence should be verified. As shown in Section 3.1, several cases have been simulated with different mesh densities for the purpose of ensuring that the mesh independent is achieved. The number of the mesh used in this simulation is determined between 1.2 and 2 million by considering the computational accuracy and computational time. In addition, in order to guarantee the computational accuracy of the boundary layer, the grid near the surface of the cylinder is greatly refined, as shown in Figure 3a–c. As a result, the numerical results of this article agree better with the previous experimental results. The maximum relative error between simulations and experiments is 10.18%, and the same value between simulations and previous numerical simulations is 5.49%. Furthermore, the computational error in this article has been improved comparing with the numerical simulation results in Ref. [27]. Hence, it is concluded that the schemes used in this article have good computational accuracy. In conclusion, the validity of the numerical method in this paper has been verified by the experimental and numerical results. It is concluded that the numerical method used in this article has good computational accuracy, and it is proved that this numerical method is feasible.

4. Results and Discussion

4.1. Average Quantities

The drag and lift coefficients are regarded as significant parameters that can reflect the hydrodynamic characteristics of the circular cylinder. During this process, the volume of the Immersed Buoyant Platform (IBP) remains constant and the IBP is always fixed without any movement. A total of fifteen different aspect ratios, namely H/D = 0.1, 0.2, 0.3, 0.4, 0.42, 0.5, 0.6, 0.7, 0.8, 0.9, 1.0, 2.0, 3.0, 4.0 and 5.0, have been simulated. Figure 7a,b exhibit the time averaged drag coefficient and the drag force with different aspect ratios of circular cylinder. Figure 8a,b exhibit the time averaged lift coefficient and the lift force with different aspect ratios of circular cylinder. What needs to be emphasized is that Figures 7b and 8b are the partial enlargement of Figures 7a and 8a.

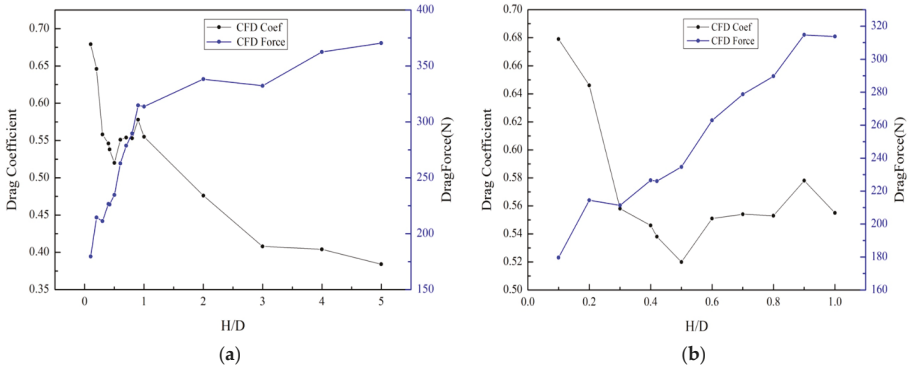

Figure 7. Time averaged drag coefficient and drag force with different aspect ratios: (**a**) the whole figure; (**b**) the partial enlargement figure.

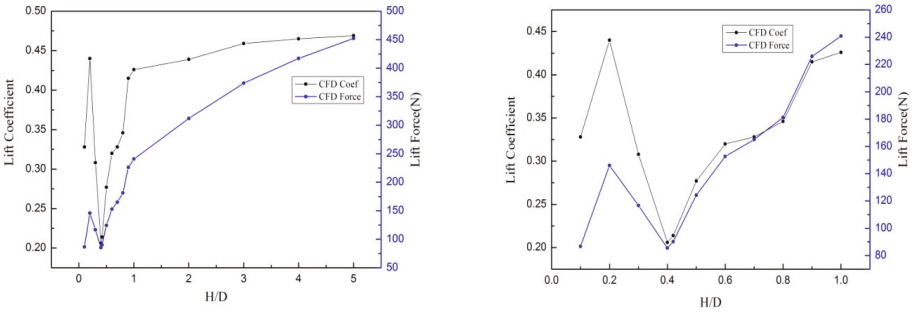

(**a**) (**b**)

Figure 8. Time averaged lift coefficient and lift force with different aspect ratios: (**a**) the whole figure; (**b**) the partial enlargement figure.

For a given H/D, the time averaged drag coefficient increases monotonically as the aspect ratio decreases, whereas the drag force decreases with decreasing the aspect ratio. The reason for decrease in the drag force is that the dynamic pressure in the wake region rises because of the downstream from the surface of the cylinder. This suggests the reattachment of flow which causes the pressure recovery of the tail end of the cylinder. In addition, spanwise vortex shedding has a pronounced impact on the drag force of the cylinder. The vortex shedding is symmetrical in the case of high aspect ratio, while the antisymmetrical ones occur with low aspect ratio. Furthermore, the fluid around the cylinder is carried to the wake region by the spanwise flow, reduces the difference of the pressure between the front and back of the cylinder and, therefore, reduces the drag force. The influence of the spanwise flow enhances gradually with decreasing the aspect ratio, which results in smaller drag forces for shorter cylinders.

It needs to be noted specifically that the change of the time averaged drag coefficient and the drag force is irregular when the aspect ratio is between 0 and 1.0. On the other hand, the time averaged lift coefficient and lift force increase gradually as the aspect ratio increases. The values of the time averaged lift coefficient and lift force reach the minimum at the same time when the aspect ratio is 0.4. Therefore, it can be concluded that the circular cylinder performs the best hydrodynamic characteristics when the aspect ratio is around 0.4.

4.2. Vortex Formation

In the following, this article studies more about the vortices generated behind the cylinder, the characteristics of the flow and the recirculation region length.

With the focus on the circular cylinder, the flow around it detaches two times. The vortices develop from the body and break away from it, generating a turbulent wake field. The structure of the flow in the wake region is affected by the Reynolds number, but the aspect ratio (H/D) has the most important influence on the vortex shedding. The flow separates from the front end of the cylinder at the first time and then moves to both sides of the cylinder. At the same time, the first level of vortices have been generated. Then, the separated flow continues to move downstream and reattaches on the surface of the circular cylinder. Under this situation, the flow separates from the trailing end of the cylinder at the second time. It results in the flow behind the cylinder oscillating violently, and generates the second level of vortices, which shed alternately. In particular, these two different kinds of vortices interact with each other [29], which causes the vortex shedding to become more complex.

Figure 9 shows the contours of vorticity in the vertical center plane at $z/D = 0$ and the horizontal center plane at $y/D = 0$ with different aspect ratios. As shown in the figure, it is concluded that the aspect ratio (H/D) has the considerable influence on the vortex

shedding. Under the condition of $0.7 \leq H/D \leq 5.0$, it is observed that only the primary separation occurs. This is due to the size of the downwash from the free end of the cylinder covering the whole length of the cylinder. The near wake field is made up of the following two parts: the downwash from the free end of the cylinder and the vortex shedding around the cylinder. In addition, the downwash from the top of the cylinder needs to go through several spirals to reach the solid wall. In this process, it will be shocked by the incoming flow from the middle part of the cylinder, thus reducing the turbulence intensity. For this reason, the downwash does not even reach the solid wall for a greater aspect ratio. Under this condition, the cylinder shows typical characteristics of three-dimensional flow around a slender cylinder. A series of regular and alternating vortex street shedding appear behind the circular cylinder. In this range of H/D, the vortices of regular shedding behind the cylinder increase the drag coefficient.

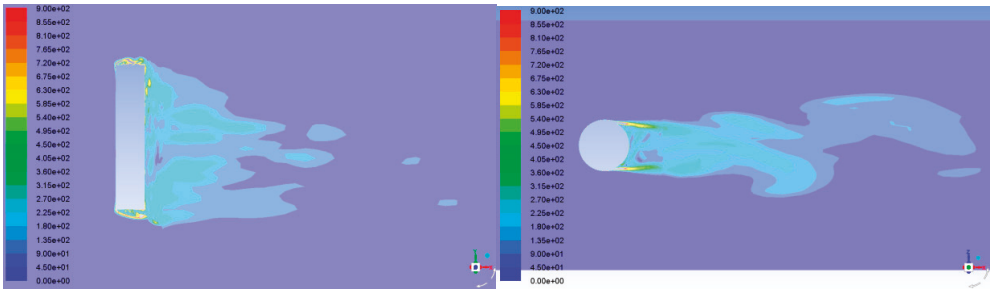

$H/D = 5$

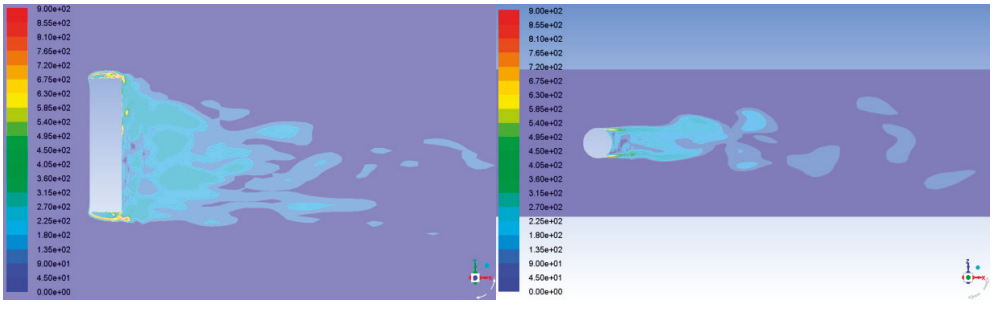

$H/D = 4$

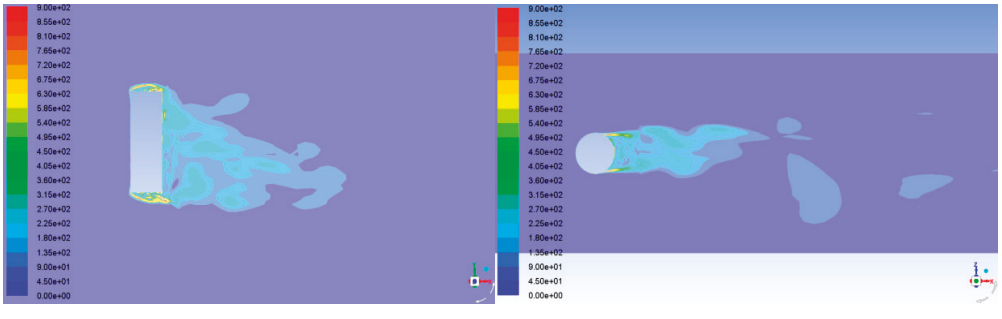

$H/D = 3$

Figure 9. *Cont.*

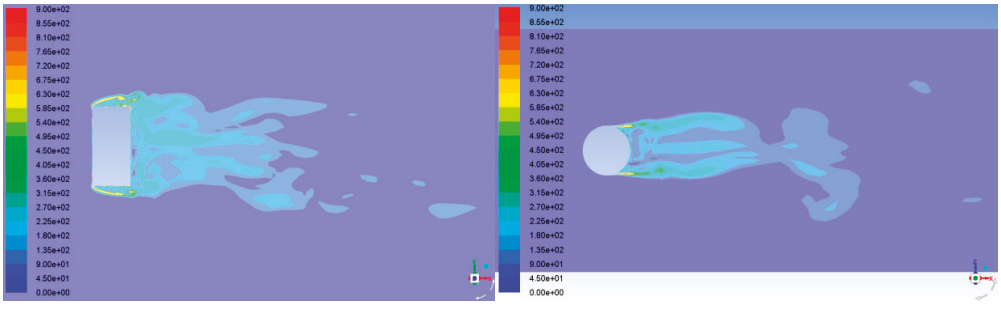

$H / D = 2$

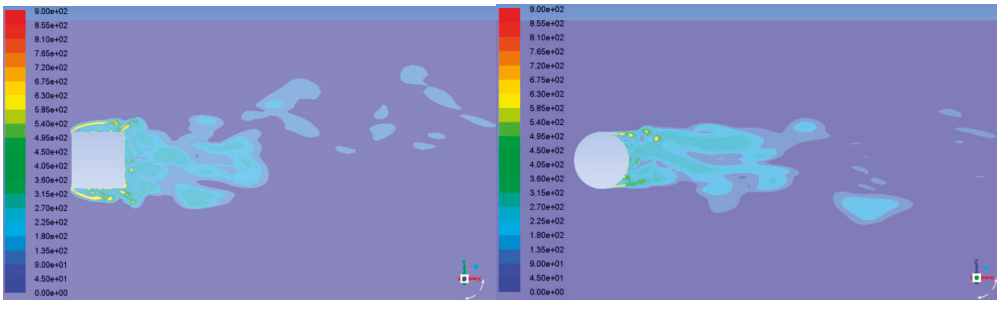

$H / D = 1$

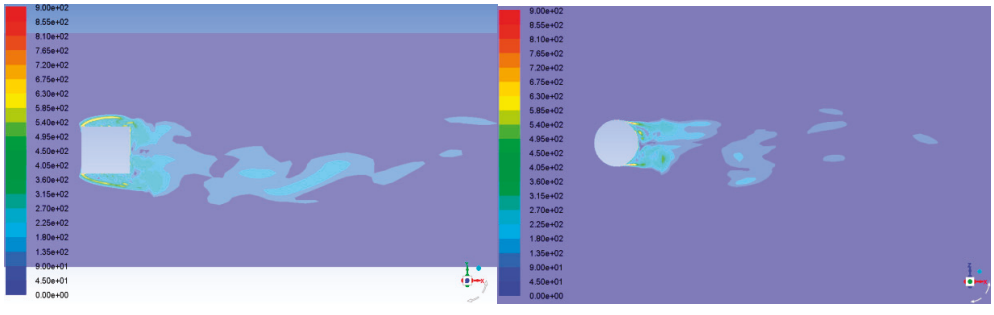

$H / D = 0.9$

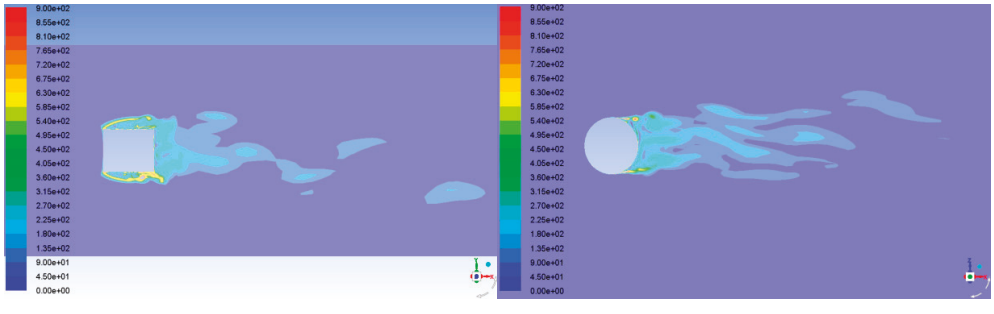

$H / D = 0.8$

Figure 9. *Cont.*

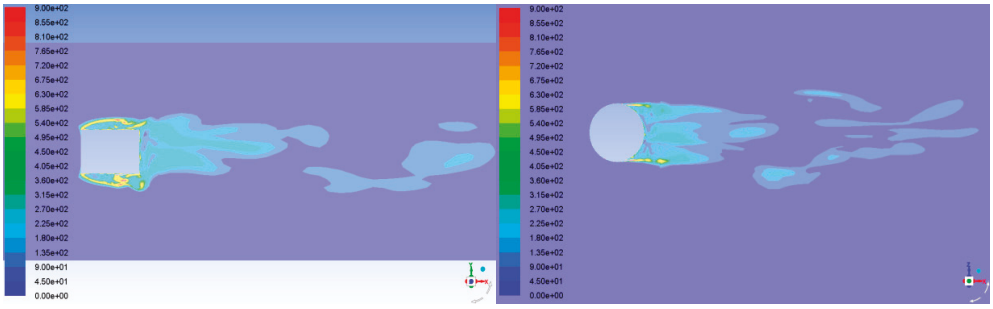

$H / D = 0.7$

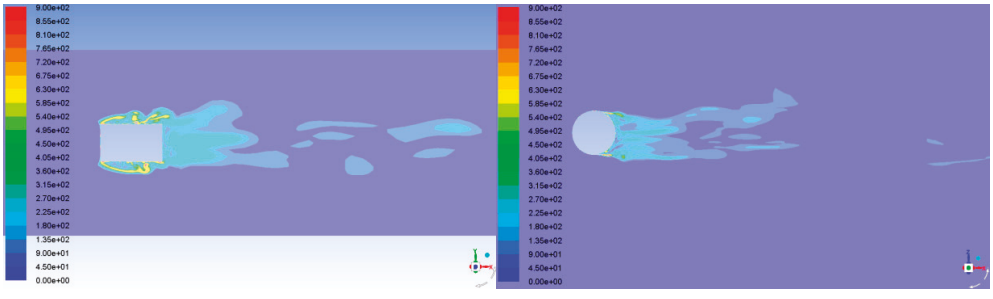

$H / D = 0.6$

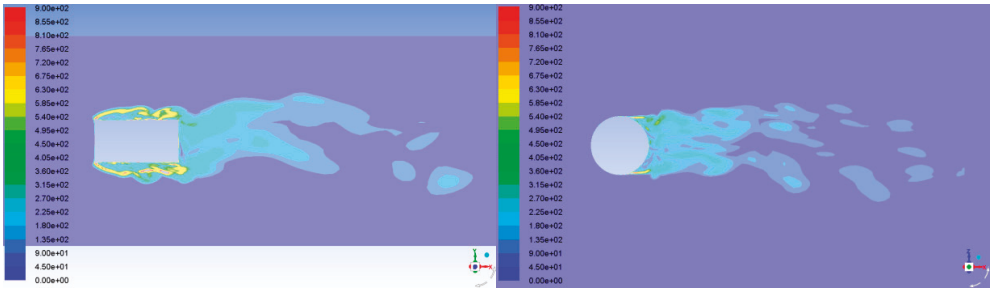

$H / D = 0.5$

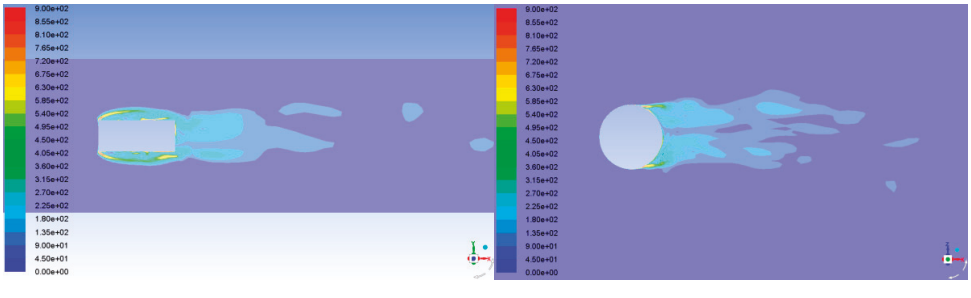

$H / D = 0.42$

Figure 9. *Cont.*

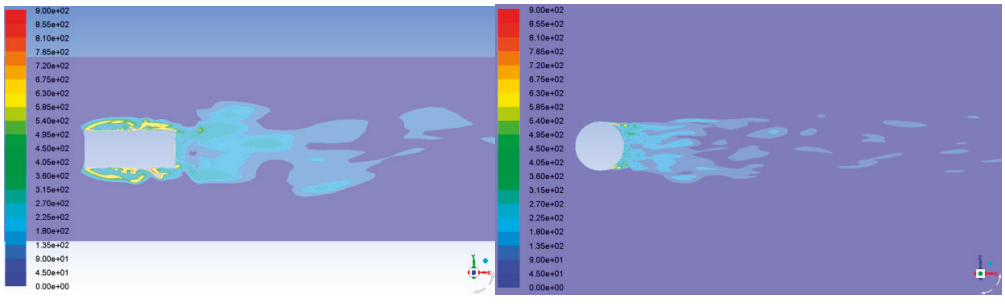

$H/D = 0.4$

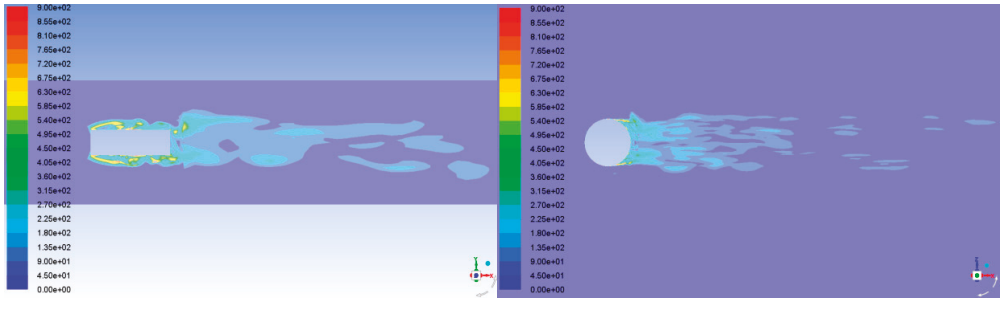

$H/D = 0.3$

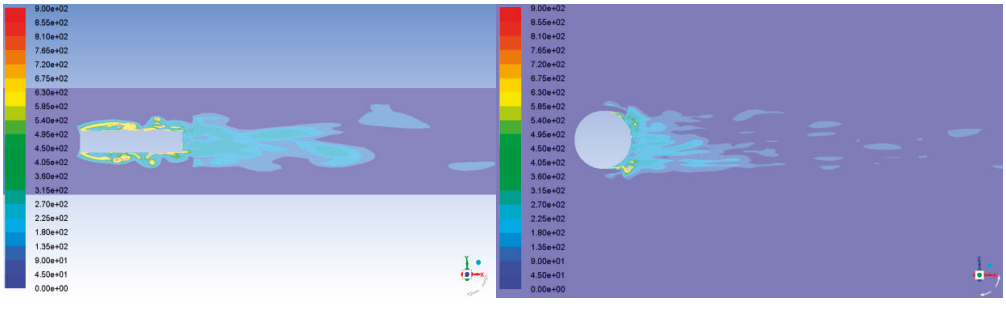

$H/D = 0.2$

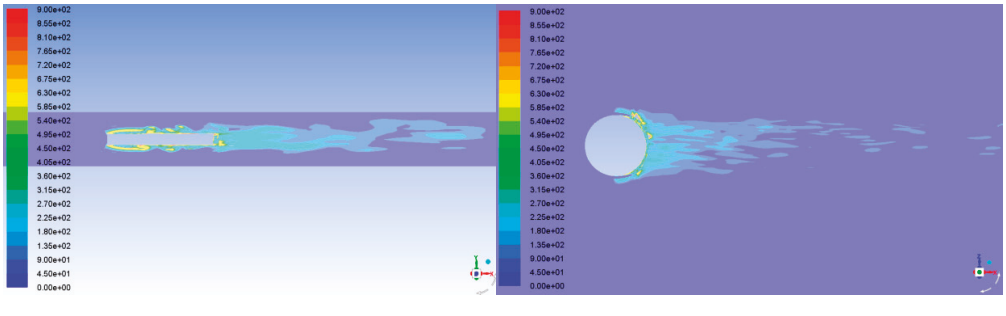

$H/D = 0.1$

Figure 9. Contours of vorticity in the vertical center plane at $z/D = 0$ and the horizontal center plane at $y/D = 0$ with different aspect ratios.

For $H/D = 0.6$ and $H/D = 0.5$, we can still observe apparent vortex shedding in the rear area of the circular cylinder, but the scale of the shedding vortex is already very small. The vortical structures in this condition are significantly less vigorous than those in the case of $0.7 \leq H/D \leq 5.0$.

When the aspect ratio is between 0.1 and 0.42, we can observe no significant vortex shedding in the rear area of the circular cylinder. As we can see, the flow separates from the front end of the cylinder and reattaches at a point on the trailing end of the cylinder. We can also find that the position of this reattachment point moves upstream gradually with the decrease in the aspect ratio. In addition, the scale of the shedding vortex is very small and distributes around the surface of the cylinder on account of the great influence of the downwash from the free end. In this range of H/D, the free end of the cylinder has a significant impact on the hydrodynamic characteristics of the near wake field. The vorticity intensity of the upper and lower ends of the cylinder is greater than that of the middle part, and the vorticity intensity of the near wake field behind the cylinder is also greater than that of the far wake field. In addition, many small scale vortices are generated behind the cylinder, and they become more and more chaotic with the decrease in the aspect ratio. Therefore, due to the influence of the free end, the three-dimensional effect of the cylinder with low aspect ratio is more obvious than that with high aspect ratio.

4.3. Flow Visualization

In this section, instantaneous streamlines and contours of velocity in the horizontal center plane at $y/D = 0$ are presented and compared for cylinders with all aspect ratios. Table 3 clears up the recirculation region length with different aspect ratios. The length of the recirculation region apparently reduces with the decrease in the aspect ratio, as shown in Table 3.

Table 3. Recirculation region length with different aspect ratios.

H/D	Recirculation Region Length/m
0.1	0.292
0.2	0.303
0.3	0.403
0.4	0.463
0.42	0.469
0.5	0.511
0.6	0.541
0.7	0.569
0.8	0.576
0.9	0.589
1	0.613
2	0.785
3	0.831
4	0.915
5	0.994

Figure 10 shows streamlines and contours of velocity in the horizontal center plane at $y/D = 0$ with different aspect ratios. The streamlines for $H/D = 5$ demonstrate the representative shape of the three-dimensional flow field around the structure; the flow separates at a critical point and forms a recirculation region in the wake field of the circular cylinder. For $H/D = 0.4$, the visible recirculation region can also be observed, but the length of this district becomes very small. The flow behind the cylinder distributes laterally due to the disturbance of the strong downwash from the upper and lower ends of the cylinder. In addition, the smaller the aspect ratio of cylinder, the more obvious this phenomenon is. For the case of $H/D = 0.1$, the presence of the recirculation region is rarely observed. The flow field behind the cylinder is extraordinary irregular and chaotic in the case of $H/D \leq 0.5$.

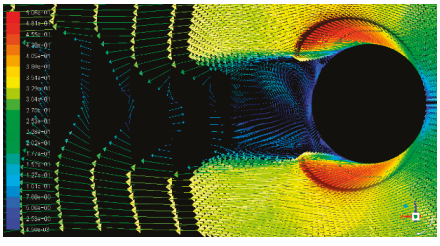

$H/D = 5$

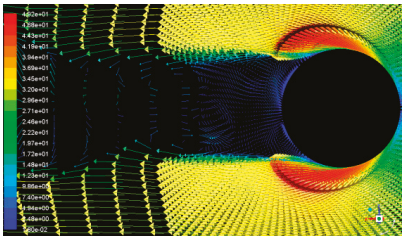

$H/D = 4$

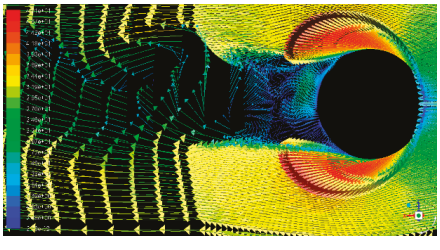

$H/D = 3$

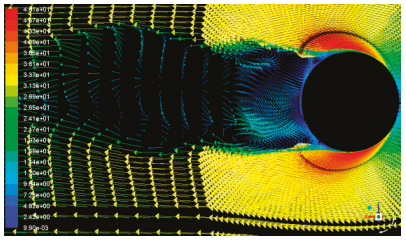

$H/D = 2$

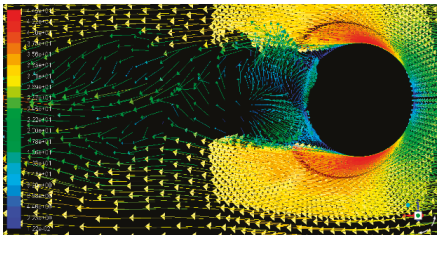

$H/D = 1$

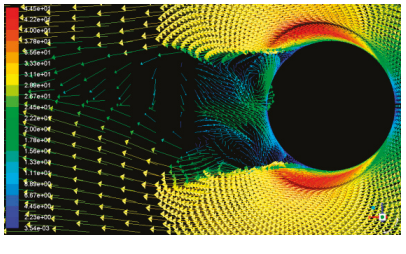

$H/D = 0.9$

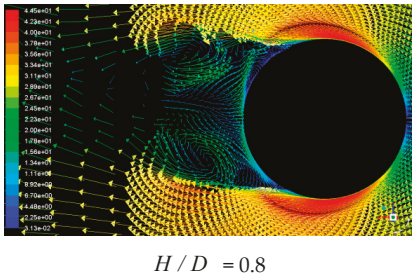

$H/D = 0.8$

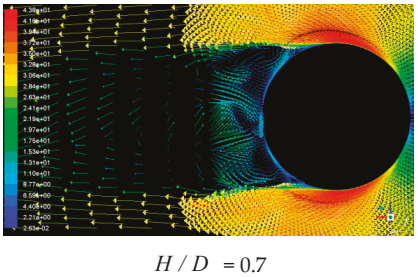

$H/D = 0.7$

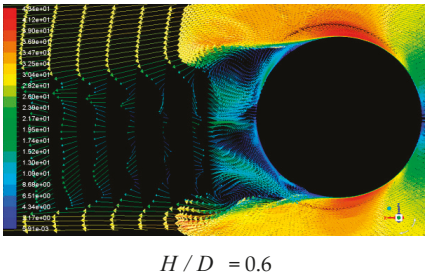

$H/D = 0.6$

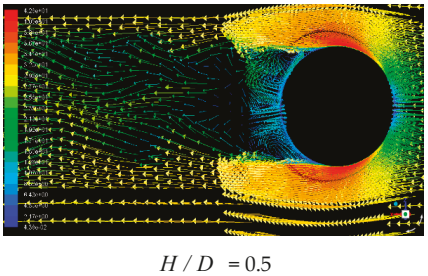

$H/D = 0.5$

Figure 10. *Cont.*

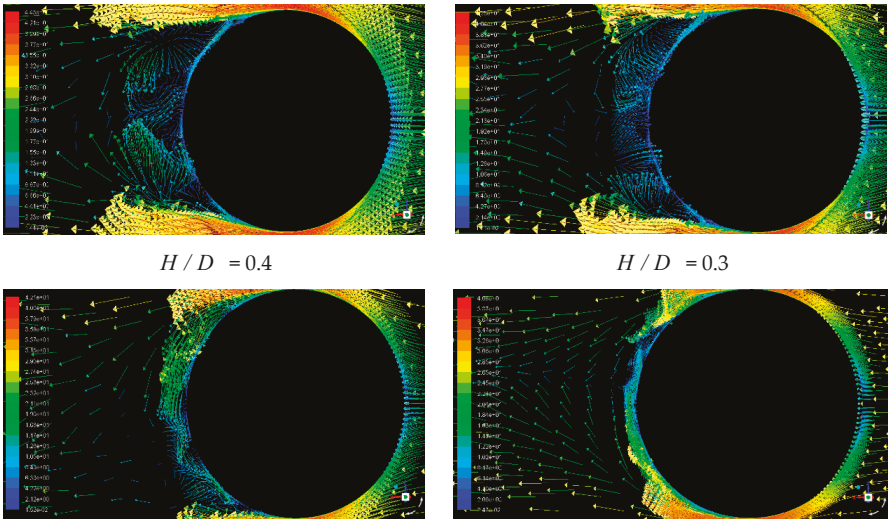

Figure 10. Instantaneous streamlines and contours of velocity in the horizontal center plane at $y/D = 0$ with different aspect ratios.

Figures 11 and 12 show instantaneous streamlines and contours of velocity in the horizontal plane at $H/D = 0.3$ and $H/D = 5$, respectively. Figures 13 and 14 show contour lines of vorticity in the horizontal plane at $H/D = 0.3$ and $H/D = 5$, respectively. As we can see from Figure 13, the vorticity magnitude in both sides of the cylinder is bigger than that in the middle part. With regard to $H/D = 0.3$, due to the small aspect ratio, the vorticity of the selected four transverse planes is all affected by the downwash from the upper and lower ends of the cylinder. Because the effect of the horizontal flow is very small, the wake field of the cylinder is mainly disturbed by the downwash. Therefore, more and more vortices shedding from the cylinder distribute in both sides of the cylinder. However, as to $H/D = 5$, the attachment of the flow from the top of the cylinder needs to perform several instances of spiral descending. During this process, the impact of the flow from the middle section of the cylinder becomes more and more stronger. The strength of the downwash from the upper and lower ends of the cylinder becomes weaker and weaker, so that the flow cannot approach to the surface of the cylinder. Therefore, we can see from Figure 14 that most of the vortex generated in the case of $H/D = 5$ appears behind the circular cylinder.

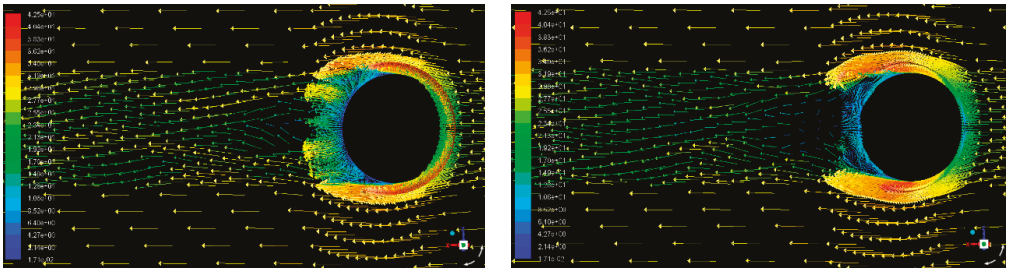

(**a**) $Z/H = 0$ (**b**) $Z/H = 0.25$

Figure 11. *Cont.*

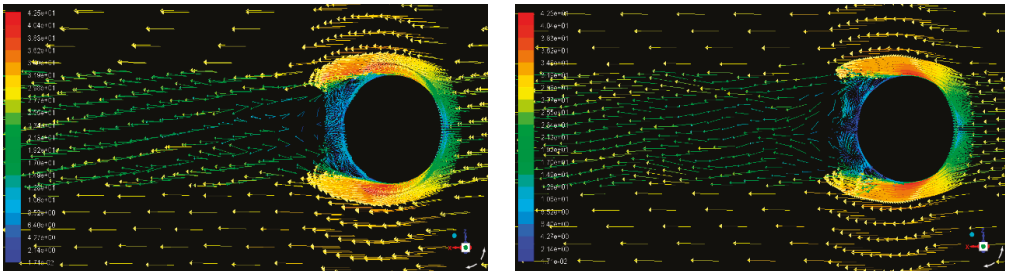

(**c**) $Z/H = 0.5$ (**d**) $Z/H = 0.75$

Figure 11. Instantaneous streamlines and contours of velocity in the horizontal plane at $H/D = 0.3$: (**a**) $Z/H = 0$; (**b**) $Z/H = 0.25$; (**c**) $Z/H = 0.5$ and (**d**) $Z/H = 0.75$.

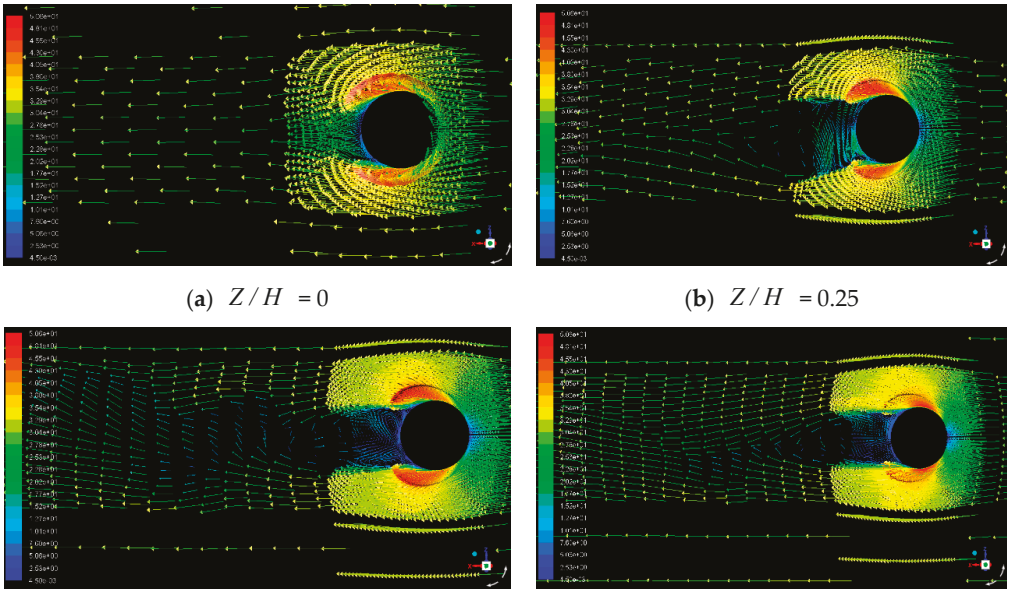

(**a**) $Z/H = 0$ (**b**) $Z/H = 0.25$

(**c**) $Z/H = 0.5$ (**d**) $Z/H = 0.75$

Figure 12. Instantaneous streamlines and contours of velocity in the horizontal plane at $H/D = 5$: (**a**) $Z/H = 0$; (**b**) $Z/H = 0.25$; (**c**) $Z/H = 0.5$ and (**d**) $Z/H = 0.75$.

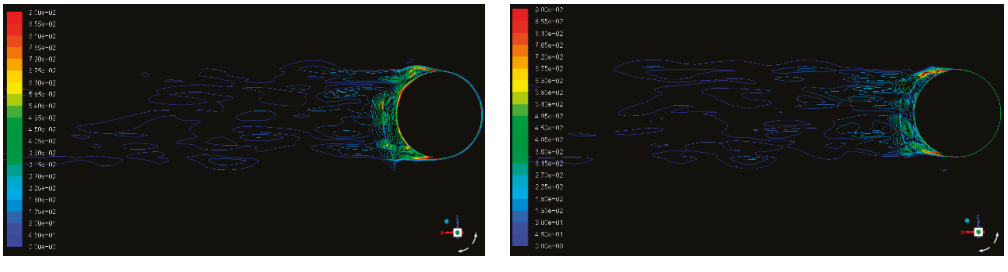

(**a**) $Z/H = 0$ (**b**) $Z/H = 0.25$

Figure 13. *Cont.*

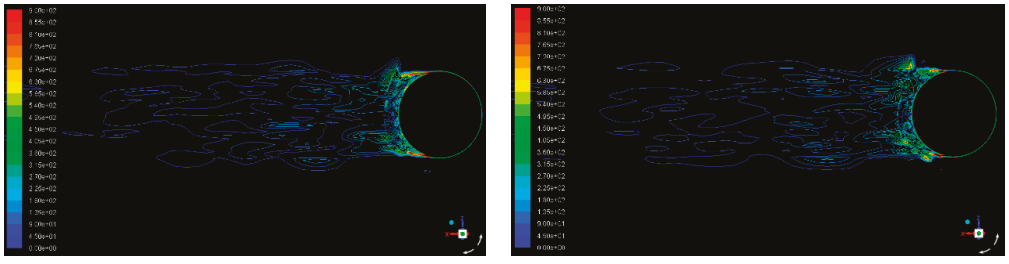

(**c**) $Z/H = 0.5$ (**d**) $Z/H = 0.75$

Figure 13. Contour lines of vorticity in the horizontal plane at $H/D = 0.3$: (**a**) $Z/H = 0$; (**b**) $Z/H = 0.25$; (**c**) $Z/H = 0.5$ and (**d**) $Z/H = 0.75$.

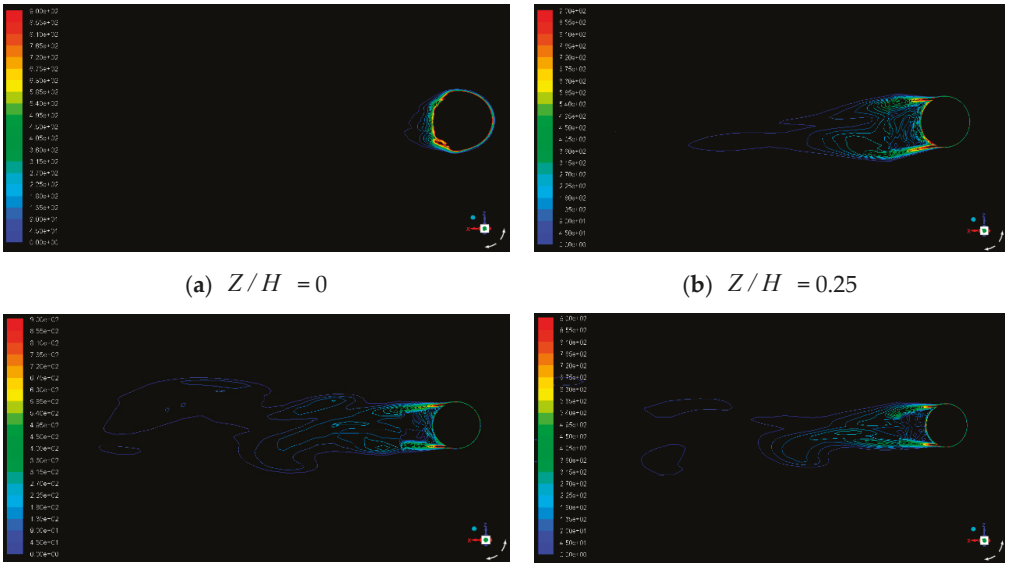

(**a**) $Z/H = 0$ (**b**) $Z/H = 0.25$

(**c**) $Z/H = 0.5$ (**d**) $Z/H = 0.75$

Figure 14. Contour lines of vorticity in the horizontal plane at $H/D = 5$: (**a**) $Z/H = 0$; (**b**) $Z/H = 0.25$; (**c**) $Z/H = 0.5$ and (**d**) $Z/H = 0.75$.

Figure 11 shows instantaneous streamlines and contours of velocity in the horizontal plane at $H/D = 0.3$. It can be observed that the streamlines of the transverse plane perform more disordered as this plane gets closer to the free end of the cylinder. The distance between the transverse plane and the free end plays a key role in the characteristics of vortex shedding. Moreover, the critical point at which the flow particles move backwards is also closer to the cylinder. Therefore, there is almost no large scale vortex shedding that can be observed and the flow vibrates very weakly. The existence of the downwash destroys the alternating shedding vortices into many irregular small scale vortices. The results show that the oscillations of the velocity in the selected four transverse planes are small. Hence, it can be found that the whole wake field is affected by the downwash when the aspect ratio is between 0.1 and 0.4. Figure 12 shows instantaneous streamlines and contours of velocity in the horizontal plane at $H/D = 5$. As we can see from Figure 12, the oscillations of the velocity on both sides of the cylinder are very violent in this condition. An obvious area of negative pressure is formed behind the cylinder. The closer the transverse plane

is to the middle part of the cylinder, the more its wake field is affected by the horizontal incoming flow. Therefore, the recirculation regions in the calculated transverse planes are bigger than that of the lower aspect ratio.

5. Conclusions

In this paper, aiming at acquiring an optimum structural form of IBP, the hydrodynamic characteristics of the flow past the cylindrical IBP with different height-to-diameter ratios are systematically investigated by use of the LES approach. Following conclusions can be obtained:

(1) The forces acting on the cylinders with low aspect ratios are significantly suppressed compared to those with high aspect ratios. Due to the recovery of the dynamic pressure in the wake region of the cylinders, the drag force and lift force decrease as the aspect ratio decreases.

(2) The vortical structures of the low aspect ratio cylinders are significantly less vigorous compared to those of high aspect ratio. The interplay between the flow coming from both sides of the cylinder and the downwash results in complicated vortex dynamics. In the case of $0.7 \leq H/D \leq 5.0$, it is observed that only the primary separation occurs. A series of regular and alternating vortex street shedding appear behind the circular cylinder. The vortex shedding leads to the generation of the area of negative pressure, which causes the increase in the drag force. For $H/D = 0.6$ and $H/D = 0.5$, the phenomenon of vortex shedding behind the circular cylinder is also observed, but the scale of the shedding vortex is already very small. In the case of $0.1 \leq H/D \leq 0.42$, we can observe no significant vortex shedding in the rear area of the circular cylinder.

(3) The recirculation region length reduces significantly with the decrease in the aspect ratio. The streamlines for $H/D = 5$ demonstrate the representative shape of the three-dimensional flow field around the structure, the flow separates at a critical point and forms a recirculation region in the wake field of the circular cylinder. For lower aspect ratio, the effects of the free end are already very obvious. In addition, the flow field behind the cylinder is extraordinary irregular and chaotic in the case of $H/D \leq 0.5$.

(4) As far as free-end effects are considered, the whole wake field is affected by the downwash when the aspect ratio is between 0.1 and 0.4. Therefore, there is almost no large scale vortex shedding can be observed and the flow vibrates very weakly. The existence of the downwash destroys the alternating shedding vortices into many irregular small scale vortices. In addition, the oscillations of the velocity in the selected four transverse planes are small. Otherwise, in the case of high aspect ratio, the oscillations of the velocity on both sides of the cylinder are very violent in this condition. Furthermore, the recirculation regions in the calculated transverse planes are bigger than that of the lower aspect ratio.

Finally, it can be concluded that the IBP will perform the best hydrodynamic characteristics when the aspect ratio is between 0.3 and 0.4. In the meantime the present study should be reliable and useful for design work of the IBP. Furthermore, the research findings will be of great significance to provide valuable reference and foundation to determine the optimum form of underwater structures, such as the buoyancy cans of the hybrid riser system.

Author Contributions: Conceptualization, X.Z., J.Y. and Y.H.; methodology, J.Y. and X.Z.; software, J.Y.; validation, X.Z., Y.H. and W.W.; formal analysis, X.Z. and J.Y.; investigation, X.Z.; resources, X.Z. and Y.H.; data curation, X.Z. and J.Y.; writing—original draft preparation, J.Y.; writing—review and editing, X.Z.; visualization, Y.H. and W.W.; supervision, X.Z. and Y.H.; project administration, X.Z.; funding acquisition, X.Z. All authors have read and agreed to the published version of the manuscript.

Funding: This research was funded by the National Natural Science Foundation of China, grant number No.51709041.

Conflicts of Interest: The authors declare no conflict of interest.

References

1. Huang, Y.; Zhen, X.; Zhang, Q.; Wang, W.-H. Optimum design and global analysis of flexible jumper for an innovative subsurface production system in ultra-deep water. *China Ocean Eng.* **2014**, *28*, 239–247. [CrossRef]
2. Zhen, X.W.; Huang, Y.; Wang, W.H.; Zhang, Q. Investigation of hydrodynamic coefficients for artificial buoyancy seabed unit. *J. Ship. Mech.* **2013**, *17*, 1381–1391.
3. Wu, J.-H.; Zhen, X.-W.; Liu, G.; Huang, Y. Optimization design on the riser system of next generation subsea production system with the assistance of DOE and surrogate model techniques. *Appl. Ocean Res.* **2019**, *85*, 34–44. [CrossRef]
4. Zhen, X.; Vinnem, J.E.; Han, Y.; Peng, C.; Yang, X.; Huang, Y. New risk control mechanism for innovative deepwater artificial seabed system through online risk monitoring system. *Appl. Ocean Res.* **2020**, *95*, 102054. [CrossRef]
5. Zhen, X.; Wu, J.-H.; Huang, Y.; Han, Y.; Yao, J.-J. Parametric Dimensional Analysis on the Structural Response of An Innovative Subsurface Tension Leg Platform in Ultra-Deep Water. *China Ocean Eng.* **2018**, *32*, 482–489. [CrossRef]
6. Naudascher, E.; Wang, Y. Flow-Induced Vibrations of Prismatic Bodies and Grids of Prisms. *J. Fluids Struct.* **1993**, *7*, 341–373. [CrossRef]
7. Adaramola, M.; Akinlade, O.; Sumner, D.; Bergstrom, D.; Schenstead, A. Turbulent wake of a finite circular cylinder of small aspect ratio. *J. Fluids Struct.* **2006**, *22*, 919–928. [CrossRef]
8. Krajnović, S. Flow around a tall finite cylinder explored by large eddy simulation. *J. Fluid. Mech.* **2011**, *676*, 294–317. [CrossRef]
9. Okamoto, T.; Yagita, M. The Experimental Investigation on the Flow past a Circular Cylinder of Finite Length Placed Normal to the Plane Surface in a Uniform Stream. *Bull. JSME* **1973**, *16*, 805–814. [CrossRef]
10. Sakamoto, H.; Arie, M. Vortex shedding from a rectangular prism and a circular cylinder placed vertically in a turbulent boundary layer. *J. Fluid Mech.* **1983**, *126*, 147–165. [CrossRef]
11. Okamoto, S.; Sunabashiri, Y. Vortex Shedding From a Circular Cylinder of Finite Length Placed on a Ground Plane. *J. Fluids Eng.* **1992**, *114*, 512–521. [CrossRef]
12. Wang, H.F.; Zhou, Y. The finite-length square cylinder near wake. *J. Fluid Mech.* **2009**, *638*, 453–490. [CrossRef]
13. Wang, H.F.; Zhou, Y.; Mi, J. Effects of aspect ratio on the drag of a wall-mounted finite-length cylinder in subcritical and critical regimes. *Exp. Fluids* **2012**, *53*, 423–436. [CrossRef]
14. Tsutsui, T. Flow around a cylindrical structure mounted in a plane turbulent boundary layer. *J. Wind. Eng. Ind. Aerodyn.* **2012**, *104*, 239–247. [CrossRef]
15. Afgan, I.; Moulinec, C.; Prosser, R.; Laurence, D. Large eddy simulation of turbulent flow for wall mounted cantilever cylinders of aspect ratio 6 and 10. *Int. J. Heat Fluid Flow* **2007**, *28*, 561–574. [CrossRef]
16. Gonçalves, R.; Franzini, G.; Rosetti, G.; Meneghini, J.; Fujarra, A. Flow around circular cylinders with very low aspect ratio. *J. Fluids Struct.* **2015**, *54*, 122–141. [CrossRef]
17. Gonçalves, R.T.; Rosetti, G.; Franzini, G.; Meneghini, J.; Fujarra, A. Two-degree-of-freedom vortex-induced vibration of circular cylinders with very low aspect ratio and small mass ratio. *J. Fluids Struct.* **2013**, *39*, 237–257. [CrossRef]
18. Zhao, M.; Cheng, L. Vortex-induced vibration of a circular cylinder of finite length. *Phys. Fluids* **2014**, *26*, 015111. [CrossRef]
19. Yu, D.; Kareem, A. Parametric study of flow around rectangular prisms using LES. *J. Wind. Eng. Ind. Aerodyn.* **1998**, *77*, 653–662. [CrossRef]
20. Yeon, S.M.; Yang, J.; Stern, F. Large-eddy simulation of the flow past a circular cylinder at sub- to super-critical Reynolds numbers. *Appl. Ocean Res.* **2016**, *59*, 663–675. [CrossRef]
21. Vakil, A.; Green, S.I. Drag and lift coefficients of inclined finite circular cylinders at moderate Reynolds numbers. *Comput. Fluids* **2009**, *38*, 1771–1781. [CrossRef]
22. Rostamy, N.; Sumner, D.; Bergstrom, D.; Bugg, J. Local flow field of a surface-mounted finite circular cylinder. *J. Fluids Struct.* **2012**, *34*, 105–122. [CrossRef]
23. Lee, T.; Lin, C.-L.; Friehe, C.A. Large-eddy simulation of air flow around a wall-mounted circular cylinder and a tripod tower. *J. Turbul.* **2007**, *8*, N29. [CrossRef]
24. Palau-Salvador, G.; Stoesser, T.; Fröhlich, J.; Kappler, M.; Rodi, W. Large Eddy Simulations and Experiments of Flow around Finite-Height Cylinders. *Flow Turbul. Combust.* **2009**, *84*, 239–275. [CrossRef]
25. Cai, S.-G.; Ouahsine, A.; Favier, J.; Hoarau, Y. Moving immersed boundary method. *Int. J. Numer. Methods Fluids* **2017**, *85*, 288–323. [CrossRef]
26. Mimeau, C.; Gallizio, F.; Cottet, G.-H.; Mortazavi, I. Vortex penalization method for bluff body flows. *Int. J. Numer. Methods Fluids* **2015**, *79*, 55–83. [CrossRef]
27. Minguez, M.; Luppi, A.; Vivet, R.; Maloberti, R. FSFR-Flat-Buoy stability model tests versus CFD/FSI method. In Proceedings of the Twenty-First International Offshore and Polar Engineering Conference, Maui, HI, USA, 19–24 June 2011; pp. 601–609.
28. Vivet, R.; Minguez, M.; Berhault, C.; Jacquin, E.; Petrie, F.; Flamand, O. Flat buoy concept for free standing riser application: An improvement of the in-place hydrodynamic behaviour. In Proceedings of the ASME 2011 30th International Conference on Ocean, Offshore and Arctic Engineering, Rotterdam, The Netherlands, 19–24 June 2011; pp. 223–232.
29. Braza, M.; Chassaing, P.; Minh, H.H. Numerical study and physical analysis of the pressure and velocity fields in the near wake of a circular cylinder. *J. Fluid Mech.* **1986**, *165*, 79–130. [CrossRef]

Journal of *Marine Science and Engineering*

MDPI

Article

A Numerical Swallowing-Capacity Analysis of a Vacant, Cylindrical, Bi-Directional Tidal Turbine Duct in Aligned & Yawed Flow Conditions

Mitchell G. Borg [1], Qing Xiao [1,*], Steven Allsop [2], Atilla Incecik [1] and Christophe Peyrard [3]

[1] Department of Naval Architecture, Ocean, and Marine Engineering, University of Strathclyde, Glasgow G4 0LZ, UK; mitchell.borg@strath.ac.uk (M.G.B.); atilla.incecik@strath.ac.uk (A.I.)
[2] Industrial Doctoral Centre for Offshore Renewable Energy (IDCORE), University of Edinburgh, Edinburgh EH8 9YL, UK; Steve.Allsop@simecatlantis.com
[3] Électricité de France Research and Development, EDF R&D, Ile-de-France, 78400 Chatou, France; christophe.peyrard@edf.fr
* Correspondence: qing.xiao@strath.ac.uk

Abstract: Introducing a duct along the perimeter of a rotor has been acknowledged to augment turbine performance. The outcome causation due to a bi-directional, cylindrical shroud, however, is uncertain. This study analyses the hydrodynamic swallowing capacity of a true-scale, vacant duct for tidal turbine applications in aligned and yawed inlet flow conditions by utilising three-dimensional unsteady computational fluid dynamics. The performance is investigated within free-stream magnitudes of 1 to 7 m.s^{-1}, and a bearing angular range of 0° to 45° with the duct axis. In proportion to the free-stream magnitude, the normalised axial velocity through the duct increases as a result of a diminishment in pressure drag. Within yawed flow, the maximum capacity falls at a bearing of 23.2°, resulting in a performance increase of 4.13% above that at aligned flow conditions. The analysis concludes that the augmentation at yawed flow occurs due to the duct cross-sectional profile lift variation with angle-of-attack. Towards nominal yaw angle, the internal static pressure reduces, permitting a higher mass-flow rate. Beyond the nominal angle-of-attack, flow separation occurs within the duct, increasing pressure drag, thereby reducing the swallowing capacity.

Keywords: swallowing capacity; duct flow; ducted turbine

Citation: Borg, M.G.; Xiao, Q.; Allsop, S.; Incecik, A.; Peyrard, C. A Numerical Swallowing-Capacity Analysis of a Vacant, Cylindrical, Bi-Directional Tidal Turbine Duct in Aligned & Yawed Flow Conditions. *J. Mar. Sci. Eng.* **2021**, *9*, 182. https://doi.org/10.3390/jmse9020182

Academic Editor: Alessandro Antonini

Received: 31 December 2020
Accepted: 2 February 2021
Published: 10 February 2021

1. Introduction

The European Commission has put forward the 2030 Climate Target Plan. This strategy has proposed the reduction of greenhouse gas emissions to 55% of the levels read in 1990 by 2030 [1]. It has sustained objectives stated within the Paris Agreement to limit the global temperature increase to below 2 °C. In relation to the strategy, application of sustainable energy-generating systems is required.

Tidal stream turbine (TST) technology has been maturing over the past decade. Despite the potential, the industry has not prospered as rapidly as had been predicted. This outcome has been deemed to be due to engineering challenges within extreme operating conditions, in combination with political and environmental factors [2]. Despite the drawbacks observed within the tidal industry, European, North American, and Asian states have largely invested in the deployment of full-scale tidal turbine arrays. A wide range of the European investment has been installed within territorial waters of France and the United Kingdom [3].

Efforts to increase the efficacy of energy-generating turbines have been ongoing. From the undergone research, bi-directional ducts have been installed along the circumference of a rotor to increase the mass-flow, establishing a ducted turbine system [4]. An effective duct design in relation to the installed rotor is required to permit the highest swallowing capacity

through the duct throat. By definition, swallowing capacity is described as the normalised axial velocity through the duct throat in relation to the external free-stream velocity.

Few research ventures have investigated the fluid dynamics of vacant, open-ended diffusers/ducts for rotor implementation within aligned and non-aligned flow conditions. Kogan and Seginer [5] described two driving factors that enhance the mass–flow rate. Primarily, a low-pressure region is produced downstream of the structure due to flow deviation from the diffuser outlet. The outlet region is therefore segregated from the energised free-stream, which draws in a larger amount of fluid. In addition, flow acceleration is induced by the areal contraction along the shroud throat within a streamtube, in accordance to Bernoulli's principle, as illustrated in Figure 1.

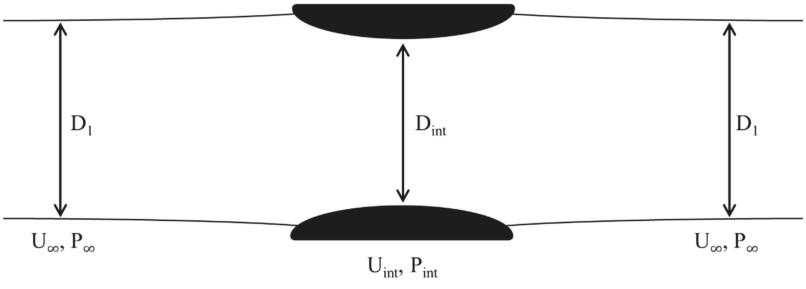

Figure 1. Bi-directional vacant duct streamtube representation.

Attributable to the potential increase in power extraction as a result of mass–flow increase through a rotor, several commercial endeavours had attempted to adopt ducted turbine technology to achieve economic prospects. Amongst the ventures, DCNS/OpenHydro Ltd. had designed an open-centre ducted design approach [6,7]. In open-water trials, a 2 MW turbine was successfully installed in the Bay of Fundy, Canada, portrayed in Figure 2, together with a pair of 500 kW rated capacity turbines in Paimpol-Bréhat, Northern France, in collaboration with EDF France.

Figure 2. The 2 MW-rated OpenHydro ducted turbine. Adapted from [8], The Canadian Press/Andrew Vaughan, 2016.

Through the small number of published works, mass–flow augmentation within an open-ended duct for turbine implementation has been put forward. Ohya et al. [9] evaluated three distinct duct structures: nozzle, cylindrical, and diffuser form types. The cylindrical duct sustained an axial velocity relatively equivalent to the free-stream throughout its length. The diffuser-type accelerated the flow by a magnitude of 1.8 as a result of

the negative static pressure induced, a −1.9 factor of the free-stream dynamic pressure. The nozzle-type attained a diminished mass–flow. Masukume et al. [10,11] varied the length to throat diameter ratio and expansion angle of a diffuser to establish the optimum geometrical shape parameters for maximum mass–flow. On average, a 1.5 magnitude over the free-stream velocity was attained through the diffuser at all combinations of length ratios and diffuser expansion angles.

In tidal current applications, Setoguchi et al. [12] developed three geometrical variations for a two-way, symmetrical, bi-directional diffuser: a shell-type, for unmodified control comparison; a straight-type, describing a solid diffuser with a straight outer duct surface; and a bulge-type, describing a solid diffuser with an outer duct surface mirroring the inner duct surface. By comparing the increase in axial velocity through the duct throat, the highest swallowing capacity was attained by the straight-type bi-directional diffuser with a vertical rim at the outlet. The flow within the duct was accelerated by a magnitude of 1.3. Cresswell et al. [13] analysed a vacant diffuser within aligned and yawed flow conditions. A static pressure variation along the internal and external surfaces of the diffuser was acknowledged with an increase in yaw bearing.

Numerically investigating the swallowing capacity of a vacant flanged duct, Kardous et al. [14] implemented an axi-symmetric computational fluid dynamic analysis utilising periodic boundary conditions. Variations in flow velocity and static pressure were established within the structure by varying the height of a straight rim at the diffuser outlet in relation to the throat diameter. A height ratio of 0.1 was found to attain the highest increase in throat velocity, equivalent to a magnitude of 1.6 to 1.7 over the free-stream velocity. Kannan et al. [15] investigated the variation in flow velocity within flanged diffuser geometrical profiles. A two-dimensional straight-body diffuser cone with a 16° aperture, coupled with a 0.5 m long 4° centre-body cone, was utilised. An increase in axial velocity of 61.25% over the free-stream was acknowledged.

Implementing axi-symmetric numerical models, Mansour and Meskinkhoda [16] applied both the Spalart–Allmaras and the RNG $k-\varepsilon$ turbulence model to determine the static pressure and axial velocity variations through a simple diffuser incorporated with a straight, vertical rim. Similarly, Khamlaj and Rumpfkeil [17] utilised the SST $k-\omega$ turbulence model to establish the generation of two static vortices downstream of the flange. Kesby et al. [18] investigated a 10° diffuser to identify the efficiency coefficients of the structure for blade-element analysis implementation.

Considering yawed flow analysis, El-Zahaby et al. [19] investigated the swallowing capacity of a flanged diffuser designed for micro-turbines by establishing an inlet velocity bearing variation. Utilising a two-dimensional axi-symmetric model, the analysis ranged from +25° to −25° with the duct axis. The optimum angle, a bearing of 15°, accelerated the flow at the diffuser entrance by 5%. Tampier et al. [20] numerically investigated the axial induction factor, average velocities at the turbine plane, and diffuser drag coefficient along a three-dimensional shroud in accordance with a variation in free-stream velocity.

Despite the undertaken research, the performance of a true-scale, three-dimensional, bi-directional, cylindrical duct has not been acknowledged. Due to its industrial implementation, the analysis was therefore deemed to be of particular interest, distinctively when considering the variable conditional parameters of an external fluid domain at differing free-stream magnitudes and yaw bearings. Therefore, the aim of this study was to analyse the swallowing-capacity performance of a true-scale bi-directional duct for tidal turbine applications in aligned and yawed flow conditions by utilising three-dimensional unsteady computational fluid dynamics (CFD). By means of the analysis, the causation of the performance variation may then be identified. The numerical analysis elaborated in this present study is a continuation of Borg et al. [21], which had developed a real-scale CFD model to assess the hydrodynamic performance of a high-solidity open-centre rotor within a bi-directional duct for tidal turbine applications in aligned flow conditions. The duct geometry was provided by EDF R&D to replicate the outcomes of a turbine similar to the design of the OpenHydro PS2 device, whilst coupling the seven-equation Reynolds

Stress "Stress-Omega" Model (τ-ω) turbulence model to close the Navier–Stokes equation and analyse the anisotropic flow domain [22].

2. Numerical Methodology

2.1. Physical Setup

The dimensions of the cylindrical bi-directional duct describe an external duct diameter (D_{ext}) of 15 m, an internal duct diameter (D_{int}) of 12 m, with a flat-convex cross-sectional profile, and a duct length (L_{dct}) of 10 m, as illustrated in Figure 3a,b. The flow parameters were considered from site analyses that had established a maximum acquired spring tide velocity of 4.0 m.s^{-1}, and a surface velocity of 5.0 m.s^{-1} [23,24]. In recognition of the literature, free-stream velocity (U_∞) magnitudes of 1.0, 2.5, 4.0, 5.5, and 7.0 m.s^{-1} were analysed to establish a variation between low and extreme current conditions. Additionally, the tidal cycle at the Paimpol–Bréhat site had been numerically simulated [25,26]. An asymmetric velocity was acknowledged in both magnitude and direction, at ebb and flood, with an average-depth angular discrepancy of 20°. Therefore, yaw bearing (γ) angles of 0°, 7°, 15°, 23.2°, 27°, 30°, 38°, and 45°, incoming from the turbine port direction at a magnitude of 4 m.s^{-1}, were investigated to establish the duct swallowing capacity under non-aligned flow conditions. The considered conditions are summarised in Tables 1 and 2. The simulations implemented an inlet turbulence intensity of 3% and an inlet turbulent length scale of 1 m.

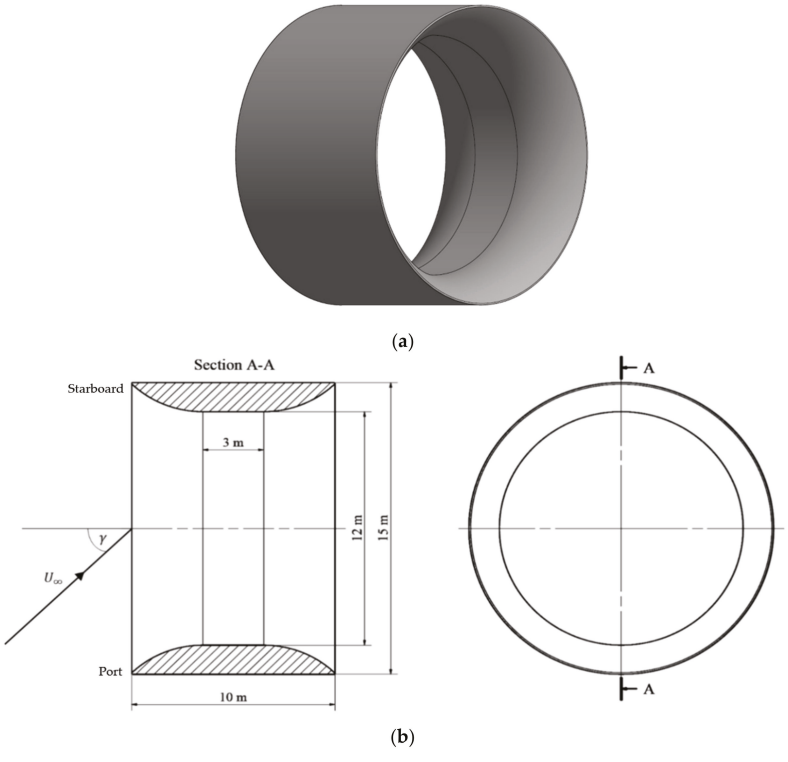

Figure 3. Geometric representation of the duct. (**a**) Rendered three-dimensional CAD representation; (**b**) First-angle sectioned projection.

Table 1. Duct model descriptions.

Description	Value
Duct external diameter (D_{ext})	15 m
Duct internal radius (D_{int})	12 m
Duct length (L_{dct})	10 m
Reynolds number (Re)	$[0.149 - 1.046] \times 10^8$

Table 2. Domain model descriptions.

Description	Aligned Flow	Yawed Flow
Free-stream velocity (U_∞)	1 m.s^{-1}, 2.5 m.s^{-1}, 4 m.s^{-1}, 5.5 m.s^{-1}, 7 m.s^{-1}	4 m.s^{-1}
Yaw bearing (γ)	0°	0°, 7°, 15°, 23.2°, 27°, 30°, 38°, 45°

2.2. Numerical Setup

The duct model was designed to be a fully submerged system within a constant fluid flow. Far-stream effects from the free-surface and seabed were therefore abdicated. This setup permitted the swallowing-capacity analysis of the duct under consistent temporal conditions. The commercial solver ANSYS Fluent 19.2 was utilised in computing the continuity and Navier–Stokes equations. A Reynolds-averaged Navier–Stokes (RANS) turbulence model was implemented in mathematical closure to represent flow property fluctuation within the three-dimensional, unsteady, incompressible flow field.

Implementing a cuboidal domain layout, a cross-sectional quadratic-face edge-length of $7D_{ext}$ was utilised. The cylindrical duct was positioned at the centre of the vertical plane. The dimensions of the computational domain attained a numerical areal blockage ratio of less than 2% to the external duct diameter to ascertain the absence of far-field effects [27]. A domain length of $9D_{ext}$ was implemented, where the inlet and outlet planes were situated at a distance $3D_{ext}$ upstream and $6D_{ext}$ downstream of the duct, respectively, as illustrated in Figure 4a. The dimensions of the domain were therefore equivalent to 105 by 105 by 135 m. The no-slip wall condition was implemented on the duct surface. Periodic conditions were allocated to the domain boundaries parallel to the duct axis. Velocity inlet and pressure outlet conditions were allocated to the perpendicular boundaries. The velocity yaw angle (γ) was induced by varying the incident velocity components at the inlet boundary. Three circular planar numerical surfaces of diameter D_{int} were introduced within the duct throat, at its upstream, middle, and downstream locations, as a rotor may be placed within this location. These surfaces were utilised for data acquisition purposes to attain mass-averaged values of normalised axial velocity and static pressure within the duct throat. The standard deviation of the mean-averaged results is presented in Appendix A.

The Reynolds–Stress Model (RSM) "Stress-Omega" (τ-ω) turbulence model was utilised with the SIMPLE pressure–velocity coupling scheme, the Green–Gauss node-based gradient, pressure staggering option (PRESTO) pressure, second order upwind momentum, second order upwind specific dissipation rate, and second order upwind Reynolds stresses spatial discretisation schemes, and the second order implicit transient formulation scheme. The Reynolds–Stress Model was utilised as the Reynolds stresses are solved in three-dimensional space due to the non-implementation of the Boussinesq approximation/assumption, prompting superiority in analysing anisotropic flows, such as flows over curved surfaces, flows in rotating fluids, and flows in ducts with secondary (rotational) motion [22]. In addition, the effects of streamline curvature, swirl, rotation, and rapid changes in strain rate are considered in a more effective manner than one-equation or two-equation models. The simulation time-step (Δt_{step}) was considered in relation to the duct length and free-stream velocity, where each transient iteration was attained by:

$$\Delta t_{step} = 0.01 \cdot \frac{L_{dct}}{U_\infty} \quad (1)$$

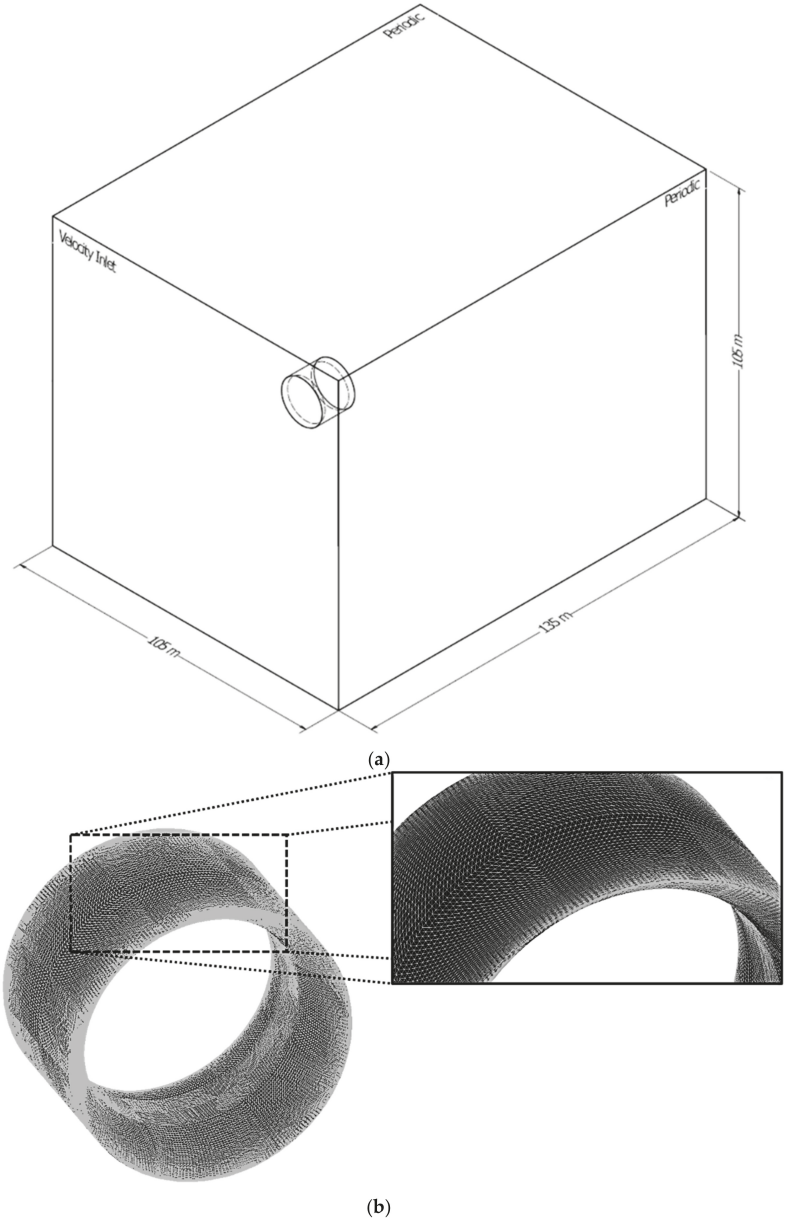

Figure 4. Representation of the domain (above, (**a**) CFD domain layout) and duct mesh (below, (**b**) Surface mesh along the duct.

The described numerical setup had been validated in previous works. The validation procedure consisted of a numerical-experimentation comparison of a small-scale tidal turbine. Details in relation to the setup of the numerical validation model may be attained in Ref. [21].

A tetrahedral mesh was utilised throughout the duct domain. A mesh independence procedure, described in Table 3, was carried out on the duct domain by considering the parameter with the highest degree of dynamics; the highest free-stream velocity. Mesh in-

dependent parameters were established utilising ITTC recommended meshing procedures and guidelines [28]:

$$\varepsilon_n = S_n - S_{n-1} \tag{2}$$

$$\psi = \frac{\varepsilon_n}{\varepsilon_{n-1}} \tag{3}$$

where ψ is the convergence ratio, ε is the difference between the considered variable (S) at different mesh independence study iterations, and the subscript n is the mesh independence study iteration.

Table 3. Mesh independence analysis for the duct domain.

n	Cell Number	Cell Number Ratio	S	ε	ψ
3	6,533,300	1.247	1.493	0.0062	0.569
2	5,240,241	1.277	1.487	0.0109	
1	4,103,210		1.476		

Subsequent to the procedure, the final surface mesh count upon the duct was marginally above 150,000 cell faces, illustrated in Figure 4b, with more than 6.5 million volumetric cells within the domain. The mesh was implemented with a prism layer at non-slip surfaces with an appropriate cell height to achieve a y-plus value of $60 \leqslant y^+ \leqslant 400$. This range was considered due to the high Reynolds number (>10^7) of the system; hence, modelling the viscous sublayer was abdicated to reduce computation time.

3. Numerical Model Characterisation

3.1. Physical Modelling

The induced normalised axial velocity through the duct throat (U_x) was associated to the free-stream velocity (U_∞) to attain a quantitative measure of the swallowing capacity along the duct axis as a coefficient of axial velocity ($C_{U,x}$):

$$C_{U,x} = \frac{U_x}{U_\infty} \tag{4}$$

Similarly, the static pressure at the duct throat (P_s) was associated to the dynamic pressure of the free-stream $\left(\frac{1}{2}\rho U_\infty^2\right)$ as a coefficient of static pressure ($C_{P,s}$):

$$C_{P,s} = \frac{P_s}{\frac{1}{2}\rho U_\infty^2} \tag{5}$$

where ρ is the fluid density.

The Reynolds number (Re) of the domain was defined as:

$$Re = \frac{D_{ext} U_\infty \rho}{\mu} \tag{6}$$

where D_{ext} is the duct external diameter and μ is the fluid dynamic viscosity.

Establishing the width of the streamtube at the far upstream position (R_1) in relation to the duct external diameter, the conservation of mass equation, relating the mass flow-rate ($\dot{m}$) at the upstream position with that at the duct throat, was utilised:

$$\dot{m}_\infty = \dot{m}_x \tag{7}$$

$$\rho\pi R_1^2 U_\infty = \rho\pi R_{int}^2 U_x \tag{8}$$

$$\frac{R_1}{R_{ext}} = C_R = \frac{R_{int}}{R_{ext}} \cdot \sqrt{C_{U,x}} \tag{9}$$

where R_{int} is the duct internal radius, R_{ext} is the duct external radius, and C_R is the radius coefficient.

The drag and lift induced upon the duct were established within coefficients of drag and lift:

$$C_D = \frac{F_D}{\frac{1}{2}\rho A_x U_\infty^2} = \frac{F_D}{\frac{1}{2}\rho \pi R_{ext}^2 U_\infty^2} \tag{10}$$

$$C_L = \frac{F_L}{\frac{1}{2}\rho A_y U_\infty^2} = \frac{F_L}{\frac{1}{2}\rho D_{ext} L_{dct} U_\infty^2} \tag{11}$$

where C_D and C_L are the drag and lift coefficient, F_D and F_L are the drag and lift forces, and A_x and A_y are the frontal areas in the axial and lateral directions, respectively.

3.2. CFD Modelling

3.2.1. Conservation Modelling

The conservation of mass and momentum were implemented within the CFD model in solving the flow domain:

$$\frac{\partial U_i}{\partial x_i} = 0 \tag{12}$$

$$\rho \frac{\partial U_i}{\partial t} + \rho U_j \frac{\partial U_i}{\partial x_j} = -\frac{\partial P_s}{\partial x_i} + \frac{\partial}{\partial x_j}\left(\mu\left(\frac{\partial U_i}{\partial x_j} + \frac{\partial U_i}{\partial x_j}\right) - \rho u_j' u_i'\right) \tag{13}$$

where U_i is the Reynolds-averaged velocity, x_i is the Cartesian coordinate, t is the elapsed time, μ is the fluid dynamic viscosity, and $-\rho u_j' u_i' = \rho \tau_{ij}$ is the Reynolds stress tensor.

3.2.2. Turbulence Modelling

To close the momentum conservation equation, the $\tau - \omega$ turbulence model was implemented:

$$\rho \frac{\partial \tau_{ij}}{\partial t} + \rho U_k \frac{\partial \tau_{ij}}{\partial x_k} = \frac{\partial}{\partial x_k}\left[\left(\mu + \frac{\mu_\tau}{\sigma_k}\right)\frac{\partial \tau_{ij}}{\partial x_k}\right] - \rho P_{ij} - \rho \Pi_{ij} + \frac{2}{3}\beta^* \rho \omega k \delta_{ij} - 2\rho\omega_k\left(\tau_{ij}\epsilon_{ikm} + \tau_{im}\epsilon_{jkm}\right) \tag{14}$$

$$\rho \frac{\partial \omega}{\partial t} + \rho U_j \frac{\partial \omega}{\partial x_j} = \frac{\partial}{\partial x_j}\left[\left(\mu + \frac{\mu_\tau}{\sigma_k}\right)\frac{\partial \omega}{\partial x_j}\right] + \alpha_1 \frac{\rho\omega}{k}\tau_{ij}\frac{\partial U_i}{\partial x_j} - \beta_o f_\beta \rho \omega^2 \tag{15}$$

where τ_{ij} is the specific Reynolds stress tensor, k is the turbulence kinetic energy, ω is the specific dissipation rate, Π_{ij} is the pressure–strain correlation tensor, μ_T is the eddy viscosity, ω_k is the rotation vector, ϵ_{ikm} is the Levi–Civita pseudotensor, f_β is the mean rotation tensor factor, and σ_k, α_1, β^*, and β_o are closure coefficients.

4. Modelling Validation

Validation of the CFD model was attained in Ref. [21], where the numerical drag coefficient of a tidal turbine was compared to experimentation performed by Mycek et al. [29].

The drag coefficient curve was numerically established, illustrated in Figure 5. The CFD model attained a coefficient of determination of 0.946 with the experimentation data points within the entire curve. All CFD data points analysed, except for the low TSR value of 1.00, fell within $2\sigma_{C_D}$ (the 95th-percentile confidence range) of the experimentation points.

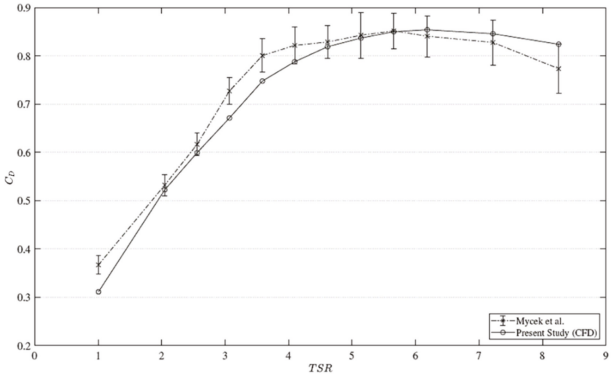

Figure 5. Drag coefficient (C_D) in relation to tip–speed ratio (TSR) for validation of the CFD model by comparing a numerical tidal turbine model [21] to experimentation [29].

5. Vacant Duct Performance in Aligned Flow Conditions

5.1. Drag Coefficient

Analysing the vacant duct, the drag coefficient decreased from a value of 0.0641 to 0.0490 with a Reynolds number increase from 1.494×10^7 to 1.046×10^8, as illustrated in Figure 6. A laminar boundary layer transitions to a turbulent boundary layer earlier with an increase in Reynolds number, thereby enhancing flow attachment and diminishing drag. This phenomenon was acknowledged to be the driving factor behind the reduction in drag with an increase in free-stream velocity. The value of drag was minute due to the throat orifice constituting 64% of the frontal area. Distinguishing the total drag in its pressure and viscous components, both drag components reduced with an increase in Reynolds number, yet the pressure drag diminished more substantially in magnitude.

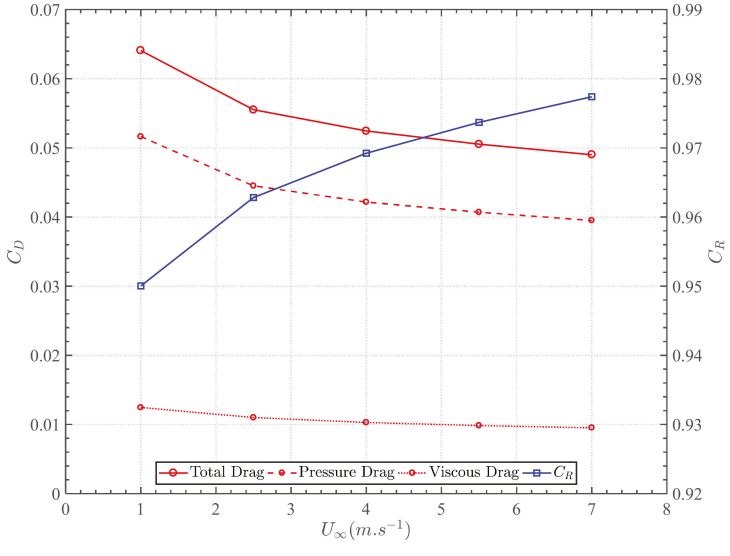

Figure 6. Evaluation of the duct drag coefficient (C_D) and radius coefficient (C_R) with free-stream velocity (U_∞) within aligned flow conditions.

5.2. Axial Velocity and Static Pressure

Evaluating the variation in normalised axial velocity with free-stream velocity, the coefficient increased from a value of 1.410 to 1.493 in accordance with the Reynolds number increase, as illustrated in Figure 7. Similarly, the static pressure within the duct throat decreased along the Reynolds number range from a coefficient of −1.00 to −1.24.

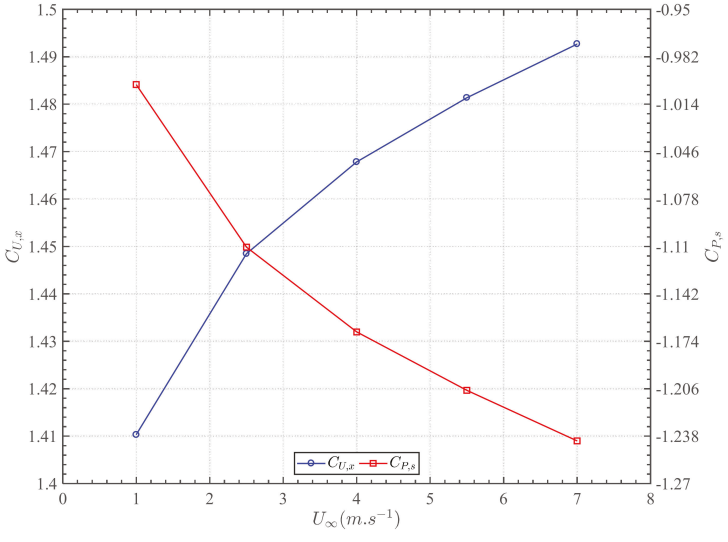

Figure 7. Evaluation of the throat axial velocity coefficient ($C_{U,x}$) and static pressure coefficient ($C_{P,s}$) with free-stream velocity (U_∞).

Primarily, the resultant normalised axial velocity occurred above the free-stream magnitude due to the contraction within the duct throat as a result of Bernoulli's principle. The supplementary increase, in relation to the Reynolds number, transpired due to the diminishing pressure drag, which permitted a higher normalised axial velocity within the duct throat, hence enhancing the swallowing capacity of the duct.

Furthermore, the one-dimensional mass-conservation formula was utilised to acquire the width of the fluid streamtube at a far upstream location in relation to the Reynolds number. The radius coefficient increased proportionally, as illustrated in Figure 6, establishing a larger mass–flow passing through the duct from an upstream position. In accordance with the increase due to the Bernoulli effect, however, it is unattainable for the upstream width (D_1) to surpass the external duct width (D_{ext}). Therefore, when considering an open-ended, cylindrical, bi-directional duct, the maximum axial velocity coefficient potentially attained is equivalent to the duct external–internal areal ratio (D_{ext}^2 / D_{int}^2).

5.3. Duct Surface Static Pressure Coefficients

The variation in static pressure along the inner and outer duct surfaces was analysed along a plane parallel to the free-stream vector, as illustrated in Figure 8. The stagnation point occurred at the leading edge of the internal duct surface. Wall static pressure diminished within the duct constriction towards the throat. Along the external surface, a dip in static pressure was acknowledged due to flow acceleration at the leading edge. A null gauge pressure was consistent along the external duct surface.

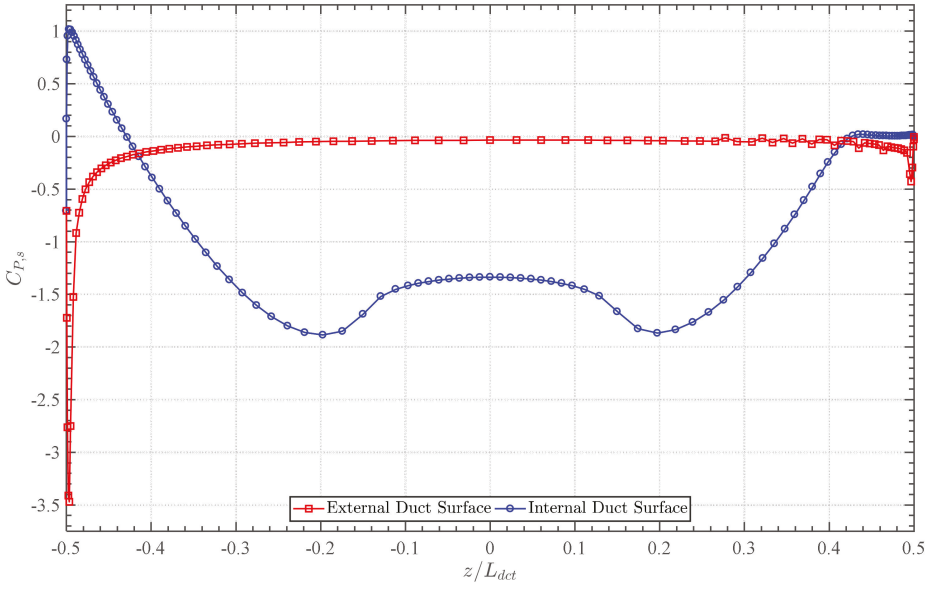

Figure 8. Pressure coefficient ($C_{P,s}$) values along the external straight and internal curved duct surfaces ($U_\infty = 4$ m.s^{-1}; $\gamma = 0°$).

5.4. Wake Velocity Profiles

The normalised axial velocity profiles of the duct wake were analysed from $0.5D_{ext}$ to $6D_{ext}$ downstream, as illustrated in Figure 9. Within the near-wake, at $0.5D_{ext}$, the maximum axial velocity surpassed the free-stream along the duct throat region as a result of the internal flow acceleration. The velocity then diminished beyond the orifice region due to the presence of the duct ridges. The point of minima axial velocity was situated at the trailing edge of the ridge. Further downstream, the wake kinetic energy levelled along the plane, resulting in the velocity profile to be consistent with the free-stream at the far-wake location of $6D_{ext}$.

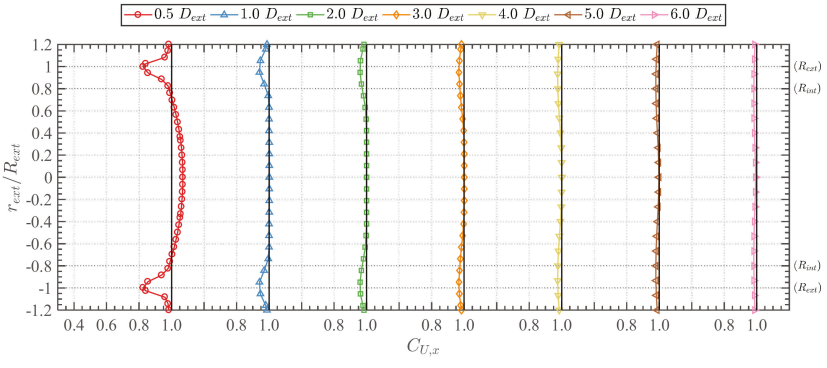

Figure 9. Axial velocity coefficient ($C_{U,x}$) profiles within the duct wake at different downstream displacements ($U_\infty = 4$ m.s^{-1}; $\gamma = 0°$).

6. Vacant Duct Performance in Yawed Flow Conditions

6.1. Drag and Lift Coefficients

Analysing the variation in drag in relation to the free-stream angular bearing, the coefficient decreased from a value of 0.0524 to −0.0690 at bearings from 0° to 30°, as illustrated in Figure 10. The coefficient subsequently increased from −0.0690 to 0.303 at bearings from 30° to 45°. The lift coefficient increased from a value of 0.0841 to 0.815 at bearings from 0° to 30°, and decreased from 0.815 to 0.585 at bearings from 30° to 45°. It should be stated that drag and lift were analysed parallel and perpendicular to the duct axis, rather than the free-stream vector, as upon installation the duct would be fixed to the seabed. The considered directions would be those of interest.

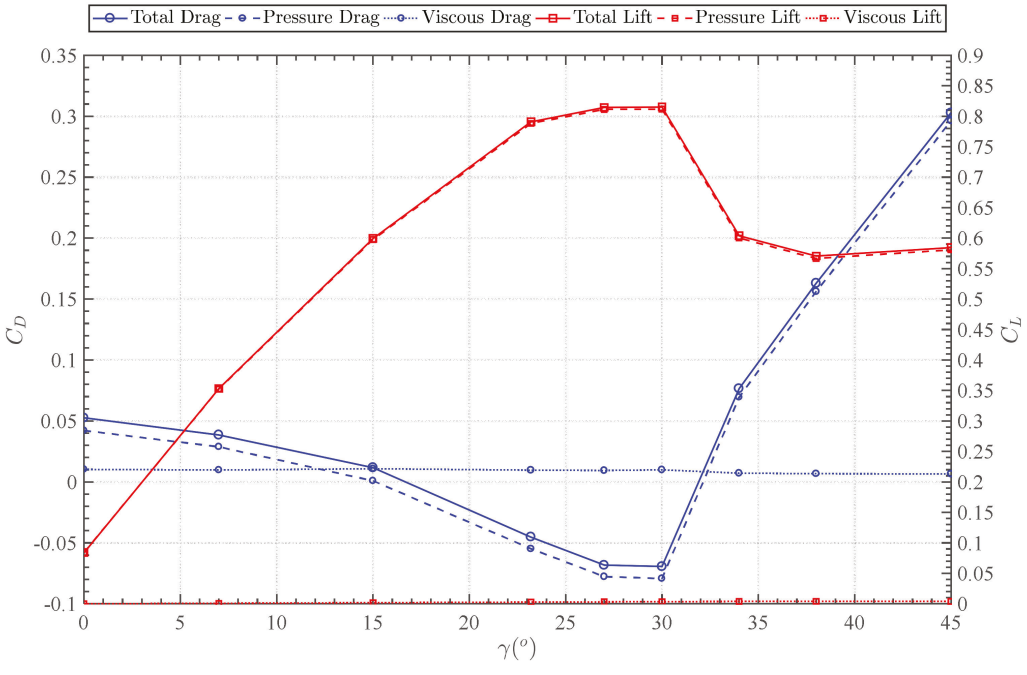

Figure 10. Evaluation of the duct drag coefficient (C_D) and lift coefficient (C_L) with yaw bearing (γ) within a free-stream velocity (U_∞) of 4 m.s^{-1}.

In recognition of the similarity to the drag and lift response of an aerofoil with angle-of-attack, it was acknowledged that the duct static stall limit had therefore occurred at 30°, with the peak lift region initiating at a bearing of 23.2°. Distinguishing the total forces into pressure and viscous forces, the component of pressure was established to be the main variant factor within the dynamic system. The viscous component was consistently negligible. Therefore, in addition to the low pressure induced within the duct throat at aligned flow ($\gamma = 0°$), an increase of the free-stream bearing augmented the low pressure further within the duct throat. This resulted in a total drag reduction with an increase in total lift.

Between a 23.2° and 30° bearing, a laminar separation bubble initiated along the internal wall region of the throat at port-side. Beyond a bearing of 30°, detachment of the laminar bubble occurred, increasing the pressure component of drag due to the flow separation, diminishing lift.

6.2. Axial Velocity and Static Pressure

In accordance with the discrepancy in drag and lift, the variation in normalised axial velocity and static pressure within the duct throat was established, as illustrated in Figure 11. The velocity coefficient increased from a value of 1.47 to 1.53 at bearings from 0° to 23.2°. The coefficient then decreased from 1.53 to 1.09 at bearings from 23.2° to 45°. The static pressure coefficient decreased from −1.17 to −1.37 at bearings from 0° to 23.2°, and increased from −1.37 to −0.49 at bearings from 23.2° to 45°.

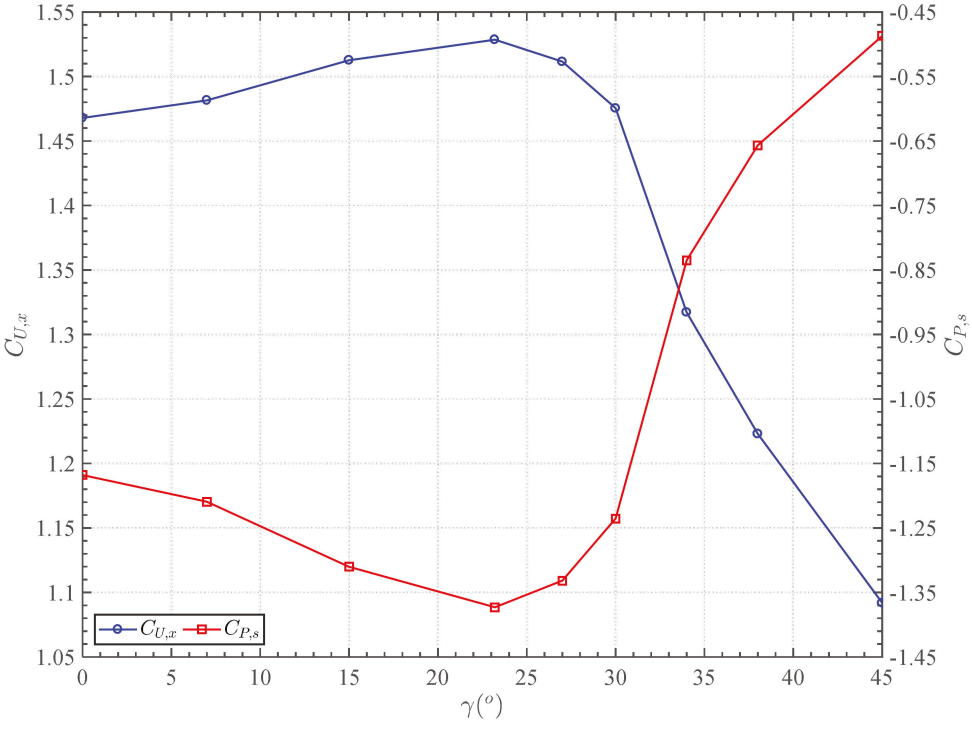

Figure 11. Evaluation of the throat axial velocity coefficient ($C_{U,x}$) and static pressure coefficient ($C_{P,s}$) with yaw bearing (γ) within a free-stream velocity (U_∞) of 4 m.s^{-1}.

In contrast to the drag and lift curves, the maxima normalized axial velocity was attained at 23.2°, rather than at 30°. The generation of a laminar separation bubble, beyond the 23.2° bearing, therefore resulted in the increase of static pressure within the cross-section of the throat orifice. Beyond 30°, the normalized axial velocity rate of change varied significantly due to the separation of the laminar bubble, increasing static pressure substantially. Contours depicting the flow variation through the cross-sectional duct domain at distinct bearings are illustrated in Figures 12 and 13.

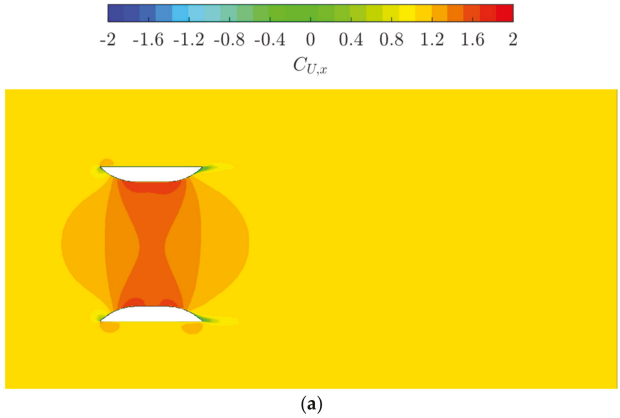

(**a**)

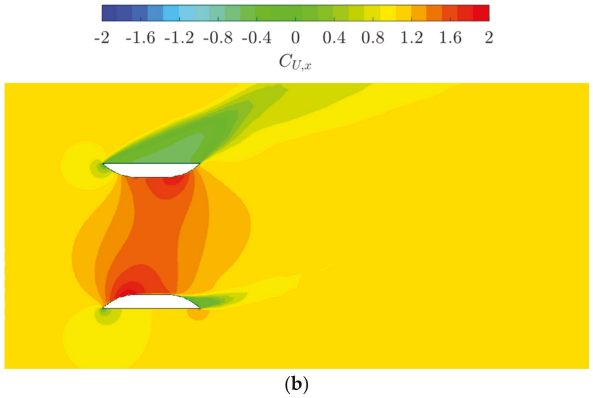

(**b**)

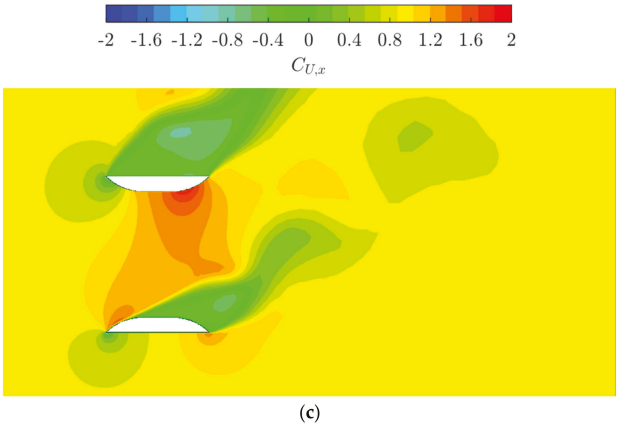

(**c**)

Figure 12. Illustrative cross-sectional representation of the axial velocity coefficient ($C_{U,x}$) within the duct domain at distinct yaw angles ($U_\infty = 4$ m.s^{-1}). (**a**) $\gamma = 0°$; (**b**) $\gamma = 23.2°$; (**c**) $\gamma = 38°$.

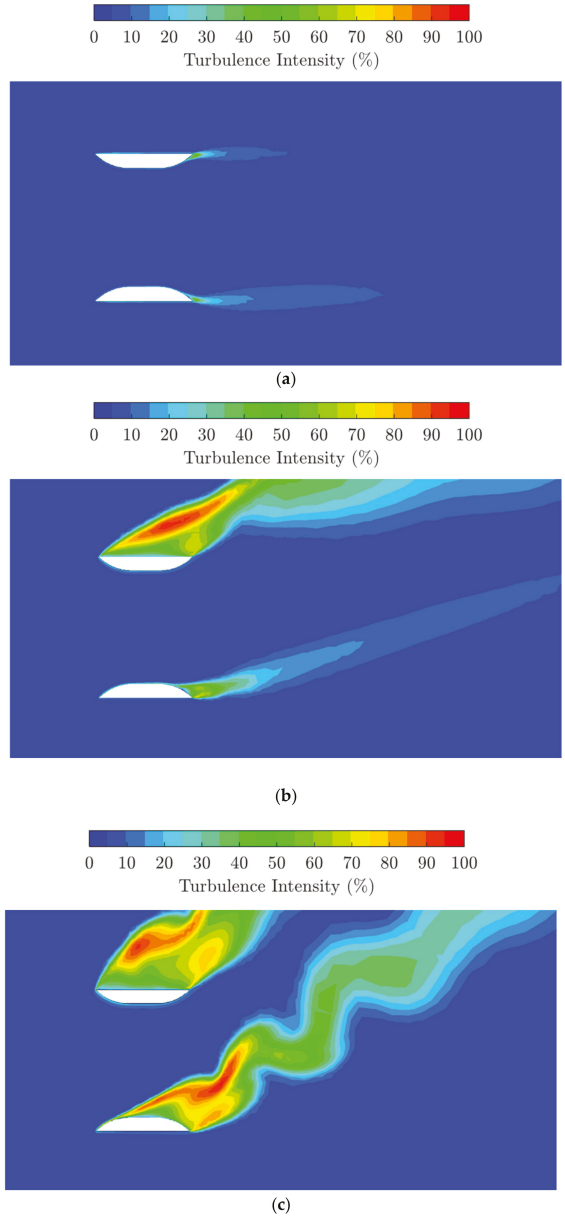

Figure 13. Illustrative cross-sectional representation of the turbulence intensity within the duct domain at distinct yaw angles (U_∞ = 4 m.s^{-1}). (**a**) $\gamma = 0°$; (**b**) $\gamma = 23.2°$; (**c**) $\gamma = 38°$.

6.3. Duct Pressure Coefficients

To establish the angular flow-stream effects upon the wall static pressure induced along the duct surfaces, the distribution along the duct cross-section was analysed as depicted in Figure 14. The surfaces were discretised by their internal and external positions, in starboard and port directions. Furthermore, the static pressure within the domain cross-section is illustrated in Figure 15.

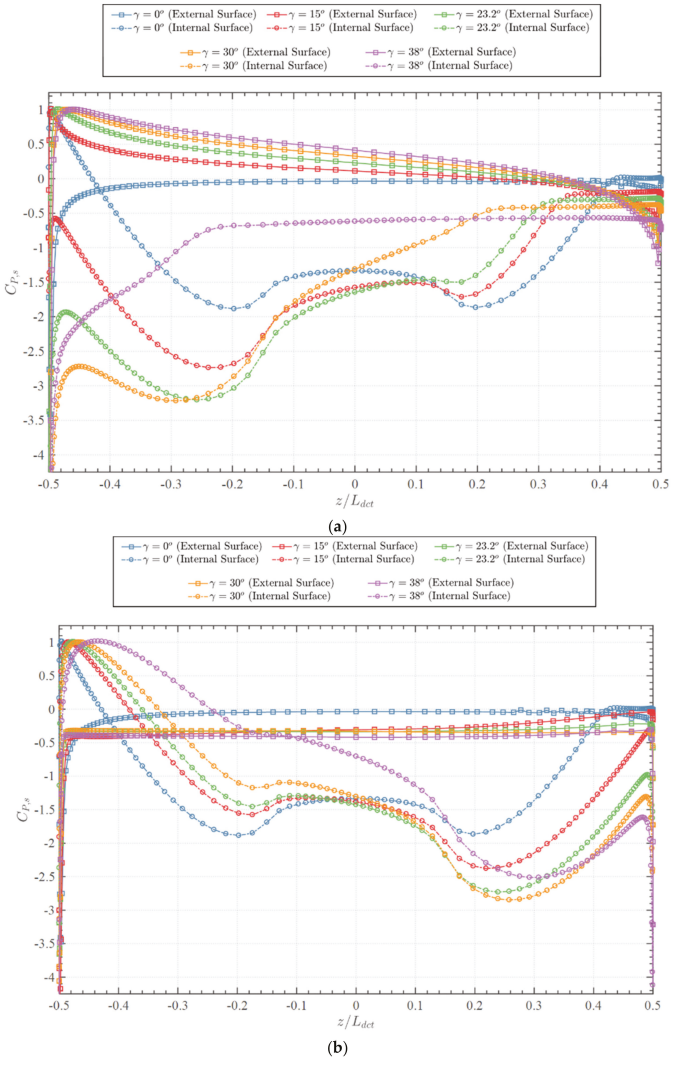

Figure 14. Evaluations of static pressure coefficient ($C_{P,s}$) distribution along the duct surfaces at $\gamma = 0°$, 15°, 23.2°, 30°, 38°. (**a**) Static pressure coefficient along the duct surfaces at port-side; (**b**) Static pressure coefficient along the duct surfaces at starboard-side.

At port, the stagnation point was located along the external surface, towards the leading edge, which shifted further downstream with an increase in yaw angle. This resulted in most of the external surface within the cross-section to be pressurised. The pressure at its trailing edge diminished with yaw bearing. Along the internal upstream curved surface, the pressure reduced in proportion to yaw angle up to a bearing of 30°. At the throat, the lowest wall pressure was attained at a bearing of 23.2°. Along the internal downstream curved surface, the pressure increased in proportion to the yaw angle. The effect of the laminar bubble and flow separation upon the static pressure at the throat was identified as the pressure increased marginally from 23.2° to 30°, yet significantly from 30° to 38°.

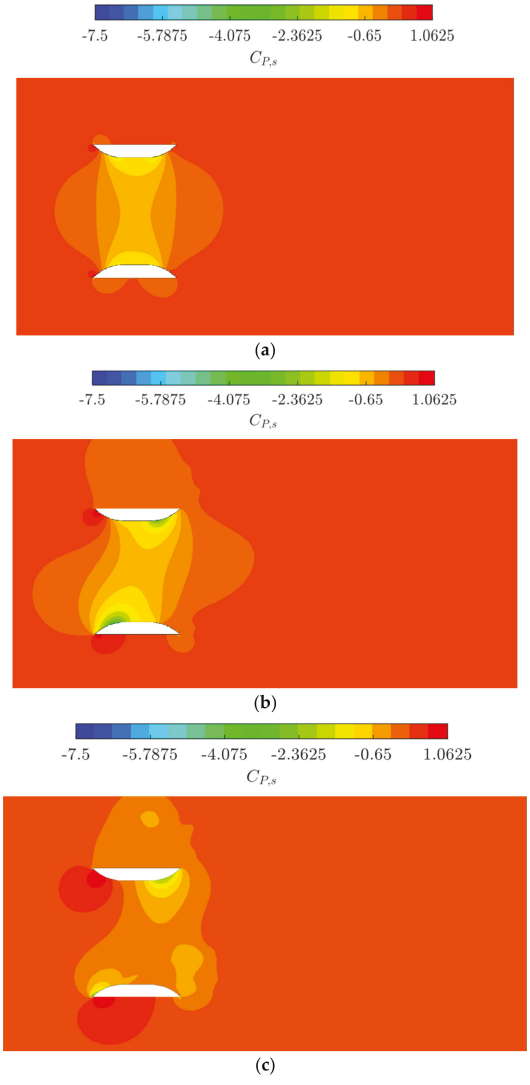

Figure 15. Illustrative cross-sectional representation of the pressure coefficient ($C_{P,s}$) within the duct domain at distinct yaw angles (U_∞ = 4 m.s^{-1}). (**a**) $\gamma = 0°$; (**b**) $\gamma = 23.2°$; (**c**) $\gamma = 38°$.

At starboard, quasi-identical outcomes were established. The stagnation point, however, occurred upon the internal surface. In addition, the variation in pressure at the curved starboard surfaces were inverted to that shown at port. Along the internal upstream curved surface, the pressure increased in proportion to yaw angle. The lowest wall pressure at the throat was also attained at a bearing of 23.2°. Along the internal downstream curved surface, the pressure decreased in proportion to the yaw angle.

7. Discussion

The swallowing capacity of a vacant bi-directional duct utilised for the purpose of ducted tidal turbine systems was numerically analysed by implementing computational fluid dynamic modelling. The analysis was undertaken to establish the potential augmen-

tations in a rotor streamtube induced by the duct installation in both aligned and yawed flow conditions.

Within aligned flow conditions, the normalised axial velocity through the duct was acknowledged to increase beyond the free-stream as a result of the Bernoulli effect. The velocity increased further, proportional to the Reynolds number, due to a diminishment in pressure drag. The mass conservation equation was utilised to establish the width of the streamtube at the far-field position, which was found to increase with Reynolds number. Therefore, a higher mass–flow from an upstream position passed through the duct throat.

Within yawed flow conditions, the normalised axial velocity was further augmented by a maximum of 4.13% at a 23.2° bearing. This increase in axial velocity came about due to the diminishment in static pressure within the duct throat, as the angle-of-attack between the duct section and the free-stream vector increased, permitting a higher flow-rate. The normalised axial velocity then decreased at yaw angles beyond the 23.2° bearing due to the initiation of a laminar separation bubble, which increased static pressure within the throat. Flow separation was induced within the shroud beyond a flow bearing of 30°. As a result, pressure drag increased, leading to a significant reduction in the normalised axial velocity through the duct. With the reduced velocity, insufficient boundary layer momentum was present for the flow to re-attach at the downstream internal section of the duct, instituting diffuser stall.

8. Conclusions

The study analysed the hydrodynamic swallowing-capacity of a true-scale, vacant, cylindrical, bi-directional duct for tidal turbine applications in aligned and yawed inlet flows by utilising three-dimensional unsteady computational fluid dynamics. The performance was investigated within free-stream magnitudes of 1 to 7 $m.s^{-1}$, and a bearing angular range of 0° to 45° with the duct axis. This analysis was imperative to acknowledge the potential axial velocity increase through a rotor for augmented power generation.

The swallowing capacity was found to increase due to the reduction in pressure drag upon the duct with an increase in Reynolds number. Within yawed flow conditions, the augmentation occurred due to the duct-profile lift variation with angle-of-attack. At a nominal yaw angle of 23.2°, the static pressure at the throat was at its minimum, permitting the maximum mass–flow rate. Beyond the nominal angle-of-attack, the initiation of a laminar separation bubble, and subsequent flow separation, occurred within the duct. The flow features increased the static pressure within the throat, thereby reducing the swallowing capacity. The swallowing capacity of the duct was therefore acknowledged to be dependent on the Reynolds number and its nominal angle-of-attack to the free-stream yaw bearing.

Author Contributions: M.G.B.: conceptualization, methodology, software, validation, formal analysis, investigation, writing—original draft. Q.X.: writing—review and editing, supervision, resources, project administration. S.A.: conceptualization, writing—review and editing, resources, formal analysis, investigation. A.I.: funding acquisition, resources. C.P.: resources, supervision. All authors have read and agreed to the published version of the manuscript.

Funding: This research was funded by the EPSRC Supergen ORE Hub Flexible Fund Program Grant (Grant No. EP/S000747/1).

Acknowledgments: The research work disclosed in this publication is partially funded by the Endeavour Scholarship Scheme (Malta). Scholarships are part-financed by the European Union—European Social Fund (ESF)—Operational Programme II—Cohesion Policy 2014–2020: "Investing in human capital to create more opportunities and promote the well-being of society", CCI number: 2014MT05SFOP001. Results were obtained using ARCHIE-WeSt High Performance Computer (www.archie-west.ac.uk).

Conflicts of Interest: The authors declare no conflict of interest. The funders had no role in the design of the study; in the collection, analyses, or interpretation of data; in the writing of the manuscript; or in the decision to publish the results.

Appendix A

In addition to the mean values of the analyses conducted within this study, the standard deviations of the results are illustrated in Figure A1. In comparison to the mean values, the deviations were acknowledged to be relatively minute.

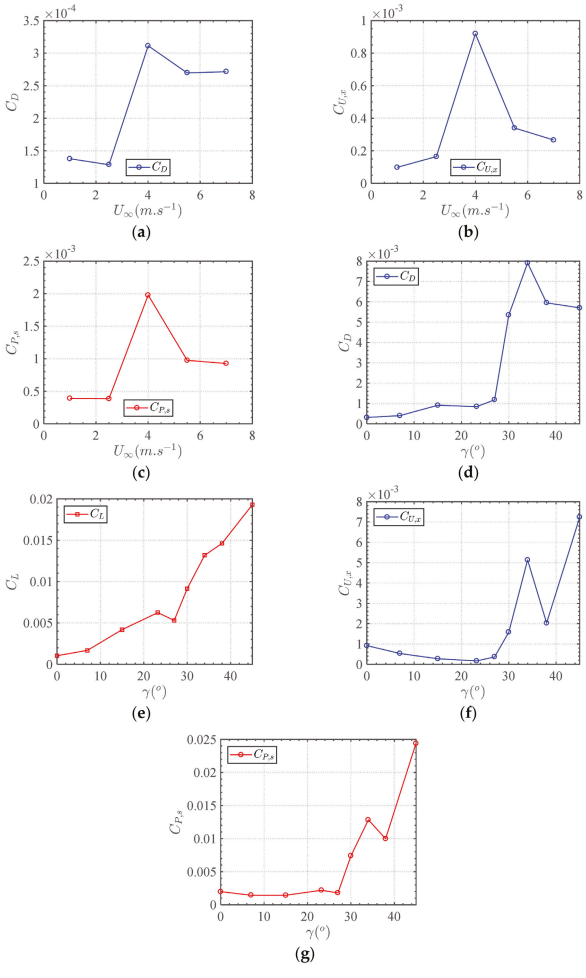

Figure A1. Evaluations of the standard deviation of the analyses conducted at aligned and yawed flows. (**a**) Evaluation of the duct drag coefficient (C_D) with free-stream velocity (U_∞) within aligned flow conditions; (**b**) Evaluation of the duct axial velocity coefficient ($C_{U,x}$) with free-stream velocity (U_∞) within aligned flow conditions; (**c**) Evaluation of the duct static pressure coefficient ($C_{P,s}$) with free-stream velocity (U_∞) within aligned flow conditions; (**d**) Evaluation of the duct drag coefficient (C_D) with angular bearing (γ) within yawed flow conditions; (**e**) Evaluation of the duct lift coefficient (C_L) with angular bearing (γ) within yawed flow conditions; (**f**) Evaluation of the duct axial velocity coefficient ($C_{U,x}$) with angular bearing (γ) within yawed flow conditions; (**g**) Evaluation of the duct static pressure coefficient ($C_{P,s}$) with angular bearing (γ) within yawed flow conditions.

References

1. European Commission (Luxembourg: Office for Official Publications of the European Communities). A European Green Deal. Available online: https://ec.europa.eu/info/strategy/priorities-2019-2024/european-green-deal_en (accessed on 21 December 2020).
2. Rourke, F.O.; Boyle, F.; Reynolds, A. Tidal energy update 2009. *Appl. Energy* **2010**, *87*, 398–409. [CrossRef]
3. European Marine Energy Centre (EMEC) Ltd. Tidal Clients. Available online: http://tidalenergy.net.au/index-subpage-2.html (accessed on 2 February 2014).
4. Goundar, J.N.; Ahmed, M.R. Design of a horizontal axis tidal current turbine. *Appl. Energy* **2013**, *111*, 161–174. [CrossRef]
5. Kogan, F.A.; Seginer, A.T.A.E. *Rep. No. 32A: Final Report on Shroud Design: Tech. Rep.*; Department of Aeronautical Engineering, Technion-Israel Institute of Technology: Haifa, Israel, 1963.
6. Bloomberg, L.P. OpenHydro Group Ltd. Available online: https://www.bloomberg.com/profile/company/4074464Z:ID2018 (accessed on 24 December 2020).
7. OpenHydro Group Ltd. Projects. Available online: http://www.openhydro.com/Projects (accessed on 13 August 2017).
8. The Canadian Press. Cape Sharp Tidal Turbine in Bay of Fundy Now Being Monitored Remotely. Available online: https://www.cbc.ca/news/canada/nova-scotia/cape-sharp-tidal-turbine-remote-monitoring-environment-1.4814069 (accessed on 15 September 2018).
9. Ohya, Y.; Karasudani, T.; Sakurai, A.; Abe, K.; Inoue, M. Development of a shrouded wind turbine with a flanged diffuser. *J. Wind Eng. Ind. Aerodyn.* **2008**, *96*, 524–539. [CrossRef]
10. Masukume, P.; Makaka, G.; Tinarwo, D. Optimum Geometrical Shape Parameters for Conical Diffusers in Ducted Wind Turbines. *Int. J. Energy Power Eng.* **2016**, *5*, 177–181.
11. Masukume, P.-M.; Makaka, G.; Mukumba, P. Optimization of the Power Output of a Bare Wind Turbine by the Use of a Plain Conical Diffuser. *Sustainability* **2018**, *10*, 2647. [CrossRef]
12. Setoguchi, T.; Shiomi, N.; Kaneko, K. Development of two-way diffuser for fluid energy conversion system. *Renew. Energy* **2004**, *29*, 1757–1771. [CrossRef]
13. Cresswell, N.W.; Ingram, G.; Dominy, R. The impact of diffuser augmentation on a tidal stream turbine. *Ocean Eng.* **2015**, *108*, 155–163. [CrossRef]
14. Kardous, D.M.; Chaker, R.; Aloui, F.; Nasrallah, S.B. On the dependence of an empty flanged diffuser performance on flange height: Numerical simulations and PIV visualizations. *Renew. Energy* **2013**, *56*, 123–128. [CrossRef]
15. Kannan, T.S.; Mutasher, S.A.; Lau, Y.K. Design and flow velocity simulation of diffuser augmented wind turbine using CFD. *J. Eng. Sci. Technol.* **2013**, *8*, 372–384.
16. Mansour, K.; Meskinkhoda, P. Computational analysis of flow fields around flanged diffusers. *J. Wind Eng. Ind. Aerodyn.* **2014**, *124*, 109–120. [CrossRef]
17. Khamlaj, T.A.; Rumpfkeil, M.P. Analysis and optimization of ducted wind turbines. *Energy* **2018**, *162*, 1234–1252. [CrossRef]
18. Kesby, J.E.; Bradney, D.R.; Clausen, P.D. Determining diffuser augmented wind turbine performance using a combined CFD/BEM method. *J. Phys. Conf. Ser.* **2016**, *753*, 10736–10774. [CrossRef]
19. El-Zahaby, A.M.; Kabeel, A.; Elsayed, S.; Obiaa, M. CFD analysis of flow fields for shrouded wind turbine's diffuser model with different flange angles. *Alex. Eng. J.* **2017**, *56*, 171–179. [CrossRef]
20. Tampier, G.; Troncoso, C.; Zilic, F. Numerical analysis of a diffuser-augmented hydrokinetic turbine. *Ocean Eng.* **2017**, *145*, 138–147. [CrossRef]
21. Borg, M.G.; Xiao, Q.; Allsop, S.; Incecik, A.; Peyrard, C. A numerical performance analysis of a ducted, high-solidity tidal turbine. *Renew. Energy* **2020**, *159*, 663–682. [CrossRef]
22. Wilcox, D.C. *Turbulence Modeling for CFD*, 3rd ed.; DCW Industries, Inc.: San Diego, CA, USA, 2006.
23. Neill, S.P.; Jordan, J.R.; Couch, S.J. Impact of tidal energy converter (TEC) arrays on the dynamics of headland sand banks. *Renew. Energy* **2012**, *37*, 387–397. [CrossRef]
24. Bahaj, A.; Myers, L. Analytical estimates of the energy yield potential from the Alderney Race (Channel Islands) using marine current energy converters. *Renew. Energy* **2004**, *29*, 1931–1945. [CrossRef]
25. Pham, C.T.; Martin, V.A. Tidal current turbine demonstration farm in Paimpol-Brehat (Brittany): Tidal characterisation and energy yield evaluation with TELEMAC. In Proceedings of the 8th European Wave and Tidal Energy Conference, Uppsala, Sweden, 7–8 September 2009.
26. Pham, C.; Pinte, K. Paimpol-Bréhat tidal turbine demonstration farm (brittany): Optimisation of the layout, wake effects and energy yield evaluation using TELEMAC. In Proceedings of the 3rd International Conference on Ocean Energy, Bilbao, Spain, 6–7 October 2010.
27. Mason-Jones, A.; O'Doherty, D.M.; Morris, C.E.; O'Doherty, T.; Byrne, C.B.; Prickett, P.W.; Grosvenor, R.I.; Owen, I.; Tedds, S.; Poole, R.J. Non-Dimensional Scaling of Tidal Stream Turbines. *Energy* **2012**, *44*, 820–829. [CrossRef]
28. Resistance Committee of the 28th ITTC. *Uncertainty Analysis in CFD Verification and Validation, Methodology and Procedures*; Technical Report; ITTC: Zürich, Switzerland, 2017.
29. Mycek, P.; Gaurier, B.; Germain, G.; Pinon, G.; Rivoalen, E. Experimental study of the turbulence intensity effects on marine current turbines behaviour. Part I: One single turbine. *Renew. Energy* **2014**, *66*, 729–746. [CrossRef]

Journal of *Marine Science and Engineering*

MDPI

Article

Investigating the Effect of Heterogeneous Hull Roughness on Ship Resistance Using CFD

Soonseok Song [1], Yigit Kemal Demirel [1,*], Claire De Marco Muscat-Fenech [2], Tonio Sant [2], Diego Villa [3], Tahsin Tezdogan [1] and Atilla Incecik [4]

[1] Department of Naval Architecture, Ocean and Marine Engineering, University of Strathclyde, Glasgow G1 0LZ, UK; soonseok.song@strath.ac.uk (S.S.); tahsin.tezdogan@strath.ac.uk (T.T.)
[2] Department of Mechanical Engineering, University of Malta, Msida, MSD 2080, Malta; claire.demarco@um.edu.mt (C.D.M.M.-F.); tonio.sant@um.edu.mt (T.S.)
[3] Department of Electrical, Electronic, Telecommunication Engineering and Naval Architecture, University of Genoa, Via all'Opera Pia, 11A, 16145 Genova, Italy; diego.villa@unige.it
[4] Faculty of Engineering, University of Strathclyde, Glasgow G1 1XJ, UK; atilla.incecik@strath.ac.uk
* Correspondence: yigit.demirel@strath.ac.uk; Tel.: +44-(0)1415483463

Abstract: Research into the effects of hull roughness on ship resistance and propulsion is well established, however, the effect of heterogeneous hull roughness is not yet fully understood. In this study, Computational Fluid Dynamics (CFD) simulations were conducted to investigate the effect of heterogeneous hull roughness on ship resistance. The Wigley hull was modelled with various hull conditions, including homogeneous and heterogeneous hull conditions. The results were compared against existing experimental data and showed a good agreement, suggesting that the CFD approach is valid for predicting the effect of heterogeneous hull roughness on ship resistance. Furthermore, the local distributions of the wall shear stress and roughness Reynolds number on the hull surface were examined to assess the flow characteristics over the heterogeneous hull roughness.

Keywords: roughness effect; Wigley hull; ship resistance; heterogeneous hull roughness; computational fluid dynamics (CFD)

Citation: Song, S.; Demirel, Y.K.; De Marco Muscat-Fenech, C.; Sant, T.; Villa, D.; Tezdogan, T.; Incecik, A. Investigating the Effect of Heterogeneous Hull Roughness on Ship Resistance Using CFD. *J. Mar. Sci. Eng.* **2021**, *9*, 202. https://doi.org/10.3390/jmse9020202

Academic Editor: Dong-Sheng Jeng

Received: 28 January 2021
Accepted: 10 February 2021
Published: 16 February 2021

1. Introduction

One of the major barriers to energy-efficient shipping is hull roughness, which is caused by various factors including mechanical causes, chemical and electrochemical processes (i.e., corrosion), and the colonisation of biofouling [1,2]. The associated economic and environmental problems include the added ship resistance and increased fuel consumption and CO2 emissions, as well as the cost for the hull maintenance. From a naval architect or a ship owner's point of view, a proper life cycle assessment is needed to improve the profitability of the ship. In other words, the economic penalties associated with the increased fuel consumption and/or the speed loss of ships should be accurately predicted and compared with the costs associated with the antifouling activities.

Accordingly, there have been investigations and studies to predict the impact of hull roughness on ship performance. The similarity law scaling procedure proposed by Granville [3,4] has been preferred by many researchers, e.g., [5–9], owing to its merits including the computational cost-effectiveness and the robustness for arbitrary ship lengths and speeds [10]. However, Granville's method is still limited by the flat plate simplification, which disregards the 3D effects, e.g., form resistance [11].

On the other hand, a Computational Fluid Dynamics (CFD) approach has been routinely employed in the field of naval architecture and ocean engineering owing to the merits that CFD can overcome the difficulties of nonlinear problems in theoretical studies while it is more cost-efficient compared to physical experiments [12–15]. Furthermore, the afore-mentioned shortcomings of Granville's method can be avoided using CFD. In CFD

simulations, the 3D effects can be considered and thus the ship resistance predictions can be more accurate. Furthermore, the CFD method is not only limited to ship hulls, but it can be applied for an arbitrary object in fluid. Accordingly, the CFD method has been used for investigating the roughness effect on ship resistance, e.g., [16–18], propeller performance, e.g., [19,20], and ship self-propulsion performance, e.g., [21,22], as well as the tidal turbine performance, e.g., [23].

Recently, Song et al. [24,25] validated Granville's method and the CFD method by comparing the predictions against a ship model test with a rough surface.

However, the majority of the studies have treated the hull surfaces as uniformly rough, while the real ships' surfaces are not uniform due to the heterogeneous biofouling accumulation on the hull. The simplification of treating the surfaces as uniformly rough can introduce inaccuracies in predicting the added resistance, as claimed by Demirel et al. [26].

Recently, Song et al. [27] conducted towing tests using a Wigley hull model with various hull roughness conditions including homogeneous conditions (i.e., smooth and full-rough) and heterogeneous conditions (i.e., $\frac{1}{4}$-bow-rough, $\frac{1}{4}$-aft-rough, $\frac{1}{2}$-bow-rough and $\frac{1}{2}$-aft-rough) by applying sand-grit on the hull surface systematically. Owing to the symmetric shape of the Wigley hull, the total resistance with the bow and aft-rough conditions could be compared to each other with the same rough surface areas. The result showed that the bow-rough conditions (i.e., $\frac{1}{4}$-bow-rough and $\frac{1}{2}$-bow-rough) showed larger added resistance than the aft-rough conditions (i.e., $\frac{1}{4}$-aft-rough and $\frac{1}{2}$-aft-rough). This finding suggests that the hull roughness in the forward part of the hull is more significant than other parts in terms of added resistance. This finding is attributed to the higher local skin friction near the leading edge, which is found either on smooth or rough surfaces. Song et al. [26] suggest that this higher local skin friction near the leading edge results in a higher roughness Reynolds number and thus a more significant roughness effect acts at the forward part of the hull. However, the study could not confirm the underlying cause since the local skin friction on the hull was not determined whilst measuring the total drag of the model.

On the other hand, there have been recent studies modelling the heterogeneous hull roughness in CFD simulations. Östman et al. [28] conducted CFD simulations of a full-scale tanker to investigate the potential in a low-cost approach for ship resistance reduction with selective applications of different quality coatings. In the CFD simulations, a high-quality coating (low roughness) surface was applied on the regions where high skin friction is concentrated, while the rest of the hull was modelled with a low-quality coating (high roughness). The result showed that the low-cost approach can reduce the ship resistance compared to the case when the low-quality coating is applied on the entire hull. Vargas et al. [29] investigated the impact of homogeneous and heterogeneous roughness distributions using CFD. A full-scale combatant was modelled with divided hull sections to evaluate different hull roughness scenarios. The result showed that the increase in the local skin friction due to hull roughness is highest at the bow, followed by sides, flat bottom, stern and transom, suggesting the benefits of partial hull cleaning. However, while these studies showed that the CFD simulations can be used to model the heterogenous hull roughness, their results were not validated against experimental data. Therefore, there is a need for a dedicated validation study to demonstrate the validity of the CFD approaches for predicting the effects of heterogeneous hull roughness.

The aim of the present study is, therefore, to fill this research gap by conducting CFD simulations to predict the effect of heterogeneous hull roughness on ship resistance and also performing a validation study by comparing the results with experimental data. In addition, the CFD simulations enable us to examine the local skin friction and roughness Reynolds number on the hull, and thus the locally varying flow regime over the heterogeneous hull roughness can be examined.

In this study, CFD simulations of the Wigley hull were developed with different hull roughness conditions using the modified wall-function approach with the roughness function model of the sand-grain surface, which were determined from previous

studies [24,25]. The CFD simulations of the Wigley hull model were performed with different hull conditions. The predicted total resistance coefficients for the various hull conditions were compared with the experimental data [27] for validation purposes. Finally, the local skin friction and the roughness Reynolds number distribution on the hull surfaces were correlated with the findings of the effect of heterogeneous roughness.

2. Methodology

2.1. Approach

Figure 1 schematically illustrates the methodology used in this study. An Unsteady Reynolds Averaged Navier–Stokes (URANS)-based CFD model was developed to replicate the physical Wigley hull model test of Song et al. [27]. The different hull roughness conditions were modelled using the modified wall-function approach with the roughness function model (ΔU^+) of Song et al. [25]. The CFD simulations were performed with different hull conditions and compared with the towing test results [27]. Finally, the local wall shear stress and the roughness Reynolds number on the hull surfaces were examined to be correlated with the findings.

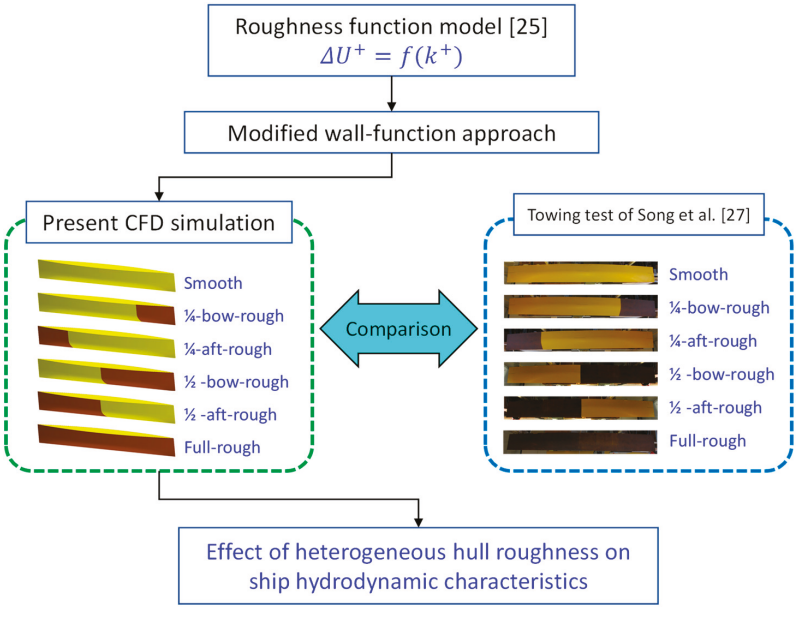

Figure 1. Schematic illustration of the current methodology.

2.2. Numerical Modelling

2.2.1. Mathematical Formulations

The URANS method was used to solve the governing equations using STAR-CCM+. The averaged continuity and momentum equations for incompressible flows can be given as

$$\frac{\partial(\rho\overline{u}_i)}{\partial x_i} = 0 \tag{1}$$

$$\frac{\partial(\rho\overline{u}_i)}{\partial t} + \frac{\partial}{\partial x_j}\left(\rho\overline{u}_i\overline{u}_j + \rho\overline{u_i'u_j'}\right) = -\frac{\partial\overline{p}}{\partial x_i} + \frac{\partial\overline{\tau}_{ij}}{\partial x_j} \tag{2}$$

where, ρ is the fluid density, $\overline{u}_i$ is the time-averaged velocity vector, $\rho\overline{u_i'u_j'}$ is the Reynolds stress, $\overline{p}$ is the time-averaged pressure, $\overline{\tau}_{ij}$ is the mean viscous stress tensor components. This viscous stress for a Newtonian fluid can be expressed as

$$\overline{\tau}_{ij} = \mu\left(\frac{\partial\overline{u}_i}{\partial x_j} + \frac{\partial\overline{u}_j}{\partial x_i}\right) \tag{3}$$

In which, μ is the dynamic viscosity. The governing equations were discretised using the finite volume method with a second-order convection scheme and a first-order temporal discretisation. The k-ω SST turbulence model [30] was adopted to capture the turbulent flow, which combines the advantages of the k-ω and the k-ε turbulence models. For the free surface effects, the Volume of Fluid (VOF) method was used.

2.2.2. Modified Wall-Function Approach

The roughness effect causes a downward shift of the velocity profile in the turbulent boundary layer. This downward shift is often called the "roughness function", ΔU^+. With the roughness function, ΔU^+, the log-law of the turbulent boundary layer can be written as

$$U^+ = \frac{1}{\kappa}\ln y^+ + B - \Delta U^+ \tag{4}$$

In which, U^+ is non-dimensional velocity defined as the ratio between the mean velocity, and the frictional velocity (i.e., $U^+ = U/U_\tau$). U_τ is defined as $\sqrt{\tau_w/\rho}$ where τ_w is the wall shear stress and ρ is the fluid density. y^+ is the non-dimensional length defined as yU_τ/ν, in which y is the normal distance from the wall and ν is the kinematic viscosity. κ is the von Karman constant (=0.42) and B is the log-low intercept.

The roughness function, ΔU^+ is a function of roughness Reynolds number, k^+, defined as

$$k^+ = \frac{kU_\tau}{\nu} \tag{5}$$

In which, k is the roughness height of the surface. The modified wall-function Equation (1) can be employed in CFD simulations to predict the roughness effect in the flow over the rough wall.

Song et al. [24] evaluated the roughness function of the sand grit (60/80 grit aluminium oxide abrasive powder) from the results of flat plate towing tests. Later on, a mathematical model of the roughness function (i.e., roughness function model) was proposed by Song et al. [25] to be used in CFD simulations.

As the same sand grit was used for the Wigley hull towing test [27], the same modified wall-function approach [25] was employed in this study to model the heterogeneous hull roughness conditions in CFD simulations. As proposed by Song et al. [25], the roughness function model for the 60/80 grit sand grain surface can be written as

$$\Delta U^+ = \begin{cases} 0 & \rightarrow \quad k^+ < 3 \\ \frac{1}{\kappa}\ln\left(0.49k^+ - 3\left(\frac{k^+-3}{25-3}\right)\right)^{\sin\left[\frac{\pi}{2}\,\frac{\log(k^+/3)}{\log(25/3)}\right]} & \rightarrow \quad 3 \le k^+ < 25 \\ \frac{1}{\kappa}\ln(0.49k^+ - 3) & \rightarrow \quad 25 \le k^+ \end{cases} \tag{6}$$

where k^+ is the roughness Reynolds number based on the peak roughness height over a 50 mm interval (i.e., $k = Rt_{50} = 353$ μm). As shown in Figure 2, the roughness function model of Song et al. [25] agrees well with the experimental roughness function [24].

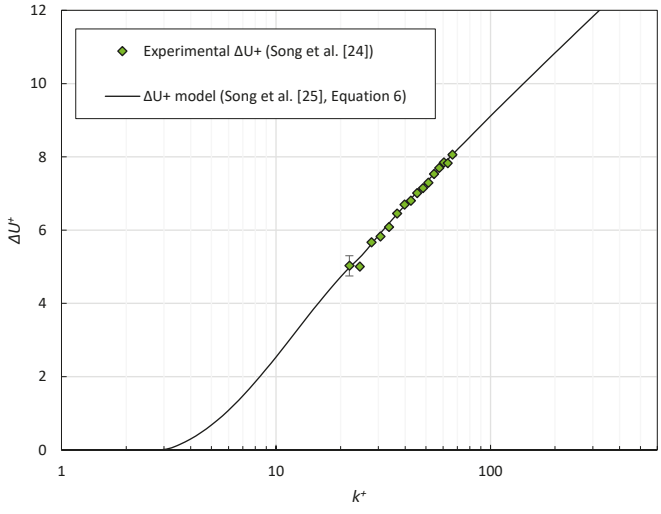

Figure 2. Experimental roughness function of Song et al. [24] and the roughness function model of Song et al. [25] Equation (6).

2.2.3. Geometry and Boundary Conditions

The Wigley hull is a parabolic hull form represented as

$$y = \frac{B}{2}\left[1 - \left(\frac{2x}{L}\right)^2\right]\left[1 + \left(\frac{z}{T}\right)^2\right] \quad (7)$$

where, L, B and T are the length, waterline beam and the draught of the model. In the current CFD simulations, the Wigley hull was modelled using the principal particulars used for the physical towing tests of Song et al. [27] as shown in Table 1.

Table 1. Principal particulars of the Wigley model and simulation conditions.

Length	L (m)	3.00
Beam at waterline	B (m)	0.30
Draft	T (m)	0.1875
Beam/draft ratio	B/T	1.6
Total wetted surface area	S (m^2)	1.3383
Wetted surface area of first quarter	S_{Q1} (m^2)	0.3066
Wetted surface area of first half	S_{H1} (m^2)	0.6691
Displacement	∇ (m^3)	0.0750
Block coefficient	C_B	0.4444
Towing speed	V (m/s)	1.08–2.17
Froude number	Fr	0.2–0.4
Reynolds number	Re_L	2.6–5.3 × 106
Water temperature	T_w (°C)	12

As shown in Figure 3, the different hull roughness conditions tested by Song et al. [27] were modelled in CFD simulations. It is of note that the four regions of the Wigley hull have the same longitudinal length (i.e., $L/4$).

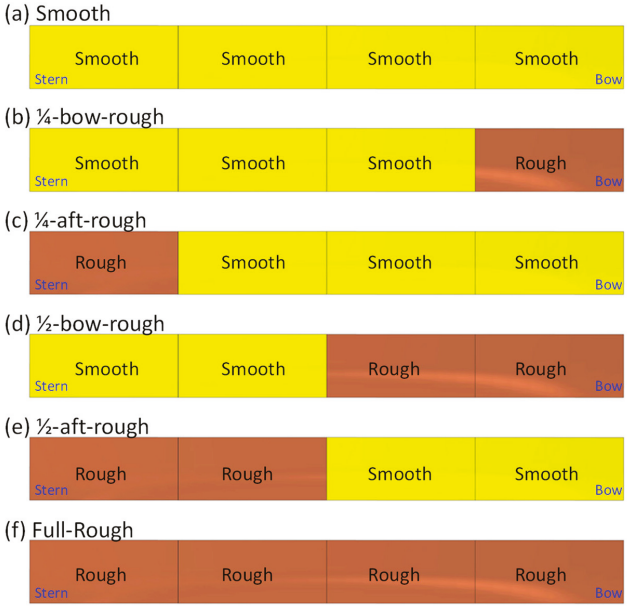

Figure 3. Different hull conditions of the Wigley hull simulations.

Figure 4 depicts the computational domain and the boundary conditions of the Wigley hull simulations used in this study. The computational domain size was chosen to be similar to that used by Dogrul et al. [31]. The velocity inlet boundary conditions were used for the inlet, top and bottom boundaries while the pressure outlet boundary condition was used for the outlet boundary. The centre midplane was defined as a symmetry plane. The no-slip wall boundary condition was used for the hull surface whilst simultaneously using different wall-functions. In other words, the modified wall-function, i.e., Equation (1) was used for the rough surfaces and the smooth-type wall-function (i.e., Equation (1) with $\Delta U^+ = 0$) is used for the smooth surfaces. The model was free to heave and sink in the simulations.

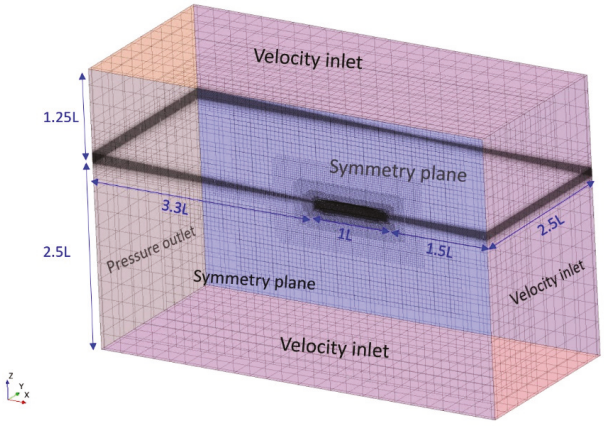

Figure 4. Computational domain and the boundary conditions of the Wigley hull simulation.

2.2.4. Mesh Generation

Figure 5 shows the grid structure used for the CFD simulations. The mesh generation was performed using the automated mesher of STAR-CCM+, with the Cartesian cut-cell method. The wall y^+ values were kept higher than 30 as well as the k^+ values as recommended by Siemens [32], as shown in Figure 6. It should be noted that the same mesh was used for all the simulations regardless of the surface conditions.

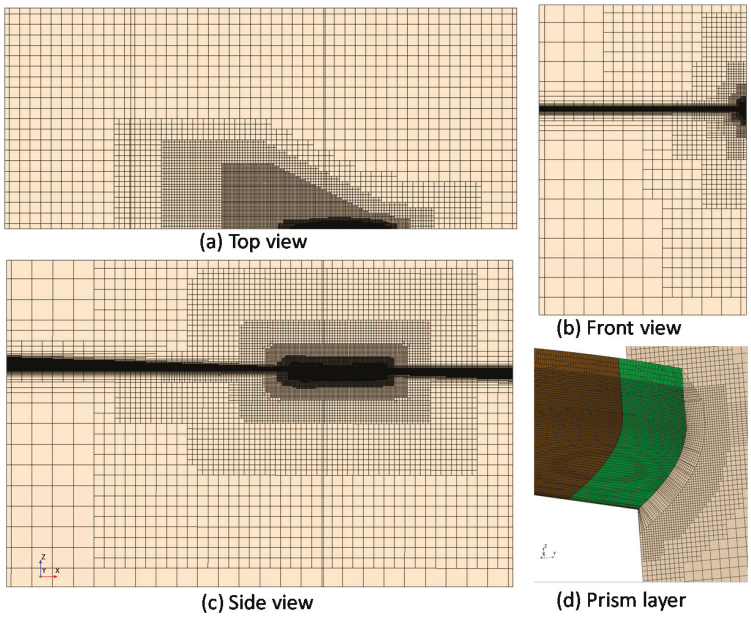

Figure 5. Volume mesh of the Wigley hull simulation.

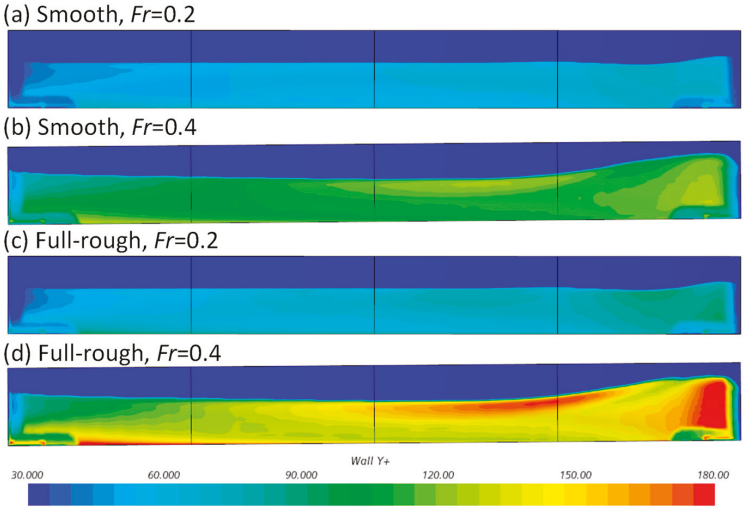

Figure 6. Wall y + on the Wigley hull.

3. Results

3.1. Verification Study

Spatial and temporal verification studies were performed to estimate the numerical uncertainties of the CFD model. The Wigley hull CFD simulations were conducted using three different resolutions of grids and time steps (i.e., Fine, Medium and Coarse), at $Fr = 0.3$ with the smooth hull condition. The Grid Convergence Index (GCI) method [33] was used to determine the spatial and temporal uncertainties (U_{Grid} and $U_{\Delta t}$) in the total resistance coefficient, C_T, predictions as similarly used by other recent studies.

Table 2 shows the U_{Grid} and $U_{\Delta t}$ values estimated from the convergence studies. As shown in the Table 2, U_{Grid} and $U_{\Delta t}$ for the Wigley hull simulation are 0.053% and 0.022%, respectively, resulting in U_{Total} of 0.057%. It is of note that the following simulation results were obtained using the fine mesh and fine time step.

Table 2. Spatial and temporal convergence study of the Wigley hull simulation, Fr = 0.3, smooth hull.

Spatial Convergence		**No.Cells**	**Δt (s)**	C_T
	Coarse	414,173	0.01	5.292×10^{-3}
	Medium	776,227	0.01	5.273×10^{-3}
	Fine	1,587,310	0.01	5.267×10^{-3}
U_{Grid} **(Fine)**				0.053%
Temporal Convergence		**No.Cells**	**Δt (s)**	C_T
	Coarse	1,587,310	0.04	5.169×10^{-3}
	Medium	1,587,310	0.02	5.258×10^{-3}
	Fine	1,587,310	0.01	5.267×10^{-3}
$U_{\Delta t}$ **(Fine)**				0.022%
U_{Total}				0.057%

3.2. Effect of Heterogeneous Roughness on Ship Resistance

The Wigley hull CFD simulations were performed with various hull conditions at the speed range of $Fr = 0.2 - 0.4$, with the corresponding Reynolds numbers of $Re_L = 2.6 - 5.3 \times 10^6$. Figures 7–9 compare the total resistance coefficient, C_T, of the Wigley hull with the different hull roughness conditions obtained from the current CFD simulations and the Experimental Fluid Dynamics (EFD) results of Song et al. [27]. The C_T values were calculated by as

$$C_T = \frac{R_T}{\frac{1}{2}\rho S V^2} \tag{8}$$

where R_T is total resistance, ρ is the density of water, S is the wetted surface area, and V is the towing speed (i.e., inlet velocity). As can be seen in Figure 7, the current CFD result agrees well with the experimental data of Song et al. [27]. This confirms the validity of the modified wall-function approach as previously demonstrated by Song et al. [25].

Figures 8 and 9 show the C_T values of the Wigley hull with the heterogeneous hull roughness conditions (i.e., $\frac{1}{4}$-bow-rough, $\frac{1}{4}$-aft-rough, $\frac{1}{2}$-bow-rough and $\frac{1}{2}$-aft-rough). As observed from the physical towing tests of Song et al. [27], the current CFD simulations predicted larger C_T values for the bow-rough conditions ($\frac{1}{4}$-bow-rough and $\frac{1}{2}$-bow-rough) than the aft-rough conditions ($\frac{1}{4}$-aft-rough and $\frac{1}{2}$-aft-rough). The percentage differences between the CFD and EFD results can be found from Table A1 in Appendix A.

Figures 10 and 11 compare the frictional and residuary resistance coefficients, C_F and C_R, with the different hull conditions, respectively. The frictional and residuary resistance were calculated by simply decomposing the total drag into the shear and pressure components. The C_F and C_R were calculated as

$$C_F = \frac{R_F}{\frac{1}{2}\rho S V^2} \tag{9}$$

$$C_R = \frac{R_R}{\frac{1}{2}\rho S V^2} \tag{10}$$

where, R_F and R_R are the frictional (shear) and residuary (pressure) resistance, respectively.

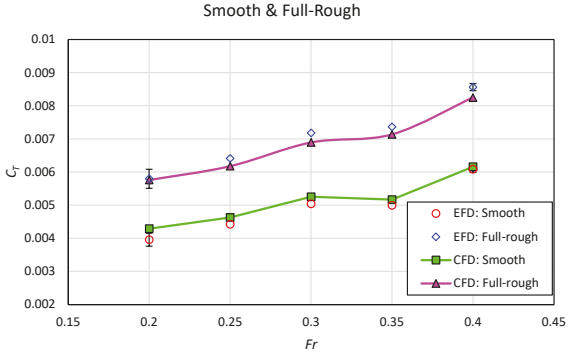

Figure 7. C_T of the Wigley hull with smooth and full-rough conditions obtained from the current Computational Fluid Dynamics (CFD) simulations and the Experimental Fluid Dynamics (EFD) result [27].

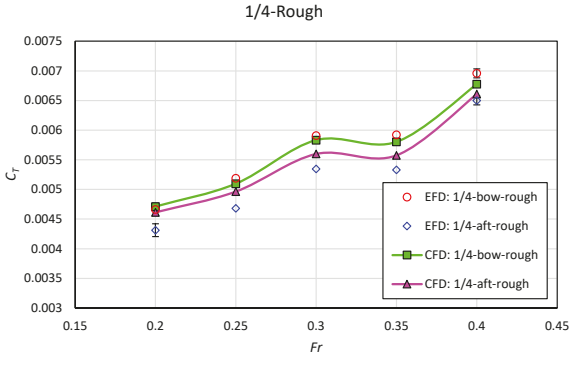

Figure 8. C_T of the Wigley hull with $\frac{1}{4}$-bow-rough and $\frac{1}{4}$-aft-rough conditions obtained from the current CFD simulations and the EFD result [27].

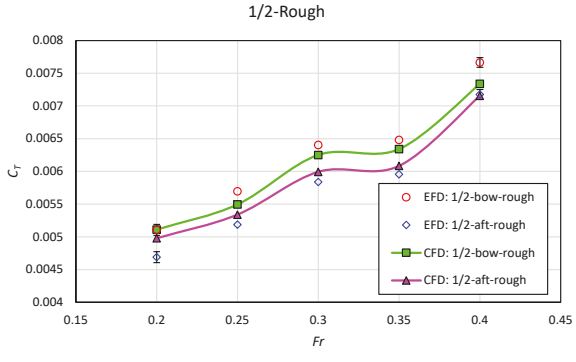

Figure 9. C_T of the Wigley hull with $\frac{1}{2}$-bow-rough and $\frac{1}{2}$-aft-rough conditions obtained from the current CFD simulations and the EFD result [27].

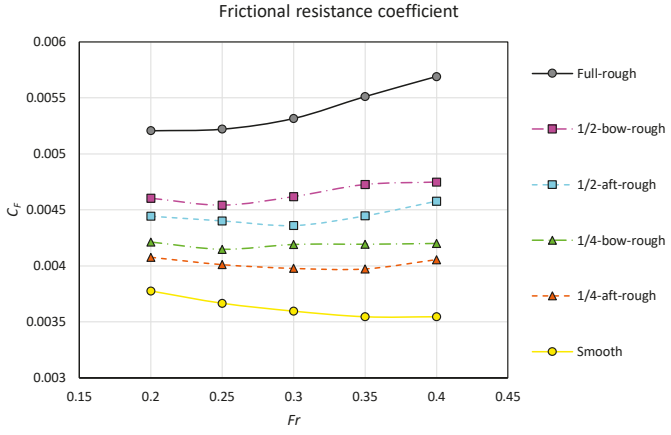

Figure 10. C_F of the Wigley hull with different hull conditions predicted from the current CFD simulations.

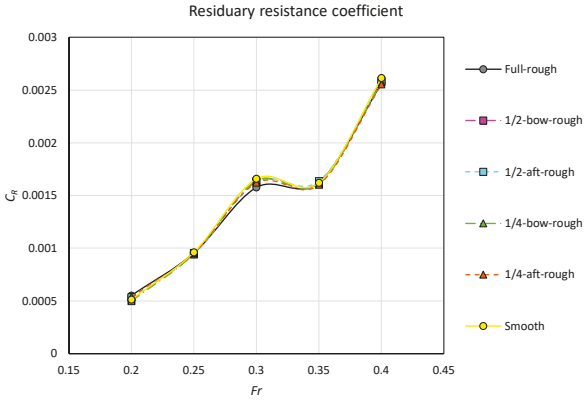

Figure 11. C_R of the Wigley hull with different hull conditions predicted from the current CFD simulations.

As shown in Figures 10 and 11, the effect of different hull conditions on the C_F values is apparent as expected, while the effect on the C_R value is negligible. As expected, in Figure 10, the C_F values of the smooth case show a descending trend while the C_F values of the full-rough case show an ascending trend, which implies that the flow of each case is within the hydraulically smooth and transitionally rough flow regimes, respectively.

The bow-rough conditions show larger C_F values than the aft-rough conditions with the same area of the rough surface. Accordingly, the differences in the added resistance between the bow-rough and aft-rough conditions can be mainly attributed to the different effects on the frictional resistance of the ship. Therefore, it is worthwhile to examine the effect of heterogeneous hull roughness on the distributions of the local skin friction on the hull.

Furthermore, in Figure 10, the C_F trends of the different hull conditions show different transition behaviours in terms of roughness flow regimes. In other words, the bow-rough cases show more developed flow features at the same speed range than the aft-rough cases. For example, the C_F values of the $\frac{1}{4}$-bow-rough case converge when $Fr > 0.3$ (i.e., the fully rough regime is reached), while those of the $\frac{1}{4}$-aft-rough case keep increasing (i.e., still within transitionally rough regime). For a similar reason, C_F values of the full-rough case

keep increasing, although its forepart is expected to reach the fully rough regime because its aft part is still within the transitionally rough regime. The locally different flow regimes on the hull can be further correlated with the roughness Reynolds number, k^+, on the hull.

3.3. Rationale behind the Effect of Heterogeneous Roughness

As discussed in the previous section, the effect of heterogeneous hull roughness on ship resistance is believed to be closely related to the distributions of the local skin friction and the roughness Reynolds number. Therefore, this section discusses and compares the local skin friction, and the roughness Reynolds numbers with different hull conditions.

Figure 12 compares the local skin friction, C_f, values on the Wigley hull with different hull conditions. The local skin friction was obtained by dividing the wall shear stress, τ_w, by the dynamic pressure, $\frac{1}{2}\rho V^2$, where ρ is water density and V is the towing speed (i.e., inlet velocity). As shown in Figure 12, significant increases in the local C_f due to the roughness effect were observed. In the case of the homogeneous conditions (smooth and full-rough), the highest local C_f values are observed in the first quarter of the hull. The heterogeneous hull conditions (Figure 12b–e) showed blended C_f distributions, where the smooth surfaces show similar C_f distributions as the smooth condition, while the rough surfaces show those similar to the full-rough condition. For example, the first quartile of the $\frac{1}{4}$-bow-rough case (Figure 12b) has a similar C_f distribution as that of the full-rough case, while the rest of the hull has a similar C_f distribution as that of the smooth case. As the full-rough condition has higher values in the bow region, the increase in the C_f values of the bow-rough cases (Figure 12b,d) are more apparent compared to the aft-rough cases.

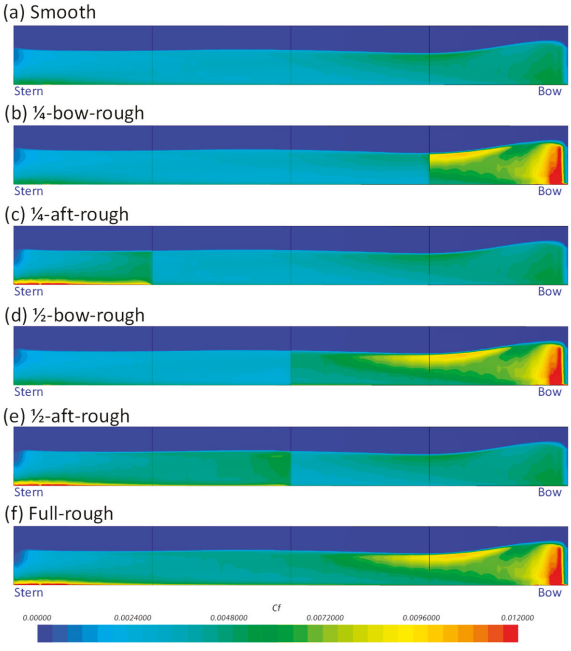

Figure 12. C_f distribution on the Wigley hull with different hull conditions, $Fr = 0.3$.

Figure 13 clearly shows the increase in the C_f values due to the presented hull roughness (i.e., $\Delta C_f = C_{f,\,\text{rough}} - C_{f,\,\text{smooth}}$). The full-rough case shows greater ΔC_f in the bow region, and thus the bow-rough conditions show larger ΔC_f values compared to the aft-rough conditions. The locally different ΔC_f values suggest different roughness effects in the different regions, and it can be best attributed to the different roughness Reynolds numbers, k^+, in the local regions.

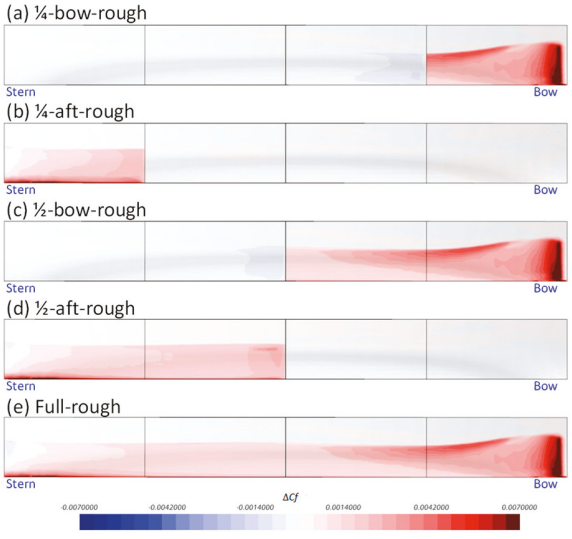

Figure 13. Increase in the C_f on the Wigley hull ($\Delta C_f = C_{f,\,\text{rough}} - C_{f,\,\text{smooth}}$), $Fr = 0.3$.

Figure 14 shows the distributions of the roughness Reynolds number, k^+, on the Wigley hull with different hull roughness conditions. As expected, the full-rough case shows larger k^+ values in the bow region due to higher local skin friction (i.e., $k^+ = k\tau_w/\nu$). For a similar reason, the bow-rough cases show larger k^+ values compared to the aft-rough cases, and these differences result in different ΔC_f values. This observation supports the hypothesis of Song et al. [27].

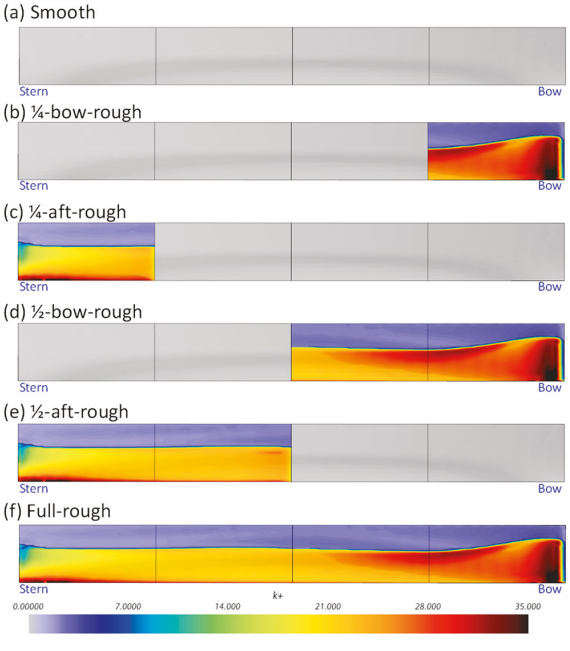

Figure 14. k^+ distribution on the Wigley hull with different hull conditions, $Fr = 0.3$.

The observations in Figures 12–14, with regards to C_f and k^+, are in correspondence with the effect of different heterogeneous hull roughness on ship resistance shown in Figures 7–10. In other words, it can be seen that the greater increases in the C_f and k^+ of the bow-rough cases resulted in the greater added resistances compared to the aft-rough cases as shown in Figures 7–10.

Furthermore, the k^+ values in Figure 14 can be also correlated with the different trends of the C_F with different hull conditions in Figure 10. As shown in Equation (6), when k^+ value is higher than 25, it is considered that the fully rough flow regime is reached. Therefore, for example, it can be seen that the fully rough flow regime is reached for most of the rough wetted surface of the $\frac{1}{4}$-bow-rough condition (Figure 10), while the transitionally rough flow regime is expected for most of the wetted surface of the $\frac{1}{4}$-aft-rough condition (Figure 10).

Figure 15 shows the boundary layers represented by the axial velocity contours limited to V_x/V_{ship} = 0.9. When it comes to the homogeneous hull conditions, the results were as expected. The full-rough case (Figure 15b) shows a thicker boundary layer compared to the smooth case (Figure 15a) and the difference becomes more apparent along with the flow, as similarly observed from previous studies, e.g., [17,18,25]. On the other hand, differences were observed with the heterogeneous hull conditions. As shown in Figures 14f and 15d, the boundary layer thicknesses around the forward part of the aft-rough conditions (where the surface is smooth) showed almost no differences compared to that of the smooth case (Figure 15a). In contrast, the bow-rough conditions (Figure 15c,e) showed increases in the boundary layer thickness not only around the forward parts (where the surface is rough) but also around the aft parts (where the surface is smooth), compared to the smooth case (Figure 15a). Interestingly, the bow-rough conditions showed thicker boundary layers on the aft parts compared to the aft-rough conditions. For example, the $\frac{1}{2}$-bow-rough condition (Figure 15e) shows a thicker boundary layer than the $\frac{1}{2}$-aft-rough condition (Figure 15f) even around the aft part.

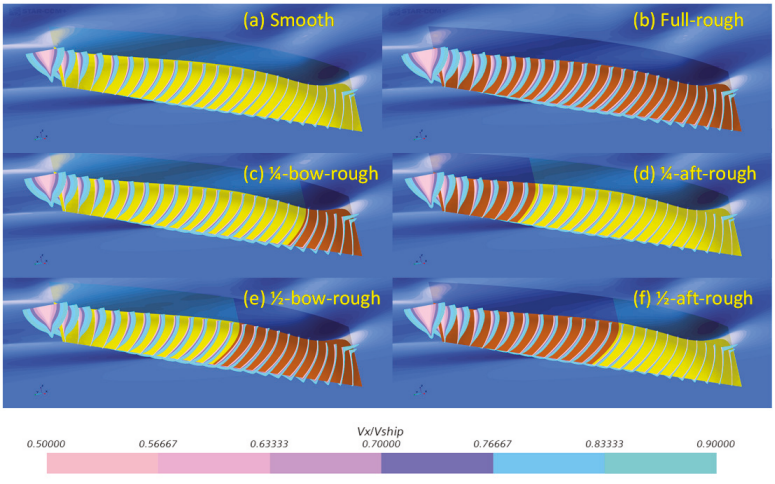

Figure 15. Boundary layer represented by slices limited to axial velocity ($V_x/V_{ship} = 0.9$), $Fr = 0.3$.

4. Concluding Remarks

A numerical investigation was completed on the effect of heterogeneous hull roughness on ship resistance. A URANS-based CFD model was developed to investigate the effect of heterogeneous hull roughness using the modified wall-function approach. The predicted total resistance coefficients with different hull conditions were compared with the experiment of Song et al. [27] and showed a good agreement. As similarly observed

by Song et al. [27], the bow-rough conditions showed larger added resistance compared to the aft-rough conditions with the same wetted surface area of the roughness region, confirming that the hull roughness of the fore part of the ship has a greater impact on the results than the hull roughness in other regions.

The observations on the effects of heterogeneous hull roughness were correlated with the distributions of the local wall shear stress and the roughness Reynolds number. The results showed that the local differences in the wall shear stress result in different roughness Reynolds numbers and thus different roughness effects depending on the locations of the hull roughness. Therefore, the hypothesis of Song et al. [27] was confirmed in this study.

This study provides a numerical investigation into the effect of heterogeneous hull roughness using the modified wall-function approach. The results can be useful from an industrial point of view, since they give insight into different priorities of partial hull cleaning depending on the impact of the roughness in different hull regions.

The investigation was carried out in model-scale using idealised surface conditions. However, the same methodology can be extended to incorporate real hull conditions of ships where heterogeneous biofouling accumulations are present. Furthermore, the numerical approach presented in this study can also be adopted for predicting the effect of heterogeneous roughness on propellers.

Author Contributions: Conceptualisation, S.S. and Y.K.D. methodology, S.S. and Y.K.D.; software, S.S.; validation, S.S.; formal analysis, S.S. and Y.K.D.; investigation, S.S. and Y.K.D.; resources, C.D.M.M.-F. and A.I.; data curation, S.S.; writing—original draft preparation, S.S.; writing—review and editing, S.S., Y.K.D., C.D.M.M.-F., T.S., D.V., T.T., A.I.; visualisation, S.S.; supervision, Y.K.D., C.D.M.M.-F., T.S., D.V., T.T. and A.I.; project administration, C.D.M.M.-F.; funding acquisition, C.D.M.M.-F. All authors have read and agreed to the published version of the manuscript.

Funding: The authors gratefully acknowledge that the research presented in this paper was carried out as part of the EU funded H2020 project, VENTuRE (grant no. 856887).

Institutional Review Board Statement: Not applicable.

Informed Consent Statement: Not applicable.

Acknowledgments: Results were obtained using ARCHIE-WeSt High Performance Computer (www.archie-west.ac.uk).

Conflicts of Interest: The authors declare no conflict of interest.

Appendix A

Table A1. Percentage differences between the current CFD simulations and the EFD result [27].

	Smooth			1/4-bow-rough			1/4-aft-rough		
Fr	CFD	EFD	%D	CFD	EFD	%D	CFD	EFD	%D
0.2	4.29×10^{-3}	3.95×10^{-3}	−8.0%	4.71×10^{-3}	4.66×10^{-3}	−1.1%	4.61×10^{-3}	4.31×10^{-3}	−6.5%
0.25	4.63×10^{-3}	4.38×10^{-3}	−5.3%	5.09×10^{-3}	5.19×10^{-3}	1.8%	4.96×10^{-3}	4.68×10^{-3}	−5.7%
0.3	5.25×10^{-3}	5.03×10^{-3}	−4.3%	5.83×10^{-3}	5.91×10^{-3}	1.3%	5.60×10^{-3}	5.35×10^{-3}	−4.5%
0.35	5.17×10^{-3}	4.95×10^{-3}	−4.2%	5.80×10^{-3}	5.92×10^{-3}	2.0%	5.58×10^{-3}	5.33×10^{-3}	−4.4%
0.4	6.16×10^{-3}	6.08×10^{-3}	−1.4%	6.77×10^{-3}	6.96×10^{-3}	2.7%	6.61×10^{-3}	6.50×10^{-3}	−1.7%
	1/2-bow-rough			1/2-aft-rough			Full-rough		
Fr	CFD	EFD	%D	CFD	EFD	%D	CFD	EFD	%D
0.2	5.11×10^{-3}	5.11×10^{-3}	−0.1%	4.98×10^{-3}	4.69×10^{-3}	−5.8%	5.76×10^{-3}	5.81×10^{-3}	0.9%
0.25	5.50×10^{-3}	5.70×10^{-3}	3.6%	5.34×10^{-3}	5.19×10^{-3}	−2.8%	6.18×10^{-3}	6.40×10^{-3}	3.6%
0.3	6.25×10^{-3}	6.40×10^{-3}	2.4%	5.99×10^{-3}	5.84×10^{-3}	−2.6%	6.89×10^{-3}	7.20×10^{-3}	4.5%
0.35	6.34×10^{-3}	6.48×10^{-3}	2.2%	6.08×10^{-3}	5.96×10^{-3}	−2.1%	7.13×10^{-3}	7.38×10^{-3}	3.4%
0.4	7.34×10^{-3}	7.66×10^{-3}	4.4%	7.15×10^{-3}	7.18×10^{-3}	0.3%	8.25×10^{-3}	8.58×10^{-3}	4.0%

References

1. Townsin, R.L. The ship hull fouling penalty. *Biofouling* **2003**, *19*, 9–15. [CrossRef]
2. Tezdogan, T.; Demirel, Y.K. An overview of marine corrosion protection with a focus on cathodic protection and coatings. *Brodogradnja* **2014**, *65*, 49–59.
3. Granville, P.S. The frictional resistance and turbulent boundary layer of rough surfaces. *J. Ship Res.* **1958**, *2*, 52–74. [CrossRef]
4. Granville, P.S. *Similarity-Law Characterization Methods for Arbitrary Hydrodynamic Roughnesses*; Bethesda: Rockville, MD, USA, 1978.
5. Schultz, M.P. The relationship between frictional resistance and roughness for surfaces smoothed by sanding. *J. Fluids Eng.* **2002**, *124*, 492–499. [CrossRef]
6. Schultz, M.P. Frictional resistance of antifouling coating systems. *J. Fluids Eng.* **2004**, *126*, 1039–1047. [CrossRef]
7. Schultz, M.P.; Flack, K.A. The rough-wall turbulent boundary layer from the hydraulically smooth to the fully rough regime. *J. Fluid Mech.* **2007**, *580*, 381–405. [CrossRef]
8. Flack, K.A.; Schultz, M.P. Review of hydraulic roughness scales in the fully rough regime. *J. Fluids Eng.* **2010**, *132*, 041203. [CrossRef]
9. Schultz, M.P.; Bendick, J.A.; Holm, E.R.; Hertel, W.H. Economic impact of biofouling on a naval surface ship. *Biofouling* **2011**, *27*, 87–98. [CrossRef]
10. Oliveira, D.; Larsson, A.I.; Granhag, L. Effect of ship hull form on the resistance penalty from biofouling. *Biofouling* **2018**, *34*, 262–272. [CrossRef]
11. Atlar, M.; Yeginbayeva, I.A.; Turkmen, S.; Demirel, Y.K.; Carchen, A.; Marino, A.; Williams, D. A rational approach to predicting the effect of fouling control systems on "in-service" ship performance. *GMO J. Ship Mar. Technol.* **2018**, *24*, 5–36.
12. Cella, U.; Cucinotta, F.; Sfravara, F. Sail plan parametric CAD model for an A-class catamaran numerical optimization procedure using open source tools. In Proceedings of the 16th Asian Congress of Fluid Mechanics, Bangalore, India, 13–17 December 2019; pp. 547–554.
13. Cirello, A.; Cucinotta, F.; Ingrassia, T.; Nigrelli, V.; Sfravara, F. Fluid–structure interaction of downwind sails: A new computational method. *J. Mar. Sci. Technol.* **2019**, *24*, 86–97. [CrossRef]
14. Stern, F.; Wang, Z.; Yang, J.; Sadat-Hosseini, H.; Mousaviraad, M.; Bhushan, S.; Diez, M.; Sung-Hwan, Y.; Wu, P.-C.; Yeon, S.M.; et al. Recent progress in CFD for naval architecture and ocean engineering. *J. Hydrodyn.* **2015**, *27*, 1–23. [CrossRef]
15. Wang, J.; Wan, D. Application progress of computational fluid dynamic techniques for complex viscous flows in ship and ocean engineering. *J. Mar. Sci. Appl.* **2020**, *19*, 1–16. [CrossRef]
16. Demirel, Y.K.; Turan, O.; Incecik, A. Predicting the effect of biofouling on ship resistance using CFD. *Appl. Ocean Res.* **2017**, *62*, 100–118. [CrossRef]
17. Song, S.; Demirel, Y.K.; Atlar, M. An investigation into the effect of biofouling on the ship hydrodynamic characteristics using CFD. *Ocean Eng.* **2019**, *175*, 122–137. [CrossRef]
18. Song, S.; Demirel, Y.K.; Muscat-Fenech, C.D.M.; Tezdogan, T.; Atlar, M. Fouling effect on the resistance of different ship types. *Ocean Eng.* **2020**, *216*, 107736. [CrossRef]
19. Song, S.; Demirel, Y.K.; Atlar, M. Propeller performance penalty of biofouling: Computational fluid dynamics prediction. *J. Offshore Mech. Arct. Eng.* **2020**, *142*, 1–22. [CrossRef]
20. Farkas, A.; Degiuli, N.; Martić, I. The impact of biofouling on the propeller performance. *Ocean Eng.* **2021**, *219*, 108376. [CrossRef]
21. Song, S.; Demirel, Y.K.; Atlar, M. Penalty of hull and propeller fouling on ship self-propulsion performance. *Appl. Ocean Res.* **2020**, *94*, 102006. [CrossRef]
22. Farkas, A.; Song, S.; Degiuli, N.; Martić, I.; Demirel, Y.K. Impact of biofilm on the ship propulsion characteristics and the speed reduction. *Ocean Eng.* **2020**, *199*, 107033. [CrossRef]
23. Song, S.; Demirel, Y.K.; Atlar, M.; Shi, W. Prediction of the fouling penalty on the tidal turbine performance and development of its mitigation measures. *Appl. Energy* **2020**, *276*, 115498. [CrossRef]
24. Song, S.; Dai, S.; Demirel, Y.K.; Atlar, M.; Day, S.; Turan, O. Experimental and theoretical study of the effect of hull roughness on ship resistance. *J. Ship Res.* **2020**, 1–10. [CrossRef]
25. Song, S.; Demirel, Y.K.; Atlar, M.; Dai, S.; Day, S.; Turan, O. Validation of the CFD approach for modelling roughness effect on ship resistance. *Ocean Eng.* **2020**, *200*, 107029. [CrossRef]
26. Demirel, Y.K.; Uzun, D.; Zhang, Y.; Fang, H.-C.; Day, A.H.; Turan, O. Effect of barnacle fouling on ship resistance and powering. *Biofouling* **2017**, *33*, 819–834. [CrossRef]
27. Song, S.; Ravenna, R.; Dai, S.; De Marco Muscat-Fenech, C.; Tani, G.; Demirel, Y.K.; Atlar, M.; Day, S.; Incecik, A. Ex-perimental investigation on the effect of heterogeneous hull roughness on ship resistance. *Ocean Eng.* **2021**, in press. [CrossRef]
28. Östman, A.; Koushan, K.; Savio, L. Study on additional ship resistance due to roughness using CFD. In Proceedings of the 4th Hull Performance & Insight Conference (HullPIC'19), Gubbio, Italy, 6–8 May 2019.
29. Vargas, A.; Shan, H.; Holm, E. Using CFD to predict ship resistance due to biofouling, and plan hull maintenance. In Proceedings of the 4th Hull Performance & Insight Conference (HullPIC'19), Gubbio, Italy, 6–8 May 2019.
30. Menter, F.R. Two-equation eddy-viscosity turbulence models for engineering applications. *AIAA J.* **1994**, *32*, 1598–1605. [CrossRef]
31. Dogrul, A.; Song, S.; Demirel, Y.K. Scale effect on ship resistance components and form factor. *Ocean Eng.* **2020**, *209*, 107428. [CrossRef]
32. Siemens. *STAR-CCM+, User Guide*, Version 13.06.
33. Celik, I.B.; Ghia, U.; Roache, P.J.; Freitas, C.J.; Coleman, H.; Raad, P.E. Procedure for estimation and reporting of uncertainty due to discretization in CFD applications. *J. Fluids Eng.* **2008**, *130*, 078001. [CrossRef]

MDPI
St. Alban-Anlage 66
4052 Basel
Switzerland
Tel. +41 61 683 77 34
Fax +41 61 302 89 18
www.mdpi.com

Journal of Marine Science and Engineering Editorial Office
E-mail: jmse@mdpi.com
www.mdpi.com/journal/jmse

MDPI
St. Alban-Anlage 66
4052 Basel
Switzerland

Tel: +41 61 683 77 34
Fax: +41 61 302 89 18

www.mdpi.com

ISBN 978-3-0365-2336-1